MATERIALS RESEARCH SOCIETY
SYMPOSIUM PROCEEDINGS VOLUME 442

Defects in Electronic Materials II

Symposium held December 2-6, 1996, Boston, Massachusetts, U.S.A.

EDITORS:

Jürgen Michel
Massachusetts Institute of Technology
Cambridge, Massachusetts, U.S.A.

Thomas Kennedy
Naval Research Laboratory
Washington, D.C., U.S.A.

Kazumi Wada
NTT LSI Laboratories
Kanagawa, Japan

Klaus Thonke
Universität Ulm
Ulm, Germany

19970819 071

MRS
MATERIALS RESEARCH SOCIETY

PITTSBURGH, PENNSYLVANIA

DTIC QUALITY INSPECTED 4

DISTRIBUTION STATEMENT A
Approved for public release;
Distribution Unlimited

This work was supported in part by the Office of Naval Research under Grant Number ONR: N00014-97-1-0035. The United States Government has a royalty-free license throughout the world in all copyrightable material contained herein.

Single article reprints from this publication are available through University Microfilms Inc., 300 North Zeeb Road, Ann Arbor, Michigan 48106

CODEN: MRSPDH

Copyright 1997 by Materials Research Society.
All rights reserved.

This book has been registered with Copyright Clearance Center, Inc. For further information, please contact the Copyright Clearance Center, Salem, Massachusetts.

Published by:

Materials Research Society
9800 McKnight Road
Pittsburgh, Pennsylvania 15237
Telephone (412) 367-3003
Fax (412) 367-4373
Website: http://www.mrs.org/

Library of Congress Cataloging in Publication Data

Defects in electronic materials II : symposium held December 2–6, 1996, Boston, Massachusetts, U.S.A. / editors, Jürgen Michel, Thomas Kennedy, Kazumi Wada, Klaus Thonke
p. cm—(Materials Research Society symposium proceedings ; v. 442)
Includes bibliographical references and index.
ISBN 1-55899-346-0
1. Electronics—Defects—Congresses. 2. Semiconductors—Defects—Congresses. I. Michel, Jürgen II. Kennedy, Thomas III. Wada, Kazumi IV. Thonke, Klaus V. Series: Materials Research Society symposium proceedings ; v. 442.
TK7871.D4 1997 97-6020
621.3815'2—dc21 CIP

Manufactured in the United States of America

CONTENTS

Preface xv

Acknowledgments xvii

Materials Research Society Symposium Proceedings xviii

PART I: NEW TECHNIQUES IN DEFECT STUDIES

*Radioactive Isotopes in Photoluminescence Experiments: Identification of Defect Levels 3
R. Magerle

*True Atomic Resolution Imaging on Semiconductor Surfaces with Noncontact Atomic Force Microscopy 15
Y. Sugawara, H. Ueyama, T. Uchihashi, M. Ohta, Y. Yanase, T. Shigematsu, M. Suzuki, and S. Morita

Optical NMR from Single Quantum Dots 25
S.W. Brown, T.A. Kennedy, and D. Gammon

Low-Temperature Infrared Absorption Measurement for Oxygen Concentration and Precipitates in Heavily-Doped Silicon Wafers 31
M. Koizuka, M. Inaba, and H. Yamada-Kaneta

A New Measurement Method of Microdefects Near the Surface of Si Wafers; Optical Shallow Defect Analyzer (OSDA) 37
Kazuo Takeda, Hidetsugu Ishida, and Atsushi Hiraiwa

Inspection of Recombination Active Defects for SiGe and Solar Cells 43
O.V. Astafiev, V.P. Kalinushkin, and N.V. Abrosimov

PART II: PROCESSING INDUCED DEFECTS: PLASMA-INDUCED POINT DEFECTS

*Electrical Characterization of Defects Introduced During Plasma-Based Processing of GaAs 51
F.D. Auret, G. Myburg, W.E. Meyer, P.N.K. Deenapanray, H. Nordhoff, M. Murtagh, Shu-Ren Ye, H.J. Masterson, J.T. Beechinor, and G.M. Crean

Damage Induced by a Low-Biased 92-MHz Anode-Coupled Reactive Ion Etcher Using Chlorine-Nitrogen Mixed Plasmas 63
Tadashi Saitoh, Hideki Gotoh, Tetsuomi Sogawa, and Hiroshi Kanbe

*Invited Paper

Donor Reactivation in Plasma-Irradiated GaAs Under Laser Illumination 69
K. Wada and H. Nakanishi

Optical and Electrical Characterization Study of $SiCl_4$ Reactive-Io-Etched GaAs 75
M. Murtagh, Shu-Ren Ye, H.J. Masterson, J.T. Beechinor, G.M. Crean, F.D. Auret, P.N.K. Deenapanray, W.E. Meyer, S.A. Goodman, and G. Myburg

Field Drift of Plasma-Induced Defects in Phosphorous-Doped Si by Reverse Bias Annealing (RBA) 81
J. Takeuchi, Y. Zaitsu, T. Shimizu, S. Matsumoto, and K. Wada

Electronic Properties of Defects Formed in n-Si During Sputter-Etching in an Ar Plasma 87
P.N.K. Deenapanray, F.D. Auret, C. Schutte, G. Myburg, W.E. Meyer, J.B. Malherbe, and M.C. Ridgway

PART III: PROCESSING INDUCED DEFECTS: DEFECTS AND GATE OXIDE INTEGRITY

***Octahedral Void Defects Causing Gate Oxide Defects in MOSLSIs** 95
Manabu Itsumi

Structure of the Defects Responsible for B-Mode Breakdown of Gate Oxide Grown on the Surface of Silicon Wafers 107
T. Mera, J. Jablonski, M. Danbata, K. Nagai, and M. Watanabe

Characterization of Grown-in Defects in CZ-Si Crystals by Bright Field IR Laser Interferometer 113
Katsuhiko Nakai, Masami Hasebe, Toshio Iwasaki, and Yasuo Tsumori

TEM Observation of Grown-in Defects in CZ-Si Crystals and Their Secco Etching Properties 119
Masahiro Kato, Hiroshi Takeno, and Yutaka Kitagawara

Crystallographic Analysis of Flow Pattern Defects in Dislocated Czochralski Silicon Crystals 125
Y. Ikematsu, T. Iwasaki, H. Harada, K. Tanaka, M. Fujinami, and M. Hasebe

Behavior of Point Defects in CZ Silicon Crystal Growth - Formation of Polyhedral Cavities and Oxidation-Induced Stacking Fault Nuclei 131
K. Tanahashi, N. Inoue, and Y. Mizokawa

*Invited Paper

Impact of Chemical and Epitaxial Treatment on Surface Defects on Silicon Wafers 137
R. Schmolke, D. Gräf, M. Suhren, R. Kirchner, H. Piontek, and P. Wagner

Positron Beam Technique for the Study of Defects at the Si/SiO_2 Interface of a Polysilicon Gated MOS System 143
M. Clement, J.M.M. de Nijs, H. Schut, A. van Veen, R. Mallee, and P. Balk

PART IV: PROCESSING INDUCED DEFECTS: POINT DEFECTS AND REACTION

An Investigation of Vacancy Population During Arsenic Activation in Silicon 151
O. Dokumaci, H-J. Gossmann, K.S. Jones, and M.E. Law

Enhanced Dissolution of Extrinsic Dislocation Loops in Silicon Annealed in NH_3 157
S.B. Herner, V. Krishnamoorthy, K.S. Jones, T.K. Mogi, and H-J. Gossmann

Depth Profile of Point Defects in Ion Implanted n^+p and p^+n Junctions Formed by 450°C Post-Implantation Annealing and Impact of Defects on Junction Characteristics 163
Mauricio Massazumi Oka, Akira Nakada, Yukio Tamai, Kei Kanemoto, Tadashi Shibata, and Tadahiro Ohmi

Gettering of Fe by Aluminum in p-Type Cz Silicon 169
S.H. Ahn, S. Zhao, A.L. Smith, L.L. Chalfoun, M. Platero, H. Nakashima, and L.C. Kimerling

Effects of Gettering on Device Characteristics 175
Mitsuhiro Horikawa, Akihiko Yaoita, Tsuyoshi Nagata, and Tomohisa Kitano

Comparison of Gettering Ability Between I/I Defects and Si Substrate 181
Mitsuhiro Horikawa and Tomohisa Kitano

Dark Current Spectroscopy of Metals in Silicon 187
William C. McColgin, James P. Lavine, and Charles V. Stancampiano

Influence of Si Substrate Crystallinity on Device Performance 193
T. Iwamoto, J. Takano, K. Makihara, and T. Ohmi

Investigation on Subsurface Damage in Silicon Wafers 199
Xin Zhang, Tong-Yi Zhang, Yitshak Zohar, and Sanboh Lee

Shallow Donor Formation in Hydrogen-Implanted Silicon 205
Yutaka Tokuda, Hiroyuki Iwata, and Akira Ito

PART V: POINT DEFECTS AND INTERACTIONS IN Si

*Cooperative Chemical Rebonding in the Segregation of Impurities in Silicon Grain Boundaries 213
A. Maiti, M.F. Chisholm, S.J. Pennycook, and S.T. Pantelides

Mechanism of Defect Reactions in Semiconductors 225
Yuzo Shinozuka

Interstitial Defect Reactions in Silicon 231
S. Zhao, A.M. Agarwal, J.L. Benton, G.H. Gilmer, and L.C. Kimerling

Formation of Er-Related Donor Centers During Postimplantation Annealing of Si:Er 237
N.A. Sobolev, O.V. Aleksandrov, and E.I. Shek

Shallow Donor Centers in Erbium-Implanted Silicon Subjected to High-Temperature Annealing 243
V.V. Emtsev, D.S. Poloskin, N.A. Sobolev, and E.I. Shek

Defects in Erbium/Oxygen Implanted Silicon 249
X. Duan, J. Palm, B. Zheng, M. Morse, J. Michel, and L.C. Kimerling

Cubo-Octahedral B_{12} Clusters in Silicon Crystal 255
M. Okamoto, K. Hashimoto, and K. Takayanagi

Interactions of Structural Defects with Metallic Impurities in Multicrystalline Silicon 261
S.A. McHugo, H. Hieslmair, E.R. Weber, M.D. Rosenblum, and J.P. Kalejs

PART VI: IMPURITY DIFFUSION AND HYDROGEN IN Si

Formation of Hydrogen Molecules in Crystalline Silicon Treated with Atomic Hydrogen 269
K. Murakami, N. Fukata, S. Sasaki, K. Ishioka, K.G. Nakamura, M. Kitajima, S. Fujimura, J. Kikuchi, and H. Haneda

Vibrational Spectroscopy of Gold Hydrogen Complexes in Silicon 275
M.J. Evans, M.G. Gornstein, and Michael Stavola

Effects of H^+-Implantation on Electron Traps in n-Type Si Induced by P^+ Preimplantation 281
Akira Ito, Hiroyuki Iwata, and Yutaka Tokuda

Evaluation of Proton-Induced Deep Levels in n-Si 287
K. Kono, N. Kishimoto, H. Amekura, and T. Saito

EPR Study of Defect Formation in H Implanted and Annealed CZ Si 293
B. Pivac, B. Rakvin, F. Corni, R. Tonini, and G. Ottaviani

*Invited Paper

Activation Energies of Interstitial Oxygen Diffusion in Silicon Containing Hydrogen 299
W. Wijaranakula

Effect of Pressure on Boron Diffusion in Silicon 305
Yuechao Zhao, Michael J. Aziz, Salman Mitha, and David Schiferl

PART VII: DISLOCATIONS IN GROUP IV SEMICONDUCTORS

*Dislocation Interactions and Their Impact on Electrical Properties of GeSi-Based Heterostructures 313
S.A. Ringel and P.N. Grillot

Dislocation-Related Photoluminescence in Strain-Relaxed $Si_{1-x}Ge_x$ Buffer Layer Structures 325
Kai Shum, P.M. Mooney, and J.O. Chu

Room Temperature Electroluminescence from D1 Dislocation Centers in Silicon 331
Einar Ö. Sveinbjörnsson and Jörg Weber

Dislocation Velocities in GeSi Bulk Alloys 337
I. Yonenaga

Influence of Substrate Off-Cut on the Defect Structure in Relaxed Graded Si-Ge/Si Layers 343
Srikanth B. Samavedam, F. Romanato, M.S. Goorsky, and E.A. Fitzgerald

HRTEM Study of Dislocations in GeSi/Si Heterostructures Grown by VPE 349
Junwu Liang and Xueyuan Wan

PART VIII: POINT DEFECTS AND DEFECT INTERACTIONS IN SiGe

*Defects in Low-Temperature MBE-Grown Si and SiGe/Si Structures 355
W.M. Chen, I.A. Buyanova, and B. Monemar

The Effect of Ion-Implantation-Induced Defects on Strain Relaxation in Ge_xSi_{1-x}/Si Heterostructures 367
J.M. Glasko, J. Zou, D.J.H. Cockayne, J. Fitz Gerald, P. Kringhøj, and R.G. Elliman

Effect of Stresses on Defect Nucleation in $Si_{1-x}Ge_x/Si$ Heteroepitaxial Systems 373
Cengiz S. Ozkan, William D. Nix, and Huajian Gao

Hall Effect Measurements on Si_xGe_{1-x} Bulk Alloys 381
T. Mchedlidze and I. Yonenaga

*Invited Paper

PART IX: POINT DEFECTS IN III-V COMPOUNDS

*Growth-Induced Alignment of the First Neighbor Shell of C_{As} in $Al_xGa_{1-x}As$ 387
J-F. Zheng, Michael Stavola, C.R. Abernathy, and S.J. Pearton

Residual Impurities and Transport Properties of High Purity MOVPE GaAs 399
G. Steude, D.M. Hofmann, M. Drechsler, B.K. Meyer, H. Hardtdegen, and M. Hollfelder

An Anomalous Deep Center (E_C-0.31 eV) in Semi-Insulating GaAs 405
Z-Q. Fang and D.C. Look

EL2-Induced Upconversion Luminescence in GaAs 411
V. Alex, T. Iino, and J. Weber

Relationship Between Hydrogen-Related Metastable Defect and EL2 Level in GaAs Crystals 417
Tatsuyuki Shinagawa and Tsugunori Okumura

Nonradiative Investigation of Hole Photoionization Spectrum of EL2 in Semi-Insulating GaAs 423
T. Ikari, A. Fukuyama, Y. Morooka, K. Yoshino, K. Maeda, and Y. Akashi

Influence of the Temperature and the Light Intensity on the Metastable Transformation of EL2 429
A. Alvarez, J. Jimenez, M.A. Gonzalez, and M. Chafai

Diffusion Process of Interstitial Atoms in InP Studied by Transmission Electron Microscopy 435
Y. Ohno, S. Takeda, and M. Hirata

Properties of InP Simultaneously Doped with Zinc and Sulfur Grown by MOCVD 441
C.M. Alavanja, C.J. Pinzone, S.K. Sputz, and M. Geva

Characterization of Hydrogen-Related Defects in Iron-Doped Indium Phosphide 447
W.B. Leigh, D. Bliss, G. Bryant, G. Iseler, J. Larkin, and J. Wolk

Evidence for Noncorrelation Between the 0.15 eV and 0.44 eV Cu-Related Acceptor Levels in GaAs 453
K. Leosson and H.P. Gislason

Effect of the Carbon Acceptor Concentration on the Photoquenching and Enhancement of the Piezoelectric Photoacoustic Signals of Semi-Insulating GaAs 459
A. Fukuyama, Y. Morooka, Y. Akashi, K. Yoshino, K. Maeda, and T. Ikari

*Invited Paper

Long-Living Shallow Donor Excited States and FIR-IR Upconversion in GaP:Te 465
S.D. Ganichev, I.N. Yassievich, W. Raab, E. Zepezauer, and W. Prettl

PART X: COMPENSATION AND STRUCTURAL DEFECTS IN III-V COMPOUNDS

A Refined Model for Threading Dislocation Filtering in $In_xGa_{1-x}As$/GaAs Epitaxial Layers 473
G. MacPherson and P.J. Goodhew

Structural and Optical Characterization of $Al_xGa_{1-x}As$ Grown at Low Temperatures by Organometallic Vapor-Phase Epitaxy 479
A. Wankerl, D.T. Emerson, M.J. Cook, and J.R. Shealy

Electrical and Structural Properties of LT-GaAs: Influence of As/Ga Flux Ratio and Growth Temperature 485
M. Luysberg, H. Sohn, A. Prasad, P. Specht, H. Fujioka, R. Klockenbrink, and E.R. Weber

Influence of Donor, Acceptor, and Isovalent Impurity Doping on Arsenic Excess and Point Defects in Low-Temperature Grown GaAs 491
V.V. Chaldyshev, A.E. Kunitsyn, N.N. Faleev, V.V. Preobrazhenskii, M.A. Putyato, B.R. Semyagin, and V.V. Tretyakov

High-Temperature Reorientation of Distortions in the Excited State of the $V_{Ga}Te_{As}$ Complexes in n-Type GaAs 497
A.A. Gutkin, M.A. Reshchikov, and V.E. Sedov

Characterization of APB's in GaP 503
Dov Cohen and C. Barry Carter

PART XI: DEFECTS IN III-V LAYERS AND STRUCTURES

Electrically Detected Magnetic Resonance on GaAs/AlGaAs Heterostructures 511
T. Wimbauer, D.M. Hofmann, B.K. Meyer, M.S. Brandt, T. Brandl, M.W. Bayerl, N.M. Reinacher, M. Stutzmann, Y. Mochizuki, and M. Mizuta

Behavior of Fluorine in N-AlInAs Layers Under Bias-Temperature Stresses 517
Y. Yamamoto, N. Hayafuji, K. Sato, and M. Otsubo

S-Doped GaInAs Grown by Chemical Beam Epitaxy: Electrical and Structural Characterization 523
E.C. Paloura, G. Petkos, P.J. Goodhew, B. Theys, and J. Chevallier

First-Principles Calculations of Diffusion of Chlorine Atoms in GaAs 529
Takahisa Ohno, Taizo Sasaki, and Akihito Taguchi

Low-Temperature Photoluminescence Properties of *In Situ* Zn-Doped InP Layers Grown by LP-MOCVD 535
Y.B. Moon, S.K. Si, E. Yoon, and S.J. Kim

The Differences Between the $In_yGa_{1-y}As/GaAs$ Interface and $GaAs/In_yGa_{1-y}As$ Interface in Superlattice over a $In_xGa_{1-x}As(x<y)$ Buffer Layer 541
X.J. Wang, L.X. Zheng, Z.B. Xiao, Z.P. Zhang, X.W. Hu, and Q.M. Wang

Defect Characterization of InAs Wafers Using Positron Lifetime Spectroscopy 547
J. Mahony and P. Mascher

PART XII: WIDE-BANDGAP MATERIALS: II-VI COMPOUNDS

Photoluminescence and Electron Paramagnetic Resonance of Nitrogen-Doped Zinc Selenide Epilayers 555
M. Moldovan, S.D. Setzler, Z. Yu, T.H. Myers, L.E. Halliburton, and N.C. Giles

Defect States in p-ZnSe:N Grown by MOVPE 561
Shizuo Fujita, Ken-ichi Ogata, Daisuke Kawaguchi, Zhi Gang Peng, and Shigeo Fujita

Identification of the Native Vacancy Defects in ZnS_xSe_{1-x} and $Mg_yZn_{1-y}S_xSe_{1-x}$ by Positron Annihilation 567
K. Saarinen, T. Laine, K. Skog, J. Oila, P. Hautojärvi, K. Rakennus, P. Uusimaa, A. Salokatve, and M. Pessa

Electrical Characterization of Nitrogen Acceptors in p-ZnSe/p-GaAs Grown by Molecular-Beam Epitaxy 573
D. Seghier and H.P. Gislason

Deep Centers Influence on Photoresponse Characteristics in High-Resistivity ZnSe 579
V.A. Korotkov, L.I. Bruk, A.V. Simashkevich, O.S. Gorea, L.E. Kovalev, and L.V. Malikova

Complex Defects in Cl-Doped ZnTe and CdTe 585
V. Valdna

The Effects of Substitutional Alkaline Metals in Zinc Vacancy of Zincselenide Single Crystals Grown by the Sublimation Method 593
Kenji Yoshino, Kouji Maeda, Atsuhiko Fukuyama, Yoshito Akashi, Kiyohisa Imada, and Tetsuo Ikari

Surface of Li-Doped ZnSe Grown on Misoriented GaAs(001) Substrates 599
Minoru Yoneta, Masakazu Ohishi, Hiroshi Saito, Mitsuhiro Ohura, Katsumoto Fujii, and Yoshihiko Hioe

Investigation of Deep Energy Levels in II-VI Compounds 605
A. Castaldini, A. Cavallini, P. Fernandez, B. Fraboni, and J. Piqueras

Nondestructive Characterization of the Surface Aging of HgI_2 Crystal 611
H. Yao, J.C. Erickson, R.B. James, and M. Natarajan

PART XIII: WIDE-BANDGAP MATERIALS: SiC

The Microscopic Structure of Shallow Donors in Silicon Carbide 619
J-M. Spaeth, S. Greulich-Weber, M. März, E.N. Kalabukhova, and S.N. Lukin

Vacancies in Electron Irradiated 6H-SiC 625
T. Friessnegg and S. Dannefaer

Defects in 4H Silicon Carbide CVD Epilayers 631
L. Zhou, P. Pirouz, and J.A. Powell

Theory of 3*d* Transition Metal Defects in 3C SiC 637
Harald Overhof

Imaging of Micropipes in Silicon Carbide Under High Field Stress 643
G. Gradinaru, M. Helmi, Y. Khlebnikov, G. Korony, W.C. Mitchel, and T.S. Sudarshan

Deep-Level Transient Spectroscopy Study of High-Temperature Aluminum Implanted 6H-SiC 649
Yuri A. Stotski, Igor O. Usov, and Alexander V. Suvorov

HRTEM Characterization of 6H-15R Polytype Boundaries in Silicon Carbide Grown by Physical Vapor Transport 655
E.K. Sanchez, M. De Graef, W. Qian, and M. Skowronski

X-ray Topography of a Single Superscrew Dislocation in 6H-SiC Through All {100} Faces 661
W.M. Vetter and M. Dudley

The Influence of the Incorporation and Desorption of CH_n Groups on the Defect Structure of *a*-SiC:H Films 667
T. Friessnegg, M. Boudreau, P. Mascher, P.J. Simpson, and W. Puff

PART XIV: WIDE-BANDGAP MATERIALS: DIAMOND

Behavior of the Potential n-Type Dopants P and As in Diamond After Low-Dose Ion Implantation 675
H. Hofsäss, M. Dalmer, M. Restle, C. Ronning, K. Bharuth-Ram, H. Quintel, and The Isolde-Collaboration

Correlation Between Defects and Electrical Conduction in Surface Conductive Layer of CVD Diamond Films 681
Y. Show, F. Matsuoka, S. Ri, Y. Akiba, T. Kurosu, M. Iida, and T. Izumi

Charge Transient Spectroscopy Study of Deep Centers in CVD Diamond and Diamondlike Films 687
V.I. Polyakov, A.I. Rukovishnikov, N.M. Rossukanyi, V.P. Varnin, I.G. Teremetskaya, B.L. Druz, E. Ostan, and A. Hayes

Coexistence of Two Carbon Phases at Grain Boundaries in Polycrystalline Diamond 693
O. Shenderova and D.W. Brenner

Hydrogen-Induced Luminescent States in the Subsurface Region of Homoepitaxial Diamond Films 699
Kazushi Hayashi, Hideyuki Watanabe, Sadanori Yamanaka, Takashi Sekiguchi, Hideyo Okushi, and Koji Kajimura

Author Index 705

Subject Index 709

PREFACE

This proceedings volume contains oral and poster contributions from a symposium on "Defects in Electronic Materials" at the combined meeting of the Materials Research Society (MRS) and the International Conference on Electronic Materials (ICEM) in December, 1996, in Boston. The international character of the symposium is reflected in the fact that 70% of the proceedings contributions are from outside the United States. Research groups from some 25 countries, led by the United States and Japan and followed by Germany and Russia, contributed to the success of the symposium. The volume comprises the areas of defects in group IV, III-V, and wide bandgap semiconductors. Defects in III-V nitrides can be found in the MRS Proceedings Volume 449.

The symposium was planned to represent the general field of defects in electronic materials, with a focus on issues that are currently widely discussed. The pervasive role of defects in determining the thermal, mechanical, electrical, optical and magnetic properties of materials is significant. The knowledge of generation and control of defects in electronic materials has contributed to the success of these materials. Developing novel semiconductor materials requires new insights into the role of defects to achieve new properties. New experimental techniques have to be developed to study defects in small structures.

This proceedings volume provides a vivid picture of the current problems, progress and methods in defect studies in electronic materials. Of most interest were the sessions on new techniques in defect studies and on process-induced defects in Si and GaAs. Papers on new techniques addressed the issues of surface defects, defects in small dimensions and the detection of near-surface defects in Si. In process-induced defects, three areas received significant attention. Plasma processes in Si and GaAs produce defective layers. Many papers deal with the understanding of these defects. Grown-in defects are widely studied because of their deteriorating effect on the gate-oxide integrity (GOI). These defects were identified as octahedral voids in as-grown silicon. Another recurring issue is gettering of metallic impurities to prevent contamination during processing.

The volume is organized into 14 parts. The first part deals with new characterization techniques. Process-induced defects are organized in the next three parts (II-IV). Defects in group IV semiconductors are divided into 4 parts (V-VIII) while defects in III-V semiconductors (IX-XI) and defects in wide-bandgap semiconductors (XII-XIV) occupy three parts each.

Jürgen Michel
Thomas Kennedy
Kazumi Wada
Klaus Thonke

January 1997

ACKNOWLEDGMENTS

The symposium organizers would like to express their appreciation to the authors, speakers and poster presenters who presented their technical work at the meeting, composed the papers in this volume, and reviewed the manuscripts; the sessions chairpersons who ran the individual sessions (W.M. Chen, E.A. Fitzgerald, S.A. Ringel, R.A. Brown, H.J. Gossmann, N.C. Giles, J.A. Freitas, G.D. Watkins, E.R. Weber, and B.K. Meyer); the MRS staff for their invaluable assistance in organizing the meeting and processing the proceedings; and all of the government and corporate sponsors listed below, whose financial contributions enabled the organizers to provide support for invited speakers and scientists from the international community, and cover the meeting expenses.

Symposium Support

Bruker Instruments, Inc.
Bunkoh-Keiki Co., Ltd.
JEOL USA, Inc.
Komatsu Electronic Metals Co., Ltd.
Nippon Steel Corporation
Office of Naval Research
Oxford Instruments, Inc.
SEH America, Inc.
Sin-Etsu Handotai Co., Ltd.
Sumitomo SiTiX Corporation
Temic Mikroelectronik
Wacker Siltronic AG

MATERIALS RESEARCH SOCIETY SYMPOSIUM PROCEEDINGS

Volume 420— Amorphous Silicon Technology—1996, M. Hack, E.A. Schiff, S. Wagner, R. Schropp, A. Matsuda 1996, ISBN: 1-55899-323-1

Volume 421— Compound Semiconductor Electronics and Photonics, R.J. Shul, S.J. Pearton, F. Ren, C–S. Wu, 1996, ISBN: 1-55899-324-X

Volume 422— Rare-Earth Doped Semiconductors II, S. Coffa, A. Polman, R.N. Schwartz, 1996, ISBN: 1-55899-325-8

Volume 423— III-Nitride, SiC, and Diamond Materials for Electronic Devices, D.K. Gaskill, C.D. Brandt, R.J. Nemanich, 1996, ISBN: 1-55899-326-6

Volume 424— Flat Panel Display Materials II, M. Hatalis, J. Kanicki, C.J. Summers, F. Funada, 1997, ISBN: 1-55899-327-4

Volume 425— Liquid Crystals for Advanced Technologies, T.J. Bunning, S.H. Chen, W. Hawthorne, T. Kajiyama, N. Koide, 1996, ISBN: 1-55899-328-2

Volume 426— Thin Films for Photovoltaic and Related Device Applications, D. Ginley, A. Catalano, H.W. Schock, C. Eberspacher, T.M. Peterson, T. Wada, 1996, ISBN: 1-55899-329-0

Volume 427— Advanced Metallization for Future ULSI, K.N. Tu, J.W. Mayer, J.M. Poate, L.J. Chen, 1996, ISBN: 1-55899-330-4

Volume 428— Materials Reliability in Microelectronics VI, W.F. Filter, J.J. Clement, A.S. Oates, R. Rosenberg, P.M. Lenahan, 1996, ISBN: 1-55899-331-2

Volume 429— Rapid Thermal and Integrated Processing V, J.C. Gelpey, M.C. Öztürk, R.P.S. Thakur, A.T. Fiory, F. Roozeboom, 1996, ISBN: 1-55899-332-0

Volume 430— Microwave Processing of Materials V, M.F. Iskander, J.O. Kiggans, Jr., J.Ch. Bolomey, 1996, ISBN: 1-55899-333-9

Volume 431— Microporous and Macroporous Materials, R.F. Lobo, J.S. Beck, S.L. Suib, D.R. Corbin, M.E. Davis, L.E. Iton, S.I. Zones, 1996, ISBN: 1-55899-334-7

Volume 432— Aqueous Chemistry and Geochemistry of Oxides, Oxyhydroxides, and Related Materials, J.A. Voight, T.E. Wood, B.C. Bunker, W.H. Casey, L.J. Crossey, 1997, ISBN: 1-55899-335-5

Volume 433— Ferroelectric Thin Films V, S.B. Desu, R. Ramesh, B.A. Tuttle, R.E. Jones, I.K. Yoo, 1996, ISBN: 1-55899-336-3

Volume 434— Layered Materials for Structural Applications, J.J. Lewandowski, C.H. Ward, M.R. Jackson, W.H. Hunt, Jr., 1996, ISBN: 1-55899-337-1

Volume 435— Better Ceramics Through Chemistry VII—Organic/Inorganic Hybrid Materials, B.K. Coltrain, C. Sanchez, D.W. Schaefer, G.L. Wilkes, 1996, ISBN: 1-55899-338-X

Volume 436— Thin Films: Stresses and Mechanical Properties VI, W.W. Gerberich, H. Gao, J–E. Sundgren, S.P. Baker 1997, ISBN: 1-55899-339-8

Volume 437— Applications of Synchrotron Radiation to Materials Science III, L. Terminello, S. Mini, H. Ade, D.L. Perry, 1996, ISBN: 1-55899-340-1

Volume 438— Materials Modification and Synthesis by Ion Beam Processing, D.E. Alexander, N.W. Cheung, B. Park, W. Skorupa, 1997, ISBN: 1-55899-342-8

Volume 439— Microstructure Evolution During Irradiation, I.M. Robertson, G.S. Was, L.W. Hobbs, T. Diaz de la Rubia, 1997, ISBN: 1-55899-343-6

Volume 440— Structure and Evolution of Surfaces, R.C. Cammarata, E.H. Chason, T.L. Einstein, E.D. Williams, 1997, ISBN: 1-55899-344-4

Volume 441— Thin Films—Structure and Morphology, R.C. Cammarata, E.H. Chason, S.C. Moss, D. Ila, 1997, ISBN: 1-55899-345-2

Volume 442— Defects in Electronic Materials II, J. Michel, T.A. Kennedy, K. Wada, K. Thonke, 1997, ISBN: 1-55899-346-0

Volume 443— Low–Dielectric Constant Materials II, K. Uram, H. Treichel, A.C. Jones, A. Lagendijk, 1997, ISBN: 1-55899-347-9

MATERIALS RESEARCH SOCIETY SYMPOSIUM PROCEEDINGS

Volume 444— Materials for Mechanical and Optical Microsystems, M.L. Reed, M. Elwenspoek, S. Johansson, E. Obermeier, H. Fujita, Y. Uenishi, 1997, ISBN: 1-55899-348-7

Volume 445— Electronic Packaging Materials Science IX, P.S. Ho, S.K. Groothuis, K. Ishida, T. Wu, 1997, ISBN: 1-55899-349-5

Volume 446— Amorphous and Crystalline Insulating Thin Films—1996, W.L. Warren, J. Kanicki, R.A.B. Devine, M. Matsumura, S. Cristoloveanu, Y. Homma, 1997, ISBN: 1-55899-350-9

Volume 447— Environmental, Safety, and Health Issues in IC Production, R. Reif, A. Bowling, A. Tonti, M. Heyns, 1997, ISBN: 1-55899-351-7

Volume 448— Control of Semiconductor Surfaces and Interfaces, S.M. Prokes, O.J. Glembocki, S.K. Brierley, J.M. Woodall, J.M. Gibson, 1997, ISBN: 1-55899-352-5

Volume 449— III–V Nitrides, F.A. Ponce, T.D. Moustakas, I. Akasaki, B.A. Monemar, 1997, ISBN: 1-55899-353-3

Volume 450— Infrared Applications of Semiconductors—Materials, Processing and Devices, M.O. Manasreh, T.H. Myers, F.H. Julien, 1997, ISBN: 1-55899-354-1

Volume 451— Electrochemical Synthesis and Modification of Materials, S.G. Corcoran, P.C. Searson, T.P. Moffat, P.C. Andricacos, J.L. Deplancke, 1997, ISBN: 1-55899-355-X

Volume 452— Advances in Microcrystalline and Nanocrystalline Semiconductors—1996, R.W. Collins, P.M. Fauchet, I. Shimizu, J–C. Vial, T. Shimada, A.P. Alvisatos, 1997, ISBN: 1-55899-356-8

Volume 453— Solid–State Chemistry of Inorganic Materials, A. Jacobson, P. Davies, T. Vanderah, C. Torardi, 1997, ISBN: 1-55899-357-6

Volume 454— Advanced Catalytic Materials—1996, M.J. Ledoux, P.W. Lednor, D.A. Nagaki, L.T. Thompson, 1997, ISBN: 1-55899-358-4

Volume 455— Structure and Dynamics of Glasses and Glass Formers, C.A. Angell, T. Egami, J. Kieffer, U. Nienhaus, K.L. Ngai, 1997, ISBN: 1-55899-359-2

Volume 456— Recent Advances in Biomaterials and Biologically–Inspired Materials: Surfaces, Thin Films and Bulk, D.F. Williams, M. Spector, A. Bellare, 1997, ISBN: 1-55899-360-6

Volume 457— Nanophase and Nanocomposite Materials II, S. Komarneni, J.C. Parker, H.J. Wollenberger, 1997, ISBN: 1-55899-361-4

Volume 458— Interfacial Engineering for Optimized Properties, C.L. Briant, C.B. Carter, E.L. Hall, 1997, ISBN: 1-55899-362-2

Volume 459— Materials for Smart Systems II, E.P. George, R. Gotthardt, K. Otsuka, S. Trolier-McKinstry, M. Wun-Fogle, 1997, ISBN: 1-55899-363-0

Volume 460— High–Temperature Ordered Intermetallic Alloys VII, C.C. Koch, N.S. Stoloff, C.T. Liu, A. Wanner, 1997, ISBN: 1-55899-364-9

Volume 461— Morphological Control in Multiphase Polymer Mixtures, R.M. Briber, D.G. Peiffer, C.C. Han, 1997, ISBN: 1-55899-365-7

Volume 462— Materials Issues in Art and Archaeology V, P.B. Vandiver, J.R. Druzik, J. Merkel, J. Stewart, 1997, ISBN: 1-55899-366-5

Volume 463— Statistical Mechanics in Physics and Biology, D. Wirtz, T.C. Halsey, J. van Zanten, 1997, ISBN: 1-55899-367-3

Volume 464— Dynamics in Small Confining Systems III, J.M. Drake, J. Klafter, R. Kopelman, 1997, ISBN: 1-55899-368-1

Volume 465— Scientific Basis for Nuclear Waste Management XX, W.J. Gray, I.R. Triay, 1997, ISBN: 1-55899-369-X

Volume 466— Atomic Resolution Microscopy of Surfaces and Interfaces, D.J. Smith, R.J. Hamers, 1997, ISBN: 1-55899-370-3

Prior Materials Research Society Symposium Proceedings available by contacting Materials Research Society

Part I

New Techniques in Defect Studies

RADIOACTIVE ISOTOPES IN PHOTOLUMINESCENCE EXPERIMENTS: IDENTIFICATION OF DEFECT LEVELS

R. MAGERLE
Fakultät für Physik, Universität Konstanz, D-78434 Konstanz, Germany

ABSTRACT

The characteristic life-times of radioactive isotopes can be used to label and identify defect levels in semiconductors which can be detected by photoluminescence (PL). This technique is illustrated with three examples: ZnS doped with radioactive ^{65}Zn by neutron irradiation and GaAs doped with radioactive ^{111}In by ion implantation. Finally we report that doping GaAs with radioactive ^{71}As which decays to stable ^{71}Ga can be used to create Ga_{As} antisites in GaAs in a controlled way and to identify their levels.

INTRODUCTION

Photoluminescence (PL) spectroscopy is a standard technique to detect defect levels in semiconductors. However, the assignment to a particular defect is often a puzzle. In semiconductors with residual impurities below the threshold concentration for PL detection intentional doping and its correlation to the intensity of PL transitions is used to identify the chemical nature of defect levels. In this way many defect levels in Si, Ge, and GaAs have been identified during the last decades. However, in other semiconductors, like InP, GaN or the II-VI compounds, which are of growing interest for opto-electronic applications, many defect levels are still not identified, due to the difficulty to grow high purity crystals. For example, the acceptor level A_1 is present in all InP samples and is caused by a residual impurity, which is supposed to be either Be or Mg [1]. In the II-VI compounds the problem is still unsolved, whether the difficulty to dope a compound *p*-type as well as *n*-type is due to self-compensation by intrinsic defects [2] or to the high concentration of residual impurities [3].

In general, an unambiguous chemical identification of a defect level is provided only by the observation of an element specific property, like the isotope mass, the nuclear spin, or the isotope abundance. In case light impurities are involved in the defect one possibility is the observation of the isotope shift of no-phonon lines or local mode phonon replicas [4]. Another possibility exists in the determination of the hyperfine interaction by electron paramagnetic resonance (EPR) or electron-nuclear double resonance (ENDOR) experiments where the defect level is determined by selective photo-excitation or photo-ionization of a paramagnetic level [5]. These two methods, however, require a paramagnetic level, suitable nuclear properties of the involved elements, and a control over the Fermi-level for selective photo-excitation. Due to these limitations any additional method to identify defect levels is highly welcome.

NUCLEAR LIFE-TIME AS AN ELEMENT SPECIFIC LABEL

Another element specific property that can be used to identify defect levels is the nuclear life-time of a radioactive isotope undergoing a chemical transmutation. If the level is due to a defect in which the parent or daughter isotope is involved the concentration of that defect will change with the characteristic time constant of the radioactive decay.

This technique will be illustrated by three examples: The first successful application of this technique by I. Broser and K.-H. Franke [6] who doped ZnS homogeneously with radioactive

Mat. Res. Soc. Symp. Proc. Vol. 442 © 1997 Materials Research Society

^{65}Zn by neutron irradiation. Then our own example of GaAs doped with radioactive ^{111}In [7] where we demonstrated that ion implantation can be used for doping with radioactive isotopes and how a quantitative link between PL intensity and defect concentration can be obtained under these circumstances. This offers a lot more possibilities for doping with radioactive isotopes than neutron transmutation since facilities like ISOLDE [8] at CERN exist which deliver mass separated ion beams of radioactive isotopes for almost all elements. Finally we report that doping GaAs with radioactive ^{71}As which decay to stable ^{71}Ga can be used to form Ga_{As} antisites in GaAs in a controlled way and to identify their levels [9].

LUMINESCENCE OF SUBSTITUTIONAL Cu IN ZnS

After first attempts to use this technique of radioactive labeling to identify the luminescence of substitutional Cu in ZnS has been done by J. S. Prener *et al.* [10] and R. M. Potter *et al.* [11] the first successful application of it has been published 1965 by I. Broser and K.-H. Franke [6]. They irradiated ZnS single crystals with thermal neutrons to dope them homogeneously with radioactive ^{65}Zn created by the nuclear reaction $^{64}Zn + n \rightarrow {}^{65}Zn + \gamma$. The lattice defects introduced during the neutron irradiation were annealed at 1173 K. After this treatment all radioactive ^{65}Zn occupies substitutional Zn-sites in ZnS as every other Zn isotope does. However, ^{65}Zn is not a stable isotope and decays to stable ^{65}Cu with a life-time $\tau = 352$ days. Provided that the lattice site does not change during the decay of $^{65}Zn_{Zn}$ to $^{65}Cu_{Zn}$ this chemical transmutation causes the concentration N_{Cu} of substitutional Cu_{Zn} to increase according to

$$N_{Cu}(t) = N_{Cu}(t=\infty)\left(1-e^{-t/\tau}\right) . \qquad (1)$$

I. Broser and K.-H. Franke used a Xe discharge lamp to excite PL at 80 K and observed the PL in the infrared region around 1.6 μm as a function of time after doping with ^{65}Zn (Fig. 1(a)). They report, that the increase of PL intensity at 1.5 μm increases with time according to

$$I(t) = I(t=\infty)\left(1-e^{-t/\tau}\right) \qquad (2)$$

with τ being exactly the nuclear life-time of ^{65}Zn. From this they concluded that the increase of PL intensity around 1.5 μm is caused by the decay of ^{65}Zn to ^{65}Cu and that it is directly propor-

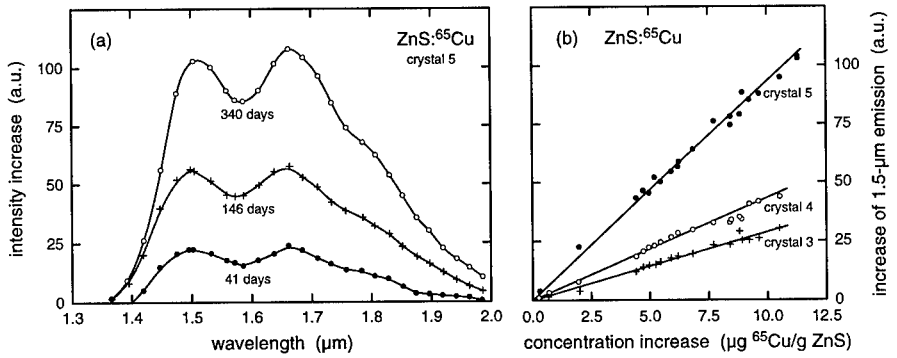


Fig. 1 (a) Infrared PL spectrum of ZnS doped with ^{65}Cu (crystal 5). The increase of PL intensity with time is governed by the nuclear lifetime τ = 352 days of the parent isotope ^{65}Zn which was produced by irradiation of ZnS with thermal neutrons (after Ref. 6). (b) Increase of PL intensity at 1.5 μm as function of the increase of the ^{65}Cu concentration (after Ref. 6).

tional to the concentration of ^{65}Cu produced by the decay of ^{65}Zn. To demonstrate this they calculated the ^{65}Cu content per g of ZnS with the help of the know neutron dose, the cross section for production of ^{65}Zn, and Eq. (1) and plotted the increase of PL intensity at 1.5 μm versus the increase of the ^{65}Cu content of the samples (Fig. 1(b)).

A potential complication of such an experiment is the emission of high energetic neutrino, β, and γ particles during the radioactive decay which might cause two effects. The recoil energy of the daughter nucleus due to the emission of these particles might be large enough to displace the nucleus from the lattice site of the parent isotope. Although it can not be excluded totally, I. Broser and K.-H. Franke argued that the displacement of ^{65}Cu due to the recoil is unlikely to happen for most of the decays and most of the ^{65}Cu created by the decay of radioactive $^{65}Zn_{Zn}$ is incorporated on substitutional lattice sites. The second effect is the irradiation of the crystal with β and γ particles which might create lattice defects. In this case the concentration of these defects would increase exactly in the same way as the concentration of daughter isotope does. By irradiating ZnS crystals with high doses of such particles I. Broser and K.-H. Franke proved with additional experiments that the increase of the 1.5 μm PL intensity in ^{65}Zn doped ZnS can not be caused by an accumulation of radiation damage.

THE Cd ACCEPTOR IN GaAs

It took about 25 years until this type of experiment was reinvented, first, to identify defect levels in Si observed with deep level transient spectroscopy (DLTS) [12, 13] and then with PL spectroscopy in Si [14, 15] and GaAs [7]. In all these experiments ion implantation was used for doping with radioactive isotopes. This offers a lot more possibilities for doping with radioactive dopants then neutron irradiation does. However, with ion implantation only a thin layer (depending on mass and energy of the implant only a few tens up to a few hundred nm thick) can be doped and the concentration of the dopant can be quite large in this layer (10^{18} cm^{-3} is easily achieved). Both facts can complicate the procedure to determine the defect concentration from the intensity of the corresponding PL emission.

We have chosen the example of GaAs doped with radioactive ^{111}In and demonstrated that ion implantation is a suitable doping technique for such experiments [7]. In this experiment an undoped GaAs layer grown by molecular beam epitaxy (MBE) on GaAs was implanted either with radioactive ^{111}In or stable Cd and In. Commercially available carrier-free ^{111}In, an ion implanter with mass separation, and a hot W surface ionization source were used to produce an isotopically pure beam of 350 keV $^{111}In^+$. It was implanted into GaAs at 300 K to a dose of $3(1)\times 10^{11}$ cm^{-2} resulting in a Gaussian shaped ^{111}In concentration profile centered at 100 nm depth with a width of 40 nm and a peak concentration of 3×10^{16} cm^{-3}. The implantation damage was removed by annealing the samples at 1125(25) K for 10 min in evacuated quartz ampoules under As atmosphere. After this treatment all In and Cd atoms are located on lattice sites with an unperturbed surrounding and the Cd atoms are electrically activated and act as acceptors [16].

^{111}In is isoelectronic to Ga and hence occupies Ga lattice sites in GaAs. It decays to ^{111}Cd with a life-time $\tau_{^{111}In}$ = 98 h by electron capture [17]. The recoil energy transferred to the ^{111}Cd nucleus by the emission of the 400-keV neutrino is only 1 eV which is much smaller than the typical energy of about 10 to 20 eV that is needed to displace an atom in GaAs [18]. Therefore ^{111}Cd atoms on Ga sites (Cd_{Ga}) are created by the decay of ^{111}In on Ga sites ($^{111}In_{Ga}$) and act there as shallow acceptors. This chemical transmutation was monitored by PL spectroscopy. The sample was kept at 5 K and the 488-nm Ar ion laser line was used for excitation with an excitation density of 10 Wcm^{-2}.

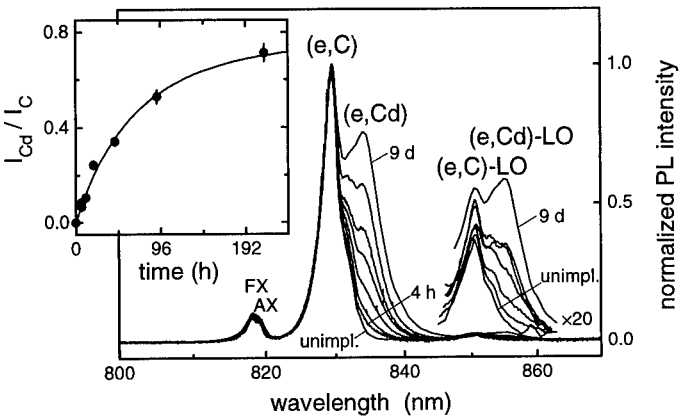


Fig. 2 PL spectra of undoped and ^{111}In doped GaAs successively taken 4 h, 7 h, 12 h, 22 h, 2 d, 4 d, and 9 d after doping. All spectra are normalized to the intensity of the (e,C) peak. In the inset, the height I_{Cd}/I_C of the (e,Cd) peak in these spectra is shown as function of time after doping with ^{111}In. The solid line is a fit to the data using Eq. (10) (from Ref. [7]).

Figure 2 shows successively taken PL spectra from the ^{111}In doped sample. A spectrum from the undoped part is also shown. Since the intensity of different PL spectra taken from the same sample varies within 25%, mainly because of the difficulty to focus reproducibly on the entrance slit of the monochromator, all spectra have been normalized to the height I_C of the (e,C) peak. The PL spectrum of the undoped part of the sample shows the features well known for undoped MBE-grown GaAs [19]. The peaks FX and AX around 819 nm are due to the recombination of free and bound excitons. The peak (e,C) at 830 nm and its LO phonon replica (e,C)-LO at 850 nm are due to recombination of electrons from the conduction band into C acceptor states. The recombination of electrons from donor states into C acceptors states appears as a small shoulder at the right hand sides of either these two peaks. C is a residual impurity in GaAs present in MBE-grown material with a typical concentration between 10^{14} and 10^{15} cm^{-3} [19].

$^{111}In_{Ga}$ is isoelectronic to Ga and causes no PL peaks in GaAs. Therefore, 4 h after doping with ^{111}In the only difference to the undoped part is a small increase of the low energy shoulder of the (e,C) peak. This shoulder increases steadily with time and develops into a peak after 9 days. The same happens at the lower energy side of the (e,C)-LO peak. During this time all other features in the spectra remain unchanged (the apparent increase of the (e,C)-LO peak is due to the increase of the (e,Cd)-LO peak). Since nothing else is changing in the ^{111}In doped sample but N_{Cd}, the two growing peaks must be caused by $^{111}Cd_{Ga}$ acceptors created by the decay of $^{111}In_{Ga}$. The position of these two peaks differ by the energy of one LO phonon. Therefore, the peak (e,Cd)-LO at 855 nm is the LO phonon replica of the (e,Cd) peak at 834 nm, in agreement with the literature [19].

We determined the height I_{Cd}/I_C of the (e,Cd) peak normalized to I_C as function of time after doping. This was done by subtracting the normalized spectrum of the undoped part from the normalized spectra of the ^{111}In doped part. The height I_{Cd}/I_C of the (e,Cd) peak remaining in these difference spectra is displayed in the inset of Fig. 2. We fitted this data by

$$\frac{I_{Cd}}{I_C}(t) = \frac{I_{Cd}}{I_C}(t=\infty)\left(1-e^{-t/\tau}\right) \qquad (3)$$

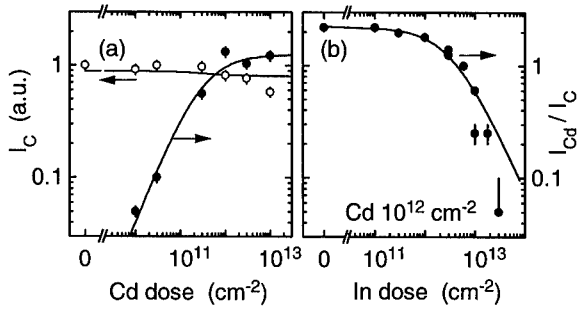


Fig. 3 (a) Height I_C [○] of the (e,C) peak and height I_{Cd}/I_C [●] of the (e,Cd) peak normalized to the height of the (e,C) peak in GaAs implanted with stable Cd to different doses. The solid lines are fits to the data using Eqs. (6) and (7), respectively. (b) I_{Cd}/I_C [●] as a function of the In dose in GaAs implanted with In and Cd ($\Phi_{Cd} = 10^{12}$ cm^{-2}). The solid lines is a fit to the data using Eq. (7) (from Ref. 7).

and obtained a time constant $\tau = 52(17)$ h which is *not* the nuclear life-time $\tau_{^{111}In} = 98$ h of ^{111}In. Evidently, I_{Cd}/I_C is not proportional to N_{Cd}. This can also be seen in Fig. 3(a) showing I_C and I_{Cd}/I_C obtained from samples implanted with stable Cd with dose Φ_{Cd} between 10^9 and 10^{13} cm^{-2}. Up to $\Phi_{Cd} = 10^{12}$ cm^{-2} I_{Cd}/I_C increases with Cd dose and is practically constant for higher doses. I_C, which is a measure of the total PL intensity in these samples, is practically constant within the entire dose range. I_{Cd}/I_C is not only determined by the Cd concentration. It is also influenced by the concentration of non-radiative centers due to residual implantation damage. This can be seen in Fig. 3(b) showing I_{Cd}/I_C from samples implanted with stable Cd ($\Phi_{Cd} = 10^{12}$ cm^{-2}) *and* In (Φ_{In} up to 3×10^{13} cm^{-2}). Additional non-radiative centers are created by the In implantation and cause a decrease of I_{Cd}/I_C with increasing In dose Φ_{In}.

This behavior can be explained by a model describing the dynamic equilibrium between generation of excess carriers by the incoming photon flux and their recombination through the different recombination channels. In other words, we determine the quantum efficiency for (*e*,Cd) recombination with respect to (*e*,C) recombination as a function of N_{Cd}. We assume the sample to consist of two layers (Fig. 4(b)): a homogeneously Cd-doped layer of thickness d with $N_{Cd} = \Phi_{Cd}/d$ and the undoped bulk below this layer. Assuming that no carrier diffusion occurs through the AlGaAs barriers, we neglect surface recombination and carrier diffusion between the two layers.

The PL intensity I_{Cd} is proportional to the recombination rate of excess carriers per unit area through Cd acceptors states $\Delta n_L B_{Cd} N_{Cd}$, where B_{Cd} is a recombination coefficient. The excess sheet carrier concentration in the implanted layer Δn_L can be expressed in terms of the total carrier life-time in the implanted layer τ_L and the generation rate of excess carriers per unit area in the implanted layer $f_L G$ by using the first of the two equilibrium conditions

$$f_L G = \frac{\Delta n_L}{\tau_L} \quad \text{and} \quad f_B G = \frac{\Delta n_B}{\tau_B} \; . \tag{4}$$

The second one describes the balance between the generation rate $f_B G$ and the recombination rate of excess carriers $\Delta n_B/\tau_B$ in the bulk. The total generation rate G is proportional to the incident photon flux and $f_L + f_B = 1$.

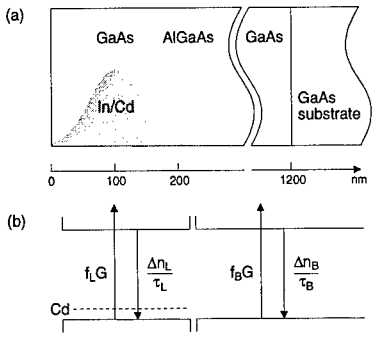


Fig. 4 (a) Layer sequence of the MBE-grown GaAs sample. On semi-insulating (100)-oriented GaAs a GaAs-$Al_xGa_{1-x}As$ superlattice buffer layer was grown, followed by 1 μm GaAs, 10 nm $Al_{0.3}Ga_{0.7}As$, 200 nm GaAs, 10 nm $Al_{0.3}Ga_{0.7}As$, and 5 nm GaAs (all undoped). (b) Illustration of the model for the carrier recombination process (from Ref. 7)

To get an expression for τ_L, we assume two additional recombination processes in the implanted layer: the radiative recombination via Cd acceptors and the non-radiative recombination due to residual implantation damage. The first one is proportional to N_{Cd} and the second one is proportional to the total dose $\Phi_{Cd}+\Phi_{In}$. Thereby, we assume that the same kind of non-radiative recombination centers is produced by In doping as it is by Cd doping and that the Cd concentration profiles are identical to the ^{111}In concentration profile. With this ansatz we write the recombination rate in the implanted layer in the usual small signal approximation as

$$\frac{\Delta n_L}{\tau_L} = \frac{\Delta n_L}{\tau_B} + \Delta n_L B_{Cd} N_{Cd} + \Delta n_L B_{nr} f_{nr}(N_{Cd} + N_{In}) \quad . \tag{5}$$

Here, $\Delta n_L B_{nr} f_{nr}(N_{Cd}+N_{In})$ is the non-radiative recombination rate per unit area due to residual implantation damage, $f_{nr}(N_{Cd}+N_{In})$ is the concentration of these non-radiative recombination centers, $N_{In} = \Phi_{In}/d$, and B_{nr} is the corresponding recombination coefficient. Hence, Δn_L and Δn_B can be expressed as function of N_{Cd} and N_{In} and the recombination rates through all the different recombination channels and thereby the relative PL peak intensities can be deduced.

I_C is proportional to the sum of the (e,C) recombination rates per unit area in the implanted layer and the bulk and within our model we obtain for $\Phi_{In} = 0$ (the case of Fig. 3(a))

$$I_C \propto \frac{\Delta n_L + \Delta n_B}{\tau_C} = G\frac{\tau_B}{\tau_C}\left(\frac{f_L}{1+\frac{\Phi_{Cd}}{f_B b}} + f_B\right) . \tag{6}$$

Thereby, $\tau_C = 1/(B_C N_C)$ is an effective lifetime describing the recombination probability through C acceptor states and b is a constant defined in Eqs. (8). With the help of Eqs. (4) and (6) we obtain the following dependence of I_{Cd}/I_C on Φ_{Cd} and Φ_{In}:

$$\frac{I_{Cd}}{I_C} = \frac{\Delta n_L B_{Cd} N_{Cd}}{\left(\frac{\Delta n_L + \Delta n_B}{\tau_C}\right)} = \frac{a}{1+\frac{b}{\Phi_{Cd}}+c\frac{\Phi_{In}}{\Phi_{Cd}}} \tag{7}$$

with

$$a = \frac{f_L}{f_B} \cdot \frac{B_{Cd}}{(B_{nr} f_{nr} + B_{Cd})} \cdot \frac{\tau_C}{\tau_B},\ b = \frac{d}{f_B (B_{nr} f_{nr} + B_{Cd}) \tau_B},\ \text{and}\ c = \frac{B_{nr} f_{nr}}{B_{nr} f_{nr} + B_{Cd}} \quad . \qquad (8)$$

For a better understanding of Eq. (7) we discuss two cases for $\Phi_{In} = 0$ (the case of Fig. 3(a)): (i) At low N_{Cd}, i.e., when $1/\tau_B >> (B_{Cd}+B_{nr}f_{nr})N_{Cd}$, the recombination via defects introduced by Cd doping can be neglected. In this case the effective lifetime τ_L defined in Eq. (5) and the excess sheet carrier concentration Δn_L (defined by Eq. (4) and (5)) are practically independent of N_{Cd}. As a consequence of that the (e,Cd) recombination rate $\Delta n_L B_{Cd} N_{Cd}$ is proportional to N_{Cd} in this regime. (ii) At high N_{Cd}, i.e., when $1/\tau_B << (B_{Cd}+B_{nr}f_{nr})N_{Cd}$, the ($e$,Cd) recombination and the non-radiative recombination due to residual implantation damage become the main recombination pathways and determine τ_L (see Eq. (5)). Then all excited electrons recombine through these two pathways and the (e,Cd) recombination rate is determined by the generation rate G, which is independent of N_{Cd}. Therefore, the (e,Cd) intensity saturates at high N_{Cd}.

The data in Fig. 3(b) can be explained in a similar way. At low Φ_{In} the additionally introduced non-radiative recombination due the In implantation does not influence τ_L and the intensity of (e,Cd) recombination. With increasing In dose Φ_{In} more and more non-radiative recombination centers are introduced causing a decrease of the (e,Cd) recombination rate.

The parameters a, b, c, and f_B can be obtained by fitting Eqs. (6) and (7) to the data shown in Fig. 3. By fitting Eq. (7) to I_{Cd}/I_C displayed in Fig. 3(a) we obtain a = 1.25(8) and b = 3.0(3)× 10^{11} cm^{-2}. Using this value for b we obtain f_B = 0.95(5) by fitting Eq. (6) to I_C displayed in Fig. 3(a). Both fits are shown as solid lines in Fig. 3.

The parameter c was obtained by fitting Eq. (7) to the data shown in Fig. 3(b) while keeping a = 1.25 and b = 3.0×10^{11} cm^{-2} fixed. We accounted for the slightly higher value of I_{Cd}/I_C for Φ_{In} = 0 in Fig. 3(b) than for the corresponding sample in Fig. 3(a) by a four times smaller value of τ_B. We attribute this to an aging of the material since 9 months passed between the two experiments. As a result, we obtain c = 0.5(2) in agreement with Ref. 7. This shows that in the case of $\Phi_{In} = 0$ the non-radiative recombination rate due to residual implantation damage $\Delta n_L B_{nr} f_{nr} N_{Cd}$ is roughly equal to the radiative recombination rate through Cd acceptor states $\Delta n_L B_{Cd} N_{Cd}$.

This model describes quantitatively the dependence of (e,Cd) intensity on N_{Cd} and the total implanted dose and we use it to describe the increase of I_{Cd}/I_C with time in the ^{111}In doped sample. Here, in contrast to the samples doped with stable Cd, N_{Cd} is increasing with time, while the number of non-radiative centers due to residual implantation damage is constant. In analogy to Eq. (5) we model the change of the carrier lifetime τ_L with time t in the ^{111}In doped sample as

$$\frac{1}{\tau_L} = \frac{1}{\tau_B} + B_{Cd} N_{In}^0 \left(1 - e^{-t/\tau}\right) + B_{nr} f_{nr} N_{In}^0 \ , \qquad (9)$$

where $N_{In}^0 = \Phi_{In}^0 / d$ is the initial ^{111}In concentration, τ is the nuclear life-time of ^{111}In, and B_{Cd}, B_{nr}, and f_{nr} are the same constants as above. With that we obtain

$$\frac{I_{Cd}}{I_C} = \frac{a}{1 + \dfrac{b}{\Phi_{In}^0 \left(1 - e^{-t/\tau}\right)} + \dfrac{c}{\left(e^{t/\tau} - 1\right)}} \ , \qquad (10)$$

where a, b, and c are the same constants as above. The structure of Eq. (10) is similar to that of Eq. (7). Basically, the only difference is that the Cd dose Φ_{Cd} in the b term of Eq. (7) is replaced by a time dependent Cd dose due to the changing Cd concentration. The time dependence of the c term accounts for the fact that in the ^{111}In doped sample the concentration of non-radiative recombination centers is not changing with Cd concentration. We fitted Eq. (10) to the data shown in the inset of Fig. 2, keeping a = 1.25, b = 3.0×10^{11} cm^{-2}, and c = 0.5 fixed and obtained

Φ_{In}^{U} = 4.6(17)×10^{11} cm^{-2} and τ = 91(23) h. This fit is shown as a solid line in the inset of Fig. 2 and agrees perfectly with the experimental data. The fit result for Φ_{In}^{U} corresponds with the implanted ^{111}In dose and that for τ agrees indeed with the nuclear life-time of ^{111}In, $\tau_{^{111}In}$ = 98.0 h.

CREATION OF Ga ANTISITES IN GaAs BY TRANSMUTATION DOPING

An important class of intrinsic defects in a compound semiconductor of type AB are antisites where an A atom is placed on a B site or vice versa. Such defects might form during non-stochiometric crystal growth conditions or during electron irradation and it is an interesting topic to know the energy levels of these defects. For instance it is still an open question what the levels of the Ga_{As} antisite in GaAs are. From valence arguments Ga_{As} should act as a double acceptor. In agreement with this GaAs grown from a Ga rich melt is often p-type with an acceptor state at 78 meV and exhibits a PL emission at 1.441 eV [20]. Therefore this level and this emission is often assigned to the Ga_{As} antisite [21], however, there is also evidence that this level is due to B_{As} [22].

The only way to create Ga_{As} antisite defects in GaAs in a controlled way and to avoid the introduction of any other defect during the production process is the transmutation of radioactive ^{71}As to stable ^{71}Ga. In addition, this approach offers the possibility to use the nuclear life-time of the involved isotopes as element specific labels to identify the levels of the Ga_{As} defect.

To create Ga_{As} antisite defects we implanted radioactive ^{71}As (260 keV, 3×10^{12} cm^{-2}) into semi-insulating LEC grown GaAs at the on-line mass separator ISOLDE [8] at CERN. The implantation damage was annealed at 1073 K and during this anneal all ^{71}As nuclei are placed on As lattice sites in GaAs. However, they are not stable and transmute via the radioactive decay chain $^{71}As_{As}$ (64 h) → $^{71}Ge_{As}$ (11.2 d) → $^{71}Ga_{As}$ to stable ^{71}Ga. The half-lives of the isotopes are given in brackets. The resulting concentrations of these isotopes as function of time can be calculated from the decay laws and are given in Fig. 5. During the first days after the implantation the concentration of ^{71}As is decreasing with a half-life of 64 h (dashed line) and the concentration of its daughter isotope ^{71}Ge is increasing (solid line). After about 5 days the concentration of ^{71}Ga starts to decrease again and after 20 days its decrease is a almost pure exponential function with a half-life of 11.2 days. Provided that the lattice site of the nucleus does not change during this chemical transmutation, $^{71}Ga_{As}$ antisite defects are formed in GaAs and their concentration increases with time as shown in Fig. 5 (dotted line).

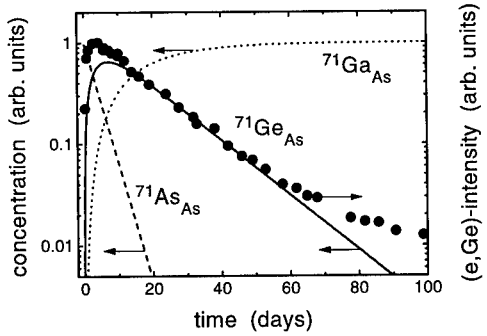


Fig. 5 Concentration of ^{71}As, ^{71}Ga, and ^{71}Ge as function of time (dashed, solid, and dotted line, respectively) resulting from the radioactive decay chain $^{71}As \rightarrow {}^{71}Ga \rightarrow {}^{71}Ge$. PL intensity of (e,Ge) recombination (solid dots) in a ^{71}As doped GaAs sample as function of time.

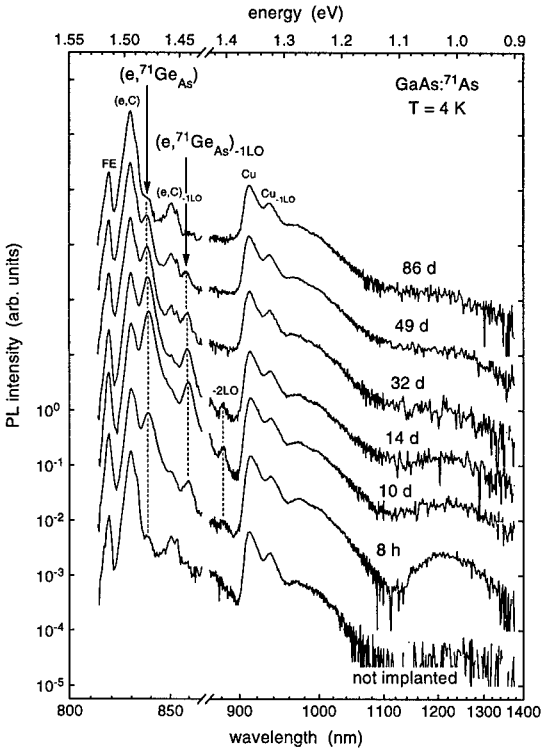


Fig. 6 PL spectra of ^{71}As doped GaAs 8 hours, 10, 14, 32, 49, and 86 days after doping with ^{71}As. A spectrum of the not ^{71}As-implanted part of the sample is shown for comparison. For clarity a logartimic scale is used and all spectra have been shifted by the same distance (corresponding to a factor 10) against each other.

We have monitored this chemical transmutation with PL spectroscopy at 4.2 K. PL was excited with 690-nm light from a laser diode and 5 mW (50 Wcm^{-2} excitation density). In Fig. 6 PL spectra taken at different times after doping the GaAs crystal with ^{71}As are shown. As reference a spectrum taken from an unimplanted part of the sample is also shown in Fig. 6. It shows the PL lines that can be observed without doping with ^{71}As: the recombination of free and bound excitons near the band edge (FE at 1.515 eV), the free-to-bound recombination into C acceptor states ((*e*,C) at 1.485 eV), the common impurity in GaAs, and the line Cu at 1.36 eV that is assigned to Cu [19], which was introduced as a contaminant during the annealing of the samples. The remaining lines are 1LO and 2LO phonon replicas of these peaks except for two broad bands centered at 1.28 and 1.02 eV which we assign to a contaminant or damage introduced during annealing.

The main difference between this spectrum and the spectra of the ^{71}As doped part of the sample is the peak (e,$^{71}Ge_{As}$) at 1.479 eV and its LO phonon replicas. This peak is due to the recombination of electrons into $^{71}Ge_{As}$ acceptor states that have been created by the transmutation of $^{71}As_{As}$ to $^{71}Ge_{As}$. The intensity of (e,$^{71}Ge_{As}$) recombination as function of time after doping

with ^{71}As is plotted in Fig. 5. Within the first days after doping with ^{71}As the intensity of $(e,^{71}Ge_{As})$ increases and after 5 days it starts to decrease with a half-life of 11.2 days due to the transmutation of $^{71}Ge_{As}$ to $^{71}Ga_{As}$. After 100 days practically all $^{71}Ge_{As}$ has transmuted to $^{71}Ga_{As}$ and the $(e,^{71}Ge_{As})$ intensity is as large as in the not ^{71}As-doped part of the sample. We attribute this remaining intensity to a contamination of the sample with stable Ge isotopes.

The $(e,^{71}Ge_{As})$ intensity is increasing within the first days and after 5 days it is as large as we expected it to be for such a sheet concentration of shallow acceptors, e.g., Cd implanted to the same dose and depth (see Fig. 3). This shows that during the transmutation of ^{71}As to ^{71}Ge most of the nuclei do not change their lattice site, although up to 30 eV recoil energy can be transferred to a ^{71}Ge nuclei during this decay [17]. This increase of the intensity of the 1.479-eV line and the fact that it decreases exactly with the half-life of ^{71}Ge (11.2 d) proves the common assignment of this line [19] to the shallow acceptor state of Ge_{As}. In addition to this qualitative interpretation of the time dependence of $(e,^{71}Ge_{As})$ intensity a detailed model of the different recombination processes similar to that one established for the case of ^{111}In doped GaAs is needed for a quantitative description of this behavior.

The fact that the $(e,^{71}Ge_{As})$ line disappears totally after 100 days shows that finally all $^{71}Ge_{As}$ acceptors have transmuted to $^{71}Ga_{As}$ antisite defects. The largest possible recoil energy that can be transferred to the Ga nucleus during this last decay is 0.4 eV. This is much less then the energy necessary to displace a atom from a regular lattice site. From electron irradiation experiments it is known that at least 10 eV are needed for this [18]. Therefore it can be excluded that the lattice site of the nucleus changes during the decay of $^{71}Ge_{As}$ to $^{71}Ga_{As}$. This proves that after 100 d the implanted layer is doped with Ga_{As} antisite defects with a sheet concentration of 3×10^{12} cm^{-2} distributed in a Gaussian shaped profile centered at 110 nm depth with a width of 50 nm and a peak concentration of 2×10^{17} cm^{-3}.

It is very remarkable that at this final state *no* PL line at 1.441 eV can be observed! Such a line is present in GaAs crystals grown from a Ga-rich melt [20]. Therefore this line and the corresponding 78-meV acceptor level is often assigned to Ga_{As} antisite defects. However, our results show, that this assignment is not correct and that the 78-meV acceptor level in Ga-rich GaAs belongs to another defect (a possible candidate might be B_{As} [22]). Another PL line that is also often related to Ga_{As} antisite defects and that we do *not* see in our samples is the 1.36-eV line [21]. Therefore, we can exclude that it is due to an isolated Ga_{As} antisite, however it might be due to a complex including Ga_{As} as already proposed by P. W. Yu *et al.* [21].

At the final state the only difference between the $^{71}Ga_{As}$ doped part and the unimplanted part of the sample is the intensity of two broad bands centered at 1.28 and 1.08 eV, which is in the $^{71}Ga_{As}$ doped part of the sample about twice as large as in the unimplanted part. However, the intensity of these two bands is constant during the 100 days of the experiment and therefore we attribute it either to residual implantation damage or a contaminant introduced during annealing.

One explanation why we do not observe an increase in intensity of any peak is that Ga_{As} does not cause any PL emission between 1.515 and 0.9 eV. Another explanation is that the emission is either very weak or very broad which makes it difficult to detect. A support for this explanation might come from calculations of S. B. Zhang and D. J. Chadi [23]. They predict Ga_{As} to be a *shallow* acceptor in *n*-type and a *deep* acceptor in *p*-type GaAs. If Ga_{As} is the dominant defect in our sample then it should be at 4 K in its deep and neutral state which might cause only a very weak and/or broad PL emission. According to this explanation the Ga_{As} state has to be filled with one electron to form a shallow acceptor state. One possibility to achieve this is to raise the temperature, however, in PL spectra taken at up to 300 K we have not seen any evidence of a peak corresponding to a such a shallow level [9].

In summary, our results show how Ga_{As} antisites can be created in GaAs with a high concentration. They show that neither the 1.441-eV line nor the 1.36-eV line is due to the isolated Ga_{As} defect and furthermore that there is no strong PL emission form Ga_{As} antisites between 1.515 and 0.9 eV. Other spectroscopic techniques like DLTS might be necessary to detect and identify the levels of Ga_{As}.

SUMMARY

We have illustrated by three examples how defect levels can be identified with PL spectroscopy by labeling it with the nuclear life-time of a radioactive isotope: radioactive $^{65}Zn_{Zn}$ which transmutes to substitutional $^{65}Cu_{Zn}$ in ZnS, radioactive $^{111}In_{Ga}$ transmuting to $^{111}Cd_{Ga}$ in GaAs, and finally the formation of Ga_{As} antisites in GaAs by transmutation of $^{71}As_{As}$ to stable $^{71}Ga_{As}$. This identification technique is applicable to a large variety of defect levels since for most elements suitable radioactive isotopes exist [17]. For example, doping of InP with ^{7}Be (τ = 76.9 d) or ^{28}Mg (τ = 30.2 h) will unambiguously identify the respective acceptor levels and answer the question whether one of those is the A_1 acceptor. To form As_{Ga}, the other antisites in GaAs, GaAs can be doped with ^{75}Ga which decays to ^{75}As.

For doping with radioactive isotopes either a conventional ion implanter or a facility like ISOLDE [8] at CERN can be used and diffusion or neutron irradiation might also work in selected cases. The isotope in mind needs a convenient life-time (between one day and one month), the spectroscopic technique has to be sensitive enough to detect the change in defect concentration, and contamination with stable isotopes of the element studied should be avoided. If the defect studied is populated by radioactive decay the recoil energy transferred to the daughter nucleus has to be small enough to keep the atom on its lattice site. In general, the response $I(N_D)$ of the spectroscopic technique on the defect concentration N_D has to be known for a quantitative labeling of a defect by its characteristic time dependence $I(N_D(t))$. Nevertheless, a qualitative identification is always possible because nothing else is changed in a radioactive doped sample but the concentration of the parent and daughter isotopes.

ACKNOWLEGDEMENTS

Most of the work presented here was done in close collaboration with A. Burchard, M. Deicher, T. Kerle, and W. Pfeiffer and their help and contributions are gratefully acknowledged. The experiments with ^{71}As would not have been possible without the help of D. Forkel-Wirth and the ISOLDE collaboration. This work has been financially supported by the Bundesminister für Bildung, Wissenschaft, Forschung und Technologie (03-RE3KON-8) and the Deutsche Forschungsgemeinschaft (SFB 306).

REFERENCES

1. B. J. Skromme, G. E. Stillman, J. D. Oberstar, and S. S. Chan, Appl. Phys. Lett. **44**, 319 (1984); S. S. Bose, I. Szafranek, M. H. Kim, and G. E. Stillman, *ibid.* **56**, 752 (1990).
2. G. Mandel, Phys. Rev. **134**, A1073 (1964); D. J. Chadi, Phys. Rev. Lett. **72**, 534 (1994), and references therein.
3. See, e.g., R. N. Barghava, J. Cryst. Growth **59**, 15 (1982); J. L. Pautrat, J. M. Francou, N. Magnea, E. Molva, and K. Saminadayar, *ibid.* **72**, 194 (1985).

4. See, e.g., P. J. Dean, Phys. Rev. B **4**, 2596 (1971); K. Thonke, H. Klemisch, J. Weber, and R. Sauer, *ibid.* B **24**, 5874 (1981); L. Canham, G. Davies, and E. C. Lightowlers, J. Phys. C **13**, L757 (1980).

5. See, e.g., H. G. Grimmeis, E. Janzén, H. Ennen, O. Schirmer, J. Schneider, R. Wörner, C. Holm, E. Sirtl, and P. Wagner, Phys. Rev. B **24**, 4571 (1981); B. K. Meyer, D. M. Hoffmann, J. R. Niklas, and J.-M. Spaeth, *ibid.* **36**, 1332 (1987).

6. I. Broser and K.-H. Franke, J. Phys. Chem. Solids 36, 1013 (1965).

7. R. Magerle, A. Burchard, M. Deicher, T. Kerle, W. Pfeiffer and E. Recknagel, Phys. Rev. Lett. **75**, 1594 (1995); R. Magerle, A. Burchard, M. Deicher, and T. Kerle, in Proc. of the 18th Intl. Conf. On Defects in Semiconductors, ed. by M. Suezawa and H. Katayama-Yoshida (Mat. Sci. Forum **196-201**, Trans Tech Publications, Zürich, 1995) p. 1503.

8. ISOLDE is an ion implanter delivering mass separated beams of radioactive isotopes which are produced on-line in the ion source by nuclear reactions with 1-GeV protons. See, e.g., H. L. Ravn and B. W. Allardyce, in Treatise on Heavy-Ion Science, edited by D. A. Bromley (Plenum, New York, 1989) Vol. 8, p. 363.

9. R. Magerle, A. Burchard, D. Forkel-Wirth, and M. Deicher, to be published.

10. J. S. Prener and F. E. Williams, J. Electrochem. Soc. **103**, 342 (1956).

11. R. M. Potter, M. Aven, and J. Kastner, J. Electrochem. Soc. **109**, 1154 (1962).

12. W. Petersen and J. Nielsen, Appl. Phys. Lett. **56**, 1122 (1990).

13. M. Lang, G. Pensl, M. Gebhard, N. Achtziger, and M. Uhrmacher, Appl. Phys. A **53**, 95 (1991).

14. S.E. Daly, M.O. Henry, K. Freitag, and R. Vianden, J. Phys.: Cond. Matter **6**, L643 (1994).

15. M. O. Henry, S. E. Daly, C. A. Frehill, E. McGlynn, C. McDonagh, E. Alves, J. C. Soares, and D. Forkel-Wirth, in Proc. of the 23rd Intl. Conf. On The Physics of Semiconductors, ed. by M. Scheffler and R. Zimmermann (World Scientific, Singapore, 1996) p. 2713.

16. N. Moriya, I. Brener, R. Kalish, W. Pfeiffer, M. Deicher, R. Keller, R. Magerle, E. Recknagel, H. Skudlik, Th. Wichert, H. Wolf, and ISOLDE Collaboration, J. Appl. Phys. **73**, 4248 (1993).

17. Table of Isotopes, edited by C. M. Lederer and V. S. Shirley (Wiley, New York, 1978).

18. D. Pons and J. C. Bourgoin, J. Phys. C **18**, 3839 (1985).

19. Properties of Gallium Arsenide, EMIS Data Reviews Series No. 2, (INSPEC, The Institute of Electrical Engineers, London, 1990).

20. for a short review, see J. C. Burgoin, H. J. Bardeleben, and D. Stievenard, J. Appl. Phys. **64**, R65 (1988), Section III. H, and references therein.

21. See, e.g., P. W. Yu, D.W. Fischer, and J.R. Sizelove, Semicond. Sci. Technol. **7**, 556 (1992).

22. R. C. Newman, B. R. Davidson, R. Addinall, R. Murray, J. W. Emmert, J. Wagner, W. Götz, G. Roos and G. Pensl, Proc. of the 17th Intl. Conf. On Defects in Semiconductors, ed. by H. Heinrich and W. Jantsch (Mat. Sci. Forum **143-147**, Trans Tech Publications, Aedermannsdorf, 1994) p. 229.

23. S. B. Zang and D. J. Chadi, Phys. Rev. Lett. **64**, 1789 (1990).

True Atomic Resolution Imaging on Semiconductor Surfaces with Noncontact Atomic Force Microscopy

Y. SUGAWARA[a], H. UEYAMA[a], T. UCHIHASHI[b], M. OHTA[a], Y. YANASE[c], T. SHIGEMATSU[c], M. SUZUKI[d] and S. MORITA[a]

a) Department of Electronic Engineering, Faculty of Engineering, Osaka University, 2-1 Yamada-Oka, Suita 565, Japan, sugawara@ele.eng.osaka-u.ac.jp
b) Department of Physics, Faculty of Science, Hiroshima University,1-3-1 Kagamiyama, Higashi-Hiroshima 739, Japan
c) Sumitomo Sitix Co. Ltd., 2201 Kamioda, Kohoku, Kashima 849-05, Japan
d) NTT Advanced Technology Co. Ltd., 3-1 Wakamiya, Morinosato, Atsugi 243-01, Japan

ABSTRACT

The constant vibration mode and the constant excitation mode in noncontact atomic force microscopy were compared to investigate the force interaction between tip and surface. As a result, we found that the constant excitation mode is much more gentle than the constant vibration mode. We also succeeded in atomic resolution imaging on InP(110) surface not only in the noncontact region but in the contact region for the first time. Furthermore, we found the discontinuity of the force gradient curve on reactive Si(111)7x7 reconstructed surface. We proposed a model to explain the discontinuity with the crossover between the physical and chemical bonding interaction.

1. INTRODUCTION

The atomic force microscope (AFM) in the contact mode [1], has been developed into a novel technique for obtaining high resolution images of both conductors and insulators. However, the question has been raised whether the AFM is really a microscope like the scanning tunneling microscope (STM) with a true atomic resolution [2, 3]. That is, most of the reported data with the AFM operating in the contact mode showed either perfectly ordered periodic lattice structures or defects on large lateral scale, but did not show any atomic-scale point defects which were routinely observed by the STM. This is due to that the contact mode imposes the repulsive interaction force greater than that acceptable for a single-atom tip.

On the other hand, in the noncontact mode, interaction force between the AFM tip and the surface can be reduced. However, till recently, an atomic-scale lateral resolution has not been achieved, because of technical difficulties for measuring the weak distance dependence of the attractive force between the tip and the sample with a good S/N ratio. Very recently, according to the technical improvements of the force sensitivity in an ultrahigh vacuum condition (UHV), several groups including ourselves succeeded in true atomic resolution imaging on Si(111) 7×7 reconstructed [4-6] and InP(110) 1×1 [7, 8] surfaces.

In this report, we investigate the force interaction between tip and sample in the different operation modes of UHV-AFM. Further, we investigate the mechanism of the force interaction between tip and reactive surface with dangling bonds such as Si(111)7×7 surface.

2. EXPERIMENTAL

Figure 1 shows a schematic diagram of the noncontact mode AFM. We have used home-built UHV-AFMs as described briefly in ref. [9]. The cantilever scanning was made by a piezoelectric tube scanner, and its deflection was detected by an optical-fiber interferometer [10], which is one of the most sensitive displacement sensor. The frequency modulation (FM) detection method [11] was used to measure the force gradient $F'=\partial F/\partial Z$ acting on the tip, where F and Z are the

Mat. Res. Soc. Symp. Proc. Vol. 442 © 1997 Materials Research Society

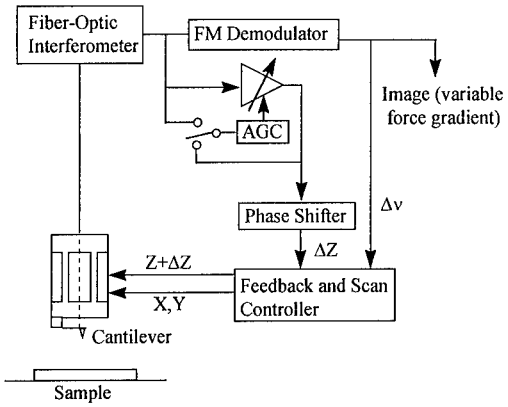


Fig. 1. Schematic diagram of noncontact mode AFM using the FM detection.

force and the distance between tip and surface, respectively. The FM detection method has a high sensitivity with very high Q value of the cantilever in a UHV. The cantilever was oscillated by the piezoelectric tube scanner at the mechanical resonant frequency ν_0 under the positive feedback condition. Two operation modes (constant vibration and constant excitation modes) were used by changing the input signal into automatic gain control (AGC) circuit. In constant vibration mode, the vibration amplitude of the cantilever was maintained to be constant [11]. In constant excitation mode, the excitation voltage supplied to the piezoelectric tube scanner for the cantilever oscillation was maintained to be constant [5]. The frequency shift $\Delta\nu$ of the cantilever resulting from the tip-sample force interaction was detected by a tunable analog FM demodulator.

As force sensors, conductive silicon cantilevers were used. A cantilever with a weak spring constant jumps into the sample surface when the force gradient being applied on the probing tip exceeds the spring constant of the cantilever. In order to suppress the jump of the cantilever into the sample surface and hence to avoid crushing the initial sharp tip, we used cantilever stiffer than that used in the contact mode (typically less than 1N/m). Its spring constant and mechanical resonant frequency were k=41 - 46 N/m and ν_0=158 - 172 kHz, respectively. Nominal radii of curvature of the tips were 5-10 nm. The Q factor of the cantilever was estimated to be about 38000. Since the oxide surface of the conductive silicon cantilever was not removed, the surface of the tip was covered with a nonconductive thin oxide layer. No bias voltage was applied between tip and surface.

AFM measurements were performed at room temperature under a pressure lower than 4×10^{-10} Torr. The samples were Fe-doped InP(001), Si-doped GaAs(001) and Si(111) wafers. InP(001) and GaAs(001) wafers were cleaved parallel to the {110} faces, and Si(111) wafer was annealed at 1200°C by the direct heating method for surface cleaning. The AFM images were taken under the variable force gradient mode. That is, during the scan, the distance between tip and surface was controlled to keep the mean frequency shift $<\Delta\nu>$ at constant level under the weak feedback condition, and AFM images were obtained from the frequency shift $\Delta\nu$.

3. RESULTS AND DISCUSSION

3.1 Comparison between constant excitation mode and constant vibration mode

In order to investigate the force interaction in the different operation modes, we compared with the constant excitation mode and the constant vibration mode. Figures 2(a) and 2(b) show the distance dependence of the frequency shift $\Delta\nu$ and the vibration amplitude of the cantilever

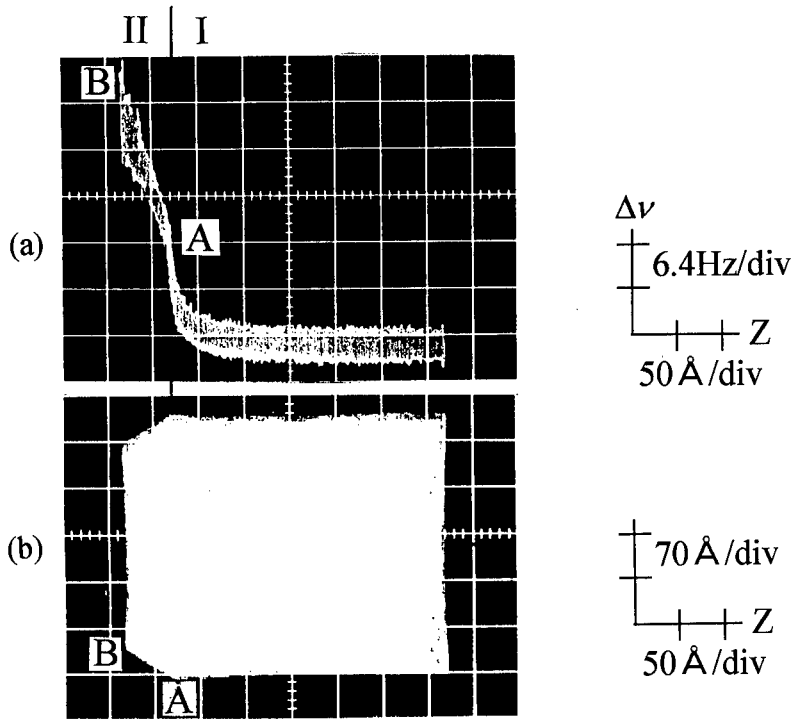


Fig. 2. In constant excitation mode, (a) frequency shift $\Delta\nu$ and (b) vibration amplitude of the cantilever as a function of the distance Z between tip and GaAs(110) surface. Spring constant and mechanical resonant frequency of the cantilever were k=46 N/m and ν_0=158 kHz, respectively. vibration amplitude A_0=190Å.

simultaneously measured in the constant excitation mode, respectively. Figures 3(a) and 3(b) show the distance dependence of the frequency shift $\Delta\nu$ of the cantilever and the excitation voltage supplied to the piezoelectric tube scanner for cantilever oscillation simultaneously measured in the constant vibration mode, respectively. In Figs. 2(a) and 3(a), upward and downward movements on the vertical axis of the frequency shift correspond to the increase and the decrease in attractive force gradient F', respectively. Initial vibration amplitude A_0 of the cantilever without the force interaction between tip and sample was set to be about 190Å in both operation modes. Sample was GaAs(110) surface.

In the constant excitation mode in Fig. 2, the vibration amplitude of the cantilever was held constant until point A (region I), and then decreased almost linearly from point A (region II). The frequency shift slowly and then quickly increased until point A (region I), but rather slowly increased from point A (region II). The distance dependence of the frequency shift in region I is attributed to the attractive van der Waals force and/or the attractive electrostatic force induced by the contact potential (the difference in work function) between tip and sample. It should be noted that in region I, the weak distance dependence are due to the long-range force interaction independent on the lateral position over the sample, while the strong distance dependence are due to the short-range force interaction containing the information on the atomic structure of the sample [6]. In region II, the vibration amplitude of the cantilever decreased and the distance dependence of frequency shift became weak. This behavior in region II is due to cyclic repulsive

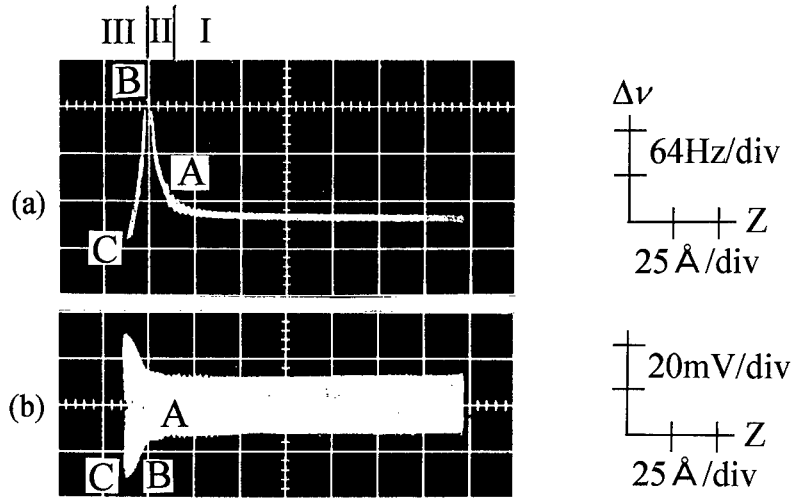


Fig. 3. In constant vibration mode, (a) frequency shift $\Delta\nu$ of the cantilever and (b) excitation voltage supplied to piezoelectric tube scanner as a function of the distance Z between tip and GaAs(110) surface. k=46 N/m, ν_0=158 kHz and A_0=190Å.

contact between tip and surface with loss of the energy stored in the oscillating cantilever.

In the constant vibration mode in Fig. 3, on the other hand, the excitation voltage supplied to the piezoelectric scanner was held almost constant until point A (region I), and slowly increased from point A to point B (region II), then quickly increased from point B (region III). The frequency shift slowly and then quickly increased until point A (region I), and further quickly increased from point A to point B (region II), then quickly decreased from point B (region III). It is found from other data that region I in Fig. 3 is coincident with the region I in Fig. 2, although it is impossible to distinguish the each region with high accuracy in Fig. 3. The distance dependence of the frequency shift in region I are also attributed to the attractive electrostatic force induced by the attractive van der Waals force and/or the contact potential between tip and sample. In region II, the excitation amplitude increased and the frequency shift quickly increased. In region III, the excitation amplitude quickly increased and the frequency shift quickly decreased. This behavior in regions II and III is due to weak and strong repulsive contact between tip and surface.

Thus, if the tip accidentally touch the surface in noncontact AFM imaging, in the constant excitation mode the repulsive force interaction between tip and surface will be weakened because of the decrease of the vibration amplitude of the cantilever, while in the constant amplitude mode the repulsive force interaction will be maintained. This means that the constant excitation mode AFM is much more gentle than the constant vibration mode AFM.

Next, we investigated the contrast of the AFM image as a function of the frequency shift in the constant excitation mode. In Fig. 4(a), we show the measured AFM image on InP(110) surface. Fast scan direction was from left to right, and slow scan direction was from bottom to top. Initial vibration amplitude A_0 was about 240 Å. As shown in Fig. 4(b), the frequency shift was linearly changed from $\Delta\nu$=19 Hz to $\Delta\nu$=6 Hz. It should be noted that the distance between tip and surface in region II was largely changed because of the weak distance dependence of the frequency shift. Here, regions I, I' and II in Fig. 4(a) correspond to the regions I, I' and II in Fig. 4(b), respectively. We can see that the image contrast strongly depends on the frequency shift. That is, the image contrast is strong in region II, but becomes weak in transition region from II to I', and again becomes strong in region I', then disappears in region I. Interestingly, even in region II where the tip is in cyclic repulsive contact with surface, strong contrast with atomic structure has been obtained.

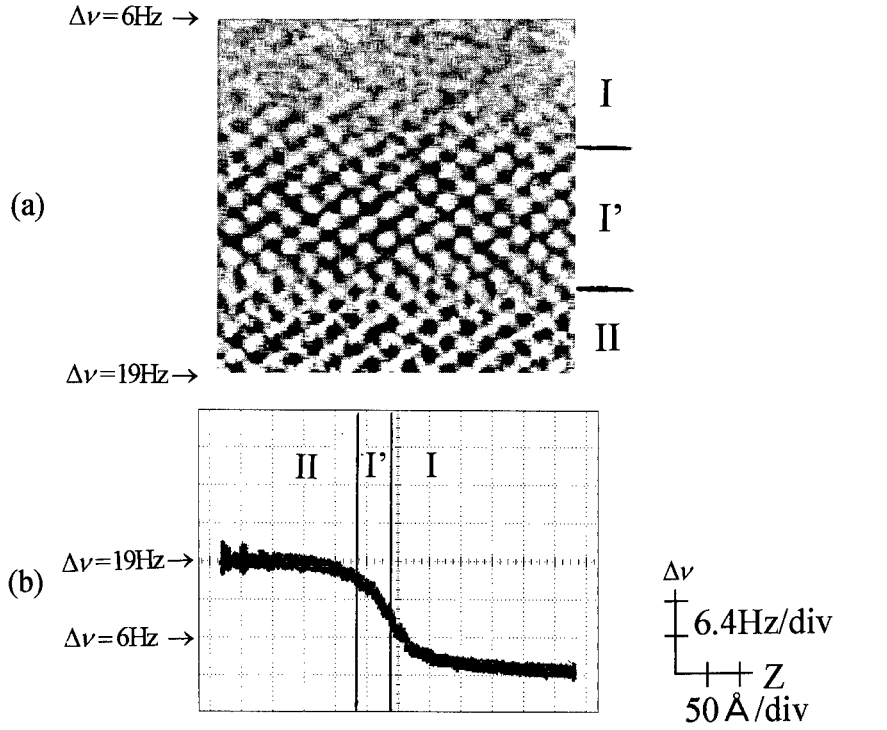


Fig. 4. (a) AFM image on InP(110) surface measured in constant excitation mode while the frequency shift was changed from $\Delta\nu$=19 Hz to $\Delta\nu$=6 Hz. Scan area is 70 Å × 70 Å. (b) Frequency shift $\Delta\nu$ as a function of distance between tip and surface. k=45 N/m, ν_0=169 kHz and A_0=240Å.

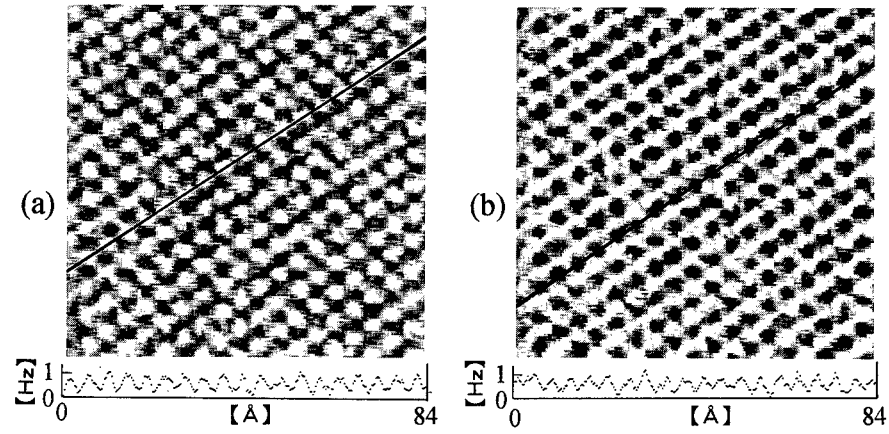


Fig. 5. AFM images of the InP(110) surface observed at frequency shift of (a) $\Delta\nu$=12 Hz and (b) $\Delta\nu$=19 Hz.

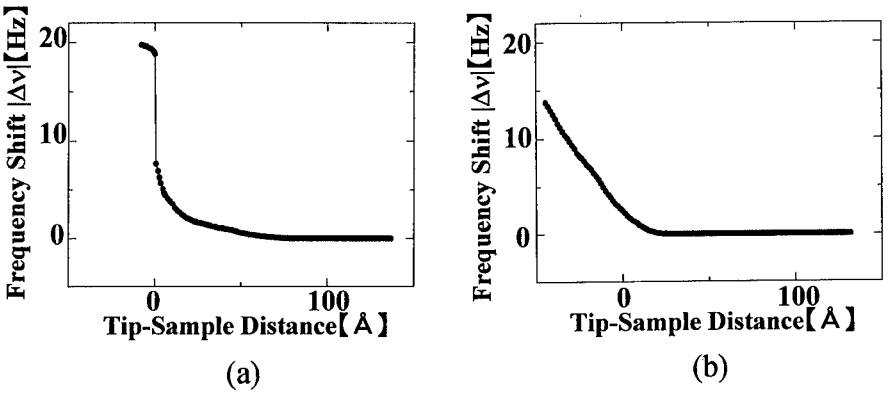


Fig. 6. Two types of force gradient curves (a) with and (b) without the discontinuity measure on reactive Si(111)7×7 reconstructed surface.

In Figs. 5(a) and 5(b), we show the AFM images of the InP(110) surface observed in noncontact region I' and in the contact region II, respectively. The rectangular lattice is clearly resolved in the entire scan area in both contact and noncontact regions. From the cross-sectional profiles, the measured variations of the frequency shift were estimated to be about 0.9 Hz in noncontact region I' and about 0.8 Hz in contact region II, respectively. Recently, it has been reported that atomic resolution imaging in the contact region is possible using dynamic mode UHV-AFM, in which tip-sample distance is controlled under slow feedback condition by point contact current or attractive electrostatic force superimposed on repulsive force of Pauli exclusion principle [12,13]. However, in the constant excitation mode, without the point contact current or the superimposed attractive electrostatic force, atomic resolution imaging is possible not only in the noncontact region but in the contact region.

3.2 Si(111) 7×7 reconstructed surface

We carefully investigated the distance dependence of the force gradient F' acting on the tip to clarify the force interaction between tip and reactive Si(111)7×7 reconstructed surface. Here, the constant excitation mode was used. As shown in Figs. 6(a) and 6(b), we found that the two types of force gradient curves have been obtained. In Fig. 6(a), the frequency shift $\Delta\nu$ at first increased slowly and then increased discontinuously and again increased slowly when the tip approached the surface. Here, frequency shift for the distance Z<-10 Å was not measured to avoid the degradation of the initial sharp tip, because the frequency shift $\Delta\nu$ became considerably unstable due to intensive interaction between tip and surface. We confirmed that there was no jump of the cantilever deflection. As far as we know, there is no report on the discontinuity of the force gradient curve on the Si(111)7×7 surface. In Fig. 6(b), on the other hand, the frequency shift $\Delta\nu$ increased monotonously when tip approached the surface. Similar tendency of the force gradient curve is generally obtained for the relatively inert InP(110) and GaAs(110) surfaces without dangling bonds near Fermi level, like Fig. 2(a). This suggests that this discontinuity of the frequency shift seems to be caused by covalent bonding (chemical bonding) between tip and reactive surface.

In Figs. 7(a) and 8(a), we show the noncontact AFM images of the Si(111)7×7 surface. Figs. 7(a) and 8(a) are for the force gradient curves with and without discontinuity, respectively. In both images, the individual adatoms and the corner holes in the 7×7 reconstruction, described by the dimer-adatom-stacking fault (DAS) model [14] and also missing adatoms, can be observed. A strong contrast has been obtained in Fig. 7(a), while weak contrast has been obtained in Fig. 8(a). Thus, the image contrast is drastically increased by the presence of the discontinuity of the force

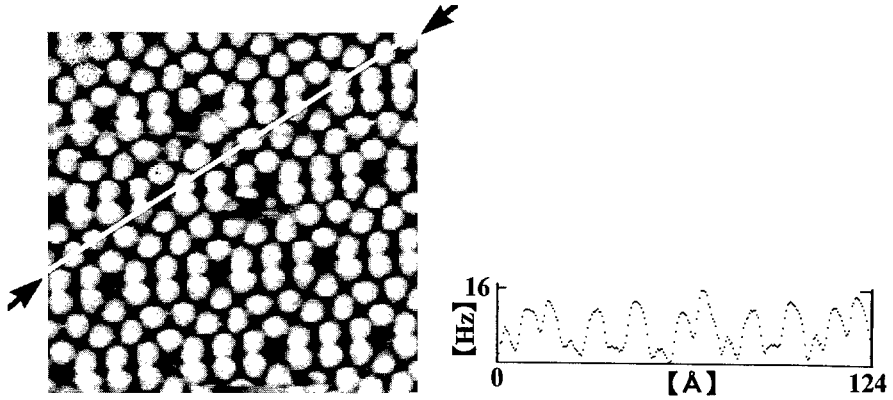


Fig. 7 (a) AFM image and (b) cross-sectional profile on Si(111) 7×7 reconstructed surface with the discontinuity of force gradient curve. The scan area was 102Å×102Å. k=41 N/m, ν_0=172 kHz, $<\Delta\nu>$=13 Hz and A_0=188Å.

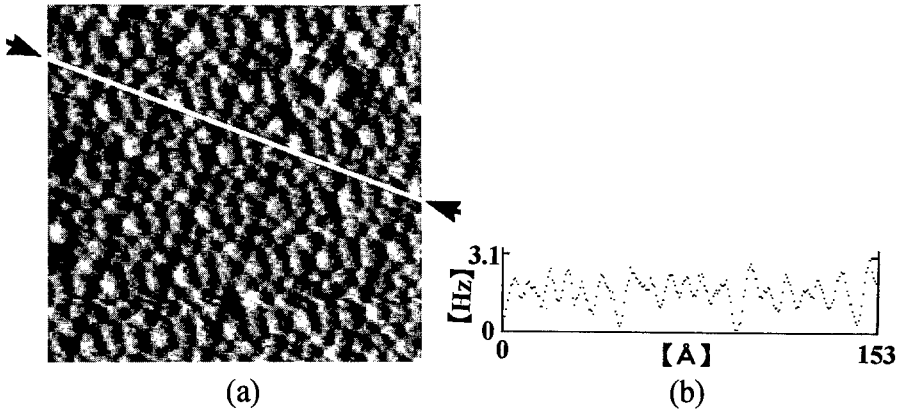


Fig. 8 (a) AFM image and (b) cross-sectional profile on Si(111) 7×7 reconstructed surface without the discontinuity of force gradient curve. The scan area was 121Å×121Å. k=41 N/m, ν_0=172 kHz, $<\Delta\nu>$=4.4 Hz and A_0=209Å.

gradient curve.

In Figs. 7(b) and 8(b), we show the cross-sectional profile along the long diagonal of the 7×7 unit cell. This cross sections indicate the frequency shift above the corner holes and the four equivalent adatoms, allowing the detailed comparison of the contrast observed in the noncontact AFM images. The frequency shift along the long diagonal of the 7×7 unit cell are estimated to be about 15 Hz in Fig. 7(b) and about 3 Hz in Fig. 8(b), respectively. Thus, the frequency shift with the discontinuity is five times larger than that without discontinuity. This means that the interaction with the discontinuity of the frequency shift give a very significant contribution of the contrast of the noncontact AFM images.

The discontinuity of the frequency shift in the above experiments can be explained by

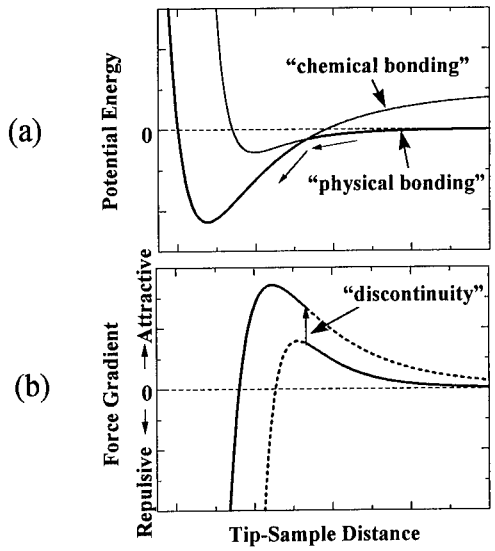


Fig. 9. Model to explain the discontinuity of the force gradient curve measured on Si(111) 7×7 reconstructed surface. (a) Potential energy curves for the physical and chemical bonding interactions. (b) Discontinuity of force gradient curve at the crossover between the physical and chemical bonding interactions.

considering the crossover between the physical and chemical bonding interactions. Figure 9(a) represents the potential energy curves for the physical and chemical bonding interactions. Here, the physical bonding interactions are due to the van der Waals and/or electrostatic interactions, while the chemical bonding interaction is due to the covalent bonding interaction. The range of the physical bonding interaction is long, while the range of the chemical bonding interaction is short. Furthermore, the potential energy minimum for the chemical bonding interaction is closer to the surface and deeper than that for the physical bonding interaction. So, the potential energy curves for the physical and chemical bonding interactions intersect each other. If tip covered with unreactive thin oxide layer approaches the Si(111)7×7 surface, tip-sample interaction will be almost dominated by the physical bonding interaction. On the other hand, if tip with reactive dangling bond approaches the Si(111)7×7 surface, far from the intersect point, tip-sample interaction will be also dominated by the physical bonding interaction. However, nearer the intersect point, chemical binding between the dangling bond out of the tip apex atoms and the dangling bond in the adatoms will occur, and hence tip-sample interaction will be dominated by the chemical bonding interaction. In the latter case, as shown in Fig. 9(b), discontinuous increase of the frequency shift (force gradient) will occur at the intersect point. It is well known that tip happens to pick up Si atoms from the surface. So, the discontinuity will be originated from the covalent bonding between the dangling bond out of Si atoms picked up on tip and the dangling bond in the adatoms on Si(111)7×7 reconstructed surface. This means that the strong image contrast in Fig. 7(b) is due to a variation in the chemical reactivity of the adatoms on the Si(111)7×7 reconstructed surface, while the weak image contrast in Fig. 8(a) is due to a variation in the van der Waals and/or electrostatic force interaction.

4. CONCLUSIONS

We compared with the constant vibration mode and the constant excitation mode to

investigate the force interaction in the different operation modes. When the tip touch the surface, the repulsive force interaction is weakened in the constant excitation mode because of the decrease of the vibration amplitude of the cantilever, while it is maintained in the constant amplitude mode. This means that the constant excitation mode is much more gentle than the constant vibration mode. We also succeeded in atomic resolution imaging on InP(110) surface not only in the noncontact region but in the contact region for the first time. We found the discontinuity of the force gradient curve on reactive Si(111)7×7 reconstructed surface. The discontinuity of the force gradient curve can be explained by the crossover between the physical and chemical bonding interaction.

ACKNOWLEGHMENTS

The authors would like to thank Mr. S. Mishima of Olympus Optical Co., Ltd. for construction of the AFM units. A part of this work was supported by a Grant-in-Aid for Scientific Research from the Ministry of Education, Science, and Culture.

REFERENCES

1. G. Binnig, C.F. Quate, and Ch. Gerber, Phys. Rev. Lett. **56**, 930 (1986).
2. G. Binnig, Ultramicroscopy **42-44**, 281 (1992).
3. F. Ohnesorge, and G. Binnig, Science **260**, 1451 (1993).
4. F.J. Giessibl, Science **267**, 68 (1995).
5. S. Kitamura, and M. Iwatsuki, Jpn. J. Appl. Phys. **34**, L145 (1995).
6. Y. Sugawara, H. Ueyama, T, Uchihashi M. Ohta, S. Morita, N. Suzuki and S. Mishima, Appl. Surf. Sci.(accepted for publication).
7. H. Ueyama, M. Ohta, Y. Sugawara and S. Morita, Jpn. J. Appl. Phys. **34**, L1086 (1995).
8. Y. Sugawara, M. Ohta, H. Ueyama and S. Morita, Science, **270**, 1646 (1995).
9. M. Ohta, Y. Sugawara, S. Morita, H. Nagaoka, S. Mishima, and T. Okada, J. Vac. Sci. Technol. B **12**, 1705 (1994).
10. D. Rugar, H.J. Mamin, P. Guethner, Appl. Phys. Lett. **55**, 2588 (1989).
11. T.R. Albrecht, P. Grütter, D. Horne, and D. Rugar, J. Appl. Phys. **69**, 668 (1991).
12. P. Güthner, J. Vac. Sci. Technol. B **14**, 2428 (1996).
13. R. Lüthi, E. Meyer, M. Bammerlin, A. Baratoff, T. Lehmann, L. Howald, Ch. Gerber and H.-J.Güntherodt, Z. Phys. B **100**, 100 (1996).
14. K. Takayanagi, Y. Tanishiro, M. Takahashi and S. Takahashi, J. Vac. Sci. Technol. A **3**, 1502(1985).

OPTICAL NMR FROM SINGLE QUANTUM DOTS

S. W. BROWN, T. A. KENNEDY, and D. GAMMON
Naval Research Laboratory, Washington, DC 20375.

ABSTRACT

We have observed nuclear magnetic resonance (NMR) signatures from constituent Ga and As nuclei in single GaAs quantum dots formed by interface fluctuations in GaAs/AlGaAs quantum wells. Orientation of the nuclear spin system by optical pumping causes an Overhauser shift in the excitonic energy levels proportional to the degree of nuclear orientation. NMR was detected by monitoring changes in the combined Overhauser plus Zeeman splitting of an exciton localized in a single quantum dot as the RF frequency was swept through a nuclear resonance. The NMR signals originate from ~10^5 nuclei in the quantum dot — (20 nm)^3 volume — representing an increase in sensitivity of five orders of magnitude over previous optical NMR measurements and thirteen orders of magnitude over conventional NMR. The data were fit to Lorentzian lineshapes, giving ^{75}As linewidths on the order of 20 kHz.

INTRODUCTION

Advances in nanocrystal fabrication and in lithographic processing techniques have enabled elegant and detailed studies of the optical and electronic properties of single quantum dots and nanocrystals [1,2]; however, the underlying physical structure and its contribution to the measured optical and electronic properties have been neglected to a large extent [3,4]. Nuclear magnetic resonance (NMR) measurements can provide strain, symmetry and chemical information about the local structural quantum dot environment, complementing studies of the optical and electronic properties. Limitations inherent to conventional NMR preventing its application to the study of single quantum dots are surmounted with optical NMR. To optically detect NMR, the optical properties of the system must change in some measurable fashion when an external RF field is in resonance with a nuclear transition. In this work, NMR spectra were obtained by monitoring changes in the Overhauser shift of excitonic energy level splittings as an RF field was swept through resonance. ^{75}As NMR spectra from single quantum dots are presented. These signals, originating from ~10^5 nuclei in a (20 nm)^3 volume, may represent the most sensitive NMR measurements reported to date.

Because this is a novel approach to the detection of NMR, we briefly review the Overhauser shift of electronic energy levels. In general, the hyperfine interaction between a delocalized electron and a single nucleus produces a negligible energy shift. However, large, readily observable Overhauser shifts of electronic energy levels can arise from the interaction of a large number of oriented nuclear spins — in this case created by optical pumping — with an electron. For electrons with s-like wavefunctions — as is the case for electrons in the bottom of the conduction band in GaAs — only the Fermi contact interaction, proportional to the electron density at the nucleus, needs to be considered. In this case, summing the contribution of all nuclei N within the electronic wavefunction Ψ_e, the Overhauser shift of the electron energy levels can be written as:

$$\Delta E_{OH} = \frac{8\pi}{3}\hbar^2\gamma_e\left[\sum_N |\Psi_e(r_N)|^2\gamma_N I_N\right]S_z, \qquad (1)$$

where I_N is the nuclear spin, S_Z the electronic spin, and γ_e and γ_N the electronic and nuclear gyromagnetic ratios, respectively.

Mat. Res. Soc. Symp. Proc. Vol. 442 © 1997 Materials Research Society

The electron wavefunction can be expressed as the product of a spatially extended envelope function $\phi_e(\vec{R})$ and a rapidly varying cell periodic part $u_o(\vec{r})$. Assuming a uniform nuclear polarization and separating the contribution to the Overhauser shift from different nuclei α, equ. (1) can be expressed as:

$$\Delta E_{OH} = \frac{8\pi}{3}\hbar^2\gamma_e\left(\Sigma_\alpha \gamma_{N_\alpha} \langle I\rangle_\alpha |u_o(r_\alpha)|^2\right)S_z, \qquad (2)$$

where $\langle I\rangle_\alpha$ is the ensemble-averaged spin polarization of one of the constituent nuclei and $|u_o(r_\alpha)|^2$ is the cell-periodic electron density at the nucleus α [5]. Thus, while individual nuclear contributions to the Overhauser shift depend on the magnitude of the envelope function of the electron — and hence on details of the electron localization — the total Overhauser shift for a particular nuclear species does not depend on the size of the quantum dot.

For the measurements presented in this work, it is convenient to express the Overhauser shift in terms of the nuclear magnetization $M_Z = N\gamma_N \langle I\rangle_z$, where N is the number of nuclear spins. The Overhauser shift from a particular nuclear species can be written:

$$\Delta E_{OH} = \Gamma_\alpha M_{\alpha z} S_z, \text{ where } \Gamma = \frac{1}{N_\alpha}\frac{8\pi}{3}\hbar^2\gamma_e|u_o(r_\alpha)|^2. \qquad (3)$$

Considering only spin-dependent terms, the total energy splitting for an exciton in an external magnetic field can be expressed as:

$$\Delta E_{total} = g^* \mu_B B_o + \sum_\alpha \Gamma_\alpha M_{\alpha z}. \qquad (4)$$

The first term, linear in applied magnetic field, describes the Zeeman interaction, with g* the exciton g-value and μ_B the Bohr magneton; the second term describes the Overhauser shift of the electron energy levels arising from orientation of the nuclear system. Depending on the polarization of the incident light (through the optical selection rules), the Overhauser shift will add to or subtract from the Zeeman splitting, leading to differences in the observed excitonic splittings. These effects are shown schematically in Fig. 1.

EXPERIMENT

The sample consists of a series of five single GaAs/AlGaAs quantum wells with widths varying from 3 to 15 nm, grown by MBE under conditions promoting the development of large monolayer-thickness, nanometer-size islands at each interface [6]. Potential differences arising from these monolayer thickness fluctuations confine the excitons in the plane of the quantum well; excitons are therefore confined in all three dimensions in these islands. To observe luminescence from single islands — or quantum dots — the excitation volume was reduced by lithographically creating small apertures in an opaque aluminum film previously deposited on the sample. Luminescence corresponding to exciton recombination from individual quantum dots was spectrally resolved when the sample was excited through apertures smaller than 5 μm [1,7]. Results are presented in this work for excitons localized in a 4.2 nm quantum well, excited through a 1.5 μm aperture (Fig. 2).

The sample was placed in the bore of a superconducting magnet between a 4 turn Helmholz coil capable of generating RF fields as high as 5 G. The sample temperature (~ 6 K)

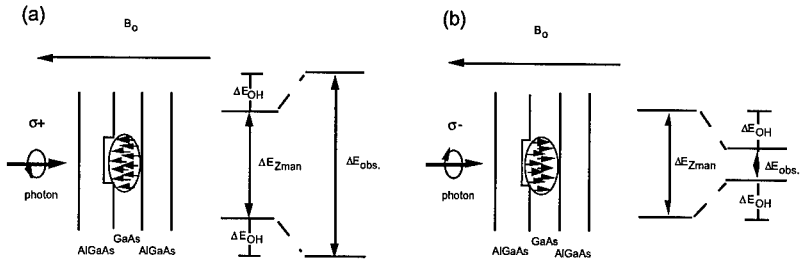


Fig. 1. Schematic diagram of the Overhauser shift of excitonic Zeeman splittings. (a) For σ^+ polarization, nuclear moments (arrows) within the envelope wave function of the exciton (solid oval) are aligned parallel to the external magnetic field B_O and the Overhauser shift adds to the Zeeman splitting. The resultant excitonic splitting is illustrated on the right. (b) The opposite effect occurs for σ^- excitation. In this case, the nuclear moments are aligned anti-parallel to the external magnetic field, the Overhauser shift opposes the Zeeman splitting, and a reduced excitonic splitting is observed.

was maintained by continuously flowing cold He gas over the sample. Measurements were taken in a standard backscattering geometry (Fig. 2 inset), with the magnetic field parallel to the wave vector of the incident and scattered radiation (Faraday geometry). Luminescence was excited with circularly polarized light from a Ti:sapphire laser, dispersed by a triple grating spectrometer and detected by a liquid nitrogen-cooled CCD array.

RESULTS AND DISCUSSION

Polarization-dependent differences in excitonic splittings from single quantum dots attributed to the Overhauser effect have been recently observed [8], as shown in Fig. 2(inset). For σ^+ excitation, the nuclear magnetization is such that the Overhauser shift increases the excitonic splitting. The sign of the nuclear magnetization is reversed when the sample is excited with σ^--polarized light and the Overhauser shift now opposes the Zeeman interaction, resulting in a reduced excitonic splitting.

To demonstrate the principle of the detection scheme, the RF was swept through the resonant frequencies of all three constituent nuclei within the quantum dot — ^{69}Ga, ^{71}Ga, and ^{75}As — at a rate of two Hz. Under these conditions, some degree of the nuclear magnetization is canceled and the measured excitonic splitting is reduced, as clearly shown in Fig. 3(a). Finally, in Fig. 3(b), the energy level splitting of the exciton is plotted as the RF frequency was stepped through the ^{75}As resonance. As expected (Fig. 1(a)), a decrease in the energy of the upper level and an increase in the energy of the lower level are observed as the magnetization is reduced when the RF frequency is close to the ^{75}As resonance frequency (~7.275 MHz).

In Fig. 4, the magnitude of the excitonic splitting is plotted the RF frequency is stepped through the ^{75}As resonance. A least-squares fit of the data to a Lorentzian functional form gave a ^{75}As NMR linewidth for this quantum dot of 22 ± 2 kHz in an external magnetic field of 1.0 T and 22± 3.5 kHz in an external field of 2.5T. The linewidths, an order of magnitude larger than measured dipolar linewidths in bulk GaAs [9], are most likely a consequence of the hyperfine interaction, though effects of RF power broadening may also contribute to the increased linewidths [10].

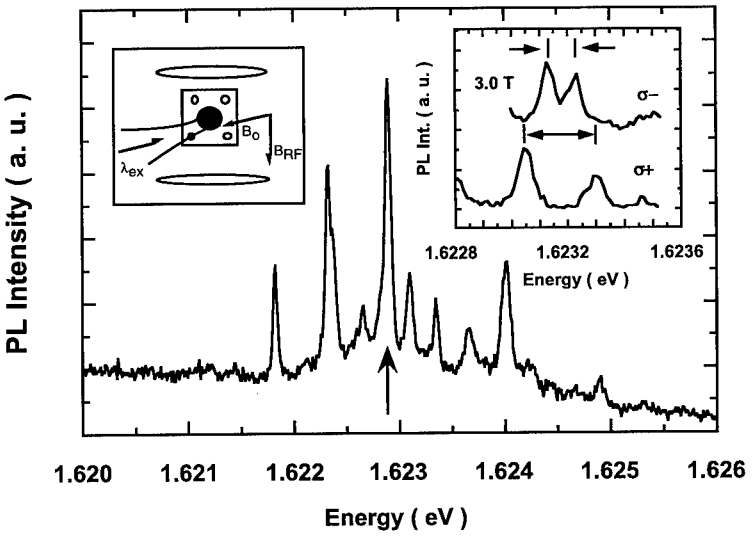


Fig. 2. Low temperature (6 K) PL spectrum from a 4.2 nm quantum well excited through a 1.5 μm aperture. Left inset: Schematic diagram of the experimental setup. The patterned sample is placed in a magnet between a pair of Helmholz coils such that the DC and RF magnetic fields are perpendicular to one another. The sample is excited along the DC field direction; luminescence is collected in a backscattering geometry. Note that while the laser spot size may be much larger than the aperture, the excitation and collection volumes are still defined by the size of that aperture. Right inset: Polarization-dependent differences in the measured excitonic splittings of the quantum dot indicated by the arrow. These data were taken in a magnetic field of 3.0 T. The slight shift in luminescence energy from the 0 T data is attributed to the magnetic field dependent diamagnetic shift.

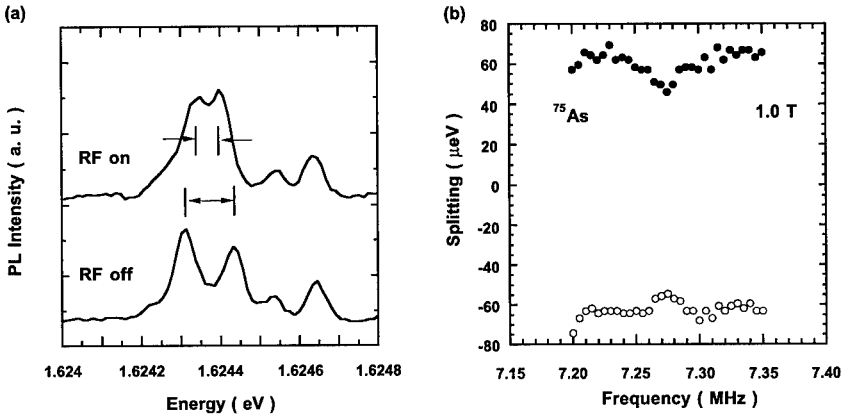


Fig.3. (a) Single quantum dot PL spectra — σ^+ excitation — in an external field of 1.0 T. A reduction in measured excitonic splittings is clearly observed when an RF field is swept through all three nuclear resonances at a rate of 2 Hz. (b) Splitting of the two excitonic energy levels as the RF field is stepped through the ^{75}As resonance.

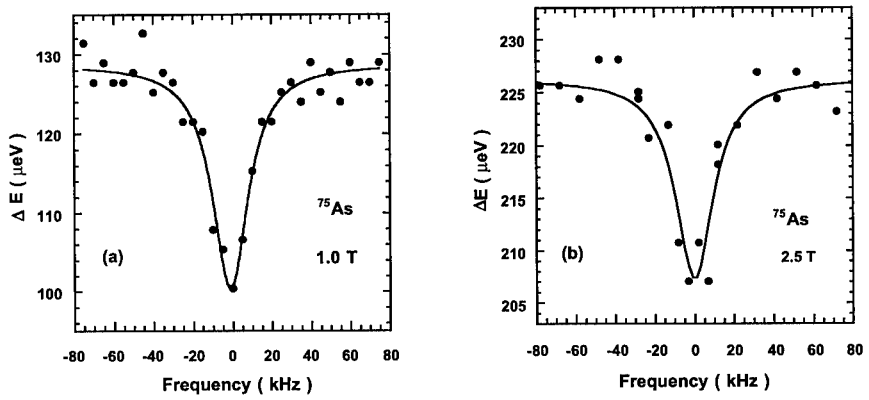


Fig.4. (a) ^{75}As NMR spectrum for σ^+ excitation in an external magnetic field of 1.0 T. The frequency offset was 7.274 ± .001 MHz. (b) ^{75}As NMR spectrum for σ^+ excitation in an external magnetic field of 2.5 T. The frequency offset was 18.208 ± .001 MHz. Solid lines are Lorentzian fits to the data.

Finally, frequency shifts on the order of tens of kHz and differences in NMR lineshape have been observed from spectrally distinct quantum dots [10]. These differences must correspond to differences in the local quantum dot environment, illustrating the point that the quantum dots serve as probes of the local environment on the nanometer scale.

CONCLUSIONS

In conclusion, we report the observation of ^{75}As NMR from single quantum dots. These data, originating from ~10^5 nuclei within a ~$(20\ nm)^3$ volume, are five orders of magnitude more sensitive than previously reported optical NMR measurements. The results presented in this work, combined with recent optically-detected electron spin resonance (ODESR) measurements from a single molecule [11,12], suggest that nuclear magnetic resonance from single impurities or molecules may be possible.

ACKNOWLEDGMENTS

We would like to acknowledge and thank B. V. Shanabrook, E. S. Snow, S. Walck, Al. L. Efros and M. Rosen for thoughtful and insightful discussions; M. Goldenberg and D. S. Katzer for the growth of the sample; and D. Park and the NRL Nanoprocessing Facility for patterning the material. This work was supported, in part, by the Office of Naval Research. S. W. Brown is an NRL/NRC research associate.

REFERENCES

[1] D. Gammon, E. S. Snow, B. V. Shanabrook, D. S. Katzer, and D. Park, Science **273**, 87 (1996); Phys. Rev. Lett. **76**, 3005 (1996).
[2] S. A. Empedocles, D. J. Norris, and M. G. Bawendi, Phys. Rev. Lett. **77**, 3873 (1996).
[3] A. M. Thayer, M. L. Steigerwald, T. M. Duncan, and D. C. Douglass, Phys. Rev. Lett. **60**, 2673 (1988).
[4] L. D. Potter, A. A. Guzelian, A. P. Alivisatos, and Y. Wu, J. Chem. Phys. **103**, 4834 (1995).
[5] D. Paget, G. Lampel, B. Sapoval, and V. I. Safarov, Phys. Rev. B **15,** 5780 (1977).
[6] D. Gammon, B. V. Shanabrook, and D. S. Katzer, Phys. Rev. Lett. **67**, 1547 (1991).
[7] D. Gammon, E. S. Snow, and D. S. Katzer, Appl. Phys. Lett. **67**, 2391 (1995).
[8] S. W. Brown, T. A. Kennedy, D. Gammon, and E. S. Snow, Phys. Rev. B (in press).
[9] R. G. Shulman, B. J. Wyluda, and H. J. Hrostowski, Phys. Rev. **109**, 808 (1958).
[10] S. W. Brown, D. Gammon and T. A. Kennedy, in preparation.
[11] J. Wrachtrup, C. v. Borczyskowski, J. Bernard, M. Orrit, and R. Brown, Phys. Rev. Lett. **71**, 3565 (1993).
[12] J. Koehler, A. C. J. Brouwer, E. J. J. Groenen, J. Schmidt, Science **268**, 1458 (1995).

LOW-TEMPERATURE INFRARED ABSORPTION MEASUREMENT FOR OXYGEN CONCENTRATION AND PRECIPITATES IN HEAVILY-DOPED SILICON WAFERS

M. KOIZUKA, M. INABA, and H. YAMADA-KANETA
Device Development Div., Fujitsu Ltd. 4-1-1 Kamikodanaka,
Nakahara-ku, Kawasaki 211-88, Japan

Abstract

We present a new IR absorption technique of measuring the dissolved interstitial oxygen concentration [O_i] and its reduction Δ [O_i] due to oxygen precipitation of the heavily-doped silicon crystal with doping level of about 10^{19} atoms/cm^3. The method consists of the three steps: bonding the silicon wafer to a thick FZ silicon substrate by heat-treatment, thinning the wafer, and measuring the height of the 1136-cm^{-1} absorption peak of O_i at a temperature below 5 K. For a heavily doped wafer and the heavily doped substrate of an epitaxial wafer, we demonstrate examples of measuring the initial [O_i] and Δ [O_i] due to heat-treatment. Using this method, we investigate oxygen precipitation characteristics of the wafer heavily doped with boron. We found that the enhanced oxygen precipitation due to heavy boron-doping is expected if we perform preanneal at temperatures below 700 ℃.

I. Introduction

As the integration grade of the silicon devices progresses, the production yield is becoming more and more sensitive to the crystal defects near the silicon wafer surface, e.g., the octahedral-structure gigantic defects [1] and the oxygen precipitates. A direct way of avoiding troubles arising from these near-surface defects is to use the epitaxial wafers, which is becoming popular nowadays even for the memory devices as well as for the logic devices. As the substrates of these epitaxial wafers, the heavily doped silicon with resitivity of about 0.01 Ωcm is often employed. Although the substrates heavily doped with boron have rather strong gettering power for particular metal impurities [2], we still have to rely upon the gettering by oxygen precipitates which is effective to other kinds of metal contaminants. Therefore, to optimize the dissolved interstitial oxygen concentration ([O_i]) and the device fabrication processes, we have to precisely evaluate the [O_i] and its reduction Δ [O_i] during heat-treatment.

However, the [O_i] of these heavily doped substrates can not be measured by the conventional room-temperature (RT) infrared (IR) absorption method using the 1106-cm^{-1} absorption peak. This is because of the strong free carrier absorption. To avoid this problem, a few trials have been made: (1) the RT IR absorption method for the 0.2-mm thick sample doped with Sb to a doping level of 2 x 10^{18} atoms/cm^3 [3], and (2) the RT IR absorption method for the Sb-doped sample heavily irradiated with electron beam [4]. The first method would fail for the p-type sample with higher doping level of 1.0 x 10^{19} cm^{-3}. The second technique is limited to the n-type material. The secondary ion mass spectroscopy and the gas fusion analysis are often adopted for the oxygen content measurements. However, these methods can not distinguish the dissolved interstitial oxygen (O_i) and the oxygen in the precipitates.

In this article we show a new IR absorption method of measuring [O_i]. This method is applicable to high doping level of about 1.0 x 10^{19} cm^{-3} for both cases of p- and n-type dopants. We demonstrate an example of measuring [O_i] and Δ [O_i] of the heavily doped p-type substrates.

II. Low-Temperature Infrared Absorption Method for [O_i]

The free carrier absorption is reduced by reducing the sample thickness. For the B-doped wafer with a resistivity of about 0.01 Ωcm, however, we have to use very thin sample with thickness 10-20 μm, for which the RT 1106-cm^{-1} peak in fig.1 (a) becomes too weak to give sufficient measuring accuracy. This problem of peak-height reduction due to reducing sample thickness is resolved by using the low-temperature 1136-cm^{-1} peak of the O_i whose height at 4.2 K is about 35 times that of the RT 1106-cm^{-1} peak, as shown in fig.1. For low temperature range 20-70 K, the IR

Mat. Res. Soc. Symp. Proc. Vol. 442 © 1997 Materials Research Society

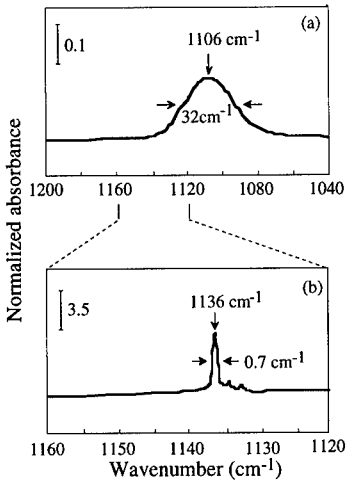


Fig.1. IR absorption peaks of the dissolved interstitial oxygen in silicon wafers measured at (a) room temperature with a resolution of 4 cm^{-1}, and (b) at 4.2K with a resolution of 0.25 cm^{-1}. The oxygen concentrations are 1.65 x 10^{18} atoms/cm^3 for both (a) and (b). Normalized absorbance means the absorbance per sample thickness of 1mm.

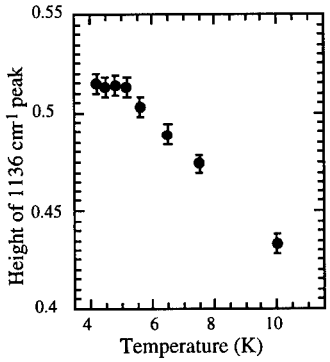


Fig.2. Measured temperature dependence of the height of the 1136cm^{-1} peak. Here, the peak-height means the peak absorbance relative to the baseline, see fig.1 (b).

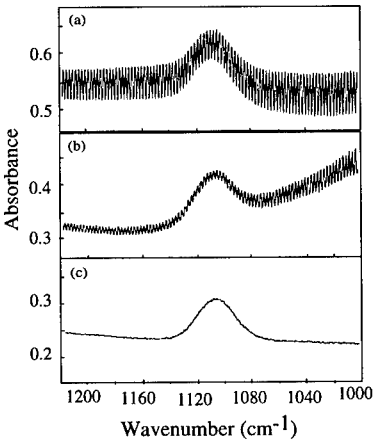


Fig.3. Reduction of interference pattern by bonding thin sample to FZ substrate. Measurements were performed with a resolution of 0.25 cm^{-1} and an acqisition of 100 times. The spectra were taken for (a) the 500-μm thick CZ sample only, and the 500-μm thick CZ sample piled on the 5-mm thick FZ substrate (b) before and (c) after the heat-treatment bonding.

absorption peak of the O_i observed at 1106 cm^{-1} at RT splits into three peaks at about 1136, 1128 and 1122 cm^{-1} [5] which correspond to optical transitions from the ground, the first excited, and the second excited states, respectively [6, 7]. For temperatures lower than 8 K, the 1128- and 1122-cm^{-1} peaks vanish, and only the 1136-cm^{-1} peak is observed [8], reflecting the Boltsmann occupations for the vibrational energy levels [7,9]. The height of the 1136-cm^{-1} peak strongly depends on temperature in the range 10-50 K. Thus, the [O_i] measurement using the 1136-cm^{-1} peak at a temperature in this range encounters cumbersome problem of reducing the error and fluctuation of the measuring temperature. However, the height of the 1136-cm^{-1} peak is almost constant below 5 K, as shown in fig.2. Accordingly, it is convenient to use this temperature region for [O_i] measurement.

As shown in fig.1(b) the 1136-cm^{-1} peak is very sharp: The full width at half maximum is 0.6 cm^{-1} at 4.2 K [8]. This means that we need measurement resolution not lower than 0.1 cm^{-1}. Such high-resolution measurement for the thin sample of the thickness 10-20 μ m causes significant interference pattern on the spectrum due to multiple reflection of the IR beam in the sample. This problem is resolved by bonding the sample to the silicon substrate with a thickness of about 5 mm and low enough [O_i]. This substrate crystal is made by the floating zone (FZ) method. The bonding can be

accomplished by a heat-treatment at 1100 ℃ for 30 min in nitrogen ambient after cleaning the mirrored surfaces of the sample and the substrate. The condition of this heat-treatment bonding is the same for all experiments presented below. Figure 3 shows high-resolution IR absorption spectra measured for a 500- μ m thick sample only (fig. 3(a)), the superposed specimen of the this sample and the 5-mm thick substrate before (fig. 3(b)) and after (fig. 3(c)) the heat-treatment bonding. We see that the heat-treatment allows good bonding such that the interference pattern remaining before it disappears completely.

To summarize, our IR absorption method for $[O_i]$ comprises the three steps: bonding the sample onto a thick FZ silicon substrate by heat-treatment, thinning the sample, and measuring the height of the 1136-cm^{-1} peak at a temperature below 5 K.

III. Experiments

A. Conversion Constant

Here, we determine the conversion constant between the $[O_i]$ and the height of the 1136-cm^{-1} peak measured below 5 K. We used B-doped Czochralski-grown silicon wafer with a resistivity of 10 Ω cm and a thickness of 520 μ m. We first determined the $[O_i]$ of this wafer by the conventional RT IR absorption method using the 1106-cm^{-1} peak and the conversion constant 9.6 ppma/cm^{-1} (American Standard for Testing and Materials F121-79 procedure). The determined value of $[O_i]$ was 1.68 x 10^{18} atoms/cm^3. By means of the above-mentioned heat-treatment, we bonded this CZ wafer to the mirror-polished FZ-grown silicon substrate of the thickness 4988 μ m. From this bonded wafer, we cut out four specimens with the edge lengths of about 17 mm x 17 mm x 5.5 mm. By means of chemical etching and/or mechanical polishing (grinding), the CZ wafer part of the four specimens were thinned to the thicknesses of 11, 43, 61, and 94 μ m, respectively. At 4.2 K, we measured the height of the 1136-cm^{-1} peak of these specimens with the resolution 0.25 cm^{-1}. We adopted Happ-Genzel apodization for the Fourier transform. This condition of the peak-height measurement, i.e., the measuring temperature of 4.2 K, the resolution of 0.25 cm^{-1} and the Happ-Genzel apodization is employed for all experiments in this paper. Figure 4 shows the measured peak heights as a function of the thickness of the CZ wafer part. From the gradient of the line fit to the experimental plots in fig. 4, together with the preliminary measured value of the $[O_i]$, we obtained the conversion constant 3.33 x 10^{16} atoms/cm^2. As mentioned in Sec. II, our resolution 0.25 cm^{-1} is insufficient to accurately measure the true height of the 1136-cm^{-1} peak at 4.2 K. For this resolution, however, we could obtain good reproducibility for repeated measurements of the peak-height. Thus, for our present IR measurements performed with the same apparatus (JEOL JIR-100 Fourier transform spectrophotometer) and the above-mentioned fixed condition, we can use this value as a conversion constant.

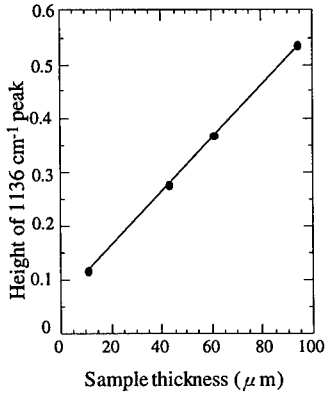


Fig.4. Measured height of the 1136 cm^{-1} peak as a function of the sample thickness.

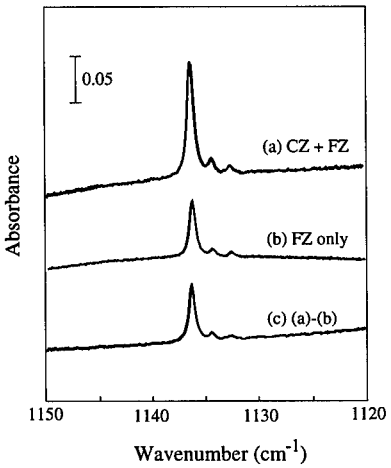


Fig.5. Infrared absorption spectra of (a) the 24-μ m thick CZ sample bonded onto 4991-μ m thick FZ substrate, (b) the 4991-μ m thick FZ substrate only, and (c) the difference spectrum of (a) - (b).

B. [O_i] Measurement for Heavily Doped Silicon Wafers

By using the above-mentioned low-temperature IR absorption method, the [O_i] of the FZ substrate was found to be 3 x 10^{15} atoms/cm^3. We bonded the B-doped CZ wafer with the resistivity 0.03 Ω cm and the thickness 520 μ m to an FZ substrate of the thickness 4991 μ m. We then thinned the CZ wafer part to a thickness of 24 μ m. Figures 5(a) and (b) show the 1136-cm^{-1} peak measured for the bonded specimen and for the FZ substrate only, respectively. By subtracting the latter spectrum from the former, we obtained the spectrum in fig. 5(c) which is the contribution from the heavily-doped CZ wafer part on the FZ substrate. It should be noted that the position (wave number) and the shape (FWHM) of the 1136-cm^{-1} peak of the heavily-doped crystal (fig. 5(c)) was unchanged from those of the conventional lightly-doped crystal. From the height of the 1136-cm^{-1} peak in fig. 5 (c) and the conversion constant determined above, we obtained [O_i] = (9.9 ± 0.5) x 10^{17} atoms/cm^3. The measurement error of the [O_i] for this case was estimated to be less than 5 %, which mainly comes from the measurement of the two peak-heights (Figs. 5(a) and (b)) and the measurement of the thickness of the CZ wafer part.

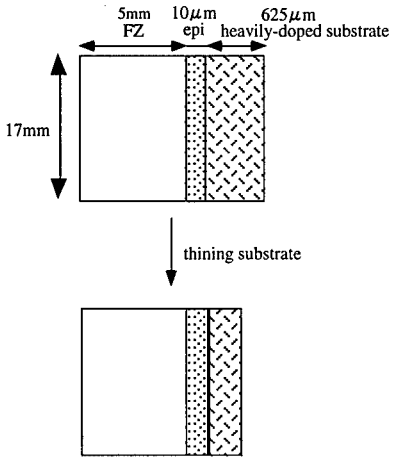


Fig.6. Schematic drawings of samples. The epitaxial layer thickness is 10 μ m.

C. [O_i] Measurement for Heavily Doped Substrate of Epitaxial Wafer

When the as-received heavily-doped substrate has lightly-doped epitaxial layer grown on it, the measurement procedure is somewhat modified. Here, we demonstrate the case of the epitaxial wafer composed of the heavily-doped (B-doped) substrate and the lightly-doped (B-doped) epitaxial layer with the resitivities of 0.01 Ω cm and 10 Ω cm, respectively. Their thicknesses are 625 μ m and 10 μ m, respectively. By the heat-treatment (Sec. II A), we first bond the surface of the epitaxial layer to a 5-mm thick FZ substrate, as illustrated in fig. 6. Next, after thinning the heavily-doped substrate to a thickness of 14 μ m, we measure the height of the 1136-cm^{-1} peak. By gradually thinning the heavily-doped substrate, we repeated this procedure for the substrate thicknesses of 10, 6 and 3 μ m. Figure 7 shows the 1136-cm^{-1} peak observed for each substrate thickness. With reducing the thickness of the heavily-doped substrate, the slope of the spectrum baseline, as well as the 1136-cm^{-1} peak, becomes weak. The steep slope of the baseline may be due to the optical excitation of the boron-bound holes to the valence band. Figure 8 is the experimental plots showing dependence of the height of the 1136-cm^{-1} peak on the thickness of the heavily-doped substrate. From the gradient of the line fit to these plots (fig. 8) and the determined conversion constant, we obtained [O_i] = (1.20 ± 0.06) x 10^{18} atoms/cm^3 for this heavily doped substrate.

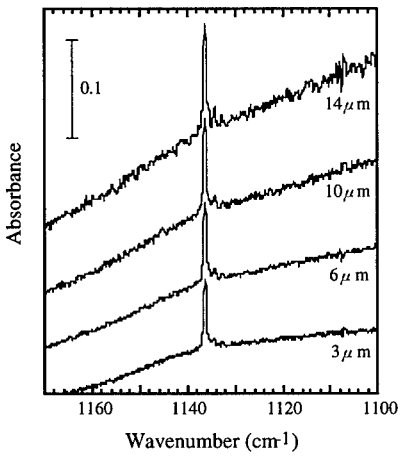


Fig.7. The 1136 cm^{-1} peak observed for various thicknesses of the thinned substrate.

D. Oxygen Precipitation in Heavily-Doped Substrate of Epitaxial Wafer

We employed the same epitaxial wafer whose [O_i] was measured in Sec. III C. We bonded the surface of the epitaxial wafer to the 5-mm thick FZ substrate, as illustrated in fig.6. From this bonded wafer, we cut out six specimens. The nitrogen-ambient preanneals at 500, 600, 700, 800 and 900 ℃ for 6 h were performed for each of five specimens, respectively. These heat-treatments aim formation of oxygen precipitation nuclei. Subsequently, each of the five specimens was subjected to the nucleus-growing anneal in nitrogen ambient where the annealing temperature was raised from each preannealing temperature to 1100 ℃ with a ramping rate of 2 ℃/min and was kept there for 1 h. After that, there were taken out of the furnace with a rate 20 cm/min, as shown by the dotted line in fig.9. Then, all the six specimens were together subjected to the two-step anneal of (1100 ℃, 6 h) + (900 ℃, 4 h) in nitrogen ambient. This corresponds to a part of typical heat-treatment processes: the well diffusion and the field oxidation heat-treatments. The total annealing sequence is described in fig.9. After thinning the heavily-doped substrate of these bonded specimens to the thicknesses of 24-27 μ m, we measured the heights of the 1136-cm^{-1} peak. For each specimen, we repeated this procedure of thinning the heavily-doped substrate and measuring the peak-height, to get the data like fig.8. Finally, by the same method as in Sec. III C, we determined the [O_i] of the heavily-doped substrates after the heat-treatments. For each specimen, we obtained the concentration of oxygen atoms involved in the oxygen precipitates (Δ [O_i]) by subtracting the measured [O_i] after the heat-treatment from the initial [O_i] = 1.20 x 10^{18} atoms/cm^3. For comparison, we measured Δ [O_i] of the conventional lightly doped wafers. The lightly doped wafers with the initial [O_i] of 1.50 x 10^{18} atoms/cm^3 and 1.25 x 10^{18} atoms/cm^3 (B-doped, 10 Ω cm) were subjected to the same heat-treatments (fig.9) as performed above for the bonded specimens. The Δ [O_i]s in this case were obtained from the conventional RT IR absorption method (American Standard for Testing and Materials F121-79 procedure).

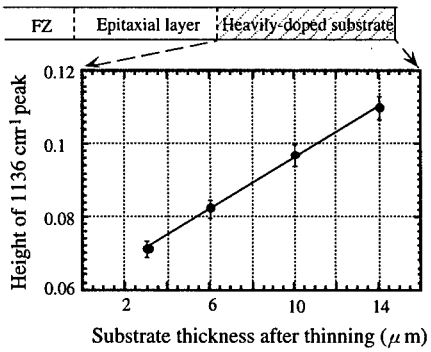


Fig.8. Linear behavior of the peak-height reduction due to sample thinning.

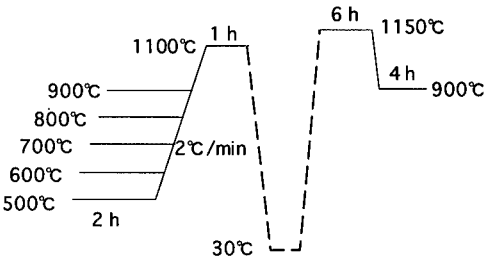


Fig.9. Total annealing sequence.

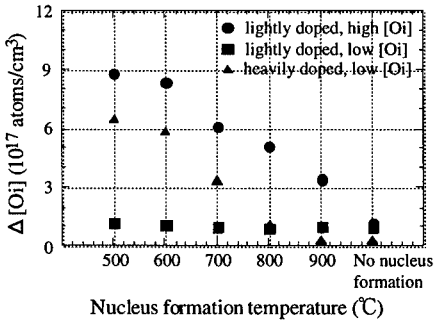


Fig.10. Dependence of the amount of oxygen precipitation Δ [Oi] on the temperature of preanneal for nuclei formation.

The results of the experiment are shown in fig. 10. For the lightly-doped wafer with a high [O_i] of 1.50 x 10^{18} atoms/cm^3, we obtained substantial amount of Δ [O_i] for the lower preannealing temperatures. On the other hands, for the lightly-doped wafer with a low [O_i] of 1.25 x 10^{18} atoms/cm^3, Δ [O_i] is almost zero for any case of the present preannealing temperatures. The Δ [O_i] of the

heavily-doped substrates is compared with the latter case, since the initial $[O_i]$ of the heavily-doped substrates, 1.20×10^{18} atoms/cm^3, is nearly equal to that in the latter case. For the heavily-doped substrates, we can obtain abundant $\Delta [O_i]$ if we choose the preannealing temperature below 700 ℃. This precipitation behavior is different from that of the lightly-doped wafer with the low $[O_i]$, and similar to that of the lightly-doped wafer with the high $[O_i]$. In other words, for the heavily-doped wafers, we can obtain oxygen precipitation enhanced by the heavy boron-doping if we perform preanneal below 700 ℃. By utilizing this enhanced oxygen precipitation due to high boron-doping, we can generally expect abundant oxygen precipitation even for the heavily-doped wafer with low $[O_i]$.

IV. Summary

We presented a new IR absorption method of measuring the dissolved interstitial oxygen concentration $[O_i]$ of the heavily-doped silicon crystal with high doping level up to 10^{19} atoms/cm^3. It consists of the three steps: We first bond the silicon wafer to a thick FZ silicon substrate by heat-treatment, and then, thin the wafer so that the IR beam can penetrate, and measure the height of the 1136-cm^{-1} absorption peak of O_i at a temperature below 5 K. For a heavily doped wafer and the heavily doped substrate of an epitaxial wafer, we demonstrated examples of measuring the $[O_i]$ and its reduction $\Delta [O_i]$ due to oxygen precipitation. We found that for the B-doped wafer with a resitivity 0.01 Ω cm, enhanced oxygen precipitation due to heavy B-doping is expected if we perform the preanneal at temperatures below 700 ℃.

References

1. M. Itsumi, H. Akiya, T. Ueki, M. Tomita and M. Yamawaki, Jpn. J. Appl. Phys. 35, 812-817 (1996).

2. D. Gilles, W. Schröter and W. Bergholz, Phys. Rev. B 41, 5770 (1990).

3. A. Borgeshi, M. Geddo, G. Guizzetti and P. Geranzani, J. Appl. Phys. 68 (4), 1655 (1990).

4. H. Tsuya, M. Kanamori, M. Takeda and K. Yasuda, in VLSI Science and Technology (Electrochemical Society, Pennington,1985) pp. 517-525.

5. H. Hrostowski and R. H. Kaiser, Phys. Rev. 107, 965 (1957); B. Pajot, J. Phys. Chem. Solids 28, 73 (1967).

6. D. R. Bosomworth, W. Hayes, A. R. L. Spray, and G. D. Watkins, Proc. Loy. Soc. London A 317, 133 (1970).

7. H. Yamada-Kaneta, C. Kaneta, and T. Ogawa, Phys. Rev. B 42, 9650 (1990); H. Yamada-Kaneta, C. Kaneta, and T. Ogawa, Mater. Sci. Forum 38-41, 637 (1989).

8. Pajot, in Oxygen in Silicon, edited by F. Shimura, Semiconductors and Semimetals 42 (Academic, Boston, 1994) pp. 201-202.

9. P. Wagner, Appl. Phys. A 53, 20 (1991).

A NEW MEASUREMENT METHOD OF MICRO DEFECTS NEAR THE SURFACE OF Si WAFERS; OPTICAL SHALLOW DEFECT ANALYZER (OSDA)

Kazuo Takeda*, Hidetsugu Ishida* and Atsushi Hiraiwa**
*Central Research Lab., Hitachi, Ltd., Kokubunji ,Tokyo 185, Japan
** Semiconductor & I.C.Div., Hitachi, Ltd., Kodaira, Tokyo 187, Japan

ABSTRACT

To inspect quality of the surface region (the depth < 0.5μm) of Si wafer, where devices are to be fabricated, a new measurement method named Optical Shallow Defect Analyzer (OSDA) is developed. This method is based on light scattering at two wavelengths having different penetration depths in silicon. The system measures the depth distribution and the size distribution of defects near the surface by comparing intensities of the two scattered lights. The depth resolution of 0.1 μm, the high measuring throughput (total 6" ϕ surface area/1hr) and the minimum detectable defect size of 20 nm are achieved. The OSDA is a powerful measurement system for nondestructive quality check of silicon wafers. We first present the data of epitaxial grown-in defects in μm order thickness epitaxial layers about the defect densities, the size distribution and the depth distribution.

INTRODUCTION

As the integration level of LSIs and miniaturization of semiconductor devices proceed, the quality of Si surface region is becoming more important to ensure high production yield of LSIs. This is because the defects near the surface cause the device failures such as gate oxide breakdown and degradation of p-n junction. The OSDA is developed to inspect quality of the surface region (the depth < 0.5μm) where devices are to be fabricated.[1] In this paper, we describe the principle of the OSDA and the measured results of grown-in defects in Czochralski (CZ) silicon wafers and epitaxial wafers.

Conventional measurement methods for defects in silicon crystals utilize infrared (IR) light as a irradiation source.[2-6] This is because silicon does not absorb IR light, and a inner defect of the crystal can be detected by scattered light from the defect. However, these methods have some problems. The scattered lights from rough back side of a wafers cause large noise for detecting a defect. Moreover, the detector of IR light is less sensitive than that of visible light and the measurement throughput is small; i.e. ~mm^2 x 5μm per 1 hour. On the other hand, laser scattering particle counters for Si wafer are very high throughput measurement systems using a single visible wavelength light that photomultiplier tubes are available for high sensitive detection. The system can estimate sizes of particles on the surface by detecting the scattered light. However, for defects in Si crystal, it is impossible to estimate the size by the conventional counters using single laser light whose wavelength is within the absorption band of silicon. This is because the intensity of the light scattered by a defect depends on the depth as well as the size of the defect. So, we need at least two experimental data to determine these two factors.

THEORY AND EXPERIMENTAL

The OSDA can measure the size and the depth of the defects in the wafer using intensities of two scattered lights with different wavelengths (532nm and 810nm) which have different absorption coefficients (0.045 at 532nm, 0.006 at 810nm[7]) in silicon. Figure 1 shows the measurement system of the OSDA using double lasers for irradiation and double photo multiplier tubes for the detection of the two scattered lights.

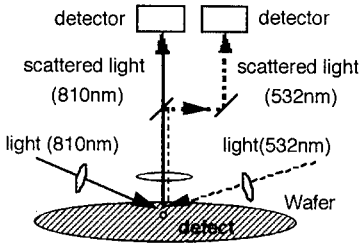


Fig.1 The OSDA system

Mat. Res. Soc. Symp. Proc. Vol. 442 © 1997 Materials Research Society

Principle of the depth measurement

The intensity of irradiation lights decrease exponentially by the depth as following equation,

$$I_Z = I_0 \exp(-\alpha Z), \tag{1}$$

where I_0 and I_Z is the intensity of irradiation light intensity at the surface and that at the depth Z, respectively, α is the absorption coefficient of silicon at the irradiation wavelength. Now, we consider two wavelengths, λ_1 and λ_2, where absorption coefficient at λ_2 is at least ten times larger than that at λ_2. In the Fig.1, λ_1 and λ_2 are 810nm and 532nm, respectively. Scattered light intensities at the two wavelength are expressed as following equations,

$$S_1 = Ti_1 Ts_1 I_1 \sigma_1 \exp[-\frac{2Z}{\Gamma_1}\left(1+\frac{1}{\cos\{\sin^{-1}(\sin\theta/n_1)\}}\right)], \tag{2}$$

$$S_2 = Ti_2 Ts_2 I_2 \sigma_2 \exp[-\frac{2Z}{\Gamma_2}\left(1+\frac{1}{\cos\{\sin^{-1}(\sin\theta/n_2)\}}\right)], \tag{3}$$

where $n_{1,2}$: the refractive index of silicon at $\lambda_{1,2}$, $\Gamma_{1,2}$: the penetration depth at $\lambda_{1,2}$, $\sigma_{1,2}$: the scattering cross section of a defect at $\lambda_{1,2}$, $Ti_{1,2}$:the transmittance of incident light of $\lambda_{1,2}$ at the surface, $Ts_{1,2}$:the transmittance of scattered light of $\lambda_{1,2}$ at the surface. From the Eqs.(2) and (3), we obtain,

$$Z = C_1 \ln[C_2\left(S_1/S_2\right)\left(\sigma_2/\sigma_1\right)], \tag{4}$$

where, C_1 and C_2 are constants which are independent of defects.

In the case of the Rayleigh scattering where a defect size is smaller than the irradiation wavelength, the following relation is derived from the Rayleigh scattering relation,

$$\frac{\sigma_2}{\sigma_1} = \left(\frac{\lambda_1}{\lambda_2}\right)^4 = cons\tan t.. \tag{5}$$

Therefore,

$$Z = C_3 \ln\left(S_1/S_2\right) + C_4, \tag{6}$$

where, C_3 and C_4 are constants which depend only on the instrument.

Light interference between a defect and the inner surface was neglected on the Eqs.(2) and (3). This is because the intensity of scattered light from a defect is usually negligible small as compared with irradiation light intensities and multiple scattering of scattered light reflected at inner surface can be neglected. So, Eq.(6) is valid.

Principle of the size measurement

Size of a defect, d, is estimated using following equation,

$$\ln d = \frac{1}{6}\ln S_1 + C_6. \tag{7}$$

The Eq.(7) is valid under the condition, $\Gamma_2 << \Gamma_1$. This is because the intensity of λ_1 light scattered by the defect (the depth $< \Gamma_2 << \Gamma_1$) is almost independent of the depth and expressed as followed,

$$S_1 = C_5 \sigma_1. \tag{8}$$

The Eq.(7) is derived from the Eq.(8) and the relation of Rayleigh scattering region, $\sigma_1 \propto d^6$. By using Eqs.(5) and (7), we can measure the depth and size of each defect by only single surface scanning. The principle of the OSDA is convenient for high speed measurement of defects near the surface.

RESULTS and DISCUSSION

To check the depth resolution, we measured the depth distribution profile of thin epitaxial layer. Figures 2 show the depth profile of defects in epitaxial layer whose thickness is 0.3 μm. This profile indicates that the defect density of epitaxial layer is much smaller than that of CZ substrates. This profile is consistent with the thickness of epitaxial layer. Counting level near the 0.5 μm become lower. This is because the 532 nm scattered light from the defects (the depth > 0.5 μ m) can not be detected. Therefore, the measurable depth range is about < 0.5 μm.

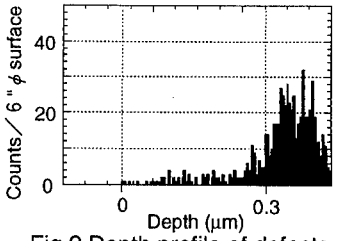


Fig.2 Depth profile of defects in epitaxial wafer
Thickness of the epitaxial layer is 0.3μm.

Figures 3 (a) and (b) shows the lateral distribution maps and the radial profiles of size distributions of 6 inch CZ wafer and 6 inch epitaxial wafer. The thickness of the epitaxial layer is 5 μm and larger than the measurable depth. So the defects in Figure 3 (b) are in the epitaxial layer. Density of defects in the epitaxial layer is of the order of 10^4 (counts/cm^3) and about 50 times lower than that of grown-in defects of the CZ wafer. The radial profile of defect size distribution of the CZ wafer shows that the sizes of defects near the wafer center are lager than that in the vicinity of the wafer edge. This result is consistent with the result by the IR laser scattering tomography.[5] For the defects in epitaxial layer, however, the radial profile of the size distribution is independent of the radial position. This result indicates that the grown-in defects in epitaxial layers are independent of the defects in CZ substrates.

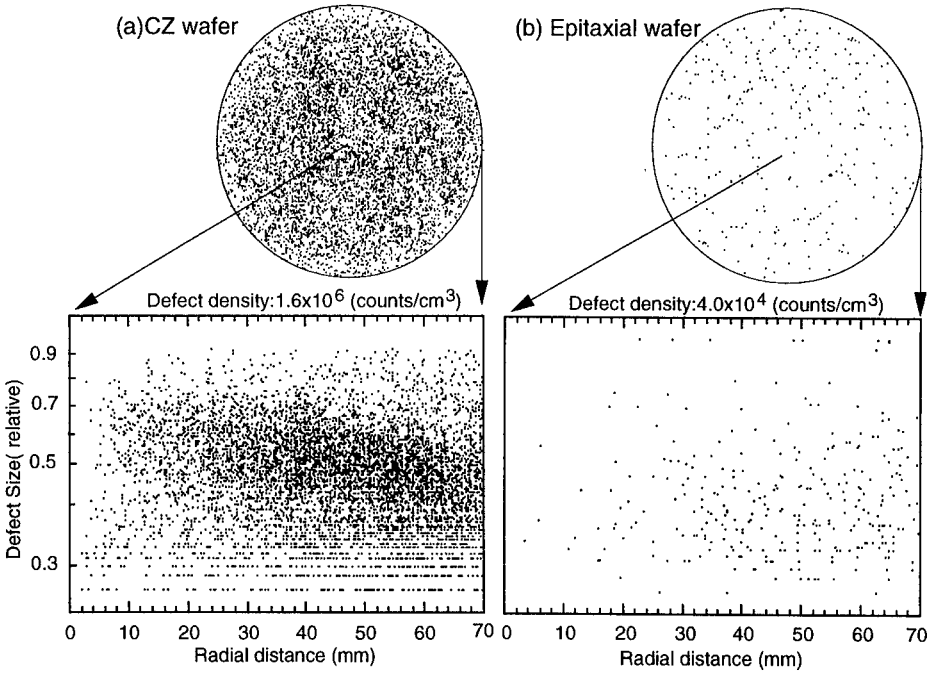


Fig.3 Lateral distribution maps and the radial pofiles of size distributions

(a) Defects (depth <0.5μm) in normal CZ wafer ([Oi]=18ppma -JEIDA,Pulling Rate:1.0 mm/min)

(b) Defects (depth <0.5μm) in Epitaxial layer (thickness of the layer=5.0 μm)

Figures 4 (a) and (b) are the size distributions of the CZ wafer and the epitaxial wafer in Figure 3 (a) and (b), respectively. The shape of defect distribution in CZ grown-in defects appears to consist of a Gaussian distribution and a simple distribution having the smaller density with the size. Kitagawara *et al.* reported the size distribution of CZ grown-in defects obtained by the Optical production profiler.[6] But, the distribution shape is not clear because the number of defects detected is few. The size distribution of epitaxial layer defects is different from that of CZ grown-in defects. This shape indicates that epitaxial grown-in defects are various sized. This result suggests that the epitaxial grown-in defects are different from the CZ grown-in defects.

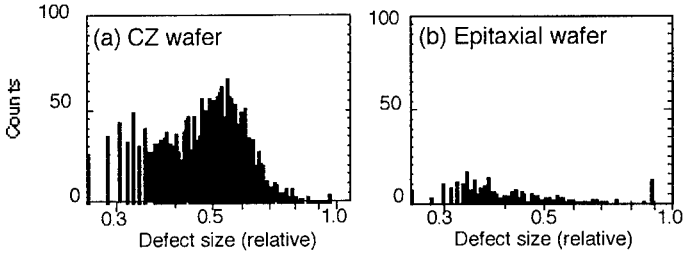


Fig.4 Comparison of defect size distributions of CZ wafer and Epitaxial wafer

(a) Defects (depth <0.5μm) in CZ wafer ([Oi]=18ppma -JEIDA,Pulling Rate:1.0 mm/min)

(b) Defects (depth <0.5μm) in Epitaxial layer(thickness of the layer:5.0 μm)

Figures 5(a) and (b) show the lateral distribution maps and the radial profiles of defect size distributions of CZ wafer with different growth conditions, slow cooling furnace and slow pulling rate, respectively. The density of defects in the slow cooling furnace wafer is of the order of 10^5 (counts/cm^3) and about 5 times lower than the normal wafer. The radial profile of the defect sizes in the slow cooling furnace wafer shows that small sized defects in the normal wafer vanished in the slow cooling furnace wafer and the defect sizes are larger than the normal wafer. However, the outline of the profile is similar with that of the normal wafer. This may indicate that defects in the normal wafer and in the slow cooling furnace wafer are same kind. The other hand, the density of defects in the slow pulling rate wafer is of the order of 10^3 (counts/cm^3) and about 200 times lower than that of the normal wafer. The radial profile of the defect sizes in the slow pulling rate wafer shows random distribution, different from that of the normal wafer. This may indicate that defects in the normal wafer and in the slow pulling wafer are different kind.

The OSDA can detect defects induced by device fabrication process, for example, heating induced slip lines near the surface of wafers. Figures 6(a) and (b) are the lateral distribution maps of defects in epitaxial layer (thickness: 10μm) after heating with the condition, 1200℃6hr+700℃ 64hr+1000℃16hr. Figure 6(a) shows that a few slip lines can be detected in the vicinity of the wafer edge by 532nm light. Figure 6(b) shows that many slip lines can be detected by 810nm light which can detect defects ten times deeper than the defects detected by 532 nm light. This result indicates that almost slip lines in the epitaxial layer exist in the depth (> 0.5 μm) and the slope of the slip lines is like a scheme shown in Fig.7. We can know the depth information about slip lines near the surface by the OSDA measurement. X-ray topography also can detect slip lines, but have no information about the depth of the slip lines.

CONCLUSIONS

The OSDA is the first measurement system which can obtain wafer-scale distributions of defects near the Si surface. The system will be a very powerful as a non destructive inspection tool of Si wafers.

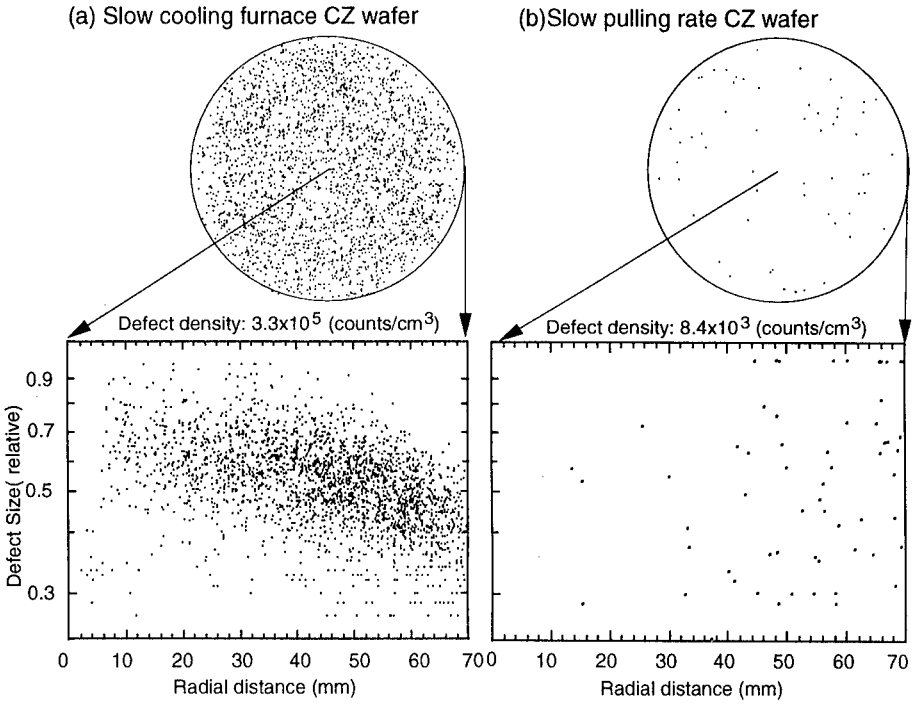


Fig.5 Lateral distribution maps and the radial pofiles of size distributions

(a) Defects (depth <0.5μm) in slow cooling furnace CZ wafer ([Oi]=18ppma-JEIDA)

(b) Defects (depth <0.5μm) in slow pulling rate CZ wafer ([Oi]=18ppma -JEIDA,pulling rate:0.4mm/min)

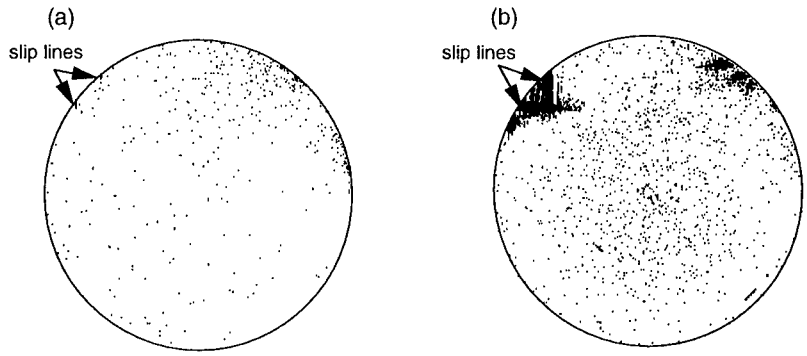


Fig.6 Observation of slip lines in Epi layer(thickness:10 μm)

Wafer heat treatment: 1200℃6h+700℃64h+1000℃16h

(a) Defects detected at 532 nm (the depth < 0.5 μm)

(b) Defects detected at 810 nm (the depth < 5 μm)

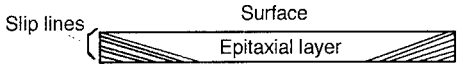


Fig.7 Scheme of slip lines in Epitaxial layer

ACKNOWLEDGMENTS

We thank Mr.T.Tajima & Mr.S.Watase at Hitachi Tokyo Electronics Ltd., for their technical support of the OSDA instrumentation, Mr. Y.Sugino & Mr. T.Tanaka at Semiconductor & I.C.Div., Hitachi, Ltd. for sample supply, Mr. Matsuda, Mr. Suzuki and Dr. H.Shimizu at Semiconductor & I.C.Div., Hitachi, Ltd., and Ms. T.Sato at Hitachi ULSI Engineering Co., for their helpful discussion, Dr. S.Isomae & Dr. M.Ohkura at Central Research Lab., Hitachi, Ltd., for their support.

REFERENCES

1) K.Takeda, H.Ishida, and A.Hiraiwa:Extended Abstract of SSDM p.151(Yokohama, 1996)
2) T.Ogawa & N. Nango: Rev. Sci. Instrum. 57, 1135 (1986)
3) K. Moriya: J. Crystal Growth, 94, 182 (1989)
4) D.Guidotti *et al.*: Appl. Phys. A 55, 139 (1992)
5) S.Sadamitu *et al.*:Jpn.J.Appl.Phys.32(1993)3675
6) Y.Kitagawara *et al.*: Proceedings of SPIE 2631, p.263 (Austin, 1996)
7) *HANDBOOK OF CONSTANTS OF SOLIDS* (Edited by E.D.Palik, Academic Press,Inc.,1985)

INSPECTION OF RECOMBINATION ACTIVE DEFECTS FOR SiGe AND SOLAR CELLS

O.V. Astafiev*, V.P. Kalinushkin*, N.V. Abrosimov**
*General Physics Institute of RAS, 38, Vavilov str., Moscow, 117942, GSP-1, Russia
E-mail: astf@kapella.gpi.ru
**permanent addr: Institute of Solid State Physics of RAS, 142432, Chernogolovka, Russia
present address: Institute of Crystal growth, Rudower Chaussee 6, Berlin, Germany

ABSTRACT

Mapping Low Angle Light Scattering method (MLALS) is proposed to study defect structure in materials used for solar cell production. Several types of defects are observed in Czochralski $Si_{1-x}Ge_x$ ($0.022<x<0.047$) single crystals. Recombination activity of these defects is investigated. The possibility of contactless visualisation of grain boundary recombination in polysilicon is also demonstrated.

INTRODUCTION

The method of electrically active defect visualisation in semiconductors has been previously proposed in [1]. The possibility of the defect visualisation in bulk of semiconductors by non-destructive contactless way has been demonstrated.

Base principle of the defect detection is the following. Local dielectric constant variations lead to optical inhomogeneities that can be detected due to plane wave scattering. These inhomogeneities can consist of free carrier accumulations existing in electrically active defect locations. Dielectric constant of the free carrier accumulations depends on wavelength and middle Infrared (mid-IR) plane wave is suitable to detect the free carrier accumulations. The reflective index change may also occur because of content fluctuation in multicomponent systems such as $Si_{1-x}Ge_x$.

Visualisation of the free carrier inhomogeneities in bulk of semiconductors is the first way of the method application. Another way for the method application is visualisation of recombination active defects for non-equilibrium free carriers (recombination contrast mode). This regime allows one to map the recombination activity. These two general ways of the method application give a good chance to investigate the semiconductors. Possible abbreviation of the method name can be MLALS (Mapping Low Angle Light Scattering). The proposed method is a direct development of the integral (non-mapping) light scattering method LALS [2] that was successfully used as an electrically active defect investigation method in semiconductors, especially in Si grown by floating zone and Czochralski technique. The most obvious and simple way for the method application is the defect structure control and study in solar silicon.

EXPERIMENTAL SET-UP

Two regimes of the experimental set-up under operation are shown in fig.1. The mid-IR plane wave (1) from a CO_2-laser passes through a semiconductor wafer (3) with parallel optically polished surfaces. Wavelength of the radiation (λ) is equal to 10.6μm. If any optical inhomogeneity (2) (for example, a free carrier accumulation with typical size a) is in the wafer bulk, the mid-IR plane wave is scattered at the diffraction angle λ/a (10). The sample (3) is placed in the forward focus of a lens $L1$ (4). Therefore, the scattered wave from the inhomogeneity transforms after the $L1$ in a parallel beam with diameter $f_1\lambda/a$.

Mat. Res. Soc. Symp. Proc. Vol. 442 © 1997 Materials Research Society

The second lens *L2* condenses the beam on an IR-receiver (7). On the other hand the non-disturbed plane wave is focused by the lens *L1*. A small opaque screen or reflective mirror (9) is placed at 45° in the back focus of the *L1* to remove the non-scattered wave. As a result, only the wave (10) reflected from the optical inhomogeneity is detected. In other words, the described scheme can serves as a filter of a wave with low spatial frequencies that removes images of big objects and selects small scattering objects.

This filter passes scattering waves with spatial frequencies that correspond to the object sizes from $f_1\lambda/b_1$ to $f_1\lambda/b_0$ where f_1 is focus length of *L1*, b_1 is the opaque screen diameter (9) and b_0 is the diaphragm diameter (5) in the back focus of *L1*.

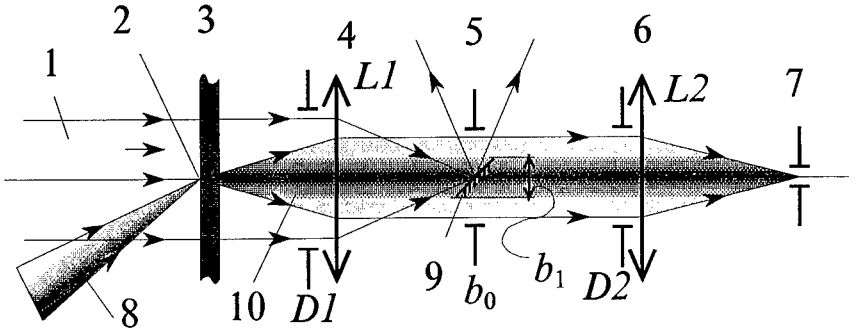


Fig.1. 1 is the mid-IR plane wave; 2 is an optical inhomogeneity (for the case of recombination contrast mode, it is a photo-induced droplet of free carries); 3 is a sample under test; 4 is the first lens *L1*; 5 is a diaphragm to restrict high spatial frequencies; 6 is the second lens *L2*; 7 is the IR-receiver; 8 is a light source that photo-induced free carriers (it uses for recombination contrast mode only); 9 is an opaque screen which differs system resolution; 10 is a scattered wave.

The set-up is used in two general modes. The first mode serves to visualise of free carrier inhomogeneities that appear in semiconductor bulk due to electrically active defects. The second mode is used to visualise of recombination active defects. To register free carrier inhomogeneities in semiconductor bulk, the probe mid-IR beam is modulated and the alternating signal of the scattering wave is detected. As a result of step by step scanning the free carrier inhomogeneity pattern can be seen. This pattern allows one to imagine the electrically active defect distribution in the bulk of the sample.

To obtain a recombination contrast pattern, a droplet of non-equilibrium free carriers is induced by an external light source. The role of such source can play a focused light beam from either a HeNe-laser or a semiconductor laser with quantum energy larger than the sample bandgap. Modulation of this light beam results in modulation of the wave scattered by the droplet. Total free carriers in the droplet and its size depend on the local lifetime value, so the sample scanning leads to reconstruction of recombination active defect pattern at the sample surface. There are materials with strong contrast caused by recombination active defects for example polycrystalline Si that contains a lot of grain boundaries. They may be observed by direct absorption. In this case, the set-up may be simplified and the opaque screen may be removed. All the radiation from the tested point comes to the receiver. The direct alternating signal from non-equilibrium carrier absorption is detected.

EXPERIMENT

Defect investigation and classification in SiGe by MLALS method

Wafers of monocrystalline alloys of $Si_{1-x}Ge_x$ with 2.2-4.7at% of Ge are investigated by MLALS methods. The alloys are grown for solar cells with high efficiency. The efficiency maximum is at $x \approx 0.62$ [3], but even small Ge content should increase its value.

The samples are chemically-dynamic polished with both sides. It was found by X-ray methods that these crystals contained several types of defects, including striations and dislocations [4]. A typical X-ray pattern schematically shown on fig.2. There are no striations and dislocations in a central area (I). A periphery area includes striations and dislocations (II). It is very important to determine defects that influence on the carrier lifetime and consequently on efficiency of solar cell.

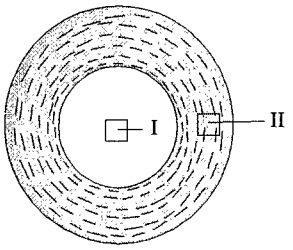


Fig.2. It is a typical scheme of X-ray pattern for wafers of monocrystalline alloys of $Si_{1-x}Ge_x$. Striation and dislocation free area observed in a central part of the crystals (I). A periphery area (II) contains dislocations and striations.

Appropriate defect contrast patterns for $Si_{1-x}Ge_x$ observed at both regimes of MLALS technique are shown in figure 3. Pairs of patterns from different parts of the samples are presented for every investigated place. The right picture in every pair corresponds to the inhomogeneity distribution in the sample bulk. The second picture corresponds to the recombination contrast at the same area. All observed areas are $1 \times 1 mm^2$ of size.

The following defect types are seen by MLALS method:

1. The first type is striations visualised clearly by the direct light scattering in the (II) areas of the samples (see fig.3(a), (c), (g), (k)). The striations usually do not create considerable recombination contrast, although there are samples (or places) where one can see the striation recombination contrast (see fig.3(h), (l)). This recombination activity can be consequence of a big lattice distortion due to high Ge content in the stripes that formed grown-in striations. Recombination activity correlation to the striation locations in the sample bulk one can clearly see on fig.3(g-h). It is obvious that grown-in striations are the Ge content variations due to the growth conditions. These stucture defects also revealed by X-ray methods.

2. The second defect type includes extended black areas at the recombination contrast pictures (see fig. 3 (b), (l)). These defects are possibly extended dislocations existed near the edge of the wafers in the (II) areas. Dislocations and dislocation walls can be revealed by etching and X-ray techniques at the same areas of the samples. The defects are not seen usually at the pictures from the direct scattering (see fig. 3(a)).

3. The third defect type combines black spots (they look like "black holes"). These defects are observed only at the recombination contrast pictures (see fig. 3(b), (d), (f), (h), (j)). These defects are the most widespread recombination defects which exist almost

everywhere (in the (I) and (II) areas). Sizes and shapes of the "black holes" are different. Usually, they look like oblong spots and their sizes vary from 20μm up to 100-200μm. From etching and X-ray methods, it is known that the central areas (II) of all tested samples have no dislocations and striations. Absence of bright striations in these regions is demonstrated by MALLS direct scattering (see fig. 3(e), (i)), but nevertheless the "black holes" can be observed (see fig. 3(f), (j)). Nature of the defects is not determined. In these areas some nondislocation defects can be revealed by etching. One can propose that these defects are the same as it is observed by MLALS direct scattering. These "black holes" are seemed to be the most dangerous defects for free carrier lifetime.

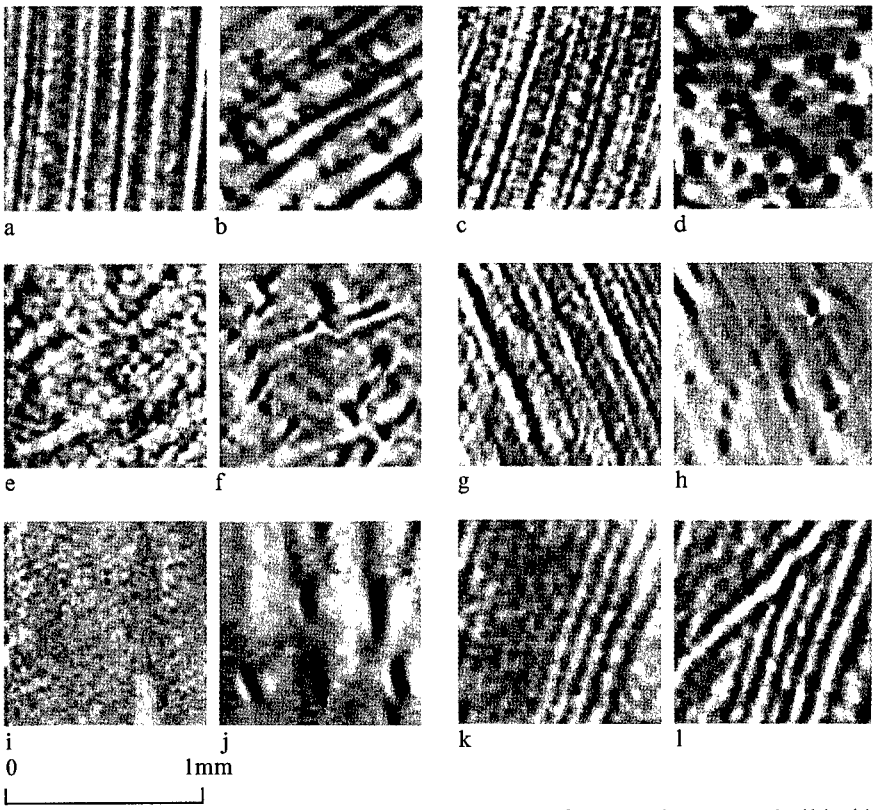


Fig. 3. Images of $Si_{1-x}Ge_x$, $0.022<x<0.047$, $1\times1mm^2$. Left images in every pair ((a), (c), (e), (g), (i), (k)) appear to be from the bulk defects scattering. Right images ((b), (d), (f), (h), (j), (l)) appear to be the recombination contrast mode.
Images (a-b), (c-d) are Cz Si (100), p-type, 4at% Ge.
Images (e-f), (g-h) are Cz Si (111), p-type, 4.7at% Ge.
Images (i-j), (k-l) are Cz Si (111), n-type, 2.2at% Ge.
(a-b), (c-d), (g-h), (k-l) are chosen far from the centres of the samples and bright striations are clearly seen.
(e-f), (i-j) are near the centre of the samples. This area is dislocation and striation free.

Visualisation of polysilicon recombination active defects

To demonstrate additional possibilities of the MLALS method the polysilicon samples are investigated. Polycrystalline silicon is a very important material for the cheap solar cell manufacturing. It is well known that the main killing free carrier defects are grain boundaries and low angle boundaries. To increase an appropriate solar cell efficiency and for technological monitoring purposes, it is important to control the boundary activity. The MLALS technique allows one to visualise the defects without contacts. It is not a problem to see them with EBIC. Unfortunately EBIC needs a p-n-junction or a Schottky barrier preparation. So it is a contact method and it is difficult to use EBIC in the manufacturing process.

Application of recombination contrast mode of MLALS for the polysilicon is the most obvious and simple way for the grain boundary activity visualisation. For this purpose the experimental set-up shown in fig.1 can be simplified. Due to strong recombination contrast of grain boundaries, they may be visualised by the direct mid-IR absorption. It means that the opaque screen can be removed.

Typical MLALS recombination contrast images observed in polycrystalline silicon samples with grain boundaries are shown in fig. 4.

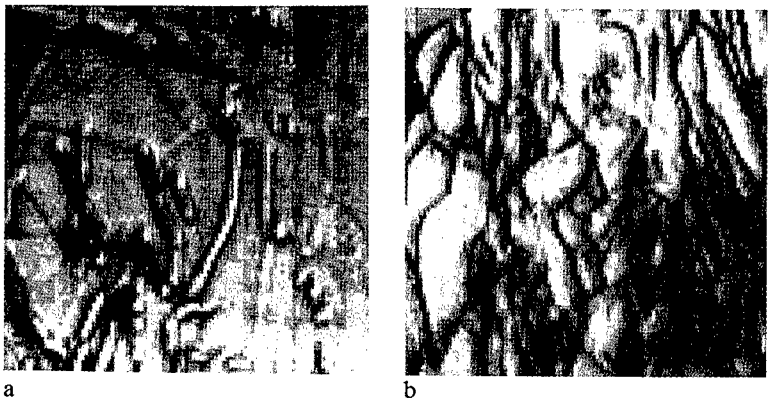


Fig. 4. Polycrystalline silicon sample surfaces, 4×4mm². These images are observed when MLALS recombination contrast mode is used. Grain boundaries are seen as lines.

It is possible to obtain a numerical value for the carrier lifetime in every point and we are planing to improve the set-up to observe the kinetic process.

CONCLUSIONS

It was demonstrated the effective possibility to investigate defect structure of solar cell material by the contactless MLALS method. The most obvious field for it application is the direct control of the polycrystalline silicon grain boundaries. Combination of two described techniques of MLALS gives unique possibilities to find and to classify defects.

It is established that $Si_{1-x}Ge_x$ alloys with Ge content within 2.2-4.7at% have a lot of widespread recombination active defects that look like "black holes". Sizes of the "black holes" are varied in the range from 20μm to 100μm. These defects appear even in the striation and dislocation free areas of the tested samples.

ACKNOWLEDGEMENTS

The authors want to thank Institute of Crystal growth, Berlin, Germany for the samples allowing.

REFERENCES

1. O.V. Astafiev, V.P. Kalinushkin, V.A. Yuryev in Proc. of the Conference on Microscopy of Semiconducting Materials (Oxford University Press, Oxford, 1995), pp.775-780.

2. V.V. Voronkov, G.I. Voronkova, V.N. Golovina, B.V. Zubov, V.P. Kalinushkin, T.M.Murina and A.M.Prokhorov, J. Cryst.Growth, **52** (1981), pp.939-942.

3. J.H. Werner, B. Winter, M. Wolf, S. Kolodinski, R. Brendel, M. Hirsh, H. Queisser, J. Wollweber, W. Schroder in 13th European Photovoltaic Solar Energy Conf., Nice, 1995, pp.111-114.

4. J. Wollweber, D. Schulz, W. Schroder, N.A. Abrosimov, in First World Conf. on Photovoltaic Energy Conversion, Hawaii, 1994, pp.1372-1374.

Part II

Processing Induced Defects: Plasma-Induced Point Defects

ELECTRICAL CHARACTERIZATION OF DEFECTS INTRODUCED DURING PLASMA-BASED PROCESSING OF GaAs

F. D. AURET [a], G. MYBURG, W. E. MEYER, P. N. K. DEENAPANRAY AND H. NORDHOFF*
M. MURTAGH, SHU-REN YE, H. J. MASTERSON, J. T. BEECHINOR, AND G. M. CREAN**
* Physics Department, University of Pretoria, Pretoria 0002, South Africa
** National Microelectronics Research Centre (NMRC), Lee Maltings, Prospect Row, Cork, Ireland

ABSTRACT

We report the results of experiments during which epitaxially grown n-GaAs was exposed to He- and $SiCl_4$-plasmas at similar sets of well defined RF powers and plasma pressures. To study the defects introduced during these plasma exposured, we employed deep level transient spectroscopy (DLTS). The effect of the plasma etch induced defects on the performance of Schottky barrier diodes (SBDs) fabricated on plasma processed GaAs was evaluated by current-voltage (IV) and capacitance-voltage (CV) measurements.

DLTS revealed that each plasma type (He and $SiCl_4$) introduced its own characteristic set of defects. Some of the defects created during He processing and one defect introduced by $SiCl_4$ etching had identical electronic properties to those introduced during high energy (MeV) He ion bombardment. $SiCl_4$ etching introduced only two prominent defects, one of which is metastable with electronic properties similar to a metastable defect previously reported in high and low energy He-ion bombardment of Si-doped GaAs. IV measurements demonstrated that the characteristics of SBDs fabricated on He-ion processed surfaces were very poor compared to those of control diodes (diodes fabricated on surfaces cleaned by conventional wet etching). In contrast, the properties of SBDs fabricated on $SiCl_4$ etched surfaces were as good as, and in some cases superior to, those of control diodes. SBDs fabricated on annealed (at 450 °C for 30 minutes) He-processed samples exhibited improved but still poor rectification. In contrast, SBDs fabricated on annealed $SiCl_4$ etched surfaces had virtually the same characteristics as those fabricated on unannealed $SiCl_4$ etched samples.

[a] Electronic mail: fauret@scientia.up.ac.za

INTRODUCTION

Plasma based processing plays an important role in several areas of semiconductor device fabrication, e.g. dry etching (by ion beams and reactive ions) and sputter deposition. Dry etching has several advantages over conventional wet chemical etching, e.g. increased anisotropic etching and the ability to obtain very narrow linewidths during microelectronics processing [1]. Dry etching using noble gas ions, such as Ar, is based on the removal of substrate particles by sputtering. During dry etching as well as during other plasma-based processes like sputter deposition, particles originating from the plasma impinge on the semiconductor and some become imbedded into it. This interaction introduces crystal damage at and close to the semiconductor surface, which in turn results in a degradation of the electrical and optical properties of the semiconductor [2]. The defects thus introduced will also influence the characteristics of devices fabricated on the etch-damaged semiconductor surface [3].

Mat. Res. Soc. Symp. Proc. Vol. 442 © 1997 Materials Research Society

It has been shown that processing involving energetic particles impacts differently on the properties of n- and p-type GaAs and on the characteristics of devices fabricated on them [4,5]. When the surfaces of n- and p-GaAs are exposed to low energy ions, either prior to or during metallisation, the barrier height (ϕ_b) of Schottky barrier diodes (SBDs) formed on them are decreased [4,5] and increased [4,5], respectively. Using deep level transient spectroscopy (DLTS) [6], Grussell *et al* [7] have shown that the barrier lowering observed for n-Si is due to the introduction of donor-like defects below the interface. Subsequently, electrically active defects were also observed in ion beam processed GaAs [8,9]. The degree of barrier modification was found to increase with increasing defect concentration [9], which in turn is determined by the energy and fluence of ions. This suggests that the barrier height of a SBD can be tailored to a specific value by exploiting the defects introduced during low energy ion processing. Any such (and other) form of defect engineering requires detailed information regarding the defects involved. Firstly, to ensure that these defects can be reproducibly introduced, their physical nature (including their dependence on impurities in the semiconductor), as well as their introduction rates and spatial distribution, should be known as functions of ion species and process conditions. Secondly, in order to predict, via numerical modeling [10], the influence of these defects on semiconductor properties and device characteristics, their electronic properties (energy levels and capture cross-sections) and concentrations are required.

Although the electronic properties of numerous defects introduced during low energy Ar- [8,9] and He-ion [11] bombardment of GaAs have been reported, the physical nature of most of these defects is still unknown. Moreover, the type and concentration of these defects have not been correlated with the bombarding ion species and impurities in GaAs. It is, therefore, not yet possible to predict the type and concentration of all the defects that will be produced by specific ions and processes in GaAs containing a given matrix of dopants and other impurities. If the defects introduced by low energy ions are to be used to *predictably and controllably* govern the electrical properties of metal-GaAs junctions, then investigations are required to establish the physical nature of these defects and their dependence on ion species and process parameters.

In contrast to noble gas ion beam based plasma etching, reactive ion etching (RIE) requires much lower particle energies since it relies mainly on surface chemical reactions and desorption [1]. Dry etching of GaAs has frequently been performed using Cl_2-based plasmas, mainly because of the volatile nature of Ga and As chlorides [12]. A noble gas is often mixed with the Cl_2-based plasmas to control the etching rate and enhance the thermal properties of the discharges. It has been shown that the etch rates of $SiCl_4$ plasmas can be increased in a controlled fashion through the addition of Ar in specific amounts [12]. The enhanced etch rates result in the creation of less residual damage in the etched substrates. Although RIE using Cl_2 and $SiCl_4$ has been extensively researched, these investigations were mostly concentrated on etch rates, surface morphology and composition, carrier compensation and the effect of etching on barrier properties of SBDs [12,13]. As yet, little is known about the electrically active defects introduced by these etchants [14].

To learn more about the defects introduced during plasma-based processing of GaAs and their influence on SBD performance, we have exposed GaAs to two totally different plasmas - He and $SiCl_4$ - at different RF powers and plasma pressures. Whereas He etching, if any, occurs via sputtering, $SiCl_4$ etching is expected to occur predominantly by chemical reactions and subsequent desorption. Our results show that both processes introduced electrically active defects

and we were able to identify some of them by comparing their DLTS "signatures" to those of defects introduced during high energy particle irradiation which have been extensively studied.

EXPERIMENT

The Si-doped n-GaAs layers used for this study were grown by organo-metallic vapor phase epitaxy (OMVPE) on n^+-substrates and had free carrier concentrations of (1.2–1.5) × 10^{16} cm^{-3}. After wet chemical cleaning, Ni/AuGe/Au ohmic contacts were formed on the n^+– substrates. For control purposes, Pd Schottky contacts were fabricated on unetched substrates by means of resistive evaporation, which is known to introduce no defects in GaAs.

He and $SiCl_4$ plasma processing were performed in a Plasma-Therm reactor (RIE mode) for 10 minutes at different pressures (30 mTorr, 60 mTorr and 90 mTorr) and RF powers (80 W, 140 W and 200 W) as outlined in Tables 1 and 2. After plasma etching, we deposited Pd Schottky contacts, 60 nm thick and 0.77 mm in diameter, by resistive evaporation through a metal contact mask. The Pd SBDs were thin enough to allow optical excitation of carriers in the depletion region for DLTS studies of minority carrier related effects.

The quality of the Schottky barrier diodes (SBDs) was assessed by current-voltage (IV) and capacitance-voltage (CV) measurements. DLTS in a lock-in amplifier based system was employed to analyze the plasma processing induced defects. During these measurements a quiescent reverse bias V_r, with a filling pulse of amplitude V_p superimposed onto it, was applied to the SBD. The energy level (E_t) in the bandgap and apparent capture cross-section (σ_a) of a defect (the combination of which is referred to as its DLTS "signature") were calculated from conventional DLTS Arrhenius plots of T^2/e vs $1/T$, where e is the emission rate at a temperature T. The depths to which these defects extend in the GaAs were determined from fixed-bias variable-pulse DLTS depth profiling [15].

RESULTS

The results presented below will show that exposing n-GaAs to He and $SiCl_4$ plasmas introduces different sets of defects and that the rectification properties of SBDs fabricated on surfaces exposed to these etchants are totally different.

He-ion processing

Fig. 1 shows that the IV characteristics of SBDs fabricated on surfaces processed in a He plasma are vastly poorer than those of control (unprocessed) diodes displayed in Fig. 4. SBDs fabricated on surfaces exposed to the He plasma exhibited a large reduction in barrier height (0.3 – 0.4 eV), a drastic increase in the reverse leakage current (up to 7 orders of magnitude) and nonlinear forward log(I)-V characteristics. The SBD characteristics depicted in Fig. 1 are characteristic of diodes fabricated on disordered surface regions with a high resistivity. From Table 1, where we have summarized the results, definitive trends emerge. For a fixed RF power (80 W, 140 W or 200 W) the device quality decreases with decreasing pressure, whereas for a fixed pressure (30 mTorr, 60 mTorr or 90 mTorr) the device quality decreases with increasing RF power. The diodes with the poorest characteristics were those fabricated on surfaces processed at maximum power and minimum pressure, whereas the least deterioration was observed when processing at minimum power and maximum pressure.

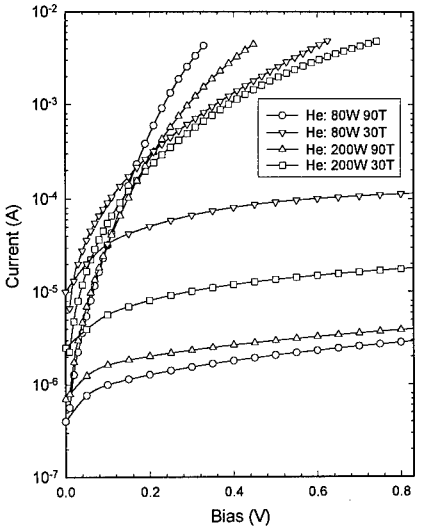


Fig. 1. IV characteristics of Pd SBDs fabricated on n-GaAs exposed to He-ions at the conditions indicated in the legend. Characteristics of control (unprocessed) samples are shown in Fig. 4.

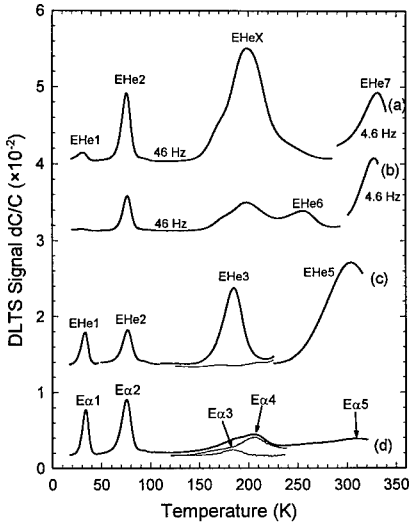


Fig. 2. DLTS spectra of SBDs fabricated on n-GaAs exposed to a He-plasma at: (a) 200 W and 30 mTorr, (b) 80 W and 90 mTorr. Curves (c) and (d) are for identical GaAs bombarded with 5 keV He ions and 5.4 MeV alpha particles, respectively. All spectra, unless otherwise indicated, were recorded at a lock-in frequency of 46 Hz, i.e. a decay time constant of 9.23 ms.

First, consider the dependence of the barrier properties on plasma pressure. At lower pressures the mean free path of the particles increases and, since they are accelerated all along their paths, their kinetic energies increase with increasing distance traversed. Therefore, particles reaching the sample during low pressure etching transfer more energy to the substrate, and hence create more damage. On the other hand, particles reaching the substrate during high pressure processing have lower kinetic energies and therefore create less damage. Since surface and sub-surface damage has been shown to reduce the barrier height of metals on n-GaAs, the increased damage expected during low pressure processing accounts for the lower barrier heights observed. Secondly, the dependence of the barrier height on RF power may be explained by noting that as the power is increased, the energy of the particles reaching the substrate increases. Consequently, more surface and sub-surface disorder is created, which in turn results in lower barrier heights. Using the same argument, it follows that low power processing will result in less damage and thus relatively higher SBD barrier heights, as we observed here. The tendencies reported here for He ion processing are in qualitative agreement with those reported for Ar ion milling of GaAs and InP [16].

The differences in barrier heights obtained from IV and CV measurements are often used as an indication of the concentration of interface states. An accurate determination of the CV barrier height requires capacitance measurements up to at least zero bias, but preferably to a few tens of a volt into forward bias. Since most of the diodes fabricated on He etched surfaces were too leaky to allow measurements in the vicinity of zero bias, no reliable CV measurements, and

Table 1. Summary of IV and DLTS results for different He RF powers and plasma pressures

Power	*Pressure*	*IV*			*DLTS peak height, dC/C ($\times 10^{-2}$)*	
(W)	*(mTorr)*	*ϕ (eV)*	*n*	*I_{-IV} (A)*	*EHe2*	*EHeX*
unprocessed (control)		0.922	1.015	4.2×10^{-11}	–	–
80	90	0.59	1.10	3.2×10^{-6}	1.04	0.76
80	60	0.58	1.12	5.6×10^{-6}	1.86	1.12
80	30	0.55	1.44	2.4×10^{-5}	2.64	3.24
140	90	0.59	1.27	3.3×10^{-6}	1.71	2.34
140	60	0.58	1.24	8.2×10^{-6}	2.08	2.90
140	30	0.56	1.32	1.7×10^{-5}	3.35	4.52
200	90	0.58	1.26	4.0×10^{-6}	1.78	2.32
200	60	0.56	1.21	1.2×10^{-5}	2.51	4.32
200	30	0.52	1.85	1.4×10^{-4}	3.69	5.93

thus, no accurate CV barrier height determinations were possible. Therefore, no meaningful comparison of IV and CV barrier heights could be made. CV measurements did, however, indicate a reduction in free carrier concentration towards the surface.

DLTS showed that the only major defect present in the control samples was the EL2 in a concentration of about $1x10^{14}$ cm^{-3}. In Fig. 2 we depict the DLTS spectra of SBDs fabricated on He-processed GaAs at 80 W and 90 mTorr (yielding "best" SBDs) and at 200 W and 30 mTorr (yielding "poorest" SBDs). It is clear that the He plasma introduced several electron traps, labeled EHe1, EHe2, EHeX, EHe6 and EHe7. Curves (a) and (b) in Fig. 2 show that the DLTS peaks of defects (i.e. the defect concentrations) are the highest for 200 W – 30 mTorr processing and the lowest for 80 W – 90 mTorr processing. Although not detailed here, our DLTS results showed the same trends for the conditions investigated as deduced from the IV measurements: The defect concentrations increase with increasing RF power and with decreasing plasma pressure. Our DLTS results thus confirm the explanation forwarded above for the dependence of IV characteristics on etch conditions based on the introduction of electrically active ion-processed induced defects.

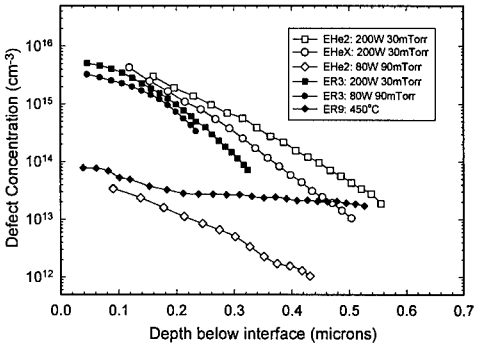


Fig. 3. DLTS depth profiles of some prominent defects in He– and $SiCl_4$–etched n-GaAs, constructed using the fixed-bias variable-pulse method.

The energy levels and capture cross sections of the defects introduced by the He plasma are summarized in Table 3. The EHe1 and EHe2 defects have the same "signatures" as the two main defects introduced by high energy alpha-particle irradiation of 1×10^{16} cm^{-3} doped GaAs (Eα1 and Eα2) [22] which have been attributed to two charge states of the isolated V_{As} [17]. EHe1 and EHe2 were also detected in low energy (1 keV) He ion beam bombarded GaAs [11]. Curves (a) and (b) of Fig. 2 show that the ratio of the concentrations of EHe1 to EHe2 is far less than unity (as may be expected for

two charge states of the same defect). We speculate that this "suppression" of the EHe1 peak is caused by two phenomenon. Firstly, the incomplete filling of EHe1 level due to stresses caused by extended defects in the vicinity of V_{As}, similar to that observed for the incomplete filling of the $V_2^{=/-}$ charge state of the divacancy in heavy ion bombarded Si [18]. Secondly, in 10^{16} cm^{-3} doped GaAs it has been shown that the emission of electrons for the Eα1 (EHe1) is more strongly influenced by an electric field than emission from Eα2 (EHe2) [22]. The influence of this field enhanced emission is even more pronounced in the low energy particle processed GaAs studied here since most of the defects are located close to the surface, i.e. in the region where the electric field is the highest. The net effect of the electric field on the DLTS peaks of these defects is a broadening towards the low temperature side and a reduction in peak height. Since the EHe1 is influenced more strongly by the electric field, its defect peak will be reduced more than that of EHe2.

Fig. 2 also shows that the temperature range 180 – 220 K contains a group of unresolved defect peaks which we labeled EHeX. In this temperature range we have previously detected the peaks Eα3 and Eα4 [curve (d)] in high energy α-particle irradiated GaAs [21]. The fact that the combination of peaks in Fig. 2 are considerably broader than those of the EHe3 (Eα3) and EHe4 (Eα4) combination, suggests that He etched GaAs may contain other defects in addition to EHe3 and EHe4 with peaks in the same temperature region. Above room temperature we observed the DLTS peak of a defect, EHe7 with the same activation energy (0.80 eV) as the EL2, but with a much larger capture cross section (8×10^{-13} cm^{-2}). Due to the large degree of lattice damage present in this material and the low barrier height of the SBDs, we are not certain whether this defect is different from the EL2 or whether its large capture cross section is an artifact due to the above mentioned constraints. Its DLTS peak at a lock-in frequency of 4.6 Hz was 20 K lower than that of the EL2.

In Fig. 3 we depict the DLTS depth profiles of some of the defects discussed above. In this figure, the sections of the profiles closer than 200 nm below the interface should be interpreted qualitatively rather than quantitatively because of the sharp reduction of the free carrier density in this region. Despite this restriction, these depth profiles all show that the concentrations of all the He plasma-induced defects decrease sharply from a maximum close to the interface into the GaAs. For example, the EHe2 concentration increases from about 10^{13} cm^{-3} at 0.6 μm below the interface towards the interface where it may approach, or even exceed, the free carrier density. The total concentration of the EHeX set of defects shows the same qualitative trend but increases sharper towards the interface than the EHe2 concentration and from the profiles it seems that its concentration at the interface may exceed that of EHe2. If we consider the high concentrations of these defects at and below the interface, it is understandable why the CV data for He-processed GaAs revealed carrier compensation in this region.

$SiCl_4$ etching

Although the same sets of power and pressure ratings as for He processing were used, the effect of plasma processing on the IV characteristics of SBDs fabricated on $SiCl_4$ etched surfaces is negligible compared to that of He processing. In fact, some etching conditions yielded SBD with characteristics superior to those of the control (unetched) samples (higher barrier heights and lower reverse leakage currents). As we show in Fig. 4, the forward and reverse IV characteristics of some of these SBDs are as good as textbook examples of pure thermionic

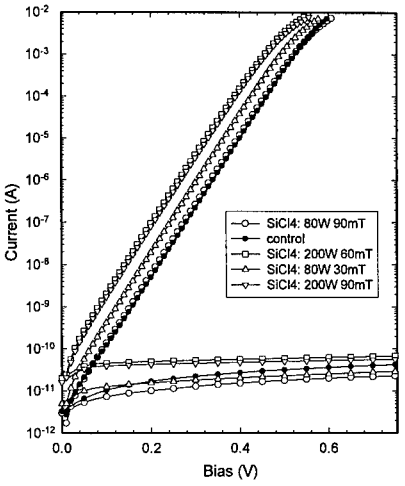


Fig. 4. IV characteristics of Pd SBDs, 0.77 mm in diameter, fabricated on n-GaAs etched with $SiCl_4$ at the plasma pressure and RF power conditions indicated in the legend.

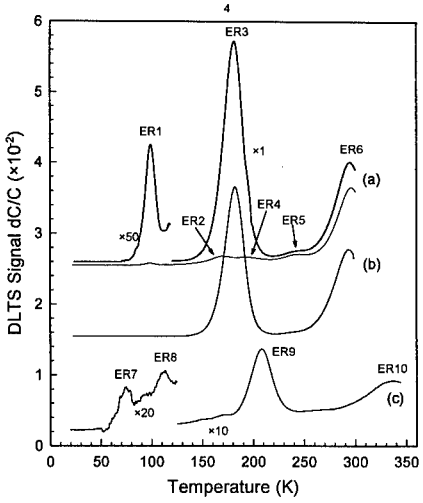


Fig. 5. DLTS spectra of Pd SBDs fabricated on n-GaAs etched with $SiCl_4$ at: (a) 200 W and 30 mTorr, (b) 80 W and 90 mTorr. The thin line in curve (a) was recorded after minority carrier injection at 120 K. Curve (c) was recorded after fabricating SBDs on a $SiCl_4$ etched sample annealed at 450 °C for 30 min.

emission across the barrier. Fig. 4 and Table 2, in which the results are summarized, do however show the same dependencies of SBD rectification properties on RF power and plasma pressure as observed for He processing - *only on a much weaker scale*. Compared to He-processed surfaces, IV measurements show that $SiCl_4$ etching has only a small influence on the rectification properties of SBDs fabricated on the etched surfaces. SBDs fabricated at all conditions have ideality factors of between 1.01 and 1.02, indicating that charge transport across the barrier takes place almost exclusively via thermionic emission. These SBDs exhibit series resistances of 4-6 Ω which are marginally higher than the 2-3 Ω of control diodes.

CV measurements showed a much more pronounced effect than IV measurements of plasma etch-induced defects. The shapes of all $1/C^2$ vs V_R curves of samples etched in $SiCl_4$ are non-linear in the vicinity of zero bias and thus indicate that the free carrier concentration of the sub-surface regions decreases towards the surface, i.e. that these regions contain compensating electron traps [19]. The $1/C^3$ vs V_R plots were closer to linear than $1/C^2$ vs V_R, confirming the reduction of free carriers towards the interface. The profiles showed that the carrier density started to decrease from about 450 nm below the surface. Despite the high quality of these diodes, the high Debye uncertainty which accompanies low carrier concentrations, prevented us from obtaining any quantitative carrier density information closer than 300 nm from the interface. From the information obtained from the carrier density profiles together with the fact that the $1/C^3$ vs V_R curves were almost linear, we deduce that the free carrier concentration decreases from 10^{16} cm^{-3} at and beyond 450 nm below the interface to being almost fully compensated at or close to the interface.

Table 2. Summary of IV and DLTS results for different $SiCl_4$ etch powers and plasma pressures

Power	*Pressure*	*IV*			*DLTS peak height, dC/C ($\times 10^{-2}$)*	
(W)	*(mTorr)*	*ϕ (eV)*	*n*	*I_{-IV} (A)*	*ER3*	*ER6*
unetched (control)		0.922	1.015	4.2E-11	0.0	0.0
80	90	0.922	1.016	2.1E-11	2.2	1.2
80	60	0.911	1.013	1.4E-11	2.2	1.7
80	30	0.886	1.017	3.0E-11	1.7	1.4
140	90	0.877	1.017	2.7E-11	1.6	1.8
140	60	0.886	1.013	2.4E-11	1.7	1.7
140	30	0.850	1.016	5.8E-11	2.3	1.7
200	90	0.848	1.017	6.5E-11	2.6	1.5
200	60	0.842	1.019	7.5E-11	1.4	1.2
200	30	0.850	1.020	6.5E-11	3.1	1.3

DLTS (Fig. 5) revealed that $SiCl_4$ etching introduced, in contrast to He processing, only two prominent (ER3 and ER6) and some minor (ER1, ER2, ER4 and ER5) electron traps. The most prominent of these defects has the same electronic properties (DLTS "signature", annealing and metastable behavior) as EHe3 (Eα3) which was observed in ion-bombarded Si-doped n-GaAs [19,20]. ER6 has a DLTS peak in the vicinity of room temperature (at a lock-in frequency of 46 Hz). Its DLTS peak height increases strongly with increasing frequency, i.e. increasing temperature, indicating either that it has a strongly temperature dependent capture cross-section, or that its capture kinetics are governed by a free carrier concentration that increases strongly with increasing temperature. Since we have found that its concentration was gradually reduced during DLTS temperature cycling, we recorded spectra only up to 305 K.

Our DLTS observations contrast those reported by Lootens *et al* [14] who found that $SiCl_4$ etching of n-GaAs removed some defects in the unetched epitaxial layer but did not introduce any new defects. Their etching did however seem to enhance the EL2 concentration.

DLTS depth profiling (Fig. 3) indicated that the concentration of ER3 and ER6 (not shown) both decrease from a maximum at the surface into the semiconductor. Once again we emphasize that, since we do not have have exact information about the free carrier concentration in the first 200 nm below the interface, the defect profiles in this region should be interpreted qualitatively rather than quantitatively. Beyond 200 nm from the interface, where we expect the profiles to be quantitatively correct, Fig. 3 shows that the defects introduced by $SiCl_4$ etching do not extend as far into the GaAs as those introduced by He etching. However, the estimated surface concentration of these defects are about the same as those of the defects introduced during He etching and seems to approach or exceed that of the GaAs doping concentration.

The most striking property of ER3 is that it can be reversibly removed by hole injection at low temperatures (120 K) and re-introduced by annealing above 200 K. This behaviour is the same as that of the alpha-particle irradiation induced defect Eα3 for which complete transformation kinetics were determined as [20]:

$E\alpha 3 \rightarrow E\alpha 3^{*}$ *(hole injection):*

$$\nu(T) = (2 \pm 1) \times 10^{4} \exp[-(0.04 \pm 0.01) / kT] \qquad (1)$$

Table 3. Electronic properties of defects introduced during He and $SiCl_4$ plasma processing of epitaxially grown n-GaAs

Etchant	*Defect*	E_t *(eV)*	σ_a *(cm^2)*	T_{peak}[(a)] *(K)*	*Similar defects*
He	EHe1	0.026	1.3×10^{-17}	30	Eα1 [22]
	EHe2	0.117	1.7×10^{-14}	72	Eα2 [22]
	EHeX	–	–	200	–
	EHe4	–	–	220	–
	EHe6	–	–	260	–
	EHe7	0.794	7.7×10^{-13}	354	EL2?
$SiCl_4$	ER1	0.190	6.5×10^{-14}	105	–
	ER2	–	–	170	–
	ER3	0.354	7.1×10^{-14}	184	Eα3 [20]
	ER4	–	–	200	–
	ER5	–	–	250	–
	ER6	0.630	1.8×10^{-13}	302	–

(a) Peak temperature at a lock-in amplifier frequency of 46 Hz, i.e. a decay time constant of 9.23 ms.

$$E\alpha 3^{*} \rightarrow E\alpha 3 \quad \textit{(zero bias):}$$
$$\nu(T) = (6 \pm 2) \times 10^{8} \exp[-(0.40 \pm 0.01) / kT] \qquad (2)$$

$$E\alpha 3^{*} \rightarrow E\alpha 3 \quad \textit{(2 V reverse bias):}$$
$$\nu(T) = (6 \pm 2) \times 10^{9} \exp[-(0.53 \pm 0.01) / kT] \qquad (3)$$

In these rate equations $\nu(T)$ denotes the transformation rate, either to remove Eα3 (eqn. 1) or to re-introduce it (eqns. 2 and 3). The significance of the metastability of ER3 is that processing GaAs in a $SiCl_4$ plasma offers a method of controllably introducing a prominent metastable defect in only the first few hundred nm below its surface, while still allowing the fabrication of high quality SBDs on its surface.

Difference in barrier heights of SBDs on He and $SiCl_4$ etched surfaces

We have shown that SBDs fabricated on $SiCl_4$ etched GaAs surfaces had close to ideal characteristics. In contrast, SBDs fabricated on He etched surfaces exhibited poor rectification properties. At the same time we have shown that etching in both plasma types introduced roughly the same surface concentrations of defects. The question that therefore arises is *why do SBDs fabricated on $SiCl_4$ etched surfaces have almost perfect characteristics while SBDs fabricated on He-processed surfaces exhibit very poor rectification properties?*

To address this question, consider the following. Firstly, the lower etch rate of He results in the accumulation of residual damage in a near-surface region. Not all these defects will necessarily be detected by DLTS because its sensitivity decreases linearly with distance towards the surface. This accumultion of near-surface damage with time is also accompanied by the in-diffusion of the defects produced. We propose that etching in a He plasma introduces large numbers of interface or near-surface states which result in pinning of the Fermi level of the SBDs

fabricated on the corresponding etched surfaces above the mid-gap position. Consequently, the SBDs fabricated on the He-processed surfaces have much lower barrier heights and significantly higher leakage currents. In contrast, the high quality of SBDs fabricated on $SiCl_4$-etched surfaces could be attributed to the continuous removal of the topmost layer in which the plasma etch-induced defect concentration is a maximum. The presence of low concentrations of interface states thus formed together with a possible surface passivation effect of chlorine ions result in high quality SBDs. Secondly, although the estimated total defect concentration at surfaces etched in both plasma types are approximately equal, the electronic properties of the defects in GaAs etched by these two etchants are different, resulting in different generation-recombination contributions to the forward and reverse currents of SBDs fabricated on He and $SiCl_4$ processed surfaces.

Defect annealing

We have annealed samples etched in He and $SiCl_4$ plasmas (at 200 W and 60 mTorr) for 30 min at 450 °C in an Ar atmosphere. This is approximately the highest temperature at which GaAs can be annealed in a conventional furnace, without capping, before its surface starts to degrade due to As loss. From the IV results we observed that SBDs fabricated on annealed $SiCl_4$ etched samples had virtually perfect characteristics. The only noticeable effect of annealing was a slight reduction in barrier height (0.02 eV) compared to unannealed etched samples. In addition, CV measurements indicated that the compensation close to the surface was reduced but $1/C^2$ vs V_R were still not quite linear. This indicates that the subsurface region still contains compensating centers. Annealed He-processed samples, on the other hand, have higher barrier heights and lower reverse leakage currents than unannealed He-processed samples. However, the general shapes of these curves were poor. They have very limited linear log(I) vs V regions in which the lowest ideality factor was n = 1.2, exhibit high series resistances and show clear evidence of high generation - recombination currents.

The DLTS results of annealed samples indicate that whereas $SiCl_4$ etched samples yielded normal DLTS spectra, He-processed samples exhibited erratic transient behavior indicative of a highly compensated material which in turn suggests that it contains a high concentration of defects. Annealing of $SiCl_4$ etched samples at 450 °C removed both the main etch-induced defects and reduced the overall defect concentration. The most prominent defect observed after annealing is ER9. Its concentration decreased from about 10^{14} cm^{-3} at the interface to $2x10^{13}$ cm^{-3} at a depth of 0.5 μm. The ER9 defect has about the same DLTS "signature" as the P1 defect observed after annealing high energy electron irradiated [23] and alpha-particle bombarded [24] GaAs. The concentration of the only other prominent peak, ER10, observed after annealing exhibits the same spatial distribution as the ER9, but its concentration is lower by about a factor of two. From this we conclude that the contributions of these two defects together is not sufficient to explain the carrier compensation still present (from CV measurements) after annealing. This suggests that there are other defects present, which we did not detect in the upper half of the bandgap, which causes the carrier compensation observed after annealing.

CONCLUSIONS

From the results presented here, we can draw several important conclusions. The first, and perhaps expected, result was that when n-GaAs is processed under identical conditions (RF power and plasma pressure) in He and $SiCl_4$ plasmas, then SBDs fabricated on $SiCl_4$–etched surfaces have far superior characteristics than those fabricated on He-processed surfaces. In fact, some $SiCl_4$ etch conditions yielded diodes with the same, or better, characteristics than diodes fabricated on surfaces cleaned by conventional wet chemical etching. We suggest that this is the result of the rapid and continuous removal of the topmost section of the plasma-damaged region by Cl-based reactions and desorbtion in conjunction with passivation of defect-related surface and sub-surface states by Cl deposited onto and below the surface during etching.

Secondly, for both He and $SiCl_4$ plasma processing, optimum SBD characteristics were obtained by etching at the lowest power (80 W) and highest pressure (90 mTorr). This is be explained in terms of the fact that particles from the plasma that reach the surface during the lowest pressures and highest deposition powers have the highest energies, and thus create the most damage in the GaAs substrate. This was confirmed by our DLTS results which showed the same trends: The highest and lowest defect concentrations were introduced during low pressure - high power and high pressure - low power procesing, respectively.

DLTS analyses of defects introduced during He and $SiCl_4$ plasma processing revealed that these two plasmas introduce two totally different set of defects. Several defects are introduced during He-processing and they include the well known E1 and E2 [23] defects, which are the two charge states of the isolated As_V. The dominant defects introduced during this process are EHe2 (E2) and a group of defects, labeled EHeX, with closely spaced peaks in the 200 K temperature range.

In contrast, $SiCl_4$ etching introduced only two major defects, ER3 and ER6. The most striking aspect of our DLTS results is that the main defect introduced during $SiCl_4$ etching, ER3, is metastable. ER3 can be reversibly removed by minority carrier injection at low temperatures (< 120 K) and re-introduced by annealing above 230 K. The concentration of this defects seems to approach 10^{16} cm^{-3} at the surface and drops to 10^{14} cm^{-3} at 0.3 μm below the interface. These results demonstrate that $SiCl_4$ etching facilitates the controllable introduction of a prominent metastable defect with a shallow spatial distribution while still allowing the fabrication of high quality SBDs on the surfaces thus etched.

Annealing the $SiCl_4$-etched samples at 450 °C for 30 min left their IV characteristics virtually unchanged while reducing the overall deep level concentration by about two orders of magnitude. This resulted in a reduced level of sub-surface free carrier compensation. The same annealing procedure also improved the IV characteristics of He etched samples but not nearly to a level acceptable for device fabrication. The DLTS spectra recorded from SBDs fabricated on annealed He-processed GaAs surfaces showed a strong indication of carrier compensation and minority carrier effects.

The results presented above lead us to conclude that, from a defect and electrical characterization point of view, $SiCl_4$ plasma etching allows the fabrication of SBDs with excellent IV characteristics as well as the introduction of a prominent metastable defect which could be of technological importance. We have also made progress in identifying some of the defects introduced in GaAs when exposing it under typical RIE conditions to He, the lightest of the noble gasses.

ACKNOWLEDGEMENTS

We gratefully acknowledge the financial assistance of the Foundation for Research Development and the Carl and Emily Fuchs Institute for Microelectronics.

REFERENCES

[1] S. J. Fonash, J. Electrochem. Soc. **137**, p. 3885 (1990).

[2] M. B. Johnson, T. C. McGill and N. G. Paulter, Appl. Phys. Lett. **54**, p. 2424 (1989).

[3] S. Ashok, H. Kräutle and J. Beneking, Appl. Phys. Lett. **45**, p. 431 (1984).

[4] Y. G. Wang and S. Ashok, J. Appl. Phys. **65**, p. 2371 (1989).

[5] F. D. Auret, S. A. Goodman and G. Myburg, unpublished.

[6] D. V. Lang, J. Appl. Phys. **45**, 3014 (1974).

[7] E. Grusell, S. Berg and L. P. Andersson, J. Electrochem. Soc. **127**, p. 1573 (1980).

[8] A. Vaseashta, A. Elshabini-Riadanf and L. C. Burton, Materials Science and Engineering **B 9**, p. 489 (1991).

[9] F. D. Auret, S. A. Goodman, G. Myburg and W. E. Meyer, J. Vac. Sci. Technol. **B 10**, p. 2366 (1992).

[10] D. Bauza and G. Pananakakis, J. Appl. Phys. **69**, p. 3357 (1991).

[11] F. D. Auret and S. A. Goodman, Appl. Phys. Lett. **68**, p. 3275 (1996).

[12] S. J. Pearton, U. K. Chakrabarti, W. S. Hobson and A. P. Kinsella, J. Vac. Sci. Technol. **B 8**, p. 607 (1990).

[13] M. Meyyappan, H. S. Lee, D. Eckart, M. Namaroff and J. Sasserath, J. Vac. Sci. Technol. **B 10**, p. 1215 (1992).

[14] D. Lootens, P. Van Daele and P. Demeester, J. Appl. Phys. **70**, p. 221 (1991).

[15] Y. Zohta and M. O. Watanabe, J. Appl. Phys. **53**, p. 1809 (1982).

[16] S. J. Pearton, U. K. Chakrabarti and A. P. Perley, J. Appl. Phys. **68**, p. 2761 (1990).

[17] B. Ziebro, J. W. Hemsky and D. C. Look, J. Appl. Phys. **72**, p. 78 (1992).

[18] B. G. Svensson, B. Mohadjeri, A. Hallen, J. H. Svensson and J. W. Corbett, Phys. Rev **B 43**, p. 2292 (1991).

[19] S. J. Fonash, S. Ashok and R. Singh, Appl. Phys. Lett. **39**, p. 423 (1981).

[20] F. D. Auret, R. M. Erasmus, S. A. Goodman and W. E. Meyer, Phys. Rev. **B 51**, p. 17 521 (1995).

[21] F. D. Auret, S. A. Goodman, R. M. Erasmus, W. E. Meyer and G. Myburg, Nucl. Instr. and Meth. in Phys. Res. **B 106**, p. 323 (1995).

[22] S. A. Goodman, F. D. Auret and W. E. Meyer, Nucl. Instr. and Meth. in Phys. Res. **B 90**, p. 349 (1993).

[23] D. Pons and J. C.Bourgoin, J. Phys. C: Solid State Phys. **18**, p. 3839 (1985).

[24] S. A. Goodman, F. D. Auret, M. Hayes, G. Myburg and W. E. Meyer, Phys. Stat. Sol. (a) **140**, p 381 (1993).

DAMAGE INDUCED BY A LOW-BIASED 92-MHz ANODE-COUPLED REACTIVE ION ETCHER USING CHLORINE-NITROGEN MIXED PLASMAS

Tadashi SAITOH, Hideki GOTOH, Tetsuomi SOGAWA, and Hiroshi KANBE
NTT Basic Research Laboratories
3-1 Morinosato-Wakamiya, Atsugi, Kanagawa 243-01, Japan
saitoh@wave.brl.ntt.co.jp

ABSTRACT

Dry-etch damage, introduced by a low biased 92-MHz anode-coupled reactive ion etching (RIE), in MBE-grown undoped GaAs has been characterized by photoreflectance (PR) and photoluminescence (PL) measurements. PL spectra show emission peaks at 1.516 eV (excitons) and at 1.494 eV (D-A, B-A) before etching, whereas a new emission peak at around 1.488-1.490 eV appears after the RIE. The depth distribution of this new emission center, examined by PL measurements with a combination of step wet etching, has a Gaussian-shape with a 1/e value of 56 nm. A very small number of nonradiative recombination centers are considered to be generated, because the integrated PL intensity including both emission peaks at 1.490 eV and at 1.516 eV is the same before and after the RIE. The surface recombination rate of the sidewall formed by the RIE is almost the same as that of the wet-etched surface. This low-damage etching has been applied to fabricate ultra-fine GaAs patterns to provide a nanometer-scale ridge structure with a cross-section 15-nm wide by 150-nm high. The low damage etching condition is also suitable for precise fabrication.

INTRODUCTION

Much attention has been paid to semiconductor low dimensional structures from the viewpoint of electronic and optoelectronic applications that take advantage of their distinctive shapes in the density of states. Sufficiently small structures on a nanometer scale can be fabricated using a combination of electron beam lithography and conventional reactive ion etching (RIE). However, conventional RIE damages the semiconductor surface, resulting in poor emission efficiency. We have been developing a low-biased anode-coupled RIE using a very high frequency (VHF) of 92 MHz, aiming at both precise fabrication and low etching damage. Self-bias voltage is reduced in the VHF plasma [1-2], leading to low ion energies, which are essential for reducing damage and contamination. Additionally, the VHF plasma can be generated at lower pressures than the conventional 13.56 MHz plasma. This low pressure operation is favorable for anisotropic etching. Furthermore, due to the anode-coupled electrode configuration, the ion energy incident on the substrate can be controlled almost independently of the rf conditions. No studies have ever tried to clarify the degree of process damage introduced by this kind of anode-coupled VHF-RIE.

In this paper, the damage caused by the anode-coupled VHF-RIE on the etched GaAs surface is assessed by photoreflectance (PR) and photoluminescence (PL) measurements. In addition, the recombination rate of the sidewall formed by the RIE is also characterized by the PL intensity dependence on the stripe width of quantum well in comparison with those made by wet chemical etching. This low-damage RIE process has been used to fabricate a nanometer-scale GaAs ridge structure.

EXPERIMENTAL

For PR measurements and the fabrication of the ridge structure, Si-doped ($3x10^{17}$ cm^{-3}) (001) oriented horizontal-bridgman (HB) GaAs wafers were used. MBE-grown undoped (001) GaAs layers with a thickness of 2 μm were used for PL measurements. The samples used for the sidewall damage assessment were prepared from single-quantum well structures grown by MBE on semi-insulating GaAs substrates. The quantum well wafers consisted of a 6-nm-thick GaAs well sandwiched between $Al_{0.35}Ga_{0.65}As$ barrier layers. They were also covered with a 8-nm GaAs cap layer. The submicron pattern for the sidewall characterization and the nanometer-scale

Mat. Res. Soc. Symp. Proc. Vol. 442 © 1997 Materials Research Society

pattern for the fabrication of the GaAs ridge structure were made on the resist (ZEP520: Nippon Zeon) using electron beam lithography. The pattern was then transferred to a 20-nm-thick nickel mask by the lift-off technique. All samples were degreased and cleaned in an ultrasonically stirred organic alkali solution (Furuuchi: Semicoclean 23) for 15 min just before loading them into the load-lock chamber.

The RIE system comprises a pair of parallel electrodes 4 cm apart. The rf power was supplied to the lower electrode through a blocking capacitor. The ion energy incident on the substrate was changed by a dc bias voltage applied to the upper electrode. The gas pressure during etching was controlled by mass flow controllers and a variable conductance valve.

After evacuating the load-lock chamber below $1x10^{-5}$ Pa, samples were transferred to the etching chamber via a transfer tunnel having a base pressure of $1x10^{-8}$ Pa. The chamber was evacuated by a turbomolecular pump; a base pressure of $8x10^{-6}$ Pa was obtained before the process gases were introduced. The flow rates of chlorine and nitrogen were 9 and 1 sccm, respectively. The gas pressure during etching was measured with an MKS Baratron gauge, and was adjusted to 0.27 Pa with the variable conductance valve. The applied rf power was 30 W, and the negative dc bias applied to the substrate was varied from 20 to 80 V. A commercial argon ion milling system (Millatron) was used to make damaged wafers for comparison with the RIE samples.

PR measurements were performed at room temperature. The pump beam was supplied by chopping a defocused He-Ne laser (632.8 nm) with intensities ranging from 0.03 to 10 mW/cm^2. The probe beam was the monochromatic light output from a halogen lamp through a 25-cm grating monochromator. It was focused on the GaAs wafer with an incident angle of 45 degrees, while the pump beam was normally incident on the surface. The reflected probe beam was detected with a Si detector via an optical filter in order to eliminate the scattered pump beam.

For the PL measurements the samples were excited with an Ar ion laser (all line). A He-Ne laser with a wavelength of 632.8 nm was used for the characterization of sidewall damage. Measurements were carried out at room temperature and 16 K. The luminescence was detected with a liquid-nitrogen cooled optical multichannel analyzer equipped with a grating monochromator, providing a wavelength resolution of 0.83 nm. Control spectra were measured in the region adjacent to the RIE etched area. This region was masked by thermally-evaporated SiO film.

RESULTS

The PR signal ($\Delta R/R$) dependence on the modulation intensity of the pump beam is shown in Fig. 1. The signal intensity was measured by taking the peak intensity of E_0 transition. The PR measurement is more sensitive to the surface region than PL measurements. The dielectric constant change of the region less than 30 nm from the surface contributes to the PR signal [3]. Curves in Fig. 1 were well fitted to the plots using the function [4]

$$\frac{\Delta R}{R} = A \cdot \log\left(1 + \log\frac{I_{\mathrm{mod}} B}{N_t}\right), \qquad (1)$$

where, A and B are constants, I_{mod} is the modulation intensity of the pump beam, N_t is the density of the recombination center, and the amount of surface electric field strength variation is assumed to be small. The spacing of Franz-Keldysh oscillation, which reflects the electric field of the surface region, did not change in this experiment. The density of the nonradiative recombination center can be assessed by using the value of the fitting parameter, B/N_t. The B/N_t values were the same, 11.07 for both the RIE sample and the control sample, which implies that the density of the nonradiative recombination center did not increase during RIE. The B/N_t values for the samples Ar-milled with a dc bias voltage of 100 and 200 V were 0.095 and 0.014, respectively, indicating that the recombination center density of Ar-milling samples were from two to three orders of magnitude greater than that of the control sample.

The PL spectra of undoped GaAs wafers etched by the RIE with a dc bias voltage of 40 V and the ones that were Ar-milled with a dc bias voltage of 100 V are shown in Fig. 2 along with the

control sample spectra. At room temperature [Fig. 2(a)] the emission spectrum of the RIE sample is in agreement with that of the control sample, suggesting no increase in the recombination center density during the RIE, which is consistent with the above mentioned PR measurement. On the other hand, the luminescence intensity of the Ar-milled sample was reduced to about 40% of the control sample intensity due to the increase of the nonradiative recombination center density. At 16 K the luminescence spectra have two peaks. The intensity of the exciton emission at 1.516 eV for the RIE sample was reduced to 80% of the control sample intensity [Fig. 2(b)]. The control sample spectrum in Fig. 2(b) has an emission peak related to a conduction-band to neutral-carbon-acceptor transition, (e, A^0), at 1.494 eV, whereas a new emission peak at 1.488-1.490 eV appears for the RIE and the Ar-milled samples. It should be noted that the wavelength of the new emission peak and the (e, A^0) peak could not be resolved well; however, they are apparently different emission centers, as will be discussed later. The exciton emission peak intensity of the Ar-milled sample was again reduced to about 35% of the control sample intensity.

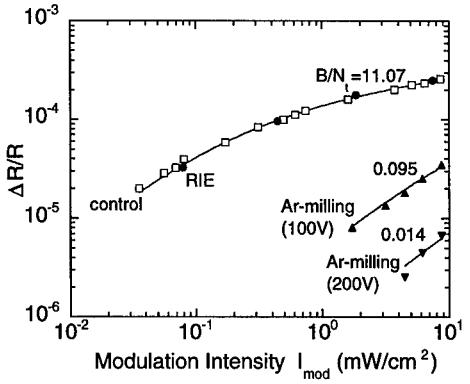


Fig. 1 Photoreflectance signal dependence on the modulation intensity of the pump beam. □: control; ●: RIE (bias: 40 V); ▲: Ar-milling (bias: 100 V); ▼: Ar-milling (bias: 200 V). Curves are theoretical fit using Eq. (1).

Integrated PL intensities are shown in Fig. 3 as a function of the dc-bias voltage. Integration was carried out in the ranges shown in Fig. 2; 750-950 nm for the spectra at room temperature

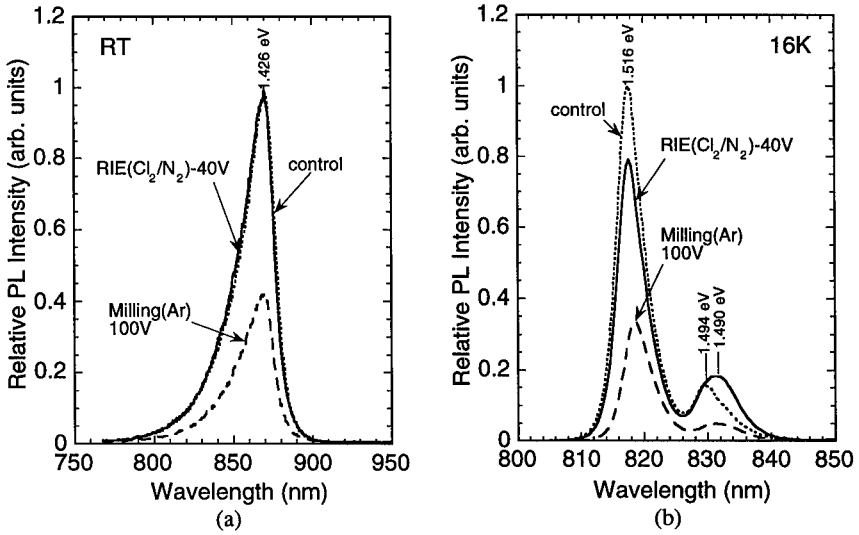


Fig. 2 Photoluminescence spectra of MBE grown undoped GaAs (a) at room temperature and (b) at 16 K. Solid lines: control; dotted lines: RIE (bias: 40 V); broken lines: Ar-milling (bias: 100 V).

and 800-850 nm at 16 K. The integrated values were normalized by that of the control sample. The integrated PL intensity levels of the RIE sample and the control are the same at both room temperature and 16 K in the bias range from 20 to 80 V, which implies that little damage was caused by this RIE treatment. On the other hand, the Ar milling caused heavy damage, resulting in the reduction of integrated PL intensity to less than 40% of the control intensity.

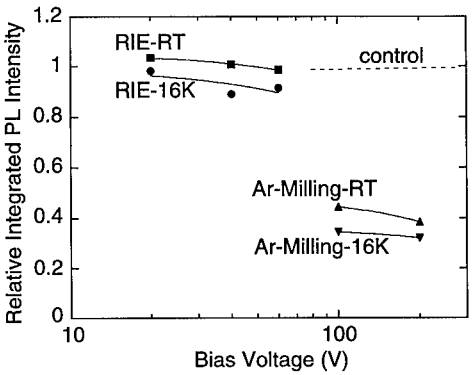


Fig. 3 Bias dependence of integrated PL intensity for RIE and Ar-milling samples. ■: RIE measured at room temperature; ●: RIE measured at 16 K; ▲: Ar-milling measured at room temperature; ▼: Ar-milling measured at 16 K.

Figures 4(a) and (b) show the excitation intensity dependence of the PL spectra for the control sample and the RIE sample, respectively, with a dc bias voltage of 40 V measured at 16 K. The excitation Ar-laser intensities were in the range of 0.01-10 W/cm^2. The emission spectra of the control sample display typical luminescence features of undoped GaAs [5]; the exciton transition, (x), at 1.516 eV remains fixed in energy and the residual carbon related emission peak, (D^0, A^0), at around 1.49 eV moves to higher energies because the recombination emission of the more distant donor-acceptor pairs saturate as the excitation intensity increases. The luminescence spectra of the RIE sample exhibited a different feature. The second emission peak is steady at 1.488 eV for all excitation intensities, though it

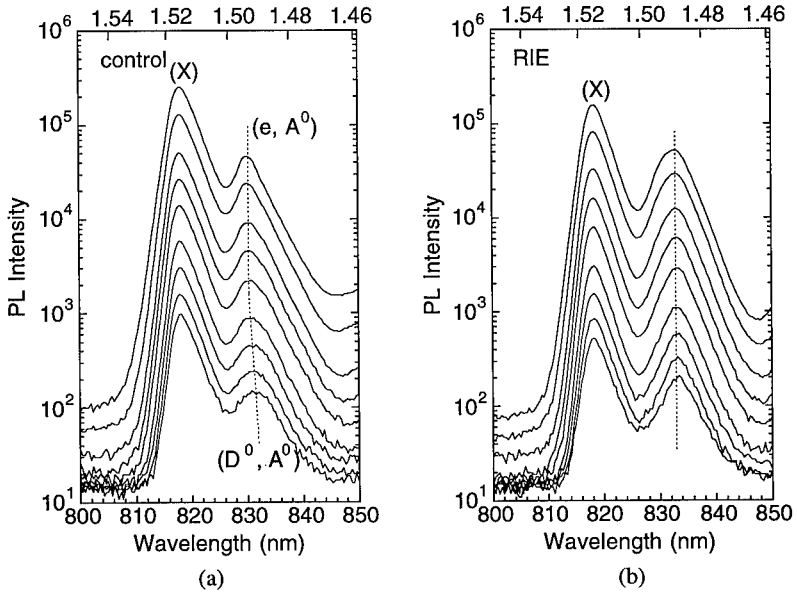


Fig. 4 Excitation intensity dependence of PL spectra of the (a) control sample and (b) RIE sample (bias: 40 V).

seems to move slightly toward higher energies due to the increase of the band-to-acceptor emission at 1.494 eV.

A separate experiment was conducted to elucidate the origin of this new emission center. We prepared five GaAs wafers, each implanted with nitrogen, carbon, oxygen at 40 keV, with chlorine at 50 keV, and with arsenic at 100 keV. The doses were the same for all the wafers: $1x10^{16}$ cm^{-2}. The PL emission intensity of all the as-implanted samples decreased due to the ion-irradiation damage and a new emission peak appeared at around 1.488 eV irrespective of the implanted species. This suggests that the new emission center is not due to contamination, but rather to defect-related vacancies or anti-sites generated during the RIE process.

In order to estimate the depth profile of this new emission center density, we measured the PL spectra at 16 K after wet etching the RIE sample with a dc bias voltage of 40 V. The emission center density, N_{EC}, in the wet etched layer with a thickness of Δx was calculated assuming

$$N_{EC} \propto \frac{\Delta I_{PL}}{\Delta x}, \qquad (2)$$

where ΔI_{PL} is the decrement of the PL intensity of the new emission center after wet etching. Generally the PL signal includes information from as deep as a micron or so below the surface due to carrier diffusion. The emission center density profile, however, can be obtained using Eq. (2), assuming that the PL signal change after wet etching is due only to the removal of the surface region.

The obtained emission-center density profile is shown in Fig. 5. It is obvious that the emission centers distribute as deep as 100 nm from the surface. The curve is a Gaussian curve fitted to the plots, giving a 1/e value of 56 nm. The emission centers penetrate deeper than the ion-projected range at this ion energy. This deep penetration phenomenon agrees well with results reported in a number of other papers [6-11].

For the characterization of the sidewall damage induced by the RIE process, we measured the relative quantum efficiency of an etched GaAs/$Al_{0.35}Ga_{0.65}As$ quantum well for stripe widths between 30 nm and 10 μm at a temperature of 16 K. The stripe structures were fabricated by RIE with a bias voltage of 40 V or by wet chemical etching using a solution of H_2SO_4: H_2O_2: H_2O. The samples were excited with a 500-μW He-Ne laser with a wavelength of 632.8 nm focused to a diameter of about 100 μm. Only the quantum efficiency of the GaAs well region can be determined because the excitation energy is smaller than the $Al_{0.35}Ga_{0.65}As$ barrier band gap. The PL spectra did not exhibit significant changes in shape and energetic position after etching for all stripe widths.

Figure 6 shows the integrated emission intensity of GaAs/$Al_{0.35}Ga_{0.65}As$ quantum well stripes made by the RIE and wet etching as a function of geometrical stripe width. The quantum efficiency was obtained by integrating the emission spectra related to the lowest excitonic transition, and it was normalized by the integrated value at a stripe width of 10 μm. The error bars represent the experimental error over three runs for RIE samples. The quantum efficiency decreases with decreasing stripe width. This width dependence is attributed to surface recombination at the stripe sidewalls. The quantum efficiencies of GaAs/ $Al_{0.35}Ga_{0.65}As$ quantum wells etched by the RIE and wet etching are the same within experimental error, which indicates that the sidewall damage induced by this RIE process is as negligibly small

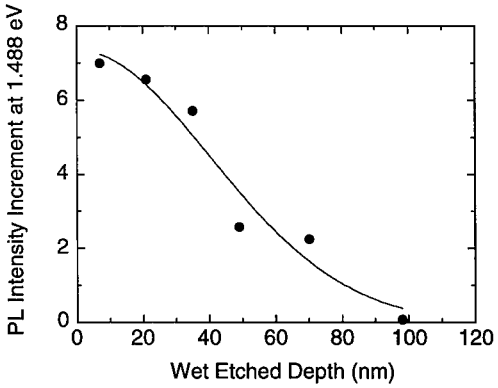


Fig. 5 Depth profile of the new emission center induced by RIE. The curve is a Gaussian fit to the plots with a 1/e value of 56 nm.

as that induced by wet etching as far as emission efficiency is concerned. The quantum efficiency of PL, $I(W)/I(\infty)$, can be approximated [12] by

$$\frac{I(W)}{I(\infty)} = \frac{W_{eff}}{S \cdot \tau + W_{eff}} . \qquad (3)$$

Here, W_{eff} is the effective stripe width which is obtained by subtracting surface dead-layer thickness from the geometrical stripe width, W, S is a surface recombination velocity, and τ is a carrier lifetime of the bulk material. The curve in Fig. 6 represents $S \cdot \tau$ of 2×10^{-5} cm.

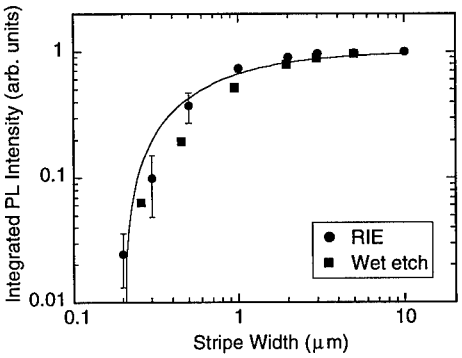


Fig. 6 PL intensity versus the width of quantum well stripe fabricated by RIE (●) and wet etching (■).

An ultra-fine GaAs ridge structure was fabricated [13] using a typical low-damage condition, i.e., chlorine and nitrogen flow rates of 9 and 1 sccm, a total pressure of 0.27 Pa, an rf power of 30 W, and a dc-bias voltage of 40 V applied to the substrate. The GaAs ridge structure has vertical sidewalls. The period is 150 nm, the height,150 nm, and the minimum width, 15 nm. The low damage etching condition in this RIE has been proved to be suitable for precise etching.

CONCLUSIONS

In conclusion, we have characterized the etching damage introduced by anode-coupled VHF (92 MHz) RIE by using photoreflectance and photoluminescence measurements. Nonradiative recombination centers were not generated by this RIE process, even though a new emission center appeared in PL spectra. A nanometer-scale GaAs ridge structure was fabricated using the low-damage condition. The low-damage condition of the anode-coupled VHF-RIE has been revealed to be suitable for precise etching.

ACKNOWLEDGMENTS

We are indebted to Dr. H. Nakanishi for his advise in the photoreflectance measurement. We also acknowledge Dr. H. Ando for useful discussions, and Professor Y. Horikoshi and Dr. N. Uesugi for their encouragement and support.

REFERENCES

[1] J. Kuske, U. Stephan, K. Schde, and W. Fuhs, Mat. Res. Soc. Sump. Proc., **258**, 141 (1992).
[2] H. H. Goto, M. Sasaki, T. Ohmi, A. Yamagami, N. Okamura, and O. Kamiya, IEEE Trans. Semicon. Manufac., **4**, 111 (1991).
[3] H. Nakanishi and K. Wada, The 57th Fall Meeting of Jpn. Soc. Appl. Phys., 7p-ZK-14 (1996) (Japanese).
[4] H. Nakanishi and K. Wada, The 55th Spring Meeting of Jpn. Soc. Appl. Phys., 30p-ZD-2 (1994) (Japanese).; Mat. Res. Soc. Sump. Proc., **324**, 161 (1994).
[5] E. W. Williams and H. B. Bebb, Semiconductors and Semimetals, vol. 8, edited by R. K. Willardson and A. C. Beer (Academic Press, New York, 1972), Chap. 5.
[6] F. Lauruelle, A. Bagchi, M. Tsuchiya, J. Merz, and P. M. Petroff, Appl. Phys. Lett., **56**, 1561 (1990).
[7] T. Kanayama, Y. Takeuchi, and Y. Sugiyama, Inst. Phys. Conf. Ser., No. 129, 573 (1992).
[8] N. G. Stoffel, S. A. Schwarz, M. A. A. Pudensi, K. Kash, L. T. Florez, J. P. Habison, and B. J. Wilkens, Appl. Phys. Lett., **60**, 1603 (1992).
[9] M. Rahman, M. A. Foad, S. Hicks, M. C. Holland, and C. D. W. Wilkinson, Mat. Res. Soc. Sump. Proc., **279**, 775 (1993).
[10] D. L. Green, E. L. Hu, and N. G. Stofell, J. Vac. Sci. Technol. B, **12**, 3311 (1994).
[11] C. H. Chen, D. L. Green, E. L. Hu, J. P. Ibbetson, and P. M. Petroff, Appl. Phys. Lett., **69**, 58 (1996).
[12] B. E. Maile, A. Forchel, R. Germann, and D. Grutzmacher, Appl. Phys. Lett., **54**, 1552 (1989).
[13] T. Saitoh and H. Kanbe, Jpn. J. Appl. Phys., Pt. 2, **35**, L60 (1996).

DONOR REACTIVATION IN PLASMA-IRRADIATED GaAs UNDER LASER ILLUMINATION

K. Wada and H. Nakanishi
NTT System Electronics Laboratories, 3-1 Morinosato-Wakamiya, Atsugi, Kanagawa 243-01, Japan, kwada@aecl.ntt.jp

ABSTRACT

Reactivation of Si donors in Ar plasma-irradiated GaAs under reverse bias annealing (RBA) is substantially enhanced by Ar laser illumination. Reactivation occurs only in the surface layer and charge density overshoots its original donor density. These are identical to those observed by high temperature RBA without laser illumination. The activation energy of the reactivation rates is about 0.1 eV, whereas it is about 0.7 eV without laser illumination. The energy reduction is explained by charge state change of deactivators in terms of two hole capturing under minority carrier injection. These findings suggest that deep levels induced by complexes of Si donors with point defects should be present above midgap. The deep penetration mechanism of plasma-induced point defects is discussed, based on the present findings.

INTRODUCTION

It is quite well known that plasma irradiation leads to deactivation of dopants in both n- and p-GaAs. One of the deactivation factors is to be hydrogen.[1] However, it may be difficult to say that all deactivation phenomena induced by plasma irradiation would be hydrogen especially in case of irradiation of plasma but hydrogen.[2] In the present paper, we refer to all kinds of plasma-induced damage as point defects, including hydrogen for the time being. In order to understand what kind of point defects are generated and how they interact with dopants, we have been studying point defects induced by Ar plasma irradiation in GaAs.

One of the most interesting phenonema is deep penetration of point defects into GaAs, as typically shown in Fig. 1; around 100 nm deep during one-minutes-plasma irradiation at room temperature.[3] We have studied the behavior of point defects by using so called reverse bias annealing (RBA)[3]: Annealing of samples with Schottky contacts under reverse bias application. This indicated that the drift velocity of deactivators is fairly high but not enough to explain the deep penetration noted above. It should be noted here that plasma ir-

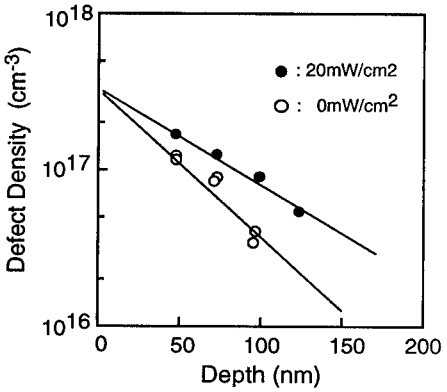


Fig. 1 Deep Peneration of Plasma-induced Point Defects and Its Enhancement by Laser Illumination

Mat. Res. Soc. Symp. Proc. Vol. 442 © 1997 Materials Research Society

radiation is often accompanied with light illumination induced by plasma emission. However, it is not clear the effect of light. We have reported that light illumination, about 20 mW/cm^2, to sample surfaces during plasma irradiation indeed causes deeper penetration of point defects into samples also shown in Fig. 1.[4] However, it is still open question what is enhanced by light illumination, e.g., diffusivity of point defects, detrapping process from donors and so on. In order to understand the effect of light, we have performed illumination of the samples during RBA. It is found that Si donor reactivation is substantially enhanced by light illumination even below room temperature. Based on the results, we will discuss a mechanism of the deep penetration.

EXPERIMENT

Samples studied in this study were Si-doped GaAs ($n = 2 \times 10^{17}$/cm^3) grown by the Horizontal Bridgman method. Samples with Ohmic contacts on back side were subjected to Ar plasma irradiation for 1 min., which was generated using the parallel plate reactor (RF power: 50 W, Pressure: 10 Pa). Such a plasma treatment introduces a sufficient quantity of point defects into GaAs, deactivating Si donors in the subsurface layer extending to a depth of 150 nm below the surface[1]. Ti Schottky diodes, 1 mm in diameter and 20 nm in thickness, were then deposited on these samples by using an electron beam evaporator. Prior to the deposition, extensively damaged surface layers on the samples were etched off to a depth of 20 nm. Such a slight etch-off process of the surface layer was essential for these samples to avoid shift and drift of built-in potential during bias application at elevated temperatures[5].

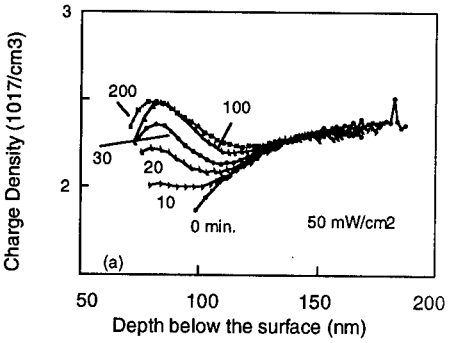
The prepared diodes were subjected to RBA under the following conditions: 0 and -4 V for 0 to 100 min. at -20 to 100 °C with or without the light illumination. Then, C-V measurements were followed to measure the depth profiles of point defects deactivating the Si donors. Thus, our measurements were insensitive to neutral point defects.

Light illumination was carried out by Ar^+ laser with a power density of 50 mW/cm^2 through the thin Schottky contacts. The temperature rise induced by laser illumination was estimated by photoreflectance measurements to be less than 10 °C and negligibly small. The incident photon flux was monitored by measuring the photocurrent of the diodes at room temperature before and after RBA. The photocurrent used in the present study was about 100 μA which was two orders of magnitude larger than that of the diode dark current biased at -4 V.

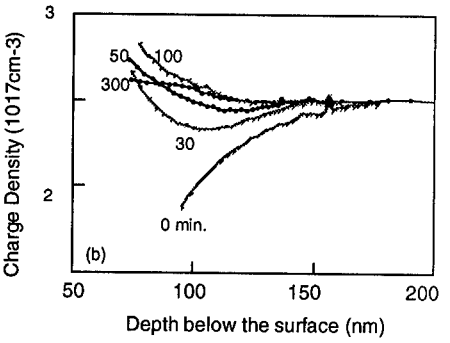
RESULTS

The effects of enhancement induced by laser illumination were observed at all temperatures used in the study. Figure 2 shows the change in the charge density depth profile with time, taking RBA at 25 °C as an example. We found that diodes subjected to RBA with light illumination gave indications of recovery, that is, the increase at room temperature in the charge density reduced by plasma-irradiation. The rate of reactivation is similar to that at 150 °C shown in Fig. 2(b), indicating substantial enhancement. In contrast to this, no changes were observed neither in diodes subjected to RBA without illumination at room temperature nor in diodes annealed even at 200 °C without light illumiation and bias application. These observations of "no changes" led us to conclude that

the point defects should form some kinds of complexes with Si donors to deactivate Si donors.[4] Based on the results, we proposed a model for reactivation[4]: Si donor reactivation by RBA at 150 °C without light illumiation would be induced by emission of two electrons from the complexes to the conduction band. Such a charge state change of the complexes could induce coulombic replusion between point defects and Si donors. This results in dissociation of a single-positive-charged point defects from a complex, leaving a single-positive-charged Si donor. In other words, Si donors are reactivated.



(a) with illumination(25°C, -4V)



(b) without illumination (150°C, -4V)

Fig. 2 Change in Charge Density Profiles during RBA

Now, we adopt the model to the present reactivation enhancement under light illumiation. Then the reactivation is explanable if a capture cross section of the complexes for hole is large. One complex of one point defect with one Si donor could capture two photo-excited holes under light illumination instead of emitting two electrons. In Figs. 2 (a) and (b), charge densities in the surface layer exceed the original donor density in samples without plasma irradiation. These reslts also confirm that point defects become positive-charged by RBA. Restoring the density after a long period of RBA as typically shown in Fig. 2 (b) proves charge states of the point defects to be positive: Point defects are conveyed away toward the surface by electric field drift. Thus, the present observations under light illumination is explained by the model noted above. Light illumiation enhances at least dissociation of point defects from the complexes but it is not yet clear if its diffusivity is enhanced. The model demands that there should be at least one defect state within the bandgap. Otherwise, hole capturing will not occur. This is in clear contract to hydrogen passivation, since hydrogen passivation would eliminate states from the bandgap as noted above.

To represent the minority carrier injection effect on complex decomposition more quantitatively, we examined the rate constant of reactivation kinetics. This was carried out by monitoring the charge density in a limited region in the damaged layer throughout the RBA. Figure 3 shows the annealing kinetics of defects deactivating Si donors at various temperatures ranging from -20 to 100 °C. The defect density was calculated by subtracting the charge density from original donor density. Here, we observed a region at a depth of 100 nm below the surface to calculate defect densities. It is clear that the reactivation of dopants is dominated by the first order kinetics of defect reaction at the initial stage of RBA, i.e., the reaction is decomposition reaction of

the complexes.

It should be marked here that defect annealing occurs even below room temperature. This must be one clue to explain deep penetration. We will come back this point later.

Figure 4 shows the Arrhenius plot of rate constants of defect decrease. We found that the activation energy is about 0.11 eV under laser illumination, which is substantially reduced from about 0.73 eV for RBA obtained at high temperature without laser illumination. This strongly suggests that the barrier height for the complexe decomposition is greatly reduced by the aid of minority carrier injection.

To assess the details of the deactivation mechanism, we have studied the thermal stability of reactivated Si donors. Figure 5 shows an example. The charge density near the surface region, which was increased once by RBA with light illumination, decreased after heat treatment around 100 °C and its profile is nearly the same as before RBA. This suggests that the dissociated point defects are metastable and change their charge states from positive to negative by heat treatment even at low temperatures of around 100 °C, again making complexes with Si donors. The stability of the reformed complexes will be reported elsewhere.

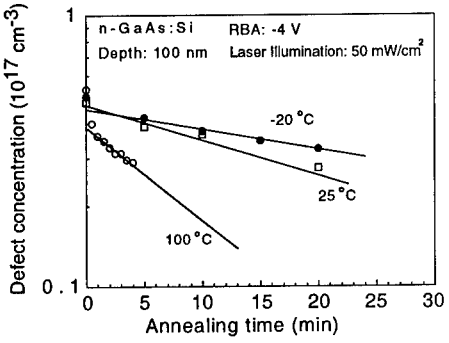


Fig. 3 Reactivation Kinetics of Si Donors

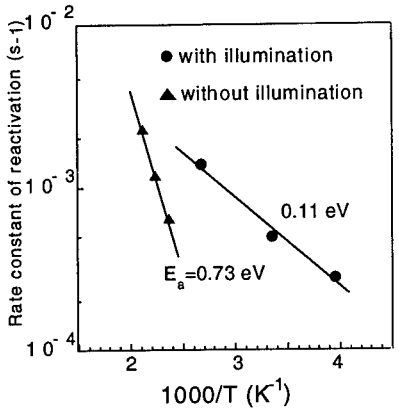


Fig. 4 Temperature Dependence of Reactivation Rates

DISCUSSIONS

The origin of point defects and mechanism of deep penetration are briefly discussed here. Regarding the possibility of point defects with extrinsic natures, candidates that may need to be considered are hydrogen atoms, which might unintentionally be introduced into GaAs during plasma processing. The activation energy of Si-H decomposition by RBA, which was reported by Pearton, was 1.25 eV[1]. This is rather large compared with our results of 0.73 eV by RBA, as shown in Fig. 4. This may deny the possibility

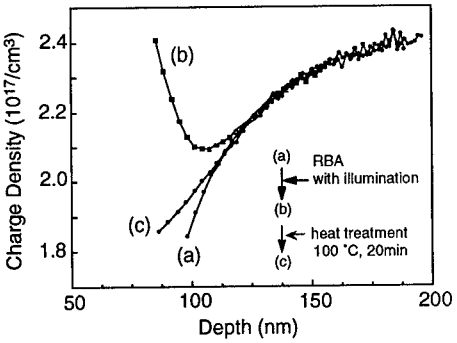


Fig. 5 Deactivation of Reactivated Donors by Annealing

of hydrogen atoms being the cause of plasma-induced point defects in this experiment. So, intrinsic point defects are discussed as possible candidates.

It was found, using the positron annihilation technique, that the plasma-induced defects induced in Si doped GaAs were of the interstitial type[6]. Recent caluclations[7,8] indicate that self-interstitials can be both positive- and negative- charged, depending on their lattice configuration. In other words, when interstitials are in the split configurations and off-site bond centers, they would be negative-charged. Then, they could form complexes with Si donors to generate neutral deep states, i.e., deactivation of Si donors. Capturing holes induced by plasma irradiation at the deep states may induce decomposition of the complexes and end up with dissociation of positive-charged point defects at tetrahedral sites (TD1) and (TD2). This supports the occurrence of charge reversal under light illumination.

Without light illumination the decomposition reaction consume 0.73 eV as shown in Fig. 4. Our model suggestes that this coresponds to the emission barrier for electrons from the complexes. However, under illumination the decomposition reaction is not athermal, but the reaction has activation energy about 0.1 eV. This suggests two possibilities. One, there is an energetic barrier to capture holes at the complexes. Two, there is an excess energetic barrier to decompose the complexes. However, deep levels induced by the complexes should be present above midgap, since Si donor reactivation occurs only in the depletion layer. This means that the first possibility would not be valid. Accordingly, the deep level by the complexes should bethe difference between the two activation energy, i.e., about 0.6 eV.

On the other hand, simple thermal annealing around100 °C deactivates Si donors again, as shown in Fig. 5. However, no deactivation of reactivated Si donors was observed in samples shown in Fig. 2(b) by thermal annealing at the same temperature. We assume metastablity of the complexes of point defects (referred to Y) and Si donors .

$$(SiY) + 2h^{+} \leftrightarrows (Si^{+} \cdot Y^{+}) \rightarrow Si^{+} + Y^{+} \qquad (1)$$

In other words,during low temperature RBA with light illumination the reaction just occurs upto intermidiate stage, i.e., $(Si^{+} \cdot Y^{+})$, while during high temperature RBA without illumination the end reaction occurs. Small diffusivity of point defects at low temperature may help the end reaction not occur in reaction (1). Thus, the end reaction requires some energy, meaning that the activation energy is the lowest limit of decomposion energy. This suggests that the deep levels 0.6 eV estimated above is the deepest limit.

Finally, let us briefly comment on deep penetration mechanism. Diffusion length of plasma-induced point defects should be limited by trapping and detrapping processes by and from Si donors at these low temperatures; so called "trap-limited diffusion". This suggests that the penetration depth of point defects should be strongly dependent on dopant density in GaAs, i.e., the less doping, the deeper penetration. This was indeed observed (not shown here). As is observed, light illumiation substantially helps point defects dissociate from the complexes, i.e., enhancing detrapping process. This means that the diffusion process of point defects under light illumination is no more trap-limited, i.e., simple diffusion. On the other hand, the results in Fig. 2(b) indicate that positively charged point defects themselves are not very fast diffusers, since they do not easily drift even at

150 °C. Based on these results, we would propose a model on the deep penetration: Point defect Y is negative charged when its state is located below the Fermi level, which results in complex formation of Y with a Si donor, i.e., SiY. Light illumination enhances detrapping process of Y from Si donors. Thus, the diffusion process of Y is not trap-limited under plasma light illumination, since detrapping of Y quickly occurs when Y is trapped by a Si donor. Negative-charged Y diffuses fast or change in charge state of Y makes Y diffuse fast and deeply penetrates, since positive-charged Y is not a fast diffuser.

SUMMARY

We found that light illumination combined with RBA strongly enhances the reactivation of Si donors in n-GaAs. A model proposed for reactivation of Si donors under RBA without light illumitation can explain the enhancement. The light-illumination- enhanced reactivation is caused by charge reversal effect of point defects under minority carrier injection. This model requires that complexes of plasma-induced point defects with Si donors have a deep state above midgap. These findings provide us a new insight for deep penetration of point defects induced by plasma irradiation.

ACKNOWLEDGMENTS

The authors would like to thank L.C. Kimerling of Massachusetts Institute of Technology for his valuable discussion. They would also like to thank M. Mitsuhashi of NTT Advanced Technology for her experimental contributions and H. Fushimi of NTT System Electronics Laboratories for discussions.

REFERENCES

1. S. J. Pearton, C. R. Abernathy, and J. Lopata, Appl. Phys. Lett. **59**, 3571 (1991).
2. For example, T. Shinagawa and T. Okumura, in this proceedings.
3. H. Nakanishi, K. Wada and W. Walukiewicz, J. Appl. Phys. **78**, 5103 (1995).
4. K. Wada, H. Nakanishi and L.C. Kimerling, Materials Science Forum **196-201** (1995) 1401.
5. K. Yamada and K. Wada, 8th Conference on Semi-insulating III-V Materials (World Scientific, Singapore, 1994), p. 251.
6. A. Uedono, T. Kawana, S. Tanigawa, K. Wada, and H. Nakanishi, Jpn. J. Appl. Phys. **33**, L1374 (1994).
7. G. Baraff and M. Schulter, Phys. Rev. Lett. **55**, 1327 (1985).
8. D.J. Chadi, Phys. Rev. **B46**, 9400 (1992).

OPTICAL AND ELECTRICAL CHARACTERISATION STUDY OF $SiCL_4$ REACTIVE ION ETCHED GAAS

M. Murtagh, Shu-Ren Ye, H.J. Masterson, J.T. Beechinor, G.M. Crean
F.D. Auret, P.N.K. Deenapanray, W.E. Meyer, S.A. Goodman and G. Myburg†

National Microelectronics Research Centre (NMRC), Lee Maltings, Prospect Row, Cork, Ireland.

† Physics Department, University of Pretoria, 0002, South Africa.

ABSTRACT

In this study $10^{16}cm^{-3}$ n-type epitaxial GaAs was reactive-ion-etched (RIE) in a parallel plate type reactor as a function of rf power and gas pressure using a $SiCl_4$ plasma. The sample matrix followed a 3 level 3 factorial statistical experimental design. Photoreflectance (PR) was employed to characterise the etch induced modification to the electronic band structure at the fundamental band-edge transition. Variable angle spectroscopic ellipsometry (VASE) and photoluminescence (PL) optical diagnostic techniques are also employed to characterise the plasma processed GaAs. PR results detail a decrease in the surface electric field (F_s) with etch severity arising from an RIE induced electron trap that increases in concentration with energetic ion sputtering. For the highest rf power densities PR further distinguishes between reactant desorption and adsorption limited etching regimes. VASE and PL data reveal the extent and degree of surface modification of the etched substrates. Atomic-Force-Microscopy showed the etched surfaces to have an average roughness, R_a of 15nm. Optical characterisation data are correlated with electrical measurements using fabricated Schottky barrier diodes for deep-level-transient spectroscopy (DLTS) as well as current-voltage and capacitance-voltage (CV) analysis. CV results detail a reduced surface carrier concentration after RIE while DLTS revealed the emergence of six electron trap defect levels. One of the two prominent RIE induced trap levels exhibited similar DLTS behaviour as that produced after ion bombardment of n-type (Si) GaAs.

INTRODUCTION

Surface processing and in particular plasma etching of GaAs is a key technology for producing optoelectronic integrated circuits, lasers and high speed devices. Silicon tetrachloride ($SiCl_4$) has been shown to be a viable etchant of GaAs resulting in anisotropic, polymer free and low residual damaged surfaces [1]. Residual lattice disorder, however, introduced for example, by energetic ion bombardment during $SiCl_4$ RIE, can directly impact the electronic, transport and optical properties in the near surface region of semiconductor materials. Such surface modification can adversely effect device manufacturing yields via degradation mechanisms such as increased junction leakage, threshold voltage shifts and variations in optical properties [2]. Furthermore, the exact nature of etch induced damage and possible causes such as introduction and propagation mechanisms are not yet understood. One reason for this is the lack of suitable methods for identifying damage confined within the near-surface region.

Mat. Res. Soc. Symp. Proc. Vol. 442 © 1997 Materials Research Society

Optical techniques [3,4] appear to be ideally suited for this purpose, especially due to their non-contact and non-invasive nature and in this work we report the application of Photoreflectance (PR) spectroscopy to characterise the surface electric field of GaAs arising from etch induced modification to the electronic band structure. Experimental PR results are correlated with extracted etch damage optical model parameters from variable angle spectroscopic ellipsometry (VASE), Photoluminescence as well as Atomic-Force-Microscopy data. Finally, optical characterisation data are correlated with electrical measurements using fabricated Schottky barrier diodes for Deep-Level-Transient spectroscopy (DLTS) as well as current-voltage and capacitance-voltage analysis.

EXPERIMENTAL

(100) orientated 1.2-1.5x$10^{16}$$cm^{-3}$ n-type (Si) epitaxial GaAs on $10^{18}$$cm^{-3}$ substrates were utilised in this study. Plasma processing was carried out in a parallel plate reactor (Plasma-Therm 790) operated at 13.56MHz in RIE mode. The samples were subjected to a pre-etch clean using : trichloroethylene, iso-propanol and de-ionised water rinses. Etching was performed as a function of plasma power, 80-200W (DC bias 148-484V) and pressure, 30-90mTorr, using a $SiCl_4$ etch chemistry with a 10sccm gas flow. The samples were etched for 10 mins on a 22°C cooled anodised aluminium base electrode. The etch rate was determined using mechanical profilometry on patterned $10^{16}$$cm^{-3}$ GaAs.

VASE was performed using a variable angle phase-modulated ellipsometer at incidence angles of 65°, 70°, and 75° from 1.6 to 4.5 eV at 20 meV intervals.

The PR spectrometer employed a double scanning monochromator arrangement to probe the 1.2eV to 1.6eV photon energy range at 2meV resolution. The incident probe beam consisted of a tungsten light source with a spot size of 3x1mm incident at 45°. A Si photodetector was used to record the reflected light intensity. The modulation source was a HeNe (632.8nm) laser, mechanically chopped at 1.4kHz, with an intensity of 1mW/cm^2 and 4mm^2 spot size. Photoluminesence measurements were also recorded using the PR experimental arrangement but with increased laser power (25mW/cm^2).

Contact mode Atomic-Force-Microscopy (AFM) was performed over a 10μm^2 area (constant cantilever force) yielding the average deviation, R_a, from the average surface roughness height.

Schottky barrier diodes were fabricated on the $10^{16}$$cm^{-3}$ epi-GaAs substrates by metal deposition of ohmic Ni/AuGeRu/Ni back contacts before etch processing and by resistive evaporation of Pd contacts (60nm thick and 0.77mm in diameter) on the post-etched epi-layers. DLTS analysis involved a two-phase lock-in amplifier based system operating between temperatures of 12 and 400K.

RESULTS AND DISCUSSION

Table I summarises the results of the VASE analysis. A three layer optical model consisting of a GaAs oxide on a two component effective medium approximation (EMA) of amorphous (α) GaAs and GaAs oxide on GaAs substrate was employed in order to interpret the experimental VASE data. The VASE results presented in Table I represent a Levenburg-Marquardt regression to the recorded Tan(ψ) and Cos(Δ) ellipsometric parameters. For the plasma etched substrates there is a small though discernable degradation to the surface as indicated by both an increase in the EMA layer thickness as well as in the degree of amorphisation (% α-GaAs) within this layer.

It is observed that for the high rf powers and at lower plasma pressures, the higher electrode bias results in higher ion energies within the plasma sheath giving rise to increased physical sputtering.

The etch rate data, also presented in Table I, reveal increased etching with decreasing plasma pressure. This increase in the etch rate maybe accounted for by increased ion sputtering which otherwise is reactant desorption limited at the higher plasma pressures [5]. Small reductions in the etch rate for the 200W rf powers (354-484V) suggest a possible adsorption limited [5] etch rate mechanism, whereby the active etchant species viz. $Cl^{\cdot}$, including Si^{+} (ion) sputtering, are inhibited at the surface.

AFM analysis was employed to investigate the surface morphology and revealed the etched surfaces to have an average roughness value, R_a, of about 15nm consistent with physical ion sputtering of the GaAs surface, note a maximum roughness of R_a=40nm was observed for the lowest etch rate condition 80W (148V) 90mTorr. The 200W (354-484V) series resulted in smoother surfaces, typical R_a=3nm, suggesting a minimum of ion sputtering and consistent with an adsorption limited etch rate, described above.

Table I also summarises the results of the RT PL study performed on the etched GaAs epilayers. The intensity of the broad near gap transition feature, centered around 870nm, is seen to decrease monotonically with etch rf power (bias). This is consistent with a decrease in the radiative to non-radiative recombination ratio arising from the formation of etch induced non-radiative processes such as deep level traps, lattice imperfections, incorporated impurities etc. The PL data also show monotonic reductions in the transition intensity as the pressure decreases, at constant power, for both the 80W and 140W series. This maybe correlated directly with the higher ion energies and consequently increased sputtering resulting in increased lattice disorder. For the 200W (354-484V) series of etches, the degradation mechanism reflects the differing etch rate regimes.

Sample Etch Conditions				VASE			PL	Etch Rate
#	rf (W)	Pressure (mTorr)	Bias (V)	Oxide (Å)	EMA Layer Thick (Å)	α-GaAs(%)	Int. (Arb.Units)	(nm/min)
1	-	-	-	26	0	0	1	-
2	80	30	246	23	13	10.8	0.44	250
3	80	60	188	23	13	12.0	0.51	221
4	80	90	148	23	13.9	11.2	0.57	183
5	140	30	384	21	11.5	11.1	0.36	385
6	140	60	302	23	13.4	11.5	0.38	378
7	140	90	252	23	12.8	10.7	0.39	357
8	200	30	484	-	37.6	13.9	0.30	363
9	200	60	405	22	11.9	8.9	0.24	376
10	200	90	354	20	10.1	13.1	0.27	345

Table I. Summary of VASE and PL analysis performed on the $SiCl_4$ treated GaAs. The unbiased estimator was better than $5x10^{-2}$ for all the VASE simulations.

Fig. 1 presents typical PR experimental spectra for the $SiCl_4$ processed epi-GaAs. The spectra reveal a medium to high surface electric field response as indicated by the exponentially broadened band-edge transition, E_0 along with Franz-Keldysh oscillations (FKO) located above

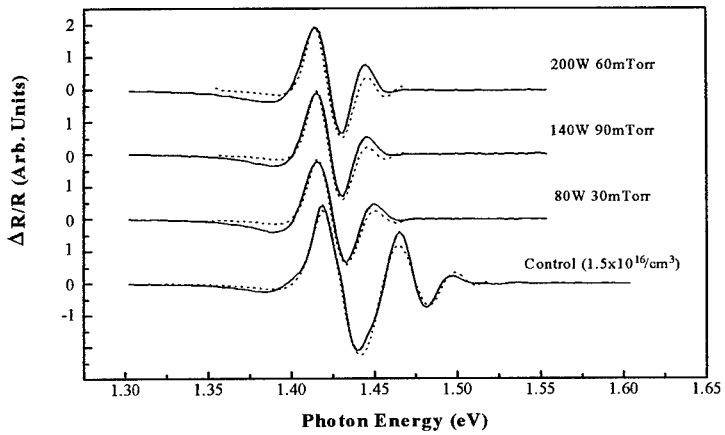


Figure 1. Typical experimental (—) and best fit (---) PR spectra for the $SiCl_4$ processed GaAs showing the medium field electric response at the fundamental E_0 (1.417eV) transition. Note the decrease in the FKO period for the RIE GaAs.

the fundamental band edge (E_0=1.417eV) [4]. The unetched GaAs also exhibited an excitonic transition located approx. 4meV below the band edge, however, for all the etched treated samples this structure was not present in the PR response due to RIE induced surface modification resulting in a quenching of the excitonic feature. The results of a Newton-Gauss least squares regression analysis of a medium field functional form (Airy functions) to the experimental data are also shown in Fig. 1. The surface electric fields (F_s) were obtained from an analysis of the FKO period, specifically from the electro-optic energy [6] using electron and heavy-hole effective masses of 0.067 and 0.34, respectively. Extracted F_s data are presented in Table II along with band-edge transition enegies and spectral broadening parameters. Note that for the 200W (354-484V) samples best fits were achieved assuming the electro-optic function to be dominated by the heavy-hole effective mass. Clearly from the PR spectral data, $SiCl_4$ RIE results in a reduced surface electric field, decreasing with rf power (bias). This reduction of the electric field maybe accounted for by RIE sputter induced electron trap formation [4] resulting in increased charge pinning at the surface and consistent with the PL data of Table I. By employing a Schottky barrier approximation to the surface field [7] and assuming negligible RIE induced changes to the built-in potential, this reduction in F_s maybe correlated to reductions in the majority carrier concentration at the surface, of the order of $1.1x10^{16}/cm^3$, depending upon the etch conditions. Note that due to an adsorption limited etch-rate mechanism for the highest rf power densities, the 200W etch samples experienced less RIE sputtering (smoother surfaces) and consequently exhibited less carrier trap generation than for the 140W series (252-384V). Also, consistent with the PL data of Table I, is that for a given rf power level, the F_s is seen to decrease further as the plasma pressure is reduced, indicating increased physical sputter induced trap generation. The extracted broadening parameters (Γ) from the PR spectra are observed to increase after etching, indicative of a reduced minority carrier lifetime arising from RIE induced scattering mechanisms.

Etch	Photoreflectance			IV & CV		DLTS	
#	E_g (eV)	Γ (meV)	F_s (x10^4 V/cm)	ϕ_b (eV)	I_R (-1V) (x10^{-11}A)	ER3 (x10^{-2})	ER6 (x10^{-2})
1	1.417	6.43	3.21 (±0.1)	0.922	4.0	-	-
2	1.415	8.04	1.94	0.886	3.0	1.70	1.40
3	1.414	7.23	2.75	0.911	1.4	2.15	1.74
4	1.414	8.65	3.09	0.922	2.1	2.20	1.23
5	1.414	7.40	1.46	0.850	5.8	2.30	1.70
6	1.414	7.18	1.51	0.880	2.4	1.70	1.70
7	1.414	7.50	1.63	0.877	2.4	1.60	1.80
8	1.413	7.10	1.65	0.850	6.0	3.13	1.26
9	1.414	6.95	1.66	0.842	7.5	1.40	1.20
10	1.414	7.82	1.78	0.848	6.5	2.60	1.50

Table II. Summary of PR and electrical - IV/CV and DLTS - analysis for the RIE $SiCl_4$ GaAs. DLTS data summarises the relative defect concentrations for the two prominent RIE induced traps - ER3 and ER6. Ideality factor, n, for the SBD's : $1.01<n<1.02$.

Schottky Barrier diodes (SBD's) were fabricated on the etched GaAs in order to determine the current-voltage (IV) and capacitance-voltage (CV) characteristices of the $SiCl_4$ RIE surfaces and also in order to perform deep-level-transient-spectroscopy (DLTS). The variation of the barrier height, ϕ_b, along with the reverse leakage current, I_R, (measured at -1V) for the RIE GaAs SBD's are presented in Table II. It is observed that the effect of RIE was to reduce the barrier height and, for the 140W 30mTorr and 200W series of samples, to increase I_R. This is consistent with the previous optical data detailing RIE induced degradation mechanisms - carrier trap

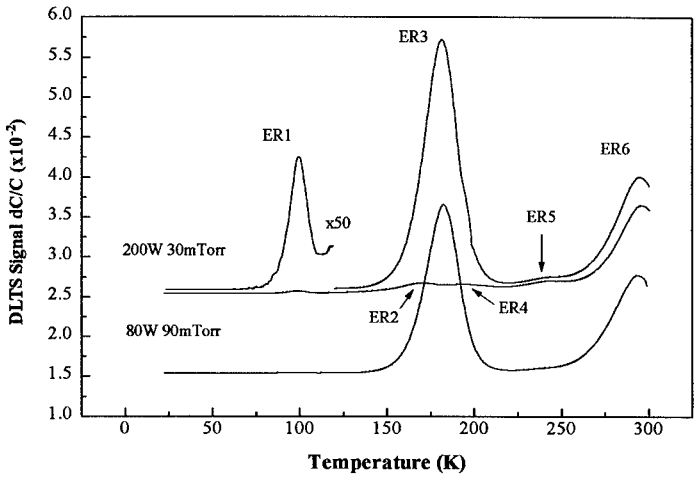


Figure 2. Typical DLTS response revealing the ER1-ER6 defect traps for the $SiCl_4$ etched epi-GaAs. Note the two prominent ER3 and ER6 defect levels.

generation - resulting in increased recombination in the depletion region as well as to increased tunnelling through the potential barrier [8]. Reductions in I_R, observed for the 80W and 140W RIE conditions (148-384V) however, are indicative of possible Si^+ incorporation and thus of possible increased n-type (Si) surface doping. Note that AFM for these etches revealed the roughest (highest R_a) surface morphologies, arising from significant Si ion sputtering. It is interesting to note also that the SBD's also exhibited series resistances of the order of 4-6Ω, compared with 2-3Ω for the unetched control epi-GaAs.

The CV results, however, were characteristic of a sub-surface region in which the carrier concentration decreases towards the surface i.e electron traps [4], consistent with both the PR (F_s) and PL data, presented earlier. CV carrier density profiles further showed the concentration to decrease from about 450nm below the surface.

DLTS revealed the presence of six $SiCl_4$ RIE induced electron trap defect levels (labelled ER1-ER6). Typical DLTS responses are presented in Fig. 2, showing the two prominent carrier traps ER3 and ER6, along with the minor ER1, ER2, ER4 and ER5 trap levels. The respective defect concentrations for the major defect levels are presented in Table II. Note that the ER3 defect displayed the same electronic properties (both DLTS annealing and metastable behaviour) as an alpha-particle irradiation induced defect, Eα3 [9] which could only be observed after ion bombardment of n-type (Si) GaAs [10].

CONCLUSIONS

$SiCl_4$ reactive ion etched (RIE) $10^{16}cm^{-3}$ n-type epitaxial GaAs was characterised using Photoreflectance, Ellipsometry, Photoluminescence (PL), Atomic Force Microscopy (AFM) and correlated with electrical I-V, C-V and DLTS measurements. Ellipsometric and PL data reveal the extent and degree of surface modification of the etched GaAs. AFM showed the etched surfaces to have a rough morphology with typical R_a of 15nm. The PR data reveal a decrease in the surface electric field arising from RIE induced electron trap formation with a reduction in the surface carrier concentration of the order of $1.1x10^{16}/cm^3$. For the highest rf power densities, PR further distinguishes between the different desorption/adsorption limited etch regimes. The results of the optical analysis were consistent with the C-V data detailing a reduced surface carrier concentration. DLTS revealed RIE induced electron traps detailing two prominent RIE induced trap levels (ER3, ER6), the former showing similar DLTS behaviour as that produced after ion bombardment of n-type (Si) GaAs.

REFERENCES

[1] M. B. Stern and P. F. Liao, J. Vac. Sci. Technol. B1 (4), Oct.-Dec. 1983, 1053.
[2] G. M. Crean, I. Little and P. A. F. Herbert, Appl. Phys. Lett. 58, (1991), 511.
[3] M. Murtagh, G. M. Crean and C. Jeynes, Mat. Res. Soc. Symp. Proc. Vol. 324, 1994, 167.
[4] M. Murtagh, P.A.F. Herbert and G. M. Crean, Mat. Res. Soc. Proc. Vol 406 1996, 327.
[5] S. J. Pearton, U. K. Chakrabarti and A. P. Kinsella, J. Vac. Sci. Technol. B 8 (4), 1990.
[6] D. E. Aspnes, Phys. Rev. Lett. 28, (1972), 168.
[7] S. M. Sze, Physics of Semiconductor Devices, 2nd Ed. Wiley Interscience, 77, 1981.
[8] F.D. Auret, W. O. Barnard, G. Myburg and L. J. Bredell, S. Africa J. Sci. Vol. 87, 1991.
[9] F. D. Auret, R. Erasmus, S. A. Goodman and W. E. Meyer, Phys. Rev. B51, 1995, 1721.
[10] F. D. Auret, S. A Goodman et al. Nucl. Instr. and Meth. Phys. Res. B106, 323, 1995.

FIELD DRIFT OF PLASMA-INDUCED DEFECTS IN PHOSPHORUS DOPED Si BY REVERSE BIAS ANNEALING (RBA)

J. TAKEUCHI*, Y. ZAITSU*, T. SHIMIZU*, S. MATSUMOTO*, and K. WADA**
* Faculty of Science and Technology, Keio University, Yokohama 223, JAPAN
** NTT LSI Laboratories, Kanagawa 243-01, JAPAN

ABSTRACT

The property of plasma induced defects in phosphorus doped CZ silicon has been investigated by reverse bias annealing (RBA). After CF_4 plasma exposure, charge density at the surface decreased since plasma induced negatively charged defects inactivated phosphorus. With the increase of annealing time, inactivated phosphorus area moved into the bulk with reverse bias of -3V. Thus it is clearly observed that negatively charged defects drifted from the surface into the bulk. The thermal dissociation energy for phosphorus-defect complexes is estimated to be 1.22eV from the Arrhenius plot of dissociation rate. These defects are likely to be Si self interstitials or vacancies.

INTRODUCTION

Dry etching technology has greatly attributed to the scale down of device dimensions and reactive ion etching (RIE) is indispensable to recent ULSI process technology. However, as device processing progresses toward the manufacture of increasingly shallow junctions, it becomes serious problem that energetic ions and photons during RIE process introduce damage and contamination in the Si surface[1,2], which have been found to degrade device performance[3,4]. This damage induced by RIE is divided into two distinct regions in terms of the depth from the surface[5]. First is the displacement damage region which extends to approximately $100\,nm$ and second is the defect reaction region which continues from displacement damage to depths greater than $1\,\mu m$. Although the first region can be removed by wet etching easily, deep damage region is difficult to be removed and affects device characteristics. Thus it is important to investigate the deep damage region.

We introduced reverse bias annealing (RBA) to measure defects which exist in this deep damage region. RBA was first used to investigate the reactivation of dopants inactivated by hydrogen passivation[6,7]. This method is as follows. Si samples are exposed to hydrogen plasma and annealed at low temperature with reverse bias applied to Schottky diodes. Then hydrogen dissociate from donors and drift into the bulk. As a result, donors are reactivated near the surface and inactivated in the bulk. In this way, the behavior of hydrogen can be observed. On the other hand, RBA was also applied to the study of plasma induced defects since they are mobile defects too. *Wada et al.* reported that plasma induced defects in GaAs had an effect on charge density profiles by RBA[8]. Therefore, this method must be also effective to reveal the characteristics of plasma induced defects in Si. In this paper, we have investigated the property of CF_4 plasma induced defects which exist in the deep damage region in phosphorus doped CZ Si at 60-80℃ by RBA.

Mat. Res. Soc. Symp. Proc. Vol. 442 © 1997 Materials Research Society

EXPERIMENTAL DETAILS

Phosphorus doped (100) CZ silicon samples with a resistivity in the range of 0.4-0.5 Ω cm were degreased with dichloromethane, acetone and methanol before RIE. Then they were exposed to CF_4(100%) plasma for 1 minute under the conditions of gas flow rate of 20 sccm, chamber pressure of 15mTorr and rf power of 100W. After plasma irradiation, about 100 Å of Si from the surface was chemically etched off (6cc of HF, 10cc of HNO_3, 16cc of CH_3COOH, 6cc of H_2O) to remove displacement damage region which mainly causes leakage current. Gold and aluminum were evaporated on the front and back surface for Schottky contacts and Ohmic contacts, respectively. Figure 1 shows the sample structure.

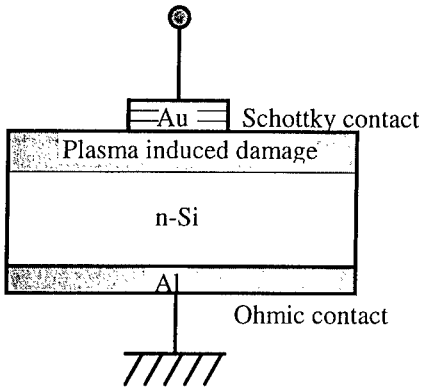


Fig. 1. Structure of a sample

After fabricating Schottky diodes, samples were placed in the vacuum(10mTorr) annealing chamber and RBA was performed. Annealing temperatures were 60-80℃ with reverse bias of 0V, -3V applied to Schottky diodes. Capacitance-voltage (C-V) measurements were performed at 1 MHz to assess profiles of the net electrically active phosphorus concentration. Current-voltage (I-V) and conductance-voltage (G-V) measurements were performed to survey diode leakage and back contact quality. Each time before measurements, annealing chamber was immediately cooled down to the room temperature by liquid nitrogen. Secondary ion mass spectroscopy (SIMS) was employed with a cesium beam to measure the depth profiles of carbon and fluorine after plasma exposure and after RBA.

RESULTS AND DISCUSSION

Charge Density Profile

Figure 2 shows charge density profiles after RBA(60℃) for 0-40min with no bias applied. In the initial profile, charge density decreased at the surface compared with that of bulk. This is due to the

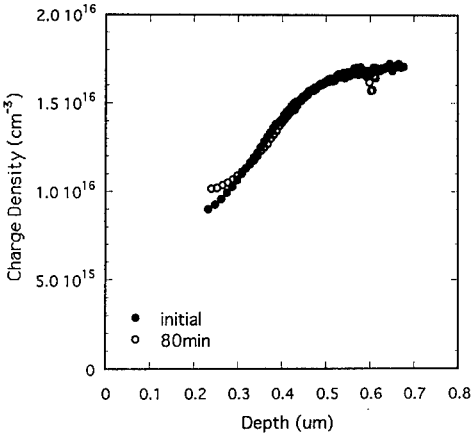


Fig. 2. The depth profiles of charge densities under RBA at 60℃ (0V).

formation of PX complexes (Here, X denotes a defect and P a phosphorus atom). Before plasma exposure, constant active phosphorus ions were present initially with the bulk donor concentration of $1.6\text{-}1.9\times10^{16}\text{cm}^{-3}$. After plasma exposure, negatively charged point defects X^- inactivated phosphorus ions P^+ to the depth of $0.6\,\mu m$. With the increase of annealing time, no change could be seen in the profiles since in this case there was no electric field and negatively charged defects did not drift.

On the other hand, the variation of charge density profiles could be seen when a sample was annealed at 60℃ with applied bias of -3V as indicated in Fig.3. Increasing annealing temperature with reverse bias of -3V, drastic variation of charge density could be seen as indicated in Fig.4 (65℃) and Fig.5 (70℃).

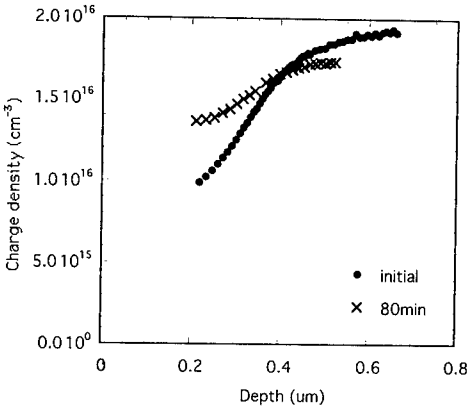


Fig. 3. The depth profiles of charge densities under RBA at 60℃ (-3V).

With the increase of annealing time, inactivated phosphorus began to be reactivated at the surface and inactivated phosphorus area moved into the bulk. This time, an applied electric field strongly affected the rate of removal of PX complexes in silicon. Plasma induced defects dissociated from PX complexes and drifted to the deep region.

To analyze the depth profiles, we adopt a simple model of the P dissociation kinetics. We assume that the PX complexes dissociate through the reaction

$$PX \rightarrow P^+ + X^- \qquad (1)$$

where P denotes dopants and X defects in Si. The dissociated defects X^- drift in the applied electric field toward the bulk. In this study, charge state conversion is not considered since no overshooting could be seen near the surface in depth profiles. Most of the defects must be the state of PX complexes due to large Coulomb force. Thus, the concentration of defects $[X]$ is given by

$$[X]\cong[PX]=[P_0]-[P_{eff}]=A(t) \qquad (2)$$

where P_{eff} denotes charge density derived from experiment, P_0 initial phosphorus concentration and $A(t)$

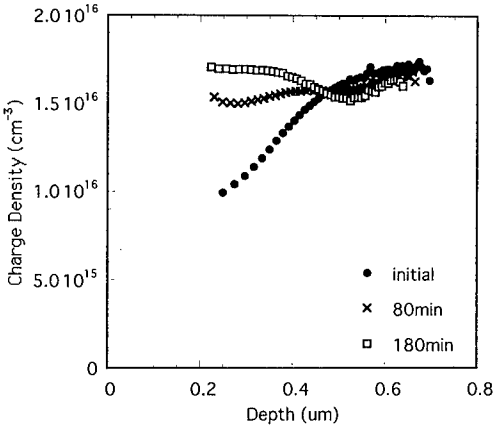


Fig. 4. The depth profiles of charge densities under RBA at 65℃ (-3V).

inactive phosphorus concentration. The reactivation of the donor follows first-order kinetics, which is characterized by

$$A(t) = A_0 \exp[-\nu(T)t] \quad (3)$$

where $\nu(T)$ expresses dissociation rate. Figure 6 shows inactive phosphorus concentration vs. annealing time measured at the depth of 0.35 μm from the surface. From these profiles, we estimated the dissociation rates of each annealing temperatures (T = 60, 65, 70, 80℃).

The dissociation rates $\nu(T)$ follow Arrhenius equation

$$\nu(t) = \nu_0 \exp(-E_d / kT) \quad (4)$$

Arrhenius analysis of the dissociation rate of PX complexes is shown in Fig.7 and thermal dissociation energy E_d is estimated to be 1.22eV from the slope.

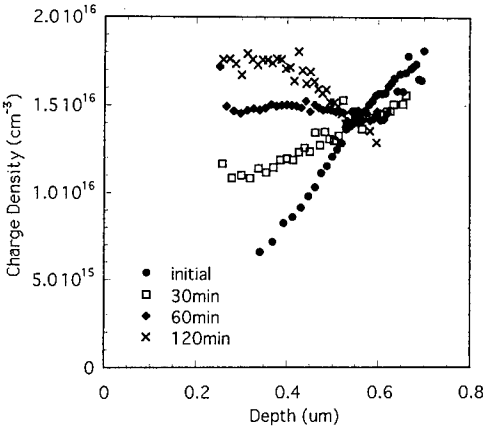


Fig. 5. The depth profiles of charge densities under RBA at 70℃ (-3V).

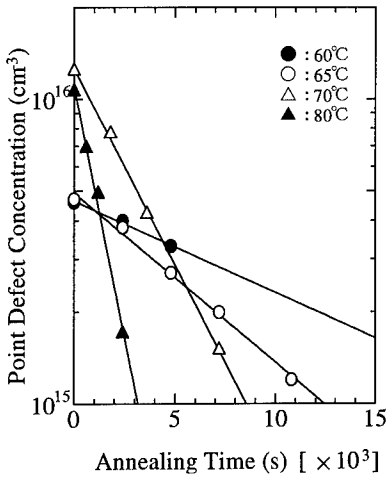


Fig. 6. Concentrations of point defects at the depth of 0.35 μm vs. annealing time.

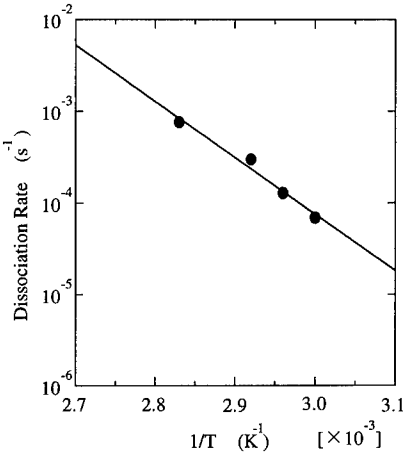


Fig. 7. Annealing temperature dependence of dissociation rates of point defects.

The Type of Defects

The issue is what kind of defects these negatively charged defects are. They could be intrinsic point defects (interstitial or vacancy) or impurities (carbon, fluorine and hydrogen).

In order to check the possibility of carbon and fluorine, SIMS was employed. Figures 8 and 9 show SIMS profiles of carbon and fluorine. The dotted line and solid line denote the profile after CF_4 plasma exposure and the profile after RBA (-3V, 70℃, 120min), respectively. After plasma process, carbon and fluorine were abundant to the depth of 0.1 μm. On the other hand, negatively charged defects existed up to 0.6 μm from C-V measurements. And it should also be pointed out that little change could be seen in carbon and fluorine profiles after RBA. Considering these results, carbon and fluorine are not likely to negatively charged defects monitored in charge density profiles.

Then, we would like to mention the possibility of hydrogen adsorbed by chemical etching. The dissociation energy of phosphorus-hydrogen complexes was estimated to be 1.18eV[6], which is similar to ours (1.22eV). However, charge density profiles of only wet etched samples were also measured and no inactivation could be seen. Therefore, hydrogen is not likely to negatively charged defects, either.

It seems that the defects are not impurities but intrinsic point defects. It is, however, still unclear what they really are. Thus, other measurements such as positron annihilation technique or optical measurements are needed to be done.

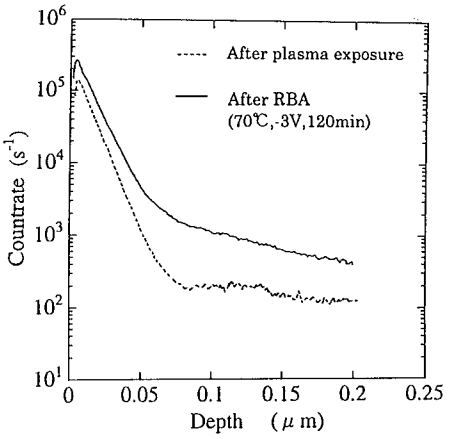


Fig. 8. Depth profiles of carbon measured by SIMS:
(1) after plasma exposure and before RBA
(2) after RBA (70℃, -3V, 120min).

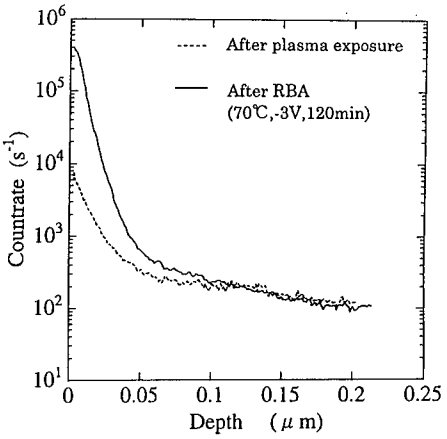


Fig. 9. Depth profiles of fluorine measured by SIMS:
(1) after plasma exposure and before RBA
(2) after RBA (70℃, -3V, 120min).

CONCLUSIONS

Plasma induced damage in silicon surface has been investigated by reverse bias annealing (RBA). We fabricated Schottky diodes from phosphorus doped CZ silicon containing RIE plasma induced defects in the surface and annealed them with reverse bias at low temperatures (60-80℃). After plasma exposure, phosphorus were inactivated in the surface region. With the increase of annealing time, phosphorus inactivated area moved to the bulk and phosphorus began to reactivate from the surface. It is explained as follows: Plasma induced negatively charged defects form complexes with phosphorus (*PX*) and inactivate phosphorus in the surface area. They dissociate from *PX* and, affected by electric field, drift from surface into the deep region where they inactivate phosphorus.

From the Arrhenius analysis of the dissociation of *PX* complexes, we estimated thermal dissociation energy of *PX* complexes to be 1.22eV. These negatively charged defects seem to be Si interstitials or vacancies from the results of C-V and SIMS measurements.

ACKNOWLEDGEMENTS

The authors would like to thank H. Sasaki of Mitsubishi Materials Silicon Corporation for sample preparation. We are also grateful to J. Lee for his SIMS measurements.

REFERENCES

1. I-Wen H. Connick, Anjan Bhattacharyya, Kenneth N. Ritz and W. Lee Smith, J. Appl. Phys. **64**(4), 2059 (1988).
2. G. S. Oehrlein, R. M. Tromp, J. C. Tsang, Y. H. Lee, and E. J. Petrillo, J.Electrochem. Soc. 132, 1441 (1985)
3. J. L. Benton, B. E. Weir, D. J. Eaglesham, R. A. Gottscho, J. Michel and L. C. Kimerling, J. Vac. Sci. Technol. **B10**, 540 (1992).
4. O. W. Purbo, C. R. Selvakumar, and D. Misra, J. Electrochem. Soc. **140**, 2659 (1993).
5. J. L.Benton, J.Michel, L. C. Kimerling, B.E. Weir and R.A. Gottscho, J. Elect. Mat. **20**, 643 (1991).
6. J. Zhu, N. M. Johnson and C.Herring, Phys. Rev. **B41**, 12354 (1990).
7. T. Zundel and J.Weber, Phys. Rev. **B46**, 2071 (1992).
8. K. Wada, H. Nakanishi and L. C. Kimerling, Materials Science Forum, **196-201**, 1401 (1995).

ELECTRONIC PROPERTIES OF DEFECTS FORMED IN n-Si DURING SPUTTER-ETCHING IN AN Ar PLASMA

P.N.K. DEENAPANRAY *, F.D. AURET *, C. SCHUTTE *, G. MYBURG *,
W.E. MEYER *, J.B. MALHERBE *, and M.C. RIDGWAY **
*Department of Physics, University of Pretoria, Pretoria 0002, sdeenapa@scientia.up.ac.za
**Department of Electronic Materials Engineering, Australian National University, Canberra, ACT 2601

ABSTRACT

We have employed current-voltage (IV), capacitance-voltage (CV) and deep level transient spectroscopy (DLTS) techniques to characterise the defects induced in n-Si during RF sputter-etching in an Ar plasma. The reverse leakage current, at a bias of 1 V, of the Schottky barrier diodes fabricated on the etched samples was found to decrease with etch time reaching a minimum at 6 minutes and thereafter increased. The barrier heights followed the opposite trend. The plasma processing introduced six prominent deep levels below the conduction band of the substrate. A comparison with the defects induced during high energy (MeV) alpha-particle, proton and electron irradiation of the same material revealed that plasma-etching created the VO- and VP-centres, and $V_2^{-/0}$. Some of the remaining sputter-etching-induced (SEI) defects have tentatively been related to those formed during either 1 keV He- or Ar-ion bombardment.

INTRODUCTION

Plasma processes are versatile techniques which are routinely used for submicron scale device fabrication. For instance, sputter deposition is used during metallization for the stoichiometric deposition of compounds and refractory metals on semiconductors. However, it has been shown that sputter deposition introduces donor-type defects at and close to the metal-semiconductor interface [1]. Plasma-based dry etching techniques such as sputter etching, ion beam etching (IBE) and reactive ion etching (RIE), are also used for the anisotropic etching of semiconductors. These plasma processes also result in lattice damage at and below the semiconductor surface which alters its electrical, optical and structural properties [2,3]. Little information on the structure of defects caused by sputter-etching is available [4,5]. The extent of the sputter-etching damage depends on the etching parameters such as etching time and rate, etching mode and bias conditions, as well as gas pressure and species. The type and extent of the sputter-etching induced (SEI) defects as a function of etch time are presented in this paper. To better understand the structure and electronic properties of the SEI defects we have compared them to those introduced during high energy (MeV) alpha-particle, proton and electron irradiation [6], and low energy (1 keV) He- and Ar-ion bombardment of the same material. We have also monitored the barrier heights and reverse leakage currents of the Schottky barrier diodes (SBD) fabricated on the etched surfaces.

EXPERIMENTAL PROCEDURE

Epitaxially grown (111) oriented n-type Si, doped to $5x10^{15}$ cm^{-3} with P, and grown on n^+-substrates were used in this study. The samples were chemically cleaned before being sputter-etched for 2, 4, 6, 8 and 10 minutes in an rf-excited (13.56 MHz) plasma. The plasma pressure and dc bias were kept constant at $5x10^{-3}$ mbar and 400 V, respectively. Circular Pd Schottky contacts of 0.77 mm diameter and 100 nm thickness, were then resistively deposited on the etched

Mat. Res. Soc. Symp. Proc. Vol. 442 © 1997 Materials Research Society

samples through a metal contact mask. For control purposes, 100 nm thick Pd contacts were resistively deposited through the same mask on chemically cleaned but unetched (t = 0 min) Si. Ohmic contacts were formed on the n^+-substrates using a liquidus In-Ga alloy.

I-V and C-V measurements were used to monitor the quality of the SBDs. The C-V barrier height (ϕ_b^{CV}) was calculated from a graph of $1/C^2$ vs V_R by using a reverse bias, V_R, of between 0 and 1 V. The SEI defects were characterised using deep level transient spectroscopy (DLTS) [7]. The energy levels, E_T, and apparent capture cross-sections, σ_a, of the defects were determined from DLTS Arrhenius plots of $\log(e/T^2)$ vs $1/T$, where e is the emission rate at a temperature T. The depth profiles were determined using the method of Zotha *et al* [8].

RESULTS AND DISCUSSION

I-V and C-V results

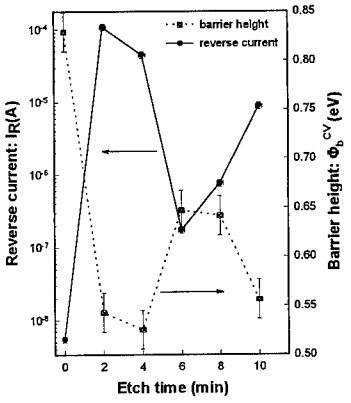


Figure 1: Variation of leakage current (I_R) at 1 V reverse bias and C-V barrier heights (ϕ_b^{CV}) of Schottky barrier diodes (SBD) fabricated on the sputter-etched samples in an Ar plasma at a pressure of $5x10^{-3}$ mbar and a dc bias of 400 V, as a function of time.

The diodes fabricated on the etched samples were found to be very leaky at room temperature. Hence, the leakage currents at 1 V reverse bias together with their C-V barrier heights were extracted at 250 K. The high ideality factors (n > 1.1) of the diodes suggested that the current transport mechanism over the barrier was not dominated by thermionic emission [9], so that the measured I-V barrier heights were not meaningful. Figure 1 shows that the leakage current decreases with sputter time to reach its minimum at 6 min, and increases thereafter. The diode barrier heights were found to follow the opposite trend. It has been proposed by Fonash *et al* [10] that sputter-etching may induce donor levels at and below the Si surface resulting in a lowering of barrier height. However, the high carrier compensation (C-V depth profiles) in the sample etched for 2 min indicates that sputter-etching introduced acceptor levels. We have, therefore, accounted for the changes in the measured barrier heights to be due to the introduction of a continuous distribution of near-surface states during etching, which pin the Fermi level in the band gap. Consequently, the least amount of defects are produced for 6 min etch times, when the effect of Fermi level pinning is least. This would correspond to a steady state regime proposed by Hirai *et al* [5]. It is speculated that for t > 6 min, the higher doses (constant etch rate) of Ar ions impinging the exposed surface results in the formation of extended defects and may even amorphise the sub-surface region. These results are in agreement with the defect depth profiling studies which are discussed below. The presence of extended defects has been correlated to baseline skewing of the DLTS spectra corresponding to etch times of 8 and 10 min, respectively, as has been proposed by Auret *et al* for GaAs [11]. Glancing angle Rutherford backscattering spectroscopy (RBS) and transmission electron microscopy (TEM) experiments to detect the presence of amorphous layers in our etched samples are in progress.

DLTS results

A typical DLTS spectrum for a sputter-etched sample is shown in curve (b) of Fig. 2. The defects are labelled P1 through to P8, and are identified in the form, for instance EP088 (P1), where "E" denotes an electron trap, "P" for plasma-etching induced and 088 the position in meV of the specific level below the conduction band. Three well resolved peaks EP088 (P1), EP143 (P2) and EP454 (P8) were identified, whereas EP183 (P3) and EP310 (P6) could be resolved only after using filling pulses of narrow widths (ns). Furthermore, the "signature" of P7 (EP326) was extracted after annealing the etched sample at 260 °C for 30 minutes.

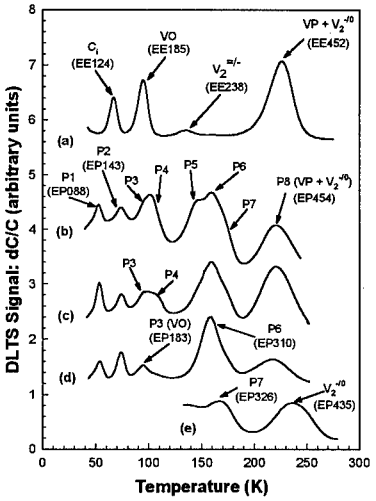


Figure 2: DLTS spectra of epitaxially grown n-Si bombarded with high energy (MeV) electrons [curve (a)], and sputter-etched in an Ar plasma [curve (b)] using 0.2 ms filling pulses. Curves (c) and (d) were obtained using filling pulse widths of 500 ns and 25 ns, respectively. Curve (e) was obtained after annealing the etched sample at 260 °C. All curves were recorded at a lock-in amplifier frequency of 46 Hz, $V_r = 1$ V and $V_p = 1.4$ V.

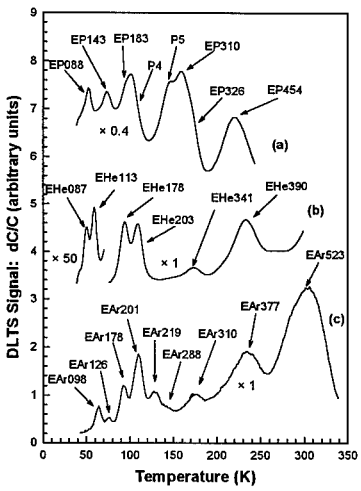


Figure 3: Comparison of DLTS spectra of epitaxially grown n-Si doped to $5x10^{15}$ cm^{-3} with P. (a) Sputter-etched in an Ar plasma at a pressure of $5x10^{-3}$ mbar (dc bias of 400 V), (b) bombarded with 1 keV He ions and (c) 1 keV Ar ions. A lock-in amplifier frequency of 46 Hz was used to extract the data.

Though the SBDs had leaky I-V characteristics, the DLTS results presented here are reliable because the activation energies of the SEI defects are less than the calculated barrier height of the most degraded diode (t = 4 min) [12]. To learn more about the structure of the SEI defects, we compared them with the primary defects induced in Si during high energy (MeV) electron, proton and alpha-particle irradiation [6,13]. Curve (a) [Fig. 2] shows the DLTS spectrum of the defects induced in n-Si during irradition with high energy (MeV) electrons. In addition to VO- and VP-centres, $V_2^{=/-}$ and $V_2^{-/0}$, high energy alpha-particle and proton irradiation introduced levels at E_c - 0.08 eV and E_c - 0.14 eV. However, no level at E_c - 0.124 eV was introduced during high energy proton and alpha-particle irradiation. After annealing the

electron irradiated sample at 180 °C for 30 minutes, EE124 annealed out and levels at E_c - 0.141 eV and E_c - 0.085 eV, which have similar electronic "signatures" (activation energy, E_T and apparent capture cross-section, σ_n) as EP143 and EP088, respectively, emerged [14]. A comparison between the SEI defects and primary defects revealed that P3 is electronically the same as the VO-centre while P8 is the superposition of the VP-centre and $V_2^{-/0}$ (EP435 resolved as per curve (e) [Fig. 2]). EP088 and EP143 are tentatively assigned the C_i-C_s structure [15]. Note that no direct evidence could be obtained from our results to show the detection of $V_2^{=/-}$. Since $V_2^{-/0}$ is observed after the VP-centre anneals out, the proposal from Svensson *et al* [16] is used to argue that the high level of damage induced in our samples results in stress fields which prevent the complete filling of $V_2^{=/-}$.

During the sputter-etching process, the Si samples were subjected to bombardment by energetic Ar ions and Ar atoms (energy between 0.4 and 1 keV) from the plasma. In order to characterise the SEI defects we have compared them with those introduced during 1 keV Ar-ion bombardment of the same material. In order to establish whether any of the SEI defects are noble gas species dependent, we have also compared them with defects created by 1 keV He-ion bombardment. Figure 3 shows the DLTS spectra of defects created during low energy Ar- [curve (c)] and He-ion [curve (b)] bombardment. From the curves in Fig. 3, P4 is tentatively matched to EAr201 and EHe203, which have similar "signatures". Annealing studies at 350 °C are scheduled to monitor the annealing of the VO-centre and to resolve P4 if it is indeed similar to EAr201/EHe203 (anneal out at 500 °C). EP310 could be similar to EAr310 since they have similar electronic properties. The properties of the SEI defects are summarised in Table I.

Table I : Summary of electronic and structural properties of the main SEI defects

Defect	P1	P2	P3	P4	P6	P7	P8
E_T (meV)	88	143	183		310	326	452
σ_a (cm^2)	$3.7x10^{-16}$	$5.7x10^{-15}$	$3.4x10^{-15}$		$1.6x10^{-15}$	$1.5x10^{-15}$	$4.2x10^{-16}$
T_{peak}[(b)] (K)	54	74	94		158	167	237
Similar defects	C_i-C_s [14]	C_i-C_s [14]	VO [6]	EAr201/ EHe203?	EAr310?		VP + $V_2^{-/0}$ [6]

(b) Peak temperature at a lock-in amplifier frequency of 46 Hz (decay time constant of 9.23 ms).

The peak DLTS signal intensities of the main SEI defects for Vr = 1 V and Vp = 1.4 V are plotted as a function of etch time in Fig. 4. It is observed that the intensities of the main defects reach a minimum in the sample etched for 6 min, and thereafter increase with etch time, which is in agreement with our I-V and C-V results. The DLTS signal for t = 2 minutes should be treated with caution because of the high carrier compensation in that sample. This result suggests that a high concentration of defects are introduced in the samples for t < 6 min, and decrease with time to reach a minimum at 6 min. The gradual increase in the defect densities for t = 8 min and t = 10 min, respectively, could be due to the creation of extended defects.

Figure 5 shows the depth profiles of P6 as a function of etch time. For the reason already specified, the depth profile corresponding to an etching time of 2 minutes is not included. The depth profiles shown here are accurate since the diodes had relatively lower leakage currents and higher barrier heights at 160 K compared to those at 250 K. A close inspection of Fig. 5 shows that the depth profiles can be separated into two distint regions - (1) a region labelled A which is

within a depth of 0.1 μm of the metal-semiconductor interface, and (2) a region B starting at a depth 0.1 μm and extending into the semiconductor. Close to the etched surface (region A), the

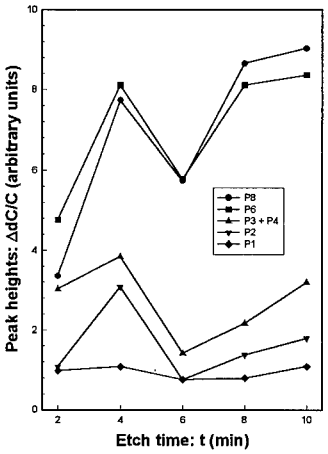


Figure 4: Peak DLTS intensity of the prominent SEI defects at V_r = 1 V and V_p = 1.4 V. None of the defects could be observed in the unetched sample. The data points for t = 2 min are not meaningful because of the heavy carrier compensation in the corresponding etched sample.

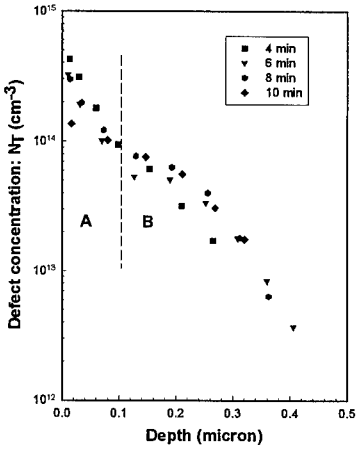


Figure 5: Depth profile (constructed from DLTS measurements using a lock-in amplifier frequency of 46 Hz) of defect P6 introduced in epitaxially grown n-Si doped to $5x10^{15}$ cm^{-3} with P, during plasma-etching in an Ar plasma at a pressure of $5x10^{-3}$ mbar and a dc bias of 400 V.

concentration of P6, [P6], is a maximum for t = 4 min, and that at 8 min slightly larger than at 6 min as expected. The lower than expected [P6] at t = 10 min is attributed to the presence of extended defects which resulted in baseline skewing of our DLTS spectra. Consequently, lower peak intensities of P6 were extracted under the successive application of forward filling pulses. Region B shows an opposite time dependence in the depth distribution of P6. The increasingly higher [P6] from t = 2 min to t = 10 min is expained by its in-diffusion, which is proportional to $\sqrt{t}$, into the epi-layer. This in-diffusion may also be assisted by recombination-enhanced diffusion [17].

CONCLUSIONS

The defects induced in n-Si by sputter-etching in an Ar plasma at a pressure of $5x10^{-3}$ mbar and a dc bias of 400 V, together with the electrical characteristics of the Schottky barrier diodes fabricated on the etched samples, have been studied as a function of etch time. We have proposed that sputter-etching has introduced acceptor-type defects in n-Si which caused an increase in the leakage currents of the diodes fabricated on the etched surfaces. The lowering of barrier heights has been explained by the introduction of a continuous distribution of near-surface states which result in the Fermi level pinning. The extent of the Fermi level pinning has been proposed to increase with the concentration of near-surface states. It has been shown that minimum damage was created for an etch time of 6 min and that extended defects could be introduced for etch times longer than 6 min. Some of the defects were successfully matched with primary defects which are introduced during high energy alpha-particle or electron irradiation,

whereas others have been tentatively identified to be noble gas-related. DLTS depth profiling of a defect P6 has revealed two distinct regions in its spatial distribution. The leakage currents of the diodes follow the same trend as the concentration of defect P6 in a region extending to approximately 0.1 μm below the interface. However, the concentration in a region extending beyond 0.1 μm increases with etch time, and has been attributed to the in-diffusion of the P6.

ACKNOWLEDGMENTS

The financial assistance of the FRD and CEFIM are gratefully acknowledged, as well as the technical assistance of J.P. le Roux and C.M. du Toit.

REFERENCES

1. F.H. Mullins and A. Brunnschweiler, Solid State Electron. **19**, p. 47 (1976).
2. S.J. Pearton, W.S. Hobson, U.K. Chakrabarti, G.E. Derkits, Jr., and A.P. Kinsella, J. Electrochem. Soc. **137** (12), p. 3892 (1990).
3. G.S. Oehrlein, Materials Science and Engineering B4, p. 441 (1989).
4. O.O. Awadelkarim, T. Gu, P.I. Mikulan, R.A. Ditizio and S.J. Fonash, Appl. Phys. Lett. **62** (9), p. 958 (1993).
5. M. Hirai, H. Iwakuro, J. Ohno, and T. Kuroda, IEEE Transactions on Components, Hybrids, and Manufacturing Technology **13** (4), p. 629 (1990).
6. J.R. Troxell, Solid State Electronics **26**, p. 539 (1983).
7. D.V. Lang, J. Appl. Phys. **45**, p. 3014 (1974).
8. Y. Zohta and M.O. Watanabe, J. Appl. Phys. **53**, p. 1809 (1982)..
9. E.H. Rhoderick and R.H Williams, Metal-Semiconductor Contacts, 2nd ed. (Clarendon Press, Oxford, 1988), p. 38.
10. S.J. Fonash, S. Ashok and Ranbir Singh, Thin Film Solids **90**, p. 231 (1982).
11. F.D. Auret, S.A. Goodman, R.M. Erasmus, W.E. Meyer and G. Myburg, Nucl. Instr. and Meth. **B 106** (1995) 323.
12. Q.Y. Ma, M.T. Schmidt, X. Wu, H.L. Evans and E.S. Yang, J. Appl. Phys. **64**, p. 2469 (1988).
13. L.C. Kimerling, Inst. Phys. Conf. Ser. **13**, p. 221 (1977).
14. P.N.K. Deenapanray, F.D. Auret, G. Myburg and W.E. Meyer, C.M. Demanet, unpublished.
15. J.L. Benton, M.T. Asom, R. Sauer and L.C. Kimerling in Identification of Interstitial Carbon Related Defects in Silicon, edited by M. Stavola, S.J. Pearton and G. Davies (Mater. Res. Soc. Proc. **104**, Pittsburgh, PA, 1988) pp. 85-91.
16. B.G. Svensson, B. Mohadjeri, A. Allen, J.H. Svensson and J.W. Corbett, Phys. Rev. **B 43**, p. 2292 (1991).
17. J.L. Benton, J. Michel, L.C. Kimerling, B.E. Weir and R.A. Gottscho, Journal of Electronic Materials **20**, p. 643 (1991).

Part III

Processing Induced Defects: Defects and Gate Oxide Integrity

OCTAHEDRAL VOID DEFECTS CAUSING GATE-OXIDE DEFECTS IN MOSLSIs

MANABU ITSUMI
NTT System Electronics Laboratories, Atsugi-Shi, Kanagawa, 243-01 Japan

ABSTRACT

We found oxide defects originating in standard Czochralski silicon and proposed the sacrificial oxidation method to eliminate these defects in about 1979. Later, N_2 annealing and H_2 annealing methods were proposed successively, and these three elimination methods have been successfully introduced into actual fabrication lines for highly reliable integrated circuits. However, the origin of the defect was not clarified until recently. We combined copper decoration and TEM in order to observe the origin of the oxide defects and for the first time, observed octahedral void defects systematically at the oxide defects with standard Czochralski silicon. The sizes of the defects are typically 0.1-0.2 microns. These Si-crystalline defects are the origin of oxide defects and, at the same time, may be the origin of crystal originated particles. Recently, we have observed octahedral void defects in the bulk of the standard Czochralski silicon too. Some experimental findings suggest that some impurities on the side wall of the octahedral void defect induce dielectric breakdown of the gate-oxides.

INTRODUCTION

We found oxide defects originating in standard Czochralski silicon (CZ-Si) and proposed sacrificial oxidation method to eliminate these defects in about 1979 [1-3]. Several years later, N_2 annealing and H_2 annealing methods were proposed successively [4-6]. These three elimination methods have been successfully introduced into actual fabrication lines for highly reliable integrated circuits. Ion implantation through oxides were also proposed [7]. In addition, it was found that Si-growth-rate reduction suppresses the defects [8]. Wafer rotation with water for eliminating the oxide defects was also proposed [9-10]. At any rate, the origin of the defect was not clarified.

We developed a novel method (Cu decoration followed by TEM) for observing the origin of the oxide defects and for the first time observed diamond-shaped void defects or V-shaped void defects (that is, a part of an octahedral void defect) systematically at the oxide defects with standard CZ-Si [11-13]. The sizes of the defects are typically 0.1-0.2 microns. These Si-crystalline defects are the origin of oxide defects and, at the same time, may be the origin of crystal originated particles (COPs). Recently, we have observed octahedral void defects in the standard CZ-Si too [14]. The dependence on gate-oxidation atmosphere and an experiment intentionally introducing impurities suggest that some impurities on the side wall of the octahedral void defect induce dielectric breakdown of the gate-oxides. The purpose of this article is to overview the history of the gate oxide defects originating in CZ-Si and to propose a model in which impurities in the defects are responsible for the gate oxide defects.

A HISTORY ON THE GATE-OXIDE DEFECTS ORIGINATING FROM CZ-Si

A history on the gate oxide defects originating from CZ-Si is summarized in Table 1. Defects in gate oxides (Figs. 1 and 2) with unknown origin were detected about 1977. The defects were characterized by a higher oxide-defect density in the oxide thickness region between 20-100 nm, as shown in Fig. 3. Assuming that the origin of the gate-oxide defects were: 1) metallic impurities, 2) Particles, 3) Si surface roughness, and 4) something from the Si substrate, we tried various kinds of experiments. As a result, we were forced to consider that the gate-oxide defects are originated in CZ-Si, because we found that the gate-oxide defect density with CZ-Si was clearly larger than that with float-zone Si, as shown in Fig. 4. Another supporting data was that the gate-oxide defect density with CZ-Si can be reduced to the level of that with float-zone silicon (FZ-Si) by using the sacrificial oxidation procedure (Fig. 5). The proposed sacrificial oxidation

Mat. Res. Soc. Symp. Proc. Vol. 442 © 1997 Materials Research Society

Table 1. History of oxide defects related to CZ-Si

Year	Item	Affiliation	References
1979	Observation of Oxide Defects for CZ-Si	NTT	[1-3]
1980	Proposal of Sacrificial Oxidation	NTT	[2-3]
1982	Proposal of Nitrogen Annealing	OKI	[4-5]
1986	Proposal of Hydrogen Annealing	Toshiba	[6]
1986	Proposal of Ion Implantation through SiO_2	NTT	[7]
1990	Proposal of Si Growth Rate Reduction	Nippon Steel	[8]
1993	Proposal of Wafer Rotation with Water	NTT	[9-10]
1995	Observation of Octahedral Void Defects at Si Surface (Related to Oxide Defects)	NTT	[11-13]
1996	Observation of Octahedral Void Defects in Bulk Si (Related to LSTDs)	NTT	[14]

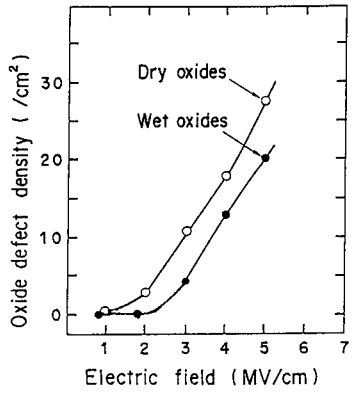


Fig. 1. The dependence of oxide defect density on electric field. Oxide thickness was 50 nm.

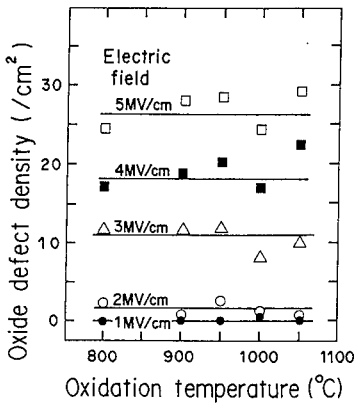


Fig. 2. The dependence of oxide defect density on oxidation temperature. Dry oxides (40-nm-thick) used.

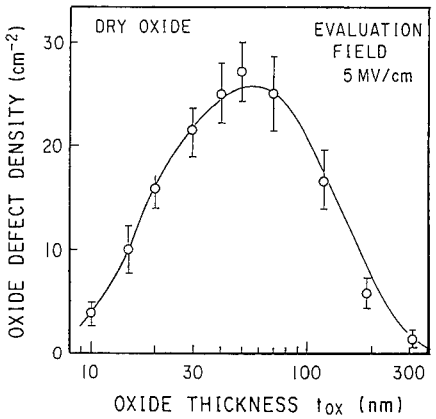


Fig. 3. The dependence of oxide defect density on oxide thickness.

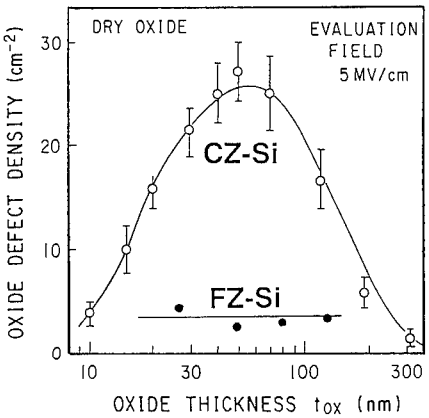


Fig. 4. The dependence of oxide defect density on oxide thickness. CZ-Si and FZ-Si were compared.

procedure for eliminating the gate-oxide defects was then introduced into the metal-oxide-semiconductor large-scale integration (MOSLSI) fabrication line and increased production yield and long-term reliability.

Several years later, nitrogen annealing [4-5], and hydrogen annealing [6] were developed to eliminate these defects, and these methods have been successfully introduced into fabrication lines producing flash memories and metal-oxide-semiconductor random-access-memories (MOSRAMs). Ion implantation through gate-oxides [7], a decreased Si growth rate [8], and wafer rotation with de-ionized water [9-10] were proposed successively for eliminating the gate-oxide defects.

The defects were originally thought to be caused by gigantic oxygen precipitates. In order to find out whether this is true or not, we recently began directly observing the origin of the gate oxide defects. First, we observed octahedral void defects just under the gate oxide defects. Next, we also observed octahedral void defects in the bulk of CZ-Si. These findings are shown and discussed in the following section.

OCTAHEDRAL VOID DEFECTS ON SURFACE OF CZ-Si

We used a copper decoration followed by focussed ion beam to directly observe the origin of the gate oxide defects . We located the origin of the gate oxide defects at a decoration point (Fig. 6) and tried TEM observations at that spot. A typical TEM observation, a plan-view of the oxide-defect origin, is shown in Fig. 7, indicating a square-like shape. Its side is oriented along the (110) axis. Another typical TEM observation is shown in Fig. 8, which is a cross-sectional view of the oxide-defect origin. The defect looks like a diamond and the angle between the face and the Si surface is 55 degree, which indicates the face has a (111) orientation. Another typical TEM observation is shown in Fig. 9, which is a cross-sectional view of the oxide-defect origin. The defect is V-shaped and the angle between the face and the Si surface is 55 degree, which indicates the face has a (111) orientation. The size of the structure is typically 0.1 to 0.2 microns. Figures. 7, 8 and 9 suggest an octahedral structure, which is shown schematically in Fig. 10. We tilted the TEM observation angle for the sample about the horizontal axis and the vertical axis. (Fig. 11) The spatical relationship between the octahedral defects and Si substrate surface is schematically illustrated in Fig. 12. When the defects are in the Si, as shown in Fig. 11(a), the defects cannot be detected as gate-oxide defects. When the defects are on the Si surface, as shown in Figs. 11(b) and (c), the defects can be detected as gate-oxide defects. Configurations shown in Figs.11(b) and (c) correspond to the TEM micrographs of Figs.8 and 9, respectively. EDS analysis of the octahedral defects revealed that the defects are empty. We observed twenty samples of TEM micrographs and the majority of them were twin-type octahedral void defects, as shown in Fig. 13.

OCTAHEDRAL VOID DEFECTS FOUND IN BULK CZ-Si

Copper decoration followed by TEM observation revealed an octahedral void structure just beneath the oxide defects. This observation is based on the copper decoration and some people suggested that the copper decoration might have some influence on the defect structure and its composition. To find out whether this is true or not, we tried to directly observe the grown-in defect in the bulk of CZ-Si, without the influence of the copper decoration. We used IR tomography followed by focussed ion beam (FIB) thinning [14].

A typical example of the grown-in defects in the standard CZ-Si is shown in a cross-sectional TEM micrograph in Fig. 14(a). The defects are twin-type octahedral defects about 100 nm in size. The face of the side walls was identified as the (111) plane. These features were common for five TEM images obtained from wafers of one of the Si vendors and for five TEM images obtained from wafers of the other Si vendor. The concentration of the defects detected by laser scattering tomography (LSTDs) was about $5x10^5$ cm^{-3}. Enlargement of the image revealed the existence of a 2-nm-thick layer on the side walls (Fig. 14(b)). The thin layer completely covers the side walls uniformly. EDS spectra and AES analysis showed that the thin layer is a kind of oxide (SiOx). We tilted the TEM observation angle for the sample about the horizontal axis and the vertical axis

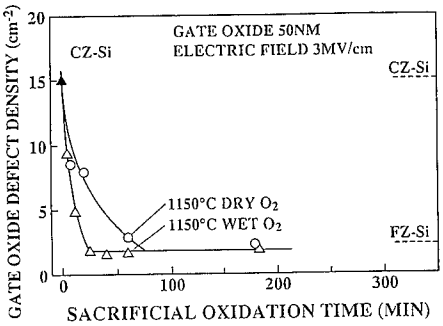


Fig. 5. Gate oxide defect density vs sacrificial oxidation time. Sacrificial oxides grown at 1150 C were removed before gate oxides were formed.

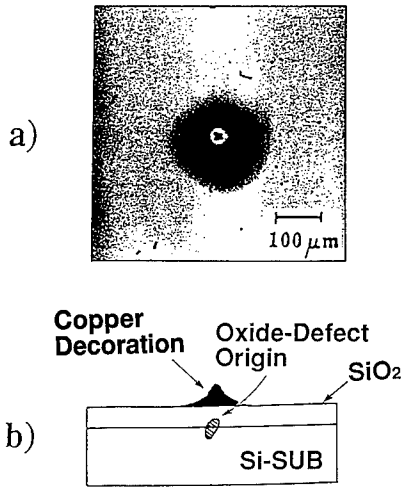


Fig. 6. Illustration of decorated copper.
a) Top view
b) cross-sectional view.

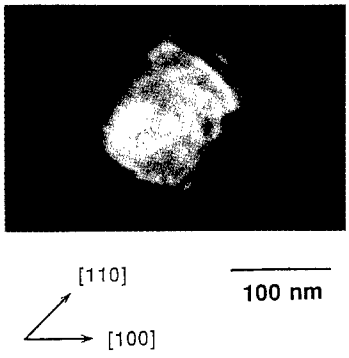


Fig. 7. TEM micrograph, plan view.

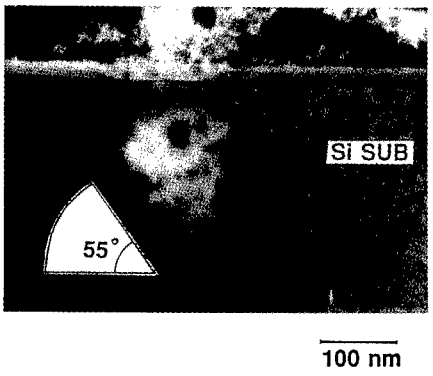


Fig. 8. TEM micrograph, cross-sectional view.

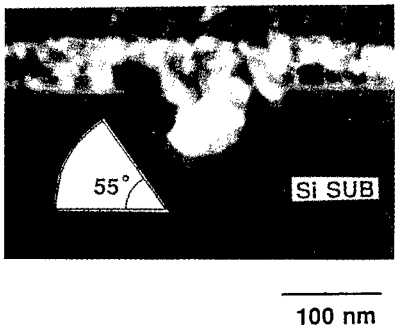


Fig. 9. TEM micrograph, cross-sectional view.

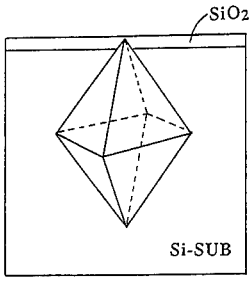


Fig. 10. Illustration of octahedral structure.

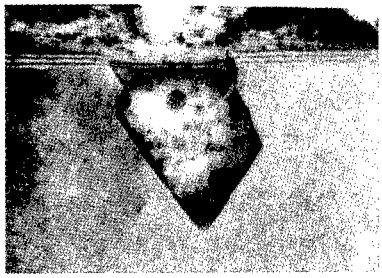


Y-axis

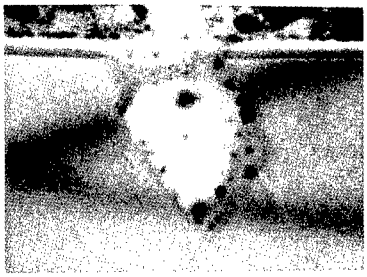
X-axis

Tilt axis

a) (X, Y)=(0, 0)



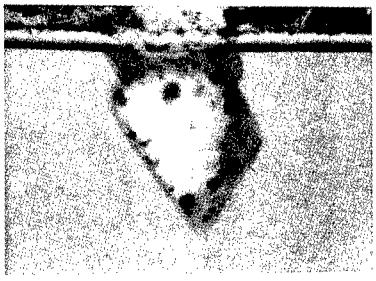
b) (X, Y)=(5, 0)



c) (X, Y)=(0, 5)



d) (X, Y)=(-5, 0)



e) (X, Y)=(0, -5)

Fig. 11. TEM micrograph, cross-sectional view.
Tilt angles are changed.
a) (X, Y)=(0, 0), b) (X, Y)=(5, 0), c) (X, Y)=(0, 5), d) (X, Y)=(-5, 0), e) (X, Y)=(0, -5)

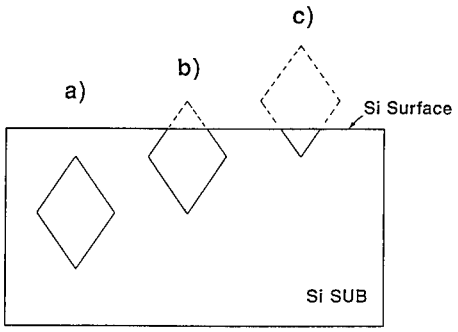


Fig. 12. Relation of octahedral defect to Si surface.

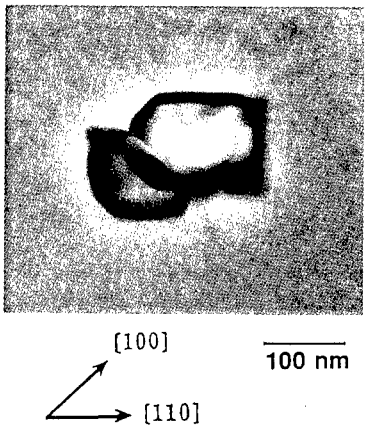


Fig. 13. TEM micrograph, plan view. Twin-type defects observed.

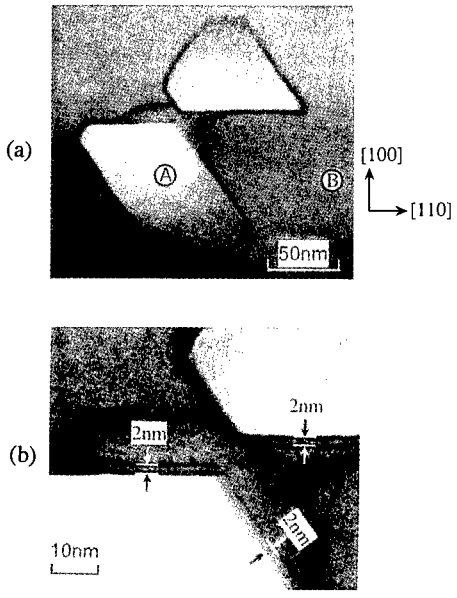


Fig. 14. TEM micrograph, cross-sectional view. A grown-in defect in CZ-Si.
A and B are analysis point.
b) Enlargement of a)

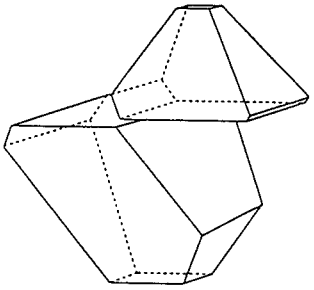


Fig. 15. Illustration of the grown-in defect shown in Fig. 14.

many times and examined what each plane looked like with the tilt. (Fig. 15)

The above results show that the octahedral void structure is formed during Si-ingot growth. Agglomeration of vacancies during the Si-ingot growth may result in the formation of the voids. The 2-nm-thick layer may be formed at the final stage of the formation of the octahedral void structure during the Si-ingot growth. Diffusion and agglomeration of vacancies during the Si-ingot growth should be further investigated through experimentation and simulation.

MECHANISM FOR GATE-OXIDE DEFECT GENERATION

A question arose about what in the octahedral void defects is responsible for the gate-oxide defects. One possible origin of the defects is oxide thinning at the edge of the silicon surface adjacent to the octahedral void defect or at the corner in the void defect. For convenience, this model is called the corner model here. Another possible origin is impurities accumulated in the octahedral void defect which act as weak spots in the growing gate-oxides during oxidation. This model is called the impurity model here. We investigated to find out which model was more consistent with experimental findings.

The dependence of the oxide defect density on the oxide thickness is shown in Fig. 16, and the dependence of the oxide defect density on the evaluation electric field across the oxide is shown in Fig. 17. In both figures, the oxide defect density for HCl oxides is lower than that for dry oxides. In Fig. 17, the oxide defect density obtained with two-step HCl-oxidation is lower still than that obtained with ordinary HCl oxidation. Several investigators have reported that Cl species removed metallic impurities or sodium ions from the growing oxides and Si substrates during HCl oxidation, resulting in the passivation of MOS devices. Their reports, in combination with our experimental results, imply that the origin of the oxide defects is metallic impurities or sodium ions in the octahedral structures and that these impurities are removed during HCl oxidation.

We intentionally introduced impurities into some samples to find out how the dependence of oxide defect density on oxide thickness changes. Figure 18 shows the dependence of the oxide defect density on oxide thickness when metallic impurities with a concentration of 10^{12} cm^{-2} were intentionally introduced. The oxides were thermally grown in dry O_2. An increase in the oxide defect density in the contaminated samples was found in the oxide thickness range of 20 to 50 nm. These experimental results suggest that intentionally introduced impurities are closely related to the generation of oxide defects, and that the original gate-oxide-defect-density vs oxide-thickness characteristic is due to the original impurities located in the octahedral void defect.

Many investigators have reported that various impurities are responsible for weak spots in the oxides. Considering this, we assume that heavy metals (Fe, Cu, Ni and so on) and alkaline metals (Na or K) accumulated in the octahedral void defects during Si growth are responsible. We also assume that these impurities located in the octahedral void defects on the Si surface layer are introduced into the growing gate-oxides during thermal oxidation and would act as a conductive path in the oxides (Fig. 19).

Ten years ago, we found that ion implantation through oxides has a noteworthy effect in eliminating the causes of oxide defects [7]. (Fig. 20) We observed that ion implantation through oxides does not change the shape of oxide thinning at the corners. One model (Fig. 21) we can propose is that some atom clusters are responsible for local conductive paths in the oxides and that ion implantation through oxides may change the arrangement of the atoms and eliminate the path. The effect of ion implantation through oxides is not consistent with the corner model but is consistent with the impurity model.

It is well-known that the oxide thinning at the corners is enhanced when the oxidation temperature is low. But the data shown in Fig. 2 indicate that the defect density is not dependent on oxidation temperatures between 800 and 1050 C. This experimental result is not consistent with the corner model. It is also well-known that the oxide thinning at the corners is more extensive in a wet oxidation ambient than in a dry oxidation ambient. But the data shown in Fig. 1 indicate that the defect density is lower for wet oxides than for dry oxides. These experimental results are also not consistent with the corner model. They are summarized in Table II.

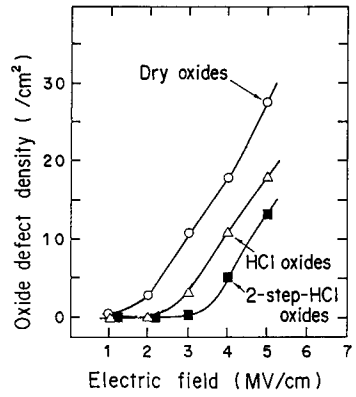


Fig. 16. The dependence of oxide defect density on electric field. Oxide thickness was 50 nm.

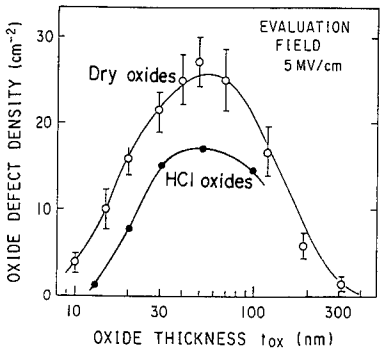


Fig. 17. The dependence of oxide defect density on oxide thickness. CZ-Si used.

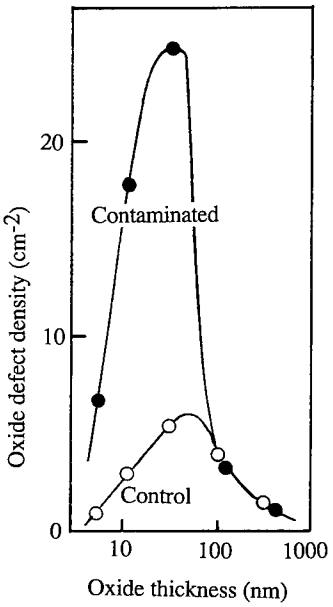


Fig. 18. Oxide defect density vs oxide thickness. Sacrificial oxidation used. Dry oxide formed. Electric field 5 MV/cm.

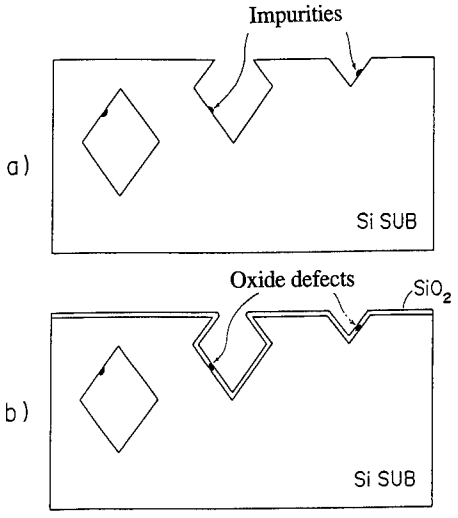


Fig. 19. Model for the introduction of impurities into the oxides.

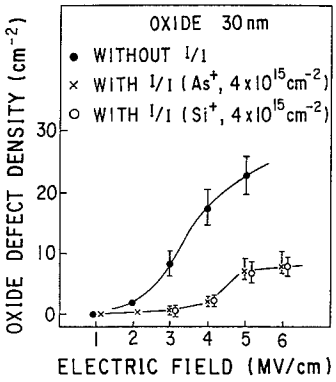


Fig. 20. Oxide defect density vs electric field. Ions were implanted through the 30-nm thick oxide.

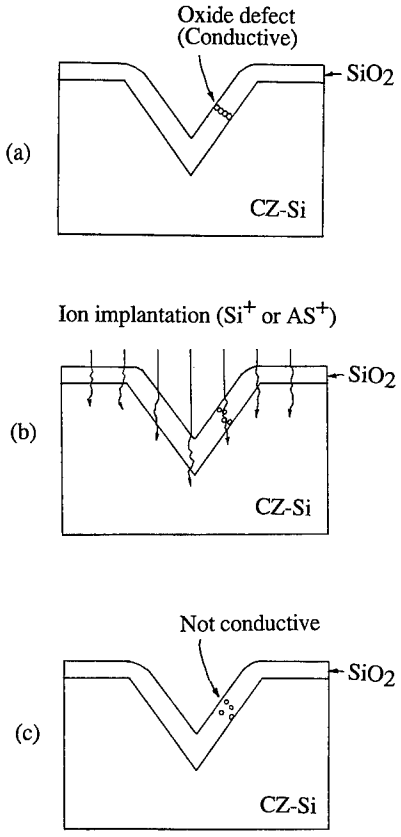


Fig. 21. Model for elimination of oxide defects with ion implantation.
(a) before I/I, (b) during I/I, (c) after I/I

Table II. Comparison of the two models.

No.	Experiment	Reference	Impurity model	Corner model
1.	Oxidation ambient dependence	Fig. 1	Yes	No
2.	Oxidation temperature dependence	Fig. 2	Yes	No
3.	Intentional introduction of impurities	Fig. 17	Yes	---
4.	Effect of sacrificial oxidation	[3]	Yes	No
5.	Ion implantation through oxides	[7, 10]	Yes	No
6.	Wafer rotation with D.I. water	[10]	Yes	Yes
7.	Surface etching of oxides	[18]	Yes	No

Yes : experimental results are consistent with the model
No : experimental results are not consistent with the model
--- : Consistency between experimental results and the model is not clear

SIGNIFICANCE OF THE DISCOVERY OF OCTAHEDRAL VOID DEFECTS

As mentioned above, we observed twenty-three samples of gate-oxide defects with TEM and twenty samples were octahedral defects. We also observed ten samples of grown-in defects in standard CZ-Si from two Si vendors and all ten of the samples were characterized with octahedral void defects. We had the data that gate-oxide defect density does not depend on Si wafers from several well-known Si vendors as long as the wafers are standard CZ-Si.

Metallic impurities, some particles and plasma damage from LSI processes will induce gate-oxide defects, but the concentrations of metallic impurities, the number of particles on wafers and the degree of plasma damage strongly depend on LSI manufacturer and on time (whether during development or production phase) alike. Compared with these factors, octahedral void defects are a common problem for all LSI manufacturers.

The octahedral void defects may also be the cause for crystal-originated-particles [15-16] and flow-pattern-defects [17] observed by many researchers. MOS transistors formed on the octahedral void defect on the Si surface will largely be different from the original designed transistor structure and the designed device characteristics as well as gate-oxide defect generation.

We can employ sacrificial oxidation, N_2 annealing, H_2 annealing, epitaxial-layer growth (Fig. 22) and so on, but we should clarify what mechanism is involved in the generation of octahedral void defects during Si growth, and improve the Si growth conditions.

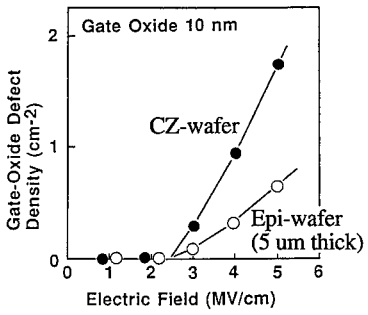


Fig. 22. Gate-oxide defect density vs electric field.

CONCLUSIONS

Gate-oxide defects originating in CZ-Si substrates are due to octahedral void defects of 0.1-0.2 microns across. Impurities located on the side wall of the octahedral void defects may be introduced into the growing gate-oxides during gate oxidation and form a conductive path in the gate-oxides. Si growth conditions should be improved, even if costly and time-consuming pre-oxidation or post-oxidation treatments are employed in the LSI fabrication processes.

ACKNOWLEDGEMENTS

We are indebted to Dr. Masato Tomita, Mr. Masataka Yamawaki, Mr. Takemi Ueki and Dr. Hidetoshi Takaoka for their help in TEM observation, to Mr. Hideo Akiya, Dr. Kazuo Imai, Mr. Hakaru Kyuragi and Mr. Norikuni Yabumoto for their continuous encouragement, and to Dr. Naohisa Inoue of Osaka Prefectual University and Dr. Kazumi Wada for their useful suggestions on the gigantic oxygen precipitates. Thanks are also due to Dr. George A. Rozgonyi of North Carolina State University for his useful comments about D-defects.

REFERENCES

1. O. Nakajima, M. Itsumi, N. Shiono, and Y. Yoriume, Ext. Abstr. (The 26th Spring Meeting, Mar. 1979), Japan. Soc. of Appl. Phys., 30p-R-1, 512 (1979). [in Japanese]
2. M. Itsumi, Y. Yoriume, O. Nakajima, and N. Shiono, Ext. Abstr. (The 27th Spring Meeting, Mar. 1980), Japan. Soc. of Appl. Phys., 3p-E-1, 553 (1980). [in Japanese]
3. M. Itsumi and F. Kiyosumi, Appl. Phys. Lett., 40 (6), 496 (1982).
4. F. Kiyosumi and M. Ino, Oki Denki Kenkyu Kaihatu, 118, Vol. 49 (3), 25 (1982).
5. F. Kiyosumi, H. Abe, H. Sato, M. Ino, and K. Uchida, Denshi-Tsushin Gakkai, Gijutsu Kenkyu Houkoku, SSD 83-66, 1 (1983).
6. Y. Matsushita, M. Watatsuki, and Y. Saito, Ext. Abstr., 18th Conf. Solid State Devices and Materials, Tokyo, 529 (1986).
7. M. Itsumi, Ext. Abstr. (The th Autumn Meeting,Sep 1986), Japan. Soc. of Appl. Phys., 459 (1986). [in Japanese]
8. M. Tachimori, T. Sakon, T. Kaneko, The Japan Soc. of Appl. Phys. and Related Soc., The 7th Kessho Kougaku (Crystal Engineering) Symposium, 27 (1990).
9. M. Itsumi and S. Aoyama, Ext. Abstr. of 184th Fall Meeting of The Electrochem. Society Inc., October, New Orleans, Vol. 93-2, Abstr. No. 256, 412 (1993).
10. M. Itsumi, J. Electrochem. Soc. 141 (9), 2460 (1994).
11. M. Itsumi, M. Tomita, and M. Yamawaki, J. Appl. Phys., 78, 1940 (1995).
12. M. Itsumi, H. Akiya, T. Ueki, M. Tomita, and M. Yamawaki, J. Appl. Phys., 78(10), 5984 (1995).
13. M. Itsumi, H. Akiya, T. Ueki, M. Tomita, and M. Yamawaki, Jpn. J. Appl. Phys., Vol. 35, Part 1, No. 2B, 812 (1996).
14. T. Ueki, M. Itsumi, and T. Takeda, 1996 Int. Conf. on Solid State Devices and Materials, Yokohama, LA-1, 862 (1996).
15. J. Ryuta, E. Morita, T. Tanaka and Y. Shimanuki, Jpn. J. Appl. Phys., Vol. 29, L1947 (1990).
16. M. Miyazaki, S. Miyazaki, T. Kitamura, Y. Yanase, T. Ochiai and H. Tsuya, Proc. 5th Int. Symp. Semiconductor Manufacturing (ISSM'96), Tokyo, Oct., 157 (1996).
17. H.Takeno, Mat. Res. Symp., Proc., Vol. 262, 51 (1992).
18. M. Itsumi, O. Nakajima, and N. Shiono, J. Appl. Phys., 72, 2185 (1992).

STRUCTURE OF THE DEFECTS RESPONSIBLE FOR B-MODE BREAKDOWN OF GATE OXIDE GROWN ON THE SURFACE OF SILICON WAFERS

T. MERA, J. JABLONSKI, M. DANBATA, K. NAGAI, and M. WATANABE
Komatsu Electronic Metals Co. Ltd., 2612 Shinomiya, Hiratsuka, Kanagawa 254, Japan

ABSTRACT

Crystal-originated pits are known as the defects responsible for B-mode Time Zero Dielectric Breakdown (TZDB) of the gate oxide grown on the surface of Si wafers. In order to clarify the breakdown mechanism, we have analyzed the structure of those defects formed at the surface of bare and oxidized wafers. In the latter case the analysis has been done both before and after gate oxide breakdown. Electric breakdown has been accomplished by Cu decoration method, recognized as an effective tool for unambiguous detection and positioning of the defects causing B-mode TZDB. As revealed by cross-sectional transmission electron microscopy (XTEM), crystal-originated pits at the bare wafer surface are polyhedral pits having about 5-nm-thick oxide layer on the inner walls. During gate oxidation the thermal oxide is growing faster on the pit walls than on the wafer surface, except for the pit corners where the oxide thinning has been observed. Resulting concave corners of the oxidized pits are suggested to be the weak spots where B-mode TZDB occurs.

INTRODUCTION

Large diameter silicon single crystals grown by Czochralski method typically contain grown-in defects with the density of about 10^6 cm^{-3}. They have been recently identified as aggregates of two or more polyhedral defects, probably voids [1,2,3]. Polyhedron aggregates located near the wafer surface produce pits at the surface of mirror polished silicon wafers subjected to standard SC-1 cleaning. Both single and double pits have been observed with well-defined polyhedral shape [4-6]. They can be detected by the laser particle counter as so called Crystal-Originated Particles (COP). Those crystal-originated pits are widely believed to be responsible for B-mode Time Zero Dielectric Breakdown (TZDB) of gate oxide grown on the wafer surface. However, the breakdown mechanism has not been understood yet.

In order to clarify the role of crystal-originated pits in B-mode TZDB of gate oxide, we analyzed the structure of those defects formed at the surface of bare and oxidized wafers. In the latter case the analysis was done both before and after gate oxide breakdown. Electric breakdown was accomplished by Cu decoration method [5,7]. Defect structure was analyzed by means of cross-sectional transmission electron microscopy (XTEM) and nano-probe energy-dispersive x-ray spectrometry (EDX).

EXPERIMENTAL

For this study, p-type (100)-oriented 150-mm-diameter mirror-polished CZ-Si wafers were selected with four different levels of gate oxide integrity (GOI) (C-mode TZBD yields were 5, 37, 60, and 100%). All wafers were subjected to standard SC-1 cleaning. 20-nm-thick thermal gate oxide was grown at 900°C for about 30 min in dry oxygen. Some of oxidized wafers were subjected to the TZDB test (polysilicon electrode area of 10 mm^2) or to the Cu decoration. For Cu decoration the wafer was im-

Mat. Res. Soc. Symp. Proc. Vol. 442 © 1997 Materials Research Society

mersed in methanol and brought into direct contact with a gold-coated cathode. A copper mesh as an anode was immersed in the liquid 5 mm above the wafer. The voltage of 10 V was applied, as measured with a surface voltage probe. Decoration time was 10 min.

The defects on the bare wafer surface were detected and positioned as Light Point Defects (LPD) by Tencor SFS6200 laser particle counter. The minimal size of detected LPD was 0.12 μm. Subsequent identification of LPD as crystal-originated pits was done by means of scanning electron microscope (SEM) using the defect location information obtained from laser particle counter. Similar procedure was used for detection, positioning and identification of crystal-originated pits on the surface of wafers subjected to gate oxidation. Positioning of the Cu-decorated defects was done by optical microscope. After subsequent removal of deposited copper in dilute HNO_3, the defects were observed by SEM. All Cu-decorated defects were identified by SEM as surface pits.

The structure of crystal-originated pits was analyzed by means of XTEM with EDX. The defect positions were marked by focused ion beam (FIB) utilizing the defect locations obtained by SEM. XTEM samples were prepared by FIB technique.

RESULTS AND DISCUSION

Figure 1 shows the correlation between densities of the defects responsible for B-mode TZDB of gate oxide and those revealed by applied Cu decoration method. The former was calculated for different wafers based on TZDB test. The following equation was used:

$$C\text{-mode yield } (\%) = \exp(-A \times D) \times 100\%, \quad (1)$$

where A is the electrode area and D is the defect density. The correlation curve in Fig. 1 shows small deviation from the slope α=1. Further experiments disclosed that the observed deviation can be eliminated by the proper adjustment of the bias voltage applied during Cu decoration. Thus, the defects causing B-mode failure in TZDB measurements are practically the same with those revealed by Cu decoration. It should be emphasized here that in all Cu-decorated positions observed by SEM after Cu removal we found single or double surface pits identical with crystal-originated pits observed on the bare and oxidized wafers. It confirms that, indeed, crystal-originated pits are responsible for B-mode TZDB of gate oxide.

We also tried to verify the possibility that Cu-decorated defects (≡ B-mode-failure-TZDB defects ≡ crystal-originated pits) can be detected prior to Cu decoration by means of laser particle counter as LPD defects. Figure 2 shows superimposed position maps of LPD defects subsequently confirmed by SEM to be the surface pits, and Cu-decorated defects. The maps were obtained for the same wafer. Only about 60% of crystal-originated pits revealed by Cu decoration were detected as LPD on as-oxidized wafer surface. Similar maps obtained for other analyzed wafers showed comparable or even worse coincidence. Thus, although the laser particle counter is still the only tool to detect crystal-originated pits on the bare wafer surface, its application for this purpose seems to be limited. Apparently, this is because the pits smaller than about 0.1 μm can hardly be detected as LPD.

XTEM micrographs of typical crystal-originated pits observed on the surface of bare, oxidized and Cu-decorated wafers are shown in Figs. 3, 4 and 5. At first it should be noted that during XTEM sample preparation the tungsten was deposited to protect the surface in FIB processing. Nevertheless, some gallium atoms were implanted producing thin amorphous Si layer. Due to the damage induced by Ga ion beam, part of the pit located close to the wafer surface became round. However, it did not usually damage the whole defects. All three crystal-originated pits presented in Figs. 3, 4 and 5 have very similar double

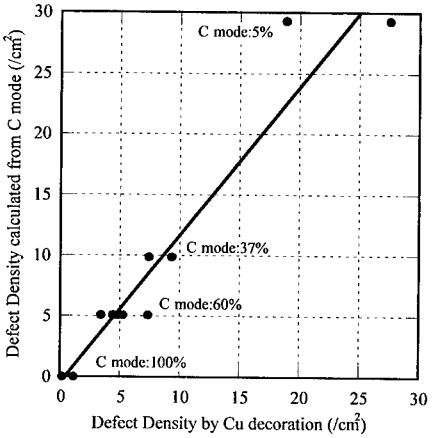


Fig. 1 Correlation between densities of the defects causing B-mode TZDB of gate oxide and those revealed by applied Cu decoration method. Four groups of wafers with different C-mode yields were tested.

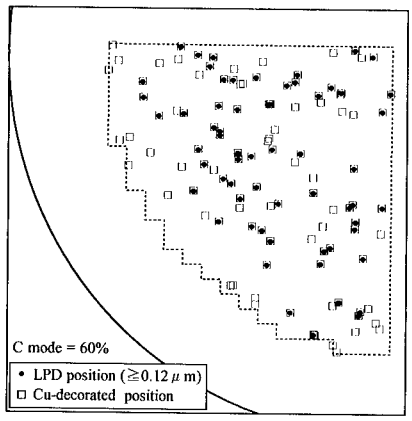
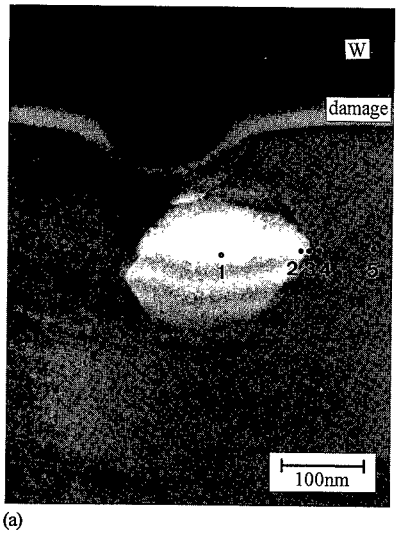
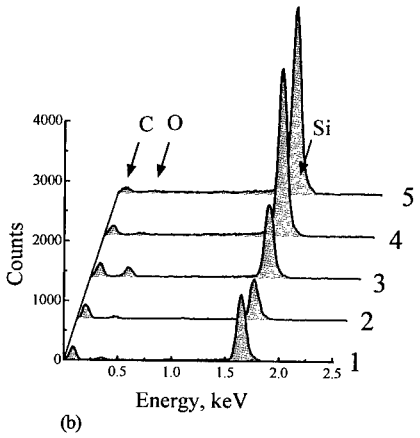


Fig. 2 Superimposed position maps of LPD defects subsequently confirmed by SEM to be the surface pits, and the defects revealed by Cu decoration. LPD were detected prior to Cu decoration. Both measurements were done on the same wafer having 60% C-mode yield.



(a)



(b)

Fig. 3 XTEM micrograph of typical crystal-originated pit formed on the surface of bare wafer (a) as well as EDX spectra taken at different defect positions (b). The positions where EDX spectra were measured are denoted by the numbers 1 to 5.

structure. Adjacent to the wafer surface upper part of the pit is nearly pyramidal-shaped, whereas the shape of deeper located part is polyhedral with the number of facets being probably equal or larger than eight. Those defects appear at the wafer surface as single pits, as revealed by SEM. Most of analyzed single pits had the described double structure. However, some single pits were found to consist of only one part with nearly pyramidal shape. About 50% of all observed crystal-originated pits appeared on the wafer surface as double pits. XTEM observations showed that their structure is very similar to the described above, except that two parts of defect are almost horizontally oriented and both are adjacent to the wafer surface. Surface pits having analogous morphologies were also found by Itsumi et al. [5]. Observed variations of crystal-originated pit structure become obvious if one believes that the defects are simply grown-in aggregates of two or more polyhedral voids cut in two by the wafer surface.

XTEM micrograph of one of crystal originated pits found on the bare wafers is presented in Fig. 3a. Figure 3b shows EDX spectra measured at different defect positions. Upper part of the pit is damaged by Ga ion beam. However, deeper located part has well-defined polyhedral shape, presumably with {111}-type facets. About 5-nm-thick layer at the walls of the polyhedron is clearly visible. As revealed by EDX, this is probably oxide layer (Fig. 3b). Similar SiO_x layers were also found at the walls of other analyzed crystal originated pits existing on the bare wafers, but newer on the (100) wafer surface. Analogous thin oxide layers were observed at the walls of polyhedral grown-in voids [3]. It should be noted here that, unlike other analyzed defects, tungsten did not penetrate at all an inside of the polyhedron shown in Fig. 3a. This strongly suggests the polyhedron to be polyhedral grown-in defect, which is isolated from the surface, rather than the part of the pit. If so, the significant differences in EDX Si peak intensities measured at various defect positions may provide additional argument that the grown-in defects are indeed voids.

Figure 4 shows XTEM micrograph of typical crystal-originated pit found on the oxidized wafer. As revealed by EDX, 30 to 40-nm-thick layer seen at the pit walls is oxide layer grown during gate oxidation. As a result of wall oxidation, originally sharp pit edges become round. The oxide layer grown at the pit walls is generally thicker than 20-nm-thick gate oxide formed on the wafer surface. This is probably because the growth of thermal oxide is faster on {111} silicon surfaces than on {100} ones, or because of contamination. However, it should be emphasized here that the thermal oxide layer formed at the pit corners (or edges) appears to be significantly thinner than that grown on the adjacent walls (Fig. 4). Similar anomalous oxide growth was observed by Sakina et al. [8] at the edges of step-shaped silicon wafer surface subjected to dry oxidation at relatively low temperatures (900 to 950°C). The effect was explained as being due to the concentration of a stress at the edge region, which may suppress oxygen diffusion through the oxide or chemical reaction at SiO_2-Si interface [8]. Obviously, this effect should be much stronger at the corners, where three or four planes intersect.

The electrical breakage of the oxide during Cu decoration does not significantly affect the structure of crystal-originated pits (Fig. 5). The oxide at the pit walls has almost the same thickness as that observed inside as-oxidized pits (Fig. 4). The new features seen in Fig. 5 are dark spots located at the interface between silicon and the inner oxide. They were identified by EDX as copper residues, which were electrochemically deposited during Cu decoration along the electrical leak paths. Cu residues were predominantly observed at the concave pit corners having thinner oxide layer. Thus, the concave corners of oxidized crystal-originated pits seem to be the weak oxide spots, where the dielectric breakdown actually occur. The dielectric breakdown of thin thermal oxides formed at the concave and convex corners of three-dimensional Si/SiO_2 structures, such as the trenched capacitors or buried oxide isolation, was described by Yamabe and Imai [9].

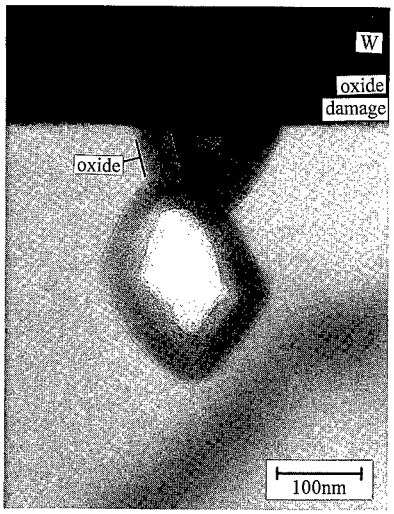


Fig. 4 XTEM micrograph of typical crystal-originated pit observed on the surface of wafer subjected to gate oxidation.

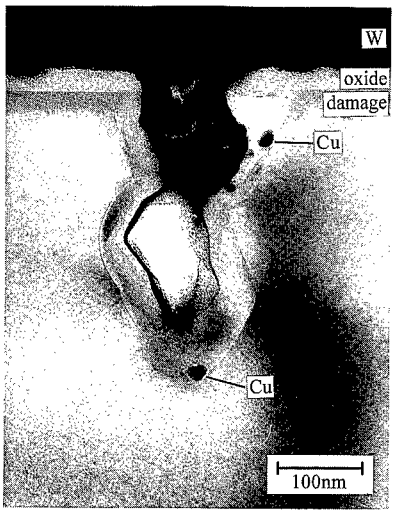


Fig. 5 XTEM micrograph of typical crystal-originated pit observed on the oxidized wafer surface after subsequent gate oxide breakdown accomplished by Cu decoration.

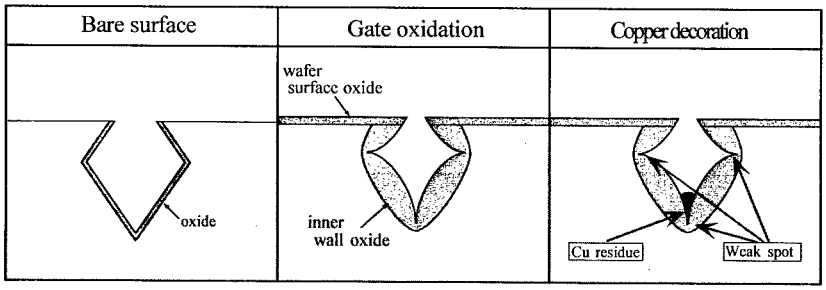


Fig. 6 Structure of crystal-originated pits on the surface of bare, oxidized and Cu decorated wafer - formation of weak spots inside the oxidized pits where the dielectric breakdown occurs (schematically).

SUMMARY

Performed study can be summarized as follows.

- Crystal-originated pits responsible for B-mode gate oxide TZDB can be unambiguously detected and positioned on the wafer surface by Cu decoration method.
- Structure of crystal-originated pits on the surface of bare wafer suggests that they are caused by the aggregates of two or more polyhedral voids having thin oxide layer on the inner polyhedron walls (Fig. 6).
- The inner walls of pits are thermally oxidized during the gate oxidation. The inner wall oxide is generally thicker than that grown on the wafer surface, except for the polyhedron corners, where the thermal oxide is thin (Fig. 6). Cu decoration takes place preferentially at those corners (Fig. 6).
- Obtained results suggest that B-mode time-zero dielectric breakdown of gate oxide occurs predominantly at the concave oxidized corners of polyhedral crystal-originated pits.

ACKNOWLEDGMENTS

The authors wish to thank Prof. K. Yamabe for fruitful discussions.

REFERENCES

1. K. Nakamura, T. Saisyoji, and T. Kubota, to be published in J. Cryst. Growth, (1996)
2. M. Nishimura, S. Yoshino, H. Motoura, S. Shimura, T. Mchedlidze, and T. Hikone, J. Electrochem. Soc. **143**, p. 243 (1996).
3. M. Kato, T. Yoshida, Y. Ikeda, and Y. Kitagawara, Jpn. J. Appl. Phys **35**, p. 5597 (1996).
4. M. Itsumi, M. Tomita, and M. Yamawaki, Microelectronic Engineering **28**, p. 39 (1995).
5. M. Itsumi, H. Akiya, T. Ueki, M. Tomita, and M. Yamanaki, J. Appl. Phys. **78**, p. 5984 (1995).
6. M. Miyazaki, S. Miyazaki, Y. Yanase, T. Ochiai, and T. Shigematsu, Jpn. J. Appl. Phys. **34**, p. 6303 (1995).
7. W. J. Shannon, RCA Review, p. 431, June 1970.
8. Y. Sakina, T. Ohno, and S. Matsumoto, Jpn. J. Appl. Phys. **22**, p. L514 (1983).
9. K. Yamabe and K. Imai, IEEE Trans. Electron Devices **ED-34**, p. 1681 (1987).

CHARACTERIZATION OF GROWN-IN DEFECTS IN CZ-SI CRYSTALS BY BRIGHT FIELD IR LASER INTERFEROMETER

KATSUHIKO NAKAI*, MASAMI HASEBE*, TOSHIO IWASAKI**, YASUO TSUMORI**
*Advanced Technology Research Laboratories, Nippon Steel Corporation, 3434 Shimata, Hikari, Yamaguchi 743, Japan
**Manufacturing Department, NSC Electron Corporation, 3434 Shimata, Hikari, Yamaguchi 743, Japan

ABSTRACT

We have developed a quantitative measurement method for the number density, size and morphology of grown-in defects in czochralski-grown silicon (CZ-Si) crystals with a bright-field infrared-laser interferometer (known as Oxygen Precipitate Profiler; OPP). Using this method we investigated the effect of crystal cooling condition during crystal growth on the formation of grown-in defects by growth holding experiments. The relation between gate oxide integrity (GOI) and grown-in defects was studied. It was revealed that the grown-in defects have octahedral shape and degrade the GOI performance. We estimate the density as well as cumulative volume of the grown-in defects and discuss the formation mechanism of them.

INTRODUCTION

With the progress of device miniaturization, the gate oxide integrity (GOI) has become an important characteristics. Recently the crystal defects which degrade GOI yield were reported to exist in as-grown CZ-Si crystals [1-4]. But the formation mechanism during CZ crystal growth is still unknown because the quantitative study of the grown-in defects, such as volume density, size distribution and morphology has not been concluded yet.

We have measured exact volume density, size distribution and morphology of the grown-in defects using OPP[5]. In this paper, we will show quantitative characterization-method by the OPP and the results of the change in volume density, size distribution and morphology of the grown-in defects with growth holding crystals in a pulling furnace. The crystal holding experiments accumulate the effect by providing the crystals much longer heating than normal one. From the observation results, we will discuss the formation process of the grown-in defects during crystal growth.

EXPERIMENT

The crystal holding experiments were carried out to investigate the GOI and the grown-in defects. The crystals were 135 mm in diameter, N type (phosphorus doped) and oxygen concentration was 9.5×10^{17} atoms/cm^3 with a conversion factor of 3.03×10^{17}/cm^2. These crystals were grown at the pulling rate of 1.0mm/min and the rate was abruptly slowed down from 1.0 to 0.2 mm/min. The slow rate was kept for certain time to hold the crystals in the furnace. Afterwards the pulling rate was changed to 1.0 mm/min again and maintained until the end of the body. Figure 1 shows an example of the cooling condition at the different crystal-positions of 210mm, 150mm and 80mm from the melt when the crystal is held for 100 minutes during growth. Each position of the crystals was designated a different temperature, and therefore the effect of holding temperature on the crystal quality can be clarified by investigating the crystal along the growth axis. The holding time was varied from 7 to 100 minutes to study the holding time dependence of the size and density of grown-in defects.

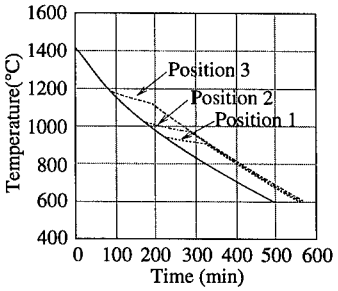


Figure 1
The cooling curve of crystal which held for 100 min during crystal growth at position 1(210mm from the halting position), 2(155mm) and 3 (80mm).

Mat. Res. Soc. Symp. Proc. Vol. 442 © 1997 Materials Research Society

To examine the GOI characteristics, metal-oxide-semiconductor (MOS) capacitors were fabricated on the sliced and mirror-polished wafers with polycrystalline silicon gates with area of 20 mm^2. The gate oxide films with thickness 25 nm were thermally grown in a dry oxygen at 1000°C. The dielectric breakdown field was determined from the applied voltage that induced the leakage current density of $1x10^{-6}$ A/cm^2.

The volume density, size distribution and morphology of the defects of these crystals were investigated by the OPP after both front side and back side surfaces of as-grown wafers were polished. The physical basis of the infrared interferometer is optical interference resulting from the mixing of a forward scattered light from a crystal defect at the focus position with a transmitted probe beam. The forward scattering of the crystal defect can be detected by the bright field phase interference[5]. The mixing of the scattered wave E_{sc} from the defect at the focus with the transmitted incident wave E_{∞} causes a phase shift, $\Delta\phi$, and results a intensity signal S. The phase shift $\Delta\phi$ and resulting signal S are described by the following equation assuming the defect is a spherical.

$$\Delta\phi = \frac{k^2 a^3}{2}\left(\frac{\varepsilon_1 - \varepsilon_m}{\varepsilon_1 + 2\varepsilon_m}\right)\left(\frac{NA}{n}\right)^2 \qquad (1).$$

$$S = P\Delta\phi \qquad (2).$$

k :$2\pi n/\lambda$, where λ is the wavelength of incident laser beam,
a : the defect radius,
ε_1 : the dielectric constant for the defects, ε_m : the dielectric constant for Si,
N.A. :numerical aperture of object lens, n :refractive index of Si,
P :the incident laser beam power.

In our system λ is 1.32μm and N.A. is 0.85.

The phase shift $\Delta\phi$ and thus the resulting signal S are proportional to the third power of the defect radius. From this relation, exact size of the defects can be obtained from the OPP intensity-signal S. Specimen wafers are scanned in X direction with a frequency of 10Hz and the scan is iterated after the wafers are moved in Y or Z direction with a pitch of 1 μm to obtain plane or cross-section view of the defect distribution.

In order to know exact size distribution of the defects by OPP, so-called the "ghost signals", which are observed in the smaller signal range than the true signal, must be subtracted from the raw data. As shown in figure 2, the defects away from the focal point are measured to be smaller than the true size because of the intensity distribution of the incident laser. The frequencies of these ghost signal appearing in each signal interval can be calculated by taking account of the Gaussian distribution of the incident laser intensity. Using this calculating procedure, the ghost signals were subtracted and the true size distribution was obtained. The detailed calculation method will be described elsewhere [6].

To make a calibration curve between the OPP signal intensity and true size of defect, the oxygen precipitates were observed both by the OPP and by transmission electron microscope (TEM) . The oxygen precipitates were introduced by two-step annealing at 1000°C or 1100°C for 1 to 64 hours after annealing 900°C for 1 hour in a nitrogen ambient. The precipitates change the morphology from platelet to octahedron, corresponding each to the second treatment temperature 1000°C and 1100°C respectively[7]. In the TEM observation, the diagonal length and thickness of the platelet precipitates and the diagonal size of octahedral precipitates were measured. After the TEM ob-

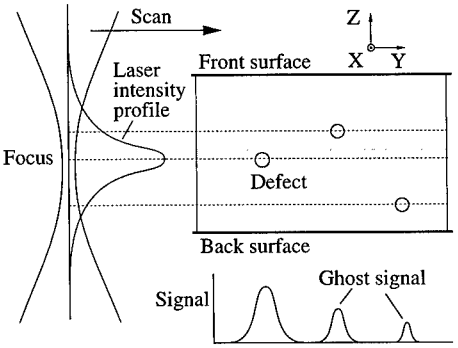


Figure 2
The Illustration to explain OPP signal intensity dependence to the incident laser intensity profile. The signal intensity when incident laser is scanned along Y direction through the sample is shown.

servation, the average signal intensity was determined by the OPP, and a calibration curve to define the defect size was obtained. Figure 3 is the results for the platelet and octahedral precipitates.

To know the morphology of grown-in defects is important because it leads to the information of the formation temperature range. In order to examine the defect morphology by the OPP, the specimen wafers were scanned in two directions by changing wafer setting angle. One is in a polarization direction of the incident laser beam set along <110> and the other is along <100> direction. The appearance of the two signal intensity histogram measured along <110> and <100> directions differs between the platelet and the octahedral precipitates as shown in Figure 4. The origin of the difference is due to that of the cross-sectional volume between the incident laser beam and the defects. The platelet precipitates lie on (100) planes and the octahedral precipitates are surrounded by {111} planes. The plane view of each precipitate from [100] direction is shown in figure 4(a) and 4(b). When the polarization direction, indicated by S in the figure, was changed from <110> to <100>, the signal amplitude of the platelet precipitates become larger. In the former case, the angle of every edge-on platelet precipitate to the polarization direction <110> is 45°; however, in the latter case, the both angles of 0° and 90° exist. And thus, the total cross-sectional volume between the incident laser beam and the defects is changed in the two cases. This results in the difference of the OPP signal intensity. On the other hand, the signal intensity from the octahedral precipitates does not vary in any polarization direction because they have a near symmetrical shape along the different polarization directions.

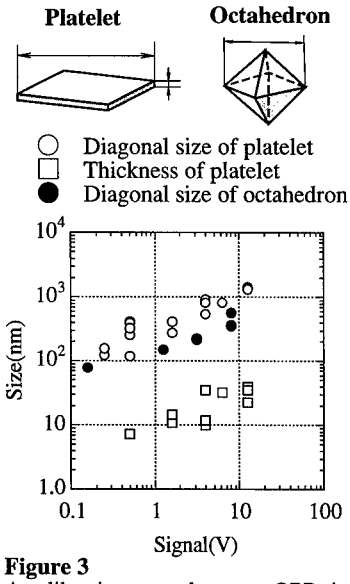


Figure 3
A calibration curve between OPP signal amplitude and precipitate size with platelet and octahedral shape. The size of precipitates were obtained by TEM.

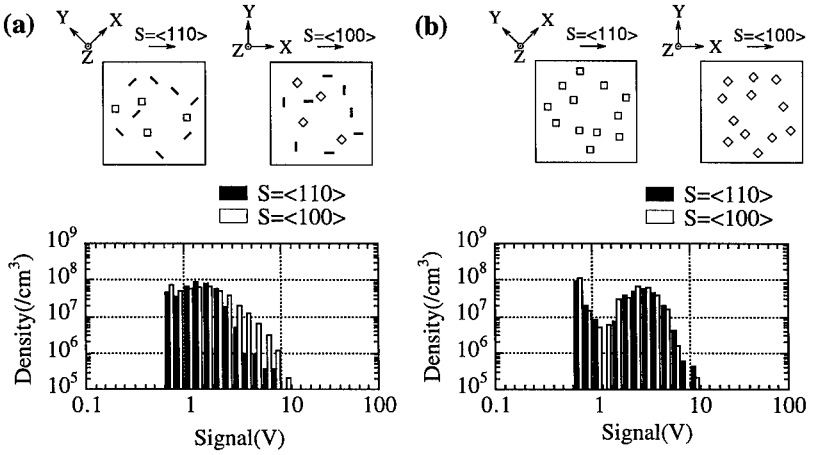


Figure 4
The OPP signal histogram of platelet (a) and octahedral (b) precipitates when the polarization of incident laser set along <110> and <100> direction.

RESULTS

The total grown-in defects density detectable by the OPP, which signal is larger than 0.2V in signal intensity, decreases in the holding temperature range between 1070°C and 1100°C compared to other temperature range as shown in figure 5(a). But the large defects over 10.0V are seen in the same temperature range.

The GOI improvement is also seen in the same temperature range; the frequency of dielectric breakdown under 8 MV/cm decreases and that over 8MV/cm increases [8] in the region where the density of grown-in defects is diminished as shown in figure 5(b).

The morphology of grown-in defects is determined to be an octahedral by the comparison of signal intensity obtained in two polarization directions. Figure 6 shows the signal intensity histograms of the grown-in defects at the position held at 1000°C. No signal intensity change is seen and so that the defects should have an octahedral shape. We have observed the grown-in defects in other holding temperature ranges and confirmed that the detected grown-in defects by the OPP are all octahedral.

The size distribution of the grown-in defects at the positions held at 1080°C for 7min and 100min is shown in figure 7. The size of grown-in defects was estimated by the calibration curve in figure 3. The average size becomes larger and the defects smaller than 300nm disappear as the holding time increases.

The size change of the defects with the holding time is plotted in figure 8, compared with that of octahedral oxygen precipitates formed at 1100°C annealing. The time is determined by calculating the total time passing the temperature range between 1070°C and 1100°C based on the cooling curve of figure 1. The average size of the defects is obtained from the size histograms. The size of the grown-in defects is about 10 times as large as that of the oxygen precipitates. However, the slopes of the size change with respect to time are similar with the value of about 1/2.

We examined the total volume of the defects per unit matrix silicon volume. It was derived from the size and number density distribution shown previously in figure 8. Figure9 is the estimated result of the total volume of grown-in defects (nm^3) per unit silicon volume ($1cm^3$) as a function of the holding temperature. There is no change in the total volume through whole the observed temperature regions (see >0.2V), even in the temperature range between 1070°C and 1100°C, where the defect number-density decreases.

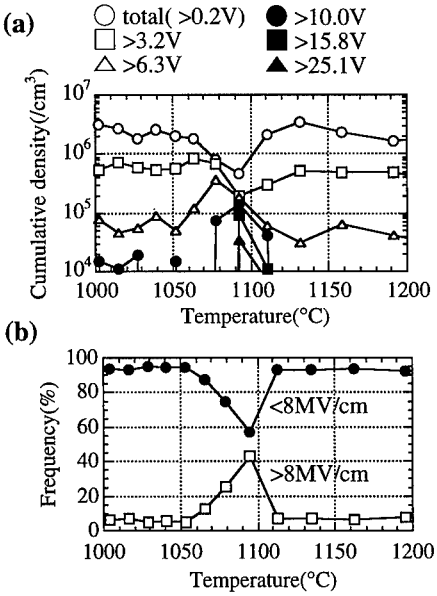


Figure 5
The cumulative grown-in defects density larger than each signal(a) and GOI yield(b) of crystal hold for 60 min during crystal growth. The horizontal axis shows the holding temperature of each position.

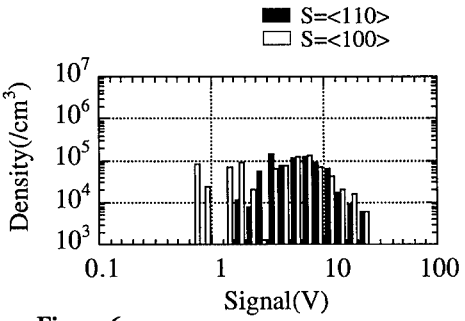


Figure 6
The OPP signal intensity histogram of grown-in defects at the crystal position held at 1000°C with the two different polarization conditions.

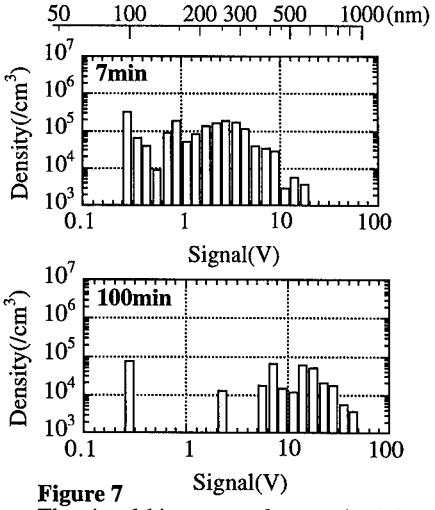


Figure 7
The signal histogram of grown-in defects at the position held at 1080°C for 7min and 100min.

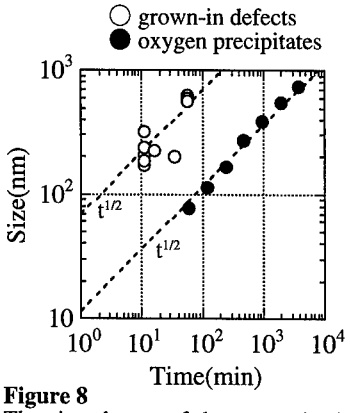


Figure 8
The size change of the grown-in defects with the total time passing the temperature range between 1070°C and 1100°C during crystal growth, and that of the oxygen precipitates with annealing time at 1100°C.

DISCUSSION

The OPP observation of the growth-held crystals clarified that the GOI yield improvement at the temperature region between 1070°C and 1100°C is due to decrease in the number density of grown-in defects larger than 84nm, and the grown-in defects observed by OPP cause dielectric breakdown of gate oxides.

The morphology of grown-in defects, which are all octahedral, indicate that they grow at the temperature higher than 1000°C during crystal growth. It is revealed by the growth holding experiments that the large grown-in defects appear mainly in the temperature range between 1070°C and 1100°C and the size are nearly same as the normal growth crystal in the other temperature range. It is convincing that the grown-in defects are formed in the temperature range between 1070°C and 1100°C, and the defects observed at the positions holding at other temperatures is considered to grow when the crystal passes the temperature range between 1070°C and 1100°C before or after growth holding.

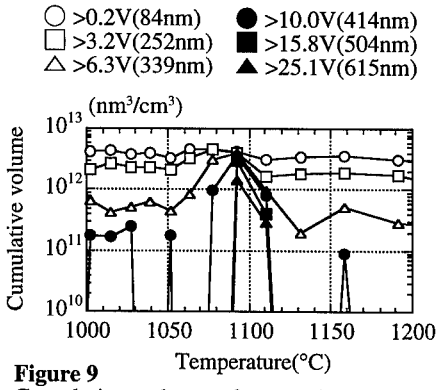


Figure 9
Cumulative volume of grown-in defects (nm^3) per unit silicon volume (cm^3) calculated by the size distribution obtained from OPP signal histogram.

We should note that the total volume of grown-in defects detected by OPP is kept constant, and the enlargement of grown-in defects could be expected by the Ostwald ripening mechanism. Therefore the increase of size and decrease of number density of grown-in defects occurred in the same temperature range and the GOI yield is improved.

The defect size is proportional to the 1/2 powers of time for both oxygen precipitates and grown-in defects. The growth of octahedral oxygen precipitates is known to be diffusion-controlled by oxygen and the size is proportional to a square root of time. On the other hand the growth of

grown-in defects is assumed to be the Ostwald ripening mechanism, the time dependence of size indicates the reaction-controlled growth [9] at the interface between defects and Si matrix.

The grown-in defects seem to be different from the oxygen precipitates because the size of grown-in defects in holding crystals is about 10 times as large as that of the octahedral oxygen precipitates which grow in the same temperature range. As will be reported, we have confirmed the grown-in defects detected by the Cu plating to be void-like defects by direct observation of the identical defects with a focused-ion-beam (FIB) TEM [10]. The similar structure is observed the grown-in defects detected by the OPP [11]. These results is in agreement with the account given Itsumi or Kato [4,12].

Assuming that the grown-in defect is composed of point defects (vacancies), the total of point defects which are constituent of grown-in defects could be derived from the total volume of the grown-in defects. The total volume of grown-in defects per unit volume ($1cm^3$) in silicon is estimated to be 10^{12}-10^{13} nm^3/cm^3. Using the atomic volume of a silicon as the volume of a vacancy (about 10^{-2}nm), the amount of vacancies calculated from the total volume of grown-in defects is 10^{14}-10^{15} $/cm^3$. This value is agree with the simulation results given by Nakamura [13]. But if the thermal equilibrium density of vacancies are induced at melting point during crystal growth, 10^{15}-10^{16} $/cm^3$ of vacancies are expected to be supersaturated in CZ-Si crystal [14]. This value is larger than our result from the volume of grown-in defects. We suspect that the reason for this difference is due to the OPP detection limit, in other words defects of size between 10^{-2}nm (single vacancy) and 84nm (10^6 vacancies), were not taken into account.

CONCLUSION

The grown-in defects induced in CZ-Si during crystal growth was investigated by a bright field infrared laser interferometer (OPP). It is revealed that the grown-in defects are octahedral one . They degrade the GOI yield and therefore the GOI improvement is achieved by the reduction of the grown-in defects. The formation of the grown-in defects is supposed to occur in the temperature range between 1070°C and 1100°C. The total volume of the grown-in defects per unit silicon volume is estimated to be constant value of 10^{12} -10^{13} nm^3/cm^3. The growth and decrease of density of grown-in defects are occurred in the same temperature range because the formation mechanism could be the ostwald ripening. Assuming the ostwald ripening mechanism, the size dependence to time is indicated to be a reaction-limited phenomena.

ACKNOWLEDGMENTS

We are indebted to Dr. W. Ohashi for the fruitful discussion throughout this study. We would like to thank Dr. Mark A. Nokes and Pamera D. Flesher of Pacific Scientific Co., Ltd., K. Ogawa of Innotech Corporation for their helpful instrumental assistance detail. We also wish to express appreciation to Y. Konishi for the OPP measurement.

REFERENCE

1. J. Ryuta *et al.* Jpn. J. Appl. Phys. 29, L1947 (1990).
2. H. Yamagishi *et al.* Semicond. Sci. Technol. 7 (1992) A135.
3. M. Hourai *et al.* Semiconductor silicon 1994 , edited by H. R. Huff, W. Bergholz and K. Sumino (the Electrochem. Soc., Pennington, NJ, 1994) pp.156.
4. M. Itsumi *et al.* J. Appl. Phys. 78, 1940 (1995).
5. J. S. Bacthelder and M. A. Taubenblatt, Appl. Phys. Lett. 55(3), 17 (1989).
6. K. Nakai *et al.* to be published.
7. M. Hasebe *et al.* Materials Science Forum vol. 83-87, 1475-1480 (1992).
8. Y. Tsumori *et al.* Mat. Res. Soc. Symp. Proc. vol. 378, 23-28 (1995).
9. R. H. Doremus, Rates of phase transformations (Academic Press, Inc., 1985) p143.
10. Deai *et al.* to be published.
11. T. Mizutani *et al.* to be published.
12. M. Kato *et al.* Abstruct of 27th National Conf. on Crystal Growth , p153 (in Japanese).
13. K. Nakamura J. Mater. Sci. Eng. B vol. 36, no1-3, p22-25.
14. Y. Okada, Phys. Rev. B 41, 10741-10743 (1990).

TEM OBSERVATION OF GROWN-IN DEFECTS IN CZ-Si CRYSTALS AND THEIR SECCO ETCHING PROPERTIES

MASAHIRO KATO, HIROSHI TAKENO and YUTAKA KITAGAWARA
Isobe R&D Center, Shin-Etsu Handotai Co., Ltd., 2-13-1 Isobe, Annaka, Gunma 379-01, Japan

ABSTRACT

Grown-in defects detected by IR laser scattering tomography (LSTDs) in Czochralski-grown Si crystals were identified by transmission electron microscopy (TEM) with a special defect positioning technique. The basic structure of the LSTD was revealed to be a composite of two or three incomplete octahedral voids with the 100-300nm total size. The TEM images of the defect showed existence of 2~4nm-thick walls surrounding the voids. These thin-walls are considered to be made of oxide, SiO_x. These LSTDs are indeed dominant grown-in defect species in most of the commercial CZ-Si wafers. The LSTD after 1200°C oxidation was also observed by TEM. The resulting image shows that the defect changed from void to filled oxide precipitate by the high temperature heat treatment. On the other hand, in very slowly pulled crystals with ~0.4mm/min rate, interstitial type dislocation loops were observed as major defect species. Non-agitated Secco etching of these grown-in defects delineates "flow patterns" (FPs) or pits without the flow patterns. The FP forming property is shown to disappear by oxidation at temperature above 1150°C, while the defect itself remains stable. This implies that the grown-in defects lose their chemical properties to form FPs by the high-temperature oxidation. It is further revealed that the grown-in defects, which once lost the FP forming property by the high-temperature oxidation, can form FPs again by an intentional Cu contamination. Thus a possible FP formation factor is Cu decoration at the grown-in defect site. Defect formation model of the as-grown twin-type LSTD is also proposed.

INTRODUCTION

It is well known that microdefects of 10^4-10^7 cm^{-3} density exist in Czochralski (CZ) silicon crystals. They are detected by various experimental methods. The defects are named according to their observation techniques such as "flow-pattern defects (FPDs)" [1], "Secco etch-pit defects (SEPDs)" [2] observed after non-agitated Secco etching, "crystal originated particles (COPs)" after NH_4 / H_2O_2 / H_2O (SC1) cleaning [3], and defects observed by IR laser scattering tomography (LSTDs) [4]. Since the density of these defects correlates with gate oxide integrity (GOI) of metal-oxide-Si (MOS) [1, 5], much effort has been made to investigate the defect nature and the mechanism of the GOI degradation by extensive TEM studies [6-11]. These TEM observations were made on wafer samples for which the defect locations were positioned by electrical techniques at the weak sites of the oxide film [9-11], or by defect delineation with chemical etching [6, 7]. In such observation techniques, however, it is probable that the original morphology of the near-surface defects are altered during the wafer surface processing such as polishing, oxidation, electrochemical defect-positioning or chemical etching. It is thus desired to directly observe the grown-in defects in the bulk Si crystals.

In this study, we first show the morphology of the grown-in LSTDs revealed by TEM, which are not altered by the surface processes. We then show a TEM image of LSTD after a high temperature heat treatment to understand how the grown-in defect changes during the heat process. The chemical etching property of the grown-in defects is studied to investigate flow pattern formation factor of the FPDs. Finally, a model to form characteristic morphology of the as-grown LSTD is proposed.

EXPERIMENTAL RESULTS AND DISCUSSION

Morphology of Grown-in Defects

To observe grown-in LSTDs, the sample wafers were sliced from 6-in. diam. (100)-oriented boron-doped p-type CZ-Si crystal which was pulled with 1.1 mm/min growth rate. Oxygen

Mat. Res. Soc. Symp. Proc. Vol. 442 © 1997 Materials Research Society

concentration was in the range 19-21 ppma in JEIDA scale [12]. The resistivity ranged from 14 to 22 Ω·cm.

To aim a specific grown-in defect by laser scattering tomography (LST) and TEM, aluminum was first evaporated onto the wafer surface. Stripe pattern shown in Fig. 1 was then fabricated by photolithography and the succeeding aluminum etching. Wafer was finally cleaved across the stripe lines which are perpendicular to the cleavage direction. Figure 1 shows a schematic illustration of the experimental setup for the LST observation. The IR beam was incident upon the cleaved surface and the defect-induced scattered light from the polished wafer surface was detected using MO-411 LST observation system by Mitsui Kinzoku Co., Ltd. Applying "illumination mode" of the MO-411 system, one can observe both defect scattering image and aluminum pattern under an identical observation condition as shown in Fig. 2. X-coordinate of the defect position was determined by addressing on the aluminum stripe pattern. Y- and Z(depth)-coordinates of the defect were measured by the LST machine from the cleaved plane and the polished surface respectively.

Cross sectional TEM samples were made exactly at the defect position with the X, Y and Z coordinates using a dicing saw and a focused ion beam (FIB) system. Final thickness of the observation area was 0.1-0.8μm. LSTDs were observed using JEOL 2000FXII and Hitachi H-1250 TEM with the accelerating voltages 200kV and 1MV respectively. The elemental analyses were performed by the energy dispersive X-ray spectrometry (EDX) using VOYAGER from NORAN Instruments mounted on Hitachi HF-2000 TEM.

Figures 3, 4 and 5 show TEM images of the (110) cross sectional observation. The defects are entirely inside the bulk Si without influence of the wafer surface processing. One LSTD consists of two or three defect components. The largest component in Fig. 3 exhibits a diamond shape with interference contrast inside. It is considered that the octahedral defect component is surrounded by the (111) facets. The LSTD images in Figs. 4 and 5 are similar to the one shown in Fig.3 with their structural components based on the octahedral geometry.

All defects observed in this study were twin or triplet type with 100-300nm sizes. It is interesting in Fig. 4 that a rather bright contrast is observed at the connecting part of the two octahedral defect-components. Similar bright contrast is observed in Fig. 5. These results suggest existence of a hole connecting the two octahedral defect-components as illustrated by a model diagram in Fig. 6. All twin-type and triplet-type defects are thought to have the structures like thi

It is also interesting that no strain field is observed around the grown-in LSTD. In contrast to this, in case of a well known octahedral oxide precipitate after a high-temperature heat treatment, strain is generally observed around the precipitate by TEM [13]. One should note that the octahedron-like defects observed in Figs. 3, 4 and 5 are surrounded by thin and clear outlines. The outline image is especially distinctive in Fig. 4. It suggests existence of several nanometers thick walls surrounding the defects. Such clear image suggesting the surrounding walls is not seen for the oxide precipitate [13]. The as-grown LSTD is thus a quite unique defect.

EDX measurement was performed to further analyze the defect. The beam diameter of the EDX analyses was set to be 1nm. The EDX spectra from the defect and the Si matrix are shown in Figs. 7 (a) and (b). We notice that the oxygen peak in spectrum (a) is significantly higher than the one in the reference spectrum (b) of the Si matrix. This means that oxygen is a defect forming

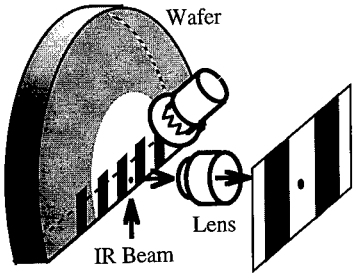


Fig. 1. A schematic illustration of the LST observation to locate a defect.

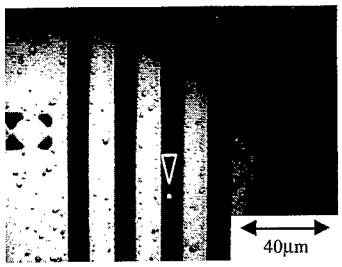


Fig. 2. An example of the LST image. White spot indicated by the arrow is a LSTD.

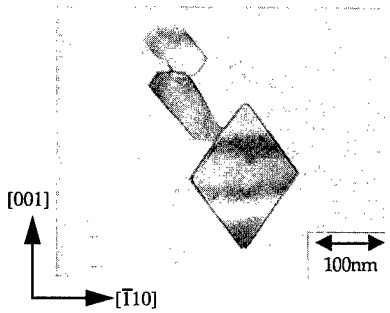


Fig. 3. (110) cross sectional TEM image of an as-grown LSTD. The accelerating voltage was 1MV.

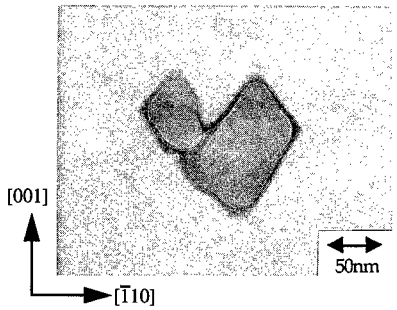


Fig. 4. (110) cross sectional TEM image of an as-grown LSTD. The accelerating voltage was 1MV.

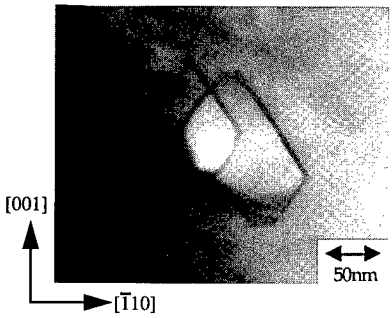


Fig. 5. (110) cross sectional TEM image of an as-grown LSTD. The accelerating voltage was 200kV.

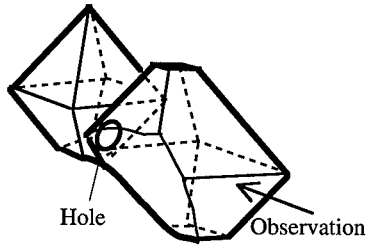


Fig. 6. A schematic illustration of a defect shown in Fig. 5

species. Nevertheless, the oxygen signal from the LSTD is very weak compared to the one for an ordinary oxide precipitate after a high-temperature heat treatment [13]. The LSTD is then considered to be not filled with SiO_2 but to be rather a void.

From the results shown above, the LSTDs are considered to be incomplete octahedral voids surrounded by several nanometers thick walls formed by SiO_x. It is noteworthy that the structure of the as-grown bulk LSTD revealed in this study is similar to a surface defect detected by the Cu-decoration method [9] or a microscopic COP structure [7, 8]. They are thus considered to be the same type of defects in the as-grown state.

It has been known that another type of defects exists in as-grown CZ-Si crystals. Figures 8 (a) and (b) show TEM images of interstitial type dislocations observed in crystals grown with pulling speeds ~1.4 and ~0.4mm/min respectively [6]. We thus understand there exist at least two types of grown-in defects in CZ-Si crystals, voids and dislocations. In a crystal with relatively fast pulling speed >1.0 mm/min, or in a crystal region inside the OSF-ring [14], the void defects are dominant species with dislocations as the minority. On the other hand, in a slowly pulled crystal with pulling speed <0.5mm/min, or in a crystal region outside the OSF-ring, the interstitial type dislocations are the only species observed.

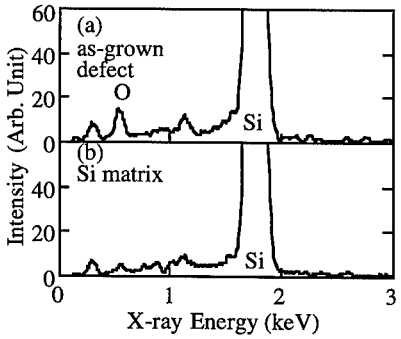


Fig. 7. EDX spectra of (a) an as-grown LSTD and (b) the Si matrix.

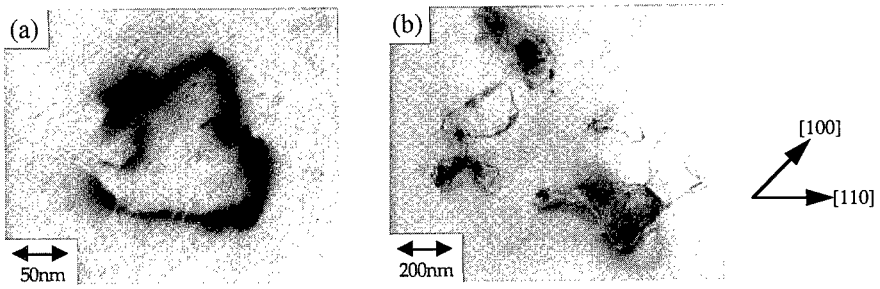


Fig. 8. TEM images of FPDs in crystals grown with pulling rates ~1.4mm/min for (a) and ~0.4mm/min for (b).

By non agitated Secco etching, the grown-in voids and grown-in dislocations are detected either as FPDs or SEPDs. Defect is called FPD when H_2 gas is generated from the defect to form "flow pattern (FP)" in Secco etchant [15]. On the other hand, defect is called SEPD when no H_2 gas bubble is formed in the etchant. The defect terminology FPD / SEPD is thus based on the defect chemical property but not on the defect type, void / dislocation. The defect chemical property and its thermal behavior are studied in the next subsection.

Thermal Behavior of Grown-in Defect Etching Property

According to refs. [15] and [16], roughly half of the LSTDs are detected as FPDs, and the others are detected as SEPDs in a CZ-Si crystal. After a high temperature oxidation above 1100°C, however, almost all the LSTDs are detected as SEPDs with the LSTD density being unchanged by the heat treatment. It means that FPDs lose the flow pattern formation property becoming SEPDs during the heat treatment. The original defects before the high-temperature oxidation are dominantly the octahedral voids as we discussed in the previous subsection.

To know how the octahedral void changes by the high-temperature oxidation, we have observed the LSTD in a crystal after the heat treatment by TEM. The sample wafer was 8-12Ω·cm <100>-oriented boron doped CZ-Si crystal pulled with 1.0mm/min rate. The oxygen concentration of the crystal was ~17ppma-JEIDA. The wafer was heat treated at 1200°C for 1h in a dry O_2 atmosphere. It was confirmed that the FPDs lost their flow pattern formation property.

Figure 9 shows the TEM image of the LSTD at the position 4-5μm deep from the wafer surface after the high-temperature oxidation. The LSTD has twin-type incomplete octahedral shape with 300nm total size. The defect shape is similar to that of the as-grown LSTD, but some strain field is observed around the defect after the high-temperature oxidation. It is also interesting that the outline contrast suggesting the thin wall for the as-grown defect is no longer observed after the heat treatment. We consider that the voids changed into filled oxide precipitates by the high-temperature oxidation. It is thus possible that the flow pattern formation property is lost by this defect morphology change.

Thermal behavior of non-agitated Secco etching property of the interstitial type grown-in dislocations has been studied. Sample wafers were sliced from 5-in. diam. ~10Ω·cm boron-doped p-type CZ-Si crystals grown with pulling rate ~0.4mm/min in <100> direction. Initial oxygen concentration was ~18ppma-JEIDA. The wafers were first subjected to the heat treatment at 1200°C for 2h in dry O_2 atmosphere to eliminate the flow pattern forming property of the grown-in dislocation loops. After the heat treatment, the wafer surface was intentionally contaminated with Cu by dipping in a solution (3% Cu nitride solution : 50% HF solution =1:100). Cu was then driven into the bulk by a heat treatment at 1000°C for 1h in N_2 atmosphere. After etching off the ~50μm-deep wafer surface region by mixed

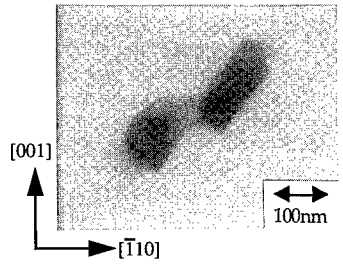


Fig. 9. TEM image of LSTD after a heat treatment at 1200°C for 1h in dry O_2 atmosphere.

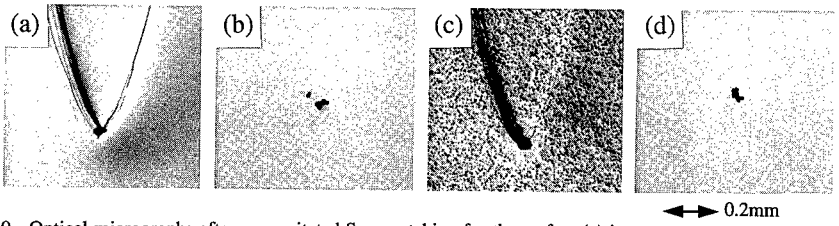


Fig. 10. Optical micrographs after non-agitated Secco etching for the wafers (a) in as-grown state, (b) after heat treatment at 1200°C for 2h in dry O_2 (c) after heat treatment at 1000°C for 1h in N_2 with Cu contamination which followed (b), and (d) after heat treatment at 1000°C for 1h in N_2 without Cu contamination which followed (b).

acids, non-agitated Secco etching was carried out.

As shown in optical micrographs in Figs. 10(a) and (b) for the non-agitated Secco etched surfaces, the grown-in dislocations lost their chemical property to form flow patterns by a heat treatment at 1200°C for 2h in dry O_2 atmosphere. However, the dislocations formed flow patterns again by subsequent intentional Cu contamination as shown in Fig. 10(c). Even when a sample followed the same heat cycle as that for sample in Fig. 10(c), the flow patterns did not form in case of the no intentional Cu contamination as shown in Fig. 10(d). Hence, another possibility of flow pattern formation factor is Cu decoration at the grown-in defect sites.

Relation between Cu contamination and octahedral voids should be investigated to clarify the difference between FPDs and SEPDs in as-grown crystals grown with relatively fast pulling rates

Formation Model of Grown-in Octahedral Voids

The grown-in LSTD structure presented in this study should provide some information about the defect formation mechanism. One should especially note the characteristic defect structure consisting of the two octahedral voids connected through a small hole as shown in Fig. 6. This seems to imply that each defect was first formed as a single octahedral void then the second octahedral void generated from the first component at some defect growth stage. On the other hand, aggregation of two separately formed octahedral voids is statistically unlikely for the twin type LSTD formation. We thus propose a defect formation model as follows.

During a crystal growth, a small void should generate by vacancy aggregation as illustrated in Fig. 11(a). It grows further by absorption of vacancies, but simultaneously, very thin oxide film is gradually formed at the defect boundary by oxygen diffusion to the void as shown in (b). After a while, the void is surrounded by oxide film several nanometers thick as shown in (c). The oxide film starts to obstruct the vacancy absorption into the void. Thus the vacancies have to attack the weakest site of the oxide wall for the defect to grow further. From this weak site of the oxide film, second void swells out to form a twin type LSTD as illustrated in (d) and (e).

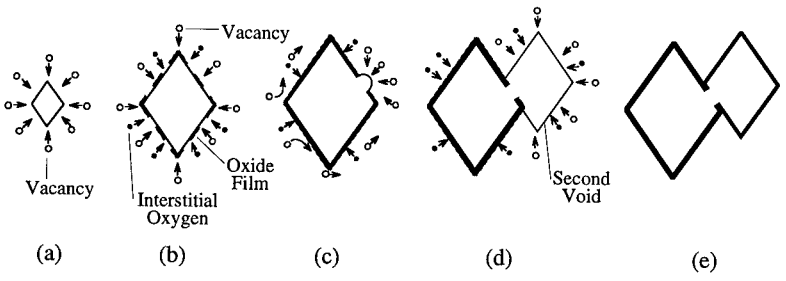


Fig. 11. Model for twin type void formation. (a) Aggregation of vacancies. (b) Formation of thin oxide film. (c) Obstruction of vacancy absorption by oxide film. (d) Growth of second void. (e) Twin type void.

CONCLUSIONS

Defect structure of LSTDs in as-grown bulk CZ Si crystals was observed by TEM . Two or three incomplete octahedral components are consecutively connected to form a twin or triplet type LSTD structure. TEM-EDX analyses revealed weak oxygen signals from the defects. This suggests that the as-grown LSTD is composed of incomplete octahedral voids and 2-4 nm-thick oxide walls surrounding the voids. These octahedral voids are considered to be dominant defect species in conventional crystals grown with relatively fast pulling rates, or in crystal regions inside the OSF-rings. On the other hand, grown-in interstitial type dislocations are dominant species in slowly pulled crystals with ~0.4mm/min rates, or in crystal regions outside the OSF-rings.

It is suggested that the as-grown void defect changes into filled oxide precipitate by a 1200°C heat treatment in oxygen atmosphere. Simultaneously the defect loses flow pattern formation property by this heat treatment. Grown-in dislocation loop, which is found dominantly in a slowly pulled crystal, also loses the flow pattern formation property by the 1200°C heat treatment. Furthermore, the grown-in dislocation, which once lost the flow pattern formation property by the high temperature heat treatment, can form flow pattern again by an intentional Cu contamination. Thus the Cu contamination at the grown-in defect site is considered to be a possible flow pattern formation factor.

Defect formation model of the as-grown LSTD is proposed to explain the characteristic twin type morphology.

ACKNOWLEDGEMENTS

The authors wish to thank Prof. Yoshio Nakamura of Tokyo Institute of Technology for supporting the 1MV TEM observation. They appreciate Jun Hatakeyama of Shin-Etsu Chemical Co., Ltd. for his help in sample preparation. They also thank Tomosuke Yoshida, Yasuhiro Ikeda, Dr. Satoshi Ushio and Dr. Takao Takenaka for invaluable comments and encouragement.

REFERENCES

[1] H. Yamagishi, I. Fusegawa, N. Fujimaki and M. Katayama: Semicond. Sci. & Technol. **7**, A135 (1992).
[2] S. Sadamitsu, S. Umeno, Y. Koike, M. Hourai, S. Sumita and T. Shigematsu, Jpn. J. Appl. Phys. **32**, 3675 (1993).
[3] J. Ryuta, E. Morita, T. Tanaka and Y. Shimanuki, Jpn. J. Appl. Phys. **29**, L1947 (1990).
[4] P. Gall, J-P. Fillard, J. Bonnafe, T. Rakotomavo, H. Rufer and H. Schwenk, in Defect Control in Semiconductors edited by K. Sumino (North-Holland, Amsterdam, 1990) p.255.
[5] S. Umeno, S. Sadamitsu, H. Murakami, M. Hourai, S. Sumita and T. Shigematsu, Jpn. J. Appl. Phys. **32**, L699 (1993).
[6] H. Takeno, S. Ushio and T. Takenaka, in Defect Engineering in Semiconductor Growth, Processing and Device Technology edited by S. Ashok, J. Chevallier, K. Sumino and E. Weber (Mater. Res. Soc. **262**, Pittsburgh, 1992) p. 51.
[7] M. Miyazaki, S. Miyazaki, Y. Yanase, T. Ochiai and T. Shigematsu, Jpn. J. Appl. Phys. **34**, 6303 (1995).
[8] M. Hourai, Ext. Abstr. 43rd Spring Meet. (Japan Society of Applied Physics and Related Societies, Aasaka, March, 1996) No. 0, P. 1405, 28p-Z-2 [in Japanese]
[9] M. Itsumi, H. Akiya, T. Ueki, M. Tomita and M. Yamawaki, Jpn. J. Appl. Phys. **35**, 812 (1996).
[10] M. Tamasuka, M. Kimura, S. Oka and G. A. Rozgonyi, in HIGH PURITY SILICON, edited by C. L. Claeys, P. Stallhofer, P. Rai-Choudhury and J. E. Maureis (Electrochem. Soc., Pennington, 1996) PV96-13, p. 345.
[11] J. G. Park, H. Kirk, K-C. Cho, H-K. Lee, C-S. Lee and G. A. Rozgonyi, Semiconductor Silicon/1994 edited by H. R. Huff, W. Bergholz and K. Sumino (Electrochem. Soc., Pennington, 1994) p.370.
[12] T. Iizuka, S. Takasu, M. Tajima, T. Arai, T. Nozaki, N. Inoue and M. Watanabe, J. Electrochem. Soc. **132**, 1707 (1985).
[13] M. Kato, T. Yoshida, Y. Ikeda and Y. Kitagawara, Jpn. J. Appl. Phys. **35**, (1996), 5597 (1996).
[14] M. Hasebe, Y. Takeoka, S. Shinomiya and S. Naito, in Defect Control in Semiconductors edited by K. Sumino (North-Holland, Amsterdam, 1990) p. 157
[15] H. Takeno, M. Kato and Y. Kitagawara, Proceeding The 2nd International Symposium on Advanced Science and Technology of Silicon Materials edited by M. Umeno p. 294 (Kona-Hawaii, 1996)
[16] S. Umeno and M. Okui, Ext. Abstr. 43rd Spring Meet (Japan Society of Applied Physics and Related Societies, Asaka, March, 1996) No. 1, P. 183, 26p-X-4 [in Japanese]

CRYSTALLOGRAPHIC ANALYSIS OF FLOW PATTERN DEFECTS IN DISLOCATED CZOCHRALSKI SILICON CRYSTALS

Y. Ikematsu[1], T. Iwasaki[2], H. Harada[2], K. Tanaka[1], M. Fujinami[3] and M. Hasebe[4]
[1]Advanced Technology Research Laboratories, Nippon Steel Corporation, 5-10-1 Fuchinobe, Sagamihara, Kanagawa 229, Japan
[2]NSC Electron Corporation, 3434 Shimata, Hikari, Yamaguchi 743, Japan
[3]Advanced Technology Research Laboratories, Nippon Steel Corporation, 1618 Ida, Nakahara-ku, Kawasaki, Kanagawa 211, Japan
[4]Advanced Technology Research Laboratories, Nippon Steel Corporation, 3434 Shimata, Hikari, Yamaguchi 743, Japan

ABSTRACT

In dislocated Cz-Si crystals, rows of flow patterns (FP) and Secco etch pits (SEP) (2-3 mm in length, along <110> direction) can be revealed by Secco etch without agitation. In this study, the crystal defects forming FP-SEP rows in dislocated Cz-Si crystals are investigated by transmission electron microscopy. Microdefects, 0.1 μ m in size, are observed in a row along a FP-SEP row, <110> direction. These defects were identified as oxygen precipitates with or without dislocation loops (interstitial-type), and voids with oxidized interiors. We conclude that FP originate from interstitial-type dislocation loops, and SEP are due to oxygen precipitates or voids.

1. INTRODUCTION

It is well known that flow patterns (FP) and Secco etch pits (SEP) in silicon crystals can be revealed by Secco etching without agitation [1]. In as-grown Czochralski silicon (Cz-Si) crystals, it has been reported that grown-in defects generating FP are identified as interstitial-type dislocation loops [2] or D-defects [3] by TEM observation of the FP tip. The relation between grown-in defects causing SEP and microdefects which scatter infrared laser (IR defects) was investigated as well. The results indicate that SEP occur at the position of IR defects by Secco etching with no agitation. Additionally, the IR defects have been analyzed by secondary ion mass spectrometry, and oxygen ions were detected at the IR defect positions. From these results, it has been suggested that SEP could originate from oxygen precipitates [4]. However, the origin of SEP has not yet been clarified.

In dislocated Cz-Si crystals, rows of FP and SEP (2-3mm in length, along <110> direction) can be revealed by Secco etching with no agitation. As a result of X-ray transmission topography, it has been recognized that the origin of FP-SEP rows is not slip dislocations but other crystal defects [5]. Thus, it is still unclear what type of microdefects generate FP or SEP by Secco etching.

The present work aims to characterize the microdefects forming the FP-SEP rows in dislocated Cz-Si crystals by means of transmission electron microscopy. From this result, the relation between microdefects and the origin of FP or SEP will be discussed.

2. EXPERIMENTAL PROCEDURE

Wafers were prepared from Czochralski-grown silicon crystals (B-doped (100), 2 to 10

Mat. Res. Soc. Symp. Proc. Vol. 442 © 1997 Materials Research Society

Ω-cm, [Oi] = 8×10^{17} atoms/cm^3 (JEIDA)), which were dislocated during the crystal growth. First, they were etched in the Secco etch solution for 90 seconds without agitation [1]. Then, a specimen 2×2 mm in size was cut from an etched wafer with a FP-SEP row positioned at the center. Thin films for TEM observations were thinned from the back surface of the specimens by mechanical grinding followed by argon ion milling. TEM observations were conducted at 200kV with an H-800 (Hitachi) or an HF-200 (Hitachi) microscope equipped with an energy-dispersive X-ray spectroscopy (EDS).

3. RESULTS AND DISCUSSION

Characterization of microdefects forming FP-SEP rows

Figure 1 shows an optical micrograph of a FP-SEP row revealed after Secco etch without agitation. In this figure, wedge-shaped patterns and shallow etch pits are seen in a row as a result of the evolution of etching. At the region indicated by an open circle in Fig.1, the microdefects able to generate FP and SEP were not appeared on the surface but buried in the silicon matrix.

Figures 2(a) and 2(b) are TEM micrographs of the region marked by the open circle in Fig.1. Microdefects 0.1 μ m in size are observed in a row along a FP-SEP row, corresponding to the <011> direction (Fig.2(a)). Two types of microdefects were observed along the FP-SEP row; one is accompanied with strain fields around it, the other is strain free. Some microdefects surrounded by strain fields have adjacent dislocation loops. In order to characterize each microdefect, more detailed TEM observations were carried out.

TEM micrographs of a microdefect accompanied by a surrounding strain field are shown in Figures 3(a) and 3(b). These micrographs were taken under the conditions of just and off Bragg reflection with $\mathbf{g}$=(400) for Fig.3(a) and Fig.3(b), respectively. As shown in Fig.3(b), the morphology of the microdefect is octahedral. The energy dispersive X-ray spectra corresponding to the defect and the matrix are shown in Fig.4, which indicates that the microdefect contains oxygen atoms. These results imply that the microdefect with a strain field is an octahedral oxygen precipitate. In addition, the peak at 0.3keV in the EDS spectra (Fig.4) is identified as carbon which originated from the contamination in the EDS analysis.

Figures 5(a) and 5(b) are TEM micrographs of a microdefect without a strain field. Similarly to the case shown in Fig.3, just and off Bragg conditions with $\mathbf{g}$=(400) were used to take the micrographs showing Fig.5(a) and Fig.5(b), respectively. From Fig.5, it is clear that the morphology of the microdefect is polyhedral (Fig.5(a)), and the microdefect has a contrast indicating dual structure in it (Fig.5(b)). In order to investigate the dual structure in the microdefect, the EDS analysis is carried out at points 1 and 2, edge and center, respectively (Fig5(b)). In the EDS spectra shown in Figure 6, the oxygen peak at the edge (point 1) is higher than that at the center (point 2), and the oxygen peak at the center (point 2) of the microdefect is lower than that at oxygen precipitates shown in Fig.4. Therefore, these results suggest that the microdefect surrounded by no strain field is a polyhedral void with an oxidized interior. In addition, the thickness of the inner oxide film was determined to be 10 -20 nm.

The nature of the dislocation loops that accompany the microdefects with strain fields is examined by an inside-outside contrast method [6]. The results are shown in Figure 7, where the upper two photographs are the pair for stereoscopic view and the lower two are the pair for inside-outside contrast. The microdefect marked by an arrow in Fig. 7(a) is an oxygen precipitate, which is the same as the microdefect shown in Fig.3, and the others are dislocation loops. These micrographs were taken with the conditions $\mathbf{g}$=(022) for the stereoscopic view,

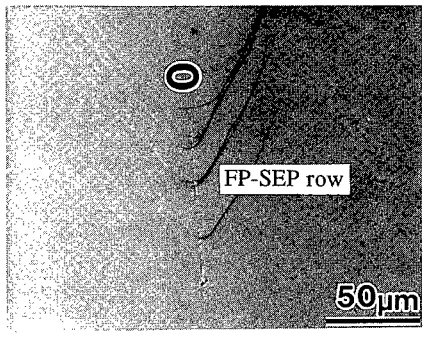


Fig. 1. Optical micrograph of a FP-SEP row in a dislocated Cz-Si crystal.

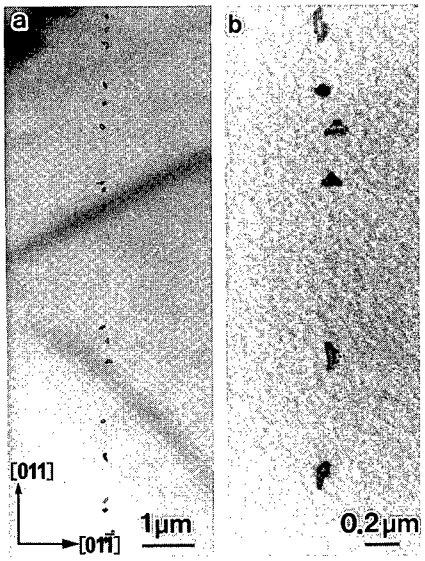


Fig. 2. TEM micrographs of microdefects along a FP-SEP row.

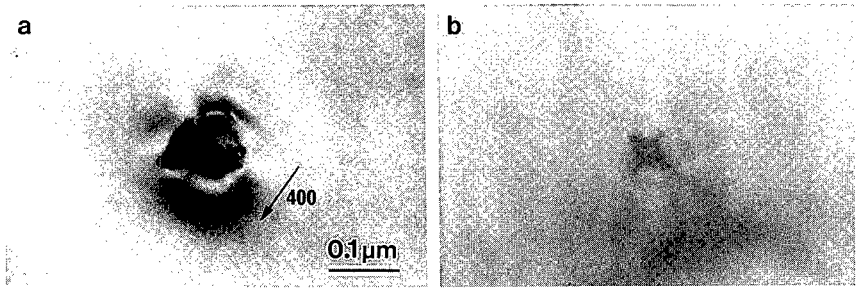


Fig. 3. TEM micrographs of a microdefect with accompanying strain field.

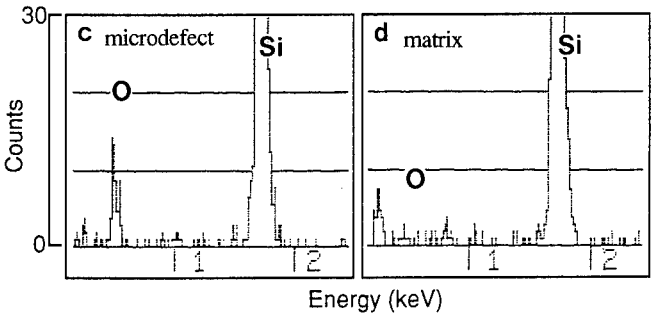


Fig. 4. EDS spectra of a microdefect with accompanying strain field.

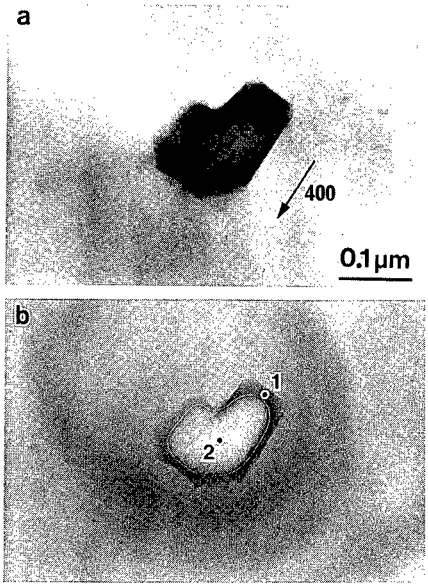


Fig. 5. TEM micrographs of a microdefect without a strain field.

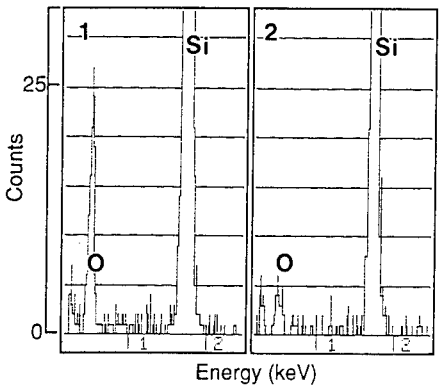


Fig. 6. EDS spectra of a microdefect without a strain field as shown in Fig.5(b).

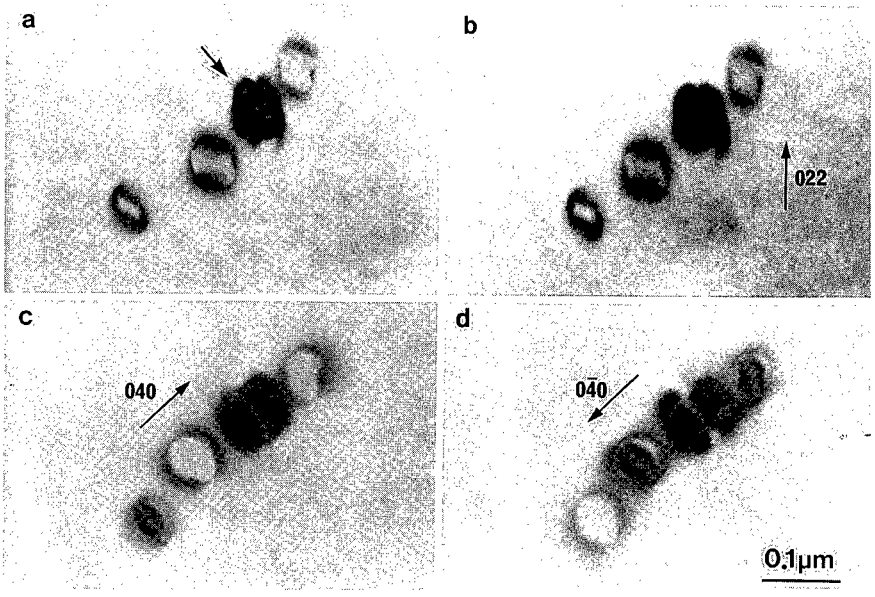


Fig. 7. A set of TEM micrographs to determine the nature of dislocation loops. ((a,b) stereo pair, (c,d) inside-outside pair)

$\mathbf{g}=(040)$ or $-\mathbf{g}=(0\bar{4}0)$ for the contrast analysis, and $s > 0$ was maintained during the observation. The loop inclination is determined by the stereoscopic view. The vector inner product can be expressed as $\mathbf{g} \cdot \mathbf{n} > 0$, where $\mathbf{g}=(040)$ is one of the reflection vectors and $\mathbf{n}$ is the normal vector to the loop. The relation between the contrast and the reflection vector is summarized in Table 1. The resulting direction of the Burgers vector of the loop is $\mathbf{b} > 0$, which indicates that the loop is an interstitial-type. In addition, the contrast of the loop at the left end is opposite to the contrast of other loops in Fig.7(c) and Fig.7(d), since its inclination is opposite to that of others.

Table 1. Results from the observation of both stereoscopic and inside-outside contrast analyses.

Photo #	Reflection	Contrast position	Contrast condition	Burgers vector
c	$\mathbf{g}=(0,4,0)$	outside	$(\mathbf{g} \cdot \mathbf{b})\, s > 0$	$\mathbf{b} > 0$
d	$-\mathbf{g}=(0,-4,0)$	inside	$(-\mathbf{g} \cdot \mathbf{b})\, s < 0$	$\mathbf{b} > 0$

Relationship between microdefects and the origin of FP or SEP

To summarize the results of TEM observations, the microdefects forming FP-SEP rows in dislocated Cz-Si crystals are identified as octahedral oxygen precipitates with or without dislocation loops (interstitial-type), and polyhedral voids with oxidized interiors.

Finally, the relation between these microdefects and the origin of FP,SEP is addressed. The ratio of each observed microdefect along FP-SEP rows is shown in Table 2. The ratio of FP or SEP in FP-SEP rows is also examined by optical microscope. The resulting ratio of FP to SEP was found to be 1 to 15 on average. Based on the comparison of the two results, the origin of FP is concluded to be interstitial-type dislocation loops, and that of SEP is concluded to be oxygen precipitates or voids.

In addition, to verify this conclusion, thin films which had been observed by TEM were slightly etched in Secco etch solution, and the relation between the location of each microdefect and the position of FP formed by Secco etching was investigated. It was recognized that small wedge-shaped patterns occurred near the positions where interstitial-type dislocation loops were observed by TEM. This result supports the conclusion stated above.

Table 2. Ratio of each microdefect along FP-SEP rows

polyhedral voids	・・・(75%)
octahedral oxygen precipitates	・・・(17%)
octahedral oxygen precipitates with interstitial-type dislocation loops	・・・(8%)

* The number in parentheses shows the ratio of each microdefect

4. CONCLUSIONS

The microdefects forming FP-SEP rows in dislocated Cz-Si crystals have been investigated by means of transmission electron microscopy. Microdefects 0.1 μ m in size are observed along a FP-SEP row corresponding to the <110> direction. These microdefects were identified as octahedral oxygen precipitates with or without dislocation loops (interstitial-type), and polyhedral voids with oxidized interiors . From the ratio of each microdefect along FP-SEP rows, we conclude that FP originate from interstitial-type dislocation loops, and SEP originate from oxygen precipitates or voids.

ACKNOWLEDGMENTS

The authors wish to thank Emeritus Professor Koji Sumino for informative discussions.

REFERNCES

1. H. Yamagishi, I. Fusegawa, N. Fujimaki and M. Katayama, Semicond. Sci. Technol. **7**, A135 (1992).
2. H. Takeno, S. Ushio and T. Takenaka in Defect Engineering in Semiconductor Growth, Processing and Device Technology, edited by S. Ashok, J. Chevallier, K. Sumino and E. Weber (Mater. Res. Soc. Symp. Proc. **262**, 1992) pp. 51-56.
3. W. Wijaranakula and H. -D. Chiou, Appl. Phys. Lett. **64**, 1030 (1994).
4. S. Sadamitsu, S. Umeno, Y. Koike, M. Hourai, S. Sumita and T. Shigematsu, Jpn. J. Appl. Phys. **32**, 3675 (1993).
5. T. Iwasaki, H. Deai, K. Simanoe, H. Harada and H. Haga, Ext. Abstr. 56th Autumn Meeting of the Japan Society of Applied Physics, 27a-ST-18.
6. P. B. Hirsch, A. Howie, P. B. Nicholson, D. W. Pashley and M. J. Whelan, Electron Microscopy of Thin Crystals, (Butterworth, London, 1965), p.265.

BEHAVIOR OF POINT DEFECTS IN CZ SILICON CRYSTAL GROWTH– Formation of polyhedral cavities and oxidation-induced stacking fault nuclei

K. Tanahashi*, N. Inoue and Y. Mizokawa***

*College of Intergrated Arts and Science, Osaka Prefecture University
1–1, Gakuencho, Sakai, Osaka, 593 Japan
**Research Institute for Advanced Science and Technology, Osaka Prefecture University
1–2, Gakuencho, Sakai, Osaka, 593 Japan

Abstract

The origin of oxidation–induced stacking faults (OSF) and polyhedral cavities in as–grown Czochralski silicon (CZ–Si) crystals is discussed with comparison to the behavior of previously investigated grown–in oxide precipitates. The incorporation, diffusion and reaction in the vacancy, self–interstitial and oxygen ternary system are considered to discuss the origin of grown–in defects.

1. Introduction

There are various kinds of defects included in as–grown Czochralski silicon (CZ–Si) crystals. Some of such grown–in defects degrade the ultra large scale integrated (ULSI) device performance. Therefore it is important to investigate the structure and origin of such defects and to eliminate them.

Grown–in defects are caused by intrinsic point defects; self–interstitials (I) and vacancies (V). It has been a question which is dominant point defects. Previously, the grown–in defects in floating zone silicon crystals (FZ–Si) have mainly been investigated. The dominant point defects in Fz–Si are considered to be self–interstitials, because swirl defects were identified to be interstitial–type dislocation loops [1]. However the presence of vacancy type defects has also been suggested [2]. On the other hand in CZ–Si, the substance of grown–in defects is less understood, though a great deal of work has been devoted. Among them, nuclei of oxidation induced stacking faults (OSF) and defects responsible for break down of gate oxide film have to be clarified due to their technical importance. Some of grown–in defects have been identified to be oxide precipitates : We found that there are silicon oxide microprecipitates of around 1 nm size and about $10^{10}/cm^3$ density [3]. There are also large platelet oxide precipitates of about 100 nm size and about $10^6/cm^3$ density [4]. Electrical activity of these oxide precipitates was evaluated [5]. It has been thought that the latter causes the degradation of the breakdown field of a dioxide film in metal oxide semiconductor (MOS) structure [6].

Recently, however, a new kind of defects has been discovered at the breakdown sites of the thin oxide films [7]. They are polyhedral–shaped cavities with thin oxide inner wall [8] and are a few hundred nm in size and about $10^6/cm^3$ density. It may be a direct evidence that there are vacancy–type defects in CZ–Si.

On the other hand, as for OSF, though it is suggested that grown–in self–interstitials are responsible for the formation of OSF [9], it has not yet been clarified.

The purpose of this paper is to propose the formation mechanism of cavities and OSF nuclei in the I–V–O ternary system.

2. Nucleation of cavities

2.1. Structure and Behavior of cavities

Recently, much information about the structure and behavior of the cavities has been accumulated [7,8,10–12]. It is summarized as follows.

As for the structure they are basically octahedral cavities whose principal faces have {111} orientations. Transmission electron microscopic (TEM) observation revealed that most of them have twin structure which is connected with one plane each other [10]. Energy dispersive x–ray spectroscopy (EDS) measurement revealed that intensity of silicon in the interior is smaller than it around, suggesting that the density of silicon is lower than the surrounding silicon matrix. Thus they were considered to be the cavities. At the inner surface, a small amount of oxygen was detected and a thin film was observed by TEM [7,10,11]. It is considered to be a dioxide film with a few nanometer thickness. Some tops of the octahedron are cut resulting in a complicated polyhedral shape. Growth condition dependence and annealing behavior have also been reported.

The presence of these cavities are consistent with the previous prediction: The vacancies in Si is

Mat. Res. Soc. Symp. Proc. Vol. 442 © 1997 Materials Research Society

considered to precipitate to an octahedral-shaped cavity, which is the equilibrium shape of a cavity in Si [13]. The so called "D-defects" have been considered to be produced as a result of vacancy aggregation [14]. The voids or cavities are usually observed in metals with face centered cubic (fcc) structure [15].

2. 2. Nucleation Mecahnism

(1) Comparison of cavities with large platelet oxide precipitates

Here, we discuss the nucleation mechanism of the cavities with comparison to previously investigated oxide precipitates. Fig.1 shows the radial distribution, density and formation temperature of cavities, large oxide precipitates and oxide microprecipitates in as-grown CZ-Si. It is to be noted that the polyhedral cavities are formed mainly in the interior of the crystal where oxide microprecipitates or bulk microdefects (BMDs) are present in as-grown crystals. However, the latter density is about $10^{10}/cm^3$ and they are formed through the homogeneous nucleation below 900^0C [3]. The density of cavities is 4 orders of magnitude smaller than that of BMDs. Therefore their formation mechanism is different from each other. Their density is equal to that of large oxide precipitates which are mainly located in the outer region of the crystal. We determined the nucleation temperature of the large oxide precipitates to be about 1250 - 1000 °C depending on the oxygen content and/or position along the growth direction, and concluded to be nucleated heterogeneously at some growth fluctuations, especially thermal fluctuation at the interface [4]. Nucleation temperature of cavities is reported to be around 1100 °C[16]. The resemblance of the density and nucleation temperature suggests that the cavities should be nucleated heterogeneously also.

(2) Nucleation mechanism

Concering the nucleus, no dislocation loop exists around a cavity. No nucleus of any kinds of grown-in defects has been identified yet. As for the large oxide precipitates, we suggested the nucleus to be structural disordering due to fluctuation of crystal growth as shown above [4]. The same defects may be the nucleus for cavities. Although dislocation loops due to point defect aggregation are probable as the nulei, it is not conclusive. Carbon clusters might also be one of the candidate for the heterogeneous nucleus.

2. 3. Growth Mechanism of cavity

(1) Structure in the initial stage of formation

There are a few models for the formation of the cavity, its main body [7], oxide inner wall [12] and twin structure [10]. In the model by Itsumi [7], a nucleus is generated in CZ-Si ingot and forms SiO_2 around nucleus. In the next stage, it develops voids, because it aquires vacancies. In the model, however, the substance of nucleus has not been described and the inner oxide film has not been referred.

There is a question whether the cavities are precipitates or cavities from the beginning. If its formation condition, for example temperature, is nearly the same as that for large oxide precipitates, the origin of cavity is the same as that of large oxide precipitates, i.e.,oxide precipitates. On the other hand, in the case that formation temperature is lower than that of large oxide precipitates, vacancies aggregate to the nucleus from the beginning.

Recently, it has been possible to observe grown-in laser scattering tomography defects (LSTD) directly [10,11]. As a result , it is probable that grown-in LSTD is cavity, not oxide precipitate, and it is formed about 1200 - 1100 °C during crystal growth. It is not clear whether the cavities nucleate at higher or lower temperature than the large oxide precipitates. Therefore, we can not know if oxide precipitates are included in the cavity and therefore it is not concluded whether origin of cavities is oxide precipitates or not. Tab.1 summarizes the comparison of cavities and large oxide precipitates.

(2) Competition between growth of cavity and oxidation

Whether the oxide inner wall is formed simultaneously with the cavity or formed after the cavity is completely growth ? As both vacancies and oxgens are supersaturated, they have the same tendency to accumulate. Nishikawa et al has observed that the oxide thickness is smaller at higher temperature and suggested the wall is formed after the cavity growth [12].

We would like, in addition, to point out that there are following problems. If both vacancies and oxygens precipitate simultaneously: the boundary between the oxide film and silicon matrix should retard as the cavity grows. In short, its interface must retreat in order that the cavity grows. Moreover, vacancies have to diffuse through oxide films to reach the cavity. These processes must be possible only to a slight degree. Thus, it is plausible that the main part of the oxide film is formed after the growth of cavity.

However there must be some barriers for oxygens to precipitates. While the cavity grows, silicon atoms on the inner surface are always removed which should make oxygen atoms hard to make oxide. This competition is discussed again.

(3) Morphology of the cavity

The observed cavities have basically an octahedral-shape but their some corners are cut off. The vacancies in Si were supposed to precipitate to an octahedral-shaped cavity, which is the equilibrium shape of a cavity in Si [13]. Since {111} planes have surface energy minimum, it is reasonable to develop an octahedral-shape surrounded by {111} planes.

Wulff's construction indicates that an octahedron is an equilibrium form in a diamond structure. Frank reported that the corner of octahedron grows round at high tenperature [17]. Cut corners of the cavity should be formed by the same reason.

(4) Detailed growth process of cavity with oxide inner wall

The formation process of cavity with oxide inner wall is considered as follows, as shown in Fig. 2. Initially, it is assumed that oxide precipitates are formed around the heterogeneous nuclei due to oxygen supersaturation as seen in Fig. 2(b).

As a result compressive stress appears around the precipitate as seen in Fig. 2(c). This attracts the supersaturated vacancies. Thus the cavities are formed adjacent to the precipitates. The Octahedral precipitates are better sources of twin cavities than the platelet precipitates.

The cavities grow further, then, to some size as seen in Fig. 2(d).

The cavity growth is completed as seen in Fig. 2(e) due either to a consumption of vacancies or to retardation of vacancy diffusion as the crystal is cooled.

In the last stage, the oxidation of inner wall is completed as seen in Fig. 2(f) by consumption of supersaturated oxygen as will be discussed later.

(5) Quantitative analysis on the behavior of vacancies and oxygens

Here, the behavior of vacancies and oxygens are discussed in terms of cavity formation. The cavities are formed in the interior of the crystal, because point defect concentration decreases in the outer part due to a very large diffusion coefficient [18]. Large oxide precipitates, on the other hand, are formed in the outer part. It suggests that $C_V D_V$ is larger than $C_O D_O$, where C_V, C_I and C_O are the concentrations of vacancies, interstitials and oxygens and D_V, D_I and D_O are the diffusion coefficients, respectively. Absence of interstitial-type dislocation loops indicates $C_V D_V > C_I D_I$. We determined C_V and D_V from the depth profile of bulk stacking faults as follows [19].

$$C_V = 8.56 \times 10^{21} \exp[-(1.56 \pm 0.66)\text{eV}/kT]$$

$$D_V = 257 \exp[-(2.86 \pm 0.66)\text{eV}/kT]$$

Using these values the migration length of vacancies are estimated at 1200 and 1100 °C and for 1 hr to be 0.03 and 0.01 cm, respectively.

From the observed size of the cavities, about 100 nm, the number of vacancies accumulated in the cavity is estimated to be 10^7 as shown in Fig.2(e). Assuming that the vacancy concentration is $4 \times 10^{16}/cm^3$ at 1200 °C from the above equation, the range of vacancy diffusion field is estimated to be 10^{-3} cm and the diffusion (growth) time is about 5 sec as shown in Fig. 2(e).

From the observed oxide wall thickness of 2nm, the number of oxygen accumulated in the cavity inner wall is estimated to be 10^5 atoms as shown in Fig. 2(f). This corresponds to the range of diffusion field of supersaturated oxygen of $5 \times 10^{17}/cm^3$ to be 10^{-4} cm. This migration length at the diffusion temperature of 1100 °C corresponds to the very short diffusion time of about 1 min. This suggests that the wall is formed after the cavity growth is completed. This is consistent with that the inner wall oxidition is interfered by the cavity growth described above. Moreover many oxygen atoms are left supersaturated which form microprecipitates homogeneously later.

Though there have been much effort to determine the concentration and diffusivity of intrinsic point defects in silicon, no data have explained the observed grown-in defect formation process and distribution.

They are a few orders of magnitude smaller than the width of OSF ring [20], suggesting that further investigation is necessary.

Table 1 Comparison of cavity and large oxide precipitate

	radial distribution	density	nucleation temperature	shape
cavity	interior	$10^6/cm^3$	1200-1100℃	octahedron
large oxide precipitate	periphery	$10^6/cm^3$	1250-1100℃	square plate

Table 2 Comparison of OSF and bulk SF

	treatment	location	nucleus	density
OSF	oxidation	surface	platelet precipitate	$\leq 10^2/cm^2$
bulk SF	annealing	interior	platelet precipitate	$10^6/cm^3$

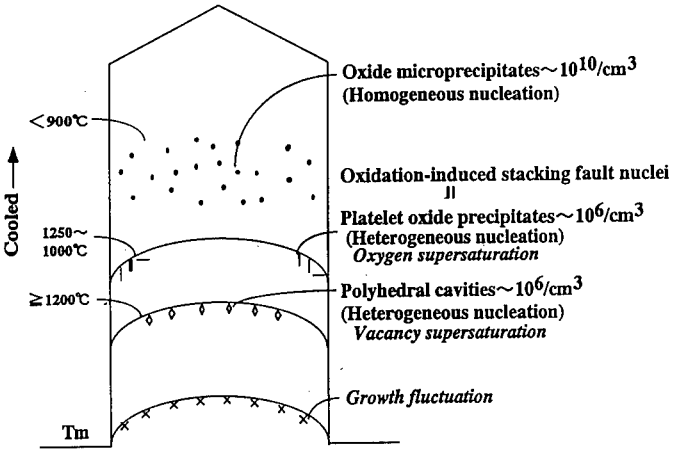


Fig.1 Schematic diagram of the distribution of cavities, large oxide precipitates and oxide microprecipitates in as-grown CZ silicon

Table 3 Enthalpy for pair formation (eV)

pair	enthalpy
I - I	—
I - V	1.5[27] 1 3[28]
V - O	0.7[28]
V - V	~1[13]
O - O	—

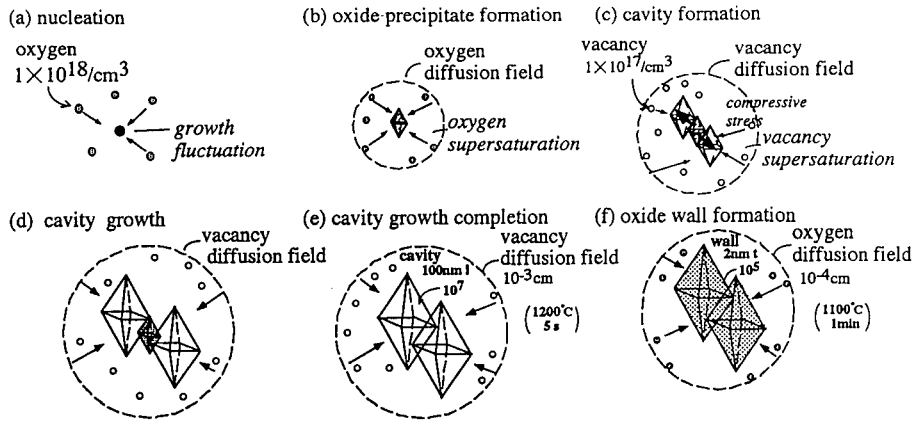


Fig.2 Shematic diagrams of the formation process of polyhedral caviyies with oxide inner wall.
(a) nucleation, (b) oxide precipitate formation, (c) cavity formation,
(d) cavity growth, (e) cavity growth completion, (f) oxide wall formation.

It is generally believed that vacancies are easily combined with oxygen. The binding energy of vacancy–vacancy complex (V–V) is about 1 eV, but that of vacancy–oxygen complex (V–O) is not definitely determined [13].

3. Nucleation mechanism of oxidation–induced stacking faults

3.1. Nucleus

Previously many people condisered that self–interstitials in as–grown Si form nuclei for the oxidation–induced stacking faults (OSFs) [21]. This is mainly due to that stacking faults are composed of interstitials, and is strongly affcted by the presence of interstitial dislocation loops observed in as–grown FZ Si by TEM. On the other hand a few people considered that OSF formation is dominated by vacancies [22]. This is based on that the OSFs are nucleated at the oxide platelet precipitates [23], and that the anomalous oxygen precipitation occurs under the excess of vacancies [24]. In short, the interstitial model poses emphasis on the substance of OSF, while the vacancy model aims with nucleation site of OSF. Whether the nucleus of OSF ring is the same as cavities or not is not conclusive, because no nucleus of cavities has been identified yet. Recent advancement described in section 2, the observation of cavities in as–grown crystal not only makes us free from insisting with interstitial model, but also makes us taking care of the role of vacancies.

3.2. Comparison of OSF and bulk SF

Previously we clarified that bulk stacking faults nucleate from the large platelet oxide precipitates during annealing by the Berdeen–Herring mechanism [25]. Tab.2 summarizes comparison OSF and bulk SF. Recently, Okui et al revealed that plate like oxide precipitates have expansive stress field parallel to its edge and form interstitial–type dislocation loops by absorption of excess self–interstitials [23].

It is to be noted that the large oxide precipitates are formed in the outer region of crystal, which is similar to the distribution of OSFs. It was shown that OSFs are located on the traces of the growth interface, and growth fluctuation introduces vacancies [21]. The former is also consistent with our assumption that the large oxide precipitates are heterogeneously nucleated at the growth fluctuation. The latter suggests that OSFs are related to the vacancies. Therefore we consider that the large platelet oxide precipitates in as–grown crystal serve as OSF nuclei. Excess interstitial distribution in the OSF ring region can be formed by the oxide precipitation which emitt interstitials to accomodate compressive stress. There is no positive role of self–interstitials in oxygen precipitation.

3. 3. Behavior of Point defects

During crystal growth, point defects incorporated into the crystal at the growth interface are supersaturated in the cooling stage. So mutual reaction and diffusion take place.

Concernig reaction processes, pair recombination reaction between self–interstitials and vacancies, formation of vacancy–oxygen complex V–O ,aggregation of vacancies (cavity formation) and oxygen (oxygen precipitation) are to be considered in the I–V–O ternary system. Tab.3 summarizes the enthalpy for these reaction.

Formation of V–O is most energetically favorable among them. However, suppose that V–O is immediately formed after crystalization, the diffusion of vacancies are limited by oxygen diffusion or complex diffusion which is much smaller than that of vacancies. It is impossible to explain the macroscopic distribution of BMDs, OSF–ring and large oxide precipitates. Therefore vacancies are isolated from oxygen at high temperature and can move freely at least down to the cavity formation temperature.

Concering the equilibrium concentration of point defects, Cv^{eq} is larger than C_I^{eq} below some temperature. It is because as the cavity formation and oxygen precipitation is related to vacancies, the dominant intrinsic point defects must be vacancies. Because growth rate is slow during CZ silicon crystal growth and the pair recombination reaction process occurs sufficeintly.

As shown above, it is possible to explain the formation of technologically important defects in as–grown CZ silicon by behavior of vacancies.

As for the macroscopic defect distribution, an extraordinarily large diffusion coefficeint is necessary for the intrinsic point defects. There is not a solution yet, but one candidate has been proposed by Habu [26]: Due to the gradient of chemical potential by temperature gradient, uphill diffusion should take place, which will reduce the free energy of thermally excess point defects. He assumed, however, that the self–interstitials are the dominant intrinsic point defects and responsible for OSF nucleation. Therefore modification to the case of vacancy is necessary after cooling to room temperature.

4. Summary

In summary, the formation mechanism of oxidation induced stacking fault nuclei and polyhedral cavities in as-grown CZ Silicon is discussed in detail. The nucleation mechanism of cavities is considered with comparison to that of grown-in large platelet oxide precipitates. Detailed growth process of twin polyhedral cavity with oxide inner wall is proposed. Behavior of vacancies and oxygen atoms is quantitatively discussed. As for the OSF nuclei, OSF formation at the edge plane of platelet oxide precipitate is emphasized, because we previously clarified that bulk stacking faults are nucleated at platelet oxide precipitates by Bardeen-Herring mechanism. And OSF nuclei are suggested to be the grown-in platelet precipitates. There is no need to assume that self-interstitials form nuclei for OSFs. Rather vacancies may play a role in the nucleation of precipitates which are OSF nuclei. Vacncies can move freely down to the formation temperature of grown-in defects in I-V-O ternary system and Cv^{eq} is larger than C_I^{eq} below some temperature. It is possible to explain the formation of grown-in defects by behavior of vacancies.

The authors are grateful to Manabu Itsumi, Kazumi Wada and Ryuichi Habu for stimulating discussions and to Atsuko Nishida for help in preparation of the manuscript.

References

[1] H.Foll and B.O.Kolbesen, Appl. Phys. **8**, 319 (1975).
[2] P.J.Rocksnoer and M.M.B.Van den Boom, J. Cryst. Growth, **53**, 563 (1981)
[3] N. Inoue, J. Osaka, and K. Wada, J. Electrochemical Soc., **129**, 2780 (1982).
[4] K. Wada, H. Nakanishi, H. Takaoka and N. Inoue, J. Cryst. Growth, **57**, 535 (1982).
[5] M. Miyagi, K. Wada, J. Osaka and N. Inoue, Appl. Phys. Lett., **40**, 719 (1982).
[6] M. Itsumi and S. Aoyama, Extended Abstract, 184th Meeting of The Electrochemical Society, #256 (1993).
[7] M. Itsumi, H. Akiya, T. Ueki, M. Tomita and M. Yamawaki, J. Appl. Phys., **78**, 5984 (1995).
[8] T. Kitamura, Y. Yanase, H. Horie, M. Miyazaki and T. Ochiai, Extended Abstract Vol. 1, 43th Spring Meeting, Japan Soc. Appl. Phys., 26P-X-6, p. 184 (1996).
[9] W. Wijaranakula, J. Electrochemical Soc., 139, 604 (1992)
[10] M. Kato, Y. Ikeda and Y. Kitagawa, Extended Abstract Vol. 1, 57th Fall Meeting, Japan Soc. Appl. Phys., 8a-ZG-6, p. 212 (1996).
[11] M. Nishimura, S. Yoshino, S. Shimura, H. Motoura and T. Hikone, Extended Abstract Vol. 1, 57th Fall Meeting, Japan Soc. Appl. Phys., 8a-ZG-7, p. 213 (1996).
[12] H. Nishikawa, T. Tanaka, Y. Yanase and M. Hourai, Extended Abstract Vol. 1, 57th Fall Meeting, Japan Soc. Appl. Phys., 8p-ZG-2, p. 214 (1996).
[13] J. A. Van Vechten, Phys. Rev. B, **17**, 3197 (1978).
[14] W. Wijaranakula and H. D. Chiou, Appl. Phys. Lett., **64**, 1030 (1994).
[15] M. Kiritani, Y. Shimomura and S. Yoshida, J. Phys. Soc. Japan, **19**, 1624 (1964).
[16] K. Nakamura, T. Saisyoji, T. Kubota and J. Tomioka, Extended Abstract Vol. 1, 57th Fall Meeting, Japan Soc. Appl. Phys., 7p-ZG-4, p. 161 (1996).
[17] F. C. Frank, Metal Surface, ASM 1 (1963).
[18] S. M. Hu, J. Appl. Phys., **52**, 3974 (1981).
[19] K. Wada and N. Inoue, J. Appl. Phys., **58**, 1183 (1985).
[20] R. Habu, I. Yunoki, T. Saito and A. Tomiura, Jpn. J. Appl. Phys., **32**, 1740 (1993).
[21] T.Abe, Oyobutsuri **59**, 272 (1990).
[22] N. Ono, K. Harada and M. Kida, Extended Abstract vol.1, 57th Fall Meeting, Japan Soc. Appl. Phys., 10a-ZH-11, p. 309 (1996).
[23] M. Okui, M. Hourai, T. Koike, E. Kajita, T.Kanda, S.Miki and T. Shigemitsu, Oyodenshibussei bunkakai 4 (1995).
[24] H. Harada, T.Abe and J. Chikawa, Proc. 5th Int. Symp. Silicon Materials Science and Technology, Boston, 1986, p. 76 (Electrochemical Society, Pennington, 1986).
[25] K. Wada, H. Takaoka, N. Inoue and K. Kohra, Jpn. J. Appl.Phys. **18**, 1629 (1979).
[26] R. Habu and A. Tomiura, Jpn. J. Appl. Phys., **35**, 1 (1996).
[27] D. A. Antoniadis and I. Moskowitz, J. Appl. Phys., **53**, 9214 (1982).
[28] S. M. Hu, J. Vac. Sci. Technol., **14**, 17 (1977).

Impact of Chemical and Epitaxial Treatment on Surface Defects on Silicon Wafers

R. Schmolke, D. Gräf, M. Suhren, R. Kirchner, H. Piontek and P. Wagner
Wacker Siltronic AG, Burghausen, Germany

ABSTRACT

Defects on polished as well as hot SC1 treated silicon wafers were investigated with an Atomic Force Microscope (AFM) and Surface Scanning Inspection Systems (SSIS). Measurement with two SSIS of different type allows to identify most of the surface defects as non particulate scatterers. AFM of these defects reveals tiny pits or groups of pits. An almost linear relation is found between the geometrical lateral defect dimension and their average size in units of LSE (Latex Sphere Equivalent; an effective measure for the scattering cross section) as reported by one of the SSIS for the defects on wafers treated with hot SC1. Growth rates of about 40 nmLSE/h are observed for the defects during subsequent treatments of wafers with hot SC1. The LSE-size distribution of as-grown defects with a peak at about 105 and 110 nmLSE is obtained for two types of wafer by modeling the defect evolution during hot SC1 treatment. The number of surface flaws $\geq$ 0.12 µmLSE on a substrate is reduced by two orders of magnitude for epitaxial layers as thin as 1.5 µm.

INTRODUCTION

Present commercially available final polished and cleaned Si wafers contain very few surface defects which cover less than 1ppb of the entire wafer surface. Most of these remaining sparse defects on the wafers, denoted generally as Localized Light Scatterers (LLS), are tiny etch pits, so-called Crystal Originated Particles (COP) delineated in the polishing process [1].

COP densities obtained after appropriate delineation with hot SC1 [2], a more systematic technique to delineate COP than polishing, can be correlated to Gate Oxide Integrity (GOI), Flow Pattern (FP), Light Scattering Tomography (LST) and therefore as-grown defect densities [1,3]. So far the size of the as-grown bulk defects has only been studied using LST [3] and Transmission Electron Microscopy (TEM) [4]. These as-grown defects are assumed to consist of vacancy agglomerates [4].

The number of LLS $\geq$ 0.12 µmLSE of a polished substrate is significantly reduced after depositing an epitaxial layer [5]. However, etch pits of polished substrates are expected to appear on the surface of the epitaxial layer to some extent. This effect could become more and more visible if the thickness of the epitaxial layer is reduced and/or the sensitivity of the SSIS is enhanced. Both trends are a consequence of the ongoing linewidth reduction in semiconductor industry.

In the present paper the relation between LLS and COP will be confirmed by investigating the microscopic defect morphology. The geometrical defect size of COP will be related to the LSE-size as measured by a commercially available SSIS. A technique will be outlined allowing to extract the LSE-size distribution of the as-grown defects by following the growth of COP during successive exposure to hot SC1. Further, results will be discussed on the relation between the number of LLS on a wafer with an epitaxial layer and its substrate for different epitaxial layer thicknesses.

Mat. Res. Soc. Symp. Proc. Vol. 442 © 1997 Materials Research Society

EXPERIMENT

Si(100) wafers cut from Czochralski crystals grown with different pulling conditions were investigated. The crystals were either lightly B-doped (resistivity 10 Ωcm) and pulled with fast cooling rates (200 mm: CZ1 type, 150 mm: A type) as well as slow cooling rates (200 mm: CZ2 type, 150 mm: B type) or heavily B-doped (resistivity 15 mΩcm, 150 mm: C type).

About 50 surface defects on two polished wafers (CZ1 and CZ2 type) and 20 surface defects on a hot SC1 treated CZ2 type wafer (CZ2/SC1) were imaged with an AFM (Nanoscope III; Digital Instruments) after the LSE-sizes and approximate defect coordinates were determined with different SSIS (Tencor SFS6200, Tencor SFS6420) and the accuracy of defect coordinates was improved by using a third SSIS with a linear stage of high precision.

Two additional wafers (CZ1 and CZ2 type) were successively immersed in hot (85°C) SC1 four times for one hour. In-between the subsequent hot SC1 treatments defect maps with respective LSE-sizes ≥ 0.12 μmLSE were generated using a SSIS (Tencor SFS6200).

Epitaxial layers were deposited on three polished wafers of type A, six of type B, twenty-four of type C, three hot SC1 treated wafers of type A (A/SC1) and 6 hot SC1 treated wafers of type B (B/SC1). The layer thicknesses grown ranged from 1.5 to 4.5 μm. The number of LLS ≥ 0.12 μmLSE on the wafers were measured before and after deposition with a Tencor SFS6200.

RESULTS AND DISCUSSION

Defect Morphology and its Relation to Light Scattering

Single pits or pits closely grouped together were found on the two kinds of polished wafers as well as on the hot SC1 treated wafer. "Closely" means that the distances involved are smaller than the spot size of the different SSIS. Some of the adjacent pits are overlapping. The pits which were closely grouped together always appeared as dual, overlapping pits in the AFM in the case of the CZ2/SC1 wafer. The lateral defect dimension of each pit is in the order of some tenths of a micron and the vertical defect dimension is approximately 100 nm. The features of the defects on polished wafers are smoother as compared to the hot SC1 treated ones. Most of the defect shapes are in agreement with an underlying octahedral symmetry as reported in [4,6].

For some of the defects on the polished wafers, however, an underlying octahedral symmetry is not obvious from the AFM images (Fig. 1). This may be due to the fact that also other constituents, e.g., oxide layers or "particles" are present at the defect sites [4,7].

The defect morphology on the two polished wafers (CZ1 and CZ2) differs - on the average - mainly with respect to their geometrical sizes. The defects on polished CZ1 wafers are smaller than on polished CZ2 wafers.

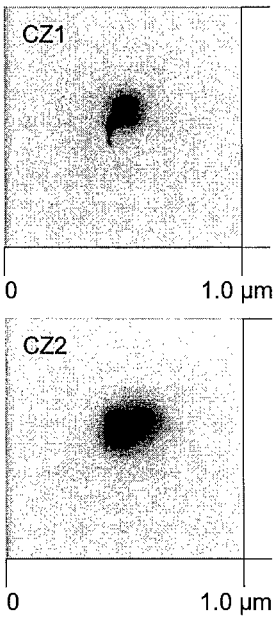


Fig. 1: Top view of two LLS on polished wafers.

The LSE-sizes as reported by a Tencor SFS6200 for the COP on CZ2/SC1 were plotted versus those evaluated by a Tencor SFS6420 (Fig. 2). These two SSIS have significantly differing collection optics. Therefore, a 1:1 correlation is obtained only for small particulate scatterers such as latex spheres used for calibration [6] (straight, dashed line in Fig. 2). The regime in-between the two full lines in Fig. 2 contains more than 66% of about 2000 defects detected on the CZ2/SC1 wafer including the data points for 14 of the defects imaged with the AFM which are denoted "characteristic". The fact that the straight line does not cross the regime enclosed by the two full lines confirms that most of the defects on the CZ2/SC1 wafer are not small particulate scatterers but other objects such as pits or pits closely grouped together.

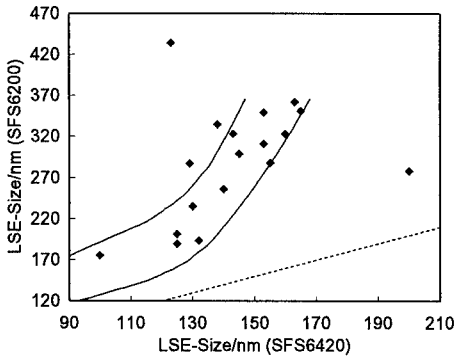


Fig. 2: LSE-size as reported by two different SSIS for the defects on hot SC1 treated CZ2 imaged with the AFM (◆). The two bold lines enclose more than 66% of about 2000 defects. The straight line represents the 1:1 correlation obtained for latex spheres.

The Largest Lateral Defect Dimension (LLDD) d and the mean LSE-size $< LSE >$ as reported by a Tencor SFS6200 can be correlated via $< LSE > \approx 0.5d$ for the defects imaged with the AFM on the CZ2/SC1 wafer (Fig. 3). For the fit only the above mentioned 14 defects were used. Such a relation cannot be established for the defects imaged on the two polished wafers.

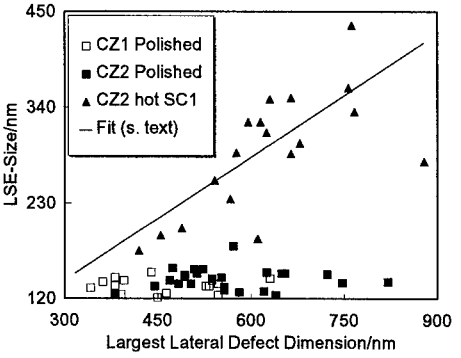


Fig. 3: Geometrical defect dimension versus LSE-size as reported by the SFS6200 for defects on polished and hot SC1 treated wafers imaged with the AFM.

These results indicate that there exist distinct geometries for defects on CZ2/SC1: (i) only single pits or dual, overlapping pits were found with the AFM, (ii) the width of the regime enclosed by the two full lines in Fig. 2 is partly due to the accuracy of the LSE-size determination and (iii) different frequency bands of the defects' Fourier spectra are recorded by the two SSIS and - according to Fig. 2 - linked to each other. This and the fact that most of the defects imaged with the AFM are characteristic ones (Fig. 2) allows to extend the relation between the mean LSE-size and the LLDD to all the defects on the CZ2/SC1 wafer.

As-grown Defect Size Distribution

The size of the COP (width and depth of the etch pits) increases during successive hot SC1 steps. Almost linear relationships are found between the LSE-size after the first and the n-th hour (average LSE-size) of hot SC1 treatment by following the LSE-size evolution of every defect (n > 1, Fig. 4). The size dependent average growth per hour ranges from 0.2 up to 0.3

times the LSE-size after the first hour of hot SC1 treatment for a variety of lightly B-doped materials, including CZ1.

The LSE-size distributions $\rho(x,t)$ of COP found after a specific time t of hot SC1 treatment for a LSE-size x originates (i) from defects which have already been present before t and have grown with respect to their LSE-size and (ii) defects which are generated at time t (Fig. 5, symbols).

This can be modeled using the 1-dimensional continuity equation

$$\partial\rho(x,t)/\partial t = -\partial j(x,t)/\partial x + h(x)$$

for $x > 0$ (see below). $j(x,t)$ corresponds to a flux density. The generation rate $h(x)$ is linearly related to the LSE-size distribution of the as-grown defect density in the bulk $B(x)$. The constant is given by the volume removal rate by etching (Si etch rate for hot SC1: 45 nm/h). One obtains

$$\rho(x,t) = A\frac{\sqrt{\pi b}}{2v}\left[erf(\frac{x-x_0}{\sqrt{b}}) - erf(\frac{x-x_0-vt}{\sqrt{b}})\right]$$

by further assuming $j(x,t) = v\rho(x,t)$, a constant growth velocity v and a defect generation rate $h(x) = A\exp[-(x-x_0)^2/b]$. A is an amplitude with the unit [number/second], x_0 is the LSE-size at which $h(x)$ exhibits a peak and b is a measure for the width of the generation rate with respect to its LSE-size dependence.

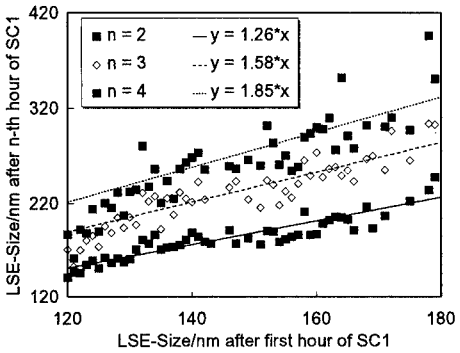


Fig. 4: Mean value of the defect size after the n-th hour of hot SC1 treatment for those defects which appeared above the threshold of the SFS6200 after the first hour of hot SC1 treatment (CZ2). The lines indicate linear regressions.

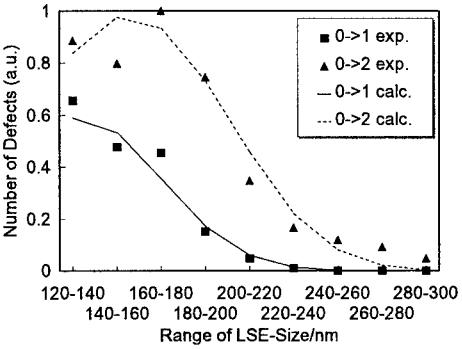


Fig. 5: LSE-size distribution for CZ2 after one (0->1) and two (0->2) hours of hot SC1 treatment (symbols) and fits according to the model (lines).

A least square fit was performed for the model parameters x_0, v, b and A using the LSE-size defect distribution functions obtained for CZ1 and CZ2 for the first and second hour of hot SC1 treatment (Fig. 5, lines). The defect distribution functions of further hours of hot SC1 treatment were not taken into account for the fit to minimize the effect of assuming a constant growth velocity v as compared to the time dependent average growth rate observed (Fig. 4). The fit results in an estimate of the LSE-size dependent defect generation rate $h(x)$ and as-grown bulk defect density $B(x)$ (Fig. 6, $B(x) \propto h(x)$, see above). The lower LSE-size which can be expected to be estimated by $h(x)$ depends on the data set used: (i) only the data of the first two hours were used for the fit, (ii) within this time the LSE-defect size grows by a factor of about 1.4 - 1.6 for the variety of lightly B-doped materials investigated (see also Fig. 4) and (iii) LSE-sizes monitored in the experiment are $\geq$ 0.12 µmLSE. Consequently, the fit of the model applies in fact to those LSE-sizes x of $h(x)$ which are above (0.12 µmLSE)/1.4 ~ 0.085 µmLSE.

The center of the defect distribution $h(x)$ for CZ1 is shifted towards smaller LSE-sizes, the width of the distribution is smaller and the amplitude of the defect distribution is larger as compared to CZ2 (Fig. 6). Integrating the distribution functions over LSE-sizes ≥ 0.085 μmLSE results in as-grown defect densities of 1.1 and $0.4 \cdot 10^6/cm^3$ for CZ1 and CZ2, respectively, consistent with [3].

The model used to extract the as-grown distribution is appropriate to reproduce the expected differences between the materials CZ1 and CZ2. However, it has deficiencies such as a negligible but in principle non zero $\rho(x, t)$ for negative x. Modifications to improve the model may include a 3-dimensional generalization with a LSE-size dependent growth rate and a dispersion as well as a more elaborate term for the generation rate. Further improvement could be obtained by using a set of coupled continuity equations for different defect species such as single and multiple pits.

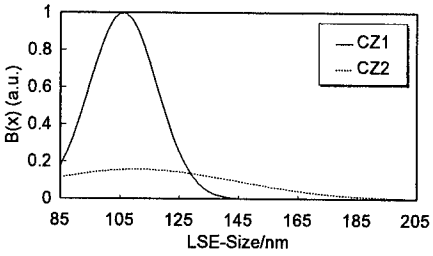


Fig. 6: Calculation of the as-grown LSE-size distribution B(x) for CZ1 and CZ2 type wafers.

Epitaxial Treatment

The modification of the shape of surface defects by depositing epitaxial layers was investigated for polished as well as for hot SC1 treated wafers. Hot SC1 treated wafers were used to have a considerably higher starting level of LLS ≥ 0.12 μmLSE as compared to polished wafers (Fig. 7). The average number of LLS ≥ 0.12 μmLSE is significantly reduced by deposition of an epitaxial layer to a low level similar for all the epitaxial thicknesses and the polished materials used.

The number of LLS ≥ 0.12 μmLSE is reduced by more than two orders of magnitude even in the case of the hot SC1 treated wafers. However, it appears that the number of LLS ≥ 0.12 μmLSE after deposition normalized with respect to the number of LLS before deposition is the larger the thinner the epitaxial layer thickness.

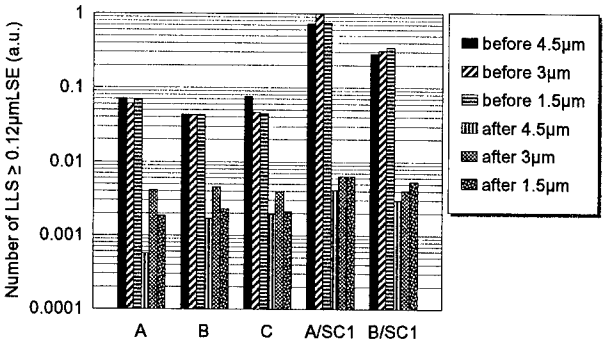


Fig. 7: Average number of LLS before and after epitaxial deposition listed according to the material used and the epitaxial layer thickness.

These results do not change when the sensitivity of the SSIS is enhanced as long as no artifacts occur due to surface roughness [8]. For the wafers and SSIS used a lower detection limit of less than 0.11 μmLSE could be achieved.

SUMMARY

Comparing COP-sizes in units of LSE as reported by two SSIS with substantially different collection optics allows to classify and to select characteristic defects for further investigation with AFM. Most of these defects on polished and hot SC1 treated lightly B-doped wafers are pits or pits closely grouped together. The shape of the pits is in accordance with an underlying octahedral symmetry. Part of the pits on the polished wafers appear to have additional constituents leading to deviations from the octahedral structure.

The geometrical lateral defect dimension correlates with the LSE-size as reported by an SSIS for defects on the hot SC1 treated wafer. The individual defect evolution with respect to LSE-size was monitored during successive hot SC1 treatments and modeling of the time evolution of the defect distribution function with the continuity equation allows to extrapolate an approximation of the LSE-size distribution of the as-grown defects with an integral defect density in the order of $10^6/cm^3$. Therefore a new approach to investigate intrinsic defects in Si is opened by delineating the COP with repeated hot SC1 treatments.

Grown-in bulk defects do not occur on the surface of an epitaxial wafer. Epitaxial layers as thin as 1.5 μm effectively reduce the LSE-size of defects on the substrate below the detection limit of present commercially available SSIS. The reduction of the number of LLS $\geq$ 0.12 μmLSE can be quantified to be two orders in magnitude for hot SC1 treated substrates which have a significantly higher level of LLS as compared to polished wafers. In this case a slight dependence of the remaining, detectable LLS on the thickness of the epitaxial layer can be observed.

ACKNOWLEDGMENTS

The support of U. Lambert, F. Passek, C. Brunner, A. Luger, C. Schnepf and G. Valouch is gratefully acknowledged. This work was supported by the Federal Department of Education and Research of Germany under the contract number M 2793 F/G and under ESPRIT project 20182 (ASPYR). The authors alone are responsible for the contents.

REFERENCES

1. D. Gräf, M. Suhren, U. Lambert, R. Schmolke, A. Ehlert, W. v.Ammon, P. Wagner in High Purity Silicon IV, edited by C.L. Claeys, P. Rai-Choudhury, P. Stallhofer, and J.E. Maurits (The Electrochem. Soc. Proc. Vol. **PV96-13**, San Antonio, TX, 1996), pp. 117-131.
2. J. Ryuta, E. Morita, T. Tanaka, and Y. Shimanuki, Jpn. J. Appl. Phys. **29**, L1947 (1990).
3. J. Vanhellemont, G. Kissinger, D. Gräf, K. Kenis, M. Depas, P. Mertens, U. Lambert, M. Heyns, C. Claeys, H. Richter and P. Wagner, Inst. Phys. Conf. Ser. No. **149**, 331 (1996).
4. M. Itsumi, H. Akiya, T. Ueki, M. Tomita, and M. Yamawaki, J. Appl. Phys. **78**, 5984 (1995).
5. P. Wagner, M. Brohl, D. Gräf, U. Lambert, Mat. Res. Soc. Symp. Proc. Vol. **378**, 17 (1995).
6. P. Wagner, H.A. Gerber, D. Gräf, R. Schmolke, and M. Suhren, International Symposium on Optical Science, Engineering, and Instrumentation, Conference on Flatness, Roughness, and Discrete Defect Characterization for Computer Disks, Wafers and Flat Panel Displays, Denver, CO, 1996, SPIE Proc. Vol. 2862 (in press).
7. M. Miyzaki, S. Miyzaki, Y. Yanase, T. Ochiai, and T. Shigematsu, Jpn. J. Appl. Phys. Vol. **34**, 6306 (1995).
8. L.W. Shive, G. Anderson, R.W. Shaw, I.J. Malik, and S. Pirooz, Semicon, Zürich, 1993.

POSITRON BEAM TECHNIQUE FOR THE STUDY OF DEFECTS AT THE Si/SiO_2 INTERFACE OF A POLYSILICON GATED MOS SYSTEM

M. CLEMENT [1,2], J.M.M. DE NIJS [1], H. SCHUT [2], A. VAN VEEN [2], R. MALLEE [1], P. BALK [1]
[1] DIMES, Delft University of Technology, P.O. Box 5053, 2600GB Delft, The Netherlands
[2] IRI, Delft University of Technology, P.O. Box 5042, 2600AG Delft, The Netherlands

ABSTRACT

This work demonstrates that positrons implanted into a 60 nm n-type polysilicon layer with large grains, can be pushed out of this layer by an externally induced electric field. In the case of a metal-oxide-silicon (MOS) system with a such a polysilicon gate, polysilicon-implanted positrons can be efficiently transported towards the SiO_2/Si interface where they all are collected. This technique offers new and interesting possibilities to study defects at the SiO_2/Si interface of technologically important MOS systems.

INTRODUCTION

In positron beam Doppler broadening measurements, defects in materials are investigated by implanted positrons [1-3]. After thermalization the positrons diffuse through the material until being trapped by defects. Subsequently, they annihilate with an electron, thus producing two γ-photons with an energy of about 511 keV. The information on the defects is obtained from the Doppler broadening of the photo-peak which is related to the momentum of the annihilated particles [1,2]. The broadening is characterized using two parameters, the shape parameter (S) and the wing parameter (W), as defined in Fig.1 [1,4,5].

The use of a mono energetic positron beam allows for controlled implantation. Thus, information on the depth distribution of defects can be obtained by scanning the beam energy. In the specific case of thermal SiO_2, it is also possible to control the transport of the positrons after thermalization by applying an electric field [5,6]. Fig. 2a schematically shows the electrochemical potential as experienced by the positrons in an Al gated metal-oxide-silicon (MOS) system for positive gate bias voltage. For such a positive bias voltage, the positrons implanted in the oxide are pushed towards the SiO_2/Si interface, but they are not injected into the silicon substrate because of the potential barrier. Instead, they remain trapped at the SiO_2/Si interface. As shown in some preceding papers, a sufficiently thick oxide

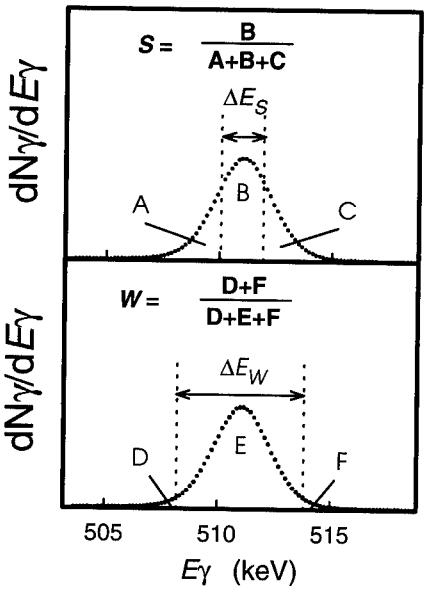


Fig. 1. Definition of shape parameter S and wing parameter W of the photopeak. The areas A,B,.. F indicate sections defined with the aid of a fixed integration window. A typical experimental spectrum is shown.

Mat. Res. Soc. Symp. Proc. Vol. 442 © 1997 Materials Research Society

layer can thus be used as an implantation buffer to collect all positrons, from which they are driven to the SiO_2/Si interface [5,6].

Guiding effectively all positrons to the SiO_2/Si interface opens new and interesting possibilities to study defects at this interface [7]. Unfortunately, the technologically most relevant MOS systems have an oxide layer of 15 nm or less, which is insufficient to collect the positrons. Moreover, they have a polysilicon gate, that may not be simply replaced by an aluminum one because of the much worse electrical properties of the SiO_2/Si interface; apparently the structural properties are affected by the moderate temperature (≈600°C) polysilicon chemical vapour deposition process.

Conceivably also the polysilicon layer can be used as an implantation buffer from which the positrons can be injected into the oxide, see Fig. 2b. To this end, the grain size and the dopant concentration of the poly layer have to be optimized. Grain bounderies act as efficient positron traps and their number has to be minimized. A stable electric field in silicon requires a space charge region associated with a depletion zone. To induce a sufficiently strong electric field in this manner, in the range of 10^{17} cm^{-3} activated dopant atoms are needed. In this work we will show the feasibility of using a polysilicon layer as an implantation buffer.

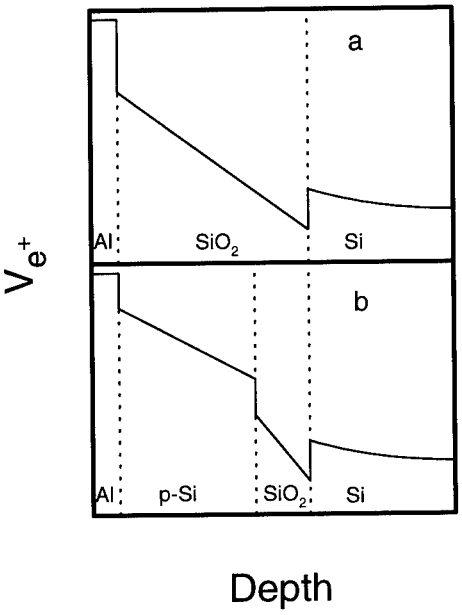


Fig 2. Schematic potential diagram for positrons in MOS system for positive bias voltage, for an Al/SiO_2/Si (a) and for Al/poly-Si/SiO_2/Si (b).

EXPERIMENTAL

For our studies we used MOS capacitors on (100) 2-5 Ωcm n-Si with a 100 nm thick gate oxide prepared by oxidation in dry O_2 at 1000°C. To produce polysilicon with large grains (60 nm or larger) we followed a deposition strategy earlier developed at our laboratories: a 60 nm amorphous silicon layer was grown by low temperature (540°C) chemical vapour deposition and subsequently subjected to crystallization anneal at 900°C [8]. Next, the polysilicon was implanted with 10^{13} cm^{-2} phosphorus atoms, followed by an activation anneal. To minimize the number of potential positron traps in the polysilicon (cf. unsaturated silicon dangling bonds), we subsequently applied an anneal at 400°C in forming gas (10%H_2/90%N_2). As a reference, the polysilicon layer of some wafers was removed by wet chemical etching at room temperature. Finally, the polysilicon gated and the bare oxides were covered with a 15 nm Al layer by evaporation from a tungsten boat.

The positron measurement were carried out using the Delft Variable Energy Positron beam [9]. This facility provides an 8 mm positron beam with energy ranging from 0 up to 30 keV and with a typical flux of 10^4 $s^{-1}cm^{-2}$. The background pressure in the vacuum system is about 10^{-7} Torr. The spectrum of the γ-photons is measured with a Ge detector with an energy resolution of about 1.1 keV at E_γ =511 keV. Bulk crystalline silicon was used as a reference; all *S*- and *W*-data are normalized to reference *S*- and *W*-values independently established on device-quality silicon.

RESULTS

To establish whether trapping in the polysilicon layer can be sufficiently suppressed and whether the polysilicon gated system indeed provides accurate information about the substrate/oxide interface, we will make a comparison of data obtained from the Al and polysilicon gated capacitors. First, we will briefly present the results from the Al gated system.

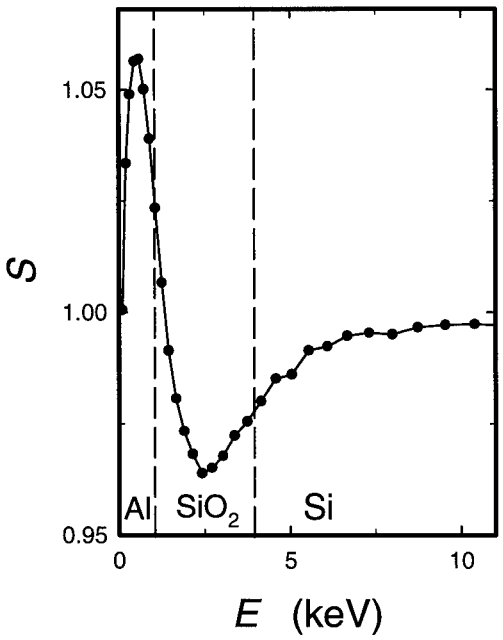


Fig. 3. *S(E)* curve for an Al gated MOS system subjected +15 V bias.

Fig. 3 shows the *S*-parameter versus implantation energy *E*, *S(E)*, for an Al gated MOS system subjected to a 15 V positive bias. In the case of implantation into the Al we obtained an *S*-value of about 1.08. Implantation into the oxide layer results in an value exhibiting a minimum. As shown elsewhere, this minimum corresponds to positrons that are transported from the oxide layer towards the silicon where they are trapped at the SiO_2/Si interface [5,6].

In Fig. 4 we show the *S(E)* and *W(E)* data as trajectories in the *S-W* plane, using the energy as a running parameter. Annihilation at a distinguishable site or layer can now be represented by a characteristic (*S,W*) point [4,5]. The triangular shape of the trajectory reveals that only three distinguishable trapping layers are involved. The cluster point at the high energy end is due to the silicon substrate. For low implantation energy the specific (*S,W*) point of Al is approached. The characteristic coordinates of the third trapping layer are given by the intersection point of the straight high and low energy parts of the trajectory; it is associated with the positrons that are trapped at the SiO_2/Si interface. In the figure we have also indicated the characteristic coordinates of SiO_2, as obtained from an independent measurement on a sample without gate. The location of this point proves that trapping in the oxide layer is fully suppressed by the electric field.

The liability of the polysilicon layer for positron trapping can be deduced from comparison of *S(E)* data from polysilicon/SiO_2/Si structures without Al, but with chemically modified outer polysilicon surface. The results of these measurements are presented in Fig. 5. The figure shows the *S(E)* curves for an as-fabricated specimen with a thin native oxide layer on the polysilicon 'a', the curve after removel of this oxide layer by an HF etch 'b', and the curves after an HF etch followed by chemical oxidation at a temperature of 60°C in HCl/H_2O_2 'c' or NO_4/H_2O_2 'd'. The data show that the surface modification strongly affects the *S*-parameter for implantation in the polysilicon layer whereas the data for deeper implantation are not affected. Apparently, a substantial part of the polysilicon-implanted positrons migrate to the outer surface. Such a drastic effect of the surface condition would be impossible in the case that the polysilicon layer would contain large numbers of efficient positron traps. In that case the positrons would be immediately trapped at the defects, unable to diffuse to the (modified) surface. This result thus suggests that positron trapping in the polysilicon layer does not play an important role and that the positrons have a sufficient long diffusion length.

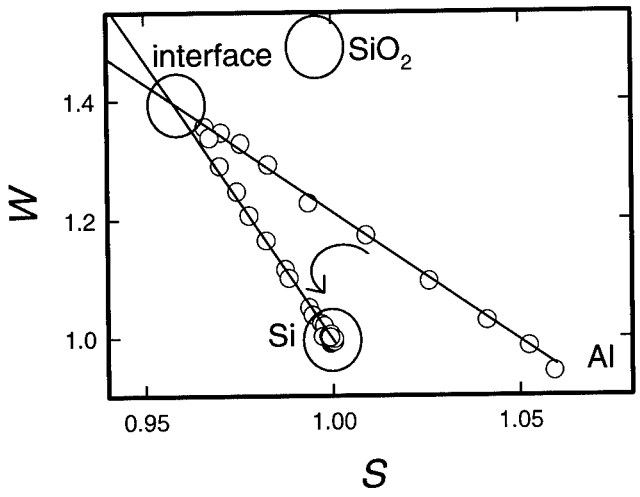


Fig. 4. *S-W* trajectories of an Al gated MOS system subjected +15 V bias. The arrow indicates the direction of increasing implantation energy. The large circles correspond with the characteristic points of Al, bulk SiO_2, the SiO_2/Si interface and the silicon substrate.

Next, we performed measurements at different bias conditions on capacitors provided with a thin Al toplayer. Fig. 6 shows the resulting *S(E)* data for 0 and +15 V bias. Implantation in the 15 nm Al toplayer results in a high *S*-value for both bias conditions. For implantation in the polysilicon, in the oxide and in the silicon, the curves reveal a clear field effect. The 15 V positive bias curve exhibits a broad minimum (S= 0.955) for implantation in the polysilicon layer, while for 0 V bias an intermediate *S*-values is observed. These data clearly demonstrate the feasibility of properly doping the polysilicon.

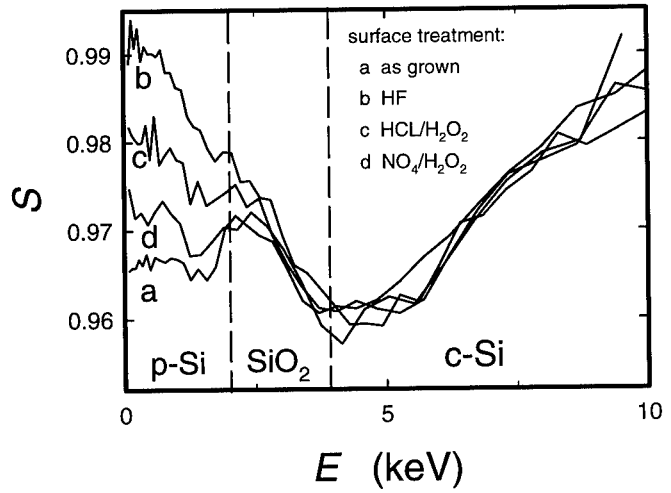


Fig. 5. *S(E)* curves of polysilicon/SiO_2/Si with different surface states. Shown are: as-fabricated specimen with native oxide layer on the polysilicon (a), after removal of this oxide by an HF etch (b), and after an HF etch followed by 60°C chemical oxidation in HCl/H_2O_2 (c) or NO_4/H_2O_2 (d).

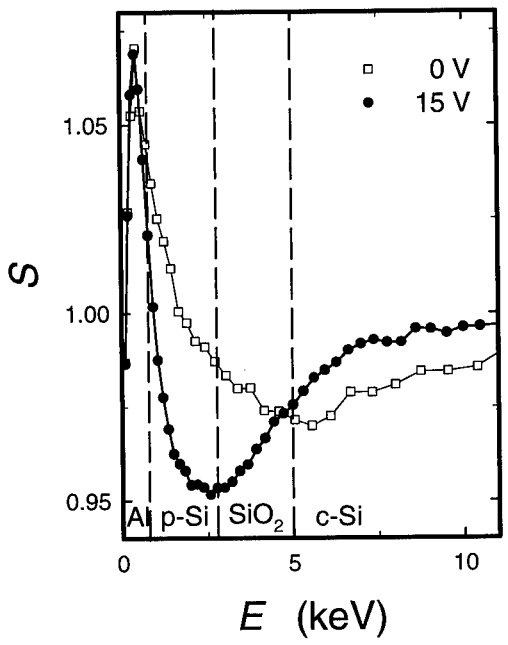


Fig. 6. *S(E)* curves for an MOS system with polysilicon layer subjected 0V and +15 V bias.

For the interpretation of the *S(E)* curves it is convenient to consider the corresponding *S-W* plot of Fig.7. The data for +15 V bias are all situated on two straight lines that intersect at $(S,W) = (0.955,1.38)$. The intersection point also coincides with a clustering point. Comparison whith the trajectory of Fig. 4 shows that the intersection point perfectly agrees with the (S,W) point of the SiO_2/Si interface of the specimen without polysilicon gate. The medium energy cluster point of Fig. 7 is associated with the broad minimum of the +15 V bias *S(E)* curve for polysilicon and oxide-implanted positrons. Apparently, the positrons implanted in the polysilicon and in the oxide are efficiently transported by the field to the SiO_2/Si interface where they are trapped. Most remarkable is that the +15 V *S-W* trajectories of the specimen with (Fig. 7) and without (Fig. 4) polysilicon layer are identical within exprimental error; it looks as if there is no polysilicon layer at all.

In Fig. 7 we have also drawn the 0 V trajectory, which reveals some additional features of the transport and the trapping of the positrons. For low energies, which corresponds with implantation in the polysilicon, the trajectory is almost straight,

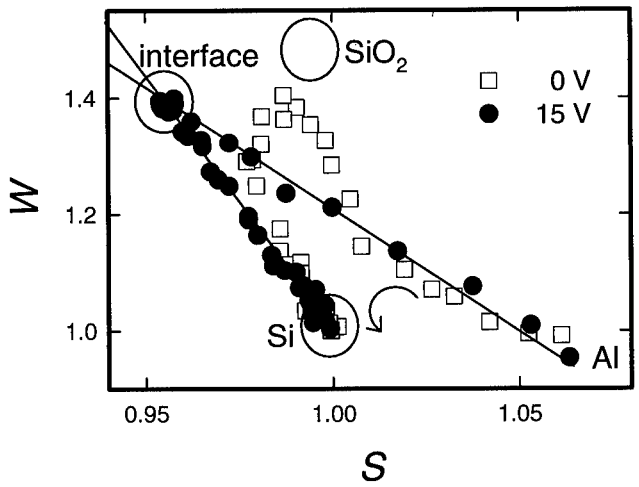


Fig. 7. *S-W* trajectories for an MOS system with polysilicon gate subjected 0 V and +15 V bias. The large circles correspond with the points of Al, bulk SiO_2, SiO_2/Si interface and the silicon.

possibly with a small deviation towards the silicon point. This deviation could point towards some trapping in the polysilicon layer; however, such a contribution may be well neglected for the present discussion. The majority of the positrons are trapped either in the Al toplayer or in a trapping layer with a characteristic point situated on the line defined by the Al and the SiO_2/Si characteristic coordinates. This suggest that the polysilicon-implanted positrons are trapped in the Al toplayer or at the polysilicon/SiO_2 interface. For moderate implantation energies, the trajectory runs outside the triangle Al-SiO_2/Si-Si, towards the bulk oxide characteristic point. Apparently without the applied field, a substantial fraction of the positrons is trapped in the bulk oxide layer. For higher energies the trajectory returns to the bulk silicon coordinates, with however a clear deviation towards the SiO_2/Si interface point and appoaching the substrate point according to the line defined by the characteristic points of the SiO_2/Si interface and of the silicon substrate. These features show that trapping at the SiO_2/Si interface still is important, but not as dominant as in the case of positive bias. Likely, a major fraction of the positrons trapped at the interface can be ascribed to substrate-implanted positrons that diffuse back to the oxide.

One should note that the SiO_2/Si characteristic (S,W) coordinates, (0.955,1.38) of Figs. 4 and 7, substantially differs from the earlier reported values of (0.95, 1.55) for specimens that were not provided from a polysilicon gate [5-7]. Apparently, structural changes are clearly sensed by the positrons. Unfortunately, we can not interpret this information as yet.

CONCLUSIONS

Our results clearly demonstrate the possibility to use a polysilicon layer as an implantation buffer for positrons; trapping can be sufficiently suppressed and the layer can be doped to induce a sufficiently strong field. We have shown that indeed all positrons implanted in the polysilicon and oxide layer can be collected at the SiO_2/Si interface. For the present studies, we did not use an optimized processing scheme; instead a deposition strategy which suited our purposes was copied from literature. This technique offers new and very promising opportunities to study defects at the SiO_2/Si interface of technological important MOS systems.

ACKNOWLEDGEMENTS

We would like to acknowledge the advise of P.J. French for the deposition of large grain-size polysilicon and the assistance of B.A.C. Rousseeuw in defining the MOS structures in the polysilicon.

REFERENCES

1. P. J. Schultz and K. G. Lynn, Rev. Mod. Phys. **60**, p. 701 (1988).
2. M. J. Puska and R. M. Nieminen, Rev. Mod. Phys. **66**, p. 814 (1994).
3. P. Asoka-Kumar, K. G. Lynn and D.O. Welch, J. Appl. Phys. **76**, p. 4935 (1995).
4. L. Liszkay, C. Corbel, L. Baroux, P. Hautojärvi, M. Bayhan, A. W. Brinkman and S. Tararenko, Appl. Phys. Lett. **64**, p. 1380 (1994).
5. M. Clement, J. M. M. de Nijs, P. Balk, H. Schut and A. van Veen, J. Appl. Phys. **79**, p. 9029 (1996).
6. M. Clement, J. M. M. de Nijs, P. Balk, H. Schut and A. van Veen, Sceduled for J. Appl. Phys. **81**, issue February 1997.
7 M. Clement, J. M. M. de Nijs, A. van Veen, H. Schut and P. Balk, IEEE Trans. on Nucl. Sc. **NS-42**, p. 1717 (1995).
8 P.J. French, B.P. Drieënhuizen, D. Poenar, J.F.L. Goosen, R. Mallee, P.M. Sarro and R. Wolffenbuttel, J. Microelectromechanical Systems, **5**, p. 187 (1996).
9. A. van Veen, J. Trace Microprobe Techn. **8**, p. 1 (1990).

Part IV

Processing Induced Defects: Point Defects and Reaction

AN INVESTIGATION OF VACANCY POPULATION DURING ARSENIC ACTIVATION IN SILICON

O. DOKUMACI *, H. -J. GOSSMANN **, K. S. JONES ***, AND M. E. LAW *
* 339 Larsen Hall, Department of Electrical Engineering, University of Florida, Gainesville, Florida 32611
** Bell Laboratories, Lucent Technologies, 600 Mountain Av., Murray Hill, NJ 07974
*** Department of Materials Science, University of Florida, Gainesville, Florida 32611

ABSTRACT

Recent experimental investigations have shown that electrical deactivation of arsenic in silicon creates excess silicon interstitials. This study investigated the possibility of excess vacancy generation during arsenic activation. We used Sb doping superlattice structures containing six 10 nm wide Sb doped spikes separated by 100 nm. It was found that antimony diffusion was not enhanced as active arsenic concentration increased, indicating there is no observable vacancy injection out of the arsenic layer during the activation process. Plan-view transmission electron microscopy study of the samples revealed dislocation loops before the activation anneal. Although the loops completely dissolved during the activation anneal, they do not seem to be sufficient enough to absorb all the vacancies generated by the activated arsenic. When germanium was present at the surface instead of arsenic, antimony diffusion was enhanced.

INTRODUCTION

High concentration arsenic layers are widely used in contemporary silicon device technology. In order to get high conductivity, arsenic is incorporated into these layers in excess of its substitutional solubility. Recent investigations have shown that electrical deactivation of arsenic in silicon creates excess silicon interstitials [1]. This has been attributed to the formation of arsenic-vacancy clusters and generation of silicon interstitials during this process. The high level of interstitial injection is also confirmed by TEM studies of type-V dislocation loops formed during arsenic deactivation in initially defect-free laser annealed samples [2].

The formation of a large number of arsenic-vacancy clusters has been confirmed with positron annihilation measurements [3]. Furthermore, extended x-ray absorption fine-structure (EXAFS) results combined with Rutherford backscattering (RBS) measurements also indicate that the deactivation of arsenic proceeds through the formation of arsenic vacancy complexes below 750^{o}C [4,5]. Upon electrical activation of arsenic, these complexes are expected to dissolve and generate free vacancies. In this study, antimony doping superlattice (DSL) structures were used to detect any possible vacancy injection into the bulk during the activation of arsenic. Since antimony diffuses predominantly through a vacancy mechanism, its diffusion is enhanced when there is a supersaturation of vacancies [6].

EXPERIMENT

The DSL structures used in the experiment contained six narrow Sb regions with 10 nm widths, peaks spaced 100 nm apart and doped to a concentration of $1.5x10^{19}$ cm^{-3}. They were grown by low temperature molecular beam epitaxy on Si(100) floatzone substrates [7]. The samples were split in three during ion-implantation: no implant, arsenic implant, and germanium

Mat. Res. Soc. Symp. Proc. Vol. 442 © 1997 Materials Research Society

implant. Since germanium is similar to arsenic in mass and size, it allows us to monitor any possible effects of similar ion-implantation damage on antimony diffusion if the damage is not completely wiped out during the damage anneal. Arsenic was implanted at 50 keV at 7° tilt with doses of $3x10^{15}$ cm^{-2} and $8x10^{15}$ cm^{-2}, while germanium was implanted at only $8x10^{15}$ cm^{-2}. All the samples were capped with an approximately 2000 Å layer of oxide and then a nitride layer to prevent the evaporation of arsenic. They were annealed at 1150°C for 5s in order to eliminate the implantation damage. After the samples were subjected to a deactivation anneal at 750°C for 2h, some of them were further annealed either at 850°C for 4 h or 950°C for 30 min to electrically activate some of arsenic.

After the nitride and the oxide were stripped, arsenic and antimony profiles were measured by SIMS. Plan-view samples were studied by TEM with a JEOL 200CX electron microscope operating at 200 keV. Spreading and sheet resistance measurements were done on arsenic doped samples.

In order to find the antimony diffusivity during the activation anneals, the following procedure was employed: For each spike, the SIMS profile after the deactivation anneal was supplied as an initial profile to the process simulation program FLOOPS. The antimony diffusivity was assumed to have the form $D_{Sb} = \alpha D_{Sb}^{ref}$, where α is an enhancement factor and the reference diffusivity D_{Sb}^{ref} is the default inert antimony diffusivity in FLOOPS, and is given by

$$D_{Sb}^{ref} = 0.21\exp\left(-\frac{3.65}{kT}\right) + (n/n_i)15\exp\left(-\frac{4.08}{kT}\right) \qquad (1)$$

The diffusion of the initial profile was simulated with FLOOPS with different values of α until the error between the simulated and the experimental profiles was minimized. The enhancement or the retardation in antimony diffusivity in the arsenic or germanium doped samples was found by dividing the diffusivity in these samples to the diffusivity extracted from the unimplanted samples which were annealed under the same conditions.

RESULTS AND DISCUSSION

Figure 1 shows the antimony SIMS profiles in the as-deposited DSL sample, and in the high dose arsenic sample which has been subjected to the 950°C activation anneal. Antimony inside the arsenic layer exhibits considerable amount of more diffusion than antimony found outside the arsenic layer. Figure 2 presents the arsenic profiles in the both the high ($8x10^{15}$ cm^{-2}) and low ($3x10^{15}$ cm^{-2}) dose samples after the deactivation and the 950°C activation anneal. A significant amount of arsenic diffusion can be observed during the activation anneal.

Figure 3 shows the ratio of the antimony diffusivity extracted from the arsenic doped samples to the inert antimony diffusivity for the activation anneals. As mentioned earlier the inert diffusivity was extracted from the unimplanted samples. For all our experimental conditions, the antimony diffusivities obtained from arsenic doped samples are very close to the corresponding inert diffusivities, meaning that there is no observable vacancy supersaturation during arsenic activation. The activation of arsenic is confirmed by both sheet resistance (Table I) and spreading resistance measurements (Figure 4). The spreading resistance data shows that diffusion of arsenic into the bulk contributes significantly to the amount of electrically active arsenic.

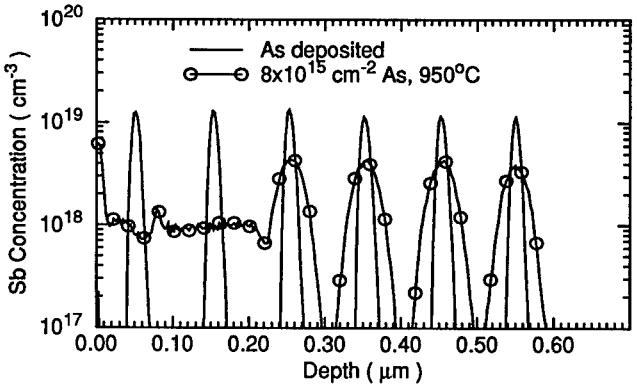


Figure 1. Antimony SIMS profiles in the as-deposited DSL sample and the sample implanted with $8x10^{15}$ cm^{-2} arsenic and annealed at 950°C after the damage and deactivation anneals.

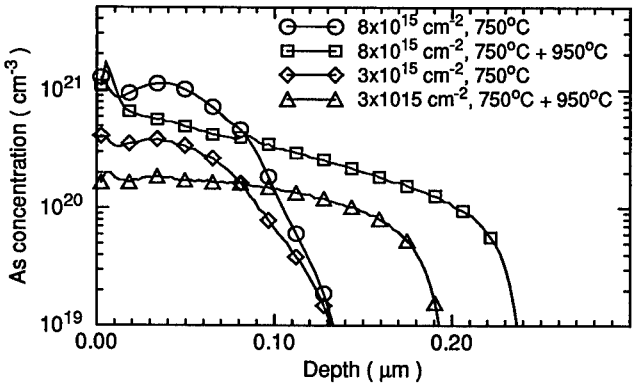


Figure 2. Arsenic SIMS profiles. The temperatures in the legends represent the anneals after the damage anneal at 1150°C.

The positron annihilation experiments show that the average number of vacancies per inactive arsenic atom is between 1/2 and 1/4 in an arsenic doped silicon sample which has been laser annealed and then thermally annealed at 750°C (Concentration of arsenic = $8x10^{20}$ cm^{-3}) [3]. RBS and EXAFS measurements have led Brizard *et al.* to propose the existence of arsenic-vacancy clusters which have a vacancy/arsenic ratio of around 1/3 [4]. Thus, it is unexpected that there is not any significant enhancement in our samples since a very large amount of free vacancies is expected to be released upon the dissolution of these clusters.

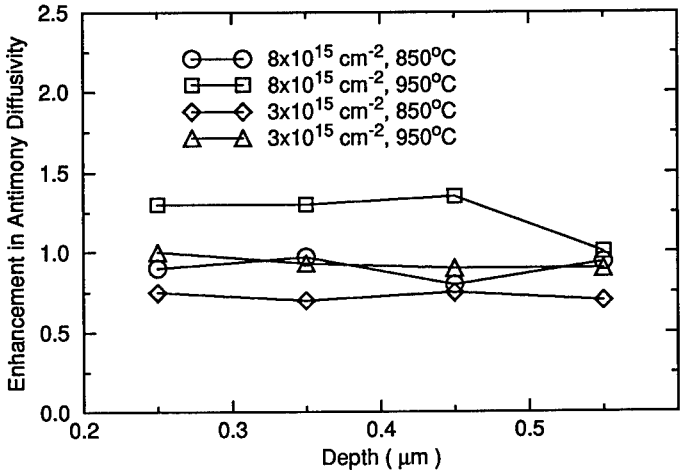


Figure 3. Enhancement in the antimony diffusivity as a function of depth in the arsenic doped samples. The temperatures shown in the legends represent the activation anneal temperatures..

Table I: Summary of the electrical and TEM measurements on the arsenic doped samples

Arsenic dose (10^{15} cm^{-2})	Anneal sequence after the damage anneal (°C)	Sheet Resistance (Ω/sq)	Density of atoms bound by dislocation loops (cm^{-2})	The total amount of electrically active arsenic (cm^{-2})
8	750	71.8	$1.1x10^{14}$	$1.1x10^{15}$
8	750 + 850	48.7	Very few loops	-
8	750 + 950	30.0	No loops	$3x10^{15}$
3	750	76.4	$2.3x10^{13}$	$1.1x10^{15}$
3	750 + 850	63.4	No loops	$1.5x10^{15}$
3	750 + 950	50	No loops	$2x10^{15}$

In order to investigate the possibility that the generated vacancies may be absorbed by the extrinsic extended defects either left over from the damage anneal or created by the subsequent deactivation anneal, we made a plan-view TEM study of the arsenic doped samples (Table I). Dislocation loops were observed in the samples after the deactivation anneal, and they completely dissolve during the activation anneals with the exception of the 850°C high dose sample where only a very small amount of loops has survived the activation anneal.

Table I also shows the total amount of electrically active arsenic obtained by integrating the electron concentration from the spreading resistance measurements with depth. In the high dose sample, the ratio of the atoms bound by the dislocation loops to the activated amount of

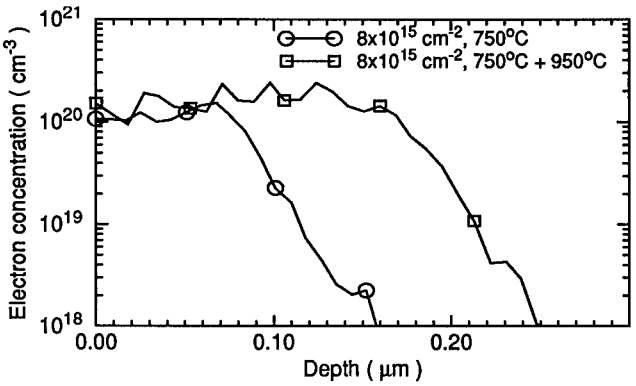


Figure 4. Spreading resistance measurements of the arsenic doped layer for the $8x10^{15}$ cm^{-2} dose. The temperatures in the legends represent the anneals after the damage anneal at 1150°C.

arsenic during the 950°C activation anneal is roughly 1/17, whereas in the low dose sample this ratio is 1/40. These ratios are much smaller than the vacancy/arsenic ratio in the clusters calculated from either the positron annihilation or EXAFS measurements. So, even if the loops are annihilated by only absorbing the vacancies generated by the activation process, this mechanism alone is not enough to explain the lack of vacancy injection into the bulk assuming that vacancies are generated with a ratio indicated by the positron annihilation and EXAFS measurements. The unaccounted vacancies may be either recombining at the surface or with the interstitials created during the deactivation anneal and possibly trapped by an impurity like carbon. In fact, SIMS analysis shows a high concentration of carbon in the samples. Another explanation might be a possible increase in the ratio of the concentration of clusters that have a higher vacancy/arsenic ratio, such as As_2V, to the concentration of higher order clusters which have a smaller vacancy/arsenic ratio, such as As_4V. This can especially happen in the regions where chemical arsenic concentration is not very high and the formation of arsenic rich clusters is kinetically limited. Therefore, instead of being injected into the bulk, the excess vacancies may be recaptured by the relatively more vacancy rich arsenic-vacancy complexes..

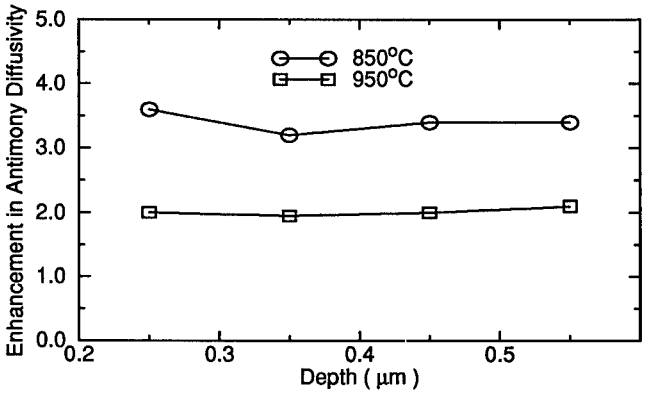


Figure 5. Enhancement in the antimony diffusivity as a function of depth in the germanium doped samples. Only the activation anneal temperatures are shown in the legends.

Figure 5 shows the enhancement in antimony diffusivity in germanium doped samples during the activation anneals. Unlike arsenic, antimony diffusion is enhanced in these samples.

CONCLUSIONS

The effect of arsenic activation on vacancy population has been studied using antimony doping superlattice structures. The antimony diffusivity has been found to be very close to its inert diffusivity during arsenic activation, suggesting that there is not significant vacancy injection. The dislocation loops observed after the deactivation anneal are not sufficient enough to absorb all the vacancies which are expected to be generated in an amount indicated by the positron annihilation and EXAFS measurements. Other possible mechanisms that can explain the lack of vacancy injection include surface recombination, recombination with trapped interstitials generated during the deactivation anneal and absorption of vacancies by relatively more vacancy rich arsenic defects, such as As_2V clusters. On the other hand, antimony diffusion is enhanced when germanium is present at the surface.

ACKNOWLEDGEMENTS

We thank V. Krishnamoorthy and S. Bharatan for assistance in the TEM work.

REFERENCES

1. P.M. Rousseau, P.B. Griffin and J.D. Plummer, Appl. Phys. Lett. 65, 578 (1994).
2. O. Dokumaci, P. Rousseau, S. Luning, V. Krishnamoorthy, K.S. Jones and M.E. Law, J. Appl. Phys. 78, 828 (1995).
3. D. W. Lawther, U. Myler, P.J. Simpson, P.M. Rousseau, P.B. Griffin, and J.D. Plummer, Appl. Phys. Lett. 67, 3575 (1995).
4. C. Brizard, J.R. Regnard, J.L. Allain, M. Dubus, A. Armigliato, and A. Parisini, J. Appl. Phys. 75, 126 (1994).
5. J.L. Allain, J.R. Regnard, A. Bourret, A. Parisini, A. Armigliato, G. Tourillon, and S. Pizzini, Phys. Rev. B 46, 9434 (1992).
6. P.M. Fahey, P.B. Griffin, and J.D. Plummer, Rev. Mod. Phys. 61, 289 (1989).
7. H. -J. Gossmann, F.C. Unterwald, and H.S. Luftman, J. Appl. Phys. 73, 8237 (1993).

ENHANCED DISSOLUTION OF EXTRINSIC DISLOCATION LOOPS IN SILICON ANNEALED IN NH_3

S.B. Herner*[a)], V. Krishnamoorthy*, K.S. Jones*, T.K. Mogi[†], and H.-J. Gossmann[‡]
*Dept. of Materials Science and Engineering, University of Florida, Gainesville, FL 32611
[†]Dept. of Materials Science and Engineering, Cornell University, Ithaca, NY 14853
[‡]Bell Laboratories, Lucent Technologies, Murray Hill, NJ 07974

ABSTRACT

The behavior of extrinsic dislocation loops in silicon was investigated by transmission electron microscopy. Loops were formed by an amorphizing implant and recrystallization anneal of Si wafers. Wafers were further annealed in either Ar or NH_3. Wafers annealed in NH_3 formed a thin (~4 nm) SiN_x film. The loops in samples in Ar showed a constant net number of interstitials bound by the loops, while those in samples annealed in NH_3 showed a marked decrease. The results are explained by a supersaturation of vacancies recombining with the interstitials in loops. By integrating the measured difference between interstitials bound by the loops in samples annealed in Ar vs. NH_3 over the distance from the surface to the loop layer, an estimate for the relative vacancy supersaturation is extracted. Comparison with estimates of vacancy supersaturations with nitridation from the change in Sb diffusivity show good agreement between the two methods.

INTRODUCTION

The diffusivity of substitutional dopants in silicon is determined by the concentration of native point defects, namely vacancies and self interstitials.[1] The formation of shallow junctions in silicon in increasingly being limited by the diffusion of the dopant after its introduction into the substrate. It is therefore crucial to understand how the concentration of native point defects changes with each processing step in the fabrication of integrated circuits (ICs).

Determination of the native point defects concentration is nontrivial, as direct observation of point defects is impossible. Indirect methods, including dopant diffusion and dislocation loop kinetics,[1,2] have therefore been developed. In this report, we examine the behavior of pre-existing extrinsic dislocation loops in silicon annealed in either Ar or NH_3. Samples annealed in NH_3 formed a silicon nitride (SiN_x) film, which is used as a masking or dielectric layer during typical IC processing. By comparing the loops in each annealing ambient, we can extract information on how the silicon nitride film affects the native point defects concentrations.

Several studies have shown that the presence of silicon nitride films results in a vacancy supersaturation and an interstitial undersaturation in the substrate.[3-5] In a recent paper, Mogi et al.[5] reported that the anneal of silicon in NH_3 at 910°C resulted in $\frac{< C_V >}{C_V^*} \sim 3.8$ and $\frac{< C_I >}{C_I^*} \sim 0.1$ after one hour, where C_V denotes the volume concentration of vacancies, C_I that of intersti-

[a)] current address: Bell Laboratories, Lucent Technologies, Murray Hill, NJ 07974

Mat. Res. Soc. Symp. Proc. Vol. 442 © 1997 Materials Research Society

-tials, and * denotes equilibrium. These values were determined by measuring the diffusivity of Sb and B in Si. Antimony was assumed to diffuse completely by a vacancy mechanism and boron by an interstitial mechanism. The diffusivities of Sb and B are therefore proportional to the concentration of vacancies and self interstitials, respectively.

The primary quantity measured by dislocation loop kinetics is the *flux* of native point defects introduced by a particular processing step. In this case, we are measuring the flux of vacancies recombining with extrinsic dislocation loops. However, the possibility of loop dissolution by interstitial undersaturation must be accounted for.

EXPERIMENTAL

A Czochralski grown p-type Si wafer ($\rho < 100\ \Omega$-cm) was implanted with 140 keV Ge^+ ions to a dose of 1 x $10^{15}/cm^2$ in order to amorphize the Si. The wafer was annealed in N_2 (99.999% purity) for 60 m at 800°C to recrystallize the wafer and form the EOR loops. Annealing under these conditions has been previously shown to return the native point defect concentration to equilibrium after the disturbance caused by ion implantation.[6] Half the samples were annealed in NH_3 (99.9995% purity) and the other half were annealed in Ar (99.995% purity) for 30 to 180 m at 810 and 910°C. Samples were examined by plan view and cross sectional TEM (PTEM and XTEM, respectively). Quantitative analysis of the loops was performed using weak beam dark field (g_{220}) PTEM micrographs. All the of loops in a representative area of ~1 μm^2 in each sample were measured. The longest axis of each loop was measured and sorted by increments of 5 nm from 10 to 70 nm. The total number of loops of each size was mutliplied by the area of that size loop and the areas added to get the total area of the loops. Previous experiments have shown that the loops lie on {111} planes. Details of the analysis and error bar generation are described in more detail in ref. [6].

RESULTS AND DISCUSSION

A typical XTEM micrograph is shown in figure 1. The loops are in a discrete layer approximately 160 nm below the surface. The film thickness was measured to be ≤ 4 nm by high resolution TEM. Representative PTEM micrographs are shown in figure 2. The loops in general show an increase in average size and a decrease in density with increased anneal time and temperature in both sets of samples. To extract point defect information, we must examine the net density of interstitials bound by the loops, and not the net density of loops. Little thermal dissolution of the loops is occurring at both temperatures in the Ar annealed samples as shown by the ~constancy of the net interstitials bound by the loops (fig. 3), while the samples annealed in NH_3 show a net decrease (fig. 4). Loop dissolution may be occurring by vacancy supersaturation and/or interstitial undersaturation.[7] We deal with each case individually:

1. Vacancy Supersaturation:

By assuming that a flux, Φ, of vacancies from the interface to the bulk is completely captured and annihilated by the loops and that all loop dissolution is due to vacancy-loop

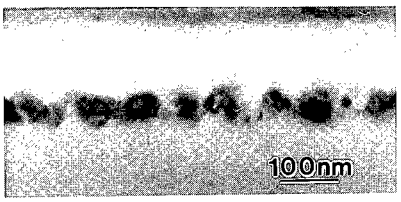


Figure 1. XTEM micrograph of a sample annealed at 910°C for 180 m in NH_3.

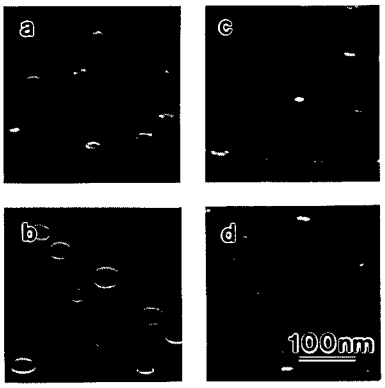


Figure 2. PTEM micrographs of samples annealed at 910°C for a) 30 m in Ar, b) 180 m in Ar, c) 30 m in NH_3, and and d) 180 m in NH_3.

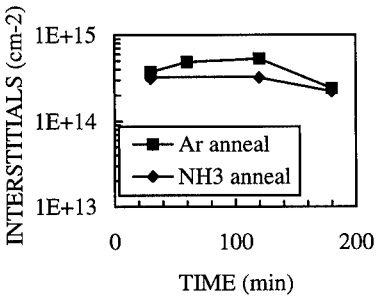


Figure 3. Net density of interstitials bound by the loops in the 810°C samples.

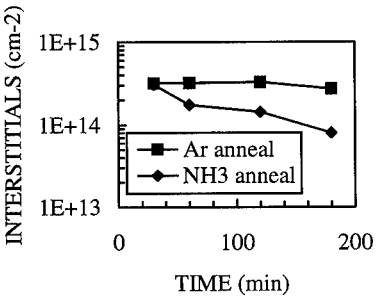


Figure 4. Net density of interstitials bound by the loops in the 910°C samples.

interaction, one can estimate the relative vacancy supersaturation via:

$$\int_o^d \Phi dx = \left(C_V - C_V^*\right) D_V$$

where $\Phi = \dfrac{\text{interstitials}_{\text{loops}}^{\text{Ar}} - \text{interstitials}_{\text{loops}}^{\text{NH}_3}}{\text{time}}$, or the net number of interstitials lost by the loops in nitrided samples per unit area and time, d is the distance between the interface and loop layer, and D_V is the vacancy diffusivity. This assumes a negligible loss of vacancies from free

interstitial-free vacancy recombination. A schematic of the vacancy concentration depth profile is shown in figure 5. We now compare the loop results to previous studies by Mogi et al.,[5,8] using an estimate of $C_V^* D_V$ from Tan and Gösele.[9] The measurements of Mogi et al., are taken at a depth of 155 nm in the wafer. Using the integrated flux values and $C_V^* D_V$ estimate, we extract values for $\frac{< C_V >}{C_V^*}$ at 910°C, shown in figure 6. The two sets of data show excellent agreement. We can conclude that loop dissolution can be attributed to a vacancy supersaturation on the order of $\frac{< C_V >}{C_V^*} \sim 4$ at 910°C.

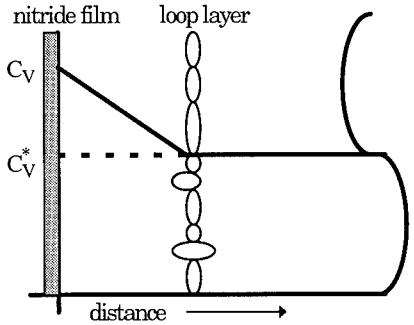


Figure 5. Concentration of vacancies as a function of depth into the sample.

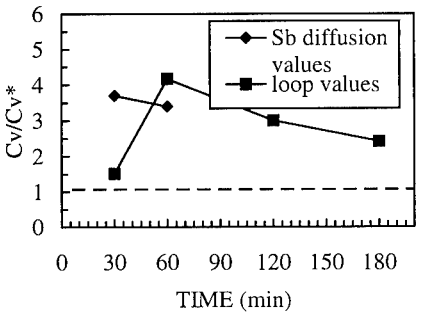


Figure 6. Time variation of the vacancy supersaturation, compared with the values from ref. [5] and [8].

2. Interstitial Undersaturation

In this case, interstitials are leaving the loops to replenish an undersaturation in the area between the interface and the loops. The integrated flux values then measure the rate at which interstitials are supplied to this region. Similar to vacancy-induced loss, we assume that (1) "lost" interstitials from loops are due solely to interstitial undersaturation, and (2) negligible "free" intersititial - "free" vacancy recombination. We cannot extract a $\frac{< C_I >}{C_I^*}$ value in analogy to the $\frac{< C_V >}{C_V^*}$ value because we do not know the relative strength of interface recombination vs. the ability of the loops to supply interstitials. The interface attempts to maintain a value of C_I^s by acting as a sink for interstitials while the loops attempt to maintain a value of C_I^* by supplying interstitials. The actual value of C_I at the interface is therefore some concentration C_I^{ss}. Figure 7 shows a schematic of the concentration depth profile of interstitials. A value for $\frac{< C_I >}{C_I^*}$ is impossible to derive because C_I^{ss} is unknown.

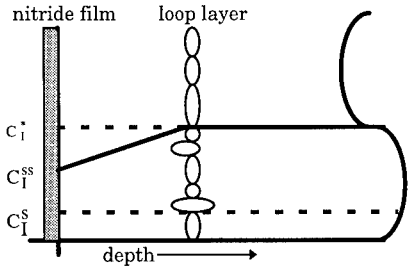


Figure 7. Concentrations of interstitials as a function of depth into the sample.

We conclude that interstitial undersaturation-induced loop dissolution can be disregarded based on two observations: (1) The number of interstitials bound by the loops is approximately constant between the Ar anneals from 810 to 910°C, indicating that the loops are not a significant source of interstitials for the rise in C_I^* between 810 and 910°C (a factor of 50x by one estimate[9]). (2) A previous study of oxidation-induced loop growth,[10] in which $\frac{< C_I >}{C_I^*}$ ~ 10 at 900°C, resulted in a 60% increase in the number of interstitials bound by the loops after a one hour anneal. We therefore expect that a value of $\frac{< C_I >}{C_I^*}$ ~ 0.1 would result in little loop dissolution. All of these observations indicate that we can disregard loop dissolution due to interstitial undersaturation.

The estimates of $\frac{< C_V >}{C_V^*}$ shown in figure 6 show that the vacancy supersaturation is a partially continuous flux from the interface. The larger error bars on the short time anneals arise from the fact that we are measuring a small difference in the net interstitials bound by the loops. The data also indicates a slight decrease in the vacancy supersaturation in anneal times longer than 60 m, which is in agreement with the earlier study. This could be due to a decline in the flux.

CONCLUSION

The anneal of silicon with pre-existing extrinsic dislocation loops in NH_3 results in the accelerated dissolution of the loops compared with samples annealed in Ar. This enhanced dissolution is due to a superaturation of vacancies caused by the presence of the SiN_x film. We extract estimates of the relative $\frac{< C_V >}{C_V^*}$ values at 910°C by measuring the enhanced dissolution by TEM. The results show excellent agreement with a previous study that used the change in Sb diffusivity to estimate the relative concentration of vacancies.

ACKNOWLEDGMENTS

The work at the University of Florida was funded by SEMATECH and the work at Cornell University was funded by SRC. We thank Bell Laboratories, Lucent Technologies, for partial financial support of two of the authors (SBH and TKM).

REFERENCES

1. P.M. Fahey, P.B. Griffin, and J.D. Plummer, Rev. Mod. Phys. **61**, 289 (1989).

2. J.K. Listebarger, K.S. Jones, and J.A. Slinkman, J. of Appl. Phys. **77**, 1948 (1993).

3. P. Fahey, G. Barbuscia, M. Moslehi, and R.W. Dutton, Appl. Phys. Lett. **46**, 784 (1985).

4. S.T. Ahn, H.W. Kennel, J.D. Plummer, and W.A. Tiller, Appl. Phys. Lett. **53**, 1594 (1988).

5. T.K. Mogi, H-J. Gossmann, D.J. Eaglesham, C.J. Rafferty, H.S. Luftman, F.C. Unterwald, T. Boone, J.M, Poate, and M.O. Thompson, in Proceedings of the 5th International Symposium on Ultra Large Scale Integration Science and Technology, eds. Edward M. Middlesworth and Hisham Massoud, (The Electrochemical Society, Pennington, NJ 1995) 145.

6. J.K. Listebarger, H. G. Robinson, K.S. Jones, M.E. Law, D.D. Sieloff, J.A. Slinkman, and T.O. Sedgwick, J. Appl. Phys. **78**, 2298 (1995).

7. B.L. Eyre and D.M. Maher, Phil. Mag. **24**, 767 (1971).

8. T.K. Mogi, PhD Dissertation, Cornell University, 1996.

9. T.Y. Tan and U.M. Gösele, Appl. Phys. A **37**, 1 (1985).

10. H. Park, K.S. Jones, and M.E. Law, J. Electrochem. Soc. **141**, 759 (1994).

Depth profile of point defects in ion implanted n^+p and p^+n junctions formed by 450℃ post-implantation annealing and impact of defects on junction characteristics

Mauricio Massazumi Oka, Akira Nakada, Yukio Tamai, Kei Kanemoto, Tadashi Shibata, and Tadahiro Ohmi
Department of Electronic Engineering, Faculty of Engineering, Tohoku University,
Aza-Aoba, Aramaki, Aoba-ku, Sendai 980-77, JAPAN
(TEL: +81-22-217-7124 / FAX: +81-22-263-9395)

ABSTRACT

It is shown that defects generated by ion implantation, remaining after annealing at low temperature, are deep-distributed in the bulk silicon and their amount is demonstrated to be function of the substrate type and the implanted ion species. The confirmation that defects penetrate deeply into the silicon is made by a new method that consists in damaging by ion implantation a previously formed pn junction that shows very low leakage current and has a deep junction. It is proposed that the dopants in the substrate act as nucleation centers for the formation of point defect clusters and that these clusters actually degrade the junction. It was found that point defects penetrate much more deeply in p^+n junctions than in n^+p junctions. It was also found that BF_2^+ introduces much more defects into the silicon than As^+, owing to the presence of fluorine. The leakage currents at 5 V of n^+p and p^+n diodes made by implantation of P^+ and B^+, respectively, could be lowered by one to two orders of magnitude with respect to values obtained by implantation of As^+ and BF_2^+ because the former ones produce less defects than the latter.

INTRODUCTION

It is known that a layer fully amorphized by ion implantation can be completely restored, from the crystallinity point of view, by solid phase epitaxy, even at a temperature as low as 500℃ [1], and that implanted dopants can be activated at temperatures in this range [2]. However, junctions annealed at temperatures lower than 800℃ are known to exhibit leakage currents much higher than those annealed at high temperatures (900 - 1000℃) [3-5]. This is due to the residual damages existing beyond the location of the amorphous/crystalline interface that are known as end-of-range defects [6 - 8].

On the other hand there is a strong interest to reduce the temperature of post-implantation annealing below 500℃ because this will allow the use of metal (e.g. aluminum) in the heart of

Mat. Res. Soc. Symp. Proc. Vol. 442 © 1997 Materials Research Society

devices, for instance as gate material and metallic substrate in metal-substrate SOI (silicon-on-insulator) CMOS (Complimentary Metal Oxide Semiconductor) structure, which is expected to operate at clock rates as high as 10 GHz [9, 10]. Therefore the better understanding of defects generated by the ion implantation and the development of a technology to make junctions at low temperature presenting a performance comparable to those annealed at high temperature is of capital importance. We have shown that junctions presenting leakage currents three to four orders of magnitude lower than values reported in the literature can be formed using an ultra clean ion implanter [11] having a background pressure of $\sim 10^{-10}$ Torr and metallic-contamination level below 10^{10} atoms/cm^2 on the wafer surface. In this work it is reported that further improvements in the leakage current can be achieved by selecting ions that produce less defects during the ion implantation.

EXPERIMENT

Two distinct experimental procedures were employed. In the first procedure, described in Fig. 1 [12], junctions with low leakage current with area of 1x1 mm^2 were firstly made by post-implantation annealing at 1000℃ with the annealing time being varied in order to achieve junctions with varying depths. n^+p junctions were made by As^+ implantation and p^+n junctions, by BF_2^+ implantation, both at 25 keV with a dose of $2x10^{15}$ cm^{-2}. 800 nm thick silicon dioxide was then deposited by APCVD (Atmospheric Pressure Chemical Vapor Deposition). In half of the wafer, square shaped openings with area of 0.95x0.95 mm^2 were patterned over the pre-formed junctions. A damaging implantation was carried out into the pre-formed junctions by different ions. Therefore in half of the wafer the damage did not reach the silicon surface, since it was completely covered by the oxide, and in the other half, this implantation actually caused damage. The samples were then annealed at 450℃ for 5 h, which is the annealing condition to form n^+p junction by As^+ implantation. This method allows to verify the penetration depth of the damage generated by the ion implantation, and we will refer to diodes made by this method as damaged diodes. In the second procedure, n^+p and p^+n diodes were made by implantation of dopants at 25 keV with a dose of $2x10^{15}$ cm^{-2}. As^+, BF_2^+, P^+, and B^+ were implanted. Cz silicon substrates with (100) orientation and B concentration of the order of 10^{15} cm^{-3} were used to form n^+p diodes, and Cz silicon with (100) orientation and P concentration of the order of 10^{15} cm^{-3}, to form p^+n diodes. The diodes were square shaped, having an area of 1x1 mm^2. Post implantation annealing was made at the temperature range of 450℃ to 1000℃. The annealing time for each temperature was chosen in order to achieve the minimum sheet resistance of the implanted layers at this temperature. Diodes made by this method will be referred as conventional diodes.

RESULTS AND DISCUSSION

Figure 2 shows the leakage current density measured at 5 V for n^+p damaged diodes as function of the junction depth, with damage caused by As^+ [12]. It is seen that defects generated by the ion implantation penetrate at least down to 300 nm from the surface. This penetration depth is much larger than the projected range of the As^+ implanted at 25 keV, which is about 18.7 nm, and thus these defects should have extremely high mobility. It can be inferred that they are point defects that have, probably, agglomerated into clusters.

Someone would be led to conclude from Fig. 2 that the curve of the leakage current is also the depth profile of the defects, however this is not correct. In Fig. 3 it is shown the linear plot of the leakage current density as a function of the width of the space charge region in the damaged n^+p diode with junction depth of 180 nm. The observed linear increase, is not particular of this diode, but it is seen also in diodes with other junction depths. Thus the concentration of defects is almost constant through the whole bulk and not rapidly decreasing in depth. The seeming contradiction can be explained by the following model. The ion implantation generates a great amount of point defects at the region close to the surface, and as point defects are extremely mobile, they can reach even the wafer backside during the implantation. Clusters of point defects nucleate heterogeneously at the dopants present in the bulk, and these clusters cause the increase of the leakage current. In the damaged diodes there is a layer with high concentration of dopants at the surface, the pre-formed junction, that acts as a buffer for the flux of point defects, reducing the amount of point defects in the bulk, and thus lowering the concentration of the defects. As a consequence, damaged junctions with deeper junctions present lower leakage currents. We have previously reported that the leakage current of conventional n^+p and p^+n diodes annealed at 450℃ [12, 13] increases explosively when the substrate doping concentration increases. This result led us to conclude that dopant atoms act as nucleation centers of defects. From this model it becomes clear that the approach to lower the leakage current of diodes made by post-implantation annealing at low temperature is to reduce the amount of nucleated clusters of point defects.

The leakage currents in n^+p and p^+n damaged diodes with damaging implantation by As^+ and BF_2^+ are shown in Fig. 4-a and Fig. 4-b. In both, n^+p and p^+n damaged diodes, BF_2^+ degrades the junction more than As^+, indicating that the amount of defects generated during the implantation depends on the implanted species. It is also seen that defects penetrate more deeply in p^+n structures than in n^+p structures, which means that the concentration of defects depends also on the type of dopant present in the substrate, but this behavior will not be further detailed in this paper.

In order to evaluate the influence of each implanted species, p^+n damaged diodes with a

junction depth of 900 nm and with damaging implantation carried out by B^+, F^+, Si^+, P^+, and As^+ at 25, 35, 59, 68, and 146 keV, respectively, were made, all of them with a dose of $2x10^{15}$ cm^{-2}. All species were implanted with energies to attain projected ranges of about 83 nm. In this experiment no annealing was carried out after the damaging implantation. Figure 5 shows that F^+ degrades the junction more strongly than other ions, thus explaining why BF_2^+ degrades the junction more than As^+ does. It is noteworthy that in this experiment the damage caused by As^+ can not be directly compared with the damage caused by other ions because a too high implantation energy was necessary to achieve the projected range of 83 nm, causing much more defects than in other cases. This fact can be inferred from the fact that in the case of As^+ damaging implantation even the reference value is degraded, indicating that the masking APCVD oxide layer has been traversed. From Fig. 5 it can be concluded that n^+p junctions must be made by P^+ implantation instead of As^+ implantation, and that p^+n junctions must be made without implantation of fluorine into the junction to achieve the lowest leakage currents.

Figure 6 shows the leakage current density measured at a reverse bias of 5 V of conventional n^+p diodes made by As^+ and P^+ implantation in the cases with substrate doping concentrations of the order of 10^{15} cm^{-3} and 10^{16} cm^{-3} as a function of the annealing temperature. For both substrate doping concentrations it is seen that the leakage current density at 450℃ can be lowered by one order of magnitude for the case of P^+ implantation.

In the case of conventional p^+n diodes made at 500℃, it was observed that the leakage current density can be reduced from $4.64x10^{-8}$ A/cm^2, in the case of BF_2^+ implantation, down to $1.53x10^{-9}$ A/cm^2, in the case of B^+ implantation (Fig.7). However although a carrier concentration of the order of 10^{20} cm^{-3} is achieved for the case of BF_2^+ implantation (Fig. 8-a), this values is lowered to 10^{19} cm^{-3} in the case of B^+ implantation (Fig. 8-b) because the implanted layer could not be amorphized. In Fig. 8-b it is also shown the carrier profile of the sample with implantation of B^+ into a layer pre-amorphized by Si^+ down to 287 nm. In this case a carrier concentration of the order of 10^{20} cm^{-3} can be achieved. However, the implantation to pre-amorphize the silicon surface degrades strongly the junction and an annealing at 500℃ is not enough to recover the junction, resulting a leakage current density at 5 V as high as $3.06x10^{-2}$ A/cm^2 (Fig. 7). Thus, further improvements are still necessary to achieve simultaneously low leakage current and high activation of implanted dopants in p^+n diodes.

CONCLUSION

It was shown that the leakage current of n^+p and p^+n junctions made by post-implantation annealing at low temperature depends on the implanted species and on the type of the substrate. It is proposed that point defects are generated at the region close to the surface, and they penetrate

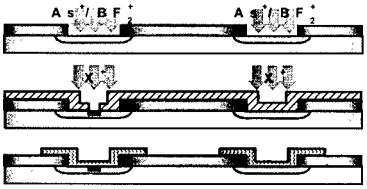


Fig. 1) Experimental procedure for the damaging implantation.

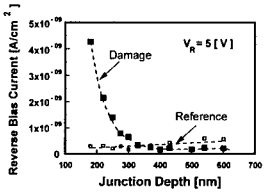


Fig. 2) Leakage current density measured at 5 V for n^+p damaged diodes, where As^+ was used as the damaging species, as function of the junction depth.

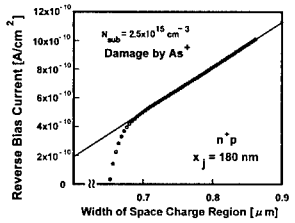


Fig. 3) Linear plot of the leakage current density as function of the width of the space charge region in damaged n^+p diode with junction depth of 180 nm damaged by As^+.

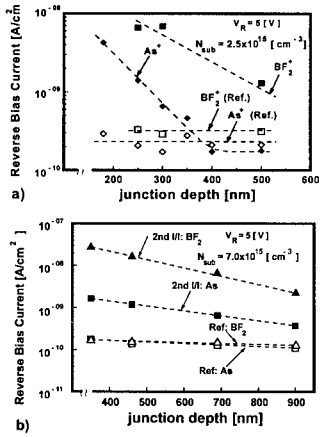


Fig. 4) Leakage currents in n^+p (a) and p^+n (b) damaged diodes with damaging implantation by As^+ and BF_2^+ as function of the junction depth.

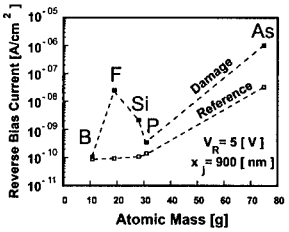


Fig. 5) Leakage current density measured at 5 V of p^+n damaged diodes with a junction depth of 900 nm with damaging implantation carried out by B^+, F^+, Si^+, P^+, and As^+.

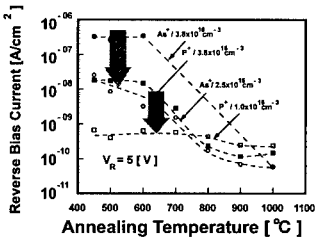


Fig. 6) Leakage current density measured at a reverse bias of 5 V of conventional n^+p diodes made by As^+ and P^+ implantation in the cases with substrate doping concentrations of the order of 10^{15} cm^{-3} and 10^{16} cm^{-3} as function of the annealing temperature.

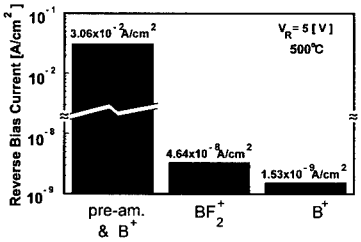
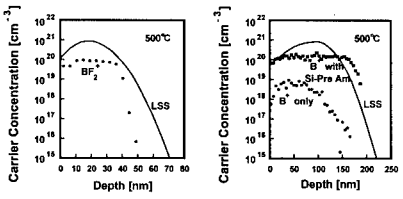


Fig. 7) Leakage current density at 5 V for conventional p^+n diodes made by implantation of B^+ into a layer of 287 nm pre-amorphized by Si^+, BF_2^+, and B^+, annealed at 500°C.



a) b)

Fig. 8) Depth profile of the carrier concentration for the case of BF_2^+ implantation (a), and B^+ implantation into a layer pre-amorphized and not-pre-amorphized by Si^+ implantation (b).

deeply into the Si. Substrate dopants act as centers for heterogeneous nucleation of point defect clusters. n^+p junctions made by P^+ implantation and p^+n junctions made by B^+, that cause less degradation, resulted leakage currents one order of magnitude lower than the counterparts made by implantation of As^+ and BF_2^+.

ACKNOWLEDGMENT

This study was carried out in the Super Clean Room of Laboratory for Electronic Intelligent Systems, Research Institute of Electrical Communication, Tohoku University.

REFERENCES

[1] L. Csepregi, E. F. Kennedy, T. J. Gallagher, and J. W. Mayer, J. Appl. Phys. **48**, 4234 (1977).

[2] H. Nishi, T. Sakurai, and T. Furuya, J. Electrochem. Soc. **125**, 461 (1978).

[3] A. E. Michel, F. F. Fang, and E. S. Pan, J. Appl. Phys. **45**, 2991 (1974).

[4] K. Tsukamoto, Y. Akasaka, Y. Watari, Y. Kusano, Y. Hirose, and G. Nakamura, Jpn. J. Appl. Phys. **17**, 187 (1987).

[5] E. Landi and S. Solmi, Solid-State Electron. **29**, 1181 (1986).

[6] Y. Wada and N. Hashimoto, J. Electrochem. Soc. **127**, 461 (1986).

[7] C. Carter, W. Maszara, D. K. Sadana, G. A. Rozgonyi, J. Liu, and J. Wortman, Appl. Phys. Lett. **44**, 459 (1984).

[8] K. S. Jone, S. Prussin, and E. R. Weber, J. Appl. Phys. **62**, 4114 (1987).

[9] T. Ohmi, Jpn. J. Appl. Phys. **33**, 6747 (1994).

[10] K. Kotani, T. Ohmi, S. Shimonishi, T. Mgita, H. Komori, and T. Shibata, IEICE Trans. Electrn. **E76-C**, 541 (1993).

[11] K. Tomita, T. Migita, S. Shimonishi, T. Shibata, T. Ohmi, and T. Nitta, J. Electrochem. Soc. **142(5)**, 1692 (1995).

[12] A. Nakada, M. M. Oka, Y. Tamai, T. Shibata, and T. Ohmi, J. Appl. Phys. **80(3)**, 1594 (1996).

[13] Y. Tamai, M. M. Oka, A. Nakada, T. Shibata, and T. Ohmi, to be presented at the ULSI Science and Technology - 191st Meeting of the Electrochem. Soc., May, 1997, Montreal, Quebec, Canada.

GETTERING OF FE BY ALUMINUM IN P-TYPE Cz SILICON

S.H. Ahn, S. Zhao, A.L. Smith, L.L. Chalfoun, M. Platero, H. Nakashima*, L.C. Kimerling
Materials Science and Engineering, Massachusetts Institute of Technology, Cambridge, MA, 02139. *Advanced Science and Technology Center for Cooperative Research, Kyushu University, Kasuga Fujuoka 816 Japan.

ABSTRACT

In this study, we investigate the gettering process of Fe in p-type Cz silicon after iron has been introduced at the solubility limit at 1000°C. Deep Level Transient Spectroscopy (DLTS) was used to measure [FeB], a fingerprint of [Fe_i], at the center of samples. The minority carrier diffusion length and lifetime were calculated from Electron Beam Induced Current (EBIC) measurements. The fact that [FeB] is proportional to the negative second power of the minority carrier diffusion length at the high [FeB] regime confirms that FeB donors are the dominant recombination centers limiting solar cell performance with high Fe contamination. By quenching after heat treatment, we can maintain and measure the kinetics and thermodynamics of gettering exclusively. The getter/silicon interface was studied by comparison of the gettering rates of molten Al at 620°C, 700°C, and 800°C, and iron silicide at 700°C. We model Fe gettering with respect to temperature, time, solubility and precipitate nuclei density. In the early stage of Fe gettering, the process is dominated by precipitate formation around oxygen precipitate nuclei. The precipitate density is estimated to be on the order of $5x10^8 cm^{-3}$. In later stages, Fe outdiffusion contributes to the [Fe_i] reduction. The early stage precipitation limits [Fe_i] reduction after short time to the solubility at the gettering temperature.

INTRODUCTION

Al is the standard backside contact for Si solar cells due to three advantages. First, it makes a good ohmic contact to p^- base material. Second, it alloys with Si at high processing temperatures to form a p^+ layer which generates backside field (BSF) effect to reduce minority carrier recombination velocity at the contact interface [1,2]. Third, it getters transition metals including Fe [3,4]. Even trace amounts of most transition metals, which are all too easily incorporated during solar cell processing, can degrade cell performance significantly by introducing carrier recombination centers into the silicon energy gap. The high diffusivity and moderate solubility of transition metals in silicon make silicon susceptible to transition metal contamination. The natural abundance of Fe makes it one of the most troublesome contaminants. It reduces the solar cell efficiency by pairing with boron in the p-type silicon base since the resultant FeB donor is an efficient recombination center. Gettering becomes quite important as contamination prevention is difficult and expensive.

Fe segregation in molten Al with respect to Si is expected to be high, but it has never been measured in a physical system, and its effectiveness in the presence of other competing getters is unknown. Therefore, it is very important to understand the complexity of gettering reactions. Fe gettering by Al depends on the initial conditions. Al effectively getters Fe at contamination levels less than or equal to the Fe solubility in Si at the annealing temperature, in the absence of other Fe trapping mechanisms such as microdefects, dislocations or grain boundaries [5-7]. For [Fe_i] at the equilibrium concentration relative to $FeSi_2$ precipitates in the bulk, which is most likely to be the case for solar grade Si as modeled by Tan, [Fe_i] is predicted to remain at the solubility level until

Mat. Res. Soc. Symp. Proc. Vol. 442 © 1997 Materials Research Society

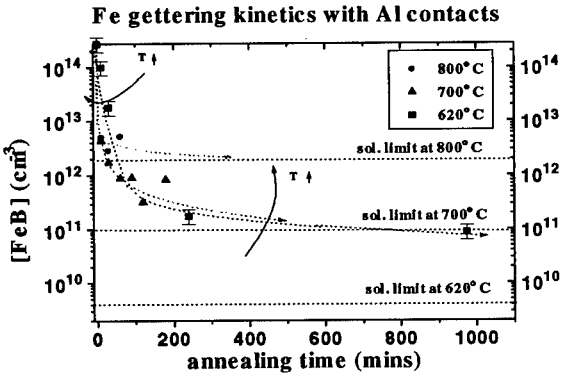


Figure 1 [FeB] in Fe-contaminated p-type Cz Si with Al contacts is plotted against annealing time at 800°C, 700°C, & 620°C.

complete dissolution of Fe precipitates while Fe outdiffuses to the Si/Al interface [8]. Our experimental study addresses the question of what kinetic mechanisms dominate Fe gettering with Al contacts when initial [Fe_i] is above its solubility. We used an idealized system of evaporated Al and p-type single crystalline Cz Si.

EXPERIMENTS

P-type Cz silicon with N_B=1.3x10^{15}cm^{-3} was used for the following experiments. Clean p-type Cz samples were treated with organic cleaning: ultrasonic in trichloroethane, acetone, and methanol for 10 minutes, respectively. Then, the samples were etched for 2 to 3 minutes in a solution of HNO_3 and HF mixed in 20:1. Immediately before the samples were mounted into an evaporation chamber, they received 5% dilute HF dip. Fe was evaporatively deposited on both sides of the samples under the vacuum level of 7.5x10^{-7} mbar. The samples with Fe on both sides were put into quartz tubes, which were evacuated and sealed. The sample in the quartz ampoule was hung in a vertical furnace, annealed at 1000°C for 2 hours to introduce Fe at the solubility limit and finally quenched into oil to preserve the dissolved [Fe].

Samples with two different gettering interfaces have been prepared: Al-contacts, and Fe-contacts. For the samples with Al contacts, Fe-deposited samples were stripped of Fe and iron silicide in a solution of HNO_3 and HF mixed in 10:1, and then 0.4 μm thick Al was evaporated on both sides of stripped samples after the stripped samples received the cleaning steps listed above. The samples with Al contacts were annealed in ampoules under vacuum at 620°C, 700°C, and 800°C for various time lengths and quenched into water. The samples with Fe contacts were annealed at 700°C the same way and quenched into water. Al Schottky contacts were deposited on the samples after they were mechanically polished down to the center. BioRad DL8000, Digitized Deep Level Transient Fourier Transform Spectroscopy, was used to measure [FeB]. This concentration is equal to [Fe_i] since Fe_i pairs with boron within 24 hours at room temperature after the heat treatment. Minority carrier diffusion length, a key parameter for solar cell performance, was measured by the EBIC technique.

RESULTS AND DISCUSSION

The initial [FeB] in Fe-contaminated samples before annealing was 2.7x10^{14}cm^{-3} by DLTS measurement. [FeB] vs. time in Figure 1 summarizes the time dependence of [Fe_i] with

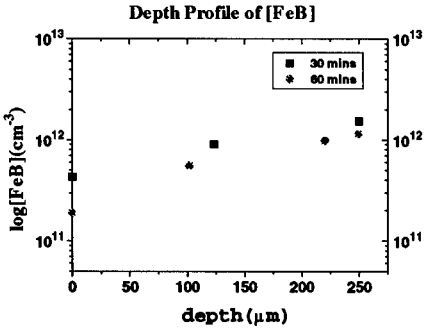


Figure 2 [FeB] in Fe-contaminated p-type Cz Si with Al contacts is plotted against the depth of the sample after annealing at 700°C for 30 and 60 minutes.

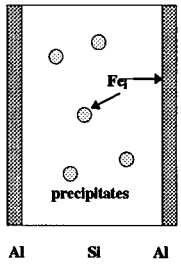


Figure 3 Fe_i can either precipitate around preferable sites or outdiffuse to the Si/Al interface.

Si/Al interface at 800°C, 700°C, and 620°C. Three regimes were observed for the annealing time periods used: 1) initial fast decay, 2) slow decay with varying rates, 3) asymptotic decay. In the first regime, the decay rate was the fastest of all annealing time periods and became faster with increasing temperature. In the second regime, the decay rate decreased gradually with annealing time. This transition regime from the first to the third regime was shortened with increasing temperature. In the third regime, [FeB] asymptotically approached a concentration that was higher with increasing temperature. At 800°C and 700°C, the residual [FeB] approached the solubility limit of Fe at the heat treatment temperature. The [FeB] at the surface after 60 minutes annealing at 700°C as shown in Figure 2 supports that [FeB] at the center would approach the [Fe_i] solubility limit. At 620°C, even though accurate evaluation requires longer annealing, the residual [FeB] seems to be reaching the solubility limit of Fe. In order to understand the mechanism controlling [Fe_i] in the initial fast decay regime, the exponential decay time constant, τ, was estimated from the initial slope of log [FeB] vs. annealing time at the heat treatment temperatures. The activation energy, E_a from a plot of τ vs. 1/T was 0.65eV. Since the migration energy for Fe_i is 0.68eV [9], an Fe diffusion-limited process is most likely responsible for the initial fast decay.

Two Fe diffusion-limited mechanisms available are possible precipitate formation and outdiffusion, as schematically shown in Figure 3. The dissolved Fe can heterogeneously nucleate precipitates at preferred sites. Fast heterogeneous nucleation allows the process to be diffusion-limited. The process time constant is approximated to follow Ham's law, equation (1), if heterogeneous nucleation by Fe is faster than Fe diffusion to the precipitates [10].

$$\tau_{ppt} = \frac{1}{4\pi(nr)_{ppt}D_{Fe}} \qquad (1)$$

where n_{ppt}, r_{ppt}, D_{Fe} are density and size of precipitates, and Fe diffusivity, respectively. The kinetics of outdiffusion are controlled by Fick's law. Considering only outdiffusion as the Fe gettering mechanism and the symmetric boundary conditions in Figure 3, one can analytically express [FeB] as an infinite series of the product of a Fourier cosine term and a time dependent exponential term. One needs the exact [Fe_i] at the Si/Al interface, $[Fe_i]_I$, to express [FeB] accurately. However, $[Fe_i]_I$ decreases with time, approaching the solubility as shown in Figure 2. Consequently, the rate estimated for Fe outdiffusion is maximized by setting $[Fe_i]_I$ to be the solubility of Fe, $[Fe_i]_{sol}$, for short time. We could reasonably assume $[Fe_i]_I$ was $[Fe_i]_{sol}$ for the purpose of comparing initial Fe gettering kinetics from the experimental data with that from

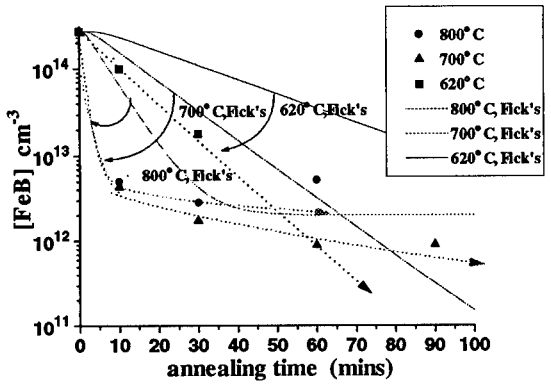


Figure 4 Both of [FeB]'s, experimental and Fick's law-governed, are plotted against annealing time at 800°C, 700°C, & 620°C.

Fick's law. Except for the very beginning of Fe gettering kinetics, one can describe [FeB] quite accurately with only the first cosine term until [FeB] at the center of sample gradually approaches the value at the boundary. Then, the time constant can be approximated as shown in equation (2).

$$\tau_d = \frac{\kappa \cdot (t_{si}/2)^2}{D_{Fe}} \qquad (2)$$

where $\kappa \approx 0.41$ and t_{si} is sample thickness. The Fe gettering kinetics data were compared with the plots of [FeB] vs. annealing time by numerical analysis of Fick's law in Figure 4, which showed that the decay slope of experimental data was greater than that of the Fick's law estimates for all three temperatures. This comparison indicates that initial fast decay is not due to outdiffusion. Both time constants for precipitates and outdiffusion are summarized in Table II. We model our kinetics by assuming that Fe precipitates heterogeneously around oxygen precipitate nuclei. The initial density and size of precipitates are estimated using fitted $\tau_{meas.}$ from log $\tau_{meas.}$ vs. 1/T , Ham's law and mass balance in Fe precipitate formation that equates the decrease in [FeB] with the increase in [$FeSi_2$]. $n_{ppt.}$ and r_{ppt} were estimated and summarized in Table I. The consistent values of n_{ppt} and r_{ppt} for three temperatures implies that the samples were identical and n_{ppt} was about $5x10^8 cm^{-3}$. This value is the same order of magnitude as the density of oxygen precipitate nuclei in single crystalline Cz Si. Therefore, heterogeneous Fe precipitate formation around oxygen nuclei reasonably accounts for the initial fast decay. The process is also consistent with the fact that [FeB] approaches the solubility limit of Fe at the heat treatment temperature for short term anneal. To observe the interface dependence of Fe gettering, samples with Fe contacts as well as Al contacts were annealed. It is shown that [Fe_i] loss with Fe contacts is faster than that

Table I Initial precipitate size & density at 620°C, 700°C, & 800°C

	$(nr)_{ppt}(cm^{-2})$	$r_{ppt}(nm)$	$n_{ppt}(cm^{-3})$
620°C	870	13	$6.6x10^8$
700°C	910	16	$5.7x10^8$
800°C	790	17	$4.6x10^8$

Table II precipitate vs. outdiffusion

620°C	$\tau_{meas.}$<10 min.	τ_d=22min.
700°C	$\tau_{meas.}$<2.4 min.	τ_d=10min.
800°C	$\tau_{meas.}$<2.5 min.	τ_d=5 min.

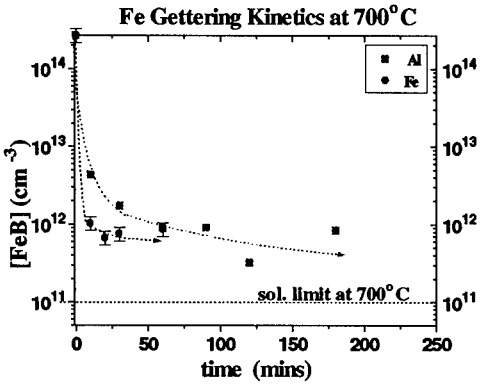


Figure 5 [FeB] in Fe contaminated p-type Cz Si are plotted against annealing time at 700°C for Fe and Al contacts

with Al contacts in Figure 5. A possible explanation is that near interface outdiffusion of Fe is faster with Fe contacts than with Al contacts. Supersaturated Fe at the interface can immediately precipitate without a nucleation barrier. However, Fe at the Si/Al interface may experience a "barrier" to segregation to Al layer as indicated by the slower Fe_i loss kinetics. The fact that [FeB] at the interface gradually decreases with annealing time, while still above the solubility limit at the annealing temperature as shown in Figure 2, also supports the existence of a "barrier" to segregation to Al. The presence of an Fe concentration gradient after 30 and 60 minutes annealing is evidence of the occurrence of outdiffusion in the second regime.

It is of great interest how much the minority carrier diffusion length is improved by Fe gettering with Al contacts. One can analytically correlate [FeB] with the minority carrier diffusion length in equation (3) assuming [FeB] is the dominant recombination center.

$$[FeB] \approx \frac{D_e}{\sigma_e < v_e >} L^{-2} \qquad (3)$$

where σ_e, v_e, D_e, and L_e are capture cross-section, electron velocity, electron diffusivity, and minority carrier diffusion length, respectively. Log L_e corresponds with log[FeB] with a negative two slope in the high [FeB] regime of Figure 6. It deviates from the correspondence in the low [FeB] regime with L_e being lower than that given by equation (3). L_e improvement with the reduction of [FeB] in the high [FeB] regime shows that FeB is the dominant carrier recombination center and that precipitated Fe is not so electrically active in the recombination process. In the low [FeB] regime, other recombination centers can be dominant or at least

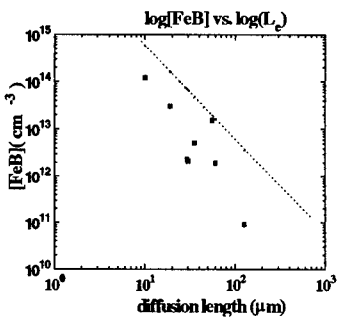


Figure 6 log[FeB] vs. L_e. The dotted line is a plot for only FeB recombination centers with $\sigma_e = 5 \times 10^{-15} cm^2$ & $N_{boron} = 1.3 \times 10^{15} cm^{-3}$

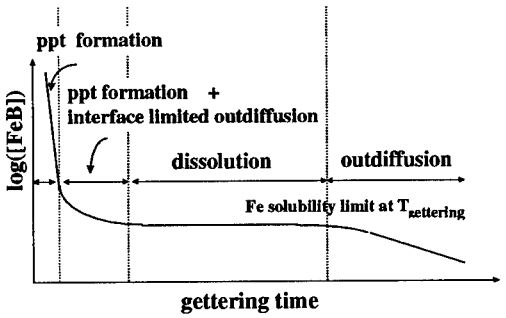


Figure 7 Schematic of Fe gettering kinetics in p-type Cz Si with Al contacts: this study shows that the first regime is dominated by Fe precipitate formation around oxygen precipitate nuclei and the second regime is governed by both Fe precipitate formation and interface-limited outdiffusion.

comparable with FeB since L_e is either independent of [FeB] or improves at a slower rate with decrease in [FeB].

CONCLUSIONS

Fe gettering kinetics in intentionally Fe-contaminated p-type Cz single crystalline Si with Al contacts has been studied. Fe predominantly precipitates around bulk oxygen precipitate nuclei in the initial stage of annealing and then diffuses to the Si/Al interface. FeB is the dominant recombination center in the high [FeB] regime and other recombination centers become significant in the low [FeB] regime. Finally, [Fe_i]-dependent Fe gettering kinetics with Al contacts are schematically summarized in Figure 7.

ACKNOWLEDGEMENT

This project has been supported by National Renewable Energy Laboratory (NREL). Authors are grateful for NREL sponsorship.

References

1. M.P. Godlewski, C.R. Baraona, H.W. Brandhorst, Jr., "Low-high junction theory applied to solar cells," *10th IEEE Photovoltaic Specialists Conf.*, Palo Alto, California (1973), pp. 40-47
2. J. Mandelkorn and J.H. Lamneck, Jr., "A new electric field effect in silicon solar cells," J. Appl. Phys., **44**, 10 (1973), pp. 4785-4787
3. P. Sana, J. Salami and A. Rohatgi, IEEE Transactions on Electron Devices **40**, p. 1461 (1993)
4. M. Apel, I. Hanke, R. Schindler and W. Schroter, J. Appl. Phys. **76**, p. 4432(1994)
5. S.M. Joshi, U.M. Gosele and T.Y. Tan, J. Appl. Phys. **77**, p. 3858(1995)
6. S.A. McHugo, H. Hieslmair and E.R. Weber, in Defects in Semiconductors 18, International Conference on Defects in Semiconductors, edited by M. Suezawa and H. Katayma-Yoshida, Sendai, Japan, 1995, p. 1979
7. H. Hieslmair, S. Mchugo, and E. Weber, 6th Workshop on the Role of Impurities and Defects in Silicon Device Processing, Snowmass, Colorado, Aug. 12-14, 1996, p. 210
8. T.Y. Tan, R. Gafiteanu, U. Gosele, 6th Workshop on the Role of Impurities and Defects in Silicon Device Processing, Snowmass, Colorado, Aug. 12-14, 1996, p. 116
9. G. Klaus, *Metal Impurities in Silicon-Device Fabrication, Springer Series in Materials Science 24*, Springer-Verlag, 1995, p. 67
10. F.S. Ham, J. Phys. Chem. Solids **6**, p. 335 (1958)

EFFECTS OF GETTERING ON DEVICE CHARACTERISTICS

Mitsuhiro Horikawa, Akihiko Yaoita, Tsuyoshi Nagata and Tomohisa Kitano
ULSI Device Development Laboratories, NEC Corporation,
1120 Shimokuzawa, Sagamihara, Kanagawa 229, Japan

ABSTRACT

Effective methods of gettering metallic impurities were proposed. To achieve effective gettering, an annealing process to induce gettering was modified taking fundamental gettering steps and the difference in the gettering mechanism into account. As the concentration of heavy metal is below solubility in a state-of-the-art clean room, a combination of segregation type gettering and slow cooling heat treatment is an effective technique to remove metal impurities from the device active region. Using this technique, DRAM device characteristics such as leakage current and data retention time can be improved.

INTRODUCTION

It is well known that metallic impurities introduce generation-recombination (GR) centers within the band gap. The GR centers increase the junction leakage current. The reduction of junction leakage current is necessary in achieving 256 M and 1 G bits DRAMs. Therefore, it is important to suppress or eliminate GR centers in silicon wafers.

Gettering is a useful technique to remove GR centers in the device active regions. There are two types of gettering techniques which are widely used in silicon-device fabrication. One is using poly-silicon back seal (PBS) wafers [1], and the other is using DZ-IG wafers whose getter sites are closer to the device active region than those of PBS wafers [2]. Gettering mechanisms can be divided into two categories, labeled relaxation type gettering and segregation type gettering [3, 4]. PBS employs segregation type gettering, and DZ-IG employs relaxation type gettering. In the relaxation type, gettering occurs when the concentration of metallic impurities exceeds the solubility at temperature. On the other hand, in the segregation type, the gettering depends not on supersaturation, but rather on the partitioning coefficient of the metal between the device region and the gettering layer.

Some transition metals, e.g. Fe, are easily gettered at the LOCOS edge, which increases the junction leakage current [5]. Therefore, to reduce junction leakage current, metallic impurities must be gettered at not LOCOS edge but gettering layer. In real device fabrication processes, the gettering process involves three steps ; the first step is the release of metallic impurities from its associated form, the second step is the diffusion of metallic impurities to the gettering region, and the third step is the capture of defects at the gettering sites [6, 7].

In this study, an annealing process to induce gettering was modified taking these three gettering steps and the difference in the gettering mechanism into account. This study also demonstrates the effectiveness of using modified annealing, to reduce junction leakage and to improve data retention time characteristic.

EXPERIMENT

Junction leakage current was evaluated using an n^+/p diode, with a size of 32 mm^2. A junction was isolated by LOCOS. In leakage current evaluation, two types of junctions were evaluated to investigate the effect of the release process of impurities from the LOCOS edge. One junction has 4 factors of perimeter to area ratio (P/A), and the other has 400 factors. Data retention time characteristics were examined using DRAM devices with conventional planar capacitors.

The starting material used in all experiments was CZ-grown , <100>-oriented Si, 150 mm in diameter, with a thickness of 675 μm. A PBS, A DZ-IG, and N-IG wafers were used in this study. The PBS wafer had poly-silicon film of 1 μm thickness on the back. The DZ-IG wafer received high-temperature annealing followed by low-temperature annealing to form oxygen precipitates. The N-IG wafers which do not have gettering ability were annealed to annihilate thermal donors. In addition, to evaluate junction leakage, a PBS wafer with a grown float zone (FZ) was

Mat. Res. Soc. Symp. Proc. Vol. 442 © 1997 Materials Research Society

examined.

In the test device fabrication processes, the annealing for gettering was treated between contact window formation and the metallization processes. Figure 1 shows the annealing processes for gettering which were used in this study. Two types of processes were used. In the conventional process, wafers were unloaded from a furnace at the maximum temperature and were quickly cooled. In the slow-cooling process, to achieve efficient diffusion and capture processes, wafers were slowly cooled down to 600 ℃ in a furnace and unloaded. The maximum temperatures corresponding to the release process of impurities were the same in both conventional and slow-cooling processes. For both leakage current and data retention time evaluations, the effects of a conventional and a slow-cooling on device characteristics were compared. The maximum temperatures of annealing for gettering in the leakage current and data retention time evaluations were 900 ℃ and 850 ℃, respectively. In addition, for data retention time evaluation, two conventional processes were evaluated to investigate the effect of the diffusion process of impurities. One had 10 minutes of maximum temperature, the other had 70 minutes.

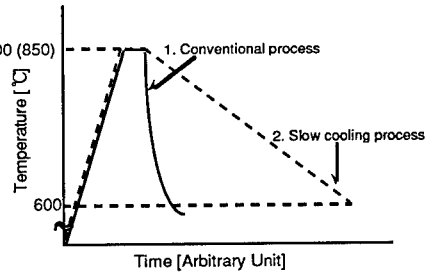


Fig. 1 Annealing processes for gettering

RESULTS

LEAKAGE CURRENT EVALUATION

Figure 2 shows the junction leakage current characteristics after the conventional process. There are no notable differences between the characteristics of the PBS, DZ-IG, and N-IG wafers.

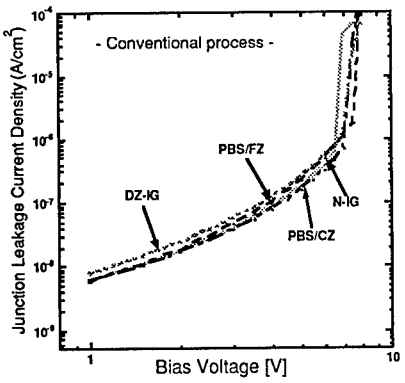


Fig. 2 Junction leakage current characteristics. Annealing for gettering was carried out by a conventional process.

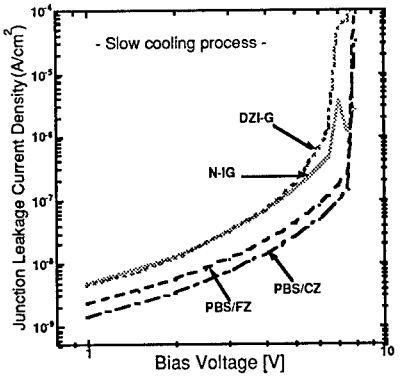


Fig. 3 Junction leakage current characteristics. Annealing for gettering was carried out by a slow-cooling process.

The leakage current characteristics after a slow-cooling process are shown in Fig. 3. The leakage current reduced when the PBS wafer was used, but it did not reduce when DZ-IG and N-IG wafers were used. It is assumed that the metal impurity concentration was below solubility in the Si wafer, so that gettering efficiency is insufficient for DZ-IG wafers whose gettering mechanism is of the relaxation type. On the other hand, gettering efficiency is sufficient for PBS wafers because the gettering mechanism is of a segregation type which can capture metal impurities below solubility.

Figure 4 shows the leakage current characteristics of different P/As. After the conventional process, there was no dependency on P/A. When the slow-cooling process was applied, the leakage current was reduced in both P/A, however, the leakage current of small P/As was greatly reduced. This result indicates that the leakage current is increased by the LOCOS structure. One possible reason is that maximum temperature of annealing for gettering is insufficient to release metal impurities from the LOCOS edge. Another possible reason is that the capture process by the LOCOS edge is as effective as that of a PBS wafer.

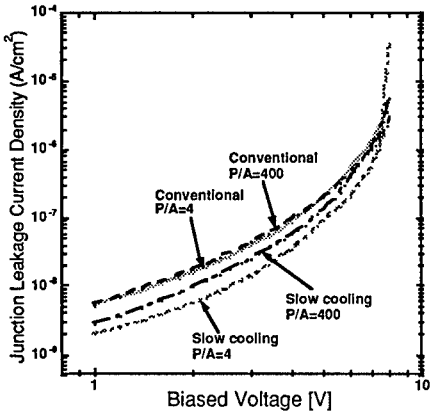


Fig. 4 Dependency of junction leakage current characteristics on perimeter to area ratio (P/A). All wafers in this figure are PBS wafers.

EVALUATION OF DATA RETENTION TIME CHARACTERISTICS

The retention time distribution can be divided into two regions: "majority distribution" and "minority distribution". The retention time of almost all memory cells belongs to "majority distribution", and "majority distribution" was dominated by G-R current at the LOCOS edge [8].

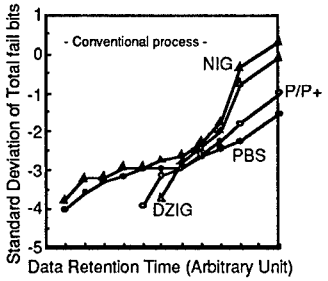


Fig. 5 DRAM data retention time characteristics. Annealing for gettering was carried out by a conventional process.

Figure 5 shows the data retention time characteristics after the conventional process. The p/p^+ material was examined as a reference sample. When we looked into the number of memory cells which belonged to "majority distribution", the leakage current of PBS and p/p^+ wafers was smaller than those of DZ-IG and N-IG wafers. The gettering mechanism of these wafers is the segregation type. Figure 6 shows the effectiveness of the slow-cooling process for gettering. When DZ-IG wafers were used, the slow-cooling process had no effect on gettering. However, when PBS wafers were used, leakage current was reduced. This is the same reason as that for junction leakage current reduction.

To reconfirm the effects of diffusion length of impurities on data retention time characteristics, the maximum temperatures length in the conventional process was varied. The time dependence for

effective gettering by the conventional process is shown in Figure 7. Significant reduction in the leakage current occurred for 70 minutes of maximum temperature over the process with 10 minutes of annealing.

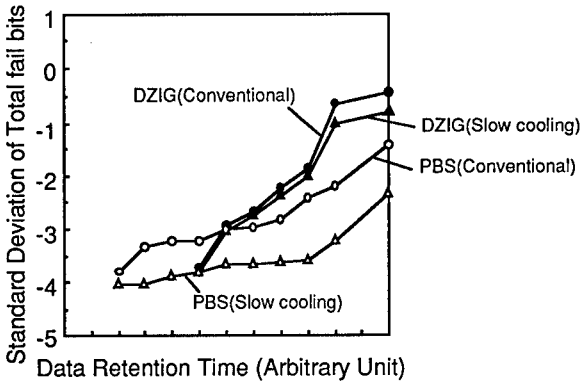


Fig. 6 Effects of annealings for gettering on DRAM data retention time characteristics.

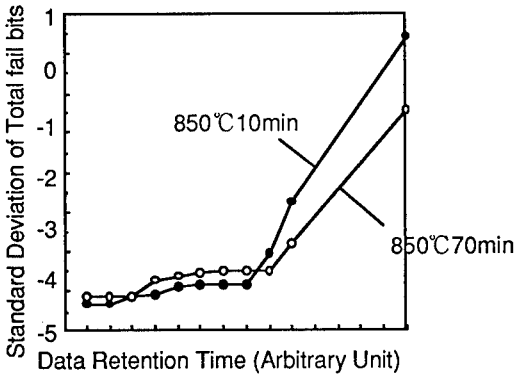


Fig. 7 Effect of maximumtemperature length on DRAM data retention time characteristics. The length in conventional process was varied to 10 minutes and 70 minutes. PBS wafers were used for this evaluation.

CONCLUSION

Effective methods of gettering metallic impurities were proposed and studied. As the concentration of heavy metal is below solubility in state-of-the-art clean rooms, a combination of segregation-type gettering and slow cooling heat treatment is an effective technique to remove metal impurities from device active regions. Using this technique, device characteristics such as leakage current and the data retention time of DRAMs can be improved.

In addition, the slow-cooling process revealed that leakage current is increased by the LOCOS structure. For more effective gettering, it is necessary to raise the maximum temperature of slow-cooling so that it is sufficient to release metal impurities from the LOCOS edge.

ACKNOWLEDGMENTS

The authors are grateful to Tatsunori Murotani, Yoshonori Muramatsu, and Koujiro Matsui for their help in the evaluation of DRAM data retention time characteristics. The authors would also like to thank Drs. Osamu Mizuno, Kenji Okada, and Kazuko Ikeda for their encouragement.

REFERENCES

[1] M. C. Chen and V. J. Silverstri, J. Electrochem. Soc. 129, 1294 (1982)
[2] K. Nagasawa, Y. Matsushita, and S. Kishino, Appl. Phys. Lett. 37, 622 (1980)
[3] D. Gilles, in Defect Engineering in Semiconductor Growth, Processing and Device Technology, edited by S. Ashok, J. Chevallier, K. Sumino, and E. Weber, MRS Symposia Proceedings Vol. 262 (Material Research Society, Pittsburgh, 1992) p. 917.
[4] K. Graff, in Metal Impurities in Silicon-Device Fabrication, Springer Series in Materials Science Vol. 24 (Springer-Verlag, New York 1995) p. 164
[5] A. Ohsawa, K. Honda, R. Takizawa, T. Nakanishi, M. Aoki, and N. Toyokura, in Semiconductor Silicon 1990, edited by H. R. Huff, K. Barracclough, and J. Chikawa, Proceedings of The Electrochemical Society (The Electrochemical Society, Pennington, 1990) p. 601
[6] H. R. Huff, Solid-State Technol. 26, 211 (1983)
[7] J. S. Kang and D. K. Schroder, J. Appl. Phys. 65, 2974 (1989)
[8] T. Hamamoto, S. Sugiura, and S. Sawada, in Proceedings of IEEE, Int. Elecron Devices Meeting, p. 915 (1995)

COMPARISON OF GETTERING ABILITY BETWEEN I/I DEFECTS AND Si SUBSTRATE

Mitsuhiro Horikawa and Tomohisa Kitano
ULSI Device Development Laboratories
NEC Corporation, 1120, Shimokuzawa, Sagamihara, Kanagawa 229, Japan

ABSTRACT

A Si wafer is contaminated with 1.5 X 10^{13} Fe/cm^3 and the Fe gettering ability of low dose I/I defects is compared with that of a Si substrate with/without a poly-silicon back seal. Poly-silicon has higher gettering ability than I/I defects and prevents Fe from gettering at these defects. When there is no poly-silicon and temperature is as low as 700℃, however, I/I defects act as gettering sites for Fe, even if the dose is as low as 2 X 10^{13} cm^{-2}. Fe gettering by I/I defects leads to a decrease in minority carrier diffusion length. DLTS measurement reveals that Fe getters at I/I defects in the interstitial atom state.

INTRODUCTION

The reduction of junction leakage current is necessary in achieving 256 M and 1 G bits DRAMs. Gettering technology is very effective in reducing junction leakage current [1] and fundamental gettering properties have been investigated by many researchers [2, 3, 4, 5]. However, these investigations were conducted without taking account of the defects induced by device fabrication processes, for example, ion implantation. It is necessary that these defects recover and don't act as new gettering sites to induce generation-recombination current in the depletion region. Instead, these process-induced defects must be recovered without gettering the metal contaminant.

In this study, the Fe gettering ability of defects induced by ion implantation, that is, I/I defects, was compared with that of a Si substrate with/without a poly-silicon back seal [3]. The surface photo-voltage (SPV) method [6] and deep level transition spectroscopy (DLTS) [7] were applied to this study. The dose of I/I was as low as 2X10^{13} cm^{-2} corresponding to the dose for the node formation of DRAMs. We show that Fe was gettered at the low dose I/I defects as interstitial Fe (Fe_i) when there was no poly-silicon back seal. However, when there was a poly-silicon back seal, Fe was not gettered at I/I defects.

EXPERIMENT

The experimental procedure is shown in Fig. 1. Two kinds of 150-mm-diameter wafers (675-μm thick, B-doped, 10~15 Ω cm) were used, one was the PBS(poly-silicon back seal) wafer for external gettering [2] and other was a wafer with no gettering site, that is, an NG wafer. The poly-silicon thickness was 1 μm. The front surfaces of both wafers were contaminated with Fe of 1X10^{12} cm^{-2} using spin coating [8]. The wafers received heat treatment at 1000℃ for 1 hr in dry oxygen and were quenched to uniformly contaminate the entire wafer at 1.5X10^{13} cm^{-3}. After Fe contamination, Si^+ ions were implanted only into the 125-mm-diameter region of the wafers at 50 keV at a 2X10^{13} cm^{-2} dose. The samples were annealed at 700, 800, 900, and 1000℃ to induce gettering. The effective diffusion length of Fe was 675 μm at each temperature.

Mat. Res. Soc. Symp. Proc. Vol. 442 © 1997 Materials Research Society

When I/I defects do not recover enough, there are two types of gettering sites (I/I defects and poly-silicon) in the PBS wafer and one type of gettering site (I/I defects) in the NG wafer. When there are no I/I defects, Fe in B-doped Si has at least three different types of impurity state : Fe_i, Fe_i-B pairs and precipitations. At room temperature and [B] > 10^{14} cm^{-3}, all Fe is bound in Fe_i-B pairs.

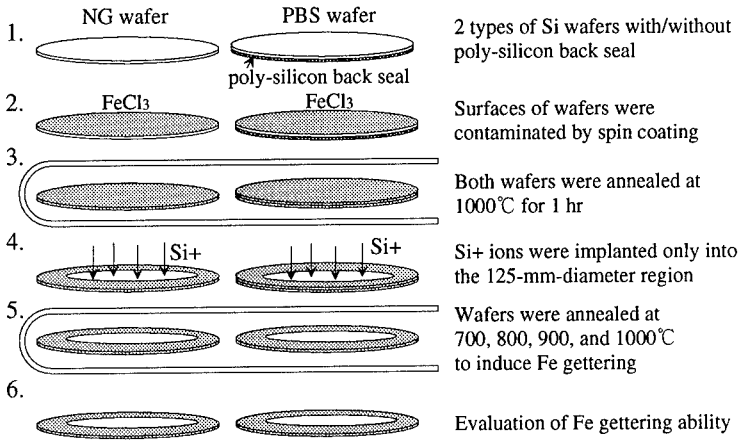


Figure 1. Experimental procedure

In this study, we assumed that the I/I defects, which gettered Fe, produced new Fe related levels and/or reduced [Fe_i-B] (Fe_i-B pair concentration) around themselves, so that the minority carrier diffusion length in the implanted region is different from that in the un-implanted region. Therefore, the gettering ability of I/I defects and poly-silicon was investigated by evaluating the minority carrier diffusion length and the Fe-related levels.

The minority carrier diffusion length was measured by the SPV method. It is well known that the dissociation reaction

$$Fe_i\text{-}B \rightarrow Fe_i^{+} + B^{-}$$

is almost complete after annealing at 210℃ followed by quenching on an Al plate. [Fe_i-B] may be determined by the difference in minority carrier diffusion length before and after 210℃ annealing. This is because the dissociation reaction induces a reduction in minority carrier diffusion length. The Fe-related levels were investigated by DLTS, using the evaporated Al layers as Schottky contacts.

RESULTS

Figure 2 shows the minority carrier diffusion length of the PBS wafer before thermal dissociation of Fe_i-B pairs. The diffusion length after annealing at 700℃ is longer than those at other temperatures. This result indicates that Fe gettering was well induced at 700℃, so that Fe concentration decreased. No differences in minority carrier diffusion length were obtained between the implanted region and the un-implanted region.

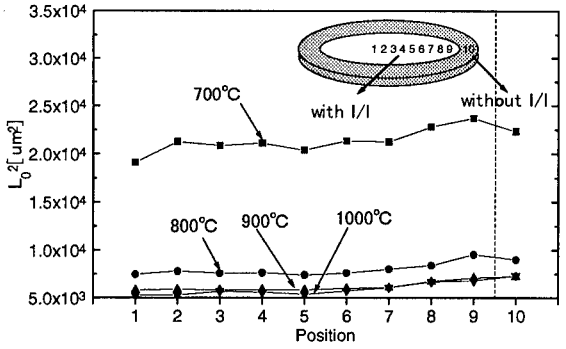


FIG. 2 Minority carrier diffusion length of PBS wafer before thermal dissociation of Fe_i-B pairs. Positions 1-9 indicate the implanted regions, number 10 indicates the un-implanted region.

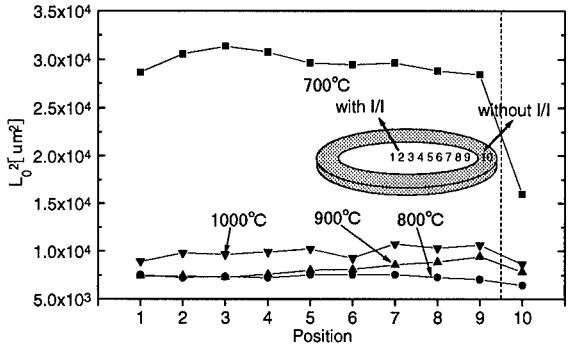


FIG. 3 Minority carrier diffusion length of NG wafer before thermal dissociation of Fe_i-B pairs. Positions 1-9 indicate the implanted regions, number 10 indicates the un-implanted region.

The minority carrier diffusion length of the NG wafer before the thermal dissociation reaction are shown in Fig. 3. The diffusion length of the implanted region after annealing of 700℃, as well as the length of the PBS wafer, is longer than those at other temperatures. However, the diffusion length of the un-implanted region is not as long. This shows that the Fe gettering process was only induced in the implanted region, and that [Fe_i-B] around the I/I defects was reduced. Therefore, we next estimated [Fe_i-B] by the SPV method.

Figure 4 shows the [Fe_i-B] after 700℃ and 800℃ annealing. [Fe_i-B] in the PBS wafer was lower than that in the NG wafer. This result indicates that poly-silicon is effective for Fe gettering. After annealing, both the PBS and NG wafers at 800℃, no differences in [Fe_i-B] could be detected between the implanted and un-implanted regions. These results suggest that Fe was not gettered at the I/I defects after 800℃ annealing. When the samples were annealed up to 1000℃, similar results were obtained.

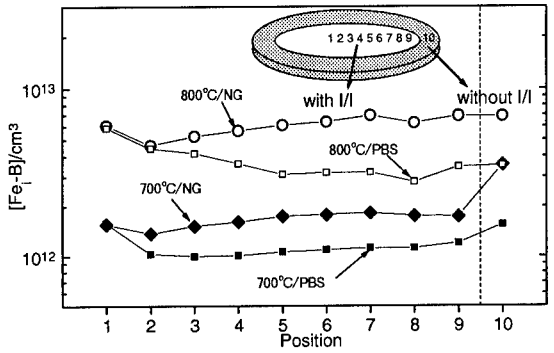


FIG. 4 Concentration of Fe_i-B pairs measure by the SPV method. Positions 1-9 indicate the implanted regions, number 10 indicates the un-implanted region.

After annealing at 700℃, differences in [Fe_i-B] could also not be detected between the implanted region and un-implanted region of the PBS wafer. However, in the NG wafer, [Fe_i-B] was lower in the implanted region than the un-implanted region. Also, [Fe_i-B] in the implanted region after 700℃ annealing was lower than that after 800℃ annealing. These results suggest that the gettering ability of poly-silicon is higher than that of the I/I defects. However, when there was no poly-silicon, Fe was gettered at the I/I defects.

The Fe state gettered at I/I defects in the NG wafer was investigated in more detail, using the DLTS technique. Figures 5(a) and (b) show the DLTS signal obtained from the un-implanted region and the implanted region. There was one peak at 58.9K (H1) in the un-implanted region. In addition, another peak was detected at 250K (H2) in the implanted region. Next, we measured the depth profiles of these peaks. The depth profiles of H1 and H2 are shown in Fig. 6. H1 was detected even in a deep bulk as well as in the subsurface. On the other hand, H2 could only be detected in the sub-surface of the wafer. These results indicate that the peak at 250K was produced by the I/I defects which gettered Fe.

In order to identify the peaks obtained from this study, the thermal emission characteristics were measured as shown in Fig. 7. These measurements were taken at a series of

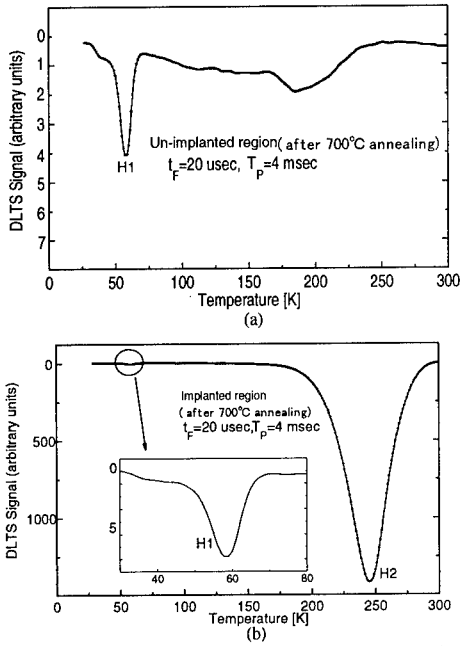


FIG. 5 (a) DLTS traces obtained from un-implanted region of NG wafer. (b) DLTS traces obtained from implanted region of NG region. T_p means the frequency of filling pulse, and t_F means the width of filling pulse.

fixed temperatures under constant capacitance conditions. The activation energy and the hole capture cross-section of each peak obtained are shown in Table 1. The peak at 250K (H2) was so broad, that it was analyzed as two peaks (H21 and H22) which were convoluted by fitting.

Table 1. Activation energy and hole capture cross-section of each peak.

Defect	E_a (eV)	σ (cm^2)
H1	$E_v + 0.087$	2.5×10^{-15}
H21	$E_v + 0.27$	1.7×10^{-18}
H22	$E_v + 0.38$	6.2×10^{-17}

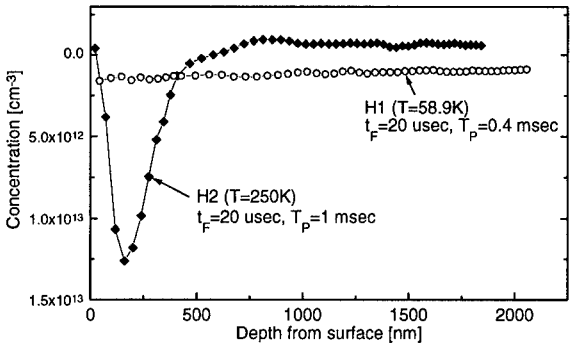


FIG. 6 Depth profiles of H1 and H2 in implanted region of NG wafer. T_P means the frequency of filling pulse, and t_F means the width of filling pulse.

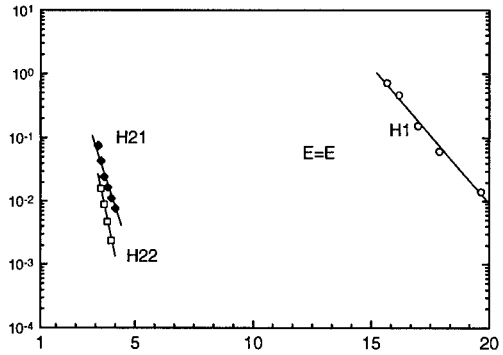


FIG. 7 Thermal emission rates for hole traps obtained from the indicated levels.

The activation energy and the hole capture cross section of H1 agreed with those of Fe_i-B pairs in previous work [9]. H21 has not yet been identified, however, the activation energy and hole capture cross-section of H22 agreed with those of the Fe_i obtained by S. D. Brotherton et al. [10]. This result led to the conclusion that a part of Fe was gettered at the I/I defects as Fe_i.

CONCLUSION

A Si wafer was contaminated with 1.5 X 10^{13} Fe/cm^3 and the Fe gettering ability of low dose I/I defects was compared with that of a Si substrate with/without a poly-silicon back seal. Poly-silicon had higher gettering ability than I/I defects and prevented Fe from gettering at I/I defects. When there was no poly-silicon and temperature is as low as 700℃, however, I/I defects acted as gettering sites for Fe, even if the dose was as low as 2 X 10^{13} cm^{-2}. Fe gettering by I/I defects led to a decrease in minority carrier diffusion length. DLTS measurement revealed that Fe was gettered at I/I defects in the interstitial atom state.

ACKNOWLEDGMENT

The authors would like to thank Drs. Osamu Mizuno, Kenji Okada and Kazuko Ikeda for their encouragement.

REFERENCES

[1] R. W. Gregor and W. H. Stinebaugh, Jr., J. Appl. Phys., 64, 2079 (1988)
[2] D. Gilles, E. R. Weber, and S. Hahn, Phys. Rev. Lett., 64, 196 (1990)
[3] Y. Hayamizu, S. Ushio, and T. Takenaka, in MRS Symposia Proceedings Vol. 263 (1992) p. 1005.
[4] M. Aoki, A. Hara, and A. Ohsawa, J. Appl. Phys. 72, 895 (1992)
[5] S. Sano, S. Sumita, T. Shigematsu, and N. Fujino, in Semiconductor Silicon/1994, Proceedings of The Electrochemical Society, edited by H. R. Huff, W. Bergholz, and K. Sumino (The Electrochemical Society, Pennington, 1994), p. 784
[6] G. Zoth and W. Bergholz, J. Appl. Phys., 67, 6764 (1990)
[7] D. V. Lang, J. Appl. Phys. 45, 3023 (1974)
[8] M. Hourai, T. Naridomi, Y. Oka, K. Murakami, S. Sumita, N. Fujino and T. Shiraiwa, Jpn. J. Appl. Phys. 27 (1988) L2361
[9] J. L. Benton and L.C. Kimerling, J. Electrochem. Soc. 129, 2098 (1982)
[10] S. D. Brotherton, P. Bradley, and A. Gill, J. Appl. Phys. 57, 1941 (1985)

DARK CURRENT SPECTROSCOPY OF METALS IN SILICON

WILLIAM C. MCCOLGIN, JAMES P. LAVINE, AND CHARLES V. STANCAMPIANO
Eastman Kodak Company, Microelectronics Technology Division,
Rochester, NY 14650-2008

ABSTRACT

Dark current spectroscopy (DCS) is used to identify the signature of metals that generate dark or leakage current in silicon image sensors. Individual metal atoms or defects are detected by DCS on a pixel-by-pixel basis. DCS is applied here to show how the number of electrically active iron atoms in a pixel changes with light and with low-temperature anneals. The measurements explore the dissociation and association of iron-boron pairs and the diffusion of iron near room temperature.

INTRODUCTION

Iron continues to be a concern for silicon devices and investigations of its concentration and gettering are moving to ever lower levels of iron in silicon [1]. Charge-coupled devices (CCDs) are excellent vehicles for the investigation of electrically active defects that result from silicon device processing. Dark current spectroscopy (DCS) is used to identify the signature of metals in silicon that generate dark or leakage current [2]. Individual metal atoms or defects are detected by DCS at concentrations of the order of $1 \times 10^9/cm^3$. DCS permits the study of metals such as iron at low concentrations and near room temperature. This provides the opportunity to gather more information on the behavior of iron in silicon. In this work, metals are introduced by controlled process-induced contamination. Substitutional gold and interstitial iron are identified on the basis of a comparison of the measured temperature-dependent dark current generation rates with data in the literature [2-3]. The dissociation of iron-boron pairs with a strong visible light source [4] is observed, since the DCS shows additional dark current from the liberated interstitial iron. Iron is of particular interest, because earlier work has shown it is capable of producing imager defects [2-3,5-6].

The image sensor provides dark current values, which can be stored, with a spatial resolution of one pixel. This permits the determination of local changes in the dark current due to events such as light illumination or an anneal. This enables the monitoring of the number of electrically active iron atoms in a pixel as a function of the process step and of time.

Mat. Res. Soc. Symp. Proc. Vol. 442 ©1997 Materials Research Society

The following presents several examples of the movement of iron and its association with and dissociation from boron [4]. The technique of dark current spectroscopy (DCS) is first described. Then the experimental results are presented and discussed. Finally, future directions for this research are outlined.

DARK CURRENT SPECTROSCOPY

When the dark current sources in an image sensor are reduced through proper design and operating conditions, the contributions of deep level traps in the imager are revealed. These traps can be studied by integrating the imager for long periods of time in the dark and forming a histogram from the image of the pixel dark current. The histogram shows the number of pixels with given dark current levels and a sample histogram, which is based on 185,000 pixels, is presented in Figure 1. Histograms with quantized dark current were first seen by McGrath et al. [7]. Previous work [2] leads us to identify the successive peaks as due to pixels with no electrically active iron atoms, with one electrically active iron atom, with two, with three, and with four, respectively. However, one gold atom generates with a rate approximately equal to that for three iron atoms. Curve-fitting may be used to see if gold is present. Generally, the number of pixels with a given number of specific metal atoms, such as iron atoms, follows a Poisson distribution [2]. In fact, the deviations from the Poisson distribution may indicate a second metal is present as in the case of iron and gold. The horizontal scale in Figure 1, and in the subsequent figures, indicates the number of electrically active iron atoms in a pixel. The quantized dark current peaks in the histograms enable one to follow the number of iron atoms in a pixel as a function of anneals or illumination. The histograms are captured at 55^0C and the dark current comes from the imager's photodiodes. At 55^0C, one electrically active interstitial iron atom generates at the rate of 213 electrons/s.

EXPERIMENTAL RESULTS

The first results show what happens during a 4.5 hour anneal at 55^0C. Figure 1 is the histogram before the anneal, while Figure 2 is the histogram after the anneal. Estimates based on the peak heights suggest there are 1.2 iron atoms per pixel. The histograms are quite similar, which suggests that nothing has changed, but a pixel-by-pixel comparison in Figure 3 shows otherwise. This figure is a correlation plot and it uses

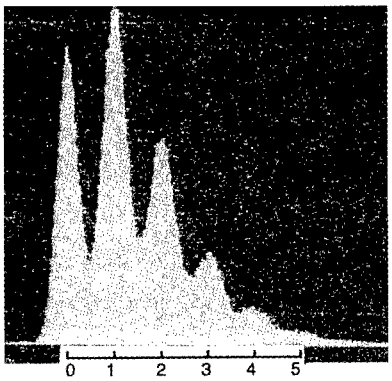


Fig. 1. Dark current histogram before the start of the experiments.

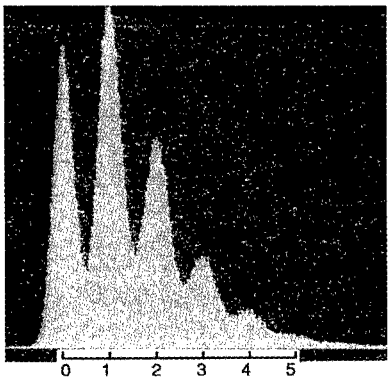


Fig. 2. Dark current histogram after 4.5 hours at 55^{0}C.

the pixel dark current value before the anneal for the x-axis and the pixel dark current value after the anneal for the y-axis. Thus, each point is the before and after dark current values for the same pixel. The brightness in the figure indicates the number of pixels with these dark current values. The projection of the correlation plot on an axis gives the respective histogram. Pixels whose dark current does not change lie on a 45^0 line. Figure 3 reveals many changes over the time of the anneal and shows there is a considerable amount of iron movement at 55^{0}C. Many pixels gain or lose an electrically active iron atom. Those that gain form a line parallel to and one iron spacing above the 45^0 line, while those that lose form a line parallel to and one iron spacing below the 45^0 line. A few pixels gain or lose more than one electrically active iron atom. The additional iron is presumed to come from the dissociation of iron-boron pairs at 55^{0}C. The boron is present within the photodiode and on its periphery. The correlation plot serves as a vivid reminder that iron is mobile in silicon at 55^{0}C and that iron-boron pairs break up and reform at this temperature. Thus, the correlation plot is an excellent illustration of dynamic equilibrium.

The next series shows the results of illumination from an intense light source coupled to a round fiber optic bundle. The initial histogram closely resembles that in Figure 1 and has about 1.2 electrically active iron atoms per pixel. Figure 4 shows the dark current image from the previously illuminated spot and a histogram based on 40,000 pixels within the residual, high dark current spot. The image sensor was illuminated with the fiber optic source for one minute. The histogram only hints at

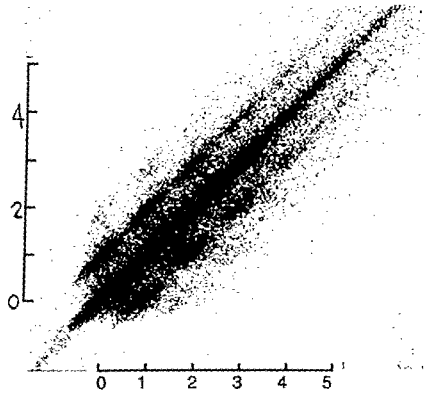


Fig. 3. Correlation plot between Figs. 1 and 2.

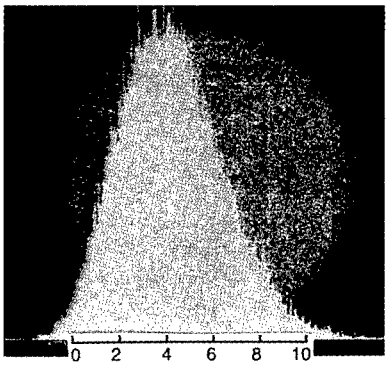


Fig. 4. Dark current histogram after one minute of visible illumination.

quantization and the mean number of electrically active iron atoms has risen to about five per pixel. The additional iron is presumed to come from the dissociation of iron-boron pairs under the influence of light at the temperature of 55^0C [4,8]. (It is worth noting that iron diffuses about 0.08 μm in 30 m at 55^0C [9-10].) The lack of quantization in Figure 4 may reflect the rapid changes the non-equilibrium iron atom population is undergoing, i.e., the iron and boron may be recombining during the measurement time.

The last measurement took three minutes and the imager was allowed to recover for eight minutes at 55^0C. The histogram was then captured and is nearly identical to that in Figure 4. A correlation plot between the data of Figure 4 and those for the post-recovery appears in Figure 5. Figure 5 has a bright line parallel to and below the 45^0 line. The lower line corresponds to pixels that have lost one electrically active iron atom in the short time between measurements. Two more hours of recovery lead to more signs of quantization and discrete peaks reappear after overnight recovery, as seen in Figure 6. The iron atom population is still out of equilibrium, since the illuminated spot is still visible. However, the rate of change of iron to iron-boron has slowed down and permitted the discrete peaks to reappear. The correlation plot between the initial histogram and Figure 6 appears in Figure 7. The plot indicates pixels are more likely to gain electrically active iron atoms due to the illumination. For example, some pixels with none to start, have one or two electrically active iron atoms, even after the overnight recovery. Very few pixels show a loss.

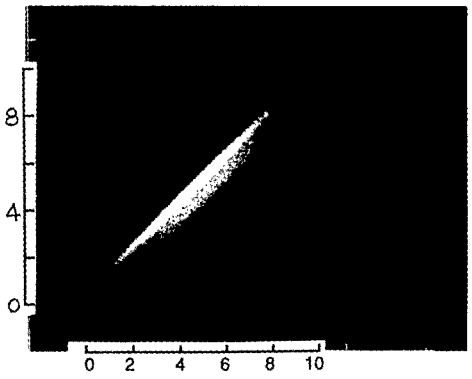


Fig. 5. Correlation plot between after illumination and after a short recovery.

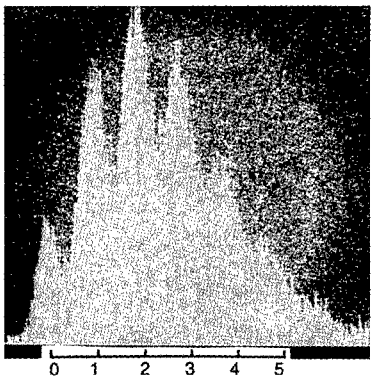


Fig. 6. Dark current histogram after illumination and overnight recovery.

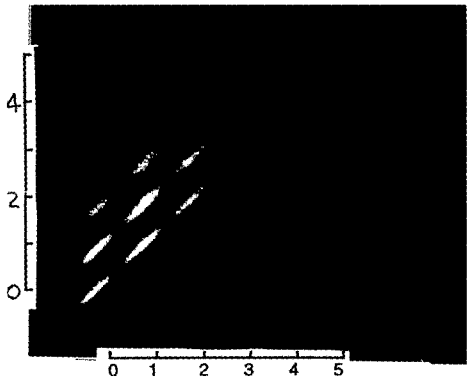


Fig. 7. Correlation plot between the initial histogram and that in Fig. 6.

CONCLUSION

The present work has used dark current spectroscopy (DCS) to study iron in silicon at low concentrations. The amount and the location of the electrically active iron atoms vary with time and with illumination. DCS permits the monitoring of the iron on a pixel-by-pixel basis in an image sensor. The qualitative plots presented here may be supplemented by quantitative studies that are based on the same data. This will permit the gathering of information on the kinetics of the iron-boron dissociation and association reactions in actual devices at temperatures around 55^0C.

REFERENCES

1. J. L. Benton, P. A. Stolk, D. J. Eaglesham, D. C. Jacobson, J.-Y. Cheng, J. M. Poate, N. T. Ha, T. E. Haynes, and S. M. Myers, J. Appl. Phys. **80**, 3275 (1996).
2. W. C. McColgin, J. P. Lavine, and C. V. Stancampiano, in *Defect and Impurity Engineered Semiconductors and Devices,* edited by S. Ashok, J. Chevallier, I. Akasaki, N. M. Johnson, and B. L. Sopori (Mater. Res. Soc. Proc. **378**, Pittsburgh, PA, 1995) pp. 713-724.
3. W. C. McColgin, J. P. Lavine, J. Kyan, D. N. Nichols, and C. V. Stancampiano, Tech. Dig. IEDM, 113 (1992).
4. L. C. Kimerling and J. L. Benton, Physica **116B**, 297 (1983).
5. Y. Okada, M. Okigawa, K. Kazui, Y. Kitamura, T. Furusawa, Opto-electronics **6**, 231 (1991).
6. W. C. McColgin, J. P. Lavine, J. Kyan, D. N. Nichols, J. B. Russell, and C. V. Stancampiano, in *Defect Engineering in Semiconductor Growth, Processing and Device Technology*, edited by S. Ashok, J. Chevallier, K. Sumino, and E. Weber (Mater. Res. Soc. Proc. **262**, Pittsburgh, PA, 1992) pp. 769-774.
7. R. D. McGrath, J. Doty, G. Lupino, G. Ricker, and J. Vallerga, IEEE Trans. Electron Devices **ED-34**, 2555 (1987).
8. G. Zoth and W. Bergholz, J. Appl. Phys. **67**, 6764 (1990).
9. E. R. Weber, Appl. Phys. A **30**, 1 (1983).
10. S. V. Koveshnikov and G. A. Rozgonyi, Appl. Phys. Lett. **66**, 860 (1995).

Influence of Si Substrate Crystallinity on Device Performance

T. Iwamoto [1,2], J. Takano [1,2], K. Makihara [1,2], and T. Ohmi [1]

1) Department of Electronic Engineering, Faculty of Engineering, Tohoku University,
Aza-Aoba, Aramaki, Aoba-ku, Sendai 980-77, Japan.
Phone:+81-22-217-7124 / Fax:+81-22-263-9395
2) Laboratory for Electronic Intelligent Systems, Research Institute of Electrical Communication,
Tohoku University, Katahira 2-1-1, Aoba-ku, Sendai, 980-77 Japan.

ABSTRACT

We have demonstrated the influence of surface microroughness on the electrical characteristics of MOS devices and investigated the influence of wafer's manufacturing methods, such as Czochralski(Cz), floating-zone(FZ), and epitaxial(Epi) silicon wafers, on the susceptibility to the surface microroughness when some chemical treatment was performed. As a result, it was found that Cz and FZ wafers are very susceptible to the surface microroughness and the amount of the vacancy of Epi wafer is much smaller than that of another wafers. It was also demonstrated that the electrical characteristics of very thin gate oxide films are strongly influenced by the silicon substrate quality. Epi wafer is a strong candidate for fablication of highly-reliable devices on 300mm wafers.

INTRODUCTION

In order to obtain a highly-reliable device performance, an atomic scale flattening of silicon surface/interface is very important. It has been known that gate oxide reliability is very susceptible to the surface microroughness before the oxidation process. Moreover, it has been also reported that the channel mobility of MOSFETs is very sensitive to the interface microroughness between the gate oxide and silicon substrate[1-2]. And as the inversion layer becomes thinner, the influence of Si-SiO_2 interface will be more conspiquous[3]. Therefore, the perfect control of silicon surface is essential to fablicate scaling down ULSI devices.

We have already reported that the surface microroughness of silicon wafer is mainly caused by an alkaline solution treatment such as NH_4OH in RCA cleaning and that a modifiction of the mixing ratio in APM (NH_4OH / H_2O_2 / H_2O) solution can reduce the increase of the surface microroughness[1]. In this paper, we have demonstrated that the increase of the surface microroughness depends on the kinds of silicon substrate such as Cz(100), FZ(100) and Epi(100) wafers. From these studies, it is clarified that Epi wafer is very useful for silicon substrate because of the week susceptibility to microroughness for some chemical treatments.

Mat. Res. Soc. Symp. Proc. Vol. 442 © 1997 Materials Research Society

EXPERIMENT

In this experiment, p-type and n-type, silicon (100) wafers made by three different methods, namely Cz, FZ, and Epi, were employed. The surface microroughness was controlled by varying the alkaline solution, namely NH_4OH / H_2O_2 / H_2O (APM cleaning in a RCA cleaning process) before gate oxidation process. The amount of microroughness was measured by Scanning Tunneling Microscope (STM) and Atomic Force Microscope (AFM). The gate oxidation process was carried out at 900 °C in dry O_2 ambient. In order to evaluate the influence of microroughness on the electrical characteristics, MOS diodes and MOSFETs were prepared. Sb and B were diffused into the Cz, FZ and Epi wafers by using OCD (oxide coating diffusion). After diffusion, OCD was removed by BHF solution and sheet resistance was measured by four point probe measurement.

RESULTS

Figure 1 shows the time zero breakdown characteristics (E_{BD}) of MOS (Al / SiO_2 / p-type or n-type Si) diodes having 10nm gate oxide films on Cz , FZ and Epi wafers as a function of surface microroughness (Ra value). The gate oxides was formed on having various surface microroughness by varying the NH_4OH concentration in the APM solution at RCA cleaning. The microroughness (Ra value) was measured by STM. When the data are compared within the same group of n-type and p-type samples, the breakdown depends only on the surface microroughness and not on the growth technique such as Cz, FZ and Epi. And the difference between the breakdown field for p- and n-type groups is due to the different barrier heights (Al/SiO_2 or n-Si/SiO_2) for electron injection into the oxide.

The charge-to-breakdown characteristic(Q_{BD}) is strongly related to the ULSI reliability[4]. Especially, the tunnel oxide in a flash memory[5] requires the high Q_{BD} values under both gate and substrate injections. Figure 2 shows the charge-to-breakdown characteristics (Q_{BD}) of MOS diodes with an area of $1.60 \times 10^{-4} cm^2$ under constant electrical field (9.5 MV/cm^2) as a function of surface microroughness. The breakdown is defined by the diode current increasing up to $1 \times 10^{-5} A$. The Q_{BD} values increase with decrease in the surface microroughness. This result indicates that the charge-to-breakdown characteristic is strongly influenced by surface microroughness.

With a reduction of device dimension, the thickness of the inversion layer decreases due to an increase of impurity concentration in the substrate. Therefore, the surface microroughness of silicon substrate has influence on the channel mobility of carriers[2]. Figure 3 shows the channel mobility as a function of surface microroughness of silicon substrate. The channel mobility increases as the surface microroughness decreases. This result indicates that the channel mobility is also strongly influenced by surface microroughness.

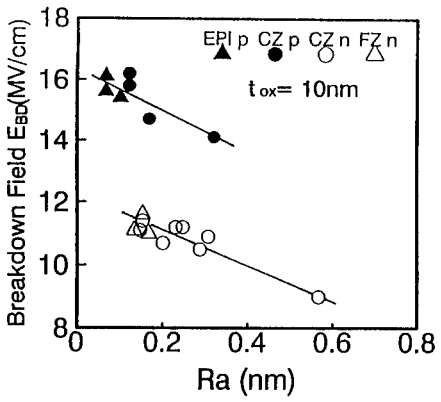


Fig.1 Time zero breakdown caricaturists (EBD) of MOS diodes having 10nm gate oxide films on Cz , FZ and Epi wafers as a function of surface microroughness.

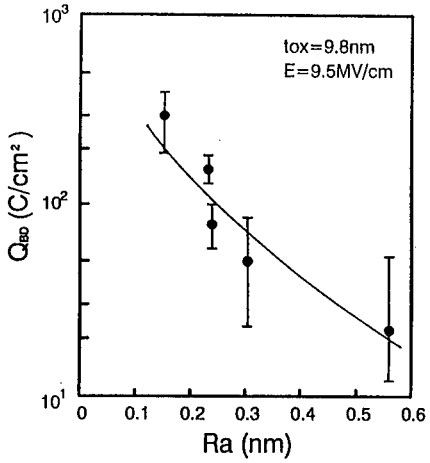


Fig. 2 Charge-to-breakdown characteristics (QBD) of MOS diodes as a function of surface microroughness.

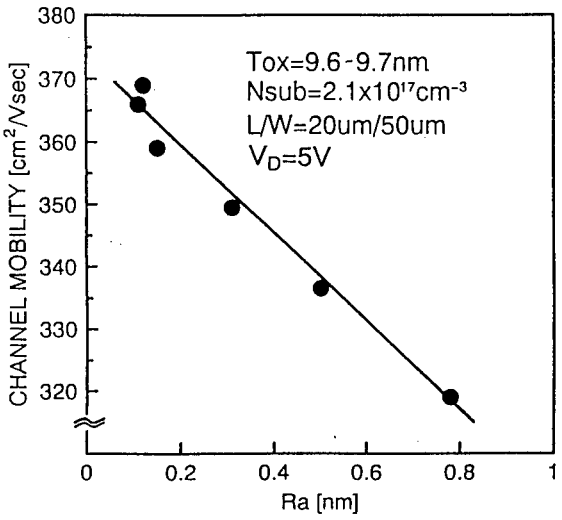


Fig. 3 Channel mobility as a function of surface microroughness of silicon substrate.

These results indicate surface microroughness strongly influences MOS device performance, particularly its speed performance as well as its reliability. Therefore, an atomic scale flattening of silicon surface for some treatments is very important for a future ULSI device fabrication. Next, we have investigated that the influence of silicon substrate (Cz, FZ and Epi wafers) on the surface microroughness for some chemical treatments.

In device fabrication, substrate surface cleaning is generally carried out based on RCA cleaning. We have already reported that the surface microroughness of silicon substrate is mainly caused by an alkaline solution treatment such as NH_4OH in RCA cleaning[1]. Figure 4 shows surface microroughness as a function of etching depth by APM cleaning solution at 80-90 °C. The mixing ratio of NH_4OH / H_2O_2 / H_2O is 1 : 1 : 5. As etching time is longer, surface microroughness increases for all substrates but Ra value of Epi wafer is very low. This result indicates that Epi wafer is very stable against this chemical treatment.

Figure 5 shows surface microroughness of Cz , FZ and Epi wafers as a function of O_2+H_2O partial pressure at 900 °C under high vacuum condition (<10^{-6} Torr). As partial pressure is high, surface microroughness increases. In the case of 10^{-7} Torr (O_2+H_2O partial pressure), surface microroughness on Epi wafer is very smooth as compared with Cz and FZ wafers. This result also indicates that Epi wafer is very stable. These data (Fig.4, 5) suggest that there are some differences in Cz, FZ and Epi wafers.

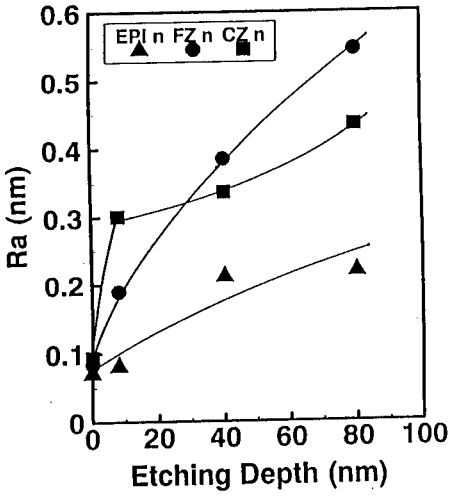


Fig. 4 Surface microroughness as a function of etching depth.

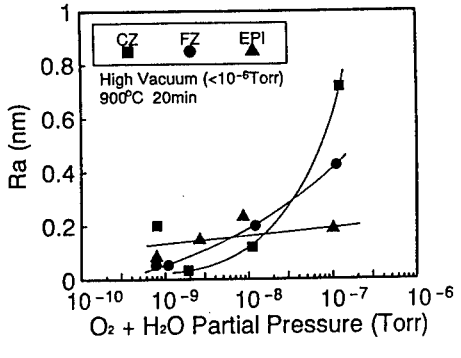


Fig. 5 Surface microroughness of Cz , FZ and Epi wafers as a function of O2+H2O partial pressure at 900 °C under high vacuum condition.

We investigated the amount of vacancies in Cz, FZ and Epi wafers. Figure 6 shows the sheet resistance of Cz, FZ and Epi wafers diffused Sb and B atoms in p-type and n-type wafers, respectively. After the diffusion of B into n-type wafers at 900 °C for 30min, the sheet resistances of Cz, FZ and Epi become almost same. This result can be explained that B atoms diffuse interstitially in silicon crystal because atomic radius of B atoms is smaller than that of Si atoms. Therefore, there is no difference on the substrate type. However, in the case of Sb diffusion at 1000 °C for 2 hours, whose atomic radius is lager than that of Si atoms, the sheet resistance of Epi wafer is higher than that of Cz and FZ wafers. Since Sb atoms diffuse in silicon crystal by changing the position with vacancies, this result suggests that the amount of vacancies in the Epi wafer is lower than that in the Cz and FZ wafers.

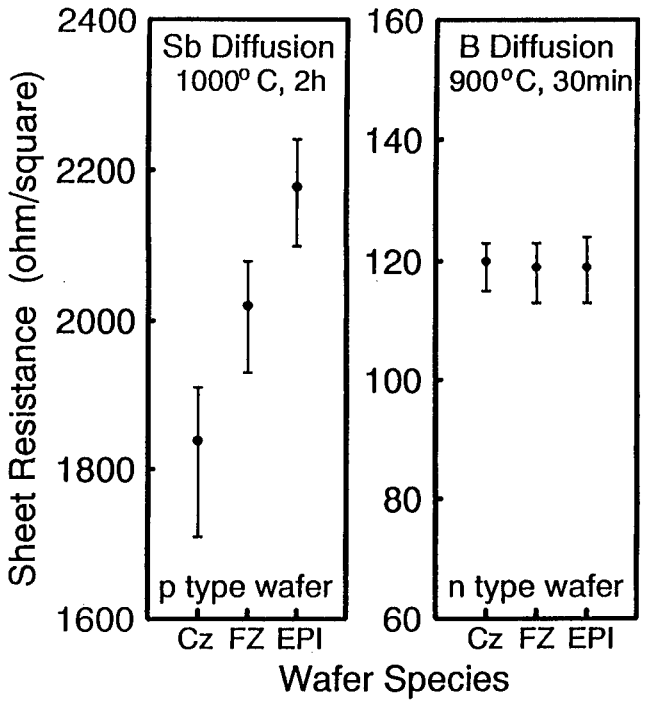


Fig. 6 Sheet resistance of Cz, FZ and Epi wafers diffused Sb and B atoms in p-type and n-type wafers, respectively.

CONCLUSION

We have demonstrated that the influence of surface microroughness on the electrical characteristics of MOS devices and investigated that the influence of silicon substrate (Cz, FZ and Epi wafers) on the surface microroughness for some chemical treatment. Epi wafer is very useful for Si substrate because of low microroughness for some chemical treatments. However, there is a problem in Epi wafer. Epi wafer include metal contamination (Fe etc.) from gas feed line and the inside-wall of a chamber. To solve this problem, we are trying to change all metal surface of epitaxial machine to Cr_2O_3 passivatied surface[6] which is very stable to specialty gas (HCl etc.).

ACKNOWGEMENT

This study was carried out at Super Clean Room, Laboratory for Electronic Intelligent Systems, Research Institute of Electrical Communication, Tohoku University.

REFERENCES

1. T. Ohmi, M. Miyashita, M. Itano, T. Imaoka and I. Kawanabe, IEEE Trans. Electron Devices, vol.39, P.537, 1992.
2. K. Ohmi, K. Nakamura, T. Futatsuki, K. Makihara and T. Ohmi, Ext. Abst. Int. Conf. SSDM, p.149, 1993.
3. T. Ohmi, K. Kotani, A. Teramoto and M. Miyasha, IEEE Electron Device Letter, vol.12, p.652, 1991.
4. K. Ohmi, T. Iwamoto, T. Yabune, T. Miyake and T. Ohmi, Ext. Abst. Int. Conf. SSDM, p.258, 1995.
5. F. Masuoka and K. Sakui, Ext. Abst. Int. Conf. SSDM, p.877, 1993.
6. T. Ohmi, A. Ohki, M. Nakamura, K. Kawada, T. Watanabe, Y. Nakagawa, S. Miyoshi, S. Takahashi and M. S. K. Chen, J. Electrochem. Soc., vol.140, No. 6, p.1691, 1993.

INVESTIGATION ON SUBSURFACE DAMAGE IN SILICON WAFERS

Xin Zhang*, Tong-Yi Zhang*, Yitshak Zohar*, and Sanboh Lee**

*Department of Mechanical Engineering, Hong Kong University of Science and Technology, Clear Water Bay, Kowloon, Hong Kong. **Department of Materials Science and Engineering, National Tsinghua University, Taiwan.

ABSTRACT

Micro-Raman spectroscopy and chemical etching were applied to determine the depth of subsurface damage in silicon wafers undergoing different machining processes: cutting, grinding, polishing and lapping. In comparison with the Raman spectrum of perfect single crystal silicon, both the shape and intensity at the shoulder (500 cm^{-1}) and the subpeak (300 cm^{-1}) spectral regions were changed in all the machined wafers. The intensities at shoulder and subpeak gradually decreased and finally resumed to normal, as the depth of the investigated layer increased. According to the chemical etch rate, the depth of the subsurface damage was thus evaluated for the different wafers. TEM observations further confirmed the obtained results.

1. INTRODUCTION

During the manufacturing of silicon wafers, various machining processes, such as grinding, lapping, and polishing, usually produce the subsurface damage and consequently change the physical and chemical properties of the surface and sub-surface layers [1-2]. The depth of damage layer is defined as the distance from the surface to the deepest damage below where the translational symmetry of the lattice is conserved [3]. Various techniques are employed to measure the damage depth, which depends on the mechanical treatment, semiconductor material, orientation of crystals, particle size of abrasives, and other factors [4-7]. In the present work, we applied micro-Raman spectroscopy as well as chemical etching to measure the depth of the subsurface damage layers.

2. EXPERIMENTAL PROCEDURE

Different machining processes, including grinding, lapping and polishing, were applied during the manufacturing of semiconductor slices. Five wafers used in this study varied in the final machining process: grinding 1200# (G1200), grinding 4000# (G4000), grinding 8000# (G8000), double-side lapping (Lap), and grinding and polishing (G+P). The wafer diameter for G4000 and G8000 is 8 inches; while the others are all 4 inches.

A series of silicon square samples (10 × 10 mm) were cut from the five machined wafers. The chemical etching was carried out in potassium hydroxide (KOH) 40 wt.% solution at 60°C inside a sealed container. First we determined the etch rate from the etching time and the etching depth, which was measured by a surface profiler, the α-stepper. For the machined wafers, different etching periods were selected and they were 1, 3, 5, 10, 30, 60, 180, and 300 minutes. After each etching step, Raman spectroscopy measurements were performed with a spectrometer working in multichannel mode at room temperature. The laser beam with a power of 0.5 mW at 514.5 nm was focused onto a 2 μm-spot on the sample using a 50× objective lens mounted on an optical microscope. The wavelength scanned in this work ranged from 200 to 800 cm^{-1}.

Mat. Res. Soc. Symp. Proc. Vol. 442 © 1997 Materials Research Society

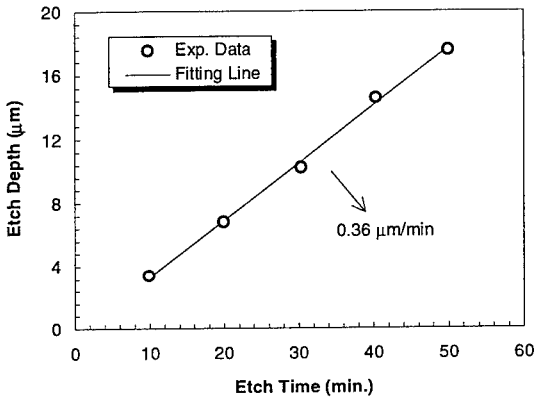


Fig. 1 Etch rate of silicon in 40 wt.% KOH solution at 60°C.

Observations of transmission electron microscope (TEM) and high resolution electron microscope (HREM) were further carried out for both G1200 and G+P wafers. Samples were prepared by mechanical polishing to about 30 μm and then further thinned by ion milling.

3. RESULTS AND DISCUSSION

Fig. 1 shows the relation between the etching depth and the etching time for silicon in 40 wt.% KOH solution at 60°C. From the slope of the fitting line, the etch rate of silicon wafer in the KOH solution was determined to be about 0.36 μm/min.

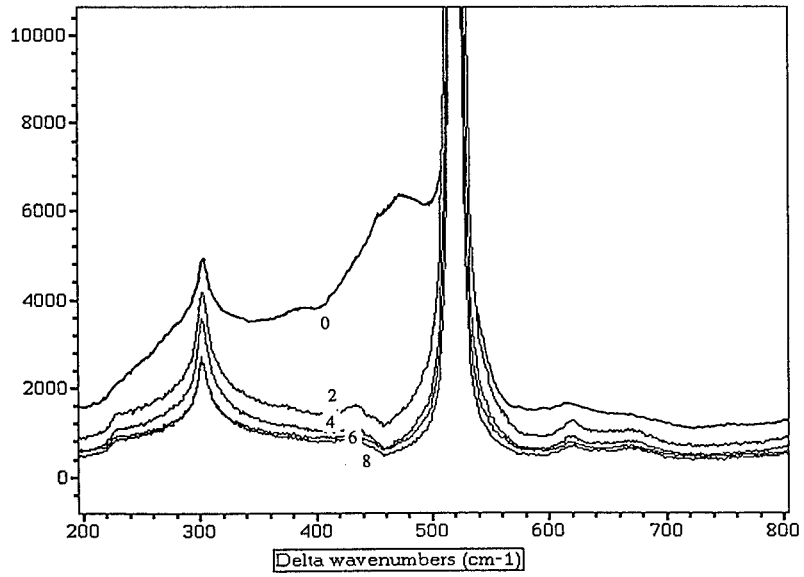


Fig. 2 Raman spectra of G1200 sample. (0) before etching; (2) 3 min; (4) 10 min; (6) 60 min; (8) 300 min.

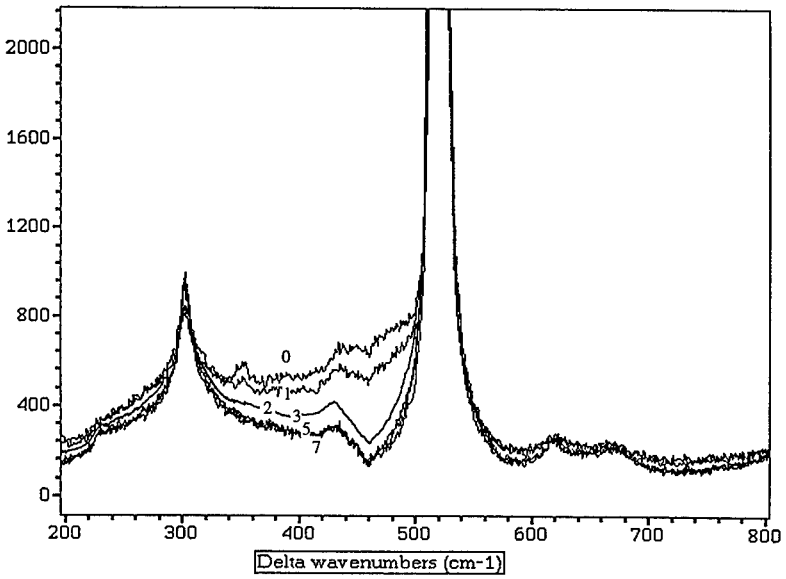


Fig. 3 Raman spectra of G4000 sample. (0) before etching; (1) 1 min; (2) 3 min; (3) 5 min; (5) 30 min; (7) 180 min.

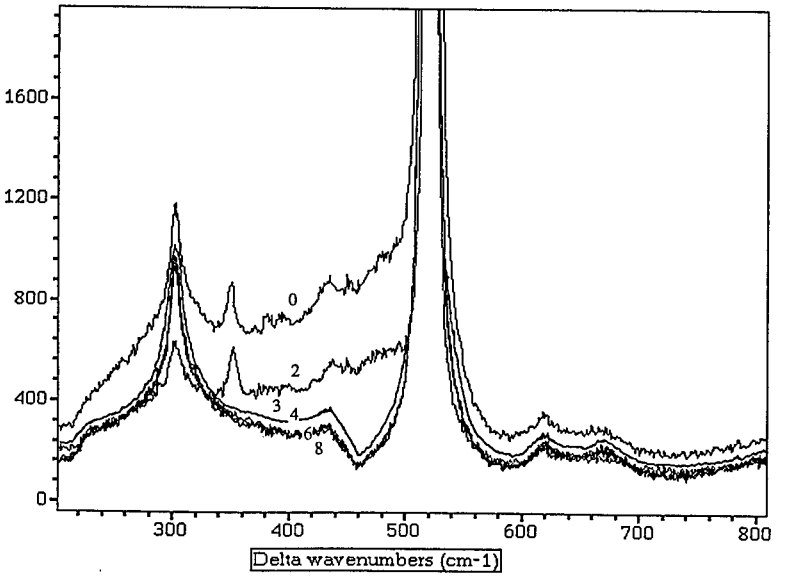


Fig. 4 Raman spectra of G8000 sample. (0) before etching; (2) 3 min; (3) 5 min; (4) 10 min; (6) 60 min; (8) 300 min.

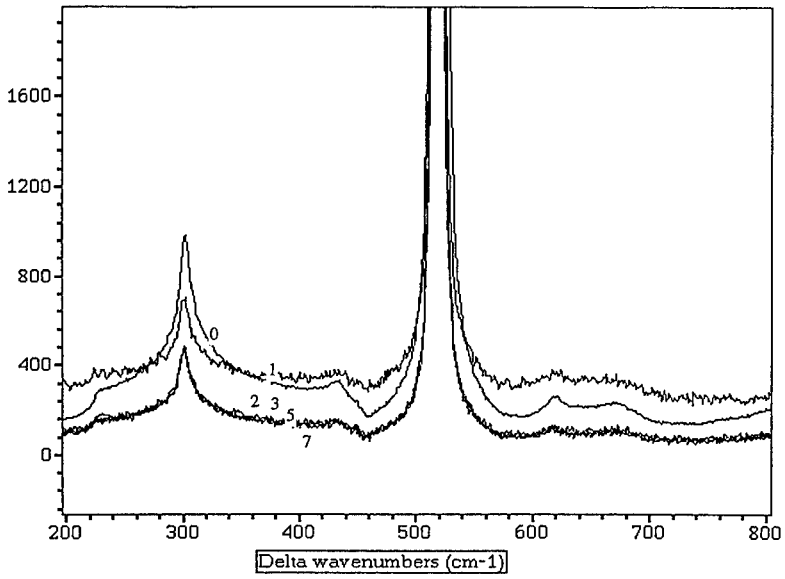


Fig. 5 Raman spectra of G+P sample. (0) before etching; (1) 1 min; (2) 3 min; (3) 5 min; (5) 30 min; (7) 180 min.

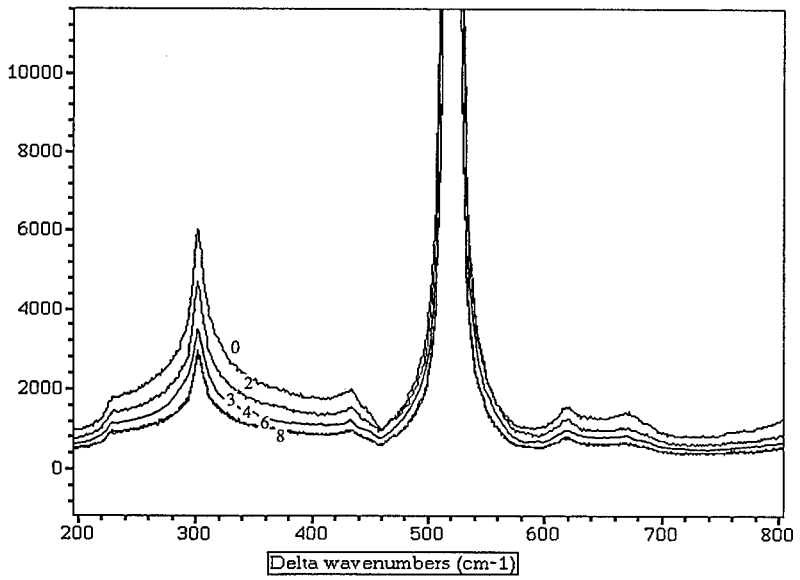


Fig. 6 Raman spectra of Lap sample. (0) before etching; (2) 3 min; (3) 5 min; (4) 10 min; (6) 60 min; (8) 300 min.

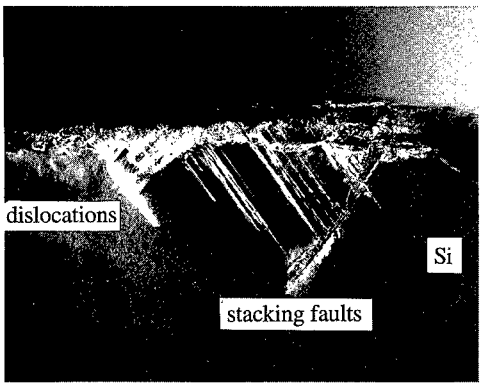


Fig. 7 Cross-sectional TEM micrograph of G1200 sample (11,500×).

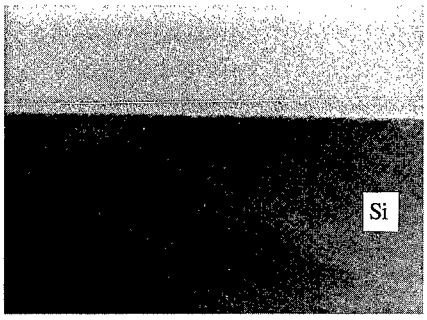


Fig. 8 Cross-sectional TEM micrograph of G+P sample (50,000×).

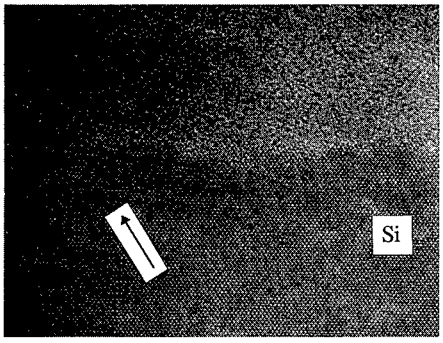


Fig. 9 Cross-sectional HREM micrograph of G+P sample (540,000×).

Raman spectra were taken for the five wafers before etching and after each etching step. Fig. 2 shows the Raman spectra of G1200 sample, where numbers 1-8 denote correspondingly the etching time of 1, 3, 5, 10, 30, 60, 180, and 300 minutes, and hereafter the same notation is used. As can be seen, within the first 10 minutes of etching, there is obvious decrease in the spectral intensities at the shoulder part and at the subpeak region as the etching time increases. After 10 minutes of etching, the spectra were stable and no noticeable changes could be observed. We, therefore, believe that the damage layer was removed after 10 minute etching. Using the etch rate of silicon in the KOH solution, the depth of subsurface damage for G1200 sample was evaluated to be about 3.60 μm.

Similarly, Fig. 3-6 show the Raman spectra of G4000, G8000, G+P and Lap samples under different etching step, respectively. The spectra became stable after 3, 5, 1 and 10 minute

etching, for the G4000, G8000, G+P and Lap samples. Thus, the depths of subsurface damage for G4000, G8000, G+P and Lap samples were evaluated to be 1.08, 1.80, 0.36 and 3.60 μm, respectively. Clearly, the G+P samples had the lowest level of damage. The G4000 and G8000 samples, i.e. high level grinding, produced a 1-2 μm thick damage layer. Both the Lap and G1200 samples, however, had the deepest damage with a magnitude of nearly 4 μm.

Fig. 7 shows the cross-sectional TEM micrograph for the G1200 sample. The subsurface damage induces the defects, dislocations and (111) stacking faults in the original perfect crystal. The depth evaluated from the TEM picture is about 3.5 μm, similar to the value measured from the micro-Raman spectroscopy and the chemical etching. Fig. 8 illustrates the cross-sectional TEM micrograph for the G+P sample, where no dislocations and stacking faults were observed. However, dislocations were observed under the HREM. Fig. 9 shows the HREM micrograph at the cross section for the G+P sample, where the arrow indicates the dislocations. By measuring the distance from the dislocations to the surface, the depth of the subsurface damage was evaluated to be about 0.30 μm. The result is also consistent with the micro-Raman analysis.

4. CONCLUDING REMARKS

Combined application of micro-Raman spectroscopy and chemical etching enables the measurement of the depth of the subsurface damage in silicon wafers under different machining processes: G1200, G4000, G8000, G+P, and Lap. In comparison with the Raman spectrum of perfect single-crystal silicon, both the shape and intensity at the shoulder (500 cm^{-1}) and the subpeak (300 cm^{-1}) spectral regions were changed in the machined wafers. As the layer depth increased, the shoulder and subpeak intensities gradually decreased and the spectra finally resumed the shape of the perfect single-crystal spectra. Basing on the etch rate of silicon in the KOH solution, the depth of the subsurface damage for the five wafers was evaluated to be: 3.6 μm for G1200, 1.08 μm for G4000, 1.80 μm for G8000, 0.36 μm for G+P and 3.6 μm for Lap.

Since the micro-Raman spectrum has already provided the deformation information for the whole damage layer, it is possible to determine the depth of subsurface damage only by the micro-Raman spectrum without chemical etching. More work is under progress to understand the correlation between the micro-Raman spectrum and the defects in silicon crystals.

ACKNOWLEDGMENTS

This work was sponsored by the Hong Kong Research Grants Council through RGC grant HKUST713/95E. The authors are also grateful to Dr. Ning Wang for his assistant work in TEM observation.

REFERENCES

1. P. A. McKeown, Annals of CIRP, **36**, p. 495 (1987).
2. N. Taniguchi, Annals of CIRP, **32**, p. 573 (1983).
3. U. Bismayer, E. Brinksmerier, B. Guttler, H. Seibt, and C. Menz, Precision Engineering, **16**, p. 139 (1994).
4. S. Johansson and J. A. Schweitz, J. Am. Ceram. Soc., **71**, p. 617 (1988).
5. E. Brinksmerier, Precision Engineering, **11**, p. 211 (1989).
6. R. G. Sparks and M. A. Paesler, Precision Engineering, **10**, p. 191 (1988).
7. H. K. Tonshoff, W. V. Schmieden, I. Inasaki, W. Konig, and G. Spur, Annals of CIRP, **39**, p. 621 (1990).

SHALLOW DONOR FORMATION IN HYDROGEN-IMPLANTED SILICON

YUTAKA TOKUDA*, HIROYUKI IWATA** and AKIRA ITO***
*Department of Electronics, Aichi Institute of Technology, Yakusa, Toyota 470-03, Japan, tokuda@el.aitech.ac.jp
**Research Institute for Industrial Technology, Aichi Institute of Technology, Yakusa, Toyota 470-03, Japan
***Department of Electronics and Information Engineering, Suzuka College of Technology, shiroko, Suzuka 510-02, Japan

ABSTRACT

Formation of shallow donors has been studied in 100-keV hydrogen-implanted n-type silicon with a dose of $1x10^{15}$ cm^{-2}. Annealing experiments are made in the temperature range 100 to 800℃. Gold Schottky contacts are fabricated on these samples to obtain carrier concentration profiles. The hydrogen profiles are measured by secondary ion mass spectroscopy. In the annealing temperature range 350 to 450℃, an increase of the carrier concentration is observed near the surface region with almost flat depth profiles. The well-known hydrogen-related donors (1st shallow donors) disappear around 400℃, while shallow donors (2nd shallow donors)observed here decrease above 500 ℃. Hydrogen profiles show almost no change in the 2nd donor formation temperatures, although hydrogen starts to outdiffuse at 250℃. This indicates that the 2nd shallow donors are related to hydrogen atoms and to implantation-induced damage. The implantation-induced defects trap diffusing hydrogen atoms, which leads to the formation of the 2nd shallow donors.

I. INTRODUCTION

Hydrogen is one of the most important light elements in silicon. There have been intensive studies on the behavior of hydrogen, especially on the passivation of shallow acceptors and donors [1,2]. Furthermore, it has been reported that hydrogen introduces so-called hydrogen-related shallow donors in silicon.

There are several cases in formation of hydrogen-related shallow donors, that is, hydrogen implantation [3-6], neutron transmutation doping in silicon grown in a hydrogen atmosphere [7,8], electron irradiation in silicon doped with hydrogen by annealing in a H_2 gas ambient at 1000℃ [9,10], and neutron transmutation doping and subsequent hydrogen-plasma treatment [11]. Hydrogen-related shallow donors are formed in the temperature range 300 to 500 ℃,although it is unclear whether the same kinds of donors are produced or not among these cases. However, there is a common feature in four cases that lattice defects are present in samples.

In the present paper, we investigate the formation of shallow donors in 100-keV hydrogen-implanted n-type silicon in the annealing temperature range 100 to 800℃. The carrier concentration profiles are compared with the hydrogen profiles. These results are discussed in connection to lattice defects introduced by implantation.

II. EXPERIMENTAL PROCEDURE

Samples used in this study were prepared from phosphorus-doped, n-type (100) Czochralski-grown (CZ) silicon crystals which had a resistivity of between 1 and 2 Ωcm. 100-keV H^+ ions were implanted into silicon wafers at room temperature to a dose of $1x10^{15}$ cm^{-2}. Annealing was performed in the temperature range 100 to 800 ℃ in flowing N_2.

Gold Schottky contacts were fabricated on these samples by evaporation in vacuum to obtain carrier concentration profiles from capacitance (C)-voltage(V) measurements. The capacitance was measured by using a Boonton 72B capacitance meter. C-V measurements were made at 90K to avoid the effects of deep traps on the estimation of carrier concentration profiles [12].

Secondary ion mass spectroscopy (SIMS) analysis were made to measure hydrogen profiles with a Cameca IMS-4F ion microanalyzer using a 14.5-keV Cs^+ ion beam. Hydrogen profiles are compared with carrier concentration profiles obtained from C-V measurements at 90K.

Mat. Res. Soc. Symp. Proc. Vol. 442 © 1997 Materials Research Society

III. EXPERIMENTAL RESULTS AND DISCUSSION

A. Carrier Concentration Profiles

Figure 1 shows the variations of the zero-bias depletion layer width at 90K for hydrogen-implanted samples as a function of annealing temperatures. The depletion layer width is about 0.5 μ m before hydrogen implantation. The zero-bias depletion layer width increases to 2.4 μ m after implantation, which indicates the introduction of large densities of acceptor-type defects.

The zero-bias depletion layer width gradually recovers to the pre-implantation value in the annealing temperature range 100 to 250 ℃ and becomes smaller in the range 300 to 450 ℃. The decrease of the zero-bias depletion layer width in the range 100 to 250℃is ascribed to the passivation of implantation-induced acceptor-type defects by hydrogen since the growth of hydrogen-related shallow donors has been reported to occur at annealing temperatures around 250℃ [3-6]. The smaller values of the zero-bias depletion layer width indicates the presence of donors over the phosphorus donor concentration in the range 300 to 500℃,consistent with the growth temperature range of hydrogen-related shallow donors. It is thought that both passivation of acceptor-type defects by hydrogen and growth of the hydrogen-related shallow donors act at annealing temperatures of 200 and 250 ℃.

In the annealing temperature range 500 to 600℃, the zero-bias depletion layer width increases with annealing temperatures, according to the disappearance of the hydrogen-related shallow donors and exceeds the pre-implantation value at the temperatures of 550 and 600 ℃. This shows that the hydrogen-implantation-induced damage still remains at the annealing temperatures below 600℃. The zero-bias depletion layer width has almost the same value as that before implantation in the annealing temperature range 650 to 800℃, which suggests the annealing of the implantation damage.

For samples before implantation, the carrier concentration profile is flat and its value is 3.5×10^{15} cm^{-3}. The carrier concentration profiles are shown in Fig. 2 for hydrogen-implanted samples which are annealed at 300, 350, 400, 450, 500 and 550 ℃. An increase in carrier concentration is observed at the annealing temperature of 300℃ with its peak around the mean projected range Rp of hydrogen implanted in this work. This reveals the growth of the hydrogen-related shallow donors as reported previously [3-6]. It is noted that an increase in carrier concentration is seen in the shallower region than Rp. The carrier concentration increase in the shallower region is more significant at annealing temperatures at 350, 400 and 450℃, while a decrease in carrier concentration is already observed around Rp. This suggests that the growth of another kind of shallow donors occurs at these annealing temperatures.

Hereafter, we call two kinds of shallow donors the 1st shallow donors and the 2nd shallow donors, respectively. The 1st shallow donors mean the well-known hydrogen-related shallow donors which are formed around 300 ℃ and start to disappear at the annealing temperature of 350℃. The 2nd shallow donors correspond to those which grow in the annealing temperature range 350 to 450℃. However, it is unclear that the 2nd shallow donors are related to hydrogen, although the formation of several kinds of

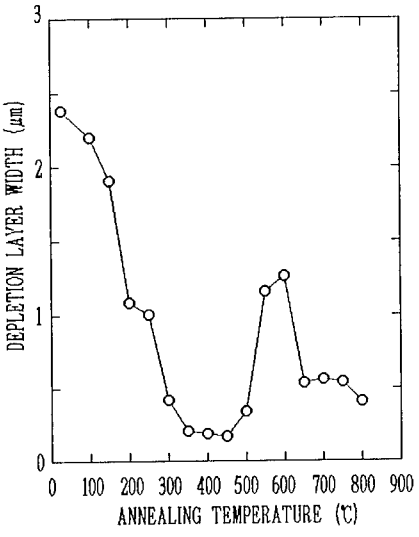


Figure 1. Variations of the zero-bias depletion layer width at 90K for hydrogen-implanted samples as a function of annealing temperatures.

hydrogen-related shallow donors has been reported [5,8,9-11]. This is discussed in connection with the results of the SIMS analysis.

There is a difference in concentration profiles between two kinds of shallow donors in addition to the difference of the growth temperature. The carrier concentration profiles in the growth region of the 2nd shallow donors are relatively flat compared to that of the 1st shallow donors with the carrier concentration peak around Rp as shown in Fig. 2.

The annealing of the 2nd shallow donors occurs at annealing temperatures above 450 ℃ and progresses from the deeper region toward the surface. At an annealing temperature of 500℃, a significant reduction in the 2nd shallow donor concentration is seen, and the carrier concentration profile with its peak around Rp appears in the deeper region. This profile may be due to the formation of the 3rd shallow donors. At an

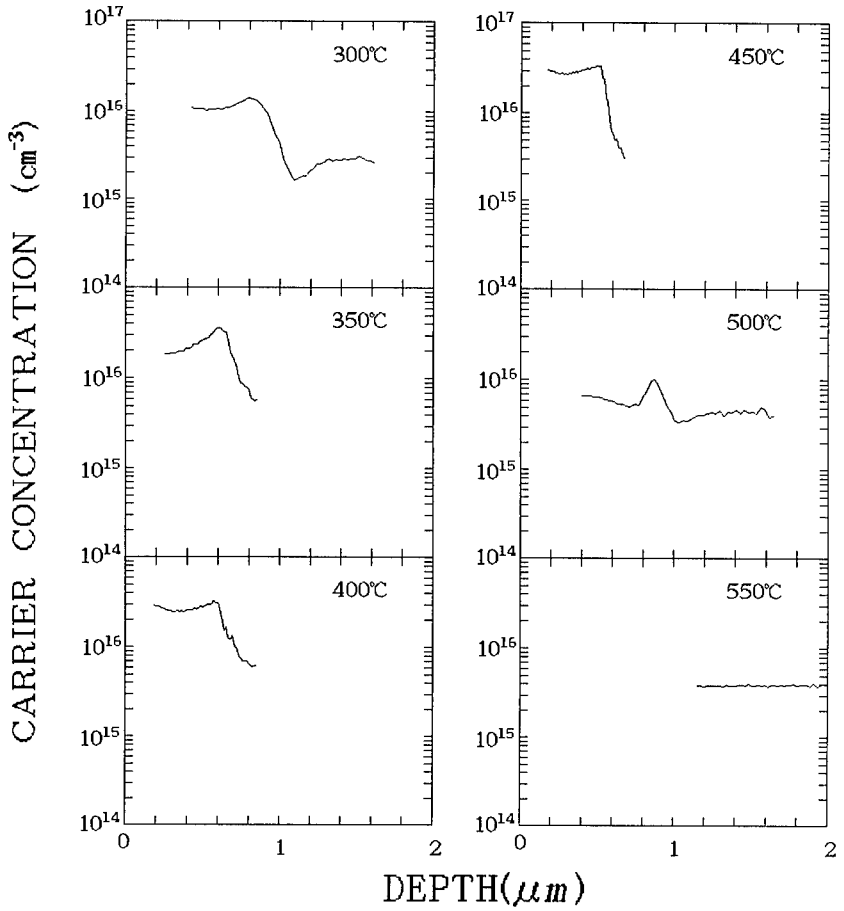


Figure 2. Carrier concentration profiles for hydrogen-implanted samples which are annealed at 300, 350, 400, 450, 500 and 550℃ .

annealing temperature of 550℃, the carrier concentration profile can be measured in the region above 1.1 μ m as discussed earlier and is flat with the carrier concentration equal to that before implantation.

B. Hydrogen Profiles

Figure 3 shows hydrogen profiles for as-implanted and subsequently annealed samples at 250,300,350,400,450,500 and 550 ℃. There is almost no change in hydrogen profiles in the annealing temperature range up to 200 ℃. The diffusion of hydrogen toward the surface is clearly observed at the annealing temperature of 250℃ and continues up to the 350℃ annealing.

It is found that hydrogen profiles have almost the same one at the annealing temperatures of 350,400 and 450℃. There are large densities of implantation-induced defects with its peak at the slightly shallower depth than Rp [13]. No significant change in hydrogen profiles in the annealing temperature range 350 to 450 ℃ is ascribed to trapping of diffusing hydrogen atoms by implantation-induced defects in the shallower region than Rp since hydrogen starts to diffuse toward the surface at the annealing temperature of 250℃.

At the annealing temperature of 500℃, the outdiffusion of hydrogen is observed again, and the appreciable amount of hydrogen is found to be lost from the implanted region. There remains the slight amount of hydrogen at the annealing temperature of 550℃. The hydrogen concentration is below detection limit of the SIMS analysis used in the present experiments at the annealing temperatures above 750℃.

C. Comparison of carrier concentration profiles and hydrogen profiles

The 1st shallow donors are the well-known hydrogen-related shallow donors [3-6] considering their growth temperature range as stated in Ⅲ.A. The concentration profiles of the 1st shallow donors are consistent with the hydrogen depth profiles for as-implanted samples as seen in Figs. 2 and 3. The 1st shallow donors grow at relatively lower annealing temperatures and seem to be formed through short range interaction between hydrogen atoms and implantation-induced defects. This confines the 1st shallow donors to the small region around Rp.

The 2nd shallow donors are formed at annealing temperatures higher than the 1st shallow donors. The growth region of the 2nd shallow donors spreads toward the surface. The annealing temperature range where the growth of the 2nd shallow donors occurs is in good agreement with the range where there is no significant change in hydrogen profiles as shown in Figs. 2 and 3 in spite of the occurrence of hydrogen diffusion at lower annealing temperatures. As suggested in Ⅲ.B, it is thought that implantation-induced defects trap diffusing hydrogen atoms in this annealing temperature range. The trapping of hydrogen by implantation-induced defects leads to the formation of complex defects. We believe that these complex defects including hydrogen and implantation-induced defects correspond to the 2nd shallow donors, that is, the 2nd shallow donors are also hydrogen-related shallow donors. The spreading of the distribution of the 2nd shallow donors toward the surface suggests that implantation-induced defects also outdiffuse. The 2nd hydrogen-related shallow donors are formed when implantation-induced defects traps hydrogen atoms under the flow of both species from the implanted region toward the surface.

The 2nd shallow donors are stable in the annealing temperature range 350 to 450 ℃. They start to disappear at the annealing temperature of 500℃. Then, the hydrogen starts to outdiffuse again as shown in Fig. 3. This means that the hydrogen atoms are liberated from complex defects and diffuse toward the surface. This supports again the idea that the 2nd shallow donors are hydrogen-related shallow donors.

Several authors have reported introduction of some kinds of hydrogen-related shallow donors, dependent on the annealing temperatures [5,8-11]. Markevich et al. [9,10] have studied the evolution of hydrogen-related shallow donors with annealing in electron-irradiated CZ Si saturated with hydrogen by far-infrared absorption measurements. They have reported introduction of three kinds of hydrogen-related shallow donors labeled D1,D2 and D3 which are developed and annihilated in the annealing temperature ranges 250 to 425, 350 to 600 and 425 to 600℃, respectively. The annealing temperature ranges where D1 and D2 are observed correspond well to the ranges where the 1st and 2nd shallow donors are observed, respectively. It is suggested in Ⅲ.A that there are the 3rd shallow donors around Rp at the annealing temperature of 500℃. Since rather

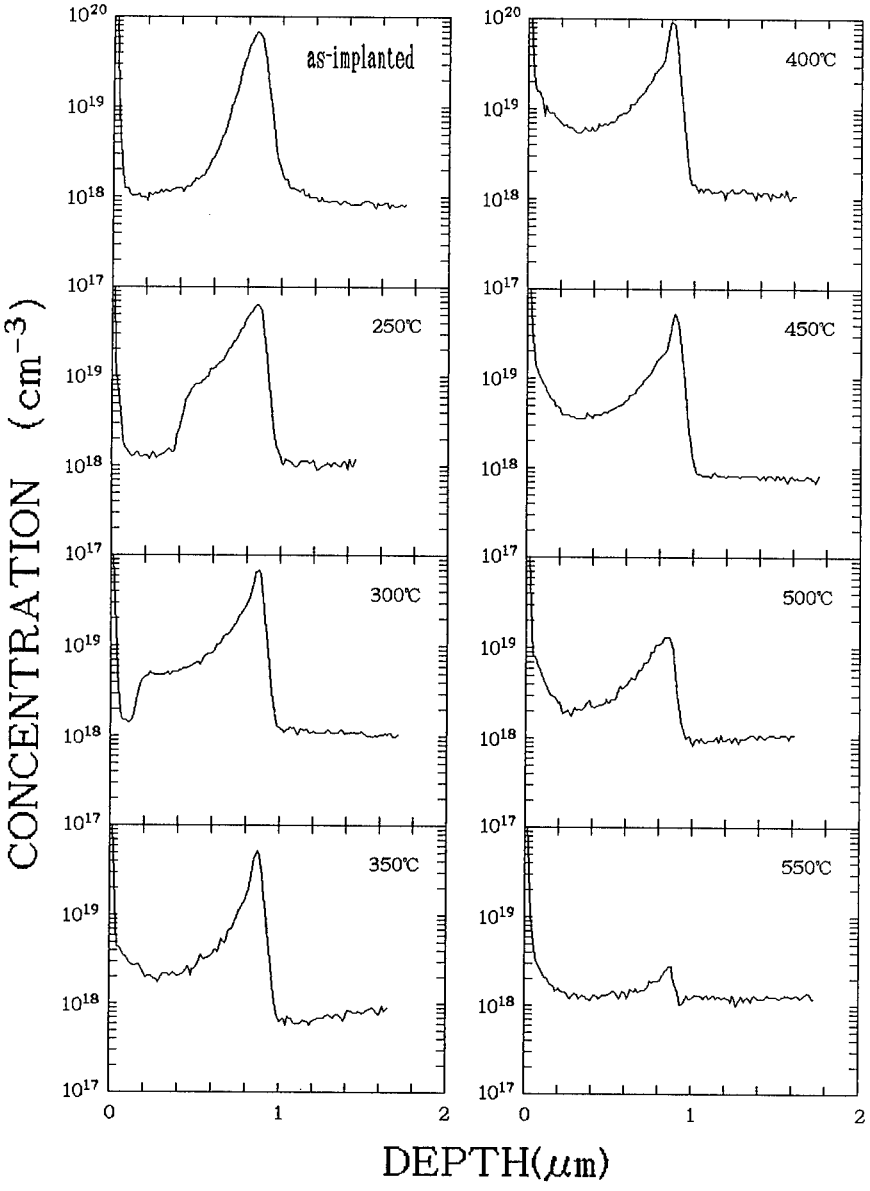


Figure 3. Hydrogen plofiles for as-implanted and subsequently annealed samples at 300, 350, 400, 450, 500 and 550℃.

large amount of hydrogen still remains in the region around Rp, it is possible that the 3rd shallow donors are hydrogen-related. The observed annealing temperature of the 3rd shallow donors is within the annealing temperature range of D3. This seems to indicate that the 3rd shallow donors correspond to the hydrogen-related shallow donors labeled D3.

It has been suggested that D1,D2 and D3 are complex defects containing hydrogen, oxygen and vacancy with no observation of hydrogen-related shallow donors in float-zone-grown (FZ) silicon [9,10]. However, the growth of hydrogen-related shallow donors has been reported in hydrogen-implanted FZ and epitaxial silicon [3- 5],and NTD-FZ silicon incorporated with hydrogen [7,8,11]. There may be some difference in the structure of complex defects for hydrogen-related shallow donors, according to a difference in ways to introduce them. Further investigation is necessary to obtain more detailed pictures of hydrogen-related shallow donors although hydrogen-related donors observed in electron-irradiated silicon doped with hydrogen are suggested to correspond to those observed here in hydrogen-implanted silicon.

IV. SUMMARY

Formation of hydrogen-related shallow donors has been studied in hydrogen-implanted n-type silicon through C-V measurements of fabricated Schottky diodes and SIMS analysis. Comparison is made between carrier concentration profiles and hydrogen profiles.

The growth and annihilation of two kinds of hydrogen-related shallow donors(1st and 2nd donors) is observed at the annealing temperatures around 300 and 400 ℃, respectively. Similarity is found in the observed annealing temperature ranges of hydrogen-related shallow donors between hydrogen-implanted n-type silicon, presented here and electron-irradiated n-type silicon saturated with hydrogen, reported previously [9,10] including the 3rd shallow donors. It is suggested that the 1st hydrogen-related shallow donors are complex defects formed through short range interaction between hydrogen atoms and implantation- induced defects and the 2nd ones through trapping of hydrogen atoms by implantation-induced defects under the flow of both species from the implanted region toward the surface.

REFERENCES

1. J .I .Pankove and N .M. Johnson, Hydrogen in Semiconductors (Academic, New York, 1991).
2. S .J .Pearton, J.W. Corbett and M. Stavola, Hydrogen in Crystalline Semiconductors (Springer, Berlin, 1992).
3. Y. Zohta, Y. Ohmura and M. Kanazawa, Japan J. Appl. Phys. **10**, 532 (1971).
4. Y. V. Gorelkinskii and N. N. Nevinnyi, Nucl. Instrum. Methods. **209/210**, 677 (1983).
5. E. Ntsoenzok, P. Desgardin, M. Saillard, J. Vernois and J. F. Barbot, J.Appl. Phys. **79**, 8274 (1996).
6. Y. Tokuda, Y. Hasebe, A. Ito, H. Iwata, A. Usami, A. Terashima, H. Ohshima and T. Hattori, to be published in Semicond. Sci. Technol.
7. L. Chuengang, L. Yaoxin, S. Chengtai and Y. Janhua, in Proceedings of the 4th International Conference on Neutron Transmutation Doping in Semiconductors, edited by R. D. Larrabe (Plenum, New York, 1983), p.193.
8. W. Zhengyuan and L. Lanying, in Proceedings of the 4th International Conference on Neutron Transmutation Doping in Semiconductors, edited by R.D. Larrabe (Plenum, New York, 1983), p.311.
9. V. P. Maekevich, M. Suezawa, K. Sumino and L. I. Murin, J. Appl. Phys. **76**. 7347 (1994).
10. H. Hatakeyama, M. Suezawa, V. P. Markevich and K. Sumino, in Proceedings of the Materials Science Forum Vols, edited by M. Suezawa and H. Katayama-Yoshida (Trans Tech Publications, Switzerland, 1995), p.939.
11. J. Hartung and J. Weber, Phys. Rev. B **48**, 14161 (1993).
12. L. C. Kimerling, J. Appl. Phys. **45**, 1839 (1974).
13. L. Palmetshofer and J. Reisinger, J. Appl. Phys. **72**,2167 (1992).

Part V

Point Defects and Interactions in Si

COOPERATIVE CHEMICAL REBONDING IN THE SEGREGATION OF IMPURITIES IN SILICON GRAIN BOUNDARIES

A. Maiti,[1,2] M. F. Chisholm,[1] S. J. Pennycook,[1] and S. T. Pantelides[1,2]

[1]Solid State Division, Oak Ridge National Laboratory, Oak Ridge, TN 37831
[2]Department of Physics and Astronomy, Vanderbilt University, Nashville, TN 37235

ABSTRACT

With *ab initio* calculations we show that the experimentally observed large segregation energies of As at Si grain boundaries can be explained by the formation of isolated dimers or ordered chains of dimers of *threefold-coordinated* As along the cores of grain boundary dislocations. We also find the intriguing possibility that As segregation may drive structural transformation of certain grain boundaries. Recently we have obtained the first atomic-resolution STEM images of As in a Si grain boundary, consistent with the formation of As dimers. Segregation energy of As dimers was found to be significantly higher in isolated dislocation cores, where larger site-variation in strain than in grain boundaries lead to further lowering of the electronic levels of As deep into the bandgap.

INTRODUCTION

Polycrystalline semiconductors are used in microelectronics. Dopants, which control the electrical properties of these materials, are known to segregate in grain boundaries in electrically inactive configurations [1-4]. The fraction of dopants in the grain boundaries is governed by the *segregation energy*, i.e., the energy difference between a dopant atom in the grain boundary and a dopant atom in the bulk crystal. For the specific case of As segregation in Si and Ge grain boundaries, experimental values of the segregation energies range from 0.41 to 0.65 eV [1-4].

Clearly, it would be very important for technologists to know if the large segregation energy is an intrinsic property of a defect-free grain boundary or is caused by defects that could, in principle, be avoided. Experiment [5] and theory [6, 7] have established that tilt grain boundaries in undoped Si and Ge rebond so that all host atoms are fourfold-coordinated. The only first-principles theoretical study of segregation was reported recently by Arias and Joannopoulos [8]. These authors examined the segregation energies of isolated As atoms placed at different substitutional sites in a Ge grain boundary and found values only of order 0.1 eV. They proposed that the observed segregation energies are likely to arise from As atoms bound to steps or other defects. No calculations were pursued to explore such possibilities.

MOTIVATION

The motivation for the present work was the recognition that the observed large segregation energies may occur in defect-free grain boundaries because As atoms achieve their preferred threefold coordination, as they are known to do in amorphous Si and Ge [9]. Simple bond counting suggests that, if a single As atom were to achieve threefold coordination in a Si or Ge grain boundary, at least one Si (Ge) atom would have to have odd coordination (3 or 5), which is energetically costly. Clearly, threefold-coordinated As atoms would be far more likely if they were incorporated in a grain boundary in a

Mat. Res. Soc. Symp. Proc. Vol. 442 © 1997 Materials Research Society

cooperative manner, at least two at a time. The simplest possibility would be two As atoms at nearest neighbor sites. The As atoms might relax away from each other so that the "bond" between the As atoms is broken. In this way, each As atom attains its preferred threefold-coordination, with all the Si atoms fourfold-coordinated [10].

COMPUTATIONAL PROCEDURE

The calculations were based on density functional theory [11] with local exchange-correlation energy as parametrized by Perdew and Zunger [12]. The atomic cores are represented by non-local, norm-conserving pseudopotentials of the Kerker type [13] in a separable Kleinmann-Bylander form [14], and defined on a real-space grid [15]. The integration over the Brillouin Zone was performed using two special k-points chosen according to the Monkhorst-Pack scheme [16]. The electronic wavefunctions were expanded in a plane wave basis set with an energy cutoff of 150 eV, verified to yield accurate lattice constant and bulk modulus for the pure crystal. For each geometry, the electronic wavefunctions were first relaxed by the conjugate gradient scheme of Payne, *et al.* [17], until they reached a local minimum (the Born-Oppenheimer surface). The ions were then moved according to the Hellman-Feynman forces until the largest force on any ion in any direction was less than 0.08 eV/Å.

SEGREGATION AT A Σ=5 {310} <001> TILT BOUNDARY

Relaxed Structures

For simplicity and computational feasibility we first considered the symmetric Σ=5 tilt boundary in Si, which is parallel to the {310} plane of the original crystalline lattice and has the tilt axis parallel to the <001> direction. It has a minimum periodicity of one conventional lattice parameter (a = 5.431 Å) in the <001> direction and a periodicity of $a\sqrt{5/2}$ = 8.587 Å in the direction perpendicular to the <001> axis. The details of the supercell used for our calculations are described in Ref. 10. The relaxed ground-state structure, which we call GB1, is shown in Fig. 1 in a projection perpendicular to the tilt

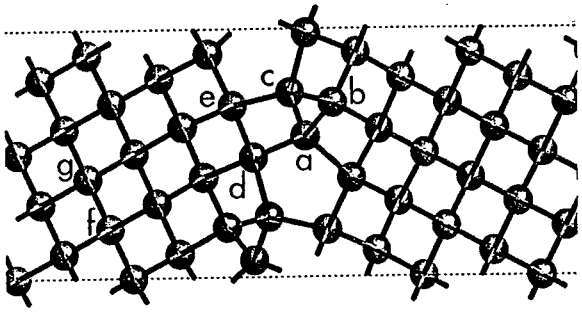


Fig. 1. Projection (normal to the tilt axis) of the relaxed structure of a Σ=5 {310} <001> symmetric grain boundary of Si in its ground state (GB1). Letters a-g denote various sites where segregation of isolated As atoms and As dimers were investigated. Results are listed in Table I.

axis. Figure 2 shows a second low-energy structure, we label GB2, with a total energy that is higher by only 0.15 eV per periodic segment of the grain boundary plane. The two

structures differ in the relative <001>-shift of the two grains forming the boundary, by a/8 = 0.68 Å, and also in the nature of the dislocation cores comprising the boundaries. The cores of GB1, are of the *pure edge* type (**b** = a/2 <110>), while the cores of GB2 with Burger's vector **b** = a/2 <101> have *mixed* screw and edge character.

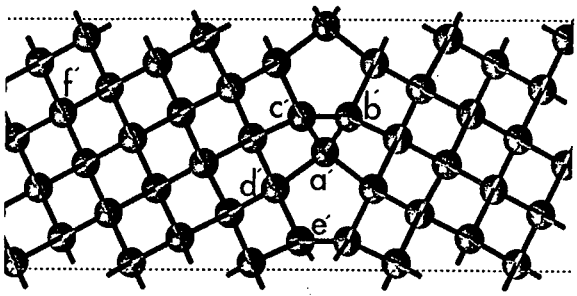


Fig. 2. Grain boundary of Fig. 1 in a metastable state (GB2) in the same projection view. Letters a'-f' denote various sites at which segregation of isolated As atoms and As dimers were investigated. Segregation energies are listed in Table II.

We studied segregation of As atoms in both GB1 and GB2 because the two structures contain different dislocation cores that are components of many different grain boundaries. Figures 1 and 2 show labels for the sites where As atoms were placed: [a] through [e] are sites in the GB1 grain boundary whereas [f] and [g] are sites in the bulk; [a'] through [f'] denote corresponding sites for GB2. Symmetry has been used to reduce the number of possible distinct As sites and site pairs. Thus, using the symbol '~' to indicate symmetry equivalence, we have for GB1: a ~ c and d ~ e. It follows that for GB1 the possible distinct sites for atom segregation are [a] ([c]), [b], and [d] ([e]). The distinct site pairs for dimer segregation are [a, c], [a, d], [b, c] and [d, e]. In addition, we have also studied the dimer [f, g] where two atoms are placed at nearest-neighbor sites in the bulk crystal. For GB2 we have the equivalence b' ~ c' ~ e'. The resulting distinct site pairs are [a', d'], [d', e'], [b', c'] and [a', c'].

Isolated As atoms and dimers

The results for isolated As substitutionals are shown in the top halves of Tables I and II. We find that all sites except [a] ([c]) on GB1 and [a'] on GB2 have a binding energy of ~ 0.1 eV, the same value obtained for isolated As atoms in a similar boundary in Ge [8]. The smaller binding of [a] can be explained from the *similarity* of its environment, characterized by the surrounding bond-length and bond-angle distribution, to that of a bulk site [f] or [g], while an opposite effect occurs for [a']. In all cases of isolated As substitutionals, the lattice is found to undergo only a very small relaxation, in agreement with the results of Ref. 8.

We now turn to the dimer configurations. As we noted earlier, we performed calculations with both minimal and double periodicity in the grain-boundary plane, corresponding to dimer chains and isolated dimers, respectively. The latter calculations are extremely time consuming, and were, therefore, performed only for selected pairs of sites. We found that dimer formation in the grain boundary is energetically favored. If two As atoms are placed at neighboring substitutional sites in the bulk crystal, they repel each other seeking to achieve threefold coordination (pair [f, g] in Table I). The

equilibrium As-As distance is 2.71 Å compared to a Si-Si bond-length of 2.35 Å. The overall energy goes up by a tiny amount (0.01 eV per As atom) as compared with isolated substitutional atoms because of the elastic energy cost. In contrast, As dimers in the grain boundary lead to an overall lowering of the energy. The selected calculations we performed for the isolated dimers yielded net binding of order 0.05-0.2 eV/atom, indicating that the elastic energy cost in the grain boundary can be smaller than in the bulk. Dimer formation in the grain boundary is the result of *repulsion* between neighboring As atoms and occurs because this repulsion can be accommodated easier in the grain boundary than in the bulk crystal.

Table I. Segregation energies of single As atoms and As dimers placed substitutionally at various sites of a Σ=5 {310} <001> tilt boundary in Si with the GB1 structure (Fig. 1). For the dimer geometries the *relaxed* distance between the two dimer companion atoms ($d_{As\text{-}As}$) and the corresponding distance between the first As atom and the periodic image of its dimer companion ($d_{As\text{-}As*}$) are also indicated. See Fig. 1 for site denominations.

As site(s)	Segregation Energy (eV/As atom)	$d_{As\text{-}As}$ (Å) (dimer geometries)	$d_{As\text{-}As*}$ (Å) (dimer geometries)
[f]	0.00		
[a], [c]	0.03		
[b]	0.11		
[d], [e]	0.11		
[f, g]	-0.01	2.71	4.59
[a, d]	0.10	2.71	5.20
[d, e]	0.19	2.79	4.70
[a, c]	0.20	2.89	3.76
[b, c]	0.32	3.43	3.43

Table II. Lists the same information as Table I for the GB2 structure of a Σ=5 {310} <001> tilt boundary in Si. See Fig. 2 for site denominations.

As site(s)	Segregation Energy (eV/As atom)	$d_{As\text{-}As}$ (Å) (dimer geometries)	$d_{As\text{-}As*}$ (Å) (dimer geometries)
[f']	0.00		
[b'], [c'], [e']	0.12		
[d']	0.13		
[a']	0.22		
[a', d']	0.08	2.43	5.25
[d', e']	0.09	2.72	4.84
[b', c']	0.11	2.42	4.29
[a', c']	0.52	2.76	3.54

Dimer Chains

The results for chains of As dimers are even more dramatic and are displayed in detail in Tables I and II for the two grain-boundary structures, respectively. We see that segregation energies range from 0.1 to 0.5 eV/atom, the latter being in agreement with the measured values [1-3]. In tables I and II, the third column contains the As-As distance in the dimer, which is to be compared with the normal Si-Si distance of 2.35 Å. The fourth column contains the distance between an As atom and the periodic image of its dimer companion (As*).

We note three classes of results: (i) cases where the As-As* distance is significantly larger than the As-As distance, suggesting that the dimers in the chain are fairly well-separated. The segregation energy is small, less than 0.2 eV/atom, comparable to that of truly isolated dimers that we discussed earlier; (ii) cases where the As-As and As-As* distances are comparable but different (e.g. [a, c] in GB1 and [a', c'] in GB2) where the segregation energy ranges from 0.2 to 0.5 eV/atom; and (iii) a case where the As-As and As-As* distances are identical ([b, c] in GB1), corresponding to a fully ordered chain of As atoms, with an intermediate segregation energy of 0.32 eV/atom.

An examination of the local three-dimensional topologies corresponding to Figures 1 and 2 suggests that the most stable dimer geometries in a chain are the ones in which one or both of the component As atoms can relax *into* the dislocation cores, where the average atomic density is lower than the crystalline bulk. Such relaxation reduces the strain in the Si backbonds, thereby yielding a larger segregation energy. It is interesting to note that the most stable chain of dimers [a', c'] in GB2 has its component atoms on two different dislocation cores, a configuration possible only in relatively-large-angle grain boundaries, while the chain of dimers [b, c] on GB1 has only one of its atoms (c) lying on a dislocation core, and could occur in any dislocation core of the perfect edge type.

Possibility of Structural Phase Transition

It is particularly interesting to note that the highest segregation energy in GB2 is significantly larger than in GB1, and might actually drive a structural transformation. In other words, the injection of a high concentration of As into polycrystalline Si may convert a grain boundary with perfect edge dislocations into one with mixed dislocations. Similar solute-induced grain boundary transformations have long been known to occur in metals [18], but we are not aware of any prior reports in semiconductors. From the relative total energies of the two grain boundaries we estimate that the transformation from GB1 to GB2 would require a critical As concentration of ~ 19% in the column of the favored dimer sites. However, such a transformation involves a relative shift (sliding) of the two grains at the boundary, and the above estimate does not take into account any elastic energy cost that may be required to maintain integrity at triple junctions during the sliding process.

SEGREGATION AT AN ISOLATED DISLOCATION CORE

In the above section we studied the segregation of As at a high-angle grain boundary. For plastically deformed materials, as well as in low-angle grain boundaries the primary extended defects are dislocations [19]. In semiconductor devices, dislocations can severely affect the behavior of dopant impurities because: (1) the dislocation cores may provide a fast diffusion pathway to dopant impurities, which severely influences the dopant profile in an uncontrolled way, and (2) impurities may get trapped in the core regions leading to preferential segregation and electrical deactivation of the impurity. It

is, therefore, important to investigate dopant segregation at an isolated dislocation core, and it is interesting to compare and contrast with segregation at a high-angle grain boundary. For concreteness, we chose a 90° partial, a commonly occurring dislocation in Si.

Relaxed Structures

We used a noncubic periodic supercell with two oppositely oriented 90° partial cores separated by a distance of 13 Å [20] (Fig. 3). Previous studies found two models of reconstruction in the 90° partial dislocation core: (1) the *asymmetric reconstruction*, in

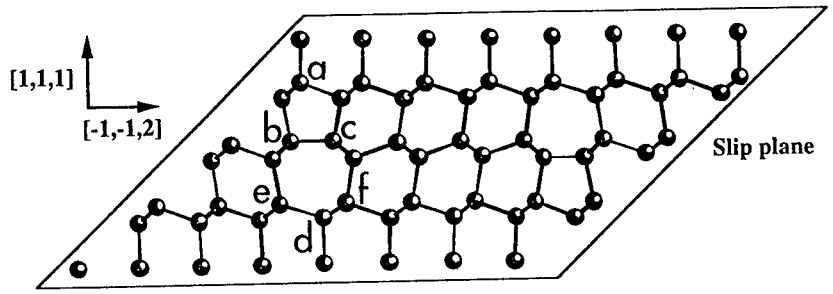


Fig. 3. Various sites of an isolated 90° partial core, viewed along the dislocation line, on which single As atoms and As dimers are placed. Segregation energies are listed in Table III.

which the mirror symmetry along the dislocation line is broken [21, 22]; and (2) the *symmetric reconstruction*, in which the mirror symmetry is kept intact [23]. The asymmetric structure has all the atoms fourfold-coordinated, while the symmetric structure has two quasi fivefold-coordinated atoms per periodic segment of the core. Both these reconstructed cores look almost the same in the projection along the dislocation line (Fig. 3), but are clearly distinguishable in the bonding structures in the slip plane. From *ab initio* relaxations we found that the asymmetric structure was stable, while the symmetric structure spontaneously transformed into the asymmetric structure, in agreement with an earlier *ab initio* study [24]. All our segregation studies were thus performed exclusively on the asymmetric structure by substitutionally placing single As atoms and As dimers at various sites and nearest neighbor site pairs of the dislocation core, as indicated in Fig. 3.

Isolated As atoms

Let us first consider the single As atoms in the dislocation core. Four different sites were chosen. The strain distribution is very different at different sites, as is apparent from comparing the site-associated bond-lengths with the bulk Si-Si bond-length of 2.35 Å, making the segregation energy strongly site-dependent. Thus the strain is: (i) compressive at site a, with bond-lengths (2.29, 2.31, 2.31, 2.34) Å; (ii) tensile at site d, with bond-lengths (2.37, 2.41, 2.43, 2.44) Å; (iii) mixed compressive/tensile at sites b and c with bond-lengths (2.31, 2.34, 2.41, 2.43) Å. The resulting segregation energy for As, listed in Table III, is largest for sites b and c, moderate but positive at site a, and even negative for site d. The largest segregation energy of 0.33 eV (sites b, c) is much larger than the average binding at a grain boundary [8, 10]. Also, the wide variation of

segregation energy from site to site is to be contrasted with a much smaller dispersion in a grain boundary [10], where the strain distribution is much more uniform. In all cases of single substitutional As, the relaxation from the initial Si site is very small, just as in a high-angle grain boundary.

Dimer Chains

Segregation studies of periodic chains of As dimers yield more dramatic results. To interpret these results, it should be re-emphasized that two As atoms placed on nearest neighbor Si sites, which we call As *dimers*, seek to repel and relax away from each other. In this way, each As atom achieves its preferred threefold coordination, leaving all the Si atoms fourfold-coordinated [10]. The three largest bonds in the dislocation core, *i.e.* [d, f], [d, e] and [b, c] were chosen for investigation. Table III displays the segregation energies for these three dimers, and the relaxed As-As and the As-As* distances. The distinct behaviors of the three dimers are clearly evident from Table III, as discussed below.

Table III. Lists the same information as Table I for As atoms and dimers segregated at the asymmetric structure of an isolated 90° partial dislocation core in Si. See Fig. 3 for site denominations.

As site(s)	Segregation Energy (eV/As atom)	$d_{As\text{-}As}$ (Å) (dimer geometries)	$d_{As\text{-}As^*}$ (Å) (dimer geometries)
bulk	0.00		
[d]	- 0.15		
[a]	0.14		
[b], [c]	0.33		
[d, f]	0.01	2.57	2.42
[d, e]	0.13	2.90	4.53
[b, c]	0.88	2.87	2.95

(i) [d, f]: In this case the orientation of the dimer is such that site d is the nearest neighbor of both f and its nearest periodic image f* in the dislocation line direction. Thus, in the periodic chain of dimers, all the As atoms are too close to each other. This allows only a small stretching of the As-As separation, to only 2.57 Å, while the As-As* distance (2.42 Å) changes very little from the equilibrium Si-Si bond distance of 2.35 Å. Consequently, the relaxed structure consists of a chain of essentially fourfold-coordinated As atoms, resulting in negligible binding.

(ii) [d, e]: In this case the orientation of the dimer is nearly perpendicular to the dislocation line direction, and sites d and e* are only second neighbors. This allows the As dimer atoms to relax away from each other, stretching the As-As separation to 2.90 Å, thereby leading to threefold coordination of each As atom. However, the transverse orientation of the dimer keeps it well separated from its periodic images in the dislocation line direction, as evident from the large As-As* distance. We therefore have an array of nearly *isolated* As dimers. This leads to a positive but low segregation energy (0.13 eV per As), just as in a grain boundary [10].

(iii) [b, c]: In this case the dimer is oriented such that although b and c* are second nearest neighbors, their distance before relaxation is much less than the separation of d and e* in case (ii). Consequently, the As-As stretch is accompanied by As and As*

getting closer to each other. In the final relaxed geometry, the As-As* separation (2.95 Å) is only slightly larger than the As-As separation (2.87 Å) and we have a nearly perfect *chain* of *As atoms* leading to a large segregation energy (0.88 eV per As).

Electronic States

In order to elucidate further the source of energy gain through the formation of dimer chains, we have examined the electronic energy levels in the As dimers in the dislocation core and compared them with those of isolated As atoms in the bulk. As one would expect, the isolated As atom has a shallow donor level at less than 0.1 eV below the conduction band edge. In the [b, c] dimer chains, on the other hand, each As atom has an electron at a level in the mid-gap region [25]. Further analysis indicates that the level in the gap is a member of the lone-pair states that As atoms have when they are threefold-coordinated. Because of the close proximity of the threefold coordinated As atoms, these lone-pair states split, with half of them in the bandgap and half of them in the valence band. Thus, the gain in energy could be viewed as a result of the shallow donor level being driven deep into the bandgap by the lattice relaxation accompanying dimer formation, or, equivalently, as arising from the fact that dimer formation leads to lone-pair states that are lower in energy than the states that are available when an As atom is fourfold-coordinated.

DIRECT IMPURITY DETERMINATION WITH HIGH RESOLUTION STEM

Experiment

The sample consisted of a silicon bicrystal wafer containing a Σ=13 {510} <001> symmetric grain boundary. Plan view samples with a <001> surface normal were characterized by high resolution Z-contrast imaging using a VG Microscopes HB603U scanning transmission electron microscope operating at 300 kV. The compositional sensitivity of the images, which is a function of the inner detector angle, can approach the atomic number (Z) squared dependence of Rutherford scattering. With the resulting image, no preconceived model structures are required for image interpretation. The actual defect arrangements are apparent immediately [26]. Figure 4 displays a computer

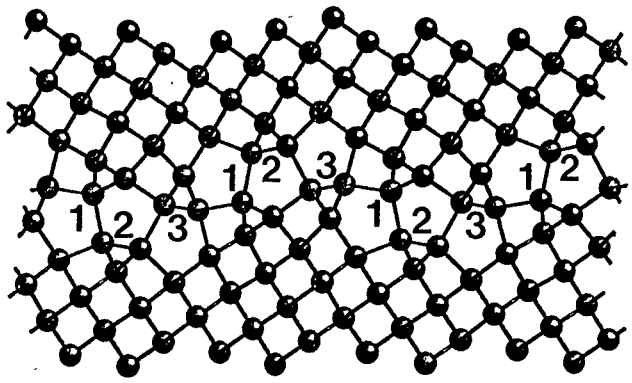


Fig. 4. Atomic model of a Σ=13 {510} <001> boundary imaged (Z-contrast) by STEM, viewed in a projection normal to the tilt axis.

model of the atomic structure obtained from the Z-contrast image of the grain boundary in a projection normal to the tilt (<001>) axis [27]. Each periodic segment consists of two equivalent sets of three triangles, denoted by 1, 2, 3 in Fig. 4.

The pure Si bicrystal was implanted at 450°C with arsenic ions (450 keV, $3x10^{16}$ ions/cm^2). Subsequent to implantation, the wafer was annealed first for one week at 1000°C followed by one week at 700°C. In the doped crystal, the average intensity from triangles 2 is 20% brighter than the average intensity from the triangles 1 or 3 [28]. These bright features, which are periodically repeated every 0.69 nm, are not observed in the undoped bicrystal. From careful intensity analysis, we have estimated an As concentration of ~ 5-6% in the bright triangles and ~1-2% or less in the dark triangles, respectively.

Theoretical Studies

In order to explain why triangles 2 light up specifically, we have performed *ab initio* calculations for segregation of As in a Σ=13 {510} <001> boundary in Si, similar to that described in the previous two sections for a Σ=5 boundary and a 90° partial dislocation core. Due to constraints imposed by heavy computational requirements, we used the minimum periodic repeat lengths in the grain boundary plane, i.e. 0.54 nm and 1.38 nm along and perpendicular to the tilt axis, respectively. In a direction normal to the grain boundary plane, we used two oppositely oriented grain boundaries separated by 2.94 nm.

The calculations indicate that for isolated substitutional As atoms the segregation energies vary somewhat from site to site, but is always around 0.1 eV, irrespective of the location. The result is similar to earlier results for the Σ=5 boundary in Si [10] and Ge [8]. *This result clearly implies that the higher intensity observed in triangles 2 must be due to arsenic segregation in some form other than as isolated substitutional atoms.*

Guided by the segregation studies described earlier, the obvious thing to look for was the segregation of dimers. Indeed, dimer chains yielded threefold coordinated As and larger segregation energies. However, estimates from our intensity analysis implied dilute As limit. Assuming that equilibrium had been established on and around the grain boundary, statistical mechanics can be used to show that, in the dilute limit, dopants segregate either as isolated atoms or more strongly as *isolated* dimers. The formation of *chains* of two or more dimers are *entropically almost precluded*. By a straightforward maximization of the partition function, the concentration of As as isolated As atoms (n_1) and isolated As dimers (n_2) can be expressed in terms of the bulk As concentration (n_B) as:

$$n_1 = \frac{n_B}{1 - n_B} \exp(\Delta_1/k_B T), \qquad (1)$$

and

$$n_2 = 2 \left(\frac{n_B}{1 - n_B}\right)^2 \exp(2\Delta_2/k_B T), \qquad (2)$$

where, Δ_1 and Δ_2 are the segregation energies per As atom for the isolated atom and *isolated* dimer respectively, T is the equilibrium temperature, and k_B the Boltzmann constant. From *ab initio* calculations we estimated Δ_1 ~ 0.1 eV for all triangles, and Δ_2 ~ 0.3 eV and ~ 0.1 eV respectively for the bright (2) and dark (1, 3) triangles. Assuming an equilibrium temperature of 700°C and a bulk As concentration of ~ 0.4% (close to the heavy doping limit of As in crystalline Si), the total As concentration ($n_G = n_1 + n_2$) given by eqs. (1) and (2) is ~ 5% in the bright triangles and ~ 1.5 % in the dark triangles, in agreement with estimates from the intensity analysis of our Z-contrast images. Thus,

our STEM observations and calculations strongly indicate that As and presumably other n-type dopants (e.g. P) can attain their preferred threefold-coordination in the cores of dislocations and grain boundaries without forcing neighboring Si atoms to become over- or under-coordinated [28].

SUMMARY

In summary, cooperative phenomena involving chains of *threefold-coordinated* As atoms or dimers result in much larger segregation energies than isolated As substitutionals, both in high-angle grain boundaries and in isolated dislocation cores. Segregation energies, thus obtained for a Σ=5 tilt boundary, are in agreement with experimental values for As segregation in poly-Si. This provides a mechanism for As segregation that does not require the presence of steps or other defects. Dimer chains in mixed dislocation cores are found to have lower energies, raising the intriguing possibility of segregation-induced structural transformation in grain boundaries containing pure edge dislocations. The overall behavior of single impurities, isolated dimers, and chains in an isolated dislocation core is similar to the behavior in a high-angle grain boundary. However, the segregation energy of both single As atoms and those in a chain are much larger in an isolated dislocation core, with the result for the chain being as high as 0.9 eV per As atom. Finally, high resolution STEM imaging of a Σ=13 tilt boundary in Si doped with As have conclusively shown that As segregates preferentially only to certain dislocations (triangles) within the grain boundary core, which can be explained by the formation of As dimers.

ACKNOWLEDGMENTS

We would like to thank the ORNL Center for Computational Sciences for providing valuable supercomputer hours. This research was supported in part by Lockheed Martin Energy Research Corp. under DOE contract No. DE-AC05-96OR22464, and ONR grant No. N00014-95-1-0906, and by an appointment to the ORNL Postdoctoral Research Associates Program administered jointly by ORNL and ORISE.

REFERENCES

1. C. R. M. Grovenor, J. Phys. C **18**, 4079 (1985).

2. C. R. M. Grovenor, P. E. Batson, D. A. Smith, and C. Y. Wang, Phil. Mag. A **50**, 409 (1984).

3. M. M. Mandurah, K. C. Saraswat, C. R. Helms, and T. I. Kamins, J. Appl. Phys. **51**, 5755 (1980).

4. J.-L. Maurice, in *Polycrystalline Semiconductors II*, edited by J. H. Werner and H. P. Strunk, Springer Proceedings in Physics Vol. 54 (Springer, Berlin, 1992), p. 166.

5. A. Bourret and J. L. Rouvière, Springer Proc. Phys. **35**, 8 (1989).

6. M. Kohyama, Phys. Stat. Sol. (b) **141**, 71 (1987).

7. A. T. Paxton and A. P Sutton, J. Phys. C **21**, L481 (1988).

8. T. A. Arias and J. D. Joannopoulos, Phys. Rev. B **49**, 4525 (1994).

9. N. F. Mott, Adv. Phys. **16**, 49 (1967).

10. A. Maiti, M. F. Chisholm, S. J. Pennycook, and S. T. Pantelides, Phys. Rev. Lett. **77**, 1306 (1996).

11. P. Hohenberg and W. Kohn, Phys. Rev. **136**, B864 (1964).

12. J. P. Perdew and A. Zunger, Phys. Rev. B **23**, 5048 (1981).

13. G. P. Kerker, J. Phys. C **13**, L189 (1980).

14. L. Kleinmann and D. M. Bylander, Phys. Rev. Lett. **48**, 1425 (1982).

15. R. D. King-Smith, M. C. Payne, and J. S. Lin, Phys. Rev. B **44**, 13063 (1991).

16. H. J. Monkhorst and J. D. Pack, Phys. Rev. B **13**, 5188 (1976).

17. M. C. Payne, M. P. Teter, D. C. Allan, T. A. Arias, and J. D. Joannopoulos, Rev. Mod. Phys. **64**, 1045 (1992).

18. V. Vitek and G. J. Wang, Surf. Sci. **144**, 110 (1984); K. E. Sickafus and S. L. Sass, Acta Met. **35**, 69 (1987); C. Rottman, J. de Phys. **49**, C5, 313 (1988).

19. J. P. Hirth and J. Lothe, *Theory of Dislocations* (McGraw-Hill, New York, 1982).

20. A. Maiti, T. Kaplan. M. Mostoller, M. F. Chisholm, S. J. Pennycook, and S. T. Pantelides, Appl. Phys. Lett., tentative Jan. 20 (1997).

21. R. Jones, J. Phys. (Paris), Colloq. **40**, C6-33 (1979).

22. P. B. Hirsch, J. Phys. (Paris), Colloq. **40**, C6-27 (1979).

23. M. S. Duesbery, B. Joos, and D. J. Michel, Phys. Rev. B **43**, 5143 (1991).

24. J. R. K. Bigger, D. A. McInnes, A. P. Sutton, M. C. Payne, I. Stich, R. D. King-Smith, D. M. Bird, and L. J. Clarke, Phys. Rev. Lett. **69**, 2224 (1992).

25. In the local density approximation used in the calculations, the bandgap is smaller than the experimental bandgap, so we cannot unambiguously determine the precise location of the level relative to the conduction band edge. Note that, however, for total-energy calculations performed here, only the occupied states are pertinent.

26. D. E. Jesson and S. J. Pennycook, Proc. R. Soc. Lond. A **449**, 273 (1995).

27. M. F. Chisholm, M. Mostoller, T. Kaplan, and S. J. Pennycook, Phil. Mag. A, in press.

28. M. F. Chisholm, A. Maiti, S. J. Pennycook, and S. T. Pantelides, *Science*, submitted.

MECHANISM OF DEFECT REACTIONS IN SEMICONDUCTORS

Yuzo SHINOZUKA
Department of Applied Science, Faculty of Engineering, Yamaguchi University
Tokiwadai 2557, Ube 755, Japan
yuzo@butsuri.yamaguchi-u.ac.jp

ABSTRACT

An overview is presented on mechanisms of electronically induced (enhanced) defect reactions in semiconductors, which are classified into the local heating, the structural instability, and the recombination enhanced. A mechanism for the annihilation of a hydrogen-carbon complex in silicon is given as an example of the second one. The last two mechanisms can be treated in a unified scheme by using the correct configuration coordinate diagram, which enable us to treat correctly the correlation in successive captures of an electron and a hole. The energy conversion mechanism during the reaction is precisely discussed paying attention to the relation between the lattice relaxation mode and the symmetry breaking reaction coordinate.

INTRODUCTION

The semiconductor technology is based on a physics hypothesis where carriers move in a almost static array of atoms and the electron-lattice interaction can be treated as a small perturbation. Recently, however, there have been found various phenomena which break this hypothesis. A localized electronic excitation in nonmetallic materials sometimes induces a large atomic displacement, such as a large lattice distortion at a point defect, desorption of an atom from a surface, defect reaction, structural phase transition, and so on. Among them, the most striking phenomena might be the off-center instability of a substitutional impurity and defect reactions. The former phenomenon has been found at several donors in III-V semiconductors and invalidates the traditional common sense of the valence control by shallow impurity doping. The off-center instability can be explained from various point of views: the extrinsic self-trapping of a carrier, the shallow-deep transition of bound electrons, the Jahn-Teller effect for symmetry breaking, Anderson's negative U between two electrons, and the bond change between sp^3 and sp^2 [1]. The second phenomenon, the defect reaction, generates degradations of semiconductor devices. Optically created dangling bonds bring about the degradation of amorphous Si solar cells. Degradations of light emitting semiconductor diodes and lasers have been found to caused by the climb and glide motions of dislocations. The control of defect reactions is an important key of the high efficiency and reliability of devices [2].

The purpose of the present paper is to give an overview on mechanisms of electronically induced (enhanced) defect reactions. Proposed mechanisms so far are reexamined including the local heating, the structural instability, and the recombination enhanced. A mechanism for the annihilation of a hydrogen-carbon complex in silicon is presented as an example of the second one. The last two mechanisms can be treated in a unified scheme by using the correct configuration coordinate diagram, which enable us to treat correctly the correlation in successive captures of an electron and a hole. The energy conversion mechanism during the reaction is precisely discussed paying attention to the relation between the lattice relaxation mode and the symmetry breaking reaction coordinate.

DEFECT REACTION INDUCED BY ELECTRONIC EXCITATION

Figure 1 schematically shows typical examples of defect reactions: impurity diffusion, climb and glide motions of dislocation, and structural change of a defect (creation, annihilation, and multiplication). It has been shown that defect reactions are induced or enhanced by electronic excitations such as photoexcitation, electron beam excitation and carrier injection. Hereafter we will call these phenomena DRIEE in abbreviation and indicate the reaction symbolically as $D_i \rightarrow D_f$. The off-center displacement of a substitutional impurity may fall within the category of DRIEE,

Mat. Res. Soc. Symp. Proc. Vol. 442 © 1997 Materials Research Society

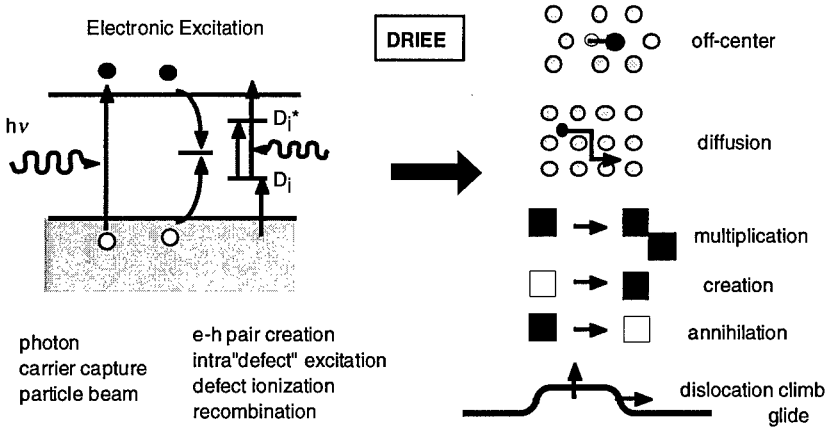


Fig. 1. Defect reaction induced by electronic excitation (DRIEE).

which is caused by a charge change of a defect.

Hereafter we discuss the mechanism of DRIEE in general starting from the energy conversion process. During the DRIEE the electronic energy is converted into the atomic kinetic energy in the reaction coordinate as:

$$\text{electronic energy} \xrightarrow{(A)} \text{lattice vibration } (q) \xrightarrow{(B)} \text{motion in reaction coordinate } (Q_R). \qquad (1)$$

Since the electronic energy is necessary to be localized for the process (A), it must take place via localized electronic states.

LOCAL HEATING

Some defect reactions have been considered to occur by a local heating. In the first step (A), the electronic energy is transformed into the vibrational energy of local phonons by nonradiative recombinations of electrons and holes at so called killer centers. Thermal equilibrium in a quasi "defect molecule" is locally realized so that a local temperature T_{loc} ($>T$) can be defined. Next the motion in the reaction coordinate (B) is activated. In this mechanism two processes (A) and (B) are usually considered to be different and then there is no coherence between two. Since the thermal equilibrium is locally realized, there are ample times of the backward reaction $D_f \rightarrow D_i$, then the population ratio would be given by the Boltzmann relation $n(D_i)/n(D_f)=\exp(\Delta E/k_B T_{loc})$, where ΔE is the energy necessary to change $D_i \rightarrow D_f$. Usually created defects are found to be annealed out, then it should be that $\Delta E > 0$. If the mechanism were the local heating, $n(D_f)$ should decrease by cooling process after a stop of the electronic excitation (carrier injection, photo illumination). Thus the local heating mechanism can not explain those reactions in which created defects can be annealed out.

If the size of a quasi "defect molecule" is so small that the local temperature can not be defined, we must treat exactly the kinetics of a defect and the time sequence of (A) and (B). Several models have been proposed so far, which can be classified into two categories as schematically shown in Fig. 2. One is the structural instability mechanism (Fig. 2(a)) where a special electronic state of a defect induces a symmetry breaking atomic distortion such as off-center distortion. For example, an electronic excitation to ex_1 promptly induces the reaction and that to ex_2 decreases the potential barrier height ($E_t \rightarrow E_t^*$) of the reaction. Examples are Bourgoin-Corbett model [3] and Sheinkman model [4]. The other mechanism is the recombination enhanced (or phonon kick) mechanism (Fig. 2(b)) where an electron-hole recombination at a defect excites a transient atomic motion in the reaction coordinate Q_R. Examples are Weeks-Tully-Kimerling model [5] and Sumi

(a) *Structural Instability Mechanism* (b) *Recombination Enhanced Mechanism (Phonon Kick)*

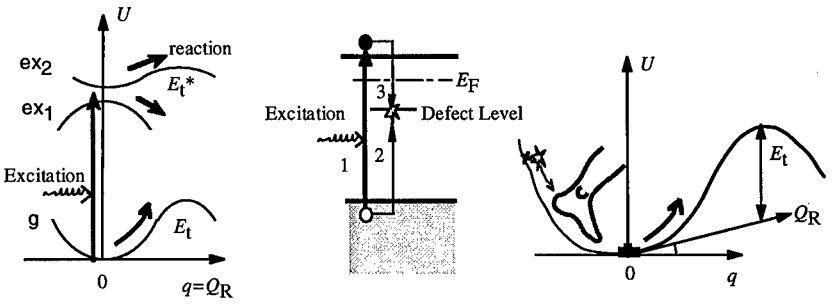


Fig. 2. (a) structural instability mechanism and (b) recombination enhanced (phonon kick) mechanism for DRIEE.

model [6]. Though two mechanisms (a) and (b) look different, they can be treated in a unified scheme as follows.

STRUCTURAL INSTABILITY

The most simple case would be those where the relaxation mode q in (A) is nothing but the reaction coordinate Q_R in (B) itself. This is so in the off-center instability of a substitutional impurity such as the EL2 center in GaAs [7, 8], the DX-center in III-V semiconductors [9-11] and a substitutional nitrogen impurity in Si [12, 13]. It is found in N impurity in Si that if the impurity charge is neutral, the on-center T_d configuration is metastable and presents a shallow donor state, whereas the off-center C_{3v} configuration is stable and presents a deep-donor state. For ionized states (positively charged) the on-center configuration is stable and the off-center unstable. A carrier capture or emission by the impurity induces the on-off bistability, which is a simple example of defect reactions. The off-center instability of N in Si can be also explained in terms of the J-T effect as is in the DX-center [14], however, only one localized electron is enough to stabilize the off-center configuration. A detailed discussion is given in reference [1].

Quite recently a bistability mechanism of a dangling bond in amorphous silicon (a-Si) has been proposed [15] for the key mechanism of the Staebler-Wronski effect [16] where the optical absorption creates dangling bonds which are ESR active. The authors show theoretically that dangling bonds in a-Si have two stable configurations. One is a normal dangling bond, n-DB, with a negative electron correlation energy ($2\ \text{n-DB}^0 \rightarrow \text{n-DB}^+ + \text{n-DB}^-$). Then they are usually ESR inactive. The other is a flipped dangling bond, f-DB, with positive correlation. An optical excitation is shown to induce a defect reaction $\text{n-DB}^{+(-)} \rightarrow \text{f-DB}^0$. The proposed mechanism is attractive, however, it remains in controversy.

In the on-off bistability case the reaction is reversible ($D_i \leftrightarrow D_f$) and then it can be easily controlled. Even if the reaction is irreversible, we discuss in the following section that the off-center displacement has a role of a precursor in defect reactions.

ANNIHILATION OF IMPURITY COMPLEX

A hydrogen atom in semiconductors can passivate or activate donors, acceptors and other impurities. In silicon a hydrogen impurity can occupy several stable sites in the diamond lattice. If it occupies a bond center site between a substitutional carbon (isoelectronic) impurity and a Si atom, this H-C complex act as a shallow donor whose thermal depth is E_c- 0.15eV. The positively charged H-C complex is stable above the room temperature, while the neutral state is unstable at the room temperature and the activation energy for the annihilation is estimated as 0.5 ~ 0.7eV [17]. Since the "united atom" of an H-C complex is a nitrogen atom in the molecular chemistry, the

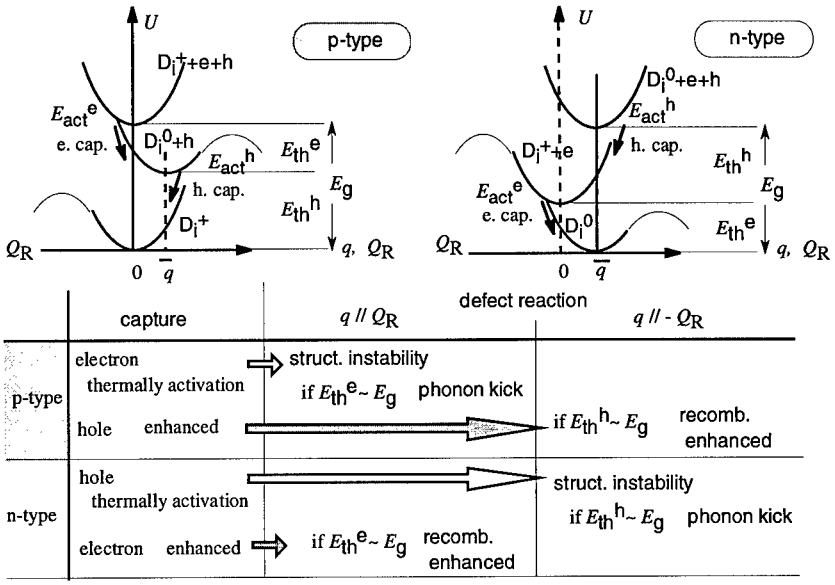


Fig. 3. An example of the configuration coordinate diagrams for a defect in p-type and n-type semiconductors. Thick adiabatic potentials are for the interaction mode q (relaxation mode) and thin adiabatic potentials for the reaction coordinate Q_R. The table summarizes the most probable path for DRIEE.

effective potential seen by a conduction electron away from the $(H\text{-}C)^+$ complex is similar to those by the N^+ impurity. Then we can derive an analogy between the stabilities of a N impurity and of a H-C complex in Si. For a shallow donor state or a positively charged state (an electron is away) the central position is stable for a N impurity, and the H-C complex is stable. If an electron comes close to them, on the other hand, it induces the off-center displacement of a N impurity, and the off-center displacement of a hydrogen atom. That is, a hydrogen atom is pushed away from a carbon: the annihilation of an H-C complex. This would be a typical example of a defect reaction caused by the structural instability mechanism.

RECOMBINATION ENHANCED DEFECT REACTION

Carrier captures by a defect as well as localized electronic excitations take place via a localized electronic state whose level is located in the band gap. Therefore it is convenient to introduce a configuration coordinate diagram (CCD) [18]. A typical example is illustrated in Fig. 3: for simplicity the initial defect is assumed to have D_i^0 and D_i^+ charged states.

In a p-type semiconductor, the defect is stationary occupied by a majority hole (D_i^0). The interaction mode, q, and its origin are defined such that the equilibrium positions of atoms for D_i^+ is given by q=0 and those for D_i^0 by $q=\bar{q}$. A capture of a minority electron occurs by a thermally activated process (the activation energy is E_{act}^e) which is followed by a transient lattice vibration of q around $\bar{q}$. Because q is not a normal mode but a linear combination of many normal modes of different frequency, the vibration of q is quickly damped. (If q mainly consists of a local vibrational mode at the defect, however, the vibration lasts rather long periods.) During the lattice relaxation, an energy equal to the thermal depth E_{th}^e of an electron is converted to phonons. These transient vibrations can enhance a succeeding majority hole capture: capture enhanced capture. If a

hole is captured before the transient lattice vibration has been damped out, the activation energy E_{act}^{h} is not necessary (cf. Dexter-Krick-Russel mechanism for the F-center in alkalihalides [19]). After a hole capture, q again vibrates around q=0. During the second lattice relaxation, an energy equal to the thermal depth E_{th}^{h} of a hole is converted to phonons as if a hole is bound in the D^+ configuration. An electronic energy $E_g=E_{th}^{e}+E_{th}^{h}$ is converted to the atomic energy in total. It is also noted that the D_i^++e+h is a doubly continuum state and the D^0+h is a singly continuum state. That is, both an electron capture (D_i^++e+h$\rightarrow D_i^0$+h) and a hole capture (D_i^0+h$\rightarrow D_i^+$) are electronic transitions from continuum free states to a single localized state.

When we use the CCD to discuss defect reactions, we should mind that there are many situations depending on the variety of charged states of a defect, the magnitude of E_{th}^{e} and E_{th}^{h}, the relation between the relaxation mode q and the reaction coordinate Q_R, the magnitude of capture cross sections, and so on. When the relaxation mode q is a symmetric mode such as a breathing mode, q is orthogonal to Q_R which is a symmetry breaking mode by definition. Then the symmetrical relaxation process does not affect defect reactions.

Let us consider that the on-off bistability takes place by the charge change of a defect. The keypoint is which corresponds to the off-center configuration, q=0 or $\bar{q}$? If the reaction coordinate Q_R is almost parallel to q, a defect reaction occurs by the structural instability mechanism induced by a minority electron capture (cf. Fig. 2(a): the excitation to ex_1). If E_{th}^{e} is large and q // Q_R but there is a potential barrier, the phonon kick mechanism takes place with the aid of E_{th}^{e} induced by an electron capture. This corresponds to the structural instability mechanism shown in Fig. 3(b) (the excitation to ex_2). If E_{th}^{h} is large and q // - Q_R, the phonon kick mechanism takes place by a hole capture which has been enhanced by an electron capture. If a majority carrier capture occurs very quickly within the local transient vibration, the band gap energy $E_g=E_{th}^{e}+E_{th}^{h}$ can be used for exciting a defect reaction. This could be the most effective path to the defect reaction and nothing but so called the recombination enhanced mechanism.

In an n-type semiconductors, defect reactions can be discussed in a similar way as above, starting from $q=\bar{q}$ and D_i^0+e+h. In contrast to the p-type, the first capture of a minority hole by a neutral center D_i^0 is not accelerated by the Coulomb attraction while the second electron capture by D_i^+ is accelerated.

We have assumed that the initial defect has D_i^0 and D_i^+ charged states. If it has D_i^- and D_i^0, the above discussion can be also valid with respective translations $D_i^0 \rightarrow D_i^-$ and $D_i^+ \rightarrow D_i^0$. As described just above, it should be minded that either in n-type and p-type, the capture of a majority carrier always enhanced by a minority carrier capture, but only a hole capture is accelerated by the Coulomb attraction of D_i^-.

CONCLUSION

So far we have discussed the mechanisms of defect reactions in semiconductors, which are classified into the local heating, the structural instability, and the recombination enhanced. The annihilation mechanism of a hydrogen-carbon complex in silicon has been given as an example of the second one. Using the correct configuration coordinate diagram we have also shown that the last two mechanisms can be treated in a unified scheme, if we treat correctly the correlation in successive carrier captures and the relation between the lattice relaxation mode and the reaction coordinate.

The off-center instability would be an important role in DRIEE. Further study is necessary to clarify the relation between the relaxation mode q and the reaction coordinate Q_R. A systematic experimental study is also necessary to distinguish whether each DRIEE is caused by a single capture or by a successive two captures: recombination.

ACKNOWLEDGMENTS

The author would like to thank Professor K. Maeda and Dr. K. Wada for valuable discussions. The present work is supported by the Proposal-Based Advanced Industrial Technology R&D Program of NEDO Japan and by a Grand-in-Aid by the Japanese Ministry of Education, Science and Culture.

REFERENCES

1. Y. Shinozuka, Proc. 19th Taniguchi Symposium (Springer, 1996) ed. by K. Nasu, in press.
2. O. Ueda, *Reliability and degradation of III-V optical devices* (Artech House Publishers, Boston-London) 1996.
3. J. C. Bourgoin and J. M. Corbett, Phys. Lett. **38A**, 135 (1972), and Radiation Effects **36**, 157 (1978).
4. M. K. Sheinkman, JETP Lett. **38**, 330 (1983), and M. K. Sheinkman and L. C. Kimerling, *Defect Control in Semiconductors*, ed. K. Sumino (North-Holland, 1990) p. 97.
5. J. D. Weeks, J. C. Tully, and L. C. Kimerling, Phys. Rev. B**12**, 3286 (1975).
6. H. Sumi, Phys. Rev. B**29**, 4616 (1985), J. Phys. C**17**, 6071 (1984).
7. D. J. Chadi and K. J. Chang, Phys. Rev. Lett. **61**, 873 (1988), Phys. Rev. B**39**, 10063 (1989).
8. M. Saito, A. Oshiyama, and O. Sugino, Phys. Rev. B**47**, 13205 (1993).
9. D. V. Lang and R. A. Logan, Phys. Rev. Lett. **39**, 635 (1977).
10. J. Dabrowski and M. Scheffler, Phys. Rev. Lett. **60**, 2183 (1988).
11. D. J. Chadi and K. J. Chang, Phys. Rev. Lett. **60**, 2187 (1988).
12. K. L. Brower, Phys. Rev. B**26**, 6040 (1982).
13. K. Murakami, H. Kuribayashi, and K. Masuda, Phys. Rev. B**38**, 1589 (1988).
14. Y. Shinozuka, Materials Science Forum **83-87**, 527 (1992).
15. T. Matsumura, H. Katayama-Yoshida, and N. Orita, Proc, of MRS Symposium (Amorphous Silicon Technology '95) **377**, 275 (1995); N. Orita and H. Katayama-Yoshida, J. Non-Crystalline Solids **198-200**, 347 (1996).
16. D. L. Staebler and C. R. Wronski, Appl. Phys. Lett. **31**, 292 (1977).
17. Y. Kamiura, M. Tsutsune, M. Hayashi, Y. Yamashita, and F. Hashimoto, Materials Science Forum **196-201**, 903 (1995).
18. Y. Shinozuka, J. Phys. Soc. Jpn. **51**, 2852 (1982); Jpn. J. Appl. Phys. **32**, 4560 (1993).
19. D. L. Dexter, C. C. Klick, and G. A. Russel, Phys. Rev. **100**, 603 (1956).

INTERSTITIAL DEFECT REACTIONS IN SILICON

S. ZHAO, A. M. AGARWAL, J. L. BENTON*, G. H. GILMER*, and L. C. KIMERLING
Department of Materials Science and Engineering, Massachusetts Institute of Technology, Cambridge, MA 02139, szhao@photonics.mit.edu
*Bell Laboratories, Lucent Technologies, Murray Hill, NJ 07974

ABSTRACT

The interaction between self-interstitials (Si_i), impurities, and dopants in Si leads the formation of undesirable point defects which affect device operation. Electron beam irradiation has been used to generate Si_i and initiate defect reactions, and the hierarchy and competition of interstitial defect reactions involving O, C, B, and P in Si have been explored by DLTS measurements. We describe the interstitial defect reactions as a three-step process: (i) displacement reaction for the generation of Si_i, (ii) Watkins replacement reaction for the generation of C and B interstitials (C_i and B_i), and (iii) diffusion limited reaction for the formation of pairs. Within the framework of reaction kinetics, for the first time, we have successfully set up a nonlinear system model to simulate the reaction processes. The interstitial migration enthalpy and the pair formation capture radius are two parameters used in the model to describe long range migration and near neighbor interaction. The good agreement between the model and experiments not only supports the defect assignments by DLTS, but also provides an initial glimpse into the interaction of point defects in Si.

INTRODUCTION

C and O are introduced into bulk Si in significant concentrations during crystal growth and device fabrication with steps such as ion implantation and reactive ion etching with fluorocarbons. The impurity introduction creates carrier recombination centers in the bandgap. The interaction among O, C, B, P, and Si_i also exhibits a complex hierarchy of interstitial defect reactions. The interstitial defect reactions are found to be common phenomena during heat treatment in both p-type and n-type Si using electron beam irradiation and DLTS measurements [1, 2, 3, 4, 12]. Based on the DLTS defect assignments and a series of defect anneal data, a complex interstitial defect reaction hierarchy diagram has been constructed [1]. The DLTS measurements also show the competitions between different pairing reactions, and a first order defect reaction mechanism has thereby been suggested [1, 3]. In this paper, we propose a first order kinetic model to simulate the interstitial defect reactions and explain the experimental data in Si.

DEFECT REACTION KINETICS

The electron beam penetration depth in Si is in the millimeter range for beam energies in the MeV range, and the point defect distribution generated in the experiments can be approximately assumed uniform. Si_i and vacancies (V) are produced in displacement reactions by electron irradiation, B_i and C_i are subsequently created by Watkins replacement reactions. Both B_i and C_i migrate in the Si and undergo diffusion limited pairing reactions with background impurities B_s, C_s and O_i [1, 3].

$$Si_s \rightleftharpoons^{\sigma,\phi,t_0}_{k_0} Si_i + V; \qquad B_s + Si_i \rightleftharpoons^{k_1}_{k_2} B_i + Si_s, \qquad C_s + Si_i \rightleftharpoons^{k_3}_{k_4} C_i + Si_s; \tag{1}$$

$$B_i + B_s \rightleftharpoons^{k_5}_{k_6} B_iB_s, \qquad B_i + O_i \rightleftharpoons^{k_7}_{k_8} B_iO_i, \qquad B_i + C_s \rightleftharpoons^{k_9}_{k_{10}} B_iC_s, \tag{2}$$

$$C_i + C_s \rightleftharpoons^{k_{11}}_{k_{12}} C_iC_s, \qquad C_i + O_i \rightleftharpoons^{k_{13}}_{k_{14}} C_iO_i, \qquad C_i + P_s \rightleftharpoons^{k_{15}}_{k_{16}} C_iP_s. \tag{3}$$

Mat. Res. Soc. Symp. Proc. Vol. 442 © 1997 Materials Research Society

σ, ϕ, t_0, and k_i are the displacement reaction cross section, irradiation fluence, irradiation time, and reaction rate parameter, respectively. In principle, both isothermal and isochronal anneals of the defect reactions in Eqs. (1)-(3) can be simulated if all the reaction parameters are known. It is difficult to simulate coupled pair dissociation processes due to limited knowledge on various pair bonding mechanisms and binding energy data. However, except for the displacement reaction, all the forward reactions are diffusion limited in which the migration of mobile interstitials play a dominant role in determining reaction branch ratio in the pairing reactions (Eqs. (2)-(3)). The reaction branch ratio changes slowly with temperature due to the quite large difference (0.1-0.2 eV) in migration enthalpy among Si_i, B_i and C_i. Therefore we can study defect introduction by the final pairing reactions by simulating isothermal anneal processes if pair dissociation is negligible in that temperature range. The isothermal anneal at room temperature is performed for a long time until the mobile interstitials disappear.

The isothermal anneal processes in p-type Si can be described by the following equations,

$$\frac{d[B_i]}{dt} = k_1[Si_i][B_s] - k_5[B_i][B_s] - k_7[B_i][O_i] - k_9[B_i][C_s]; \tag{4}$$

$$\frac{d[C_i]}{dt} = k_3[Si_i][C_s] - k_{11}[C_i][C_s] - k_{13}[C_i][O_i]; \tag{5}$$

$$\frac{d[B_iO_i]}{dt} = k_7[B_i][O_i], \quad \frac{d[B_iB_s]}{dt} = k_5[B_i][B_s], \quad \frac{d[B_iC_s]}{dt} = k_9[B_i][C_s]; \tag{6}$$

$$\frac{d[C_iO_i]}{dt} = k_{13}[C_i][O_i], \quad \frac{d[C_iC_s]}{dt} = k_{11}[C_i][C_s]; \tag{7}$$

$$\frac{d[B_s]}{dt} = -k_1[Si_i][B_s] - k_5[B_i][B_s], \quad \frac{d[O_i]}{dt} = -k_7[B_i][O_i] - k_{13}[C_i][O_i], \tag{8}$$

$$\frac{d[C_s]}{dt} = -k_3[Si_i][C_s] - k_9[B_i][C_s] - k_{11}[C_i][C_s]; \tag{9}$$

$$\frac{d[Si_i]}{dt} = \sigma N[\frac{d\phi}{dt}(t)] - k_1[Si_i][B_s] - k_3[Si_i][C_s]. \tag{10}$$

where $N = 5.0\times10^{22}$ cm^{-3} is Si atom concentration, $\sigma = 2.4\times10^{-24}$ cm^2 for beam energy $E = 1.0$ MeV [5]. The irradiation flux is $\frac{d\phi}{dt}(t) = (\frac{\phi}{t_0})f(t)$, and $f(t) = \{1 + \exp[(t - t_0)/(t_0/400)]\}^{-1}$. The diffusion limited reaction rate parameter can be expressed as [6, 7],

$$k = 4\pi r_c D_i, \qquad D_i = (1/6)\nu_i r_i^2 \exp(-H_i^m/kT) \tag{11}$$

where r_c is the capture radius, D_i is the interstitial diffusion coefficient, $r_i \approx 2.5$ Å is the distance between two interstitial sites, $\nu_i \approx 1.0\times10^{13}$ sec^{-1} is attempt frequency, and H_i^m is the interstitial migration enthalpy. The migration enthalpy for B_i, C_i, and Si_i are 0.63 eV [8], 0.73 eV [9, 10], and 0.40 eV [11], respectively.

The initial conditions are: $[B_s]|_{t=0} = [B]$, $[C_s]|_{t=0} = [C]$, $[O_i]|_{t=0} = [O]$, $[B_i]|_{t=0} = 0$, $[C_i]|_{t=0} = 0$, $[Si_i]|_{t=0} = 0$, $[B_iO_i]|_{t=0} = 0$, $[B_iB_s]|_{t=0} = 0$, $[B_iC_s]|_{t=0} = 0$, $[C_iO_i]|_{t=0} = 0$, and $[C_iC_s]|_{t=0} = 0$. [B], [C] and [O] are the total B, C and O concentrations, respectively. Eqs. (4)-(10) plus the initial conditions satisfy the following mass conservation,

$$[B_i] + [B_s] + [B_iO_i] + [B_iC_s] + 2[B_iB_s] = [B] \tag{12}$$

$$[C_i] + [C_s] + [C_iO_i] + [B_iC_s] + 2[C_iC_s] = [C] \tag{13}$$

$$[O_i] + [B_iO_i] + [C_iO_i] = [O] \tag{14}$$

$$\{[Si_i] + [B_i] + [B_iO_i] + [B_iC_s] + [B_iB_s] + [C_i] + [C_iO_i] + [C_iC_s]\}|_{t=t_{final}} = \sigma N\phi \tag{15}$$

Therefore, a *closed, self-consistent* nonlinear system is constructed to describe the interstitial defect reactions in p-type Si.

The pairing in n-type Si [1, 3] can be simulated based on the forward reactions in Eq. (3). C_i and C_i-related pairs are generated by reactions described in Eqs. (1) and (3). In order to study pair formation processes, current injection was applied to dissociate C_i-related pairs. Right after the current injection, the isothermal anneal of C_i can be described by the following equations,

$$\frac{d[C_i]}{dt} = -k_{11}[C_i][C_s] - k_{13}[C_i][O_i] - k_{15}[C_i][P_s]; \tag{16}$$

$$\frac{d[C_iO_i]}{dt} = k_{13}[C_i][O_i], \quad \frac{d[C_iC_s]}{dt} = k_{11}[C_i][C_s], \quad \frac{d[C_iP_s]}{dt} = k_{15}[C_i][P_s]; \tag{17}$$

$$\frac{d[O_i]}{dt} = -k_{13}[C_i][O_i], \quad \frac{d[P_s]}{dt} = -k_{15}[C_i][P_s], \quad \frac{d[C_s]}{dt} = -k_{11}[C_i][C_s]. \tag{18}$$

Eqs. (16)-(18) plus proper initial conditions (Fig. 1 caption) also satisfy corresponding conservation relations. The reaction parameters are listed in TABLE 1.

TABLE 1 DLTS Defect Assignment and Defect Reaction Parameter

DLTS Signal & Assignment [1]	Defect Reaction	Capture Radius (Å)	Reaction Rate Parameter	
			forward (300K) (cm^3/sec)	backward (sec^{-1})
	$Si_s \rightleftharpoons^{\sigma,\phi,t_0}_{k_0} Si_i + V$		$\sigma = 2.4 \times 10^{-24}$ cm^2 $\phi = 4.8 \times 10^{15}$ cm^{-2} $t_0 = 20$ min	$k_0 = 0$ cm^3/sec
B_i: E(0.13), E(0.45)	$B_s + Si_i \rightleftharpoons^{k_1}_{k_2} B_i + Si_s$	2.0	$k_1 = 5.0 \times 10^{-17}$	$k_2 = 0$ cm^3/sec
C_i: E(0.12), H(0.27)	$C_s + Si_i \rightleftharpoons^{k_3}_{k_4} C_i + Si_s$	2.0	$k_3 = 5.0 \times 10^{-17}$	$k_4 = 0$ cm^3/sec
B_iB_s: H(0.30)	$B_i + B_s \rightleftharpoons^{k_5}_{k_6} B_iB_s$	20.0 ↓	$k_5 = 7.0 \times 10^{-20}$	$k_6 = 0$
B_iO_i: E(0.26)	$B_i + O_i \rightleftharpoons^{k_7}_{k_8} B_iO_i$	2.0	$k_7 = 7.0 \times 10^{-21}$	$k_8 = 0$
B_iC_s: H(0.29)	$B_i + C_s \rightleftharpoons^{k_9}_{k_{10}} B_iC_s$	40.0 ↓	$k_9 = 1.5 \times 10^{-19}$	$k_{10} = 0$
C_iC_s: ME(0.17), ME(0.10), MH(0.09), MH(0.05)	$C_i + C_s \rightleftharpoons^{k_{11}}_{k_{12}} C_iC_s$	4.0	$k_{11} = 3.1 \times 10^{-22}$	$k_{12} = 0$
C_iO_i: H(0.36)	$C_i + O_i \rightleftharpoons^{k_{13}}_{k_{14}} C_iO_i$	4.0	$k_{13} = 3.1 \times 10^{-22}$	$k_{14} = 0$
C_iP_s: ME(0.30), ME(0.29), ME(0.23), ME(0.21)	$C_i + P_s \rightleftharpoons^{k_{15}}_{k_{16}} C_iP_s$	6.0	$k_{15} = 4.7 \times 10^{-22}$	$k_{16} = 0$

RESULTS AND DISCUSSION

The defect introduction can be quantitatively described by a defect introduction rate defined as: Introduction Rate (cm^{-1}) = Concentration (cm^{-3})/Fluence (cm^{-2}). The defect introduction rate depends on the background impurity concentration. Fig. 1(a), (b), and (c) show the measured

and calculated defect introduction rate in p-type Si versus [B], [C], and [O], respectively. In Fig. 1(a), consistent trends and magnitudes exist between the model and experiments. As [B] increases, the C_iO_i introduction rate decreases due to the competition by the B_iO_i defect. However, in high [B] ($10^{17} - 10^{18}$ cm^{-3}) region, both the B_iO_i and B_iC_s introduction rates decrease because of the competition from B_iB_s pair. This competition based on the first order B_i-B_s pairing kinetics is not enough to fit experiment. Higher order kinetic processes such as B_i clustering may be important in the high [B] region. The inclusion of B_i clustering helps to minimize the deviation between the model and experiments, i.e., both B_iO_i and B_iC_s introduction rates will drop rapidly in high [B] region, and the calculated B_iB_s curve will shift to the high [B] region by using a smaller capture radius for B_i-B_s pairing.

Fig. 1(b) shows the dependence on [C]. The model predicts the same trends as observed in experiment. There are competitions between B_iO_i and B_iC_s, and between C_iO_i and B_iO_i. C_iC_s is in competition with all other C-related defects in the high [C] ($10^{17} - 10^{18}$ cm^{-3}) region, where C_i clustering is also possible. In order to show the trend of C_i with increasing [C], the 4-hour anneal data are extracted from the model since C_i is not a final reaction product. In Fig. 1(c), except for several experimental data at [O]$\approx 10^{18}$ cm^{-3}, the model gives trends consistent with experiment. There is a competition between B_iC_s and B_iO_i formation. [B_iO_i] tends to saturate in the high [O] region, while [B_iC_s] saturates in the low [O] region. The B_iC_s introduction rate depends slightly on [O] when [O]$< 10^{17}$ cm^{-3}.

In Fig. 1(a), (b), and (c), the higher concentration from the model is caused by the neglect of Si_i-V recombination and reverse Watkins replacement process, and also by the large capture radius assumption for B_i-B_s and B_i-C_s pairing (TABLE 1). It should be pointed out that the comparison between the model and experiments is indirect. The experimental data are the maximum values observed over stable temperature range from a series of isochronal anneal experiments [1, 2, 4]. The calculated curves are based on isothermal anneal simulations at room temperature. The comparison of trends between the model and experiment is meaningful only for the final reaction products. An exact numerical match between the model and experiment should not be expected.

Fig. 1(d) shows the simulated pair formation processes in n-type Si and comparison with the isothermal anneal experiment at room temperature. With the consumption of C_i, C_iO_i and C_iP_s pairs appear. The experimental data of C_i and C_iO_i are from sample 5Si-P-FZ-DJ, and the C_iP_s ME(0.23) data are from sample 3Si-P-FZ-DJ (Fig. 1 caption) [3]. The C_i migration enthalpy of 0.73 eV extracted from the experimental data is the same value used in the simulation of p-type Si. The pair formation kinetics are determined by the forward reactions under isothermal anneal. Therefore good agreement between the model and experiment exists. The C_iP_s pair data are based on one (ME(0.23)) of its multiple configurations, while the model gives the total concentration. Thus the moderate fit is not a surprise.

The DLTS defect assignments [1] have been used in the first order interstitial defect reaction model. The calculated concentrations and introduction rates of the final reaction products from the model agree qualitatively with the DLTS measurements. This fact not only supports the DLTS defect assignments, but also confirms the proposed first order interstitial defect reactions based on DLTS measurements. Pairs with multiple configurations (C_iC_s and C_iP_s) have larger capture radii, consistent with physical picture. The Watkins replacement reaction of capture radius 2.0 Å is assumed to happen at the nearest neighbor. The large capture radii for B_iB_s and B_iC_s formation are consistent with long range Coulomb interaction [1], but other effects may also play a role. As discussed before, if B_i clustering is included in the model, it is not necessary to assign a large capture radius for B_i-B_s pairing to compete with B_i-O_i pairing. From experiment, the maximum values of B_iC_s and B_iO_i do not occur at the same temperature [1]. In order to compare

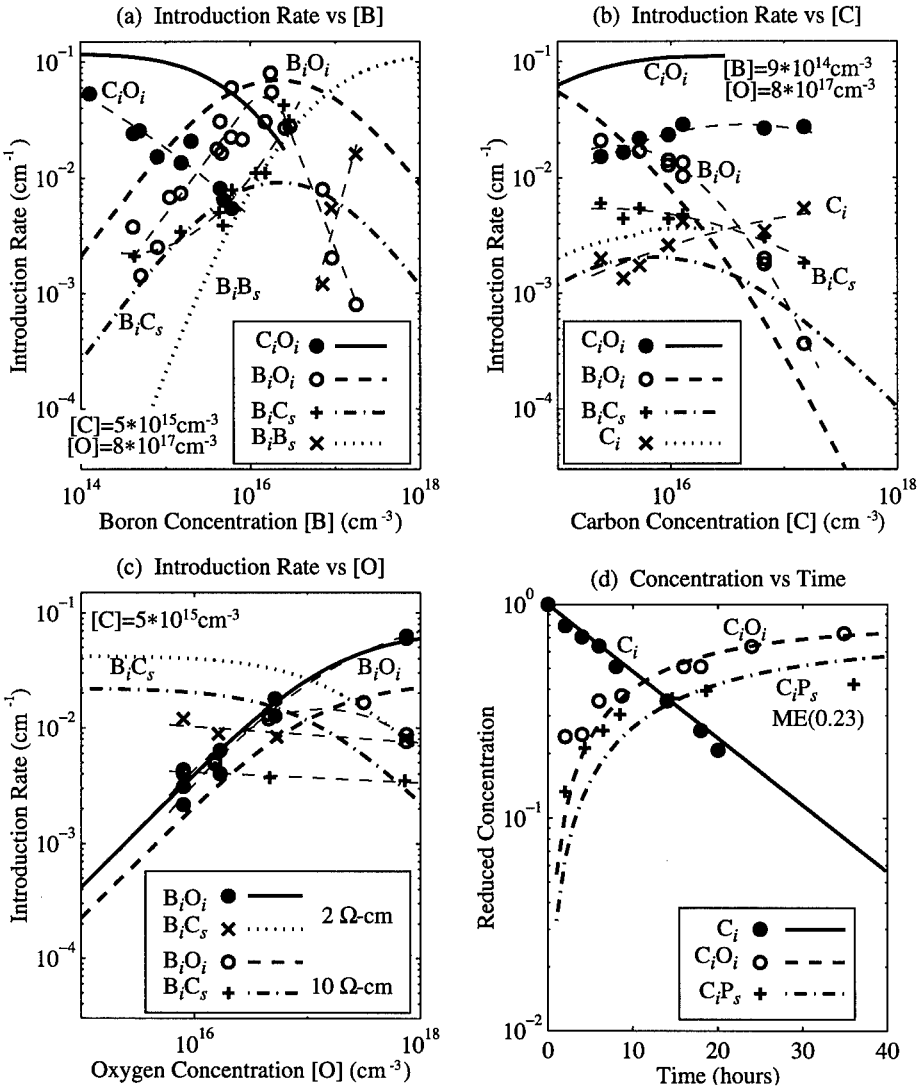


Fig. 1 Defect introduction in *p*-type Si and pair formation processes in *n*-type Si. The thick lines show results from the model, the thin dashed lines are fit curves to the experimental data represented by different dots. Fig. 1(a), 1(b) , and 1(c) show that, in *p*-type Si, defect introduction rate depends on the background impurity concentration [B], [C], and [O], respectively [1,2,4]. In order to show the trend of C_i with increasing [C], the thick C_i curve in Fig. 1(b) represents the 4 hour anneal data from the model since C_i is not a final reaction product. Fig. 1(d) shows pair formation processes in *n*-type Si. The experimental data of C_i and C_iO_i are from sample 5Si-P-FZ-DJ ([P]=3*10^{15}cm^{-3}, [O]=5*10^{16}cm^{-3}, [C]=1*10^{16}cm^{-3}), and the C_iP_s ME(0.23) data are from sample 3Si-P-FZ-DJ ([P]=2*10^{16}cm^{-3}, [O]=8*10^{15}cm^{-3}, [C]=8*10^{15}cm^{-3}) [3].

the calculated B_iC_s trend with [B] to experiment, a large capture radius for B_i-C_s pairing has been assumed in the isothermal anneal simulations. Therefore the real capture radii for B_iB_s and B_iC_s formation are expected to be smaller than the values in TABLE 1.

CONCLUSIONS

A first order nonlinear system model has been constructed to simulate the interstitial defect reactions in Si. The interstitial migration enthalpy and the pair formation capture radius are two parameters used in the model to describe long range migration and near neighbor capture of interstitials. First order diffusion limited pairing reactions are the predominant processes in the interstitial defect reactions. The reaction kinetics are determined by the interstitial migration enthalpy, pairing capture radius, and background impurity concentration. The model supports the DLTS defect assignments. However, the model can be improved by including back reactions and higher order kinetic processes such as pair dissociation, Si_i-V recombination, and B_i-, C_i-clustering, etc.. Other defects such as Si_i-clusters on C-complexes, Si_i- and V-related defects (e.g., Si_iO_i, VV, etc.) are also playing roles in the interstitial defect reactions [1, 12]. A series of isothermal anneal experiments should be performed on p-type Si to determine the reaction parameters of the model. The complete defect knowledge base is crucial to the development of an interstitial defect reaction simulator. The simulator can not only be used to construct the interstitial defect reaction hierarchy diagram and to understand defect behaviors in Si device processing during ion implantation and anneal, but also to characterize background impurity concentration (e.g., [O], [C], etc.) in Si by combined electron irradiation and DLTS techniques.

REFERENCES

[1] L. C. Kimerling, M. T. Asom, J. L. Benton, P. J. Drevinsky, and C. E. Caefer, Mater. Sci. Forum, **38-41**, 141(1989).

[2] P. J. Drevinsky, C. E. Caefer, L. C. Kimerling, and J. L. Benton, in Defect Control in Semiconductors, edited by K. Sumino, (Elsevier Sci. Pub. B. V. North-Holland, 1990) p341.

[3] M. T. Asom, J. L. Benton, R. Sauer, and L. C. Kimerling, Appl. Phys. Lett. **51**, 256 (1987).

[4] P. J. Drevinsky, C. E. Caefer, S. P. Tobin, J. C. Mikkelsen, Jr., and L. C. Kimerling, Mat. Res. Soc. Symp. Proc., **104**, 167 (1988).

[5] $\sigma N = 0.12$, J. W. Corbett, in Electron Radiation Damage in Semiconductors and Metals, Solid State Phys. Suppl. 7, (Academic Press, NY 1966), p74.

[6] L. A. Girifalco, Statistical Physics of Materials (Wiley, NY 1973).

[7] M. Lannoo and J. Bourgoin, Point Defects in Semiconductors II. Experimental Aspects (Springer-Verlag, Berlin, 1982).

[8] R. D. Harris, G. D. Watkins, and L. C. Kimerling, Mater. Sci. Forum, **10-12**, 163 (1986).

[9] L. C. Kimerling, P. Blood, and W. M. Gibson, in Defects and Radiation Effects in Semiconductors 1978, Inst. Phys. Conf. Ser. **46**, p273-280.

[10] L. W. Song and G. D. Watkins, Phys. Rev. B, **42**, 5759 (1990).

[11] Si_i is very mobile at low temperatures under irradiation conditions and exhibits much slower diffusion at high temperatures. The Watkins replacement reaction is the fastest process of $H_i^m(Si_i) \leq 0.40$ eV, under irradiation conditions.

[12] G. Davies, Mater. Sci. Forum, **38-41**, 151 (1989).

FORMATION OF Er-RELATED DONOR CENTERS DURING POSTIMPLANTATION ANNEALING OF Si:Er

N.A. SOBOLEV, O.V.ALEKSANDROV, E.I. SHEK
Ioffe Physicotechnical Institute, Russian Academy of Sciences,
194021 St.Petersburg, Russia, nick@sobolev.ioffe.rssi.ru

ABSTRACT

Dependence of the donor center concentration, the Er activation coefficient and the n-layer thickness on the implantation and subsequent annealing conditions was studied. A model of formation of donor centers has been developed. The model is based on the interaction of Er atoms with self-interstitials. It describes the dependence of electrical parameters of Er-doped layers on temperature and time of postimplantation annealing.

INTRODUCTION

The understanding of the formation of Er-related electrically active centers is essential to improve the luminescence intensity of Si:Er structures. Some electrical properties of Si:Er have been studied in [1-4]. It has been shown that donor centers are formed after the implantation of erbium ions in silicon followed by annealing temperatures of 800-1100 °C. Existing expertimental results show that erbium atoms are constituents of the donor centers. It was established that the presence of oxygen in the initial silicon promotes the formation of donor centers which are associated with the implantation of erbium [2,3]. There are no data on the formation of Er-related donor centers for a wide range of experimental conditions. The purpose of the present work is to study the effects of implantation and consequent annealing conditions on electrical properties of Si:Er.

EXPERIMENT

Wafers of p-Si grown by the float-zone (FZ) and Czochralski (Cz) techniques were used. The initial resistivity was of 20 Ωcm and 10 Ωcm for FZ-Si and Cz-Si, respectively.

Erbium ions with an energy of 1 or 1.2 MeV and a dose of $1x10^{13}$ cm^{-2} were implanted in Si at room temperature. Oxygen ions with an energy of 0.17 MeV and a dose of $1x10^{14}$ cm^{-2} were co-implanted in some Si:Er (1.2 MeV) samples. To prevent channeling the <100> oriented substrates were inclined at an angle of 7 degrees relative to the ion beam.

The implanted samples were annealed in the temperature range of 400-1250 °C for 0.25-17 h in a chlorinated atmosphere containing 0.5 mole % carbon tetrachloride.

The implantation of erbium ions and subsequent annealing led to the formation of a n-type layer near the surface. SIMS, thermal probe, four-probe, capacitance-voltage and beveling and staining techniques were used to study the properties of Si:Er(:O). The activation coefficient of the erbium impurity in the n-layer was calculated from the relation $f=Q_{don} / Q_{tot}$ where $Q_{don}=(e\mu R_s)^{-1}$ is the number of donor centers in the n-layer, e is the electron charge, μ=1350 $cm^2/(Vs)$ is the electron mobility (it was assumed to be independent of donor center concentration), R_s is the layer resistance, and Q_{tot} is the total number of erbium atoms in the implanted layer.

Mat. Res. Soc. Symp. Proc. Vol. 442 © 1997 Materials Research Society

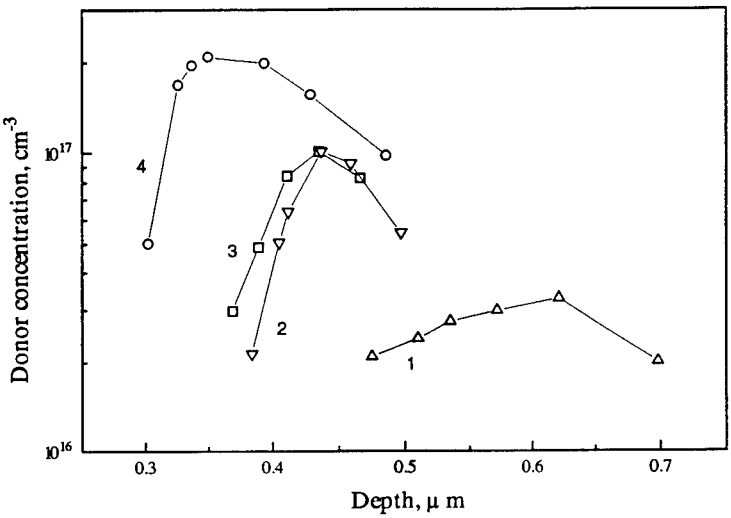


Fig. 1. Concentration profiles of Er-related donors after postimplantation annealing of FZ-Si:Er (1,3) and FZ-Si:Er:O (2,4) for 0.5 h at 700°C (3,4) and 900°C (1,2).

RESULTS AND DISCUSSION

The SIMS measurements showed that the distribution of the erbium after annealing remains the same as after implantation.

Post-implantation annealing results in the formation of donor centers and a n-type layer. The measurements of the capacitance-voltage characteristics showed that each of the donor center concentration profiles in the n-layer n(x) have a disting maximum. The character of the change in the distribution n(x) as a function of the temperature of isochronous (t=30 min) annealing for FZ-Si:Er (1.2 MeV) and FZ-Si:Er (1.2 MeV):O (0.17 MeV) is shown in Fig. 1 (curves 1-4). Co-implantation of oxygen leads to an increase of the donor concentration at the same annealing conditions. As the annealing temperature increases, the concentration at the maximum decreases. The position of the maxima of the distribution n(x) is also shifted into the bulk of the sample as compared with the position of the maximum for the total concentration of erbium atoms N(x).

The activation coefficient of the erbium and the n-layer thickness are plotted in Fig. 2 as function of the temperature of isochronous annealing of Cz-Si:Er (1 MeV). The maximum activation of erbium, reached at 700 °C, is equal to ~20% of the total concentration of the implanted erbium. A maximum thickness of the n-layer is seen at 600°C, in Fig. 2b.

The activation coefficient and the n-layer thickness, plotted as functions of the isothermal annealing time at 900°C for Cz-Si:Er (1 MeV) are shown in Fig. 3. The activation coefficient decreases as the annealing time increases. The thickness of the n-layer at 900 °C increases at the initial stage of annealing (t<1 h) and decreases at t>2 h.

We shall now discuss the experimental results. It was observed that no changes occur in the SIMS profile as a result of post-implantation annealings of structures in which the

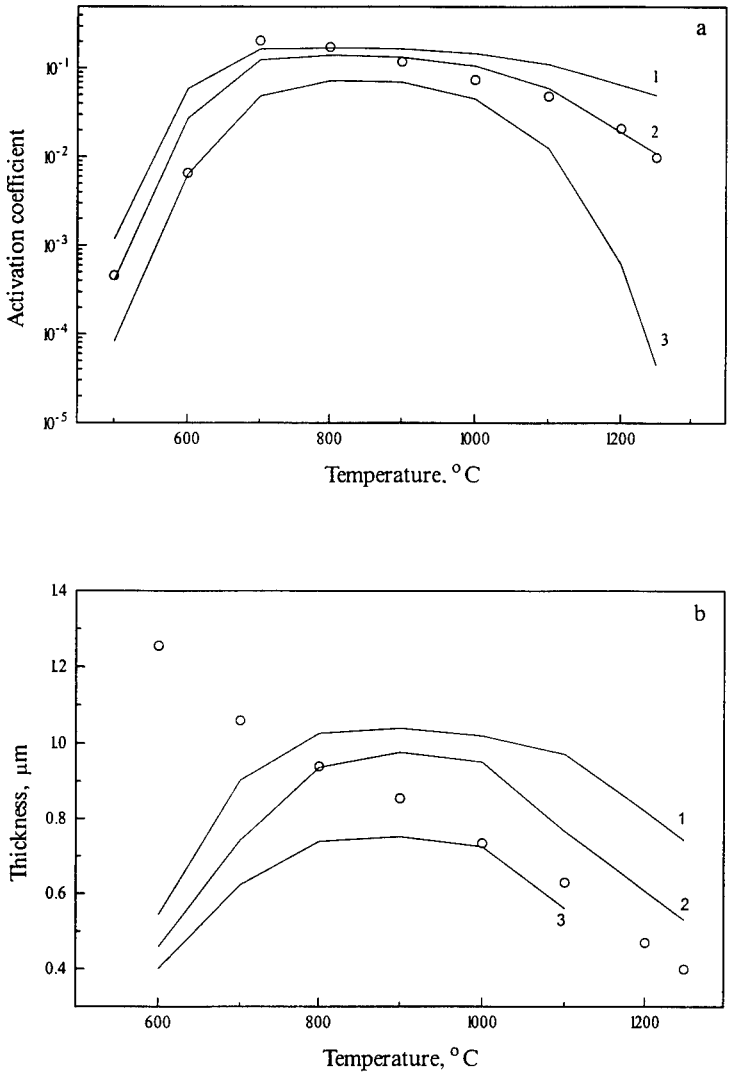


Fig. 2. Temperature dependences of the activation coefficient (a) and of the n-layer thickness (b) after isochronous annealing of Cz-Si:Er for 0.5 h. Open circles correspond to the experimental data. Constant K_{01}, cm^3s^{-1}: 15.45 (1), 5.15 (2), 1.03 (3).

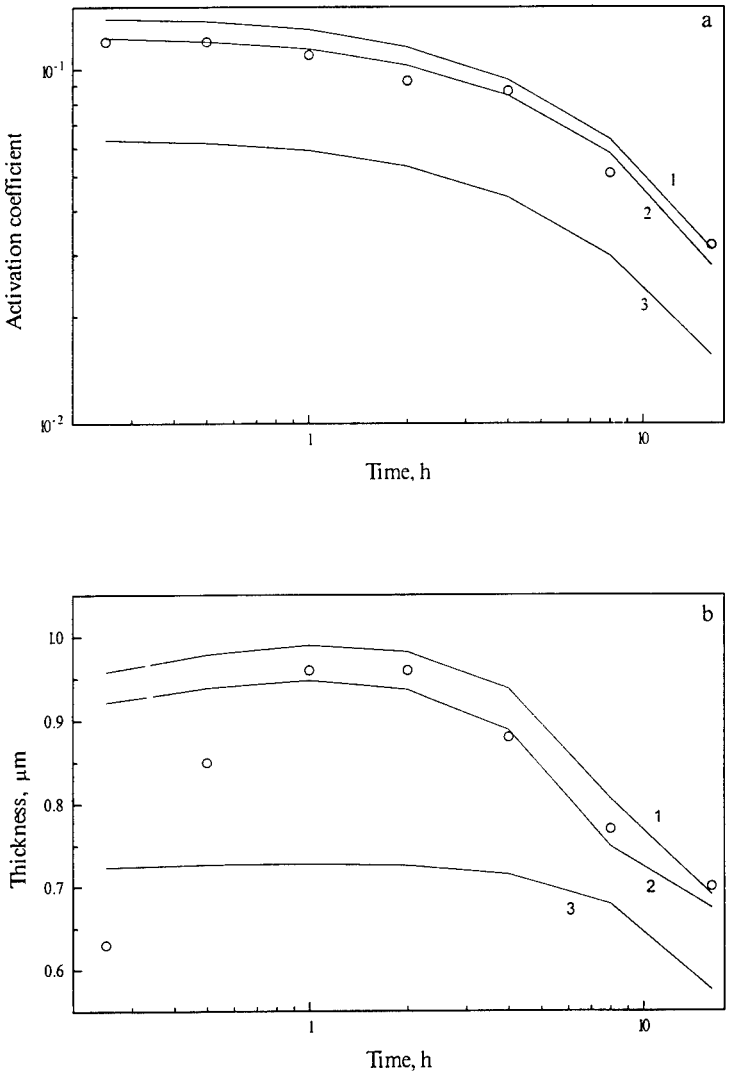


Fig. 3. Activation coefficient (a) and n-layer thickness (b) as functions of the isothermal (T=900°C) annealing time of Cz-Si:Er. Open circles correspond to the experimental data. Constant τ, s: 95 (1), 19 (2), 3.8 (3).

concentration of the implanted erbium ions did not exceed the critical value (which depends on the ion energy). The absence of broadening of the concentration profile as a result of post-implantation annealings is explained by the low values of the diffusion coefficient of the erbium in silicon. Moreover, it was ruled out that the implanted erbium is present in silicon not in the form of isolated atoms, but rather in the form of clusters or of complexes of point defects, or that it can be trapped by more complex structural defects.

The experimental data analysis has shown that the observed (in Figs. 2 and 3) behaviour of the activation coefficient of the Er atoms and the n-layer thickness can be described by the following model of formation of Er-related donor centers.

1. Donor center (W) is the complex containing Er atom and self-interstitial (I). Its formation is associated with the interaction of a immobile Er atom with more mobile self-interstitial and is described by the quasichemical reaction

$$Er + I \underset{K_2}{\overset{K_1}{\leftrightarrow}} W, \qquad (1)$$

where $K_1=K_{10}\exp(-E_{K1}/kT)$ is the forward reaction constant and $K_2=K_{20}\exp(-E_{K2}/kT)$ is the reverse reaction constant.

2. Postimplantation annealing leads to generation of intrinsic point defects. A sample surface is a sink for excess vacancy. A part of excess self-interstitials recombines at the surface and the other part participate in donor center formation. The assumption that nonequlibrium intrinsic point defects participate in the formation of donor centers correlates well with the data of the postimplantation annealing atmosphere effect on the formation of optically [5,6] and electrically [4] active Er-related centers.

3. The kinetics of donor center formation are described by the following system of differential equations:

$$\frac{\partial[W]}{\partial t} = K_1[Er][I] - K_2[W], \qquad (2)$$

$$\frac{\partial[Er]}{\partial t} = -K_1[Er][I] + K_2[W], \qquad (3)$$

$$\frac{\partial[I]}{\partial t} = D\frac{\partial^2[I]}{\partial x^2} - K_1[Er][I] + K_2[W] + G, \qquad (4)$$

where [Er] is the Er concentration, D is the self-interstitial diffusivity,

$$G(x,t) = \frac{\chi \cdot G(x,t=0)}{\tau}\exp\left(-\frac{t}{\tau}\right) \qquad (5)$$

is the intrinsic point defect generation rate during annealing of the implantation defects, G(x,t=0) is the initial distribution of implantation defects, $\tau=\tau_o\exp(E_\tau/kT)$ is the constant of implantation defect concentration decay, χ is the mean number of intrinsic point defects generated by one Er ion.

The boundary conditions are

$$[I(x=0,t)] = [I^*] \quad \text{and} \quad \frac{\partial[I(x=0,t)]}{\partial x} = 0, \qquad (6)$$

where $[I^*]$ is the equilibrium self-interstitial concentration, d is the sample depth.

4. The activation coefficient (f) and the n-layer thickness (x_j) were calculated using the following equations

$$f(t) = \frac{1}{Q_{tot}} \int_0^{x_j} W(x,t)dx, \quad (7)$$

$$W(x_j,t)=C_B, \quad (8)$$

where C_B is the acceptor concentration in initial sample.

The best fitting of the experimental results for Cz-Si:Er (1 MeV) have been obtained at the following parameters: $D=2.75\times10^{-5}$ exp(-1.5/kT) cm^2/s, $K_1=5.15\times10^{-13}$ exp(-1.5/kT) cm^3/s, $K_2=5.85\times10^{3}$ exp(-1.75/kT) s^{-1}, $\tau=5\times10^{-5}$ exp(1.3/kT) s, $\chi=0.19$. Figs. 2 and 3 also show the changes of the model curves due to variation of the K_1 and τ constants.

The different character of the dependences of the activation coefficient and the n-layer thickness on the temperature and time of post-implantation annealing indicates that the change in these parameters is controlled by different types of donor centers. The formation of several types of donor centers after erbium implantation and subsequent annealing at 900 °C was observed in [1,2,7].

CONCLUSION

The effect of the oxygen implantation, annealing temperature and annealing time on the formation of donor centers in Er-implanted silicon was studied. It was shown that the variation of annealing temperature as well as additional oxygen implantation lead to a change of Er-related donor center distribution. The suggested model of formation of the centers accurately fits the dependences of the activation coefficient and the n-layer thickness on the annealing conditions.

ACKNOWLEDGMENTS

The authors are indebted to Mr E.O. Parshin for his help in the sample preparation.The work was partly supported by The International Science and Technology Center (grant 168) and The Russian Foundation for Fundamental Research (grant 96-02-17901a).

REFERENCES

1. F.Widdershoven and J.P.M.Naus, Mater. Sci. Eng. **B 4**, p. 71 (1989).
2. J.L. Benton, J. Michel, L.C. Kimerling, D.C. Jacobson, Y.H. Xie, D.J. Eaglesham, E.A. Fitzgerald and J.M. Poate, J. Appl. Phys. **70,** p. 2667 (1991).
3. F. Priolo, S. Coffa, G. Franzo, C.Spinella, A.Carnera and V.Bellani, J. Appl. Phys. **74**, p. 4936 (1993).
4. O.V.Aleksandrov, N.A.Sobolev, E.I.Shek and A.V.Merkulov, Fiz. Tekh. Poluprovodn. **30**, p. 876 (1996) [Semiconductors **30**, p. 468 (1996)].
5. J.Michel, J.L.Benton, R.F.Ferrante, D.S.Jacobson, D.S.Eaglesham, E.A.Fitzgerald, Y.H.Xie, J.M.Poate and L.C.Kimerling, J. Appl. Phys. **70**, p. 2672 (1991).
6. N.A.Sobolev, M.S.Bresler, O.B.Gusev, E.I.Shek, M.I.Makoviichuk and E.O.Parshin, Fiz. Tekh. Poluprovodn. **28**, p. 1995 (1994) [Semiconductors **28**, p. 1100 (1994)].
7. V.V.Emtsev, O.V.Aleksandrov, D.S.Poloskin, E.I.Shek and N.A.Sobolev, Materials Science Forum, Trans Tech publications, Switzerland, **196-201**, p. 615 (1995).

SHALLOW DONOR CENTERS IN ERBIUM-IMPLANTED SILICON SUBJECTED TO HIGH-TEMPERATURE ANNEALING

V.V. EMTSEV, D.S. POLOSKIN, N.A. SOBOLEV, E.I. SHEK
A.F. Ioffe Physicotechnical Institute, Russian Academy of Sciences,
194021 St.Petersburg, Russia, emtsev@jsc.pti.spb.su

ABSTRACT

Consideration has been given to production processes of shallow donor centers formed in silicon after implantation of erbium ions or co-implantation of erbium and oxygen ions followed by annealing at 700° and 900°C. Analysis of the experimental data obtained in this work made it possible to put forward some suggestions concerning the nature of these defects.

INTRODUCTION

Erbium-doped silicon (Si:Er) has been studied for a long time and many properties of this material are known in considerable detail.This knowledge forms a basis for finding applications in optoelectronics.

Most of the information concerning deep centers in Si:Er comes from DLTS measurements; see for instance [1-3]. However, formation processes of shallow donor centers with ionization energies less than 90 meV are scantily known. Further experimental information is needed to elucidate this aspect of the problem.

The aim of the present work is to study the behavior of shallow donors in Si doped with Er by implantation and subjected to annealing at high temperatures.

EXPERIMENT

Boron-doped Si ingots, both grown by the Czochralski (Cz-Si) and float-zone (FZ-Si) techniques, were used in this work. The initial resistivity was of 7.5 Ohm·cm and 20 Ohm·cm for Cz-Si and FZ-Si, respectively. Samples were square-shaped and 7x7x1 mm^3 in size. Electrical contacts were applied at the corners of samples and the Van-der-Pauw method was used for Hall effect measurements.

Er and O ions with energies of 1.2 MeV and 0.17 MeV, respectively, were co-implanted in Si at room temperature over the dose range from 10^{12} to 10^{13} Er ions / cm^2, the dose of oxygen ions always being by an order-of-magnitude higher than that of Er ions. For comparison, we used in some cases only Er ions during the implantation.

After implantation all samples were subjected to annealing at 700° and 900°C for 30 min. in a chlorine-containing atmosphere to remove radiation damage and to activate Er impurity atoms. Some non-implanted samples of FZ-Si were used as reference ones and were annealed under the same conditions. In this way it was proved that the possible contamination due to the annealing only does not exceed $1 \cdot 10^{14}$ cm^{-3}. The implantation and subsequent annealing lead to formation of n-type surface layers with low resistivities. The average thickness of these layers on p-type substrates was of about 1 μm. The electron concentration n(T) as a function of temperature was measured over the temperature range of 20 K to 300 K. As an illustration, some typical curves of n(T) for FZ-Si:Er and FZ-Si:Er:O after annealing at 700° and 900°C are shown in Fig. 1 and Fig. 2. Similar curves were also obtained for Cz-Si:Er and Cz-Si:Er:O. All the experimental curves were analyzed with the help of relevant electroneutrality equations.

Mat. Res. Soc. Symp. Proc. Vol. 442 © 1997 Materials Research Society

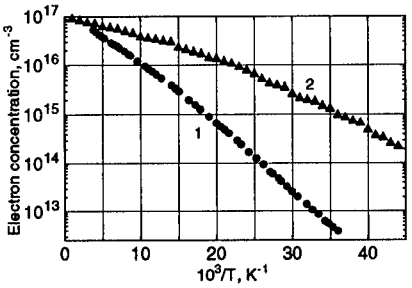


Fig. 1. Temperature dependence of the electron concentration in FZ-Si:Er (curve 1) and FZ-Si:Er:O (curve 2) after implantation and subsequent annealing at 700°C for 30 min. Implantation dose: Φ=1·10^{13} Er ions/cm^2, Φ=1·10^{14} O ions/cm^2.

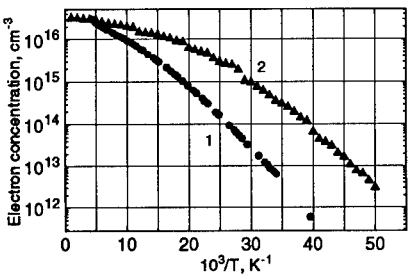


Fig. 2. Temperature dependence of the electron concentration in FZ-Si:Er (curve 1) and FZ-Si:Er:O (curve 2) after implantation and subsequent annealing at 900°C for 30 min. Implantation dose: Φ=1·10^{13} Er ions/cm^2, Φ=1·10^{14} O ions/cm^2.

RESULTS AND DISCUSSION

FZ-Si:Er after annealing at 700°C

First we consider FZ-Si after implantation at a dose of $1\cdot10^{13}$ Er ions / cm^2; see Fig. 1. The almost featureless shape of the n(T) curve over a wide temperature range tells us immediately that it cannot be fitted with a one-level model of donor centers.Instead, one must take into consideration a system of several donor states, closely separated on the energy scale. As usual the lower-temperature portion of the curve makes possible estimating the ionization energy of shallow donor states , about 30 meV. Assuming that most of the boron -related defects in the implanted layer are annealed out at 700°C (see for instance [4]) one can use the initial concentration of boron for estimations of the concentration of shallow donors at $\approx E_c$ –0.03 eV by fitting the experimental n(T) curve at low temperatures until some deviations appear. At this point the energy and concentration of shallow donors are fixed and further calculations of the remaining portion of the n(T) curve is proceeded with the involvement of other donor states.

Preliminary calculations showed that an extended model including two kinds of donor states, shallow and deep ones, cannot yet provide a satisfactory description of n(T) over the entire temperature range. Because of this, a more realistic model should consist of three kinds of donor states: besides shallow donors at $\approx E_c$ –0.03 eV, there are donors at $\approx E_c$ –(0.05~0.07) eV describing the middle portion of experimental curves of n(T) and deeper donors which contribute to an increase in n(T) at T≥100 K when the former ones tend to be exhausted. The parameters of these deep donors cannot be explicitly evaluated from n(T). One could roughly estimate that the donor states should be in the range of E_c –(0.09~0.12) eV. The final fitting was based on a model consisting of three levels within the energy intervals given above and carried out with the aid of a special computer program. For the model we used the possible variations in the concentration of donors with ionization energies less than 90 meV are about 10

percent, those for deeper donors can be by several times larger. For the latter ones, there is an expected trend for fitting the experimental data: the higher the ionization energy, the larger the donor concentration. In this way, the concentration of donors at $\approx E_c$ –0.09 eV is minimal for reasonable fitting. In spite of some uncertainties while modeling, general trends in the appearance of donor centers should also be true for donors distributed over some energy intervals, since in this case the donor concentration estimated by means of a three-level model may be representative for each group of centers.

This step-by-step analysis of n(T) curves allowed to outline the distribution of donor centers produced; see Fig. 3. We think that shallow donors at $\approx E_c$ –0.05 eV may be attributed to Er- and O-related defects, in spite of low oxygen contents (in our case a few 10^{16} cm^{-3}). Actually, the mean diffusion length of oxygen in Si at 700°C for 30 min. is sufficient for the formation of such complexes if Er-related defects whose concentration in FZ-Si may be a few 10^{16} cm^{-3} can trap the mobile oxygen atoms. It is conceivable that the ErO unit is a constituent of these defects.

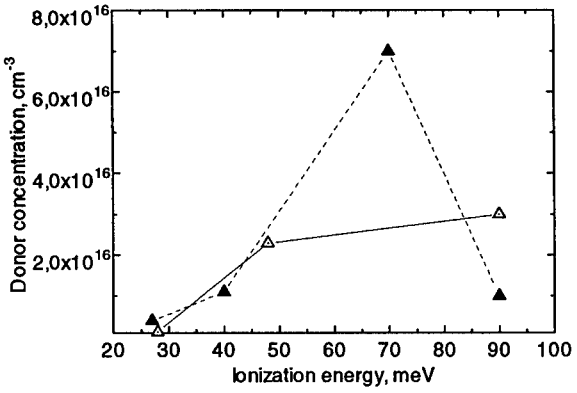


Fig. 3. Distribution of shallow donor centers over their ionization energies for FZ-Si:Er (open triangles) and FZ-Si:Er:O (solid triangles) after implantation and subsequent annealing at 700^0 C for 30 min. Implantation dose: $\Phi=1\cdot10^{13}$ Er ions / cm^2, $\Phi=1\cdot10^{14}$ O ions / cm^2.

FZ-Si:Er:O after annealing at 700°C

For this case a typical curve of n(T) is depicted in Fig. 1 (curve 2). It was also analyzed by means of a three level model and the results are shown in Fig. 3.

Under similar irradiation and annealing conditions, the co-implantation of Er and O ions in FZ-Si leads to the appearance of new donor centers at $\approx E_c$ –0.07 eV in a considerable concentration. At the same time the total concentration of shallow donors at E_c –(0.03~0.04) eV remains of minor importance, in spite of the fact that their concentration is increased by an order-of-magnitude. The oxygen atoms present in high concentrations in FZ-Si:Er:O can aggregate at 700°C as they do in oxygen-rich Cz-Si ; see for instance [5]. Along with this, in the FZ-Si:Er:O, in contrast to Cz-Si , there is a lot of nucleation sites in form of Er-related defects, certainly different from those formed in FZ-Si:Er. Really, subsequent oxygen implantation in the Er-implanted FZ-Si, the second step in co-doping, gives rise to additional production of intrinsic defects in the Er-doped layer and may in this way modify the Er-related defects formed at the first step, after implantation of Er ions. Two points are of special interest. First , new donor centers at $\approx E_c$ –0.07 eV are absolutely dominating among the donors with ionization energy less than 90 meV. Second, in the case of oxygen aggregation at Er-related nucleation

sites one may expect that these donor states are distributed over a certain energy interval due to different size of growing oxygen aggregates, as is observed in Cz-Si ; see for instance [6]. The involvement of Er in aggregation processes seems greatly contribute to both high formation rates and high thermal stability of the oxygen aggregates, since in Cz-Si (without Er) the maximal concentration of thermal donors formed at 700°C is smaller by at least two orders-of-magnitude; cf [7].

Cz-Si:Er:O after annealing at 700°C

We analyzed the obtained curves of n(T) in a similar way we did for FZ-Si and the results of our analysis are shown in Fig. 4.

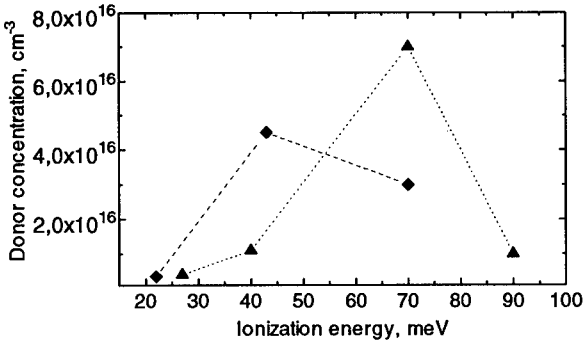


Fig. 4. Distribution of shallow donor centers over their ionization energies for FZ-Si:Er:O (triangles) and Cz-Si:Er:O (diamonds) after implantation and subsequent annealing at 700° C for 30 min. Implantation dose: $\Phi=1\cdot10^{13}$ Er ions / cm^2, $\Phi=1\cdot10^{14}$ O ions / cm^2.

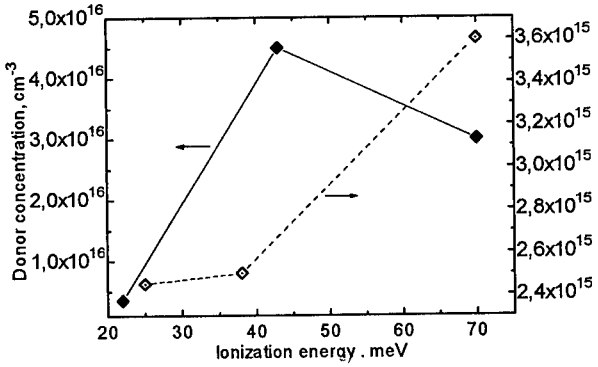


Fig. 5. Distribution of shallow donor centers over their ionization energies for Cz-Si:Er:O after implantation and subsequent annealing at 700°C. Implantation dose: $\Phi=1\cdot10^{12}$ Er ions / cm^2 and $\Phi=1\cdot10^{13}$ O ions / cm^2 (open diamonds); $\Phi=1\cdot10^{13}$ Er ions / cm^2 and $\Phi=1\cdot10^{14}$ O ions / cm^2 (solid diamonds).

When Er and O ions were co-implanted in Cz-Si the total concentration of donor centers was found to be nearly the same as observed in FZ-Si:Er:O after implantation at the same dose; see Fig. 4. However, their distribution is clearly changed and the maximum shifted to shallower donor states at $\approx E_c$ –0.04 eV. The formation of these donors seems to be occured at the expense of donor states at $\approx E_c$ –0.07 eV. Such a comparison can be justified if one takes into

account that both implanted layers are oxygen-rich. Nonetheless, after implantation of oxygen in Cz-Si there is considerable increase in the total oxygen content when the implanted oxygen was added to the oxygen available in Cz-Si. This increase should lead to substantial enhancement of oxygen aggregation processes, as is usually observed in Cz-Si with increasing oxygen content ; see for instance [8]. In consequence, oxygen aggregates of larger size are mostly formed at the same Er-related nucleation sites, as happens with FZ-Si:Er:O. These larger oxygen aggregates are thought to be responsible for the appearance of shallower donor states, similar to the oxygen aggregation processes in heat-treated Cz-Si ; see for instance [9,10]. If this model is true one could expect that the maximum of the donor distribution should be shifted to higher ionization energies with decreasing implantation dose of oxygen ions. Our experimental data for Cz-Si after co-implantation of Er and O ions at a dose of $1\cdot10^{12}$ cm^{-2} and $1\cdot10^{13}$ cm^{-2} , respectively, display the expected behavior, the maximum of the donor distribution being shifted to $\approx E_c$ –0.07 eV; see Fig. 5. Under the same implantation conditions (energy, dose, temperature etc) the total concentration of Er-related nucleation sites should be equal for both FZ-Si:Er:O and Cz-Si:Er:O. This is why the formation of shallow centers at $\approx E_c$ –0.04 eV takes place at the expense of donor centers at $\approx E_c$ –0.07 eV.

FZ-Si:Er, FZ-Si:Er:O and Cz-Si:Er:O after annealing at 700°C

Our analysis of the experimental curves of n(T) like those given in Fig. 2 allowed to conclude that the prominent Er- and O-related donor centers with shallow states at E_c –(0.04÷0.07) eV are not stable at 900°C; cf Fig. 4 and Fig. 6. The distributions of shallow donors in all the implanted materials after annealing at this temperature are very similar to one another. These donor centers are thought to be very stable Er-related complexes with intrinsic defects. Taking into account their electrical activity as shallow donors the involvement of oxygen in the electrically active core cannot be ruled out.

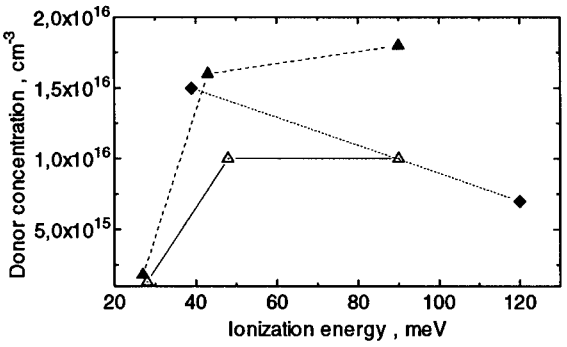


Fig. 6. Distribution of shallow donor centers over their ionization energies for FZ-Si:Er (open triangles), FZ-Si:Er:O (solid triangles) and Cz-Si:Er:O (diamonds) after implantation and subsequent annealing at 900^0 C for 30 min. Implantation dose: $\Phi=1\cdot10^{13}$ Er ions / cm^2, $\Phi=1\cdot10^{14}$ O ions / cm^2.

CONCLUSION

It has been shown that co-implantation of Er and O ions in Si and subsequent annealing at 700°C result in the appearance of shallow donor centers with ionization energies less than 90 meV. Their total concentration is increased by an order-of-magnitude over the dose range of

$1 \cdot 10^{12}$ Er ions/ cm^2 to $1 \cdot 10^{13}$ Er ions/ cm^2, with corresponding increases in the oxygen doses, and can be about 10^{17} cm^{-3} at doses which are far from those needed for amorphization of implanted layers.

The data obtained are inviting to conclude that both Er and O are involved in the formation of these shallow donors. Most likely, oxygen aggregation takes place at Er-related defects as nucleation sites during the post-implantation annealing at 700°C. Because of this, one may expect that the dominant donor states are distributed over the energy interval of $\approx E_c - 0.04$ eV to $\approx E_c - 0.07$ eV due to the presence of oxygen aggregates of different size. The Er doping of Si with high contents of oxygen contributes to a high formation rate of oxygen aggregates as well as to their thermal stability, as compared to Cz-Si without Er. Annealing at elevated temperatures showed that they can be dissolved at 900°C.

ACKNOWLEDGMENTS

The authors are indebted to Mr E.O. Parshin for his help in the sample preparation.The work was partly supported by The International Science and Technology Center (grant 168) and The Russian Foundation for Fundamental Research (grant 96-02-17901a).

REFERENCES

1. J.L. Benton, J. Michel, L.C. Kimerling, D.C. Jacobson, Y.H. Xie, D.J. Eaglesham, E.A. Fitzgerald and J.M. Poate, J. Appl. Phys. **70,** p. 2667 (1991).

2. S. Libertino, S. Coffa, G. Franzó and F. Priolo, J. Appl. Phys. **78**, p. 3867 (1995).

3. W. Jantsch, H. Przybylinska, Yu. Suprun-Belevich, M. Stepikhova, G. Hendorfer and L. Palmetshofer, Materials Science Forum, Trans Tech publications, Switzerland, 1995, vol. 196-201, pp. 609-614.

4.T.E. Haynes, D.J. Eaglesham, P.A. Stolk, H.-J. Gossmann, D.C. Jacobson and J.M. Poate, Appl. Phys. Lett. **69**, p. 1376 (1996).

5. A. Borghesi, B. Pivac, A. Sassella and A. Stella, J. Appl. Phys.**77**, p. 4169 (1995).

6. B.A. Andreev, V.G. Golubev, V.V. Emtsev, G.I. Kropotov, G.A. Oganesyan and K. Schmalz, Fiz. Tekh. Poluprovodn. **27**, p. 567 (1995) [Semiconductors (American Institute of Physics) **27**, p. 315 (1995)].

7. K. Schmalz and P. Gaworzewski, Phys. Stat. Sol. (a) **64**, p.151 (1981).

8. P. Gaworzewski and K. Schmalz, Phys. Stat. Sol. (a) **77**, p. 571 (1983).

9. P. Wagner and J. Hage, Appl. Phys. A **49**, p. 123 (1989).

10. Yu. N. Daluda, V.V. Emtsev and K. Schmalz, Radiat. Eff. **107**, p. 93 (1989).

DEFECTS IN ERBIUM/OXYGEN IMPLANTED SILICON

X. DUAN, J. PALM, B. ZHENG, M. MORSE, J. MICHEL AND L. C. KIMERLING
Department of Materials Science and Engineering, Massachusetts Institute of Technology
77 Massachusetts Avenue, Cambridge, MA 02139

ABSTRACT

A systematic study of defects in the Er/O implanted silicon was conducted using TEM, HRTEM and SIMS. Defect-free material was obtained after the annealing of 400 keV Er^+ implanted (100)Si. In sharp contrast, several forms of secondary defects consisting of dislocations, dislocation loops and precipitates were induced upon annealing at different temperatures in the 4.5 MeV implanted (100)Si sample. The isothermal evolution of the defects and reactions between dopants and defects were studied. Oxygen tends to segregate into the dislocation loop zones, where platelet precipitates with habit planes of {111} were found. Following dissociation of oxygen and erbium, plate-like Er precipitates were generated, which are most likely $ErSi_2$ with a habit plane of {111}.

INTRODUCTION

Erbium in silicon has attracted considerable interest because of its potential to give high-efficiency sharp luminescence at 1.54 μm which can be excited either optically or electronically [1,2]. This possibility inspires the long sought goal of integrating silicon optoelectronics with very large scale integration (VLSI) electronics to overcome high interconnection density and bandwidth limitations. In order to have strong luminescence, large amounts of optical active Er must be incorporated into the silicon lattice. Ligands, such as oxygen which has been found to significantly increase Er luminescence[2], also need to be incorporated to modify the local environment around Er[3].

Several techniques have been used to incorporate Er into silicon[4-9], but ion implantation, to date, has received the most attention due to its compatibility with IC technology. However, during the implantation process the crystalline lattice of the Si is damaged and an annealing at high temperature is necessary to repair the damage as well as to optically activate the dopant. The secondary defects, such as dislocations, dislocation loops and precipitates, could thus be induced upon annealing which then significantly inhibit the luminescence of Er in Si. Therefore, the optimal processing for the maximum luminescence cannot be realized unless the relationships between processing, structure and properties are thoroughly understood. The main focus of this paper, hence, is on fully understanding the defect behavior of Er/O implanted Si during the thermal annealing.

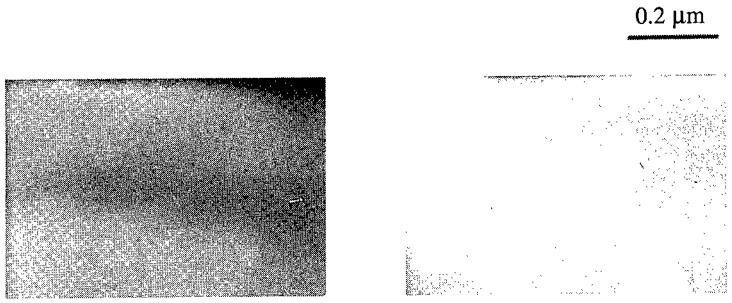
EXPERIMENTAL

Erbium was implanted into p-type Cz (100) silicon substrate at an energy of both 4.5 MeV and 400 keV with an implantation dose to produce a profile with an Er peak concentration of 5 x 10^{17} cm^{-3} to establish whether implantation energy affects the defects. Oxygen was co-implanted to form a peak concentration of 3 x 10^{18} cm^{-3} spatially overlapping Er to form Er/O complexes. Samples were then annealed for 30 minutes in Ar ambient at different temperatures: 600, 800, 900 and 1000°C to examine the dependence of defects on annealing temperatures. An isothermal study at 900°C, which was previously determined to optimize luminescence, was done for times ranging from 15 minutes to 16 hours. Characterization for both as-implanted and annealed materials was conducted using cross-sectional transmission electron microscopy (XTEM), high resolution transmission electron microscopy (HRTEM) and secondary ion mass spectroscopy (SIMS).

Mat. Res. Soc. Symp. Proc. Vol. 442 © 1997 Materials Research Society

RESULTS AND DISCUSSION

Figure 1 shows the TEM cross-section images of 400 keV implanted (100)Si after annealing for 30 minutes at 800°C (Figure 1a) and 900°C (Figure 1b). No advanced secondary defects were observed in the sample although it was implanted in a depth of 1500 Å with peak concentrations of 5×10^{17} cm^{-3} and 3×10^{18} cm^{-3} for erbium and oxygen, respectively. This implied that either the implantation dose, hence the displacement damage density in the 400 keV implanted sample had not reached the critical value required for the formation of category I defects[10], or the surface-mediated annihilation dominated the annealing of defects.



(a) **(b)**

Figure 1. XTEM week-beam images for 400 keV implanted (100)Si after annealing for 30 minutes at 800°C (a) and 900°C (b) , showing a defect-free material.

In sharp contrast, however, a variety of secondary defects consisting of dislocations, dislocation loops and precipitates are induced during annealing in 4.5 MeV implanted Si. The evolution from a supersaturation of point defects to a layer of dislocation loops with increasing temperatures in a range of 600 to 1000°C is presented in Figure 2. When the anneal was done at 600°C for 30 minutes, a population of randomly sized, cluster-like structures was observed as shown in Figure 2a. This defect feature is similar to the primary damage distributed in the clustering arrangements to minimize the number of dangling bonds. An 800°C anneal for the same duration resulted in a dissolution of these unstable clusters and a formation of a great number of dislocation loops (Figure 2b) and a few dislocations. These small dislocation loops, with an average size of 200 Å, are the predominant secondary defects; They were distributed over a wide depth range between 1.4 μm to 1.8 μm, which was deeper than the peak depth of the dopant distribution (the projected range R_p) of 1.35 μm as determined from the SIMS data. The dislocation loops continued to grow in size and distribute in a deeper layer as the annealing temperature was increased to 900°C, while narrowing in distribution depth (Figure 2c). After annealing at 1000°C for 30 minutes, these defects significantly coarsened to an average size of about 1500 Å, with a greatly reduced loop density (Figure 2d).

The shrinkage of the dislocation loop band with increasing temperatures was asymmetric; the upper half of the dislocation loop band was annihilated while the lower half of dislocation loops grew in size. This can be explained by the outdiffusion of point defects towards the surface, causing the annihilation of the upper half loop zone. At the same time, the indiffusion of point defects toward deeper layer does not have a sink. Therefore the coalescence of these defects led to growth of the loops in the lower half zone (see Figure 2).

Microstructural data for the buried loop band were derived from XTEM images, as illustrated by the set given in Figure 3 (a) and (b) which show the change of the dislocation loop bands in the 4.5 MeV implanted material annealed at 900°C for 10 hours and 16 hours, respectively. Isothermal annealing at 900°C revealed a symmetrical shrinkage of the first loop band along with a

growth in size and reduction of loop density as annealing time increased for the 4.5 MeV implanted sample (compare Figure 2c to 3a and 3b). A second discrete band of dislocation loops formed in the deeper layers of the sample after longer periods of isothermal annealing mentioned above. Figure 3a shows the primary loop band (1st band) became narrow and the second loop zone started to appear. An annealing for six more hours caused an enlargement in the loop size and an increase in loop numbers in the second loop band (Figure 3b). As a result, the second loop band became wider.

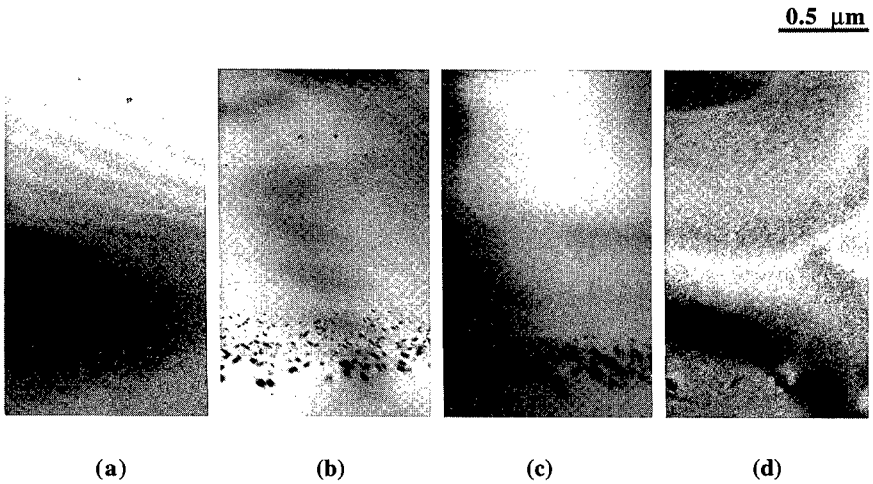


Figure 2. XTEM weak beam images demonstrating an evolution of the morphologies and distribution of defects for a 4.5 MeV Er/O implanted (100)Si sample after 30 minutes annealing at different temperatures: (a) 600°C, (b) 800°C, (c) 900°C and (e) 1000°C.

Reactions between dopants and defects has been closely investigated for the 4.5 MeV implanted Si. The SIMS profile of oxygen for the sample annealed at 900°C for 16 hours (Figure 3c) shows a well defined two peak feature that well matches the depths for two dislocation loop bands in the TEM image shown in Figure 3b. This feature forms a sharp contrast with the profile taken after a 15 minutes annealing which shows only one peak of oxygen distribution with a lower concentration of oxygen (dashed line in Figure 3c). The result documents that oxygen segregated into both defect bands which acted as a sink for oxygen during long-term annealing. The driving force for the migration of oxygen into the defect zone may be supersaturation of oxygen and strain cancellation at the dislocation cores. Erbium, however, was not gettered by the dislocation loops, which can be evaluated from the symmetry of the erbium profile for the same sample annealed at 900°C for 16 hours (Figure 3c).

Comparison of the microstructures of the loops in the first loop band for the 4.5 MeV sample annealed at 900°C for a short-term and a long-term is shown in Figure 4a and 4b, respectively. The TEM contrast of the defects could be influenced by specimen tilting for the short-term annealing sample (Figure 4a) indicating that they were dislocation loops. The dislocation loops were identified to be Frank loops on {111} planes with a burgers vector of a/3<111>.

After a long-term, 16 hours annealing at 900°C, a significantly lower density of loop-like defects with much larger size were obtained, as shown in Figure 4b. Tilting of the sample showed that the coarsened loops still lay on {111} planes, but were visible in all reflections. The absence of a criterion of $\mathbf{g}\cdot\mathbf{b} = 0$, the absorption contrast at weekly diffraction orientations and the strong inside-outside contrast at $\pm\ \mathbf{g}$ are all consistent with these defects being precipitates. These precipitates can be basically divided into two types, as marked "A" and "B" respectively in Figure 3b, based on the contrast features for the same reflection. The small "A" type precipitates have a

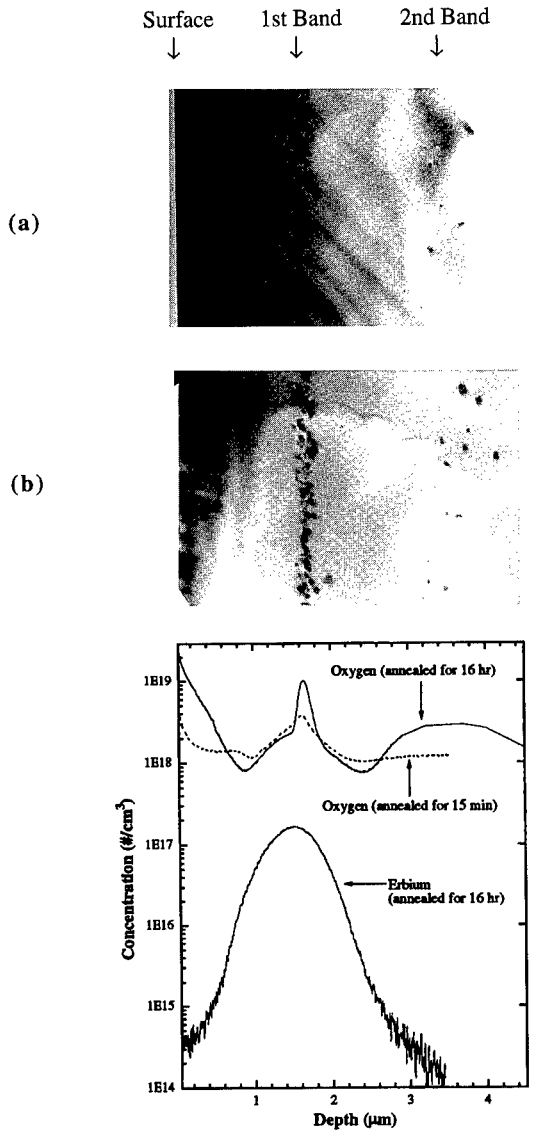


Figure 3. XTEM weak beam images taken after annealing at 900°C for 10 hours (a) and 16 hours (b), showing the development of a second loop band in the 4.5 MeV implanted (100)Si; SIMS profiles (c) documenting the segregation of oxygen into both loop bands in (b).

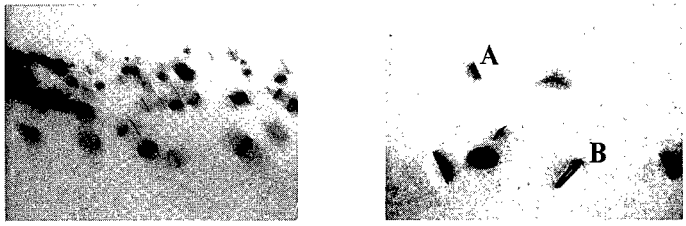


Figure 4. XTEM weak beam images, showing the different defects features in the 4.5 MeV implanted samples annealed at 900 °C for 30 minutes (a) and 16 hours (b).



Figure 5. HRTEM image of the platelet $ErSi_2$ precipitates observed from the <011> direction in the 4.5 MeV implanted (100)Si after annealing at 900°C for 16 hours. The $ErSi_2$ phase has a habit plane of {111}.

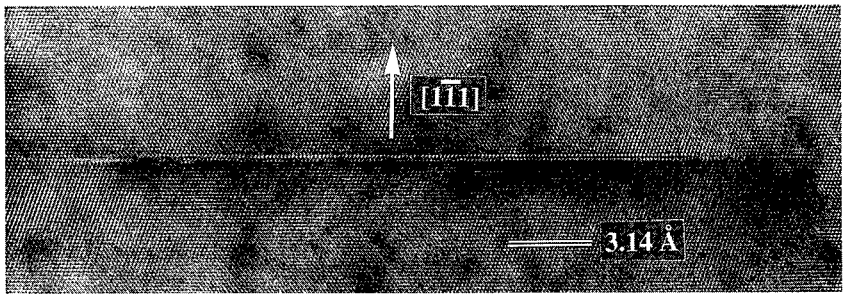


Figure 6. HRTEM image along <011> showing the plate-like oxygen precipitate on the{111} plane formed after annealing for 16 hours in the 4.5 MeV implanted sample.

size of 250 Å, located in slightly shallow layers, while the larger "B" type precipitates have a size range between 500 - 600 Å, distributed at the bottom of the band.

Figure 5 represents a HRTEM image of a typical small "A" type precipitate (Figure 4b) along <011> in which the platelet image can be seen edge on. The precipitate took a platelet morphology with a habit plane of {111} and with a thickness normal to the plane below 10 Å. The structure of the precipitate is identical to the HRTEM image of Er precipitates reported in the Er implanted Si[11] which were believed to be $ErSi_2$. The coherent $ErSi_2$ has a hexagonal crystal structure and aligned with its [0001] axis parallel to <111> Si[12].

A HRTEM image of an isolated, typical larger "B" type precipitates (Figure 4b), revealed that the type of precipitates grew on {111} plane as displayed in Figure 6. Considering the evidence of segregation of oxygen into the loop area (Figure 3) and the identical shape between the primary loops (Figure 4a) and the final precipitates (Figure 4b), the "B" type precipitates were most likely oxygen precipitates, might be derived from oxygen precipitation and evolved from the Frank stacking faults. The nucleation of oxygen precipitates took place heterogeneously on existing dislocation loops which acted as a sink for oxygen interstitials.

CONCLUSIONS

A defect-free material was observed in the 400 KeV implanted sample annealed for 30 min. At 800 and 900°C. In sharp contrast, a variety of secondary defects consisting of dislocations, dislocation loops and precipitates are induced upon annealing in the 4.5 MeV Er/O implanted Si; The defects grew in size and distributed in a deeper layer as the temperature was increased. During the isothermal annealing at 900°C, as the primary dislocation loop zone shrank with an increased annealing time, a second loop zone formed in a deeper layer in the 4.5 MeV implanted samples. The oxygen tended to segregate into the dislocation loop zones, where platelet precipitates with habit planes of {111} were found during long-term annealing in the 4.5 MeV implants. Upon dissociating oxygen from erbium, platelet-like Er precipitates generated in the 4.5 MeV implants which were, most likely, $ErSi_2$ with a habit plane of {111}.

REFERENCES

[1]. H. Ennen, J. Schneider, G. Pomrenke, A. Axmann, Appl. Phys. Lett. **43**, 943 (1983).
[2]. J. Michel, J. L. Benton, R. F. Ferrante, D. C. Jacobson, D. J. Eaglesham, E. A. Fitzgerald, Y. H. Xie, J. M. Poate, and L. C. Kimerling, J. Appl. Phys. **70**, 2672 (1991).
[3]. F. Priolo, S. Coffa, G. Franzo, C. Spinella, A. Carnera, and V. Bellani, J. Appl. Phys. 74, 4936 (1993).
[4]. B. Zheng, J. Michel, F. Ren, L. C. Kimerling, D. C. Jacobson, J. M. Poate, Appl. Phys. Lett. **64**, 2842 (1994).
[5]. A. Polman, J. S. Custer, E. Snoeks, G. N. Van Den Hoven, Appl. Phys. Lett. **62**, 509 (1993).
[6]. P. Wetzel, L. Haderbache, C. Pirri, C. J. Peruchetti, D. Bolmont, G. Gewinner, Phys. Rev. B **43**, 6620 (1991).
[7]. D. B. Beach, R. T. Collins, F. K. Legoues, J. O. Chu, MRS Symposium Proceedings **282**, 397 (1992).
[8]. M. Morse, B. Zheng, J. Palm, X. Duan, L. C. Kimerling, MRS Symposium Proceedings **422,** 41 (1996).
[9]. J. L. Rogers, P. S. Andry, W. J. Varhue, E. Adams, M. Lavoie, P. B. Klein, J. Appl. Phys. 78, 6241 (1995).
[10]. K. S Jones, S. Prussin, and E. R. Weber, Appl. Phys. A 45, 1 (1988).
[11]. D. J. Eaglesham, J. Michel, E. A. Fitzgerald, D. C. Jacobson, J. M. Poate, J. L. Benton, A. Polman, Y. H. Xie, and L. C. Kimerling, Appl. Phy. Letter **58**, 2797, (1991).
[12]. J. L. Park, S. J. Pennycook, and C. W. White, J. Appl. Phys. 70, 3, 1 August, 1853 (1991).

CUBO-OCTAHEDRAL B_{12} CLUSTERS IN SILICON CRYSTAL

M. OKAMOTO, K. HASHIMOTO, K. TAKAYANAGI
Takayanagi Particle Surface Project, ERATO, Japan Science and Technology Corporation, 2-13-3 Akebono, Tachikawa, Tokyo 190, Japan

ABSTRACT

A new stable structure and the electronic structure of boron clusters in silicon crystal have been calculated using the first-principles local density functional approach for $Si_{54}B_{12}H_{60}$ clusters. According to our calculation, the cubo-octahedral B_{12} cluster was found to be more stable than the icosahedral one proposed previously. The total energy difference was about 4.6 eV. The analysis of the partial density of states showed that the cubo-octahedral B_{12} cluster should act as a double acceptor.

INTRODUCTION

The experimental discovery[1] of truncated icosahedral C_{60} has generated an innovation in clusters science. Since the icosahedral symmetry of the C_{60} has approximately a spherical nature, the cluster is expected to be treated as a pseudo-atom for designing new materials. The icosahedral structure has often been found even in bulk boron compounds [2], where the building unit is an icosahedral B_{12} cluster. The unit is formed by the intraicosahedral "three-center bonds" which are characteristic of boron. The boron compounds have sometimes been called "inverted molecular solids" [3], because the bonds between the icosahedral units are as strong as those within the icosahedra. An example on the importance of the surroundings is that B_{12} clusters have not been observed in vacuum, whereas they have often been found in solids. A laser ablation experiment [4] demonstrated that the magic numbers of boron clusters were $N = 5$, 10, 11, and 13.

Recently, Mizushima *et al.*[5] proposed a fascinating boron cluster model for a high-dose boron as-implanted system in silicon. They assumed that the icosahedral B_{12} clusters would exist in Si_5 substitutional sites in silicon crystal which is shown in Fig. 1. They also insisted that their experimental data of fourier transform infrared spectroscopy, X-ray photoelectron spectroscopy, and stripping Hall measurements could be explained by the model. The band calculation[6] for the model showed that the calculated hole concentration was consistent with the experimental results [5]. However, there are some remaining problems related to the stability of the icosahedron surrounded by silicon. There is a mismatch in the symmetries between point group I_h of the icosahedral B_{12} cluster and point group T_d of the Si_5 vacancy. Some distortions of the icosahedron must be caused in the silicon vacancy because of no correlation in subgroup between them [7]. In this letter, we show our calculated results for the stable structure and the electronic states of B_{12} clusters in silicon crystal.

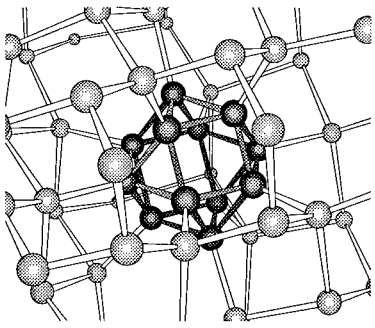


Fig. 1. Boron cluster in silicon

CLUSTER MODEL AND CALCULATION DETAILS

We modeled the system as a $Si_{54}B_{12}H_{60}$ cluster. The cluster was constructed as follows. First, a Si_{59} cluster of

Mat. Res. Soc. Symp. Proc. Vol. 442 © 1997 Materials Research Society

symmetry C_{3v} was extracted from silicon crystal. Then, we substituted a B_{12} cluster for a Si_5 cluster of symmetry T_d at a center of the Si_{59}. Two initial structures for the B_{12} cluster were selected; one was an icosahedron, and the other a cubo-octahedron[8], considering their special structures. The icosahedron has the highest number of three-center bonds, while the symmetry of the cubo-octahedron matches very well with that of the Si_5 vacancy. Finally, we terminated all dangling bonds of surface silicon atoms using hydrogen atoms. Since both models had the same symmetry C_{3v}, we kept the symmetry unchanged throughout the calculations.

To optimize a structure,we used the first-principles local density functional approach. In our approach, frozen core approximation, localized numerical basis functions of 6-31G** level, and exchange-correlation functional of Vosko, Wilk, and Nusair [9] were used. We considered only spin singlet states. Two electrons were added to both of the model clusters to facilitate the calculations. The operation enabled the highest occupied molecular orbitals to be filled completely and the calculation to converge quickly. It took about four hours for one step of the self-consistent field calculation, and more than fifty steps were necessary for well converged structure optimization. No atoms were fixed during the structure optimization.

RESULTS AND DISCUSSIONS

The optimized structure for the icosahedron model is summarized in Table I and Fig. 2(a). Figure 2(a) illustrates a view from Si[111] direction of the icosahedron model. Hydrogen atoms are not shown in the figure. The lengths of intraicosahedral B-B bonds and nearest neighbor (n.n.) B-Si bonds are presented in Table I. Since a regular icosahedral structure for B_{12} cluster was assumed in the previous band calculation by Yamauchi, Aoki, and Mizushima [6], all of the intraicosahedral bonds had the same length, which was 1.81 Å. However, our results in Table I show that the icosahedron should be distorted to minimize energy. The optimized icosahedral B_{12} cluster has a symmetry C_{3v},because the distortion become large around the triangle 10-11-12. The intraicosahedral bond lengths are in the range from 1.72 to 1.89 Å. These values are slightly longer than the optimized bond lengths of the B_{12} cluster in vacuum, which are in the range of 1.59-1.67Å

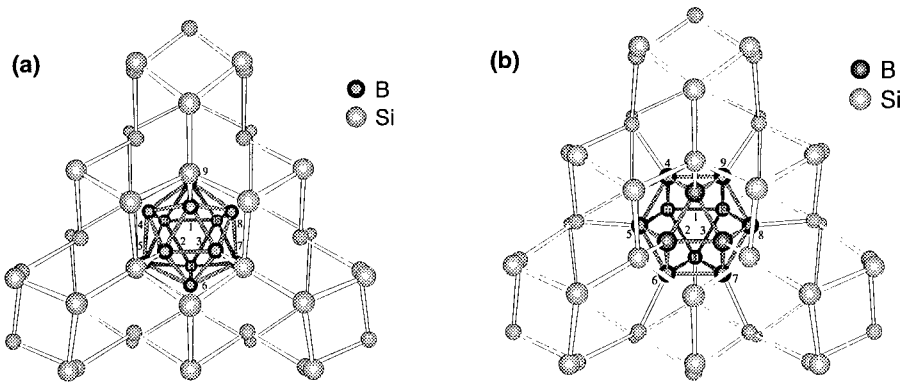


Fig. 2. Optimized structure viewed from Si[111] direction for (a) icosahedron model, and (b) cubo-octahedron model. Numbers of the boron atoms are marked. Hydrogen atoms are not shown here.

TABLE I. Optimized bond length of the icosahedron model. Nearest neighbor is denoted by "n.n.".

Connection[a]	Bond length (Å)	
	This work	Previous calc.[b]
10-(9,5), 11-(5,7), 12-(7,9)	1.89	1.81
Triangle 10-11-12	1.72	1.81
Other intra-bonds of B_{12}	1.77	1.81
(1,2,3,10,11,12) - n.n. Si	2.03	2.05
(4,6,8) - n.n. Si	2.43	2.05
(5,7,9) - n.n. Si	2.26	2.05

[a]See Fig. 2(a) for definitions of atom numberings.
[b]Reference 6.

TABLE II. Optimized bond length of the cubo-octahedron model. Nearest neighbor is denoted by "n.n.".

Connection[a]	Bond length (Å)
Triangles 1-2-3, 4-5-10, 6-7-11, 8-9-12	1.77
Triangles 1-9-4, 2-5-6, 3-7-8, 10-11-12	1.74
(1, 2, ... , 12) - n.n. Si	2.03

[a]See Fig. 2(b) for definitions of atom numberings.

[2], 1.66-1.77Å [10], or 1.68-1.69 Å (by our method). The B-B bonds are considered to be stretched by the interaction with the surrounding silicon atoms. The silicon cage around B_{12} cluster was shrunk slightly due to the B-Si interaction. There are three kinds of n.n. B-Si lengths in the optimized model. The shortest length of 2.03 Å suggests that they are tightly bonded, because the electron density is as high as 0.1 $bohr^{-3}$ at the bond. Since the remaining n.n. B-Si bonding lengths are longer than those mentioned above, they are considered to be weakly bonded or not to be bonded. The electron density at such bonds is less than 0.05$bohr^{-3}$ which is shown in Fig. 3(a). The weak/ dangling bonds are created because of the symmetrical mismatch between point group I_h of the icosahedral B_{12} cluster and point group T_d of the Si_5 vacancy.

The density of states (DOS) of the icosahedron model is plotted in Fig. 4(a). The B_{12} partial DOS calculated from Eq.(1) is illustrated as gray area whose value is magnified twice. The DOS curves are smoothed by a gaussian function with energy width of 0.1 eV. The broken line marks the

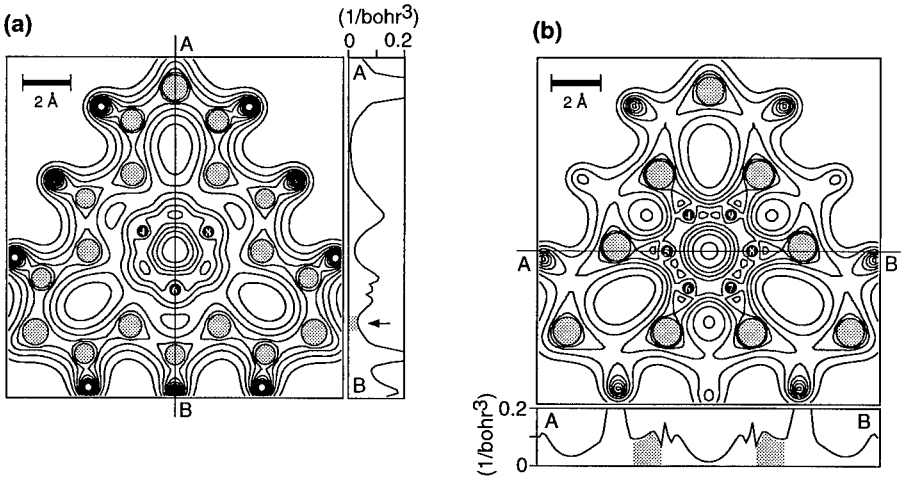


Fig. 3. Valence electron density on (a) 4-6-8 plane of the icosahedron model, and (b) 4-5-6-7-8-9 plane of the cubo-octahedron model. Contours in step of 20 milielectrons per cubic bohr.

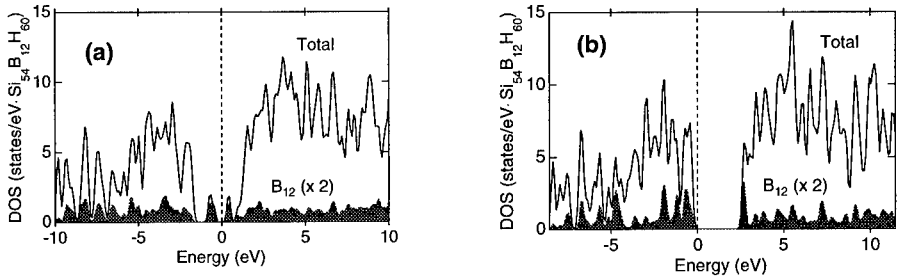


Fig. 4. Density of states for (a) icosahedron model, and (b) cubo-octahedron model. Partial DOS of B_{12} cluster is shown as gray area, and is magnified twice. The dashed line marks Fermi level when two electrons are added to the cluster.

Fermi level when two electrons are added to the cluster. The wide energy gap about 2 eV in width corresponds to that of bulk silicon. Dangling bond states appear in the gap. The high peaks in the partial DOS of these states indicate that they are mainly created by the boron atoms 4, 5, 6, 7, 8, and 9. The cohesive energy of -505.56 eV has been calculated using this model.

The optimized structure of the cubo-octahedron model is summarized in Table II and Fig. 2(b). The structure of the cubo-octahedral B_{12} cluster is optimized to have a symmetry T_d which is slightly distorted from the original symmetry O_h. The bond lengths in the cubo-octahedron are in the range from 1.74 to 1.77 Å. On the other hand, it is remarkable that all n.n. bonds have the same length of 2.03 Å. The electron density at these bonds exceeds the value of 0.1 $bohr^{-3}$ which is shown in Fig. 3(b). It is confirmed that each boron atom in this model is tightly bonded to its n.n. silicon atom.

The density of states of the cubo-octahedron model is plotted in Fig. 4(b). We can not find any mid-gap states in the figure. Therefore the cohesive energy of -510.13 eV for this model becomes lower than that of the icosahedron model. The energy difference is about 4.6 eV. The results suggest that the cubo-octahedral B_{12} cluster is more stable than the icosahedral one because the crystal field of silicon crystal is stronger than the three-center bonding. According to group theory, the strong crystal field can be explained by the relation in which the point group T_d of the Si_5 vacancy is a subgroup of the point group O_h of the cubo-octahedron. So far the cubo-octahedral structures for B_{12} clusters have been found in UB_{12} compensated metal [11], mixed valence system such as YbB_{12} [12], and superconductors such as ZrB_{12} and ScB_{12} [13]. The reason why the B_{12} cluster in these systems does not form an icosahedron is considered to be due to their surroundings.

To estimate carrier concentration, we used the Löwdin's definition for the partial DOS, $D_\alpha(E)$, of atomic orbital ϕ_α,

$$D_\alpha(E) = \sum_{\mu\nu}^{N} (\mathbf{S}^{1/2})_{\alpha\mu}(\mathbf{P})_{\mu\nu}(\mathbf{S}^{1/2})_{\nu\alpha}\delta(E - E_\alpha) \qquad (1)$$

where **P** is the density matrix and **S** is the overlap matrix. Number of electrons which belong to B_{12} cluster can be calculated by integrating $D_\alpha(E)$ with respect to the energy E below the Fermi level and summing up the result for all boron orbitals. We found 38.0 electrons belonging to the B_{12} orbitals of the icosahedron model, and 37.8 electrons belonging to those of the cubo-octahedron model. Since one boron atom has three valence electrons, one B_{12} cluster is occupied by 36 electrons. The remaining electrons of 1.8 - 2.0 were considered to be transferred from the surrounding silicon

atoms into the B_{12} cluster. The above result demonstrates that the B_{12} clusters in both models should act as a double acceptor in silicon. This is consistent with the results of experiments[5] and band calculations [6]. In general, since the localized basis functions do not have orthogonal relations, an ambiguity in the definition of the partial DOS exists. Therefore, it should be noted that this result was obtained using such an approximation.

CONCLUSIONS

In conclusion, we have investigated the stability and the electronic states of boron clusters in silicon crystal using the first-principles local density functional approach. We modeled the system as a $Si_{54}B_{12}H_{60}$ cluster. Two initial structures for the B_{12} clusters were examined; one was the icosahedron, and the other the cubo-octahedron. The structure optimization within the symmetry constraint of C_{3v} results showed that the cubo-octahedron model was more stable than the icosahedron model. Their energy difference was about 4.6 eV. The crystal field effect of the cubo-octahedron model was considered to be much stronger than that of the icosahedron model, although the latter had strong three-center bonding. In other words, the interface between the B_{12} cluster and silicon was very important. The symmetry T_d of the Si_5 vacancy is a subgroup of the symmetry O_h of the cubo-octahedron, so that no dangling bonds are created in the Si_5 vacancy of the cubo-octahedron model. Moreover, the analysis of the partial DOS suggests that the cubo-octahedral B_{12} cluster should act as a double acceptor, which is consistent with the experimental data [5]. Therefore, we conclude that B_{12} clusters in silicon crystal with symmetry C_{3v} have the cubo-octahedral structure.

ACKOWLEDGMENTS

We would like to express our sincere thanks to Dr. H. Hirayama of the Tokyo Institute of Technology for discussions about experimental details, and Dr. M. Fujimori of the University of Tokyo for discussions about the cubo-octahedral B_{12} clusters [14].

REFERENCES

1. H. W. Kroto, J. R. Heath, S. C. O'Brien, R. F. Curl, and R. E. Smalley, Nature **318**,162 (1985).

2. R. Kawai and J. H. Weare, J. Chem. Phys. **95**, 1151 (1991).

3. D. Emin, Phys. Today (January), **55** (1987).

4. L. Hanley, J. L. Whitten, and S. L. Anderson, J. Phys. Chem. **92**, 5803 (1988).

5. I. Mizushima, M. Watanabe, A. Murakoshi, M. Hotta, M. Kashiwagi, and M. Yoshiki, Appl. Phys. Lett. **63**, 373 (1993); I. Mizushima, A. Murakoshi, M. Watanabe, M. Yoshiki, M. Hotta, and M. Kashiwagi, Jpn. J. Appl. Phys. Part 1 **33**, 402 (1994).

6. J. Yamauchi, N. Aoki, and I. Mizushima, in Abstract of 51st annual meeting, (Phys. Soc. Japan, Tokyo, 1996), p.68.

7. Common subgroup of I_h and T_d is C_{3v}. Sequences of subgroups of point group I_h and T_d are $I_h \supset D_{3d} \supset C_{3v} \supset C_3$ and $O_h \supset T_d \supset C_{3v} \supset C_3$, respectively.

8. W. N. Lipscomb and D. Britton, J. Chem. Phys. **33**, 275 (1960).

9. S. J. Vosko, L. Wilk, and M. Nusair, Can. J. Phys. **58**, 1200 (1980).

10. H. Kato, K. Yamashita, and K. Morokuma, Chem. Phys. Lett. **190**, 361 (1992); H. Kato, K. Yamashita, and K. Morokuma, Bull. Chem. Soc. Jpn. **66**, 3358 (1993).

11. Y. Onuki, I. Umehara, Y. Kurosawa, N. Nagai, K. Satoh, M. Kasaya, and F. Iga, J. Phys. Soc. Jpn. **59**, 2320 (1990).

12. K. Sugiyama, F. Iga, M. Kasaya, T. Kasuya, and M. Date, J. Phys. Soc. Jpn. **57**, 3946 (1988).

13. K. Hamada, M. Wakata, N. Sugii, K. Matsuura, K. Kubo, and H. Yamauchi, Phys. Rev. B **48**, 6892 (1993).

14. M. Okamoto, K. Hashimoto, and K. Takayanagi, to be published in Appl. Phys. Lett.

INTERACTIONS OF STRUCTURAL DEFECTS WITH METALLIC IMPURITIES IN MULTICRYSTALLINE SILICON

S.A. McHugo *, H. Hieslmair**, E.R. Weber**, M.D. Rosenblum*** and J.P. Kalejs***

* Advanced Light Source, Lawrence Berkeley National Laboratory, Berkeley, CA 94720
** Dept. of Materials Science and Mineral Eng., University of California, Berkeley, CA 94720
*** ASE Americas Inc., Billerica, MA 01821

ABSTRACT

Interactions between structural defects and metallic impurities were studied in multicrystalline silicon for solar cell applications. The objective was to gain insight into the relationship between solar cell processing, metallic impurity behavior and the resultant effect on material/device performance. With an intense synchrotron x-ray source, high sensitivity x-ray fluorescence measurements were utilized to determine impurity distributions with a spatial resolution of $\approx$ 1μm. Diffusion length mapping and final solar cell characteristics gauged material/device performance. The materials were tested in both the as-grown state and after full solar cell processing. Iron and nickel metal impurities were located at structural defects in as-grown material, while after solar cell processing, both impurities were still observed in low performance regions. These results indicate that multicrystalline silicon solar cell performance is directly related to metal impurities which are not completely removed during typical processing treatments. A discussion of possible mechanisms for this incomplete removal is presented.

INTRODUCTION

Multicrystalline silicon is one of the most promising materials for terrestrial solar cells. The material's low cost and good efficiency make it cost competitive without inherent environmental disposal difficulties. An important property of this material is that once the material's minority carrier diffusion length (L_n) drops below the material's thickness, the cell efficiency is drastically reduced. L_n values of as-grown multicrystalline silicon are typically shorter than the material's thickness which necessitates steps for material improvement. These low L_n values have been attributed to the presence of dislocations and microdefects [1-2]. Furthermore, the carrier recombination rate of these defects is intensified when metal impurities are precipitated at or decorating the defects [3-7]. Therefore, it is critical to getter impurities from the material as well as inhibit contamination during growth and solar cell processing.

Standard solar cell processing steps such as, phosphorus in-diffusion for p-n junction formation and aluminum sintering for backside ohmic contact fabrication, intrinsically possess

Mat. Res. Soc. Symp. Proc. Vol. 442 © 1997 Materials Research Society

gettering capabilities [8-12]. These processes have been shown to improve L_n values in regions of multicrystalline silicon with low structural defect densities but not in highly dislocated regions, suggesting that if impurities are present at these dislocations they are not effectively gettered [1,2,13-15]. Recent Deep Level Transient Spectroscopy (DLTS) results indirectly reveal higher concentrations of iron in highly dislocated regions [16] while further work suggests that the release of impurities from structural defects, such as dislocations, is the rate limiting step for gettering in multicrystalline silicon [16-18]. The work presented here directly demonstrates the relationship between metal impurities, structural defects and solar cell performance in multicrystalline silicon. Additionally, a brief discussion is presented on the thermodynamics and kinetics of impurity release from structural defects.

EXPERIMENT

Edge-defined Film-fed Growth (EFG) multicrystalline silicon in the as-grown state and after full solar cell processing was used in this study. Standard solar cell processing steps were carried out at ASE Americas Inc. The materials possessed oxygen concentrations of $< 10^{17}$ cm^{-3}, carbon concentrations of $\approx 8x10^{17}$ cm^{-3} and boron doping levels of $1x10^{15}$ cm^{-3}. As-grown cast multicrystalline silicon was also used for comparison. Prior to analysis, as-grown materials were etched to remove ≈ 5 μm from both the front and backside. Fully processed samples were etched with a metal etchant to remove the front and backside contacts followed by a silicon etch of ≈ 15μm from both the front and backside in order to remove the heavily phosphorus doped region and the aluminum doped backside layer. Samples were subjected to a piranha cleaning (5:H_2SO_4, 1:H_2O_2 @ 120°C) for 15 minutes, prior to all Surface Photovoltage (SPV) and X-Ray Fluorescence (XRF) micro-probe measurements. This treatment has been shown to effectively remove organics and metal impurities from silicon surfaces [19]. SPV measurements, a standard technique for measurement of diffusion length [20-22], quantified L_n values over an entire 10x10 cm solar cell wafer. Metal impurity concentrations and distributions were determined by use of the Center for X-ray Optics' x-ray fluorescence microprobe (beamline 10.3.1) at the Advanced Light Source, Lawrence Berkeley National Laboratory. The sample was not under vacuum, so only elements with Z greater than silicon could be detected, which includes all metal impurities of interest. Multi-layer mirrors arranged in a Kirkpatrick-Baez orientation focused the x-rays down to ≤ 1μm. The typical sampling depth for metal impurities in silicon is ≈ 50μm. Standard samples with known amounts of various impurities ranging from Al to Zn were used to quantify

the impurity concentration in the multicrystalline silicon samples. The sensitivity of the system for metal impurities in silicon is less than $1x10^{14}$ atoms/cm^2. This allowed for micron-scale mapping of metal impurities with sensitivities far surpassing conventional mapping techniques. It should be noted that observations of metal impurity agglomerates have been observed with this apparatus previously [23], however, correlation with structural defects was not achieved. Structural defect densities were determined by preferential etching and surface analysis using a Scanning Electron Microscope (SEM) in secondary electron mode. Mapped areas were exactly relocated between the XRF and SEM to allow for direct comparison of impurity and structural defect distributions.

RESULTS AND DISCUSSION

Minority carrier diffusion length (L_n) values were measured on a number of as-grown EFG samples using SPV. Typical L_n values ranged from 10-100μm. XRF studies of this material as well as other as-grown multicrystalline silicon materials reveal the presence of Fe and Ni. The observation of Fe in as-grown multicrystalline silicon are in accord with indirect measurements of other work [16]. An XRF map of Fe is shown below in Figure 1a.

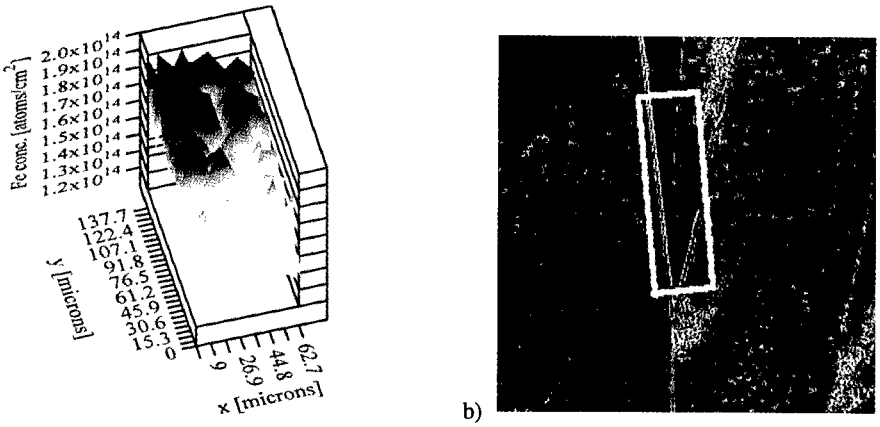


Figure 1: a) X-Ray Fluorescence map of Fe in an EFG multicrystalline silicon sample b) SEM micrograph of a preferentially etched EFG sample showing dislocations and grain boundaries. The XRF scan area of Figure 1a is denoted by the white box.

Following the XRF mapping, the sample from Figure 1a was preferentially etched and analyzed with an SEM in secondary electron mode as shown in Figure 1b where the lines are etched-out grain boundaries and the pits delineate dislocations. By comparison of Figures 1a and b, it is

apparent that the Fe is primarily present along two grain boundaries. This is direct evidence that metal impurities agglomerate at structural defects in as-grown multicrystalline silicon. One would expect this agglomeration since any impurities present during the slow cool from crystal growth would prefer to precipitate at the highly disordered core of a grain boundary. This defect seems to provide an extraordinarily low energy site for Fe which would be required in order to trap impurities at high growth temperatures when the impurities are highly mobile and the impurity supersaturation is low. This concept has been shown for Cu precipitation at structural defects in single and multicrystalline silicon [7,24].

SPV measurements of L_n were also taken on fully processed EFG, as shown in Figure 2.

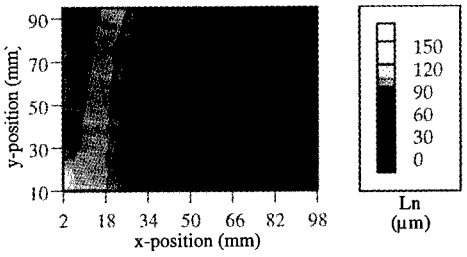


Figure 2: SPV map of L_n across a 10x10 cm EFG solar cell after complete solar cell processing.

Of particular interest is the one poorly performing region down the center of the wafer which is along the growth direction. This region has drastically reduced the solar cell efficiency by ≈ 3% absolute. XRF line scans were taken across this poor region as well as other good regions. A summed spectra taken in the poor region, shown in Figure 3, reveals the presence of Ni and Fe.

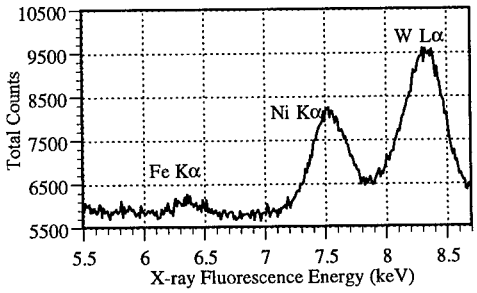


Figure 3: XRF spectra of a fully processed EFG solar cell. This spectra is the sum of 228 spectra taken over a line scan through the low L_n regions in Figure 2.

For this scan, 228 points in 1.25 μm steps were taken with a 5 minute dwell time at each point. The W Lα is a stray signal from the apparatus. XRF scans taken in good regions detected neither

these impurities nor any other impurities. The Ni was widely distributed while the Fe signal was too weak at any point for spatial resolution. This is direct proof that metal impurities are not adequately gettered during typical solar cell processing steps.

Considering the results presented here and other past work [16-18], which show incomplete gettering for lengthy anneal times such that impurity diffusion from the original site to the gettering layer should be sufficient, it is highly probable that these impurities are not gettered from this material because of sluggish impurity release from defects. Previous work on this subject [25] suggested the diffusion of impurities away from precipitates can slow the dissolution process of a precipitate such that this process cannot be considered as the exact opposite of impurity precipitation, as originally suggested [26]. However, this mechanism of dissolution sluggishness is an important factor only for very slowly diffusing impurities which is not the case for Ni, Fe or Co in silicon at usual processing temperatures.

The surface reaction rate must also be considered as possibly retarding impurity release. If one considers the metal to be in the form of metal silicide at the structural defect, then a simple analysis would indicate that the dissolution rate is dictated by the metal silicide-silicon reaction rate. Based on metal impurity diffusion into silicon from metal silicide sources [27], there is no indication that the surface reaction rate at this interface is slower than impurity diffusion away from the silicide and into the silicon. However, the metal silicide could be stabilized by the structural defect's strain field such that dissolution is not comparable with metal in-diffusion studies. Additionally, the assumption that the impurity is in the form of a silicide may not be correct. Rather, the metal may reside in a dissolved state where the defect acts as a region of higher solubility than the surrounding matrix, essentially existing as a segregation-type gettering mechanism just as aluminum or phosphorus gettering but within the material. Also, the metal may be in the form of a metal carbide or metal oxide which would completely alter the surface reaction rates and metal solubility in the matrix.

CONCLUSIONS

This work reveals metal impurities agglomerated at structural defects in multicrystalline silicon used for solar cells. These impurities are seen to remain in poorly performing regions of finished solar cells. Based on this work, further understanding of the gettering process is required for implementation of effective processing steps.

ACKNOWLEDGMENTS

The authors would like to thank S.M. Myers, F.G. Kirscht, A.C. Thompson and T. Heiser for wonderfully enlightening conversations. This work was supported by the Director, Office of Energy Research, Office of Basic Energy Sciences, Materials Sciences Division, of the U.S. Department of Energy, under Contract No. DE-AC03-76SF00098.

REFERENCES

1. B.L. Sopori, L. Jabstrzebski, T. Tan and S. Narayanan: in *Proc. of the 12th European Photovoltaic Solar Energy Conference*, Netherlands, 1994, p. 1003
2. S.A. McHugo, J. Bailey, H. Hieslmair and E.R. Weber: in *1994 IEEE First World Conf. on Photovoltaic Energy Conversion,* Waikoloa, Hawaii, U.S.A., 1994, p. 1607
3. C. Cabanel and J.Y. Laval, J. Appl. Phys. **67**, 1425 (1990)
4. V. Higgs and M. Kittler, Appl. Phys. Lett. **63**, 2085 (1993)
5. M. Kittler, W. Seifert and V. Higgs, Phys. Stat. Sol. (a) **137**, 327 (1993)
6. T.H. Wang, T.F. Ciszek and T. Schuyler, Solar Cells **24**, 135 (1988)
7. S.A. McHugo and W.D. Sawyer, Appl. Phys. Lett. **62**, 2519 (1993)
8. L. Baldi, G. Cerofolini and G. Ferla, J. Elec. Chem. Soc. **127**, 164 (1980)
9. W. Schröter and R. Kühnapfel, Appl. Phys. Lett. **56**, 2207 (1990)
10. E.Ö. Sveinbjörnsson, O. Engström and U. Södervall, J. Appl. Phys. **73**, 7311 (1993)
11. R.D. Thompson and K.N. Tu, Appl. Phys. Lett. **41**, 440 (1982)
12. M. Apel, I. Hanke, R. Schindler and W. Schröter, J. Appl. Phys. **76**, 4432 (1994)
13. M. Loghmarti, R. Stuck, J.C. Muller, D. Sayah and P. Siffert, Appl. Phys. Lett. **62**, 979 (1993)
14. O. Porre, M. Stemmer and M. Pasquinelli, Materials Science and Eng. B24, 188 (1994)
15. S.A. McHugo, H. Hieslmair and E.R. Weber: in *Defects in Semiconductors 18, International Conference on Defects in Semiconductors,* edited by M. Suezawa and H. Katayama-Yoshida, Sendai, Japan (1995) p. 1979
16. S.A. McHugo and E.R. Weber: in print, Applied Physics A, 1996
17. M. Seibt and W. Schröter: *6th Workshop on the Role of Impurities and Defects in Silicon Device Processing,* Aug. 1996
18. S.A. McHugo, H. Hieslmair and E.R. Weber: ibid 17
19. M.M. Heyns, S. Verhaverbeke, M. Meuris, P.W. Mertens, H. Schmidt, M. Kubota, A. Philipossian, K. Dillenbeck, D. Gräff, A. Schnegg and R. de Blank, Mat. Res. Symp. Proc., vol. 315, p. 35, (1993)
20. E.O. Johnson, J. Appl. Phys. **28**, 1349 (1957)
21. A.M. Goodman, J. Appl. Phys. **32**, 2550 (1961)
22. J. Lagowski, A.M. Kontkiewicz, L. Jabstrzebski and P. Edelman, Appl. Phys. Lett. **63**, 2902 (1993)
23. A.C. Thompson and R. Holm, to be published
24. B. Shen, T. Sekiguchi, J. Jablonski and K. Sumino, J. Appl. Phys. **76**, 4540 (1994)
25. H.B. Aaron and G.R. Kotler, Met. Trans. **2**, 393 (1971)
26. G. Thomas and M.J. Whelan, Phil. Mag. **6**, 1103 (1961)
27. E.R. Weber, Appl. Phys. A **30**, 1 (1983)

Part VI

Impurity Diffusion and Hydrogen in Si

FORMATION OF HYDROGEN MOLECULES IN CRYSTALLINE SILICON TREATED WITH ATOMIC HYDROGEN

K. MURAKAMI*, N. FUKATA*, S. SASAKI*, K. ISHIOKA** , K.G. NAKAMURA**, M . KITAJIMA**, S. FUJIMURA***, J. KIKUCHI***, and H. HANEDA****
* Institute of Materials Science, University of Tsukuba, Tennoudai 1-1-1, Tsukuba, Ibaraki 305, Japan; murakami@mat. ims.tsukuba.ac.jp
**National Research Institute for Metals, Sengen 1-2-1, Tsukuba, Ibaraki 305, Japan;
***Process Development Division, Fujitsu Ltd., Kawasaki, Kanagawa 211, Japan;
****National Institute for Research in Inorganic Materials, Namiki 1-1, Tsukuba, Ibaraki 305, Japan

ABSTRACT

Hydrogen molecules have been formed in crystalline silicon at various temperatures by a hydrogen-atom remote treatment. The Raman spectrum of the vibrational lines of hydrogen molecules in crystalline silicon is detected for silicon samples treated at temperatures between 250 and 500° C. The maximum production is obtained at 400° C. The Raman spectrum of hydrogen molecules in silicon observed at room temperature exhibits a frequency shift of around 4158 cm^{-1} and a very broad half-width of approximately 34 cm^{-1}. Isotope shift also can be observed at around 2990 cm^{-1} in silicon treated with deuterium atoms at 400° C. The frequency shifts of the observed lines are in close agreement with those reported for molecular hydrogen and deuterium in gas, liquid, and solid phases. We discuss a model for the hydrogen molecule configuration and rule out the possibility of high-pressure hydrogen molecular gas in microvoids in crystalline silicon. These results indicate that hydrogen molecules exist at the tetrahedral interstitial sites in crystalline silicon .

INTRODUCTION

Hydrogen has been a very important impurity in crystalline semiconductors, because hydrogen impurities are incorporated during the various stages of semiconductor processing and exhibit interesting phenomena such as passivation of defects and impurities, Fermi resonance, and tunneling.[1] Incorporated atomic hydrogen is not stable in crystalline semiconductors and forms complexes with other defects or forms hydrogen clusters. Recent calculations have predicted that in silicon, among the various forms of hydrogen-related defects, a hydrogen molecule at the tetrahedral interstitial site has a relatively low energy.[2,3] However, no direct observation of hydrogen molecules has been reported so far, except for our previous studies [4,5]. A metastable configuration for another type of hydrogen molecule has also been studied.[6] This consists of a bond-center (BC) hydrogen and a hydrogen at a neighboring tetrahedral interstitial site, and has an energy that is 0.01 eV higher than the most stable hydrogen molecule.

In this paper, we report direct spectroscopic evidence for the existence of hydrogen molecules in crystalline silicon through their Raman spectra and the dependence of the formation of hydrogen molecules upon the substrate temperature during hydrogen atom treatment (HAT). The isotope shift of the Raman lines is also reported because of the importance for the identification of hydrogen molecules. The values of the observed Raman shifts are consistent with those reported for H_2 and D_2 in gas, liquid, and solid states, while the half-widths of the lines are two orders of magnitude broader than those reported in the literature.[7,8] We discuss a model for the hydrogen molecular configuration and rule out the possibility of high-pressure hydrogen molecular gas included in microvoids that are induced in crystalline silicon by the hydrogen atom treatment. These results

Mat. Res. Soc. Symp. Proc. Vol. 442 © 1997 Materials Research Society

indicate that hydrogen molecules exist at the tetrahedral interstitial sites in crystalline silicon, which will give us a new possibility of science and technology of hydrogen molecules in crystalline semiconductors.

EXPERIMENT

We have examined two types of silicon samples. The first is implanted and thermally annealed silicon, and the other is unimplanted silicon. Hydrogenation was done for these samples at various substrate temperatures ranging from 60 to 600° C for 3 hours, using the remote-treatment with downstream hydrogen atoms from hydrogen plasmas which were generated by microwave irradiation in a microwave cavity. Floating-zone (FZ), p-type silicon wafers were used in this study, and some had been implanted with phosphorus (P) ions at 50 keV with doses of 1 to $5x10^{14}/cm^2$ and thermally annealed at 900° C for 30 minutes. Deuterium atom treatment was also done in the same way as the hydrogenation.

Raman scattering measurements were carried out at room temperature in a 90°-scattering configuration with the 514.5 nm line of a cw argon-ion laser as the Raman excitation light. The measured frequency shift ranges from 300 to 4210 cm^{-1} and the wave-number resolution is 0.2 - 0.3 cm^{-1}. In order to investigate the effect of hydrogen- and deuterium-molecules on the linewidth of electron spin resonance (ESR) of donor/conduction electrons, ESR measurements at 4.2 K were also performed for implanted silicon with P donors with an X-band spectrometer. Details of these experiments and hydrogenation were reported in detail elsewhere.[4,5,9,12]

RESULTS AND DISCUSSION

Figure 1 shows typical Raman spectra obtained for the samples with P donors which were treated at various substrate temperatures. In Fig. 1(a), a Raman line is clearly seen at 590 cm^{-1} for HAT-400°C sample, as well as the optical phonons at 521 cm^{-1}. The small band at 590 cm^{-1} was assigned to the rotational line ($S_0(1)$) of ortho-H_2.[5,7,8] In contrast to this, the line corresponding to the rotation of para-H_2 , ($S_0(0)$), was not observed because it overlaps with the strong Raman signal of bulk silicon. As shown in Fig. 1(b), a Raman line was observed at around 4158 cm^{-1} for the samples treated at temperatures from 250 to 500° C. We assigned this to the vibrational Raman line Q_1 of the hydrogen molecule in crystalline silicon based upon its frequency which is close to those reported for hydrogen-molecules in gas,[7] liquid, and solid phases.[8] It should be stressed that the half-width of the Raman line is two orders of magnitude broader than for the corresponding lines reported for liquid and solid H_2 at lower temperatures. On the other hand, no vibrational molecular lines were observed in the samples treated with hydrogen atom below 180° C and above 600°C, as can be seen in Fig. 1(b). The vibrational Raman line near 4158cm^{-1} was seen most clearly for both the samples of HAT-400° C with and without P ion implantation.[4] It should be also noted that the deuterium isotope effect can be clearly observed in Fig.1(c) for the sample DAT-400° C which was done by deuterium atom treatment (DAT) at 400°C; i.e., at around 2990 cm^{-1}, we see a broad Raman line associated with the deuterium molecule. The observed isotope shift is in excellent agreement with those reported for hydrogen and deuterium molecules.[4,7,8] Thus, these results provide strong evidence for the existence of hydrogen molecules in the crystalline silicon treated with atomic hydrogen at a substrate-temperature range approximately from 250 to 500° C. Stutzmann et al. [10] reported that interstitial deuterium molecules may be the main component of the incorporated deuterium in p-type silicon after dissociation of B-D complexes by thermal annealing, although they could not detect the Raman

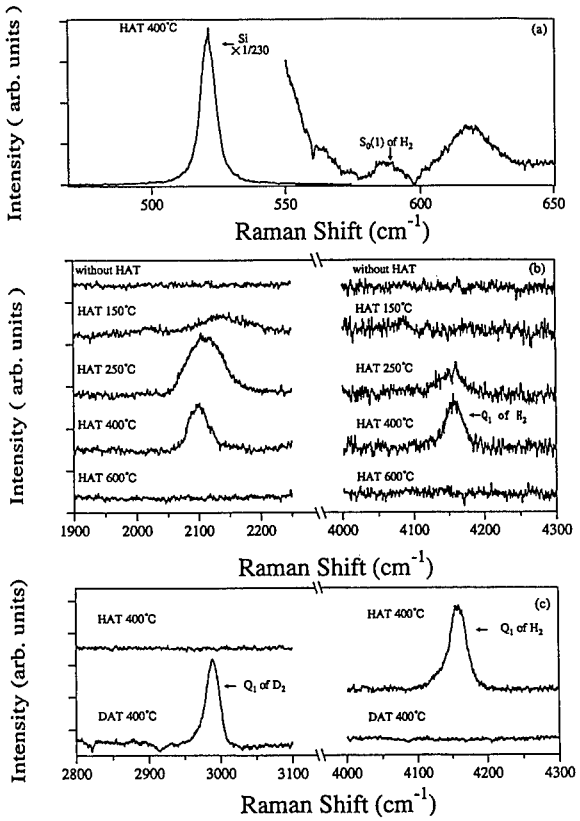


Fig.1 Raman scattering spectra observed at wide frequency shift for samples (HAT and DAT) treated at various temperatures. HAT and DAT mean "hydrogen-atom treatment" and "deuterium-atom treatment", respectively.

spectrum for deuterium molecules in their experiments. Our finding strongly supports their proposal that D_2 is a product of the dissociation of B-D.

For the sample HAT-150°C, a broad Raman line can be seen at around 2140 cm^{-1}, although the vibrational line of hydrogen molecule is not observed in Fig. 1(b). This Raman shift is similar to one previously assigned to Si-H vibrations associated with platelets.[9,11] Another Raman line associated with Si-H bond vibration is also observed at around 2100 cm^{-1} for the sample HAT-400° C. The shift to lower wave number compared to that of the HAT-150° C sample suggests that the Si-H bond is changed to a more relaxed state than for the Si-H bond with strong compression in the platelets. For a sample treated with atomic hydrogen at 600°C, no Raman lines were observed near 2140 or 2095 cm^{-1}.

It is found from the results shown in Fig. 1 that the Raman intensities of hydrogen molecules and Si-H bonds are strongly dependent on the substrate temperature during hydrogen atom treatment. We now show the substrate-temperature dependence of the formation of hydrogen molecules and

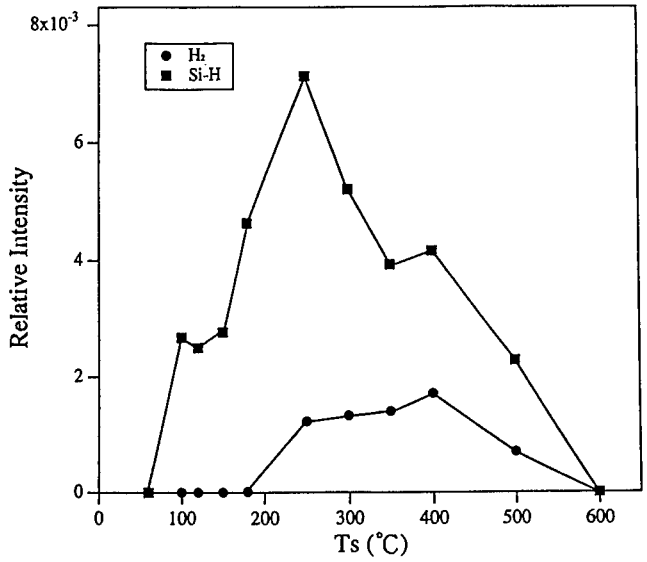


Fig.2 Intensity of vibrational Raman lines of hydrogen molecule and Si-H as a function of the substrate temperature during HAT.

Si-H bonds in Fig.2. The intensity is normalized by the Raman intensity of the Si optical phonon line at 521 cm^{-1} for each sample. The intensity of the vibrational Raman lines reaches a maximum at 250 ℃ for Si-H and at 400°C for hydrogen molecules. Since the Raman shifts were observed to vary at each substrate temperature T_S, the values of their Raman shifts are plotted in Fig. 3 as a function of T_S. The variation of the shift is small for hydrogen molecules, whereas the shift varies greatly for the Si-H. The Raman line at about 2140 cm^{-1} seen below 250°C is due to the Si-H in the platelets.[11] It is likely that the line at about 2100 cm^{-1} seen above 300° C originates from either isolated, two Si-H bonds located near the Si bond center or in very small seeds of the platelets. These ideas need no vacancies for forming the structure in crystalline silicon.

Here, we discuss models for hydrogen molecule configuration in crystalline silicon. There are two possibilities. The first is a model in which the hydrogen molecules exist at several metastable states in the tetrahedral interstitial sites, as proposed by theoretical calculations[2,3]. The second is that of a high pressure gas of hydrogen molecules included in microvoids that are created by the hydrogen atom treatment. The first model is supported and the second can be ruled out as follows;

(1) We first considered the possibility that the origin for the Raman line at 4158 cm^{-1} might exist in a very thin surface layer with a thickness less than 10 nm which might have been damaged, even with the remote plasma. In order to investigate this possibility, we etched off a surface layer of approximately 10 nm by sequential rinses in HNO_3 followed by HF and then measured the Raman spectrum. It was found that there were no significant changes in the vibrational Raman line at 4158 cm^{-1}. Therefore, we conclude that the hydrogen molecules are located deeper sites in the bulk of the crystalline silicon.[4]

(2) The hydrogen atom treatment used, i.e., the remote plasma method, is known to induce no significant damages in deeper regions of crystalline silicon.

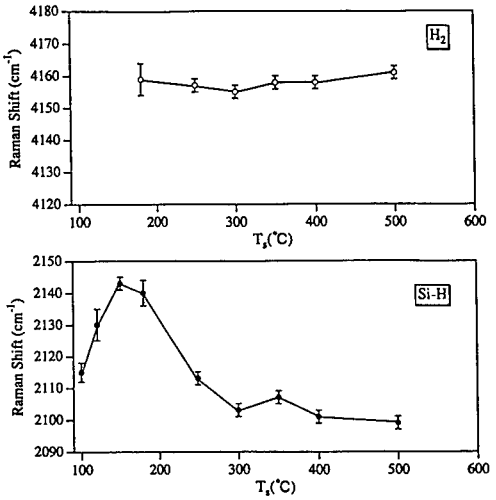


Fig.3 Raman shifts of hydrogen molecule and Si-H as a function of the substrate temperature during HAT.

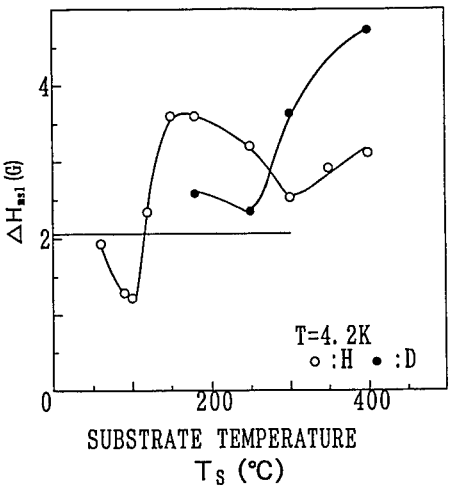


Fig.4 ESR linewidth of the donor/ conduction electrons measured at 4.2K for HAT-400 and DAT-400°C samples as s finction of T_S.

(3) No hydrogen molecules were detected for silicon samples implanted with $1x10^{16}$ and $1x10^{17}H_2^+/cm^2$ at 10 keV which include microvoids.[12]

(4) We can devide the vibrational Raman lines of hydrogen molecules into two distinct lines by more detail measurements.[12] One of them was found to correlate with platelets, suggesting hydrogen molecules being located just near or within platelets.

(5) The ESR linewidth of donor/conduction electrons measured at 4.2 K indicates an isotope effect. Figure 4 shows the ESR linewidth as a function of T_S for HAT and DAT samples. At the range of platelets formation (T_S of 150 to 250° C), the increase in ESR linewidth is due to the hyperfine interaction between donor/conduction electrons and the nuclear spin of hydrogen atoms (I=1/2) or of deuterium atoms (I=1).[4] At the range of molecules formation (T_S of 250 to 500° C), the linewidth for DAT samples is larger than that for HAT ones. This is an indirect evidence of molecule formation, because of the following reason. At lower temperatures, the para-H_2 is dominant since its ground state is about 180 K lower in energy than that of the ortho-H_2, while ortho-D_2 is more stable than para-D_2. The observed difference of the ESR linewidth may be due to the difference in the magnitude of the hyperfine interactions with donor/conduction electrons for the lowest-energy para-H_2 (I=0) with the rotational quantum number of J=0 and for the lowest-energy ortho-D_2 (I=0 and 2) with J=0. If these molecules were included in microvoids, there would be no hyperfine intereaction since the wavefunction of donor electrons or conduction electrons could not penetrate enough into the microvoids.

(6) The Raman line exhibits a very broad linewidth. Hartwig and Vitko [13] also reported a similar broad linewidth for hydrogen molecules in vitreous silica and that the hydrogen molecules are

located in the small interstices in vitereous silica.
(7) A cluster calculation using the ab initio Hartree-Fock model [14] indicates the possibility of broad Raman line of about 30 cm^{-1} for hydrogen molecules in the tetrahedral interstitial sites.
(8) High pressure hydrogen-molecule gas is thought to show a strong temperature dependence of the Raman linewidth. However, the Raman linewidth observed did not change between two observations at 77 K and room temperature.[12]

Thus, the results shown above support the first model as the most probable configuration and indicate that the second model can be ruled out. The very broad Raman line may come from the metastabilities of hydrogen molecules located at several sites near the tetrahedral interstitial site and with several stable directions for the molecular axis, in addition to the interaction between hydrogen molecules and silicon lattice phonons. This leaves us with an interesting question and is thought to be important for molecules in crystalline semiconductors.

CONCLUSIONS

We have provided direct evidence for the existence of hydrogen molecules in crystalline silicon treated at relatively high temperatures with atomic hydrogen by means of Raman scattering measurements. The Raman spectrum of the molecules exhibits a vibrational line near 4158 cm^{-1}, which is close to Raman lines associated with para- and ortho-hydrogen molecules in gas, liquid , and solid states. The results of Raman measurements for various silicon samples treated at temperatures of 60 to 600° C indicate that the hydrogen molecules are formed predominantly above 250°C, where the formation of platelets is suppressed, and below 500° C . It is also found that the quantity of formed molecules reaches a maximum value at substrate temperature of 400°C. These molecules are thought not to be included in microvoids, but to be in the tetrahedral interstitial sites.

ACKNOWLEDGEMENTS

We are grateful to Professors G.D. Watkins, M.J. Stavola, and C.A.J. Ammerlaan for helpful discussions. This work is a part of a research contract from the NEDO.

REFERENCES

[1] See for example, J.F. Zheng and M. Stavola, Phys. Rev. Letters **76**, 1154 (1996).
[2] K.J. Chang and D.J. Chadi, Phys. Rev. Lett. **60**, 1422 (1988).
[3] C.G. Van de Walle, Phys. Rev. B **49**, 4579 (1994).
[4] K. Murakami,N. Fukata, S. Sasaki, K. Ishioka, M. Kitajima, S. Fujimura, J. Kikuchi, and H. Haneda, Phys. Rev. Letters **77**, 3161 (1996).
[5] N. Fukata, S. Sasaki, K. Murakami, K. Ishioka, M. Kitajima, S. Fujimura, and J. Kikuchi, Jpn. J. Appl. Phys. **35**, L1069 (1996).
[6] D.J. Chadi and C.H. Park, Phys. Rev. **52**, 8877 (1995), and J.D. Holbeck, B.B. Nielsen, R. Jones, P. Sitch, and S. Orberg, Phys. Rev. Lett. **71**, 875 (1993).
[7] B.P. Stoicheff, Can. J. Phys. **35**, 730 (1957).
[8] S.S. Bhatnagar, E.J. Allin, and H.L. Welsh, Can. J. Phys. **40**, 9 (1962).
[9] N. Fukata, S. Sasaki, S. Fujimura, H. Haneda, and K. Murakami, Jpn. J. Appl. Phys. **35**, 3937 (1996).
[10] M. Stutzmann, W. Beyer, L. Tapfer and C.P. Herrero, Physica B **170**, 240 (1991).
[11] J.H. Heyman, J.W. Ager III, E.E. Haller, N.M. Johnson, J. Walker, and C.M. Doland, Phys. Rev. B **45**, 13363 (1992).
[12] N. Fukata, S. Sasaki, K. Murakami, K. Ishioka, M. Kitajima, S. Fujimura, J. Kikuchi, and H. Haneda, to be submitted to Phys. Rev. B.
[13] C.M. Hartwig and J. Vitko, Jr., Phys. Rev. B **18**, 3006 (1978).
[14] K.G. Nakamura, K. Ishioka, M. Kitajima, and K. Murakami; Solid State Comm. (in press).

VIBRATIONAL SPECTROSCOPY OF GOLD HYDROGEN COMPLEXES IN SILICON

M. J. EVANS, M. G. GORNSTEIN, AND MICHAEL STAVOLA
Department of Physics, Lehigh University, Bethlehem, Pennsylvania 18015

ABSTRACT

Several vibrational bands have been observed in the region 1750-1900 cm^{-1} for n-type silicon into which gold and hydrogen had been introduced by high temperature diffusion. This paper focuses primarily on a defect which gives rise to bands at 1813.3 and 1827.1 cm^{-1}. This center contains a single hydrogen atom and has two charge states in the gap with trigonal symmetry. We propose a tentative model in which this complex contains a substitutional Au atom and a single hydrogen atom at one of two possible antibonding sites, bonded either to Au or to Si. A defect observed previously in Si samples doped with Pt and H which gives rise to hydrogen stretching bands at 1880.7 and 1897.2 cm^{-1} has similar properties to the Au-H complex discussed here, suggesting that these defects have the same structure. Other hydrogen-stretching modes observed in Si samples that contain Au and H are also discussed.

INTRODUCTION

Hydrogen has been found to be an important impurity in semiconductors and its interaction with shallow impurities has received much attention.[1] The interaction of hydrogen with deep-level impurities such as transition metals, however, has remained poorly understood.[2] Recently, it has been recognized by two different experimental approaches that transition-metal-hydrogen complexes in Si are not necessarily passivated and can contain states in the gap. In several studies, H has been introduced into the depletion region of Schottky diodes to produce hydrogenated transition metals that have been studied by DLTS.[3-5] An alternative approach, which has been used here, has been to introduce H into the bulk of a Si sample with a high temperature (1250°C) anneal in molecular H_2. While a more limited variety of defects can be hydrogenated by high temperature hydrogen indiffusion, a sufficient number of defects is introduced into bulk samples for study by structure-sensitive spectroscopic methods.[6-9] In this paper the hydrogen-stretching vibrations of several centers in Si containing Au and H are discussed.[10]

EXPERIMENT

Samples were prepared from floating-zone, n-type Si with [P] = 3 x 10^{16} cm^{-3}. Au was introduced by evaporating a layer of Au metal onto the sample surface, followed by a high temperature (900-1200°C, 18-24 h) anneal in a sealed quartz ampoule that contained 1/3 atm. of He. (In samples prepared with a Au indiffusion temperature of 1100°C, the Au concentration was found by DLTS to be approximately 1 x 10^{15} cm^{-3}.) A subsequent anneal in 2/3 atm. H_2 was performed at 1250°C for 30 minutes. The samples were then quenched to room

Mat. Res. Soc. Symp. Proc. Vol. 442 © 1997 Materials Research Society

temperature in ethylene glycol. When a very fast quench was desired, the ampoules were made thin at one end so that they would break upon contact with the ethylene glycol. Other samples were prepared similarly in D_2 or in mixtures of H_2 and D_2. Vibrational spectra were measured using a Bomem DA3.16 Fourier transform infrared spectrometer equipped with a MCT detector. Table 1 summarizes the vibrational frequencies for the H- (and D-) stretching bands commonly observed.

Si: Au + H	Si: Au + D
1785.6 cm^{-1}	1292.1 cm^{-1}
1787.7	1292.9
1803.3	1298.6
1813.3	1310.9
1817.3	1313.6
1827.1	1319.4
1831.8	1323.0

Table 1.Vibrational frequencies for bands seen in Si containing Au and H (or D).

TRIGONAL CENTER CONTAINING Au AND H

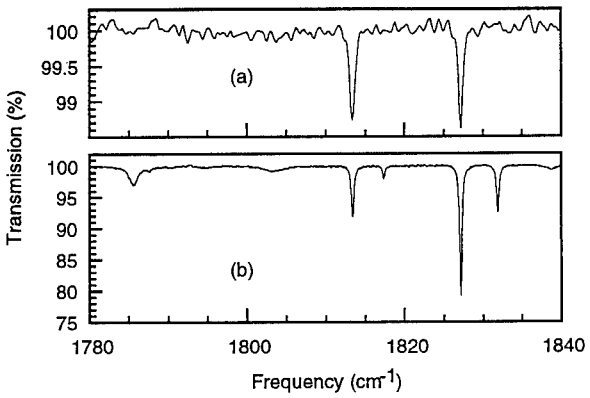


Figure 1. H-stretching bands in n-type Si containing Au and H.
(a) Spectrum of a 2mm thick sample showing bands at 1813.3 and 1827.1 cm^{-1} (1225°C Au indiffusion).
(b) Spectrum of a 13mm thick sample showing additional bands at 1785.6, 1787.7, 1803.3, 1817.3 and 1831.8 cm^{-1} (1000°C Au indiffusion).

Fig. 1(a) shows an IR absorption spectrum of Si that contains Au and H with two narrow (FWHM ~ 0.3 cm^{-1}) absorption bands at 1813.3 and 1827.1 cm^{-1}. These bands have not been seen in control samples that have been annealed in ampoules at high temperature without a Au diffusion source, or in samples diffused with other transition metals. Presumably they arise from a complex that includes Au. In samples with deuterium substituted for hydrogen, the bands were shifted to 1310.9 and 1319.4 cm^{-1}, respectively, confirming the involvement of hydrogen. Furthermore, samples prepared in a mixture of H_2 and D_2 exhibit no additional vibrational modes, indicating that each of these bands arises from defects that contain a single H atom. The intensities of the two hydrogen bands track each other when the samples are isochronally annealed (30 min.). There was an initial increase in intensity at ~150°C as hydrogen is released from elsewhere in the sample[11] followed by a decrease for an annealing temperature of 250°C where the Au-H center begins to be annealed away. The similar annealing behavior suggests that both lines originate from a single defect.

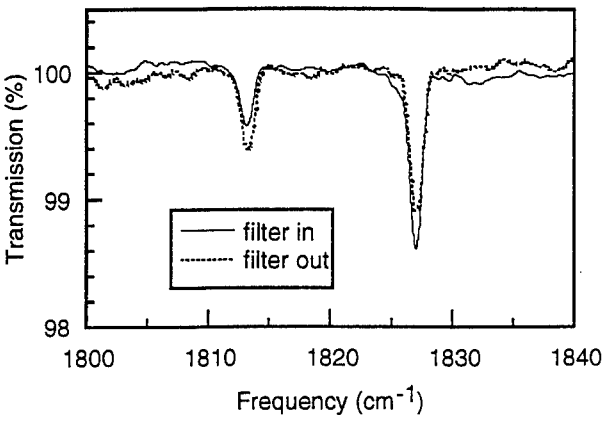


Figure 2. Effect of secondary illumination on bands at 1813.3 and 1827.1 cm^{-1}. The spectrum drawn with the dashed line was measured with the complete spectrometer source spectrum incident on the sample. The spectrum shown with the solid line was taken with a 4.5 μm long-pass filter placed before the sample.

Spectra shown in Fig. 2 measured under different illumination conditions also suggest these two bands arise from the same defect. The broad band globar source used in the Bomem spectrometer can photoionize defects that have a level in the gap. By varying the amount of light striking the samples, the relative populations of different charge states can be altered. In Fig. 2 the spectrum taken with the unfiltered globar source is shown by the dashed line. The solid line shows a spectrum taken with a 4.5 μm low-pass filter placed before the sample. (This filter blocks light outside the spectral range used to measure the H-stretching spectrum.) When the amount of light incident on the sample is reduced with the filter, the 1827.1 cm^{-1} band shows an increase in intensity, while the 1813.3 cm^{-1} band shows a decrease of similar magnitude. This complementary behavior when the illumination conditions are changed shows that these bands can be assigned to two different charge states of the same defect. The occupied charge state gives rise to the 1827.1 cm^{-1} band, and the unoccupied charge state gives rise to the band at 1813.3 cm^{-1}. Furthermore, the Fermi level in the samples can be shifted by varying the Au concentration and this also changes the relative intensities of the 1813.3 and 1827.1 cm^{-1} bands. Increasing the Au indiffusion temperature increases the Au concentration and lowers the Fermi level in our n-type samples. Increasing the Au indiffusion temperature increases the intensity of the band at 1813.3 cm^{-1} relative to the band at 1827.1 cm^{-1} which provides further support for a center with a level in the upper half of the band gap and with the 1813.3 cm^{-1} band being due to the unoccupied charge state. The absolute charge state of the Au-H defect remains uncertain, but an argument about the competition to retrap photoionized electrons at low temperature, similar to that made previously for the PtH_2 complex[6], suggests that an acceptor level is being photoionized.

These vibrational bands were also studied by uniaxial stress methods. Under stress, spectra of the bands at 1813.3 and 1827.1 cm^{-1} each show splittings and intensity ratios consistent with trigonal centers.[12] For the 1813.3 cm^{-1} band, the parameters that describe the stress-induced shifts[12] were found to be A_1 = -0.4 cm^{-1}/GPa and A_2 = -2.0 cm^{-1}/GPa. For the 1827.1 cm^{-1} band, A_1 = -0.8 cm^{-1}/GPa and A_2 = -3.9 cm^{-1}/GPa.

The reorientation of this defect under stress was also studied. For the [110] stress direction, for example, each of the 1813.3 and 1827.1 cm^{-1} bands is split into two components.

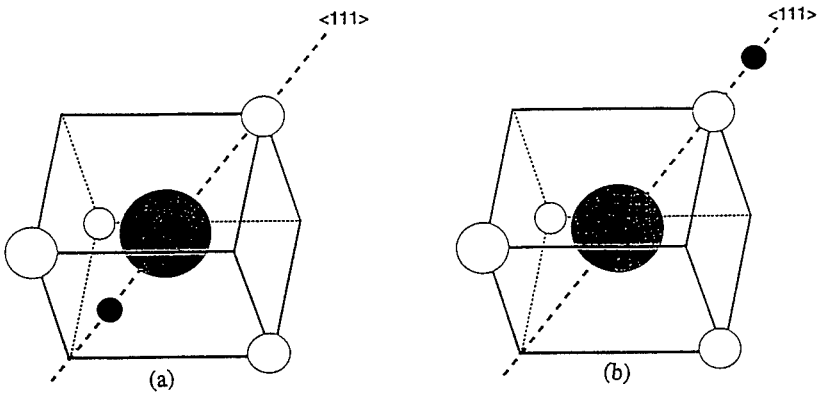


Figure 3. Models for a trigonal Au-H complex in Si with a substitutional gold atom and the hydrogen at an antibonding site along a <111> direction.

The relative intensities of these components depended on the magnitude of the applied stress, suggesting that the defects were reorienting. An alignment of the defects could not be frozen in at low temperature (3.5K), indicating a very small barrier for reorientation. The similarity of the symmetry, magnitude of the stress parameters and reorientation behavior for the 1813.3 and 1827.1 cm^{-1} H-stretching bands strongly supports our conclusion that they are the vibrational modes of different charge states of the same defect complex.

Isolated Au in silicon occupies a substitutional site[13] and DLTS experiments show that the Au acceptor is the dominant trap in our samples. Thus, we propose that the 1813.3 and 1827.1 cm^{-1} vibrational modes are due to a Au impurity complexed with a single hydrogen atom. Tentative models for a trigonal Au complex are shown in Fig. 3. We have chosen an antibonding site for the H in our models because we have found that the Au-H complex reorients at low temperatures, suggesting a small reorientation barrier. A bond-centered H atom should have a more substantial reorientation barrier, because its movement would involve the relaxation of its heavier Au and Si neighbors. Similar arguments have been made for acceptor-H complexes in semiconductors.[14,15] Whether the H atom is bonded to the Au atom as in Fig. 3(a) or to a Si atom as in Fig. 3(b) is not known. The models proposed here are necessarily tentative because of the limited amount of information that is available.

A defect very similar to this Au-H complex was seen previously in samples doped with Pt and H.[6] Vibrational bands seen at 1880.7 and 1897.2 cm^{-1} in Pt and H containing samples arise from a defect containing a single H atom and show stress splittings consistent with a trigonal center.[16] The Fermi level dependence of the relative intensities of these bands and the effect of secondary illumination show that the 1880.7 and 1897.2 cm^{-1} bands are also due to two charge states of the same defect with the lower frequency band assigned to the unoccupied charge state.[6] We propose that the Pt-H center observed previously is analogous to the Au-H center discussed here and that it has a similar structure. The observation of similar complexes in Au containing samples and in Pt containing samples, but with different vibrational frequencies, supports our proposal that the transition metal impurity is contained within the complex.

We have examined the Pt-H bands for evidence of isotopic shifts characteristic of the naturally abundant Si isotopes because they are more intense than the Au-H bands reported here.

A close examination of the lineshapes of the 1880.7 and 1897.2 cm^{-1} bands (FWHM ~ 0.4 cm^{-1}) did not reveal weak shifted bands due to the naturally abundant ^{29}Si or ^{30}Si isotopes which might be found if H were bonded to Si as in the structural model shown in Fig. 3(b). However, for several defects with H at an antibonding site, the isotope shift due to a change in the mass of the hydrogen atom's nearest neighbor has been found to be surprisingly small.[17-20] Therefore, our present results do not determine whether the H atom is bound to Si or the transition metal in these complexes.

ADDITIONAL H-STRETCHING BANDS IN Si CONTAINING Au AND H

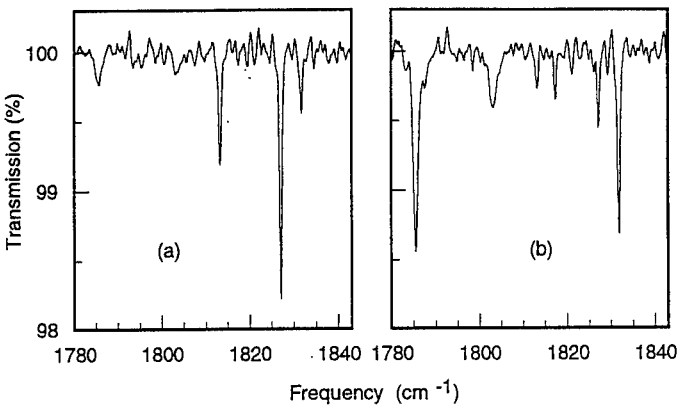


Figure 4.
(a) Spectrum of a sample taken after H indiffusion.
(b) Spectrum of the same sample after a subsequent anneal at 150°C.

In addition to the H-stretching bands discussed above, several other absorption bands have been observed in some of the Si samples containing Au and H. Fig. 1(b) shows H-stretching bands at 1785.6, 1787.7, 1803.3, 1817.3 and 1831.8 cm^{-1} in addition to the 1813.3 and 1827.1 cm^{-1} bands. Deuterium counterparts for these additional signals have also been observed. All of these signals are usually seen only in samples where the ampoule was deliberately broken during the quench. Fig. 4(a) shows a spectrum of such a sample immediately after the hydrogen diffusion. The additional signals are present, but are weak relative to the 1813.3 and 1827.1 cm^{-1} bands. In Fig. 4(b), the new signals are shown to be increased in intensity by a 30 min. anneal at 150°C. All five of the additional signals are eliminated by an anneal at 250°C. This annealing behavior is similar to that reported by Brotherton *et al.*[21] for the Au-Fe pair in Si. Iron is a common contaminant in Si, and experiments are therefore underway to investigate whether any of these new bands arise from hydrogen-passivated Au-Fe pairs.

Following the initial high temperature anneal in H_2 and following subsequent anneals, the intensities of the bands at 1817.3 and 1831.8 cm^{-1} are correlated, suggesting that they may be vibrational modes of the same defect. Their behavior during annealing is distinct from the bands at 1785.6, 1787.7 and 1803.3 cm^{-1}. Illumination and uniaxial stress experiments show that the bands at 1817.3 and 1831.8 cm^{-1} arise from two charge states of a single defect, similar to the 1813.3 and 1827.1 cm^{-1} bands proposed to be due to a Au-H complex, but with a symmetry lower than the trigonal. At present, little further is known about the defect or defects that give rise to the bands at 1785.6, 1787.7 and 1803.3 cm^{-1} bands.

ACKNOWLEDGMENTS

This work was supported by the National Science Foundation under Grant No. DMR-9415404.

REFERENCES

1. S.J. Pearton, J.W. Corbett, and M. Stavola, *Hydrogen in Crystalline Semiconductors* (Springer Verlag, Berlin, 1992).
2. S.J. Pearton, *Hydrogen in Semiconductors*, Chapt. 5, edited by J.I. Pankove and N.M Johnson (Academic, San Diego, 1991).
3. E.Ö. Sveinbjörnsson and O. Engström, Phys. Rev. B **52**, 4884 (1995).
4. W. Jost, J. Weber, and H. Lemke, Semicond. Sci. Technol **11**, 22 (1996); 525 (1996).
5. W. Jost and J. Weber, Phys. Rev. B **54**, R11038 (1996).
6. S.J. Uftring, M. Stavola, P.M. Williams, and G.D. Watkins, Phys. Rev. B **51**, 9612 (1995).
7. M. Stavola, S.J. Uftring, M.J. Evans, P.M. Williams, and G.D. Watkins, *Defect and Impurity Engineered Semiconductors and Devices*, ed. by S. Ashok, J. Chevalier, I. Akasaki, N.M Johnson, and B.L Sopori (MRS, Pittsburgh, 1995), pp. 341-352.
8. M. Höhne, U. Juda, Yu. V. Martynov, T. Gregorkiewicz, C.A. J. Amerlaan, and L.S. Vlasenko, Phys. Rev. B **49**, 13 423 (1994).
9. P.M. Williams, G.D. Watkins, S. Uftring, and M. Stavola, Phys. Rev. Lett. **70**, 3816 (1993).
10. A preliminary report of two bands at 1813.3 and 1827.1 cm-1 in Si containing Au and H was given in Ref. (7).
11. S.A. McQuaid, M.J. Binns, R.C. Newman, E.C. Lightowlers, and J. B. Clegg, Appl. Phys. Lett. **62**, 1612 (1993).
12. A.A. Kaplyanskii, Opt. Spectrosk. **16**, 606 (1964).
13. H. Feichtinger, in *Electronic Structure and Properties of Semiconductors*, edited by W. Schröter (VCH, Weinheim, 1991), p.143.
14. P. J. H. Denteneer, C. G. Van de Walle, and S.T. Pantelides, Phys. Rev. Lett. **62**, 1884 (1989).
15. G.D. Watkins, in Defects in Semiconductors 15, ed. by G. Ferenczi (Trans Tech, Aermansdorf 1989) p.39.
16. S.J. Uftring, M.J. Evans, and M. Stavola, unpublished.
17. B. Pajot, R.C. Newman, R. Murray, A. Jalil, J. Chevalier, and R. Azoulay, Phys. Rev. B **37**, 4188 (1988).
18. R.C. Newman, Semicond. Sci. Technol. **5**, 911 (1990).
19. S.N. Walck and W.B. Fowler, Phys. Rev. B **51**, 13146 (1995).
20. J. Vetterhöffer and J. Weber, Phys. Rev. B **53**, 12835 (1996).
21. S.D. Brotherton, P. Bradley, and A. Gill, J. Appl. Phys. **57**, No. 6, 1783 (1985).

EFFECTS OF H^+-IMPLANTATION ON ELECTRON TRAPS IN N-TYPE Si INDUCED BY P^+ PRE-IMPLANTATION

AKIRA ITO*, HIROYUKI IWATA**, YUTAKA TOKUDA***
*Department of Electronic and Information Engineering, Suzuka College of Technology, Shiroko, Suzuka 510-02, Japan, aito@info.suzuka-ct.ac.jp
**Research Institute for Industrial Technology, Aichi Institute of Technology, Yakusa, Toyota 470-03, Japan
***Department of Electronics, Aichi Institute of Technology, Yakusa, Toyota 470-03, Japan

ABSTRACT

The change of the concentration of electron traps in n-type Si induced by P^+ implantation (300keV, $1x10^9cm^{-2}$) with subsequent H^+-implantation has been studied by deep level transient spectroscopy. H^+-implantation is performed at room temperature to a dose of $2x10^{10}cm^{-2}$ in the range 30 to 120keV. First P^+ implantation induces six electron traps (Ec-0.12, 0.15, 0.21, 0.26, 0.39, 0.49eV). H^+-implantation additionally induces an electron trap (Ec-0.32eV) which is related to hydrogen. The subsequent H^+-implantation partly decreases the concentration of the electron traps induced by P^+ implantation, although it increases the concentrations near the H^+ projected range. 30 keV H^+-implantation is most effective to reduce the trap concentration. The reduction of the concentration of the traps is ascribed to the reaction of pre-existing defects with interstitial or vacancy defects formed by subsequent H^+-implantation.

I. INTRODUCTION

Ion implantation technique has been used widely in the fabrication of very large scale integrated (VLSI) circuits. This technique is advantageous to the fabrication of shallow junctions, while implanted dopants introduce interstitial and vacancy related defects[1]. In order to electrically activate the implanted dopants and anneal the damage caused by implantation, heat treatment process is necessary. However, during the annealing, some implanted dopants redistribute. As a result, lower temperature heat treatment is desired in the fabrication of VLSI circuits.

It has been reported that amorphous Si layers can be crystallized by ion implantation at elevated temperatures[2-4]. We have reported a partial activation of phosphorous(P^+) implanted into silicon by subsequent hydrogen(H^+) implantation at a very low temperature (400 ℃), and further electrical activation by annealing at 800 ℃ with sharper carrier concentration depth profile[5]. It can be expected that the interstitials and vacancies caused by subsequent implantation react with pre-existing vacancy or interstitial related defects. In this paper, we study the effects of subsequent H^+-implantation on interstitial-related defect and vacancy-related defects formed by P^+ implantation in n-type Si.

II. EXPERIMENTAL PROCEDURE

The substrates used in this study were phosphorous doped n-type (100) Czochralski-grown silicon wafers which had a resistivity of between 1 and 2 ohm•cm. 300keV P^+ ions were implanted to a dose of $1x10^9$ cm^{-2} with a dose rate of $1x10^9cm^{-2}s^{-1}$ at room temperature. The

Mat. Res. Soc. Symp. Proc. Vol. 442 © 1997 Materials Research Society

P^+ ion beam incident angle was tilted by 7 degrees to the substrate normal. Subsequently, H^+ ion implantation was performed to a dose of $2x10^{10}cm^{-2}$ with a dose rate of $1x10^{10}cm^{-2}s^{-1}$ with varying energies from 30 to 120 keV at room temperature. The H^+ ion beam incident angle was normal to the surface to suppress the destruction of the annealed layer by H^+-implantation. The projected range of P^+ ion implanted at 300keV is about 0.38μm. And the projected ranges of H^+ ion implanted at 30keV and 120keV are about 0.4μm and 1.2μm, respectively. Schottky contacts were fabricated by evaporation of Au, and the Ohmic contacts were fabricated by rubbing on eutectic gallium-indium at the back side of the sample. Deep level transient spectroscopy (DLTS) was carried out with a bipolar weighting function[6,7]. The changes of the concentration depth profiles of dominant traps were evaluated.

III. RESULTS AND DISCUSSIONS

Figure 1 shows DLTS spectra of the P^+-implanted sample (a) and the subsequently H^+-implanted samples at 30keV (b) and 90keV (c). The observed electron trap parameters are listed in Table I. The five traps E1, E2, E3, E6 and E7 are observed in all samples studied. These traps are usually observed after low dose ion implantation and electron irradiation[1,8-11]. The E1 trap corresponds to interstitial-related defect, complex of substitutional carbon and silicon interstitial(C_{Si}-Si_I-C_{Si}) [11]. The E2, E3, E6 traps are vacancy-related defects. The E2 trap corresponds to oxygen-vacancy pair(O-V) and the E3 trap to divacancy ($V-V^{-/--}$). The observed DLTS signal of the E6 trap is attributed to the divacancy ($V-V^{0/-}$) and phosphorous-vacancy (P-V), because the emission rates of divacancy and phosphorous-vacancy are nearly equal. Svensson et al. have reported that H^+-implantation introduces two electron traps (Ec-0.32eV and Ec-0.45eV)[8]. The E5 trap observed in this study corresponds to one (Ec-0.32eV) of the hydrogen-related traps. It is thought that the E7 trap corresponds to the Ec-0.45eV trap. However, since the E7 trap is observed by both P^+-implantation and H^+-implantation, it seems that the E7 trap is caused by implantation damage. The DLTS signal of the E5 trap overlaps with that of the E4 trap in the H^+-implanted sample and the P^++H^+

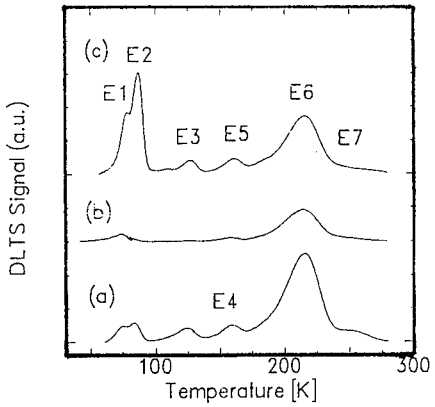


Fig.1 DLTS spectra of the P^+-implanted sample (a) and the subsequently H^+-implanted samples at 30keV (b)and at 90keV (c).

Table I. Observed electron trap parameters

Label	Activation Energy (Ec - Et) [eV]	Capture Cross Section (10^{-15} cm^2)	Remarks
E1	0.12	15	C_{Si}-Si_I-C_{Si}
E2	0.15	13	V-O
E3	0.21	3	$V-V^{0/-}$
E4	0.26	1.2	P_s-C_I
E5	0.32	61	H-related
E6	0.39	4.2	V-P, $V-V^{-/--}$
E7	0.49	8.8	

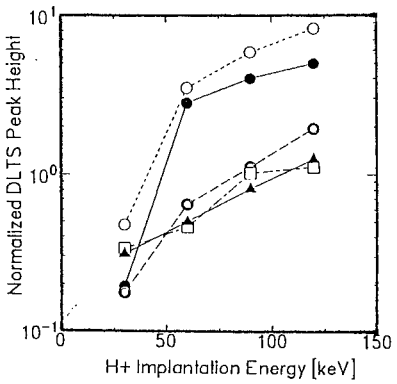


Fig.2 DLTS peak heights of each traps observed after subsequent H^+-implantation which are normalized to that of only P^+-implanted sample.

implanted sample. The E4 trap is introduced by implantation damage. Asom et al. have observed the substitutional phosphorous-interstitial carbon pair (P_S-C_I) whose trap level is E_C-0.29eV[11]. The observed E4 trap may correspond to this trap.

H^+-implantation at 30keV reduces the DLTS peak heights of all electron traps produced by first P^+-implantation at 300keV. However, H^+-implantation at 90keV increases the DLTS peak heights of the traps. Figure 2 shows the change of DLTS peak heights of each trap observed after subsequent H^+-implantation which are normalized to that of only 300keV P^+-implantation. Since the carrier concentrations of all samples used in this study are almost unchanged in used implantation doses and energies, the detectable region is nearly equal to each other. All DLTS spectra in this figure are measured with 10V reverse bias and a filling pulse amplitude of 10V. Thus, the DLTS peak heights are proportional to the total trap concentration in the depth range of 0.4μm to 1.6μm. The projected range of H^+ implanted with an implantation energy of 30keV to 120keV is within the detectable range. Thus, H^+-implantation-induced damages can be totally detected in this study. Figure 2 shows that H^+-implantation at 30keV is most effective to anneal the pre-existing traps, while H^+-implantation at higher energy tends to introduce implantation damage defects. It should be noted that both P^+ and H^+ implantation causes Si interstitial-vacancy pairs. If there is no interaction between the defects produced by P^+ implantation and H^+-implantation, the trap concentration would be the sum of both trap concentrations. It is well known that hydrogen atoms passivate the electrical traps, and Si interstitials and vacancies easily diffuse even at room temperature. Kouketsu et al. have reported that 100 keV H^+-implantation annihilates the iron-related hole traps which can not be annihilated by hydrogen plasma[12]. They proposed that the passivation treatments are activated by the energy transferred from implanted hydrogen to silicon lattice during implantation[12]. We have reported that Si interstitials and vacancies caused by H^+-implantation improve the activation ratio of pre-implanted P^+ ions[5]. It can be expected that the induced Si interstitials and vacancies reduce the vacancy-related traps(E2 and E6 traps) and the interstitial-related trap(E1 trap), respectively. In order to investigate more precisely the effects of subsequent H^+-implantation on defect reduction, the depth profiles of dominant traps (E1, E2 and E6) were measured by DLTS with changing bias conditions.

Figures 3(a), 3(b) and 3(c) show the concentration profiles of the E2 trap, the E6 trap and the E1 trap in the P^+ implanted samples followed by H^+-implantation with energy 30 to 120keV, respectively. The profiles of the only P^+ implanted sample are also shown in these figures. The detectable depth range is deeper than about 0.4 μm. Subsequent 30keV H^+-implantation

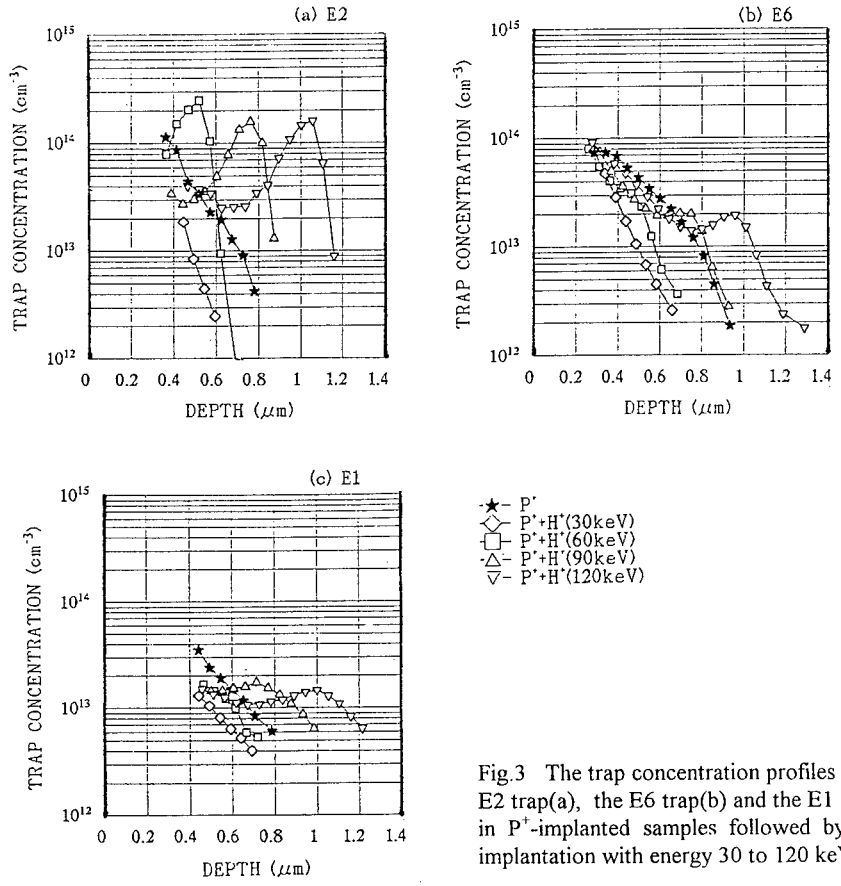


Fig.3 The trap concentration profiles of the E2 trap(a), the E6 trap(b) and the E1 trap(c) in P^+-implanted samples followed by H^+-implantation with energy 30 to 120 keV.

reduces all trap concentrations comparing with those in the only P^+ implanted sample in the detectable region. At higher implantation energy, the behavior of the change of trap concentrations is different.

In the case of the E2 trap (V-O) shown in Fig.3(a), H^+-implantation at 60keV increases the E2 trap concentration in the region 0.4μm to 0.6μm, and reduces the concentration in deeper region. The increased E2 trap concentration has a peak around 0.5μm which is slightly shallower than the projected range of implanted H^+ ions at 60keV (0.68μm). It is well known that the distributions of implantation-induced interstitials and vacancies have a peak at shallower depth than projected range(Rp) of implanted ions[10]. It can be supposed that the peak of the E2 trap concentration of H^+-implantation at 30keV is bellow 0.4μm, although no peak of E2 concentration is observed in this study. 90keV H^+-implantation decreases the already-existed E2 trap concentration in the region shallower than about 0.52μm, while it increases in the deeper region. 120keV H^+-implantation shows no significant decrease of the already-existed E2 trap concentration, while it increases the trap concentration and the observed peak moves to deeper because the Rp increases with implantation energy. The diffusion of Si interstitials

caused by subsequent implantation reduces the already existed vacancy related trap E2, although subsequent implantation introduces implantation-induced damage defect E2 trap around Rp.

In the case of the E6 trap (V-V and V-P) shown in Fig.3(b), 60keV H^+-implantation decreases the E6 trap concentration at any depth in the observed region. Above 90keV, H^+-implantation additionally induced E6 trap is observed around each Rp. Comparing with the case of E2 trap, the amount of the increased E6 trap concentration is smaller. It should be noted that the E6 trap concentration in the region from 0.3μm to 0.73μm is decreased by 120keV H^+-implantation. Few implanted hydrogen atoms overlap with the region where the annealing effect of the E6 trap was observed. This rules out the possibility of passivation of point defects by hydrogen atoms.

The observed peak depths of the E2 trap and E6 trap concentrations in the subsequently 120keV H^+ implanted sample are nearly equal. Because both E2 and E6 traps are vacancy related traps, the concentration depth profiles are related to the vacancy distributions.

In the case of the E1 trap (C_{Si}-Si_I-C_{Si}) shown in Fig.3(c), the behavior of the change of E1 trap concentration on subsequent H^+-implantation is similar to that of E6 trap as mentioned above. The observed peak position of the E1 trap (intersitial related trap) above 90keV H^+-implantation is nearly equal to that of the E2 trap (vacancy related trap) by 90keV H^+-implantation. This indicates that the distributions of implantation-induced Si interstitials and vacancies are nearly equal.

Figures 4(a) and 4(b) show the reduced trap concentration depth profiles by H^+-implantation for E1(C_{Si}-Si_I-C_{Si}) trap and E6 trap(V-V and V-P), respectively. 30keV H^+-implantation is most effective to reduce both the vacancy related trap(E6) and the interstitial related trap(E1). The amount of reduced concentration of E6 trap is larger than that of E1 trap because of the difference of the introduced trap concentration by P^+-implantation. The annealing effect is weakened with the implantation energy. This is ascribed to the reduction of the supply of interstitials and vacancies since the H^+ projected range becomes deeper with implantation energy. The reduced E6 trap concentration monotonously decreases with the subsequent H^+-implantation energy. On the other hand, the reduced E1 trap concentration decreases gradually

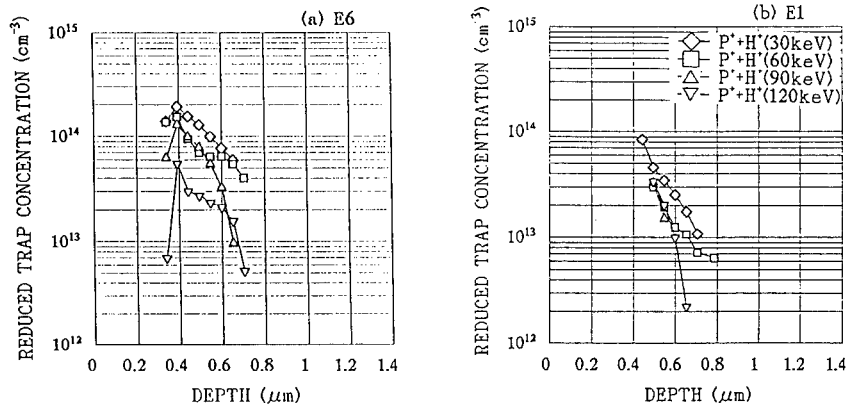


Fig.4 Reduced trap concentration depth profiles by H^+-implantation for E1 trap(a) and E6 trap (b).

with the implantation energy up to 60keV, and is saturated above the 90keV H^+-implantation. Decreases of interstitial related E1 trap (C_{Si}-Si_I-C_{Si}) and vacancy related E6 trap(V-V and V-P) need supply of vacancies and interstitials, respectively. This suggests that the amount of available Si vacancies caused by subsequent H^+-implantation is smaller than that of available Si interstitials by subsequent H^+-implantation. It has been reported that the self interstitials and vacancies can diffuse very fast even at room temperature[1]. To our knowledge, there is only a few reports about interstitial related defects[11], although many studies about vacancy related traps have been reported[1]. It can be speculated that some vacancies caused by H^+-implantation are preferably trapped with impurities such as oxygen and phosphorous and others are transformed to larger size defects such as divacancy when they combine, while little interstitials are trapped with impurities except for carbon. Thus, when the projected range of subsequent implantation is deeper than that of pre-implantation, annealing effects of vacancy related defects by subsequent H^+-implantation can be more expected compared with interstitial related traps.

VI. SUMMARY

The change of the concentration of electron traps in n-type Si induced by P^+-implantation with subsequent H^+-implantation has been studied by deep level transient spectroscopy. First P^+-implantation induces six electron traps (Ec-0.12, 0.15, 0.21, 0.26, 0.39, 0.49eV). H^+-implantation additionally induces electron trap (Ec-0.32eV) which is related to hydrogen. The concentration of the electron traps induced by P^+-implantation are partly decreased by the subsequent H^+-implantation. The reduction of the concentration of the traps is ascribed to the reaction with interstitial or vacancy defects formed by subsequent H^+-implantation.

REFERENCES

1)L.C.Kimerling, IEEE Trans. On Nuclear Sci. **NS-23**, 1497 (1976).

2)R.G.Elliman, J.S.Williams, W.L.Brown, A.Leiberich, D.M.Maher and R.V.Knoell, Nuclear Instruments and Methods in Physics Research **B19/20**, 435 (1987) .

3)J.Linnors and G.Holmén, J.Appl.Phys. **62**, 4737 (1987)

4)J.Nakata, Phys.Rev.**B 43**,14643 (1991)

5)Y.Tokuda, Y.Hasebe, A.Ito, H.Iwata, A.Usami, A.Terashima, H.Ohshima and T Hattori, to be published in Semiconductor Science and Technology

6)D.V.Lang, J.Appl.Phys. **45**, 3023 (1974)

7)Y.Tokuda, N.Shimizu and A.Usami, Jpn.J.Appl.Phys.**18**, 309 (1979)

8)B.G.Svensson, A.Hallén and B.U.Rsundqvist, Mat.Sci.and Eng. **B4**, 285 (1989)

9)G.G.Qin, Y.C.Du, J.Wu, andX.C.Yao in Defects in Semiconductors, edited by H.J.von Bardeleben (Mat.Sci.Forum 10-12, 1986) pp.563-572

10)L.Palmetshofer and J.Reisinger, J.Appl.Phys. **72**, 2167 (1992)

11)M.T.Asom, J.L.Benton, R.Sauer and L.C.Kimerling, Appl.Phys.Lett. **51**, 256 (1987)

12)M.Kouketsu, K.Watanabe and S.Isomae, Materials Science Forum **196-201**, 861 (1995)

EVALUATION OF PROTON-INDUCED DEEP LEVELS IN n-Si

K. Kọno, N. Kishimoto, H. Amekura, T. Saito
National Research Institute for Metals (NRIM),
High Resolution Beam Research Station,
1-2-1 Sengen, Tsukuba, Ibaraki, 305, Japan, kono@nrim.go.jp

ABSTRACT

Deep level transient spectroscopy (DLTS) has been conducted to reveal electronic states of deep centers in n-Si, under 17 MeV-proton irradiation. The DLTS device was installed into the beam line of the cyclotron. The *in-situ* experiment was concentrated on, to study the dynamical defect evolution and the effect of irradiation temperature on the deep centers. DLTS signals of four deep levels E0-E3 were observed when n-Si was irradiated at 300 K. Three of the four peaks were identified as V-O, V-V^{2-} and P-V centers, in comparison with the past data of electron irradiation. The other unknown level (E0) was located at 0.16 eV below the conduction band, and 0.02 eV lower than the V-O level. The E0 peak showed a characteristic behavior dependent on the irradiation temperature. The E0 did not emerge when irradiated at 200 K, but appeared after being annealed at 300 K following the 200 K irradiation. The evolution of these levels was consecutively investigated with accumulating the proton fluence and with annealing after the irradiation.

INTRODUCTION

Extensive research with DLTS measurement has been accumulated on radiation damage of n-Si and the energy schemes of the deep centers were basically established. Particularly for electron irradiation, the defects produced were Frenkel pairs and the natures of the relevant deep centers were well understood, including the defects and the defect-solute clusters [1-5]. However, not much has been known of the defects produced by high-energy protons (e.g. 17 MeV), where collision cascades possibly give rise to complex defects. There were some proton irradiation experiments but the starting temperature for DLTS scan was not enough low ($T \geq 78$ K) to evaluate relatively shallow levels [6,7]. In our previous work [8,9], it was found from the *in-situ* photoconductivity that the shallow-impurity doping is rather effective to passivate the deep centers via strong defect-solute coupling. The photo-sensitivity of the doped Si survived even after a fair amount of proton fluence, while that of non-doped Si rapidly deteriorated. To reveal the mechanism, it is requisite to identify the energy states of the defects relevant to the defect-impurity interaction. Furthermore, the remaining important aspects, in general, are the dynamical evolution of the defects with accumulation of the fluence and their annealing behaviors, especially starting from irradiation temperatures which are lower than room temperature.

The purpose of this research is to investigate the dynamical effects of 17 MeV-proton irradiation on shallow-impurity doped Si and the effects of low-temperature irradiation on the formation of deep centers, taking advantage of the *in-situ* DLTS system.

Mat. Res. Soc. Symp. Proc. Vol. 442 © 1997 Materials Research Society

EXPERIMENT

Sample preparation

Samples of 3x13x0.6 mm^3 were cut out from commercially available wafers, of phosphorus-doped n-type Czochralski (CZ) silicon (100). Resistivity of the wafer is less than 10 Ωcm. A Schottky barrier was formed by vacuum evaporation of gold, after the ohmic contact was conventionally formed on the other surface. The dopant concentration was determined to be $7x10^{14}$ cm^{-3} from C-V characteristics. The sample was mounted onto the copper block of the sample stage. To avoid ballistic injection of the gold atoms into the capacitance layer, the Schottky barrier side was set towards the stage surface, inserting an insulating sheet of BN.

Irradiation

The sample was irradiated by the 17 MeV proton beam, generated with the cyclotron at NRIM (National Research Institute for Metals, Tsukuba, Japan). The projectile range of this beam is estimated to be 1.7 mm in Si by the TRIM code [10]. This projectile range is much larger than the sample thickness of 0.6 mm. The long projectile range guarantees the following: (1) the sample is free from hydrogen injection which creates various deep levels [6], (2) the depth profile of the defects is regarded as homogeneous.

The beam current density of the proton was about 30 nA/cm^2 and the total fluence was varied between 0.9 $\mu A \cdot s/cm^2$ ($2.8x10^{-8}$ dpa) ~3.1 $\mu A \cdot s/cm^2$ ($9.6x10^{-8}$ dpa). The conversion relation used is 1 $\mu A \cdot s/cm^2$ ($6.24x10^{12}$ ion/cm^2)=$3.1x10^{-8}$ dpa for 17 MeV proton.

The high-energy proton beam causes relatively low Joule heating, when it passes through the thin sample. Also, since the current density was suppressed very low, the sample temperatures were precisely kept constant under the irradiation. The proton irradiation was conducted either at 200 K or 300 K.

Measurement

DLTS measurement was done right after the proton irradiation. Isochronal annealing (for 30 min at each temperature) was also conducted after the irradiation. The DLTS device was integrated with one of the target chambers of the NRIM cyclotron. This configuration made it capable to evaluate the deep levels right after the irradiation, discriminating from the spontaneous annealing.

A capacitance meter (Hewlett Packard 4280A 1 MHz) along with a pulse generator (HP 8112A 50 MHz) was used to measure the transient change in the capacitance. This system was designed to allow some leakage current for the irradiated samples. The sample temperature was controlled by a cryogenic He-circulator and a temperature controller (Scientific Instruments 96550).

All the measurements were conducted under the DLTS conditions of majority carrier injection. The Schottky diode was applied with an inverse voltage of 4 V and the injection pulse was 1 μs of 4 V which canceled the inverse bias. The delay time was varied from 1μs through

256 μs.

To avoid unintentional annealing of the sample, temperature sequences were carefully carried out. After the first 200 K irradiation, the temperature was scanned from 50 K through 200 K right after the irradiation. Then the sample was annealed at 250 K and the temperature was again scanned from 50 K through 250 K. Next, the 300 K annealing was done, followed by the subsequent scan from 50 K through 300 K.

All the equipments were remotely controlled by GP-IB via its extender from a personal computer in the cycrotron control room.

RESULTS

Figure 1 shows the DLTS signals of the sample irradiated at 200 K. The upper DLTS curve was taken right after irradiation. The lower curve corresponds to the one after the annealing at 300 K. The peaks in the DLTS spectra were designated as E1 to E3 for the peaks found in the literature, and the unknown as E0. It is readily seen that the deep level E0 emerges around 80 K, after the 300 K annealing.

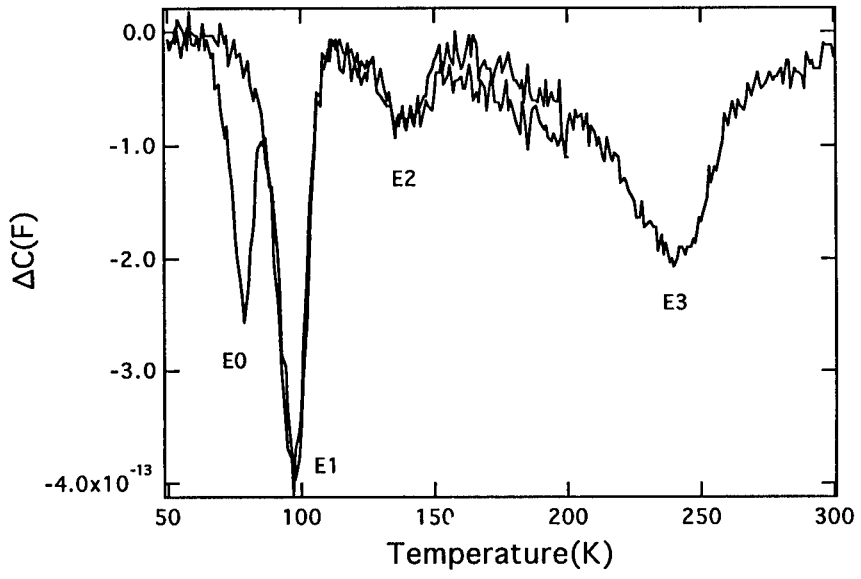


Fig. 1 DLTS spectra below the irradiation temperature down to 50 K. The upper curve was taken under the irradiation temperature 200 K, before annealing. The lower curve corresponds to the DLTS spectrum after annealing at 300 K (taken up to 300 K).

By changing the time window, the energy levels of the respective peaks were determined. Comparing the energy levels of each peak with those reported from electron irradiation [1-3], the following assignments were made: Three of the four peaks agreed with the established data in the literature, that is, E1 (0.18 eV); V-O, E2 (0.25 eV); V-V^{2-} and E3 (0.41 eV); P-V. However, the E0 center, whose energy level was 0.16 eV below the conduction band, was not found in the DLTS data for the electron irradiation.

Here, the E0 center cannot be ascribed to the residual hydrogen from the injected protons. The projectile range of proton beam is 1.7 mm and is much larger than the sample thickness of 0.6 mm. The present irradiation condition is in a sense very simple and the proton irradiation merely gives the intrinsic defects, without any implanted solutes.

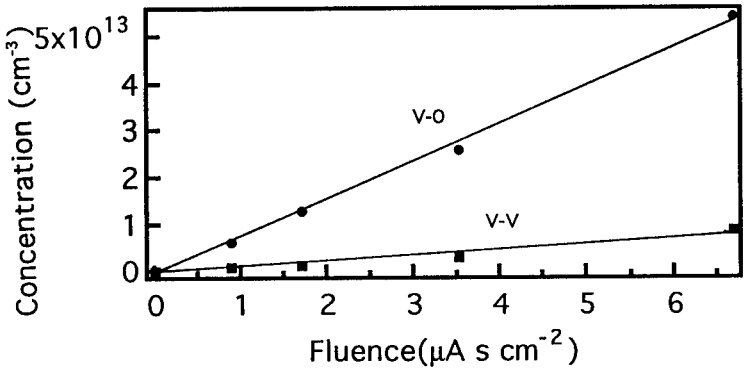


Fig 2 Defect concentration of V-V and V-O centers plotted as a function of the proton fluence. The irradiation temperature of the sample was kept at 200 K.

Figure 2 shows the evolution of deep levels in accordance with the accumulation of defects. In this case, the sample temperature was kept at 200 K during the irradiation. The temperature scan for the DLTS measurement was done between 50 K and 200 K, in order to avoid the spontaneous annealing. For this specimen, the majority defects were the V-O centers and the fewer V-V clusters. The defect density of the both V-O and V-V^{2-} was perfectly proportional to the proton fluence. The fluence dependences of those defect clusters are important to know the defect kinetics, with respect to the unknown defect centers E0.

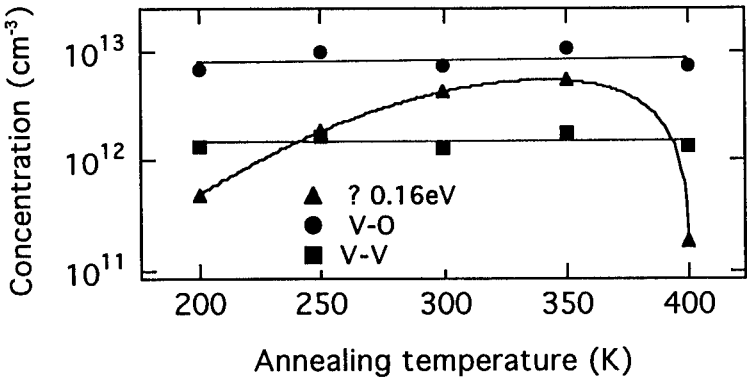


Fig. 3 Annealing behavior of concentrations of the deep centers. The sample was irradiated at 200 K and successively annealed up to 400 K.

Figure 3 shows change of deep levels with the isochronal annealing for 30 minutes. Concentrations of the V-O and V-V centers did not show significant change by the annealing, though some fluctuation was observed. On the other hand, the E0 center did show a characteristic evolution, i.e., the E0 emerged when annealed at 300 K or higher, and disappeared after the 400 K annealing.

DISCUSSION

The present DLTS system has two advantageous features:

(1) Real-time measurements without stopping the accelerator.

(2) Consecutive measurements without breaking vacuum or exposing sample to room temperature.

The former enables us to conduct the stable and accurate irradiation and to track the real-time defect evolution with the accumulation of defects. The latter advantage allows us the defect measurement, avoiding unintentional spontaneous annealing which takes place above the irradiation temperature.

As for the defect evolution under the proton irradiation, the results so far was not very unusual, except the finding of the E0 centers. With increasing the proton irradiation, the defect centers of V-O and V-V increased in proportion to the total fluence. This proportionality is the same as that of the electron irradiation.

The unknown peak E0 showed up after the irradiation at 300 K, or for the irradiation at 200 K and the following annealing at 300 K. To our knowledge, this peak was not reported in the past experiments of electron irradiation for n-Si.

There were other important conditions with this experiment, regarding the origin of the E0 centers:

(1) Residual hydrogens due to irradiation are negligible because of the large projectile range.

(2) The proton irradiation creates more complex defects due to the cascade collision, as compared to the electron irradiation.

Taking into account the above two points and the emergence and annihilation of the E0 levels, the origin is likely to be the higher-order complex of defects than the V-O or V-V centers. The specific structure of the defect complex is still under investigation.

CONCLUSION

The evolution of the defect concentration with the beam fluence was investigated by the *in-situ* DLTS method. It was found for the V-O and V-V centers to have linear relationship with the proton fluence. Annealing behaviors of the deep levels were clarified. The unknown level of energy level 0.16 eV appeared under 17 MeV proton irradiation, for limited temperature conditions. This level appeared only with the irradiation at 300 K or the irradiation at 200 K followed by the annealing at 300 K. The concrete structure of the level is not yet known.

Advantages of the DLTS system integrated to the accelerator were emphasized from the *in-situ* standpoint.

REFERENCES

1. O.O. Awadelkarim, H. Weman, B.G. Svensson and J.L. Lindstrom, J. Appl. Phys. **60**, 1974 (1986).
2. A.O. Evwaraye and Edmund Sun, J. Appl. Phys. **47**, 3776 (1976).
3. B.G. Svensson and M. Willander, J. Appl. Phys. **62**, 2758, (1987).
4. S.D. Brotherton and P. Bradley, J. Appl. Phys., **53**, 5720 (1982).
5. J.R. Troxell and G.D. Watkins, Phys. Rev. B **22**, 961 (1980).
6. K. Irmscher, H. Klosw and K. Maass, J. Phys. C: Solid State Phys., **17**, 6317 (1984)
7. A. Hallen , B.U.R. Sundqvist, Z. Paska, B.G. Svensson, M. Rosling and J. Tiren, J. Appl. Phys. **67**, 1266 (1990).
8. H. Amekura, N. Kishimoto, K. Kono, and T. Saito, J. Appl. Phys. 77, 4984 (1995).
9. H. Amekura, N. Kishimoto, K. Kono and T. Saito, Mater. Sci. Forum **196-201**, 1159 (1995).
10. J.F. Ziegler, J.P. Biersack and U. Littmark, *The Stopping and Range of Ions in Solids* (Pergamon Press, New York, 1985), Chap. 8.

EPR STUDY OF DEFECT FORMATION IN H IMPLANTED AND ANNEALED CZ Si

B. PIVAC*, B. RAKVIN*, F.CORNI**, R.TONINI**, and G. OTTAVIANI**
*R. Boskovic Institute, P.O.Box 1016, HR-10000 Zagreb, Croatia
**Dipartimento di Fisica, Universita di Modena, I-41100 Modena MO, Italy

ABSTRACT

Structural defects produced in single crystal silicon after hydrogen ion implantation were studied by electron paramagnetic resonance spectroscopy. Samples implanted at 77K show the presence of vacancy clusters that serve as precursors for nanoblister formation upon subsequent thermal treatment. Evolution of vacancy clusters at various stages of thermal annealing show the influence of implanted hydrogen redistribution that passivates the paramagnetic activity in the intermediate temparature range. At still higher temperatures hydrogen outdiffuses from the bulk activating remaining structural defects. At these temperatures, formed vacancy clusters gettered oxygen present in the bulk forming, therefore, V_xO_y complexes. Finally, at temperatures above 700^0C vacancy clusters disintegrate completely.

INTRODUCTION

Structural damage produced in crystalline silicon by ion bombardment has been extensively studied over the last two decades [1,2], as it presents a very promising way of creating novel device structures. Energetic ions penetrating into Si crystal produce a cascade of atomic displacements, resulting in damage and ultimately an amorphous zone is formed around the implantation track. Various structural defects are produced during such processes and some of them have paramagnetic properties so that they can be studied by electron paramagnetic resonance (EPR). One of them, often found in disordered material due to ion implantation as well as in amorphous materials obtained in different ways, is the D-center. It consists of a dangling bond, i.e. one unpaired electron, on a silicon atom backbonded to three other silicon atoms. The fingerprint of this defect is a characteristic EPR signal with a g value g=2.0055 [3].

On the other hand, hydrogen induced modification of the physical properties of crystalline silicon is one of the most important problems of scientific and technological relevance [4]. Hydrogen affects structural and electrical properties of crystalline silicon in a rather complex way, which depends in part on the implantation conditions (flux, fluence, energy, temperature), and in part on the thermal history of the sample. In a pioneering study, Stein [5] implanted H in Si and observed a large number of H-associated infrared bands. These experiments, as well as theoretical calculations [6], have shown that a large number of different H-related defects are present in H implanted silicon.

Previous EPR studies have shown that the dominant center present in hydrogen-implanted silicon is Si-S1 (Si-B2) [7-9]. The Si-S1 center was found to have spin S=1/2 and to be axially symmetric along the [111] axis. The eigenvalues of the g tensor are $g_{\|}$=2.0010±0.0005 and $g_{\perp}$=2.0103±0.0005 [7]. A review of EPR studies of hydrogen and hydrogen-related defects in crystalline silicon was recently given by Gorelkinskii and Nevinnyi [10].

In the last few years, a systematic effort for studying the hydrogen-defect interaction in crystalline Si has been performed by groups of researchers, including some of the present authors [11-13]. The intention of this series of experiments was to focus attention on silicon samples

Mat. Res. Soc. Symp. Proc. Vol. 442 © 1997 Materials Research Society

implanted at an energy (15.5 keV) low enough to avoid the production of dense collisional cascades. Various experimental techniques such as secondary-ion-mass spectroscopy, Rutherford backscattering (RBS) in channeling conditions, x-ray diffraction, infrared spectroscopy, elastic recoil detection analysis, transmission electron microscopy [11-13] and positron annihilation spectroscopy (PAS) [14] have been used so far to characterize these samples with respect to different aspects: density profiles of total hydrogen and of residual hydrogen content in the molecular form H_2 after thermal annealing, displacement field of Si, etc. The present work completes this series of experimental analyses with the measurement of paramagnetic characteristics of defects created during ion implantation and subsequent thermal treatment. The obtained results are discussed in light of results obtained with RBS and PAS experiments.

EXPERIMENTAL

The samples were prepared by implanting H_2^+ ions into single crystal silicon substrates. Silicon wafers were Czochralski grown, (100) oriented, and *p* type, with a resistivity in the interval 30-50 Ωcm (the corresponding dopant concentration was much lower than the concentration of implanted hydrogen, so that the substrates can be considered intrinsic). The implantations were carried out by tilting the slices by 7^0 with the respect to the beam to avoid channeling.

Samples were implanted with H_2^+ ions at an energy of 31 keV and dose of $5x10^{16}$ atoms/cm^2. Due to H_2^+ fragmentation at the surface and low density of the collisional cascades, this implantation is equivalent to the implantation of atomic hydrogen at double fluence and an energy of 15.5 keV.

The implantations were carried out at 77 K in a VESUVIUS 15 ion implanter operated at very low current density $\approx 1\mu A/cm^2$, with an end station modified to allow the target to be cooled by a good thermal contact with a liquid-nitrogen heat sink.

Annealing treatments were carried out by heating the samples in a vacuum in the temperature interval 100-900^{0}C.

EPR measurements were performed at room temperature, employing a Varian E-109 spectrometer operating in the X-band (9.4 GHz). Some EPR spectra were recorded at 10^0 intervals of rotation in the magnetic filed with the respect to Si (011) plane. The exact position of the *g*-factor and quantitative spin concentration was determined according to DPPH and a detection limit of 10^{11} spins/cm^3 was achieved.

RESULTS AND DISCUSSION

Figure 1 shows EPR spectra of H implanted and annealed samples. As shown in the figure, the as-implanted sample is characterized by a single isotropic line with *g* value $g=2.0069\pm0.0002$. Though the RBS measurements have shown significant disorder created approx. 200 nm bellow the surface [15] due to hydrogen ion implantation, no D-center was observed in as-implanted samples besides the above mentioned peak.

Luetgemeier and Schnitzke [7] have shown that Si-S1 is the dominant EPR center after implantation of hydrogen in silicon at room temperature. It should be also pointed out that the parameters of the S1 *g*-tensor are very close to those of the Si-B2 center [8] which has been found after low fluence ion implantation of N and P in silicon. Kleinhenz et al. [9] have suggested that the S1 center arises from a negative charge state of a dangling bond in a vacancy cluster and has an average *g*-value of 2.0055 similar to the D center often found in amorphous silicon.

Unlike finding of Kleinhenz et al. [9], our results clearly show that center we observe in hydrogen implanted sample has an average *g*-value clearly different from D-center. Furthermore,

we found that the same center with g=2.0069 is found only after H and D implantation while He and Kr produced dominant defects similar to D-centers. We also found that the same center is the dominant defect irrespective of whether the implantation was performed at room temperature or at 77 K.

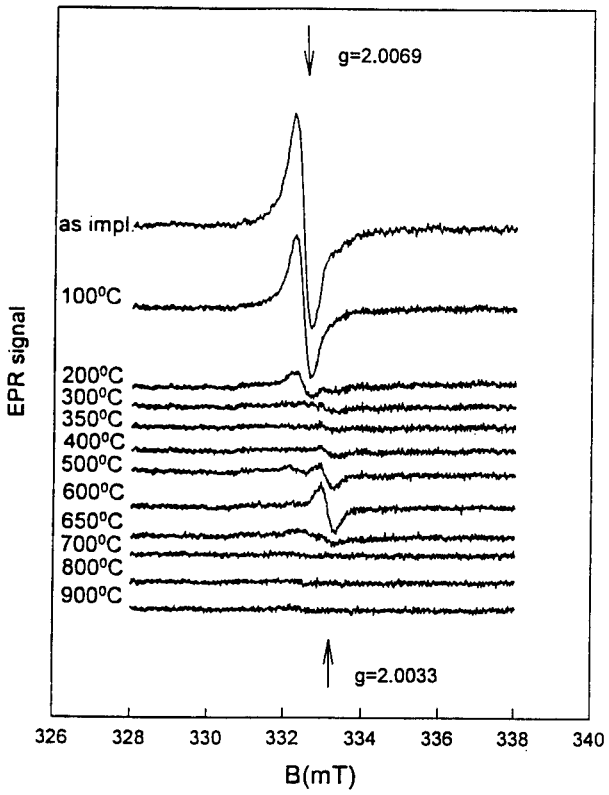


Figure 1. Figure shows EPR spectra of as-implanted and vacuum annealed hydrogen-implanted Si samples.

Though the appearance of the center we observe in as-implanted samples is isotropic, an analysis of the rotation in the magnetic field revealed a slight change in the linewidth, indicating that the observed spectrum is due to complex structure. However, very strong exchange interaction among the contributing centers produces line narrowing and perfect lorentzian line shape. Similarly to our finding, Gorelkinskii and Nevinnyi [10] found earlier that the S1 spectrum is the sum of different spectra with slightly different g-tensors. They concluded that the S1 center arises from a dangling bond of different vacancy-type defects. They also assumed that some of these dangling bonds could be occupied by hydrogen atoms.

The existence of S1 centers, i.e. vacancy clusters in as-implanted samples, is in accordance with the observation of nanoblisters formation upon hydrogen implantation [15]. Observed S1 centers would serve as a precursor for such nanoblister formation upon subsequent thermal annealing.

Moreover, this EPR finding on as-implanted samples is in very good agreement with the PAS study of Brusa et al. [14], who have shown that a small number of positron traps (probably small vacancy clusters) survives at a shallow depth, where hydrogen is practically absent.

RBS analysis performed on the same samples was unable to detect single vacancies and small vacancy clusters. However, RBS revealed, in the region from the surface down to 160 nm, the presence of silicon self-interstitials, which is consistent with the presence of vacancies observed by EPR and PAS in this region.

In our case we could not detect hyperfine splitting due to hydrogen and therefore we cannot claim its presence in the close vicinity of the observed center. Moreover, the annealing kinetics of the center we observe in as-implanted samples is different from literature data on the S1 center [7]. Unlike the S1 center described in the literature that is stable up to 200^{0}C, the density of the center shown in Fig. 1reduces significantly already at 100^{0}C, and at 200^{0}C it almost vanishes. One possible explanation for the difference in annealing kinetics between our center and literature data on the S1 center could be a short range redistribution of hydrogen atoms within the sample upon annealing.

PAS and electrical measurements show the presence of hole traps and their concentration depends upon the annealing. The traps, which are present in the as-implanted sample, decrease and completely disappear after heat treatment at 300-400^{0}C; treatments at higher temperatures promote the formation of traps indistinguishable from the previous ones which definitively disappear after 700^{0}C annealing.

From Fig. 1 we see that further thermal annealing did not produce any significant changes up to about 500^{0}C, besides gradual annealing of the S1 center. Annealing of proton implanted samples at temperatures <500^{0}C was shown to produce AA1 and AA3 type defects [10], and moreover since we are dealing with CZ (oxygen doped) material one would expect formation of V-O defects as shown by Lee and Corbett [16]. The fact that we did not detect any paramagneticaly active defect in the mentioned temperature range can be explained with the hydrogen redistribution. As shown before [15], a strong hydrogen redistribution occurred upon thermal treatment up to 500^{0}C when hydrogen starts to outdiffuse from the sample. Such hydrogen redistribution passivates structural defects and renders them paramagnetically inactive.

Therefore, only at 500^{0}C and higher, when hydrogen leaves the bulk, EPR could detect the presence of defects. Indeed, in samples annealed at 500^{0}C a complex spectrum arises, as shown in Fig. 1. The spectrum consists of two major contribution, one with average g-value 2.0033 and another with g-value 2.0068. We can observe traces of the g=2.0033 center even on samples annealed at 400^{0}C which reach a maximum value upon annealing at 600^{0}C and afterwards vanish. Again due to strong exchange interaction we cannot resolve anisotropic values of the g tensor. Its average value and kinetics of formation and annealing suggest that this might be an AA3 center. Gorelkinskii et al. [10] found this kind of center in hydrogen implanted silicon and asigned it to one of the reaction components of the reversible changing process of the H-related shallow donor. On the other hand, we observed similar centers even in the case of silicon implanted at 77 K with similar energies and doses of He, and therefore we believe that the hydrogen ion is not determinant in creating this center. Moreover, as mentioned above, upon thermal annealing at 500^{0}C and above, hydrogen outdiffuses from the bulk and SIMS measurements have revealed that at 500^0 C only about 10% of the initial concentration of H is still present [13]. Therefore, we believe that the center with g-value 2.0033 is due to some sort of multivacancy or V_xO_y complex.

As mentioned before, after annealing at 500^{0}C, an additional peak with g-value 2.0068 appeared. Centers with similar g-values were already reported by Lee and Corbett [16] and attributed to V_xO_y (centers like Si-P2, Si-P4 and Si-A14, Si-A15). Therefore, we also attribute the second peak to the formation of V_xO_y . Upon further annealing at higher temperatures no other paramagnetic activity was detected.

Our findings upon high temperature treatment are in very good agreement with PAS results too. Namely, Brusa et al. [14] showed that annealing at 500^{0}C increased activity of positron traps, while further annealing at even higher temperatures, particularly above 800^{0}C, eliminates any positron trap.

CONCLUSION

We studied structural defects developed upon low energy and high fluence hydrogen ion implantation in CZ single crystal silicon substrates at 77K. Results showed that in as-implanted samples, centers having paramagnetic properties were already developed and attributed to vacancy clusters, Si-S1 centers, that will further develop in nanoblisters after subsequent thermal treatment. Thermal annealing in the range 100-500^{0}C strongly reduces the population of S1 centers with dynamics that do not correspond to the published data on Si-S1 centers. We explain such behavior by hydrogen short range redistribution in that temperature interval. At higher temperatures, i.e. about 600^{0}C, hydrogen outdiffuses from the bulk rendering structural defects paramagnetically active. Annealing in this temperature range produces further vacancy cluster agglomeration that might be decorated with oxygen due to its gettering. Eventually at even higher temperatures vacancy clusters finally disintegrate resulting in no EPR signal. Our results agree very well with and complement recently published data on RBS and PAS studies of the same system.

REFERENCES

1. J.W. Corbett, J.K. Karius, and T.Y. Tan, Nucl. Instrum. Methods **182&183**, 457 (1981).

2. W.R. Brown, in Beam-Solid Interactions and Phase Transformations, edited by H. Kurz, G.L. Olsen, and J.M. Poate, (Mater. Res. Soc. Proc. **51**, Pittsburgh, PA 1985), p. 53-70.

3. P.A. Thomas, M.H. Brodsky, D. Kaplan, and D. Lepine, Phys. Rev. B, **18**, 3059 (1978).

4. S.J. Pearton, J.W. Corbett, and T.S. Shi, Appl. Phys. A **43**, 153 (1987).

5. H.J. Stein, J. Electron. Mater. **4**, 159 (1975).

6. T.S. Shi, S.N. Sahu, G.S. Oehrlein, A. Hiraki, and J.W. Corbett, Phys. Stat. Sol. (a) **74**, 329 (1982).

7. H. Luetgemeier and K. Schnitzke, Phys. Lett. **25 A**, 232 (1967)

8. D.F. Daly and K.A. Pickar, Appl. Phys. Lett. **15**, 267 (1969).

9. R.L. Kleinhenz, Y.H. Lee, V.A. Singh. P.M. Mooney, A. Jaworowski, L.M. Roth, J.C. Corelli, and J.W. Corbett, in Defects and Radiation Effects in Semiconductors, Conf. Ser. No 46 (Inst. Phys. London, 1979) p. 200.

10. Yu.V. Gorelkinskii and N.N. Nevinnyi, Physica B, **170**, 155 (1991).

11. G.F. Cerofolini, L. Meda, C. Volpones, G. Ottaviani, J. De Fayette, R. Dierckx, D. Donelli, M. Orlandini, M. Anderle, R. Canteri, C. Claeys, and J. Vanhellemont, Phys. Rev. B **41**, 12607 (1990).

12. L. Meda, G.F. Cerofolini, G. Ottaviani, R. Tonini, F. Corni, R. Balboni, M. Anderle, R. Canteri, and R. Dierckx, Physica B **170**, 259 (1991).

13. L. Meda, G.F. Cerofolini, C. Bresolin, R. Diercks, D. Donelli, M. Orlandini, M. Anderle, R. Canteri, G. Ottaviani, R. Tonini, C. Claeys, J. Vanhellemont, S. Pizzini, and S. Farina, in Semiconductor Silicon 1990, edited by H.R. Huff, K.G. Barraclough and J. Chikawa (Electrochem. Soc., Pennington, NJ, 1990), vol. **90/7**, p. 456.

14. R.S. Brusa, M. Duarte Naia, A. Zecca, C. Nobili, G. Ottaviani, R. Tonini, and A. Dupasquier, Phys. Rev. B **49**, 7271 (1994).

15. G.F. Cerofolini, R. Balboni, D. Bisero, F. Corni, S. Frabboni, G. Ottaviani, R. Tonini, R.S. Brusa, A. Zecca, M. Ceschini, G. Giebel, and L. Pavesi, Phys. Stat. Sol. (a) **150**, 539 (1995).

16. Y.-H. Lee and J.W. Corbett, Phys. Rev. B, **13**, 2653 (1976).

ACTIVATION ENERGIES OF INTERSTITIAL OXYGEN DIFFUSION IN SILICON CONTAINING HYDROGEN

W. WIJARANAKULA
Shin-Etsu, SEH America, Incorporated
4111 Northeast 112th Avenue, Vancouver, Washington 98682-6776, USA

ABSTRACT

The activation energies of interstitial oxygen diffusion in silicon containing hydrogen were derived from the results obtained from thermal donor generation experiments using numerical fitting based upon the classical nucleation rate theory and the time-dependent reduction of interstitial oxygen concentration resulting from oxygen aggregation. By using a new thermal equilibrium concentration of hydrogen at a pressure of 1 atm of $2x10^{21}$ exp(-1.75 *eV/kT*), and the expression for the dependence of hydrogen thermal equilibrium concentration on the partial pressure *P* given as $P^{0.65}$ times the hydrogen thermal equilibrium concentration at a pressure of 1 atm, the correlation between the activation energies of interstitial oxygen diffusion and hydrogen saturation is observed to be linear-logarithmic. In the hydrogen saturation range between 10^3 and 10^6, the activation energies of interstitial oxygen diffusion are estimated to be between 0.03 and 0.21 *eV* lower than the normal value of 2.53 *eV*. This implies that enhanced oxygen diffusion may occur primarily under hydrogen saturation conditions.

INTRODUCTION

The diffusion of interstitial oxygen atoms in silicon is an important process in the manufacturing of integrated circuit (*IC*) devices because the formation and dissolution kinetics of oxygen-related defects is governed by oxygen diffusion. Oxygen-related defects, particularly those located in the device active region, cause catastrophic device failure and poor device performance during its operation [1]. Therefore, these defects must be removed from the silicon wafer surface prior to the *IC* device manufacturing process. In the past several years, the diffusivity of interstitial oxygen (D_i) under various experimental conditions has been determined using a variety of measurement techniques [2-4]. McQuaid *et al* [3] estimated the diffusivity of interstitial oxygen in silicon after pre-annealing at 900°C in hydrogen ambient from the reduction of stress-induced 9-μm dichroism and reported the value of $D_i = 7.1x10^{-4}$ exp (-2.0 *eV/kT*). Zhong *et al* [4] derived the oxygen diffusivity from the O^{16} secondary ion mass spectroscopy (*SIMS*) out-diffusion profile from silicon samples annealed at 1000 and 1200°C in hydrogen ambient. From the *SIMS* analysis, the activation energy of oxygen diffusion (Q_i) was estimated to be 3.1 *eV* which is much higher than the typical value of 2.53 *eV* [2]. Newman *et al* [5] suggested that oxygen diffusion would be enhanced when the hydrogen concentration is greater than a critical hydrogen concentration.

In this work, the activation energies for oxygen diffusion in silicon containing hydrogen will be estimated from the results obtained from thermal donor generation experiments [6-7] using numerical fitting based upon the classical nucleation rate theory and the time-dependent reduction of interstitial oxygen concentration. The correlation between the activation energies and hydrogen saturation in the silicon will be determined.

Mat. Res. Soc. Symp. Proc. Vol. 442 © 1997 Materials Research Society

OXYGEN THERMAL DONOR GENERATION IN SILICON

It is well established that pre-annealing of silicon in hydrogen ambient leads to an enhanced generation rate of oxygen thermal donors (*TD*) [5-8]. From the argument that the presence of hydrogen in the silicon lattice does not affect either the surface-free energy of oxygen thermal donor clusters σ_{TD} (*T*) or the volume of the thermal donor containing an oxygen atom V_{TD} , the activation energy of oxygen diffusion Q_i can be derived directly from the *TD* nucleation rate (J_{TD}) which is described by the classical theory proposed by Becker [9].

$$J_{TD} = A \exp(-\frac{Q_i}{kT}) \exp(-\frac{16\pi V_{TD}^2 \sigma_{TD}^3}{3 (k T)^3 \ln(C_i / C_i^{eq})^2}) \quad (1)$$

In Eq.(1), A is a constant and V_{TD} is on the order of 5.4×10^{-23} cm^3 [10]. C_i^{eq} is the thermal equilibrium concentration of interstitial oxygen atoms, equal to $5.5 \times 10^{20} \exp(-0.89\ eV/\ kT)$ [11]. The interstial oxygen concentration C_i which reduces with increasing annealing time (t) as a result of oxygen aggregation can be expressed as [12]

$$C_i(t) = C_{io}[1 + \frac{2}{3} D_O \exp(-\frac{Q_i}{kT}) t(C_{io})^{2/3}]^{-3/2} \quad (2)$$

where D_o is the pre-exponential factor, equal to 0.13 [2]. In Eq.(2), C_{io} is the concentration of interstitial oxygen in the starting material. Using a typical value of Q_i = 2.53 *eV*, σ_{TD} and A can be determined from a numerical fitting with the results from the *TD* generation experiment.

Figure 1 shows the plot of the *TD* concentrations as a function of annealing time at 450°C for *n*-type *Cz* silicon containing interstitial oxygen at a concentration of 8.2×10^{17} cm^{-3} and substitutional carbon below the infrared detection limit which is below 1×10^{16} cm^{-3} [13]. From the numerical fitting, σ_{TD} is equal to 2.32×10^{14} *eV*/cm^2 , in agreement with 2.08×10^{14} *eV*/cm^2 as reported by Ohrlein *et al* [10]. A is estimated to be 2.28×10^{46} donors/cm^3 sec and is five-orders of magnitude higher than the value previously reported by Ohrlein *et al*, equal to 1.9×10^{41} donors/cm^3 sec. One of the explanations for this discrepancy may be because silicon wafers used in Ohrlein *et al* experiment contained a

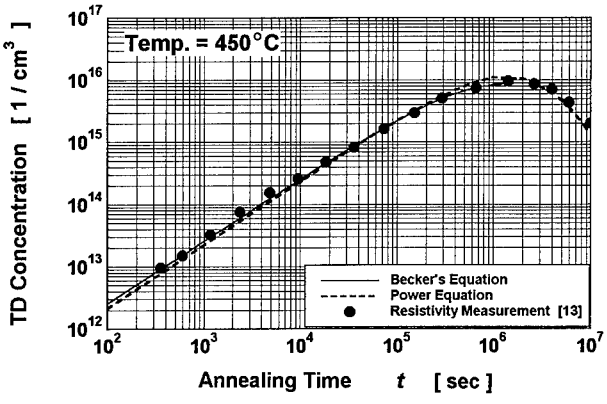


Fig.1: The relationship between *TD* concentration and annealing time *t* at 450°C.

high concentration of carbon, $4x10^{16}$ atoms/cm^3. Carbon is known to suppress the *TD* formation [14]. It should be pointed out that Ohrlein *et al* did not take into consideration the time-dependent reduction of C_i. This may also contribute to a low value of the parameter A. Therefore, the value of $A = 2.28x10^{46}$ donors/cm^3 sec will be used in this work. For the purpose of comparison, the experimental results in Fig. 1 were also fitted to the power equation proposed by Ourmazd [15], $n_{TD} = k_t C_i^x t^{1.02}$, using $x = 3.44$ [12]. In the power equation, $C_i(t)$ was determined using Eq.(2). The results in Fig.1 show an excellent agreement between the experimental data, the calculated results using the power equation and the classical theory for $t < 10^6$ sec.

ACTIVATION ENERGIES OF INTERSTITIAL OXYGEN DIFFUSION IN SILICON CONTAINING HYDROGEN

Figure 2 shows the plots of the *TD* concentrations as a function of annealing time at 422 and 507°C for *p*-type *Cz* silicon containing interstitial oxygen at a concentration of $1.5x10^{18}$ cm^{-3} and substitutional carbon below the infrared detection limit [7]. The closed symbols represent the experimental results obtained from samples pre-annealed at 1200°C in a hydrogen ambient at a partial pressure of 0.03 atm prior to *TD* annealing. The open symbols are from the control samples with no hydrogen pre-annealing. The solid lines represent the results from the numerical fitting. From the numerical fitting, σ_{TD} is between 2.43 and $2.47x10^{14}$ *eV*/cm^2 for both the pre-annealed and no pre-annealed samples. In the control samples, the activation energy for oxygen diffusion Q_i is 2.53 *eV*. In samples pre-annealed in hydrogen ambient and *TD* annealed at 422 and 507°C, the activation energies of oxygen diffusion Q_i are 2.32 and 2.43 *eV*, respectively. From the expression, $D_i = 0.13 \exp(- Q_i / kT)$ [2], these activation energies correspond to the oxygen diffusivities of $1.98x10^{-18}$ and $2.62x10^{-17}$ cm^2/sec, respectively. According to the correlation by McQuaid *et al* [3] represented by the expression, $7x10^{-4} \exp(-2.0\ eV/kT)$, the enhanced oxygen diffusivities at 422 and 507°C are $2.22x10^{-18}$ and $8.44x10^{-17}$ cm^2/sec, respectively. The result indicates that the enhanced oxygen diffusivities calculated using McQuaid *et al* 's correlation is slightly higher than those calculated from the *TD* nucleation rate.

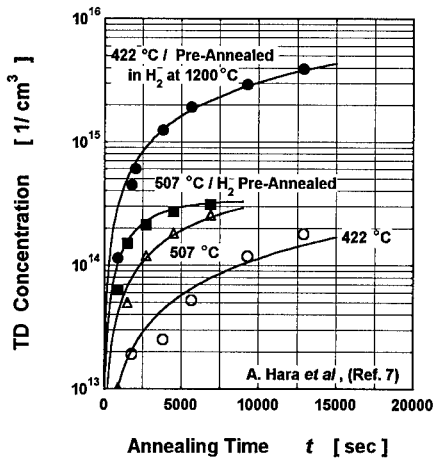


Fig. 2: The relationship between *TD* concentration and annealing time *t*.

Figure 3 shows the plots of the *TD* concentrations as a function of hydrogen concentration in silicon as reported recently by M. Koizuka *et al* [6] and A. Hara *et al* [7]. A *TD* annealing was performed in nitrogen ambient at 425°C at a partial pressure of 1 atm after pre-annealing in hydrogen ambient. The open symbols represent the experimental results obtained from samples pre-annealed at 750°C in hydrogen ambient at partial pressures ranging from 0.01 to 3.0 atm. The closed symbols are the experimental results obtained from samples pre-annealed at temperatures between 700 and 1200°C in hydrogen ambient at a partial pressure of 0.03 atm. The hydrogen concentration in the samples was calculated

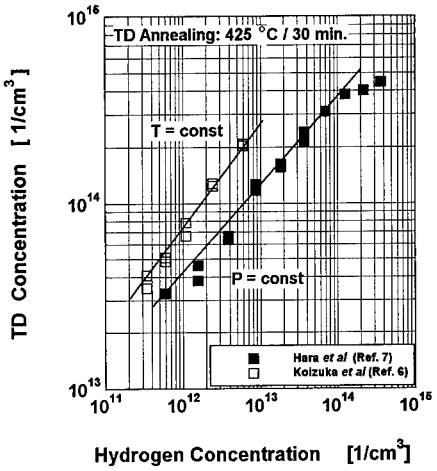


Fig. 3: The relationship between *TD* concentration and hydrogen concentration.

based upon the assumption that the hydrogen concentration in the samples are at thermal equilibrium C_H^{eq} during the pre-annealing. According to Van Wieringen and Warmoltz [16], C_H^{eq} at a partial pressure of 1 atm in the temperature range between 1050 and 1200°C is given as $4.96 \times 10^{21} \exp(-1.86\ eV/kT)$, while C_H^{eq} at a given partial pressure in the range between 0.1 and 1 atm may be represented by the expression $C_H^{eq}(P) = C_H^{eq}(1\text{ atm})\ P^{\beta}$ where P is the partial pressure and β is a constant, equal to 0.5 [6].

Figure 4a shows the plots of the activation energies Q_i as a function of hydrogen saturation H_S where H_S is defined as the ratio between C_H^{eq} (1 atm) at 425°C and hydrogen concentration in the samples. It should be pointed out that the plots include the results in Fig.2 for samples pre-annealed in hydrogen ambient at 1200°C, where H_S is the ratio between C_H^{eq} (1 atm) at 422 and 507°C and hydrogen concentration in the samples. From the figure, it may be concluded that in the hydrogen saturation range between 10^3 and 10^6, the correlation between Q_i and H_S is linear-logarithmic. Because the correlation between Q_i and H_S obtained from samples pre-annealed in hydrogen ambient at a constant pressure appears to be different from that obtained from

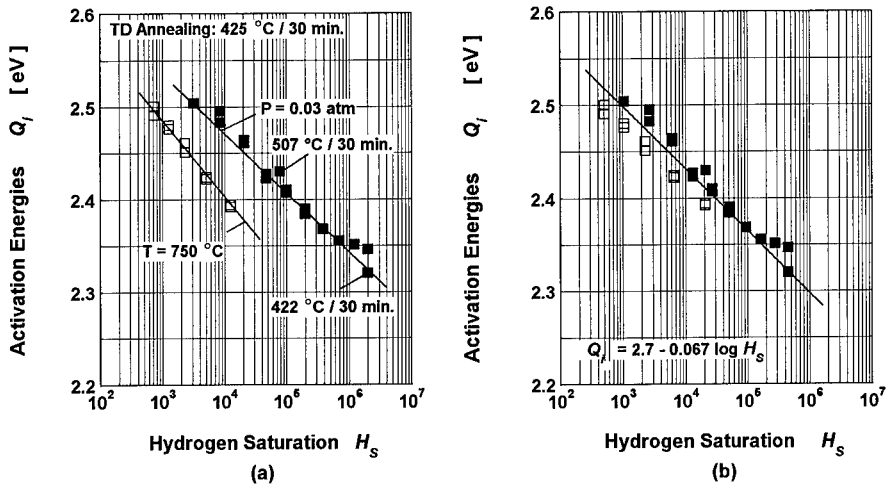


Fig. 4: The relationship between activation energies of oxygen diffusion Q_i and hydrogen saturation H_S based upon (a) Wieringen and Warmoltz's correlation [16] and (b) the present analysis.

samples pre-annealed at a constant temperature, it is suspected that the correlation between Q_i and H_S may depend on pre-annealing conditions. In order to resolve this issue, a best-fit was performed by adjusting C_H^{eq} and β . Van Wieringen and Warmoltz derived C_H^{eq} and β from experiments performed at high temperatures above 1050°C in a narrow range of partial pressures (0.1 - 1 atm). An extrapolation from a high temperature region to 425°C, or a widening of the partial pressure range to 0.01 and 3 atm, could result in an error during the calculation of the hydrogen concentration in the samples.

Figure 4b shows the results from the best-fit using the new thermal equilibrium concentration $C_H^{eq}(1\text{ atm}) = 2\text{x}10^{21}\exp(-1.75\ eV/kT)$ and the constant $\beta = 0.65$. From the figure, the correlation between Q_i and H_S may be expressed by, $Q_i = 2.7 - 0.067 \log H_S$, independent from the pre-annealing conditions. Figs. 5 and 6 show a comparison between $C_H^{eq}(T)$ and the expression $C_H^{eq}(P) = C_H^{eq}(1\text{ atm})\ P^{\beta}$ obtained from the best-fit and

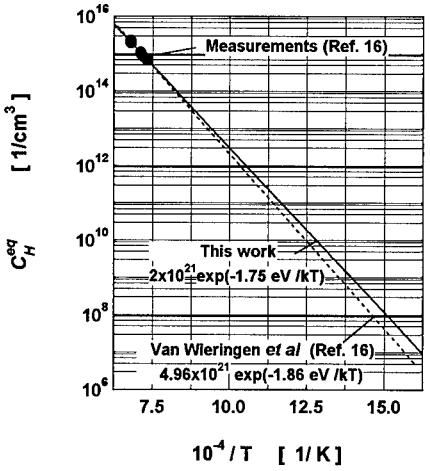


Fig. 5: Thermal equilibrium concentration of hydrogen in silicon C_H^{eq}.

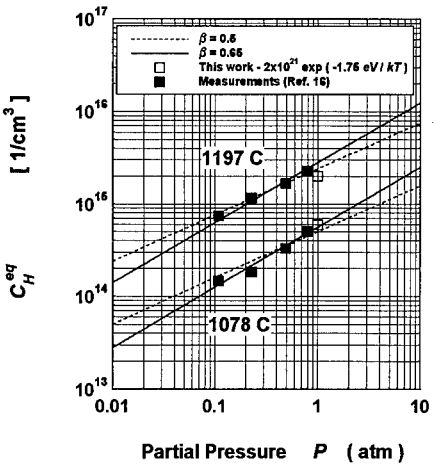


Fig. 6: The relationship between C_H^{eq} and partial pressure P.

those according to Van Wieringen and Warmoltz. The results clearly show that the new the thermal equilibrium concentration of hydrogen and the expression $C_H^{eq}(P) = C_H^{eq}(1\text{ atm})\ P^{0.65}$ fit well with the experiment results. Based upon the present analysis, it is suggested that an enhanced oxygen diffusion occurs when the hydrogen concentration in silicon is at least 10^3 times higher than the thermal equilibrium concentration.

SUMMARY

The activation energies of interstitial oxygen diffusion in silicon containing hydrogen were derived from the results obtained from thermal donor generation experiments using numerical fitting based upon the classical nucleation rate theory and the time-dependent reduction of interstitial oxygen concentration. By using a new thermal equilibrium concentration of hydrogen at a pressure of 1 atm equal to $2\text{x}10^{21}\exp(-1.75\ eV/kT)$, and the expression for the dependence of hydrogen thermal equilibrium concentration on the partial pressure P given as $P^{0.65}$ times $C_H^{eq}(1\text{ atm})$, the correlation between Q_i and H_S is observed

to be linear-logarithmic. In the hydrogen saturation range between 10^3 and 10^6, the activation energies of interstitial oxygen diffusion are estimated to be between 0.03 and 0.21 *eV* lower than the normal value of 2.53 *eV*. This implies that enhanced oxygen diffusion may occur primarily under hydrogen saturation conditions. It is proposed that the thermal equilibrium concentration of hydrogen in silicon at a partial pressure of 1 atm in the temperature range between 400 and 1200°C is best described by the expression, $2x10^{21}$ exp(-1.75 *eV/kT*). In the partial pressure range between 0.01 and 3.0 atm, the expression should be, $C_H^{eq}(P) = C_H^{eq}(1 \text{ atm}) P^{0.65}$.

ACKNOWLEDGMENT

The author would like to gratefully thank Mr. M. Koizuka of Fujitsu Ltd. for providing the results from thermal donor generation experiments.

REFERENCES

1. S.S. Kim and W. Wijaranakula, in Defect and Impurity Engineered Semiconductors and Devices, edited by S. Ashok, J. Chevallier, I. Akasaki, N.M. Johnson, and B.L. Sopori, (Mate. Res. Soc. Proc. 378, Pittsburgh, PA, 1995) p.725-730.
2. J.C. Mikkelsen, Jr, in Oxygen, Carbon, Hydrogen and Nitrogen in Crystalline Silicon, edited by J.C. Mikkelsen, Jr, S.J. Pearton, J.W. Corbett, and S.J. Pennycook, (Mate. Res. Soc. Proc. 59, Pittsburgh, PA, 1986) p.19-30.
3. S.A. McQuaid, R.C. Newman, J.H. Tucker, E.C. Lightowlers, R.A.A. Kubiak and M. Goulding, Appl.Phys.Lett., 58, 2933(1991).
4. L. Zhong and F. Shimura, J.Appl.Phys., 73, 707(1993).
5. R.C. Newman, J.H. Tucker, A.R. Brown, and S.A. McQuaid, J.Appl.Phys., 70, 3061(1991).
6. M. Koizuka, A. Hara and H. Yamada-Kaneta, in Extended Abstracts, (The Electrochem.Soc., Abstr.No. 515, 95-2, Pennington, NJ, 1995) p.821-822.
7. A. Hara, M. Koizuka, M. Aoki, T. Fukuda, H. Yamada-Kaneta, and H. Mori, Jpn.J.Appl.Phys., **33**, 5577(1994).
8. J.L.Benton, L.C. Kimerling and M. Stavola, Physica 116B, 271(1983).
9. R. Becker, Proc.Phys.Soc., 52, 71(1940).
10. G.S. Oehrlein, J.L. Linstrom, and S.A. Cohen, in Thirteenth International Conference on Defects in Semiconductors, edited by L.C. Kimerling and J.M. Parsey, Jr., (The Metal. Soc.of AIME, Warrendale, PA, 1984) p.701-708.
11. W. Wijaranakula, Appl.Phys.Lett., 59, 1608(1991).
12. W. Wijaranakula, Appl.Phys.Lett., 59, 1185(1991).
13. Y. Kamiura, F. Hashimoto, and M. Yoneta, J.Appl.Phys., 65, 600(1989).
14. W. Wijaranakula, J. Appl.Phys., 67, 7624(1990).
15. A. Ourmazd, W. Schröter, and A. Bourret, J.Appl.Phys., 58, 1670(1984).
16. A. Van Wieringen and N. Warmoltz, Physica, XXII, 849(1956).

EFFECT OF PRESSURE ON BORON DIFFUSION IN SILICON

Yuechao Zhao[1], Michael J. Aziz[1], Salman Mitha[2], and David Schiferl[3]

[1]Division of Engineering and Applied Sciences, Harvard University, Cambridge, MA 02138
[2]Charles Evans and Associates, Redwood City, CA 94063
[3]Los Alamos National Laboratory, Los Alamos, NM 87545

ABSTRACT

We are studying the effect of pressure on boron diffusion in silicon in order to better understand the nature of the point defects responsible for diffusion. Si homoepitaxial layers delta-doped with boron were grown using molecular beam epitaxy. Diffusion anneals were performed in a high temperature diamond anvil cell using fluid argon as a pressure medium. Diffusivities were deduced from B concentration-depth profiles measured with using secondary ion mass spectrometry. Preliminary results indicate that pressure enhances B diffusion in Si at 850 °C, characterized by an average activation volume of -0.125±0.02 times the atomic volume, and thus appear consistent with an interstitial-based diffusion mechanism. Results are compared with previous hydrostatic-pressure studies, with results in biaxially strained films, and with atomistic calculations of activation volumes for self diffusion.

INTRODUCTION

Because understanding and controlling diffusion related phenomena become increasingly important as semiconductor device dimensions decrease, diffusion in semiconductors has been heavily studied. Despite this emphasis there remains no consensus about the relative concentrations and mobilities of the point defects involved in the diffusion of many substitutional elements in Si [1]. A study of the dependence of the atomic diffusivity, D, on pressure, p, can provide valuable information to help elucidate the atomistic mechanism(s) of diffusion. The pressure-dependence of the diffusivity is characterized by the activation volume, ΔV^*:

$$-kT\frac{\partial \ell n\, D(T,p)}{\partial p} \equiv \Delta V^* , \qquad (1)$$

where k is the Boltzmann constant and T is the temperature. When experimental conditions are such that the point defect concentrations equilibrate rapidly with the free surface compared to the experimental time scale then ΔV^* is the sum of the formation volume ΔV^f and the migration volume ΔV^m. The formation volume is the volume change in the system upon formation, from the free surface, of a defect in its standard state, and the migration volume is the additional volume change when the defect reaches the saddle point in its migration path. ΔV^f characterizes the pressure-dependence of the equilibrium point defect concentration and ΔV^m characterizes the pressure-dependence of the point defect mobility. Here we report preliminary results for the diffusion of boron, the technologically most important p-type dopant, in silicon. Effects associated with transient enhanced diffusion were avoiding by fabricating the sample without ion implantation. Boron delta-doped samples were grown by molecular beam epitaxy (MBE), which possess many advantages in diffusion studies [2].

There has been much recent work on diffusion of boron and other species under the biaxial strain conditions characteristic of strained-layer epitaxy. We compare these to our results and to those of molecular statics calculations using a thermodynamic formalism of Aziz [3] that relates diffusion under hydrostatic and nonhydrostatic stress states. When stresses become nonhydrostatic, the activation volume becomes the activation strain tensor: upon point defect formation and migration, dimension changes parallel and perpendicular to the direction of mass

Mat. Res. Soc. Symp. Proc. Vol. 442 © 1997 Materials Research Society

transport couple to different elements of the stress tensor. For diffusion normal to the surface of an (001) biaxially strained thin film with a diamond cubic structure, the formalism provides a relation between the activation volume obtained under hydrostatic conditions and the derivative, Q', of the apparent activation energy on biaxial strain:

$$\Delta V^* + \frac{3}{2}\frac{Q'}{Y} = \pm\Omega + (\Delta V^m_{//} - \Delta V^m_{\perp}) \,, \qquad (2)$$

where $\Delta V^m_{//} - \Delta V^m_{\perp}$ is the anisotropy in the migration volume, Y is the ratio of Young's modulus to one minus Poisson's ratio in the film, and the + and - signs are for vacancy and interstitial-based mechanisms, respectively. Deviations from eq. (2) will be observed if some of the point defect equilibration occurs at threading dislocations in biaxially strained films.

EXPERIMENT

The boron-doped Si samples used in the present study contain four boron spikes, grown by low temperature MBE [4], with a spacing of 70 nm and the closest B spike being 110 nm from the surface. The peak concentration of the spikes is about 10^{19} atoms/cm^3. Diffusion anneals at 850 °C were performed in a high temperature diamond anvil cell (DAC) [5] using fluid argon, cryogenically condensed from an argon gas of nominal purity 99.95%, as an inert and hydrostatic pressure medium. The DAC was heated externally in a furnace as shown in Fig. 1. After the DAC was mounted into the furnace, the furnace was evacuated with a mechanical pump, the temperature was raised to 250-300°C, and several cycles of flushing and evacuating with helium of nominal purity 99.999% were performed. Diffusion temperatures were reached after filling the furnace with helium at an overpressure of roughly 260 torr above atmospheric. The He ambient provides a uniform temperature field around the DAC and minimizes oxygen leakage into the furnace. Atmospheric-pressure anneals were performed with the DAC loaded with 1 atm of room-temperature Ar gas and sealed initially. At high temperatures, however, the DAC may open up, so that the furnace ambient may be in contact with the sample.

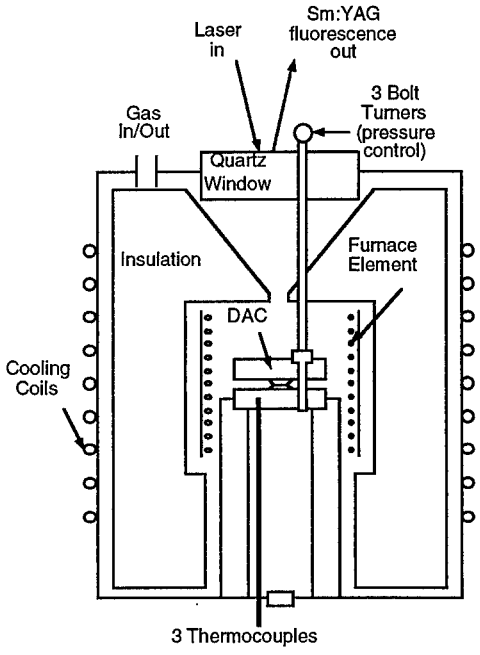


Figure 1. Schematic of high temperature-high pressure system used for pressure anneals.

True anneal durations were about 2500 seconds. Temperatures were recorded using thermocouples embedded in the lower and upper plates supporting the diamond anvils and in the gap between the plates. These thermocouple readings never disagreed by more than 7 °C. For the calculation of the diffusivity we used effective anneal times at 850 °C, which were calculated using thermal histories

recorded by a computer and an activation energy of 3.7 eV. Pressure can be adjusted *in situ* and was determined using the pressure-dependence of the wavelength of Sm-doped YAG fluorescence peaks Y1 through Y10 [6,7]. The uncertainty in the pressure determination is estimated to be ±0.3 GPa.

Concentration-depth profiles of boron were measured using secondary ion mass spectrometry (SIMS) with an 8 keV O_2^+ primary ion beam. A linear sputter time-depth scale conversion for each profile was established using a linear regression to superpose the measured peak positions on the published peak positions established by profilometry [4]. The diffusivities of B were deduced from the profiles using Wu's σ^2-analysis [8], which relates the time-dependence of the standard deviation of a profile of any shape (we performed a separate analysis for each doping spike) to the diffusivity, assuming that the diffusivity is independent of concentration. Although it may affect the absolute magnitude of the calculated diffusivities, the assumption of concentration-independence should not significantly affect the measured activation volume. The use of a lower energy primary ion beam in order to improve the depth resolution was precluded by the requirement of a tight focus on samples with a typical size of $150 \times 150 \times 40\ \mu m^3$, defined by the size of the sample chamber of the DAC. Fortunately, the diffusivities extracted from the σ^2 analysis are independent of instrumental resolution.

RESULTS AND DISCUSSION

Fig. 2 shows the B concentration-depth profiles in an as grown sample and a sample annealed at 3.5 GPa for 2496 s. Fig. 3 shows the preliminary results for the pressure-dependence of the diffusivity. Note that the closer to the surface the spikes are, the larger their diffusivities are. An argon anneal at Bell Labs [9] indicates that depth-dependence of the diffusivity appears to be a characteristic of this sample rather than of the atmosphere in this high-pressure study. However, the anomalously high diffusivity of the first spike in the 0-GPa sample, which may be related to the imperfect sealing by the DAC, has been discarded in the calculation of the apparent activation volume. Fig. 3 indicates that pressure apparently enhances B diffusion in Si at 850 °C, characterized by an average activation volume of -0.125±0.02 Ω. The values for diffusivities of B obtained in the present study are systematically lower than the literature value of B diffusivity in Si for 850 °C [10]. Instead, the diffusivity determined for the deepest spike corresponds to the literature value for about 780 °C. This inconsistency remains a puzzle because the thermocouples in the

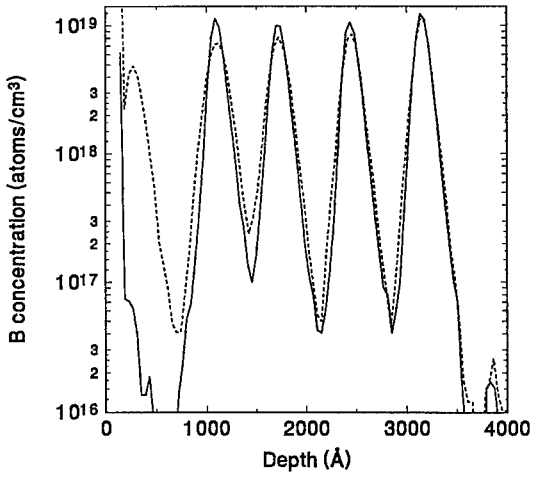


Figure 2. Typical concentration-depth profiles for as grown (solid line) and annealed (dashed line) samples.

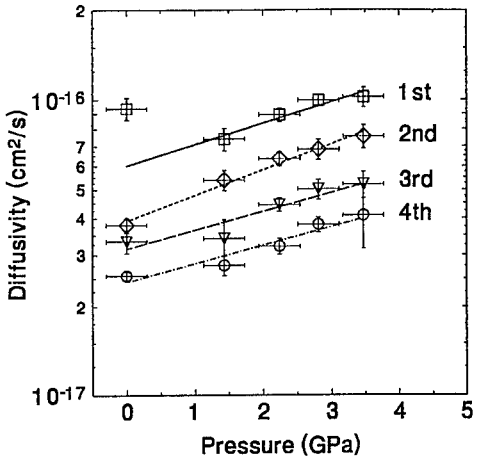


Figure 3. Preliminary results of pressure-dependence of B diffusivities in Si measured in the present study. The spikes are labeled starting from that closest to the sample surface.

DAC reproduced the melting point of 99.999% pure Ag (960 °C) within 10°. Although we have no information that the origin of this apparent inconsistency is independent of pressure, we will assume that it is pressure-independent for the purposes of the discussion below.

Our apparent activation volume differs from that of Södervall *et al.* [11], who reported $\Delta V^* = (+0.27 \pm 0.25)\ \Omega$ over 1050-1230°C. However, because their samples were fabricated by ion implantation of boron, their results may be complicated by transient enhanced diffusion.

Our results are interpretable directly in terms of defect formation and migration volumes only if experimental conditions are such that the point defect concentrations equilibrate rapidly with the free surface compared to the experimental time scale. We have no proof that this is the case in the experiment reported here. If the process is nonequilibrium then this experiment may represent the effective pressure dependence of an interstitial injection process. Despite the obvious depth dependence of the diffusivity, which suggests that interstitial concentrations vary through the sample, we will make the openly naive assumption that there is rapid equilibration with the surface, in order to compare the observed behavior with the behavior that might be anticipated from the results of other experiments and models.

Qualitatively, the pressure enhancement is normally thought of as consistent with an interstitial-based mechanism. This is based on the common assumptions that the volume change upon relaxation around a point defect (ΔV^{relax}), as well as the migration volume, are substantially smaller than Ω. When $\Delta V^{relax} + \Delta V^{m} = 0$, $\Delta V^* = +1\ \Omega$ for the vacancy mechanism and $-1\ \Omega$ for interstitial-based mechanisms, exactly. It is now possible to be quantitative because ΔV^{relax} and ΔV^{m} can be predicted using molecular dynamics or statics calculations. We know of no atomistic calculations of the volumetrics of boron diffusion in silicon. However, relaxation volumes have been calculated for self diffusion by interstitial-based mechanisms. Antonelli and Bernholc [12] used density functional theory with the local density approximation to calculate the volume of formation of the self-interstitial in the tetrahedral and bond-centered configurations. Tang *et al.* used the tight-binding approximation to calculate a formation volume of $-0.1\ \Omega$ for the <110> dumbbell self interstitial. If we assume that the formation and migration volumes for boron diffusion are close to those for self diffusion then we can at least see whether our results are reasonable.

Experimentally, Kuo *et al.* [13] isolated the effects of strain and composition on B diffusion in biaxially strained Si-Ge alloy thin films. They concluded that boron diffusion in silicon does not depend strongly on biaxial strain. Also, Cowern *et al.* [14] studied Si-Ge interdiffusion in biaxially strained multilayers under inert and oxidation-enhanced conditions and used a model to

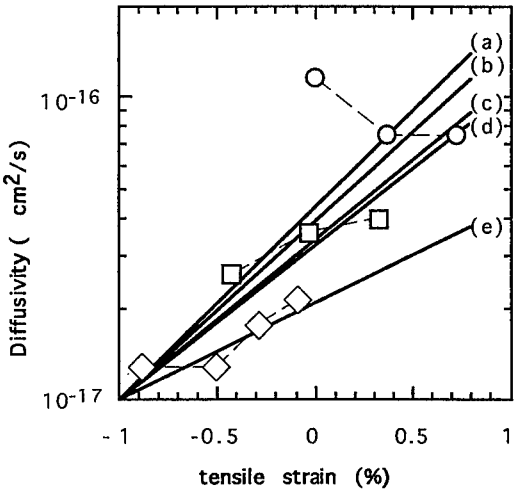


Figure 4. Preliminary comparison of interstitial mechanisms in biaxially strained Si-Ge films. Vertical offsets represent composition effect at constant strain; slopes represent strain effect at constant composition. Data from Kuo et al. [13]: circles: B in pure Si; squares: B in $Si_{90}Ge_{10}$; diamonds: B in $Si_{80}Ge_{20}$. Straight lines determined from Eq. (2) using: (a) ΔV^{relax} for <110> dumbbell interstitial in Si self diffusion from Tang et al. [15]; (b) the present preliminary data for the activation volume for B in Si; (c) Q' reported for OED of Si/Ge multilayers from Cowern et al. [14]; (d) ΔV^* for self diffusion by tetrahedral interstitial saddle point, from Antonelli and Bernholc [12]; (e) ΔV^* for self diffusion by bond-centered interstitial saddle point, from Antonelli and Bernholc. Vertical offsets of all lines are arbitrary; only the slopes are significant.

isolate the effect of strain on the interstitial-based component. They reported a value of Q' = -12 ± 6 eV per unit strain for the interstitial contribution to oxidation-enhanced diffusion (OED).

In Fig. 4 we use Eq. (2) to compare the measured and predicted strain-dependence of boron diffusion in biaxially strained Si-Ge. The comparisons are made assuming (1) the anisotropy in the migration strain $\Delta V^m_{//} - \Delta V^m_{\perp} = 0$ in all cases except that of Cowern *et al.*, where no such assumption is necessary; (2) relaxation and migration volumes for point defects involving boron are identical to those calculated for pure Si (or Ge in the case of Cowern *et al.*); this assumption is not necessary for the present experiment performed on boron diffusion in Si; (3) $\Delta V^m = 0$ for the <110> dumbbell of Tang *et al.* [13]; (4) the biaxial modulus is Y = 180.5 GPa independent of composition and temperature. Only the slopes of the curves are relevant - their vertical offsets are arbitrary. The slopes of the data of Kuo *et al.* [13] for B diffusion in $Si_{89}Ge_{11}$ and $Si_{79}Ge_{21}$ (From their Fig. 2) fall within the range of the other values whereas the slope of their data for B diffusion in pure Si under tensile strain (From their Fig. 3) is opposite in sign. Qualitatively, our data and the alloy data of Kuo *et al.* are consistent with an interstitial-based mechanism whereas their pure Si data are not. It would be very valuable to have calculations and experiments to determine the missing parameters and permit a rigorous comparison. The missing parameters are the formation or relaxation volumes for B diffusion by the interstitialcy or kick-out mechanism at the saddle point of the migration path, and the anisotropy in the migration strain.

SUMMARY

Preliminary results of effect of pressure on boron diffusion in silicon indicate that pressure enhances B diffusion in Si at 850 °C, characterized by an average activation volume of -0.125±0.02 times the atomic volume. This result is qualitatively consistent with an interstitial-based diffusion mechanism. The results are also qualitatively consistent with several different atomistic calculations for Si self diffusion by interstitial-based mechanisms, with Cowern *et al.*'s interpretation of oxidation-enhanced diffusion in strained Si-Ge alloys, and with Kuo *et al.*'s results

for B diffusion in biaxially strained Si-Ge alloys; these are all inconsistent with Kuo *et al.*'s results for B diffusion in biaxially strained pure Si films.

This research was supported by NSF-DMR-95-25907. Work at LANL was supported by the Division of Materials Sciences, DOE under contract W-7405-ENG-36 with the University of California. The authors are grateful to D.J. Eaglesham for providing the starting sample and to H.-J. Gossmann for communication of his simulation results for comparison to the σ^2 results used here, for the performance of the Ar ambient anneal on this sample, and for much helpful discussion.

REFERENCES

[1]P.M. Fahey, P.B. Griffin and J.D. Plummer, Rev. Mod. Phys. **61**, 289 (1989).

[2]H.-J. Gossmann, in Delta Doping of Semiconductors, edited by E.F. Schubert (Cambridge University Press, Cambridge, U.K., 1996), p. 253.

[3]M.J. Aziz, submitted to Appl. Phys. Lett.

[4]P.A. Stolk, D.J. Eaglesham, H.-J. Gossmann and J.M. Poate, Appl. Phys. Lett. **66**, 1370 (1994).

[5]S. Mitha, M.J. Aziz, D. Schiferl and D.B. Poker, Appl. Phys. Lett. **69**, 922 (1996).

[6]N.J. Hess and D. Schiferl, J. Appl. Phys. **71**, 2082 (1992).

[7]Y.C. Zhao, W.B. Carter, S.D. Theiss, S. Mitha, M.J. Aziz and D. Schiferl, (unpublished).

[8]D.T. Wu, in Crucial Issues in Semiconductor Materials and Processing Technologies, edited by S. Coffa, F. Priolo, E. Rimini and J.M. Poate (Kluwer, London, 1992), p. 403.

[9]H.-J. Gossmann (private communication). The Bell Labs anneal took place in a furnace in argon of 99.95% purity flowing at 1.5 liters/minute at 850 °C for 45 minutes. The temperature was calibrated using solid phase epitaxial growth rates and using a thermocouple attached to the silicon and is believed to be accurate to within ± 10°. The furnace and procedure are identical to those reported in H.-J. Gossmann, C.S. Rafferty, F.C. Unterwald and T. Boone, Appl. Phys. Lett. **67**, 1558 (1995).

[10]R.B. Fair, in Impurity Doping Process in Silicon, edited by F.F.Y. Wang (North-Holland, Amsterdam, 1981), Chapter 7.

[11]U. Södervall, M. Friesel and A. Lodding, J. Chem. Soc. Faraday Trans. **86**, 1293 (1990).

[12]A. Antonelli and J. Bernholc, Phys. Rev. B **40**, 10643 (1989).

[13]P. Kuo, J.L. Hoyt, J.F. Gibbons, J.E. Turner and D. Lefforge, Appl. Phys. Lett. **66**, 580 (1995).

[14]N.E.B. Cowern, W.J. Kersten, R.C.M. de Kruif, J.G.M. van Berkum, W.B. de Boer, D.J. Gravesteijn and C.W.T. Bulle-Liewma, in Proc. 4th Int. Symp. on Process Physics and Modeling in Semiconductor Devices, eds. G.R. Srinivasan, C.S. Murthy, and S.T. Dunham, Electrochem. Soc. Proc. Vol. 96-4 (Electrochem. Soc., Pennington, NJ, 1996).

[15]M. Tang, L. Colombo, J. Zhu and T. Diaz de la Rubia, submitted to Phys. Rev. B.

Part VII

Dislocations in Group IV Semiconductors

DISLOCATION INTERACTIONS AND THEIR IMPACT ON ELECTRICAL PROPERTIES OF GeSi-BASED HETEROSTRUCTURES

S.A. Ringel* and P.N. Grillot**
*Department of Electrical Engineering, The Ohio State University, Columbus, OH 43210, ringel@ee.eng.ohio-state.edu
** Now at Hewlett Packard Optoelectronics, San Jose, CA, 95131, pat_grillot@hp.com

ABSTRACT

Substantial improvements in the quality of relaxed, heteroepitaxial GeSi layers have occurred in the past few years due to both the development of compositionally-graded buffer layers and to an improved understanding of strain-relaxation in lattice-mismatched epitaxy, which have led to low dislocation densities within these layers. As a result, high performance GeSi devices have been achieved which has fueled yet greater device design flexibility through the use of relaxed GeSi layers over a wider range of alloy compositions and lattice constants. A complete understanding of the properties of all defects that result from strain-relaxation is essential to realize high performance and reliable devices, especially as the lattice-mismatch strain becomes more severe. While the structural properties of dislocations in relaxed GeSi layers have been studied in detail, the electronic properties of these defects and their consequences on the overall electrical properties of relaxed GeSi layers are not well understood. In this paper, we show that for high quality (low dislocation density) relaxed layers, clusters of intrinsic point defects formed by dislocation interaction, rather than the dislocations themselves, now dominate the deep level spectrum. We further show that these defects reduce the *electronic* material quality for films grown by UHVCVD at low temperatures (650 °C) in comparison to films grown at temperatures > 800 °C even though all films have similarly low threading dislocation densities. Using DLTS, spreading resistance, EBIC and Hall effect measurements, these defects are shown to introduce a low concentration of hole traps from E_v + 0.05 to E_v + 0.30 eV that compensate and type convert nominally undoped GeSi layers grown at 650 °C to p-type. Annealing studies indicate that these defects anneal out at ~ 750 - 800 °C, which is accompanied by conductivity type reversal to n-type, elimination of compensation and increased diffusion length. These observations, in addition to the precise position of each energy level, closely correlate with earlier results on plastically-deformed bulk Si, suggesting that these defect complexes are of intrinsic origin. We conclude that strain-relaxation in graded heterostructures causes considerable dislocation interaction which introduces point defect complexes associated with dislocations that, in addition to threading dislocation density, must now be considered as an important factor for achieving high electronic quality, relaxed GeSi layers.

INTRODUCTION

Substantial improvements in the quality of relaxed, heteroepitaxial Ge_xSi_{1-x} layers have occurred in the past few years due to both the development of compositionally-graded buffer layers and to an improved understanding of strain-relaxation in lattice-mismatched layers, which

Mat. Res. Soc. Symp. Proc. Vol. 442 © 1997 Materials Research Society

have led to low dislocation densities (< 10^6 cm^{-2}) within these layers [1-3]. As a result, high performance electronic Ge_xSi_{1-x} devices have now been achieved, including heterojunction bipolar transistors, 2DEG and 2DHG FET's. These successes, and the steady maturation in understanding the strain-relaxation process is currently fueling interest in yet greater device design flexibility through the use of relaxed Ge_xSi_{1-x} epilayers covering the entire range of alloy compositions (x = 0 - 1) and lattice constants [3]. For example, compositions of relaxed Ge_xSi_{1-x} films approaching pure Ge may provide a means to integrate GaAs-based optoelectronics with Si via the lattice-matching provided by the increasing lattice constant with Ge mole fraction [4]. As such interest continues to develop, the inherently larger lattice-mismatch with Si wafers and resultant increase in dislocation generation necessitates a thorough understanding of *all* defect properties in order to achieve high performance and reliable device technologies in the future. While the structural properties of dislocations in relaxed GeSi layers and the mechanism of strain-relaxation are now well understood, the electrical activity of these defects and their consequences on the overall electrical properties of relaxed GeSi layers have only recently been considered in some detail [5-11].

The purpose of this paper, therefore, is to present information on the deep levels present in relaxed GeSi layers, their impact on electrical and optical properties of GeSi layers, and comment on their potential physical origin. The results presented are based in part on our prior published results that report on the presence and properties of electron and hole traps due to dislocations and other extended defects in relaxed GeSi heteroepitaxy. It is important to realize that this paper focuses exclusively on the electrical and optical characterization studies of extremely high structural quality, relaxed GeSi layers. That is, we are primarily interested in characterizing the electronic properties of high purity (background doping ~< $1x10^{14}$ cm^{-3}), low threading dislocation density (< $1x10^6$ cm^{-3}) and fully relaxed GeSi layers grown using compositionally-graded buffer layers on Si since this process of achieving low dislocation density layers is now well established and only relaxed layers with low dislocation density will ultimately be used for subsequent devices. We show that for such high purity, low dislocation density films, clusters of intrinsic point defects formed by dislocation interactions contribute a low concentration (< mid 10^{12} cm^{-3} range) of shallow, acceptor-like states that limit the overall electrical properties and quality of undoped $Ge_{0.30}Si_{0.70}$ layers, instead of the dislocations themselves. We show that growth or post-growth anneal temperatures in excess of 800 °C are necessary to remove these defects. At low growth temperatures (650 °C), these defects tend to obscure the dislocation core defect state for these low dislocation density layers, which is revealed only after the high temperature annealing. We also demonstrate a fundamental connection and consistency between the deep level spectra (electron and hole) measured at all growth/anneal temperatures for the $Ge_{0.30}Si_{0.70}$ films and wide range of alloy compositions which implies that similar defect configurations due to strain-relaxation in the GeSi material system are formed for a wide range of alloy compositions.

EXPERIMENT

Ge_xSi_{1-x} layers were grown by Ultra High Vacuum Chemical Vapor Deposition (UHVCVD) on (100) n^+ Si wafers. Final layer compositions were obtained by grading at 10% Ge/μm from pure Si at the starting wafer surface, with the predominant cap layer composition being 30% Ge for the work presented here. The thicknesses of the constant composition cap layers ranged from 1.5 - 3 μm, and were either nominally undoped (measured background doping < $1x10^{14}$ cm^{-3}) or lightly As-doped to a measured concentration of 1-$2x10^{14}$ cm^{-3}. Samples were grown at both 650 °C and 900 °C. After the 650 °C growth, some of the films received a rapid

thermal anneal (RTA) treatment in N_2 for 60 sec. at 700 °C, 750 °C, 800 °C and 850 °C. To facilitate both Deep Level Transient Spectroscopy (DLTS) and other electrical characterization techniques, a thin p^+ layer was grown on the low doped GeSi cap layer so that the pn junction depletion region extending into the low doped, constant composition cap layer was probed. Devices were delineated by mesa etching. Materials were systematically characterized by TEM, EBIC, Hall effect, capacitance-temperature (C-T), photoluminescence (PL), cathodoluminescence (CL) and DLTS. Complete details of our growth, processing and characterization techniques can be found elsewhere [7,8]. For the purposes of this paper it is important to note that the intentional low doping concentration in our films allows our DLTS measurements to be sensitive down to trap concentrations on the order of 10^{10} cm^{-3} so that we can probe defect states introduced by the low concentration of defects present in our films.

RESULTS

Figure 1 shows a cross sectional TEM micrograph of a $Ge_{0.30}Si_{0.70}$/graded buffer/Si wafer structure grown at 650 °C. A threading dislocation density of $7x10^5$ cm^{-2} was measured in the cap layer using EBIC, with no observable change in the TEM after annealing and is representative of the structural quality of all of the films in this study. In spite of the apparent similarity in quality between different layers for all growth and anneal temperatures, however, very different electrical properties of the films were observed. Perhaps most striking among these are the spreading resistance profiles and DLTS data shown in figure 2. Note here that all films were intentionally As-doped (n-type) but demonstrate low background p-type conductivity for the as-grown layer grown at 650 °C and a trap spectrum that is dominated by a low concentration (mid 10^{12} cm^{-3}) of a number of distinct hole traps. In contrast, the layer grown at 900 °C demonstrates the expected n-type conductivity at low carrier concentration in the cap layer, coupled with a trap spectrum dominated by an even lower concentration (~ 10^{11} cm^{-3}) of a single dominant electron trap that we have previously identified as a fundamental state of the dislocation core [7]. Note that the low trap concentration in both cases, coupled with the low dislocation density generally qualifies both materials as high quality, although as we will soon see, their electrical properties can be rather

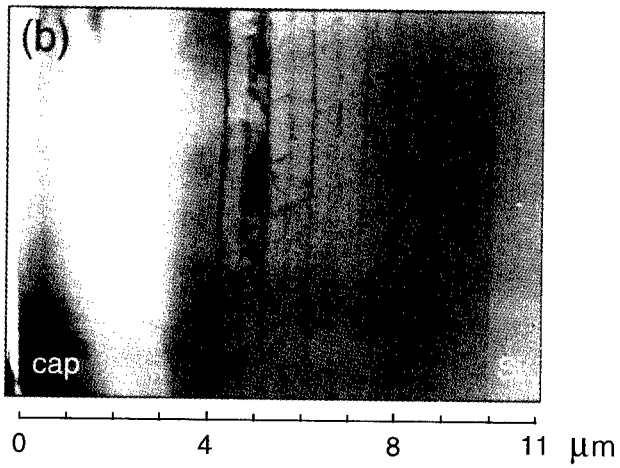


Figure 1. Cross-sectional TEM image of a representative $Ge_{0.30}Si_{0.70}$/graded GeSi/Si structure. A threading dislocation density of $7x10^5$ cm^{-2} was measured by EBIC.

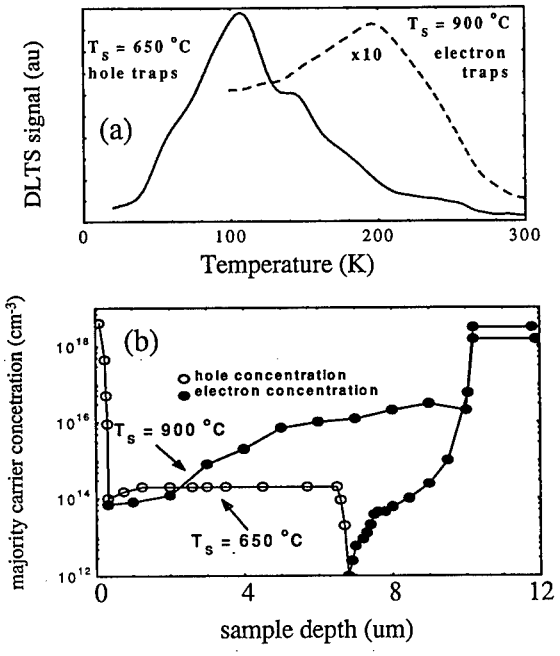


Figure 2. (a) DLTS spectra and (b) spreading resistance profiles for the GeSi heterostructure grown at 650 °C and 900 °C. Note that the n-type concentration in the cap layer of the 900 °C sample is lower than that of the 650 °C sample, indicating the apparent dopant diffusion from the substrate through the graded layer in this sample does not affect the type conversion in the cap.

different. In the remainder of this paper we address the relation between these deep states and the bulk electrical properties of the relaxed films, and attempt to identify the physical sources of these states since the low background doping offers us the opportunity to perform DLTS studies with very high sensitivity and the low dislocation density provides us with less complicated defect structures compared to high dislocation density films.

To accomplish this, we have investigated $Ge_{0.30}Si_{0.70}$ layers grown at 650 °C that have undergone systematic rapid thermal annealing as described above. Figure 3 shows the spreading resistance profiles of an as-grown 650 °C $Ge_{0.30}Si_{0.70}$/graded GeSi/Si structure and the profile of a sample having undergone an RTA at 850 °C. As in the case for the growth temperature comparison, the as-grown layer demonstrates a type conversion from n to p-type, and the desired n-type conductivity (intentional As doping was ~$1x10^{14}$ cm^{-3}) is recovered after annealing. An obvious possible cause of the type conversion is compensation via acceptor-like states. Evidence for this is shown in figure 4 where the zero-bias capacitance of $Ge_{0.30}Si_{0.70}$ diodes is plotted against sample measurement temperature as a function of post-growth RTA temperature. The as-grown and low temperature RTA samples display considerable temperature dependence which is indicative of the participation of electrically active deep states in the charging process. This dependence disappears with high RTA temperatures as shown, which indicates the source for the

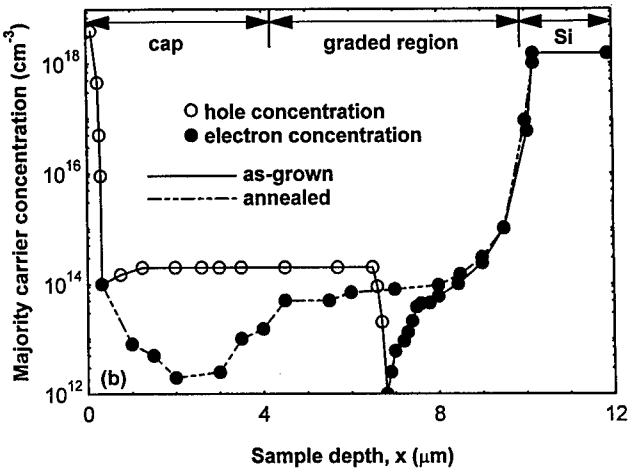


Figure 3. Spreading resistance profiles for the 650 °C grown sample prior to and after RTA.

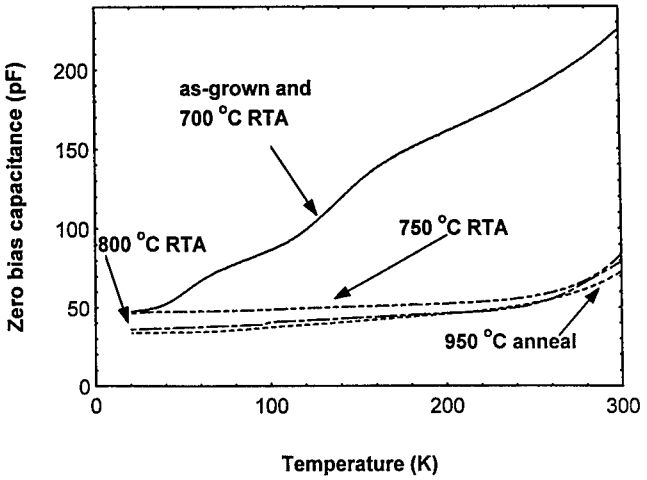


Figure 4. Zero bias C-T data for samples grown at 650 °C that were post-growth processed at the indicated annealing conditions.

compensation effect is thermally-unstable. We have also found that a significant enhancement in the minority carrier diffusion length within this structure after RTA processing. This is shown in figure 5 where the EBIC signal is plotted against position in the sample cross-section for the as-grown (650 °C) case and the 850 °C annealed sample. The extended collection length of the

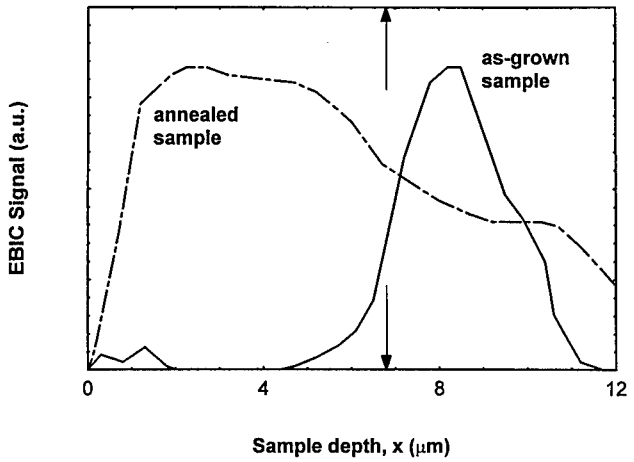


Figure 5. Cross-sectional EBIC line scan from as-grown and annealed samples. Arrows indicate position of the p-n junction in each case.

EBIC signal indicates improved collection efficiency via enhanced diffusion length after RTA. In addition we can monitor the position of the active pn junction from this figure which prior to RTA processing is at the interface between the n-type Si wafer (or the compensated n-type regions at the back of the graded layers) and the type converted, p-type GeSi layers (a p^-/n^+ junction). After annealing, the collecting junction moves to the front p^+/n interface, as originally intended. The motion of the junction supports the spreading resistance data shown earlier. We have also found a strong correlation with the evolution of both the PL and CL spectra as a function of annealing, but these results are beyond the scope of this paper and have been reported in an earlier publication [8]. The reason for mentioning these, however, along with the data shown thus far is to establish a remarkable consistency between many diverse electrical and optical measurements, all of which point to the active participation of deep states and their strong influence on the bulk electrical and optical properties of high quality, relaxed GeSi layers.

The participation of deep states is confirmed by the series of DLTS scans shown in figure 6. As indicated, there are a number of distinct hole traps present in low concentrations (note y-axis scale is in the 10^{12} cm^{-3} range) in the as-grown layer. The activation energies of the dominant hole traps are shallow and range from E_v + 0.05 eV to E_v + 0.30 eV (the notation H(0.05) - H(0.30) will be used from here on out). In fact, temperature-dependent Hall effect measurements indicate an activation energy consistent with these levels [8], demonstrating their role in dictating overall conductivity of the as-grown films. Returning to figure 6, as the RTA temperatures are increased, the concentration of all hole traps decrease rapidly and are below our detection limit (< 10^{10} cm^{-3}) after a 750 °C RTA, as shown in the figure on the left. For samples exposed to higher RTA temperatures (right hand side of figure 6), no hole traps are detected and instead we find a very low concentration of electron traps, which after an 850 °C RTA, is reduced only to the presence of the E(0.37) level that we have previously shown to be the dislocation core state [7].

Notice that the final trap concentration of this dislocation core state saturates at ~ $2x10^{11}$ cm^{-3} for anneals of 850 °C and higher (not shown) which is consistent with the low threading

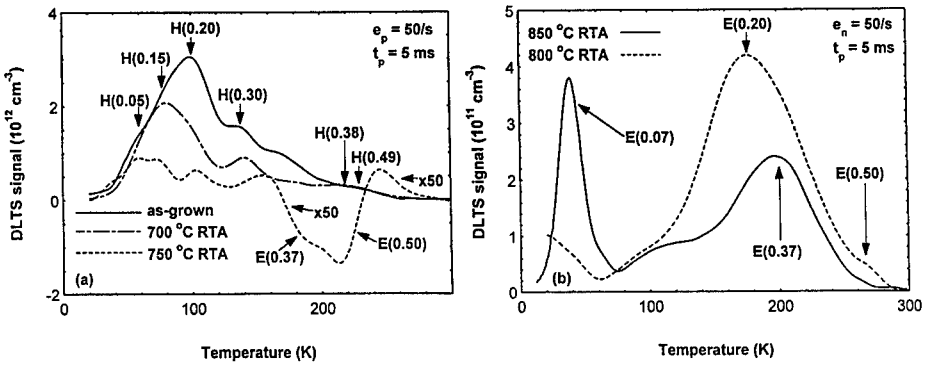


Figure 6. DLTS spectra for the 650 °C samples with no post-growth annealing and after the annealing at the conditions shown in the figure. Figure 6a was obtained prior to complete conductivity type reversal from p to n type. Figure 6b show the DLTS scans after the film has reverted to n-type due to the removal of the acceptor-like traps.

dislocation density (~ $7x10^5$ cm^{-2}) in this film. It is useful to quantitatively compare the threading dislocation density with the core state level concentration. It has been proposed that only kink sites along a dislocation core will be electrically active due to core reconstruction along the dislocation line everywhere else, which represents about 1% of all core sites [12]. If we consider the atomic density along a dislocation in the <110> direction coupled with the measured $7x10^5$ cm^{-2} dislocation density, by a simple calculation we roughly predict a concentration of ~ $1x10^{11}$ cm^{-3} electrically active dislocation core sites. This is close to the measured core state (E(0.37)) trap density of ~ $2x10^{11}$ cm^{-3} and demonstrates a good correlation between structural (TEM) and deep level (DLTS) measurements that demonstrates the consistency of our analysis.

The temperature range in which the shallow hole traps are removed by annealing is consistent with the conversion of the film conductivity from p to n-type at an anneal temperature of around 750 °C as found by spreading resistance and EBIC measurements made on the samples as a function RTA temperature. In fact, we found it difficult to obtain consistent DLTS measurements for the 750 °C RTA samples due to nonuniform type conversion throughout the bulk of the GeSi layer at this RTA temperature. Hence, from the discussion thus far the following points are clear: (1) H(.05), H(0.15), H(0.20) and H(0.30) are shallow, acceptor-like defect states that act to compensate background n-type doping, causing type conversion in these layers that are actually lightly-doped with As; (2) these defects are thermally-unstable and reduce electrical quality of the films as a whole; (3) each state displays the logarithmic capture kinetics and other characteristics indicative of extended defects as their physical sources (not shown); (4) results from very different characterization methods (DLTS, C-T, Hall, EBIC, PL and CL) completely correlate with eachother and demonstrate that the electrical quality and trap spectra depend on anneal and growth temperature; (5) there is no apparent connection between these results and TEM data which do not show differences in dislocation density; and (6) there is no evidence for the participation of the dislocation core state in these low dislocation density layers. We therefore

conclude that the source for the hole traps discussed here must be clusters of point defects based on their annealing behavior and since the traps display extended defect characteristics. In the following paragraphs, we present evidence that suggests the source of these shallow acceptor states is intrinsic to the strain-relaxed material.

Comparison of the TEM cross section in figure 1 coupled with the spreading resistance data in figure 3 indicates that the observed type conversion does not occur uniformly throughout the GeSi structure. In fact, working from the Si substrate upwards, type conversion gradually occurs as the steps within the step-graded region become thinner (a result of the changing growth rate with increasing Ge mole fraction in the UHVCVD process). If one considers the effect of thickness, for the same interface mismatch thinner layers will remain partially strained in comparison to thicker layers, with all other factors being equal. As subsequent layers are grown, dislocations gliding in the next interface plane can be injected downward into the previous layer, in order to relax this latent strain in the region below. In so doing, misfit dislocations must cut through other orthogonal misfits within the interface plane and the resulting jog motion of the dislocation will generate point defects such as vacancies. Such dislocation interactions are entirely expected within graded structures and this is but one possible mechanism that is easy to imagine upon comparison of figures 1 and 3. The individual point defects are well known to migrate together to form clusters (multiple vacancies, for example) in order to reduce total energy, and these clusters themselves can be quite mobile, dispersing throughout the film. Based on the high annealing temperatures necessary to completely remove these defects (> 750 °C), we conclude that these intrinsic point defect clusters must be associated with the dislocation core (i.e. influenced by the dislocation strain field), as has been suggested previously in plastically deformed (PD) Si for dislocation-related vacancy clusters [13]. This is also consistent with previously published annealing behavior of deep levels attributed to point defect clusters formed by dislocation intersections in PD-Si [12].

There are a number of compelling reasons the source of these point defect clusters is likely to be an intrinsic, dislocation-related process described above, and not extrinsic impurities. First, the compensation effect varies with position in the graded layer as described above. Unknown impurity incorporation during high-quality UHVCVD epitaxy is unlikely to occur in this fashion and would not be expected to depend on relaxation phenomena as described above. Second, we have observed the same states in GeSi samples grown by other techniques, including rapid thermal chemical vapor deposition (RTCVD) and molecular beam epitaxy (MBE). The likelihood of the same impurities present in these very different growth environments (especially MBE where impurities like oxygen are present in extremely small quantities) is remote. Third, the same hole traps with the same annealing properties and compensation behavior have been reported in PD float zone (FZ) Si crystals. The fact that FZ Si has very low oxygen content (as does MBE-grown SiGe) strongly suggests that the easily-suspected oxygen impurity is *not* the source of these acceptor-like defects.

Additional evidence that supports the possibility of intrinsic sources for these hole traps is presented in figure 7 which shows a re-plot of the deep level spectra of FZ PD-Si with our own DLTS spectrum from the as-grown 650 °C $Ge_{0.30}Si_{0.70}$ sample. The DLTS spectra are remarkably similar. In fact, if one translates the GeSi spectrum to higher temperatures by 70 K as shown, the spectra almost completely overlap. This temperature shift is significant since it represents a change in energy equivalent to the increase in valence band edge energy as one moves from pure Si to a relaxed 30% Ge GeSi alloy, a change of 0.12 eV. In Table I this analysis is quantified where the measured energy level of each detected hole trap within the 30% Ge alloy is listed (including the deeper states) in the left hand column. By adding the 0.12 eV difference in valence band energy to this we obtain the second column which lists the energy levels within strain

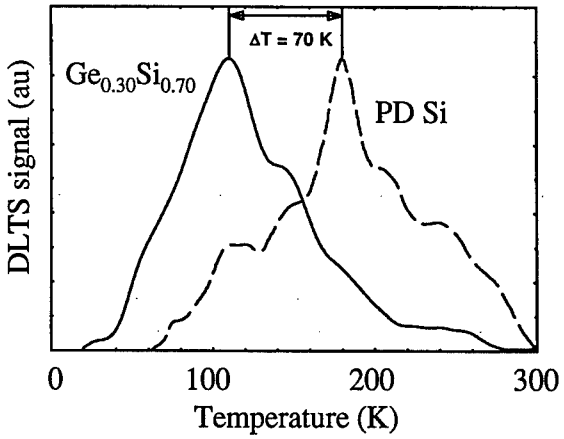


Figure 7. DLTS spectra of the 650 °C as-grown sample plotted along with previously published DLTS data obtained from PD-Si after ref. 12. The indicated 70 K difference in temperature corresponds to 0.12 eV, equivalent to the valence band offset between Si and relaxed $Ge_{0.30}Si_{0.70}$.

-relaxed Si as predicted by this simple model. The third column contains actual measured data detected from PD-Si which indicates an excellent match between the predicted and actual values for each level. This model implies that these levels do not follow the changing bandstructure as Ge mole fraction is changed; i.e. they are fixed in energy with respect to another reference, such

Table I: Hole trap energies in p-type $Ge_{0.30}Si_{0.70}$ and p-type PD Si. The predicted hole trap energy in PD Si is determined by adding 0.12 eV to the measured hole trap energy in $Ge_{0.30}Si_{0.70}$, the average change in bandgap between $Ge_{0.30}Si_{0.70}$ and bulk Si. PD Si data is from refs. 13-15. The H(0.20) trap, denoted by superscript a, is the dominant trap in the spectrum.

Measured hole trap in $Ge_{0.30}Si_{0.70}$ (eV)	Corresponding trap in PD Si (eV)		
trap energy	predicted	measured	difference
H(0.49 ± 0.02)	0.61	0.63	-0.02
H(0.43 ± 0.02)	0.55	0.56	-0.01
H(0.38 ± 0.02)	0.50	0.49	0.01
H(0.30 ± 0.02)	0.42	0.40	0.02
H(0.20 ± 0.02)[a]	0.32	0.35[a] 0.33[a]	-0.03 -0.01
H(0.15 ± 0.02)	0.27	0.26	0.01
H(0.05 ± 0.03)	0.17	0.21	-0.04

as the vacuum level [9]. Similar behavior has been reported for vacuum-referred deep states introduced by deep impurities in various III-V and II-VI semiconductor alloys where the deep states are not effective mass-like in nature and are not coupled to the band edges [17].

Not only do we observe a strong connection between the shallow hole traps between Si and SiGe, but we also find the same compositional behavior with regard to the electron traps detected in SiGe alloys. Figure 8a summarizes the position of electron traps within the relaxed GeSi bandgap detected not only in the 30% Ge alloys discussed here, but over the entire range of GeSi compositions (PD-Si and PD-Ge [18] data are included in the figure). Films having compositions other than 30% were grown at 850 °C and the behavior of the electron traps and their role as recombination-generation centers in GeSi diodes were analyzed in great detail in ref. 7. Figure 8b is a graphical summary of the hole trap data listed in Table I for PD-Si and 30%Ge alloys. In both figures 8a and 8b, the changing bandstructure of the Ge_xSi_{1-x} alloy was accounted for and we can see a general invariance of both electron and hole traps for the alloy system. This implies that the physical defects themselves, which include the dislocation core state and the point defect clusters, may be organized in a configuration that is a fundamental characteristic of dislocation structure and interaction in the Ge_xSi_{1-x} alloy system. It would be of great fundamental interest to investigate this last supposition further. From the point of view of potential physical sources for the shallow acceptor-like traps that dictate the electronic quality of the low temperature $Ge_{0.30}Si_{0.70}$ layers, this information strongly supports the notion of intrinsic point defect clusters formed by dislocation interactions as the physical source for these states.

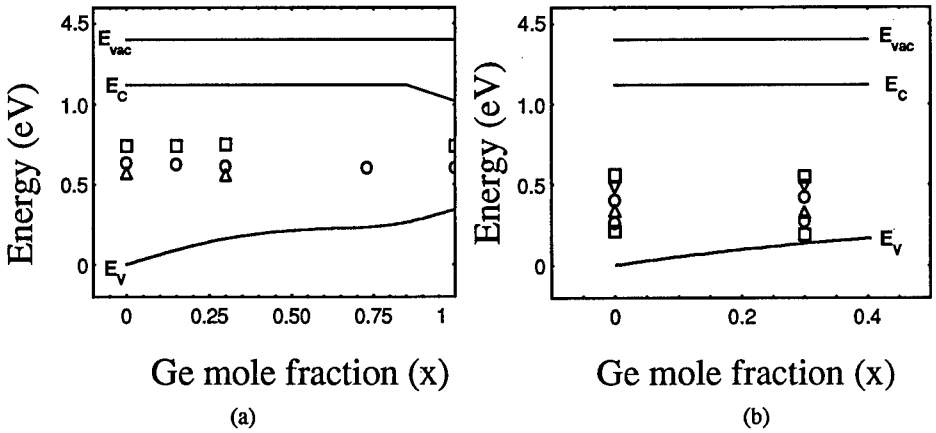


Figure 8. (a) Position of electron traps and (b) hole traps within the GeSi bandgap as a function of alloy composition in relaxed material. PD-Si data is from ref. 12 and 16, and PD-Ge data is from ref. 18. Each shape represents a single defect for the compositions measured.

CONCLUSIONS

In this paper we have systematically characterized deep levels in high structural quality GeSi layers grown and post-growth annealed at various temperatures. In all cases, very low threading dislocation density was maintained, along with low background doping to yield high DLTS sensitivity. In spite of the constant structural quality from the dislocation perspective, we have found there to be a strong dependence of electrical and optical properties on growth/process temperature in these layers. A series of acceptor-like hole traps H(0.05) - H(0.30) were detected by DLTS and subsequent annealing studies showed these states to be responsible for generally inferior electrical and optical properties of layers grown at 650 °C that include poor diffusion length, dopant compensation and type conversion, and broadened D-line luminescence. These defects were shown to anneal out above 800 °C, beyond which the only observable defect was the E(0.37) dislocation core state whose concentration ($2x10^{11}$ cm^{-3}) was found to be consistent with the $7x10^{5}$ cm^{-2} threading dislocation density determined by EBIC measurements. By comparison with PD-Si, PD-Ge and other compositions of GeSi layers grown by various methods, we have shown that the likely source of these defect states is intrinsic. We have proposed that these defects are introduced via a dislocation interaction mechanism which generates clusters of intrinsic point defects that are associated with the dislocations which anneal out to concentrations < 10^{10} cm^{-3} at 750 °C. Furthermore, DLTS measurements show that these defects introduce levels that are invariant with the Ge_xSi_{1-x} alloy composition from x = 0-1 indicating a possible characteristic defect configuration occurs for strain-relaxation in GeSi alloys. From this work we conclude that for high structural quality, low dislocation density relaxed GeSi layers, point defect generation due to dislocation interactions cannot be ignored as an important aspect of determining ultimate material quality for relaxed, low dislocation density GeSi layers grown on Si.

ACKNOWLEDGMENTS

The authors are grateful to E.A. Fitzgerald of MIT for supplying GeSi samples, J. Michel of MIT for assistance with PL and CL measurements and L.C. Kimerling of MIT for key discussions. This work was supported by NSF grant no. DMR-9458406 and an OSU Presidential Fellowship to PNG.

REFERENCES

1. R. Hull and J.C. Bean, Crit. Rev. Solid State Mater. Sci. **17**, 507 (1992).
2. E.A. Fitzgerald, Mater. Sci. Rep. **7**, 87 (1991).
3. Y.H. Xie, E.A. Fitzgerald, D. Monroe, G.P. Watson and P.J. Silverman, Jpn. J. Appl. Phys. **33**, 2372 (1994).
4. E.A. Fitzgerald, Y.H. Xie, D. Monroe, P.J. Silverman, J.M. Kuo, A.R. Kortan, F.A. Thiel and B.E. Weir, J. Vac. Sci. Technol. B **10**, 1807 (1992).
5. P.N. Grillot, S.A. Ringel, E.A. Fitzgerald, G.P. Watson and Y.H. Xie, J. Appl. Phys. **77**, 676 (1995).
6. P.N. Grillot, S.A. Ringel, E.A. Fitzgerald, G.P. Watson and Y.H. Xie, J. Appl. Phys. **77**, 3248 (1995).
7. P.N. Grillot, S.A. Ringel and E.A. Fitzgerald, J. Electron. Mater. **25**, 1028 (1996).
8. P.N. Grillot, S.A. Ringel, J. Michel and E.A. Fitzgerald, J. Appl. Phys. **80**, 2823 (1996).
9. P.N. Grillot and S.A. Ringel, Appl. Phys. Lett. **69**, 2110 (1996).

10. A. Souifi, G. Bremond, T. Benyattou, G. Guillot, D. Dutartre and I. Berbezier, J. Vac. Sci. Technol. B **10**, 2002 (1992).
11. J.C. Brighten, I.D. Hawkins, A.R. Peaker, R.A. Kubiak, E.H.C. Parker and T.E. Whall, J. Appl. Phys. **76**, 4237 (1994).
12. L.C. Kimerling ad J. R. Patel, in VLSI Electronics, ed. By N.G. Einspruch (Academic, Orlando, 1985), vol. **12**, p. 223.
13. C. Kisielowski-Kemmerich, G. Weber and H. Alexander, J. Electron. Mater. **14**, 387 (1985).
14. H. Alexander, in *Point and Extended Defects in Semiconductors*, edited by G. Benedek, A. Cavallini, and W. Schroter (Plenum, New York, 1989), p. 51.
15. H. Ono and K. Sumino, J. Appl. Phys. **57**, 287 (1985).
16. L.C. Kimerling, J.R. Patel, J.L. Benton, P.E. Freeland, Inst. Phys. Conf. Ser. **59**, 401 (1981).
17. M.J. Caldas, A. Fazzia and A. Zunger, Appl. Phys. Lett. **45**, 671 (1984).
18. F.H. Baumann and W. Schroter, Philos. Mag. B **48**, 55 (1983).

DISLOCATION-RELATED PHOTOLUMINESCENCE IN STRAIN-RELAXED $Si_{1-x}Ge_x$ BUFFER LAYER STRUCTURES

Kai Shum*[1], P. M. Mooney**, and J. O. Chu**
*Department of Electrical Engineering, The City College of the City University of New York, New York, NY 10031
**IBM Research Division, T. J. Watson Research Center, P. O. Box 218, Yorktown Heights, NY 10598

ABSTRACT

Low-temperature photoluminescence (PL) spectroscopy was used to study electronic states associated with threading dislocations (D lines) in strain-relaxed $Si_{1-x}Ge_x$ layers. The structures investigated were grown by ultra-high vacuum chemical vapor deposition (UHV/CVD) at 550 °C and consist of an Si(001) substrate followed by a step-wise graded buffer layer followed by a thick uniform composition $Si_{1-x}Ge_x$ layer. Variations in the PL intensity and peak position of the four D lines after isochronal annealing at temperatures between 600 and 800 °C have been measured. We show that the large energy shift of the D1 line is due to a change in the local band-gap energy at the dislocation core due to strain-driven diffusion of Ge away from the dislocation core with an activation energy of 2.4 eV.

INTRODUCTION

Step-wise graded $Si_{1-x}Ge_x$ layers grown on Si(001) substrates relax by the introduction of 60° misfit dislocations. The 60° dislocations dissociate into a 30° and a 90° partial dislocation separated by a stacking fault a few nanometers wide. Because such structures are used as buffer layers for field effect transistors (FETs)[1] or other devices [2], it is important to understand the behavior of the dislocations when these structures are exposed to temperatures typical of device fabrication processes. Photoluminescence (PL) spectroscopy at low temperature has been used to characterize the electronic states associated with dislocations (D lines) in pastically deformed bulk Si [3-5]. However, the microscopic origin of these lines, even in bulk Si, is still debated.

In this paper, we present low temperature PL data from uniform composition $Si_{1-x}Ge_x$ ($0 \le x \le 0.30$) layers grown on step-graded $Si_{1-x}Ge_x$ layers on Si(001) substrates by ultra-high vacuum chemical vapor deposition (UHV/CVD)[6]. The PL spectra show near band-edge recombination of no-phonon- and phonon-assisted excitons confined in three dimensional potential wells (alloy fluctuations) which have been discussed elsewhere [7]. The D-lines characteristic of dislocations are also observed. Here we present the variations of the PL intensity and peak position of the four D-lines after isochronal annealing at temperatures between 600 and 800 °C. The data show clearly that D1 is not a phonon replica of D2. We propose that the energy shift of the D1 line with annealing temperature is due to a change in the local band gap energy at the partial dislocation core due to strain driven diffusion of Ge away from the core. The activation energy for diffusion when x=0.25 is found to be 2.44±0.02 eV, consistent with other experiments [8,9].

[1]Work done while on special leave at the IBM T.J. Watson Research Center.

Mat. Res. Soc. Symp. Proc. Vol. 442 © 1997 Materials Research Society

SAMPLE PREPARATION AND EXPERIMENTAL APPARATUS

Samples for these experiments are Si(001) substrates having a step-graded $Si_{1-x}Ge_x$ layer followed by a thick uniform composition $Si_{1-x}Ge_x$ layer grown at 550 °C by UHV/CVD. The lattice mismatch strain in these structures is relieved by the formation of 60° dislocations. The misfit segments are located at the top of the silicon substrate, in the step-graded region and close to the bottom of the uniform composition layer. The threading arms extend up to the wafer surface through the uniform composition layer, which is probed in these experiments. Four different samples have been measured. The layer thickness for the x=0.17 and 0.30 samples is about 3.5 μm and about 1.1 μm for the x=0.25 sample. The x=0 sample was obtained by etching away a $Si_{0.85}Ge_{0.15}$ layer grown directly on a Si(001) substrate. Each wafer was cleaved into eight pieces. Seven of them were annealed at temperatures between 600 and 800 °C in N_2 gas for 10 min.

Our high-sensitivity PL apparatus was described previously [7], except that in this case the luminescence was collected by a lens in stead of a parabolic mirror to further enhance the collection efficiency. The samples were excited by the 457 nm line of an Ar^+ ion laser at normal incidence with an excitation area of 1 mm^2. The samples were immersed in liquid or gaseous helium. The sample temperature was measured using a calibrated silicon diode and could be varied continuously between 1.7 and 300 K. The PL was analyzed by a computer-controlled Fourier transform spectrometer and was detected by a liquid-N_2-cooled Ge detector. The measured PL spectra were corrected for the system's spectral response using a blackbody radiator at a known temperature.

RESULTS AND DISCUSSIONS

The PL spectra of the as-grown piece and the seven annealed pieces were measured under identical conditions. Fig. 1 shows the spectra of the x=0 samples taken at 4.2 K. Fig. 2(a) shows the energy position of the four D lines. The energy positions of the D2, D3, and D4 lines are essentially independent of the annealing temperature (T_a). A small shift in the energy of D1 is observed. The PL intensity of D1 and D2 decreases as T_a increases but that of D3 and D4 is constant. The linewidth of D1 and D2 both vary with T_a, as shown in Fig. 2(b). Since the energy separation between D1 and D2 depends on T_a and the variation of the line width with T_a of D1 is different from that of D2, we conclude that D1 is not a phonon-replica of D2. This conclusion is consistent with the experimental results of PL decay time measurements [10].

Fig. 3 shows the PL spectra of the x=0.25 samples taken at 4.2 K. This figure shows the large energy shift for D1 and D2 as T_a increases. The energy of D3 and D4 is essentially independent of T_a. The other two samples with x=0.17 and x=0.30 show similar behavior. Fig. 4 summarizes the energy shift of D1 as a function of T_a for the four samples studied. The dotted line indicates the energy position of 0.808 eV, the energy position of D1 at 4.2 K in plastically deformed bulk Si. It is clear in this figure that the energy of D1, which in as-grown samples varies with alloy composition, shifts continuously toward higher energy and, after annealing at 750 °C, is independent of the alloy composition. In the following discussion we focus on the energy shift of the D1 line.

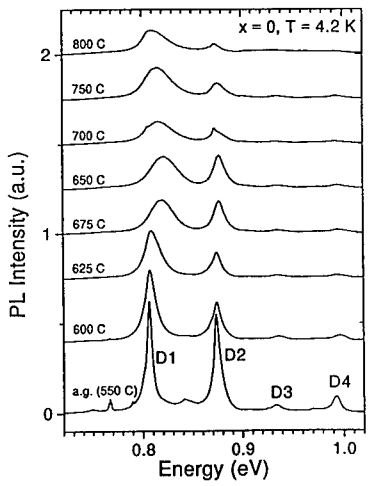


Fig. 1. PL spectra for the x=0 samples at various annealing temperatures.

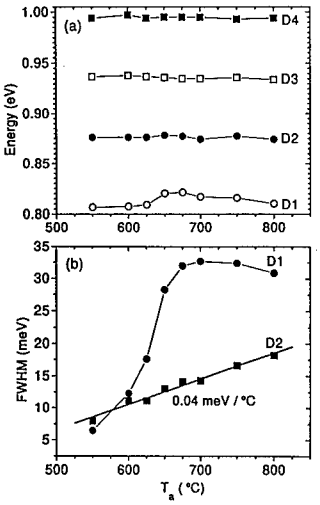


Fig. 2. (a) Energies and (b) linewidths (FWHM) of the D-lines vs. T_a for x=0.

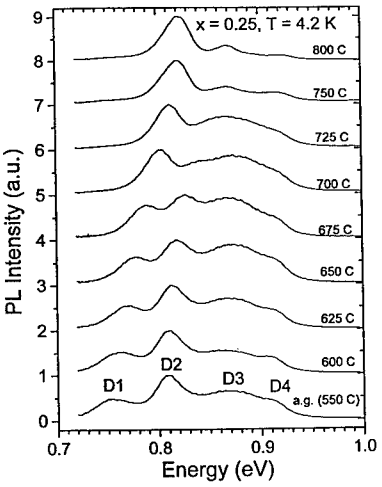


Fig. 3. PL spectra for the x=0.25 samples at various annealing temperatures.

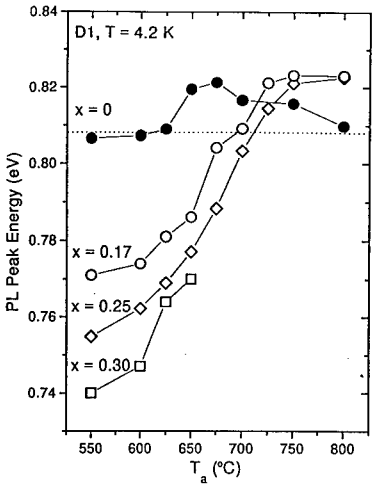


Fig. 4. Energy of D1 vs. T_a for different alloy compositions.

Here we propose a model to explain this interesting shift. In this model the D1 emission arises from radiative transitions involving electronic states spatially localized at the core of the partial dislocations. Batson has observed electronic states within the gap at the core of the 30° partial dislocation, but not at the center of the stacking fault, using spatially resolved electron energy loss measurements [11]. During annealing, Ge atoms move away from the dislocation core, resulting in an increase of the local band gap energy. This local band gap change shifts the D1 line toward higher energy as the annealing temperature increases. Energy shifts of the D1 and D2 lines having a $t^{3/2}$ dependence, where t is the annealing time, indicating Ge/Si diffusion on a nanometer scale have been reported previously [9].

To substantiate the model, let us start with Cottrell-Bilby's equation [12] on the change in concentration (ΔC) of Si or Ge atoms during the early stages of annealing:

$$\Delta C = C(x)\, 3(\pi/2)^{1/3}\, (ADt/kT_a)^{2/3}, \qquad (1)$$

where C(x) is the initial average atomic concentration which depends on the alloy composition x; D is the diffusion constant, which is assumed to be same for Ge atoms to diffuse away from and for Si atoms to diffuse toward the partial dislocation core; k is the Boltzman constant; and A is a constant, related to the unit cell volume difference between Si and Ge crystals, which has units of eV/cm^2. Based on the model, the energy shift of the D1 line [$\Delta E=E(T_a)-E(550\ °C)$] can be expressed as

$$\Delta E = E_g(x)[\Delta C/Co(x)] = E_g(x)\, 3(\pi/2)^{1/3}\, (ADt/kT_a)^{2/3}, \qquad (2)$$

where $E_g(x)$ is the band gap corresponding to the initial atomic concentration C(x). D can be written as:

$$D = D_0 \exp(-E_a/kT_a), \qquad (3)$$

where E_a is the activation for diffusion and D_0 is the diffusion coefficient. From Eq. (2) we have determined that $A=4\times10^{12}$ eV/cm^2 using the experimentally obtained value of $D_0=3.75\times10^{-7}$ cm^2/s from Ref. 8 along with our measured value of ΔE= 0.05 eV at T_a=750 °C, when x=0.25. We then uniquely fit the measured $\Delta E(T_a)$ with a single parameter, E_a.

In order to clearly show how the measured $\Delta E(T_a)$ follows the Arrhenius behavior of D, Eq. (2) is rearranged as

$$\Delta E(kT_a)^{2/3}=B \exp(-2E_a/3kT_a), \qquad (4)$$

where B is defined as $E_g(x)3(\pi/2)^{1/3}(AD_0t)^{2/3}$. Fig. 5 shows the variation of $\Delta E(kT_a)^{2/3}$ for the D1 line. The data for the D2 line is also displayed in this figure to show how the peak shift of D1 effects the movement of D2 as a function of T_a. Two conclusions can be drawn from this figure: (1) Data points for D1 at T_a<750 °C can be fit by Eq.(4) resulting in a diffusion activation energy of 2.44±0.02 eV, which is consistent with the values obtained in two other independent experiments [8,9]. This consistency confirms the model. (2) The apparent PL peak energy shift for the D2 line is due to the energy shift of the D1 line, which approaches D2, resulting in anti-crossing behavior at T_a= 675 °C. Fig. 6 demonstrates that the energy separation between D1 and D2 is a minimum at T_a=675 °C. This anti-crossing behavior rules out the proposal that D1 is a phonon-replica of D2,

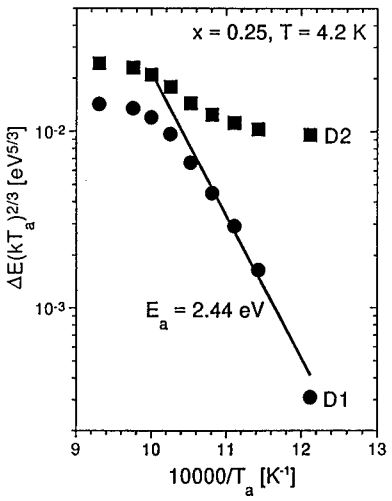


Fig. 5. Arrhenius plot showing the activation energy for Ge diffusion when x=0.25.

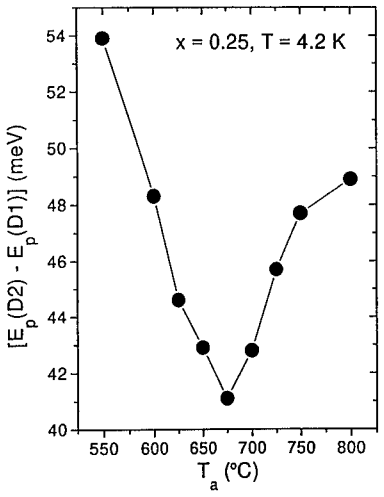


Fig. 6. Energy separation between D1 and D2 vs. T_a when x=0.25.

although it implies that electronic states associated with the D1 and D2 are strongly coupled and therefore must be spatially close to each other.

SUMMARY

In summary, we have presented PL data taken from strain-relaxed $Si_{1-x}Ge_x$ layers with $0 \leq x \leq 0.30$ grown on step-graded $Si_{1-x}Ge_x$ layers on Si(100) at a relatively low temperature of 560 °C by UHV/CVD. These data indicate that the D1 line originates from states at the core of the partial dislocations and is not a phonon replica of the D2 line. The energy shift of the D1 line is consistent with the diffusion of Ge atoms away from the core of the partial dislocations with a diffusion activation energy of 2.44 eV, when x=0.25.

ACKNOWLEDGEMENTS

We thank C.P. D'Emic for annealing these samples. This work was partially supported by a grant (No. F49620-93-1-0619) from AFOSR. Shum would like to thank B. S. Meyerson and A. Grill at IBM for their support.

REFERENCES

1. K. Ismail, S. Rishton, J.O. Chu, K. Chan, S.F. Nelson, and B.S. Meyerson, IEEE Electron Device Lett. EDL-**14**, 348 (1993).

2. E.A. Fitzgerald, Y.H. Xie, D. Monroe, P.J. Silverman, J.M. Kuo, A.R. Kortan, F.A. Thiel, and B.B. Weir, J. Vac. Sci. Technol. B **10**, 1807 (1992).

3. N.A. Drozdov, A.A. Patuin, and V.D. Tkachev, Sov. Phys. JETP Lett. **23**, 597 (1976).

4. V. Higgs, E.C. Lightowlers, C.E. Norman, and P. Knightley, Matr. Sci. Forum **83-87**, 1309 (1992).

5. J. Weber, Solid State Phenomena **37-38**, 13 (1994).

6. B.S. Meyerson, Appl. Phys. Lett., **48**, 797 (1986).

7. L.P. Tilly, P.M. Mooney, J.O. Chu and F.K. LeGoues, Appl. Phys. Lett. **67**, 2488 (1995).

8. P. Boucaud, L. Wu, C. Guedji, F.H. Julien, I. Saines, Y. Campidelli, and L. Garchy, J. Appl. Phys. **80**, 1414 (1996).

9. K. Tanaka and M. Suezawa, 7th Intl. Conf. on Shallow Levels in Semiconductors (Amsterdam, 1996).

10. S. Fukatsu, Y. Mera, M. Inoue, K. Maeda, H. Akiyama, and H. Sakaki, Appl. Phys. Lett. **68**, 1889 (1996).

11. P.E. Batson, Proc. of the Microscopy Society of America, ed. G.W. Bailey and M.N. Elliman, 1995, p.1995.

12. A.H. Cotrell and B.A. Bilby, Proc. Phys. Soc. A**62**, 49 (1949).

ROOM TEMPERATURE ELECTROLUMINESCENCE FROM D1 DISLOCATION CENTERS IN SILICON

EINAR Ö. SVEINBJÖRNSSON[a] AND JÖRG WEBER
Max-Planck-Institut für Festkörperforschung, Heisenbergstrasse 1, D-70569 Stuttgart, Germany

ABSTRACT

We report on electroluminescence at room temperature from forward biased n^+-p silicon diodes containing high densities (10^8-10^9 cm^{-2}) of dislocations at the junction interface. In addition to electroluminescence from band-to-band transitions, we observe a signal arising from the well known dislocation center D1 peaked at ~1.6 μm (0.78 eV). The D1 electroluminescence intensity at room temperature increases linearly with current density with no observable saturation as long as sample heating is avoided. The quenching of the D1 luminescence between 4 K and room temperature is highly sensitive to metal impurities which introduce competitive non-radiative recombination centers. The external power efficiency of the D1 electroluminescence was estimated to be of the order of 10^{-6}.

INTRODUCTION

Infrared light emission from silicon has recently received considerable attention. A significant progress has been made in obtaining electroluminescence (EL) at room temperature from erbium doped silicon devices [1-5] and other structures like SiGe that are compatible with silicon processing technology [6].

In this work we study luminescence from dislocations in silicon. Recently Kveder *et al* [7] reported dislocation-related electroluminescence at room temperature in plastically deformed silicon. No spectra were shown above 150 K but the authors attribute the light emission to the well known dislocation center D1. We have recently reported on such D1 electroluminescence at room temperature from laser melted silicon [8]. We find that such electroluminescence has comparable external efficiency to erbium doped devices when operated under forward bias.

The aim of this work is twofold. Firstly to investigate the feasibility of using the room temperature D1 emission in light emitting devices. Secondly, to compare the D1 luminescence with the erbium-related emission which occur at similar wavelengths (1.5 - 1.6 μm). This is important since dislocations are formed during the implantation of erbium into silicon and care must be taken to separate signals arising from the dislocations introduced and the implanted erbium ions.

EXPERIMENTAL

The starting material was high purity float-zone grown boron doped silicon wafers with resistivity of 20 Ωcm. The dislocations were generated after the sample surface had been melted using a high power (20 W) focused Ar^+ laser beam. The substrate was kept at room temperature while the beam was scanned over the wafer surface with a scanning speed of 10 cm/s. The separation between the recrystallized traces of the beam was approximately 40 μm. After recrystal-

[a] *Present address: Department of Solid State Electronics, Chalmers University of Technology, S-41296 Göteborg, Sweden.*

Mat. Res. Soc. Symp. Proc. Vol. 442 © 1997 Materials Research Society

lization such material has dislocation densities at the surface of approximately $2x10^9$ cm^{-2} estimated using transmission electron microscopy (TEM) [9]. This surface region extends to depths of 1-2 μm. Below the surface layer the dislocation densities are of the order of 10^8 cm^{-2} down to depths of 5 -10 μm. The two main types of dislocations observed are 60° dislocations that are dissociated into Shockley partials and straight 90° dislocations of the Lomer -Cottrell type [9].

After recrystallization, the samples used for the EL studies were pre-deposited with phosphorus on the dislocated side using solid diffusion sources. The diffusion temperatures were between 800 and 900°C with a duration of approximately 30 minutes. Prior to phosphorus diffusion the wafers were RCA cleaned to avoid metal surface contamination. Mesa structures were then fabricated by wet chemical etching. To investigate the effect of reduced surface recombination few samples were thermally oxidized at 900°C for 90 minutes resulting in an oxide thickness of 70 nm. Thereafter holes were etched in the oxide layer on the highly phosphorus doped side followed by evaporation of aluminum through a metal mask to achieve an ohmic contact. Gold was evaporated on the p-type substrate for ohmic contact.

The photoluminescence (PL) and EL studies were carried out in a cryostat cooled with liquid helium or nitrogen. The PL excitation was made by the Ar 514.5 nm laser line and the luminescence data were collected using a 1m SPEX monochromator and a nitrogen cooled germanium detector. The luminescence spectra are not corrected for the overall spectral response of the experimental set up.

RESULTS AND DISCUSSION

Photoluminescence (PL)

Figure 1 shows PL spectra taken at three different temperatures of a laser melted sample after subsequent phosphorus diffusion at 830°C for 25 minutes. At 4.2 K the strongest signals are the dislocation-related lines D1 and D2 [10] and the bound exciton TO emission (BE_{TO}). The dislocation lines D3 (at 0.95 eV) and D4 (at 0.99 eV) are also visible in the spectrum. At 77 K the dominant PL feature is the broad D1 signal at approximately 0.8 eV with D2 visible as a shoulder at 0.88 eV. No band-to-band transition is observed at 77 K. However, when the temperature is raised to 300 K two signals are present. The peak at 1.1 eV is due to band-to-band transitions while the peak at 0.78 eV is attributed to the D1 signal. The energy shift of the D1 line from 4.2 K to room temperature is ~ 30 meV compared to ~45 meV decrease of the silicon band gap. The D1 emission originates from the surface region where the dislocation density is highest and vanished if 14 μm were etched off the sample surface.

It should be noted that negligible D1 luminescence is observed at room temperature in samples directly after the laser melting of the surface [11]. However, heat treatment (or phosphorus diffusion) between 800 and 900°C enhances the room temperature D1 emission by two to three orders of magnitude while the intensity at 4.2 K remains unchanged. We attribute this to annealing of defects in the laser melted surface region resulting in a decrease of non-radiative recombination centers. We found that samples that were not RCA cleaned prior to the heat treatment or phosphorus diffusion did not show D1 luminescence at room temperature. However, these samples showed Cu contamination in form of Cu pair luminescence at 4.2 K [12]. This suggests that non-radiative recombination centers introduced by in-diffusion of impurities (Cu or other metals) from the sample surface are responsible for the lack of luminescence at room temperature.

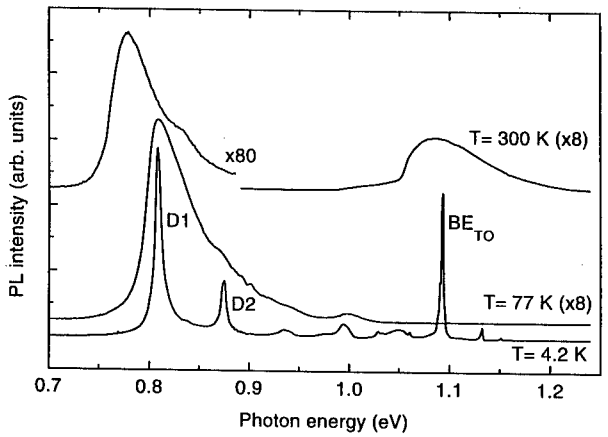


Figure 1. Photoluminescence spectra showing the evolution of the dislocation-related lines D1 and D2 with temperature. PL spectra at 4.2 K, 77 K, and room temperature from a laser melted sample after subsequent phosphorus diffusion at 830°C for 25 min. Argon ion laser excitation 150mW/mm^2. The spectra at 77 K and 300 K are scaled by the factors indicated. BE_{TO} denotes the bound exciton (boron) TO emission. The dislocation related lines D3 and D4 are also observed in the 4.2 K spectrum at ~ 0.88 eV and ~ 0.99 eV respectively.

In general we find that the thermal quenching of D1 is highly sensitive to the sample preparation, which may explain why most previous investigations have not revealed D1 emission at room temperature [10,13]. An example of this is shown in figure 2 which depicts the thermal quenching of D1 for three differently prepared samples. All samples exhibit similar D1 intensity at 4.2 K. We estimated the activation energy of the thermal quenching (above 50 K) using the expression:

$$I(T)/I(0) = [1+gT^{3/2}\exp(-E/kT)]^{-1} \qquad (1)$$

This expression is characteristic of dissociation of bound electron-hole pair into a conduction/valence band [10]. I(T) denotes the PL intensity, $BT^{3/2}$ accounts for the thermal dependence of density of states in the band and E is the characteristic dissociation energy. A similar equation describing thermal dissociation of localized electron-hole pairs between different bound states of the same center, does not contain the $T^{3/2}$ term [10]. The experimental error in the data shown in figure 2 is too large to distinguish between these two models although expression (1) gives a better fit to the data.

The key point is that we obtain substantially different thermal quenching energies depending on the sample preparation. This means that we are monitoring three different quenching processes in these samples which may not be related to the D1 emission at all. Instead it appears as if the PL quenching is determined by non-radiative recombination centers. We obtain an activation energy of 0.25 eV for the most thermally stable luminescence. Thermal quenching energies of D1 reported in literature are of the order of 10 meV [9,12] with the exception of recent work of Kveder et al [7] who obtain 0.15-0.16 eV using an expression similar to equation (1).

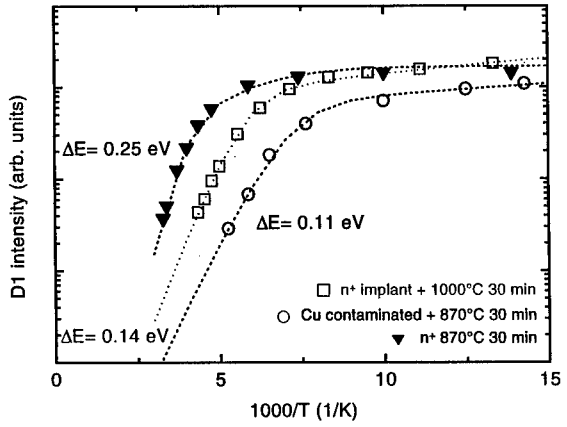


Figure 2. Thermal quenching of the D1 photoluminescence in three differently prepared samples. All samples received the same laser melting treatment and were then processed as follows: ▼ phosphorus diffusion at 870°C for 30 minutes, ○ annealing in argon ambient at 870°C for 30 minutes, □ Phosphorus implanted followed by annealing at 1000°C for 30 minutes. Sample 2) is unintentionally contaminated with copper. This is detected as Cu pair luminescence in the PL spectrum at 4.2 K.

Electroluminescence (EL)

Figure 3 shows EL spectra of a forward biased n^+-p junction diode at room temperature. The inset gives a schematic of the sample structure. The maximum EL intensity is obtained when emission is collected from the sample edge at the n^+-p junction. The n^+-p junction is located at a depth of approximately 0.4 μm and the phosphorus density at the surface is $1x10^{20}$ cm^{-3}. The diode was excited by a current source (duty cycle 50%) at a frequency of 67 Hz. The EL spectra look very similar to the PL spectra also at lower temperatures.

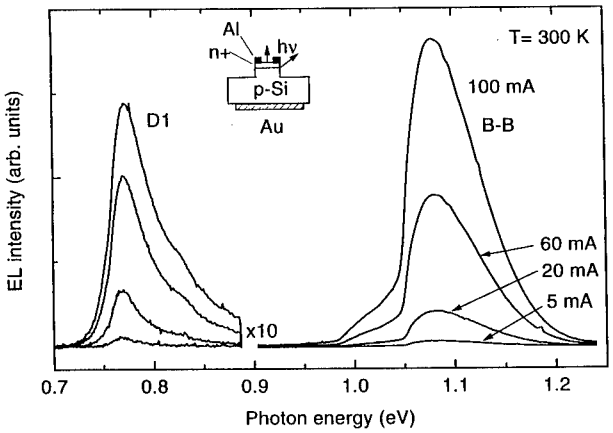


Figure 3. Electroluminescence spectra at 300 K from an n^+-p diode for different bias currents. The signal at ~ 1.1 eV is due to phonon assisted band-to-band transitions (B-B) while the peak at ~ 0.78 eV is assigned to the D1 dislocation center. The data shown were collected from the n^+-p junction on the side of the structure (see inset).

The intensity ratio between the band-to-band emission and D1 is very sensitive to temperature. Heating of the sample above room temperature results in saturation of the D1 intensity and a rapid increase of the band-to-band intensity. The D1 signal dominates for temperatures from 77 K and up to 260-270 K where the band-to-band emission becomes significant.

In order to decrease the surface recombination a few samples were thermally oxidized at 900°C after the mesa etching. The sample structure was the same as shown in the inset of figure 3 except the mesa etched region is covered with a 70 nm oxide layer. This results in an overall enhancement of the electroluminescence (typically by factor of five) although the ratio of the band-to-band emission and D1 varies from sample to sample. Figure 4 shows the integrated EL intensity of the band-to-band emission and the D1 signal as a function of the current density at room temperature. The D1 intensity increases approximately linearly with current density while the band-to-band emission shows a non-linear behavior. This is true as long as heating of the sample is avoided. Current densities above 5 A/cm^2 heat the sample, resulting in a saturation of the D1 signal and a rapid increase of the band-to-band signal.

In contrast to forward bias operation no electroluminescence is observed during reverse bias operation. Only a weak featureless background signal is detected when the reverse bias is close to the breakdown voltage (50-60 V).

We have estimated the D1 light output power at room temperature to be roughly 0.1-0.2 μW when exciting with electrical power of 150 mW [8] giving an external power efficiency of the order of 10^{-6}. This is comparable to the values reported for the band-to-band emission [14-15]. Concerning erbium doped silicon external quantum efficiencies of up to 10^{-5} have been reported during reverse bias operation [5]. However, under forward bias the efficiency is of the same order as the D1 emission on this study.

Although the erbium-related emission and the D1 signal are within similar photon energy range the signals should be easy to separate at room temperature. The D1 signal at room temperature is typically two or three times broader than the erbium peaks reported in literature [2-5]. Also, D1 is peaked at approximately 1.6 μm while the Er signal has a sharp characteristic peak at 1.54 μm. However, one should be more cautious at lower temperatures since there the D1 line coincides exactly in wavelength with the erbium-related emission.

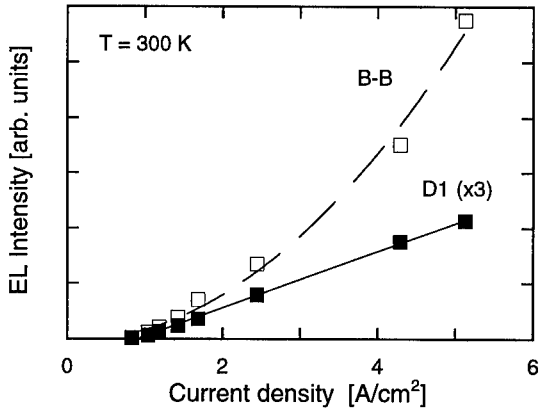


Figure 4. Integrated EL intensity of the band-to-band luminescence (B-B) and the D1 signal as a function of current density.

CONCLUSIONS

We find that high density of dislocations (10^8-10^9 cm^{-2}) in silicon can give rise to room temperature electroluminescence (EL) peaked at a wavelength of 1.6 μm. The origin of the luminescence is the well known dislocation center D1. The D1 line shifts from a wavelength of 1.54 μm to 1.6 μm when the temperature is raised from 77 K to room temperature. The intensity of the D1 electroluminescence at room temperature is comparable to the intensity of the phonon assisted band-to-band transition. This corresponds to an external power efficiency of the order of 10^{-6}.

ACKNOWLEDGEMENTS

We acknowledge H. J. Queisser for his interest and support of this work. We thank J. Vetterhöffer for helpful discussions as well as W. Heinz and W. Krause for technical assistance. B. Winter and R. Brendel are acknowledged for oxidations and phosphorus diffusions. Part of this work was financially supported by Chalmers University of Technology, Göteborg, Sweden.

REFERENCES

1. H. Ennen, G. Pomrenke, A. Axmann, E. Eisele, W. Haydl and J. Schneider, Appl. Phys. Lett. **46**, 381 (1985).
2. B. Zheng, J. Michel, F. Y. G. Ren, L. C. Kimerling, D. C. Jacobson, and J. M. Poate, Appl. Phys. Lett. **64**, 2842 (1994).
3. G. Franzò, F. Priolo, S. Coffa, A. Polman, and A. Carnera, Appl. Phys. Lett. **64**, 2235 (1994).
4. S. Coffa, G. Franzò and F. Priolo, Appl. Phys. Lett. **69**, 2077 (1996).
5. J. Stimmer, A. Reittinger, J. F. Nützel, G. Abstreiter, H. Holzbrecher, and Ch. Buchal, Appl. Phys. Lett. **68**, 3290 (1996).
6. H. Presting, T. Zinke, A. Splett, H. Kibbel and M. Jaros, Appl. Phys. Lett. **69**, 2376 (1996).
7. V. V. Kveder, E. A. Steinman, S. A. Shevchenko, and H. G. Grimmeiss, Phys. Rev. B **51**, 10520 (1994).
8. E. Ö. Sveinbjörnsson and J. Weber, Appl. Phys. Lett. **69**, 2686 (1996).
9. W. Staiger, G. Pfeiffer, K. Weronek, A. Höpner, and J. Weber, Mater. Sci. Forum **83-87**, 1571 (1994).
10. R. Sauer, J. Weber, J. Stolz, E. R. Weber, K.-H. Küsters, and H. Alexander, Appl. Phys. A **36**, 1 (1985).
11. E. Ö. Sveinbjörnsson and J. Weber, in Thin Solid Films (Proceedings of the E-MRS 1996 meeting, Strasbourg, France) in press (1996).
12. J. Weber, H. Bauch, and R. Sauer, Phys. Rev. B **25**, 7688 (1982).
13. M. Suezawa, Y. Sasaki, and K. Sumino, Phys. Stat. Solidi A **79**, 173 (1983).
14. C. Michaelis and M. H. Pilkuhn, Phys. Status Solidi **36**, 311 (1969).
15. T. C. Ong, K. W. Terrill, S. Tam, and C. Hu, IEEE Electron Dev. Lett. **EDL-4**, 460 (1983).

DISLOCATION VELOCITIES IN GeSi BULK ALLOYS

I. YONENAGA
Institute for Materials Research, Tohoku University, Sendai 980-77, Japan,

ABSTRACT

The mechanical strength and dislocation velocities in single crystal $Ge_{1-x}Si_x$ alloys grown by the Czochralski method were investigated by compressive deformation and by the etch pit technique, respectively. In the temperature range 450 - 700 °C and the stress range 3 - 20 MPa, the dislocation velocity in the GeSi alloys with $x = 0.004$ - 0.053 decreases monotonously with an increase in the Si content, reaching about a quarter of that in Ge at $x = 0.053$, and can be expressed as a function of the stress and the temperature. The yield stress of the GeSi alloy increases with increasing Si content from $x = 0$ to 0.4 and is temperature-insensitive at high temperatures, showing that the flow stress of alloy has an athermal component which is absent in elemental or compound semiconductors.

INTRODUCTION

The GeSi alloy is of interest in view of its variable band gap and lattice parameter according to the alloy composition. GeSi alloys for optoelectronic applications are mostly prepared as thin films on crystalline substrates by various epitaxial methods. Above the critical thickness, introduction of misfit dislocations is unavoidable in such hetero epitaxial structures. Very little is known on the dynamic properties of dislocations in alloy semiconductors except the generation of misfit dislocations related to the mismatch at the film/substrate interface. Few groups measured the velocity of misfit and threading dislocations in GeSi films grown by molecular beam epitaxy [1-6]. However, there exists some uncertainty due to that dislocations were activated with the unrelaxed biaxial stress in thin films on substrates. To obtain reliable data, it is necessary to measure the velocities of isolated dislocations in crystals under defined stress distribution. Dynamic properties of dislocations in a GeSi system have often been assumed to be similar to those in Si or Ge crystals. Little attention has been paid to the unique properties of dislocations that appear due to alloying. It has been reported that the flow stresses of GaAsP and InAsP alloys have the athermal component that is absent in compounds of GaAs, GaP, InAs and InP [7,8]. It is of interest to investigate the mechanical behavior of the GeSi alloy and to extract the unique dislocation process that is brought about by alloying.

Recently, we succeeded in growing GeSi bulk crystals by the Czochralski technique [9]. This has made it possible to investigate the dislocation velocities and the mechanical properties of GeSi alloys to compare them with those of elemental Ge and Si crystals. This paper reports the velocities of dislocations and the mechanical behavior in $Ge_{1-x}Si_x$ with $x = 0.004$ - 0.053 and with $x = 0.1$ - 0.4, respectively.

EXPERIMENT

Bulk $Ge_{1-x}Si_x$ crystals were grown by the Czochralski method. The details of the growth procedure and apparatus are described elsewhere [9]. The composition of grown crystals was determined by energy dispersive X-ray spectroscopy.

Dislocation velocities were measured on the GeSi with Si contents up to $x = 0.053$. Rectangular specimens of 2 x 3 x 15 mm^3 in size with the long axis along the $[\bar{1}10]$ direction and side surfaces parallel to the (111) and $(11\bar{2})$ planes were finished by chemical polishing with a reagent of $5HNO_3$:1HF at 30 - 40°C. The specimen was stressed at elevated temperature by three-point bending in a vacuum. The bending axis was parallel to $[11\bar{2}]$ direction. Dislocations were generated from a scratch drawn on the (111) surface along the long axis at room

Mat. Res. Soc. Symp. Proc. Vol. 442 © 1997 Materials Research Society

temperature with a diamond stylus. Displacements of dislocations due to stressing were measured by the etch pit technique with the Billig etchant [10] at 80°C.

The mechanical properties were investigated on the GeSi with Si contents up to x = 0.4. Rectangular specimens of 2.7 x 2.7 x 10.7 mm^3 in size with the stressing axis along the [123] direction and the side surfaces parallel to the (111) and (541) planes were finished by the chemical polishing. Compression tests were conducted under a constant strain rate using an Instron-type machine at elevated temperatures.

The dislocation velocities and the mechanical strength of crystals of high purity Ge and Si with grown-in dislocation densities of about 10^4 cm^{-2} were compared with those of the alloys.

RESULTS

Crystal Growth

Figure 1 shows the $Ge_{1-x}Si_x$ boule grown from a melt of initial composition x_{m0} = 1.0 at%. The pulling direction was <100> and pulling rate was 1.0 mm/h. Four {111} facets confirm the growth of single material up to the tail. The crystal is 40 mm in length. The composition at the growth starting position was x_0 = 0.06 and changed to low Si content along the growth direction due to the preferential consuming of Si atoms from the melt during the growth. A full single crystal 20 mm in diameter and 60 mm in length with variable composition $0.004 < x < 0.03$ along the growth direction of <111> was also successfully obtained with the pulling rate 2.0 mm/h.

With an increase in Si composition, the crystals changed from single material to polycrystal in the middle part of the boule, which may relate to the occurrence of constitutional supercooling.

The density of native dislocations in the grown crystals revealed by the etch pit technique was in the range of 10^3 - 10^5 cm^{-2}.

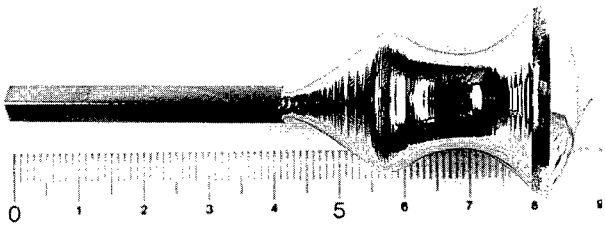


Fig. 1. $Ge_{1-x}Si_x$ alloy crystal grown by the Czochralski method. The composition at the start of growth is x = 0.06.

Dislocation Velocity

Dislocations were generated preferentially from a scratch drawn on the surface. The velocity was measured as a function of the temperature in the range 450 - 700°C and of the resolved shear stress in the range 3 - 20 MPa. Figure 2 shows how the velocity of 60° dislocations at 450°C under a shear stress of 20 MPa depends on the composition of the GeSi alloy. It is seen that the velocity of dislocations in $Ge_{1-x}Si_x$ decreases monotonously with an increase in the Si content and reaches about a quarter of the velocity of those in pure Ge at a Si content of 0.053. Figure 3 shows the velocities of 60° dislocations at various temperatures plotted against the shear stress in $Ge_{1-x}Si_x$ alloys with x = 0.016 and 0.047 together with that in pure Ge. As seen in the figure, the logarithm of the velocity of dislocations is linear with respect to the logarithm of the stress at all temperatures and for all Si contents with approximately the same slope.

As in other semiconductors, the velocity v of 60° dislocations in the $Ge_{1-x}Si_x$ alloys with x = 0.004 to 0.053 can well be expressed as a function of the stress τ and the temperature T by the empirical equation:

$$v = v_0 (\tau / \tau_0)^m \exp(- Q / k_B T), \qquad (1)$$

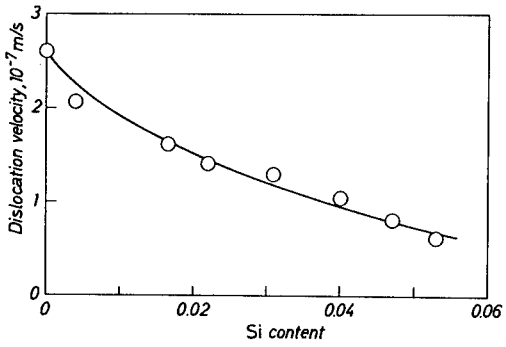


Fig. 2. Velocities of 60° dislocations in the GeSi alloys at 450°C under a shear stress of 20 MPa as dependent on the Si content.

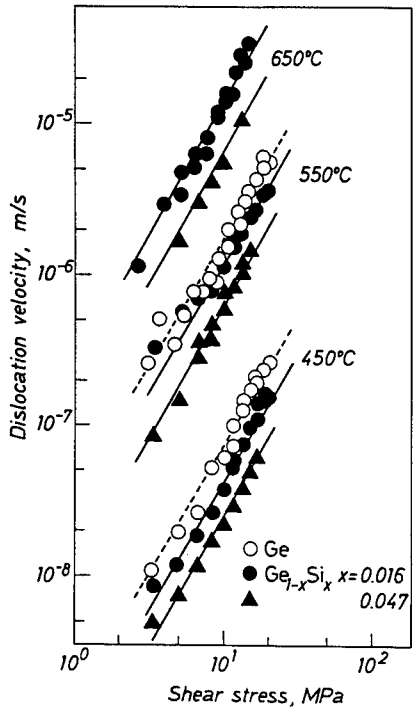


Fig. 3. Velocities of 60° dislocations in the GeSi alloys with various Si contents at 450, 550 and 650°C as dependent on the shear stress together with those in Ge.

Table I. Magnitudes of v_0, m and Q for 60° dislocations in $Ge_{1-x}Si_x$ and pure Ge.

Crystal	v_0 (m/s)	m	Q (eV)
Ge	2.9×10^2	1.7	1.62 ± 0.05
$Ge_{1-x}Si_x$ ($x = 0.016$)	4.6×10^2	1.7	1.68
($x = 0.047$)	2.8×10^2	1.7	1.68

where τ_0 = 1 MPa and k_B is the Boltzmann constant. The experimentally determined magnitudes of v_0, m and Q in GeSi and Ge are given in Table I. The magnitudes of the parameters m and Q in Eq. (1) in the alloy are same as those in Ge or only slightly different. This may be due to rather small Si contents in the alloys investigated.

Mechanical Strength

Stress-strain behavior of GeSi crystals with Si contents up to x = 0.4 was investigated at various temperatures under a shear strain rate of 1.8 x 10^{-4} s^{-1}. Figure 4 shows the stress-strain curves of the GeSi alloy with x = 0.10. At temperatures lower than 600°C the stress-strain curves of the specimens were characterized by a stress drop, followed by an increase in the stress with strain. Such a stress drop after the upper yield point is commonly observed for various semiconductors, such as Si, Ge, GaAs etc. at relatively low temperatures. On the contrary, at temperatures higher than 700°C, no stress drop is seen in the stress-strain curves and the yield stress becomes constant.

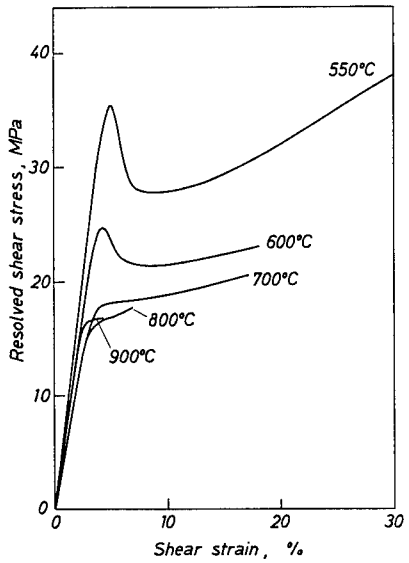


Fig. 4. Stress-strain curves of $Ge_{1-x}Si_x$ alloys with x = 0.10 at various temperatures under a strain rate of 1.8 x 10^{-4} s^{-1}.

The lower yield stresses for GeSi alloys with x = 0.01, 0.04, 0.10 and 0.40 and also those of Si and Ge for comparison sake are plotted against the reciprocal temperature in Fig. 5 for the deformation under a shear strain rate of 1.8 x 10^{-4} s^{-1}. The logarithms of the yield stresses in Si and Ge are linear with respect to the reciprocal temperature in the whole temperature range investigated. The same holds in a limited temperature range of 500 - 700°C for the alloy of x = 0.01 and in a range of 550 - 600°C for the alloy of x = 0.04 and 0.10. In such temperature ranges the yield stresses of the alloys are close to that of Ge. The temperature dependencies of the yield stresses of the alloys become much weaker in a high temperature range. This temperature range expands toward the low temperature side with an increase in the magnitude of x. Thus, the yield stresses of GeSi alloys are nearly constant with respect to the temperature and much higher than that of Ge. Siethoff observed the temperature dependence of lower yield stress of Si crystals doped with Ge up to 1.6 at.% to be similar to that of pure Si [11]. This may be attributed to rather low Ge content and also to the fact that deformation temperature was too low to render the temperature-independent yield stress appreciable in their SiGe alloys. The yield stress of GeSi alloys increased with increasing Si content in the investigated composition range x = 0 - 0.4 and seems to show the maximum in the range x = 0.5 - 1.0.

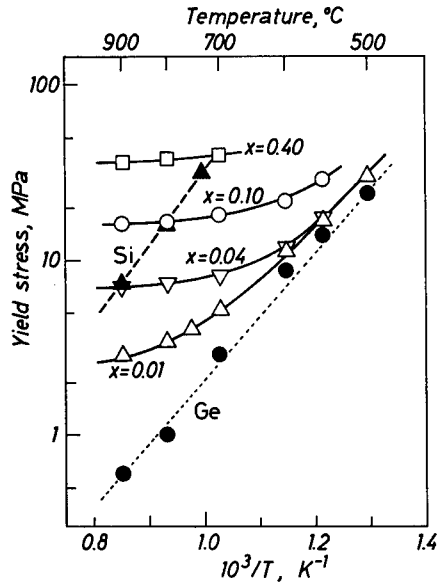


Fig. 5. Yield stresses of the GeSi alloys plotted against the reciprocal temperature for deformation under a strain rate of 1.8×10^{-4} s^{-1}.

DISCUSSION

The velocity of isolated dislocations in the GeSi alloys with $x = 0.004$ - 0.053 is observed to be a little lower in the temperature range 450 - 700°C than that in Ge crystals. This may account for rather small difference in the yield stresses of the alloys of such compositions and of Ge observed in such a temperature range. However, the difference in the dislocation velocity among various compositions of GeSi alloys seems to not account for drastic difference in the mechanical strength of the alloys at high temperatures.

The flow stress of a crystal in any deformation stage consists of two components. One is the effective stress that is necessary to move dislocations at a certain velocity against the intrinsic resistance of the crystal via a thermally activated process. The other is the athermal stress that is the component necessary to overcome any resistance not thermally surmountable and depends weakly on temperature. If we assume that alloying results in a drastic increase of the Peierls potential and brings about the reduction of dislocation velocity, we can expect that yielding with a stress drop should be more remarkable in the GeSi alloy than in the Ge. Furthermore, the strengthening effect related to alloying should diminish as the temperature is increased. Neither is in agreement with the experimental results in this work. The variation in the yield stress with temperature in the GeSi alloys seen in Fig. 5 can be interpreted to show that the flow stress of the alloy has an athermal stress component that is absent in Ge and Si. The athermal stress component seems to become large with an increase in Si content up to $x = 0.5$. It is reasonable to suppose that the athermal stress is related to the alloying effect.

There are a few possible origins for athermal stress related to alloying, as discussed in the cases of GaAsP and InAsP [7,8]. The first is short-range order of the $L1_1$ structure reported in strained layer superlattices prepared by molecular beam epitaxy [12]. Motion of a dislocation destroys the short-range order along its slip plane, which results in an extra stress of athermal nature. However, it is considered difficult to detect ordered structure in bulk GeSi alloys [13]. The second is long-range stress related to the local fluctuations of the alloy composition in a crystal. Since the bond lengths of Si and Ge differ by about 4 %, a large stress field may be introduced in the crystal if the alloy composition is not homogeneous on atomic scale. The

dislocation cannot surmount such a long-range stress field via a thermally activated process. The third is related to the dynamic development of a solute atmosphere around dislocations during deformation. An extra stress, apparently athermal nature, is needed to release the dislocations from solute atmosphere. Either or both of the local fluctuation of alloy composition or/and dynamic development of solute atmosphere around dislocations are thought to be the causes for the strengthening of bulk GeSi alloys at elevated temperatures.

Dislocations move in such built-in athermal stress fields in alloy semiconductors, which should affect their activities. Such effect on dislocation velocities cannot be detected in the investigated GeSi alloys for rather low Si contents, which is a task in the future.

CONCLUSION

The mechanical strength and the dislocation velocities in single crystal $Ge_{1-x}Si_x$ alloys grown by the Czochralski method were investigated. The dislocation velocity in $Ge_{1-x}Si_x$ with x = 0.004 - 0.053, which reaches about a quarter of that in Ge at x = 0.053, can be expressed by the empirical equation as a function of the stress and the temperature. The stress-strain behavior in the yield region of the GeSi alloys is similar to that of Ge and Si in the temperature range lower than about 600°C. The yield stress of the alloys is temperature-insensitive at high temperatures and increases with increasing Si content from x = 0 to 0.4, which is originating from alloy hardening.

ACKNOWLEDGMENTS

This work has been done in collaboration with Professor K. Sumino. The author wishes to gratefully acknowledge him.

REFERENCES

1. G. G. Tuppen and C. J. Gibbings, J. Appl. Phys. **68**, 1526 (1990).
2. D. C. Houghton, Appl. Phys. Lett. **57**, 2124 (1990).
3. R. Hull, J. C. Bean, D. Bahnck, L. J. Peitcolas, K. Short and F. C. Unterwald, J. Appl. Phys. **70**, 2052 (1991).
4. Y. Yamashita, K. Maeda, K. Fujita, N. Usami, K. Suzuki, S. Fukatsu, Y. Mera and Y. Shiraki, Phil. Mag. Lett. **67**, 165 (1993).
5. R. Hull, J. C. Bean, L. J. Peitcolas, B. E. Weir, K. Prabhakaran and T. Ogino, Appl. Phys. Lett. **65**, 327 (1994).
6. D. D. Perovic and D. C. Houghton in Microscopy of Semiconducting Materials 1995, edited by A. G. Cullis and A. E. Staton-Bevan (IOP Publishing, Bristol, 1995) pp. 117-134.
7. I. Yonenaga, K. Sumino, G, Izawa, H. Watanabe and J. Matsui, J. Mater. Res. **4**, 361(1989).
8. I. Yonenaga and K. Sumino in 8th Symposium Record of Alloy Semiconductor Physics and Electronics, edited by A. Sasaki (Organization of Special Project Research on Alloy Semiconductor Physics and Electronics, Kyoto, 1989) pp. 187-194.
9. I. Yonenaga, A. Matsui, S. Tozawa, K. Sumino and T. Fukuda, J. Crystal Growth **154**, 275 (1995).
10. P. R. Camp, J. Electrochem. Soc. **102**, 586 (1955).
11. H. Siethoff, Mater. Sci. Eng. **4**, 155 (1969).
12. A. Ourmazd and J. C. Bean, Phys. Rev. Lett. **55**, 765 (1985).
13. D. Stenkamp and W. Jäger, Phil. Mag. **A65**, 1369 (1992).

INFLUENCE OF SUBSTRATE OFF-CUT ON THE DEFECT STRUCTURE IN RELAXED GRADED Si-Ge/Si LAYERS

SRIKANTH B. SAMAVEDAM[1], F. ROMANATO[2], M. S. GOORSKY[3], E. A. FITZGERALD[1]

[1]Department of Materials Science and Engineering, Massachusetts Institute of Technology, Cambridge, MA 02139.
[2]INFM-Department of Physics "G. Galilei", University of Padova, via Marzolo 8, Padova, Italy.
[3]Department of Materials Science and Engineering, University of California, Los Angeles, CA 90095.

ABSTRACT

Relaxed graded Si-Ge/Si layers can be used in a variety of micro-electronics applications such as templates for III-V/Si integration, in high speed field effect transistor (FET) structures and as detectors in optical communication. Each of these applications requires a different final Ge concentration in the graded Si-Ge layer. With increasing Ge content in the graded layer, some of the materials concerns that need to be addressed are- (i) a high surface roughness, (ii) the formation of dislocation pile-ups, and (iii) an increase in the threading dislocation density. We have shown that there is a substantial improvement in the surface roughness and the dislocation pile-up density of the graded Si-Ge layers by depositing on (001) 6° off-cut substrates. The substrate miscut also facilitates favorable intersections of {111} planes that aid reactions between the 60° dislocations to form edge dislocations with Burgers vectors of the type 1/2<110> and <100> resulting in a novel hexagonal dislocation structure. Such reactions occurred more readily in the Ge-rich regions of the graded layers where the growth temperature was high enough to aid dislocation climb. The edge dislocations with in-plane Burgers vectors lack a tilt component and the decreased rate of tilting in the Ge-rich regions is confirmed by triple crystal X-ray reciprocal space maps. This novel dislocation structure offers opportunities to explore new processes which may eliminate spatially variant strain fields in relaxed epitaxial layers.

INTRODUCTION

Good quality strain-relaxed silicon-germanium (Si-Ge) alloys grown on silicon (Si) substrates have several micro-electronics applications. The larger lattice constant of relaxed Si-Ge provides a pseudo-substrate for III-V/Si-Ge/Si hetero-integration [1]. The higher carrier mobility of Ge and the possibility of band-gap engineering using strain, make these materials attractive for high speed device applications [1-3]. High Ge Si-Ge layers and super-lattice structures grown on relaxed $Si_{0.5}Ge_{0.5}$ can be used to make photo-detectors integrated on Si for optical communications [4].

Growing relaxed uniform layers of Si-Ge on Si results in a dislocation structure with short misfit segments and a high density of deleterious threading dislocations due to high dislocation nucleation rates. Over the years, the most successful technique for growing low-threading density relaxed Si-Ge/Si layers has been high temperature relaxed grading [5]. In the growth of relaxed graded structures, at any given time the misfit strain is small and hence, so is the dislocation nucleation rate. Further, a high growth temperature promotes easy glide

Mat. Res. Soc. Symp. Proc. Vol. 442 © 1997 Materials Research Society

of threading dislocations. The final result is a dislocation structure with long misfit segments and a low threading dislocation density. Completely relaxed Ge-Si layers with low dislocation densities have also been quoted for extremely fast grades at lower temperatures [5]. The strain fields associated with the misfit dislocations result in the characteristic <110> oriented cross-hatch pattern on the epilayer surface in Si-Ge/Si(001) growth [7]. These surface features are quite distinct from the short wavelength <100> oriented surface ripples that are observed in thin elastically strained Si-Ge/Si [8-10]. In relaxed graded Si-Ge/Si structures, the roughness associated with the long wavelength cross-hatch pattern leads to formation of dislocation pile-ups and an increased threading dislocation density under continued relaxation [11].

In this paper, we show that by growing on an (001) off-cut substrate, there is a substantial improvement in surface roughness and dislocation pile-up density. Growth on a miscut (001) substrate usually produces an epilayer that is tilted to reduce the substrate off-cut [12,13]. We have studied the tilt of the relaxed graded Si-Ge layers using triple axis X-ray diffractometry and observe that there is a decrease in the rate of tilting in layers with high Ge. TEM studies of the high Ge alloy regions of the relaxed graded structure reveal a new hexagonal edge dislocation network composed of 1/2<110> and <100> Burgers vectors with no tilt component normal to the growth surface. The decreased rate of epilayer tilt is explained by the formation of this novel hexagonal network.

EXPERIMENT

Relaxed graded Si-Ge/Si layers were grown on 2-inch (001) and (001) 6° off-cut (towards in-plane <110>, say [110]) n-Si substrates using ultra-high vacuum chemical vapor deposition (UHVCVD). The Si-Ge layers were grown at temperatures in the range of 800°-900° C and graded at 10% Ge/μm. Due to the high growth pressure used in our system, we were able to obtain growth rates in the range of 18-25 Å/sec. A 2μm uniform cap layer with the same composition as the final graded layer was grown above the graded region.

The surface morphology of the samples were characterized using atomic force microscopy (AFM) in the contact mode. EBIC was used to characterize electrically active threading dislocations and dislocation pile-ups. Threading dislocations gliding on {111} planes interact with orthogonal misfit dislocations [14] and deep trenches from the cross-hatch pattern [11] lying in their path and get blocked creating dislocation pile-ups on {111} planes. Such pile-ups appear in plan view EBIC as dark bands of recombination centers. The dislocation pile-up density was determined by the number of intersections per unit length of the sample surface. The epilayer tilt and the degree of strain relaxation was determined using triple axis X-ray diffractometry. Reciprocal Space Maps (RSMs) around (004) and (224) points of the reciprocal lattice with the diffraction plane parallel to both in-plane <110> directions were collected. The dislocation structure in different regions of the graded structure was characterized using plan view transmission electron microscopy (TEM).

RESULTS AND DISCUSSION

Fig. 1 shows a plot of rms roughness (in nm) and dislocation pile-up density (in no./cm) plotted for two sets of samples, Ge/Si-Ge(graded)/Si(001) exact and Ge/Si-Ge(graded)/Si(001) miscut (6° off towards in-plane [110]) substrate. For each set of samples data along the two in-plane <110> directions are shown. It is clearly seen that there is a

substantial reduction in rms roughness and dislocation pile-up density for the sample grown on the off-cut substrate compared to growth on the on-axis substrate.

It is known that the formation of the cross-hatch pattern is related to misfit dislocation strain fields [1,7]. In graded structures, the surface morphology of the top surface is the response of growth surface to multiple strain fields from inhomogeneous distributions of misfit dislocations at various interfaces below. In low-mismatched hetero-epitaxy on an on-axis (001) substrate the 60° dislocations that relieve misfit lie along the two in-plane <110> directions. Thus they form long parallel arrays of misfit dislocations along the two <110> directions. On a miscut substrate, 60° dislocations gliding on complementary {111} planes along a miscut <110> direction tend to come towards each other in the (001) plane and finally intersect [15]. Fig. 2 shows a TEM image of a 60° misfit dislocation array from a Ge/Si-Ge(graded)/Si(001) miscut (6° off towards a [110]) sample. It is seen that 60° dislocations gliding along the miscut [110] direction tend to have intersecting paths whereas the dislocations gliding along the [1-10] direction lie parallel to each other. Therefore, it is not possible to form long parallel arrays of misfit dislocations along the miscut [110] direction. Without close, parallel misfit dislocations, the strain fields at any given point above the misfit interface are less than those in the on-axis sample. Hence, rms roughness is reduced for the miscut sample.

Dislocation pile-ups are observed only in samples graded up to higher Ge concentrations. By comparing the SEM and plan-view EBIC images of the same area it is easy to see that the dislocation pile-ups form primarily along rare deep trenches in sample. In low-mismatched interfaces, it has been shown that a threading dislocation can be blocked by a perpendicular misfit dislocation [14]. However, this model cannot explain the formation of dislocation pile-ups except in very low mismatched cases. We have proposed a model based on both dislocation blocking and the effect of the maximum trench depth of the cross-hatch pattern that explains the formation of dislocation pile-ups in high mismatched and the moderately mismatched graded interfaces [11]. The trenches in the cross-hatch pattern that are deeper than a critical h^* can effectively block threading dislocations and form dislocation pile-ups. In the off-cut sample there are fewer deep trenches and hence fewer dislocation pile-ups. Secondly, it is difficult to create a long wall of blocking stress fields that can stop the gliding threading dislocations when the dislocations tend to lie along intersecting paths as in Fig. 2 . Further details of dislocation pile-up and surface morphology interactions are discussed elsewhere [11].

Fig. 3a shows a (004) RSM of a Ge/Si-Ge(graded)/Si(001) 6° off-cut sample with the diffraction plane perpendicular to the miscut [110] direction. The RSM in Fig. 3a is similar to the RSMs of the on-axis sample obtained with the beam along each of the <110> directions. In Fig. 3a the substrate Si peak and the epilayer Ge have approximately same $q_{<110>}$ value indicating that there is no epilayer tilt about the miscut [110] direction. This observation is confirmed by the (224) RSM of the same sample under a similar diffraction configuration. Measurement of $\varepsilon_{\parallel}$ and $\varepsilon_{\perp}$ of the Ge peak using the (224) RSM indicates that the graded layers are almost completely relaxed. Fig. 3b shows a (004) RSM of the same sample as in Fig. 3a, with the diffraction plane parallel to the miscut [110] direction. It is seen that the graded layer is tilted away from the Si(001) 6° off-cut peak so as to reduce the epilayer miscut. The net tilt of the graded layer with respect to the Si substrate is ≈1.6°. We determined the epilayer tilt as a function of the graded layer composition using the corresponding (224) RSM. The rate of epilayer tilting changed from ≈0.017°/%Ge to ≈0.011°/%Ge at about 71%Ge. The component of the Burgers vector of 60° dislocation perpendicular to the interface, b_z, is responsible for the epilayer tilt and therefore a change in the tilting corresponds to a change in the Burgers

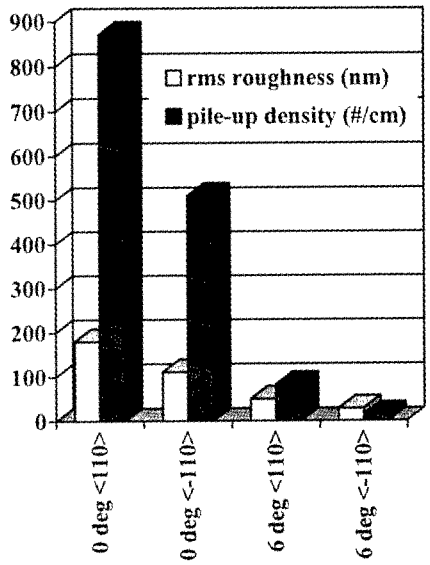


Fig. 1. A plot showing the rms roughness and dislocation pile-up density data for on-axis (0 deg.) and miscut (6 deg.) Ge/Si-Ge/Si(001) samples.

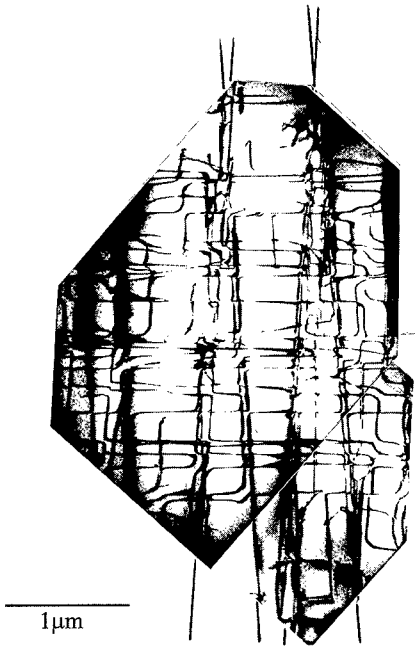


Fig. 2. A TEM image of the 60° dislocation array in a Ge/Si-Ge/Si(001) 6° off-cut (towards [110]) sample showing dislocations along the miscut [110] direction gliding along intersecting paths.

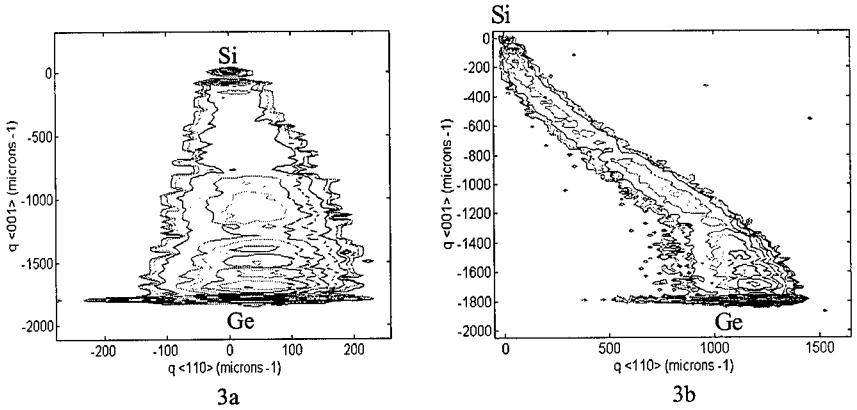


Fig. 3. Reciprocal space maps (RSMs) of Ge/Si-Ge(graded)/Si(001) 6° miscut sample. In (a) the diffraction plane is perpendicular to the miscut [110] direction. In (b) the diffraction plane is parallel to the miscut [110] direction. The RSM in (a) is very similar to the RSMs of the on-axis Ge/Si-Ge/Si(001) sample taken along any of the <110> directions.

vector population. The 60° dislocation that generally forms to reduce misfit in low mismatch systems has b_z oriented either "up" or "down" depending up on its inclination to the (001) growth surface. On an on-axis sample there are equal number of 60° dislocations with opposite tilt components such that the epilayer does not have a net tilt. An asymmetric population of dislocations with opposite tilt components causes the epilayer to tilt away from the substrate orientation [12,13,16]. If it is assumed that the graded layers are relaxed entirely by 60° dislocations, one can determine the number of dislocations with either kind of tilt as a fraction of the total number of dislocations, knowing the rate of epilayer tilt [13]. In the sample graded up to 100%Ge we find that the fraction of dislocations with "tilt-up" is ≈0.78N below 71%Ge and ≈0.65N above 71%Ge, where N is the total number 60° dislocations. This indicates that there must be a change in dislocation structure in the higher Ge regions of the graded structure. To investigate this further, we examined the dislocation structure in different regions of the graded buffer using plan view TEM.

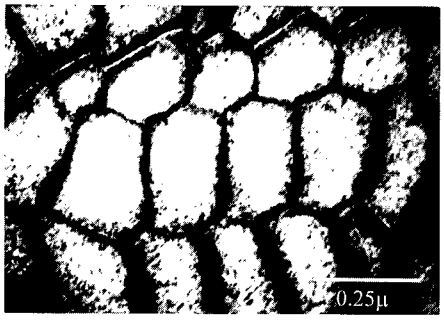


Fig. 4. A plan view TEM micrograph of the dislocation structure in the Ge rich region of a Ge/Si-Ge/Si(001) 6° off-cut sample showing a novel hexagonal dislocation structure.

In Si-rich regions of the graded structure, the dislocation structure consisted of a regular orthogonal array of 60° dislocations that one normally observes in low-mismatched diamond cubic interfaces. Fig. 4 shows a plan view TEM image of the dislocation structure in the Ge-rich region of the graded structure. A novel hexagonal dislocation network is observed. A **g.b** analysis of the dislocation structure revealed that the network is composed of edge dislocations with 1/2<110> and <100> type Burgers vectors. The <100> type edge dislocations form due to reaction between the 1/2<110> type edge dislocations. The <100> type dislocation has been observed in bulk silver bromide [17] and potassium chloride [18] crystals. However, we believe that this is the first time it has been observed in epitaxial semiconductor thin films. Since all the dislocations in the hexagonal network have in-plane Burgers vectors, they do not contribute to the tilt of the epilayer. The hexagonal network occurs only in those areas of the interface where the right kind of 1/2<110> dislocations are found. The formation of the hexagonal network explains the reduction in the tilting rate of the epilayer.

We have modeled the energetics of formation of the hexagonal network from a square 1/2<110> edge network, which in turn forms from a 60° orthogonal array. The reactions of 60° dislocations to form 1/2<110> type edge dislocations is energetically favored from the "b^2 *criterion*" or Frank's rule. However, the energy of reacting 1/2<110> edges is equal to the <100> type product using this rule. Our preliminary calculations indicate that the hexagonal network forms to convert the high energy four-fold nodes of the orthogonal network into three-fold nodes of the hexagonal network. We have determined the total network energy per unit area of the three dislocation networks as a function of plastic strain (same as b_{misfit}.

dislocation density). The hexagonal dislocation network indeed has the lowest energy minimum. The formation of the hexagonal network requires climb reactions. In the high Ge layers, the growth temperature (800° C) is closer to the melting point of the alloy ($T_{m,Si}$≈1425° C, $T_{m,Ge}$≈940° C). The point defect concentration and hence the dislocation climb velocities increase substantially aiding the formation of the 1/2<110> type edge dislocations and the hexagonal network. Therefore, because the kinetic pathway to the lower-energy network is not avaliable, the hexagonal network is not observed in the high Si regions of the graded structure.

CONCLUSIONS

There is a substantial improvement in surface roughness and dislocation pile-up density by growing graded Si-Ge layers on (001) Si substrates off-cut towards any of the <110> directions. Triple-axis X-ray diffractometry indicates that graded structures on miscut substrates tilt to reduce the substrate miscut. At high temperatures the 60° dislocations can react to give a novel low energy hexagonal dislocation network that reduces epilayer tilt. The formation of this novel hexagonal dislocation network presents opportunities to eliminate spatially variant strain fields that lead to deleterious surface morphology effects.

REFERENCES

1. E. A. Fitzgerald, Y. H. Xie, D. Monroe, P. J. Silverman, J. M. Kuo, A. R. Kortan, F. A. Thiel and B. E. Weir, J. Vac. Sci. Technol. B **10**, 1807 (1992).
2. F. Schäffler, D. Tobben, H. R. Herzog, G. Abstreiter and B. Hollander, Semicond. Sci Technol. **7**, 260(1992).
3. K. Ismail, J. O. Chu and B. S. Meyerson, Appl. Phys. Lett. **64**, 3124 (1994).
4. M. Arienzo, J. H. Comfort, E. F. Crabbe, D. L. Harame, S. S. Iyer, V. P. Kesavan, B. S. Meyerson, G. Patton, J. M. C. Stork and Y. C. Sun, Microelectronic Engg. **19**, 519 (1992).
5. E. A. Fitzgerald, Y. H. Xie, M. L. Green, D. Brasen, A. R. Kortan, J. Michel, Y. J. Mill and B. E. Weir, Appl. Phys. Lett. **59**, 811 (1991).
6. F. K. LeGoues, B. S. Meyerson, J. F. Morar and P. D. Kirchner, J. Appl. Phys. **71**, 4230 (1992).
7. E. A. Fitzgerald, D. G. Ast, P. D. Kirchner, G. D. Pettit and J. M. Woodall, J. Appl. Phys. **63**, 693 (1988).
8. A. G. Cullis, D. J. Robbins, S. J. Barnett and A. J. Pidduck, J. Vac. Sci. Technol. A **12**, 1924 (1994).
9. M. Albrecht, S. Christiansen, J. Michler, W. Dorch and H. P. Strunk, Appl. Phys. Lett. **67**, 1232 (1995).
10. D. E. Jesson, S. J. Pennycook, J.-M. Baribeau and D. C. Houghton, Phys. Rev. Lett. **71**, 1744 (1993).
11. S. B. Samavedam and E. A. Fitzgerald, submitted to J. Appl. Phys. (1996).
12. J. E. Ayers, S. K. Ghandhi and L. J. Schowalter, J. Crystal Growth **113**, 430(1991).
13. F. K. LeGoues, P. M. Mooney and J. O. Chu, Appl. Phys. Lett. **62**, 140(1993).
14. V. T. Gillard, W. D. Nix and L. B. Freund, J. Appl. Phys. **76**, 7280 (1994).
15. P. Kightley, P. J. Goodhew, R. R. Bradley and P. D. Augustus, J. Cryst. Growth **112**, 359 (1991).
16. M. Mazzer, A. Carnera, A. V. Drigo and C. Ferrari, J. Appl. Phys. **68**, 531(1990)
17. J. M. Hedges and J. W. Mitchell, Phil. Mag. **44**, 223 (1953).
18. S. Amelinckx, Acta Metall. **6**, 34 (1958).

HRTEM STUDY OF DISLOCATIONS IN GeSi/Si HETEROSTRUCTURES GROWN BY VPE

JUNWU LIANG, XUEYUAN WAN
Institute of Semiconductors, Chinese Academy of Sciences, P. O. Box 912, Beijing 100083, China

ABSTRACT

GeSi/Si heterostructures grown by atmospheric chemical vapor epitaxy have been studied by cross sectional high resolution transmission electron microscopy (HRTEM). For the first time we have observed an interstitial-type dislocation loop which is located near to a 60° misfit dislocation in the initially prepared GeSi/Si sample. After 30 minutes observation, the interstitial-type dislocation loop disappeared and the 60° dislocation climbed. Moreover, we have observed dissociated 60° dislocations with about 9 nm width of stacking fault existing in silicon substrate.

INTRODUCTION

In lattice-mismatched semiconductor heterostructures, there are misfit dislocations introduced in the interface to relieve the misfit strain energy between the growing layer and the substrate when the thickness of the growing layer reaches a critical thickness [1].

High resolution transmission electron microscope (HRTEM) is a powerful tool for the study of dislocations in crystals. HRTEM has been also widely used in the research of dislocations in lattice-mismatched semiconductor heterostructures. By cross sectional HRTEM, the core of a dislocation can be researched conveniently.

The climb phenomenon of a 1/3<111> Frank dislocation in CdTe material has been observed by Yamashita and Sinclair [2] using HRTEM. However, the existence of interstitial-type dislocation loop and its interaction with a 60° dislocation have never been reported for GeSi/Si heterostructures. In this paper we present the observation of the climb of a 60° dislocation induced by a nearby interstitial-type dislocation loop. As far as we know, this is observed for the first time.

Dissociated 60° misfit dislocations have been observed often in strained heterostructures, such as in $In_xGa_{1-x}As/GaAs$ [3, 4] in $Si_{1-x}Ge_x/Si$ [5, 6, 7] by HRTEM, plan-view TEM or weak beam TEM. Y. Xin et al.[7] reported that the leading 90° partial is at the SiGe/Si interface while the 30° partial located in the Si substrate and the dissociation width of the dissociated dislocation is 6 nm. In the present work, the dissociation of 60° dislocations in GeSi/Si heterostructures is examined by HRTEM.

EXPERIMENT

The epitaxial Ge_xSi_{1-x} layers with x=0.15-0.17 and thickness of 4000Å were grown at 870°C on Si(001) substrate by atmospheric chemical vapor phase epitaxy. The resource gases are dichlorosilane and germane. Before deposition, the Si wafers are chemically polished by HCl.

The material structures were examined by HRTEM performed using a H9000NAR microscope operated at 300kV. The cross sectional samples are prepared by mechanic polishing and argon ion beam thinning procedure.

Mat. Res. Soc. Symp. Proc. Vol. 442 © 1997 Materials Research Society

RESULTS AND DISCUSSION

Climb of a 60° misfit dislocation

Fig. 1(a) is a [110] lattice image of a $Si_{0.85}Ge_{0.15}$/Si sample in which the misfit is about 0.6%. There is a Lomer dislocation which consists of two 60° misfit dislocations. In the upper right side of the Lomer dislocation, we can see another high contrast area (indicated by dots). Here is an interstitial-type dislocation loop which squeezes in between two atomic planes. This loop is only about one lattice spacing apart from the right-sided 60° misfit dislocation which forms the Lomer dislocation with another 60° misfit dislocation. It is obvious that the lower part of the loop nearly touches the right-sided 60° dislocation. In Fig. 1(b) the schematic lattice fringe corresponding to the HRTEM image in Fig. 1(a) is shown.

Fig. 2(a) is the lattice image of the same area of the same sample taken after thirty minutes. It is evident that the interstitial loop has been attracted to the right-sided 60° dislocation and disappeared, and this right-sided 60° dislocation has climbed by about 30Å. Fig. 2(b) represents the schematic lattice fringe corresponding to Fig. 2(a).

It is well known that ion radiation during preparation of TEM specimens by ion milling and electron radiation during TEM observation of specimens might generate defects, such as interstitial-type loops [8], and can affect the configuration of defects in the specimens.

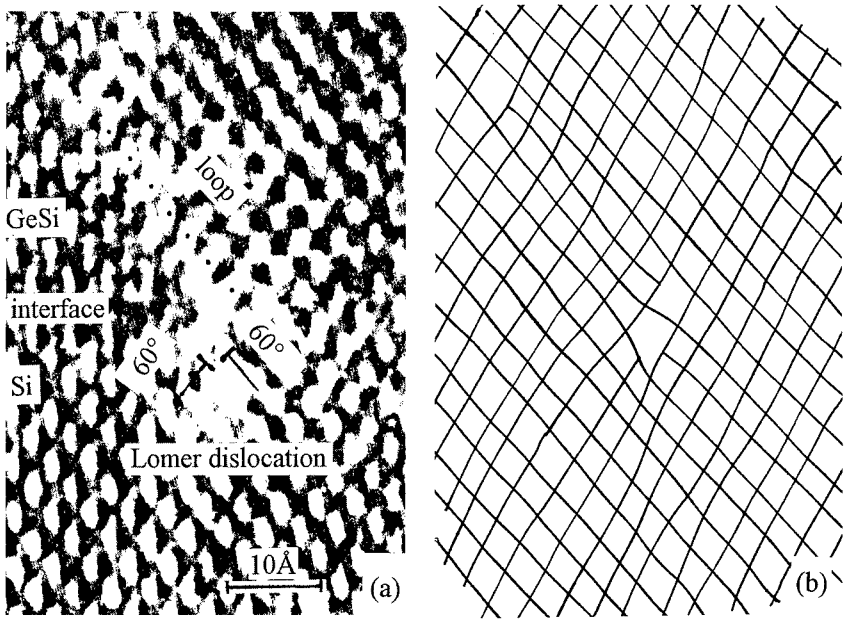


Fig. 1 HREM image taken initially showing a Lomer dislocation consisting of two 60° dislocations and an interstitial type dislocation loop and the schematic lattice fringe corresponding to it. (a) the HRTEM image. (b) the schematic lattice fringe.

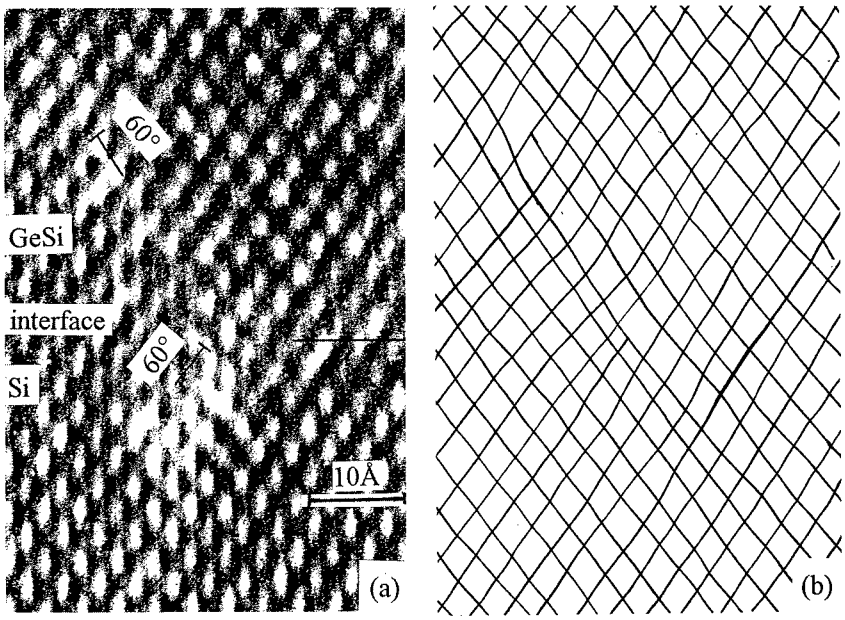


Fig. 2 HREM image taken after 30 min. showing the disappearance of the interstitial type loop and the climbing of the right-sided 60° dislocation and the schematic lattice fringe corresponding to it. (a) the HRTEM image. (b) the schematic lattice fringe.

The interstitial-type loop in Fig. 1(a) might be generated during the preparation of TEM sample or during the TEM observation. When observed by TEM the second time, the electronic beam increased locally the temperature of the sample and the loop moved to the nearby 60° dislocation, so the loop disappeared, the 60° dislocation climbed.

The Dissociated 60° Dislocation

We have observed some 60° and a few screw dislocations. Some of them dissociated. Fig. 3 shows a HRTEM image of a $Si_{0.83}Ge_{0.17}$ sample. There is a dissociated dislocation located near the interface in the epilayer. Using the Burgers vector analysis method of dislocations, a Burgers circuit around this dissociated dislocation shows it is a dissociated 60° dislocation. A Burgers circuit around the upper partial yields a vector whose magnitude is 2/3 the distance between lattice points in this $(\bar{1}10)$ projected plane, this is the nature of 90° partials. The stacking fault between the two partials is an intrinsic one.

The 90° partial is located at the $Si_{0.17}Ge_{0.83}$/Si interface whereas the 30° partial is toward the inside of silicon substrate. This is consistent with the result reported by Y. Xin et al. [7] Nevertheless, the tails associated with the 90° and 30° partials reported by them are not observed in our samples.

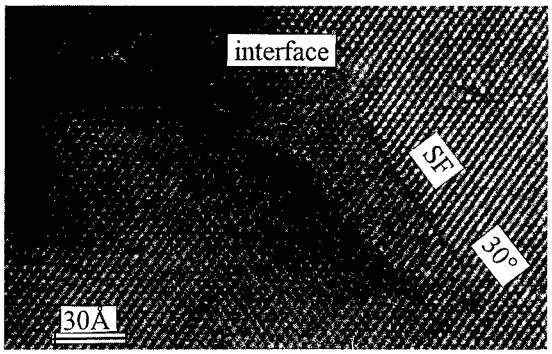


Fig. 3 A dissociated 60° dislocation. The 90° partial is located near the interface, and the 30° partial is located in the substrate.

In close vicinity to the dissociated 60° dislocation also exist some defect configurations whose nature and the reason remain unclear.

The dissociation width of the stacking fault is about 9 nm which is greater than the reported width value of 6 nm. This might be caused by the inhomogeneous strain existing in the GeSi/Si heterostructures.

CONCLUSIONS

In conclusion, by means of HRTEM, for the first time we observed climb process of a 60° misfit dislocation by a nearby interstitial-type dislocation loop in the GeSi epilayer near the interface of SiGe/Si. Also we observed a dissociated 60° misfit dislocation with 90° partial lying near the interface and the 30° partial lying in the inside of the silicon substrate. The dissociation width of the stacking fault reaches about 90Å.

REFERENCES

1. F. C. Frank and J. H. Van der Merwe, Proc. R. Soc. London Ser. **A 198**, p. 205 (1949).
2. T. Yamashita, and R. Sinclair, 1983, in Defects in Semiconductors, edited by J. Narayan and T. Y. Tan (Mat. Res. Soc. Sym. Proc. 14, North-Holland, New York:), p. 295.
3. Y. Chen, N. D. Zakharov, P. Werner, Z. Liliental-Weber, and J. Washburn, Appl. Phys. Lett. **63**, p. 1536 (1993).
4. J. Zou and D. J. H. Cockayne, J. Appl. Phys. 77, p. 2448 (1995).
5. R. Hull, J. C. Bean, D. Bahnck, J. M. Bonar, and L. J. Peticolas, D. Gerthsen, F. A. Ponce, and G. B. Anderson, in Microscopy of Semiconducting Materials 1991, edited by A. G. Cullis and N. J. Long (Inst. of Phys. Conf. Ser. No. 117, Bristol, 1991), P. 497.
6. K.Rajan, Appl. Phys. Lett. **57**, p. 1135 (1990), **59**, 2564 (1991).
7. Y. Xin, P. D. Brown, R. E. Schaublin and C. J. Humphreys, in Microscopy of Semiconducting Materials 1995, edited by A. G. Cullis and A. E. Staton-Bevan (Inst. of Phys. Conf. Ser. No. 146, Bristol, 1995), P. 183.
8. G. Lu and F. Phillipp, in Microscopy of Semiconducting Materials 1991, edited by A. G. Cullis and N. J. Long (Inst. of Phys. Conf. Ser. No. 117, Bristol, 1991), P. 367.

Part VIII

Point Defects and Defect Interactions In SiGe

DEFECTS IN LOW TEMPERATURE MBE-GROWN Si AND SiGe/Si STRUCTURES

W.M. Chen, I.A. Buyanova, and B. Monemar
Department of Physics and Measurement Technology, Linköping University, S-581 83 Linköping, SWEDEN, wmc@ifm.liu.se

ABSTRACT

We review our recent experimental results on important grown-in non-radiative defects in Si and SiGe/Si heterostructures grown by molecular beam epitaxy (MBE) at low temperature. Several types of such defects have been revealed by the optically detected magnetic resonance technique and were shown to play an important role in carrier recombination. Among them a dominant defect is identified to be the vacancy-oxygen (V-O) complex. Experimental evidence on the formation mechanisms of these non-radiative defects points at a low surface adatom mobility during low temperature growth as a major cause, and also ion bombardment as occurs e.g. during potential enhanced doping. Based on the gained knowledge, educated attempts by post-growth hydrogen and thermal treatments have been made to remove these harmful defects and to improve the radiative efficiency of the material.

INTRODUCTION

Si and SiGe layered structures grown by modern epitaxial techniques form an interesting electronic system providing considerable freedom for bandgap engineering. This is due to effects of heterojunction band offsets, widely tuneable by alloy composition and strain (due to lattice mismatch), and also to quantum phenomena arising from spatial confinement. Moreover, they offer a very promising and attractive materials system for a variety of high performance devices, as their fabrications are largely compatible to the existing, mature main-stream silicon technology, leading the way to a highly desirable monolithic integration of electronic and optoelectronic devices on the same chip. These devices are expected to be superior over the existing silicon devices for high frequency applications based on e.g. heterobipolar transistors (HBT) and modulation doped field effect transistors (MODFET), for infrared (IR) detectors, and possibly also near infrared light emitters and detectors.

So far the success of SiGe/Si structures in optoelectronic applications has been very limited, due to the poor intrinsic radiative efficiency of this indirect bandgap semiconductor system. Many attempts have in the past years been made to overcome this inherent problem, including bandgap engineering (e.g. zone-folding [1]) to achieve a quasi-direct bandgap, quantum confinement [2] to increase the overlap of wavefunctions between the recombining electron and holes, and defect engineering by incorporating light emitting dopants in the materials [3]. Very little is known, however, of important non-radiative defects in this materials system, as they have largely eluded from an investigation by sensitive optical spectroscopies which only monitor radiative channels of carrier recombination. Such non-radiative defects are known to dominate carrier recombination in the indirect bandgap materials such as SiGe/Si, and thus play a key role in performance of minority carrier devices. They may to a large degree undermine the progress of the aforementioned attempts by bandgap and defect engineering, and therefore deserve a greater attention.

In this paper, we review our recent results on important non-radiative defects in Si and SiGe/Si structures grown by molecular beam epitaxy (MBE) at low temperature. The advanced experimental technique, namely optical detection of magnetic resonance (ODMR), provides an unique opportunity of investigating non-radiative defects by optical means. The emphasis of this work is placed on low temperature MBE-grown materials, motivated largely by the fact that such a low temperature growth is required to maintain well-defined doping profiles and sharp interfaces, to enhance incorporation of dopants, and to obtain thick metastable strained structures.

Mat. Res. Soc. Symp. Proc. Vol. 442 © 1997 Materials Research Society

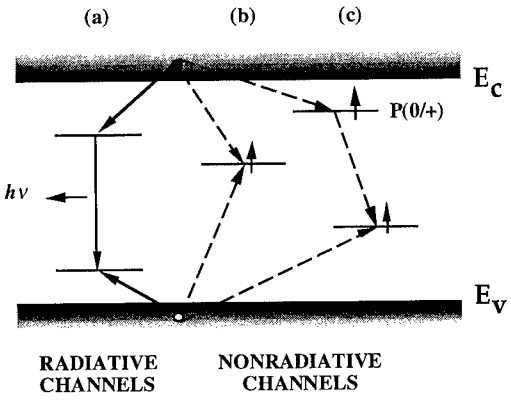


Fig.1 The competing carrier recombination processes between radiative channels (a) and non-radiative channels (b-c), explored by the ODMR technique. The non-radiative channels can be due to either a single deep-level defect (b) or due to a charge transfer process involving a shallow impurity (such as the P donor) and a deep-level defect. The arrows at the defect levels represent the unpaired electron spins of the defects which participate in the spin-resonance enhanced recombination giving rise to the observed ODMR signals.

EXPERIMENTAL

Experimental Approach

The key to the experimental approach is to utilize the competing carrier recombination processes between radiative and nonradiative defects [4], see Fig.1. In this case the non-radiative defects are monitored by magnetic resonance while the radiative channels are detected by photoluminescence (PL). A magnetic-resonance enhanced recombination via nonradiative channels, provided that they are among the dominant recombination channels, leads to a corresponding reduction in free carrier concentration available for recombination via radiative channels. This results in a decrease in PL intensity, or equivalently a negative ODMR signal. ODMR has in recent years been proven to be of great use in studies of non-radiative defects in Si [5,6].

The ODMR experiments were performed at the X-band (9.23 GHz) using a modified Bruker ER-200D ESR spectrometer, equipped with a TE_{011} microwave cavity with optical access in all directions. The PL emission from the samples under the illumination of the UV multilines (333.6 - 363.8 nm) or the 514.5 nm line of an Ar^+ laser was monitored by a liquid nitrogen cooled Ge detector. The ODMR signal was obtained by detecting a synchronous change in the PL intensity with the amplitude modulation of the microwave field or with the field modulation of the magnetic field, corresponding to a change in the PL intensity with or without the applied microwave field. With the field modulation, a derivative-like lineshape of the ODMR is observed when the magnetic field is modulated on and off the spin resonance conditions. In practice, a slightly different microwave frequency was employed in each measurement, corresponding to the resonant frequency of the loaded microwave cavity under the perturbation of a specific sample. This results in a corresponding difference in the magnetic field position of the ODMR signal for a given g-value. To calibrate this difference, the resonant field for g=2 is in some cases marked for each ODMR spectrum, and then all the ODMR spectra are shifted accordingly to line up the g=2 mark, leading to calibrated ODMR spectra for a correct and easy comparison.

Samples

The samples investigated in this work are partly listed in Table I, all grown on (100) Si substrates by MBE with a Balzers UMS 630 Si-MBE system. The undoped Si samples consist of a 1000-1200 Å undoped Si buffer layer, followed by a 2000 Å undoped Si layer. The B-doped Si

Table I. List of the samples studied and a brief summary of the ODMR results.

Samples	T_g (°C)	Doping	substrate bias (V)	ODMR "1"	ODMR "2"	ODMR "31P"	ODMR "3"	ODMR "4"	ODMR "5"
Si	420	undoped	0	strong	strong				weak
Si	420	undoped	-1000	very strong	very strong	strong			strong
Si	420	B	0				weak		
Si	420	B	-1500	very strong	very strong				
Si	520	B	0				weak		
SiGe/Si	420	undoped	0	strong	strong				
SiGe/Si	620	undoped	0					weak	

samples consist of a 1000-1200 Å undoped Si buffer layer, followed by three periods of boron δ-doped spikes (1×10^{13} cm^{-2}) separated by 1000-1500 Å undoped Si spacers. All the structures were finally capped by a 1000 Å undoped Si layer. The growth temperature T_g is typically ~420 °C, except the buffer layer at 700 °C, and the growth rate is 1-2 Å/sec. Some samples were grown at slightly higher temperatures, e.g. 520 °C. The undoped SiGe/Si quantum well (QW) structure studied in this work was grown at 420 °C or 620 °C, with a 30 Å-wide $Si_{0.8}Ge_{0.2}$ QW. Post-growth hydrogen treatment was done at around 200 °C for 60 min., with a remote dc H plasma at a pressure of 2.0 mTorr. Post-growth isochronal thermal annealing was carried out at 200-500 °C for 15 minutes in a furnace in an argon gas environment.

RESULTS AND DISCUSSION

Role in carrier recombination

In Fig.2 we show the low temperature PL spectra obtained from the Si and SiGe/Si structures studied in this work. They typically consist of near bandgap sharp PL lines at an energy higher than 1.08 eV and many broad, featureless PL bands at lower photon energy. The sharp line structure near the bandedge includes the free exciton, shallow bound excitons and sometimes electron-hole droplets. These PL emissions are mostly contributed by the substrates, and will therefore not be considered in this work. The broad bands, on the other hand, are known to originate from the MBE-layers. The presence of a specific type of the broad bands has been shown to be critically dependent on the growth conditions (e.g. the substrate bias) and the sample structures (e.g. B doping or alloy) [7]. Even within one specific sample, the broad bands over a wide spectral range (0.7-1.03 eV) have been shown to arise from at least two different defects. These broad PL bands are not related to the nonradiative defects studied in this work, as will be shown below, and will therefore not be discussed further in the paper. A detailed study of these broad PL bands is described elsewhere [7].

By monitoring these broad PL bands over a wide spectral range, between 0.7 eV and 1.03 eV, ODMR spectra can clearly be observed. As an illustration, we show in Fig.3 ODMR spectra from the B-doped Si epilayer grown with negative bias. The negative ODMR signals correspond to a decrease in the PL intensity of various PL bands over the entire spectral range monitored under the spin resonance conditions. A close-up of the ODMR signal (the lower two curves in Fig.3) shows that the non-radiative defect involving in the spin resonance is identical when two different spectral ranges of the PL emissions were monitored. This is despite the fact that the two spectral ranges of the PL emissions have been shown to be of different origin [7]. This observation thus provides clear evidence that the non-radiative defect monitored in the spin resonance is not at all related to the PL emissions. It is rather the competing process mediating the link between the radiative and non-radiative centers. By varying the modulation frequency in the ODMR experiments, the non-radiative defects studied in this work are shown to provide efficient recombination channels on a time scale shorter than the instrumental limit (< 10 μs).

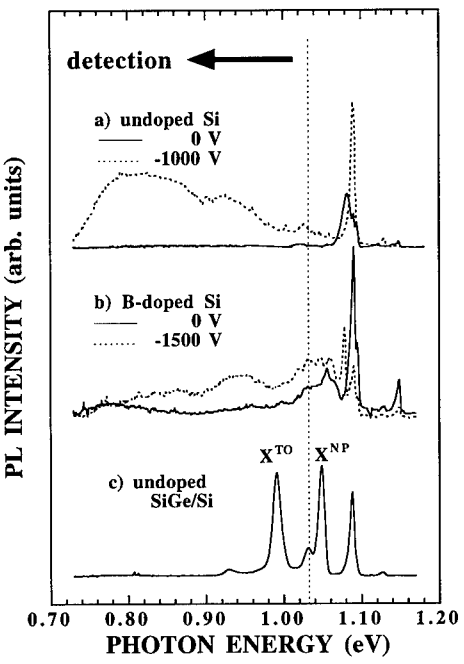


Fig.2 a) PL spectra obtained at 2K from the undoped Si epilayers grown with zero bias (solid curve) and negative bias (dashed curve). b) PL spectra obtained at 2K from the B-doped Si epilayers grown with zero bias (solid curve) and negative bias (dashed curve). c) PL spectrum obtained at 2K from undoped SiGe/Si QW grown with zero bias. X_{NP} and X_{TO} denote the excitonic emissions from the QW. The arrow indicates the range of optical detection selected in the ODMR experiments.

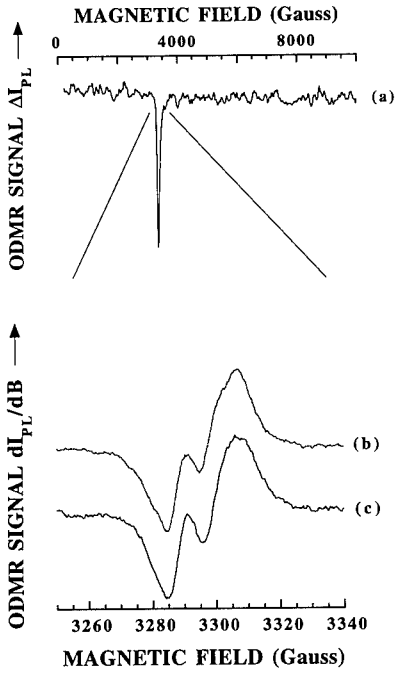


Fig.3 a) The ODMR spectrum from the B-doped Si epilayer grown at 420 °C with negative bias. A close-up of the ODMR is shown in the lower two curves b) and c), with the optical detection in the range 1.48 - 1.75 μm and 1.2 - 1.43 μm, respectively. In b) and c), a modulation of magnetic field giving rise to the derivative lineshape was employed to obtain a better spectral resolution.

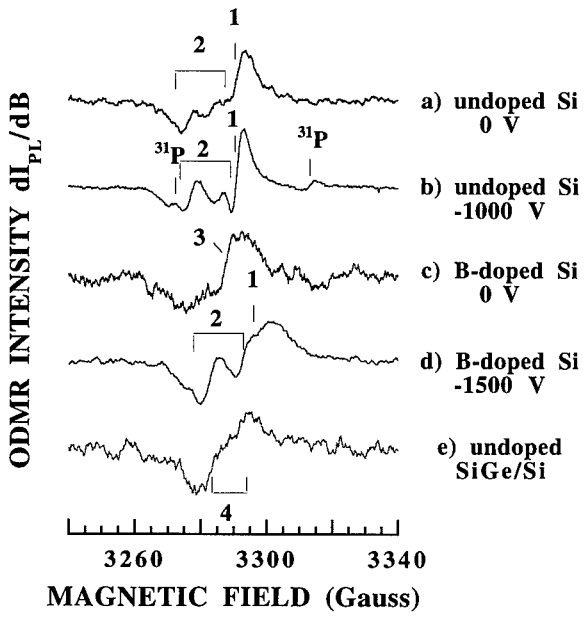


Fig.4 a)-d) The ODMR spectra obtained from the undoped and B-doped Si epilayers grown with zero bias and negative bias. e) The ODMR spectrum obtained from the undoped SiGe/Si QW grown at 620 °C with zero bias. Various ODMR signals can be observed. A relative shift of the ODMR field position between the samples, for a specific defect, is due to a slight difference in the microwave frequency employed in each case.

Identification

Several ODMR signals are observed from various samples [8], as shown in Fig.4 and briefly summarized in Table I. The relative intensity of these ODMR signals varies from sample to sample, and also depends on experimental conditions. Therefore they originate from different non-radiative defects. The resulting ODMR spectra represent an overlap of these ODMR signals and can thus be decomposed into corresponding contributions, as demonstrated in Fig.5. In the as-grown undoped samples, three types of defects denoted as "1", "2" and "^{31}P" are revealed. The ODMR spectrum (Fig.4d) from the as-grown B-doped Si epilayers grown with substrate bias is dominated by the same defects as seen in the as-grown undoped Si (Fig.4a-b). This is proven by a careful angular dependence study of the ODMR signal, from which the same defect symmetry and g-values have been deduced. The apparent broadening of the ODMR lines in the B-doped samples is very likely due to the B δ-doping, which introduces a gradient of an electric field or a strain field in the region where the defects are situated. The built-in electric field is introduced as a result of electron transfer from the neighboring "undoped" Si layer to the B δ-doing layer, leading to a band bending and a formation of a two-dimensional electrical potential (different from uniformly B-doped Si) [9]. In contrast to the B-doped Si grown with substrate bias discussed above, the situation is different in the B δ-doped sample of the same structural design but grown without substrate bias. As shown in Fig.4c, the dominant ODMR signal 1 and 2 observed in the former sample are no longer detectable. Only a weak ODMR signal 3 is now present, with an average g-value of 2.0018. This ODMR signal can still be observed in the sample grown at 520 °C.

In order to reveal the symmetry of the defects, the angular dependence of the ODMR spectra has been studied with respect to the direction of the external magnetic field **B** (Fig.6). To obtain

Table II. A summary of the electronic structure and spin Hamiltonian parameters of the non-radiative defects in the MBE-grown Si and SiGe/Si, from the best fit of the spin Hamiltonian (Eq. 1) to the experimental results.

ODMR signals	Effective spin S	g-tensor	Symmetry	Identification
^{31}P	1/2	isotropic g=1.9986±0.0005	cubic	Shallow P donor
1	1/2	slightly anisotropic average g=1.9993±0.0005	unknown	vacancy-related
2	1/2	g_x=2.0030±0.0005, x≡[001] g_y=2.0019±0.0005, y≡[1$\bar{1}$0] g_z=2.0087±0.0005, z≡[110]	orthorhombic I	the V-O complex
3	1/2	average g=2.0018±0.0005	unknown	unknown
4	1/2	average g=2.000±0.005	unknown	unknown
5	1/2	average g=2.0005±0.0005	unknown	unknown

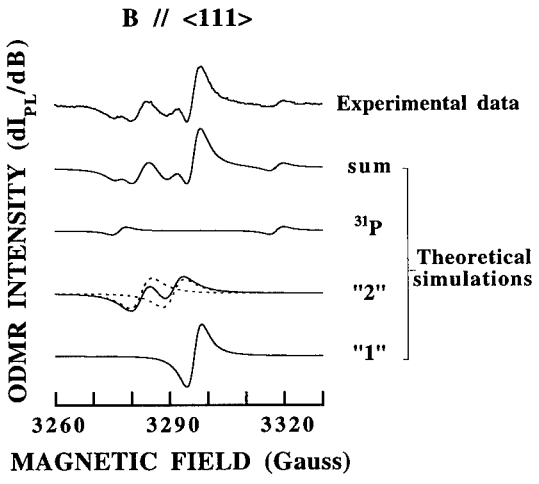


Fig.5 The ODMR spectrum from the MBE Si layers grown at 420 °C, taking as an example the undoped sample grown with negative substrate bias (-1000 V). Both the experimental data (the upper-most curve) and the theoretically simulated spectra (the lower four curves) are shown, when the external magnetic field is along a <111> crystallographic axis. The ODMR spectra are composed of three contributions, ^{31}P, 2 and 1, originating from three different defects. The dashed curves in the simulated "2" spectra represent different inequivalent orientations of the low-symmetry V-O complex with respect to the direction of the magnetic field.

the electronic structure of the corresponding defects, a detailed analysis of the experimental data from each defect has been performed by an effective spin Hamiltonian

$$H = \mu_B \mathbf{S}\mathbf{g}\mathbf{B} + \Sigma \mathbf{S}\mathbf{A}_i\mathbf{I}_i, \qquad (1)$$

where the first term is the electronic Zeeman interaction and the second term represents the magnetic interactions (or hyperfine interactions) between the electronic spin **S** and the nuclear spins ($\mathbf{I}_i$ for the ith nucleus) of the defect atom(s) and ligand Si atoms. μ_B is the Bohr magneton. **g** denotes the effective g-tensor, and $\mathbf{A}_i$ the hyperfine interaction tensor related to the ith nucleus. From a best fit of the spin Hamiltonian to the experimental results, the spin parameters and the defect symmetry can be deduced and are listed in Table II. The theoretically calculated angular

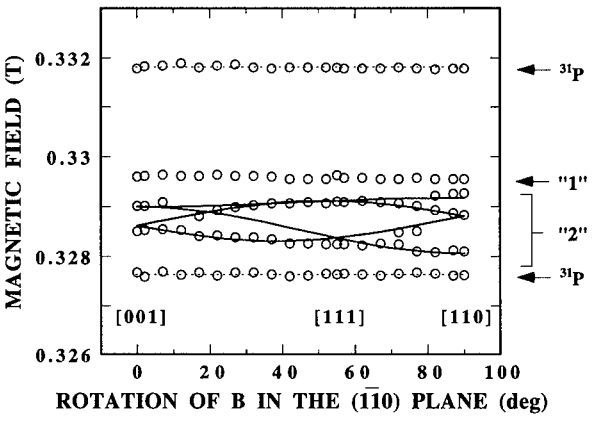


Fig.6 Angular dependence of the ODMR signals ^{31}P, 2 and 1. The open circles stand for the ODMR field positions determined experimentally. The solid and dashed lines are calculated ODMR field positions for the V-O complex and the shallow P donor, respectively, obtained from the best fit of the experimental data by the spin Hamiltonian (Eq. 1) with the parameters given in Table II.

dependences of the "^{31}P" and "2" ODMR signals by using the spin Hamiltonian parameters given in Table II are also shown in Fig.6 by dashed and solid curves, respectively.

The anisotropic "2" ODMR signal is concluded to arise from a defect with orthorhombic I symmetry. By comparing with previously reported data in bulk silicon, it is found, within experimental error, to coincide with the well-known vacancy-oxygen (V-O) complex [10], i.e. the dominant defect in oxygen-rich bulk Si (such as the common Czochralski substrate material) after electron irradiation. The observed electron spin resonance (ESR) [10] and ODMR (in this work) arises from an additional electron trapped in the V-O center, with the (-/0) level at E_c-0.17 eV [11]. This assignment is confirmed by the characteristic hyperfine structure of the ^{29}Si ligand atoms observed over a wider field range [12]. The relative intensity between the central ODMR lines and their corresponding hyperfine satellites, taking into account the natural abundance (4.67 %) of the ^{29}Si, leads to the conclusion that the observed hyperfine structure is due to the two equivalent sites of the ^{29}Si ligand atoms directly connected to the dangling bonds of the V-O complex. Due to a strong localization of the electron wavefunction near the vacancy-related defects, a sizable hyperfine interaction can usually be observed and has been regarded as a fingerprint of a vacancy-related defect.

The "1" ODMR signal is only slightly anisotropic, and contributions from inequivalent orientations of the defect can not be clearly resolved. This has prevented us from drawing a definite conclusion on the symmetry and the identity of the defect. There are, however, indications that the ^{29}Si ligand hyperfine satellites are present as shoulders in the ODMR spectra, and thus the defect could also be vacancy-related as argued above. The weak intensity of these satellites is probably due to a lower number of equivalent sites of the ^{29}Si ligand atoms.

The g-value and the hyperfine interaction deduced from the ODMR signal "^{31}P" are found to be identical to the previously reported values for the shallow P substitutional donor [13] in silicon, and this signal can therefore be positively assigned to the P donor. The incorporation of phosphorus in the crystal is likely due to contamination from the stainless steel in the growth chamber. The participation of the shallow P donor in non-radiative carrier recombination is due to an efficient inter-center charge transfer [6,14] to other deep level recombination centers, beyond the framework of the commonly used model by Shockley-Read-Hall [15]. The efficiency of such a charge transfer critically depends on the overlap of wavefunctions between the shallow P donor and the deep centers, and thus on the concentration of these centers.

Formation Mechanisms

Stronger ODMR signals are observed from the samples grown with negative bias as compared to those grown with zero bias (Fig.7). This observation can be attributed to stronger

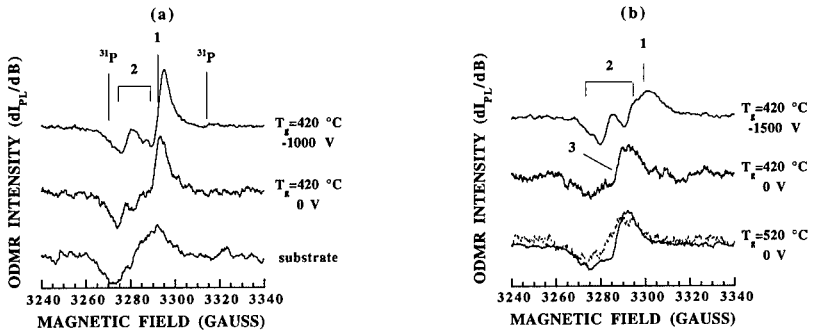


Fig. 7 ODMR spectra from (a) the undoped and (b) the B-doped MBE-Si samples, showing the effects of ion bombardment. The dashed curve for the B-doped MBE-Si represents the ODMR spectrum from the substrate.

PL emissions monitored or/and an increased concentration of the nonradiative defects in the samples grown with negative bias. The appearance of the shallow P-donor ODMR in the undoped samples grown with negative bias, but not in the undoped samples grown with zero bias though a similar P contamination is expected to occur, provides evidence that the concentration of the nonradiative defects is indeed higher in these samples. This is based on the facts that the efficiency of charge transfer between the P-donors and the deep recombination centers is determined by the overlap of wavefunctions between the participating centers, which is a sensitive function of the concentration of the centers. An increase of the defect concentration in the samples grown with negative bias can be explained as being due to effects of ion bombardment. The results from the samples grown with positive bias, not shown here, resemble those from the samples grown with zero bias, suggesting that the positive ions such as Si^+ play a major role in the damage induced by ion bombardment.

The presence of these defects in samples grown without substrate bias, thus without severe ion bombardment, is believed to be due to a low surface adatom mobility during the low temperature growth leaving many unfilled lattice sites being frozen and buried in the epilayers. The incorporation of oxygen due to contamination in the MBE epilayers also depends critically on the growth temperature [16]. A decrease in growth temperature generally leads to a higher O concentration buried in the epilayers, due to a lower rate of O desorption from the growing surface. This determines the V-O center to be the predominant defect in the MBE layers grown at low temperature.

Post-Growth Treatments

The hydrogen treatments of these undoped MBE-Si samples are shown (Fig.8a-b) to be rather effective in deactivating the dominant non-radiative vacancy-related defects. Only a relatively weak background ODMR signal (denoted as "5"), with an average g-value of 2.0005, can be detected in the biased sample after the hydrogen treatments. Though the origin of this remaining ODMR signal is still not clear, it is known to originate from the MBE layer. This is supported by a comparison to the ODMR spectrum obtained from the substrate, also shown in Fig.8a-b. The fact that this background ODMR signal is barely seen in the sample grown without the substrate bias indicates that either the related defect is directly introduced by ion bombardment, or it is a complex involving hydrogen and defects induced by ion bombardment.

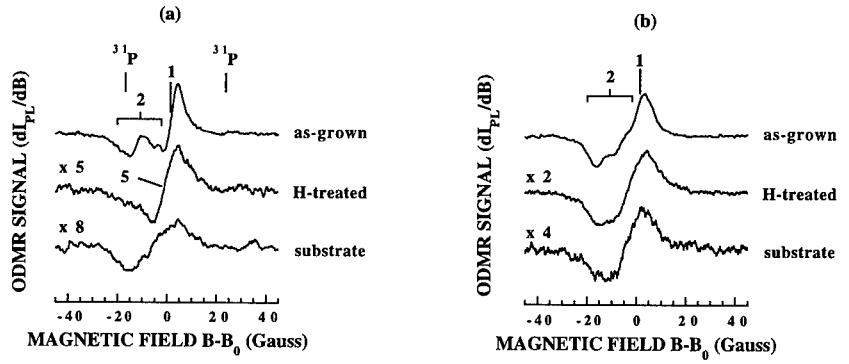


Fig.8 ODMR spectra from the undoped MBE-Si grown at 420 °C a) with and b) without substrate bias, demonstrating effects of post-growth hydrogen treatment. B_0 represents the ODMR field at g=2.

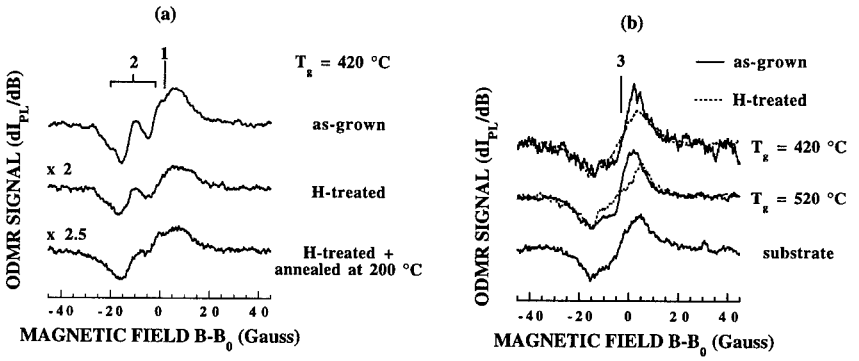


Fig.9 ODMR spectra from the B-doped MBE-Si grown a) with and b) without substrate bias, demonstrating effects of post-growth hydrogen treatment. B_0 represents the ODMR field at g=2.

The effects of hydrogenation in the B-doped samples grown with negative bias are only marginal (Fig.9a), however. The reason for this can be attributed to a strong competition in capture of hydrogen by the B dopants present in a high concentration [17]. This is supported by our observations that the shallow B acceptors have to a large extent been passivated by hydrogen, resulting in a significant reduction of the related PL emissions [18]. In contrast, non-radiative carrier recombination related to the ODMR signal "3" can be completely deactivated, as shown by the dashed curves in Fig.9b. This ODMR signal (and thus the related defect) is believed to be present in the sample grown with substrate bias, but is buried in the background of the much stronger ODMR signal "1" and "2".

Another attempt to remove the non-radiative defects is by post-growth thermal annealing, since the majority of vacancy-related defects including the V-O complex are known to anneal out at 500 °C [11]. This approach has been remarkably successful and has led to a nearly complete removal of the non-radiative defects monitored in the ODMR by annealing at 500 °C, much more effective as compared with the hydrogen treatment. This results in a significant improvement in thermal quenching behavior of luminescence from the materials [18].

SUMMARY

We have revealed several grown-in non-radiative centers in low temperature MBE-grown Si and SiGe layered structures by ODMR. A dominant defect is proven to be the V-O complex, having orthorhombic I symmetry and exhibiting the characteristic hyperfine structure from the ^{29}Si ligand connecting to the dangling bonds of the vacancy. The shallow P donor is shown to participate in efficient non-radiative recombination via charge transfer to deep centers when the latter are abundant. Experimental evidence on the formation mechanisms of these non-radiative defects has been provided as being due to a low surface adatom mobility during low temperature growth, and also due to ion bombardment as occurs e.g. during potential enhanced doping. A post-growth hydrogen treatment is demonstrated to be quite effective in passivating the defects in the undoped samples, but not in the B-doped samples due to the strong competition by the B-H complexing. Thermal annealing at high temperature (e.g. 500 °C) is, on the other hand, shown to be highly effective and leads to a nearly complete removal of the non-radiative defects monitored in the ODMR experiments and to a significant improvement in thermal quenching behavior of luminescence from the structures.

ACKNOWLEDGMENTS

We are grateful to W.-X. Ni and G.V. Hansson for providing samples and for valuable collaboration, and to G. Pozina for temperature-dependent photoluminescence experiments. This work has been supported by the Swedish Natural Science Research Council (NFR) and the Swedish Council for Engineering Sciences (TFR).

REFERENCES

1. K.B. Wong, M. Jaros, I. Morrison and J.P. Hagon, Phys. Rev. Lett. **60**, 2221 (1988).

2. Z.H. Lu, D.J. Lockwood and J.-M. Baribeau, Nature **378**, 258 (1995).

3. J. Michel, F.Y.G. Ren, B. Zheng, D.C. Jacobson, J.M. Poate and L.C. Kimerling, Mat. Sci. Forum **143**, 707 (1994).

4. W.M. Chen and B. Monemar, Appl. Phys. **A53**, 130-135 (1991).

5. W.M. Chen, O.O. Awadelkarim, B. Monemar, J.L. Lindström and G.S. Oehrlein, Phys. Rev. Lett. **64**, 3042 (1990).

6. W.M. Chen, B. Monemar, E. Janzén and J.L. Lindström, Phys. Rev. Lett. **67**, 1914 (1991).

7. I.A. Buyanova, W.M. Chen, A. Henry, W.-X. Ni, G.V. Hansson and B. Monemar, Phys. Rev. **B52**, 12006 (1995).

8. W.M. Chen, I.A. Buyanova, A. Henry, W.-X. Ni, G.V. Hansson and B. Monemar, Appl. Phys. Lett. **68**, 1256 (1996).

9. I.A. Buyanova, W.M. Chen, A. Henry, W.-X. Ni, G.V. Hansson and B. Monemar, Phys. Rev. **B53**, 9587 (1996).

10. G.D. Watkins and J.W. Corbett, Phys. Rev. **121**, 1001 (1961).

11. G.D. Watkins, J.W. Corbett and R.M. Walker, J. Appl. Phys. **30**, 1198 (1959).

12. W.M. Chen, I.A. Buyanova, W.-X. Ni, G.V. Hansson and B. Monemar, Phys. Rev. Lett. **77**, 4214 (1996).

13. G. Feher, Phys. Rev. **114**, 1219 (1959); A. Stesmans and G. De Vos, Phys. Rev. **B34**, 6499 (1986).

14. A.M. Frens, M.T. Bennebroek, A. Zakrzewski, J. Schmidt, W.M. Chen, E. Janzén, J.L. Lindström and B. Monemar, Phys. Rev. Lett. **72**, 2939 (1994).

15. W. Schockley and W.T. Read, Phys. Rev. **87**, 835 (1952); R.N. Hall, Phys. Rev. **87**, 387 (1952).

16. W.-X. Ni, G. Radnoczi, and G.V. Hansson, Thin Solid Films 184 , 403 (1990).

17. W.M. Chen, I.A. Buyanova, W.-X. Ni, G.V. Hansson and B. Monemar, Appl. Phys. Lett. Jan. 11 (1997) in press.

18. W.M. Chen, I.A. Buyanova, G. Pozina, B. Monemar, W.-X. Ni and G.V. Hansson, unpublished results.

THE EFFECT OF ION-IMPLANTATION INDUCED DEFECTS ON STRAIN RELAXATION IN Ge_xSi_{1-x}/Si HETEROSTUCTURES

J.M. GLASKO, J. ZOU[1], D.J.H. COCKAYNE[1], J. FITZ GERALD[2], P. KRINGHØJ[3] and R.G. ELLIMAN

Electronic Materials Engineering Department, R.S.Phys.S.E., Institute of Advanced Study, Australian National University, Canberra, A.C.T. 0200, Australia

[1] Electron Microscopy Unit, University of Sydney, Sydney, N.S.W. 2006, Australia

[2] Petrophysics Group, R. S. E. S., Institute of Advanced Studies, Australian National University, Canberra, A.C.T. 0200, Australia

[3] Institute of Physics and Astronomy, Aarhus University, DK-8000 Aarhus-C, Denmark

ABSTRACT

This study examined the effect of ion irradiation and subsequent thermal annealing on GeSi/Si strained-layer heterostructures. Comparison between samples irradiated at 253 °C with low energy (23 keV) and high energy (1.0 MeV) Si ions showed that damage within the alloy layer increases the strain whereas irradiation through the layer/substrate interface decreases the strain. Loop-like defects formed at the GeSi/Si interface during high energy irradiation and interacting segments of these defects were shown to have edge character with Burgers vector a/2<110>. These defects are believed responsible for the observed strain relief. Irradiation was also shown to affect strain relaxation kinetics and defect morphologies during subsequent thermal annealing. For example, after annealing to 900 °C, un-irradiated material contained thermally-induced misfit dislocations, while ion-irradiated samples showed no such dislocations.

INTRODUCTION

GeSi/Si strained-layer heterostructures have been studied extensively because of their potential for the fabrication of high-speed electronic and optoelectronic devices[1-4]. This system is particularly attractive because it could enable high-speed devices and bandgap engineering concepts to be incorporated into existing Si structures using well developed processing technology. To fully capitalise on the flexibility afforded by such structures it is important to understand how they respond to conventional processing. Since ion-implantation is extensively used in the fabrication of Si-based devices, the effect of ion-irradiation on strained layers is of particular significance.

Previous studies have demonstrated that ion irradiation can cause either an increase[2,3,4] or a decrease[5,4,6] in perpendicular lattice strain, depending on the irradiation conditions. Most studies have concentrated on low energy irradiation where peak damage production is either within the alloy layer or at the strained-layer/substrate interface. In such cases, the strain is correlated with the lattice damage and is observed to increase with increasing ion fluence. This effect decreases as the irradiation temperature is increased because dynamic annealing reduces the defect density within the layer. For higher energy irradiation, where damage within the strained layer is minimised, strain relaxation has been observed. This suggests that the net strain may be a result of the competition between two mechanisms: a) an increase in strain due to the accommodation of extrinsic defects in the alloy layer and b) a decrease in strain caused by the accommodation of extrinsic defects at, or near, the strained-layer/substrate interface. This scenario is tested in the

Mat. Res. Soc. Symp. Proc. Vol. 442 © 1997 Materials Research Society

present study by comparing the effects of low and high energy irradiations. The effect of ion-irradiation on subsequent thermally-induced relaxation is also examined.

EXPERIMENTAL

Ge_xSi_{1-x} alloy layers were grown on (001) Si substrates at 750-550 °C by molecular beam epitaxy (MBE). The layers employed in this study were 148 nm thick and had a Ge content of x=0.069. They were capped with 24 nm of Si to prevent oxidation. The Matthews and Blakeslee critical thickness[7] for this alloy composition is ~70 nm, one half of the actual thickness; the strained-layers are metastable and relax when heated to temperatures above ~800 °C.

Samples were heated to 253±1°C and irradiated with either 23 keV (R_p ~0.037μm) or 1.0 MeV Si ions (R_p ~1.3μm) to compare the effects of irradiating within the layer (WTL) or through the alloy-substrate interface (TTI). These irradiation conditions will be referred to as low- and high-energy irradiations, respectively. For 1.0 MeV irradiation, the ion flux was held constant during irradiation at 1.04 μA/cm^2, and ion fluences were 0.6, 1.0, 3.0, and 6.0x10^{16} Si/cm^2. For the 23 keV irradiation, the flux was 0.15 μA/cm^2 and fluences were scaled to give a peak nuclear energy deposition within the alloy layer equivalent to the average nuclear energy deposited within the alloy during the 1.0 MeV irradiation; this corresponded to fluences of 0.88, 1.5, 4.4 and 8.8x10^{15} Si/cm^2, respectively. Samples were tilted 7° with respect to the surface normal to avoid channeling effects, and the base pressure during irradiation was ≤ 8x10^{-8} Torr.

Samples were annealed in an Ar ambient at temperatures of 450, 600, 750 and 900 °C for 30 minutes. Layer strain was measured by double crystal x-ray diffraction (DCXRD) using the (004) reflection. Radiation damage was characterised by Rutherford backscattering spectrometry and channelling (RBS-C) using 2.0 MeV He^+ ions and by transmission electron microscopy on plan view (PV-TEM) and cross-sectional (X-TEM) samples using a Philips EM430 operating at 300 kV or a Philips CM12 operating at 120 kV.

RESULTS AND DISCUSSION

As-Irradiated Behaviour

Fig. 1 compares the damage distributions created by WTL and TTI irradiations. For WTL samples the damage is confined to the alloy layer, extending to a depth of 70 nm for a fluence of 4.4x10^{15} Si/cm^2. RBS-C analysis of the TTI samples reveals a relatively defect free Ge_xSi_{1-x} layer, with the dechanneling yield rising steadily with depth towards the peak of the damage distribution (~1.19μm). Samples irradiated to fluences exceeding 1x10^{16} Si/cm^2 exhibit a pronounced direct backscattering peak at a depth corresponding to the GeSi-substrate interface layers (see figure 1b). This has previously been shown to result from a band of defects at, or near, the alloy-substrate interface and it has been speculated that these defects are responsible for the strain relief observed for TTI irradiations[4].

The effect of irradiation on strain in the alloy layer is illustrated in Fig. 2, which shows x-ray rocking curves for as-grown and irradiated samples. The rocking curve for WTL samples (Fig 2a) shows structure on both sides of the as-grown Ge_xSi_{1-x} peak position (~680 arsecs); the structures to the right are Pendellösung fringes, while that on the left is indicative of an increase in the perpendicular strain ($\varepsilon_\perp$) in the irradiated region of the alloy layer, consistent with previous reports for WTL irradiation at room temperature[2,3]. The absence of strain relaxation in this WTL experiment raises doubt about the validity of the suggestion[6] that defects or defect structures

found within the alloy layer are the cause of the strain relaxation observed during elevated temperature irradiations. The rocking curves for the TTI samples, shown in Fig. 2b, reveal that the angular separation between the Ge_xSi_{1-x} and Si substrate peaks decreases with irradiation fluence, indicating a decrease in the $\varepsilon_\perp$ as previously reported[4]. The strain is reduced to ~50% of that in the as-grown layer after a fluence of $3x10^{16}$ Si/cm^2 and is almost completely relaxed after a fluence of $6x10^{16}$ Si/cm^2. A pronounced secondary peak develops to the right of the Si substrate peak for high fluence irradiation (> $3x10^{16}$ Si/cm^2). This is a tensile strain peak which is caused by vacancies and arises as a result of the spatial separation of the vacancy and interstitial profiles. This effect becomes measurable only at high fluence and does not affect the measured strain within the alloy layer[4,8]. In comparing the behaviour of the WTL and TTI samples, it is observed that elevated temperature irradiation can result in either an increase or a decrease in the $\varepsilon_\perp$. Further, it seems that relaxation results only if defects are produced at, or near, the alloy-substrate interface. The following discussion concentrates on TTI samples.

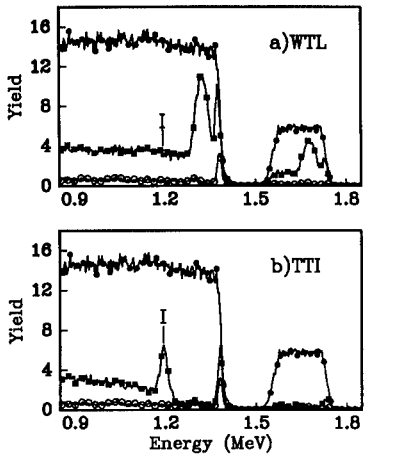


Figure 1: RBS-C spectra of the a) $4.4x10^{15}$ Si/cm^2 sample, and b) the $3x10^{16}$ Si/cm^2 TTI sample, showing the random, as-irradiated and as-grown spectra. The depth corresponding to the GeSi/Si substrate interface is indicated in the figure.

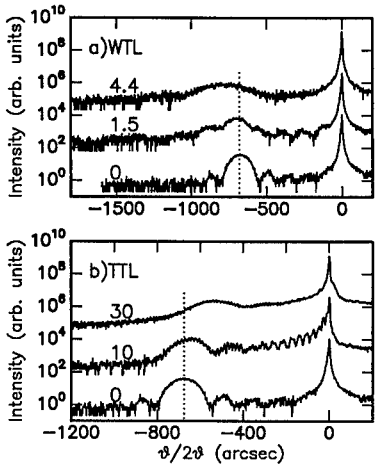


Figure 2: DCXRD rocking curves of the as-grown and as-irradiated material for a) the WTL samples, and b) the TTI samples. Fluence is indicated in units of 10^{15} Si/cm^2.

Fig. 3 shows TEM micrographs of a TTI sample irradiated to $3x10^{16}$ Si/cm^2. The X-TEM micrograph in Fig. 3a clearly shows the defect band at, or near, the GeSi-substrate interface, and large faulted loops in the underlying substrate. There is little obvious damage within the alloy layer itself, although a small population of loops is evident, concentrated mainly about the center of the alloy layer. These are noticeably smaller than the loops in the substrate. Tilting experiments with the X-TEM sample and preliminary PV-TEM analysis (see figure 3b) suggest that the defects located in the vicinity of the interface exhibit loop-like behaviour. However, they are smaller and

have a higher density than the loops in the substrate, and they are not faulted. Some appear to lie in the interface plane and others clearly lie on planes inclined to the interface.

To examine the interface defects more closely, detailed PV-TEM analysis of the TTI samples was undertaken. The faulted nature of the loops in the substrate along with the small size of the loops within the alloy layer, made it possible to discriminate between the loops above or below the interface, and the defects at, or near, the interface. PV-TEM micrographs of the $3x10^{16}$ Si/cm^2 sample are shown in figures 4a-d. They reveal that the interface defects are irregularly shaped defects with loop-like character. Some appear to be isolated defects while others clearly interact. Burgers vector analysis shown in Fig. 4, reveals that some line segments have Burgers vectors of a/2<110>, inclined to the interface plane, while segments resulting from the interactions of individual defects are of edge character and have Burgers vectors of b= a/2<110> lying in the interface plane.

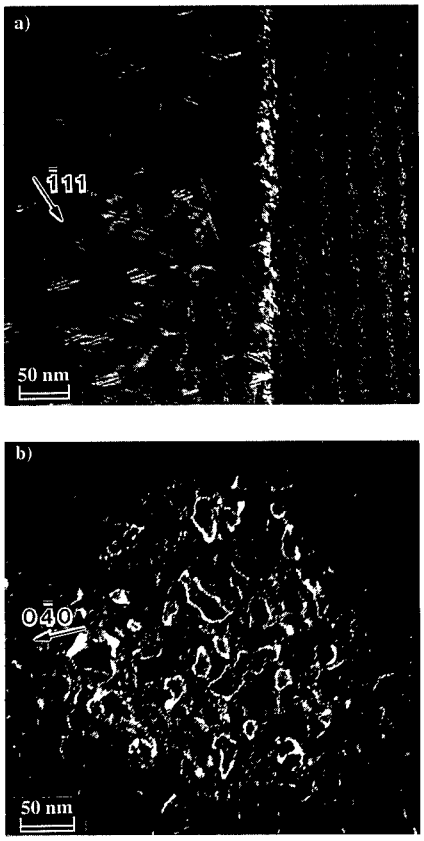


Figure 3: Weak beam TEM images of the $3x10^{16}$ Si/cm^2 TTI sample: a) in cross-section view; b) in plan-view).

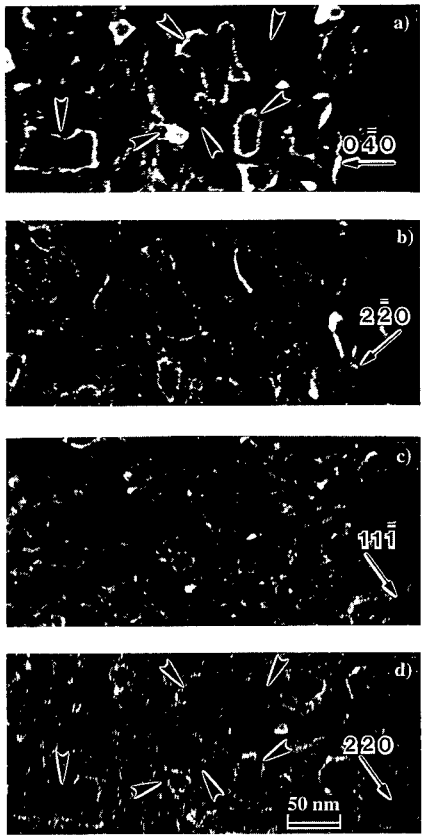


Figure 4: Weak beam plan-view TEM images of the interface defects in the $3x10^{16}$ Si/cm^2 TTI sample. g vectors indicated in figure. Arrows also indicate defect segments of interest.

Loops, with Burgers vectors of a/2[110]-type, can in principle, effect strain relief if located on the substrate side of the Ge_xSi_{1-x}/Si substrate interface. Such strain relief would be very localised, and for that reason, it is expected that a large density of such defects would be necessary to effect the strain relief observed. To confirm experimentally that these defects are the ones actually responsible for the observed relaxation behaviour, it is necessary to determine the nature and location of the loop-like defects, and the habit plane of the defects. This is difficult experimentally and is the subject of a further study, both experimental and computer modelling study.

Annealing Behaviour

The annealing behaviour of the as-grown, and irradiated material was examined by DCXRD and TEM. DCXRD analysis of the as-grown material revealed that after annealing to 450, 600, and 750 °C, the Si substrate peak and the alloy layer peak broadened, suggesting an increase in the threading dislocation density. Negligible relaxation occurred at these temperatures. However, after annealing to 900 °C (see Fig. 5), DCXRD analysis showed that the layer had relaxed partially, to ~90% of as-grown level. PV-TEM of this sample (shown in Fig. 6a), reveals a regular orthogonal array of misfit dislocations at the Ge_xSi_{1-x}/Si substrate interface with a density of $4.5x10^4$ \cm.

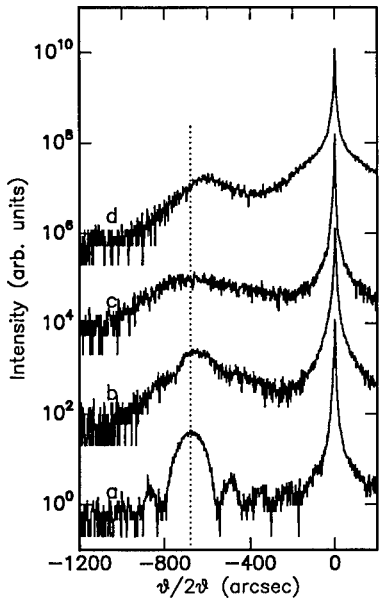


Figure 5: DCXRD spectra of samples after annealing to 900 °C: a) as-grown material; b) as-grown material after annealing; c) $4.4x10^{15}$ Si/cm^2 WTL sample; d) $3x10^{16}$ Si/cm^2 TTI sample. The peak position for the as-grown layer is indicated (~680 arsecs).

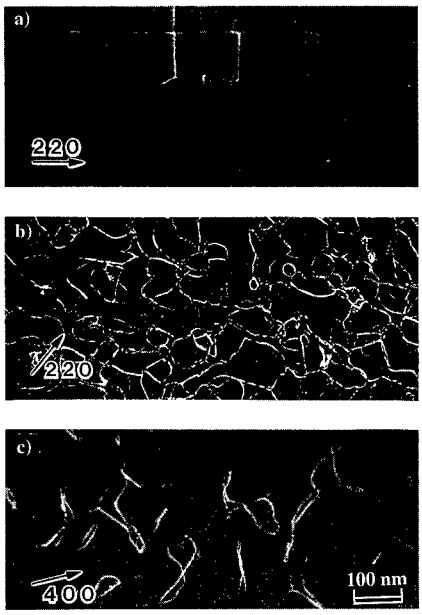


Figure 6: Weak beam plan view TEM images of samples after annealing to 900 °C: a) un-irradiated material; b) $4.4x10^{15}$ Si/cm^2 WTL sample; and c) $3x10^{16}$ Si/cm^2 TTI sample. Diffraction vectors are indicated by arrows.

DCXRD of the $4.4x10^{15}$ Si/cm^2 WTL sample and the $3x10^{16}$ Si/cm^2 TTI sample also showed little change in the strain after annealing at 450, and 600 °C. Some recovery of strain was observed after annealing at 750 °C, with the TTI sample recovering from the as-irradiated level of ~50% to ~87% of the as-grown strain. DCXRD analysis after annealing to 900 °C reveals that both WTL and TTI samples relax further although the WTL layer remains more fully strained than either the as-grown or the TTI samples (~76% of as-grown).

Fig. 6 shows PV-TEM micrographs of samples as-grown, after WTL irradiation to $4.4x10^{15}$ Si/cm^2, and TTI irradiation to $3x10^{16}$ Si/cm^2, after annealing to 900 °C. X-TEM of WTL sample (not shown) contains a mesh of interacting loops and dislocations which extend from the surface to a depth of ~70 nm. No misfit dislocations are visible at the Ge_xSi_{1-x}/Si substrate interface. X-TEM analysis of the TTI samples reveals a number of large discrete loops extending from the alloy-substrate interface towards the surface. (A network of dislocations centred approximately on the peak of damage profile of the 1 MeV Si ions (~1.1 μm) is also present). PV-TEM, Fig. 6c, reveals that segments of the loops are preferentially aligned along orthogonal <110> directions. These are presumed to effect strain relief but more detailed analysis is required before this can be confirmed. As with the WTL sample, interface misfit dislocations are also absent in this sample.

CONCLUSIONS

It has been shown that relaxation during elevated temperature ion irradiation can occur if the end-of-range of the irradiating species reaches or exceeds the depth of the GeSi/Si interface. Comparison between samples irradiated at 253 °C with low energy (23 keV) and high energy (1.0 MeV) Si ions showed that damage within the alloy layer increases the strain whereas irradiation through the layer/substrate interface results in strain relief. Loop-like defects are produced at, or near the interface during high energy irradiation. These include both isolated and interacting defects. Burgers vector analysis revealed that the loop-like structures have Burgers vectors of b= a/2<110>, inclined to the interface plane, with interacting segments of edge character of b= a/2<110>-type, lying in the plane parallel to the interface. These edge segments and edge components are believed to cause strain relief.

Irradiation was also shown to affect strain relaxation kinetics and defect morphologies during subsequent thermal annealing. For example, after annealing to 900 °C, un-irradiated material contained thermally-induced misfit dislocations, while ion-irradiated samples showed no such dislocations. Irradiated samples remained more fully strained than unirradiated samples.

REFERENCES

1. R. Metzger, Compound Semiconductor Nov/Dec, 21 (1995)
2. J. M. Glasko, R. G. Elliman, J. D. Fitz Gerald, and P. Kringhøj, Nucl. Instr. and Meth. B (1997) In press
3. D.Y.C. Lie, A. Vantomme, F. Eisen, T. Vreeland, M-A. Nicolet, T.K. Carns, V. Arbet-Engels and K.L. Wang, J. Appl. Phys. 74, 6039 (1993)
4. P. Kringhøj, J.M. Glasko and R.G. Elliman, Nucl. Instr. Meth., B96, 276 (1995)
5. S. Mantl, B. Holländer, W. Jäger, B. Kabius, H. J. Jorke and E. Kasper, Nucl. Instr. Meth. B39, 405 (1989)
6. W. Jäger, B. Kabius, W. Sybertz, S. Mantl, B. Holländer, H. J. Jorke and E. Kasper Inst. Phys. Conf. Ser. No. 100: Section 4 343 (1989)
7. J. W. Matthews and A. E. Blakeslee, J. Cryst. Growth 27, 118 (1974)
8. M. C. Ridgway, and S. L. Ellingboe, Nucl. Instr. and Meth. B (1997) In press

Effect of Stresses on Defect Nucleation in $Si_{1-x}Ge_x$/Si Heteroepitaxial Systems

Cengiz S. Ozkan, William D. Nix and Huajian Gao
Materials Science and Engineering Department
Stanford University, Stanford, CA 94305

Abstract

Strained layer semiconductor structures provide possibilites for novel electronic devices. When a semiconductor layer is deposited epitaxially onto a single crystal substrate with the same structure but a slightly different lattice parameter, the semiconductor layer grows pseudomorphically with a misfit strain that can be accomodated elastically below a critical thickness. When the critical thickness is exceeded, the elastic strain energy builds up to a point where it becomes energetically favorable to form misfit dislocations. In the absence of a capping layer, surface roughening may also take place which causes strain relaxation in the form of 2D ridges or islands via surface diffusion. At sharp valley regions on the surface, amplified local stresses can cause further defect nucleation and propagation. These defects can be detrimental to the electrical performance of devices by acting as electron-hole recombination centers or current leakage channels. In this paper, we present observations and analyses of two novel defects nucleated in heteroepitaxial $Si_{1-x}Ge_x$ thin films through surface roughening. Heteroepitaxial films 500 Å thick and containing 22% Ge are deposited by LPCVD. These initially flat films are subjected to various annealing conditions in a H_2 atmosphere to induce morphological evolution and defect formation. High resolution transmission electron microscopy and atomic force microscopy have been used to study the morphology of defects at the film surface and at the film/substrate interface.

Introduction

The growth of heteroepitaxial semiconductor structures is becoming more important due to the requirements of modern device fabrication. Heteroepitaxy is defined as growing a layer of single crystal material on another single crystal substrate with a different composition, crystal structure or crystallographic orientation. By using heteroepitaxy, it is possible to tailor the electronic or optical properties. In most cases, heteroepitaxy involves a lattice mismatch between the different materials that will produce strain in the epitaxial layer. In the case of $Si_{1-x}Ge_x$/Si heteroepitaxial structures, the lattice misfit strain ε_m is negative, and is given approximately by $\varepsilon_m = 4.2X_{Ge}$. Strained $Si_{1-x}Ge_x$ layers form the base of heterojunction bipolar transistors (HBT), which are currently used in commercial high speed analog applications. More recent research on relaxed $Si_{1-x}Ge_x$ layers has led to possible applications in CMOS and MOSFET technologies.

A key issue in heteroepitaxy is that the strain introduced by the lattice mismatch can be relaxed. Relaxation can take place by surface roughening, misfit dislocation formation at the film-substrate interface, and introduction of various defects into the epitaxial layer, such as stacking faults or dislocations. For heteroepitaxial films with subcritical thickness, the initial misfit strain at the deposition temperature can be accomodated totally as elastic strain [1], and given favorable conditions (such as annealing), strain relaxation takes place only by surface roughening in the form of 2-D ridges and 3-D islands. In the case of supercritical films, all three mechanisms can take place. Our previous studies have shown that supercritical films with 18-25 % Ge can be grown very flat and do not contain any misfit dislocations. One can study the various mechanisms of strain relaxation given above by subjecting these films to various annealing conditions [2,3]. In the present study, we focus on those defects that are formed in the film as a result of surface roughening, and present analyses for two novel defects.

Experimental Procedures

Heteroepitaxial $Si_{1-x}Ge_x$ films containing 22% and 75%Ge were deposited on to 100 mm (100) type bare silicon substrates in a single wafer chamber ASM Epsilon-1 CVD system. First, an RCA clean was done on the substrates; this was followed by a high temperature bake in the reactor for thermal

Mat. Res. Soc. Symp. Proc. Vol. 442 © 1997 Materials Research Society

desorption of the passivating oxide and a surface etch using HCl at 1185 °C. A 500 nm thick Si buffer layer was deposited at 800 °C prior to $Si_{1-x}Ge_x$ deposition to ensure a high quality nucleation layer. $Si_{1-x}Ge_x$ deposition was carried out at 550-600 °C by thermal decomposition of silane and germane at 15 Torr total pressure, using hydrogen as a carrier gas. Film deposition was followed by annealing in the reactor for the required temperature and time in a hydrogen evironment. Cross section transmission electron microscopy was done using a Philips EM430T operating at 300 KeV to study the morphology and microstructure of defects and islands. Thin foils for XTEM were fabricated using a standard procedure of stack construction, slicing, thinning, disc cutting, dimpling and ion milling [4].

Experimental Results

Figure 1 shows cross sectional bright field TEM images of a series of 500 Å thick 22% Ge films annealed at 800 °C. Figure 1(a) shows an image for the as-grown state, where the film surface is flat and there are no defects at the interface. Figure 1(b) shows a cross sectional image for a $Si_{1-x}Ge_x$

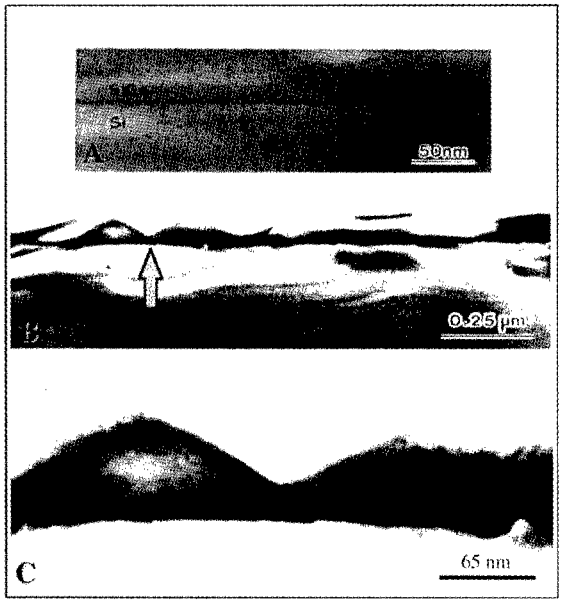


Figure 1.

film annealed at 800 °C for 20 minutes. This image reveals surface roughening and some defects, and the contrast is representative of strain distribution. Figure 1(c) is a magnified section of figure1(b) as denoted by an arrow. This image shows a very sharp cycloid-like formation, which is a potential site for defect nucleation. And, in fact, figure 2(a) shows the image of a V-shaped defect that was observed at the tip of the valley in figure 1(c). This clearly shows the role of surface roughening in nucleating defects at the sharp valley regions which act as local regions of stress concentration. This double V-shaped defect contains a 90° dislocation at its tip and two stacking faults on the side, as shown previously [2]. The 90° dislocation has a Burgers vector of (a/2)<110>, and it can be revealed by a Burgers circuit analysis around the defect. Previous research has shown that, this V-shaped defect has formed from a Lomer-Cottrell dislocation which nucleated at the valley during annealing. Depending on

its distance from the surface, a Lomer-Cottrell dislocation can become unstable, upon which the two Shockley partial dislocations in its fine structure can move to the surface under the effect of image forces, leaving trails of stacking faults behind. An analysis for the stability of a Lomer-Cottrell dislocation formed in a film under stress will be discussed shortly. Very recently, we have observed a similar defect in the midst of an island as shown in figure 3(b) (defect magnified in figure 3(c)), in the

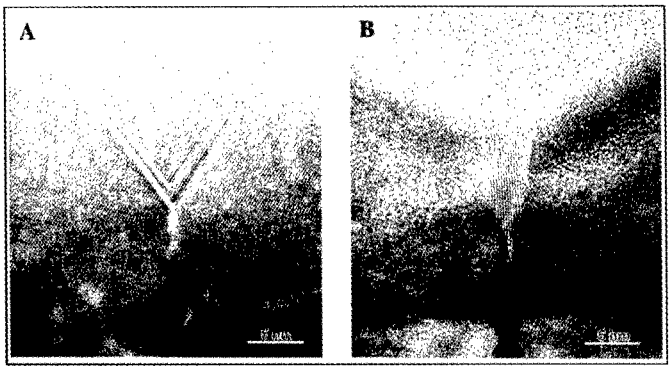


Figure 2.

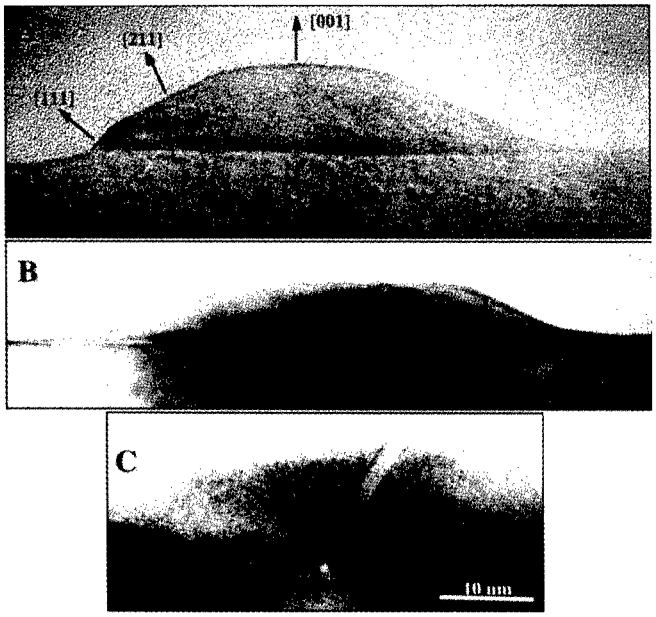


Figure 3.

case of a 75% Ge film which was initially 10 Å in thickness, and annealed at 650 °C for 1 minute. Actually, this film was subcritical with respect to dislocation formation, and figure 3(a) shows the image of a defect free island obtained on the same sample. This shows the role of surface roughening in nucleating defects even for subcritically thick heteroepitaxial films. Figure 4 depicts the nucleation and propagation mechanisms for these defects, where surface evolution proceeds in the direction of the arrow (left). We think that the mechanism shown in figure 4(b) operates whenever the the curvature at

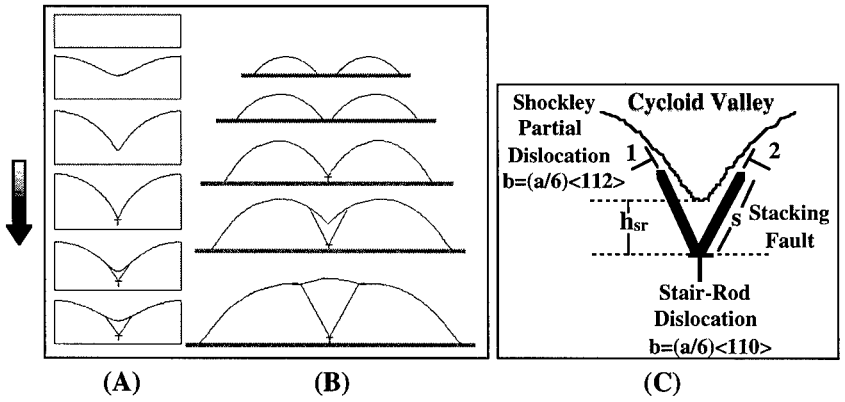


Figure 4.

the intersection of both islands is sufficiently large to produce the necessary stress concentration. This shows that, the island shown in figure 3(a) must have formed by the migration of smaller islands during annealing. Finally, Figure 2(b) shows a wedge type defect, which is encapsulated between two Σ9 twin boundaries, as determined by using image simulation. Therefore, this defect was named as a two-fold Σ9 twin [5]. Details regarding the formation of this defect will be discussed in the next section.

Theoretical Analysis

We will first present an analysis for the stability of a Lomer-Cottrell dislocation near a free surface, where the film is under a biaxial lattice mismatch stress. The stress field for a general edge dislocation can be computed by using the following Airy stress function [6],

$$\Psi(x, y, b_x, b_y, h) = C\left((b_y x - b_x y)\mathrm{Log}\left(\frac{x^2+y^2}{x^2+(2h-y)^2}\right) + \frac{4hxb_y(h-y)+2b_x h(y(2h-y)+x^2)}{x^2+(2h-y)^2}\right)$$

where $C = \dfrac{\mu}{4\pi(1-\vartheta)}$, (1)

and,

$$\sigma_{xx}(x, y, b_x, b_y, h) = \frac{\partial^2\Psi}{\partial y^2}, \quad \sigma_{yy}(x, y, b_x, b_y, h) = \frac{\partial^2\Psi}{\partial x^2}, \quad \sigma_{xy}(x, y, b_x, b_y, h) = -\frac{\partial^2\Psi}{\partial x \partial y} \tag{2}$$

Here, Ψ is the Airy stress function, μ is the shear modulus, ϑ is the Poisson ratio, b_x and b_y are the x

and y components of the Burgers vector, h is the distance of the edge dislocation from the surface, and σ_{xx}, σ_{yy} and σ_{xy} are the components of the stress field. As soon as a Lomer-Cottrell dislocation nucleates, it will have the fine structure shown in figure 4(c): A stair-rod type dislocation which is locked in place (sessile), and two Shockley partials that are separated from the stair-rod by stacking faults. If this unified defect is sufficiently close to the surface, then the Shockley partials will escape to the surface under the effect of image forces, leaving trails of stacking faults behind.

Here, we are going to investigate the equilibrium position of a Lomer-Cottrell dislocation as a function of film stress. Since the instability of this defect is governed by escaping of the Shockley partials to the surface, we would like to evaluate the stair-rod/Shockley partial distance "s" as a function of "h_{SR}", which is the distance of the stair-rod from the surface. This requires the calculation of the net driving force on a Shockley partial. If we are to do this calculation on partial number 2, we have to take into account its interaction with patial number 1, the stair-rod, and the its own image field from the surface. Furthermore, all the stress fields have to be transformed to the new coordinate system α-β in

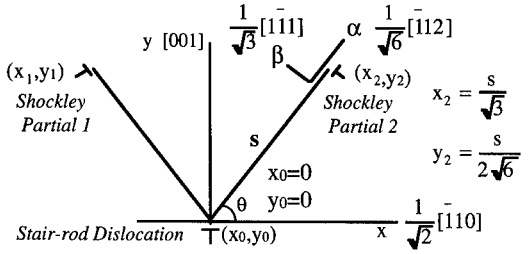


Figure 5.

order to compute the total resolved shear stress acting on Shockley partial number 2,which can be computed from,

$$\sigma_{\alpha\beta}^{(s2)} = A_{\tilde{x}\alpha}A_{\tilde{y}\beta}\sigma_{\tilde{x}\tilde{y}}^{(s1)} + A_{\tilde{x}\alpha}A_{\tilde{y}\beta}\sigma_{\tilde{x}\tilde{y}}^{(sr)} + A_{\tilde{x}\alpha}A_{\tilde{y}\beta}\sigma_{\tilde{x}\tilde{y}}^{I(s2)} \quad (3)$$

where $\sigma_{\tilde{x}\tilde{y}}^{(s1)}$ and $\sigma_{\tilde{x}\tilde{y}}^{(sr)}$ are the components of complementery stress field for the Shockley partial number 1 and the stair-rod dislocation, $\sigma_{\tilde{x}\tilde{y}}^{I(s2)}$ is the image stress field for the Shockley partial number 2 and A_{ij} are the components of the direction cosine matrix representing the coordinate transformation. The equilibrium configuration of the Lomer-Cottrell is obtained by setting the summation of Peach-Kohler forces along the α axis equal to zero:

$$\sum F_\alpha = -(\sigma_{\alpha\beta}^{(s2)} + M\varepsilon)b^{(s2)} - \Upsilon_{sf} = 0 \quad (4)$$

Where M is the biaxial modulus of the film, ε is the misfit strain and Υ_{sf} is the surface energy. The above equlibrium equation can be solved numerically for h_{SR} for a given value of biaxial film strain. Figure 6 shows a plot of the critical value of h_{SR} as a function of film stress (note that, the values are normalized with respect to the Burgers vector). For a given value of stress, the Lomer-Cottrell dislocation is stable as long as its distance from the surface is larger than the corresponding critical value; otherwise, the two Shockley partials will move to the surface and leave trails of stacking faults behind. Furthermore, this plot also shows that, for higher values of film stress, the Lomer-Cottrell dislocation is stable even at a closer distance to the surface. For a 22% Ge thin film, the misfit strainε=0.042*22%=0.924% and M=168 GPa, so that the uniform biaxial film stress is approximately

1.5 GPa. For the defect shown in figure 2(a), we have estimated a stress concetration factor of about 9 at the time this defect was nucleated, which leads to a nucleation stress value of approximately 13.5 GPa near the tip of the valley. When we look at figure 6, this corresponds to a critical depth of about two Burgers vectors. This means that, nucleation of this defect has taken place via ledge collapse at a depth closer than 2 Burgers vectors. Previous research has estimated that, the nucleation of a 90° dislocation at the surface will take place at around 7.3% strain. This requires a stress concentration factor of 7.3/0.924=7.9 for a 22% Ge alloy, which compares very well with our experimental observations.

The formation of a Lomer-Cottrell causes strain relaxation in the film. After it forms, relaxation in the film shifts the equilibrium morphology to a smoother surface, thereby decreasing the total surface energy. Therefore, a refilling process starts to operate via surface diffusion. During this refilling process, stacking faults continue to grow [2].

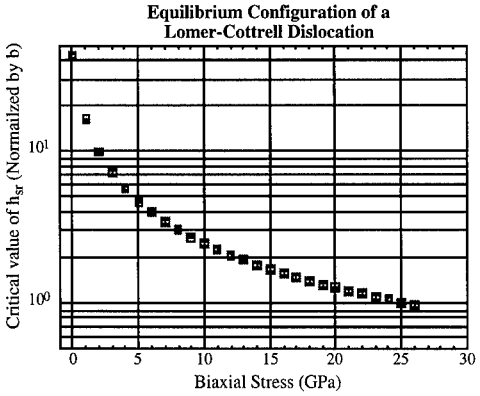
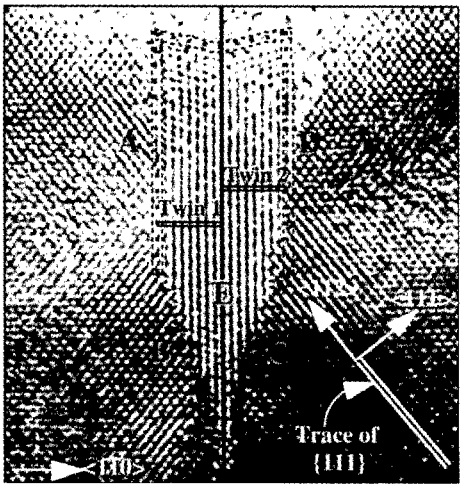


Figure 6.

The defect shown in figure 2(b) is analyzed via image simulation techniques [5]. Figure 7 shows the orientation relationships for this defect. It is in the form of a wedge, which is composed of two twins surrounded by 4 boundaries (in the original crystal matrix) and the free surface (glue part). All three crystals have a <110> type rotation axis in common. The relative rotations of the traces of{111} planes in the twins are given in the table section of figure 7. For example, in the left twin (the left part of the wedge), the relative orientation is such that, the traces of {111} planes in the original crystal are rotated by 35.264°. Hence, although boundary A is a {110} type plane in the original crystal, it becomes a {111} type plane in the left twin. In other words, there is a transformation from a {110} type plane to a {111} type plane. All the transformations given in the table are rotations relative to the common <110> type axis. Boundaries B and C are Σ9 type coincidence boundaries, and boundary E is a Σ3 type coincidence boundary. It is clear that, boundaries A and D are different than B and C, respectively. Therefore, for example, a transformation from boundary A to boundary B is associated with an elastic defect, which is a wedge disclination. Overall, there are wedge disclinations where A and B, B and C, and C and D intersect with each other. The critical strain required for the nucleation of a wedge type defect as shown in figure 7 has been determined to be larger than -2% (compressive). Now, for a 22% Ge film, the average film strain is equal to about 0.924%, hence a stress concetration factor of 2/0.924=2.16 will be sufficient to nucleate a similar defect (We have estimated a stress concentration factor of about 7-8 for the defect in figure 7). Nucleation of the wedge causes strain relaxation, and further growth of the wedge occurs as a result of surface diffusion operating to refill the valley region in

order to flatten the surface (decreasing the surface energy). A more detailed analysis of the nucleation mechanisms for this defect can be found in reference [5].



Defect Boundaries	Reference Lattice	Transformed Lattice	Rotation About [110]
A	$(0\bar{1}1)_M$	$(\bar{1}\bar{1}1)_{Twin1}$	35.264°
B	$(\bar{1}22)_M$	$(\bar{1}\bar{2}2)_{Twin1}$	38.942°
C	$(12\bar{2})_M$	$(\bar{1}2\bar{2})_{Twin2}$	-38.942°
D	$(01\bar{1})_M$	$(\bar{1}1\bar{1})_{Twin2}$	-35.264°
E	$(\bar{1}1\bar{1})_{Twin2}$	$(11\bar{1})_{Twin1}$	70.529°

Figure 7.

Conclusion

We have observed that, operation of multiple defect nucleation mechanisms take place in heteroepitaxial $Si_{1-x}Ge_x$ thin films. We have shown that cusp like features forming upon surface roughening are suitable sites for defect nucleation. One of the observed defects is a Lomer-Cottrell dislocation, and we have proposed two possible mechanisms by which it can nucleate during sharp cycloid formation via a) roughening starting from a flat surface, b) island coalescence during coarsening (or Ostwald ripening). Depending on the depth at which the Lomer-Cottrell dislocation nucleates, it can either be stable, or dissociate into a stair-rod and two Shockley partial dislocations upon which, the Shockley partials can escape to the surface leaving trails of stacking faults behind. The second observed defect is a wedge type multiple twin defect, which is composed of two twins seperated by a $\Sigma 3$ coincident boundary. The wedge is distingusihed from the matrix by four boundaries, two of which are $\Sigma 9$ type coincident boundaries. This defect has been named as a two-fold $\Sigma 9$ twin.

Acknowledgments

The support of the U.S. Office of Naval Research under the grant ONR-N00014-92-J-4094 is greatfully acknowledged.

References

1. W. D. Nix, Met. Trans., **20 A**, 2217 (1989).
2. C. S. Ozkan, W. D. Nix and H. Gao, Mat. Res. Soc. Proc., **399**, 407 (1996).
3. C. S. Ozkan, W. D. Nix and H. Gao, Mat. Res. Soc. Proc., **436**, 328 (1996).
4. J. C. Bravman, R. Sinclair, J. Elec. mic. Tech., **1**, 53 (1984).
5. P. Mullner, H. Gao, C. S. Ozkan, Philosophical Magazine **A**, in print (1996).
6. L. B. Freund, J. Appl. Phys., **68** (5), 1 (1990).

HALL EFFECT MEASUREMENTS ON Si_xGe_{1-x} BULK ALLOYS

T.MCHEDLIDZE*, I.YONENAGA**
*Komatsu Electronic Metals Co.Ltd., 2612 Shinomiya, Hiratsuka, 254, JAPAN
**Institute for Materials Research, Tohoku University, Sendai 980-77, JAPAN

ABSTRACT

Carrier transport measurement results for Si_xGe_{1-x} bulk alloys with $0.03 \le x \le 0.9$, grown by the Czochralski method are presented. Both monocrystalline (x=0.03 and x=0.23) and polycrystalline (x=0.12, 0.25, 0.4, 0.5, 0.75, 0.9) samples were analyzed. In all samples additional charge carriers were created during growth or/and cooling of crystals. With n-type starting materials only alloy with x=0.9 revealed n-type conductivity, all other alloys were of p-type. Creation of acceptors in the Si_xGe_{1-x} alloy grown by Czochralski method is maximal for $0.4 \le x \le 0.75$.

INTRODUCTION

Due to the difficulties in the growth of bulk monocrystalline SiGe alloys the electrical properties of this material remains poorly studied. Recently several successful attempts of monocrystalline Si_xGe_{1-x} growth were reported for different x values [1-3]. Although the quality of grown SiGe crystals is still much worse than that of Si or Ge crystals, probably it is quite in time to start investigation of the electrical properties of SiGe bulk crystals.

In our previous works [4,5] we reported results of carrier transport measurements in Si_xGe_{1-x} alloys with $0.03 \le x \le 0.75$. With no chemical impurity deliberately added both monocrystalline and polycrystalline alloys revealed p-type conductivity, although starting Ge and Si were n-type. Annealing of monocrystalline samples at 900C for 5 hours with subsequent quenching to room temperature caused a decrease in the acceptor concentration. From the results it was concluded that some acceptor-like species are generated during the growth or/and cooling of CZ-SiGe alloys. It is interesting to investigate the type and concentration of created charge carriers in SiGe alloy with x close to 1 grown in the same conditions and from the same starting material.

EXPERIMENTAL

Details of Si_xGe_{1-x} alloy growth by Czochralski method are described in [3]. Experiments and calculations for the Si_xGe_{1-x} alloy with x=0.9 (#029 sample) were done according to the procedures described in [4]. Namely, defect arrangement in the plane perpendicular and parallel to the growth axis was investigated using an optical microscope and densities of dislocations, twin and grain boundaries in the sample were calculated. Hall effect measurements of the sample were made by standard technique for polycrystalline and anisotropic materials [6,7].

Several pieces of #029 alloy were annealed in an evacuated quartz capsule at 900°C for 5 hours, followed by quenching to room temperature, like in the case of samples #013 and #017 in the previous work [4]. All measurements were repeated on annealed samples.

Mat. Res. Soc. Symp. Proc. Vol. 442 © 1997 Materials Research Society

Sample	Ge	#007	#016	#013	#013a*	#017	#017a*	#014	#015	#023	#029	#029a*	Si
x	0	0.03	0.12	0.23	0.23	0.25	0.25	0.40	0.5	0.75	0.9	0.9	1
CR	P	M	P	M	M	P	P	P	P	P	P	P	M
λ_{GB},cm^{-1}	3	-	14±7	-	-	25±6	16±5	30±10	28±8	67±17R 21±9L	13±8	10±6	-
λ_{TB},cm^{-1}	-	-	10±9	-	-	23±17	17±6	49±17	48±27	66±60R 18±14L	58±47	41±22	-
λ_{D},10^{3}cm^{-2}	80	10±5	16±7	71±43	63±19	19±6	31±8	42±16	22±6	79±5	26±16	34±14	3
Type	n	p	p	p	p	p	p	p	p	p	n	n	n
n_C, 10^{14}cm^{-3}	1.7	0.9 ±0.03	0.52 ±0.02	13.6 ±0.6	10.7 ±0.4	4.3 ±0.4	6.1 ±0.3	13.3 ±0.7	13.5 ±0.9	36.1 ±0.6	38.4 ±1.1	1.3 ±0.7	6× 10^{-2}
ρ,Ωcm	54	30±2	110±18	6±0.3	6±0.2	30±4	18±6	11±2	14±4	3±0.5	3±0.7	54±3	2k

Table 1. Measured characteristics of as-grown and annealed (*) 900C, 5hours in evacuated quartz capsule) samples. x represents Si content, CR - crystallinity of alloy (P - polycrystall, M - monocrystall), λ - density of defects (GB - grain boundaries, TB - twin bondaries, D - dislocations), n_C - carrier concentration, ρ - resistivity (room temperature galvanomagnetic measurements). For #023 sample GB and TB densities differ for the direction parallel (L) and perpendicular (R) to growth axis, n_C and ρ represents calculated values for the material of grains of polycrystal (see [5]).

RESULTS

Results of microscopic and of room temperature galvanomagnetic measurements for all Si_xGe_{1-x} as-grown and annealed samples with $0.03 \le x \le 0.9$ and for starting Si and Ge materials are presented in Table 1. Results for $0 \le x \le 0.5$ and $x=1$ samples are reprinted from [4]. For $x=0.75$ carrier concentration, n_c and resistivity, ρ are calculated values for the material of grains of polycrystalline alloy, taken from [5].

As seen from the table, Si_xGe_{1-x} alloy with $x=0.9$ revealed an n-type conductivity with carrier concentration higher than that in the starting material. The location of donor level, obtained from the slope of the Hall coefficient Arrenius plot curve, with a correction for the $T^{3/2}$ dependence for the density of states, gives value of 0.043eV from the bottom of the conduction band. Annealing of the sample at 900°C for 5 hours with subsequent quenching to room temperature led to large reduction in the carrier concentration and improvement of electron Hall mobility (from the value of $550 cm^2/Vs$ before annealing to almost $880 cm^2/Vs$ after). Annealing also reduced the density of grain and twin boundaries and increased dislocation density. From the variation of carrier concentration with temperature in the sample we estimated the number of compensated acceptors in #029 as-grown sample as $N_A \approx 8.2 \times 10^{13} cm^{-3}$.

DISCUSSION

Donor energy level position and annealing behavior in the as grown Si_xGe_{1-x} alloy with $x=0.9$ give possibility to suppose, that a kind of thermaldonors were created during growth or/and cooling of #029 alloy and these thermaldonors were responsible for n-type conductivity of the alloy.

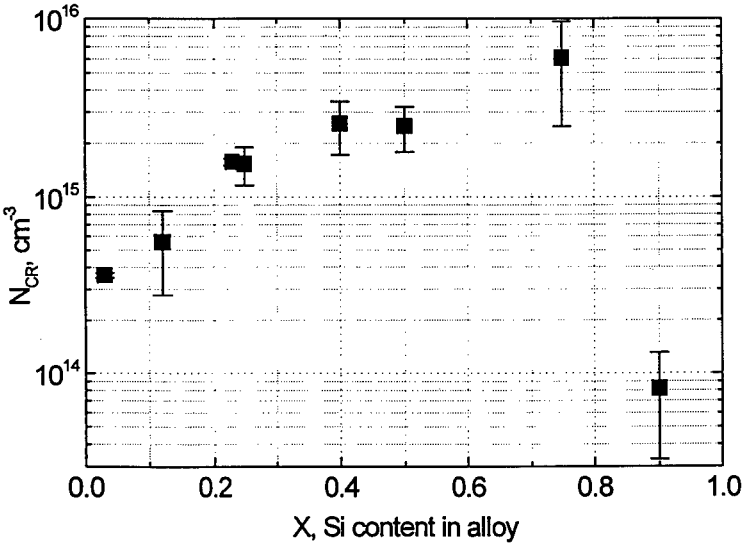


Fig.1.Created acceptor concentration in as-grown Si_xGe_{1-x} alloys with different x

Created acceptor concentration N_{CR} in Si_xGe_{1-x} alloys with different x are presented on Fig.1. The concentration is calculated according to the following equation:

$$N_{CR} = N_{MEAS} + Q_t^{GB} \cdot \lambda_{GB} + (1 - X) N_D^{Ge},$$

where N_{MEAS} is the measured acceptor concentration in the alloy, Q_t^{GB} is the acceptor trap density on grain boundaries calculated in [4] and λ_{GB} the concentration of grain boundaries in the sample, N_D^{Ge} is the donor concentration in starting Ge material. Relatively big error in the N_{CR} value is caused by estimation error in λ_{GB}.

As seen from the Fig.1, N_{CR} has maximum for middle x values. Such behavior suggests that created acceptors may be due to improper compound mixing in the alloy. High temperature annealing probably improves mixing and, as a result, concentration of the acceptors decreases (see results for #013 alloy before and after annealing in Tab.1).

Interesting point is difference in amount of created thermaldonors in the samples with $0.03 \le x \le 0.75$ and in the one with $x=0.9$. Analysis of the variation of carrier concentration with temperature for the samples with $0.03 \le x \le 0.75$ gave for the created donor concentration value $N_D < 5 \times 10^{13} cm^{-3}$ in comparison with $1.6 \times 10^{15} cm^{-3}$ donors for alloy with $x=0.9$. It will be worth to mention that thermaldonors were created in the alloy with minimal concentration of created acceptors. Of course differences in the cooling kinetics due to different compound concentration of the alloys can influence thermaldonor creation process, but it is difficult to suppose such a big difference in the cooling kinetics between alloys with $x=0.75$ and $x=0.9$.

As is well known, carbon which can be easily introduced during CZ chystal growth strongly inhibits the formation of thermaldonors (see for example [8] and references herein). We have not measured concentration of carbon in our samples, so the influence of the impurity cannot be ruled out for our case.

CONCLUSIONS

In Si_xGe_{1-x} alloys grown by the Czochralski method acceptors are created during growth or/and cooling of crystals. The amount of created acceptors is maximal for $0.4 \le x \le 0.75$. Thermaldonor generation is highly suppressed in the alloys with high acceptor concentration. At present we cannot propose clear explanation for the difference in the thermaldonor creation kinetics in the various grown Si_xGe_{1-x} alloys.

REFERENCES

1. A.Dahlen, A.Fattah, G.Hanke and E.Karthaus, Cryst. Res. Technol. **29**, p. 187 (1994)
2. M.Kurten and J.Schilz, J. Crystal Growth **139**, 1 (1994)
3. I.Yonenaga, A.Matsui, S.Tozawa, K.Sumino and T.Fukuda, J.Crystal Growth **154**, p. 275 (1995)
4. T.R.Mchedlidze, I.Yonenaga, A.Matsui and K.Sumino, Mat. Sci. Forum, **196-201**, p. 353 (1995)
5. T.R.Mchedlidze and I.Yonenaga, Jpn. J. Appl. Phys. **35**, p. 652 (1996)
6. L.J. van der Pauw, Philips Research Reports **16**, p. 187 (1961)
7. H.C.Montgomery, J.Appl.Phys., **42**, p. 2971 (1971)
8. L.I.Murin and V.P.Markevich, Mat Sci. Forum, **196-201**, p. 1315 (1995)

Part IX

Point Defects in III-V Compounds

GROWTH INDUCED ALIGNMENT OF THE FIRST NEIGHBOR SHELL OF C_{As} IN $Al_xGa_{1-x}As$

J.-F. ZHENG*, MICHAEL STAVOLA*, C.R. ABERNATHY** AND S.J. PEARTON**
*Department of Physics, Lehigh University, Bethlehem, Pennsylvania 18015, USA
**Department of Materials Science, University of Florida, Gainesville, Florida 32611, USA

ABSTRACT

We have discovered a growth-induced alignment of the Al and Ga first neighbors of C_{As} acceptors in $Al_xGa_{1-x}As$ grown by metalorganic molecular beam epitaxy. This growth induced alignment has been detected from the polarization dependence of the C atom's vibrational absorption bands that the alignment gives rise to. The alignment of the first neighbor shell of C_{As} also gives rise to aligned C_{As}-H complexes when the C is passivated by H. This leads to polarized H-stretching absorption bands which have also been observed. The growth-induced alignment provides information which helps us to assign the complicated C_{As} vibrational spectrum observed in the $Al_xGa_{1-x}As$ alloys.

INTRODUCTION

Carbon occupies an As sublattice site in epitaxial GaAs and $Al_xGa_{1-x}As$ alloys where it acts as a shallow acceptor. It can be incorporated at concentrations up to 10^{21} cm^{-3} from the metalorganic precursors or dopant gases used during growth by metalorganic molecular beam epitaxy (MOMBE) or metalorganic chemical vapor deposition (MOCVD) and has become an attractive p-type dopant.[1]

The vibrational mode of C_{As} in GaAs at 582.8 cm^{-1} has been studied extensively.[2] Isotopic fine structure due to ^{69}Ga and ^{71}Ga nearest neighbors has been observed and confirms the mode assignment and site location.[2,3] The C_{As} mode has also been observed in AlAs at 631.5 cm^{-1} (refs.4 and 5). The situation in $Al_xGa_{1-x}As$ alloys has been more complicated. Ono and Furuhata[6] observed seven vibration bands in the region 570 to 650 cm^{-1} that they assigned to the vibrations of C_{As}. Spectra of two of our samples of $Al_xGa_{1-x}As$ doped with carbon are shown in Fig. 1. The various bands that are observed are due to carbon atoms with different possible combinations of Ga and Al first neighbors.[7,8] While theoretical calculations have been performed which explain the overall extent of the spectrum, there has been insufficient information to make assignments of the observed bands to the individual modes of C_{As} acceptors with specific nearest neighbor configurations.[7] Only the bands at 632 and 574 cm^{-1} have been assigned to the A_1 and E modes, respectively, of the $AlGa_3C_{As}$ complex.[7,9] (We use the notation $Al_nGa_{4-n}C_{As}$, where n takes integer values from 0 to 4, to specify the composition of the C_{As} atom's first neighbor shell.)

It is well known that C_{As} acceptors in GaAs and $Al_xGa_{1-x}As$ alloys can be passivated by hydrogen, either intentionally or unintentionally during growth or annealing. Direct evidence for a C_{As}-H complex in GaAs was obtained by Clerjaud *et al.*[10] who observed an infrared absorption band at 2635 cm^{-1} that they assigned to the H-stretching vibration of the ^{12}C-H complex. A model was proposed in which the hydrogen atom is located at a bond-centered position between the C and a Ga nearest neighbor. The C_{As}-H complex is also present in AlAs, with the hydrogen stretching band being located at 2558 cm^{-1} (refs. 11 and 12). There are also several low frequency modes due to C_{As}-H complexes in GaAs and AlAs that have been assigned recently.[11-14] The above results are all in agreement with recent calculations.[11,15]

Mat. Res. Soc. Symp. Proc. Vol. 442 © 1997 Materials Research Society

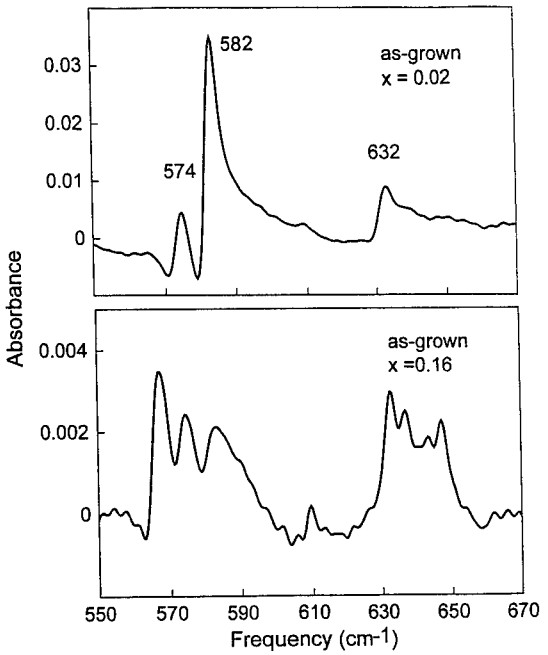


Fig. 1. Infrared absorption spectra of heavily carbon-doped $Al_xGa_{1-x}As$ samples grown by MOMBE. Spectra are label by their Al fraction, x. The sample with x=0.02 has an acceptor concentration of $N_A=1.5x10^{20}$ cm^{-3}, a thickness of 470 nm, and was grown from TEAl, TMG, and AsH_3 source gasses. The sample with x=0.16 has an acceptor concentration of $N_A=1.2x10^{19}$ cm^{-3}, a thickness of 340 nm, and was grown from TMAAl, TMG, and AsH_3 source gasses.

To better understand C_{As} in $Al_xGa_{1-x}As$, C_{As} was passivated by hydrogen and the H-stretching vibrations[16] were used as a probe of C_{As} acceptors with different combinations of Ga and Al neighbors by Pritchard *et al.*[8] Table I lists the absorption bands attributed to the H-stretching modes of C_{As}-H complexes in $Al_xGa_{1-x}As$ epilayers. Pritchard *et al.*[8] noted that the four bands with the highest frequencies have approximately equal separations but that there is then a much larger frequency shift to the fifth band at 2558 cm^{-1} due to C_{As} with four Al neighbors. Further, local-density-functional calculations show that the C_{As}-Al bond is stronger and shorter than the C_{As}-Ga bond.[8,17] Accordingly, Pritchard *et al.*[8] proposed that hydrogen atoms would be incorporated preferentially between C_{As} and Ga atoms, and that hydrogen atoms would only interupt C_{As}-Al bonds for C_{As} atoms with four Al neighbors. Thus the four bands with nearly the same separations in frequency correspond to the C_{As}-H complexes for which the C_{As} atom has one or more Ga nearest neighbors. A larger shift to the fifth band at lowest frequency (2558 cm^{-1}) occurs when the H interupts a C_{As}-Al bond for configurations with four Al nearest neighbors. The assignments made to first neighbor shell configurations are also given in Table I.

In this paper, we will make assignments of the vibrational bands of isolated C_{As} acceptors in $Al_xGa_{1-x}As$ with different nearest neighbor configurations based upon information deduced from an alignment of the atoms in the first neighbor shell that results from the crystal growth process. Defect alignments are usually produced by an externally applied stress and have often been used to determine the symmetry of a defect center and the directions of optical transition moments.[18] However, there have been a few cases where defects have been observed to be preferentially aligned following epitaxial crystal growth.[19-24] Here, we show that the first neighbor shell of a C_{As} acceptor can be aligned in $Al_xGa_{1-x}As$ alloys following crystal growth. We have also found that the H-stretching bands of the C_{As}-H complexes in $Al_xGa_{1-x}As$ show polarization dependent

absorption which indicates that the C_{As}-H complexes are also aligned. This allows the C_{As}-H complexes to be correlated with the $Al_nGa_{4-n}C_{As}$ configurations from which they arise. The growth-induced alignment of the C_{As} and C_{As}-H defects provides additional information about the directions of the transition moments of the C_{As} vibrational modes which permits the complicated mode spectrum in the alloy to be assigned.

Table I. The frequencies of C_{As}-H complexes in AlGaAs with different first neighbor shell configurations. The successive shifts in the vibrational frequency as Al atoms are added to the first neighbor shell and the configuration are given. Data and assignments are from Pritchard *et al.*[9]

ω (cm^{-1})	$\Delta\omega$ (cm^{-1})	configuration
2636	0	Ga_3C-H-Ga
2626	-10	$AlGa_2C$-H-Ga
2617	-9	Al_2GaC-H-Ga
2608	-9	Al_3C-H-Ga
2558	-50	Al_3C-H-Al

GROWTH-INDUCED ALIGNMENT OF LOW SYMMETRY DEFECT COMPLEXES

It has been found previously that a few low symmetry defect complexes are aligned following epitaxial crystal growth.[19-24] The results to be reported here are similar to recent work on a $(C_{As})_2$-H defect in epitaxial GaAs (refs. 22-24) if the C_{As} impurity in $Al_xGa_{1-x}As$ and its first neighbor shell are thought of as a low symmetry defect complex.

In heavily C-doped epitaxial layers grown by MOMBE from trimethylgallium and arsine at 500°C and with $N_A \geq 10^{20}$ cm^{-1}, a vibrational band at 2688 cm^{-1} was observed in addition to the 2636 cm^{-1} band assigned to the H-stretching vibration of C_{As}-H.[25] The intensity of the absorption band at 2636 cm^{-1} was independent of the polarization of the incident light while the 2688 cm^{-1} band was observed to be more intense for light polarized along a particular <110> direction in the (001) growth plane.[22] These results are surprising because the different <110> directions are crystallographically equivalent in the bulk of the crystal.

Skolnick *et al.* have previously studied a family of luminescence bands observed in epitaxial GaAs grown by MBE.[19] The emitted light was found to be polarized along a particular <110> direction for as-grown samples. Skolnick *et al.* noted that the equivalence of the <110> directions is broken at the growth surface.[19] Consider a (001) As-terminated surface. All of the As-Ga bonds below the surface are along a particular <110> direction, say the $[1\bar{1}0]$. All of the As-Ga bonds that will be formed above the As terminated surface will be along the perpendicular [110] direction. To explain the growth-induced alignment it was proposed that a low symmetry defect becomes aligned at the growth surface where the <110> directions are inequivalent and that its alignment is maintained as the defect is incorporated into the growing epitaxial layer.

The same mechanism has been adopted for the alignment of the defect that gives rise to the 2688 cm^{-1} band in heavily carbon-doped GaAs.[22] A low symmetry defect that can bind H is aligned at the growth surface and maintains its alignment as it is incorporated into the growing epitaxial layer. From the interpretation of a series of annealing experiments, Cheng *et al.* proposed that the 2688 cm^{-1} band was due to an aligned $(C_{As})_2H$ defect.[22] Recent theoretical work supports this assignment.[26]

Davidson *et al.* have obtained similar results for the absorption band at 2688 cm^{-1} for GaAs samples grown by MOMBE[23] and also by low pressure vapor phase epitaxy (LPVPE).[24] These

authors identified the different [110] directions in their samples and found that the 2688 cm^{-1} absorption band is strongest for light polarized along the [110] direction for both the MOMBE and LPVPE grown samples.[27] (The $[1\bar{1}0]$ direction is defined by the intersection of the (111) As terminated plane with the (001) surface.)

EXPERIMENT

We have examined several carbon-doped $Al_xGa_{1-x}As$ epitaxial layers that were grown by MOMBE on semi-insulating GaAs substrates in a Varian Gas Source Modular Gen II. The Ga and As source gases were trimethylgallium (TMG) and arsine, and the Al source gas was either triethylaluminum (TEAl) or trimethylamine alane (TMAAl). The substrate growth temperature was 500°C and the C_{As} acceptors were introduced by the TMG. The active acceptor concentrations were determined from Hall measurements. Several samples were annealed in H_2 following growth. These samples were sealed in quartz ampoules with 2/3 atm of H_2, and annealed in a muffle furnace. Following the anneal, the samples were quenched to room temperature in ethylene-glycol.

Infrared absorption spectra were measured with a Bomem DA3.16 Fourier transform spectrometer operated at a resolution of 2 cm^{-1}. The spectrometer was equipped with an InSb detector cooled to 77 K for the spectral region between 1800 and 3200 cm^{-1} and with a Si composite bolometer cooled to 4.2 K for the region between 400 and 750 cm^{-1}. The incident light was polarized with a wire-grid polarizer. The absorption measurements were made with the samples cooled to liquid N_2 temperature in an Air-Products Helitran cryostat.

ALIGNED DEFECT CENTERS IN HEAVILY CARBON DOPED $Al_xGa_{1-x}As$

It is important to recognize that both C_{As} impurities without hydrogen and C_{As}-H complexes are present in our samples and that the vibrational modes of both can be studied separately. As was discussed above, the H-stretching modes have been previously assigned to C_{As}-H complexes with specific first neighbor shell configurations.[8] Thus the dichroisms we observe for the H-stretching bands of C_{As}-H complexes, coupled with the conclusion that H preferentially enters the C-Ga bonds of the center,[8] allows the orientation of the $Al_nGa_{1-n}C_{As}$ complex to which the H is bound to be determined. Thus our strategy has been to understand the H-stretching spectrum of the C_{As}-H complexes first, and to then use the information learned about the aligned C_{As}-H centers to assign the C_{As} vibrational modes of centers without H.

Previous work showed that 5 to 10% of the carbon in epitaxial GaAs, grown under conditions very similar to our $Al_xGa_{1-x}As$ layers was passivated by H in the as-grown samples.[25] Following a treatment in H_2 at 450°C, from 15 to 30% of the C_{As} was found to be passivated.[25] We have made similar estimates of the concentration of C_{As}-H complexes from the intensities of the H-stretching modes in our $Al_xGa_{1-x}As$ samples and of the acceptor concentration from Hall measurements. We find that roughly 5 to 10% of the C is passivated in as-grown $Al_xGa_{1-x}As$ samples and that 25 to 30% is passivated in H_2 treated samples.

In the following, results for an $Al_xGa_{1-x}As$ sample with a low Al composition (x=0.02) are discussed first because the spectra are simpler than for larger Al compositions. A sample with a greater Al composition (x=0.16) is then discussed.

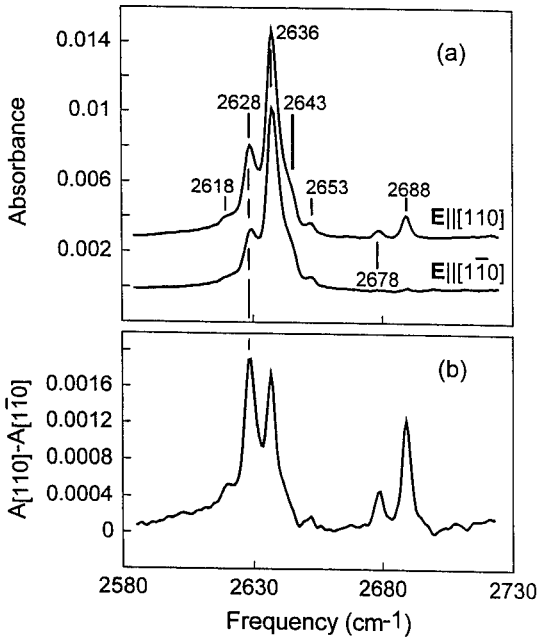


Fig. 2. (a) H-stretching spectra, measured with light polarized along the [110] and [1$\bar{1}$0] directions in the (001) growth plane for the $Al_{0.02}Ga_{0.98}As$ epi-layer whose spectrum is shown in Fig. 1. The sample was annealed at 455 °C in H_2 for 60 min to introduce hydrogen. (b) Difference of the absorbance spectra measured with [110] and [1$\bar{1}$0] polarizations.

Aligned C_{As}-H Complexes and Their Hydrogen-Stretching Modes in an $Al_{0.02}Ga_{0.98}As$ Sample

IR absorption spectra of the H-stretching modes of carbon and hydrogen containing complexes for the $Al_{0.02}Ga_{0.98}As$ sample that were measured with light polarized parallel to the two different <110> directions in the (001) growth plane are shown in Fig. 2. For this sample with a low Al composition, the bands at 2636 and 2688 cm^{-1} can be associated with C_{As}-H and $(C_{As})_2$-H complexes with only Ga nearest neighbors because of their correspondence to bands at the same frequencies observed in C-doped GaAs.

The $(C_{As})_2H$ complex with four Ga nearest neighbors that gives rise to the 2688 cm^{-1} band is nearly completely aligned as was discussed above for the same complex in epitaxial GaAs. The high carbon concentration (N_A =1.5x10^{20} cm^{-3}) is consistent with the presence of $(C_{As})_2H$ complexes similar to those seen previously in heavily-carbon-doped GaAs with $N_A \geq 10^{20}$ cm^{-3} (ref. 25). In addition to the 2688 cm^{-1} band, the band at 2678 cm^{-1} is also strongly polarization dependent. The assignment of the 2678 cm^{-1} band to the H-stretching mode of a $(C_{As})_2H$ complex with a single Al nearest neighbor is consistent with this band having the same polar ization dependence as the 2688 cm^{-1} band and a frequency of 10 cm^{-1} less than that of $(C_{As})_2H$ with all Ga neighbors. This frequency shift is similar to that shown in Table I for the addition of Al atoms to the nearest neighbor shell of C_{As}-H. If we make the reasonable assumption that the 2688 cm^{-1} band is strongest for light polarized with E//[110], as was determined by Davidson *et al.* for GaAs epitaxial layers grown by MOMBE and LPVPE,[23,24,27] then the [110] and [1$\bar{1}$0] directions are established for our samples. It is from the polarization dependence of the 2688 cm^{-1} band that the [110] and [1$\bar{1}$0] directions were determined for the data shown in Fig. 2.

Of most direct interest here is the band at 2628 cm^{-1}, previously assigned by Pritchard *et al.*[8] to the hydrogen stretching modes of a C_{As}-H complex with one Al and three Ga neighbors and with the H interupting one of the C-Ga bonds, i.e. $AlGa_2C$-H-Ga. The absorption at 2628 cm^{-1} is stronger for light polarized with **E**//[110] as can be best seen in Fig 2(b), which shows the difference of the two spectra. A convenient measure of the polarization dependence of the absorption is the dichroism D defined as

$$D \equiv \frac{\alpha_{110} - \alpha_{1\bar{1}0}}{\alpha_{110} + \alpha_{1\bar{1}0}}, \qquad (1)$$

where the α's are the absorption coefficients for the polarization directions given by the subscripts. The dichroism for the 2628 cm^{-1} band is $D = 0.2$ for this sample. We argue that the observed dichroism is due to a preferential alignment of the Ga and Al atoms in the first neighbor shell of C_{As}. This alignment of the first neighbor shell gives rise to the dichroism in the H-stretching absorption because the H preferentially occupies the C-Ga bonds. The polarization dependence of the H-stretching spectrum is explained if there are two C-Ga bonds in the $(1\bar{1}0)$ plane and just one in the (110) plane. The preferential alignment of the first neighbor shell proposed here will be confirmed by the dichroisms observed for the C_{As} modes in the next section.

For completeness, we briefly discuss the remaining H-stretching bands shown in Fig. 2 and their dichroisms. The weak band at 2618 cm^{-1} has been assigned previously to the H-stretching mode of C_{As}-H complexes with 2 Al nearest neighbors.[8] The 2618 cm^{-1} band also shows dichroism [Fig. 2(b)], but this will be more clearly seen in samples with higher Al content that will be discussed below. There is a small dichroism, $D = 0.05$, observed for the 2636 cm^{-1} band due to C_{As}-H with four Ga nearest neighbors which is presumably due to residual strain in the heavily C-doped layer. It is well-known that the C_{As}-H complex can be aligned by applied stress.[28] Finally, the weak bands at 2643 and 2653 cm^{-1} have been observed previously in heavily C-doped GaAs with $N_A \geq 1 \times 10^{20}$ cm^{-3} (ref. 25). It was suggested that these are C_{As}-H stretching modes perturbed by a distant impurity, perhaps another carbon atom.

Aligned First Neighbor Shell and the C-Modes of C_{As} Impurities in an $Al_{0.02}Ga_{0.98}As$ Sample

The infrared absorption spectra due to the carbon vibrations of $Al_nGa_{4-n}C_{As}$ complexes are shown in Fig. 3 for the same $Al_{0.02}Ga_{0.98}As$ sample discussed in the previous section. Three strong bands are observed at 574, 582, and 632 cm^{-1}. (Bands at these frequencies were observed previously by Woodhouse *et al.*[9]) Three weaker bands are observed at 567, 609, 647 cm^{-1}. The band at 582 cm^{-1} is due to C_{As} with four Ga neighbors in this sample with its low Al fraction. As can be seen in Fig. 3, the 574 cm^{-1} band is strongest for light polarized with **E**//[110], the same polarization direction for which the 2628 cm^{-1} band is strongest. The 632 cm^{-1} band is strongest for light polarized with **E**//$[1\bar{1}0]$.

The H-stretching spectra discussed above show that the Ga_4C_{As} and $AlGa_3C_{As}$ complexes are dominant in this sample and also allow the orientation of the $AlGa_3C_{As}$ complex to be determined. The $AlGa_3C_{As}$ complex has trigonal symmetry, with the C_{As}-Al bond lying along the C_3 axis of the complex. The C_{As} vibrations are A_1 and E modes, with the transition moment direction for the A_1 mode along the C_3 axis of the defect and the transition moment for the E mode in the plane perpendicular to the C_3 axis. To explain the polarization dependence of the C_{As} modes, the <111> axis of the C-Al bond must be aligned so as to be preferentially in just one of the {110} planes that is perpendicular to the (001) growth plane. When the $AlGa_3C_{As}$ complex is passivated by a

single H atom, it will interrupt a C-Ga bond because the C-Al bond is shorter and stronger.[8,15] The H-stretching absorption has been found to be stronger for light polarized along the [110] direction, establishing that the trigonal axis of the complex lies in the perpendicular (110) plane as is shown in Fig. 4(a) because there is only one C-Ga bond in this plane that might be interupted by a H atom while there are two C-Ga bonds in the perpendicular $(1\bar{1}0)$ plane.

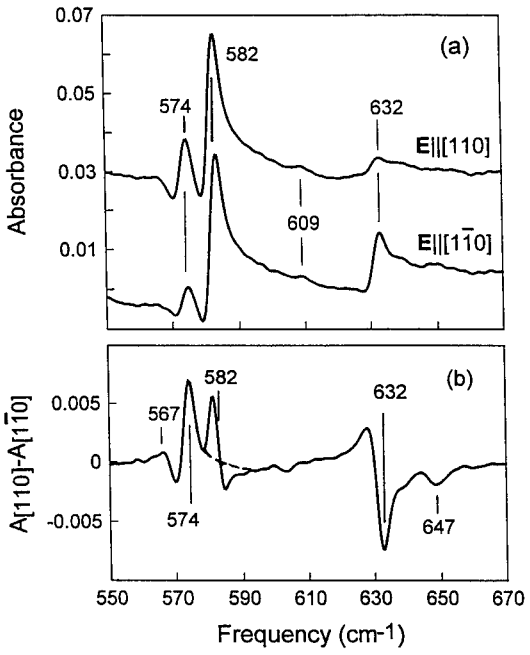


Fig. 3. (a) Infrared spectra, measured with light polarized along the [110] and $[1\bar{1}0]$ directions in the (001) growth plane, showing the C_{As} modes for the as-grown $Al_{0.02}Ga_{0.98}As$ epi-layer whose spectrum is shown Fig. 1. (b) Difference of the absorbance spectra measured with [110] and $[1\bar{1}0]$ polarizations.

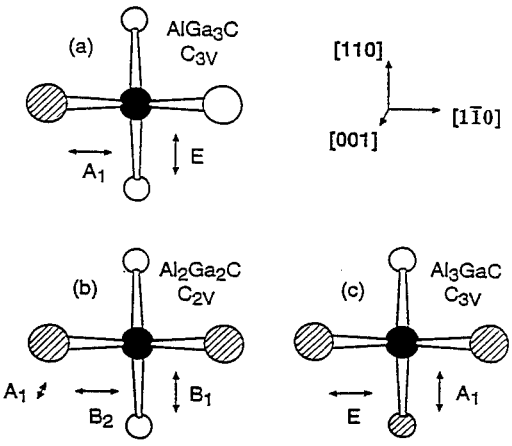


Fig. 4. View, looking down the [001] axis, of the $Al_nGa_{4-n}C_{As}$ complexes for (a) n=1, (b) n=2, and (c) n=3. The C_{As} atom is drawn black, the Al atoms are shaded, and the Ga atoms are white. The orientations of the complexes found in our MOMBE-grown samples are as shown. The projections in the (001) plane of the transition moment directions for the C_{As} modes are also shown. (The transition moment for the E mode has a smaller perpendicular component that is not shown in this figure.)

The preferential alignment we have observed now permits the 574 and 632 cm^{-1} bands to be unambiguously assigned. For the defect orientation shown in 4(a), the A_1 mode will only absorb light polarized along the $[1\bar{1}0]$ direction, and the E mode will preferentially absorb light polarized along the [110] direction. (The ratio of the absorption for the [110] polarization to the $[1\bar{1}0]$ polarization is 3:1 for the E mode.) Thus the 574 cm^{-1} band must be due to the E mode of vibration of the C_{As} atom, and the 632 cm^{-1} band must be due to the A_1 mode, confirming the previous assignment.[7,9]

Also shown in Fig. 3 are weak absorption bands at 567, 609, and 647 cm^{-1}. Their presence in this sample with a low Al content suggests that they may be due to the $Ga_2Al_2C_{As}$ complex with C_{2v} symmetry shown in Fig. 4(b). If one assumes the Al atoms in the defect lie preferentially in the same {110} plane as for the Ga_3AlC_{As} complex, their polarization dependence suggests that the 567 and 647 cm^{-1} can be assigned to the B_1 and B_2 modes, respectively. These suggestions will verified by the results shown in the next sections for a sample with a higher Al fraction.

Before completing this section we discuss the puzzling result in Fig. 3, that the band at 582 cm^{-1} that is due to Ga_4C_{As} also appears to show dichroism. This complex should not be aligned, either during growth or by residual stress in the layer, because of its high symmetry. A careful examination of the spectra shows that there is a small polarization dependent shift of the 582 cm^{-1} band which we presume is due to residual stress in the epilayer. This gives rise to a derivative-like shape in the difference spectrum and what looks to be a peak near the sharper rising edge of the asymmetric C_{As} band. We have drawn a dashed line in Fig. 3 to show where we presume the baseline to be to show that the feature near 583 cm^{-1} in the difference spectrum has no net area.

Aligned C_{As}-H Complexes and Their Hydrogen-Stretching Modes in an $Al_{0.16}Ga_{0.84}As$ Sample

The hydrogen-stretching spectra of an $Al_{0.16}Ga_{0.84}As$ sample measured with polarized light are shown in Fig. 5. The 2628, 2618, and 2610 cm^{-1} bands that are observed have been assigned to the $AlGa_2C_{As}$-H-Ga, Al_2GaC_{As}-H-Ga, and Al_3C_{As}-H-Ga complexes, respectively.[8] The intensities of the H-stretching bands are polarization dependent in the as-grown sample. The observed dichroisms are given in Table II.

Table II. Dichroisms for the H-stretching bands of the $Al_{0.16}Ga_{0.84}As$ epitaxial layer with spectra shown in Fig. 5 .

	2610 cm^{-1}	2618 cm^{-1}	2628 cm^{-1}
D	0.8	0.9	0.4

Similar to above, the polarization dependence of the H-stretching modes shows that the Al and Ga first neighbors of the C_{As} atom are aligned. Furthermore, from this polarization dependence the orientations of the $Al_nGa_{4-n}C_{As}$ complexes to which the H is bound can be determined. First, we assume the polarization dependence of the 2628 cm^{-1} band is the same as that found for the sample with x=0.02 discussed above, making the [110] direction the polarization direction for which the intensity of the 2628 cm^{-1} band is strongest. In the following we argue that the alignments of the $Al_nGa_{4-n}C_{As}$ complexes are as shown in Fig. 4. As was found for the sample with x = 0.02 above, the C_{As} atom's Al neighbors lie preferentially in the (110) plane and the Ga neighbors lie preferentially in the $(1\bar{1}0)$ plane. The magnitudes of the dichroisms of the H-stretching bands are consistent with the proposed alignments of the $Al_nGa_{4-n}C_{As}$ complexes and that H interupts the C_{As}-Ga bonds. For both the $Al_2Ga_2C_{As}$, and Al_3GaC_{As} complexes all of the C_{As}-Ga bonds lie in the $(1\bar{1}0)$ plane [Figs. 4(b) and 4(c)]. Thus the

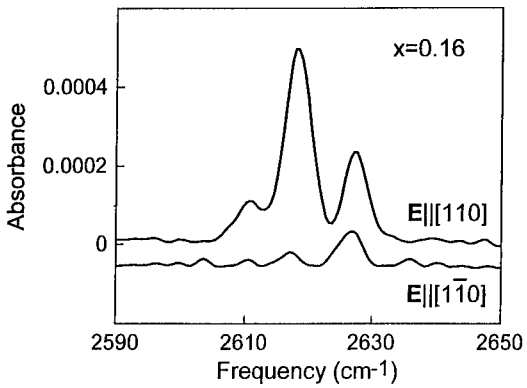


Fig. 5. (a) H-stretching spectra, measured with light polarized along the [110] and [1$\bar{1}$0] directions in the (001) growth plane for the $Al_{0.16}Ga_{0.84}As$ epi-layer whose spectrum is shown in Fig. 1. The sample was annealed at 450 °C in H_2 for 60 min to introduce hydrogen. (b) Difference of the absorbance spectra measured with [110] and [1$\bar{1}$0] polarizations.

hydrogen passivated complexes have H-stretching modes with transition moments that also lie in this plane and only absorb light with polarization **E**//[110]. The observed dichoisms are $D \approx 1$ for these complexes (see Table II), consistent with the proposed alignments. For the $AlGa_3C_{As}$ complex [Fig 4(a)], there is one C_{As}-Ga bond in the (110) plane and two C_{As}-Ga bonds in the (1$\bar{1}$0) plane. Thus in this case, the ratio of the intensities of the 2628 cm^{-1} band for **E**//[110] to **E**//[1$\bar{1}$0] would be predicted to be 2:1, giving a dichroism of $D = 0.33$. The value observed for the 2628 cm^{-1} band, $D = 0.4$, is consistent with the predicted value.

Aligned First Neighbor Shell and the C-Modes of C_{As} Impurities in an $Al_{0.16}Ga_{0.84}As$ Sample

Infrared absorption spectra of the carbon modes measured with polarized light for an $Al_{0.16}Ga_{0.84}As$ sample are shown in Fig. 6. The seven bands previously reported by Ono and Furuhata[6] are labeled in Fig. 6(b). It can be seen that the three bands with lower frequencies, at 567, 574, and 582 cm^{-1}, are strongest for light polarized with **E**//[110], and the three bands with higher frequencies, at 632, 637, and 647 cm^{-1}, are strongest for light polarized along the perpendicular direction, with **E**//[1$\bar{1}$0], while the band with frequency 609 cm^{-1}, lying between these two groups of bands, has equal intensity for both polarization directions. The two bands at 574 and 632 cm^{-1} have been assigned to the E and A_1 modes of $AlGa_3C_{As}$, respectively.

The bands at 567, 609, and 647 cm^{-1} that are strong in this sample with x=0.16 were also present as weak features in the sample with x=0.02. (Fig. 3). The presence of these bands in samples with x=0.02 and x=0.16, with their intensity increasing for the sample with greater Al fraction, leads us to assign them to the C_{As} modes of the $Al_2Ga_2C_{As}$ complex shown in Fig. 4(b). The greater concentration of the $Al_2Ga_2C_{As}$ complex, relative to the concentration of the $AlGa_3C_{As}$ complex, in the sample with x=0.16, is consistent with the relative intensities of the H-stretching modes of the hydrogen passivated complexes shown in Fig. 5. The data discussed above for the hydrogen passivated complex establishes the orientation of the $Al_2Ga_2C_{As}$ complex shown in Fig. 4(b), with the two Al atoms lying in the (110) plane. With this information about the orientation, the C_{As} modes can be assigned. The B_1 mode corresponds to the antisymmetric vibration of the C_{As} atom and its two Ga neighbors and has its transition moment oriented along the [110] direction. Thus, the 567 cm^{-1} band, which is observed for **E**//[110] in Fig 6, is assigned

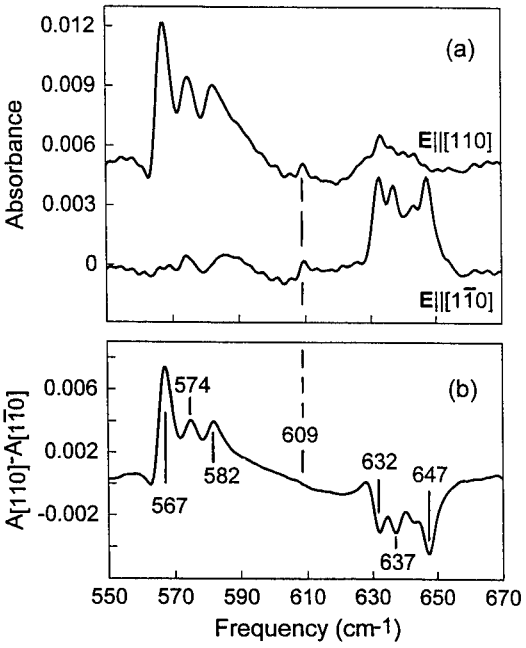


Fig. 6. (a) Infrared spectra, measured with light polarized along the [110] and [1$\bar{1}$0] directions in the (001) growth plane, showing the C_{As} modes for the as-grown $Al_{0.16}Ga_{0.84}As$ epilayer whose spectrum is shown Fig. 1. (b) Difference of the absorbance spectra measured with [110] and [1$\bar{1}$0] polarizations.

to the B_1 mode. The B_2 mode corresponds to the antisymmetric vibration of the C_{As} atom and its two Al neighbors and has its transition moment oriented along the [1$\bar{1}$0] direction. Thus, the 647 cm^{-1} band, which is observed for **E**//[1$\bar{1}$0], is assigned to the B_2 mode. The A_1 mode corresponds to the symmetric vibration of the C_{As} atom along the C_2 axis of the $Al_2Ga_2C_{As}$ complex and has its transition moment oriented along the [001] direction. The band at 609 cm^{-1} is only seen weakly in both polarization directions and is assigned to the A_1 mode. (The presence of a weak 609 cm^{-1} band for light propagating along the [001] direction indicates that the $Al_2Ga_2C_{As}$ complex is not completely aligned.)

The remaining C_{As} bands at 582 and 637 cm^{-1} in Fig. 6 can now be assigned to the Al_3GaC_{As} complex. This attribution is also consistent with the H-stretching spectrum for the hydrogen passivated C_{As} complexes for x=0.16 (Fig. 5). The 2610 cm^{-1} band previously assigned to Al_3C_{As}-H-Ga is present and the 2636 cm^{-1} band due to Ga_3C_{As}-H-Ga is absent, so the 582 cm^{-1} band is not due to Ga_4C_{As}. For the Al_3GaC_{As} orientation shown in 4(c), that was determined from the polarization dependence of the H-stretching modes of the hydrogen passivated complex, the A_1 mode will only absorb light polarized along the [110] direction, and the E mode will preferentially absorb light polarized along the [1$\bar{1}$0] direction. (The ratio of the absorption for the [1$\bar{1}$0] polarization to the [110] polarization is 3:1 for the E mode.) Thus the 582 cm^{-1} band is assigned to the A_1 mode of vibration, and the 637 cm^{-1} band is assigned to the E mode.

CONCLUSION

We have discovered, from the polarization dependence of the C_{As} vibrational bands, that the first neighbor shell of the C_{As} impurity in $Al_xGa_{1-x}As$ is aligned in several samples that were grown

by MOMBE. The C_{As} impurity's Al neighbors lie preferentially in the (110) plane, perpendicular to the (001) growth plane, whereas the Ga neighbors lie preferentially in the $(1\bar{1}0)$ plane. The C_{As}-H complexes in the same samples show corresponding alignments and the H-stretching modes are polarization dependence because the H atom interupts C_{As}-Ga bonds instead of C_{As}-Al bonds.[8]

The C_{As} impurities with an aligned first neighbor shell provide new information about the directions of the transition moments for the C_{As} vibrational modes of $Al_nGa_{4-n}C_{As}$ centers in the alloy. From the transition moment directions, the mode assignments can be deduced. The assignments of the 9 possible C_{As} modes of $Al_nGa_{4-n}C_{As}$ centers are as follows:

i) The Ga_4C_{As} and Al_4C_{As} complexes have carbon modes with frequencies of 582.8 and 631.5 cm^{-1}, respectively, that are known from previous work on C_{As} in GaAs (ref. 2) and AlAs.[4,5]

ii) The bands at 574 and 632 cm^{-1} are due to the $AlGa_3C_{As}$ complex, with the 574 cm^{-1} band being the E mode and the 632 cm^{-1} band being the A_1 mode. An appealing aspect of this assignment is that the A_1 mode is primarily a C_{As}-Al stretching vibration and that its frequency is close to the frequency of the C_{As} mode in pure AlAs.

iii) The bands at 582 and 637 cm^{-1} are due to the Al_3GaC_{As} complex, with the 582 cm^{-1} band being the A_1 mode and the 637 cm^{-1} band being the E mode. An appealing aspect of this assignment is that the A_1 mode is primarily a C_{As}-Ga stretching vibration and that its frequency is close to the frequency of the C_{As} mode in pure GaAs.

iv) The bands at 567, 609, and 647 cm^{-1} are due to the $Al_2Ga_2C_{As}$ complex, with the 567 cm^{-1} band being the B_1 mode, the 609 cm^{-1} band being the A_1 mode, and the 647 cm^{-1} band being the B_2 mode.

We conclude with a few words of caution. There are bands in the carbon vibrational region that have not been discussed here. For example, there is a shoulder in the spectra shown in Fig. 1 and Fig. 6 near 595 cm^{-1} and a peak at 643 cm^{-1}. In making our assignments, we have focussed on the vibrational bands that were also observed by Ono and Furuhata[6] and that are polarization dependent in our samples. While we believe the unassigned features are due to more complicated carbon complexes, we cannot be certain these unassigned bands are unrelated to $Al_nGa_{4-n}C_{As}$ complexes.

ACKNOWLEDGEMENTS

This work performed at Lehigh University was supported by the U.S. Navy Office of Naval Research under Contract Nos. N00014-94-1-0117 and N00014-93-1-0857.

REFERENCES

1. C.R. Abernathy, *State-of-the-Art Program on Compound Semiconductors XXIV,* edited by F. Ren, S.J. Pearton, S.N.G. Chu, R.J. Shul, W. Pletschen and W. Kamijo (Electrochem. Soc., Pennington, 1996), v. **96-2**, p. 1.
2. R.C. Newman, *Imperfections in III/V Materials,* edited by E. Weber (Academic, Boston, 1993), p. 117.
3. W. M. Theis, K.K. Bajaj, C.W. Litton, and W. G.Spitzer, Appl. Phys. Lett. **41,** 70 (1982).
4. J. Wagner, A. Fischer, and K. Ploog, Appl. Phys. Lett. **62,** 3482 (1993).
5. B.R. Davidson, R.C. Newman, D.A. Robbie, M.J.L. Sangster, J. Wagner, A. Fischer, and K. Ploog, Semicond. Sci. Technol. **8,** 611 (1993).
6. H. Ono and N. Furuhata, Appl. Phys. Lett. **59**, 1881 (1991).

7. M.J.L. Stangster, R.C. Newman, G.A. Gledhill, and S.B. Upadhyay, Semicond. Sci. Technol. **7,** 1295 (1992).
8. R.E. Pritchard, R.C. Newman, J. Wagner, F. Fuchs, R. Jones, S. Öberg, Phys. Rev. B **50,** 10628 (1994).
9. K. Woodhouse, R.C. Newman, R. Nicklin, R.R. Bradley, and M.J.L. Sangster, J. Cryst. Growth **120,** 323 (1992).
10. B. Clerjaud, F. Gendron, M. Krause, and W. Ulrici, Phys. Rev. Lett. **65,** 1800 (1990).
11. R.E. Pritchard, B.R. Davidson, R.C. Newman, T.J. Bullough, T.B. Joyce, R. Jones, and S. Öberg, Semicond. Sci. Technol. **9,** 140 (1994).
12. J. Wagner, R.E. Pritchard, B.R. Davidson, R.C. Newman, T.J. Bullough, T.B. Joyce, C. Button, and J.S. Roberts, Semicond. Sci. Technol. **10,** 639 (1995).
13. B.R. Davidson, R.C. Newman, T.J. Bullough, and T.B. Joyce, Phys. Rev. B **48**, 17106 (1993).
14. J. Wagner, K.H. Bachem, B.R. Davidson, R.C. Newman, T.J. Bullough, and T.B. Joyce, Phys. Rev. B **51,** 4150 (1995);
15. R. Jones and S. Öberg, Phys. Rev. B **44**, 3673 (1991).
16. K. Watanabe and H. Yamazaki, J. Appl. Phys. **74,** 5587 (1993).
17. R. Jones and S. Öberg, Phys. Rev. B **49,** 5306 (1994).
18. G.D. Watkins, *Early Stages of Oxygen Precipitation in Silicon,* edited by R. Jones (Kluwer, Dordrecht, 1996), p. 1.
19. M.S. Skolnick, T.D. Harris, C.W. Tu, T.M. Brennan, and M.D. Sturge, Appl. Phys. Lett. **46** 427 (1985).
20. M.S. Skolnick, D.P. Halliday, and C.W. Tu, Phys. Rev. B **38**, 4165 (1988), and references contained therein..
21. S. Charbonneau and M.L.W. Thewalt, Phys. Rev. B **41**, 8221 (1990), and references contained therein.
22. Y. Cheng, M. Stavola, C.R. Abernathy, S.J. Pearton, and W.S. Hobson, Phys. Rev. B **49,** 2469 (1994).
23. B.R. Davidson, R.C. Newman, T. Kaneko, and O. Naji, Phys. Rev. B **50,** 12250 (1994).
24. B.R. Davidson, R.C. Newman, and K.H. Bachem, Phys. Rev. B **52,** 5179 (1995).
25. D.M. Kozuch, M. Stavola, S.J. Pearton, C.R. Abernathy, and W.S. Hobson, J. Appl. Phys. **73,** 3716 (1993).
26. S.-G. Lee and K.J. Chang, Phys. Rev. B **54**, 8522 (1996).
27. B.R. Davidson, R.C. Newman, and K.H. Bachem, Phys. Rev. B **54**, 17223 (1996).
28. I.A. Veloarisoa, M. Stavola, Y.M. Cheng, S. Uftring, G.D. Watkins, S.J. Pearton, C.R. Abernathy, and J. Lopata, Phys. Rev. B **47,** 16237 (1993).

RESIDUAL IMPURITIES AND TRANSPORT PROPERTIES OF HIGH PURITY MOVPE GAAS

G. Steude, D. M. Hofmann*, M. Drechsler*, B. K. Meyer, H. Hardtdegen**,
and M. Hollfelder**

I. Physikalisches Insitut der Justus Liebig Universität Giessen, Heinrich Buff Ring 16, D-35392 Giessen, Germany

* Physics Department E 16, Technical University of Munich, D-85747 Garching, Germany

** Institut für Schicht- und Ionentechnik des Forschungszentrums Jülich, D-52425 Jülich, Germany

ABSTRACT

High purity GaAs grown by metal organic vapor phase epitaxy (MOVPE) using nitrogen as a carrier gas has been studied by optically detected cyclotron resonance (ODCR) at microwave and far infrared frequencies. Upon variation of the experimental parameters such as sample temperature, optical excitation density and microwave power the residual ionized (donor) and neutral (acceptor) impurity concentrations can be estimated, they are $2x10^{12}$ cm^{-3} and $5x10^{13}$ cm^{-3}, respectively. The luminescence results indicate C to be the dominant residual acceptor. The residual donors were identified as S, Se, Sn from the observation of the internal 1s - $3p^-$ transitions, with S showing the highest absorption strength. At low temperatures the electron mobility as determined by ODCR is about $3x10^5$ cm^2/Vs.

INTRODUCTION

Modern epitaxial semiconductor growth techniques tend to improve layer properties towards better crystaline perfection, superior optical properties, and carrier mobility. Another important aspect of innovations in crystal growth are safety issues, environmental compatibility and last not least economical aspects. The later aspects where decisive to develop growth processes for the metallorganic vapour phase epitaxy (MOVPE) using nitrogen as a carrier gas instead of the widely used hydrogen.

Excellent optical properties have been reported for GaAs, InP and AlGaAs epitaxial layers grown by a modified MOVPE process with nitrogen as carrier gas [1]. The task of the present study is to determine the carrier scattering properties of the layers.

We have used optically detected cyclotron resonance (ODCR) experiments to study the scattering processes of electrons in high purity GaAs epitaxial layers in the microwave and the far infrared spectral range. The optical detection of the cyclotron resonance has several

Mat. Res. Soc. Symp. Proc. Vol. 442 © 1997 Materials Research Society

advantages compared to the conventional detection [2]. The experiments allow to estimate the residual donor as well as the acceptor concentrations which consistently explain the the temperature and optical excitation power dependence of the electron scattering rates. The photoluminesence (PL) results indicate carbon to be the dominant residual acceptor, whereas from intra-impurity transitions observed in the far-infrared ODCR spectra the residual donors S, Se, Sn and Si could be identified.

EXPERIMENT

The samples used for the experiments were undoped GaAs layers of 10 μm thickness grown by MOVPE on semi-insulating GaAs substrate. Details of the crystal growth process can be found in ref. [1].

The optically detected cyclotron resonance experiments were performed using a far-infrared laser, pumped by a CO_2 laser which gave laser lines at 163 μm and 118.8 μm and microwaves at frequencies of 36 GHz and 140 GHz.

For the far-infrared and 140 GHz experiments the sample was placed in a 12 Tesla superconducting solenoid magnet. The photoluminescence was excited by an air cooled Argon-ion laser at 488 nm via an optical fiber, and the same fiber was used to collect the emitted light. The PL was thereafter dispersed by a 1/4 m single grating monochromator and detected with a LN_2 cooled Ge detector.

The 36 GHz experiments were performed in a 4 Tesla superconducting splittcoil cryosystem which allows optical access through windows. Here the sample was placed in the center of a TE_{011} resonator. The optical excitation and detection components were similar to those used for the far-infrared system.

For the analysis of the ODCR spectra one has to take into account that in the experiments the sample is exposed to unpolarized high frequency radiation. Thus the cyclotron resonance lineshape is decribed by the equation [3]:

$$P(\omega) \sim \frac{1+(\omega_o^2+\omega_c^2)\tau^2}{[1+(\omega_c^2-\omega_o^2)\tau^2]^2+4\omega_o^2\tau^2} \cdot \frac{Ne^2\tau}{m^*} \qquad (1)$$

Here τ is the carrier momentum relaxation time, P the power absorbed and N the number of carriers. ω_c is the cyclotron frequency, $\omega_c = eB/m^*$ with m^* the electron effective mass. If $\omega_c\tau > 1$, the resonance occurs at $\omega_o = \omega_c$ and τ can be obtained from the full width (ΔB) of the resonance line at half of its maximum, by the expression $\omega_c\tau = 2B_r/\Delta B$, where B_r is the resonance magnetic field.

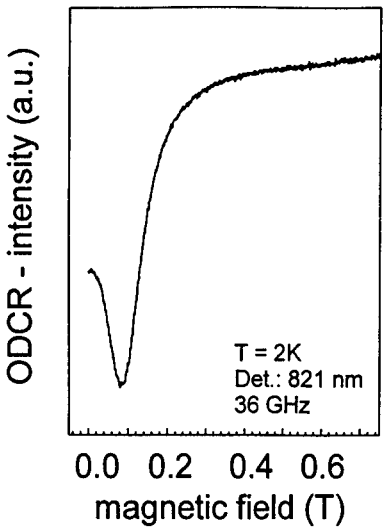


Figure 1 :
Optically detected cyclotron resonance spectrum of conduction band electrons in the MOVPE GaAs layers grown with N_2 carrier gas

RESULTS AND DISCUSSION

Low temperature high resolution photoluminesence spectra of the samples have been reported before [1]. Therefore here only the mayor features are briefly described. In the excitonic region recombinations due to free-, donor-, and acceptor bound excitons can be resolved at about 1.49 eV. At 1.493 eV the conduction band electron to acceptor recombination is observed as well as the corresponding donor - acceptor pair recombination. The energetical positions of the acceptor related recombinations are identical to those previously attributed to carbon acceptors, which is a common residual impurity in high quality epitaxial layers [4].

Fixing the optical detection energy at the position of the excitonic recombination and sweeping the magnetic field the ODCR spectra were measured. A typical 36 GHz spectrum is shown in Fig.1. From the resonance position an effective mass value of $0.066m_o$ is obtained, which is in good agreement to literature data of 0.0661 m_o [5]. From the halfwidth of the resonance a relaxation time $\tau = 1.1 \times 10^{-11}$ s is obtained, which corresponds to a mobility of $\mu_{ODCR} = 3 \times 10^5$ cm^2/Vs.

The scattering mechanisms are studied by temperature dependendent measurements of the cyclotron resonance. The experimental data are shown in Fig. 2 as full squares. From 1.5 K to 10 K the scattering rate increases only slightly, above 10K the increase is stronger. Measurements were possible up to 40 K, for higher temperatures the luminescence intensity became too small and the experimental conditions too unstable to give convincing results.

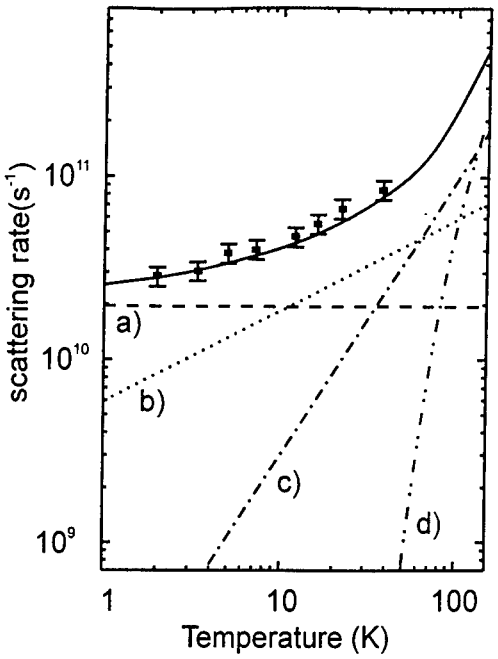


Figure 2 :
Experimental temperature dependence of the electron scattering rate in the MOVPE GaAs layers (symbols). Broken lines: calculations taking a) neutral impurity-, b) piezoelectric-, c) acoustic-phonon-, and d) LO-phonon- scattering into account. Full line: calulated total scattering rate

The temperature dependence is well explained taking three scattering mechanisms into account: a) neutral impurity scattering, b) acoustic-phonon piezoelectric scattering, and c) acoustic phonon deformation potential scattering. The contribution of each of these scattering mechanisms to the total scattering rate are given by the broken lines in Fig.2. For completteness LO-phonon scattering is also included (line d) in Fig.2, but it is not of relevance for the low temperature data. The total scattering rate has been obtained according to Mathiesen´s rule. The calculations to obtain the scattering rates have been treated as given in textbooks [6]. A good agreement to the experimental data is obtained for an neutral impurity concentration of $5x10^{13}cm^{-3}$.

On a first view it might be surprising that ionized impurity scattering does not play a role in the analysis of the data. The material is p-typ conductive due to the presence of residual carbon acceptors. At low temperature in thermal equilibrium they are in the neutral charge state, except the fraction compensated by residual donors. Thus the number of ionized impurities is roughly given by two times the number of residual donors. This fraction of ionized impurities is photo-neutralized under the experimental conditions used for the temperature dependent measurements.

The photo-neutralization effect can be reduced by reducing the power of the exciting laser beam. These experiments are shown in Fig. 3. The dependence is explained by taking

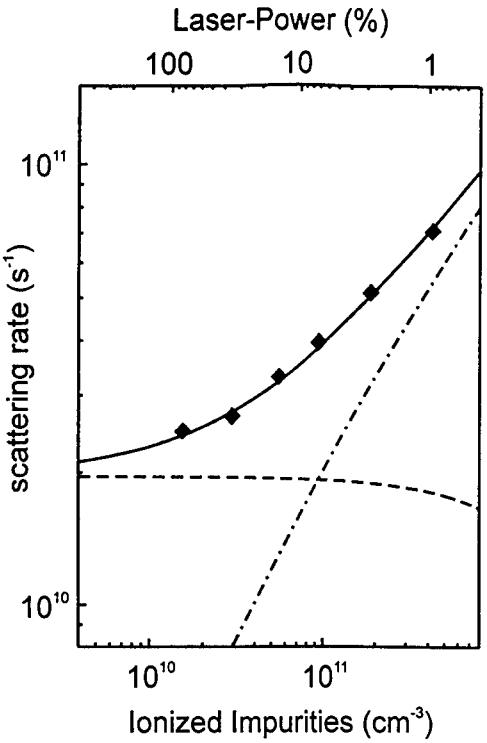


Figure 3 :
Dependence of the electron scattering rate in the laser power used for the ODCR experiments. Contributions of neutral-impurity-scattering (dashed line) and ionized-impurity-scattering (dashed dotted line). Drawn line: calculated total rate

into account neutral (dashed line) and ionized impurity scattering (dash-dotted line). To fit the experimental data the ionized impurity concentration should vary from about 2 x 10^{10} cm^{-3} for high excitation powers to 2 x 10^{12} cm^{-3} for low excitation powers. Assuming that at low excitation powers almost thermal equilibrium ("dark") conditions are present 1 x 10^{12} cm^{-3} reflects the approximate residual donor concentration in the sample.

Information on the chemical nature of the residual donors can be obtained by far-infrared experiments, since the internal transitions of the hydrogen like states of the residual donors can be observed [1,7]. Due to the chemical shift these transitions are located at different magnetic field positions. These central cell effects are best resolved on the 1s - 3p-transitions, which are shown in Fig. 4. The absorption lines due S, Sn and Se are observable. S shows the highest absorption strength. For comparison a spectrum of a MOVPE GaAs layer using H_2 instead of N_2 as carrier gas is shown in Fig. 4b). The ODCR properties of both layers were almost identical. The H_2 layer showed approximately a factor of two higher mobility at low temperatures. In the layer grown with H_2 carrier gas the residual donor element is Si. It indicates that the group VI elements are probably residual trace impurities in the N_2 gas.

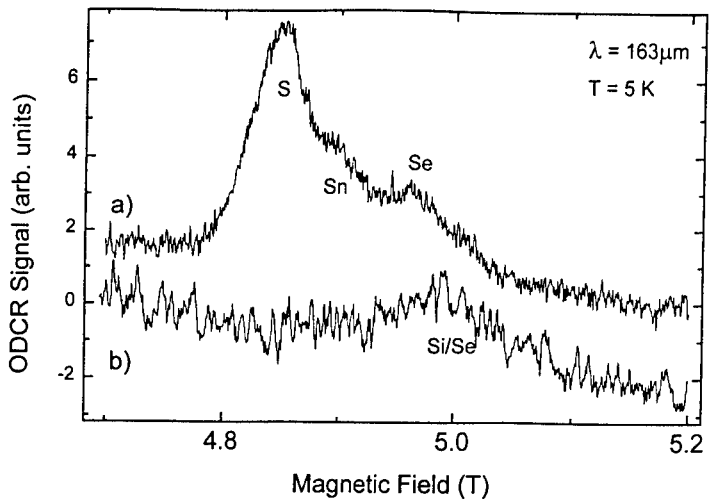


Figure 4:

Far-infrared spectra of the 1s - $3p^-$ transitions of shallow donor impurities in a) MOVPE grown GaAs using N_2 carrier gas, and b) using H_2 carrier gas.

In conclusion optically detected cyclotron resonance experiments have been used to study the carrier scattering in high purity MOVPE grown GaAs. The experiments allow to estimate the residual impurity concentrations and information on their chemical nature is obtained from far-infrared experiments.

REFERENCES

[1] H. Hardtdegen, P. Giannoules, III/Vs Review **8**, 34 (1995)

[2] M. Godlewski, W. M. Chen, and B. Monemar, Crit. Rev. Solid State Mater. Sci. **19**, 241 (1994)

[3] C. Kittel, G. Dresselhaus, A. F. Kip, Phys. Rev. **98**, 368 (1955)

[4] B. Hamilton, Properties of GaAs, (INSPEC publication, London, 1990) p. 246

[5] J. G. Michels, R. J. Warburton, R. J. Nicholas, and C. R. Stanley, Semicond. Sci. Technol. **9**, 198 (1994)

[6] K. W. Böer, Survey of semiconductor physics (Van Nostrand Reinhold, New York, 1990)

[7] Z. Wasilewski and R. A. Stradling, Semicond. Sci. Technol. **1**, 264 (1986)

AN ANOMALOUS DEEP CENTER (E_C-0.31 eV) IN SEMI-INSULATING GaAs

Z-Q. FANG AND D. C. LOOK
Physics Department, Wright State University, Dayton, OH 45435 USA

ABSTRACT

A prominent deep center in semi-insulating GaAs, T_5 at E_C-0.31 eV, has been studied by thermally stimulated current (TSC) spectroscopy using variation of illumination energy, intensity, and time. Unlike the case for most of TSC traps, the steady-state (long illumination time) peak intensity of T_5 varies with light intensity. With the additional evidence that T_5 seems to be related to both As_{Ga} and V_{As}, it is possible that a photoinduced interaction As_{Ga}-$V_{As} \rightarrow V_{Ga}$-$As_i$-$V_{As}$ is taking place.

INTRODUCTION

Although the major deep donor in undoped SI GaAs is EL2 (an As_{Ga}-related defect), there exist several other point defects having levels shallower than that of EL2. One of them is a center at E_C-0.31 eV, which is commonly seen by thermally stimulated current (TSC) spectroscopy (labelled as T_5 in our laboratory, with a peak occurring near 140 K). Much work has been devoted to understanding its nature, which can be summarized as follows: 1) typically, T_5 is one of the largest peaks in the TSC spectrum, especially for SI GaAs with As-rich crystal stoichiometry [1,2]; 2) the average published values of the energy level E_T and the capture cross section σ_T for T_5 are 0.31 eV and 4 x 10^{-15} cm^2 [3], which incidentally are close to those of the DLTS center EL6 [4]; 3) under strong infrared (IR) light ($h\nu$=1.10 eV) illumination T_5 can be fully quenched [5] and its thermal recovery rate [r = 2.0 x 10^8 exp (-0.26 eV/kT)] is very close to that for EL2 [6]; 4) an electrical-field-enhanced thermal quenching of T_5 during the TSC scan can be frequently observed in less As-rich SI GaAs, such as that grown by the vertical gradient freeze technique [7]; and 5) there is a good correlation between the trap density of T_5 and the V_{As} concentration, as measured by positron lifetime spectroscopy under 1.42 eV illumination [8].

Recently, more studies have been conducted on this center and in this paper we present the dependence of T_5 and other TSC traps on the wavelength and intensity of the trap-filling light at 83 K. Based on all these results, T_5 is thought to be a defect complex, related to both As_{Ga} and V_{As}, and to possibly be produced, in part, by a light-induced reaction.

EXPERIMENTS AND SAMPLES

In the TSC measurements, the samples were cooled to a low temperature (~ 83 K) in a Bio-Rad DL4600 system, then illuminated with 1.45 eV or weak 1.13 eV light, which mainly causes electron excitation from neutral EL2 centers. After a period of excitation long enough for the trap populations to reach steady state, but short enough to avoid quenching of either the photocurrent (PC) or the TSC signals, the illumination was removed and the sample was heated at a linear rate β (e.g. 0.3 K/s) in the dark. As the

Mat. Res. Soc. Symp. Proc. Vol. 442 © 1997 Materials Research Society

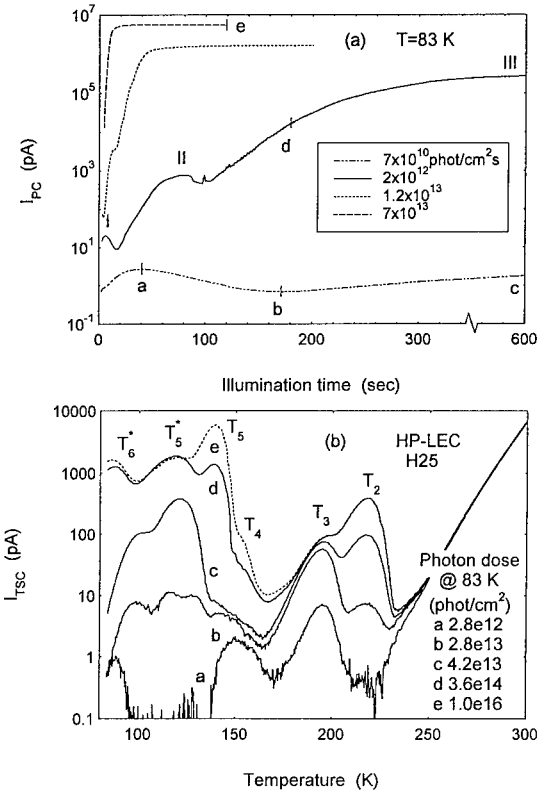


Figure 1

(a) Photocurrent responses at 83 K and (b) TSC spectra (using 1.13 eV light), measured on sample H25 as a function of photon dose, showing the trap filling of T_3 and T_2, and the development of T_5 and T_6^*

temperature is raised, TS currents are contributed by carriers being freed from individual traps. The peak temperature (T_m) in the TSC spectrum can be correlated with the energy level (E_T) of the traps by $E_T/kT_m = \ln T_m^4/\beta + \ln 1.7 \times 10^{16}\ \sigma_T/E_T$, where σ_T is the apparent capture cross section and k, Boltzmann's constant. For the spectral dependence measurements, monochromatic light with different photon energies from 0.80 eV to 1.45 eV was provided either by a tungsten halogen lamp, using appropriate interference filters, or by a 1/4-meter monochromator. The light intensities were calibrated by a power meter placed at the sample position. Three undoped SI GaAs samples were used in the study; two (H25 and H059) were grown by the high-pressure liquid encapsulated Czochralski (HP-LEC) method, using As-rich and Ga-rich melt stoichiometry, respectively, and the other one (L2901), by the low-pressure (LP) LEC technique.

RESULTS AND DISCUSSION

Fig. 1a presents the photocurrent responses at 83 K for sample H25, using 1.13 eV light with different intensities. From the figure, we see a complex photocurrent development for a moderate light intensity (2×10^{12} phot/cm^2 s), and a slight quenching for a high intensity

(7×10^{13} phot/cm^2 s). The development of the photocurrent is accelerated by increasing the light intensity and therefore cannot be observed in detail at high light intensities, an effect observed by many authors [5,9,10]. Corresponding to excitation photon doses from 2.8×10^{12} to 1.0×10^{16} phot/cm^2, as noted by symbols a through e in Fig. 1a, the various TSC spectra show dramatic changes, as pictured in Fig. 1b. From the figure, we can compare the trap filling processes for the different traps: 1) T_3 is the first trap filled; 2) T_2 is then gradually filled; and 3) T_5 and T_6^* seem to be the last traps filled. After long-term illumination, a photoquenching of the TSC spectrum can be observed (not shown), as described in Ref. [5]. We have also measured the photocurrent responses using different photon energies from 0.95 to 1.45 eV. Basically, the measured responses consist of three portions, as indicated in the curve (solid line) representing a moderate light intensity in Fig. 1a. The first portion (from zero to I), the second portion (from I to II), and the third portion (from II to III) are found to correspond to the filling of T_3, the filling of T_2, and the filling (and possibly development) of T_5 and T_6^*, respectively. Santic et al. reported very similar experimental results and proposed a model based on the filling/emptying of deep traps with charge carriers to explain the observed phenomena [11]. However, as discussed below, we believe that there may exist a photoinduced creation mechanism for T_5, which can affect the photocurrent evolution at low temperatures. The measured E_T and σ_T for the main TSC traps can be found in our recent publication [8].

The spectral dependences of the steady-state peak heights, after long-term illumination at a constant intensity of 6.25×10^{14} phot/cm^2 s for each wavelength, are shown in Fig. 2 for sample H059. From a simple rate-equation analysis, it can be shown that the steady-state occupied fraction of a single-donor trap, N^o_T/ N_T, will be given by

$$\frac{N_T^o}{N_T} = \frac{1}{1+F(\lambda)\dfrac{\sigma_{vp}(\lambda)}{\sigma_{vn}(\lambda)}} \qquad (1)$$

where $\sigma_{vp}(\lambda)$ and $\sigma_{vn}(\lambda)$ are the photoionization coefficients for hole and electron excitation, respectively, from EL2, and $F(\lambda)$ is a weak function of λ as long as the trap photoionization coefficients are smaller than those due to EL2. The TSC signal will be proportional to N^o_T if the trap is an electron trap. From Fig. 3 of Ref. 12, we can see that

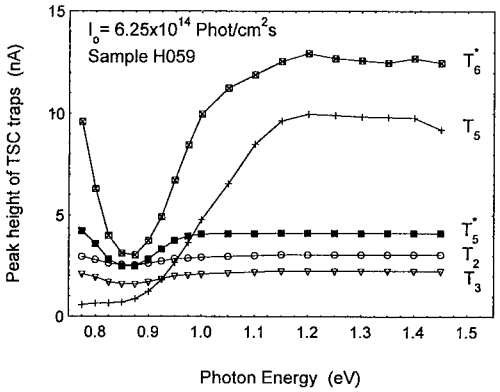


Figure 2

Spectral dependence of the peak height for major TSC traps, measured on sample H059 by using different photons with an equal photon flux for the excitation at 83 K

σ_{vp}/σ_{vn} clearly goes through a maximum near hν=0.9 eV and thus N_T should go through a minimum at this energy, which indeed is the case for traps T_2, T_3, T_5^*, and T_6^*, as shown in Fig. 2. Trap T_5, on the other hand, does not show a minimum, although the extreme weakness of the signal at hν=0.8 eV might obscure the detailed dependence on light energy.

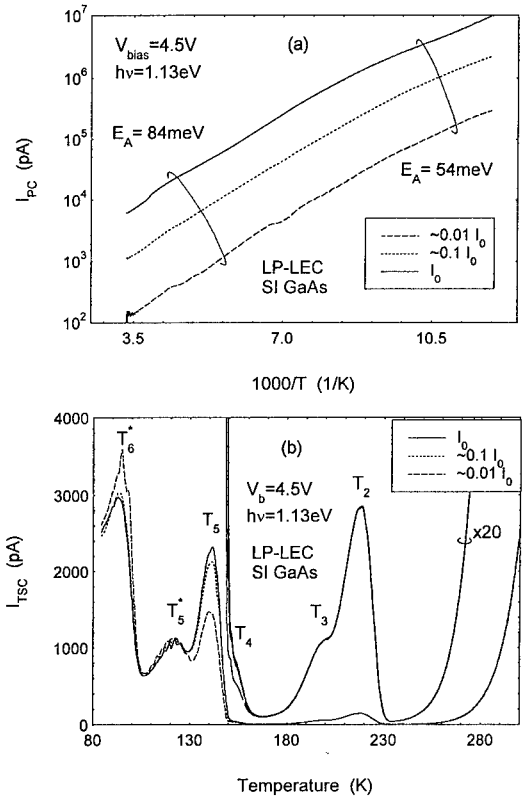


Figure 3

(a) Temperature dependent photocurrents and (b) TSC spectra (using 1.13 eV light), measured on sample L2901 as a function of light intensity

Also of interest is the fact that Eq. 1 is independent of light intensity I_o. In Fig. 3a and 3b, respectively, we show the PC and TSC as a function of I_o. Note that the PC (Fig. 3a) is proportional to I_o, as expected, and in fact has a temperature dependence that shows that the carrier lifetimes are controlled by EL2, an assumption used in the derivation of Eq. 1 and proven in an earlier work [13]. Also, from Fig. 3b we see that most of the trap intensities, under steady-state illumination at 83 K, are independent of I_o, as predicted by Eq. 1 (note that $I_{TSC} \propto N^o_T$). We thus infer that traps T_5 and T_6^* are anomalous, since their intensities vary with I_o. The density of T_6^* decreases with I_o, and that of T_5 increases, which suggests that T_6^* may be destroyed by the light, and T_5, created. Certainly such properties are not unknown, as evidenced by the light-induced changes in the atomic structure of EL2 itself.

There is evidence that T_5 is related to As_{Ga} in that it is usually the dominant trap in SI GaAs and also, its quenching properties are nearly identical to those of EL2. However, there is also evidence that T_5 is related to V_{As}, because its density increases with 1-MeV electron irradiation (although at a much lower rate than that of T_6^*, the As vacancy). Thus, it is tempting to assign T_5 to the As_{Ga}-V_{As} complex, or some variation of that complex, such as V_{Ga}-As_i-V_{As}. In this regard, we note that V_{Ga} (which is created by 1-MeV electron irradiation but evidently at a lower rate than that of V_{As} [14]) can easily be transformed by a nearest-neighbor As hop to As_{Ga}-V_{As}, and the switchover occurs for Fermi levels near midgap [15,16]. Also, the As can move to a metastable configuration, V_{Ga}-As_i-V_{As}. Baraff and Schluter [15] have suggested that As_{Ga}-V_{As} defects should be abundant in GaAs, which would support the dominance of T_5 in typical TSC spectra. Also, positron annihilation measurements have shown the presence of V_{Ga} in SI GaAs [17] so that T_5 could be increased by the light-induced transformations $V_{Ga} \rightarrow As_{Ga}$-$V_{As}$ or $V_{Ga} \rightarrow V_{Ga}$-$As_i$-$V_{As}$. Moreover, high or even moderate electrical fields can destroy T_5 (or at least cause the TSC signal to disappear) at about 140 K [7], which could be explained by a reverse defect transformation of the type we are describing. This latter effect occurs only for T_5, again confirming its anomalous nature among the TSC traps in SI GaAs.

Finally, as mentioned earlier, we note from Fig. 3b that, under increased light illumination, the T_6^* density decreases and the T_5 density increases. Again, it is tempting to suggest that some of the T_6^* may be transformed to T_5 by the light. In this regard, we recall an experiment [18,19] in which we showed that an 0.15-eV Hall-effect center, thought to be As_{Ga}-V_{As}, was transformed to a metastable 0.29-eV center, thought to be V_{Ga}-As_i-V_{As}, under IR light irradiation. Note that 0.15-eV is very close to the T_6^* energy, and 0.29-eV, close to the T_5 energy. Although 1-MeV electron-irradiation experiments show a large increase of T_6^* with electron fluence, which suggests an assignment of T_6^* to isolated V_{As}, it is probable that the defect As_{Ga}-V_{As} also has a donor level close to that of V_{As}. Thus, the Hall results [18,19] and the TSC results in Fig. 3b, are consistent in that in each case an 0.15-eV center is transformed to an 0.3-eV center by IR light illumination. Also, the thermal recovery of the 0.29-eV metastable Hall center occurs at about 140 K, near the electric-field-induced instability temperature of T_5. Here it is possible that at 140 K the electric field causes a transformation of T_5 back to T_6^*, in which case the center would immediately lose its electron to the conduction band, causing the high-temperature edge of the T_5 lineshape to be much sharper than usual. However, some of these speculations must await further experimentation and analysis.

CONCLUSIONS

A prominent deep center, T_5 at E_C-0.31 eV, in SI GaAs has been extensively studied by TSC spectroscopy using variation of illumination energy, intensity, and time, and different applied electrical fields. The experimental results obtained so far suggest that the center is related to both As_{Ga} and V_{As}. A possible light-induced metastable configuration, V_{Ga}-As_i-V_{As}, has been proposed for T_5.

ACKNOWLEDGMENT

Z-Q. F. and D. C. L. were supported by U.S. Air Force Contract No. F33615-95-C-1619, and part of the work was performed at the Avionics Directorate, Wright Laboratory, Wright-Patterson Air Force Base, Ohio.

REFERENCES

1. Z-Q. Fang and D. C. Look, J. Appl. Phys. **69**, 8177 (1991)
2. U. V. Desnica, B. Santic, D. I. Desnica, and M. Pavlovic, J. Electron. Mater. **22**, 403 (1992)
3. D. I. Desnica, J. Electron. Mater. **21**, 463 (1992)
4. G. M. Martin, A. Mitonneau and A. Mircea, Electron. Lett. **13**, 191 (1977)
5. Z-Q. Fang and D. C. Look, Appl. Phys. Lett. **59**, 48 (1991)
6. Z-Q. Fang and D. C. Look, J. Appl. Phys. **73**, 4971 (1993)
7. Z-Q. Fang and D. C. Look, Appl. Phys. Lett. **66**, 3033 (1995)
8. Z-Q. Fang, D. C. Look, S. Kuisma, K. Saarinen, and P. Hautojarvi, in Proceedings of 9th Conference on Semiconducting and Insulating Materials, Toulouse (1996) (in press)
9. U. V. Desnica, D. I. Desnica, and B. Santic, Appl. Phys. Lett. **58**, 278 (1991)
10. J. Jimenez, M. A. Gonzalez, P. Hernandez, J. A. de Saja, and J. Bonnafe, J. Appl. Phys. **57**, 1152 (1985)
11. B. Santic, U. V. Desnica, N. Radic, D. I. Desnica, and M. Pavlovic, J. Appl. Phys. **73**, 5181 (1993)
12. P. Silverberg, P. Omling, and L. Samuelson, Appl. Phys. Lett. **52**, 1689 (1988)
13. D. C. Look and Z-Q. Fang, J. Appl. Phys. **80**, 3590 (1996)
14. D. Pons and J. C. Bourgoin, J. Phys. C. Solid State Phys. **18**, 3839 (1985)
15. G. A. Baraff and M. Schluter, Phys. Rev. B33, 7346 (1986)
16. Y. Bar-Yam and J. D. Joannopoulos, Phys. Rev. Lett. **56**, 1213 (1986)
17. K. Saarinen, S. Kuisma, P. Hautojarvi, C. Corbel, and C. Le Berre, Phys. Rev. Lett. **70**, 2794 (1993)
18. Z-Q. Fang, J. W. Hemsky, and D. C. Look, Mat. Res. Soc. Symp. **325**, 431 (1994)
19. D. C. Look, Z-Q. Fang, and J. R. Sizelove, Phys. Rev. **B49**, 16757 (1994)

EL2-INDUCED UPCONVERSION LUMINESCENCE IN GaAs

V. Alex*, T. Iino**, J. Weber*
*Max-Planck-Institut für Festkörperforschung, Heisenbergstr. 1, 70569 Stuttgart, Germany, valex@vaxff1.mpi-stuttgart.mpg.de
**Sumitomo Metal Mining Co. Ltd., Ohme Research Center, Tokyo 198, Japan

ABSTRACT

Near band gap luminescence in bulk-grown semi-insulating GaAs is excited in a two step process via the EL2 defect. While the conventionally excited photoluminescence of our samples is dominated by conduction band to acceptor transitions, the upconversion process selectively excites donor acceptor pair transitions. Illumination near the maximum of the EL2-photoquenching band at 1064 nm leads to a complete disappearance of the so called upconversion photoluminescence (UPL). Excitation with light of shorter wavelengths however only partially quenches the UPL. Excitation between 850nm and 900nm completely regenerates the UPL. The characteristic photorecovery transients of the UPL are described by the EL2 regeneration mechanism via the population of the acceptor level of the metastable EL2 by hot electrons. The recovery of the EL2 by simultaneous illumination with above and below band gap light enables the observation of UPL at wavelengths, where the EL2-defect would otherwise be rapidly quenched. Under these conditions we observe a remarkable increase of the UPL-efficiency.

INTRODUCTION

The band edge photoluminescence in semiconductors is usually generated by excitation with light of considerably higher energy than the band gap. In this way the excitation photon energy is downconverted to the lower energetic luminescence photon energy. Electrons in the conduction band and holes in the valence band can also be produced by the photoionisation of electrons and holes from a deep defect in the energy gap. The photoionisation process occurs for photon energies lower than the band gap energy. The radiative recombination of the generated electrons and holes upconverts the excitation light to higher photon energies[1].
In this paper, we investigate upconversion photoluminescence in bulk-grown undoped semi-insulating GaAs. The dominant EL2-defect in this material is related to an arsenic antisite defect [2]. EL2 is a deep double donor, with a 0/+-level at mid-gap. It can compensate shallow residual acceptors and is therefore responsible for the semi-insulating property of the material. Illumination with photons of about 1μm wavelength at low temperatures transfers the neutral EL2 to a metastable lattice-relaxed configuration $EL2^*$. In the metastable configuration the EL2 has lost all its characteristic optical properties, like photoionisation cross sections. The back-transition to the fundamental state is hindered by a thermal barrier of 0.34 eV. An athermal recovery of the EL2 can however take place via the population of the acceptor level of the metastable configuration $(EL2^*)^{-/0}$. At ambient pressure, this level is resonant with the conduction band and can be populated only by hot electrons. The negatively charged $EL2^*$ can bind an exciton, whose non-radiative recombination enables an athermal regeneration [3,4,5,6]. In earlier investigations the required hot electrons and excitons were provided by an excitation of the sample with above band gap light. Khachaturyan et al. [6] also discussed the possibility, that

Mat. Res. Soc. Symp. Proc. Vol. 442 © 1997 Materials Research Society

an upconversion process via the EL2 itself could provide the necessary charge carriers. They assumed however, that this process is very inefficient.

EXPERIMENT

Undoped semi-insulating GaAs was grown by the liquid encapsulated Czochralski (LEC) and the vertical gradient freeze (VGF) technique by Sumitomo Metal Mining Co. Ltd. EL2 concentrations of $2.1\times10^{16}cm^{-3}$ for the VGF and $3.7\times10^{16}cm^{-3}$ for the LEC samples were determined by measuring the infrared absorption at 300K and using 4.9×10^{-17} cm^{-2} as conversion factor. The PL and excitation spectra are measured in the photon counting mode with a cooled GaAs-photomultiplier in combination with a SPEX 1704 double-monochromator and a multi-channel-scaler for the time-resolved measurements. A cw-Ti:sapphire, pumped by an all-line Ar^+-laser was used as a tuneable excitation source in the range between 700 and 1000nm and a cw-Nd:YAG-laser for 1064 nm.

Model of the upconversion process

Figure 1 shows the transition model for the upconversion process via a deep defect. σ_n and σ_p denote the electron and hole photoionisation cross sections of the defect and Φ the excitation photon flux. For simplicity, recapture processes of the photoionised charge carriers by the EL2 are only considered for holes by assigning to the electrons a finite lifetime τ^* at the defect level. The radiative recombination rate R of the electrons and holes follows a bimolecular law with a proportionality constant B. R is proportional to the optically active EL2-concentration N, which is the sum of the of the neutral and positively charged concentrations of the EL2 in the fundamental state.

$$R = \frac{\Phi^2\tau^*\sigma_n\sigma_p B}{\Phi\tau^*(\sigma_n+\sigma_p)+1}\cdot N \qquad (1)$$

EL2-quenching and -recovery kinetics

The optically active EL2 concentration, which is responsible for the UPL can be changed by excitation with photons from the photoquenching band of the EL2. The photoquenching process is described by an optical cross section σ^*, which leads to an exponential decay of the EL2-concentration. The situation becomes more complicated, if one considers that the positively charged EL2 cannot be directly quenched, but first has to lose its hole in a photoionisation process. The time dependence is then described by the sum of two exponential functions [7]. If the photorecovery process of the EL2 would involve a direct interaction with light, described by an optical cross section, one would expect, that the transients can be described by a constant equilibrium value and a sum of two exponential functions with modified time constants. The recovery mechanism via the population of the $(EL2^*)^{-/0}$ -level leads however to more complicated kinetics. The simplest assumption is that the recovery rate is then proportional to the generation rate of hot electrons. If these charge carriers can only be generated in an upconversion process via unquenched EL2, the recovery rate becomes proportional to the product of the quenched and unquenched EL2 concentration. Denoting the proportionality constant by σ^r and first neglecting the $EL2^+$-state, one obtains for the time dependence of the optically active EL2-concentration

$$N(t)=\frac{\sigma^{*}-N^{tot}\sigma^{r}}{C\exp\left[\left(\sigma^{*}-N^{tot}\sigma^{r}\right)t\right]-\sigma^{r}} \qquad (2)$$

where C is an integration constant, which depends on the initial EL2-concentration. Depending on C, eq.(2) represents either increasing or decreasing concentrations.

RESULTS

Below band gap excitation

Figure 2 shows PL-spectra of a typical sample, measured at 2K with different excitation wavelengths. Excitonic transitions (X), conduction band to acceptor (e-A^0) and donor acceptor pair (DAP) transitions (D^0-A^0) contribute to the conventionally excited luminescence. Near the band-gap (1.520 eV = 815nm at 0K), the contribution of donor acceptor and excitonic transitions rises. The upconversion spectrum shown for 900nm excitation consists of a single luminescence band, which is ascribed to DAP transitions by its energetic position. The DAP nature of the luminescence is confirmed by the temperature dependence of the UPL. Due to the thermal ionisation of donors and acceptors, the UPL intensity rapidly decreases above 20K. The integrated luminescence intensity follows a 1.2-power law of the excitation light flux over three orders of magnitude variation of the excitation. This super-linear dependence is expected by eq.(1).

Excitation above 900nm quenches the UPL within some minutes to a stable equilibrium level. This level gets very low for excitation above 950nm (fig. 3). We exclude the possibility, that this steady state UPL is caused by upconversion by some other unquenchable defect with a threshold at 950nm. Simultaneous illumination with the 1064 nm Nd:YAG laser, which has a maximum quenching efficiency for the EL2 leads to a complete quench of the UPL. After a complete photoquench of the UPL with the Nd:YAG laser, excitation with wavelengths shorter than

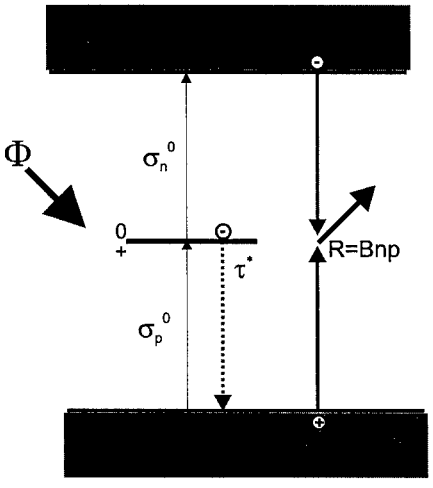


Fig. 1: Schematic model of the two step excitation process via a deep defect

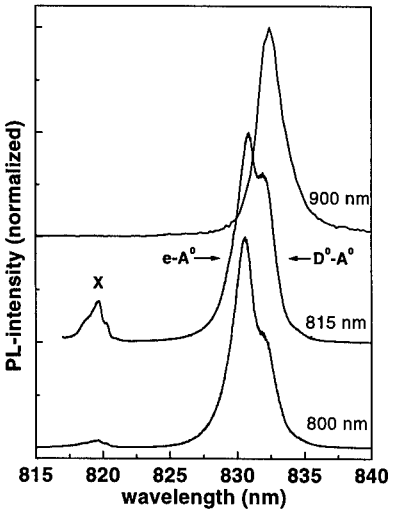


Fig. 2: PL-spectra with different excitation wavelengths

950nm causes a recovery of the UPL-intensity with a characteristic S-shaped transient (fig. 4). The timescales for the photorecovery and photoquenching are comparable, indicating the high efficiency of the recovery mechanism. The same equilibrium value is obtained for initially all EL2 quenched or thermally recovered. Excitation between 850 and 900nm leads to no photoquenching and under these excitation conditions we can achieve a 100% pure optical recovery of the EL2 with below band gap light. This could be repeated for an arbitrary number of quenching and optical recovery cycles.

The S-shaped photorecovery transients rule out the possibility of a direct interaction with light by a simple qualitative inspection. Eq.(2) can qualitatively reproduce the observed shape, but a fittable equation requires the consideration of the $EL2^{+}$-state, that was not taken into account in the rate equations leading to eq.(2). Unfortunately, the equation system is then not analytically solvable any more. A sum of two equations of type (2) with different time and integration constants can however very well fit the measured transients, as indicated by the lines in figure 4. The ad-hoc introduction of a second summand obtains some justification by the similar modification of the photoquenching rate equations[7]. A distinction between the two recovery mechanisms in the photoquenching transients is not possible, since a constant plus two exponential functions and the sum of two eq.(2) can both fit the transients quite accurately.

Above-gap excitation

Excited with the same light flux, the maximum intensity of the UPL is only 3% of the conventionally excited luminescence. Even if upconversion processes via the EL2 could take place also for above gap excitation and contribute to the conventionally excited luminescence, one would not expect to observe any considerable luminescence transient photorecovery with above gap light. However we find an increase in the luminescence intensity by about a factor of three, measured in the maximum of the DAP-transition. The luminescence transients in that case can be fitted by exponential functions with about five times shorter time-constants than shortest below gap recovery times. This is even more astonishing, if one considers that above gap light regenerates only the EL2 within its penetration depth.

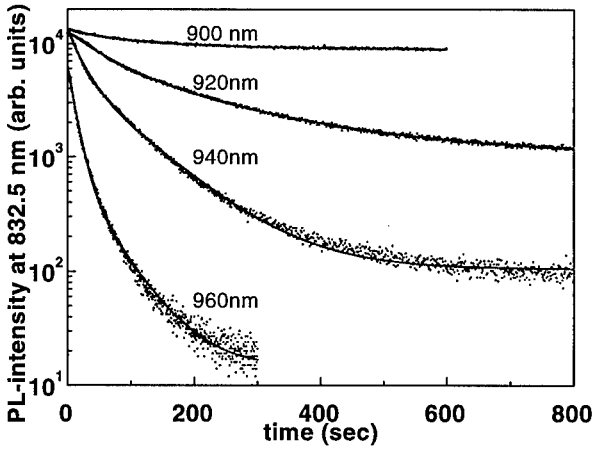


Fig.3: Photoquenching transients of the UPL-intensity during excitation at the indicated wavelength after a complete regeneration of the EL2

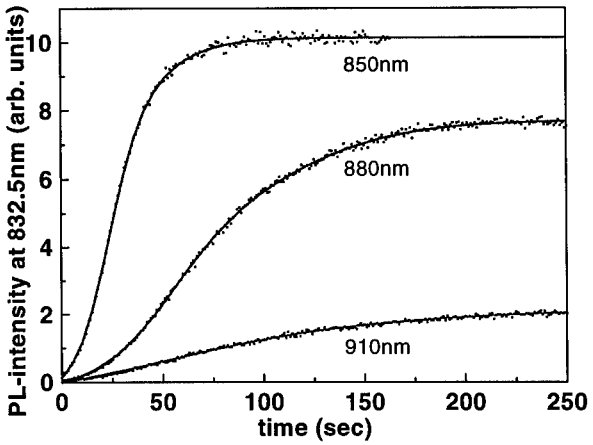


Fig.4: Photorecovery transients of the UPL-intensity at the indicated wavelength after a complete quench of the EL2

Simultaneous above and below gap excitation

The high recovery efficiency of the above gap light enables also the observation of a steady state Nd:YAG excited UPL by a simultaneous above gap illumination. The simultaneous excitation of the sample with above and below gap light leads to a strong increase of the efficiency of the UPL (fig. 5). Excitonic and DAP transitions are preferentially enhanced by the below gap excitation. This effect appears even more astonishing if one considers, that this luminescence increase stems entirely from within the small penetration depth of the above gap laser.

Initially we tried to explain the selective excitation of DAP luminescence in the UPL by the low excitation density in the sample, that would allow a complete relaxation of the generated electrons from the conduction band to the shallow donors (an enhancement of the DAP compared to the e-A^0-transitions can also be obtained by a decrease of the excitation light flux). However this can not explain the preferential DAP exciatation under the two beam condition. As an explanation we suggest a close relation between the EL2 and the shallow donors, that participate in the DAP transitions. Such a close relation was already seen by the quenching of the shallow donor Zeeman-absorption simultaneous to the EL2 quenching [8]. However we suggest, that the involved shallow donor, might be the shallow hydrogenic level of the EL2 itself, found by Nissen et al. [9], and which has a binding energy of 3.2±0.5 meV. This could also explain the luminescence transient during above gap photorecovery. The close shallow-donor-EL2 coupling might also be related to the unexpected high efficiency of the photorecovery with below gap light. The explanation of the mechanism of the strong efficiency enhancement of the UPL under simultaneous above gap excitation requires further investigations.

CONCLUSIONS

The investigation of upconversion luminescence was demonstrated to be a useful tool for the investigation of the EL2-defect. Below gap light has a high photorecovery eficiency and its characteristic transients enable an investigation of the underlying mechnism. New phenomena occurred for simultaneous above and below gap excitation.

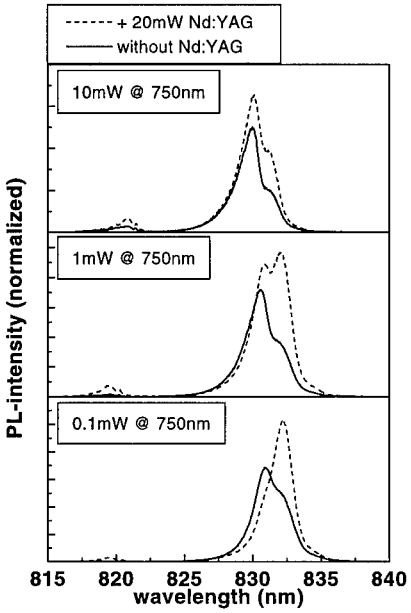


Fig. 5: PL-spectra with excitation at 750nm at three different powers and the addition of a 20mW Nd:YAG laser.

ACKNOWLEDGMENTS

The authors gratefully acknowledge the continuous support and encouragement of Prof. H.-J. Queisser. The technical assistance of W. Heinz and W. Krause is greatly appreciated.

REFERENCES

1. T. Iino and J. Weber, Mater. Sci. Forum **196-201**, 993 (1995)
2. G.M. Martin and S. Makram-Ebeid, in Deep Centers in Semiconductors, edited by S.T. Pantelides (Gordon and Breach, New York, 1985)
3. M. Baj and P. Dreszer, Phys. Rev. **B39**, 10470 (1989)
4. M. Baj, P. Dreszer, and A. Babinski, Phys. Rev **B43**, 2070 (1991)
5. C. Ziegler, U. Scherz, and M. Scheffler, Phys. Rev **B47**, 16624 (1993)
6. K. Khachaturyan, E.R. Weber, and J. Horigan, Phys. Rev. **B46**, 1365 (1992)
7. N. Radic, C. Santic, and U. Desnica, Jpn. J. Appl. Phys. **34**, 5922 (1995)
8. T. Ohyama, T. Shimizu, H. Kobori, and E. Otsuka, Jpn. J. Appl. Phys. **32**, 1889 (1993)
9. M.K. Nissen, T. Steiner, D.J. Beckett, and M.L.W. Thewalt, Phys Rev. Lett. **65**, 2282 (1990)

RELATIONSHIP BETWEEN HYDROGEN-RELATED METASTABLE DEFECT AND EL2-LEVEL IN GaAs CRYSTALS

Tatsuyuki Shinagawa and Tsugunori Okumura
Dept. of Electr. & Inform. Eng., Tokyo Metropolitan University
1.1, Minami-ohsawa, Hachiohji, Tokyo 192-03, Japan

ABSTRACT

The relationship between the hydrogen-related metastable defect (M3/M4) and the EL2 level in n-GaAs crystals has been investigated. We found with various kinds of GaAs crystals that the hydrogen-related metastable couple (M3/M4), first reported by Buchwald et al., has been observed only in the crystals containing the EL2 defect. This fact was further confirmed by using LT-MBE GaAs crystals before and after rapid thermal annealing (RTA). Only in the n-LT-n sample annealed at 900°C, in which the EL2 defect was formed, the metastable couple (M3/M4) appeared upon hydrogenation. As hydrogenated, the EL2 level was passivated or dissociated. From bias-annealing experiments, the M4 level was completely annihilated by annealing at 573K, where the EL2 level was restored to its original concentration. We speculated from these results that both diffused hydrogen and preexisting arsenic antisite defect (As_{Ga}) are responsible for the formation of the metastable defect(M3/M4).

INTRODUCTION

Recently, defect states with metastable properties have been studied in several III-V compound semiconductors. [1-6] One of these defects is the hydrogen-related metastable couple (M3/M4) first found in Si-doped GaAs grown by metalorganic chemical vapor deposition (MOCVD) by Buchwald et al.[4] Using deep-level transient spectroscopy (DLTS), they observed a completely reversible transformation between two defect configurations depending on the applied bias polarity during annealing at 400K. However, the microscopic structure of the hydrogen-related metastable defect (M3/M4) is still not clear. Tabata et al.[6] showed that the presence of an electron trap 0.33 eV below the conduction band is dependent on the As/Ga ratio in the MOCVD growth; they stated that arsenic interstitials could be responsible for this level showing metastability, which is probably identical to the M4 level reported by Buchwald et al. On the other hand, Pfeiffer and Weber [7] concluded from the experiments with GaAs containing a high concentration of oxygen that both oxygen and diffused hydrogen are involved in the formation of the M3/M4 defects; the EL3 level tentatively assigned to the off-center oxygen defect O_{As}[8] was observed in their as-grown crystals. We have studied deep-level formation upon plasma hydrogenation with n-GaAs crystals grown by various methods. It was speculated that both diffused hydrogen and intrinsic defects related to excess As are responsible for the generation of the metastable defect.[9]

In this paper, we present experimental evidence that hydrogen as well as preexisting arsenic antisite defects (As_{Ga}) are responsible for the generation of the M3/M4 defect. Plasma hydrogenation was carried out on low temperature molecular beam epitaxial (LT-MBE) GaAs crystals before and after rapid thermal annealing (RTA) in addition to the crystals used in the former study. The annealing behavior of the metastable couple (M3/M4) as well as the EL2 level was investigated to understand the relationship between these defects.

Mat. Res. Soc. Symp. Proc. Vol. 442 © 1997 Materials Research Society

EXPERIMENTAL

GaAs crystals used in this work were grown by various growth methods, which were supposed to provide different off-stoichiometry compositions. In addition to normal n-type crystals, we used a specially designed MBE crystal with an LT-layer. Figure 1 shows the growth condition as well as the sample structure of LT-MBE GaAs used in this study. The sample was grown on an n^+-GaAs(100) substrate doped with Si ($1x10^{18}$ cm^{-3}). The growth rate was 0.5μm/h with a beam equivalent pressure ratio P_{As4}/P_{Ga} of 15. On the substrate, a 1μm thick Si-doped ($1x10^{16}$ cm^{-3}) GaAs buffer layer was grown at 620°C. Then, the As cell was left open while the substrate temperature was reduced to 250°C and a 26 nm LT-GaAs epilayer was grown. The substrate temperature was raised again to 620°C and another 1μm thick Si-doped GaAs layer was grown. This n-LT-n sample was separated into several pieces, some of which were loaded into an infrared image furnace for rapid thermal annealing (RTA) in order to form the EL2 level.[11] The RTA process was performed under a hydrogen flow on the face-to-face capless condition at temperatures of 700-900°C. The heating rate and the holding time at the highest temperature were set to 20K/sec and 5 min, respectively. Then, the sample was cooled down as rapidly as possible.

The samples were exposed to hydrogen plasma in a remote RF (13.56MHz, 50W) plasma system. The chamber was evacuated below 10^{-6}Torr prior to feeding a hydrogen gas. The distance between the glow-discharge plasma and the substrate was 15 cm and the substrate temperature was kept at room temperature.

In order to characterize shallow donors as well as deep levels, Schottky diodes were fabricated by evaporating Al or Au on the top of the hydrogenated surfaces through a metal mask with openings of 0.3, 0.5, 0.7 and 1.0 mm in diameter. Current-voltage (*I-V*) and capacitance-voltage (*C-V*) characteristics were measured before deep level transient spectroscopy (DLTS) measurements. In the DLTS measurement, capacitance difference signals were obtained by using a rectangular weighting function, and the rate window was set to 400 ms for the purpose of spectrum comparison. We examined the concentration of the EL2 level from the photoquenching measurement at liquid nitrogen temperature(77K)[14]. The photons from an infrared (IR) light emitting diode (1.32 eV, 5 mW) are fed on the top of the Al or Au Schottky diodes.

The relationship between the hydrogen-related metastable defect (M3/M4) and the EL2 defect was studied by annealing these Schottky diodes at 420-573K under various bias voltages applied to the diodes. For this experiment, the DLTS measurement was carried out only below 300K in order to minimize an unintentional bias-anneal effect during the measurement.

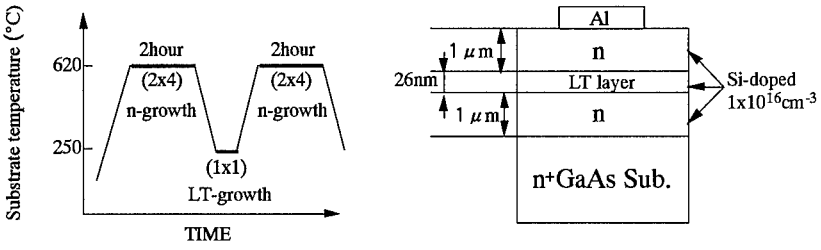


Fig. 1. The growth condition and structure of the n-LT-n sample.

RESULTS AND DISCUSSION

Figure 2 shows a typical variation of DLTS spectra of the M3/M4 levels upon bias annealing observed in the hydrogenated n-GaAs crystal grown by the horizontal Bridgeman method (HB), which contains EL2 as well as EL6 in the as grown state. In the as-irradiated state, one of the metastable couple (M4) was observed in addition to the ion-induced defect level, labeled EH1, which was annealed out after annealing at 420K.[13] The M4 level disappeared under forward bias at the same annealing temperature, while the M3 level appeared. Upon reverse-bias annealing, the spectrum change was opposite to that under forward bias. We found that the conversion was completely reversible at this temperature. Thus, the metastable nature of the M3/M4 levels was identical to the results reported by Buchwald et al.[4]

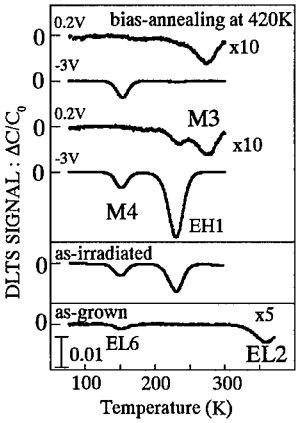


Fig. 2. Typical variation of DLTS spectra upon bias-annealing for hydrogenated n-GaAs.

Table I summarizes the relationship between the formation of the M3/M4 pair and the existence of the EL2 level in the as-grown crystals. The GaAs crystals used here can be sorted into three groups based on crystal off-stoichiometry. Here, we assume that the concentration of the EL2 level is a measure of the off-stoichiometry. An LPE crystal belongs to Group A, since it is grown from a Ga-rich solution. MBE, VPE and BG crystals (Group B) are considered to be slightly As-rich ; the EL2 defect was not detected although they were grown in an As rich atmosphere. LEC and HB crystals in Group C contain a large concentration of the EL2 defect. It is clear from Table I that the M3/M4 pair was formed upon hydrogenation only in Group C crystals containing the EL2 defect in the as-grown state. The strong correlation between the M3/M4 pair and the EL2 defect suggests that the metastable defect consists of an arsenic antisite (As_{Ga}) and/or its related defects which is likely formed in a highly As-rich composition. It is noted that the EL3 level, tentatively assigned to off-center oxygen defect O_{As}, was not detected ($<5x10^{12}cm^{-3}$) in all crystals used here.

The correlation between the M3/M4 defect and As_{Ga} was further confirmed by the experiments with the LT-MBE samples. We have already found that the EL2 level was not detected in the as-grown n-LT-n sample but was generated after RTA at 900°C.[11] Figure 3 shows the DLTS

Table I. Relationship between thehydrogen-related metastable defect and the EL2 level.

Group	Crystals	Off-stoichiometry	EL2 level	metastable pair (M3/M4)
A	LPE	Ga-rich	×	×
B	MBE	moderately As-rich	×	×
	VPE		×	×
	BG		×	×
C	HB	highly As-rich	○	○
	LEC		○	○

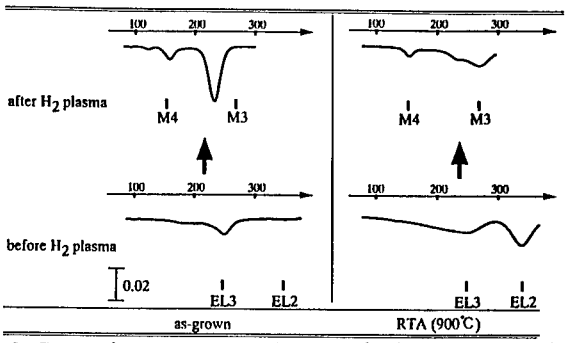


Fig. 3. Comparison among DLTS spectra in the n-LT-n samples.

spectra detected in the n-LT-n samples before and after hydrogenation with as-grown and annealed samples. The DLTS measurements revealed that no EL2 level was detected in the "as-grown" n-LT-n sample (lower-left spectrum) and that the EL2 peak was clearly generated after RTA(lower-right spectrum). The so-called photoquenching measurement confirmed that this newly generated level is identical to the EL2 defect.[11] After hydrogenation, a large amount of the M3/M4 levels were generated in the "RTA" LT-MBE sample with the EL2 level. Pfeiffer and Weber reported both the EL3 level, O_{As}, and hydrogen are involved in the formation of the M3/M4 defect.[7] On the other hand, we found that after hydrogenation the M3/M4 pair was not found in the "as-grown" n-LT-n sample even with the EL3 level.

The DLTS spectrum of the "as-grown" n-LT-n sample after hydrogenation shows a secondary peak at slightly higher temperature of about 150K than that for the M4 level. Figure 4 shows the variation of DLTS spectra upon bias-annealing for the hydrogenated n-LT-n samples. For the "as-grown" sample without the EL2, the 150K peak completely vanished after the first annealing under forward bias, but the M3 level was not generated. After the following bias-annealing, DLTS signals for neither the M3 nor the M4 level appeared in the "as-grown" sample. The annealing behavior of the150K peak is quite similar to that observed in Group B crystals. It is , therefore, concluded that the 150K peak detected in the "as-grown" n-LT-n sample is not the M4 level.[13] On the other hand, the variation of DLTS spectra for the "RTA" sample exposed to hydrogen plasma clearly showed metastability in the M3/M4 defect. It is seen from Fig.4 that the M4 level

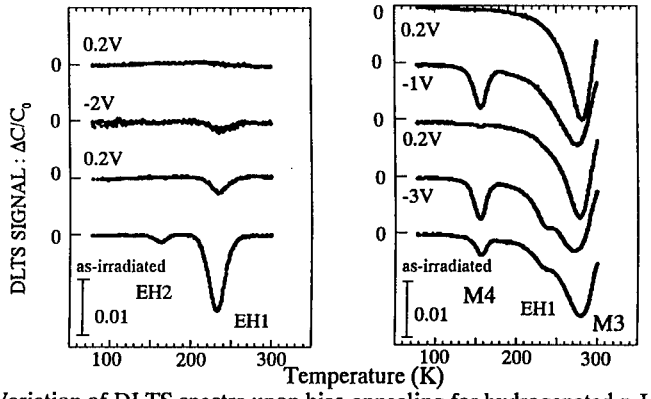


Fig. 4. Variation of DLTS spectra upon bias-annealing for hydrogenated n-LT-n samples.

disappeared during forward-bias annealing and recovered during reverse bias annealing. However, the M3 level was not completely transformed into the M4 level under reverse bias in the "RTA" n-LT-n sample; the M3 peak is seen for all spectra shown in Fig.4(b) although its height varies with bias polarity.

Figure 5 shows the DLTS peak-height variations of the M3 and M4 levels detected in the "RTA" n-LT-n sample with each annealing step. Although about three fourths of the total amount of the M3 level was not transformed into the M4 level, the variation of two levels is complementary to each other. It is noted that we used an n-LT-n structure to apply a capacitance DLTS measurement. The M3 signal which was not transformed into the M4 signal is possibly due to the region near the centered LT-layer where the Fermi-level is rather tightly pinned at a certain level. Therefore, in such a region the Fermi-level cannot go down across the M3 level even under a reverse bias.

It is noted that the EL2 level disappeared in the as-hydrogenated sample, where the M4 was formed. We determined the concentration of the EL2 level by photoquenching measurements, since we did not measure DLTS spectra above 300K in order to avoid an unintentionally annealing effect during measurements. Figure 6 shows the concentration variation (in terms of $\Delta C/C_0$) of the M4 and the EL2 levels again in HB crystals as a function of annealing temperature. The exact concentration cannot be determined since these levels are not uniformly distributed in depth. The EL2 level was passivated by a hydrogen-plasma exposure which could lead the formation of an electrically inactive EL2–H complex.[12] The EL2 level was partly reactivated after the first annealing at 420K. The regeneration of the EL2 defect in hydrogen passivated GaAs was already reported by Ball et al..[12] They reported that the electrically active EL2 defect was restored to approximately 30 percent of its original concentration by annealing at 384K. We also observed that the EL2 level did not reactivate completely at similar temperature. Although it is not clear the reason why the concentration of the M4 level increased upon annealing up to 473K, the maximum concentrations of the M4 level and the EL2 level agree with each other. In the temperature range between 523 and 573K, the M4 level decreased in concentration and disappeared, while the EL2 level was restored to its original concentration.

Figure 7 shows the variation of the deep level concentrations for the M4 level and the EL2 level as a function of annealing duration at 500 K. It is clearly seen that the decrease of the M4 level and the recovery of the EL2 level correlate to each other.

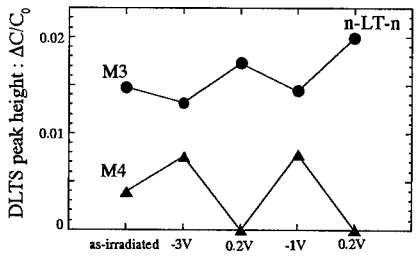


Fig. 5. DLTS peak height variation of the M3 and M4 level with bias-annealing polarity.

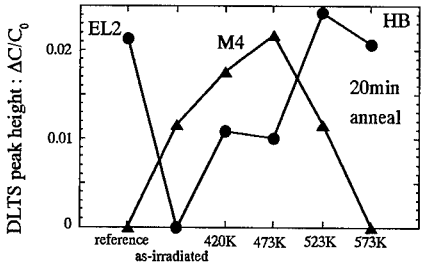


Fig. 6. Variation of concentrations for the metastable pair (M3/M4) and the EL2 level as a function of annealing temperature.

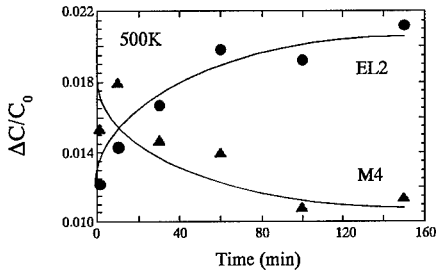


Fig. 7. Variation of concentrations for M4 level and EL2 level as a function of annealing duration at 500K.

CONCLUSION

We have studied the relationship between the hydrogen-related metastable defect M3/M4 and the EL2 level in GaAs crystals. From the experiments using LT-MBE GaAs crystals before and after rapid thermal annealing (RTA), we confirmed that the metastable couple (M3/M4) was formed only in the crystals with the EL2 level before hydrogenation. From bias-annealing experiments, the M4 level was completely annihilated by annealing at 573K. At the same time, the EL2 level was restored to its original concentration. It is, therefore, speculated that both diffused hydrogen and already existing arsenic antisite defect (As_{Ga}), which partly composed of the EL2 level, are responsible for the formation of the metastable defect (M3/M4).

ACKNOWLEDGMENTS

We wish to thank S. Kuma and Y. Otoki of Hitachi Cable Co. for providing various kinds of GaAs. We are also grateful to H. T. Kaibe of Tokyo Metropolitan University and T-C. Lin of Komatsu Electronics Co. for their assistance with the sample preparation.

REFERENCE

[1] A. Chantre, V. Vincent, and D. Bois, Phys. Rev. B **23**, 5225 (1981).
[2] M. Levinson, J. L. Benton, and L. C. Kimerling, Phys. Rev. B **27**, 6216 (1983).
[3] D. V. Lang, in *Deep Centres in Semiconductors*, edited by S.T. Pantelides (Gordon and Breach, New York, 1986) Chap. 7, p. 489.
[4] W. R. Buchwald, N. M. Johnson, and L. P. Trombetta, Appl. Phys. Lett. **50**, 1007 (1987).
[5] W. R. Buchwald, G. J. Gerardi, E. H. Poindexter, N. M. Johnson, H. G. Grimmeiss, and D. J. Keeble, Phys. Rev. B **40**, 2940 (1989).
[6] A. S. Tabata, M. A. A. Pudensi and A. M. Machado, J. Appl. Phys. **65**, 4076 (1989).
[7] G. Pfeiffer and J. Weber, Materials Science Forum, **143-147**, 873 (1994).
[8] U. Kaufmann, E. Klausmann, J. Schneider, and H. Ch. Alt, Phys. Rev. B **43**, 12106 (1991).
[9] T. Shinagawa and T. Okumura: Mat. Res. Soc. Symp. Proc. Vol.**378**, 447 (1995).
[10] G. M. Martin, A. Mitonneau and A. Mircea, Electron. Lett. **13**, 191 (1977).
[11] T. C. Lin, and T. Okumura, Jpn. J. Appl. Phys. **35**, 1630 (1996).
[12] C. A. B. Ball, A. B. Conibear, and A. W. R. Leitch, Inst. Phys. Conf. Ser. No **136**, Chap. 11, 697(1993).
[13] T. Shinagawa and T. Okumura, J. Appl. Surf. Sci. (to be published).
[14] G. Vincent, D. Bois and A. Chantre, J. Appl. Phys. **53**, 3643 (1982).

NONRADIATIVE INVESTIGATION OF HOLE PHOTOIONIZATION SPECTRUM OF EL2 IN SEMI-INSULATING GaAs

T. Ikari**, A. Fukuyama*, Y. Morooka**, K. Yoshino** K. Maeda**, and Y. Akashi*
* Department of Materials Science, Miyazaki University and
** Department of Electrical and Electronic Engineering, Miyazaki University
1-1 Gakuen-kibanadai, Miyazaki 889-21, Japan

ABSTRACT

The piezoelectric photoacoustic (PPA) measurements before and after the secondary light illumination for 3 minutes were carried out at 85 K to investigate the electron and hole photoionization processes of EL2 in carbon concentration controlled semi-insulating (SI) GaAs. The result showed a broad peak around 1.0 eV and a hump up to the band gap energy. These were due to hole and electron photoionization processes of EL2, respectively, and these processes were clearly observed from a nonradiative recombination point of view for the first time. In addition, we found that the hole photoionization process of EL2 is not influenced by the secondary light illumination at low temperature. Although the electron photoionization underwent photoquenching effect upon an illumination of 1.12 eV, the hole photoionization process did not change even after a long period of illumination. The positively charged EL2 donor state may not transform to the metastable state.

INTRODUCTION

Deep lying defect level EL2 is known to be a dominant donor to accomplish a semi-insulating nature of GaAs substrate for LSI applications. Since EL2 also transforms to its metastable state by a secondary light illumination at low temperature, so-called photoquenching effect, its electronic structure has been extensively studied. One very fundamental parameter for understanding of basic properties of EL2 is the photoionization cross-section. Although only a few investigation has been reported by using the deep level optical spectroscopy (DLOS) [1] or photocapacitance technique [2], the effect of the photoquenching on the photoionization cross-section spectra of EL2 have not been investigated yet.

Piezoelectric photoacoustic (PPA) spectroscopy has recently been used in investigating physical properties of semiconductors. One of the great advantages of the PPA spectroscopy is that it is a direct monitor of the nonradiative recombination processes. Heat generated by the nonradiative recombinations of photoexcited electrons are detected by a piezoelectric transducer (PZT) directly attached to the rear surface of the sample. The other advantage is that the PPA spectroscopy is sensitive to a very small optical absorption coefficient in a highly transparent sample. The presence of these two great advantages indicates that the PPA spectroscopy should be a very useful tool for investigating deep levels in GaAs such as EL2. The preliminary results on the PPA spectra of LEC grown SI GaAs were already reported in our previous papers and the electron transition involving EL2 could be resolved [3, 4].

In this paper, we report on the photoionization spectra of EL2 at 85K in both normal and quenched states obtained by using a piezoelectric photoacoustic (PPA) technique. The result showed a broad peak at 0.9 eV and a broad band up to the band gap energy which is due to hole and electron photoionization spectra of EL2, respectively. In addition, the most important finding was that the hole photoionization process of EL2 is not influenced by the secondary light illumination at low temperature. Although the electron photoionization underwent photoquenching effect upon an illumination of 1.12 eV, the hole photoionization process did not change even after a long period of illumination. The positively charged EL2 donor state cannot transform to the metastable state.

EXPERIMENTAL PROCEDURES AND RESULTS

The three samples were prepared from carbon concentration controlled SI GaAs wafers

Mat. Res. Soc. Symp. Proc. Vol. 442 © 1997 Materials Research Society

grown by the liquid encapsulated Czochralski (LEC) method. The carbon concentration of the samples #1, #2, and #3 were 13.0, 11.0 and 4.0 $\times$ 10^{15} cm^{-3}, respectively. Total EL2 concentration remains unchanged at 1.2-1.4 $\times$ 10^{16} cm^{-3} for three samples. Since these wafers in the present study were thermally treated by three-stage annealing method [5], a minimum amount of irrelevant intrinsic defects is expected. The detailed experimental setups for the PPA measurements have been reported previously [6].

The PPA spectra of three samples at 85 K are shown in Fig.1. After the sample was cooled down in the dark, the PPA signal intensity was measured as a function of photon energy ranging from $0.7 \leq h\nu \leq 1.45$ eV. A broad hump above 1.1 eV up to the band gap energy is observed for the samples #2 and #3. In sample #1, the PPA spectrum consists of a broad peak around 1.0 eV and the hump up to the band gap energy. These structures agree well with our previous reports [3, 4]. From the spectral similarity of the PPA spectra to the photoionization cross section spectra of EL2 level, we have concluded that the PPA signals below the band gap energy are caused by the electron nonradiative recombinations involving EL2. The peak around 1.0 eV and the hump are due to nonradiative recombinations of electrons photoexcited from the valence band to the positively charged $EL2^+$ (hole photoionization cross section; σ_p) and from the neutral $EL2^0$ to the conduction band (electron photoionization cross section; σ_n), respectively. The σ_p spectrum at 78 K determined from the photocapacitance technique [2] was also shown in Fig.1 by the dot-dashed curve to compare with the PPA spectra.

Figure 2 shows an effect of the secondary light illumination on the PPA spectrum of the sample #1. The PPA spectrum after the secondary light of 1.12 eV illumination for 3 minutes at 85 K are shown by the solid curve. The PPA spectrum at the normal state is also shown by the broken curve. The intensity of the hump decreases by the secondary light illumination for 3 minutes, while the peak around 1.0 eV remains unchanged. For the samples #2 and #3, the hump vanishes by the secondary light illumination of 1.12 eV for 3 minutes. We hereafter refer the states before and after the secondary light illumination to the normal and the quenched states, respectively. The quenched state is quite stable unless the temperature of the sample increases above 130 K. The PPA signal shows the normal state after heating the sample above 130 K and subsequent cooling down to 85 K. This means that thermal recovery from the quenched to the normal states occurs around this temperature.

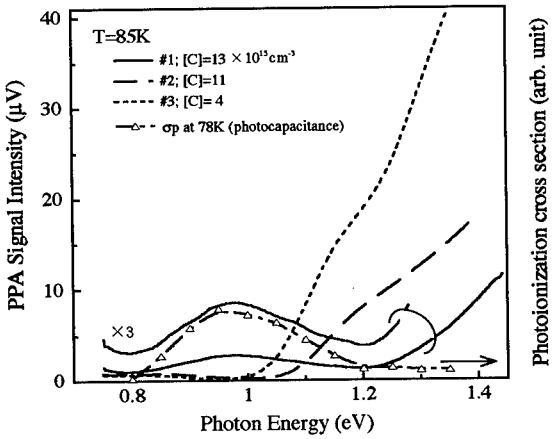


Fig.1 The PPA spectra at 85 K for samples #1([C]=13.0 $\times$ 10^{15} cm^{-3}), #2([C]=11.0 $\times$ 10^{15} cm^{-3}), and #3([C]=4.0 $\times$ 10^{15} cm^{-3}). The σ_p spectrum at 78 K determined by the photocapacitance technique was also shown by the dot-dashed curve.

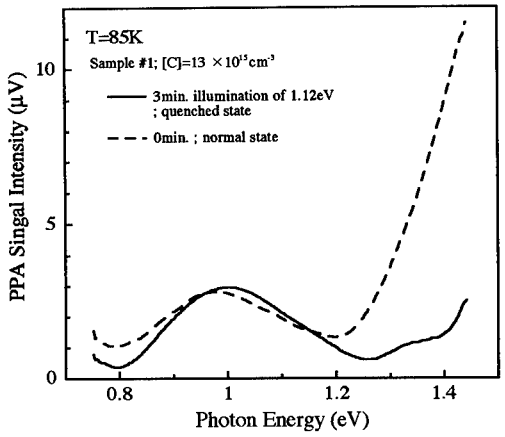


Fig.2 The effect of the secondary light of 1.12 eV illumination for 3 minutes on the PPA spectra of the sample #1. Decrease of the PPA signal above 1.1 eV was observed.

DISCUSSIONS

Since the PPA signal below the band gap energy region are proportional to the absorption coefficient β [3] and to the total EL2 concentration [7], the PPA signal intensity I_{PPA} may be given by

$$I_{PPA} \sim \beta = N f \sigma_n + N (1-f) \sigma_p, \qquad (1)$$

where N is the total EL2 concentration and f is the electron occupancy factor. Electron occupancy of the EL2 level can be controlled by the carbon acceptor concentration. For all the samples measured in the present study, deep lying EL2 level is partially ionized to compensate the carbon acceptor, i.e., $0 < f < 1$. Therefore, both terms of the right hand side of the equation (1) contribute to the PPA spectra. Since the total EL2 concentration remains unchanged at 1.2-1.4 × 10^{16} cm^{-3} for all the samples, the factor f decreases with increasing the carbon concentration. For the sample of larger carbon concentration, the factor f becomes small and results in a comparable contribution of both terms in the equation. This is clearly seen in the Fig.1. The PPA signal above 1.1 eV (σ_n) decreases with increasing the carbon acceptor concentration, while the PPA signal below 1.1 eV (σ_p) increases.

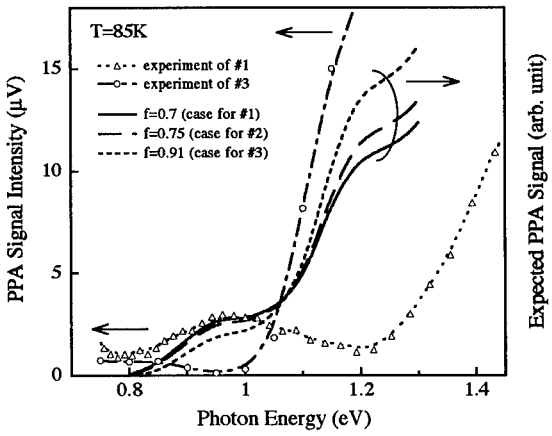


Fig.3 Evaluated PPA spectra from the equation (1) by using the value f=0.70, 0.75, and 0.91. The experimental PPA spectra for samples #1 and #3 are also shown.

In recent years, Suemitsu *et al.* [8] reported a carbon concentration dependence of the electron occupancy f of the EL2 level. According to their empirical relation of $[EL2^+] = 0.3$ [C], the factor f is calculated to be 0.70, 0.75, and 0.91 for each samples when we use the value of $N = 1.3 \times 10^{16}$ cm^{-3}. By using the equation (1) and the photoionization cross sections σ_n and σ_p determined from the photocapacitance technique [3], the PPA spectra can be evaluated and the results are shown in Fig.3. The spectral shape of the experimental and the expected PPA spectra are similar to each other, but the measured signal intensity of the sample #1 is very small in the region of σ_n. On the contrary, the PPA signal intensity of the sample #3 shown by the dot-dashed curve is very small compare with the expected PPA spectra in the region of σ_p. This fact may be interpreted by supposing that the recombination probabilities corresponding to σ_n and σ_p are not the same for the PPA signal generation mechanism.

In the present study of the PPA measurements, the σ_n and σ_p spectra could be observed from a nonradiative recombination point of view for the first time. Since the DLOS and the photocapacitance techniques were only applicable to Schottky diodes on conducting materials, the PPA technique is a unique way to investigate σ_n and σ_p for SI materials. Although an infrared optical absorption technique is extensively used to investigate an optical properties of EL2, no optical absorption due to σ_p process have been observed [7]. The reason is still uncertain in their paper.

The quenched state was generated by the secondary light of 1.12 eV illumination for 3 minutes, and the thermal recovery from the quenched to the normal states occurred by heating the sample around 130K for a few minutes. These features are in good agreement with those of the photoquenching effect of EL2 in the optical absorption measurements [6]. Therefore, we concluded that the observed quenched state of the PPA signal by the secondary light illumination at 85 K is due to so-called photoquenching effect of EL2 levels ($EL2^0$ to EL2* transition). Since EL2* is optically inactive, the photoquenching effect decreases a number of photoexcited electrons. This results in a decrease of the PPA signal intensity. When the quenched sample is heated above 130 K, thermal recovery from EL2* to $EL2^0$ occurs. The PPA signal then turns back to the value in the normal state at 85 K.

It is noted from Fig.2 that an effect of the photoquenching is different for σ_n and σ_p processes. The PPA signal above 1.1 eV corresponding to σ_n process was effectively photoquenched within a short period illumination of the secondary light as in the case for the optical absorption measurements. On the other hand, the PPA signal corresponding to σ_p cannot be photoquenched as shown in Fig.2. Since the photoquenching of EL2 was reported to occur only at neutral $EL2^0$ [7], an ionized $EL2^+$ cannot be photoquneched unless it emits a hole to the valence band and becomes neutral. For the sample with large amount of carbon, larger part of EL2 level are positively ionized. This results in a slow photoquenching effect. Although the hump corresponding to σ_n underwent photoquneching effect upon an illumination of 1.12 eV for 3 minutes, a peak around 1.0 eV corresponding to σ_p did not change even after a long period of illumination. These experimental results are explained by assuming that the photoquenching process of $EL2^+$ ($EL2^+ \rightarrow EL2^0 \rightarrow$ EL2*) have very small capture cross section. The positively charged EL2 state may not transform to the metastable state. As a result, $EL2^+$ remains in the positively charged state even after photoquenching of $EL2^0$, and electron nonradiative recombination corresponding to σ_p causes the PPA signal. This is the first time that the effect of the photoquenching on the hole photoionization spectrum was investigated from a nonradiative point of view.

CONCLUSIONS

We have observed the PPA spectra and their photoquenching effect in the carbon concentration controlled LEC grown SI GaAs. We concluded that the peak around 1.0 eV and the hump up to the band gap energy are caused by the nonradiative recombination of electrons photoexcited by σ_p and σ_n processes. The electron and hole photoionization spectra of EL2 at 85K were clearly observed by using PPA technique for the first time. In addition, we found that the hole photoionization process of EL2 is not influenced by the secondary light illumination at low temperature. Although the electron photoionization underwent photoquenching effect upon an illumination of 1.12 eV, the hole photoionization process did not change even after a long period of illumination. The positively charged EL2 donor state may not transform to the metastable state.

Since the PPA measurement could detect the nonradiative recombination pathway corresponding to σ_p process of EL2, the usefulness of the PPA measurements for studying the deep electron levels in semiconductor was pointed out.

ACKNOWLEDGMENTS

We acknowledge to Hitachi Cable Co., Ltd. for supplying the GaAs wafers and to Miyazaki Oki Electric Co., Ltd. and Komatsu Electronic Metals Co., Ltd. for the financial support.

REFERENCES

[1] A. Chantre, G. Vincent and D. Bois: Phys. Rev. **B23**, 5335 (1981)

[2] P. Omling, P. Silverberg and L. Samuelson: Materials Science Forum **38-41**, 79 (1989)

[3] A. Fukuyama, T. Ikari, K. Miyazaki, K. Maeda and K. Futagami: Jpn. J. Appl. Phys. **31**, Suppl.31-1 pp.20-22 (1992)

[4] A. Fukuyama, T. Ikari, K. Maeda and K. Futagami: Jpn. J. Appl. Phys. **32**, 2567 (1993)

[5] Y. Otoki, M. Nakamori, R. Nakazono, and S. kuma, in Proceedings of the Fourth Conference on Semi-Insulating Ⅲ - Ⅴ Materials, edited by H. Kukimoto and S. Miyazawa (Ohm-sha, Tokyo, 1986)

[6] T. Ikari, S. Shigetomi, Y. Koga, H. Nishimura, H. Yayama and A. Tomokiyo: Phys. Rev. **B37**, 886 (1988)

[7] D. W. Fischer: Appl. Phys. Lett. **50**, 1751 (1987)

[8] M. Suemitsu, M. Nishijima, and N. Miyamoto; J. Appl. Phys. **69**, 7240 (1991)

INFLUENCE OF THE TEMPERATURE AND THE LIGHT INTENSITY ON THE METASTABLE TRANSFORMATION OF EL2

A.ALVAREZ, J.JIMENEZ, M.A.GONZALEZ, M.CHAFAI*.
Física de la Materia Condensada, ETS Ingenieros Industriales, 47011 Valladolid, Spain, jimenez @hp9000.uva.es.* L.E.T.I., Faculté des Sciences, 50000 Meknes, Morocco.

ABSTRACT

The temperature dependence of the metastable transformation of EL2 is explained in terms of the thermal emission of holes from the actuator level, VA. A model including the thermal release of holes from this level is presented. The numerical solution allows to account for the low photoquenching efficiency above 80 K in an accurate way. The existence of this level was postulated on the bases of the electric compensation and the temperature dependence of the metastable transformation of EL2 in semiinsulating GaAs. This level allows a complete description of the driving mechanism of the metastable transformation of EL2.

INTRODUCTION

Electronic technology based on GaAs has received a great deal of attention in the last fifteen years, the most important application is the fabrication of optoelectronic and high speed devices. Semi insulating substrates are used for ensuring suitable isolation between the different elements of the integrated circuits. It is usually admitted that a native defect, the so-called EL2, is responsible for the high resistivity of the substrate. EL2 is a double donor, with an electronic level in the mid-gap, which is conventionally assumed to compensate the residual shallow acceptors, mainly C_{Ga}. Thus, the Fermi level is pinned at the EL2 (0/+) ionization level [1]. Besides its technological interest, EL2 exhibits unique properties, in particular it undergoes a metastable transformation under suitable optical excitation ($1<hv<1.3$ eV) at low temperature[1]. In recent papers we have modeled the metastable transformation of EL2 in terms of the role played by an additional level, the actuator level of the metastability of EL2 [2,3]. It should be noted that one of the main difficulties for the identification of EL2 is the absence of precise information about the metastable state and the mechanism driving the transformation. We present herein the main features of the temperature dependence of the metastable transformation of EL2 on the bases of the thermal emission of a hole from the actuator level of the metastability.

ELECTRIC COMPENSATION

In spite of the many efforts to identify this defect and the causes leading to the metastable transformation some controversies remain up to day. The first question concerns the electric compensation, actually it is possible to obtain high resistivity GaAs with C concentrations up to two orders of magnitude below that of ionized EL2 [4]. On the other hand the metastable transformation is achieved on neutral EL2 levels, which should mean that for exhausting the normal EL2 population a previous neutralization of ionized EL2 is required, leaving behind a

Mat. Res. Soc. Symp. Proc. Vol. 442 © 1997 Materials Research Society

high concentration of free holes (~ 10^{15}-10^{16} cm^{-3}), which is not observed as a significant increase of the conductity in the dark. It is usually claimed that such a hole population is captured by Carbon acceptors, explaining thus the absence of the free hole population. Nevertheless, such an hypothesis is not reliable since the C acceptors are fully ionized above 50 K [5]. Even with the acceptors ionized, there is no significant change of the conductivity in the dark, which suggests that other deeper hole traps must exist. In fact, several other acceptor levels were detected by EPR in concentration comparable to that of EL2 [4,6]. In spite of this evidence, the relation between these levels and the electric compensation of GaAs has not yet been assessed.

METASTABLE TRANSFORMATION

It is usually assumed that the metastable transformation is produced by an internal electronic transition, which the deexcitation supplies the energy necessary for the lattice relaxation. The intracenter transition is identified by its ZPL in the optical absorption spectrum, but its relation to the metastable transformation of EL2 has been questioned in view of some experimental results[7].

The microscopic structure of EL2 is another matter of controversy; nevertheless, there exist a general consensus about the close relation between EL2 and the As_{Ga} native defect [1]. Several authors have postulated that EL2 is the isolated $As_{Ga,}$ while others suggested that there is an association between As_{Ga} and other defects [8].

Recently we have tried to solve some of these questions with novel ideas. In spite of the microscopic structure of EL2, our model assumes the existence of an actuator level, VA, of which the prime specific role is to trigger the metastable transformation. The main features of this model have been described in previous papers [2,3]. The fingerprint of the EL2 metastable transformation is the photoquenching of the optical response of EL2. We have studied both the photoquenching and the thermal recovery of EL2 by means of extrinsic photocurrent (1-1.3 eV) measurements. We showed the existence of a thermal hystheresis associated with the configurational change of EL2, the photoquenching is not observed above 80-85 K, while the thermal recovery of EL2 takes place at 130 K. This observation was related to the existence of the actuator level, which the charge state controls the metastable transformation. Above 80-85 K, holes are thermally released from the actuator level rendering unable the transit to the metastable state. Since the metastable transformation releases a significant concentration of holes that are not observed in the valence band, it is reasonable to assume that the actuator level is a hole trap. Thus, this level will play a relevant role in the electric compensation of GaAs. The temperature range in which the hole emission occurs, along with DLTS [9] and MCD (Magnetic Circular Dichroism)[2] results lead us to tentatively identify the actuator level with the Ga_{As} defect.

This level must be in a concentration close to that of EL2, and it is completely ionized in thermal equilibrium; thus, the ionized fraction of EL2 is nearly independent of the concentration of residual shallow acceptors, as effectively occurs in low Carbon doped material. Finally, EL2 becomes quenchable when the actuator level traps a photogenerated hole, normally arising from the ionized EL2 levels. Within this frame a set of rate equations accounting for these facts was built up [3]. Assuming an intracenter transition it was not possible to reproduce the photocurrent quenching transient, since excess free electrons appear in the conduction band. As a matter of fact, it was assumed that the photoionization of neutral EL2 was the electronic transition leading to the metastability. The driving force is the coulombic interaction between the actuator level with a hole and the ionized quenchable EL2. It was thus possible to obtain accurate numerical

solutions for the photocurrent and optical absorption quenching transients. Furthermore, the theoretical quenching efficiency spectrum presented an astonishing agreement with the experimental one. The optical cross section for the metastable transformation was found to be a complex function of the optical cross sections of the ground state of EL2.

THERMAL EMISSION OF HOLES

Herein we discuss the influence of the temperature and the light intensity on the photoquenchig of EL2. In order to include the role of the thermal hole emission from the actuator level, the set of rate equations describing the metastable transformation were modified including an additional term that should account for such thermal emission above 80 K. A typical Arrhenius term was then introduced in the rate equations, the activation energy was estimated at 0.2 eV, which is in agreement with the second ionization level of the Ga_{As} acceptor [9]. The preexponential factor was estimated at $3.9*10^9\ s^{-1}$. The hole emission to the valence band requires some additional capture mechanism in order to prevent the presence of a free hole concentration, which is not experimentally observed. This hole capture without photoquenching is ensured by both EL2 and the deep donor level, D. The capture cross section of D is a fitting parameter in our model.

$$\frac{dN_{nq}^{+}}{dt} = \sigma_n^0 N_{nq}^0 \phi - \sigma_p^0 N_{nq}^{+} \phi + C_{pN} N_{nq}^0 p - C_{nN} N_{nq}^{+} n$$

$$\frac{dN_{nq}^{0}}{dt} = -\sigma_n^0 N_{nq}^0 \phi - C_{pN} N_{nq}^0 p + C_{nN} N_{nq}^{+} n + e_{pA} N_q^0$$

$$\frac{dN_{q}^{0}}{dt} = \sigma_p^0 N_{nq}^{+} \phi - \sigma_n^0 N_q^0 \phi - e_{pA} N_q^0 - C_{pN} N_q^0 p$$

$$\frac{dN^{*+}}{dt} = \sigma_n^0 N_q^0 \phi + C_{pN} N_q^0 p - C_{nN}^{*} N^{*+} n$$

$$\frac{dD^{+}}{dt} = -C_{nD} n D^{+} + C_{pD} p\left(D - D^{+}\right)$$

$$\frac{dn}{dt} = \sigma_n^0\left(N_{nq}^0 + N_q^0\right)\phi - C_{nN} N_{nq}^{+} n - C_{nN}^{*} n N^{*+} - C_{nD} n D^{+}$$

$$\frac{dp}{dt} = e_{pA} N_q^0 - C_{pN} p\left(N_{nq}^0 + N_q^0\right) - C_{pD} p\left(D - D^{+}\right)$$

$$N^{*} = N - \left(N_{nq}^{+} + N_{nq}^0 + N_q^0 + N^{*+}\right)$$

$$N_{nq}^{+} + N^{*+} + D^{+} = VA^{-} + n$$

$$e_{pA} = 3.9 \times 10^9 T^2 e^{\frac{-0.203}{kT}}$$

$\sigma_n^0 = 1.17*10^{-16}\,cm^2;\sigma_p^0 = 0.11*10^{-16}\,cm^2;C_{nN} = 2.2*10^{-14}\,cm^3s^{-1};C_{nN}^{*} = 1.2*10^{-13}\,cm^3s^{-1};C_{nD} = 1.4*10^{-13}\,cm^3s^{-1}$

$C_{pN} = 4.4*10^{-15}\,cm^3s^{-1};C_{pD} = 1*10^{-14}\,cm^3s^{-1};\phi = 3*10^{15}\,cm^{-2}s^{-1};N_{nq}^{+}(0) = 1*10^{16}\,cm^{-3};N_{nq}^0(0) = 1*10^{16}\,cm^{-3};$

$N_q^0(0) = 0;N^{*+}(0) = 0;D^{+}(0) = 1*10^{16}\,cm^{-3};n(0) = 0;p(0) = 0;N^{*}(0) = 0$

The terms are defined as follows: N_{nq}^{+}-nonquenchable ionized EL2 concentration; N_{nq}^{0}-nonquenchable EL2 concentration; N_{q}^{0}-quenchable EL2 concentration; N^{*+}-ionized metastable EL2 concentration; D^{+}-ionized donor concentration; p-hole concentration; n-electron concentration; σ_n^{p} and σ_p^{0}-optical cross sections; C_{nN}-electron capture rate by non quenchable EL2; C_{nN}^{*}-electron capture rate of ionized metastable EL2; C_{nD}-electron capture rate of ionized donors; Φ-photon flux; α-absorption coefficient; e_{pA}-thermal emission rate of holes.

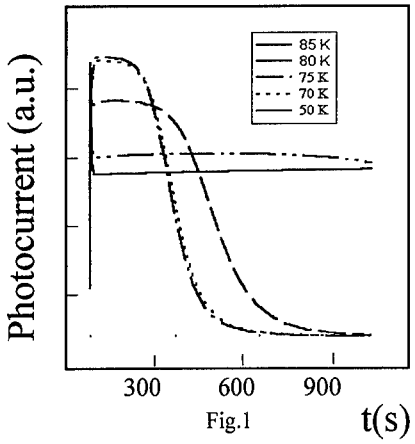


Fig.1

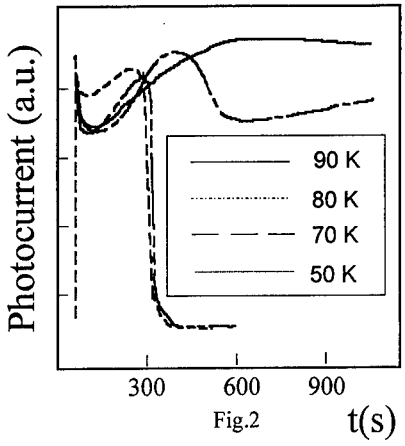


Fig.2

Fig.1.- Calculated photocurrent (1.17eV) transients at different temperatures
Fig.2.- Experimental photocurrent (1.17eV) transients at different temperatures

The solution reveals that the photoquenching begins to be delayed at 70 K, figure 1. Below this temperature the photoquenching is achieved within 400 s, and it is nearly independent of temperature, above 85 K, the photoquenching is not done, even after a long time (>2000 s). This is consistent with the experimental result [10, 11], figure 2. The increase of the time needed for photoquenching can be explained in terms of the balance between the hole transfer to the actuator level and the thermal emission and subsequent capture by EL2 or D. When the thermal emission starts the mean lifetime of the quenchable EL2 levels begins to decrease while the hole transfer rate does no significantly change, this results in the corresponding reduction of the photoquenching probability. From this competition results that the quenching occurrence at high temperature, above 70K, is strongly dependent on the light intensity, since the rate of hole transfer is proportional to the incident density of photons. This is observed experimentally and on the other hand is very accurately reproduced by the calculation, figure 3.

It was also shown that the photocurrent quenching is observed once the optical absorption quenching is almost accomplished; this should mean that the photocurrent quenching is observable once most of the EL2 levels are in the metastable state. Following this, it is possible to greatly reduce the photoquenching time at 85K by a previous illumination at lower temperature. This exactly occurs when the mentioned procedure is implemented both experimentally and numerically. These results, along with those relating to the low temperature quenching evidences the accuracy of the model with the actuator level.

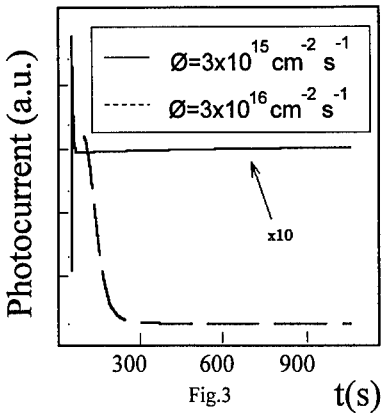


Fig.3

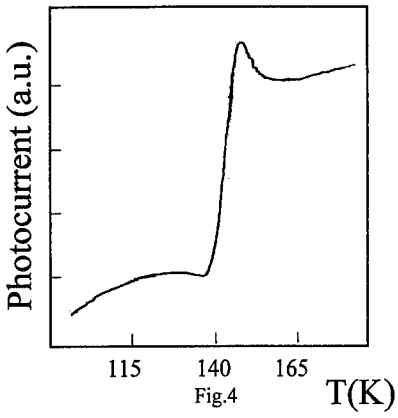


Fig.4

Fig.3.- Calculated photocurrent (1.17eV) transients at 85 K for two different incident photon flux

Fig.4.- Experimental thermal recovery of the photocurrent under illumination with 1.17eV light.

THERMAL RESTORATION OF EL2

A detailed study about the thermal restoration of the EL2 ground state is now being undertaken. In relation to this point some experimental facts have to be noted. An activation energy of 0.3 eV is usually admitted for such a process [1]. This activation energy is measured in darkness. Our measurements are under illumination. In these conditions the activation energy measured fot the photocurrent tecovery is much higher, up to 0.9 eV. This value depends on the sample and the light energy. In a first qualitative approach we ascribed this anomalously large activation energy to the combined effect of the thermal recovery of EL2 and the mobility change associated with the p to n dominant photoconduction during the recovery process [12]. However, numerical estimations rule out this hypothesis, and suggest that the restoration under light differs from that in the dark. The optical excitation seems to actively influence the mean lifetime of the photogenerated carriers released from recovered EL2 levels. Accompanying this sharp photocurrent restoration a spike photocurrent is observed, the intensity of the spike is dependent on the light wavelength in a similar way to the thermal activation energy. This is tentatively associated with the thermal quenching of the TSC reported by Fang et al [13]. Our calculations point out that such an structure is associated with an electron capture process controlled by a level different from EL2.

CONCLUSION

The role of the actuator level in the temperature dependence of the metastable transformation has been modeled, introducing an Arrhenius term in the set of rate equations describing the

metastability of EL2. The agreement with the experimental results is excellent, providing further support to the role played by the actuator level in the mechanism driving the metastable change of EL2. It is shown that the photoquenching efficiency depends on the average charge of this level. In fact, it depends on the balance between hole capture and emission by this level. Thus, temperature and light intensity are competing parameters in the transit to the metastable state. Preliminary results concerning the thermal restoration of EL2 are pointed out.

REFERENCES

1. G.M. Martin and S. Makram-Ebeid; Deep Centers in Semiconductors, edited by S.T. Pantelides (Gordon and Breach, New York 1986), ch.6

2. J. Jiménez, A. Alvarez, M. Chafai, L.F. Sanz and J. Bonnafé; J. Appl. Phys. 73, 2871 (1993).

3. A.Alvárez, J.Jiménez and M.A.González; Appl.Phys.Lett 68, 2959, 1996

4. B.K.Meyer, K.Krambrock, D.M.Hofmann and J.M.Spaeth; Defect Control in Semiconductors, edited by K.Sumino (Elsevier Science Publishers B.V., North-Holland, 1990) p. 735 .

5. J.Wagner, H.Seelwind and U.Kaufmann; Appl.Phys. Lett 48, 1054 (1986).

6. U.Kaufmann, M.Baeumler, J.Windscheif and W.Wilkening; Appl. Phys. Lett. 49, 1254, (1986).

7. G.Baraff; Proc. Seventh Conference on Semi-insulating III-V Materials, edited by C.J.Miner, W.Ford and E.R. Weber (Adam Hilger, Bristol, 1993), p.11

8. H.J. van Bardeleben, D.Stievenard, D.Deresmes, A.Hubber and J.C. Bourgoin; Phys.Rev. B 34, 7192 (1986).

9. G.Roos, A.Schoner, G.Pensi, J.Wagner, B.K.Meyer and R.C.Newman; J.Appl.Phys. 69, 1454 (1991).

10. J.Jiménez, A.Alvarez, M.Chafai and J.Bonnafé; Phys.Rev. B 50, 14112 (1994).

11. M.Suemitsu, H.Takahasi and N. Miyamoto; Phys. Rev. B 52, 1666 (1995)

12. A.Alvárez, J.Jiménez, M.Chafai, M.A.González and J.Bonnafé; J.Appl.Phys. 73, 5004 (1993).

13. Z.Q.Fang and D.C. Look; Appl.Phys. Lett 66, 3033 (1995).

DIFFUSION PROCESS OF INTERSTITIAL ATOMS IN InP STUDIED BY TRANSMISSION ELECTRON MICROSCOPY

Y. OHNO, S. TAKEDA, AND M. HIRATA
Department of Physics, Graduate School of Science, Osaka University,
1-16, Machikane-yama, Toyonaka, Osaka 560, Japan

ABSTRACT

It is found that interstitial agglomerates are formed uniformly in an irradiated area of InP by annealing at the temperature above 700 K after 200 keV-electron irradiation. TEM observation shows that the number density of interstitial atoms in the agglomerates reached a maximum value when the growth of all the agglomerates stopped. The final density did not depend on annealing temperature but on electron dose, and it increased quadratically with electron dose up to $2x10^{22}$ cm^{-2}. In order to explain the experimental results, we have proposed a new model that the agglomerates are formed by thermal diffusion and agglomeration of interstitial-pairs, i.e. In_i-P_i interstitial-pairs. From the analysis, the migration energies for the pairs are estimated to be 1.52 eV. The onset temperature for the diffusion of the pairs is estimated as 550 K.

1. INTRODUCTION

InP has been widely used for high-functional devices such as Gunn-diodes and hf-transistors. Since the existence of point defects in the crystals greatly affects on electrical [1] and/or optical properties [2], they have been extensively investigated. From the results of electron paramagnetic resonance [3] and Huang diffuse scattering [4] in electron-irradiated InP, the onset temperature for migration of isolated In- or P-interstitials is estimated to be 100~300 K. Above the onset temperature, three kinds of defects annealing are observed by various experimental techniques such as electronic conductivity measurement [1], photoluminescence spectroscopy [2], and positron annihilation spectroscopy (PAS) [5, 6]; annealing stages between 423 and 523 K, 573 and 723 K, and 723 and 823 K. These stages are considered to arise from annealing of isolated-vacancies, formation of vacancy clusters, and collapse of vacancy clusters, respectively. Even though the role played by point defects in electronic and optical properties is established, the diffusion mechanism of the defects has not yet been fully clarified.

In the present study, we found the formation of interstitial agglomerates in InP by following annealing after electron irradiation. *In-situ* observation of the growth of point defect agglomerates in a TEM contributes to the understanding of the migration of point defects [7]. We thus measured the variation of the radii and number density of the agglomerates under several annealing and irradiation conditions. From the analysis of the experimental results, we have proposed a new diffusion model in InP: the agglomerates are formed by thermal diffusion of In_i-P_i interstitial-pairs introduced during electron-irradiation.

2. EXPERIMENTS

Specimens were Cz-InP single crystals. By means of selected ion mass spectroscopy, the concentrations of native impurity atoms (C, O, Si, and S) in the specimens were estimated to be less than $5x10^{17}$ cm^{-3}. Specimens for TEM observation were prepared by chemical polishing. In order to introduce point defects intentionally, specimens were irradiated by the 200 keV-electron beam exactly parallel to the <100> direction. The irradiation was performed at 300 K with an electron dose of $1.7x10^{22}$ cm^{-2}, otherwise it is noted in the text. An irradiation area on a specimen surface was about 2 μm in diameter. Specimens were then annealed at the temperature range from 700 to 825 K. Since InP rapidly deteriorates when annealed in vacuum at temperature above 700 K, the specimens were annealed in a flowing argon atmosphere in a furnace.

TEM observation were performed with 200 keV electrons. Weak-beam images were taken with 220 reflection (g, 5g). The images were taken with the electron-beam with the direction tilted by 5° to <100> in order to avoid irradiation-effects during observation [8].

Mat. Res. Soc. Symp. Proc. Vol. 442 © 1997 Materials Research Society

3. RESULTS

3-1 Formation of the interstitial agglomerates

Figure 1(a) shows a TEM image of an electron-irradiated area. There is no distinct contrast due to lattice defects. As shown in Fig. 1(b), numerous defects were formed only in the irradiated area by annealing at 800 K after the irradiation. Figure 1(c) shows the magnified image of Fig. 1(b): the defects were identified as dislocation loops on {111} (some of them are indicated by large arrows) and {110} (small arrows) planes by observation with several reflections and incident beams. The nature of the loops was clarified as interstitial-type by means of the inside-outside method. The habit plane and nature of the {111} defect was surely confirmed by high-resolution TEM image (Fig. 1-d). Interstitial agglomerates on {111} planes were also formed in GaP by the similar procedure [9], though ones on {110} were not introduced.

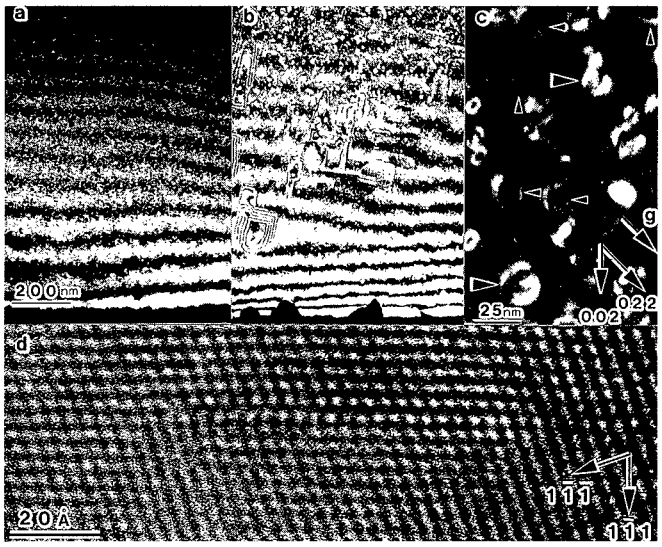


Fig. 1 Weak-beam TEM images of electron irradiated area of InP before (a) and after (b) annealing at 800 K taken with 220 reflection (g, 5g). The electron-dose D is 1.7×10^{22} cm^{-2}. (c) the magnified image of Fig. 1(b). The small and large arrows in Fig. 1(c) show a part of interstitial agglomerates on {110} and {111} planes, respectively. (e) High resolution TEM image of an interstitial agglomerates on {111} planes in InP taken with the <110> incidence.

Figure 2 shows the planar densities of the agglomerates on {111} (denoted by open circles) and {110} (closed circles) planes v.s. the specimen thickness. Both the densities can be fitted with straight lines and the fact indicates that the volume number densities of the agglomerates, C_L are independent of the specimen thickness. The agglomerates were created by annealing at the temperature above 700 K after 200 keV-electron irradiation. The electron energy of 200 keV is large enough to introduce Frenkel-type defects at both In and P sublattices [10]. The concentration of electron-irradiation-induced interstitials (~10^{19} cm^{-3}) is larger than the concentration of impurities (~10^{17} cm^{-3}). Therefore, the result demonstrated in Fig. 1 clarifies that the agglomerates were formed by thermal migration of interstitial atoms that were introduced by electron irradiation.

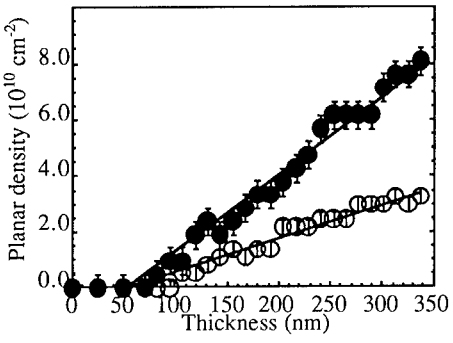


Fig. 2 Planar density of the agglomerates on {111} (open circles) and {110} (closed circles) planes v.s. the specimen tickness measured in Fig. 1(b).

3-2 Number densities of the interstitial agglomerates

Most of the interstitial agglomerates were nucleated within an annealing time of 900 s, and C_L remained constant after the nucleation. Figure 3 shows the logarithms of the number density $\ln(C_L)$ as a function of the reciprocal of annealing temperature $1/kT_{an}$. The values of C_L was measured when all the agglomerates were nucleated; specimens were annealed for a period of 1800 s after irradiation. As shown in Fig. 3, C_L increases exponentially with $1/kT_{an}$. The slope of C_L for the agglomerates on {111} planes (denoted by open circles) is the same as one for the agglomerates on {110} planes (closed circles), even though the values of C_L is different. The slopes of the straight lines in the figure provide the energies of 0.75 eV.

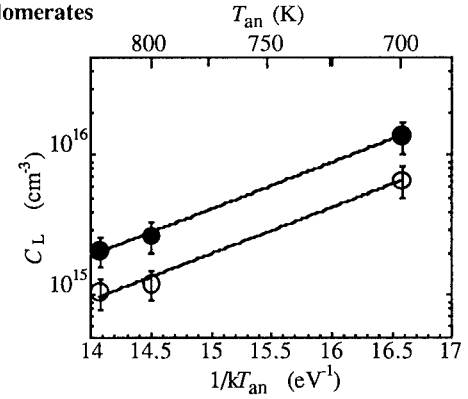


Fig. 3 Number density of the agglomerates on {111} (open circles) and {110} (closed circles) planes C_L as a function of the reciprocal of annealing temperature $1/kT_{an}$.

3-3 Radii of the interstitial agglomerates

The radii of the agglomerates increased with annealing times and then reached a final value within an annealing time of 900 s. Figure 4 shows the size distribution of the final radii r_0 at the temperature T_{an}=700 K (denoted by open marks) and 800 K (closed marks). As shown in Fig. 4, the size distribution of the radii of the agglomerates on {111} (squares) and {110} (circles) planes appear qualitatively similar; the averaged radius and standard deviation of the agglomerates on {111} planes is almost the same as that on {110}. We found that the dispersion of the radii of the agglomerates is small; the ratio of the standard deviation of r_0 (nm) to the average of r_0 (nm) is 0.3/2.2 at the temperature T_{an}=700 K and 1.0/4.7 at T_{an}=800 K.

Figure 5 shows the averaged final radius $\tilde{r}$ v.s. $1/kT_{an}$. The irradiation and annealing condition was the same as those used in Fig. 3. The means of the marks is the same as those in Fig. 3. As shown in Fig. 5, $\tilde{r}$ decrease exponentially with $1/kT_{an}$.

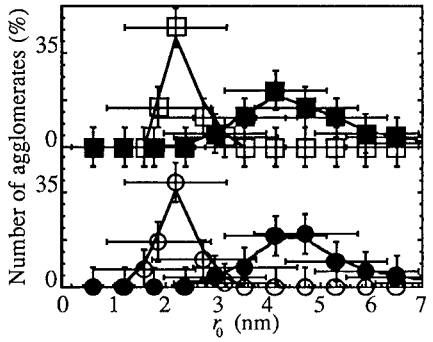


Fig. 4 Size distribution of the agglomerates on {111} (squares) and {110} (circles) planes at the annealing temperature T_{an} of 700 (open marks) and 800 (closed marks) K.

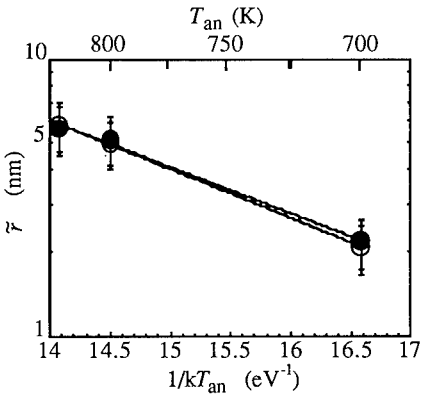


Fig. 5 Average final radii of the agglomerates on {111} (open circles) and {110} (closed circles) planes $\tilde{r}$ v.s. the reciprocal of annealing temperature $1/kT_{an}$.

3-5 Number density of interstitial atoms in all the agglomerates

We can estimate the number density of interstitial atoms in all agglomerates, C_{IL} as

$$C_{IL} = 2\sum_i \sum_j \pi \, r_{0(j)}^{\,2} \, \sigma_{(j)} \qquad (1)$$

in which σ represents the planar density of In- or P-interstitials in agglomerates on $\{j\}$ planes (j=111, 110), and is denote individual agglomerates. Since dispersion of the radii of all agglomerates is small, we can rewrite the Eq. (1) as

$$C_{IL} = 2\sum_j \pi \, \tilde{r}_{(j)}^{\,2} \, \sigma_{(j)} \, C_{L(j)} . \qquad (2)$$

C_{IL} reaches a final value $C_{IL}(\infty)$ when the growth of all the agglomerates stops. Figure 7 shows the final number density of interstitial atoms contained in all agglomerates $C_{IL}(\infty)$. Specimens were previously irradiated with an electron dose of (a) 9.5×10^{21}, (b) 1.7×10^{22}, and (c) 3.5×10^{22} cm^{-2}, respectively. The annealing condition was the same as those used in Fig. 3. As shown in Fig. 7, $C_{IL}(\infty)$ remains constant at several T_{an} when D is a constant value; $C_{IL}(\infty)$ does not depend on D but on T_{an}.

Figure 8 shows $C_{IL}(\infty)$ as a function of D and irradiation temperature T_{ir}. Specimens were previously irradiated with an electron dose of 1.7×10^{22} cm^{-2} at the temperature T_{ir} of 110 (denoted by triangles), 300 (circles), and 450 (squares) K, respectively, and then annealed at 800 K for a period of 1800 s. No interstitial agglomerates were formed when a specimen was irradiated at the temperature above 450 K. $C_{IL}(\infty)$ increased quadratically with electron doses in a dose range of $D\leq2.0\times10^{22}$ cm^{-2} when the irradiation temperature T_{ir}=300 K and $D\leq2.6\times10^{22}$ cm^{-2} when T_{ir}=110 K. $C_{IL}(\infty)$ irradiated at T_{ir}=110 K is slightly lower than one at T_{ir}=300 K in the dose range of $D\leq2.6\times10^{22}$ cm^{-2}.

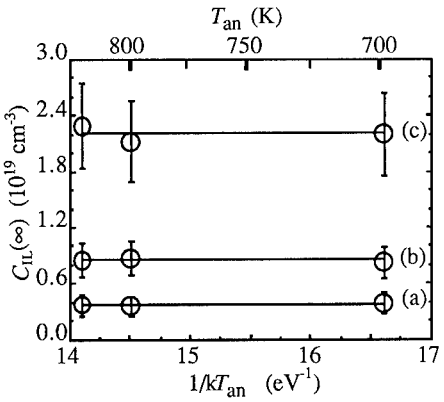


Fig. 6 Final number density of interstitials in all agglomerates $C_{IL}(\infty)$ v.s. the reciprocal of annealing temperature $1/kT_{an}$. Electron doses are (a) 9.5×10^{21}, (b) 1.7×10^{22}, and (c) 3.5×10^{22} cm^{-2}, respectively.

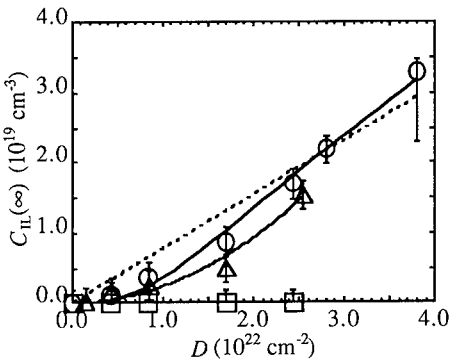


Fig. 7 Final number density of interstitials in all agglomerates $C_{IL}(\infty)$ v.s. electron dose D. Irradiation temperature T_{ir} are 110 (triangles), 300 (circles) and 450 (squares) K. Broken and solid lines represent the simulated $C_{IL}(\infty)$ curves based on the isolated-interstitials-migration and the interstitial-pairs-migration model, respectively.

DISCUSSION

As shown in Fig. 7, $C_{II_L}(\infty)$ increases quadratically with D; this is a characteristic trend in second order reaction. This result is not explained by an isolated-interstitial migration model that applies to metals and alloys [7], since the model yields the result that $C_{II_L}(\infty)$ increases linearly with D (denoted by broken line in Fig. 7). Moreover, the onset temperature for formation of the agglomerates (~700 K) is much higher than that for migration of isolated interstitials (100~300 K) [3, 4]. These results strongly suggest that the agglomerates are formed by the migration of not isolated-interstitials but interstitial-related complexes created in second order reaction. For quantitative understanding of the experimental results, we propose a new diffusion model based on migration of interstitial-pairs. The model is depicted as the following equations,

$$\frac{dC_I(\xi)}{dt} = P(\xi) - Z_I(\xi)\, M_I(\xi)\, C_I(\xi)\, C_V(\xi) - Z_{II}\,(M_I(\mathrm{In}) + M_I(\mathrm{P}))\, C_I(\mathrm{In})\, C_I(\mathrm{P}), \quad (3)$$

$$\frac{dC_V(\xi)}{dt} = P(\xi) - Z_I(\xi)\, M_I(\xi)\, C_I(\xi)\, C_V(\xi), \quad (4)$$

$$\frac{dC_{II}}{dt} = Z_{II}\,(M_I(\mathrm{In}) + M_I(\mathrm{P}))\, C_I(\mathrm{In})\, C_I(\mathrm{P}) - (2\pi r \cdot \alpha) M_{II} C_L C_{II}, \quad (5)$$

$$\frac{dC_{II_L}}{dt} = (2\pi r \cdot \alpha) M_{II} C_L C_{II}. \quad (6)$$

Equations (3) and (4) represent the variation of the concentration of isolated interstitials, $C_I(\xi)$ and one of isolated vacancies, $C_V(\xi)$, respectively. ξ denotes the species of atoms: In and P atoms. $P(\xi)$ represents the production rate of Frenkel-type defects affected by correlated recombination under electron irradiation [11], $Z_I(\xi)$ the number of capture sites around a ξ-vacancy for ξ-interstitials, and $M_I(\xi)$ the mobility of isolated ξ-interstitials. An In_i-P_i interstitial-pair is formed when an interstitial jumps into the spontaneous recombination volume around an interstitial of the other kind (third term in Eq. (3)). Equation (5) represents the variation of the concentration of the pairs C_{II}, where Z_{II} represents the number of capture sites of the interstitial pairing. The second term in Eq. (5) is the rate of disappearance of the pairs by the formation of interstitial agglomerates, where M_{II} denotes the mobility of the pairs, α the number of capture site per unit length around the agglomerates for the pairs. The variation of C_{II_L} is given in Eq. (6).

Since the onset temperature for migration of isolated vacancies is estimated to be 425~450 K [4, 5, 12], we consider that only isolated interstitials can freely migrate thermally during irradiation at the temperature $T_{ir} \leq 450$ K. Moreover, the mobility of the interstitial-pairs during electron-irradiation at the temperature $T_{ir} \leq 450$ K can be neglected, since interstitial agglomerates are not formed during irradiation. We have introduced one more important assumption; an In_i-P_i interstitial-pair never combines with an isolated single In- or P-vacancy. The experimental results demonstrated in Fig. 6 and 7 are well described by the model proposed above.

We performed the numerical calculations of the rate equations, (3) to (6) with several sets of parameters. In the following computations, we naturally assumed that $P(\mathrm{In})=P(\mathrm{P})=2.0\times10^{-6}$ s^{-1} during irradiation, $P(\mathrm{In})=P(\mathrm{P})=0\ s^{-1}$ during annealing, $Z_I(\mathrm{In})=Z_I(\mathrm{P})=10^2$, and the concentrations of point defects before irradiation were assumed to be zero. We assumed that $M_I(\mathrm{In})=M_I(\mathrm{P})$ $(=M_{ir})$ and $M_{II}=0$ during irradiation, and $M_I(\mathrm{In})=M_I(\mathrm{P})$ $(=M_{an})$ during annealing. From the analysis, we confirmed that $C_{II_L}(\infty)$ is independent of both M_{an} and M_{II} on the condition of constant D and M_{ir}. This reproduces the experiment shown in Fig. 6, since M_{an} and M_{II} are related to the annealing temperature T_{an}.

We first assumed that the pairs are created only by electron irradiation: $Z_{II}=4$ during

irradiation and Z_{II}=0 during annealing. $C_{IL}(\infty)$ increases quadratically with D in the lower dose range; $C_{IL}(\infty)$ computed with M_{ir}=1x10^{-3} and M_{ir}=5x10^{-4} s^{-1} (denoted by solid lines in Fig. 6) agree well with the measurements at the irradiation temperature T_{ir}=300 and 110 K, respectively. The similar results could be obtained whenever the values of Z_{II} and $P(\xi)$ were in the order of 10^0 and 10^{-6} s^{-1}, respectively. Suppose the interstitial-pairs are formed during not only irradiation but also annealing, $C_{IL}(\infty)$ increases linearly with D. Consequently the experimental data are consistently described by the former model: interstitial agglomerates are formed by thermal migration of In_i-P_i interstitial-pairs that are created only by electron irradiation.

In the temperature range from 700 to 825 K, C_L increased exponentially with $1/kT_{an}$ and $C_{IL}(\infty)$ was independent of T_{an} on the condition of constant D. Interstitial agglomerates whose sizes are less than 2 nm may be formed at T_{an}<700 K, though they are hardly observable by TEM. Suppose the relationships between C_L and T_{an} and between $C_{IL}(\infty)$ and T_{an} are held even at low T_{an}, we can estimate C_L and $C_{IL}(\infty)$ for temperatures T_{an}<700 K. The temperature when C_L reaches a quarter of $C_{IL}(\infty)$, at which only two interstitial-pairs are contained in an agglomerate, corresponds to the onset temperature for the migration of the interstitial-pairs. We estimated the onset temperature to be 550 K. The estimated temperature is higher than the onset temperature for migration of isolated In- or P-interstitials [3, 4] (100~300 K), and the fact obviously indicates that interstitial agglomerates are not formed by migration of isolated interstitials. The temperature is also higher than the onset temperature for migration of isolated vacancies [4, 5, 12] (425~450 K). This experimental result is consistent with our assumption that the interstitial-pairs does not combine with isolated vacancies.

The estimated onset temperature is close to the onset temperature of an annealing stage observed by electron conductivity measurements [1] (543 K~) and PAS in electron [6] or neutron [5] irradiated InP (575 K~). The stage is believed to arise from the breaking up of vacancy clusters such as V_{In}-V_P pairs [6]. This defect annealing may be simply interpreted as the recombination of a V_{In}-V_P pair and a In_i-P_i pair by migration of interstitial-pairs. In GaP, the migration energy for interstitial-pairs was estimated as the twice the energy shown by the slope of ln(C_L) v.s. $1/kT_{an}$ [9]. We thus estimate the migration energy for In_i-P_i pairs as 1.52 eV.

CONCLUSIONS

We found that interstitial agglomerates are formed uniformly in InP by following annealing at the temperature above 700 K after 200 keV electron irradiation. Results of TEM observations showed that the agglomerates are formed through the two processes; 1) introduction of interstitial atoms by electron irradiation and 2) thermal diffusion of interstitials by annealing. Experimental results are consistently explained by a diffusion model; the interstitial agglomerates are formed through the migration of In_i-P_i interstitial-pairs for InP introduced during electron irradiation.

REFERENCES

[1] E. Yu. Brailovskii, F. K. Karapetyan, I. G. Megera, and V. P. Tartachnik, Phys. Status Solidi A **71**, 563 (1982).
[2] A. Sibille and E. V. K. Rao, J. Cryst. Growth **64**, 194 (1983).
[3] T. A. Kennedy and N. D. Wilsey, Appl. Phys. Lett. **44**, 1089 (1984).
[4] K. Karsten and P. Ehrhart, Phys. Rev. B **51**, 10508 (1994).
[5] V. N. Brudnyi, V. A. Charchenko, N. G. Kolin, V. A. Novikov, A. D. Pogrebnyak, and Sh. M. Ruzimov, Phys. Status Solidi A **93**, 195 (1986).
[6] V. N. Brudnyi, S. A. Vorobiev, and A. A. Tsoi, Appl. Phys. A **29**, 219 (1982).
[7] M. Kiritani, J. Nucl. Mater. **216**, 220 (1994).
[8] K. Urban and N. Yoshida, Radiat. Eff. **42**, 144 (1979).
[9] Y. Ohno, S. Takeda, and M. Hirata, Phys. Rev. B **54**, 4642 (1996).
[10] B. Massarani and J. C. Bourgoin, Phys. Rev. B **34**, 2470 (1986).
[11] N. Noda, S. Takeda, Phys. Rev. B **53**, 7197 (1995).
[12] P. R. Tapster, J. Cryst. Growth **64**, 200 (1983).

PROPERTIES OF INP SIMULTANEOUSLY DOPED WITH ZINC AND SULFUR GROWN BY MOCVD

C. M. ALAVANJA, C. J. PINZONE, S. K. SPUTZ, AND M. GEVA*
Bell Laboratories 700 Mountain Avenue, Murray Hill, NJ 07974
* 9999 Hamilton Boulevard Breinigsville, PA

ABSTRACT

As the p-type dopant most often used in metalorganic chemical vapor deposition (MOCVD) of Group III - Group V compound semiconductors, Zn presents problems in device design and performance because of its high diffusivity in these materials. While Zn diffusion into n-type layers such as InP:S has been observed frequently, there is little known as to the electronic and optical properties of the resultant material. We have grown InP samples by MOCVD which are doped with both Zn and S to levels as high as $3x10^{18}$ cm^{-3}. These samples were analyzed by electrochemical C-V profiling, van der Pauw-Hall analysis, secondary ion mass spectroscopy (SIMS), and low temperature (10K) photoluminescence spectroscopy (PL). We have determined that good hole mobility is maintained in InP:Zn samples that are simultaneously doped with S up to a level of $4x10^{17}$ cm^{-3}. PL analysis of co-doped samples shows peaks between 0.91 and 0.92 μm which are indicative of donor-acceptor transitions, and broad peaks with energy levels of approximately 1.0 μm which may be indicative of ZnS complexes or precipitates. SIMS analysis of Zn diffusion into Fe doped substrates shows that Zn diffusion is reduced in the presence of S in the lattice.

INTRODUCTION

The ability to intentionally and precisely change the electrical properties of a semiconductor material with the addition of low levels of an electron donating or "withdrawing" species is an enabling technology for the fabrication of electronic and photonic devices in any materials system. In metalorganic chemical vapor deposition (MOCVD) of Group III- Group V compound semiconductors, this is done by the addition of appropriate precursors to the reactive gas stream[1]. Upon further growth of the device material and subsequent processing, redistribution of these dopant atoms may occur to reduce the intended carrier concentration in the material or displace the electrical junction, resulting in degradation of the device performance. The driving force for this being the reduction of free energy associated with movement of atoms to lower energy positions in response to the concentration gradient, strain field, or built in electrical field. This is a particular problem with Zn atoms which are commonly used in this technique as a p type dopant in InP. The rapid diffusion of Zn in InP has been widely reported[2,3] and is believed to be dominated by the movement of Zn interstitials through the lattice[4]. This presents a serious problem for development of MOCVD as a manufacturing platform for optoelectronic integrated devices with reduced dimensions and more demanding tolerances. Observations of an enhanced interaction of Zn with S in InP[5], and the investigation of Zn diffusion in InP in the presence of S, Si or Fe[6] has lead us to investigate the properties of InP simultaneously doped with Zn and S.

EXPERIMENT

All epitaxial InP samples grown for this work were produced in a commercial single 2" wafer low pressure MOCVD system. The source materials were adduct purified trimethylindium, 100% phosphine, diethylzinc, and 1% hydrogen sulfide in hydrogen, Substrates were either (100) oriented InP:S or InP:Fe. Growth proceeded with a V/III ratio of approximately 250, at 670° C and 80 mbar (45 torr) with the wafers rotated at approximately 80 rpm. Room temperature Hall measurements were made using the van der Pauw technique[7] with a magnetic field of 3 kGauss and test currents between 1 and 10 mA. Alloyed contacts were made using either InCd or InPb at 350° for 20 seconds under forming gas. Particular care was taken to ensure that the test

Mat. Res. Soc. Symp. Proc. Vol. 442 © 1997 Materials Research Society

contacts were ohmic. Samples were characterized by low temperature photoluminescence (PL) in a closed cycle cryostat cooled to 9-10K. The samples were excited with an Argon ion laser tuned to the 4880 Å line at 0.5 W output power. Data was taken using an ISA 0.64 meter spectrometer and a cooled germanium PIN detector. A Phillips 420 electron microscope operated at 120 KV was used for TEM characterization on several samples to check for ZnS precipitates. Secondary ion mass spectroscopy was performed using a CAMECA IMS-4f using a Cs+ primary ion beam and detecting negative secondary ions for the detection of S, and positive secondary molecular ions for the detection of Zn. S and Zn standards in InP were analyzed in order to quantify elemental concentrations. The depth scale was found by measuring the depth of the sputtered craters subsequent to the analysis.

RESULTS

Carrier concentration measurements were performed on Zn doped and Zn-S co-doped samples with similar Zn levels. The results shown in Figure 1 exhibit the characteristic drop in mobility with increasing Zn concentration as would be expected for the Zn doped samples, For the co-doped samples where InP is co-doped with 2 x 10^{-18} cm^{-3} Zn concentration and from 2-4 x 10^{-17} cm^{-3} S concentration, the measured hole mobilities are comparable to those of the InP with only Zn doping. This is signifigant because if we are to use S counter-doping to block the movement of Zn interstitials, hole mobility must be maintained in order for the device to work properly. We were unable to obtain meaningful mobility results from samples that were doped with higher levels of S (where [S] ~ [Zn]) because of formation of Schottky barriers at the alloyed contacts. A wide range of In alloys were tried in order to overcome this problem but to no avail. This would suggest that the carriers have been totally compensated or perhaps an interface state arises from the presence of a Zn-S complex. Different metallization techniques and deep level transient spectroscopy are being attempted to resolve the nature of carrier behavior in these co-doped layers. As expected a reduction of the carrier concentration in the co-doped samples is observed. However for three co-doped samples with the same Zn concentration, the carrier concentration (N_A-N_D) was seen to increase with increasing S concentration. This at first seems counterintuitive, but since for a measured Hall voltage the carrier concentration is proportional to the current:

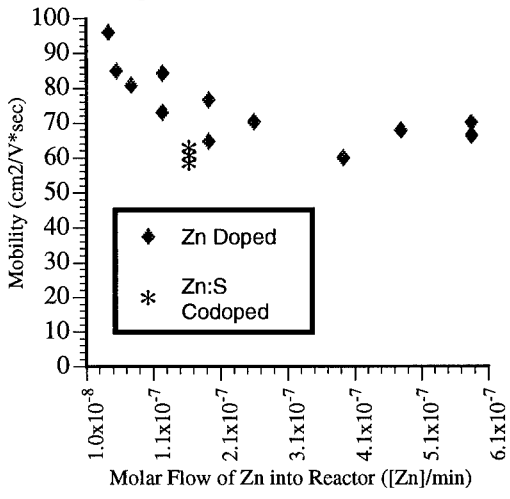


Figure 1

$$I \propto (n\,\mu_n + p\,\mu_p) \qquad (1)$$

where n and p are the electron and hole concentrations respectively the higher mobility term dominates. On the other hand the mobilities add inversely[8] so that the lower mobility term (i.e. for holes) dominates.

SIMS measurements on samples doped with either Zn or S separately, and both species simultaneously were performed. A linear incorporation of Zn is seen up to the substitutional incorporation limit of 1-4 x 10^{18} cm^{-3} as has been previously observed[9]. The presence of S at one tenth to one fifth that of the Zn concentration enhances the incorporation of Zn into the epitaxial layer. For the sample in which the S concentration is equal to that of the Zn, there is a signifigant increase in Zn incorporation. These results are similar to those seen by Blaauw et.al. in their studies of Zn and Si co-doping[10 11]. A plot of these results in Figure 2 shows the higher incorporation rate of Zn in the presence of S. A careful study of S incorporation in the presence of Zn was not made. For flow conditions where the concentration of S was higher than that of Zn in singly doped InP, these same conditions resulted in equal concentrations of Zn and S atoms in the InP co-doped layer as measured by SIMS. Conditions that resulted in higher concentrations of Zn than S did result in co-doped layers with higher atomic levels of Zn suggesting that there is no enhancement of S incorporation in the presence of Zn.

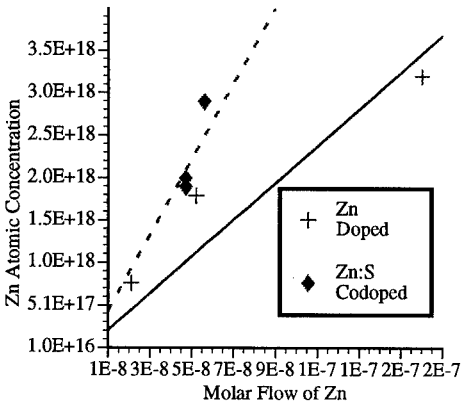


Figure 2

The extent of Zn diffusion into the underlying InP:Fe substrate can be seen from SIMS analysis of these samples. For Zn doped samples below the onset of of rapid diffusion (~1-3 x 10^{18} cm^{-3}) the Zn concentration drops abruptly. A typical spectra of a sample with a Zn concentration above this limit is seen in Figure 3. The susbstrate-epitaxial layer interface is marked by concentration spikes thought to be an artifact of the SIMS analysis. This interface location has also been verified by a calculation of the layer thickness from the growth rate and growth time. In all of the samples grown on iron doped substrates, a knee in the Zn concentration curve around 6 x 10^{16} cm^{-3} occurs as the Zn diffuses into the substrate. This corresponds to the level of Fe doping in the substrate. In this region an Fe-Zn kick out mechanism dominates the typical Zn interstitial diffusion and enhances the total Zn diffusion. The depth of this Zn plateau into the substrate increases with increasing concentration.

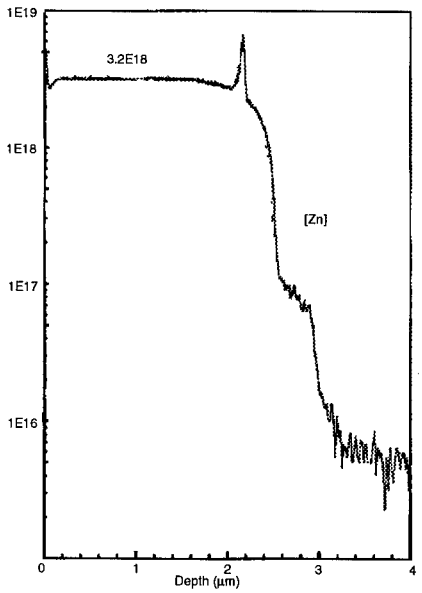


Figure 3

Co-doped layers were grown with Zn levels close to 2 x 10^{18} cm^{-3}. The normalized diffusion lengths were calculated separately for the region near the interface and for the low level diffusion region dominated by interdiffusion with Fe. This data is presented in Figures 4 and 5. The increase of the diffusion depth with increasing Zn concentration confirms the concentration dependence of the Zn diffusion. Diffusion in the low level region is less dependent on the interdiffusion mechanism dominates. The lower normalized diffusion depths for co-

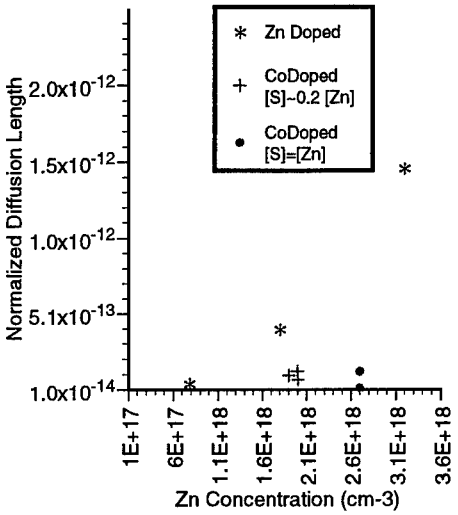


Figure 4

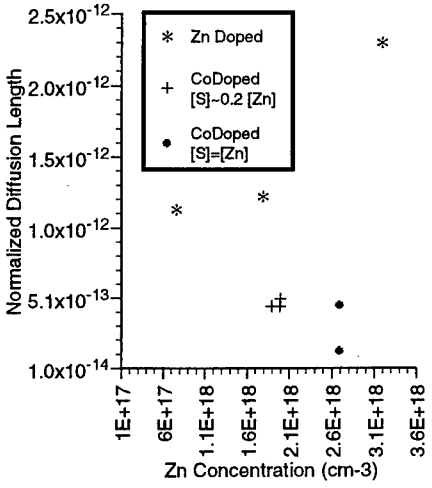


Figure 5

doped samples shows that even a low level of S co-doping can inhibit Zn diffusion. The sample with S co-doping approximately equal to the Zn concentration, shows that S can inhibit diffusion of Zn from a highly doped Zn layer.

PL spectra were taken at 10K in the range from 0.83 to 1.03 μm. At this temperature the bandgap transition for InP is 0.88 μm. In all of the Zn doped samples, the luminescence peak occured at 0.9 μm which is consistent with a conduction band-to-acceptor transition for a shallow acceptor level, that is shallow acceptors in InP contribute an energy level 35.2 meV from the edge of the band gap[12] leading to a transition at 0.902 μm. For co-doped InP samples with a low level of S, the spectra as shown in Figure 6 exhibits a strong peak between 0.91 and 0.92 μm. This corresponds to a large number of donor-acceptor transitions, which is to be expected since both have been intentionally incorporated into the layer. A broad peak close to 0.93 μm is also observed We think that this is due to transitions associated with Zn-S precipitates which were observed by TEM in this sample. This peak was not observed in samples where there was no evidence of Zn-S precipitates. The co-doped sample with equal atomic levels of Zn and S was signifigantly brighter than the previous co-doped samples. In this spectra, Figure 7, the peak energy is shifted to 0.95 μm and the peak has broadened to include wavelengths from 0.92 to 1.02 μm. The broadness of the peak is thought to be a result of the increase in the variety of states introduced by neutral Zn-S complexes. There is no transition observed at 0.92 μm (D-A) as in the other co-doped samples because since the Zn is bound to the S, all of the donors and acceptors are tied up in the Zn-S complex.

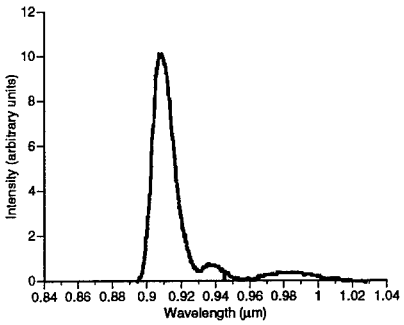


Figure 6

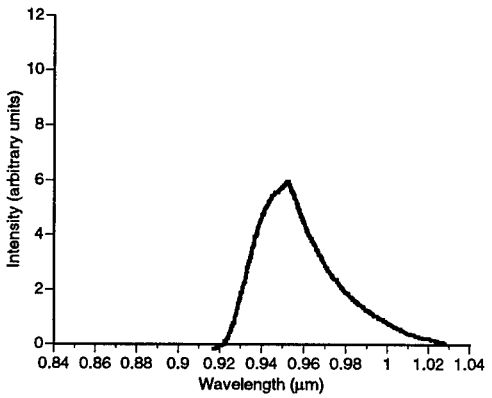


Figure 7

CONCLUSIONS

Co-doping Zn with S has been shown to increase Zn incorporation slightly for samples in which the S concentration was less than the Zn concentraion. When the S concentration is higher than the intended Zn, Zn is incorporated to the same level as the S. The increased incorporation is likely due to some complexation of Zn and S constituents on the surface of the growing crystal which decreases the re-evaporation of Zn from the surface, resulting in the observed Zn incorporation enhancement. The data presented show that for moderate levels of S added to Zn doped InP, hole mobility through the layer is still comparable to that of a singly doped InP:Zn layer. The addition of S to Zn doped InP also appears to inhibit the outdiffusion of Zn. The data also suggest a mechanism by which co-doping with S inhibits Zn diffusion. Young and coworkers[13] have shown that an S layer grown between a moderately (8×10^{17} cm^{-3}) Zn doped layer will inhibit the interdiffusion of Fe and Zn while a Zn:S doped layer will not have an effect on the interdiffusion. Their explanation is that the S absorbs the holes necessary to creat Fe interstitials by the reaction:

$$Fe^{-}_{In} + 2h \Leftrightarrow Fe^{+} + V_{in} \qquad (2)$$

The S layer thereby limits the number of Fe interstitials which drive the interdiffusion. Young et. al. propose that Zn:S co-doped InP layers fail to limit Fe-Zn interdiffusion because the co-doped layers maintain p-type characteristics and therefore do not absorb holes or inhibit Zn diffusion. The work presented in the present paper demonstrates that co-doping with S to a concentration of $2\text{-}4 \times 10^{17}$ cm^{-3} limits Zn diffusion out of the co-doped layer. The decrease in the hole population in the co-doped layer due to the S should be equal to the difference between the [Zn] and [S], which is 10 to 20% of the Zn level. If the drop in diffusion is due to the reduction of holes, one would expect a drop of similar magnitude in the normalized diffusion lengths. However the drop for the co-doped layer is more than 80% in the interface region, and 60% in the low level region. This suggests that S inhibits Zn diffusion at least in part by a different mechanism, and it is reasonable to suggest that the reduction in diffusion is due to a decrease in Zn interstitials by formation of a neutral Zn-S donor-acceptor complex. Evidence of these complexes is seen by low temperature photoluminescence of these materials. We hope to complement this work with DLTS measurements of these layers and to further investigate the carrier transport properties of the layers co-doped with high levels of Zn and S.

ACKNOWLEDGEMENTS

We would like to thank George Chu for performing TEM analysis on several samples, Tom Bitner of Lucent Technologies Microelectronics for several SIMS measurements, and Ralph DeClassis for making the electrochemical C-V measurements (Polaron). The support of Won Tsang, Mike Di Giuseppe, and Robert Fenstermacher is gratefully acknowledged.

REFERENCES

[1] For a comprehensive review of this technology see G. B. Stringfellow, Organometallic Vapor-Phase Epitaxy:Theory and Practice, Academic Press, Inc. 1989

[2] C. J. Pinzone, N. T. Ha, N. D. Ha, R. D. Dupuis, and H. S. Luftman, "Characteristics of Doping and Diffusion of Heavily Doped N and P Type InP and InGaAs Epitaxial Layers Grown by Metalorganic Chemical Vapor Deposition," MRS Symposia Proceedings Vol. 163 p. 867

[3]E. Veuhoff, H. Baumeister, J. Reiger, M. Gorgel, and R. Treichler, "Comparison of Zn and Mg Incorporation in MOVPE InP/GaInAsP Laser Structures", J. Electron. Mater., 20 (**12**) 1991 p.1037

[4] S. N. G. Chu and R. A. Logan, "Concentration Dependant Zn Diffusion in InP During MOVPE of InP", J. Crys. Growth, Vol. 108 1991 p. 449

[5] C. J. Pinzone, N. T. Ha, R. D. Dupuis, N. D. Gerrard, and H. S. Luftman, "Diffusion Studies of Heavily Doped InP and $In_{.53}Ga_{.47}As$ Grown by MOCVD, IEEE LEOS 2nd Conference on InP and Related Materials, Denver, CO April 24, 1990

[6] C. Blaauw, B. Emmerstorfer, D. Keller, L. Hobbs and A. J. Springthorpe, "Effects of S, Si, or Fe Dopants on the Diffusion of Zn in InP During MOCVD", J. Electron. Mater. **21** (2) 1992 p. 173

[7] van der Pauw

[8] B. G. Streetman, Solid State Electronic Devices 2nd edition, Prentice-Hall, Englewood Cliffs, NJ 1980

[9] E. Veuhoff, H. Baumeister, J. Reiger, M. Gorgel, and R. Treichler, "Comparison of Zn and Mg Incorporation in MOVPE InP/GaInAsP Laser Structures", J. Electron. Mater., 20 (**12**) 1991 p.1037

[10] C. Blaauw and L. Hobbs, "Donor-Acceptor Pair Formation in InP Doped Simultaneously with Si and Zn During Metalorganic Chemical Vapor Deposition", Appl. Phys. Lett. 59 (**6**) 1991 p. 674

[11]C. Blaauw, B. Emmerstorfer, D. Keller, L. Hobbs and A. J. Springthorpe, "Effects of S, Si, or Fe Dopants on the Diffusion of Zn in InP During MOCVD", J. Electron. Mater. **21** (2) 1992 p. 173

[11]V. Swaminathan and A. T. Macrander, Materials Aspects of GaAs and InP Based Structures, Prentice Hall, Inc., Englewood Cliffs, NJ 1991, p. 384

[13] E. W. A. Young, G. M. Fontinj, C. J. Virezma, and P. C. Zalm, "An Effective Barrier Against the Interdiffusion of Iron and Zinc Dopants in InP", J. Appl. Phys., 70 (**7**) 1991 p. 3593

Characterization of Hydrogen-Related Defects in Iron-Doped Indium Phosphide

W. B. Leigh*, D. Bliss**, G. Bryant**, G. Iseler**, J. Larkin**, and J. Wolk***
*Division of Electrical Engineering, Saxon Drive, Alfred University, Alfred, N.Y. 14802, fleigh@bigvax.alfred.edu
**Rome Laboratory, Hanscom AFB MA 01731
***Lawrence Berkeley Laboratory, Berkeley CA 94720.

ABSTRACT

We have investigated the effect of annealing on hydrogen-related donors in crystals of InP using Hall effect, infrared absorption, and photorefractive gain measurements. Hydrogen is believed to be incorporated during growth, forming a donor complex around an indium vacancy with hydrogen saturating all four dangling bonds. By observing the local vibrational mode of the hydrogen complex using infrared absorption at 2316 cm^{-1} was possible to observe a decrease in the concentration of the hydrogen defect after annealing. In the undoped crystal, the disappearance of this defect is accompanied by a decrease in the free carrier concentration as measured by Hall effect. These changes are correlated with a decrease in the absorption due to Fe^{2+} centers, which form when donors are compensated by the neutral acceptor Fe^{3+}. The existence of the hydrogen-related donor complex is further substantiated by photorefractive experiments using 1064nm irradiation on the iron doped samples. All of the measurements point to the role of hydrogen as a contributor to the net shallow donor concentration in InP crystals.

Introduction

Semi-insulating crystalline InP can be prepared by iron-doping the melt during the cystal growth process. As the iron impurity sits on an indium sublattice in InP, iron is a negative-charged acceptor when in its Fe^{2+} state. The iron also can exist in the Fe^{3+} state, which is neutral. The Fe^{2+} acceptor energy level is deep, compensating residual donors contributed by the growth process. This compensation is usually modeled as charge compensation of a donor impurity or defect D, which when ionizes to D^+, contributes an electron that can be captured by the neutral Fe^{3+} :

$$D \rightarrow D^+ + e^- \qquad (1a)$$

$$Fe^{3+} + e^- \rightarrow Fe^{2+} \qquad (1b)$$

Compensation by the iron acceptor is "self balancing." If the residual donor concentration varies through an ingot, the material remains semi-insulating through a balance of the Fe^{2+}/Fe^{3+} ratio. Any reduction in the donor concentration is met by a reduction in the Fe^{2+} concentration. Conversely, by measuring the concentration of Fe^{2+} in iron-doped material, the active donor concentration can be found.

The identity of residual donors in InP is not entirely clear. Previous theories implied that S and Si were possible residual donors, though the exact source of these impurities has not been traced. Also, the net donor impurity concentration in bulk grown InP is found to be too low to account for the measured Fe^{2+} concentration.[1] Recently, semi-insulating InP has been prepared by annealing semiconducting material in conditions that prevented iron from being converted to an inactive center.[2,3,4] The preparation of this material resulted in a decrease in the donor content due to the anneal. The donor was of a type easily removed by annealing.

It has been speculated that a native defect-related donor exists in InP, which could easily be

Mat. Res. Soc. Symp. Proc. Vol. 442 © 1997 Materials Research Society

removed by annealing under the proper conditions. Recent studies have indicated that this donor is a hydrogen-native defect complex, labeled H-X, which is most likely a hydrogen-indium vacancy complex.[5,6] It has been shown in these studies that the H-X defect can be identified from the local vibrational mode (LVM) associated with infrared-absorption. This absorption line is centered at 2315.6 cm^{-1}, and involves the vibrational modes of hydrogen bonded to a phosphorous atom. Darwich[6] investigated the stretch associated with this mode and concluded that it was due to a fully hydrogenated indium vacancy $V_{In}(PH_4)$. The four hydrogen atoms contribute three electrons to the vacancy plus one for conduction.

The IR absorption line is a convenient method of characterization of the H-X defect, as the Fe^{2+} absorption can also be determined using this tool. There are two well-known absorption lines at 2830 cm^{-1} and 2842 cm^{-1} due to the Fe^{2+} intracenter transition between crystal field split states, corresponding to transitions from the lowest and the first excited state of the ground level ^5E into the lowest lying $^5T_2$ state. Zach[1] has shown that the Fe^{2+} concentration can be found by integrating the area underneath both absorption peaks.

We have used the absorption-lines at 2316 cm^{-1}, 2830 cm^{-1}, and 2842 cm^{-1}, along with Hall-effect data and photorefractive gain measurements, to determine changes in the concentration of the hydrogen defect in as-grown and annealed samples of InP. Samples of InP were grown using the Magnetic Liquid Encapsulated Kyropolous (MLEK), Liquid Encapsulated Czochralski (LEC) or the Vertical Gradient Freeze (VGF) techniques. Both iron doped and undoped samples were used. Samples were annealed in quartz ampoules at 900° C then cooled. Changes in the Fe^{2+} content were then determined from the LVM absorption lines and from photorefraction measurements. Changes in the carrier concentration of undoped samples were monitored using Hall effect, and changes in the concentration of H-X defect of all samples were determined from 2315 cm^{-1} absorption.

Experimental

Indium phospide samples were annealed in sealed quartz ampoules at 900° C for 48 hrs. A small amount of phosphorous was loaded into the ampoule with the sample to provide a P overpressure of 2-5 atmospheres during the anneal. After annealing, ~50 μm were removed from each surface before the samples were re-measured. Samples cooled at a high rate were observed to change from semi-insulating to semiconducting, a condition attributed to the conversion of iron to a non-active interstitial site when samples are quenched.[3] Samples for characterization by Hall-effect and IR absorption were slow cooled at 50°/hr.

Absorption measurements were made using a Digilab 80 E-V Vacuum Fourier transform spectrometer equipped with a cooled Ge:Cu photoconductor. This spectrometer has a nominal resolution of 0.125 cm^{-1}. Samples were measured in a continuous flow helium cryostat and measurements were made at 6.5K.

Results

Figure 1 shows an example of a spectra of the intracenter Fe^{2+} absorption measured for iron-doped InP both before and after annealing. Charged iron content for MLEK, LEC, and VGF as-grown samples were measured from the 2830 cm^{-1} and 2842 cm^{-1} peaks, then re-measured after the anneal. The reduction of these peaks corresponds to a decrease in the Fe^{2+} content of ~10^{15} cm^{-3}.

Reductions in Fe^{2+} measured from IR absorption are tabulated for as-grown and annealed InP:Fe samples in Table I. The table shows the measured decrease in charged iron content, ΔFe^{2+} following the anneal. For each sample type, a measured decrease from 2 X 10^{14} to ~2 X 10^{15} cm^{-3}

was measured, corresponding to a decrease in the donor concentration as outlined in Equation (1). For annealed samples, a lower decrease in the Fe^{2+} was measured for VGF as compared to MLEK samples, presumably from differences in the cooling rates between these two growth methods.

Simultaneous with the decrease in the measured compensation of the samples in Table I was a virtual annihilation of the hydrogen-related absorption peak at 2315 cm^{-1}. This is listed in Table I as ΔA for H-X concentration. Figure 2 shows before and after FTIR spectrum showing how the hydrogen peak disappears for annealed samples. Annealing is therefore accompanied by removal of this hydrogen donor from the samples.

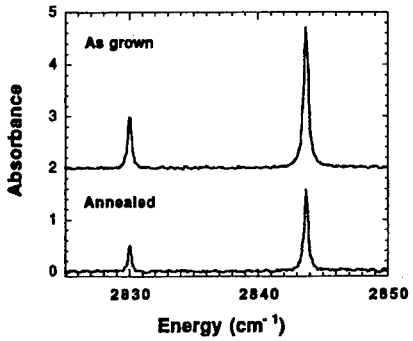


Figure 1. Infrared absorption measurements of MLEK-grown sample 4057, both before and after annealing. Peaks are intracenter Fe^{2+} absorptions.

As annealing Iron-doped material decreased the Fe^{2+} compensation, removal of the hydrogen donor by annealing was also observed to decrease the free carrier concentration for undoped samples. Table II illustrates changes in the carrier concentration for undoped samples as determined by Hall-effect. Measurements of mobility and carrier concentration were made at both 300K and 77K. As can be seen in Table II, for each sample, the 300K and 77K free carrier concentrations decreased by ~10^{15} cm^{-3} after annealing.

Like those for iron-doped material, the decrease in free carriers was accompanied by a decrease in the absorption of the hydrogen related donor, as determined by IR absorption measurements. These measurements are given as changes in the area, ΔA, in Table II.

Hall mobility was measured at 300K and at 77 K for undoped InP samples. While 300K Hall mobilities remained about the same following the anneal, measured liquid-nitrogen temperature mobilities were observed to increase for annealed samples, corresponding to a decrease in the shallow donor concentration. This is again an indication of a loss in the hydrogen-defect donor.

The above results, namely, a decrease in the Fe^{2+} compensating acceptor in iron-doped material, a decrease in the free carrier concentration for undoped material, and an increase in low-temperature electron mobilities, all point to a reduction in the shallow donor content of bulk InP. Iron-doped samples remained semi-insulating after annealing, proving little iron is lost in the anneal process. Furthermore, the annihilation of the hydrogen -defect absorption peak confirms that it is this defect that is removed from the material by annealing. Hydrogen is known to escape sealed quartz ampoules during high temperature processing.

Table I. Fe^{2+} and H-X concentrations for annealed InP:Fe. Samples 4057 and 4041 are MLEK-grown, while 45 was grown from the VGF technique.

Sample number	Sample type	d (cm)	Fe^{2+} (10^{15} cm^{-3})	ΔFe^{2+} (10^{15} cm^{-3})	ΔA H-X (a.u)
4057	as grown	0.31	3.29	-	-
4057	annealed	0.285	1.51	-1.78	-0.08
4041	as grown	0.493	3.33	-	-
4041	annealed	0.183	1.72	-1.61	-0.075
45	as grown	0.635	5.11	-	-
45	annealed	0.625	4.91	-0.2	-0.05

Recent calculations by Ewels et. al.[7] using an ab initio local density functional cluster code have confirmed the H-X complex to be a shallow donor. This confirms the measured decrease in the donor concentration as a reduction in the hydrogen-related defect concentration. Ewels also used the cluster code to further confirm the triplet vibrational mode for this donor as consistent with the 2316 cm^{-1} absorption line.

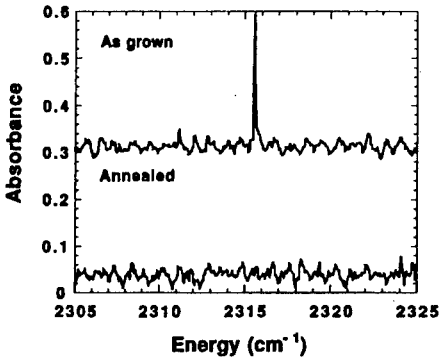


Fig. 2. FTIR spectra showing the virtual annihilation of the H-X LVM peak following a 900° C anneal.

Photorefractive Gain in Iron-Doped InP.

Photorefractive gain parameters were measured on various samples of iron-doped InP grown by the Magnetic Liquid Encapsulated Kyropolous technique at Rome Laboratory. The conventional method for describing the photorefractive effect is the one level-one band model that describes photorefractive gain from two-beam coupling.[8] Two incident beams of light form an interference pattern; a series of light and dark areas within the crystal. In the light areas, a charge is optically excited from a deep level to the band, where it drifts or diffuses to the dark areas. A space charge region is the result, which translates into a spatially varying electric field. The electric field creates a spatially variant refractive index grating via the linear Pockel's effect. The refractive index grating allows light from one transmitted beam to grow (gain) at the expense of the other.

The net carrier concentration can be roughly determined from screening length measurements of photorefractive gain. In photorefractive samples, screening lengths can be determined from the measurement of two-wave mixing gain as a function of grating spacing. This gain is a maximum at a grating spacing roughly equal to the Debye screening length. The value of the screening length is determined by the doping level of the material.

Gain vs. screening as been analyzed by Delaye et al[9]. Under no electric field, carrier motion

Table II. Measured Hall mobility and carrier concentration at 77K and 300K for as-grown and annealed samples. Samples 569 and 280 are LEC grown while 4066 and 4006 are MLEK.

Sample number	Sample type	ΔA H-X (a.u.)	n (300K) (10^{15} cm^{-3})	μ_n (300K) (cm^2/Vs)	n (77K) (10^{15} cm^{-3})	μ_n (77K) (cm^2/Vs)
569	as grown	-	2.7	2964	2.8	26500
569	Annealed	-0.05	1.3	3615	1.5	39900
280	as grown		4.7	3500		
280	annealed					
4066	as grown	-	5.4	4056	4.8	26500
4066	annealed	-0.05	3.1	4143	3.9	30000
4006	as grown	-	5.9	3270	5.5	21000
4006	annealed	-0.031	2.2	3170	2.0	20900

is solely by diffusion. The photorefractive gain can be modeled as

$$\frac{Ak}{\Gamma} = \frac{1}{\zeta}(1 + k^2 / k_o^2) \qquad (2)$$

were

$$A = \frac{2\pi k_B T n^3 r_{41}}{q\lambda \cos\theta} \qquad (3)$$

and

$$k_o = \frac{q^2}{\varepsilon k_B T} N_T \qquad (4)$$

n is the refractive index, r_{41} is the electro-optic (Pockel's) coefficient for InP, k is the grating wavevector, N_T is the Fe^{2+} concentration, and θ is the incident angle. A plot of Ak/Γ vs. k^2 will yield a value for k_O and the constant ζ. This, in turn, yields a value for N_T.

Gain was determined from two-beam coupling in the conventional manner. Two incident beams, $I_S(0)$ and $I_\Gamma(0)$, are brought together in a sample of thickness L.
With the reference beam I_Γ turned on, the transmitted signal intensity is given by

$$I_s(L,on) = I_s(0)e^{(\Gamma-\alpha)L} \qquad (5)$$

where Γ is the gain coefficient and α is the loss coefficient. With the reference beam off the transmitted signal is then

$$I_s(L,off) = I_s(0)e^{-\alpha L} \qquad (6)$$

Gamma can then be determined from measuring the ratio of $I_S(L,on)/I_S(L,off)$.

Figure 3 shows values of photorefractive gain measured for various grating spacing for various InP:Fe samples grown at Rome Laboratory. As the carriers have less distance to diffuse for shorter grating spacing, the gain first increases with decreasing spacing, until the spacing has decreased to ~0.7 micron. At this point the gain starts decreasing, due to increased screening of the net donors, as noted above. From this point the Fe^{2+} concentration can be determined.

Figure 4 shows Ak/Γ *vs.* k^2 for data from Fig. 3 as per Equation (2). Straight lines show

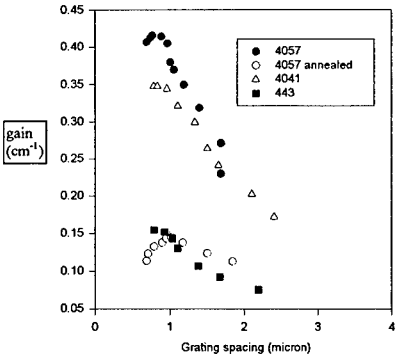


Fig. 3. Gain vs. grating spacing.

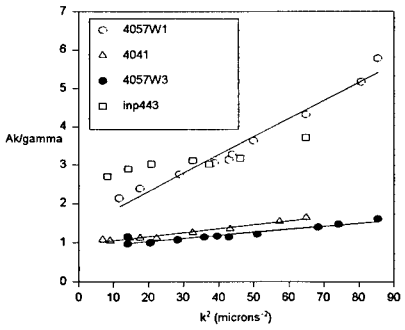


Fig. 4. Data from Fig 3 fit to Eq. (2)

Table III. Results of screening length measurements on InP:Fe.

Sample no.	Sample type	k_o^2 (μ^{-2})	$[Fe^{2+}]$ (cm^{-3})	ζ
4057	as grown	94	1.7×10^{15}	1.21
4057	annealed	49	8.6×10^{14}	1.15
4041	as grown	96	1.7×10^{15}	1.04
4041	annealed	172	3×10^{15}	0.63
443	as grown	91	1.6×10^{15}	0.45

agreement of the data to the model. Fe^{2+} concentrations measured from the slopes of Fig. 4 vary from a low of $5X10^{14}$ cm^{-3} for sample 4057 after a 900° C anneal, to 2×10^{15} cm^{-3}, which was a nominal value for un-annealed samples.

Table III shows values for the parameters k_o^2 and ζ of Eq. (2) as determined by the data of Fig 4, for various samples of Iron doped InP. Also included in the Table are Fe^{2+} concentrations determined from the values of k_o^2. Results for some samples include both before and after a 900° C anneal. Results are within a factor of 2 of concentrations measured by IR absorption.

Acknowledgment

This work was supported by the U.S. Air Force Office of Scientific Research.

[1] F. X. Zach, *J. Appl. Phys.* 75, 7894 (1994).

[2] G. Hirt, D. Wolf, and G. Müller, *J. Appl. Phys.* 74, 5538 (1993)

[3] .. Fornari, A. Brinciotti, E. Gombia, R. Mosca, A. Sentiri, *Mat. Sci. and Eng.* B28, 95 (1994).

[4] D. Wolf, G. Hirt, and G. Müller, *J. Electron. Mat.* 24, 93 (1995).

[5] F. X. Zach, E. E. Haller, D. Gabbe, G. Iseler, G. G. Bryant, and D. F. Bliss, *J. Electron. Mat.*, 25, 331 (1996)

[6] R. Darwich, B. Pajot, B. Rose, D. Robein, B. Theys, R. Rahbi, C. Porte, and F. Gendron, *Phys. Rev. B.* 48 17776 (1993).

[7] C. P. Ewels, S. Öberg, R. Jones, B. Pajot, P.R. Briddon, *Semicond. Sci. and Technol.*, 11, 502 (1996).

[8] P. Günter, J. -P. Huignard, Photorefractive Materials and Their Applications I, (Springer-Verlag, Berlin, 1988).

[9] P. Delaye, P.V. Halter, and G. Roosen, *Appl. Phys. Lett* 57 (4) 360 (1990).

EVIDENCE FOR NON-CORRELATION BETWEEN THE 0.15 eV AND 0.44 eV Cu-RELATED ACCEPTOR LEVELS IN GaAs

K. LEOSSON AND H.P. GISLASON
Science Institute, University of Iceland, Dunhagi 3, Reykjavik, Iceland

ABSTRACT

We present investigations on the two dominating acceptor levels observed in Cu-diffused GaAs which have frequently been attributed to the two ionization levels of a double Cu_{Ga} acceptor. We employed plasma hydrogenation and lithium diffusion followed by reverse-bias and zero-bias annealing to passivate and subsequently reactivate the Cu-related acceptor levels. Deep-level current-transient spectroscopy measurements reveal that the two levels are independently reactivated, strongly indicating that they arise from different defects.

INTRODUCTION

Copper is a fast interstitial diffuser in GaAs. It is present in virtually every processing environment and, therefore, is a commonly occurring contaminant in semiconductors. Despite extensive research there is still considerable controversy in the literature regarding the nature of copper in GaAs. Cu on Ga site is expected to act as a double acceptor. Charge compensation measurements by Hall and Racette[1] showed that for each Cu atom introduced into n-type GaAs, approximately two conduction electrons were lost, consistent with double-acceptor behavior. Other authors (see, e.g., Ref. 2) have correctly pointed out that double compensation can also occur through association with donors. Allison and Fuller[3] attributed acceptor levels around 0.15 eV and 0.44 eV above the valence band, observed in temperature-dependent Hall measurements, to the two ionization levels of Cu_{Ga}. Deep-level transient spectroscopy (DLTS) later confirmed the existence of these levels (see Ref. 4 and references therein), commonly referred to as Cu_A and Cu_B. The proximity of the Cu_A level to the valence band implies that the concentration of the associated defect cannot be measured accurately with DLTS. Simultaneous passivation of both levels has been observed in DLTS following hydrogenation[5] and Li-diffusion.[6] In both studies, the Cu-related levels reappeared when the passivating hydrogen or lithium was driven out by annealing the samples at elevated temperature. The simultaneous passivation of the two levels was taken as an indication that both levels belonged to the same defect, assuming that a single acceptor level around 0.44 eV, being in a neutral charge state at the diffusion temperature, would interact minimally with positively charged hydrogen or lithium. The present paper describes a detailed study of the two Cu-acceptor levels, their passivation by hydrogen and lithium and subsequent reactivation by thermal annealing at different temperatures. These investigations reveal a non-correlation between the two levels, effectively eliminating the possibility that they arise from the same defect.

Mat. Res. Soc. Symp. Proc. Vol. 442 © 1997 Materials Research Society

EXPERIMENT

The starting material used in this study was horizontal Bridgman nominally undoped n-type GaAs with an electron concentration of $n = 1.5 \times 10^{16}$ cm^{-3} at room temperature. Samples were converted to p-type through Cu diffusion at 650°C from an As-saturated Ga melt containing approximately 5% Cu by weight. The diffusion was performed in open ampoules under Ar flow. Subsequent Li diffusion was carried out at 400°C in a similar fashion using ≈0.2% Li metal in the melt. A Cu-diffused reference sample was treated in an equivalent manner but with no Li in the melt. The room temperature Hall hole concentration of the reference was $p = 2 \times 10^{16}$ cm^{-3} whereas the hole concentration of Li-passivated samples was around 7×10^{15} cm^{-3}. Cu-diffused samples were also hydrogenated from a remote hydrogen plasma for 3 hours at a sample temperature of 150°C, reducing the active acceptor concentration, as measured by capacitance-voltage profiling, by several orders of magnitude to a depth of approximately 2 μm.

Schottky diodes with a typical reverse breakdown voltage of 3–4 V were formed by evaporating 1-mm diameter Al dots on the sample surface. Ohmic contacts on the opposite side of the samples were created by welding Zn-coated gold wire directly to the surface. Charge density profiles were measured with conventional capacitance-voltage techniques using a 1 MHz capacitance bridge. Current-transient spectra were recorded using a double gate boxcar averager in conjunction with a current amplifier. Current-transient spectroscopy (CTS), introduced by Sah *et al.*,[7] has the advantage over conventional capacitance DLTS that it can be used to study shallower levels but quantitative relationships between signal intensity and defect concentration are more difficult to establish. Samples were cooled in liquid nitrogen or mounted on a high-temperature thermal stage in a Joule-Thompson cryostat cooled with nitrogen gas. Annealing from room temperature to 200°C was carried out in the cryostat under vacuum. Al dots were etched off the surface of samples subjected to zero-bias annealing at higher temperatures. The annealing was performed under Ar flow. New dots were evaporated on the surface after a brief etching of the annealed samples.

RESULTS

The CTS spectra presented here show peaks in the temperature range 100–300 K. Temperature-dependent Hall measurements revealed that no shallow acceptors were present in appreciable concentration in any of the samples. As a result, an artificial peak due to carrier freeze-out appeared in the spectra at 80-110 K. This peak was removed for clarity by fitting a Gaussian curve to the peak and subtracting the fit from the experimental data. Activation energies of defects responsible for each peak were determined by recording CTS spectra with different time windows. The analysis is limited to short time windows since the CTS peak height decreases rapidly for longer time windows. No other peaks were observed in CTS spectra up to 400 K.

Figure 1a shows CTS spectra in Cu-diffused GaAs. The two commonly occurring Cu-related hole traps, Cu_A and Cu_B with activation energies 0.15 eV and 0.44 eV, respectively, are clearly observed. It should be emphasized that the difference in peak height does not necessarily imply a difference in the concentration of the two defects. The effects of Li-diffusion and plasma hydrogenation are also shown in the figure. In Li-diffused material, the Cu_B level is partially passivated whereas the Cu_A peak disappears completely. A new level at 0.12 eV appears. The intensity of this peak is lower in more heavily passivated samples.

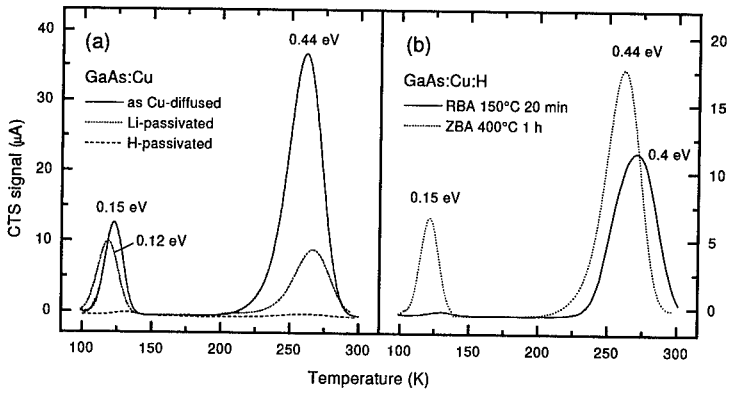


Figure 1: (a) Hole traps in Cu-diffused GaAs, measured by current-transient spectroscopy, showing the effect of passivation by hydrogen and lithium. Activation energies of the observed peaks are indicated. (b) Effects of annealing on the CTS spectrum of hydrogenated GaAs:Cu. The high-temperature peak is reactivated after annealing with bias at 150°C and both peaks reappear after zero-bias annealing at 400°C. Annealing times are given in the figure. All curves were recorded using a reverse bias of 0.3 V, pulse height of 0.3 V and pulse length of 100 μs. The time window was 0.207 ms.

As previously established,[5] Cu_A and Cu_B are effectively removed from the bandgap after hydrogenation. Only very weak signals corresponding to the original peaks are observed.

The hydrogenated sample of Fig. 1a was annealed with and without bias at different temperatures. Reverse-bias or zero-bias annealing in the temperature range used in this study has no significant effects on the as-Cu-diffused material. The effect of annealing on a hydrogenated sample is shown in Fig. 1b. Reverse-bias annealing below 100°C does not significantly alter the spectrum. After annealing with bias at higher temperatures a peak appears which exhibits an activation energy of 0.4 eV. The anomalous shift in the peak position is an artifact of the measurement since no acceptor levels shallower than 0.4 eV are present in appreciable concentration in the near-surface region of the sample. We also attribute the change in energy to experimental uncertainty and assume that the reactivated peak corresponds to Cu_B. This assumption is supported by measurements on Li-passivated material described below. There is no measurable change in the weak 0.15 eV signal after the heat treatment. Zero-bias annealing at 200°C sufficed to passivate the reactivated 0.4 eV level, restoring the CTS spectrum to that of the H passivated sample in Fig. 1a. Fig. 1b indicates that both Cu-related peaks reappear after zero-bias annealing at 400°C as previously shown by Hofmann *et al.*[5] and capacitance-voltage charge density profiles confirmed that this heat treatment effectively restored the original (as Cu-diffused) active acceptor concentration in the near-surface region of the sample.

Similar behavior is observed in Li-passivated samples as indicated in Fig. 2. The CTS spectra of partially passivated material were normalized with respect to the total charge density in the near-surface region as measured by capacitance-voltage profiling at room

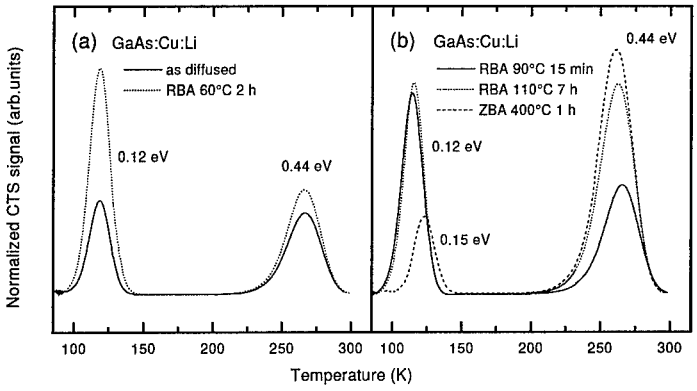


Figure 2: (a) Cu-diffused GaAs partially passivated by Li before and after reverse-bias annealing at 60°C for 2 hours. (b) Effect of reverse-bias and zero-bias annealing at higher temperature on Li-passivated GaAs:Cu. Annealing times and temperatures are indicated in the figure. Measurement parameters are identical to those given in Fig. 1.

temperature. The behavior of Schottky junctions with a high deep-level concentration was simulated numerically to confirm that variations in peak height of the spectra after normalization more accurately represent the corresponding changes in trap density. Such normalization was not attempted for hydrogenated material since the charge density varies rapidly within the depletion region.

Fig. 2a shows the effect of reverse-bias annealing below 100°C on the partially Li-passivated sample of Fig. 1a. The intensity of the 0.12 eV peak increases significantly. The slight increase in the Cu_B peak height is a product of the normalization procedure; in the as-recorded spectrum the peak height decreases slightly. The original 0.12 eV peak height is restored by zero-bias annealing at 100°C. As shown in Fig. 2b, reverse-bias annealing above 100°C does not increase further the intensity of the 0.12 eV level. However, the Cu_B peak height increases sharply. The rate of this reactivation at a given temperature in the range 100-150°C corresponds closely to the corresponding reactivation rate of the 0.4 eV level in hydrogenated material, supporting the assumption that the latter also represents the Cu_B level. No peak corresponding to the Cu_A level at 0.15 eV is observed. As before, zero-bias annealing at 200°C was sufficient to restore initial conditions in the sample, represented by the CTS spectrum of the Li-passivated sample in Fig. 1a. The deep-level spectrum of the as-Cu-diffused material is fully recovered after Li has been driven out of the sample by zero-bias annealing at 400°C as indicated in Fig. 2b and by Egilsson *et al.*[6]

CONCLUSIONS

The results presented in Figs. 1 and 2 are summarized in Fig. 3. It is clear that Cu_A and Cu_B are affected by Li diffusion and hydrogenation. Furthermore, both levels reappear after zero-bias annealing at 400°C. These facts have been previously established.[5,6] However, it is clear that reverse-bias annealing at intermediate temperatures suffices to reactivate the Cu_B

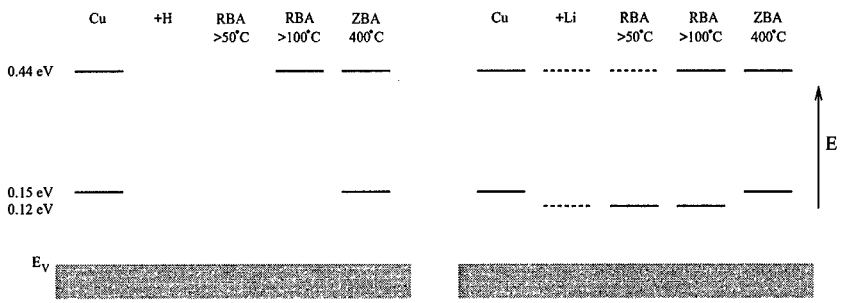


Figure 3: Results of previous figures summarized on an energy band diagram. Solid lines indicate energy levels corresponding to peaks observed in the CTS spectra. Dashed lines indicate partially passivated levels. If no line is shown the level has effectively been removed from the bandgap. The reactivation of Cu_B after reverse-bias annealing in the range 100–150°C is not accompanied by the appearance of Cu_A. Zero-bias annealing at 400°C drives out the passivating species and restores initial (as Cu-diffused) conditions in the samples.

level with no corresponding signal from the Cu_A level. Detailed numerical simulations were carried out to confirm that the appearance of a peak in the CTS spectrum corresponding to one ionization level of a double acceptor must always be accompanied by the appearance of a peak corresponding to the other ionization level. We conclude that no experimental artifact or anomalous behavior of junctions with a high concentration of deep levels can be held responsible for the non-observance of the Cu_A level. Hence, the Cu_A and Cu_B levels must arise from different defects which are passivated by hydrogen and lithium but may be independently reactivated. The assumption made in the previous passivation studies,[5,6] that defects in the neutral charge state interact minimally with the passivating species must therefore be in error. Indeed, passivation of neutral native electron traps in GaAs by both hydrogen[8–10] and lithium[11] has been reported in the literature.

Non-correlation of the Cu_A and Cu_B levels has been previously suggested in the literature. Kullendorff *et al.*[2] pointed out a striking agreement on an absolute energy scale between the positions of the Cu_A and Cu_B levels in GaAs and two Cu-related acceptor levels in each of the III-V semiconductors InP and GaP. In InP the shallower level is far enough from the valence band to be easily measured by DLTS and the concentrations of the two Cu-related levels are found to be independent of each other. Roush *et al.*[12] used different concentrations of Cu_A and Cu_B to account for compensation of shallow donors in GaAs. On the basis of optical studies, Cu_A and Cu_B have been assigned to various defects and defect complexes but there is little agreement between these assignments aside from the fact that they frequently involve As vacancies (see Ref. 2 and references therein).

In summary, we have observed that the Cu_B level in GaAs is passivated in the presence of hydrogen or lithium and may be reactivated by annealing with bias above 100°C. The thermal stability of the passivation is comparable for both passivating species. The Cu_A level is similarly passivated by the introduction of H or Li but cannot be reactivated within a reasonable time with annealing below 200°C. The Cu_A level is recovered, however, when the passivating species is driven from the samples at 400°C. A new level appears in partially

Li-passivated material which can be passivated by further addition of Li. Although no concrete assignments can be made on the basis of the present work we propose that the 0.12 eV level is due to an electrically active complex involving Li and possibly Cu_A. The complex is converted into a passive complex through the addition of Li. We assume that positively charged Li is driven from the surface toward the bulk of the sample during reverse-bias annealing, as indicated earlier,[13] reducing the Li concentration in the near-surface region where the CTS spectrum is recorded.

We consider the present data to be the most direct evidence available for the non-correlation of the Cu_A and Cu_B levels in GaAs. The possibility that Cu_A is related to a Cu_{Ga} double acceptor, as suggested in the literature,[14] is by no means precluded but we have demonstrated that the Cu_A and Cu_B levels do not correspond to the two ionization levels of a double Cu-acceptor as has frequently been claimed.

ACKNOWLEDGMENTS

This work was partially supported by the University of Iceland Research Fund and the Icelandic Research Council. The authors wish to thank Dr. B.H. Yang for carrying out the diffusions and Dr. E. Sveinbjörnsson at the Max Planck Institute, Stuttgart, for performing the plasma hydrogenation.

REFERENCES

[1] R.N. Hall and J.H. Racette, J. Appl. Phys. **35**, 379 (1963)

[2] N. Kullendorff, L. Jansson, L-Å. Ledebo, J. Appl. Phys. **54**, 3203 (1983)

[3] H.W. Allison, C.S. Fuller, J. Appl. Phys. **36**, 2519 (1965)

[4] A.G. Milnes, Advances in Electronics and Electron Physics **61**, 63 (1983)

[5] G. Hofmann, J. Madok, N.M. Haegel, G. Roos, N.M. Johnson, E.E. Haller, Appl. Phys. Lett. **61**, 2914 (1992)

[6] T. Egilsson, H.P. Gislason, and B.H. Yang, Phys. Rev. B, **50** 1996 (1994)

[7] C.T. Sah, L. Forbes, L.I. Rosier, H.F. Tasch, Jr., Solid-State Electron. **13**, 759 (1970)

[8] S.J. Pearton, J. Appl. Phys. **53**, 4509 (1982)

[9] J. Lagowski, M. Kaminska, J.M. Parsey, Jr., H.C. Gatos, M. Lichtensteiger, Appl. Phys. Lett. **41**, 1078 (1982)

[10] W.C. Dautremont-Smith, J.C. Nabity, V. Swaminathan, M. Stavola, J. Chevallier, C.W. Tu, S.J. Pearton, Appl. Phys. Lett. **49**, 1098 (1986)

[11] T. Egilsson, B.H. Yang, H.P. Gislason, Physica Scripta **T54**, 28 (1994)

[12] R.A. Roush, D.C. Stoudt, M.S. Mazzola, Appl. Phys. Lett. **62**, 2670 (1993)

[13] H.P. Gislason, T. Egilsson, K. Leosson, B.H. Yang, Phys. Rev. B, **51**, 9677 (1995)

[14] E. Janzén, M. Linnarsson, B. Monemar, M. Kleverman, Mat. Res. Soc. Sym. Proc. **163**, 169 (1990)

EFFECT OF THE CARBON ACCEPTOR CONCENTRATION ON THE PHOTOQUENCHING AND ENHANCEMENT OF THE PIEZOELECTRIC PHOTOACOUSTIC SIGNALS OF SEMI-INSULATING GaAs

A. Fukuyama*, Y. Morooka**, Y. Akashi*, K. Yoshino** K. Maeda**, and T. Ikari**
* Department of Materials Science, Miyazaki University and
** Department of Electrical and Electronic Engineering, Miyazaki University
1-1 Gakuen-kibanadai, Miyazaki 889-21, Japan

ABSTRACT

The spectral and the time dependent piezoelectric photoacoustic (PPA) measurements under the continuous light illumination were carried out at 85 K to investigate nonradiative recombination processes involving EL2 defect levels in carbon doped semi-insulating (SI) GaAs. The decrease of the PPA signal due to the photoquenching effect of EL2 was observed for a short period of illumination of 1.12 eV. It was found that the photoquenching becomes drastic with increasing the carbon concentration. After fully photoquenching, the PPA signal increased again through a local minimum by the continuous light illumination and finally exceeded the initial value before illumination until the saturation level was reached. The deep donor level EL6 and its metastable state are proposed. EL6 level donates electrons to compensate a part of carbon acceptors after photoquenching. The nonradiative recombination through this level generates the PPA signal. The usefulness of the PPA technique for studying the nonradiative transition through deep levels in semiconductor is suggested.

INTRODUCTION

Deep lying defect level EL2 is known to be a dominant donor to accomplish a semi-insulating nature of GaAs substrate for LSI applications. Since EL2 also transforms to its metastable state by a secondary light illumination at low temperature, so-called photoquenching effect, its electronic structure has been extensively studied. In recent years, Mitchel and Jimenez [1] reported an additional feature of the photoconductivity of LEC grown GaAs at 77 K. The photocurrent first decreases due to the photoquenching effect of EL2 as in the case of the optical absorption measurements. However, the photocurrent shows a very strong enhancement (EPC) upon a prolonged illumination with photon energy in the range from 1.0 to 1.25 eV. However, EPC observed in the photoconductivity (PC) measurements have never been confirmed by other experiments. Although there still remain some inconsistencies in their argument, they concluded that EPC was attributed to EL6 level which is ubiquitous in bulk GaAs.

Piezoelectric photoacoustic (PPA) spectroscopy has recently been used in investigating physical properties of semiconductors. The great advantages of the PPA spectroscopy are that (i) it is a direct monitor of the nonradiative recombination processes and (ii) it is sensitive to a very small optical absorption coefficient in a highly transparent sample. The presence of these two great advantages indicates that the PPA spectroscopy should be a very useful tool for investigating deep levels in GaAs such as EL2 and EL6. The preliminary results on the PPA spectra of LEC grown SI GaAs were already reported in our previous paper and the electron transition involving EL2 could be resolved [2, 3].

In this paper, we report for the first time on the study of the photoquenching and additional enhancement effects from a nonradiative recombination point of view. The spectral and the time dependent PPA measurements were carried out at 85 K in carbon concentration controlled SI GaAs. The decrease of the PPA signal by the 1.12 eV secondary light illumination for a short period is interpreted by the photoquenching effect of EL2. We found that the photoquenching effect becomes drastic with increasing the carbon concentration. The actuator model proposed by Suemitsu *et al.* [4] and the EL6 model by Mitchel and Jimenez [1] for PC measurements will be discussed by comparing with the present experimental results. We will then conclude that the metastable state of EL6, which appears after photoquenching, play an important role in the generation mechanisms of the enhancement of the PPA signal.

Mat. Res. Soc. Symp. Proc. Vol. 442 © 1997 Materials Research Society

EXPERIMENTAL PROCEDURES AND RESULTS

The samples were prepared from carbon concentration controlled SI GaAs wafers grown by the liquid encapsulated Czochralski (LEC) method. Table.1 summarizes the details of the samples. Since these wafers utilizing in the present study were thermally treated by three-stage annealing method [5], a minimum amount of irrelevant intrinsic defects is expected. The detailed experimental setups have been reported previously [6].

Sample No.	carbon ($10^{15}cm^{-3}$)	[EL2] ($10^{16}cm^{-3}$)	Resistivity ($10^{7}\Omega cm$)
#1	11.0	1.2-1.4	23-24
#2	4.0	1.2-1.4	9.2-10.9
#3	1.3	1.2-1.4	2.6-2.9

Table. 1 Specifications of SI-GaAs samples

The PPA spectrum at 85 K is shown in Fig.1 by the solid curve. The PPA spectrum consists of a broad band up to the band gap energy. This structure agrees well with our previous reports [2, 3] which have concluded that the PPA signals below band gap are caused by the electron nonradiative transitions involving EL2. Figure 1 also shows an effect of the secondary light illumination on the PPA spectrum. The PPA spectrum after the secondary light of 1.12 eV illumination for 3 minutes is shown by the broken curve. The PPA signal decreases by the secondary light illumination. This feature was observed for all the samples measured in the present study. We hereafter refer the states before and after the secondary light illumination of 3 minutes to the normal and the quenched states, respectively. The quenched state is quite stable unless the temperature of the sample increases above 130 K. The PPA signal shows the normal state after heating the sample above 130 K and subsequent cooling down to 85 K. This means that thermal recovery from the quenched to the normal states occurs around this temperature.

Since the PPA signal intensity is proportional to the absorption coefficient [2] and to the total EL2 concentration [7], we here define the quenching rate Q as

$$Q = 100 \times (I_N - I_Q) / I_N \quad (\%), \qquad (1)$$

where I_N and I_Q are the PPA signal intensities at 1.12 eV before and after the secondary light illumination for 3 minutes, respectively. The quenched state is most emphatically created when the secondary light is set in the photon energy at 1.12 eV. The Q as a function of the carbon concentration is plotted in Fig.2. The figure indicates a clear positive correlation between the carbon concentration and the Q.

The time dependent PPA signal was obtained as follows. After the sample was cooled in the dark to 85 K, the PPA signal intensity was recorded as a function of illumination time. The probe and the secondary lights were set at the photon energy of 1.12 eV. The result for the sample #1 is shown in Fig.3. All the data are normalized by the initial value at zero minute (I_0) without any secondary light illumination. A curve exhibits a complex feature specified by three states as labeled in Fig.3. Decrease of the signal intensity was observed for a short period to 3 minutes. This state corresponds to the quenched state. Next, the PPA signal increases through the local minimum and exceeds an initial value before the light illumination. Finally, the PPA signal further increases to a saturation level for more than 15 minutes. We refer the saturation level (above 15 minutes) to the enhanced state. We observed a same complex feature for all the samples. The enhanced state is observed when the secondary light is set in the photon energy ranging from 1 to 1.2 eV. If the temperature of the sample is kept at 85 K, the enhanced state is quite stable.

The PPA spectrum at the enhanced state was shown in Fig.1 by the dotted curve. The PPA spectrum shows a broad band around 0.9eV. Therefore, we here define the signal intensity at 0.9eV as the I_E to investigate carbon concentration dependence of the enhanced state. No clear

correlation between the carbon concentration and the I_E was observed as shown in Fig.4.

DISCUSSIONS

From the above experimental results, we can consider that there are two different photo-induced states for LEC grown SI GaAs samples. One is the quenched state generated after a short period illumination. The other is the enhanced state generated after a long period illumination. We will then discuss two photogenerated states separately.

The quenched state

The decrease of the signal intensity and the thermal stability of the quenched state in the present study are in good agreement with those of the photoquenching effect of EL2 in the optical absorption measurements [7]. Therefore, we concluded that the observed decrease of the PPA signal by the secondary light illumination at 85 K is due to so-called photoquenching of EL2 levels ($EL2^0$ to EL2* transition). Since EL2* is optically inactive, the photoquenching decreases a number of electrons excited from the valence band (VB) to $EL2^+$ and from $EL2^0$ to the conduction band (CB). This results in a decrease of the PPA signal intensity. When the quenched sample is heated above 130 K, thermal recovery from EL2* to $EL2^0$ occurs. The PPA signal then turns back to the value in the normal state at 85 K.

Once the photoquenching of EL2 is fully accomplished, the final amount of the photoquenching

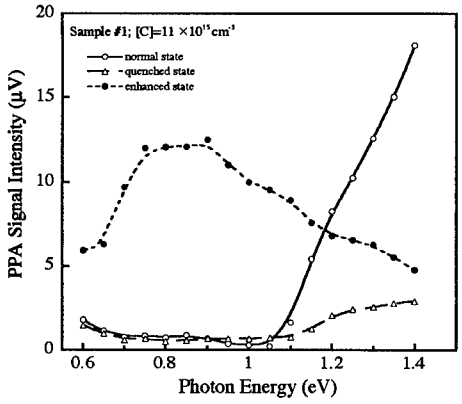


Fig.1 The PPA spectrum at 85K(solid curve). The PPA spectra after the secondary light illumination for 3 and 15 minutes are also shown by the broken and the dotted curves, respectively.

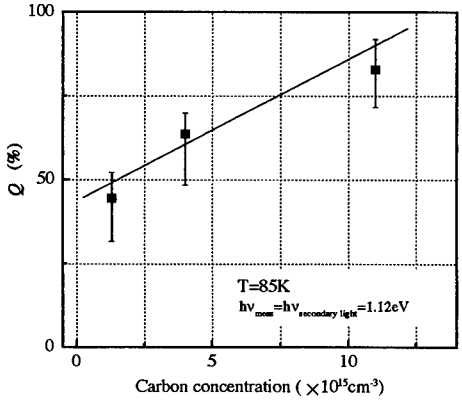


Fig.2 Carbon concentration dependence of Q

should be the same because the total EL2 concentration did not change from sample to sample. However, the Q increases with increasing the carbon concentration as shown in Fig.2. This result cannot be explained by simply supposing that the decrease of the PPA signal is due to the transformation between $EL2^0$ and EL2*.

In recent years, similar correlation between the carbon concentration and the photoquenching rate has been reported using near-infrared optical absorption measurements by Suemitsu *et al.* [4]. They supposed that an actuator level (AL), which was firstly proposed by Jimenez *et al.* [8], acts as a trigger of the onset of EL2 photoquenching. According to their model, the increase of the

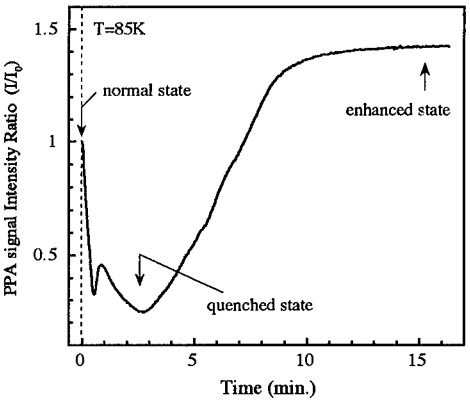


Fig.3 The time dependence of the PPA signal under a continuous secondary light illumination with photon energy of 1.12eV.

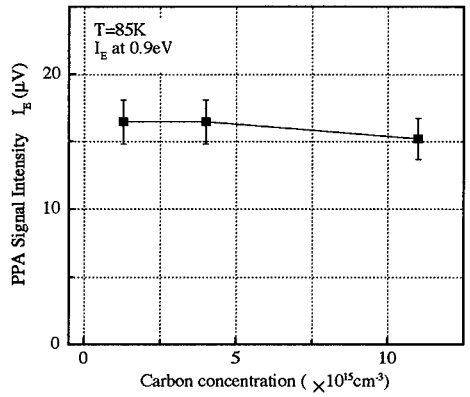


Fig.4 Carbon concentration dependence of the PPA signal intensity of the enhanced state at 0.9eV.

photoquenching rate with increasing the carbon concentration is well explained. Since the PPA signal intensity is proportional to the absorption coefficient in this photon energy region [2], the AL model may interpret the correlation between the carbon concentration and the Q in the present study. However, there still remain a difficulty. The proposed AL model requires that the AL has large concentration in the same order of EL2 levels. Since we used the carefully controlled samples which were thermally treated with three-stage annealing method [5], large amount of intrinsic defects rather than EL2 are not expected. Further experiments are now in progress.

The enhanced state

Since the EL2* state is known to be optically inactive [7], the electronic level involved in the enhanced state does not directly correspond to the EL2*. We first attempt to apply the AL model

to explain the enhancement effect of the PPA signal. However, it is not likely because the activation energy of the AL is small (70-80 meV) compared with the peak energy of the enhanced PPA spectrum. The AL model also cannot explain the time lag between the photoquenching and the activation of the enhanced state shown in Fig.3.

The observed features of the enhanced state in the PPA measurements are very similar to that observed in the PC measurements [1]. Although the signal generation mechanisms are different among the two experiments, the level involved in the enhanced state of the PPA signal may strongly correlate to that of EPC. Mitchel and Jimenez [1] concluded that EPC was generated by the charge transfer including EL6 level which is ubiquitous in bulk GaAs. Although the chemical nature of EL6 is as yet unknown, this level is identified as a deep donor at 0.35 eV below CB. Its concentration is as high as 10^{15} cm^{-3} in LEC grown SI GaAs [1] and its electron photoionization spectrum has been reported to be similar to that of EL2 in the 0.7-1.5 eV spectral range [9]. These features indicate that EL6 plays an important role on the PPA signal generation mechanism at the enhanced state as in the case for PC measurements. It is noted here that the PPA signal is generated by the nonradiative recombination of photoexcited electrons. Therefore, there should be an optical generation and following recombination of electrons in the enhanced state. It is then reasonable to consider that EL6 level is involved in the photoexcitation of electrons by the 1.12 eV light and following nonradiative recombination processes when the sample is in the enhanced state.

Photo-Hall measurements [1] showed that the carrier type of EPC state is hole, and also implies that the carbon acceptors should be compensated even after photoquenching. We then considered that EL6 donates electrons to compensate carbon acceptors. Since the concentration of EL6 is lower than that of carbon acceptors, all of EL6 are positively ionized. Electrons in VB and/or in the compensated carbon acceptors can be photoexcited to the positively ionized $EL6^+$ by the secondary light of 1.12 eV illumination, and these photoexcited electrons can recombine with holes. This recombination should be nonradiatively detected as the PPA signal at the enhanced state. However, there still remain a difficulty because that the DLOS study reported the absence of any optical refilling of $EL6^+$ from VB due to the very large Franck-Condon shift of 0.6 eV [9]. Therefore, it is not likely that electrons are photoexcited from VB and/or compensated carbon acceptors to the positively ionized $EL6^+$ and cause the PPA signal in the enhanced state.

It should be noted that the enhanced state cannot be achieved without undergoing the photoquenching. This implies a metastability of the level involved in the enhanced state. The slow activation of the enhanced state after fully photoquenching of EL2 as shown in Fig.3 is also manifestation of a metastable transition. The metastable behavior associated with EL6 level is then proposed to explain our present experimental results in more detail. We consider that $EL6^+$ transforms to optically active metastable state, say $EL6^m$, by the continuous light illumination after the fully photoquenching of EL2. If this metastable transition only occurs when EL6 is in the neutral charge state $EL6^0$, $EL6^+$ needs neutralizing by capturing an electron photoexcited from VB. However, as discussed above, there is no optical refilling of $EL6^+$ from VB [9]. Since all of EL6 are positively ionized when the sample is in the quenched state, we can consider that metastable transition occur when EL6 is positively ionized. Nonradiative recombination of electrons photoexcited from VB and/or from compensated carbon acceptor to $EL6^m$ causes the PPA signal at the enhanced state. Once the enhanced state has been established, the PPA signal intensity does not depend on the carbon concentration but on the total EL6 concentration. Therefore, I_E did not change with the carbon concentration as shown in Fig.4.

In the present model, electrons should be photoexcited to $EL6^m$ in the enhanced state. This should lead to an optical absorption. However, no signal due to EL6 could be observed in the optical absorption measurements. This may be understood to consider that the sensitivity for the defect levels of low concentration is higher for PPA than the usual optical absorption measurement. Since the concentration of EL6 is lower than that of EL2, the PPA signal intensities of the enhanced state should be small compared with the normal state. However, the observed results can reasonably be interpreted by considering that nonradiative recombination probability of electrons in the enhanced state ($EL6^m$) is larger than that of the normal state (EL2). The intensity of the PPA signal becomes larger even when the concentration of EL6 is lower than that of EL2. This is consistent with the fact that EL6 has a very larger Frank-Condon shift value at 0.6 eV than that of EL2 at 0.12 eV [9]. This is because that there is no report on the PL measurement concerning the level which causes the enhanced state observed in the PPA and PC measurements. Most of all recombination

processes of these photoexcited electrons may occur nonradiatively.

CONCLUSIONS

We have observed two kinds of photo-induced states of the PPA signal in SI GaAs samples after the secondary light illumination at 85 K. One is the quenched state generated by a short period illumination and other is the enhanced state attained by a prolonged illumination. Both two states are effectively generated in the similar photon energy region from 1 to 1.2 eV. We found that when the sample has large carbon concentration, the photoquenching is more effective. The actuator model proposed by Suemitsu *et al.* [4] can partly interpret our experimental results. The presence of deep donor EL6 and its metastable state $EL6^{m}$ are proposed to explain the enhanced state. After fully photoquenching, positively ionized $EL6^{+}$ can transform to metastable $EL6^{m}$ by the continuous light illumination. The nonradiative recombination through this level is considered to generate the PPA signal. The hole photoionization spectrum concerning EL6 defect level is observed for the first time in the present study.

Since the PPA measurement could detect lower concentration of the deep level than optical absorption measurements, the usefulness of the PPA measurements for studying the deep levels in semiconductor was suggested. The enhancement of the photosensitivity by the continuous light illumination is observed from a nonradiative recombination point of view for the first time.

ACKNOWLEDGEMENTS

We acknowledge to Hitachi Cable Co., Ltd. for supplying the GaAs wafers and to Komatsu Electronic Metals Co., Ltd. and Miyazaki Oki Electric Co., Ltd. for the financial support.

REFERENCES

[1] W. C. Mitchel and J. Jimenez: J. Appl. Phys. **75**, 3060 (1994)

[2] A. Fukuyama, T. Ikari, K. Miyazaki, K. Maeda and K. Futagami: Jpn. J. Appl. Phys. **31**, Suppl.31-1 pp.20-22 (1992)

[3] A. Fukuyama, T. Ikari, K. Maeda and K. Futagami: Jpn. J. Appl. Phys. **32**, 2567 (1993)

[4] M. Suemitsu, H. Takahashi and N. Miyamoto: Phys. Rev. **B52**, 1666 (1995)

[5] Y. Otoki, M. Nakamori, R. Nakazono, and S. kuma, in *Proceedings of the Fourth Conference on Semi-Insulating III - V Materials*, edited by H. Kukimoto and S. Miyazawa (Ohm-sha, Tokyo, 1986)

[6] T. Ikari, S. Shigetomi, Y. Koga, H. Nishimura, H. Yayama and A. Tomokiyo: Phys. Rev. **B37**, 886 (1988)

[7] D. W. Fischer: Appl. Phys. Lett. **50**, 1751 (1987)

[8] J. Jimenez, A. Alvarez, M. Chafai, Luis F. Sanz, and J. Bonnafe: J. Appl. Phys. **73**, 2871 (1993)

[9] A. Chantre, G. Vincent and D. Bois: Phys. Rev. **B23**, 5335 (1981)

LONG-LIVING SHALLOW DONOR EXCITED STATES AND FIR-IR UP-CONVERSION IN GaP:Te

S. D. GANICHEV*,**, I. N. YASSIEVICH**, W. RAAB*, E. ZEPEZAUER*, and W. PRETTL*

*Institut für Experimentelle und Angewandte Physik, Universität Regensburg, 93040 Regensburg, Germany

**A.F. Ioffe Physicotechnical Institute, Russian Academy of Sciences, St. Petersburg, 194021, Russia

ABSTRACT

Tellurium donors in GaP have been ionized by phonon assisted tunneling in the electric field of pulsed far-infrared laser radiation. In response to the laser pulse a photoconductive signal has been detected with a fast component reproducing the laser pulse and a slow component which rises after the irradiation has ceased and finally exponentially decays with a strongly temperature dependent time constant in the range of microseconds to several milliseconds. This temporal structure of the signal is explained by a cascade capture mechanism and subsequent accumulation of carriers in a long-living shallow donor excited state, identified as valley-orbit split $1s(E)$ level of Te. The final step of recombination is achieved by radiative transitions, which is proved by the observation of far-infrared to mid-infrared up-conversion.

EXPERIMENTAL SETUP AND RESULTS

The samples used were GaP highly doped with Te with a density of 3 and $7\cdot 10^{17}$ cm^{-3}. The resistance of the samples depends on the temperature as $\exp(-\Delta\varepsilon/k_BT)$ with activation energy $\Delta\varepsilon$ about the half of the binding energy which shows that the compensation in the material is very low. The density of ionized impurities, Te^+, is estimated to be less than $5\cdot 10^{16}$ cm^{-3} at T below 150 K.

Measurements have been carried out in a temperature variable optical cryostat in the temperature range between 20 K and 150 K where in thermal equilibrium most of charge carriers are bound to the impurity ground states. The radiation source was a high power pulsed far-infrared molecular laser optically pumped by a TEA CO_2 laser. Using NH_3 as active laser gas, 40 ns pulses with a peak power of 50 kW have been obtained at wavelengths, λ, of 76, 90.5, 148, and 280 μm. The photon energies corresponding to these wavelengths are much smaller than the Te binding energy of 90 meV. In this case ionization is obtained by phonon assisted tunneling in the electric field of the FIR-radiation [1].

The ionization of impurities due to the irradiation has been measured by the standard method of detecting photoconductivity using a 50 Ω load resistor circuit (see inset of Fig. 2). The bias voltage across the sample was about 5 V/cm and therefore substantially below the threshold of electric breakdown.

The conductivity of the samples is increased by irradiation with far-infrared pulses. In Figs. 1 and 2 typical pulse shapes are shown for different time scales. Fig. 1 shows the response of a sample on a short time scale and a laser pulse recorded with a linear photon drag detector. During the irradiation the response rises and falls following to the excitation laser pulse, with characteristic times less than 10 ns. After the radiation ceased the signal

Mat. Res. Soc. Symp. Proc. Vol. 442 © 1997 Materials Research Society

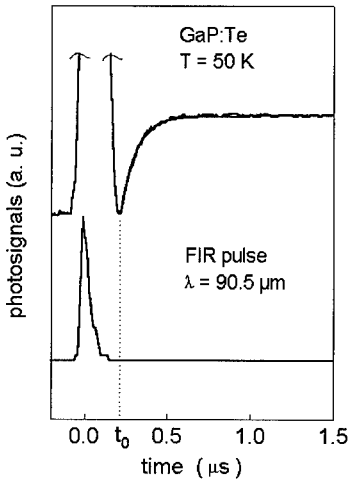


Figure 1: Upper curve: Typical photoconductivity signal of GaP:Te at T=50 K on a short time scale showing the rise after the irradiation has ceased. The smooth line for $t > t_0$ is calculated after Eq. (3). Lower curve: Exciting laser pulse of $\lambda = 90.5\mu$m detected by a linear detector.

increases again, assumes a maximum after about 1 μs and then decreases exponentially (Fig. 2). The rise can be fitted very well by the function $a \cdot (1 - \exp((t - t_0)/\tau_r))$ with a characteristic time τ_r of about 10^{-7} s. The characteristic time τ of the slow exponential decay (Fig. 2) increases by almost three orders of magnitude with falling temperature from 150 K (6 μs) to 35 K (3 ms). Fig. 3 shows $1/\tau$ as a function of the inverse temperature, fitted in first approximation by the exponential function $1/\tau = 1/\tau_0 \cdot (\exp(-\Delta\varepsilon/kT)$ with $\Delta\varepsilon = 28$ meV. The decay time τ is independent of intensity and of frequency of the radiation.

In addition, up-conversion of FIR radiation into mid-IR radiation has been observed. A bulk GaP:Te sample has been placed in front of a fast Ge:Cu extrinsic infrared detector sensitive to radiation of wavelengths less than 30 μm ($\hbar\omega$ >40 meV). A 2 mm thick KRS-5 slab has been used as a cut-off filter for wavelengths longer than 50 μm to block the exciting laser beam. Irradiation by high-power FIR radiation in the wavelength range of 76-280 μm generates a luminescence signal, detected in the temperature range between 20 K and 100 K. This signal is independent of the exciting wavelength.

DISCUSSION

Heating of the free electron gas or the whole sample can be ruled out as dominant mechanism for the observed signal. Above about 70 K the mobility of electrons in GaP decreases with rising temperature [2, 3], causing a decrease of conductivity. This is in contrast to the experimental results. Furthermore heating of the sample as a whole cannot lead to the observed particular time dependence of the slow signal.

The fast component of the signal is due to ionization and rapid capture in excited Coulombic states of Te [4]. But there is still to find a self-consistent explanation of the slow component's temporal structure:

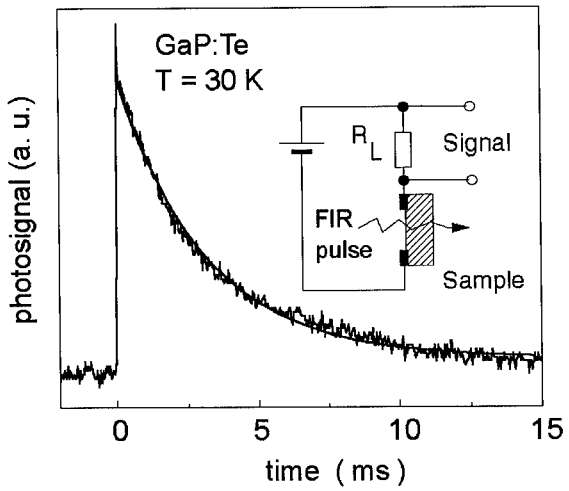


Figure 2: Typical photoconductivity signal of GaP:Te at T=30 K on a long time scale showing the slow exponential decay. The smooth curve is calculated after Eq. (3). Inset: Scheme of the experimental setup.

Additional deep impurities like oxygen with very small capture cross sections of about 10^{-22} cm^2 [5,6] can be excluded. To obtain the observed long decay time there should be an oxygen density of $5 \cdot 10^{17}$ cm^{-3} which contradicts the low compensation of the investigated material.

We will show that the whole kinetic of the signal can be described in the frame of the following model: free carriers are rapidly captured by highly excited impurity center states and subsequently cascade down to the ground state. We introduce an additional long-living-state with a vanishingly small recombination probability to the ground state. This state stores carriers and re-injects them slowly by thermal activation into the densely lying Coulombic states close to the band edge. Therefore the concentration of carriers in the band is increased by an up-shift of the nonequilibrium population distribution into this states.

In GaP the valley-orbit splitting causes a large separation of 40.7 meV between states $1s(E)$ and the ground state $1s(A)$. Cascade capture goes predominantly across s-states [7] by emission of acoustic phonons. Electrons are accumulated in the $1s(E)$-state because its energy separation to the ground state is much bigger than the largest acoustic phonon energy (31.5 meV, [8]), but still smaller than optical phonon energy (51 meV, [8]). The most probable recombination of electrons in the $1s(E)$ state is by one-phonon excitation to the next higher s-state $2s(A)$, 28 meV above the $1s(E)$ state. The energy 28 meV, is just the energy fitting the experimentally determined exponential temperature dependence of the slow decay time τ mentioned above. Thus, the $1s(E)$ state can be identified as the level of electron storage.

The $2s(A)$ state is close to several p-states therefore, by the exchange between these states due to absorption and emission of acoustical phonons, final radiative recombination

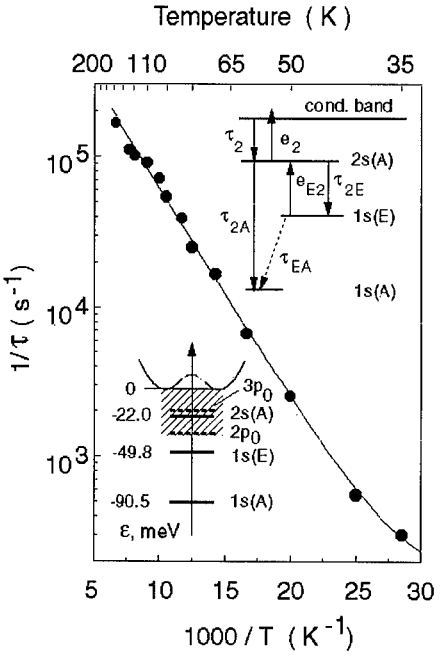


Figure 3: Temperature dependence of observed exponential decay time of the photoconductivity signal (circles) and fitting curve $1/\tau = (1.6 \cdot 10^6 \cdot \exp(-\Delta\varepsilon_{2E}/kT) + 1.44 \cdot 10^2)$ s^{-1}. Insets show the Coulombic states structure of Te in GaP (bottom, left) and a schematic representation of the model of recombination kinetic (top, right).

to the ground state is possible, explaining the observed infrared luminescence.

This kinetic model is sketched in an inset (top, right) of Fig. 3. In agreement to the experimental conditions at low temperatures and the high excitation level, it is assumed that the excess population of excited states is negligible compared to the thermal population in the dark. After irradiation, when there is no more generation, the corresponding rate equations are given by:

$$\begin{aligned} \frac{dn}{dt} &= -\frac{n}{\tau_2} + e_2 n_2 \\ \frac{dn_2}{dt} &= \frac{n}{\tau_2} - e_2 n_2 - \frac{n_2}{\tau_{2E}} + e_{E2} n_E - \frac{n_2}{\tau_{2A}} \\ \frac{dn_E}{dt} &= \frac{n_2}{\tau_{2E}} - e_{E2} n_E - \frac{n_E}{\tau_{EA}}, \end{aligned} \tag{1}$$

where n, n_2, and n_E are the densities of electrons in conduction band, the $2s(A)$ and $1s(E)$ states, respectively. The time constants τ_2, τ_{2E}, τ_{2A}, and τ_{EA} and the probabilities of reverse processes e_2 and e_{E2} are indicated in the schematic energy level scheme Fig. 3 (top, right).

Thermal emission from the ground state is neglected. The thermal transition probability e_{E2} is then given by:

$$e_{E2} = \frac{1}{\tau_{2E}} \exp(-\Delta\varepsilon_{2E}/k_B T), \tag{2}$$

where $\Delta\varepsilon_{2E}$ is the energy distance between levels $1s(E)$ and $2s(A)$.

The rate equations are solved for times $t > t_0$ where $t_0 \approx 100$ ns is the time the radiated ceased. t is larger than τ_2 and, thus, for $t > t_0$ a quasiequilibrium between free carriers and the population of $2s(A)$ is established. In this case the solution of the first rate equation in Eq. (1) is given by $n = e_2\tau_2 n_2$, showing that n_2 determines the density n of nonequilibrium free carriers in the conduction band. Then the concentration of electrons in the state $2s(A)$ as a function of time can be calculated as:

$$n_2(t) \approx \frac{e_{E2} n_E^{(0)}}{(\frac{1}{\tau_{d1}} - \frac{1}{\tau_{d2}})} [\exp(-\frac{(t-t_0)}{\tau_{d2}}) - \exp(-\frac{(t-t_0)}{\tau_{d1}})] \tag{3}$$

The dynamic relaxation times τ_{d1} and τ_{d2} are then given by:

$$\frac{1}{\tau_{d1}} = \frac{1}{\tau_{2A}} + \frac{1}{\tau_{2E}} + e_{E2} \cdot \frac{\tau_{2A}}{(\tau_{2A} + \tau_{2E})} \tag{4}$$

$$\frac{1}{\tau_{d2}} = e_{E2} \cdot \frac{\tau_{2A}}{(\tau_{2A} + \tau_{2E})} + \frac{1}{\tau_{EA}} \tag{5}$$

Here we assume that carriers are dominantly captured by $1s(E)$ state, i. e. $\tau_{2E} \ll \tau_{2A}$.

As it is seen, the exponential rise and decay dependence on the temperature follows from Eq. (3) if $\tau_{d1} \ll \tau_{d2}$. Because of this Eq. (3) can be fitted independently with either τ_{d1} or τ_{d2} as single free parameters to the experimentally observed rise and decay of the slow signal, as shown in Figs. 1 and 2. The resulting dynamic time constants are $1/\tau_{d1} = 10^7$ s^{-1} and $1/\tau_{d2} = 1.6 \cdot 10^6 s^{-1} \cdot \exp(-\Delta\varepsilon_{2E}/kT) + 1.44 \cdot 10^2$ s^{-1} with $\Delta\varepsilon_{2E} = 28$ meV. The temperature dependence of τ_{d2} after the latter relation is shown in Fig. 3 by the full line. All this numerical results are in excellent agreement with the experimental data.

For the present temperature range the last term in Eq. (4) is much smaller than $1/\tau_{2A} + 1/\tau_{2E}$ and can therefore be omitted, which allows us to determine all three kinetic time constants from the measured dynamic times and the temperature dependence of τ_{d2}. We find $\tau_{2E} = 10^{-7}$ s, $\tau_{2A} = 5 \cdot 10^{-7}$ s, and $\tau_{EA} = 0.7 \cdot 10^{-2}$ s, which is consistent with the assumptions of the model that $\tau_{2E} \ll \tau_{2A} \ll \tau_{EA}$.

Furthermore Eq. (3) yields a maximum of n_2 and the corresponding photoconductive signal which occurs at the time $t_1 = \tau_{d1}(\Delta\varepsilon_{2E}/k_{BT}) \ln(\tau_{2A}/\tau_{2E})$ and shifts with temperature. This effect has also been observed.

CONCLUSIONS

A long-living shallow donor excited state, identified as the $1s(E)$ component of the valley-orbit split ground state, has been observed with a strongly temperature dependent life time

as long as several milliseconds. The experimental observations have been described by a modified cascade capture model: carriers rapidly captured within 100 ns by highly excited Coulomb states are accumulated in the $1s(E)$ state which has a very long life time of several milliseconds for direct transitions into the ground state. The recombination of carriers from this state takes place by thermal excitation into somewhat higher lying s- and p- states and subsequent optical and, probably, acoustic multiphonon transitions. Final radiative transitions explain the observation of mid-infrared luminescence.

The high excess carrier density in the excited impurity state has been observed up to a temperature of 150 K and may be of interest for the development of a semiconductor impurity laser in the infrared. Population inversion of radiative states could be realized by re-exciting the carriers from the storage level applying an additional far-infrared or a short electric dc-pulse.

ACKNOWLEDGEMENTS

Financial support by the Deutsche Forschungsgemeinschaft is gratefully acknowledged.

REFERENCES

[1] S. D. Ganichev, W. Prettl, and P. G. Huggard, Phys. Rev. Lett. **71**, 3882 (1993).
[2] D.N. Nasledov, V.V. Negreskul, S.I. Radautsan, S.V. Slobodchikov, Phys. Stat. Sol. **10**, 37 (1965).
[3] H.C. Montgomery, J. Appl. Phys. **39**, 2002 (1968).
[4] R.Z. Bachrach, P.D. Darkus, and O.G. Lorimor, J. Appl. Phys. **45**, 4971 (1974).
[5] C.H. Henry, and D.V. Lang, Phys. Rev. B **15**, 989 (1977).
[6] P. Dean in Deep Centers in Semiconductors, Gordon and Breach Science Publishers, N.Y., 1986.
[7] V.N. Abakumov, V.I. Perel, and I.N. Yassievich, Nonradiative Recombination in Semiconductors, Modern Problems in Condensed Matter Sciences Vol. 33 (North Holland, Amsterdam, 1991).
[8] W. Scott, J. Appl. Phys. **50**, 472 (1979).

Part X

Compensation and Structural Defects in III-V Compounds

A REFINED MODEL FOR THREADING DISLOCATION FILTERING IN $In_xGa_{1-x}As/GaAs$ EPITAXIAL LAYERS

G. MACPHERSON and P. J. GOODHEW

Department of Materials Science and Engineering, University of Liverpool, PO Box 147, L69 3BX, United Kingdom

ABSTRACT

A model is presented for the filtering of threading dislocations in $In_xGa_{1-x}As/GaAs$ epitaxial single layers by accurate control of the layer thickness. The model developed differs from previous models since the $In_xGa_{1-x}As$ growth is restricted to less than ten times the Matthews and Blakeslee critical thickness (h_c) where the asymmetry in the [110] and [$\bar{1}$10] dislocation densities is the greatest. Beyond this thickness it is shown that the removal or annihilation of threading dislocations (TDs) in the epilayer is more than offset by the introduction of new TDs from spiral and Frank-Read type sources. Results from strain sensitive etching with CrO_3 aqueous solutions show that the TD density can be reduced by up to a factor of ten below that found in the substrate. Atomic force microscopy shows that these thin layers maintain a high level of surface quality with an absence of striations. Evidence is also shown that this type of defect etching is suitable for revealing large scale dislocation blocking in samples that have been grown significantly beyond $10h_c$.

INTRODUCTION

For epitaxial layers grown in the 2D (Frank-van der Merwe) growth regime with misfits of less than 1% (x<~0.15) the initial introduction of misfit dislocations (MDs) at the heteroepitaxial interface is from the "bending over" of pre-existing TDs that have replicated themselves in the epilayer[1]. Due to the lack of a four-fold symmetry axis in III-V semiconductors the core of 60° dislocations with <110> line directions have either group III or group V cores. This difference gives rise to an asymmetry in the dislocation densities in the [110] and the [$\bar{1}$10] which is most prominent in the initial stages of relaxation[2]. The first MDs to form are arsenic cored α dislocations with [$\bar{1}$10] line directions. This work aims to show that this asymmetry can be used to increase the mean free path (λ) beyond the recently calculated values of 960μm for α dislocations and 1000mm for β dislocations[3] by reducing the likelihood of blocking from orthogonal 60° or 90° dislocations. This increase in λ gives rise to an increase in the proportion of threading dislocations "falling off" the

Mat. Res. Soc. Symp. Proc. Vol. 442 © 1997 Materials Research Society

substrate and a reduction of up to a factor of ten in the threading dislocation density of the epilayer.

Preliminary results are also provided of large scale dislocation blocking revealed by the etchant. The etchant reveals what appear to be long edge dislocation segments (>50μm in length) lying out of the interface which have blocked a significant number of orthogonal 60° dislocations.

EXPERIMENTAL PROCEDURE

Seven $In_xGa_{1-x}As/GaAs$ layers were grown by chemical beam epitaxy (CBE) at a temperature of 500°C and are described in table 1. Epilayer thicknesses were determined from cleaved edge transmission electron microscopy (TEM) using the **g**002 reflection[4] and cross sectional TEM and are described in terms of h_c with a core cut-off parameter α=2. It is also assumed that h_c for buried layers is twice that for single layers. The plan view and cross sectional specimens were prepared by the standard method described elsewhere[5]. The specimens were examined in a JEOL 2000FX operating at 200kV. Samples a, b, c, e, f, and g were grown on 50.0±0.3mm (001) horizontal Bridgman (HB) n^+ substrates (Si 2-7x$10^{17}$$cm^{-3}$) grown by Sumitomo Electric which had quoted TD densities of <$10^4$$cm^{-2}$. Sample d was grown on 50.0±0.3mm (001) substrates (Si 5-400x$10^{16}$$cm^{-3}$) obtained from American Xtal Technology which are grown by the vertical gradient freeze (VGF) technique and have quoted TD densities of <500cm^{-2}. Etch pit densities for the epilayer (ρ_e) were obtained by etching in a strain sensitive CrO_3-HF solution[6,7]. This type of etchant revealed defects that were visible by Nomarski interference microscopy after the removal of approximately 200nm of the epilayer. The etch pattern revealed by the etchant actually produces hillocks[7] but these shall be referred to as pits for the sake of not introducing new terminology. Etch rates were determined by etching a sample of known thickness for a fixed time and determing from cleaved edge TEM the amount of material removed. Typical etch rates for the solution used in this study were 50nmmin^{-1}. With this particular solution the etch rate is determined solely by the concentration of HF. Etch pit densities for the substrate (ρ_s) were determined by removing the epilayer in a chlorine-methanol solution and sunsequently re-etching the substrate in the CrO_3 solution. A Nanoscope III AFM was used in contact mode to characterise the epilayer surfaces.

RESULTS AND DISCUSSION

ρ_e, ρ_s, the mean surface roughness (σ_m, obtained from AFM), and the linear misfit dislocation densities (ρ_{MD}) for the seven samples are summarised in table 2. The results for the etch pit densities for samples c and g are shown in figures 1(a) and

(b) respectively. For the first of the samples (sample a) there is only a slight decrease in ρ_e compared to ρ_s. As the $In_xGa_{1-x}As$ layer thickness increases to $3h_c$ ρ_e is found to be more than a factor of four below ρ_s. Plan view TEM of this sample failed to reveal misfit dislocations with [110] line directions showing that dislocation blocking of orthogonal dislocations is not occurring in this sample. The trend for lower ρ_e is continued in sample c which shows the largest reduction compared to ρ_s. ρ_e was found to be more than a factor of eight below ρ_s with ρ_e measured at $700cm^{-3}$. It is worth noting that reductions of this level are rarely found in $In_xGa_{1-x}As/GaAs$ and $Al_xGa_{1-x}As/GaAs$ superlattices[8]. Plan view TEM again failed to reveal misfit dislocations with [110] line directions. Associated with this reduction in TD density was an increase in the proportion of TDs found at the very edge of the wafer. A similar observation has been reported in Te-doped InP layers grown on (001) InP:Fe[9]. Sample d which was grown on the low TD density substrate showed a significant reduction in ρ_e with respect to ρ_s (a factor of eight) but the poor statistics give errors of approximately 25% in the density values.

For sample e the trend for lower ρ_e is reversed, with ρ_e only a factor of four below ρ_s and it is believed that this reversal is due to the significant introduction of TDs from dislocation multiplication. The plan view micrograph of figure 2 clearly shows an orthogonal array of misfit dislocation with no obvious difference in ρ_{MD} for the two <110> directions. With ρ_{MD} at the level found in sample e it is expected that there will be a significant interaction between the misfit dislocations with one such reaction denoted by an arrow in figure 2. This is the reaction of two parallel 60° dislocations to form an edge dislocation and it should also be noted that the reaction appears to have been initiated at the crossing of two orthogonal 60° dislocations. This edge dislocation is necessarily located out of the interface and it is believed that it may then act as dislocation pinning point for multiplication[10]. Sample f shows a further increase in ρ_e (now approximately equal to ρ_s), with sample g showing a significant increase in ρ_e to a level more than a factor of fifteen greater than ρ_s. Sample g was interesting since it showed high densities of TDs aligned along the <110> directions as shown in figure 3 which are consistent with the repeated operation of dislocation mills. The surfaces of all the samples were characterised by AFM and from table 2 it can be seen that the surfaces remain relatively flat for layer thicknesses $<\sim 10h_c$ ($\sigma_{rms} <\sim 2.5nm$) with sample f the first to show a significant increase in roughness.

Etching with aqueous CrO_3-HF also appears suitable for the revealing of large scale dislocation blocking. Figure 4 show a Nomarski micrograph of sample f showing a striated surface. These striations are produced by the etchant as a result of the strain fields generated by the linear misfit dislocations and are not the typical growth striations associated with 2D growth. It is not normally possible to find a one to one correlation between dislocations and their etched striation at these dislocation densities but there are exceptions. One such exception is the striation with strong

contrast lying horizontally in figure 4. Plan view TEM tended to show long dislocation segments lying below these striations and it is believed that these striation form above edge dislocations that lie significantly above the interface and therefore have a greater strain field at the surface relative to the interfacial dislocations. Since these edge dislocations lie above the interface it would be expected that they would be responsible for a significant amount of blocking of orthogonal dislocations as predicted by Freund[11]. Examples of blocking have been denoted by arrows in the figure confirming that this is occurring. This work will be discussed in more detail in a future publication.

CONCLUSIONS

By growing $In_xGa_{1-x}As$ epitaxial layers that are less than $10h_c$ it is possible to reduce ρ_e by a factor of approximately ten with relatively little change in the surface roughness. Once the layer thickness exceeds $10h_c$ then the introduction of TDs from multiplication sources becomes appreciable. A preliminary study of the striations formed by the etchant on the strain fields associated with the linear misfit dislocation segments shows evidence of blocking of 60° dislocations by long orthogonal segments of edge dislocations lying above the interface.

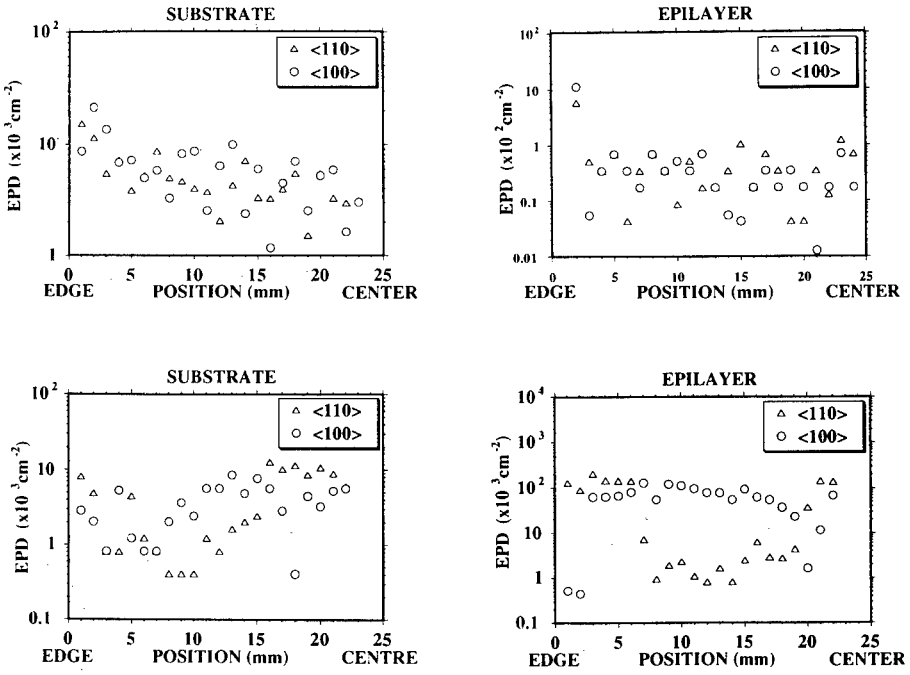


Figure 1: Etch pit densities for the substrate and epilayer for samples c and g respectively.

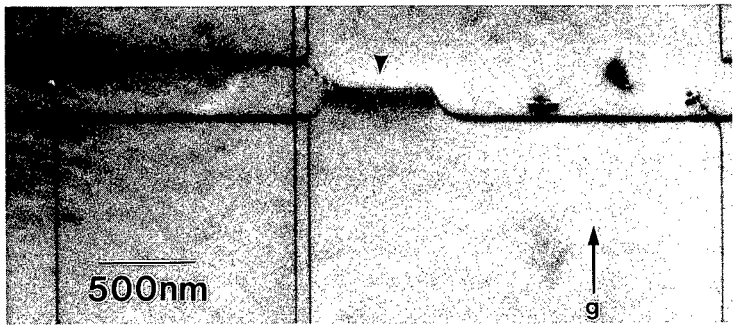


Figure 2: Plan view TEM micrograph of sample e showing the formation of an edge dislocation segment from the reaction of two correctly oriented 60° dislocations. The reaction has been initiated by the interaction of the two 60° dislocations with a 60° dislocation lying in the [110] direction.

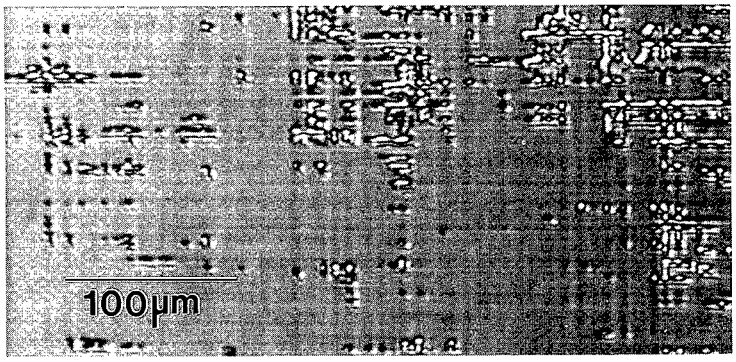


Figure 3: Nomarski interference micrograph of sample g showing etch pits aligned along <110> directions which are associated with the operation of dislocation mills within the epilayer.

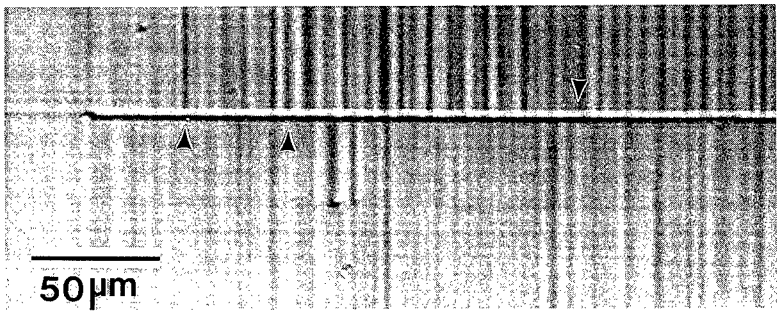


Figure 4: Nomarski interference micrograph of sample f showing a striation with strong contrast (lying horizontally in the figure) which is associated with an edge dislocation. Dislocation blocking of orthogonal 60° dislocations is denoted by arrows.

Table 1:

Sample	h/h_c	Composition (x)	Thickness (nm)	GaAs Cap	TD Density (cm^{-2})
a	2	0.10	68±4	YES	10^4
b	3	0.10	102±5	YES	10^4
c	4	0.10	136±5	YES	10^4
d	6	0.10	204±5	YES	500
e	10	0.05	400±10	NO	10^4
f	45	0.15	500±15	NO	10^4
g	175	0.12	1200±15	NO	10^4

Table 2:

Sample	ρ_s ($x10^3 cm^{-2}$)	ρ_e ($x10^3 cm^{-2}$)	ρ_{MD}($x10^4 cm^{-1}$)		σ_{rms} (nm)
			[-110]	[110]	
a	4.0	3.4	0.08	<0.001	1.2
b	6.3	1.4	0.14	<0.001	2.8
c	5.9	0.7	0.20	~0.001	2.1
d	0.45	~0.06	0.37	~0.002	2.3
e	5.4	1.4	9.7	9.5	1.4
f	8.6	7.6	135	135	5.4
g	3.9	59.6	193	193	11.8

REFERENCES

1. M. Aindow, Philos.Mag.Lett. **62**, 139 (1990).
2. K. L. Kavannagh, M. A. Capano, L. W. Hobbs, J. C. Barbour, P. M. J. Marée, W. Schaff, J. W. Mayer, D. Petit, J. M. Woodall, J. A. Stroscio, and R. M Feenstra, J.Appl.Phys. **64**, 4843 (1988).
3. M. J. Matragrano, D. G. Ast, G. P. Watson, and J. R. Shealy, J.Appl.Phys. **79**, 776 (1996).
4. H. Kakibayashi and F. Nagata, Jpn.J.Appl.Phys. **24**, L905 (1985).
5. G. MacPherson, R. Beanland, P. J. Goodhew, and P. Kidd, Scripta.Metall.Mater. **33**, 123 (1995).
6. J. van der Ven, J. L. Weyher, J. E. A. M. van der Meerakker, and J. J. Kelly, J. Electrochem.Soc. **134**, 989 (1986).
7. N. Chen, J.Cryst.Growth, **129**, 777 (1993).
8. E. A. Fitzgerald, Mater.Sci.Rep. **7**, 87 (1991).
9. S. N. Chu, S. Mahajan, K. E. Strege, and W. D. Johnston, Jr., Appl.Phys.Lett. **38**, 766 (1981).
10. R. Beanland, J.Appl.Phys. **77**, 4031 (1995).
11. L. B. Freund, J.Appl.Phys. **68**, 2071 (1990).

STRUCTURAL AND OPTICAL CHARACTERIZATION OF $Al_xGa_{1-x}As$ GROWN AT LOW TEMPERATURES BY ORGANOMETALLIC VAPOR PHASE EPITAXY

A. Wankerl*, D.T. Emerson, M.J. Cook and J.R. Shealy
OMVPE Facility, School of Electrical Engineering, Cornell University, Ithaca NY 14850
*aw20@cornell.edu

ABSTRACT

We report on the low temperature growth of $Al_xGa_{1-x}As$ by conventional Organometallic Vapor Phase Epitaxy OMVPE for a substrate temperature of 500°C and V/III ratios extending to subunity. Optical, structural and electrical qualities are assessed with double crystal X-ray diffraction, Nomarski and atomic force microscopy, 1.6K and 300K photoluminescence, Rutherford backscattering and Hall measurements. Although our low temperature grown films are of good structural and optical quality, they exhibit high background p-doping (carbon) and high levels of hydrogen passivation. A method for extracting the carbon doping levels from lattice contraction measurements is suggested. The dependence of layer composition, free carrier concentration and hydrogen passivation on growth parameters are investigated. Moreover, the effects of post-growth annealing on free carrier concentration, lattice parameter and optical qualities are studied. The influence on the bandgap of bandtail states and compressive strain due to carbon are compared.

INTRODUCTION

High purity $Al_xGa_{1-x}As$ films are typically grown by organometallic vapor phase epitaxy (OMVPE) at substrate temperatures above 600°C. The film purity has been shown to degenerate as the growth temperature is reduced due to an increase in unintentional carbon doping [1,2]. However, low temperature growth offers the advantage of reduced impurity diffusion and aids the formation of abrupt interfaces useful for HBT and MODFET applications. Moreover, the UV-laser stimulated growth process, which promises high resolution area selective growth for OEIC applications, requires a lower substrate temperature for achieving high growth contrast (growth in illuminated area / growth in dark).

The extent of unintentional carbon doping depends strongly on the metal organic precursors. GaAs growth from TMG results in higher carbon doping than growth from TEG, which is attributed to the difference in gas phase chemistry. For growth from methyl precursors, it was shown that carbon is incorporated via a secondary growth mechanism involving the formation of metal carbene. [3] As the growth temperature is decreased, this mechanism becomes more relevant, leading to higher carbon incorporation. This paper provides a study of the structural and optical properties of $Al_xGa_{1-x}As$ grown at 500°C from methyl based organometallics. It is significant in that it investigates a lower growth temperature, as well as lower V/III ratios, than seen in previous reports.

EXPERIMENTS

Epitaxial growth

The epitaxial layers were grown in a low-pressure (25 Torr), four growth zone vertical-barrel OMVPE reactor. A similar two growth zone system has been described previously [4]. Instead of a quartz cell this system has a water-cooled stainless steel cell including a quartz window for UV-laser stimulated growth experiments. All growths were conducted on (001) semi-insulating GaAs substrates by conventional and interrupted OMVPE growth in one growth zone only. The precursors trimethylgallium (TMG), trimethylaluminum (TMA) and arsine were premixed prior to injection. After a 10 min. anneal cycle at 730°C under 1.05% AsH_3, a 2400 Å GaAs buffer layer was deposited at 650°C. During a growth stop under AsH_3 overpressure, the temperature was

Mat. Res. Soc. Symp. Proc. Vol. 442 © 1997 Materials Research Society

then lowered to 500°C. Sufficient time for temperature stabilization elapsed before the $Al_xGa_{1-x}As$ layer was grown. The wafer temperature was monitored by optical pyrometer and thermocouple measurements. Palladium diffused hydrogen was used as carrier gas. Two series of varying V/III ratio at different aluminum vapor mole fractions were grown. For the first six samples, the aluminum vapor mole fraction was 0.45, and we varied the V/III ratio form 99 to 0.25, where two of the samples had a subunity V/III ratio. The three samples of the second series were prepared at a 0.75 aluminum vapor mole fraction and at V/III ratios above unity corresponding approximately to three from the first series.

Characterization

The lattice mismatch of the $Al_xGa_{1-x}As$ layer with respect to the GaAs substrate was determined by double crystal x-ray diffraction (DCXRD) using (004) Bragg reflection and Cu $K\alpha$ radiation at 1.541 Å wavelength. Since both aluminum and carbon potentially contribute to the mismatch, the aluminum mole fraction was independently assessed by Rutherford backscattering (RBS), for which we used a He^{++} ion beam at 2.5 MeV and a scattering angle of 170°. Post-growth annealing behavior as a function of temperature was studied by a sequence of 10 min. anneals in N_2 ambient and subsequent Hall measurements. Carrier concentrations and mobilities were measured on all samples both as-grown and after a 10 min. anneal at 550°C. Optical qualities of unannealed and annealed samples were studied with 1.6K and 300K photoluminescence (PL). Surface morphologies were assessed by Nomarski and atomic force microscopy.

RESULTS AND DISCUSSION

Growth quality and hydrogen passivation

The GaAs buffer layer was p-type with a $4.4*(10^{15})$ cm^{-3} room temperature carrier concentration and 415 cm^2/Vs mobility. Its high quality ensures that secondary contamination in our reactor is negligible for this study and that none of our measurements on the $Al_xGa_{1-x}As$ are influenced by buffer charges. The $Al_xGa_{1-x}As$ surfaces were specular apart from particle contamination and occasional defects, and Nomarski microscopy showed identical morphology for all samples. AFM studies yielded a mean surface roughness of about 0.15 nm. Mobilities around 60 cm^2/Vs were measured for the degenerately carbon doped $Al_xGa_{1-x}As$ layers at V/III ratios above unity.

Significant degrees of hydrogen passivation are typically observed in heavily carbon doped GaAs and $Al_xGa_{1-x}As$ grown by OMVPE. Post-growth annealing reduces hydrogen passivation by cracking the hydrogen-carbon bond and allowing the hydrogen to diffuse out. The carbon atoms become thus activated as acceptor impurities. Figure 1 shows the extent of carbon acceptor activation as a function of annealing temperature. All samples were annealed under a low N_2 flow. We found the hole concentrations to increase for annealing temperatures below 550°C and to decrease above this temperature. Around 470°C, the hole concentration increases drastically, suggesting that sufficient thermal energy is provided for the out-diffusion of hydrogen. This behavior is consistent with findings in annealing

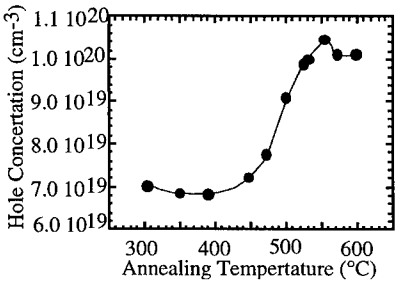


Figure 1: Hole concentration as function of annealing temperature for 10 min. anneals.

studies of heavily carbon doped GaAs [5]. The decrease in hole concentration for high annealing temperatures is attributed to the formation of carbon interstitials and precipitates [6]. For the comparison of optical and structural qualities between annealed and as-grown samples, we annealed all samples for 10 min. at 550°C, the temperature for which we obtained maximum acceptor activation.

Composition and carbon incorporation

Since the tetrahedral covalent bond radius of carbon is much smaller than that of gallium, aluminum or arsenic, high carbon concentrations in $Al_xGa_{1-x}As$ lead to significant lattice contraction. The mismatch with respect to GaAs as measured by DCXRD includes lattice expansion due to aluminum (positive mismatch) and contraction due to carbon (negative mismatch). Since it is not possible to determine the composition of heavily carbon doped $Al_xGa_{1-x}As$ from its lattice constant, we measured the aluminum mole fraction independently with RBS. Figure 2(a) shows the aluminum mole fraction for both growth series, which was found to vary with V/III ratio. This data was used to separate the lattice mismatch due to aluminum from that due to carbon, where we used $a = 5.6533 + 0.0078x$ [7] for the lattice constant of $Al_xGa_{1-x}As$. The mismatch due to carbon only is plotted for all samples in figure 2(b).

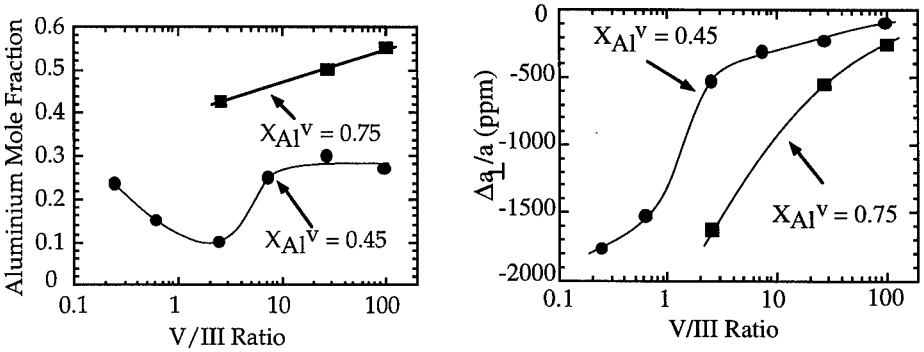


Figure 2: (a): Aluminum mole fraction measured by RBS as a function of V/III ratio.
(b): Perpendicular lattice mismatch of $Al_xGa_{1-x}As$ with respect GaAs due to carbon only as a function of V/III ratio. Aluminum vapor mole fractions (X_{Al}^V) as indicated.

We modified the lattice contraction model of de Lyon *et al.* [8] to predict the carbon concentration. This model assumes a linear variation of lattice constant with substitutional carbon doping and is based on the difference between the tetrahedral covalent bond radius of carbon and that of the atom it substitutes. If $\Delta a_\perp$ denotes the change in lattice constant of the $Al_xGa_{1-x}As$ layer with respect to the lattice constant of GaAs due to carbon only as given by figure 2(b), then the carbon concentration can be estimated by

$$c_C = \frac{\sqrt{3}}{4} \frac{\Delta a_\perp \rho_{AlGaAs}}{\left[(r_{Al} - r_C) f_{Al}^C + (r_{Ga} - r_C) f_{Ga}^C + (r_{As} - r_C) f_{As}^C\right]}. \quad (1)$$

Here, r_x is the tetrahedral covalent bond radius of element x, f_y^C is the fraction of carbon atoms substituting element y and

$$\rho_{AlGaAs} = \frac{4}{\left[(5.6533 + 0.0078x)10^{-8}\right]^3}[cm^{-3}] \qquad (2)$$

is the molecular density of $Al_xGa_{1-x}As$. The factor of $\frac{\sqrt{3}}{4}$ arises from the relation between the bond radius and the lattice constant in the zinc-blend structure. The calculated carbon concentrations are shown in figure 3 as open squares for the 0.45 aluminum vapor mole fraction samples and as open triangles for the 0.75 aluminum vapor mole fraction samples. For this calculation, we assumed that all carbon atoms are substitutionally incorporated on As sites and used $(r_{As}-r_C)=0.49$ Å. We see that all samples grown at 500°C exhibit degenerate unintentional p-type carbon doping, ranging from $5*10^{19}$ to $4*10^{20}$ cm^{-3}, which decreases as the V/III ratio is decreased. The other two curves in figure 3 display the measured room temperature hole concentrations before (solid squares) and after the 10 min. post-growth anneal at 550°C (solid circles). Except for the sample grown at a V/III ratio of 0.25, we find excellent agreement with the hole concentrations after full acceptor activation. This validates the assumption that all carbon atoms occupy As sites. The difference between carbon and hole concentration for the 0.25 V/III ratio sample, however, suggests compensation at the lowest V/III ratio. Not only the hole concentration, but also the perpendicular mismatch due to carbon increases for all samples upon annealing for 10 min. at 550°C. Figure 4 compares the gain in free carrier concentration with the increase in lattice contraction upon annealing. From the agreement in shape of these two curves, we may conclude that the lattice contraction upon annealing is solely due to the out-diffusion of hydrogen originating from C_{As} - H bonds.

Photoluminescence

Figure 5 (a) shows the 300 K photoluminescence spectra of the sample grown at 0.45 aluminum vapor mole fraction and 7.41 V/III ratio, and figure 5 (b) shows the corresponding 1.6K spectra. Each plot displays the spectra of both as-grown and annealed samples. The low temperature photoluminescence spectra of all unannealed samples exhibit a hump extending over a wide range of midgap energies. As for the spectra shown in figure 5 (b), the hump usually overlaps with the GaAs peak. This feature becomes more pronounced for the samples with higher carbon concentrations and it decreases or disappears upon annealing. Midgap peaks with similar annealing behavior have been observed in heavily carbon doped GaAs [9]. The midgap energy hump is absent in the room temperature spectra. Due to this behavior, we suspect that this peak originates from deep levels generated by the carbon-hydrogen complexes.

The photoluminescence peak positions differ for all samples, and for each sample the peak shifts upon annealing. We investigated these shifts for the series of samples grown at 0.45 aluminum vapor mole fraction. Since the aluminum mole fraction in the layer varies with V/III ratio, we consider for each sample the difference between the actual peak position and the nominal bandgap at the respective temperature. Thus we obtain with $(h\nu-E_g)$ a quantity independent of the composition and sample temperature. We used $E_g(x_{Al}) = 1.424 + 1.247x_{Al}$ (eV) [7] for the room temperature bandgap and $E_g(x_{Al}) = 1.512 + 1.455\ x_{Al}$ (eV) [10] for the low temperature bandgap. Two opposing effects influence the bandgap of our highly carbon doped $Al_xGa_{1-x}As$ layers: bandtail states introduced by the degenerate doping shrink the bandgap and the compressive strain due to the smaller carbon atoms widens the bandgap. Considering the bandgap as a function of V/III ratio, we establish, that the effect of compressive strain dominates the bandtail effect, if the derivative of $(h\nu-E_g)$ with respect to V/III ratio is negative. Conversely, if the derivative of $(h\nu-E_g)$ with respect to V/III ratio is positive, the bandtail effect dominates the effect of compressive strain. Figure 6 (a) shows the dependence of $(h\nu-E_g)$ on V/III ratio for the room temperature luminescence spectra of as-grown (open circles) and annealed (solid circles) samples, and figure 6 (b) shows the corresponding for low temperature photoluminescence. The curves are drawn qualitatively as a guide to the eye and the division into three regions is also qualitative in nature.

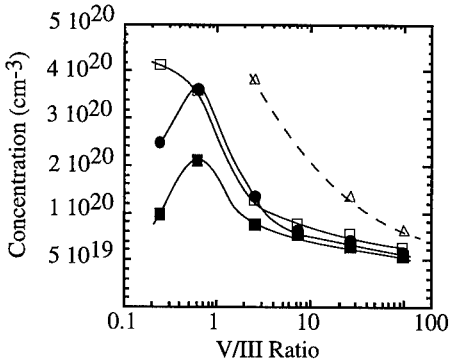


Figure 3: Measured hole concentrations (■)as-grown and (●)annealed for 0.45 aluminum vapor mole fraction. Calculated carbon concentrations for the aluminum vapor mole fractions of (□) 0.45 and (△) 0.75.

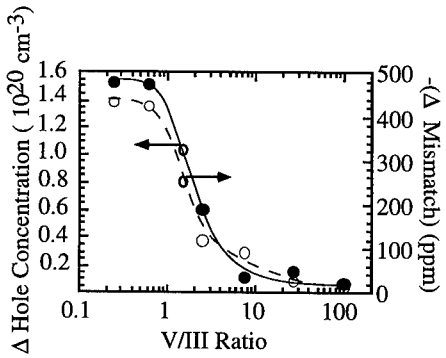


Figure 4: Change in hole concentration (solid line) and the absolute perpendicular mismatch (dotted line) upon annealing for 10 min. at 550°C.

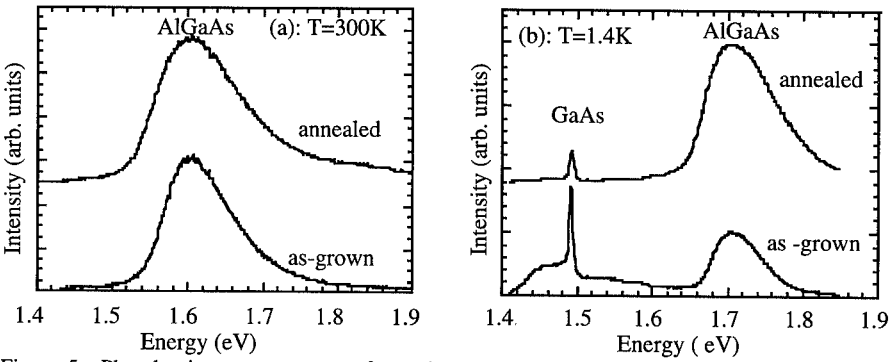


Figure 5: Photoluminescence spectra of sample grown at 0.45 vapor mole fraction and 7.41 V/III ratio. As-grown and annealed spectra for (a) 300K PL and (b) 1.6K PL. For as-grown spectrum at 1.6 K (b), the deep level 'hump' overlays the GaAs peak.

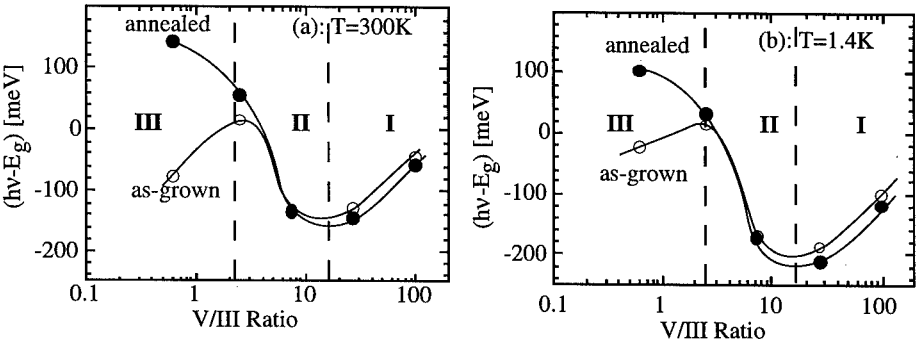


Figure 6: ($h\nu$-E_g) vs. V/III ratio for (a) 300K and (b) 1.6K photoluminescence spectra of the samples grown at 0.45 aluminum vapor mole fraction. Annealed and as-grown cases as indicated.

The dependencies of (hv-E_g) on V/III ratio agree well for room and low temperature photoluminescence spectra. From our previous discussion we conclude, that the bandtail states affect the bandgap more than compressive strain in region I, and that the strain dominates in region II. For the low V/III ratios in region III we observe a transition from the dominance of the bandtail effect to the dominance of the compressive strain effect upon annealing. At these high carbon concentrations, the additional lattice contraction due to the hydrogen purge affects the bandgap much more than the gain in free carriers through the anneal. Overall, we can conclude that the two opposing effects on the bandgap are equally important in heavily carbon doped $Al_xGa_{1-x}As$.

CONCLUSION

In summary, we have characterized the structural and optical properties of $Al_xGa_{1-x}As$ grown at 500°C by OMVPE. Despite the degenerate unintentional carbon doping, we obtained good film quality with electrical and optical properties suitable for device applications. The material properties were found to be very sensitive to the V/III ratio and to post-growth annealing. A method for extracting the carbon concentration from DCXRD and RBS measurements was suggested. The maximum activation of the hydrogen passivated acceptors was found to occur at an annealing temperature of 550°C and the additional lattice contraction upon annealing was shown to be solely due to the purging of hydrogen. Optical characterization revealed the existence of deep levels originating from carbon-hydrogen complexes. The generation of bandtail states and the compressive strain in highly carbon doped $Al_xGa_{1-x}As$ layers were found to influence the bandgap to equal extend.

ACKNOWLEDGMENTS

This work was supported by the National Science Foundation. We thank Dr. Peter Revesz for the RBS measurements. We also would like to acknowledge Dr. A. Schremer, B. Butterfield, V. Williams, J. Smart, E. Chumbes, J. Lee and M. Ezpeleta for their technical assistance.

REFERENCES

1. W.S. Hobson, Proceedings of the Twenty-First State-of -the-Art Program on Compound Semiconductors (SOTAPOCS XXI), ed. S.N.G. Chu, F. Ren, V. Malhorta and P. van Daele, The Electrochemical Society, **Proc. Vol. 94-34**, 30 (1995).

2. M. Kondo and T. Tanahashi, J. Cryst. Growth **145**, 390 (1994).

3. T.F. Kuech and J.M. Redwing, J. Cryst. Growth **145**, 382 (1994).

4. J.R. Shealy, J. Cryst. Growth **87**, 350 (1988).

5. W.Y. Han and Y. Lu, Appl. Phys. Lett. **61**, 87 (1992).

6. S. Nozaki and K.Takahashi, Appl. Phys. Lett. **62**, 1913 (1993).

7. S. Adachi, J. Appl. Phys. **58**, R1 (1985).

8. T.J. de Lyon, J.M. Woodall, M.S. Goorsky and P.D. Kirchner, Appl. Phys. Lett. **56**, 1040 (1990).

9. K. Watanabe and H. Yamazaki, Appl. Phys. Lett. **59**, 434 (1991).

10. T.F. Kuech, D.J. Wolford, R. Potemski, J.A. Bradley, K.H. Kelleher, D. Yan, J.P. Farrell, P.M.S. Lesser and F.H. Pollak, Appl. Phys. Lett. **51**, 505 (1987).

ELECTRICAL AND STRUCTURAL PROPERTIES OF LT-GaAs: INFLUENCE OF As/Ga FLUX RATIO AND GROWTH TEMPERATURE

M. Luysberg**, H. Sohn*, A. Prasad*, P. Specht*, H. Fujioka*, R. Klockenbrink*, E.R. Weber*,
*Dept. of Materials Science and Mineral Engineering, UC Berkeley, CA 94720
** present address: IFF, Research Center Jülich, 52425 Jülich, Germany, m.luysberg@kfa-juelich.de

ABSTRACT

The deposition of GaAs by MBE at low temperatures results in a material of unique properties. However, up to now the control and understanding of the electrical and structural properties are unsatisfactory. To investigate the influence of growth parameters on the formation of point defects and electrical properties, the substrate temperature and the As/Ga flux ratio were systematically varied. In a well defined parameter range the lattice expansion was found to be dominated by the formation of As antisite defects. After annealing a high resistivity is obtained independent of the growth conditions. A strong influence of the growth temperature on the band conduction mechanism is observed, whereas a variation of the As/Ga flux ratio induces only slight changes of the temperature dependence of the conductivity.

INTRODUCTION

Thin epitaxial layers of GaAs grown at low temperatures (LT-GaAs) are of current interest in view of their technological importance as insulating layers in GaAs devices or as active layers in THz photodetectors. The high resistivity and the short carrier lifetime were attributed to the formation of native defects in this As rich material [1]. The high concentration of As antisite As_{Ga} defects introduced during growth have been shown to be responsible for the hopping conductivity observed in the as-grown layers [2,3]. Ga vacancies are assumed to partly compensate the deep double As_{Ga} donors [4]. Upon annealing at temperatures above 400°C the structural and electrical properties change. The as-grown layers show a dilatation of the lattice compared to stoichiometric GaAs and are of high crystalline quality. Annealed LT-GaAs samples are characterized by the formation of As precipitates [5,6,7], which causes the relaxation of the lattice parameter to the stoichiometric value. Furthermore, the material becomes semi-insulating upon annealing. The overlap of depleted regions surrounding the As precipitates was employed to explain the high electrical resistivity [8]. In contrast, in the "arsenic antisite model" the semi-insulating properties are attributed to the pinning of the Fermi level by a sufficiently high residual concentration of As_{Ga} [2].

In order to engineer the point defect concentration and the microstructure of LT-GaAs we focused on the systematic variation of growth conditions, i.e. growth temperature and As/Ga flux ratio as measured by the beam equivalent pressure (BEP). The structural and electrical properties as well as the point defect concentrations were investigated by various methods (see below).

EXPERIMENT

LT-GaAs layers were grown by molecular beam epitaxy using a Varian Gen II MBE system. To achieve better control of the growth temperature we recently installed a precision substrate temperature measurement system using diffuse reflectance spectroscopy, which reduces the error

Mat. Res. Soc. Symp. Proc. Vol. 442 © 1997 Materials Research Society

in the temperature measurement to 2°C. In the following corrected temperature values based on a calibration of the thermocouple reading are being used. Details of the growth are described elsewhere [9]. Two different types of growth series have been deposited: a temperature series, where the growth temperature was varied from 200°C to 350°C at a BEP of 20, and several BEP series grown in the temperature range of 200°C to 250°C, where the BEP was varied from 7 to 40. In a second set of samples each growth run was repeated to embed the LT-GaAs as i layer in a n-i-n structure. Since the growth of the n^+ top layer is performed at 600°C, the underlying LT-GaAs layer is in-situ annealed for approximately 30 min. To compare electrical and structural properties proximity annealing at 600°C for 30min was preformed for selected layers.

The structural properties of as-grown and annealed layers were investigated by X-ray diffraction (XRD) and transmission electron microscopy (TEM). The [As_{Ga}^{o}] and the [As_{Ga}^{+}] concentrations were determined by near infrared absorption (NIRA) and magnetic circular dichroism (MCDA) (see [4] for details). To characterize the electrical properties of annealed material the temperature dependence of the conductivity was measured using n-i-n structures, where the i layer consists of annealed LT-GaAs.

RESULTS AND DISCUSSION

The growth of GaAs at low temperatures results in the dilatation of the lattice compared to stoichiometric material. The influence of the As/Ga flux ratio on the lattice parameter of the LT-GaAs layers is summarized in Figure 1 for series of samples grown at different temperatures. The perpendicular lattice mismatch Δd/d determined form the (004) reflections is plotted versus the BEP. In all cases investigated, the parallel lattice mismatch evaluated from the asymmetrical (224) reflections is zero, which implies a tetragonal distortion of the LT-GaAs layers. In a well defined window from a BEP of 8 to a BEP of 20 the lattice parameter of the LT-GaAs films increases with increasing As/Ga flux ratio. This is demonstrated for the samples grown at 200°C and 240°C. If the As/Ga flux ratio is further increased, the lattice mismatch remains constant at 0.14% and 0.11% for the samples grown at 195°C and 200°C, respectively. The growth at low As/Ga flux ratio with a BEP<8 results in unstrained epitaxial growth. The onset of the dilatational growth seems to be independent of temperature, since a similar threshold value is observed for the samples grown at 200°C and 240°C. A similar variation of the lattice parameter with the As/Ga flux ratio was previously reported for samples grown at 250°C, where the BEP was varied from 3 to 6 [10]. Lagadas et al [11] observed a linear increase of the lattice mismatch with the BEP up to a plateau at 0.056% for samples grown at 250°C.

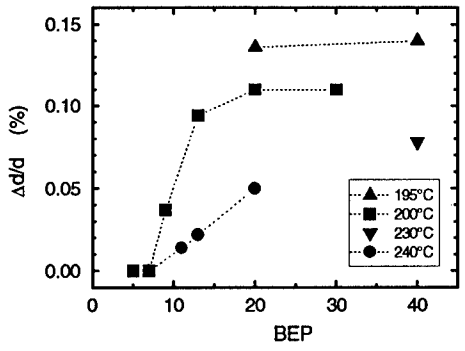


Figure 1: Lattice mismatch Δd/d as a function of the BEP

The growth temperature has also a considerable influence on the lattice dilatation of the LT-GaAs films. At a given As/Ga flux ratio the lattice mismatch decreases with increasing growth temperature, e.g. from 0.11% at 200°C to 0.05% at 240°C for a BEP of 20 (Fig.1). A further decrease of the lattice mismatch can be achieved by choosing even higher temperatures up

to 350°C, where the lattice mismatch becomes zero within the margin of errors [9].

For samples grown in a certain range of parameters the lattice constant is found to be correlated with the As_{Ga} concentration. In Figure 2 the lattice mismatch between the LT-GaAs layers and the GaAs substrate is plotted versus the neutral As_{Ga} concentration, which was measured by NIRA [9]. For each sample the growth temperature and the BEP are given. With the exception of the sample grown at 200°C and a BEP of 30, a linear correlation is observed. This supports our previous result for samples grown at different temperatures in the range of 200°C to 300°C [1,4], which are also included in Figure 2. Therefore, it is confirmed that As_{Ga} are the dominant point defects responsible for the lattice expansion. Furthermore, it has to be stressed that both, a variation of the growth temperature and a variation of the As/Ga flux ratio influence mainly the incorporation of As_{Ga}. However, this seems not to hold for samples grown at a high As/Ga flux ratio, i.e. in the "plateau region" (Figure 1), since the neutral As_{Ga} concentration decreases, although the lattice mismatch remains constant.

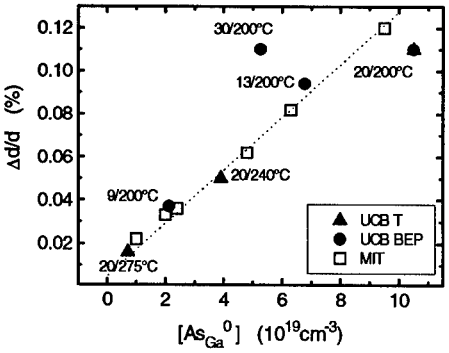


Figure 2: Linear correlation of lattice mismatch Δd/d and $[As_{Ga}^0]$ concentration. BEP and growth temperature are given for the temperature series (UCB T) and the BEP series (UCB BEP). The values of samples grown at MIT Lincoln Laboratory (MIT) [1] are shown for comparison.

In addition to the neutral As_{Ga} concentration the amount of positively charged As_{Ga}^+ was determined by MCDA [9]. In all cases investigated the $[As_{Ga}^+]$ concentration was approximately one order of magnitude lower than $[As_{Ga}^0]$, which is in agreement with previous studies [1]. Based on the observed second power dependence of the $[As_{Ga}^0]$ compared with the $[As_{Ga}^+]$ it was proposed that Ga vacancies, which are triple acceptors, are responsible for the carrier compensation [4]. Indeed, we measured recently with positron annihilation [12] that the V_{Ga} concentration is about three times smaller than the concentration of As_{Ga}^+.

The structural properties of as-grown and annealed LT-GaAs have been investigated by TEM. No defects were observed in the as-grown samples, neither in the samples grown at high

BEP	ρ (cm^{-3})	diameter	$[As]_{precipitate}$ (cm^{-3})	$[As_{Ga}]^0$ (cm^{-3})
9	$4.3\ 10^{16}$	≈ 2 nm	$8.5\ 10^{18}$	$2.1\ 10^{19}$
13	$1.2\ 10^{17}$	3.0 nm	$8.2\ 10^{19}$	$6.8\ 10^{19}$
20	$9.2\ 10^{16}$	4.1 nm	$1.6\ 10^{20}$	$1.1\ 10^{20}$
30	$7.2\ 10^{16}$	3.5 nm	$7.5\ 10^{19}$	$5.3\ 10^{19}$

Table I: Quantitative analysis of As precipitates for samples grown at 200°C and different BEP. From the volume density ρ and the size of the precipitates the number of As atoms forming the precipitates are evaluated. The concentration of neutral $[As_{Ga}^0]$ is given for comparison.

As/Ga flux ratios, nor in samples grown at low temperatures. Upon annealing at 600°C the formation of precipitates is observed in samples, which are grown below 300°C and above a BEP of 8. From the characteristic Moiré fringe distances the precipitates were identified as hexagonal As. At high growth temperatures the samples remained defect-free after annealing. Table 1 summarizes the results of the quantitative analysis (for details see [12]). The size of the precipitates, which was measured from high-resolution electron micrographs, increases upon an increase of the BEP from 9 to 20. If the As/Ga flux ratio is further increased the diameter of the precipitates becomes smaller, as observed for the sample grown at a BEP of 30. The concentration of precipitates was obtained by counting about 100 precipitates in the corresponding sample volume and is given in column 2. Within the margin of error the precipitate densities for the samples grown at high As/Ga flux ratios at a BEP >13 are the same. The sample grown at a BEP of 9 shows a significantly lower density. To evaluate the number of As atoms in the precipitates it was assumed that all of the precipitates are hexagonal As. Taking into account that the number density can only be determined with an accuracy of a factor of 2 the estimated total amount of As in the precipitates agrees with the concentration of the neutral As_{Ga} determined by NIRA (Table I).

The temperature dependence of the conductivity of n-i-n structures was measured to determine the electrical properties of the LT-GaAs layers. Figure 3 summarizes the results obtained for samples grown at different temperatures at a BEP of 20. A small contribution due to hopping conduction can be observed for the sample grown at 200°C , which is indicated by the smaller slope at decreasing measurement temperatures. The samples grown at higher temperatures show only the activation over one barrier, as is obvious from the linear behavior of the Arrhenius plot. The variation of the BEP has no significant influence on the electrical properties (Fig.4). All samples grown at a temperature of 240°C show a considerable contribution due to hopping conduction. At higher measurement temperatures the band conduction dominates the electrical behavior.

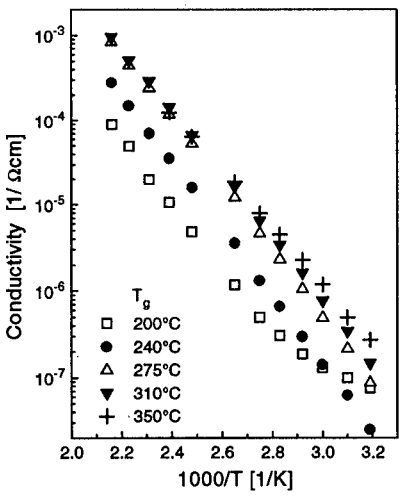


Figure 3: Arrhenius plot of the conductivity for samples grown at a BEP of 20 and different temperatures T_g

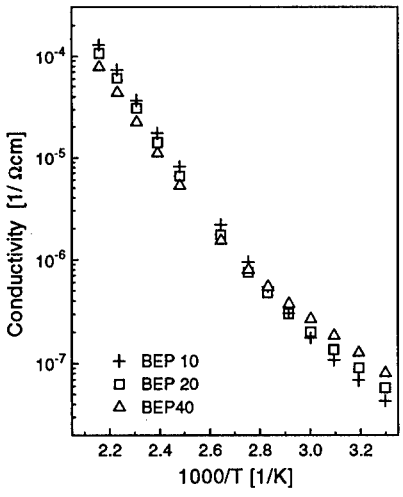


Figure 4: Arrhenius plot of the conductivity for samples grown at 240°C and different BEP

Only a slight decrease of the slope can be observed for the samples grown at a higher BEP. At room temperature, the conductivity is for all samples below 10^{-6} 1/Ωcm (Figs 3,4). Thus all samples exhibit a high resistivity. Note that no As precipitates were detected by TEM in samples grown at temperatures above 250°C. Therefore, the high resistivity observed in these samples is not related to the existence of As precipitates, in contrast to the buried Schottky barrier model [8].

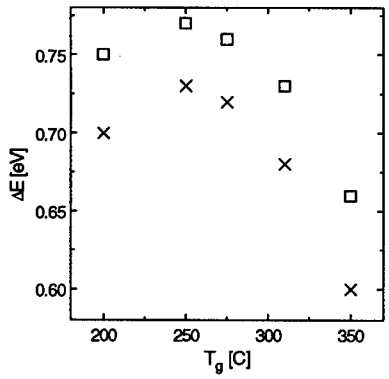


Figure 5: Activation energies ΔE determined from Figure 3 assuming a constant (□) and a $T^{-3/2}$ (×) temperature dependence of the mobility.

To determine the activation energies of the band conduction, two different models for the temperature dependence of the mobility were applied: (a) a $T^{-3/2}$ dependency due to phonon scattering and (b) a constant mobility (Fig.5). The activation energy e.g. for the sample grown at 250°C is estimated to be 0.77 eV assuming a constant mobility. This value agrees with our previous measurements of a n-i-n sample containing a semi-insulating LT-GaAs layer grown at 250°C, where an activation energy of 0.77 eV was determined [13]. Furthermore, it can be deduced, that the activation energy is significantly lower for high growth temperatures, >350°C, compared to lower growth temperatures. Similar low activation energies were previously reported by Look et al., [14] who found an activation energy of 0.65 eV for as grown samples deposited in a temperature range of 200°C to 400°C. Since this result was obtained by measuring the planar conductivity in an Hall effect experiment, the conductivity was dominated by hopping conduction over a wide range of measurement temperatures, which does not allow to clearly evaluate the band conduction contribution. Only at higher growth temperatures one single conduction mechanism, the band conduction, was observed by Look et al. [14], which is in agreement with our value.

The high activation energies at low growth temperatures of about 0.73 to 0.77 eV are close to that of undoped semi-insulating GaAs, in which EL2 is the dominant deep donor. A decrease of the activation energy for higher growth temperatures can be explained in two ways: a decrease of the acceptor concentration which would change the position of the Fermi level, or the involvement of a different deep donor level. The existence of a deep donor level 0.65 eV below the conduction band edge, which is associated with As antisites, has been suggested previously [15].

CONCLUSIONS

LT-GaAs can be deposited with high reproducibility, if the growth conditions are carefully controlled. A well defined As antisite concentration can be achieved by choice of appropriate growth parameters, i.e. substrate temperature and As/Ga flux ratio. In a wide range of growth parameters the As_{Ga} concentration is linearly correlated with the lattice expansion of the LT-GaAs layers. Furthermore, the total amount of As forming the As precipitates in annealed material is the same within the margins of error as the neutral As_{Ga} concentration in the as grown samples. These results support the view that the As_{Ga} is the dominant point defect in LT-GaAs. The LT-GaAs layers are characterized by a high electrical resistivity after annealing at 600°C. The

band conduction mechanism in the LT-GaAs layers depends on the growth temperature, since a lower activation energy is found for high growth temperatures. Only slight changes of the temperature dependence of the conductivity were observed in samples grown at different As/Ga flux ratios.

ACKNOWLEDGMENTS

This work was supported by Air Force Office of Scientific Research under grant No. F49620-95-1-0091. The authors thank Z. Liliental-Weber, J. Novak and P. Kordos for fruitful discussions. M.L. is in part supported by a F. Lynen fellowship of the Alexander von Humboldt association.

REFERENCES

[1] Z. Liliental-Weber, J. Ager, D. Look, X. W. Lin, X. Liu, J. Nishio, K. Nichols, W. Schaff, W. Swider, K. Wang, J. Washburn. E. R. Weber, and J. Whitaker, Proc. of the 8th Conf. on Semiinsulating III-V Materials, edited by M Godlewski (World Scientific, 1994)

[2] D. C. Look, D. C. Walters, M. O. Manareh, J. R. Sizelove, C. E. Stutz, and K. R. Evans, Phys. Rev. B, **42**, 3578 (1990)

[3] M.Kaminska, E.R. Weber, Proc. of the 20th Int. Conf. on the Physics of Semicond. edited by: E. M. Anastassakis and J.D. Joannopoulos (World Scientific 1990) p. 473

[4] X. Liu, A. Prasad, J. Nishio, E.R. Weber, Z. Liliental-Weber, and W. Walukiewicz, Appl. Phys. Lett., **67**, 279 (1995)

[5] Z. Liliental-Weber, A. Claverie, J. Washburn, F. Smith and R. Calawa, Appl. Phys. A, **53**, 141 (1991)

[6] M. R. Melloch, N. Otsuka, J.M Woodall, A. C. Warren, and J. L. Freeouf, Appl. Phys Lett., **57**, 1331 (1990)

[7] A. Claverie and Z. Liliental-Weber, Phil. Mag. A, **65**, 981 (1992)

[8] A. C. Warren, J. M. Woodall, F. L. Freeouf, D. Gruschkosky, D. T. McInturff, M. R. Melloch, and N. Otsuka, Appl. Phys. Lett., **57**, 1331 (1990)

[9] M. Luysberg, H. Sohn, A. Prasad, H. Fujioka, R. Klockenbrink, and E.R. Weber, Proc of the SIMC9 accepted for publication

[10] M. Missous and S. O'Hagen, J. Appl. Phys., **75**, 3396 (1994)

[11] M. Lagadas, Z. Hatzopoulos, M. Calamiotou, M. Kayiambaki, and A .Christou, Mat. Res. Soc. Symp. Proc., **325**, 383 (1994)

[12] M. Luysberg, A. Prasad, H. Sohn, P. Specht, E.R. Weber, J. Gebauer, R. Krause-Rehberg to be published

[13] H. Fujioka, E.R. Weber, A. K. Verma, Appl. Phys. Lett., **66**, 2834 (1995)

[14] D. C. Look, G. D. Robinson, J. R. Sizelove, and C. E. Stutz, J. Electron. Mat., **22**, 1425 (1993)

[15] D. C. Look,Z.-Q. Fang, J. R. Sizelove, and C. E. Stutz, Phys. Rev. Lett., **70**, 465, (1993)

INFLUENCE OF DONOR, ACCEPTOR, AND ISOVALENT IMPURITY DOPING ON ARSENIC EXCESS AND POINT DEFECTS IN LOW TEMPERATURE GROWN GaAs

V. V.CHALDYSHEV*, A.E.KUNITSYN*, N.N.FALEEV*, V.V.PREOBRAZHENSKII**, M.A.PUTYATO**, B.R.SEMYAGIN**, and V.V.TRETYAKOV*
*Ioffe Physico-Technical Institute, 194021 St.Petersburg, Russia
**Institute of Semiconductor Physics, 630090 Novosibirsk, Russia

ABSTRACT

We show that in contrast to Si donor and Be acceptor doping, isovalent In impurity doping enhances arsenic excess in the GaAs films grown by molecular beam epitaxy at low temperature. This effect is due to an increase in the concentration of arsenic antisite defects. Gallium vacancy related defects are detected only in the samples annealed at high temperature. Their concentration is found to be higher in the indium-free material than in the indium doped one.

INTRODUCTION

The main feature of GaAs grown by molecular beam epitaxy (MBE) at low temperature (LT GaAs) is a high arsenic excess that provides unique properties of this material [1-5]. The arsenic excess can be varied in a wide range by the growth temperature and As/Ga flux ratio [5,6]. The main problem in this method is the breakdown of the film crystallinity [6], when the growth temperature is too low or the As/Ga flux ratio is too high. Due to this limitation, it seems to be interesting to develop an alternative approach to the enhancement of excess arsenic incorporation at low growth temperature.

In this paper we show that isovalent In impurity doping results in a higher arsenic excess when compared to that in the conventional LT GaAs grown at the same temperature and V/III flux ratio. In contrast to shallow donor or acceptor doping, the indium doping causes an increase of arsenic antisite defect concentration in as-grown films and a decrease of gallium-vacancy-related defect concentration upon annealing.

EXPERIMENT

The GaAs films were grown in a dual-chamber 'Katun' MBE system on undoped semi-insulating 2-inch GaAs substrates with (001) orientation. The growth rate was 1 $\mu m\, h^{-1}$. The following groups of LT GaAs samples were grown at 200°C: (i) conventional undoped films; (ii) Si-doped films with donor concentration of $1\times10^{18}cm^{-3}$; (iii) In-doped films with isovalent impurity concentration of 0.2 at.% and 0.04 at.%; (iv) films doped with both Si ($1\times10^{18}cm^{-3}$) and In (0.2 at.% and 0.04 at.%); (v) films doped with Be acceptors ($1\times10^{18}cm^{-3}$) and isovalent In impurity (0.2 at.%). In addition, undoped LT GaAs films were grown at 150°C. Each sample was divided into four parts, one of which was kept as grown, the others were annealed in the MBE setup under arsenic overpressure for 15 minutes at 400, 500, 600, 700 or 810°C.

Electron probe microanalysis (EPMA) was applied to measure the indium content and to assess the arsenic excess in the samples. A Camebax microanalyser was utilized in these measurements in a special high-sensitivity regime. X-ray diffraction study was carried out using asymmetrical Ge (001) monochromator adjusted for the (004) reflection of $CuK_{\alpha 1}$ radiation. A Philips EM420 transmission electron microscope operating at an accelerating voltage of 100 and

Mat. Res. Soc. Symp. Proc. Vol. 442 © 1997 Materials Research Society

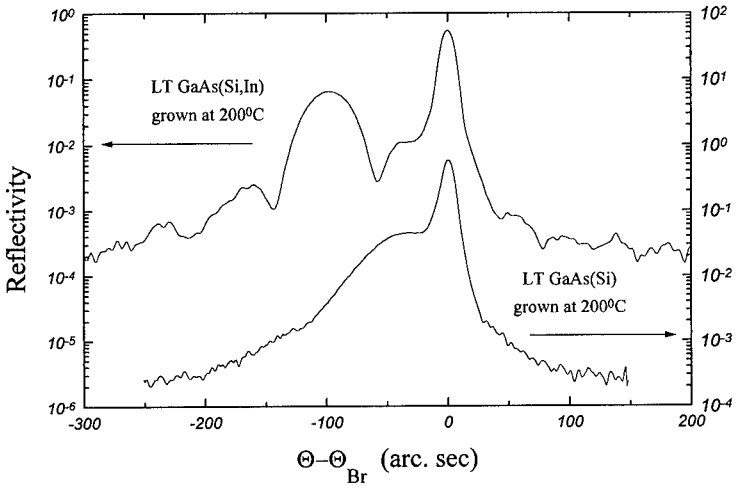


Fig. 1. X-ray rocking curves in the vicinity of GaAs (004) $CuK_{\alpha 1}$ reflection for as-grown LT GaAs films doped with In+Si and with Si only.

120 kV was employed for observation of As clusters in the annealed samples. Photoluminescence spectra were obtained at 4.2 K in the wavelength region 800–1200 nm using an Ar^+ laser for excitation and a cooled photomultiplier as photodetector. Optical absorption spectra were recorded at room temperature in the near infrared region.

RESULTS

The EPMA measurements showed that As excess in the samples was approximately 0.5 at.%, but it varied from one sample to another. It is well known [4] that arsenic excess causes a lattice expansion. Fig.1 shows the x-ray rocking curves for as-grown LT GaAs samples doped with Si and Si+In. Two major peaks on each curve correspond to the substrate and epitaxial layer. An additional interference pattern can be seen for the indium-doped sample whereas it is hardly possible to recognize such a pattern in the sample doped with Si only. The indium-doped sample exhibits, also, a higher reflectivity related to the epitaxial layer. These facts indicate the better quality of the indium-doped sample when compared to the indium-free one. So, indium doping provides abrupt interface, smooth surface, and homogeneous crystal structure. We show below that this improvement accompanies an appreciable increase in arsenic excess.

The major difference between the rocking curves in Fig.1 is that the lattice expansion for the LT GaAs(Si, In) is much larger than that for the LT GaAs(Si). This phenomenon cannot be attributed to 7% difference between In and Ga atom sizes. The indium content in this particular LT GaAs(Si, In) sample was as low as 0.04 at.% and In_{Ga} substitution causes only a tenth of the effect observed. Therefore, we can suppose that the enchanced lattice expansion is due to an increase in arsenic excess. When indium doping is higher, the lattice expansion due to In_{Ga} substitution becomes larger and can be easily deduced from the comparison of as-grown and annealed parts of the same sample, because the contribution of arsenic excess to the expansion disappears upon annealing [4]. Fig.2 shows the lattice mismatch between the LT GaAs layers with indium content of 0.2 at.% and the stoichiometric GaAs substrate. The In_{Ga}-related effect is

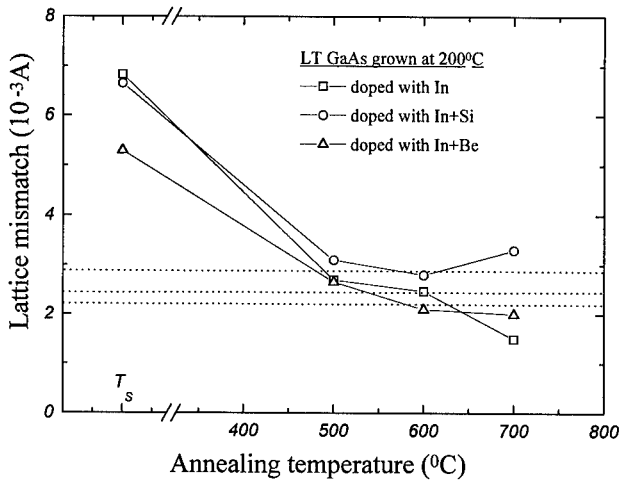


Fig. 2. Lattice mismatch between indium-doped LT GaAs films and GaAs substrate as a function of annealing temperature.

marked in Fig.2 by the horizontal dot lines. The data in Fig.2 show that in contrast to isovalent indium doping, the additional doping with Si donors or Be acceptors leads to a decrease in the lattice mismatch related to arsenic excess. This result is consistent with previous observations [7].

A strong optical absorption was observed for all the as-grown samples in the near infra-red region (Fig.3). It is well known that this absorption relates to arsenic antisite defects [8]. Fig.3(a) shows that As_{Ga}-related optical absorption is two times higher in In-doped LT GaAs(Si) than in In-free LT GaAs(Si) grown under identical conditions. This result is quantitatively consistent with the data of x-ray diffraction study. So, the two independent experimental techniques evidence an appreciable increase in arsenic excess due to indium doping of LT GaAs layers. In contrast to this phenomenon, the Si donor and Be acceptor doping leads to a decrease in arsenic excess (Fig.3(b)). This result of optical measurement is also consistent with x-ray diffraction study. The conclusions on the effect of In, Si, and Be doping are quantitatively supported by direct measurements of arsenic excess using EPMA.

Fig.3(b) shows the infra-red optical absorption in the indium-doped material grown at 200°C and in the conventional undoped LT GaAs grown at 200 and 150°C. A comparison of the spectra allows us to conclude that in respect of arsenic excess the In doping is equivalent to a decrease of the growth temperature by ~20°C.

After annealing both arsenic-excess-related lattice mismatch (Fig.2) and As_{Ga}-related optical absorption (Fig.3(a)) disappear. This is a well known result of arsenic precipitation [4]. We observed As clusters built in GaAs matrix using transmission electron microscopy (TEM). The cluster density was found to be higher and the clusters were bigger in indium doped samples than in indium free ones. This fact also evidences the increase in arsenic excess due to indium doping.

Thus, several independent techniques show a strong enhancement of arsenic excess due to isovalent indium impurity doping of LT GaAs. A possible reason for this phenomenon is the

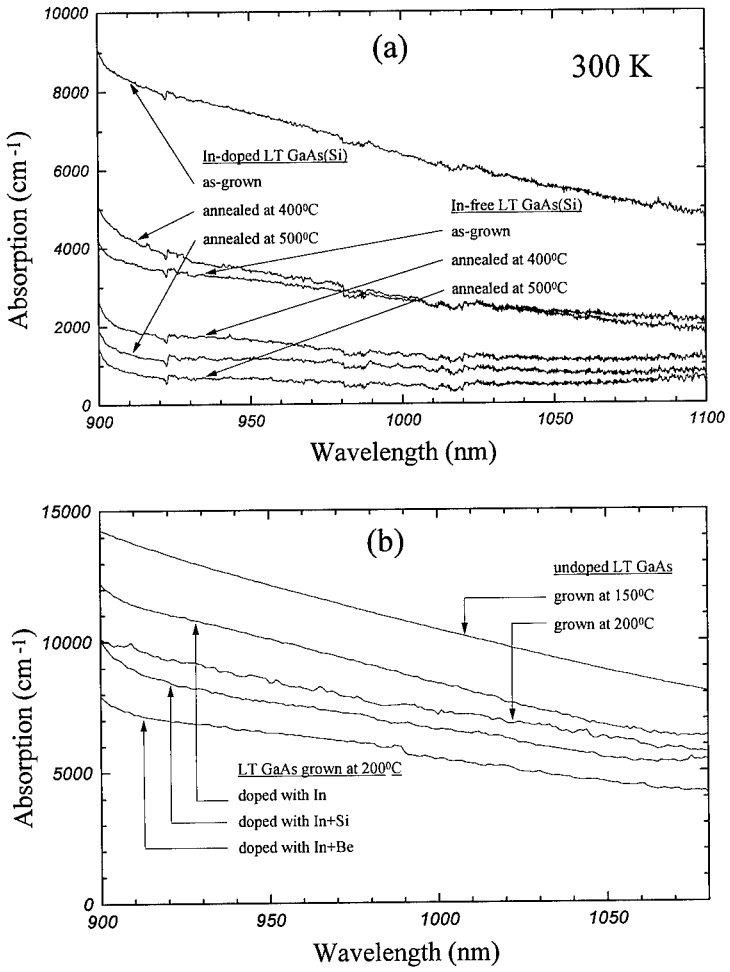


Fig. 3. Optical absorption of LT GaAs films doped with different impurities.

following. It is generally believed that As_{Ga} antisite defect has the As-As bond length larger than the Ga-As bond length in the host matrix [8]. Isovalent In_{Ga} impurity also has the bond length larger than that in the matrix. Therefore, the indium doping should provide lower deformation energy for formation of As_{Ga} defects during the MBE at low temperature. The concentrations of indium impurity and arsenic antisite defect were close to each other. Therefore, the corresponding effect should be strong enough. In contrast to isovalent In impurity, the shallow donors and shallow acceptors mainly induce a coulombic interaction with As antisite defects. This kind of interaction should lead to an increase in As_{Ga} formation energy and, consequently, to a decrease in the defect concentration.

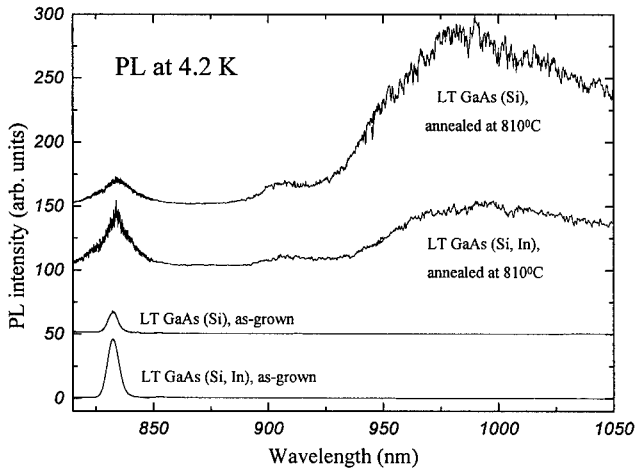


Fig. 4. Low temperature photoluminescence spectra of as-grown and annealed LT GaAs films doped with Si+In and Si only.

Fig.4 shows the photoluminescence spectra of as-grown and annealed LT GaAs films doped with Si and with Si+In. Only a single line related to a residual shallow acceptor was observed in the both as-grown samples. The intensity of this line was very weak due to a short carrier lifetime in LT GaAs [4]. After annealing this line still remains weak. However, it becomes much broader. The broadening can be attributed to electrical fields surrounding As clusters, when the clusters are formed by annealing in Si-doped matrix.

The major feature of the PL spectra of the samples annealed at high temperature is a broad emission band centered at 1.2 eV. This band is usually attributed to Si_{Ga}–V_{Ga} complexes [9]. This band is not observed in the as-grown samples and after annealing at relatively low temperature (≤ 600°C). The appearance of 1.2 eV line indicates an increase in gallium vacancy concentration upon high-temperature annealing of LT GaAs. It can be seen from Fig.4 that the intensity of 1.2 eV line is higher in In-free film than in In-doped one. On one hand, this difference can be attributed to the well known effect of isovalent indium impurity on such kind of defects in gallium arsenide [10,11]. On the other hand, we should take into account that the situation with point defects is different in as-grown state and after annealing. During the low temperature MBE, the concentration of point defects is controlled by the growth kinetics. We have shown that in this case the indium doping causes an increase in the concentration of non-stoichiometry-related defects. However, upon the high temperature annealing, the point defects are in equilibrium with the cluster system. According to the thermodynamic law, the bigger are the As clusters, the lower is the concentration of the point defects related to excess arsenic. Using TEM we do observe that the As clusters in the LT GaAs(Si,In) annealed at 810°C are bigger than those in LT GaAs(Si) grown and annealed under identical conditions.

CONCLUSIONS

We have shown that isovalent In impurity doping causes an increase of arsenic excess in GaAs films grown by molecular-beam epitaxy at low temperature, whereas Si donor or Be

acceptor doping lead to an opposite effect. The phenomenon seems to be due to different interaction mechanisms of the impurities with As antisite defects. The use of indium doping is attractive for enchancement of the arsenic excess in LT GaAs, because it is accompanied by improvement of the interface and crystalline quality of the films.

No evidence for gallium vacancy related defects was found by photoluminescence study in as-grown films and in the films annealed at low temperature (≤ 600°C). However, a high concentration of V_{Ga}-Si_{Ga} complexes was revealed in the samples annealed at high temperature (700-850°C).The concentration of these complexes was found to be higher in In-free LT GaAs(Si) films than in indium-doped ones.

ACKNOWLEDGMENT

The work was carried out under Russian National Programs: Physics of Solid State Nanostructures and Fullerenes and Atomic Clusters. It was also supported by Russian Foundation for Basic Research under Grant No. 95-02-05532. The authors are grateful to Dr. N.A.Bert and Dr. Yu.G.Musikhin for TEM study.

REFERENCES

1. F.W.Smith, A.R.Calawa, C.L.Chen, M.J.Mantra, and L.J.Mahoney, Electron Dev.Lett. ***9***, 77 (1988).

2. M.Kaminska, Z.Liliental-Weber, E.R.Weber, T.George, J.B.Kortright, F.W.Smith, B.Y.Tsaur, and A.R.Calawa, Appl.Phys.Lett. 54, 1831 (1989).

3. M.R.Melloch, K.Mahalingam, N.Otsuka, J.M.Woodall, and A.C.Warren, J.Cryst.Growth 111, 39 (1991).

4. N.A.Bert, A.I.Veinger, M.D.Vilisova, S.I.Goloshchapov, I.V.Ivonin, S.V.Kozyrev, A.E.Kunitsyn, L.G.Lavrentieva, D.I.Lubyshev, V.V.Preobrazhenskii, B.R.Semyagin, V.V.Tretyakov, V.V.Chaldyshev, and M.P.Yakubenya, Phys.Solid State 35, 1289 (1993).

5. N.A.Bert, V.V.Chaldyshev, S.I.Goloshchapov, S.V.Kozyrev, A.E.Kunitsyn, V.V.Tretyakov, A.I.Veinger, I.V.Ivonin, L.G.Lavrentieva, M.D.Vilisova, M.P.Yakubenya, D.I.Lubyshev, V.V.Preobrazhenskii, and B.R.Semyagin, in: Physics and Applications of Defects in Advanced Semiconductors (Mat. Res. Soc. Symp. Proc. 325, 1994), pp.401-406.

6. Z.Liliental-Weber, W.Swider, K.M.Yu, J.Kortright, F.W.Smith, and A.R.Calawa. Appl.Phys.Lett. 58, 2153 (1991).

7. R.E.Pritchard, S.A.McQuaid, L.Hart, R.C.Newman, J.Makinen, H.J. von Bardeleben, and M.Missous. J. Appl. Phys., ***78***, 2411 (1995)

8. X.Liu, A.Prasad, J.Nishio, E.R.Weber, Z.Liliental-Weber, and W.Walukiewicz. Appl. Phys. Lett. 67, 279 (1995).

9. A.A.Gutkin, N.S.Averkiev, M.A.Reshchikov, and V.E.Sedov. Mat. Sci. Forum 196-201, 231, (1995).

10.Yu.F.Biryulin, N.V.Ganina, M.G.Milvidskii, Yu.V.Shmartsev and V.V.Chaldyshev. Sov. Phys. Semicond., 17, 108 (1983)

11.V.V.Chaldyshev, E.V.Astrova, A.A.Lebedev, I.A.Bobrovnikova, N.A.Chernov, O.M.Ivleva, L.G.Lavrentieva, I.V.Teterkina, and M.D.Vilisova. J. Cryst. Growth, 146, 246 (1995)

HIGH-TEMPERATURE REORIENTATION OF DISTORTIONS IN THE EXCITED STATE OF THE $V_{Ga}Te_{As}$ COMPLEXES IN n-TYPE GaAs

A. A. GUTKIN, M. A. RESHCHIKOV, V. E. SEDOV
Ioffe Physical-Technical Institute, 26 Polytechnicheskaya, St.-Petersburg 194021, Russia, agut@defect.ioffe.rssi.ru

ABSTRACT

We have investigated polarization of photoluminescence from the $V_{Ga}Te_{As}$ complexes in n-GaAs induced through resonant excitation by polarized light. Experimental data in temperature range from 77 to 240 K were described by classic one-dipole approximation within the model of the $V_{Ga}Te_{As}$ complex subjected to the Jahn-Teller distortion in the ground and excited states. It is shown that depolarization of photoluminescence at temperatures over $\sim$ 120 K may be explained by concurrent action of i) thermal emission and back capture of holes bound to the complexes in the excited state and ii) reorientation of complex distortion during a life of this state. The model parameters have been estimated.

INTRODUCTION

Complexes involving a gallium vacancy (V_{Ga}) and a shallow donor (Te_{As}, Sn_{Ga}, Si_{Ga}) in bulk n-type GaAs are supposed to give rise to a wide photoluminescence (PL) band with a maximum at photon energy ($\hbar\omega$) of $\sim$1.2 eV [1]. This band is caused by recombination of an electron from conduction band or from the state close to its bottom with a hole in a deep state localized at the complex [1,2].

Investigations of the PL from the $V_{Ga}Te_{As}$ complexes at low temperatures (2 and 77 K) with application of uniaxial pressure or at polarized resonant excitation [3-6] allowed us to suggest a phenomenological model of this complex explaining qualitatively its observed properties. According to this model [4,7,8], the initial trigonal symmetry of the $V_{Ga}Te_{As}$ complex is distorted in the excited state due to the Jahn-Teller effect, i.e. to interaction of a hole captured by the complex with partly symmetrical oscillations of atoms surrounding V_{Ga}. This lowers the complex symmetry down to monoclinic and each defect has three equivalent monoclinic configurations corresponding to three possible orientations of the Jahn-Teller distortion (Fig. 1) in the same manner as for the vacancy-donor complexes in Si [9-11] binding three holes. The symmetry plane of the {110}-type in each complex holds the initial complex axis, i.e. the line which joins the lattice sites corresponding to initial positions of two complex components. Reorientation of the Jahn-Teller distortion (a change-over to another configuration) implies a rotation of the symmetry plane around the initial complex axis through $\pm 120^0$ (Fig. 1). The ground state of the complex is distorted in a similar manner [5,6]. So, an axis of dipole describing the emission (or absorption) of the light by the defect should lie in the symmetry plane and vary its direction along with rotation of this plane. Hereafter we shall describe the position of this axis by an angle φ, measured from the $< 110 >$ axis lying in the symmetry plane (Fig. 1). At temperatures up to 77 K reorientation of the distortion of the $V_{Ga}Te_{As}$ complex in GaAs occurs only in the ground state. However at elevated temperatures reorientation in the excited state may become essential. In this work for investigation of this reorientation we studied the temperature dependences of linear

Mat. Res. Soc. Symp. Proc. Vol. 442 © 1997 Materials Research Society

polarization of the $V_{Ga}Te_{As}$ PL induced by resonant polarized light (with photon energy of 1.34-1.47 eV) at temperatures up to 240 K.

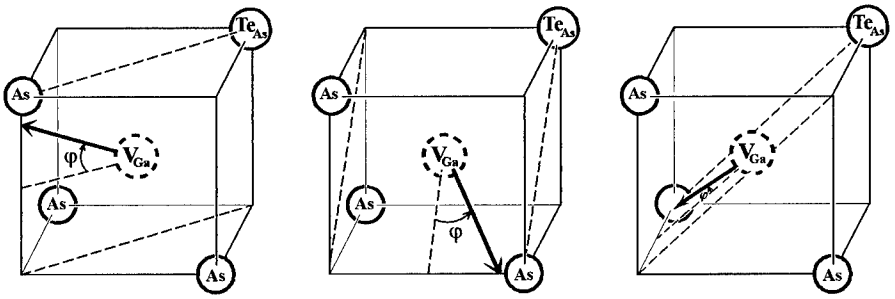


Fig. 1: Three equivalent configurations of the $V_{Ga}Te_{As}$ complex in GaAs. Arrow indicates the axis of optical dipole.

FEATURES OF PHOTOLUMINESCENCE FROM MONOCLINIC REORIENTABLE COMPLEXES WITH THE FIXED < 111 > AXIS

For analysis of the experimental data we calculated some characteristics of the steady-state PL from defects under study within the above-mentioned model. In doing so we allowed for possible reorientation of the Jahn-Teller distortion during a life of the excited state and also for thermal emission and back capture of holes by the complexes. The calculations were carried out in the framework of the classic dipole approximation in which optical characteristics of defect were simulated by a superposition of a linear oscillator and a rotator considered as incoherent [12]. Besides, we assumed the following.

1. Distortions of the complex in the ground and excited states are alike, namely, directions of axes of the emitting and absorbing dipoles coincide and relative contributions of a linear oscillator and a rotator to absorption and emission are the same (one-dipole approximation).

2. Each complex lives in the ground state sufficiently long time (since the excitation intensity is weak) and the time of reorientation in this state is small, so all possible configurations of individual complex in the ground state are equally probable.

We used the orthogonal scheme of experiment with mutually perpendicular directions of exciting light flow and observation of PL. Direction of electric vector of the exciting light wave was characterized by an angle η between this vector and the axis perpendicular both to directions of exciting and observed light flows. The measured degree of polarization appears as

$$\rho(\eta) = [I_{\|}(\eta) - I_{\perp}(\eta)]/[I_{\|}(\eta) + I_{\perp}(\eta)], \quad (1)$$

where $I_{\|}(\eta)$ and $I_{\perp}(\eta)$ are intensities of PL with electric vector of the light wave directed respectively parallel and perpendicular to the axis from which the angle η is counted. The most extensively studies have been made for two crystal orientations about directions of

excitation and observation of PL: [110]-[001] and [100]-[010] (the first is a direction of excitation and the second indicates the observation direction). For both cases the extreme values of ρ correspond to $\eta = 0$ and $\eta = 90°$. Calculations under the above-mentioned assumptions result in the following expressions

$$\rho(\eta{=}0) = \rho_1 = \frac{1 + (1-m)\tau_0 c_p p_1}{1 + \tau_0 c_p p_1} \frac{f_1 + \frac{\tau}{\tau_0}(1 + \tau_0 c_p p_1) f_2}{f_3 + \frac{\tau}{\tau_0}\left[(1 + \tau_0 c_p p_1) f_4 - \frac{1}{3} m \tau_0 c_p p_1 f_5\right]} \tag{2}$$

for the [110]-[001] scheme and

$$\rho(\eta{=}0) = \rho_2 = \frac{1 + (1-m)\tau_0 c_p p_1}{1 + \tau_0 c_p p_1} \frac{\frac{\tau}{\tau_0}(1 + \tau_0 c_p p_1) f_5}{f_3 + \frac{\tau}{\tau_0}\left[(1 + \tau_0 c_p p_1) f_4 - \frac{1}{3} m \tau_0 c_p p_1 f_5\right]} \tag{3}$$

for the [100]-[010] scheme. Here τ is a characteristic time of distortion reorientation in the excited state, τ_0 is the life time of the excited state, $c_p p_1$ is the rate of thermal emission of holes into the valence band (c_p is the rate of capture of holes by the complex and p_1 is the concentration of holes in the valence band when the Fermi level coincides with the level of the complex), m is the ratio between the rate of capture of holes by the studied complexes and the total rate of escape of holes from the valence band (due to capture by all defects and to interband recombination), $f_1 \div f_5$ are values depending only on the dipole parameters and independent of temperature

$$\begin{aligned}
f_1 &= (1-2\beta)^2 (cos\varphi - 2\sqrt{2} sin\varphi)^2 cos^2\varphi \\
f_2 &= 2(1-2\beta)^2 (cos^2\varphi + 4 sin^2\varphi) cos^2\varphi \\
f_3 &= 4(1+\beta)^2 \\
f_4 &= (cos^2\varphi + 2 sin^2\varphi + 2\beta cos^2\varphi)^2 + 2(cos^2\varphi + 2\beta sin^2\varphi)^2 \\
f_5 &= (1-2\beta)^2 (cos^2\varphi - 2 sin^2\varphi)^2,
\end{aligned} \tag{4}$$

where β is a coefficient characterizing relative contributions of a linear oscillator and a rotator to the absorption and emission of defect ($\beta = 0$ for "pure" oscillator and $\beta = 1$ for "pure" rotator).

For both considered orientations of a crystal

$$\rho(\eta{=}90^0) \equiv 0. \tag{5}$$

Expressions (2) and (3) show that the decrease of the induced polarization of PL with increase in temperature may be caused as by increase of probability of the distortion reorientation in the exciting state, so by the rise of excited complexes with arbitrary directions of the initial axis and any directions of the distortion what happens due to thermal emission and back capture of holes by the complexes.

Thermal emission of holes results also in decrease of intensity of PL from the complexes [2] which at interband excitation is governed by the following expression

$$I = I_0/[1 + (1-m)\tau_0 c_p p_1], \tag{6}$$

where I_0 is the PL intensity at low temperatures when the thermal emission and capture do not occur. It is significant that at $\eta = 0$ the ratio between polarization degrees for two schemes mentioned above is independent of β and at low temperature, when $\tau/\tau_0 \to \infty$, is

$$\frac{\rho_1}{\rho_2} = \frac{2(cos^2\varphi + 4 sin^2\varphi) cos^2\varphi}{(cos^2\varphi - 2 sin^2\varphi)^2}. \tag{7}$$

EXPERIMENTAL RESULTS AND DISCUSSION

We studied bulk Czochralski grown samples of n-GaAs:Te with different electron concentrations ($2 \cdot 10^{17} - 10^{18}$ cm^{-3}). Method of study of PL, its polarization and excitation spectra were the same as in [5]. PL spectra of the 1.2 eV band associated with the $V_{Ga}Te_{As}$ complexes and spectra of its excitation for one of the samples at different temperatures are shown in Fig. 2. At temperatures less than $\sim$ 140 K the 1.2 eV band varied little with tem-

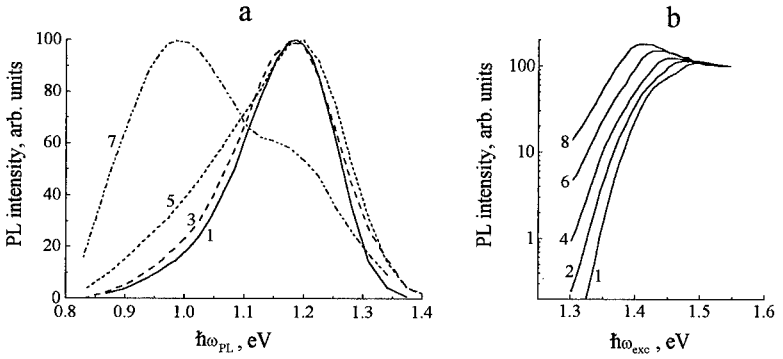


Fig. 2: PL spectra at $\hbar\omega_{exc} = 1.96$ eV (a) and PL excitation spectra at $\hbar\omega_{PL} = 1.2$ eV (b) at various temperatures. T, K: 1 - 80; 2 - 120; 3 - 150; 4 - 160; 5 - 180; 6 - 200; 7 - 230; 8 - 240.

perature. On further heating the intensity of this band falls and because of this the relative intensity of a band with a maximum at $\sim 0.95\ eV$ (related to another complex with deeper level [13]) increases. Figure 3 illustrates the temperature dependence of total intensity of the

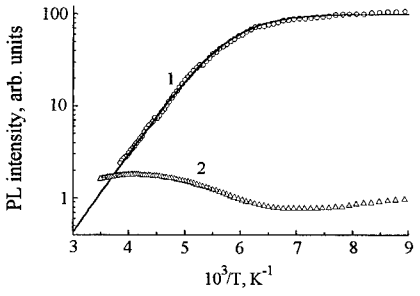


Fig. 3: PL intensity of the 1.2 eV (1) and "quasiinterband" (2) bands vs temperature for a sample with $n \approx 5 \cdot 10^{17} cm^{-3}$. $\hbar\omega_{exc} = 1.96\ eV$. Solid line is calculated using expression (6) with the following parameters. $m = 0.75$, $\tau_0 = 10^{-6}$s, $E_T = 170\ meV$, $c_p p_1 = 7 \cdot 10^{10} \cdot \exp(-E_T/kT)$ s^{-1}.

1.2 eV band. As noted in previous section, it is associated with thermal emission of holes from the complexes. One can find from this dependence the value of $(1-m)\tau_0 c_p p_1$ in the temperature range where it is of the order of 1 or more, and also an activation energy for thermal emission of holes E_T. The closest agreement was found for all investigated samples at $E_T = 170$ meV.

Behavior of the induced polarization of the PL was studied at PL excitation by light with photon energies less than the width of the gap (E_g). The value of ρ at $\eta = 0$ raised and then saturated with decrease in photon energy $\hbar\omega_{exc}$. Such a dependence is associated with unresonant excitation in a part of complexes at $\hbar\omega_{exc}$ close to E_g. For comparison with expressions (2) and (3) we used the values of $\rho(\eta{=}0)$ from the saturation region where the excitation is pure resonant. The temperature dependence of this value for one of the samples oriented as [110]-[001] is shown in Fig. 4. A similar dependence is evident for the [100]-[010]

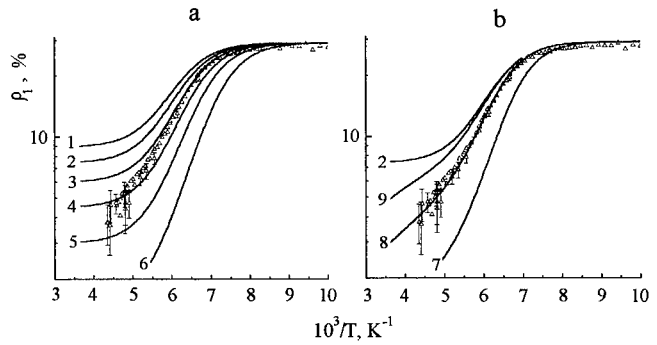


Fig. 4: Temperature dependence of $\rho(\eta = 0)$ for a sample with $n \approx 5 \cdot 10^{17} cm^{-3}$ oriented as [110]-[001]. $\hbar\omega_{exc} = 1.35 \div 1.36\ eV$, $\hbar\omega_{PL} = 1.20 \div 1.25\ eV$. Curves are calculated using expressions (2) and (8) in case of $\tau/\tau_0 \to \infty$ (a) and in general case (b). Parameters for calculations. m: 1 - 0.7; 2,7,8,9 - 0.75; 3 - 0.8; 4 - 0.85; 5 - 0.9; 6 - 0.95. E_B, meV : $1 \div 6 - \infty; 7 - 200; 8 - 225; 9 - 250$. $\varphi = 15°$. $\beta = 0.15$, other parameters are the same as in Fig. 3.

sample orientation. The value of $\rho(\eta{=}90°)$ was zero in the same region of excitation spectrum at any temperature what is consistent with (4). According to (2) and (3) an independence of ρ_1 and ρ_2 from temperature at $T \leq 120$ K indicates the lack of reorientation in the excited state ($\tau/\tau_0 \to \infty$) and of thermal emission of holes from complexes ($\tau_0 c_p p_1 \ll 1$). The values of ρ_1 and ρ_2 in this temperature range were about the same for all samples and comprise of $\rho_{10} \approx 29\%$ and $\rho_{20} \approx 9\%$ what gives according to (7) $\varphi \simeq \pm 15°$ or $\varphi \simeq \pm 51°$. One can find then from (2) or (3) using experimental values of ρ_{10} or ρ_{20} that $\beta \approx 0.15$.

As discussed above, the decrease of ρ_1 and ρ_2 at $T \geq 120$ K may be caused by two reasons. If the decrease is associated only with thermal emission and back capture of holes ($\tau/\tau_0 \to \infty$), according to (2) and (3), the temperature dependence of ρ_1, ρ_2 is governed only by the dependence of $\tau_0 c_p p_1$. The latter may be found from the $I(T)$ dependence (Fig. 3) for given m. The calculated in such a manner dependence of $\rho_1(T)$ at various m is shown in Fig. 4a. Much better agreement may be obtained if, along with the emission and back capture of holes, the reorientation of the complex distortion in the emitting state is taken into account (Fig. 4b). Supposing in so doing that

$$\tau = \nu^{-1} \exp(E_B/kT), \tag{8}$$

we have reached an adequate fit of the equation to the data for investigated camples at $E_B \approx 200 - 250\ meV$ and $\nu^{-1} \approx 10^{-11} - 10^{-13}\ s$. The value of τ_0 in this case varied from

$\sim 0.5 \cdot 10^{-6} s$ to $\sim 1.5 \cdot 10^{-6} s$ for the samples with electron concentration from $10^{18} cm^{-3}$ to $2 \cdot 10^{17} cm^{-3}$ respectively what is in good agreement with the values of τ_0 obtained in [14]. In these fits the value of m varied from 0.4 to 0.9 with increase of electron concentration from $2 \cdot 10^{17} cm^{-3}$ to $10^{18} cm^{-3}$ what is in good agreement with the values we have found from increase of quasi-interband PL observed along with decrease of intensity of the 1.2 eV band at elevated temperatures (Fig. 3). Notice that good agreement between theory and observation has been obtained only at $\varphi = +15°$.

CONCLUSIONS

The analysis performed indicates that polarization of the 1.2 eV PL band at resonant excitation by polarized light in wide temperature range may be described well within the model of the $V_{Ga}Te_{As}$ complex suggested in [4,7,8]. It is shown that depolarization of this band at temperatures over ~ 120 K may be explained by concurrent action of transport of excitation to the complexes with arbitrary orientations (due to thermal emission and back capture of holes by the complexes) and of distortion reorientation during a life of the excited state of the complex. The activation energy for such a reorientation is about 200 - 250 meV.

ACKNOWLEDGEMENTS

The work was partly supported by RFFI (Grant No. 95-02-04146-a).

REFERENCES

1. E. W. Williams, Phys. Rev. **168**, 922 (1968).
2. K. D. Glinchuk, A. V. Prokhorovich, V. I. Vovnenko, phys. stat. sol. (a) **34**, 777 (1976).
3. N. S. Averkiev, A. A. Gutkin, E. B. Osipov, M. A. Reshchikov, V. R. Sosnovskii, Fiz. Tekh. Poluprovodn. **26**, 1269 (1992) [Sov. Phys. Semicond. **26**, 708 (1992)].
4. A. A. Gutkin, N. S. Averkiev, M. A. Reshchikov, V. E. Sedov in *Defects in Semiconductors 18*, edited by M. Suezawa and H. Katayama-Yoshida (Materials Science Forum, **196-201**, pt. 1, 1995) pp. 231-235.
5. N. S. Averkiev, A. A. Gutkin, E. B. Osipov, M. A. Reshchikov, V. E. Sedov, V. R. Sosnovskii, Fiz. Tekh. Poluprovodn. **25**, 50 (1991) [Sov. Phys. Semicond. **25**, 28 (1991)].
6. A. A. Gutkin, M. A. Reshchikov, V. E. Sedov, Zeitschrift fur Physikalische Chemie (to be published).
7. N. S. Averkiev, A. A. Gutkin, M. A. Reshchikov, V. E. Sedov, Fiz. Tekh. Poluprovodn. **30**, 1123 (1996) [Semiconductors **30**, 595 (1996)].
8. A. A. Gutkin, M. A. Reshchikov, V. R. Sosnovskii, Fiz. Tekh. Poluprovodn. **27**, 1516 (1993) [Semiconductors **27**, 844 (1993)].
9. G. D. Watkins, J. W. Corbett, Phys. Rev. **134**, 1359 (1964).
10. E. L. Elkin, G. D. Watkins, Phys. Rev. **174**, 881 (1968).
11. X.-Q. Fan, S.-G. Shen, D.-X. Zhang, Phys. Rev. **B 42**, 9501 (1990).
12. E. E. Bukke, N. N. Grigor'ev, M. V. Fok, Trudy FIAN **79**, 108 (1974).
13. A. A. Gutkin, M. A. Reshchikov, V. R. Sosnovskii, Semicond. Sci. Technol. **9**, 2247 (1994).
14. K. D. Glinchuk, A. V. Prokhorovich, V. E. Rodionov, Fiz. Tekh. Poluprovodn. **11**, 35 (1977).

CHARACTERIZATION OF APB's IN GaP

DOV COHEN, C. BARRY CARTER
Department of Chemical Engineering and Materials Science, University of Minnesota
421 Washington Ave S.E., Minneapolis, MN 55455

ABSTRACT

Antiphase boundaries in GaP crystals epitactically grown on Si (001) have been characterized using transmission electron microscopy. Convergent-beam electron diffraction was used to identify the antiphase-related grains. The antiphase boundaries were observed to adopt facets parallel to specific crystallographic orientations. Furthermore, stacking-fault-like contrast was observed along the interface suggesting that the domains may be offset from one another by a rigid-body lattice translation.

INTRODUCTION

The electronic and optical properties of semiconductor crystals are strongly influenced by the presence and nature of planar faults. In order to obtain greater insight into these physical properties, and the mechanism responsible for the formation of planar faults during crystal growth, the structure properties and chemical compostion of such faults need to be understood. In the sphalerite structure, the antiphase boundary (APB) is amongst the least complex planar defect which can be studied. APBs are planar defects can form during heteroepitactical crystal growth due to a crystal symmetry mismatch between the epilayer and substrate. Compound semiconductor crystals which possess the sphalerite structure, such as GaP, consists of two chemically distinct interpenetrating face-centered cubic sublattices. In GaP, one sublattice is occupied by Ga atoms, the other by P atoms. The sublattices are offset from one another by a vector a/4[111] which defines the polar axis from cation to anion. In a crystal without antiphase disorder, the allocations of sublattices will be the same throughout the crystal. However, if the sublattice ordering is reversed somewhere within the crystal, an antiphase boundary will form along the interface between the domains of opposite polarity.[1] The only crystallographic difference between the two domains is the exchange of the Ga and P atoms in the lattice. Hence, the structure of an APB can be thought of as a Σ=1 grain boundary.[2] The bonding across APB is composed of a mixture of antisite bonds (i.e. Ga-Ga and P-P) and normal Ga-P bonds. The combination of the different bonding characteristics along this interface is believed to be responsible for the experimenatally observed structural properties. Therefore, an investigation of the structural properties of APBs will enable us obtain a greater insight into the bonding characteristics of these materials.

Antiphase boundaries can form in GaP when grown on Si (001) substrates. Due to their similar lattice parameters and thermal expansion coefficients, GaP and Si can be grown epitactically on one another. Since, the diamond lattice lacks a polar ordering of sublattices, GaP crystals can grow on Si (001) substrates in two different polar orientations. Thus, APBs can form during crystal growth along a plane where two GaP islands of opposite polarity coalesce, as illustrated in Figure 1. Alternatively, APBs can nucleate if the Si substrate contains a/4[001] steps on the surface.[3] Thus, an antiphase boundary can form even if the Si surface is completely covered by an P or Ga layer during the growth of the first monolayer of GaP.

The existence of APBs was originally suggested by Holt[1], and experimental studies of the structural properties of APBs in GaP[4,5] , GaAs,[3,6,7,8,9] SiC[7,10], as well as AlN [11] have been carried out over the past twenty years. The purpose of this paper is illustrate recent efforts to further characterize the structural properties of APBs in GaP

Mat. Res. Soc. Symp. Proc. Vol. 442 © 1997 Materials Research Society

EXPERIMENT

The GaP epilayers examined in this study have been grown by gas-source molecular-beam epitacty (GSMBE, Riber 32P) on Si (001) substrates. In the GSMBE chamber, the Ga and P sources consisted of solid Ga and phosphine (PH_3), respectively. The substrate was cleaned prior to insertion to the MBE chamber following a procedure developed by Ishizaka and Shiraki.[12] A thin layer of oxide grown during substrate preparation was thermally desorbed at 820 ^{o}C in the MBE chamber. The desorption of the oxide layer was monitored *in situ* by reflection high-energy electron diffraction (RHEED).

The GaP layers were grown using a two step growth procedure. Initially, the GaP growth proceeded at a substrate temperature 400 $\pm$ 50 ^{o}C with a growth rate of 0.3 μm/hr until a thickness of ~300 nm. Conventional homoepitactial growth at ~550 ^{o}C followed with a typical growth rate of 0.5 μm/hr. Growth rates were calibrated by RHEED oscillations measured for GaAs growth. The total thickness of the GaP epilayer grown on Si was ~2 μm.

The epilayers were prepared for examination in the transmission electron microscope (TEM) by a combination of mechanical dimpling and polishing. Three-millimeter-diameter discs were cored from the wafer. Afterwards, the sample was mechanically dimpled and polished from the Si side and ion-thinned to perforation using 4 keV Ar ions. TEM examination was performed using a Phillips CM-30 operating at 300 keV.

RESULTS

A typical (200) dark-field image of an APB in GaP observed in this study is shown in Figure 2. The APB can be identified by a dark stacking-fault-like fringe contrast enclosing an island whose crystal polarity is opposite to that of the surrounding matrix crystal. A large density of such regions were found in the GaP epilayer, with sizes ranging from 300 to 600 nm in diameter. The observed dark contrast along the boundary in the (200) dark field image is due to a phase change, α_{hkl}, arising from an exchange of the structure factors along the interface. Images formed from {hkl} reflections with $h + k + l = 4n \pm 2$ (n=0,1,2,...) are sensitive to differences in the structure factors on either side of the APB since this effect will introduce a π phase difference in the electron beam as it crosses the interface. The APB appears to be irregularly shaped, adopting habit planes which change through many different crystal orientations. However, there are segments of the interface which tend to adopt directions parallel to specific crystallographic planes with straight sections which are nearly edge-on. For example, segments A is nearly edge-on and lies parallel to the {110}. Segments B, C and D, while curved, appear to adopt facet directions which are parallel to the {110}, {1$\bar{1}$0} and {010} planes. The curved nature of these segments may be partially due to distortions in the lattice which are seen to interact with the APB.

In order to confirm that these stacking-fault-like defects corresponded to APBs, the polarity of the islands and surrounding matrix was determined using a convergent-beam electron diffraction technique (CBED).[13] In this technique, the crystal is oriented to a two beam condition using the (200) reflection and uses the constructive and destructive dynamical interactions with reflections in the high order Laue zone to indicate the sense of the crystal polarity. The CBED polarity technique requires a thick sample in order to generate sufficient dynamical scattering. Therefore, isolated antiphase domains in a thicker regions of the sample were analyzed. Images of two CBED patterns taken inside and outside the APB domain are shown in Figure 3. The direction of the dark cross in the (200) disk indicates the sense of the direction of the cation to anion. The CBED pattern of the matrix shows a dark cross residing in the (200) reflection. While the CBED pattern from the island region the dark cross lies in the ($\bar{2}$00) disk. Thus, confirming that the two domains surrounded by the boundary are in antiphase relationship to one another.

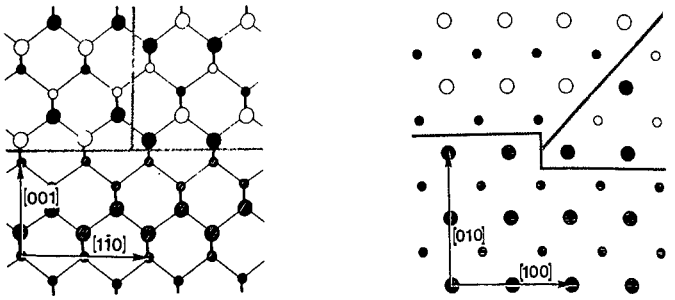


Fig. 1 Mechanisms for the initiation of antiphase boundaries on the (001) Si surface.
a) Nucleation of an vertical antiphase boundary by the coalescence of two GaP islands which are antiphase to one another. b) Formation of an inclined anitphase boundary due to the presence of a a/4[001] vertical step on the Si (001) surface.

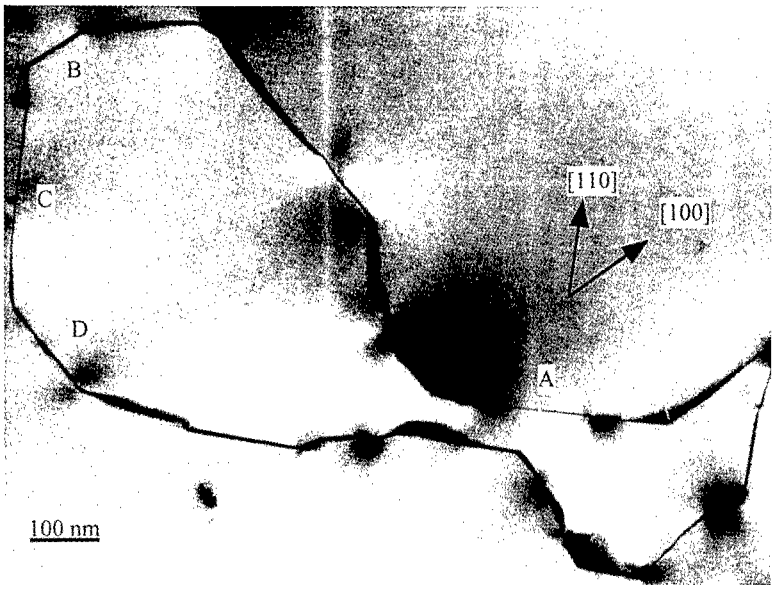


Fig. 2 (200) dark-field image of an antiphase boundary in GaP. The interface appears to be irregularly shaped. However, segments of the interface do tend to adopt directions parallel to specific crystallographic planes. Segments A and C facet nearly parallel to the {110} planes. Segments B and D facet along the {100} planes. Note that the facet along segement A is nearly edge-on.

The stacking-fault-like fringes surrounding along the APB suggests that a rigid-body lattice translation may also exist between adjacent domains. An electron beam crossing an APB may experience a phase change, α_{hkl}, arising from the differences in the structure factors as well as a phase change of $2\pi\mathbf{g}.\mathbf{R}$ due to rigid-body lattice translations, where **R** is the displacement vector describing the relative translation of the two domains with respect to one another. Since structural phase difference, α_{hkl}, is small for images formed with the (220) reflection, fringes along the APB present in the (220) dark-field image strongly suggest that **g.R** contrast may be present at this boundary.[8]

DISCUSSION

In the TEM images, APBs in GaP do possess a tendency to adopt facets along directions parallel to specific crystallographic planes. While the large regions of the boundary have a curved structure, the boundary has adopted distinctive facets which are at 45 degrees to one another.. The curved nature of this interface may be due to an artifact from the crystal growth. Furthermore, defects at the GaP/Si interface and threading dislocations may influence the observed shape of the APB structure locally distorting the crystal lattice. Since APBs are planar defects in the bulk lattice, a 2 μm thick film may be insufficient for the APBs to adopt their equilibrium configuration during crystal growth. Additional analysis of these interfaces in thicker GaP films will be necessary to further understand their structural properties.

The observed tendency of APBs in GaP to facet along specific orientations is consistent with observations of APBs in other crystals possessing the sphalerite structure. APBs in SiC exhibit pronounced faceting.[7]. While APBs in GaAs have been observed to adopt curved habit planes, distinct faceting has been observed along the {110} and to a lesser degree {111} planes.[6] Morizane original study of APBs in GaP reported an absence of faceting along any particular crystallographic planes; the GaP films grown in this study were 1 micron thick and may also have not adopted an equilibrium configuration.[4]

In order to understand the tendency of APBs to facet preferential along specific planes, it is necessary to consider the interfacial energy associated with the individual planes. A simple structural model of the APB considers the interfacial energy to be due to bonding characteristics across different crystallographic planes.[1] The bonding across an APB contains antisite bonds which pair like atoms, for example Ga-Ga and P-P. The antisite bonds introduce localized charges along the interface and may locally alter the stoichiometry of the crystal depending upon their number. Hence, the interfacial energy depends upon the number and stoichiometry of antisite bonds which is a function of the different orientations of for an APB. As illustrated in Figure 4, APBs lying parallel to the {110} and {112} planes will possess an equal number of antisite bonds, and therefore preserve the crystal's chemical stoichiometry Along the {113}plane, the number of antisite bonds are unequal. While APBs lying along the {100}and {111}planes will consist entirely of antisite bonds of one type.[1,8]

In addition to preferentially facet, the structure of APBs may be complicated by the presence of rigid-body translations of adjacent domains across the interface. Rigid-body translations may originate from the presence of antisite bonds of lengths different to the normal Ga-P bonds which could alter the volume of the interface. Alternatively, APBs may lower their interfacial energy by a lattice translation to accommodate distortions induced by an interface composed of a mixture of atomic-bonds of unequal lengths, i.e. Ga-Ga and P-P. Such rigid body lattice translations have been observed in APBs in GaAs, where the grains adjacent to the {110} facet were translated parallel to the boundary by 0.019 nm. This parallel translation sheared the two domains along the interface in order to accommodate the different antisite bond lengths between Ga-Ga and As-As.[6] Additional experiments need to be performed on the GaP APB in order to determine the direction and magnitude of rigid body lattice translations along these interfaces.

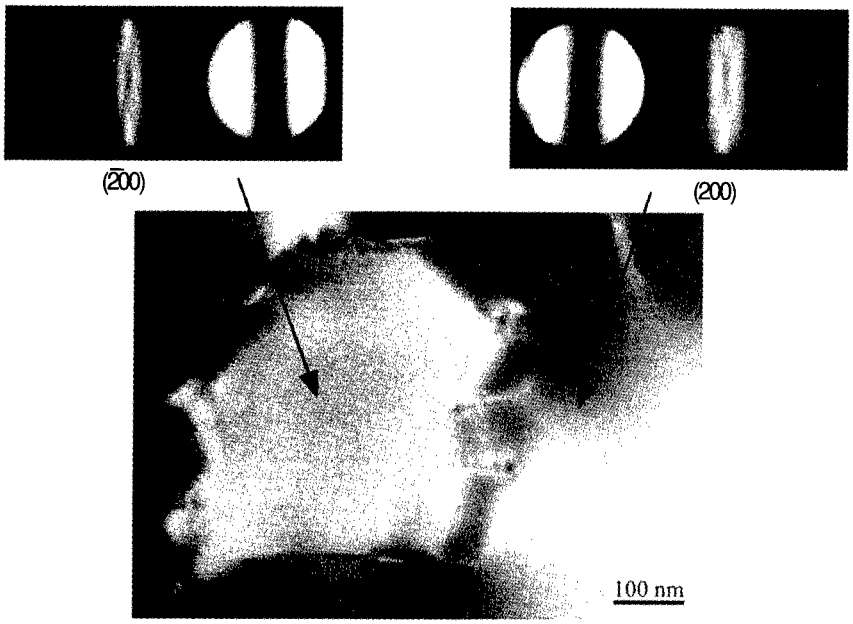


Fig. 3 CBED polarity analysis of an antiphase domain. The directionof the black cross points in the direction of the Ga to P bond. In the left pattern taken from the island region enclosed by the stacking-fault-like contrast, the dark cross appears in the (2̄00) reflection. While in the right pattern which was taken from the matrix, the dark cross appears in the (200) reflection. Upon crossing the boundary the direction of the cation to anion is reversed. Therefore, the adjacent grains are in antiphase order to one another.

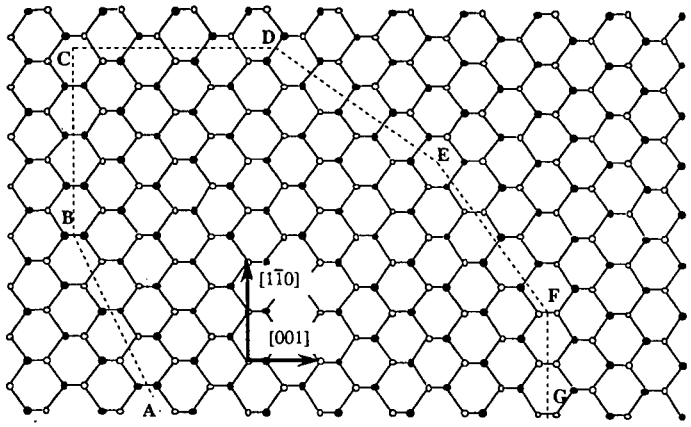


Fig. 4 [110] projection of the sphalerite structure showing various antiphase boundary facets: **AB** (1$\bar{1}$3), **BC** (001), **CD** ($\bar{1}$10),**DE** ($\bar{1}$11), **EF** ($\bar{1}$1$\bar{2}$), **FG** (00$\bar{1}$).

CONCLUSIONS

Antiphase boundaries in GaP films grown on Si (001) substrates have been characterized by TEM in plan-view. The antiphase domains in the crystal were confirmed by CBED analysis. Sections of the APB were observed to adopt facet planes nearly parallel to the {100} and {110}. Furthermore, stacking-fault-like contrast observed in the (220) dark field images suggest rigid body-lattice translations between adjacent domains are present at the interface.

ACKNOWLEDGMENTS

The authors would like to thank Dr. Fred Williamson for his technical assistance on operating the MBE and Dr. Stuart McKernan for his assistance in the TEM characterization of these defects. The GaP crystals were grown at the Microtechnology Laboratory at the University of Minnesota. The electron microscope is part of the Center for Interfacial Engineering which is a National Science Foundation Engineering Research Center. This research is supported by the National Science Foundation under contract No. NSF/DMR-9522253.

REFERENCES

1. D. B. Holt, J. Chem. Phys. Solids **30**, 1297-1308 (1969).
2. S. McKernan and C. B. Carter, Solid State Phenomena **37-38**, 67-74 (1994).
3. J. H. Neave, P. K. Larsen, B. A. Joyce, J. P. Gowers and J. F. van der Veen, J. Vac. Sci Technol. **B4**, 668 (1983).
4. K. Morizane, J. Cryst. Growth **38**, 249-254 (1977).
5. S. B. Samavedam, S.B.Kvam, F. G and e. al, Mat. Res. Soc. Symp. Proc. **91**, 431-6 (1995).
6. D. R. Rasmussen, S. McKernan and C. B. Carter, Phil. Mag. **63**, 1299-1314 (1991).
7. D. R. Rasmussen, N. H. Cho, D. W. Susnitzky and C. B. Carter, Ultramicroscopy **30**, 27-32 (1989).
8. N. H. Cho, B. C. De Cooman, C. B. Carter, R. Fletcher and D. K. Wagner, Appl. Phys. Lett. **47**, 879-881 (1985).
9. D. R. Rasmussen, S. McKernan and C.B.Carter, Phys. Rev. Lett. **66**, 2629-2632 (1991).
10. P. Pirouz, C. M. Chorey and J. W. Powell, Appl. Phys. Lett. **50**, 221-223 (1987).
11. S. McKernan and C. B. Carter, Mat. Res. Symp. Proc. **167**, 259-264 (1990).
12. A. Ishizaka and Y. Shiraki, J. Electrochem. Soc. **133**, 666 (1986).
13. J. Tafto and J. C. H. Spence, J. Appl. Cryst. **15**, 60-64 (1982).

Part XI

Defects in III-V Layers and Structures

ELECTRICALLY DETECTED MAGNETIC RESONANCE ON GaAs/AlGaAs HETEROSTRUCTURES

T. WIMBAUER*, D. M. HOFMANN*, B. K. MEYER*, M. S. BRANDT*, T. BRANDL*, M. W. BAYERL*, N. M. REINACHER*, M. STUTZMANN*, Y. MOCHIZUKI**, M. MIZUTA**
*Technical University of Munich, Walter Schottky Institute and Physics Department E 16 D-85747 Garching, Germany
**Fundamental Research Laboratories, NEC Corporation, 34 Miyukigaoka, Tsukuba, Ibaraki 305, Japan

ABSTRACT

Electrically detected magnetic resonance (EDMR) has been used to study carrier recombination in GaAs/AlGaAs quantum well structures grown by molecular beam epitaxy. The spin dependent photoconductivity signals depend strongly on the electrical contact properties. Using silver paste contacts a narrow (18 G) resonance located at g = 2.001 is observed. It has been previously attributed to surface defects on GaAs. Using alloyed In-contacts other signals are detected. The dominant resonance observed at 9 GHz has an isotropic g-value of g = 1.99 with a halfwidth of 200 G and is therefore assigned to Cr^{4+}. Other signals of considerably lower intensity are explained by the well known electron paramagnetic resonance (EPR) properties of the Ga_i-interstitial and the As_{Ga}-antisite defects. EDMR performed at 34 GHz allows the experimental separation of the two sets of hyperfine lines.

INTRODUCTION

Modern epitaxial growth techniques like molecular beam epitaxy (MBE) and metal organic vapour phase epitaxy (MOVPE) allow the growth of high quality layers of GaAs and related alloys (i. e. AlGaAs). They enabled the realization of numerous novel devices ranging from optoelectronic components to microwave devices and high speed logic circuits.

However, despite the superior crystalline quality of the layers, unintentional trace impurities and intrinsic defects still play a crucial role for the device performance and can affect the electrical properties of the material in an undesirable manner. For the identification and analysis of defects EPR has a long tradition, beginning with the investigations on silicon in the late fifties [1]. Later on, the method has also been applied very successfully to compound semiconductors like GaAs. Due to limitations in sensitivity, only very few results were obtained on epitaxial layers of only a few micron thickness.

Magnetic resonance methods which have the potential of higher sensitivity are optically detected magnetic resonance (ODMR) and electrically detected magnetic resonance (EDMR). The detection mechanism of the ODMR is based on luminescence changes under magnetic resonance conditions. On the other hand, EDMR detects resonant changes in electronic transport properties such as photoconductivity and therefore is particularly suited to study the influence of paramagnetic defects on the performance of actual electronic devices.

EDMR has previously been applied primarily to elemental semiconductors and devices made of them. However, first experimental results exist on EDMR in III - V materials. With the exception of GaN - LEDs, the technique has until now only been employed to study bulk III - V samples. Here we present an exploratory investigation on a GaAs/AlGaAs heterostructure.

Mat. Res. Soc. Symp. Proc. Vol. 442 © 1997 Materials Research Society

In a previous ODMR study on the samples used in this investigation, Ga-interstitial defects were observed [2]. The resonance of Ga_i was detected as a luminescence decrease from which was concluded that Ga_i act as a nonradiative recombination center. The task of the present study was to perform complementary EDMR investigations and to study the spin properties of the defects via the conductivity of the samples.

EXPERIMENTAL DETAILS

The structure of the MBE grown multi-layer system is shown in Fig. 1. The 50 nm thick GaAs film is co-doped with Si in concentrations of $1x10^{16}$ cm^{-3} and Be in concentrations of $3x10^{16}$ cm^{-3}. The samples investigated were small pieces (2 x 4 mm^2) cut from a GaAs/AlGaAs heterostructure wafer.

The EDMR spectrometer consists of a standard X-band EPR spectrometer (Bruker ESP 300), equipped with a TE_{102}-cavity. A Keithley source measure unit 237 was used as a low-noise voltage source. Using lock-in technique for sensitive detection either the microwave power amplitude or the magnetic field were modulated with a frequency of approximately 1 kHz. The measurement temperature could be varied with a helium flow cryostat (Oxford ESR 900) from 4 to 300 K.

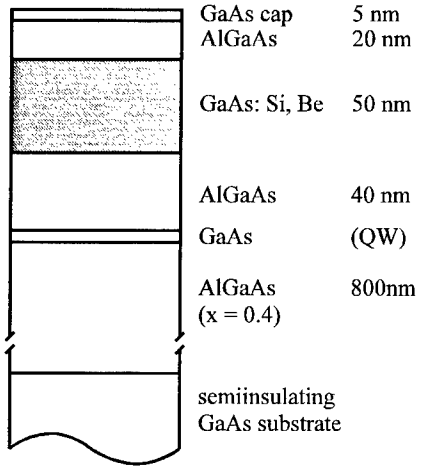


Fig. 1: Layer sequence of the investigated sample.

RESULTS AND DISCUSSION

The characteristic ODMR spectrum of the sample obtained previously [2] is shown in Fig. 2 for comparison to the EDMR results. It was recorded at a temperature of 1.6 K using a microwave frequency of 35 GHz. The resonances were detected on the shallow donor-acceptor pair-luminescence originating from the co-doped GaAs layer. Due to inter-impurity separations this luminescence provides a slowly decaying channel with recombination rates comparable to the magnetic dipole transition rate of EPR which is normally in the range of μs^{-1}. This feature enabled the indirect detection of the resonances because the defect acted as a shunt path to the radiative recombination under magnetic resonance conditions. The

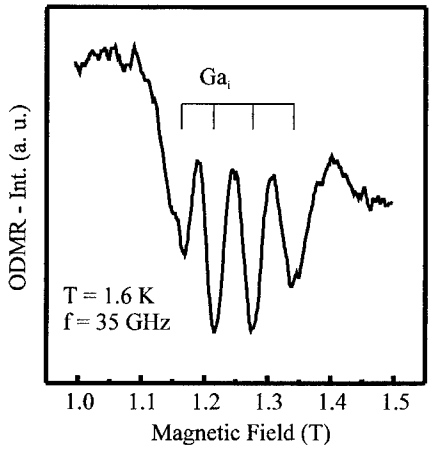


Fig. 2: ODMR spectrum of the Ga-interstitial

spectrum is described by a g-value of g = 2.009 and hyperfine interactions with the nuclear spin 3/2 of the ^{69}Ga and ^{71}Ga isotopes having a natural abundance ratio of 61/39 and hyperfine constants of 0.053 cm^{-1} and 0.067 cm^{-1}, respectively. In agreement with Kennedy et al. [3] and Trombetta et al. [4] the corresponding defect was assigned to the Ga-interstitial.

For the first type of EDMR investigations silver paste contacts on top of the GaAs cap layer were made. Fig. 3 shows an EDMR spectrum measured at a temperature of 5 K and at a frequency of 9.3 GHz while illuminating the sample with white light. In this case magnetic field modulation was performed obtaining the first derivative of the resonance curve. The signal consists of a single isotropic line located at g = 2.001 with a peak-to-peak linewidth of ΔB_{pp} = 18 G.

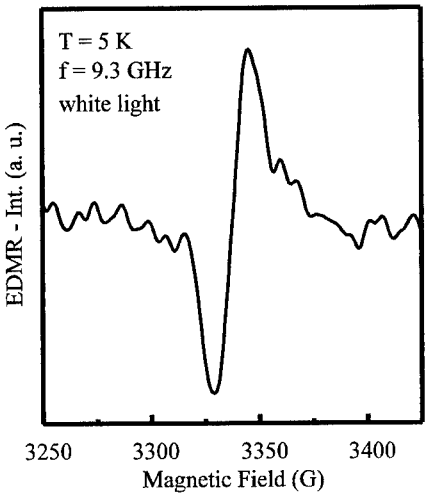


Fig 3: EDMR spectrum of the surface dangling bond.

Emanuelson et al. [5] report on a very similar signal in AlGaAs/GaAs heterostructures. The authors tentatively attributed it to a surface dangling bond in the GaAs cap layer. After the removal of the surface film by wet etching the EPR line disappeared in their case showing that the signal originates from the top layer. The observation of the surface dangling bond resonance indicates, that most of the recombination current is localized in the GaAs cap layer and no electrical contact to deeper GaAs layers was made.

In a second step, In-contacts (alloyed at 480°C for one minute) were used for EDMR measurements in order to contact all regions of the layered structure shown in Fig. 1. One can hence expect that the current flow is now more homogeneously distributed over the complete sample. For the EDMR experiment the sample was again illuminated with white light at a temperature of 4.2 K. The magnetic resonance spectrum measured in phase with the amplitude-modulated microwaves of 9.3 GHz is shown in Fig. 4 (spectrum a).

The spectrum is dominated by a line of high intensity near g = 2 ($\Delta\sigma/\sigma \approx -10^{-5}$). In addition, resonances of considerably lower intensity can be recognized at low and high fields. In order to separate the superimposed resonance lines, angular dependent, temperature dependent and microwave power dependent investigations were performed. Within the experimental accuracy the spectrum was found to be isotropic. EDMR could be detected up to 30 K without significant changes in the lineshapes and positions. Also, the variation of the microwave power from 2 mW to 2 W did not lead to a separation of the resonances.

The dominating central signal can be well described by a gaussian (see Fig. 4, simulation b). It has a g-value of g = 1.99 with a FWHM of 200 G. Very similar resonance parameters were found for Cr^{4+} ($3d^2$, S = 1) in GaAs[6]. The substrate used to grow the heterostructure is semiinsulating GaAs: Cr and the observation of this particular resonance has to be attributed to a spin-dependent recombination current in the GaAs: Cr substrate, an indication that the alloying of the In-contacts resulted in electrical contact to all parts of the sample.

In order to describe the low field and high field parts of the experimental spectrum a, the well-known EPR parameter of As_{Ga} first observed by Wagner et al. [7] were used (g = 2.047,

hyperfine constant A = 0.089 cm^{-1}, FWHM = 500 G for each of the four hyperfine lines according to the nuclear spin I = 3/2 of As). From the simulation c in Fig. 4 it can be seen that the outermost resonances of the experimental spectrum a can be described by the existence of As_{Ga}.

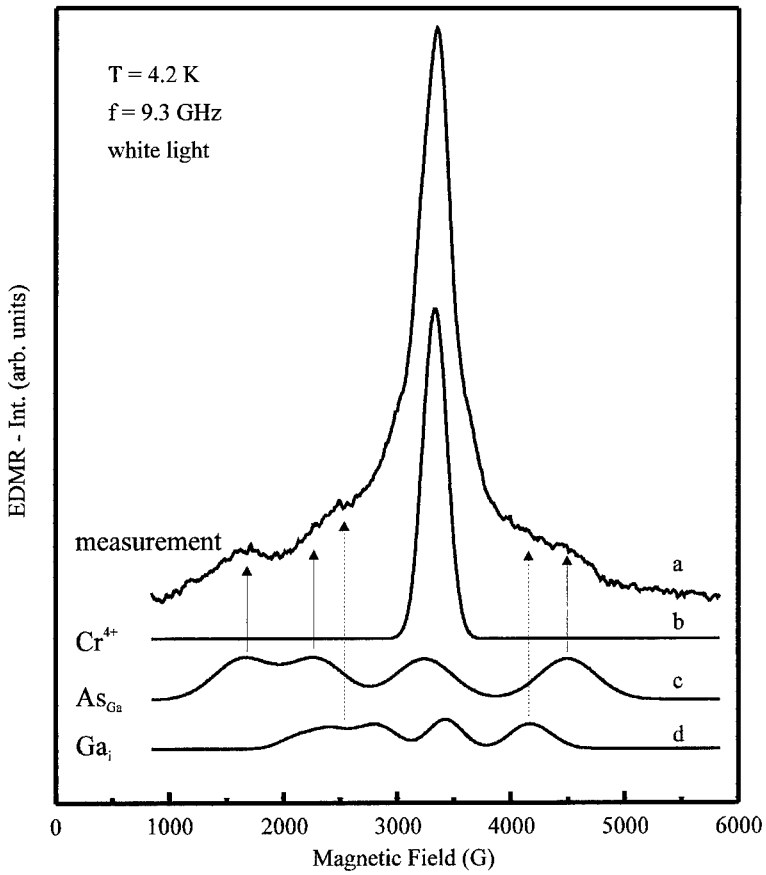


Fig. 4: EDMR spectrum measured at a microwave frequency of 9.3 GHz using alloyed In-contacts. Decomposition of the the experimental spectrum into Cr^{4+}, As_{Ga} and Ga_i.

Further including the Ga_i (simulation d) observed in the same sample by ODMR [2], a better agreement with the experimental spectrum a can be achieved with respect to the shoulders localized more closely to the central high intensity line. We would like to mention that - compared to the 35 GHz ODMR-results (see Fig. 2) - the hyperfine lines in the 9.3 GHz simulation of the Ga_i (curve d) in Fig. 4 are no longer equally spaced according to Breit-Rabi calculations.

Subtracting the contributions of Cr^{4+}, As_{Ga} and Ga_i from the experimental data a curve is obtained which can be described by a gaussian located at g = 2.01 having a FWHM = 900 G. The origin of this resonance is not known at this point.

Due to the superposition of the As_{Ga} and Ga_i resonances, a clear separation of the Ga-interstitial in EDMR is somewhat difficult from Fig. 4. Performing EDMR measurements at higher frequencies might help in the experimental resolution of the different sets of hyperfine lines. Therefore, the sample has been introduced to a non-commercial Q-band spectrometer, using the same contact geometry and light for the EDMR measurements. The observed spectrum is now dominated by the Ga-interstitial resonances as shown in Fig. 5, proving that this defect indeed influences the electronic transport processes in the sample. Weak resonances due to the Cr^{4+} and antisite defect are observed with a 90° phase shift between modulation and detection by the lock-in amplifier. This phase sensitive detection of EDMR allows in some fortuitous cases the experimental separation of the effect of different defect states on the transport properties, especially if different transport processes are monitored simultaneously. In our case, this separation into photoconductivity in the co-doped GaAs layer and in the GaAs: Cr substrate seems possible using phase shift analysis.

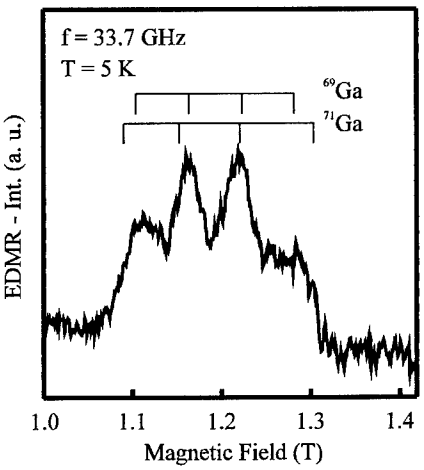


Fig. 5: EDMR spectrum of the Ga-interstitial measured at a microwave frequency of 33.7 GHz using alloyed In-contacts.

CONCLUSIONS

It was shown that the EDMR technique can be used to study defect properties in GaAs/AlGaAs multilayer systems. While ODMR is restricted to defects in the luminescent layer, the sensitivity of EDMR in the investigated structure strongly depends on contact properties. In the case of silver paste contacts surface dangling-bonds were detected. Using alloyed In contacts two intrinsic defects, the Ga-interstitial and the As-antisite defect located in different parts of the GaAs/AlGaAs multilayer system could be observed.

ACKNOWLEDGEMENTS

The authors would like to thank the Deutsche Forschungsgemeinschaft for financial support (SFB 348).

REFERENCES

1. G. W. Ludwig and H. H. Woodury, Solid State Phys. **13**, 223 (1962)

2. Y. Mochizuki, M. Mizuta and A. Mochizuki, Mat. Sci. For. **196 - 201**, 1927 (1995)

3. T. A. Kennedy, R. Magno and M. G. Spencer, Phys. Rev. B **43** 6325 (1988)

4. J. M. Trombetta, T. A. Kennedy, W. Tseng and D. Gammon, Phys. Rev. B **43** 2458 (1988)

5. P. Emanuelson, P. Omling and B. K. Meyer, Mat. Sci. For. **143 - 147**, 1541 (1993)

6. U. Kaufmann and J. Schneider, Appl. Phys. Lett. **36**, 74 (1980)

7. R. J. Wagner, J. J. Krebs, G. H. Stauss and A. M. White, Solid State Commun. **36**, 15 (1980)

BEHAVIOR OF FLUORINE IN N-AlInAs LAYERS UNDER BIAS-TEMPERATURE STRESSES

Y. Yamamoto, N. Hayafuji, K. Sato, and M. Otsubo
Optoelectronic & Microwave Devices Laboratory, Mitsubishi Electric Corporation, 4-1, Mizuhara, Itami, Hyogo, 664, Japan, E-mail: yyamamot@oml.melco.co.jp

ABSTRACT

The electrical degradation of AlInAs /GaInAs high electron mobility transistor (HEMT) due to the fluorine contamination is quantitatively explained through the comprehensive annealing experiments and bias-temperature tests. The thermal degradation rate is found to be mainly determined by the following electrochemical reaction of fluorine with donor species after the quite fast diffusion of fluorine into the AlInAs layer. It is also confirmed that the thermal degradation is stringently affected by the electric field resulting in the one-sided degradation near the anode. These findings are important knowledges to improve the reliability of AlInAs/GaInAs HEMT under the DC accelerated life test at high temperature.

INTRODUCTION

The ternary compound semiconductor alloy system of AlInAs/GaInAs has been of great interest and extensively applied for high electron mobility transistors (HEMTs) [1,2], because of a suitable band construction and superior transport properties while keeping lattice-matching to InP substrate. Those HEMTs have set record performances for the fastest transistor operating at room temperature with a cutoff frequency of 343 GHz [3], and have set the world record for the fastest monolithic integrated circuit operating at a frequency of 213 GHz [4]. There have been, however, few reports showing reliable operation in the DC accelerated life test of the AlInAs/GaInAs HEMT with the thermal and bias stresses. Some papers have shown the decrease of the drain current during the DC life test with salient increase of the drain parasitic resistance while keeping the constant source parasitic resistance [5,6]. Recently important findings have been obtained through the material studies [7-9]. The origin of the thermal instability of the AlInAs/GaInAs system has been found to be the fluorine (F) contamination [7], which is peculiar to the n-AlInAs material [8]. In addition, the F-donor bond in n-AlInAs material has been identified [9]. Consequently the degradation is thought to be strongly correlated with the thermal diffusion of F, following F-donor bond formation and those possible preferences in the drain side. In this paper, the degradation mechanism of the electrical properties of AlInAs/GaInAs HEMT material due to the F contamination is quantitatively explicated through the annealing experiments, bias-temperature stressing (BT) tests and actual DC accelerated life tests.

EXPERIMENTAL RESULTS AND DISCUSSION

a. ANNEALING EXPERIMENTS

It has been shown that the atomic concentration of F in the 0.13 μm thick n-AlInAs layer on undoped AlInAs layer saturates when annealed at 400 ℃ or higher for 15 minutes [7]. This phenomenon should be due to the thermal diffusion of F and following F-Si bond formation. At first, the thermal diffusion coefficient of F in n-AlInAs was evaluated to distinguish these two factors by the secondary ion mass spectroscopy (SIMS) measurements on 1.5 μm thick Si-doped $Al_{0.48}In_{0.52}As$ samples annealed in nitrogen atmosphere for 3 minutes at different temperatures. The

Mat. Res. Soc. Symp. Proc. Vol. 442 © 1997 Materials Research Society

samples were MBE grown on (100) oriented semi-insulating InP substrate as previously described [7]. The diffusion length is simply expressed by the equation (1):

$$L^2 = Dt, \text{----------(1)}$$

where L, D and t are the diffusion length (cm), the diffusion coefficient (cm^2/sec) and the annealing time (sec), respectively. In addition, D is expressed by the equation (2):

$$D = D_0 \exp(-E_D/k_B T), \text{----------(2)}$$

where D, D_0, E_D and k_B are the diffusion coefficient (cm^2/sec), the constant for diffusion (cm^2/sec), the activation energy (eV) and Boltzmann's constant (eV/K), respectively. Figure 1 shows the SIMS profiles of F in n-AlInAs layers annealed at 340 ℃ and 400 ℃. The source-limiting-shaped F profiles are clearly obtained for both samples, whose diffusion fronts are observed at around 0.5 μm and 1.3 μm depth, respectively. By using the equations (1) and (2), it is concluded that the values of D_0 and E_D are 0.027 (cm^2/sec) and 1.13 (eV). This result means that the diffusion depth of F in n-AlInAs is about 3 μm when annealed at 400 ℃ just for 15 minutes. Consequently it is concluded that the F accumulation rate in n-AlInAs must be mainly limited by the following F-Si bond formation.

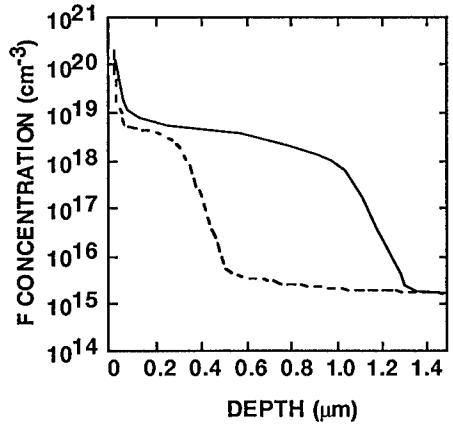


Figure 1 SIMS profiles of F in Si-doped $Al_{0.48}In_{0.52}As$ layers on semi-insulating InP substrate annealed in nitrogen atmosphere for 3 minutes at 340 ℃ (dotted curve) and 400 ℃ (solid curve).

Then, the rate determining F-Si bond formation process in n-AlInAs material was investigated theoretically and experimentally. The thermal degradation of electrical properties of the AlInAs due to the F-Si bond formation should be caused by the electrochemical reaction as described as follows:

$$F + e + Si^+ \rightarrow F\text{-}Si, \text{----------(3)}$$

because this occurs only in n-AlInAs containing free electrons[8]. Thereby the differential rate equation (4) is available with the electrochemical kinetics theory:

$$dn/dt = -k_1 n, \text{----------(4)}$$

where n is the concentration of free electron (cm^{-3}), and k_1 is the rate constant (sec^{-1}). By integrating the equation (4) with the boundary condition (5), the rate equation (6) is obtained.

$$n = n_0, \text{ when } t = 0, \text{----------(5)}$$
$$n = n_0 \exp(k_1 t), \text{----------(6)}$$

where n_0 is the initial concentration of free electron (cm^{-3}). Furthermore k_1 is generally described as the following Arrhenius equation:

$$k_1 = k_0 \exp(-E_a/k_B T), \text{----------(7)}$$

where k_0 is the constant (sec^{-1}), and E_a is the activation energy (eV). Actually a linear relation between t and $\ln(n_0/n)$ and that between $\ln(k_0/k_1)$ and 1/T were obtained through the thermal annealing experiments at various temperatures (300 ℃, 350 ℃, 400 ℃ and 450 ℃), from which E_a and k_0 were derived as 1.0 eV and 9180 sec^{-1}, respectively. Consequently by combining the equations (6) and (7), the equation (8) is now available to express the decrease of n in n-AlInAs material due to the thermal annealing:

$$n = n_0 \exp[-9180t \exp(-1.0/k_B T)]. \text{----------(8)}$$

Figure 2 shows the comparison between the theoretical curves and the experimental data. The quantitative agreements are obtained for considerably wide annealing conditions (170 ℃ ≤ T ≤ 450 ℃, 5 minutes ≤ t ≤ 500 hours). These results not only give an evidence for the idea of rate-determining F-Si bond formation in n-AlInAs, but also quantitatively explain the electrochemical reaction between F and Si.

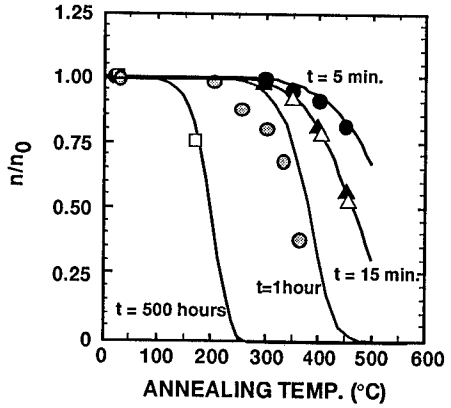


Figure 2 Annealing temperature dependence of free electron concentration decrease with the theoretical curves (solid curves). Closed symbols and open symbols are for Si doped AlInAs and AlInAs/GaInAs HEMT structure, respectively. Data after the reference [10] are also plotted with gray scaled symbols.

b. BIAS-TEMPERATURE STRESSING TESTS

Next, the one-sided increase of the drain parasitic resistance of the AlInAs/InGaAs HEMT was elucidated through the BT tests of the n-AlInAs material. Figures 3(a) and 3(b) show the selectively etched 0.5 μm thick AlInAs sample structure studied here. Before the experiments, the samples were deliberately contaminated with F by dipping in hydrogen fluoride solution in order to observe the instant deterioration. The constant voltage of 20 V (electric field of 74 V/cm) was supplied to the sample (0.6mm width x 2.7 mm length) through the two edge-placed electrodes at 250 ℃ in nitrogen atmosphere for 65 hours. The direction of the bias was reversed at the point of 39 hours. The current flow between the anode and the cathode, the voltage between the anode (anode region) and the intermediate electrode, and the voltage between the cathode and the intermediate electrode (cathode region) were monitored by the ammeter and the voltmeter, respectively.

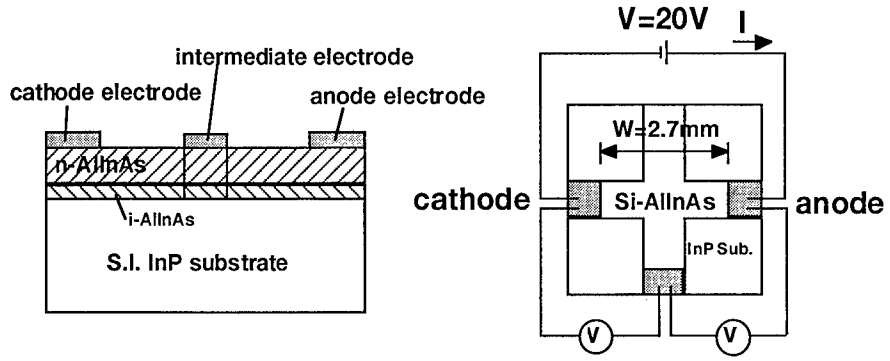


Figure 3 Sample structure for the bias-temperature test of Si-doped AlInAs. (a): cross sectional view, (b): top view. The thickness of AlInAs layer is 0.5 μm. The width and length of the bias supplied region are 0.6 mm and 2.7 mm, respectively. The ammeter and the voltmeter are symbolized by **A** and **V**, respectively.

Figures 4 (a) and (b) show the current and voltage changes during the BT test. The exponential current decreases is mainly due to the decrease of the free electron concentration by the F incorporation. The current decreases to about 65 % of the initial value within 10 hours, while the calculated time by the equation (8) is 56 hours. This degradation rate is reasonable because of the large amount of F adsorbed on the sample through the hydrogen fluoride treatment. On the other hand, the voltage in the anode region increases for 20 hours then becomes constant. There is also no marked voltage change even after bias direction conversion. These results suggest that F atoms migrate preferentially towards the anode under the electric field. The highest electronegativity and relatively small atomic radius of F possibly cause the imbalanced voltage stabilization at the biased condition because F atoms easily migrate in the AlInAs layer and capture electrons concentrating in the anode area resulting in the strong F-Si bonds formation on the spot.

c. DC ACCELERATED LIFE TESTS

Finally, the actual DC accelerated life test was performed at 200 ℃ for the Si-planar doped AlInAs/InGaAs HEMTs. The gate was T-shaped, whose length and width were 0.15 μm and 120 μm, respectively. The drain voltage and the drain current was set to 0.8 V and 12 mA, respectively.

Figure 5 shows the relative changes of the zero-gate bias saturation drain current (I_{dss}) for three individual devices with the curve derived from the equation (8) for the concentration change of free electron. The predicted curve well describes the experimental data in the range up to about 300 hours cumulative, while thereafter the data go a little bit beyond the predicted values. A possible reason of this discrepancy is the re-activation of electrons by the thermal desorption of F. It has been actually reported that the free electron concentration in the thermally degraded n-AlInAs sample is recovered by re-annealing [7].

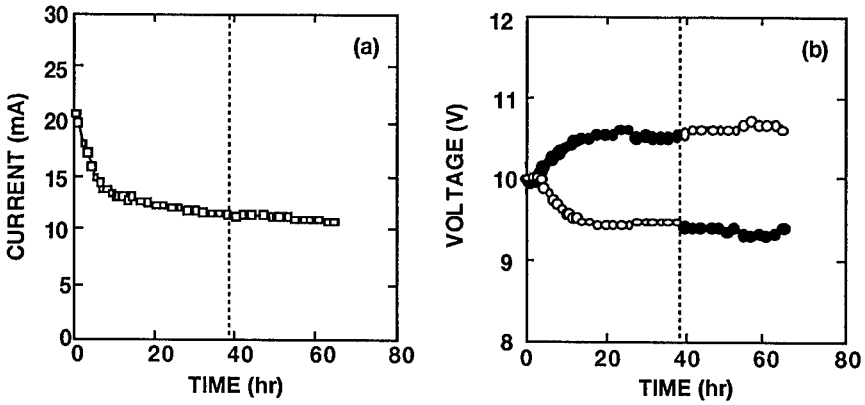


Figure 4 Current change (a) and voltage changes (b) during the BT test. A constant voltage of 20 V is supplied at 250 ℃ in nitrogen atmosphere. The bias direction is reversed at the point of 39 hours. In figure 4 (b), closed circles and open circles are for anode region and for cathode region, respectively.

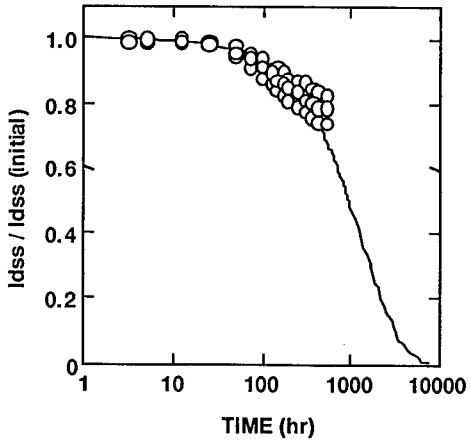


Figure 5 Relative changes of the zero-gate bias saturated drain current (I_{dss}) for three HEMTs during the DC accelerated life test at 200 ℃ with the predicted curve (solid curve) by equation (8). The input drain voltage and the drain current is 0.8 V and 12 mA, respectively, for the 120 μm wide gate devices.

CONCLUSION

The thermal degradation rate of the electrical properties of AlInAs/GaInAs HEMT material due to the F contamination was found to be mainly determined by the F-Si bond formation reaction. It is also confirmed that the thermal degradation is stringently affected by the electric field resulting in the imbalanced degradation near the anode (drain for electron). These findings are important knowledges to improve the reliability of AlInAs/GaInAs HEMT under the DC accelerated life test at high temperature.

ACKNOWLEDGMENTS

The authors would like to thank Dr. T. Sonoda and Mr. T. Ishida for fruitful discussion through this work.

REFERENCES

1. U. K. Mishra, A. S. Brown, S. E. Rosenbaum, C. E. Hooper, M. W. Pierce, M. J. Delaney, S.Vaughn, and K. White, IEEE Electron Device Lett. **9**, 647 (1988).
2. P. M. Smith, S. M. J. Liu, M. Y. Kao, P. Ho, S. C. Wang, K. H. G. Duh, S. T. Fu, and P. C. Chao, IEEE Microwave and Guided Wave Lett. **5**, 230 (1995) .
3. L. D. Nguyen, A. S. Brown, M. A. Thompson, and L. M. Jelloian, IEEE Trans. Electron Dev., **39**, 2007 (1992).
4. S. E. Rosenbaum, L. M. Jelloian, A. S. Brown, M. A. Thompson, M. A. Matloubian, L. E. Larson, R. F. Lohr, B. K. Kormanyos, G. M. Reibez, and L. P. B. Katehi, IEEE IEDM Tech. Dig. 1993, 924.
5. Y. Ashizawa, C. Nozaki, T. Noda, A. Sasaki, S. Fujita, Solid-State Electron. **38**, 1627 (1995).
6. H. Sasaki, K. Yajima, N. Yoshida, T. Ishida, R. Hattori, T. Sonoda, O. Ishihara, S. Takamiya, R. Konishi, and K. Ando, J. Electronic Mat. **25**, 559 (1996).
7. N. Hayafuji, Y. Yamamoto, N. Yoshida, T. Sonoda, S. Takamiya, and S. Mitsui, Appl. Phys. Lett. **66**, 863 (1995).
8. Y. Yamamoto, N. Hayafuji, N. Fujii, K. Kadoiwa, N. Yoshida, T. Sonoda, and S. Takamiya, J. Electronic Mat., **25**, 685 (1996).
9. N. Hayafuji, Y. Yamamoto, N. Fujii, T. Sonoda, and S. Takamiya, (Mater. Res. Soc. Symp. Proc. **417**, Pittsburgh, PA, 1996) pp. 415-420.
10. A. Wakejima, K. Onda, A. Fujihara, E. Mizuki, M. Kuzuhara, and M. Kanamori, Tech. Report of IEICE, **ED96-108**, CPM96-86, 67 (1996) (unpublished).

S-DOPED GaInAs GROWN BY CHEMICAL BEAM EPITAXY : ELECTRICAL AND STRUCTURAL CHARACTERIZATION

E. C. Paloura [a] , G. Petkos [b] , P. J. Goodhew [b], B. Theys [c], J. Chevallier [c].

[a] Aristotle Univ. of Thessaloniki, Dept. of Physics, GR-54006 Thessaloniki, Greece.
[b] Univ. of Liverpool, Dept. of Materials Science & Engineering, Liverpool, L69 3BX, U.K.
[c] C.N.R.S., Lab. de Physique des Solides de Bellevue, F.92.195 Meudon Cedex, France.

ABSTRACT

We report on the electrical and structural characterization of sulfur (S) doped $Ga_{0.73}In_{0.27}As$ layers, grown on SI (001) GaAs substrates by chemical beam epitaxy. The room temperature free electron concentration is $2x10^{17}cm^{-3}$ while the corresponding value of mobility is 3400 cm^2V^{-1} s^{-1}. The epilayer is characterized by a deep trap, which could be attributed to the electrical activity of dislocations, with an activation energy of 0.59 eV and a capture cross section $6x10^{-15}$ cm^2. TEM analysis shows that the GaInAs/GaAs interface is characterized by dislocation lines and loop-like configurations which could be attributed to climb movement by point defect absorption or emission. Annealing at 420°C (Ar ambient for 5 min) does not alter the carrier concentration (n) and mobility (μ) significantly. The invariance of n and μ, even though the temperature should be high enough to dissociate any S-atomic hydrogen complexes, indicates that the number of hydrogen-S donor complexes in the as-grown material is small compared with the donor concentration. Finally, the effect of intentional atomic hydrogen diffusion is discussed.

INTRODUCTION

$Ga_xIn_{1-x}As$ has higher than GaAs carrier mobility and saturation velocity, which render it suitable for applications in high frequency microelectronics[1] and optoelectronics devices[2 ,3]. However, the $Ga_xIn_{1-x}As$/GaAs heterostructure suffers from the presence of dislocations[4], due to the lattice mismatch in the heterosystem[5]. Gaseous sources for doping of GaAs based ternaries grown by chemical beam epitaxy (CBE) are currently widely studied. Flux control, uniformity and the ease of source replacement are some of the advantages of gaseous dopant sources over the elemental doping sources, which in addition have been found to suffer severe degradation in the CBE growth chamber[6]. Diethylsulphide (DES) has a reasonable efficiency and negligible memory effect in GaAs[7], is less toxic , has lower possibility of leakage than H_2S and has already been successfully used for the doping of GaAs, AlGaAs and GaInAs[8]. Sulfur with its low diffusivity in GaAs[9] is an attractive n-type dopant for III-V semiconductors grown by CBE.

In this paper we report on the electrical and structural characterization of sulfur doped $Ga_{0.73}In_{0.27}As$ layers grown on GaAs substrates by CBE. The epitaxial layers were characterized electrically and structurally. The free carrier concentration was deduced from resistivity and Hall effect measurements, while the ionized impurity concentration and the deep trap characteristics were obtained by capacitance-voltage (C-V) and deep level transient spectroscopy (DLTS) measurements, respectively.

Mat. Res. Soc. Symp. Proc. Vol. 442 © 1997 Materials Research Society

Finally, the presence and characteristics of dislocations in the layer were identified by plan-view transmission electron microscopy (TEM).

SAMPLE PREPARATION & EXPERIMENTAL DETAILS

The growth was carried out in a VG V80H CBE system at 500°C using trimethylgallium and trimethylindium as group III sources, at a growth rate of 1μm/h, while diethylsulphide (DES) was used for the n-type doping. Arsine pressure was generally set to give an uncorrected V:III pressure ratio of 5:1 in order to eliminate the variation of GaInAs composition with temperature and As flux. All of the metalorganic sources, including the DES, were supplied by Epichem Ltd. The samples were grown on semi-insulating GaAs (001) wafers mounted in an In-free holder.

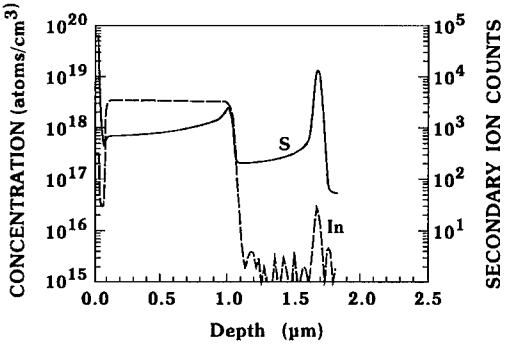


Fig.1 : SIMS profile of the S-distribution.

The structure consists of a 0.5 μm thick undoped GaAs buffer layer, a 1 μm thick S-doped $Ga_{0.73}In_{0.27}As$ and a 50 nm thick undoped GaAs cap layer which was used for Schottky contact improvement. The film composition was determined by electron microprobe analysis. The S concentration in the GaInAs epilayer, as determined by SIMS profiling using Cs^+ ions, takes values in the range 0.7-$2x10^{18}cm^{-3}$ while the carbon and oxygen concentrations were below the detection limit ($<5x10^{16}cm^{-3}$ and $5x10^{17}cm^{-3}$, respectively). The S- and In-SIMS profiles are shown in Fig.1. The Schottky contacts have been prepared using Au evaporation while the ohmic contacts were fabricated using Au/Ge alloy and annealing at 400°C in nitrogen atmosphere. The TEM study was carried out using a JEOL 200 kV electron microscope.

RESULTS AND DISCUSSION

Electrical characterization.

The ionized impurity concentration and the Schottky barrier height φ_B were determined from standard capacitance-voltage (C-V) measurements at 1 MHz. With the above S concentration, the doping concentration is found to be equal to $2x10^{17}cm^{-3}$, and remains constant as a function of depth. The value of φ_B obtained from the C-V characteristics is $\varphi_B=1.7$ eV, a value that could be attributed to the presence of defects at the GaInAs/ cap-GaAs interface[10 ,11]. However, the presence of the GaAs cap layer reduces significantly the reverse current of the

Schottky diode, which remains smaller than 500 μA for an applied reverse bias of -5V and for a diode-diameter of 1 mm. This small leakage current permits DLTS measurements using filling pulse widths which are large enough to saturate the traps.

The room temperature (300K) free electron concentration and mobility are $2.1x10^{17}cm^{-3}$ and 3400 $cm^2V^{-1}s^{-1}$, respectively. This value of mobility is very close to the theoretically predicted for a film of similar composition and it is typical for n-type $Ga_xIn_{1-x}As$ (x≅0,8), with similar thickness and carrier concentration, grown at 500°C [12 ,13]. The discrepancy between the free electron and the S-concentrations could be attributed to a small degree of compensation[11] or S-clustering, which however is not observed experimentally. The variation of carrier mobility (μ) and carrier concentration as a function of temperature are shown in Fig.2 (a) and (b), respectively. Annealing at 420°C, in Ar ambience for 5 min does not alter the carrier concentration and mobility significantly, i.e. the corresponding values after annealing are $2.2x10^{17}cm^{-3}$ and $3200cm^2V^{-1}s^{-1}$. The annealing temperature of 420°C should be high enough to dissociate any S-atomic hydrogen complexes. The invariance of the n, μ values upon annealing indicates that the in-situ incorporated hydrogen does not form any electrically active complexes or that it outdiffuses during growth.

The characteristics of the deep traps in the GaInAs epilayer have been determined using constant capacitance DLTS measurements. The DLTS spectra were recorded under -2 V bias, a filling pulse height of +0.3 V and a filling pulse width of 5 msec. We have identified a deep trap with an activation energy E_a=0.59 eV, capture cross section $\sigma_n=6x10^{-15}$ cm^2 and concentration $N_T=6x10^{13}$ cm^{-3} that could be attributed to the electrical activity of dislocations (the dislocation etch pit density was found equal to 10^4 cm^{-2}). A trap with similar signature (E_a=580 meV, $\sigma_n=2x10^{-16}$ cm^2) has been reported in the literature for MBE $Ga_{0.94}In_{0.06}$ As/GaAs[10,14 ,15]. The 580 meV trap was also attributed to the electrical activity of α-type misfit dislocations (As-core glide set dislocation) propagating along the [110] direction. The difference in the value of capture cross-section reported here could be attributed to the slightly different composition of the alloy.

Intentional atomic hydrogen and deuterium diffusion was used in order to access the degree of donor passivation due to the formation of S-H complexes. Hydrogenation using hydrogen or deuterium (hereafter called H- and ^{2}H-genation, respectively) was performed by exposure of the sample to a hydrogen or deuterium plasma (2 hrs, 200°C, 0.08W/cm^2) in a parallel plate capacitively coupled reactor. SIMS profiling of the ^{2}H-genated samples shows that deuterium diffuses through the epilayer and reaches a concentration of $1-3x10^{18}cm^{-3}$ in the bulk (Fig. 3). The deuterium signal increases very fast close to or just at the layer/buffer interface. This accumulation could occur at the misfit dislocations, defects or impurities at the interface.

However, no donor passivation was observed, unlike in n-GaAs:S where neutralization of S donors, after ^{2}H-genation with comparable conditions, was found[16]. This absence of neutralization of shallow donors in the GaInAs alloy can be understood on the basis of previous results obtained in GaAs. From hydrogen diffusion modeling, it has been shown that hydrogen introduces a deep acceptor level H^o at 0.1eV below the bottom of the conduction band[17]. Moreover, it has been also shown that an increase of the band gap in AlGaAs also induces a deepening of the H^o/H^- level with respect to the conduction band minimum [18]. So it seems reasonable to assume that in GaInAs alloys, the H^o/H^- level becomes rapidly resonant

with the conduction band as the In content increases. As a consequence H^o is the dominant species in the n-type $Ga_{0.73}In_{0.27}As$ alloy. Since there is no Coulombic attraction between the (neutral) hydrogen species and the donors, efficient donor neutralization is not expected in this alloy [18].

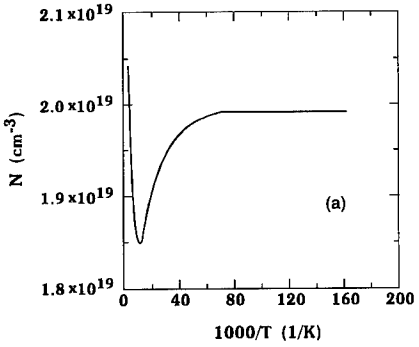


Fig. 2a : Carrier concentration as a function of temperature.

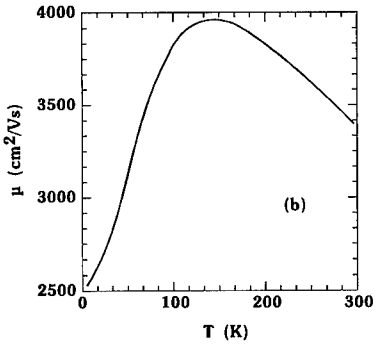


Fig. 2b : Carrier mobility as a function of temperature.

Transmission Electron Microscopy (TEM)

The etch pit density in the epilayer was measured after etching using a CrO_3-HF solution (etching rate 50 nm/min)[19]. The etch pit density, measured using Nomarski interference contrast microscopy, is 10^4 cm^{-2} and is equal to that of the substrate. A plan view TEM micrograph of the interface between the S-doped GaInAs and the GaAs cap layer is shown in Fig.4. The non-straight dislocation lines and the loop-like configurations are not normally observed in S-doped GaAs[20] or in GaInAs doped with other dopants[21]. These configurations could be attributed to climb movement of dislocations by point defect absorption or emission. Excess point defect concentration due to S-doping could result in this behavior. Coil shaped dislocations have been reported in the case of Se-doped GaAs grown by liquid-phase epitaxy (LPE), indicating the presence of a high density of excess point defects due to the heavy Se doping[22]. However, the loop configurations which we observe are widely-spaced and it is more likely that they have arisen from a complex cross-slip mechanism.

Clear evidence of sulfur precipitation has not been revealed. However, several experimental observations reported in the literature, suggest that S-precipitation can take place in S-doped GaInAs layers. In GaAs, the dislocation velocity was found to decrease upon doping with donor impurities and the magnitude of the interaction energy between a dislocation and an impurity suggested that the impurities retarding the dislocation motion are in the form of clusters[23]. In that work the dislocation velocities in Te-doped GaAs were found to be much lower than those in GaAs doped with Si at comparable concentration. In the case of S-doped InP the effects of impurities on both the dislocation velocity and the yield strength may be attributed to dynamic locking of dislocations due to sulfur dopants[24]. Large sulfur precipitates located on the dislocations were observed in S-doped InP using laser scanning topography (LST)[25].

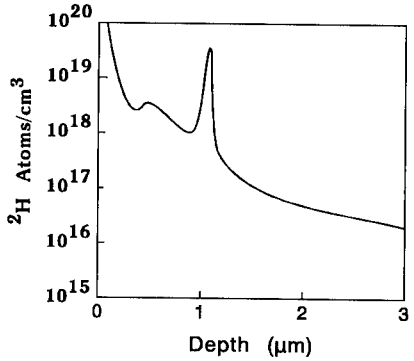


Fig. 3 : SIMS profile of the ^{2}H distribution

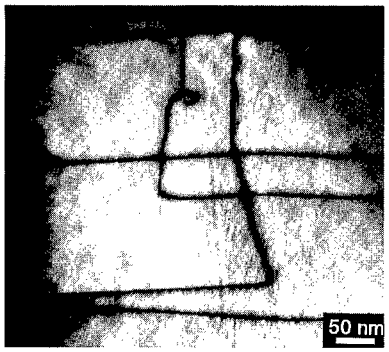


Fig.4 : Plan view TEM micrograph (g=(200), bright field). The non-straight dislocation lines and the loop-like configurations were not observed in GaInAs layers before.

It has been suggested [22] that in the case of GaAs, if the temperature is high enough to allow bulk diffusion, impurity atoms dispersed within the matrix crystal reach the core of the dislocation, move along the dislocation line and coagulate at some sites discretely separate on the dislocation line. Other residual impurities (B, O, C) in GaAs may develop complexes with S-impurities at the dislocation core, which can play an important role in the dislocation behavior. Scanning transmission electron microscopy (STEM) and high resolution electron microscopy (HREM) studies to observe S-precipitates in S-doped GaInAs are in progress.

CONCLUSIONS.

Plan view TEM has confirmed that all S-doped GaInAs layers were partially relaxed. Non-straight dislocation lines and loop like configurations were observed contrary to the case of S-doped GaAs or undoped GaInAs. This dislocation behavior observed in the interface between the S-doped GaInAs and the GaAs cap layer, can be explained in terms of climb movement by point defect absorption or emission, or by cross-slip mechanisms. The precipitation of sulfur clusters in S-doped GaInAs, although not yet observed, is to be expected and could explain some of the dislocation behavior observed in this material. The material is characterized by a rather high electron mobility (3400 $cm^2V^{-1}s^{-1}$) and a deep trap with an activation energy of 0.59 eV, which can be attributed to the electrical activity of dislocations. The thermal stability of n and μ upon annealing to 420°C indicates that the number of S-H complexes in the as-grown material is small compared to the donor concentration. Finally ex-situ hydrogenation does not cause donor passivation and therefore it can be concluded that neutral H° is the dominant species in n-type $Ga_{0.73}In_{0.27}As$ alloy.

ACKNOWLEDGMENTS : We wish to thank Ms. Monique Rommeluere from LPSB, CNRS Meudon for the electron microprobe analysis. Partial financial support from the GSRT is also acknowledged.

REFERENCES

1 . K. J. Kuhn, R. B. Darling, IEEE Trans. Electron. Devices **ED-39**, 1288 (1992).
2 . W. Dobbelaere, J. De Boeck, P. Hermans, R. Mertens, G. Borghs, W. Luyten, J. Van Landuyt. Appl. Phys. Lett. **60**, 868 (1992).
3 . W. Dobbelaere,W. De Raedt, J. De Boeck, P. Hermans, R. Mertens, G. Borghs, Ellectron. Lett. **28**, 372 (1992).
4 . G. P. Watson, D. G. Ast, T. J. Anderson, B. Pathangey, Y. Hayakawa, J. Appl. Phys. **71**, 3399 (1992).
5 . M. J. Matragrano, G. P. Watson, D. G. Ast, T. J. Anderson, B. Pathangey, Appl. Phys. Lett. **62**, 1417 (1993).
6 . P. J. Skevington, D. A. Andrews and G. J. Davies, J. Crystal Growth **105**, 371 (1990).
7 . T. B. Joyce, T. Pfeffer, T. J. Bullough and A. C. Jones, J. Crystal Growth **135**, 31 (1994).
8 . T. B. Joyce, T. L. Pfeffer, T. J. Bullough, G. Petkos, P. J. Goodhew and A. C. Jones, J. Cryst. Growth **150**, 644 (1995).
9 . J. P. Hirtz, Mater. Sci. Eng. B **17**, 9 (1993).
10 . W. R. Bachwald, J. H. Zhao, M. Harmatz and E. H. Poindexter, Sol. State Electr. **36**, 1077 (1993).
11 . D. Chattopadhyay, S. K. Sutradhar and B. R. Nag, J. Phys. C : Solid Satte Phys. **14**, 891 (1981) and references therein.
12 . R. A. Metzger, A. S. Brown, L. G. McGray and J. A. Henige, J. Vac. Sci. Technol. B **11**, 798 (1993)
13 . E. Tokumitsu, J. Shirakashi, M. Qi, T. Yamada, S. Nozaki, M. Konagai, K. Takahashi, J. Cryst. Growth **120**, 301 (1992).
14 . D. Biswas, A. Chin, J. Pamulapati and P. Bhattacharya, J. Appl. Phys. **67**, 2450 (1990).
15 . G. P. Watson, D. S. Ast, T. J. Anderson, B. Rathangey and Y. Hayakawa, J. Appl. Phys. **71**, 3399 (1992).
16 . B. Theys, B. Machayekhi, J. Chevallier, K. Somogyi, K. Zahraman, P. Gibart, M. Miloche, J. Appl. Phys. **77**, 3186 (1995)
17 . B. Machayekhi, R. Rahbi, B. Theys, M. Miloche, J. Chevallier, Mat. Sci. Forum **143-147**, 951 (1994).
18 . J. Chevallier, Defect and Diffusion Forum, **131-132**, 9, (1996).
19 . G. MacPherson, P. J. Goodhew, J. Appl. Phys. **80**, 1 (1996).
20 . G. M. Petkos, P. J. Goodhew and T. B. Joyce, J. Crystal Growth, **164**, 415 (1996).
21 . P. J. Goodhew, J. Phys. Chem. Solids **55**(10), 1107 (1994).
22 . D. K. Kim and B. T. Lee, Materials Letters **20**, 335 (1994).
23 . I. Yonenaga and K. Sumino, J. Appl. Phys. **65**(1), 85 (1989).
24 . I. Yonenaga and K. Sumino, J. Appl. Phys. **74**(2), 917 (1993).
25 . G. Jacob, A. Overs, R. Guillot, P. Gall, J. Bonnafe, H. L' Haridon and R. Coquille, Proc. of the Conf. on InP and Related Materials, 634 (1993).

FIRST-PRINCIPLES CALCULATIONS OF DIFFUSION OF CHLORINE ATOMS IN GaAs

TAKAHISA OHNO *, TAIZO SASAKI *, and AKIHITO TAGUCHI **
*National Research Institute for Metals, Tsukuba-shi, Ibaraki 305, Japan
**NTT Basic Research Laboratories, Atsugi-shi, Kanagawa 243-01, Japan

ABSTRACT

The properties of chlorine atoms in crystalline GaAs, such as stable configurations, migration paths, charge-state effects, and interaction with dopant atoms are theoretically investigated. The calculations are based on the local density functional theory using first-principles pseudopotentials in a supercell geometry. We determine the stable charge state of an isolated Cl atom as a function of the Fermi energy. When the Fermi level is situated at the top of the valence band of GaAs, the Cl atom occupies preferentially the bond-center site of a Ga-As bond in the positive charge state. The Cl atom diffuses through the GaAs crystal via a path in the region of high electron density, with a fairly large energy barrier. When the Fermi level is at the bottom of the conduction band, the lowest-energy configuration of the Cl atom is the tetrahedral interstitial site in the negative charge state and the bond center site is very slightly higher in energy. In Si-doped GaAs, the Cl atom occupies the tetrahedral interstitial site with the substitutional Si donor atom as a nearest neighbor, forming a neutral Cl-Si complex. The Cl-Si complex is weak and easily dissociates into the isolated Cl and Si atoms in GaAs. A comparison will be made between the behavior of Cl and F atoms in GaAs.

INTRODUCTION

The behavior of halogen atoms incorporated in semiconductors is of great importance in various processes in device fabrication. The reaction and diffusion of halogen atoms in the bulk semiconductor and the near-surface region is essential for chemical etching processes. The diffusion properties determine the concentration of halogen atoms near the surface during etching. The presence of large concentrations of ionized halogen atoms induces band bending near the surface, changes carrier concentrations around the halogen atoms, and affects the etching reactions of halogens [1]. The degradation of AlInAs/GaInAs system caused by thermal treatments is reported to be due to the diffusion of fluorine atoms from the surface into the Si-doped AlInAs layer, which causes the formation of complexes between the F and Si atoms and leads to the passivation of Si donors [2]. The thermal degradation is peculiar to the AlInAs ternary system, in which F atoms may exhibit high diffusivity.

Recently, a great deal of effort has been devoted to the behavior of hydrogen atoms in elemental or compound semiconductors [3]. The features of stable configurations and charge states of H atoms are well understood. It is found that the doping condition of the bulk semiconductor has a profound effect on the behavior of H atoms, and that a H atom is likely to be in the positive charge state for p-type doping and in the negative charge state in n-type materials. On the other hand, little is known about the properties of halogen atoms. In this paper, we present first-principles calculations of the properties of chlorine atoms in the GaAs bulk, such as stable configurations, migration paths, charge-state effects, and interactions with dopant atoms. The Cl atom is found to prefer the positive charge state, in spite of its high electronegativity. The behavior of F atoms in GaAs is also presented in comparison with that of Cl atoms.

CALCULATION METHODS

We perform first-principles total-energy calculations based on the density functional theory [4]. Beyond the local density approximation, we include the nonlocal exchange and correlation effects

Mat. Res. Soc. Symp. Proc. Vol. 442 © 1997 Materials Research Society

within the generalized gradient approximation of Perdew and Wang [5]. The total energy functional is minimized with respect to both the plane-wave coefficients of the occupied orbitals and the ionic degrees of freedom by using the conjugate gradient technique [6]. We employ *ab initio* norm-conserving pseudopotentials of the Kleinman-Bylander type. The pseudo wavefunctions are expanded in terms of a plane-wave basis set corresponding to a kinetic-energy cutoff of 7.29 Ry. Four special k points are employed to sample the primitive Brillouin zone.

An isolated Cl atom in the bulk GaAs is modeled using the supercell geometry containing 32 GaAs units. This 64-atom supercell corresponds to a distance between neighboring Cl atoms of 11.3 Å, which implies a weak interaction between Cl atoms in adjacent supercells. It is found that a 64-atom supercell and an energy cutoff of 7.29 Ry are sufficient to achieve the convergence of energy differences within 0.1 eV. The total-energy calculations are performed for various Cl positions in a supercell, some of which are shown in Fig. 1. For each position, all surrounding Ga and As atoms are fully relaxed in order to find the minimum-energy configuration.

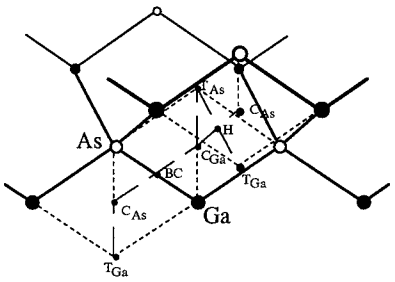


Figure.1: Relevant interstitial sites for Cl in GaAs: BC the bond center site, T the tetrahedral site (the subscript Ga and As indicate the first-nearest-neighbor atom), H the hexagonal site, C the sites defined as the center of the rhombus formed by three adjacent atoms and the nearest T site.

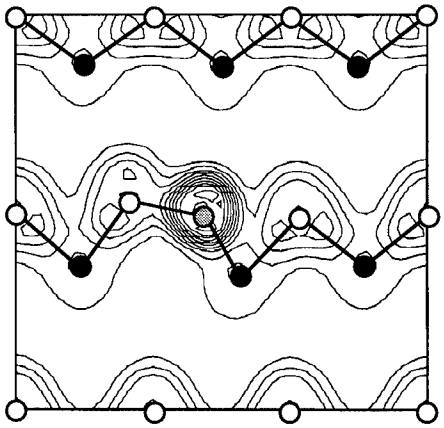


Figure 2: Contour plot of the calculated valence charge density in the (110) plane for the Cl^+ atom at the bond center site. Filled, open, and dotted circles denote Ga, As, and Cl atoms, respectively.

RESULTS AND DISCUSSION

First, we examine the stable configurations of an isolated Cl atom in bulk GaAs, in the positive, neutral, and negative charge states. The positively charged Cl (Cl^+) atom prefers the region of high electron density in bulk GaAs and interacts strongly with the lattice atoms. The lowest-energy position for the Cl^+ is the buckled bond center (BC) site, which bridges two neighboring Ga and As atoms. These Ga and As atoms have to move out over an appreciable distance. The equilibrium configuration of the Cl^+ atom at the BC site is shown in Fig. 2, together with the contour plot of the calculated valence charge density. The Ga-Cl and As-Cl bond length are 2.17 Å and 2.32 Å, respectively. The Ga-As distance is 4.08 Å, much longer than the Ga-As bond in bulk GaAs. The Ga-Cl-As bond is largely buckled with an angle of 132°. The Cl atom forms strong covalent bonds with the nearest neighbor Ga and As atoms. The Cl-related bonding states are buried deep in the GaAs valence band, and the antibonding states lie in the conduction

band, which are empty. The Cl atom at the BC site behaves like a donor impurity in GaAs. The low-density region including the tetrahedral (T) and hexagonal (H) interstitial sites is more than 1.8 eV higher in energy, compared as the BC site. The neutral Cl (Cl^0) atom exhibits the features similar to the case of Cl^+, having the BC site as the lowest-energy position.

For the case of the negatively charged Cl (Cl^-) atom, the lowest-energy position is the tetrahedral interstitial T_{Ga} site which has Ga atoms as the nearest neighbors. The host lattice atoms relax little in the vicinity of the Cl atom at the T_{Ga} site. The Cl-related energy levels at the T_{Ga} site are buried deep in the GaAs valence band, and thus the Cl atom is inevitably negatively charged at the T_{Ga} site. The other tetrahedral T_{As} site surrounded by four nearest neighbor As atoms is 0.95 eV higher in energy, compared with the T_{Ga} site. This is because the Cl^- atom prefers to have the less electronegative Ga atoms as the nearest neighbors. The H site is slightly lower in energy than the T_{As} site. Interestingly, the Cl^- is only 0.10 eV higher in energy at the BC site than at the T_{Ga} site. The As-Cl bond length is elongated to 2.72 Å, compared with the values of 2.32 Å for the Cl^+ atom at the BC site.

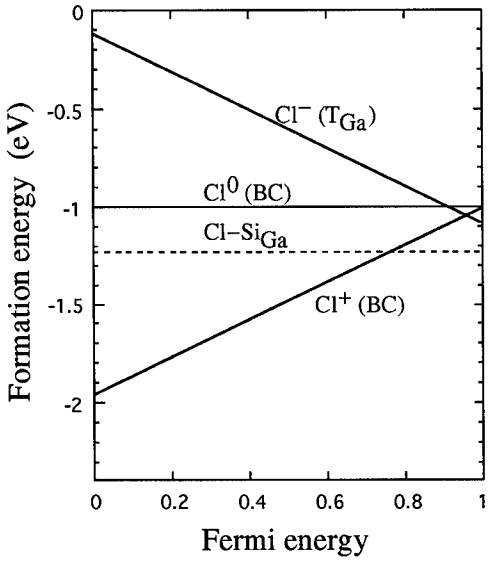


Figure 3: Formation energy of the different charge states of a Cl atom in GaAs as a function of the Fermi energy. The Cl atom is loacted at the most stable site in each charge state. The dotted line refers to the Cl-Si_{Ga} complex with a Si atom substituting for a Ga atom. The zero of the formation energy is the energy of a GaAs supercell and an isolated Cl atom in vacuum. The Fermi energy is measured from the top of the valence band, given in units of the energy gap Eg of GaAs.

In order to determine the lowest energy state of the Cl atom in GaAs, we must examine the relative energies of the different charge states. These relative energies depend on the position of the Fermi level, with which electrons are traded in order to alter the charge state of the Cl atom. Figure 3 presents the formation energy of the different charge states of Cl in GaAs as a function of the Fermi energy. When the Fermi level is situated at the top of the valence band, the lowest-energy state is the positively charged Cl^+ in the BC site. The Cl^+ atom is likely to be located in the high-density region in GaAs. As schematically shown in Fig. 4, when the Cl atom migrates from the left BC site to the right one in the high-density region, the nearest neighbor Ga atom needs to move from the right to the left. Although the process of Cl migration is rather complex in this way, we have calculated the migration barrier by assuming that the saddle point has the Cl atom and the nearest neighbor Ga atom on the vertical axis as shown in Fig. 4. This simple procedure is known to work well in many systems [7]. The saddle point is very close to the C_{Ga} site which is the center of two neighboring As atoms, with the Ga-Cl and As-Cl bond length being 2.13 Å and 2.56 Å, respectively. The migration barrier is calculated to be 0.69 eV. The Cl atom at the BC site

moves only around the nearest neighbor Ga atom via this migration path, but does not diffuse through the crystal. The migration path around the nearest neighbor As atom has a barrier of 1.22 eV at the saddle point near the C_{As} site, which is the center of two neighboring Ga atoms. As a result, the energy barrier for the Cl migration through the whole crystal is 1.22 eV. Until the Fermi level reaches just below the bottom of the conduction band, the Cl atom exhibits the same features.

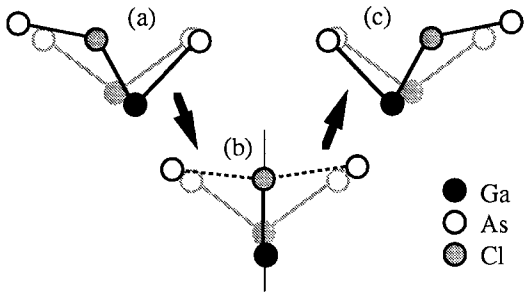


Figure 4: The geometry of the migration of Cl^+ in a (110) plane: (a) the initial stable BC, (b) the saddle point , and (c) the final stable BC geometries. The shadow figures are the nominal positions of Ga and As atoms in the perfect crystal. Filled, open, and dotted circles denote Ga, As, and Cl aroms, respectively.

When the Fermi level is at the bottom of the conduction band, there are two almost degenerated low-energy configurations; the T_{Ga} and the BC sites. The BC site is only 0.10 eV higher in energy than the T_{Ga} site. The Cl^- atom can diffuse through the lattice along a path connecting the T_{Ga} and BC sites shown in Fig. 5, with an energy barrier of less than 0.40 eV. The migration barrier, on the other hand, is 0.95 eV along a path connecting the T_{Ga} - H - T_{As} - H -T_{Ga} sites in the low-density region.

Consequently, the Cl atom prefers the positive charge state at the BC site in almost the whole region of the Fermi level, in spite of its high electronegativity. This is much different from the charge state of H atoms in GaAs [8]. The positive charge state of the Cl atom in GaAs is favored because the Cl atom forms strong bonding to the nearest neighbor Ga and As atoms. These strong bonding is not formed in the low-density region such as the T_{Ga} and the H sites.

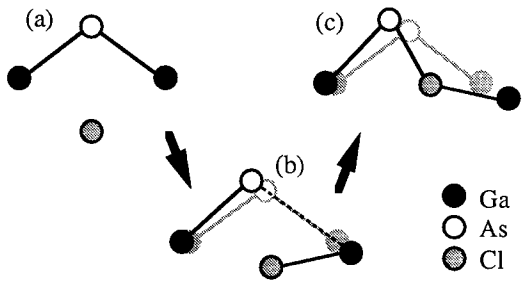


Figure 5: The geometry of migration of the negatively charged Cl^- atom, along a path connecting (a) form the T_{Ga} site, (b) through the intermediate site, and (c) to the BC site. Filled, open, and dotted circles denote Ga, As, and Cl aroms, respectively.

In order to clarify the difference of the stable T_{Ga} and BC sites in n-type GaAs, we have examined the actual interaction of the Cl atom with a Si donor atom. When Si substitutes for a Ga atom in bulk GaAs, a Si-related donor level is induced at the bottom of the conduction band. In this Si-doped GaAs, the minimum-energy configuration for the Cl atom is found near a T_{Ga} site with the substitutional Si atom as a nearest neighbor. Figure 6 shows the contour plot of the calculated valence charge density for the Cl-Si complex. Since the Cl-related energy level at the T_{Ga} site is much lower than the shallow donor level, the Cl atom behaves as an acceptor. The Cl

atom electronically passivates the Si donor and the Cl-Si complex is neutral. This passivation is accompanied by an effective charge transfer from Si to Cl . The complex of the Cl atom at the T_{Ga} site and the neighboring Si donor atom is stable by only 0.22 eV against the dissociation into the isolated Cl atom at the BC site and the isolated Si atom. After the dissociation, the Si donor is not passivated since the Cl atom behaves like a donor at the BC site. In this way, the interaction between the Cl atom and the Si donor atom favors the T_{Ga} site only little against the BC site. The low dissociation energy of the Cl-Si complex indicates that the passivation of Si donors by Cl is not effective.

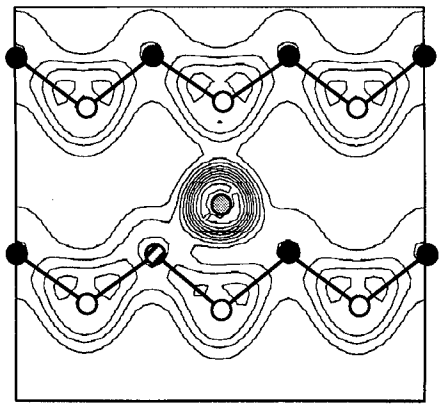


Figure 6: Contour plot of the calculated valence charge density in the (1-10) plane for the complex between the Cl atom at the T_{Ga} site and the substitutional Si atom in the Si-doped GaAs. Filled, open, hatched, and dotted circles denote Ga, As, Si, and Cl atoms, respectively.

We have also examined the behaviors of F atoms in GaAs, which is found to be quite different from those of Cl atoms. The F atom prefers the negative charge state at the T_{Ga} site, except for the Fermi level near the top of the valence band, which should be compared with the Cl atom preferring the positive charge state at the BC site. When the Fermi level is near the top of the valence band, the F atom becomes to be located at the BC site in the positive charge state. The migration barrier for the negatively charged F atom is as large as 0.7 eV, which is consistent with the low diffusivity of F atoms observed in GaAs [2]. The peculiar features of F atoms exhibiting high diffusivity in AlInAs is an open question to be solved. In Si-doped GaAs, the F atom is most likely to occupy the T_{Ga} site with the Si atom as a nearest neighbor and form an neutral F-Si complex. The dissociation energy of the F-Si complex is much larger than that of the Cl-Si complex, which implies that F atoms more effectively passivate Si donors in GaAs.

Finally, we make a comparison between Cl and F atoms in the context of etching. During etching of GaAs, the insertion of halogen atoms into Ga-As bonds is one of the most essential processes. As described above, the Cl atom at the BC site is the lowest-energy configuration for p-doped and undoped GaAs, and is one of the almost degenerated low-energy states for n-doped GaAs. This indicates that the Cl atom is likely to insert the Ga-As bond and disrupt the GaAs network, irrespective of the doping condition of the GaAs substrate. Thus, the GaAs etching rate by Cl atoms will depend slightly on the substrate doping. The etching effect of F atoms, on the other hand, will exhibit a large dependence on the substrate doping. In the case of p-type doping, the F atom is likely to break the Ga-As bond by occupying the BC site. In n-doped GaAs, however, the F atom preferentially occupies the T_{Ga} site and does not insert the Ga-As bond, which leads to a low etching rate compared with the case of p-type doping. For n-type doping, the F atoms penetrating the GaAs network stay near the surface in a large concentration, due to the large migration barrier. In heavily doped n-type GaAs, the high concentration of negatively charged F atoms near the surface induces a strong band bending and generates an inversion layer. Then, the effective Fermi level near the surface drops to the top of the valence band, the F atom becomes to occupy the BC site and initiates the disruption of the GaAs network. Only a few

experimental investigations of isolated halogen atoms in GaAs have been reported so far to allow a comparison with our calculated results. Our predictions regarding the charge state, migration path, and etching effect of Cl and F atoms provide useful information to understand technologically important halogen reactions.

CONCLUSION

The properties of Cl atoms in GaAs, such as stable configurations, migration paths, charge-state effects, and interaction with dopant atoms are theoretically investigated, based on the density functional theory using first-principles pseudopotentials in a supercell geometry. The stable charge state of an isolated Cl atom is determined as a function of the Fermi energy. When the Fermi level is at the top of the valence band, the Cl atom prefers the BC site in the positive charge state. The Cl atom diffuses through the GaAs crystal via a path in the high-density region with a fairly large energy barrier. When the Fermi level is at the bottom of the conduction band, the lowest-energy configuration of the Cl atom is the T_{Ga} site in the negative charge state, and the BC site is almost degenerated with the T_{Ga} site. The Cl atom is found to prefer the positive charge state at the BC site in almost the whole region of the Fermi energy, in spite of its high electronegativity. In Si-doped GaAs, the Cl atom occupies the T_{Ga} site with the substitutional Si donor atom as a nearest neighbor, and forms a neutral Cl-Si complex. The dissociation energy of the Cl-Si complex into the isolated Cl and Si atoms is very small.

REFERENCES

[1] C.G. Van de Walle, F.R. McFeely, and S.T. Pantelides, Phys. Rev. Lett. **61**, 1867 (1988).
[2] N. Hayafuji, Y. Yamamoto, N. Yoshida, T. Sonoda, S. Takamiya, and S. Mitsu, Appl. Phys. Lett. **66**, 863 (1995).
[3] Hydrogen in Semiconductors, edited by J.I. Pankove and N.M. Johnson, Semiconductors and Semimetals Vol.34 (Akademic, New York, 1991).
[4] P. Hohenberg and W. Kohn, Phys. Rev. **136**, B864 (1964).
[5] J.P.Perdew, J.A. Chevary, S.H. Vosko, K.A. Jackson, M.R. Pederson, D.J. Singh, and C. Fiolhais, Phys. Rev. B**46**, 6671 (1992).
[6] M.P. Teter, M.C. Payne, and D.C. Allan, Phys. Rev. B**40**, 12255 (1989).
[7] Z. Jiang and R.A. Brown, Phys. Rev. Lett. 74, 2046 (1995).
[8] L. Pavesi and P.Giannozzi, Phys. Rev. B**46**, 4621 (1992).

LOW TEMPERATURE PHOTOLUMINESCENCE PROPERTIES OF IN-SITU ZN DOPED INP LAYERS GROWN BY LP-MOCVD

Y. B. MOON*, S. K. Si**, E. YOON*, and S. J. KIM**
*School of Materials Science and Engineering & Inter-university Semiconductor Research Center, Seoul National University, Seoul 151-742, Korea
**School of Electrical Engineering & Inter-university Semiconductor Research Center, Seoul National University, Seoul 151-742, Korea

ABSTRACT

In situ Zn-doped InP layers are grown by low pressure metalorganic chemical vapor deposition at 620 °C. Hole concentration increases with dopant flow rate, but reaches a saturated hole concentration of approximately 1.5 x $10^{18}/cm^3$. Differently from the Zn-diffused InP case, photoluminescence (PL) of the *in situ* Zn doped InP shows band edge peak, e/D-A peak and distant D-A peak up to the hole concentration of 7.6 x $10^{17}/cm^3$. These results can be explained by less generation of interstitial Zn atoms during *in situ* doping. PL characteristics of the *in situ* Zn-doped InP at the saturated hole concentration is extensively studied to explain its compensation mechanism. Two new deep bands, presumably responsible for the hole saturation behavior, are observed for the first time.

INTRODUCTION

Zn is one of the most important p-type dopants in InP and its related compound semiconductors widely used in optoelectronic device fabrication. Diffusion [1,2] and *in situ* doping [3,4] are normally used for the Zn doping. It was reported that the hole concentration in a Zn-diffused InP was 0.5 - 10% of the total Zn concentration and after a high-temperature activation anneal, the hole concentration increased to the value comparable to the Zn concentration. [2] It is now widely accepted that small hole concentration in a Zn diffused sample is attributed to the self-compensation of Zn acceptors by Zn deep donors in interstitial sites. Interstitial Zn atoms are generated during the diffusion process which proceeds by interstitial-substitutional kick-out mechanism and behave as deep donors. In *in situ* Zn doping by metalorganic chemical vapor deposition (MOCVD), the doping efficiency was reported to be very low due to the high equilibrium vapor pressure of Zn. Hole concentration saturated approximately at a 1 - 2 x $10^{18}/cm^3$ level [7], presumably due to a similar self-compensation mechanism.

Photoluminescence (PL) is a characterization technique used frequently for the study of the band structure and the carrier recombination mechanism in III-V semiconductors. [8,9] A characteristic donor-acceptor transition, resulting from the presence of interstitial Zn atoms, was reported for the Zn-doped InP. [1,2] PL characteristics for the *in situ* Zn-doped InP was also reported [8], however, the PL characteristics for the sample doped close to the doping saturation level has not been reported yet.

In this paper, the low-temperature PL characteristic of the *in situ* Zn-doped InP is reported at various doping levels. InP samples are grown by low pressure metalorganic chemical vapor

Mat. Res. Soc. Symp. Proc. Vol. 442 © 1997 Materials Research Society

deposition (LP-MOCVD) with diethylzinc (DEZn) as a dopant source.

EXPERIMENT

InP samples are grown by LP-MOCVD in a horizontal quartz reactor. A graphite susceptor is heated by RF induction. Substrate temperature is monitored by a thermocouple inserted in the susceptor. The wafer temperature is calibrated by infrared interference measurement. [10] Trimethylindium (TMIn) and PH_3 (99.9997%) is used as an indium and a phosphorus source, respectively. Diethylzinc (DEZn) is used as a Zn dopant source. Palladium-purified H_2 is used as a carrier gas, and its total flow rate is fixed at 12 slm. A semi-insulating (100) InP substrate (Fe-doped) is cleaned sequentially in trichloroethane, acetone, and methanol for 10 minutes each with ultrasonic agitation and finally rinsed with deionised water. It is etched in 5 H_2SO_4 : 1 H_2O_2 : 1 H_2O solution and rinsed with deionised water. It is cleaned *in situ* for five minutes at 620 °C in a PH_3 ambient. 2 μm thick Zn doped InP layers are grown at reactor pressure of 76 Torr and growth temperature of 620 °C. Flow rates of TMIn and PH_3 are held constant at 0.91 sccm and 218 sccm, respectively. The growth rate of InP at this condition is 3.4 μm/h. DEZn flow rate is varied from 0.01 sccm to 0.36 sccm in this study.

Hole concentrations of Zn-doped InP layers are measured by an electrochemical C-V profiler. Samples are excited by an Ar^+ ion laser, and the photoluminescence is dispersed in a double monochromator and detected by a Ge photodiode cooled by liquid nitrogen.

RESULTS

InP epilayers are grown at 620 °C at various DEZn flow rates. Hole concentration in Zn-doped InP increases with DEZn flow rate, but reaches a saturation hole concentration of approximately 1.5 x $10^{18}/cm^3$, as shown in Fig.1. Similar saturation behavior for the *in situ* Zn doping was previously reported by other researchers [7], but little was discussed about its physical origin. For the Zn-diffused InP, hole concentrations greater than 3 x $10^{18}/cm^3$ were reported, however, the actual Zn concentrations measured by secondary ion mass spectrometry (SIMS) measurement were much higher than the hole concentration. [2,7] These results imply that a kind of compensation mechanism limits the maximum available hole concentration for the Zn-doped InP. From low temperature PL experiments on the Zn-diffused and annealed InP layers [1,2] Zn

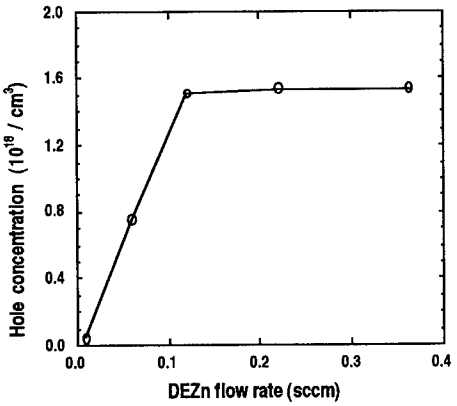


Fig.1 Hole concentration change with DEZn flow rate measured by electrochemical C-V. *In-situ* Zn doped InP epilayers were grown by MOCVD at 76 Torr, 620 °C and for all samples TMIn flow rate was 0.91 sccm and PH_3 flow rate was 182 sccm.

deep donors at interstitial sites are believed to be responsible for the compensation.

In Fig.2, PL spectra of *in situ* Zn doped InP are compared with that of Zn-diffused InP. *In situ* Zn-doped InP layers have hole concentrations below the saturation limit of $10^{18}/cm^3$ and Zn-diffused InP at 550 °C has the hole concentration of $7.5 \times 10^{17}/cm^3$. Well-resolved band edge peaks in the InP with hole concentration of $4.6 \times 10^{16}/cm^3$ are shown in Fig.2 (a). These peaks are a donor bound exciton peak at 1.417 eV and a strong Zn bound exciton peak at 1.414 eV. The intensity of the e/D-A peak (transition from band or a shallow donor level to an acceptor level) at 1.378 eV, corresponding to an ionization energy of 42 meV [9] for a Zn acceptor, is weaker than that of the Zn bound exciton peak due to low doping concentration. The intensity of the e/D-A peak increases with doping concentration and exceeds that of the band edge peak at 1.408 eV when hole concentration increases to $7.6 \times 10^{17}/cm^3$ (Fig.2 (b)). But in Fig.2 (c) from Zn-diffused InP, only one band with peak at 1.32 eV is observed and this band is known as distant deep donor to acceptor (D-A) transition. [11,12]

A weak peak at 1.334 eV is observed in Fig.2 (a) and its intensity increases abruptly as hole concentration in Fig.2 (b). As the excitation power increases, the energy of the peak indexed as high-energy band (HEB) in Fig.2 (b) increased from 1.295 eV at 2 mW to 1.367 eV at 50 mW. [11] Peak shift of 50 meV/decade is observed. The e/D-A peak and the band edge peak at 1.408 eV show no energy shift with excitation power. This large energy shift with excitation power is a typical characteristic of distant D-A transition. [12] Moreover, the peak position of the HEB is matching with the results reported for the Zn-diffused InP. [1,2] Thus, the broad band HEB in Fig.2 (b) with hole concentration of $7.6 \times 10^{17}/cm^3$ is assigned as a distant D-A peak. However, the 1.334 eV peak in Fig.2 (a) shows no energy shift with excitation power. Energy difference between this peak and the e/D-A peak is 44 meV and this energy corresponds closely to a longitudinal optical (LO) phonon energy of InP, 42.8 meV [13]. The 1.334 eV peak in Fig.2 (a) is assigned as an LO phonon replica of the e/D-A peak.

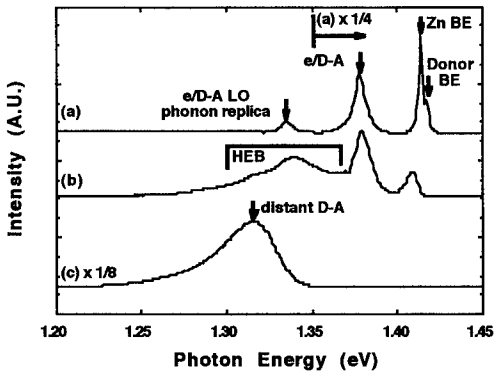


Fig.2 PL spectra of *in-situ* Zn doped InP layers with hole concentrations of (a) $4.6 \times 10^{16}/cm^3$, (b) $7.6 \times 10^{17}/cm^3$ and (c) Zn-diffused InP at 550 °C with hole concentration of $7.5 \times 10^{17}/cm^3$. The excitation power is 10mW and the sample temperature is 9K.

These PL characteristics observed in *in situ* Zn-doped InP are very different from that of Zn-diffused InP. [1,2,11] The difference can be explained by less incorporation of interstitial Zn during *in situ* doping than Zn-diffusion and the detailed results about the comparison will be published elsewhere. [11]

For the *in situ* Zn-doped InP, the hole concentration becomes saturated at high doping levels. This implies that a kind of compensation mechanism plays an important role. To investigate the compensation behavior, PL measurement are made for the samples with a saturated hole concentration of $1.5 \times 10^{18}/cm^3$, as shown in Fig.3. Samples shown in

Fig.3 have the same hole concentrations, but the actual DEZn flow rates during growth are varied. Flow rates are (a) 0.12 sccm, (b) 0.22 sccm and (c) 0.36 sccm, respectively. Comparison of Fig.3 with Fig.2 reveals some different features in PL spectra between samples at the hole saturation level and samples below the hole saturation level. First, the intensity of the e/D-A transition peak at 1.380 eV, one of the most dominant transition in the *in situ* Zn-doped InP, and the band edge peak at 1.404 eV decrease as DEZn flow rate increases. Second, the energy of the peak found at 1.336 eV, did not change with excitation power[11], and assigned as LO phonon replica of the e/D-A transition.

In Fig.3, no distant D-A transition, as appears from 1.29 eV to 1.35 eV in Zn-diffused samples, was found. Instead, other two bands, indexed as low energy band No. 1 (LEB1) and low energy band No. 2 (LEB2) are observed, as shown in Fig.3. The energy range of LEB1 and LEB2 are from 1.21 eV to 1.27 eV and from 0.882 eV to 1 eV, respectively. For LEB1 band, the peak shifts to lower energy as DEZn flow rate increases. The peak energy of LEB1 shifts by 100 meV/decade with excitation power. [11] This result indicates that the LEB1 band results from the donor to acceptor transition and the centers involved in this transition have deeper energy levels than involved in D-A transition found in Fig.2. [12] It implies that LEB1 band in Fig.3 have a different origin than the D-A transition found in Fig.2. Intensity of LEB2 band increases with DEZn flow rate but showed no energy shift with excitation power.

This abrupt changes in PL spectra has never been reported and it is presumed that there should be a change in a dominant recombination path near a hole saturation level of 1.5 x $10^{18}/cm^3$. Below the saturation level, Zn deep donors at interstitial sites and Zn acceptors are the most stable sites for electrons and holes respectively, and they predominantly recombine via these recombination centers. At the saturation level, however, the PL spectra in Fig.3 clearly indicates that there is a change in recombination path from HEB and band edge transition to LEB1 and LEB2 bands. When doping concentration reaches a saturation level, new deep centers related with LEB1 and LEB2 appears and the recombination occurs more efficiently through these deeper centers.

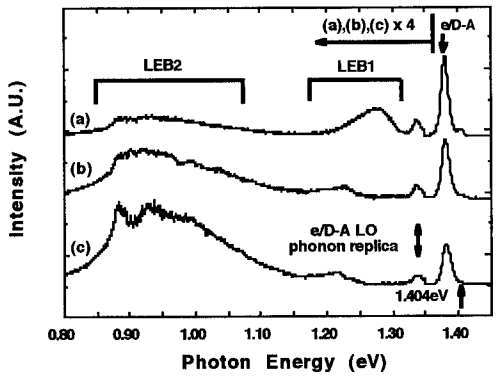


Fig.3 PL Spectra of *in-situ* Zn doped InP layers with saturated hole concentration of 1.5 x $10^{18}/cm^3$. The excitation laser power is 10mW and sample temperature is 9K. DEZn flow rates are (a) 0.12 sccm, (b) 0.22 sccm and (c) 0.36 sccm.

PL spectra of the InP samples grown at DEZn flow rate of 0.12 sccm are monitored at various measurement temperatures. As shown in Fig.4, the e/D-A peak overlaps with band edge peaks as temperature increases and eventually only a band edge peak is found at temperatures higher than 200 K. The LEB1 peak also overlaps with HEB and disappears at temperatures higher than 150 K. At room temperature HEB peak disappears. But as shown in Fig.5, LEB2 does not disappear even at room temperature and this fact is important because it implies that even at room temperatures

this band effectively captures carriers and remains as an effective recombination center.

At this time the physical origin for LEB1 and LEB2 bands is not clear. Montie *et al.* observed two bands after annealing of the Zn diffused InP samples [2]; one is the distant D-A band at 1.3 eV and the other is the peak observed in the same energy range with LEB1 band in this study. It was speculated that it might be related with P vacancies formed during annealing. In our experiments, excessive supply of Zn at high DEZn flow rates may foster local precipitation of Zn_3P_2 which is known energetically more stable at near 900 K. [14] Local strain energy from the precipitate in zincblende structure may be lowered by P vacancy formation. Such intrinsic defects formed during growth behave as donors compensating Zn acceptors, but more studies need to be done to identify the physical origin.

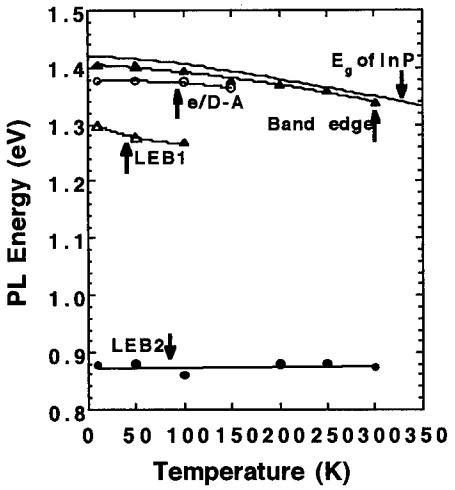


Fig.4 Changes of PL peak energy with measurement temperature. PL peaks are obtained from InP sample with hole concentration of 1.5 x $10^{18}/cm^3$ and DEZn flow rate of 0.12 sccm.

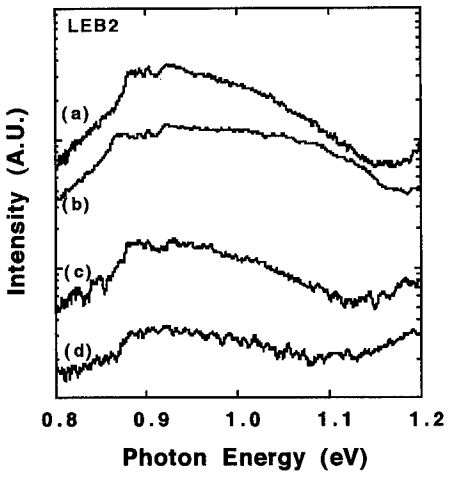


Fig.5 PL spectrum of LEB2 at various sample temperature, (a) 9K, (b) 100K, (c) 200K, (d) 300K. The spectra were obtained from InP samples with hole concentration of 1.5 x $10^{18}/cm^3$ and DEZn flow rate of 0.12 sccm.

CONCLUSIONS

In situ Zn-doped InP samples are grown by LP-MOCVD at 620 °C. Their hole concentration shows saturation behavior at 1.5 x $10^{18}/cm^3$. PL spectra of the *in situ* Zn-doped InP below the saturation level show well resolved band edge peak, e/D-A peak, and distant D-A peak. The e/D-A peak is strongest and distant D-A peak is weaker than e/D-A peak, and this intensity distribution is very different from that of Zn-diffused InP. These results can be explained by less generation of interstitial Zn atoms during *in situ* doping.

As the hole concentration becomes saturated, a peak from distant D-A transition, one of the most dominant recombination mechanism below the saturation level, disappears and the new two bands, LEB1 and LEB2 emerge. From the investigation on the characteristics of LEB1 and LEB2 bands at various temperatures, excitation powers, and DEZn flow rates, it is found that these bands are governed by the saturation of hole concentration. The bands, LEB1 and LEB2, may be related with intrinsic defect or defect complexes at high Zn concentration.

ACKNOWLEDGEMENTS

This work was supported by the Ministry of Education through Inter-university Semiconductor Research Center (ISRC 94-E-3142) and Korea Science and Engineering Foundation (KOSEF 93-01-00-17).

REFERENCES

[1] J. K. Hsu, C. Juang, B. J. Lee, and G. C. Chi, J. Vac. Sci. Technol. B **12**, 1416 (1994).
[2] E. A. Montie, and G. J. van Gurp, J. Appl. Phys. **66**, 5549 (1989).
[3] A. Molassioti, F. Scholz, and Y. Gao, J. Cryst. Growth **102**, 974 (1990).
[4] C. Blaauw, and L. Hobbs, Appl. Phys. Lett. **59**, 674 (1991).
[5] N. H. Ky, L. Pavesi, D. Araujo, J. D. Ganiere, and F. K. Reinhart, J. Appl. Phys. **69**, 7585 (1991).
[6] N. H. Ky, J. D. Ganiere, M. Gailhnou, B. Blanchard, L. Pavesi, G. Burri, D. Araujo, and F. K. Reinhart, J. Appl. Phys. **73**, 3769 (1993).
[7] A. W. Nelson, and L. D. Westbrook, J. Cryst. Growth **68**, 102 (1984).
[8] V. Swaminathan, V. M. Donnelly and J. Long, J. Appl. Phys. **58**, 4565 (1985).
[9] B. J. Stromme, G. E. Stillman, J. D. Oberstar, S. S. Chan, J. Electron. Mater. 13, 463 (1984).
[10] V. M. Donnelly, and J. A. McCaulley, J. Vac. Sci. Technol. A **8**, 84 (1990).
[11] Y. B. Moon, S. K. Si, E. Yoon, and S. J. Kim, *submitted to J. Appl. Phys.*.
[12] R. Dingle, Phys. Rev. **184**, 788 (1969).
[13] G. F. Alfred, and P. H. Borcherds, J. Phys. C **8**, 2022 (1975).
[14] I. Barin, in *Thermochemical Data of Pure Substances Part II*, (VCH, Weinheim, 1989), p. 1695.

The Differences between the $In_yGa_{1-y}As/GaAs$ Interface and $GaAs/In_yGa_{1-y}As$ Interface in Superlattice over a $In_xGa_{1-x}As$ (x<y) Buffer Layer

X.J.Wang[a] L.X.Zheng[a] Z.B.Xiao[a] Z.P.Zhang[b] X.W.Hu[a] Q.M.Wang[b]
a National Research Center for Optoelectronic Technology, Institute of Semiconductors, CAS, Beijing 100083, P.R.China
b National Integrated Optoelectronics Laboratories, Semiconductor Institute Region, Beijing 100083, P.R.China

The $In_yGa_{1-y}As/GaAs$ superlattice on $In_xGa_{1-x}As$ (x<y) buffer layer was grown by MOCVD. The well layer is under compressive strain and the barrier layer is under tensile strain. However, both layers do not exceed the calculated critical value based on the M&B equilibrium theory. According to the measuring results of TEM、SIMS, we found that: the $GaAs/In_yGa_{1-y}As$ interface was smoother than the $In_yGa_{1-y}As/GaAs$ interface; the Indium composition gradual region at the $GaAs/In_yGa_{1-y}As$ interface was narrower than that at the $In_yGa_{1-y}As/GaAs$ interface; in $In_yGa_{1-y}As$ alloy layer, the Indium composition near the $GaAs/In_yGa_{1-y}As$ interface was higher than that near another interface. For the first time, we explained the composition profile in this kind of superlattice based on the indium segregation theory. A new strain relaxation model, in which the 30-degree and 90-degree shockley partial dislocations were taken into account under both tensile and compressive strains, was presented to explain the difference of the smoothness between the $GaAs/In_yGa_{1-y}As$ interface and the $In_yGa_{1-y}As/GaAs$ interface.

I. INTRODUCTION

The thin heterojunction epitaxial material with sharp composition profiles and smooth interface is crucial to the device applications . However, some intrinsic atomic displacements affect the sharpness of the interface seriously. In this paper, unique feature in the Indium cmposition profile of $In_yGa_{1-y}As/GaAs$ superlattice was found and explained based on the Indium segregation theory for the first time.

Strain is another important factor to affect the interface quality in the InGaAs/GaAs superlattices. In this paper, we present a new strain relaxation model in which the shockley partial dislocation is considered. A good explanation to our experimental results was given based on this model.

For convenience, we suppose the item GaAs/InGaAs denotes the interface at which GaAs is grown over InGaAs surface and the item InGaAs/GaAs denotes the interface at which InGaAs is grown over the GaAs surface.

II. THEORIES

A. The Indium Segregation in Superlattices during Epitaxial Growth

During the growth of some III-V alloys,such as InGaAs and AlGaAs compounds, the more weakly bonded III-column elements will segregate on the surface.

If the growth temperature is low, the difference in composition between surface and bulk can only be formed by the accumulation of the segregated atoms on the moving growth surface. In this case ,the rapid atomic exchanges between the growth surface ML (Monolayer) and the surface ML substitute for the bulk diffusion which leads to a segregated alloy composition profile.

Mat. Res. Soc. Symp. Proc. Vol. 442 © 1997 Materials Research Society

Such atomic exchanges are so rapid that the exchange-related atoms can be considered to be in quasi-equilibrium state and its composition profile will be determined by the standard equilibrium model[1-3]:

$$\ln \frac{x_s}{1 - x_s} - \frac{E_s}{kT} + \frac{Ca^3}{4kT}\left(\frac{\delta a}{a}\right)^2 \left(1 + \frac{\delta a}{a}(x_s + x_b)(x_s - x_b)\right) = \ln \frac{x_b}{1 - x_b} \qquad (1)$$

where x_s and x_b are the Indium composition of surface and bulk respectively, C is the elastic constant, T the temperature, a the bulk lattice constant of the alloy compound, δ a/a the relative difference in lattice constant between two binary compounds of which the ternary alloy compound is composed.E_s is the energy decrease when the sub-surface atoms move to the surface(E_s>0).

So, the Indium composition x_s of the surface ML and the Indium composition x_b of the sub-surface ML are determined by equation (1) and the mass conservation law.The Indium composition of the growth surface ML is renewed in this way layer by layer.

Based on the above model, the calculated Indium composition profile for the InGaAs/GaAs superlattices for several bulk composition is shown in figure.1.

B. The difference in relaxation mechanism between the compressive and tensile strain

If the thickness of strained epitaxial layer exceeds the critical value,3D growth will take place and misfit dislocations will apear because of the strain relaxation [4-7]. The misfit dislocations may be formed by gliding and climbing of threading dislocations or nucleation at the boundary of the 3D island [8]. During both processes, the Shockley partial dislocations are possible to be formed before the creation of a perfect 60° type dislocation [9,10]

Generally, only 60° perfect dislocation is considered in M&B theory. However,it is found that the shockley partial dislocation has less formation energy than the perfect 60° dislocation if the stacking fault energy is small [10-12].In this case, we have the following dislocation reaction equation

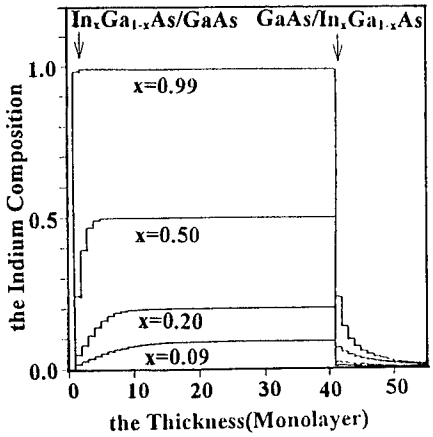


FIG. 1. The theory results of segregated Indium composition profile in InGaAs/ GaAs superlattices.

$$a/6[211] + a/6[112] \rightarrow a/2[101] \qquad (2)$$

and their burger vectors have the following relation

$$|b_1|^2 + |b_2|^2 < |b|^2 \qquad (3)$$

According to the Frank Rule [13], the dislocation energy is proportiopnal to the square of its burger vector length. Considering its lower energy compared to a perfect 60° type dislocation, the shockley partial is more possible to create before the creation of a perfect 60° type dislocation.

The atomic arrangement on the (111) glide plane determine which of the two partials will nucleate first. The first partial to be nucleated will be the 90° partial and then the 30° partial under tensile strain. But the order of the partial nucleation will be reversed for the case of compressive stress because the resolved shear stress under compressive strain is opposite to that under tensile strain[14].

Considering the shockley partial dislocation, we calculate the critical thickness Hc by using the mechanic equilibrium equation[6]:

$$HC = \frac{b(1 - \nu\cos^2\theta)}{8\pi\varepsilon(1+\nu)\cos^2\lambda} Ln(\frac{\alpha HC}{b}) \qquad (4)$$

Where b is the burger vecter length, ν the possion ratio, ε the strain, α the dislocation core energy θ is the angle between the dislocation line and the burger vector, and λ is the angle between the burger vector and direction normal to the dislocation line on the interface. The calculated results are shown in figure 2.

III. EXPERIMENTS

A. Sample

The sample was grown by low pressure Metalorganic Chemical Vapour Depositon. A $In_{0.06}Ga_{0.94}As$ buffer layer,with thickness 900nm greatly exceeding its critical value, was grown over (001) GaAs substrate at 600°C.Then, a $In_{0.09}Ga_{0.91}As$/ GaAs superlattice with well width 12.4nm,barrier width 16.4nm and period numbers 30, was grown over the $In_{0.06}Ga_{0.94}As$ buffer layer.

B. The measurement results

We have characterized the interface of the sample by using Transmission Electron Microscopy, Secondary Ion Mass Spectroscopy measurements.

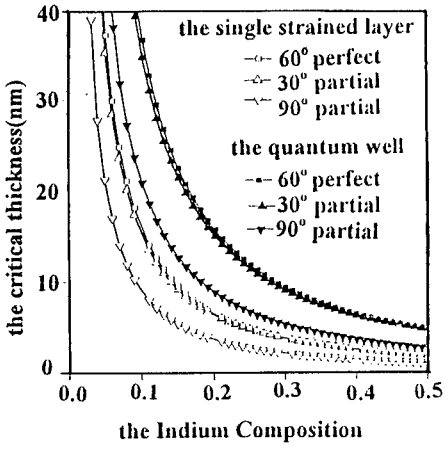


FIG. 2. The calculated critical thickness considering different kinds of misfit dislocations.

As shown in figure 3, there are several distinctive features in the cross section TEM picture of the GaAs/ $In_{0.09}Ga_{0.91}As$ superlattice:

The GaAs/$In_{0.09}Ga_{0.91}As$ interface is smoother than the $In_{0.09}Ga_{0.91}As$/GaAs interface;the region in the well layer near the GaAs/ $In_{0.09}Ga_{0.91}As$ interface is blacker (the blacker the TEM picture,the higher the Indium composition) than that near the $In_{0.09}Ga_{0.91}As$ /GaAs interface;the contrast at GaAs/ $In_{0.09}Ga_{0.91}As$ interface is more remarkable than that at another interface.

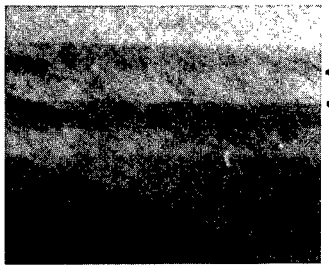


FIG. 3. The cross section TEM picture of the InGaAs/GaAs superlattice.

The SIMS measurements are given in the figure 4. Here, the SIMS measurements are obtained by sputtering the sample from the epitaxial surface to the substrate.The most unique feature in figure 4 is that the Indium gradient at GaAs/$In_{0.09}Ga_{0.91}As$ interface is larger than the gradient at $In_{0.09}Ga_{0.91}As$ /GaAs interface.

VI .DISCUSSIONS ABOUT THE EXPERIMENTAL RESULTS

A.The Indium profile in InGaAs/GaAs superlattice

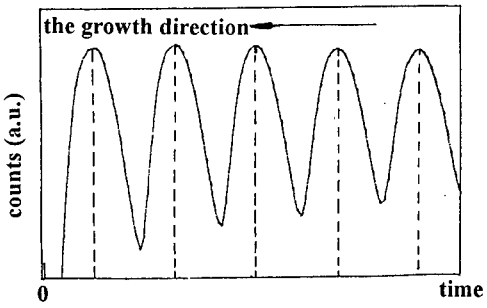


FIG. 4. The SIMS measurement result of the InGaAs/GaAs.

The calculated results in figure 1, show clearly that the Indium composition near the GaAs/$In_{0.09}Ga_{0.91}As$ interface is higher than that near the $In_{0.09}Ga_{0.91}As$/GaAs interface and the gradient for the former is larger than that for the latter.These will well explain the second and third features in the TEM picture depicted in III.B. In the meantime, it is also qualitatively identical with the characteristics of SIMS in figure 4.

B. The smoothness of the interface

We think the growth modes of both the barrier and well layers are determined by their relative mismatch. And we also think that only the calculated results for single epitaxial layer need to be considered. This is because the growth modes have been determined before the growth of the cap layer for a cladding structure.

If we consider only perfect 60° dislocation, both the GaAs barrier width 16.4nm and the $In_{0.09}Ga_{0.91}As$ well width 12.4nm are less than the calculated critical thickness.However, the case is different if we consider shockley partials.The GaAs layer is in a tensile state,so the 90° partial would nucleate first and determine its critical thickness.The $In_{0.09}Ga_{0.91}As$ layer is in a compressive state,so the 30° partial would nucleate first and determine its critical thickness. It can be seen from figure 2 that the GaAs layer already exceeds the calculated critical thickness based on the 90° partial and $In_{0.09}Ga_{0.91}As$ layer is still less than the calculated critical thickness based on the 30° shockley partial.This is the reason why GaAs has a rough surface (namely a rough $In_{0.09}Ga_{0.91}As$/GaAs interface) and $In_{0.09}Ga_{0.91}As$ has a smooth surface (namely a smooth GaAs/$In_{0.09}Ga_{0.91}As$ interface). We also know from the discussion in II.B section that misfit dislocation will glide with a perfect 60° type in compressive state. So, there are chances for it climbing from one (111) plane to another (111) plane. This leads to a curved dislocation line and preclude the dislocation extension to the $In_{0.09}Ga_{0.91}As$ layer from GaAs layer,perhaps another factor to smoothen $In_{0.09}Ga_{0.91}As$ surface.

V. CONCLUSIONS

The TEM measurement and `SIMS characterization show that Indium composition gradual region at GaAs/$In_{0.09}Ga_{0.91}As$ interface is narrower than that at $In_{0.09}Ga_{0.91}As$/GaAs interface.In the $In_{0.09}Ga_{0.91}As$ alloy layer , the Indium composition near GaAs/$In_{0.9}Ga_{0.91}As$ interface is higher.We explain these features in Indium profile in the superlattices by using Indium segregation theory for the first time.

Another feature in the TEM picture is that the GaAs/$In_{0.09}Ga_{0.91}As$ interface is smooth and the other interface is rough.Considering the Indium profile of this sample,we present a new relaxation model in which the shockley partials are taken into account to explain it .Our model may be very helpful to the optoelectronic device design using strained materials.

REFERENCES

1. J.Bonard, 《Adsorption on Metal Surfaces》 , Blsorier Press, New York,1983
2. R.Bruisma and A.Zangwill, Europhys.Lett.4(1987)729
3. J.Hornstra and W.I.Bartcls,J.Cryst.Growth.44(1978)513
4. M.Grabow and G.Gilmer, Mat.Res.Soc. Proc.94(1987)13

5. J.H.Van der Merwe and C.A.B.Bal in《Epitaxial Growth》, Part B, Academic Press ,New York, (1975)193
6. J. W. Mattews and A.B.Blakcslee,J.Cryst.Growth 27(1974)118;32(1976)265
7. Brian W. Dodson and I.J.Fritz , Crystal Properties & Preparation , vol.21, (1989)29
8. J.W.Matthews, 《Epitaxial Growth 》 , Academic Press, New York, (1975)581
9. D.Hull and D.J.Bacon, 《Introduction to Dislocations》 , Pergamon Press , Oxford, (1984)91
10. E.A.Fitzgerald, D.G.Ast, P.D.Kirchner, G.D.Pettit, and J.M.Woodall, J.Appl.Phys. 63(3)(1988)693
11. M.P.A.Viegers, C.W.T.Bulle lieuwma, P.C.Zalm and P.M.J.Maree, Mat.Res.Soc.Proc.37(1985)331
12. P.M.J.Maree, Olthof,J.W.M.Frenken,J.F.van der Veen,C.W.T.Bulle-Lieuwma,M.P.A.Viegers,and P.C.Zalm, J.Appl.Phys.58(1985)3097
13. J.P.Hirth, 《Theory of Dislocation》 , 2nd. ed., Wiley Press, New York, 1982
14. J.Petruzllo, M.R.Leys, Appl.Phys.Lett.53(24)(1988)2414

DEFECT CHARACTERIZATION OF InAs WAFERS USING POSITRON LIFETIME SPECTROSCOPY

J. MAHONY and P. MASCHER
Department of Engineering Physics, McMaster University, Hamilton, Ontario, Canada L8S 4L7

ABSTRACT

Positron lifetime measurements on InAs wafers have shown that the positron bulk lifetime in InAs is 246±2 ps. Most samples exhibit a defect lifetime of 287±6 ps, which is attributable to monovacancy-impurity complexes with a concentration of $7\pm2\times10^{16}$ cm^{-3}. Very heavily doped n-type samples exhibit a defect lifetime of 332-340 ps, characteristic of divacancies. The concentration of these defects is also close to 10^{17} cm^{-3}. Both types of defects are stable for rapid thermal annealing up to 850 °C, and both defects are neutral. The formation of the divacancy-type defects may be correlated with a discrepancy between the carrier concentration and the total dopant concentration.

INTRODUCTION

InAs is a high mobility, narrow bandgap semiconductor that is suitable for many different electrical and far infrared optical applications, including heterojunction field effect transistors [1], resonant tunneling diodes [2], bipolar transistors [3], and far infrared lasers [4]. Compared to more common III-V semiconductors such as GaAs and InP, however, very little is known about the point defect characteristics of InAs.

Positron lifetime spectroscopy (PLS) is an effective tool for characterizing vacancy-type defects in III-V compound semiconductors. Lifetimes that result from annihilations of positrons in trapped defect states can indicate the size of the open volume of the defect when compared to the lifetime for annihilations in the delocalized Bloch state, often called the "bulk lifetime". To use PLS as a defect characterization tool, it is therefore crucial that the bulk lifetime of the material be accurately known. There are several published results of positron lifetime measurements in InAs [5-8]. However, most of these measurements were made on single samples and the reported bulk lifetime values vary significantly, from 247 to 285 ps. Due to this very significant scatter, PLS at this point has not contributed reliable information about the defect characteristics of InAs.

In this contribution, PLS measurements on a large number of variously doped single crystalline InAs wafers are described. The purpose of this study is twofold: First, to accurately determine the bulk and defect positron lifetimes in InAs, and second, to investigate the doping dependence of the defect characteristics.

EXPERIMENTAL DETAILS

The InAs samples were grown at the Institute of Electronic Materials Technology in Warsaw, Poland, and contained a wide range of dopant concentrations. Carrier concentrations and mobilities were measured using the Hall effect. Rapid thermal annealing was performed in flowing nitrogen for 10 seconds with a temperature ramp of 100°C/s.

Mat. Res. Soc. Symp. Proc. Vol. 442 © 1997 Materials Research Society

Positron lifetime spectroscopy was performed using three different spectrometers with time resolutions (FWHM) of between 205 ps and 230 ps, and channel widths of approximately 19 ps. The positron sources were ^{22}NaCl encapsulated in Al foil of thickness 0.65 mg/cm^2, and had activities between 10 μCi and 20 μCi, yielding peak to background ratios of 3×10^3 to 7×10^3. To account for annihilations in the Al foil, lifetimes of 155 ps and 256 ps with absolute intensities of 1.60 % and 4.12 % were subtracted from the spectra.

The positron lifetime spectra were analyzed using PATFIT88 [9]. At least two spectra were measured for each sample condition. Measurements were made as a function of the spectrum area to determine the minimum number of lifetimes required to obtain a good fit. For two-lifetime fits, good chi-squared values were only possible for spectrum areas less than approximately 2×10^6. As was previously observed in InP [10], two-lifetime fits became statistically unacceptable for larger spectrum areas. Three-lifetime fits yielded good chi-squared values for all spectra, some with areas as large as 3×10^7 counts. However, an area of 7×10^6 counts was sufficient to obtain consistent results, and this spectrum area was used for the measurements reported in this study. The longest lifetime, τ_3, was essentially constant at 1.7 ns, with an intensity of approximately 0.1 %. This component is likely due to annihilations in the ^{22}NaCl, and was therefore removed from the spectra.

RESULTS

Table I shows the physical characteristics and the positron lifetime parameters for several p-type and n-type InAs wafers. τ_1, τ_2 and I_2 are parameters fit to the lifetime spectra, where τ_2 corresponds to the lifetime of positrons trapped at a defect, and I_2 is the corresponding intensity. $\tau_B{}^{TM}$ is the bulk lifetime of positrons calculated from the fit parameters using the conventional trapping model [11], and should equal the actual bulk lifetime, τ_B, when this model is valid. For every sample, $\tau_B{}^{TM}$ is constant at 246±2 ps. The current value is in excellent agreement with that of 247 ps reported by Dannefaer [5]. Therefore, we will adopt the value of 246±2 ps for the bulk lifetime of positrons in InAs. τ_{AVG} is the average lifetime of positrons in the sample, a parameter often used to monitor qualitative changes in the lifetime spectra. The trapping rate of positrons into the defects, κ, is proportional to the concentration of positron traps, and has been calculated using the conventional trapping model.

The samples in Table I all show very similar positron lifetime characteristics, with a defect-related lifetime component of 287±6 ps. The defect lifetime may be slightly shorter than the average in the p-type samples, and slightly longer than the average in the Se, S, and Sn doped samples, however, this apparent trend toward a longer defect lifetime in n-type samples is obscured by the uncertainty in the measurements. The trapping rate into the defects exhibiting the 287 ps lifetime is 0.7±0.2 ns^{-1}.

The very heavily S and Sn doped wafers (Table II) show markedly different positron lifetime characteristics. In these samples, the defect lifetime is much longer at 332 - 340 ps, with a trapping rate of approximately 0.7 ns^{-1}. The average lifetime is longer by about 8 ps in these samples compared to those in Table I, however, the bulk lifetime is consistent, indicating that the standard trapping model is also valid in the heavily doped samples.

Rapid thermal annealing up to 850 °C was performed on samples 1, 3, 6, 7, 9, 11, 13, 14 and 16. In all of these samples, the positron lifetime characteristics did not change appreciably,

indicating that the defects which exhibit the 287 ps positron lifetime and those exhibiting the 340 ps lifetime did not anneal out.

Table I. Physical characteristics and room temperature positron lifetime parameters for several InAs wafers. The values are determined from the average of several spectra. The uncertainties represent the standard deviation in repeated measurements.

Sample I.D.	Dopant	Carrier Type	Carrier Density (cm^{-3})	Mobility (cm^2/Vs)	τ_1 (ps)	τ_2 (ps)	I_2 (%)	τ_B^{TM} (ps)	τ_{AVG} (ps)	κ (ns^{-1})
1	Zn	p	2.2×10^{18}	140	199±23	282±12	61±17	245±2	251±1	0.9±0.4
2	Zn	p	4.5×10^{17}	180	200±22	280±11	62±17	245±2	251±1	0.9±0.4
3	Zn	p	1.9×10^{17}	180	208±23	286±14	54±21	247±2	252±1	0.8±0.5
4	none	n	6.4×10^{14}	8500	213±8	290±8	49±10	245±1	251±1	0.6±0.2
5	none	n	7.0×10^{14}	9400	210±6	285±5	55±7	245±1	251±1	0.6±0.2
6	none	n	8.0×10^{14}	10 000	211±11	287±9	53±12	245±2	251±1	0.7±0.2
7	none	n	4.0×10^{16}	18 000	195±18	279±7	64±10	242±5	249±3	0.9±0.3
8	none	n	4.8×10^{16}	18 000	199±12	286±6	60±8	244±3	252±2	0.9±0.2
9	Se	n	7.3×10^{16}	21 000	216±9	289±12	50±14	247±1	252±1	0.6±0.2
10	Se	n	7.6×10^{17}	14 000	215±9	292±10	48±12	246±2	251±1	0.6±0.2
11	Se	n	9.0×10^{17}	13 000	220±7	299±13	41±12	246±1	251±1	0.5±0.2
12	Sn	n	3.0×10^{18}	8200	219±3	293±3	44±3	246±1	251±1	0.5±0.1
13	S	n	5.0×10^{18}	7000	215±19	292±13	48±19	246±3	252±2	0.6±0.3

Table II. Physical characteristics and room temperature positron lifetime parameters for heavily doped n-type InAs:(S+Sn) wafers. The values are determined from the average of several spectra. The uncertainties represent the standard deviation in repeated measurements.

Sample I.D.	Carrier Density (cm^{-3})	Mobility (cm^2/Vs)	τ_1 (ps)	τ_2 (ps)	I_2 (%)	τ_B^{TM} (ps)	τ_{AVG} (ps)	κ (ns^{-1})
14	4.2×10^{19}	2100	214±3	340±6	36±3	247±2	260±2	0.6±0.1
15	4.2×10^{19}	1800	210±2	332±3	39±2	245±1	257±1	0.7±0.1
16	5.9×10^{19}	1500	212±5	340±6	38±4	247±1	260±2	0.7±0.1

DISCUSSION

The defect lifetime of 287±6 ps observed in samples 1 through 13 likely originates from a defect that has an open volume comparable to a monovacancy, based on the ratio $\tau_2/\tau_B = 1.17$. Theoretical calculations of the positron lifetimes for vacancies on the As and In sub-lattice yielded values of 299 ps and 285 ps, respectively [12]. While the theoretical lifetime for V_{As} is closer to the present experimental value, the inherent uncertainty in the calculation and the fact that lattice relaxations were not taken into account do not allow a definitive identification of the sub-lattice on which the monovacancy resides. In addition, the lifetime may be slightly altered if the monovacancies are complexed.

Theoretical calculations for the ionization levels of vacancies in InAs have predicted that V_{As} is always positive and that V_{In} has (0/-), (-/2-) and (2-/3-) levels at $E_V + 0.10$ eV, $E_V + 0.13$ eV, and $E_V + 0.23$ eV, respectively [13]. The fact that the trapping rate into the defects exhibiting the 287 ps lifetime does not change with temperature [14] indicates that the defects are neutral for a wide range of Fermi levels [15]. It is therefore unlikely that the defects are pure monovacancies, but rather are vacancies trapped by other defects, since such complexes may have significantly different electronic properties. One would also expect that pure monovacancies would anneal out at 850 °C, which is 92 % of the melting temperature, while vacancy complexes are more likely to be stable at high temperatures. The defect exhibiting the 287 ps lifetime is therefore a complex involving a single vacancy and some other defect species. Using the specific trapping rate of 10^{17} cm^{-3}/ns^{-1} estimated by Dannefaer *et al.* [16] for neutral vacancy-type defects in GaAs, the trapping rate of 0.7±0.2 ns^{-1} suggests that the concentration of these complexes is $7\pm2\times10^{16}$ cm^{-3}.

In most samples, the carrier concentration is of the same magnitude or larger than the defect concentration, so the vacancies may be complexed with dopant impurity atoms. Samples 4, 5 and 6 have lower mobilities than the other undoped samples, and therefore may also contain impurities in concentrations comparable to that of the vacancy defects which may play a role in the formation of the complexes. However, it is also possible that the monovacancy complexes involve native defects such as antisites rather than impurity atoms.

The defect lifetime of ~340 ps found in the very heavily doped n-type samples is close to the theoretically predicted divacancy lifetime of 347 ps [12], suggesting that the open volume of the defects is comparable to that of a divacancy. Again, the fact that the trapping rate is constant with decreasing measuring temperature [14] indicates that the defects are neutral. The trapping rate of ~0.7 ns^{-1} therefore indicates that their concentration is also close to 10^{17} cm^{-3}.

It appears to be no coincidence that only the most heavily doped n-type samples show different defect characteristics, which would indicate that the large doping concentration must somehow be responsible for the anomalous positron lifetimes. There are several possible reasons why this may be the case.

The very large S and Sn dopant concentrations may lead to precipitate formation in concentrations sufficient to affect the positron lifetime characteristics. However, calculations of the solubility of Sn [17] and S [18] in InAs estimate the solubility limits to be in the 10^{20} cm^{-3} and 10^{21} cm^{-3} ranges, respectively, so precipitate formation is unlikely. Even though only the carrier concentration, but not the actual dopant concentrations in our samples are known, it is unlikely that concentrations of dopants sufficiently large for precipitate formation could be present in our samples.

Another possibility is that defects that are normally positively charged are neutral in samples 14, 15 and 16 due to the much higher Fermi energy, and therefore only trap positrons in these samples. Since most of the n-type samples are highly degenerate, calculation of the Fermi level position is not trivial. However, the Fermi level is clearly much higher in samples 14, 15 and 16 than in samples 12 and 13. It is therefore possible that the positron trap detected in samples 14 - 16 actually exists in all of the samples, but has a (+/0) level resonant with the conduction band.

A more likely explanation may be that the large dopant concentrations facilitate the formation of different defect complexes, especially if there is a saturation in the carrier concentration with increasing dopant concentration, as was observed in heavily Zn-doped InP [10]. Studies of Sn-doped bulk material [19] showed equal dopant and carrier concentrations up to 1.1×10^{19} cm^{-3}, and Sn and Te doped molecular beam epitaxy grown material [20] showed no carrier concentration saturation up to 2.9×10^{19} cm^{-3}. However, discrepancies between the carrier concentration and total dopant concentration have been observed for dopant concentrations larger than 2×10^{19} cm^{-3} for bulk InAs:Te and $1\text{-}2\times10^{18}$ cm^{-3} for bulk InAs:S and InAs:Se [21]. In fact, the same authors performed precision density and lattice period measurements on these samples and found a negative differential concentration of point defects, indicating the presence of vacancies [19,21]. The concentration of vacancies increased with the dopant concentration for S, Se and Te doped material [21], and was comparable in magnitude to the discrepancy between the dopant and carrier concentrations (10^{19} cm^{-3} range).

Although the vacancy concentration measured in our samples is much lower, these results demonstrate that the formation of vacancy-type defects does correlate with a discrepancy between the dopant and carrier concentration in n-type InAs, as was also the case in p-type InP. Currently, Elastic Recoil Detection experiments are underway to measure the S and Sn concentrations in samples 14, 15 and 16 in order to further substantiate this correlation.

CONCLUSION

A survey of InAs wafers has accurately determined the bulk lifetime of positrons in InAs to be 246±2 ps. All wafers in this survey exhibit defect-related positron lifetimes. Most wafers contain $7\pm2\times10^{16}$ cm^{-3} of monovacancy complexes that have an associated positron lifetime of 287±6 ps. In very heavily S and Sn doped n-type wafers, the open volume defects are larger, exhibiting a positron lifetime of 332 - 340 ps. This survey has established reliable experimental values for positron lifetimes in InAs, enabling the further study of the defect characteristics of this material using the positron lifetime spectroscopy technique.

ACKNOWLEDGEMENTS

This work was financially supported by the Natural Sciences and Engineering Research Council of Canada.

REFERENCES

1. L.F. Luo, R. Beresford, W.I. Wang, and H. Munekata, Appl. Phys. Lett. **55**, 789 (1989).
2. J.F. Chen, L. Yang, M.C. Wu, S.N.G. Chu, and A.Y. Cho, J. Cryst. Growth **111**, 659 (1991).
3. J.J. Pekarik, H. Kroemer, and J.H. English, J. Vac. Sci. Technol. B **10**, 1032 (1992).
4. A. Kastalsky, V.J. Goldman, and J.H. Abeles, Appl. Phys. Lett. **59**, 2636 (1991).

5. S. Dannefaer, J. Phys. C **15**, 599 (1982).
6. V.N. Brudnyi, S.A. Vorobiev, and A.A. Tsoi, Phys. Status Solidi A **72**, 529 (1982).
7. G. Dlubek and O. Brümmer, Ann. Phys. (Leipzig) **43**, 178 (1986).
8. M. Misheva, G. Pasajov, G. Tubmev, and R. Yakimova, in *New Developments in Semiconductor Physics, Proceedings of the Third Summer School, Szeged, Hungary, 31 Aug. - 4 Sept., 1987* (Springer-Verlag, Berlin, 1988), p. 232.
9. P. Kirkegaard, N.J. Pedersen, and M. Eldrup, *PATFIT-88: A Data-Processing System for Positron Annihilation Spectra on Mainframe and Personal Computers* (Risø National Laboratory, Denmark 1989).
10. J. Mahony, P. Mascher, and W. Puff, J. Appl. Phys. **80**, 2712 (1996).
11. R.N. West, Adv. Phys. **22**, 263 (1973).
12. M.J. Puska, S. Mäkinen, M. Manninen, and R.M. Nieminen, Phys. Rev. B **39**, 7666 (1989).
13. M.J. Puska, J. Phys.: Condens. Matter **1**, 7347 (1989).
14. J. Mahony and P. Mascher, submitted to Phys. Rev. B
15. M.J. Puska and R.M. Nieminen, Rev. Mod. Phys. **66**, 841 (1994)
16. S. Dannefaer, P. Mascher, and D. Kerr, J. Phys.: Condens. Matter **1**, 3213 (1989).
17. A.N. Morozov, V.T. Bublik, T.P. Grigor'eva, V.V. Karatev, and M.G. Mil'vidskii, Sov. Phys. Crystallogr. **30**, 317 (1985).
18. L.D. Talis, V.V. Karataev, and M.G. Mil'vidskii, Inorg. Mater. **25**, 1362 (1990).
19. V.T. Bublik, V.V. Karataev, M.G. Mil'vidskii, G.A. Nemtsova, L.N. Perova, O.G. Stolyarov, and T.G. Yugova, Sov. Phys. Crystallogr. **24**, 621 (1979).
20. H.G. Lee, R.J. Fischer, L.C. Hopkins, and A.Y. Cho, J. Cryst. Growth **130**, 416 (1993).
21. V.T. Bublik, V.V. Karataev, M.G. Mil'vidskii, G.A. Nemtsova, L.N. Perova, O.G. Stolyarov, and T.G. Yugova, Sov. Phys. Crystallogr. **24**, 302 (1979).

Part XII

Wide-Bandgap Materials: II-VI Compounds

PHOTOLUMINESCENCE AND ELECTRON PARAMAGNETIC RESONANCE OF NITROGEN-DOPED ZINC SELENIDE EPILAYERS

M. MOLDOVAN, S.D. SETZLER, Z. YU, T.H. MYERS, L.E. HALLIBURTON, N.C. GILES
Department of Physics, West Virginia University, Morgantown, WV 26506-6315

ABSTRACT

Photoluminescence (PL) and electron paramagnetic resonance (EPR) studies were performed on a series of ZnSe samples grown by molecular beam epitaxy. The PL has been studied as a function of excitation wavelength, power, temperature, and time. The PL data indicates that the broad emission from a heavily nitrogen-doped ZnSe film is composed of three distinct recombination processes. The EPR spectra taken at 8 K and 9.45 GHz show an isotropic signal at g = 2.0027(3) which we attribute to singly ionized selenium vacancies (V_{Se}^{+}). The PL and EPR data help to clarify the role of defects in the compensation of heavily nitrogen-doped ZnSe thin films.

INTRODUCTION

In recent years, considerable effort has focused on developing zinc selenide for blue and blue-green lasers and LEDs. Achieving high p-type conductivity continues to be a problem in this material. Nitrogen is a promising dopant for p-type ZnSe, but unwanted compensating centers[1] have limited the maximum achievable carrier density to the low 10^{18} cm^{-3} level. Electron paramagnetic resonance (EPR),[2] optically detected magnetic resonance (ODMR),[3,4] and positron annihilation[5] techniques are being used to establish the identities of these device-limiting centers. Photoluminescence (PL) complements these efforts by providing information about the recombination processes involving the compensating centers.

The PL from ZnSe epilayers grown by molecular beam epitaxy (MBE) changes dramatically as the level of nitrogen doping increases. Heavy nitrogen doping (> mid-10^{18} cm^{-3}) is accompanied by a broad luminescence in the region from 2.45 to 2.68 eV. Early explanations[6-8] of this deep luminescence have invoked a distribution of spatially separated potential wells due to a local variation in the distribution of charged impurities. A broad band of states leading to DAP recombination involving the isolated nitrogen acceptor and a donor was suggested.

We have performed a PL study of heavily doped ZnSe:N epilayers grown by MBE. Our data suggest that the deep PL emission is more complicated than previously thought. The PL dependence on excitation wavelength, excitation power density, and temperature have been monitored. The time decay of the PL also has been measured. These data distinguish the separate recombination channels involved in the deep-level luminescence. We find that the deep PL consists of three distinct radiative recombination processes. In addition, one of the bands is accompanied by phonon replicas of energy 69 ± 3 meV. We also have performed EPR studies on a series of ZnSe samples. A signal near g=2 is observed in almost all the samples and is assigned to a singly ionized selenium vacancy (V_{Se}^{+}) center. Its presence correlates with an increase in the Zn-to-Se ratio in the undoped material and with an increase in nitrogen in the doped material. Our observation of large concentrations of single ionized selenium vacancies in ZnSe epilayers provides experimental verification that these native defects may play a significant role in this material.

EXPERIMENT

A series of ZnSe epilayers were grown at West Virginia University in a custom MBE system. These films were grown at 300°C on semi-insulating (100) GaAs substrates using high purity (7N) elemental Zn and Se from conventional MBE sources.[9] An atomic nitrogen flux from an rf plasma source (Oxford model CARS25) was used for nitrogen doping.

Mat. Res. Soc. Symp. Proc. Vol. 442 © 1997 Materials Research Society

The PL data were obtained under both cw and pulsed excitation conditions. The 325-nm output from a HeCd laser (Liconix model 4240) was focused onto the sample surface for above-band-gap cw excitation. Below-band-gap excitation (458 nm) was provided by an argon ion laser (Coherent Innova 400-10). Time-resolved PL studies were conducted using the 355-nm output from a Q-switched Nd:YAG laser (Continuum model Powerlite 8000-10) operating at 10-Hz repetition rate. The average power incident on the sample was 128 $\mu W/cm^2$, corresponding to 12.8 $\mu J/cm^2$ per pulse. The PL produced by pulsed excitation was measured using a digital oscilloscope (Tektronix TDS 684A). The system time-decay response, determined by monitoring the laser pulse, was about 3.5 ns. All PL spectra have been corrected for the response of the detection system.

For the EPR study, a Bruker ESP-300 spectrometer, operating at a microwave frequency of 9.45 GHz, a static-field modulation frequency of 100 kHz, and a microwave power of 5 mW, was used. Glassware from an Oxford Instruments ESR-900 helium gas flow system extended through a standard rectangular TE_{102} microwave cavity and maintained the sample temperature near 8 K during the measurements. The microwave frequency was measured with a Hewlett Packard 5340A counter and the magnetic field was measured with a Varian E-500 digital gaussmeter. A small MgO:Cr crystal was used to correct for the difference in magnetic field between the sample and gaussmeter probe (the isotropic g value for Cr^{3+} in MgO is 1.9800).

RESULTS

Figure 1 shows the PL spectra obtained from a ZnSe epilayer doped with nitrogen (1.5×10^{19} cm^{-3} as determined by SIMS). The data were taken at 4.8 K with 325-nm (curve a) and 458-nm (curve b) excitation, and at 90 K with 458-nm excitation (curve c). The incident power density was 2 W/cm^2. The change in appearance of the luminescence for above- and below-band-gap excitation (compare curves a and b) suggests that two PL bands are present. These bands are labeled N_I and N_{II}. Phonon replicas, spaced by approximately 70 meV, are associated with N_I and are easily seen at higher temperature (curve c). This defect-associated phonon has an energy considerably larger than the 32-meV LO phonon of the ZnSe lattice.

The power dependence of the N_I and N_{II} bands is shown in Fig. 2. These spectra were obtained using above-band-gap excitation (325 nm) and the incident power density was varied by more than three orders of magnitude. The spectra are displaced vertically and are enhanced by the

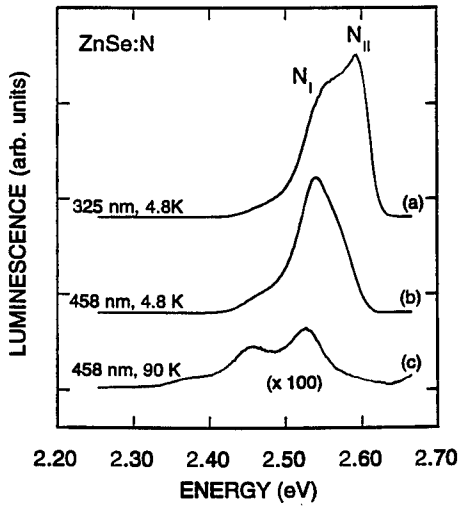


Fig. 1. PL from a heavily nitrogen-doped ZnSe epilayer (a) at 4.8 K using 325-nm excitation, (b) at 4.8 K using 458-nm excitation, and (c) at 90 K using 458-nm excitation.

factors shown on the plots. At the lowest power density shown here (1.4 mW/cm^2), the emission peak corresponding to N_I occurs at about 2.54 eV. As the power density is increased, the peak N_{II} emerges on the high energy side of the spectrum. At the highest power density (5 W/cm^2), the N_{II} band is dominant. The N_{II} band does shift slightly with changes in excitation power.

To determine the peak positions and relative amplitudes of the N_I and N_{II} bands at each incident power density, we performed a least-squares, sum-of-gaussians curve-fitting analysis of the data. As a representative example, the inset to Fig. 2 shows that the PL corresponding to the higher power densities can be described as the sum of three bands. The data from curve c are the dots in the inset, and the superposition of the three bands is the solid line. A similar power dependence study was performed using 458-nm excitation. Based on a curve-fitting analysis of all the power dependence data, the N_I peak does not shift (within our experimental error) as a function of incident excitation power and the N_{II} peak does shift from about 2.55 eV (at low power) to nearly 2.61 eV (at the highest cw powers used in our study). The phonon replica associated with N_I (the lower energy band in the inset to Fig. 2) was found to be 69 ± 3 meV.

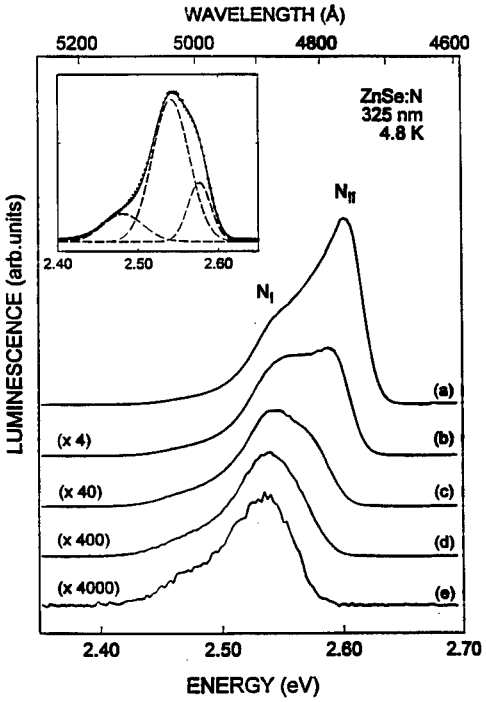


Fig. 2. PL from a heavily nitrogen-doped ZnSe epilayer using 325-nm excitation with incident power densities of (a) 5 W/cm^2, (b) 1 W/cm^2, (c) 0.1 mW/cm^2, (d) 10 mW/cm^2, and (e) 1.40 mW/cm^2. The inset shows that the PL from curve c can be described as the sum of three bands.

Figure 3 shows the time dependence of the PL emission from the heavily nitrogen-doped ZnSe epilayer. The decay of the PL was sequentially monitored at a series of energies extending from 2.75 eV (4500 Å) to 2.40 eV (5165 Å) while pumping with 355-nm light. We then constructed the time evolution of the PL spectrum, by extracting the PL intensity at seven selected times, and the results are shown in Fig. 3(a) on a linear scale and in Fig. 3(b) on a logarithmic scale. The top curves in Figs. 3(a) and 3(b) show the PL spectrum obtained immediately after the laser pulse. In addition to the N_I and N_{II} bands, the pulsed excitation has produced a third emission band at 2.65 eV which decays quickly. This third band is labeled N_{III}. The time evolution of N_I and N_{II} in Fig. 3 is of interest. Initially, the peak of N_{II} occurs at about 2.61 eV but shifts to lower energy with increasing time. In contrast, the peak position of the N_I band does not shift measurably with time. This difference in behavior for N_I and N_{II} clearly establishes the separate nature of the two recombination paths.

The N_{II} band displays the following characteristics which are consistent[10] with DAP recombination: (i) peak shift to higher energies with increasing excitation power and (ii) peak shift to lower energies with increasing time after pulsed excitation. The lifetime of the N_{III} band is 3.5 ns or less. This short-lifetime behavior is consistent with conduction band to valence band recombination, excitonic recombination, or band-to-impurity recombination. Excitonic recombination is unlikely at this high doping level. A likely possibility for the origin of N_{III} is electron-acceptor

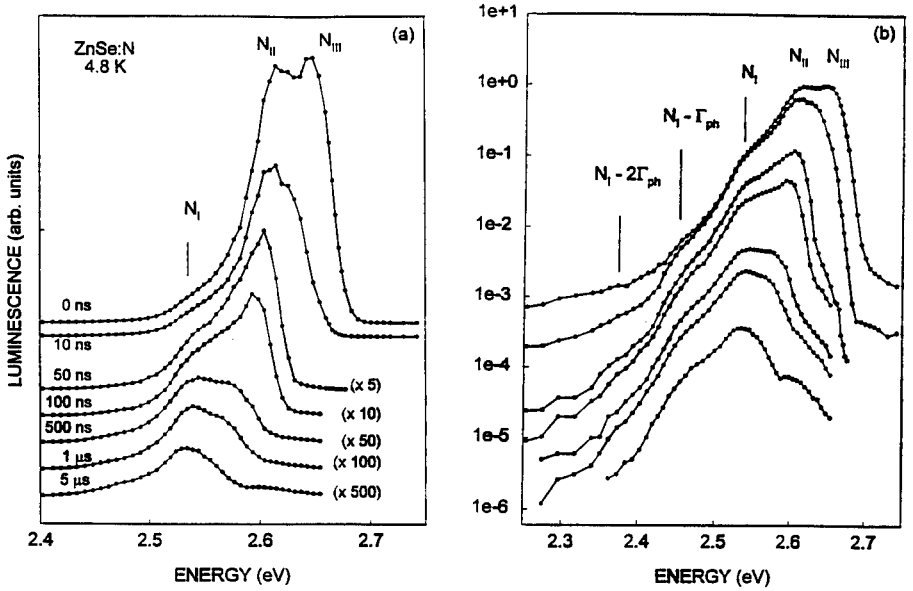


Fig. 3. Time-resolved PL from a ZnSe:N epilayer. (a) Intensities are plotted on a linear scale. Curves are displaced vertically for clarity. Several of the curves have been enhanced by the factors shown. (b) The same spectra are shown on a logarithmic scale.

(e,A) recombination since this band occurs 50 meV above N_{II}, which is DAP recombination. This 50-meV energy agrees closely with the range of values (44 to 57 meV) previously associated with a deep donor in ZnSe:N.[11-14] The N_I band shows no shift in peak position with increasing excitation power, no shift in peak position with time, and is accompanied by phonon replicas with energy of about 69 ± 3 meV. The relative intensities of the N_I phonon replicas exhibit a strong temperature dependence. Evidence for the origin of this phonon energy comes from the infrared absorption study of Stein,[15] who identified a Zn-N local vibration at 553 cm^{-1} (68.6 meV) in polycrystalline ZnSe. We suggest, based on these observations, that the N_I band at 2.54 eV is an intra-center recombination involving a localized excitation coupled with a Zn-N local mode.

We can interpret our N_{II} and N_{III} data in terms of defect energies that have been identified by earlier investigators. If the band gap of ZnSe is taken to be 2.82 eV, then a 170-meV acceptor gives electron-acceptor (e,A) emission at 2.65 eV (i.e., the N_{III} position) and this same 170-meV acceptor gives DAP emission at 2.60 eV (i.e., the N_{II} position) when the deep donor energy of roughly 50 meV is assumed. The energy levels being discussed here may vary by 5 to 10 meV depending on the strength of the pair term in DAP recombination and the uncertainty in the deep donor value. It is interesting to note that a 170-meV acceptor in ZnSe:N has already been suggested by Zhu et al.[16]

PL does not provide definitive identifications of the defects in ZnSe epilayers. We thus performed EPR in order to help make defect asignments.[2] An isotropic signal at g = 2.0027(3) was detected from several layers, as shown in Fig. 4. By assuming a system minimum detection limit of 5 x 10^{10} spins for a 1 gauss linewidth, we can determine approximate concentrations for the paramagnetic defect centers in the ZnSe layers. The upper trace in Fig. 4 was recorded from an undoped ZnSe epilayer grown under a Zn/Se ratio of 0.63. We conservatively estimate the defect concentration in this film to be about 6 x 10^{17} cm^{-3}. No EPR signal was detected in a lightly

doped layer grown using a Zn/Se ratio of 0.49, as shown in the second trace in Fig. 4. An increase in nitrogen doping up to 1.5 x 10^{19} cm^{-3} produced the signal shown in the third trace of Fig. 4. We estimate the defect concentration in this case to be about 1 x 10^{17} cm^{-3}. Several additional heavily doped ZnSe:N samples showed similar EPR spectra. The bottom trace in Fig. 4 is from a hydrogen-doped ZnSe epilayer and shows two EPR signals, the one at g = 2.0027(3) and another at g = 1.9796(3). These signals represent concentrations of spins approaching 10^{18} cm^{-3} and mid-10^{17} cm^{-3}, respectively (note the different signal-to-noise ratio in the lower trace).

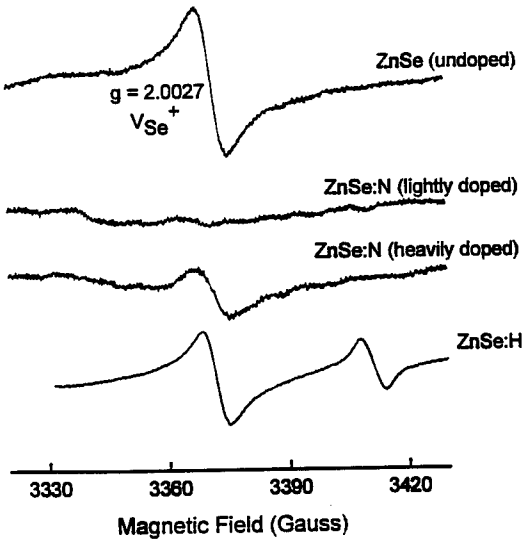


Fig. 4. EPR recorded at 8 K and 9.45 GHz from four ZnSe epilayers.

We assign the EPR signal at g = 2.0027(3) in the ZnSe epilayers grown by MBE to the singly ionized selenium vacancy, V_{Se}^{+}, because of the small shift from the free spin g value. The broader linewidth prevents us from determining whether the signal is due to an isolated V_{Se}^{+} or a V_{Se}^{+}-impurity complex in the various samples. A previous EPR report[17] for electron-irradiated bulk ZnSe assigned the V_{Se}^{+} to g = 2.0085, which is slightly higher than our observation. We note that our g value is in good agreement with the anion vacancy in ZnS (see Table I). This discrepancy in g-value assignments for the selenium vacancy in ZnSe must be resolved in future studies.

Table I. g values for paramagnetic defects involving the anion vacancy in ZnS and ZnSe.

Material	Defect	$g_{\parallel}$	$g_{\perp}$	Reference
ZnS	V_S	2.0034	...	18
	V_S-Cu_{Zn}	2.0061	2.0026	19
	V_S-Ag_{Zn}	2.0072	2.0024	19
ZnSe	V_{Se}	2.0027(3)	...	this work
	V_{Se}	2.0085(5)	...	17
	V_{Se}-X	2.0072(2)	2.0013(2)	4

CONCLUSIONS

We have identified three PL recombination paths in a heavily nitrogen-doped ZnSe epilayer. The PL bands can be interpreted as intra-center, DAP, and (e,A) recombinations. Our data suggest that spatially separated fluctuations in the band gap are not needed to explain the deep PL data, at least for nitrogen concentrations up to 1.5×10^{19} cm^{-3}. The defect responsible for the intra-center band is not known at this time. Hauksson et al.[11] have suggested that the $(V_{Se}\text{-}Zn\text{-}N_{Se})^{+}$ complex could be the 50-meV deep donor in ZnSe:N. Our observation of an EPR signal near g = 2 suggests that singly ionized selenium vacancies are present in large concentration. The neutral charge state of this complex, $(V_{Se}^{+}\text{-}Zn\text{-}N_{Se}^{-})^{0}$, might be the defect responsible for the intra-center recombination. The EPR data indicate this technique will prove useful in studying a variety of undoped and doped ZnSe epilayers.

ACKNOWLEDGEMENTS

This work was supported by the NSF/WV EPSCoR program (NSF Grant OSR-9255224).

REFERENCES

1. K. Prior, phys. stat. sol. (b) **187**, 379 (1996).
2. S. D. Setzler, M. Moldovan, Z. Yu, T.H. Myers, N.C. Giles, and L.E. Halliburton, submitted to Applied Physics Letters.
3. B.N. Murdin, B.C. Cavenett, C.R. Pidgeon, J. Simpson, I. Hauksson, and K.A. Prior, Appl. Phys. Lett. **63**, 2411 (1993).
4. T.A. Kennedy, E.R. Glaser, B.N. Murdin, C.R. Pidgeon, K.A. Prior, and B.C. Cavenett, Appl. Phys. Lett. **65**, 1112 (1994).
5. K. Saarinen, T. Laine, K. Skog, J. Makinen, P. Hautojarvi, K. Rakennus, P. Uusimaa, A. Salokatve, and M. Pessa, Phys. Rev. Lett. **77**, 3407 (1996).
6. P. Baume, J. Gutowski, D. Wiesmann, R. Heitz, A. Hoffmann, E. Kurtz, D. Hommel, and G. Landwehr, Appl. Phys. Lett. **67**, 1914 (1995).
7. C. Kothandaraman, G.F. Neumark, and R.M. Park, Appl. Phys. Lett. **67**, 3307 (1995).
8. C. Kothandaraman, I. Kuskovsky, G.F. Neumark, and R.M. Park, Appl. Phys. Lett. **69**, 1523 (1996).
9. Z. Yu, S. L. Buczkowski, N.C. Giles, and T.H. Myers, Appl. Phys. Lett. **69**, 82 (1996).
10. P.J. Dean, in Progress in Solid State Chemistry, edited by J. O. McCaldin and G. Somorjai, (Pergamon Press, New York, 1973), Vol. 8, pp. 1-126.
11. I.S. Hauksson, J. Simpson, S.Y. Wang, K.A. Prior, and B.C. Cavenett, Appl. Phys. Lett. **61**, 2208 (1996).
12. Z. Zhu, K. Takebayashi, K. Tanaka, T. Ebisutani, J. Kawamata, and T. Yao, Appl. Phys. Lett. **64**, 91 (1994).
13. Z. Zhu, G.D. Brownlie, P.J. Thompson, K.A. Prior, and B.C. Cavenett, Appl. Phys. Lett. **67**, 3762 (1995).
14. C. Morhain, E. Tournie, G. Neu, C. Ongaretto, and J.P. Faurie, Phys. Rev. B **54**, 4714 (1996).
15. H.J. Stein, Appl. Phys. Lett. **64**, 1520 (1994).
16. Z. Zhu, G.D. Brownlie, G. Horsburgh, P.J. Thompson, S.Y. Wang, K.A. Prior, and B.C. Cavenett, Appl. Phys. Lett. **67**, 2167 (1995); J. Cryst. Growth **159**, 248 (1996).
17. I.A. Gorn, V.N. Martynov, E.S. Volkova, and V.I. Grinev, Sov. Phys. Semicond. **24**, 336, (1990).
18. J. Schneider and A. Rauber, Solid State Commun. **5**, 779 (1967).
19. J. Dielman, S.H. de Bruin, C.Z. van Doorn, and J.H. Haanstra, Philips Res. Rep. **19**, 311 (1964).

DEFECT STATES IN p-ZnSe:N GROWN BY MOVPE

Shizuo FUJITA, Ken-ichi OGATA, Daisuke KAWAGUCHI, Zhi Gang PENG,
and Shigeo FUJITA
Department of Electronic Science and Engineering, Kyoto University, Kyoto 606-01, Japan

ABSTRACT

Concentration and origin of defect states in p-type nitrogen-doped ZnSe (p-ZnSe:N) grown by metalorganic vapor-phase epitaxy (MOVPE) are discussed by means of time-resolved photoluminescence and deep level transient spectroscopy. Thermal annealing, which is a useful tool for realizing p-type conductivity, results in deep defect states which seem to be associated with Zn vacancies and with nitrogen acceptors. By lowering the annealing temperature, the trap concentrations can be successfully reduced without seriously sacrificing the acceptor activation efficiency, although further reduction of Zn vacancies is pointed out as a remaining requirement for the improvement of quality of MOVPE-grown p-type layers.

INTRODUCTION

For p-type doping of ZnSe-based semiconductors by metalorganic vapor-phase epitaxy (MOVPE), efforts have been made to minimize the hydrogen passivation [1,2] of doped acceptors by applying novel dopant precursors [3-8], adopting post-growth thermal annealing [9,10], doping plasma-activated N_2 [11], or using N_2 carrier gas instead of H_2 [11]. Our research has been conducted based on low temperature photoassisted MOVPE which allows enhanced incorporation of nitrogen acceptor dopants, followed by thermal annealing to activate the doped nitrogen. The results showed the maximum net acceptor concentration ($N_A - N_D$) of 4×10^{17} cm^{-3} [12], but the material characterization has proven the deep defect states which originate from annealing damege [13].

From the most recent results, for high quality p-type doping by MOVPE it seems to be the key issues to understand the nature of the deep defects and to optimize the annealing conditions in terms of the defect concentration. In this paper, photoluminescence (PL) lifetime measurements and deep level transient spectroscopy (DLTS) are applied to p-type nitrogen-doped ZnSe (p-ZnSe:N) for characterization of the defect states.

EXPERIMENT

The p-ZnSe:N layers were prepared by photoassisted MOVPE [14] at 350 °C on (100)-GaAs substrates. Diethylzinc (DEZn) and dimethylselenide (DMSe) were used as source precursors and tertiarybutylamine (t-$BuNH_2$) as a dopant source. The detailed growth conditions have appeared in ref.[12]. Several ZnSSe samples lattice-matched to GaAs substrates were also prepared. Here, for the sulfur source we used diisopropylsulfide, which resulted in good control of the alloy composition. The post-growth thermal annealing in N_2 atmosphere successfully allowed p-type conductivity. The annealing temperature for most of the MOVPE-grown samples was 500 °C, except for the discussion on optimization of the annealing temperature. For comparison, MBE or MOMBE-grown samples were prepared by the remote microwave plasma doping technique [15,16]. The MOMBE growth was made by Zn-DMSe source combination.

Mat. Res. Soc. Symp. Proc. Vol. 442 © 1997 Materials Research Society

The net acceptor concentration was characterized by low frequency (10 kHz) C–V characteristics of vertical configuration (Au/p-ZnSe:N/p^+-GaAs/AuZn) Schottky diodes. These diodes were also used for DLTS measurements. PL lifetime measurements were done at 20 K by a time-resolved PL measurement system with a mode-locked titanium sapphire laser pumped by a CW argon laser and a synchroscan streak camera.

RESULTS AND DISCUSSION

PL Lifetime

Free excitonic emission (FX) lifetime is one of the important parameters which reflect the material properties, because it is significantly influenced by concentrations of nonradiative recombination centers and of acceptors [17]. The effects of donors may be neglected because their concentration seems to be much lower than that of acceptors.

Fig. 1 shows the FX lifetime of p-ZnSe:N grown by MOVPE, MBE, or MOMBE, as a function of the net acceptor concentration. Several data for the ZnSSe:N samples are simultaneously shown in this figure. First, it is clear that the quality of MOMBE-grown samples, which is symbolized by very short (~10 ps) lifetime at $N_A - N_D = 4.5 \times 10^{16}$ cm^{-3}, is far inferior to that of MOVPE or MBE-grown samples. This has been predicted by broad PL spectra of MOMBE-grown p-ZnSe:N [16]. While for MOVPE and MBE-grown samples, the FX lifetime decreases as the net acceptor concentration increases, suggesting increase of acceptor-related recombination centers. At the same net acceptor concentration, on the other hand, the variations are attributed to the different concentrations of other nonradiative recombination centers. Comparing the lifetime for MOVPE and MBE-grown p-ZnSe:N, it seems to be shorter for the former. This is interpreted as more generation of nonradiative recombination centers by thermal annealing [13]. Further, the lifetime tends to be longer in ZnSSe where the concentration of dislocation defects is markedly suppressed because of lattice-matching to GaAs.

In Fig. 1, it is worth noticing that the FX lifetime for unannealed nitrogen-doped ZnSe, where nitrogen is heavily passivated by hydrogen and the layer exhibits high resistivity, is as long as that for undoped pure ZnSe. This result indicates that the hydrogen-passivated nitrogen acceptors hardly contribute as nonradiative recombination centers.

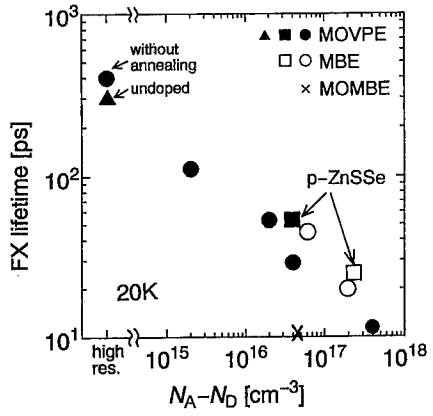


Fig. 1 FX lifetime of p-ZnSe:N as a function of the net acceptor concentration. Annealing temperature for MOVPE-grown samples is 500 °C.

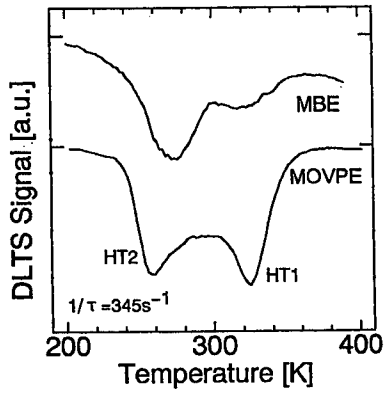


Fig. 2 Typical examples of DLTS spectra of p-ZnSe:N grown by MOVPE or MBE.

DLTS Measurements

Fig. 2 shows the typical examples of DLTS spectra of p-ZnSe:N grown by MOVPE or MBE. Two hole traps labeled as HT1 and HT2 are clearly detected. For the trap HT1, the energy level and capture cross section are around 0.4 eV and 10^{-19} cm^2, respectively. For the trap HT2, they are around 0.5 eV and 10^{-15} cm^2, respectively. It should be noted that the capture cross section of trap HT2 is much larger than that of trap HT1. These trap states HT1 and HT2 may be identical to the traps C_2 and C_1, respectively, discussed for MBE-grown p-ZnSe:N by Matsumoto *et al.* [18], although large difference remains for energy levels of HT1 and C_2.

The DLTS signal originated from the trap HT1 appears stronger for MOVPE-grown samples. Since this peak tends to be stronger for the samples grown by MBE under Se

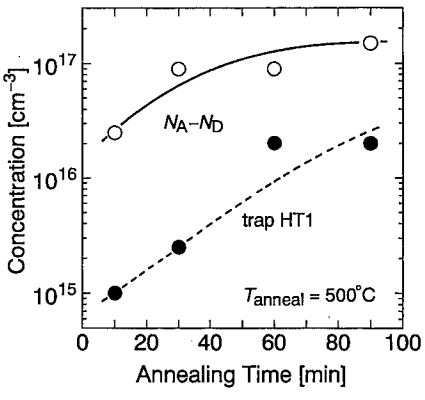


Fig. 3 Concentration of trap HT1 and net acceptor concentration of MOVPE-grown p-ZnSe:N against the annealing time. Annealing temperature is 500 °C.

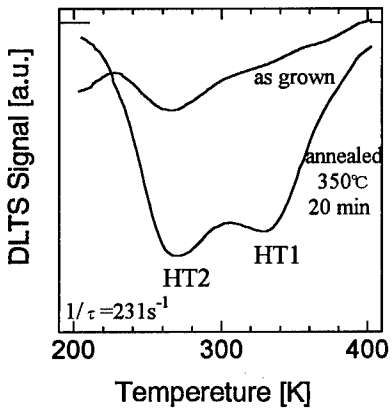


Fig. 4 Variation of DLTS spectra with thermal annealing at 350 °C in N_2 of MBE-grown p-ZnSSe:N.

overpressure conditions, or for those which exhibit stronger Zn vacancy-related emissions (SA and I_1^d) in PL, the traps seem to be related to Zn vacancies (V_{Zn}). It should be noted that Matsumoto *et al.* [18] proposed that the trap C_2, which may be identical to the trap HT1, is related to the complex of nitrogen and Se vecancies. We have no further data to discuss this discrepancy, and thus continue the discussion in this paper based on the assumption of V_{Zn}. It seems that the MOVPE-grown p-ZnSe:N includes more V_{Zn} than the MBE-grown samples, and that the thermal annealing is responsible for generation of V_{Zn}.

In order to confirm the above assumption, the concentration of trap HT1, together with the net acceptor concentration, is given in Fig. 3 against the annealing time. The net acceptor concentration tends to saturate at the annealing time longer than 30 min, but the concentration of trap HT1 continues to increase. This result can be explained by generation of the trap HT1 associated with thermal annealing. For further understanding of this phenomenon, Fig. 4 demonstrates variation of the DLTS spectra with thermal annealing at 350 °C in N_2 of MBE-grown p-ZnSSe:N. Since the MBE samples are as-grown p-type, the successive thermal annealing can clearly elucidate the effects of itselves. The ZnSSe sample was used for this experiment in order to minimize the dislocation-enhanced degradation in low temperature-grown MBE samples. The data exhibit the remarkable enhancement of the peak HT1 with the annealing. From these experiments, it is reasonable to conclude that the thermal annealing results in generation of the trap HT1, which seems to be associated with V_{Zn}.

For the trap HT2 in MOVPE-grown p-ZnSe:N, the concentration is shown in Fig. 5 against the net acceptor concentration. Note that this level has been observed for MBE-grown samples [18-20] and shown to be introduced associated with nitrogen incorporation. Compared to MBE-grown samples, whose data reported in ref.[18] are shown by the dashed line, the concentration of trap HT2 in the MOVPE-grown samples is much higher. Further, the tendency of increasing HT2 with annealing time is being obtained in our recent results. Although the detailed model for the trap states HT2 has not been proposed, it may be assumed to be nitrogen-related complexes with other elements or defects. Consequently, the

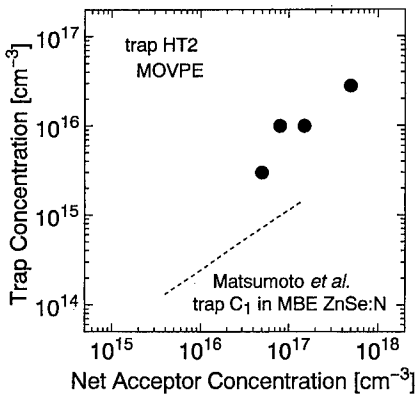


Fig. 5 Concentration of trap HT2 in MOVPE-grown ZnSe:N against the net acceptor concentration. Annealing temperature is 500 °C.

Table 1 Effects of annealing temperature on concentration of traps HT1 and HT2 in MOVPE-grown p-ZnSe:N. Data are for the samples whose net acceptor concentration is almost the same at 5×10^{16} cm^{-3}.

annealing condition	HT1 [cm^{-3}]	HT2 [cm^{-3}]
500 °C 30 min	3×10^{15}	8×10^{15}
450 °C 90 min	5×10^{15}	8×10^{15}
450 °C 30 min	1×10^{15}	1×10^{15}

annealing of MOVPE-grown samples seems to be responsible for higher concentration of the trap HT2, due to introducing impurities or defects.

From the above discussion on traps HT1 and HT2, it is clearly concluded that the optimization of annealing conditions is a key for higher quality p-type layers grown by MOVPE. Since the annealing seems to induce V_{Zn}, attempts were made to reduce the annealing temperature. Table 1 shows effects of the annealing temperature and annealing time on the concentration of traps HT1 and HT2 in MOVPE-grown p-ZnSe:N. Here, the DLTS measurements were made choosing the samples whose net acceptor concentration obtained after the annealing is almost the same at 5×10^{16} cm^{-3}. The remarkable decrease of concentration both of traps HT1 and HT2 is observed by reducing the annealing temperature from 500 °C to 450 °C. For the sample subjected to the annealing at 450 °C for 30 min, it is understood from Fig. 5 that the concentration of HT2 is close to that of MBE-grown p-ZnSe:N. However, the concentration of HT1 is still about one order of magnitude higher than that in MBE-grown samples (1×10^{14} cm^{-3} for $N_A - N_D = 5 \times 10^{16}$ cm^{-3}) [18]. This implies that the generation of V_{Zn} cannot be completely suppressed even in the up-to-date best MOVPE-grown p-type samples. Further optimization of the annealing conditions will be continued concentrating on this problem.

CONCLUSION

Since the thermal annealing process is a useful tool to achieve p-type conductivity in MOVPE-grown ZnSe:N layers, the annealing conditions should be chosen so that the annealing minimizes the generation of deep defects while maximizing the acceptor activation. The annealing condition of 450 °C for 30 min is a present solution for the best quality p-type layers, although the problem of V_{Zn} has not be solved completely.

One may argue that the temperature 450 °C is still so high that defects can be easily generated in *soft* II-VI semiconductors. However, recently from PL spectra we found that the thermal degradation can be suppressed in nitrogen-doped layers compared to undoped ones, probably due to the effects similar to solution hardening. For the FX lifetime, the thermal annealing of undoped ZnSe results in drastic decrease from 300 ps to 12 ps; the latter, as shown in Fig. 1, is far shorter than the p-type ZnSe:N experienced the thermal annealing at the same conditions. Consequently, by further optimizing the annealing conditions, we may not be very pessimistic for the annealing process itself.

Recent experiments of secondary ion mass spectroscopy (SIMS) of MOVPE-grown p-ZnSe:N layers have proven the activation ratio being close to unity. Together with the progress of the growth technique, high quality p-type layers may be realized with extending the present way.

ACKNOWLEDGEMENTS

This work was partly supported by the Grant-in-Aid for Scientific Research from the Ministry of Education, Science, Sports, and Culture, and by KU-VBL (Kyoto University Venture Business Laboratory) Project.

REFERENCES

1. J.A. Wolk, J.W. Ager III, K.J. Duxstad, E.E. Haller, N.R. Taskar, D.R. Dorman, and D.J. Olego, Appl. Phys. Lett. **63**, 2756 (1993).

2. A. Kamata, H. Mitsuhashi, and H. Fujita, Appl. Phys. Lett. **63**, 3353 (1993).
3. Sz. Fujita, S. Matsumoto, and Sg. Fujita, J. Electron. Mater. **22**, 521 (1993).
4. Y. Fujita, T. Terada, and T. Suzuki, Jpn. J. Appl. Phys. **34**, L1034 (1995).
5. S. Akram and I. Bhat, J. Cryst. Growth **138**, 105 (1994).
6. A. Kamata, J. Cryst. Growth **145**, 557 (1994).
7. H. Stanzl, K. Wolf, B. Hahn, and W. Gebhardt, J. Cryst. Growth **145**, 918 (1994).
8. A. Toda, T. Margalith, D. Imanishi, K. Yanashima, and A. Ishibashi, Electron. Lett. **31**, 1921 (1995).
9. N.R. Taskar. B.A. Khan, D.R. Dorman, and K. Shahzad, Appl. Phys. Lett. **62**, 270 (1993).
10. Sz. Fujita, T. Tojyo, T. Yoshizawa, and Sg. Fujita, J. Electron. Mater. **24**, 137 (1995).
11. W. Taudt, B. Wachtendorf, R. Beccard, A. Wahid, M. Heuken, A.L. Gurskii, and K. Vakarelska, J. Cryst. Growth **145**, 583 (1994).
12. K. Ogata, D. Kawaguchi, T. Kera, Sz. Fujita, and Sg. Fujita, J. Cryst. Growth **159**, 312 (1996).
13. K. Ogata, T. Kera, D. Kawaguchi, Sz. Fujita, and Sg. Fujita, presented at *8th Int. Conf. Metal Organic Vapour Phase Epitaxy, Cardiff, UK, 1996*; J. Cryst. Growth, in press.
14. Sz. Fujita and Sg. Fujita, Appl. Surf. Sci. **86**, 431 (1995).
15. Y. Kawakami, T. Ohnakado, M. Tsuka, S. Tokudera, Y. Ito, Sz. Fujita, and Sg. Fujita, J. Vac. Sci. & Technol. B **11**, 2057 (1993).
16. J. Suda, M. Tsuka, D. Honda, M. Funato, Y. Kawakami, Sz. Fujita, and Sg. Fujita, J. Electron. Mater. **25**, 223 (1996).
17. I.S. Hauksson, J. Suda, M. Tsuka, Y. Kawakami, Sz. Fujita, and Sg. Fujita, J. Cryst. Growth **159**, 329 (1996).
18. T. Matsumoto, K. Egashira, and T. Kato, J. Cryst. Growth **159**, 280 (1996).
19. K. Ando, Y. Kawaguchi, T. Ohno, A. Ohki, and S. Zembutsu, Appl. Phys. Lett. **63**, 191 (1993).
20. B. Hu, G. Karczewski, H. Luo, N. Samarth, and J.K. Furdyna, Appl. Phys. Lett. **63**, 358 (1993).

IDENTIFICATION OF THE NATIVE VACANCY DEFECTS IN ZnS_xSe_{1-x} AND $Mg_yZn_{1-y}S_xSe_{1-x}$ BY POSITRON ANNIHILATION

K. SAARINEN *, T. LAINE *, K. SKOG *, J. OILA *, P. HAUTOJÄRVI *,
K. RAKENNUS **, P. UUSIMAA **, A. SALOKATVE **, M. PESSA **
*Laboratory of Physics, Helsinki University of Technology, 02150 Espoo, Finland
**Dept. of Physics, Tampere Univ. of Technology, P. O. Box 692, 33101 Tampere, Finland

ABSTRACT

We show how positron annihilation can distinguish vacancies in the different sublattices of a compound semiconductor by performing experiments in ZnS_xSe_{1-x} and $Mg_yZn_{1-y}S_xSe_{1-x}$ layers. We identify the Se vacancies (V_{Se}) in N-doped and the Zn vacancies (V_{Zn}) in Cl-doped material by the shape of the core electron momentum distribution. The charge of the defect involving V_{Se} is neutral or negative in the p-type alloys, suggesting that the Se vacancy is complexed with an acceptor. The concentration of the V_{Se} complexes is high ($\geq 10^{18}$ cm^{-3}), indicating that their role is important in the electrical compensation of p-type ZnS_xSe_{1-x} and $Mg_yZn_{1-y}S_xSe_{1-x}$.

INTRODUCTION

ZnSe is a potential material for blue-green diode lasers, since its band gap is wide and its lattice constant matches closely to that of GaAs substrates. However, fundamental problems exist in the doping: ZnSe can be easily doped n type but the fabrication of p-type material is difficult. With nitrogen doping the active acceptor concentration saturates at about 10^{18} cm^{-3}, although more than 10^{19} cm^{-3} N atoms have been incorporated during the growth. Several theoretical models have been proposed for the origin of the doping problems [1-7]. However, very little experimental data exist on the microscopic origin of the compensation in ZnSe.

In this work we have applied positron annihilation spectroscopy to study the vacancy defects in ZnS_xSe_{1-x} [8] and in $Mg_yZn_{1-y}S_xSe_{1-x}$. We detect Se vacancies in N-doped alloys and Zn vacancies in Cl-doped ZnS_xSe_{1-x}. The charge state of the Se vacancy is neutral or negative, suggesting that it is complexed with an acceptor, possibly with the nitrogen dopant. The vacancy concentration in heavily N-doped ZnS_xSe_{1-x} is at least 10^{18} cm^{-3}. The Se vacancy can thus play an important role in the electrical compensation of p-type ZnSe based alloys.

EXPERIMENT

The samples in this work were 2 μm ZnS_xSe_{1-x} (x = 0.06) and $Mg_yZn_{1-y}S_xSe_{1-x}$ (x = 0.16, y = 0.11) overlayers grown by molecular beam epitaxy (MBE) as lattice matched on GaAs substrate. The alloy compositions varied less than 1 % from one sample to another according to the X-ray diffraction experiments. A $ZnCl_2$ effusion cell was used for Cl doping and a N_2 plasma source for the N doping. The impurity concentrations were determined by the secondary ion mass spectrometry (SIMS). The N concentrations varied in the range of [N] = (1-30)×10^{18} cm^{-3} in the studied 6 samples, depending on the power of the N_2 plasma source. The electrochemical capacitance-voltage profiling (ECV) showed that the hole concentration is at maximum 2×10^{17} cm^{-3}, thus indicating that most of the nitrogen acceptors are electrically inactive. In the two Cl-doped samples both the n-type carrier and the Cl concentrations were roughly 10^{18} cm^{-3} according to ECV and SIMS experiments.

The positron experiments were performed using a low-energy positron beam. The Doppler

Mat. Res. Soc. Symp. Proc. Vol. 442 © 1997 Materials Research Society

broadened shape of the 511 keV annihilation radiation was measured with a Ge detector and described with the conventional valence and core annihilation parameters S and W [9]. The S parameter represents the fraction of positrons annihilating mainly with the valence electrons with a longitudinal momentum component of $p_L \leq 3.7\times10^{-3}\ m_0c$ (m_0 is the electron mass and c the speed of light). The W parameter is the fraction of annihilations with the core electrons with a large momentum component of $11\times10^{-3}\ m_0c \leq p_L \leq 29\times10^{-3}\ m_0c$. The detailed shape of the core electron momentum distribution was studied by the coincidence measurement of Doppler broadening, in which the two annihilation quanta are detected simultaneously [10]. This technique enables the observation of longitudinal electron momenta up to $p_L \approx 40\times10^{-3}\ m_0c$.

Positrons get trapped at neutral and negative vacancy defects because of the missing positive charge of the ion cores. The reduced valence and core electron density at a vacancy increases the positron lifetime and narrows the positron-electron momentum distribution. Consequently, the valence annihilation parameter S increases and the core annihilation parameter W decreases. The momentum distribution of the annihilated core electrons contains information on the atomic numbers of the ions. A trapped positron at a vacancy overlaps mainly with the core electrons of the nearest neighbor atoms. Hence, the shape and magnitude of the core electron momentum distribution can be used to identify the sublattice of the vacancy acting as a positron trap [10].

RESULTS AND DISCUSSION

All samples were investigated at room temperature as a function of the positron beam energy E (Fig. 1). When positrons are implanted close to the sample surface with E = 0 - 5 keV, S parameter shows complicated effects related to the defects and chemical nature of the sample surface. However, at E = 5 - 20 keV the S parameter is constant indicating that all positrons annihilate in the homogeneous ZnS_xSe_{1-x} layer. At larger positron energies of E = 20 - 40 keV

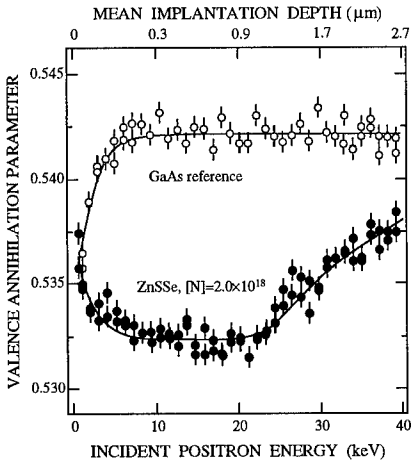


Fig. 1. The valence annihilation parameter S vs. incident energy of the positron beam in N-doped ZnS_xSe_{1-x} (x=0.06) overlayer on GaAs and in defect-free Zn-doped GaAs reference sample. The positron mean implantation depth is indicated on the top axis.

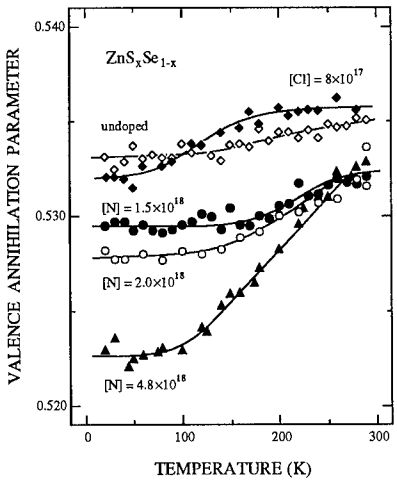


Fig. 2. The valence annihilation parameter S vs. measurement temperature in various N-doped, Cl-doped and undoped ZnS_xSe_{1-x} (x=0.06) layers. The doping concentrations of the samples are indicated [8].

S parameter increases towards the value corresponding to the GaAs lattice, since more and more positrons are implanted at the GaAs substrate. At E = 15 keV effects due to the surface and the substrate can be neglected and this energy was fixed in the furher measurements.

Fig. 2 shows the temperature dependence of the valence annihilation parameter S in some of the studied samples. In N-doped ZnS_xSe_{1-x} the S parameter increases with temperature more strongly than in undoped and Cl-doped material, while its absolute value is smaller. A similar but reverse effect is observed in the W parameter, which is larger in N-doped than in undoped and Cl-doped ZnS_xSe_{1-x}. At low temperature of 20 - 100 K, the S parameter anticorrelates with the nitrogen concentration: when [N] increases, the S parameter is lower.

The S parameter in the [N] = 4.8×10^{18} cm^{-3} doped sample increases by more than 2 % with temperature at 20 - 300 K. This increase is much larger than that of roughly 0.1 % / 100 K we have measured for delocalized positrons in defect-free Si, GaAs and InP. The temperature dependence can thus only be explained by positron trapping at vacancy defects. The S parameter behaves typically as in Fig. 2, when the fraction of positron annihilations at vacancies increases with temperature. This can be due to shallow positron traps or in p-type samples also due to the ionization of the vacancy [9,11]. In the other layers the S-parameter values are even larger than those obtained in the [N] = 4.8×10^{18} cm^{-3} doped sample. This behavior implies that vacancy defects acting as positron traps are present also in these layers.

The number of different vacancy-type positron traps in the material can be studied by investigating the linearity between the valence and core annihilation parameters [12]. If only a single type of a vacancy defect is present, the W parameter depends linearly on the S parameter, when the fraction η of positron annihilations at the vacancy varies: $\eta = (S - S_b) / (S_v - S_b) = (W_b - W) / (W_b - W_v)$. The inverse slope of the S-W plot is the defect specific parameter $R = (S_v - S_b) / (W_b - W_v)$. This analysis is presented in Fig. 3 by plotting the W parameter as a function of the S parameter measured at the same temparature.

In Fig. 3 the data in all nitrogen doped ZnS_xSe_{1-x} samples form a straight line in the (S, W) plane, which indicates that a single type of vacancy explains the positron results in N-doped material. This vacancy can be characterized by the slope $R = |\Delta S / \Delta W| \approx 5$ of the solid line in Fig. 3. Similarly, the W parameter depends linearly on the S parameter in all chlorine doped samples, implying that again a single type of vacancy, now with $R = |\Delta S / \Delta W| \approx 2.5$, is present in all of them. The vacancy in Cl-doped ZnS_xSe_{1-x} is clearly different from the one observed in N-doped material.

The straight line in the (S, W) plane is formed between the endpoints (S_b, W_b) and (S_{vi}, W_{vi}) corresponding to the delocalized positron state in the bulk and the localized state at the vacancy i, respectively. When different types of vacancies exist in the same material, all straight lines in the (S, W) plane have the same endpoint at (S_b, W_b). The crossing point of the two lines in Fig. 3 determines thus the annihilation parameters of the delocalized positron in defect-free ZnS_xSe_{1-x}: (S_b, W_b) = (0.520, 0.042).

The maximum change of the annihilation parameters S and W compared to (S_b, W_b) = (0.520, 0.042) gives information on the size of the detected vacancy defects. In Cl-doped ZnS_xSe_{1-x} $S / S_b = 1.029$ and $W / W_b = 0.85$ at 300 K and in N-doped samples we obtain $S / S_b = 1.025$ and $W / W_b = 0.93$. We think that these values are close to the defect-specific ones (S_{vi}, W_{vi}), because they are rather independent of the doping level (see T = 300 K in Fig. 2). Further, they are close to those observed previously for monovacancies in Si, GaAs and InP [9]. The slopes $|\Delta S / \Delta W| \approx 2 - 5$ (Fig. 3) are also typical for monovacancies in GaAs and InP [10,9]. The vacancies in N and Cl-doped ZnS_xSe_{1-x} have thus the open volume of monovacancies.

The relative amount of core electron annihilations at a vacancy defect depends on the open volume of the defect and on the chemical nature of the surrounding atoms. On the other hand,

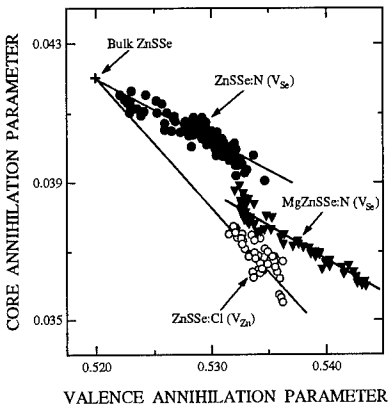


Fig. 3. The W parameter vs. S parameter in N and Cl doped ZnS_xSe_{1-x} (x=0.06) as well as in N-doped $Mg_yZn_{1-y}S_xSe_{1-x}$ (x = 0.16, y = 0.11) layers. The annihilation parameters in the defect-free ZnS_xSe_{1-x} and the straight lines characteristic to Zn and Se vacancies are indicated.

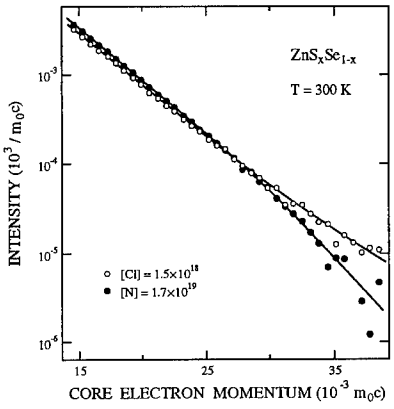


Fig. 4. The core electron momentum distribution at the vacancy defects observed in Cl-doped and N-doped ZnS_xSe_{1-x} (x=0.06) layers. The doping concentrations of the samples are indicated in the figure [8].

mainly the valence electrons contribute to the value of the S parameter, which thus depends predominantly on the open volume. Fig. 3 shows that for the same value of S, the W parameter is clearly higher for the vacancy in N-doped ZnS_xSe_{1-x} than for that in Cl-doped material. Many more positron annihilations with core electrons are thus recorded at the vacancies in N-doped than in Cl-doped ZnS_xSe_{1-x}. However, this difference can not be explained by the vacancy-impurity complexes at the same sublattice: the electrons around Cl can be expected to give a larger contribution to the W parameter than those around N, leading to the opposite behavior as seen in Fig. 3.

The theoretical calculations show that in a defect-free compound semiconductor like ZnSe the largest contribution to the core annihilation rate λ_c of the delocalized positron comes from the *3d* electrons of the Zn atoms [10]. The *3d* shell of the Se atoms is more localized in r-space and overlaps less with the positron wave function, which leads to considerably smaller contribution to λ_c. Similarly [10], the magnitude of core electron annihilations is much larger in the Se vacancy (V_{Se}) surrounded by Zn atoms than in the Zn vacancy (V_{Zn}) surrounded by Se atoms. These arguments suggest that the vacancy defect detected in N-doped ZnS_xSe_{1-x} is the Se vacancy, whereas the one observed in Cl-doped ZnS_xSe_{1-x} is the Zn vacancy.

Fig. 4 shows the high-momentum part of the Doppler broadening spectrum, which was recorded at 300 K in the [N] = 1.7×10^{19} cm^{-3} and [Cl] = 1.5×10^{18} cm^{-3} doped ZnS_xSe_{1-x} using the coincidence technique [10]. The data in the N-doped material are above those in Cl-doped ZnS_xSe_{1-x} at the momentum range of p_L = (10-25)$\times10^{-3}$ m_0c, indicating that the magnitude of the core electron annihilations is about 20 % larger at the vacancy in N-doped than in Cl-doped ZnS_xSe_{1-x}. However, at the large momenta of p_L = (25-40)$\times10^{-3}$ m_0c the data obtained in N-doped material fall below those recorded in Cl-doped ZnS_xSe_{1-x}. The two curves in Fig. 4 have different shapes: in Cl-doped ZnS_xSe_{1-x} the core electron momentum distribution is clearly broader than in N-doped ZnS_xSe_{1-x}.

The broader momentum distribution indicates that the core electrons around the vacancy

have higher average momentum in Cl-doped than in N-doped ZnS_xSe_{1-x}. This implies that the chemical nature of the atoms surrounding the vacancy are different in the two cases. The *3d* electrons of Zn atoms are less localized than those of Se atoms, which leads accordingly to a narrower momentum distribution. Hence, the data of Fig. 4 indicate that positrons trapped at vacancies annihilate preferentially with the core electrons of Zn atoms in N-doped ZnS_xSe_{1-x} and with those of Se atoms in Cl-doped ZnS_xSe_{1-x}. The core electron momentum distribution gives thus a direct identification of the Se vacancy in N-doped ZnS_xSe_{1-x} and the Zn vacancies in Cl-doped material.

The positron experiments were performed also in heavily N-doped $Mg_yZn_{1-y}S_xSe_{1-x}$ (x = 0.16, y = 0.11) layers. The temperature dependence of S and W parameters in $Mg_yZn_{1-y}S_xSe_{1-x}$ are qualitatively similar as those in ZnS_xSe_{1-x} (Fig. 2), indicating that vacancies are present also in these layers. To identify the vacancies found in $Mg_yZn_{1-y}S_xSe_{1-x}$, the W parameter is plotted in Fig. 3 as a function of the S parameter measured at the same temperature. Two observations can be made. First, the absolute level of the W parameter in $Mg_yZn_{1-y}S_xSe_{1-x}$ is less than in ZnS_xSe_{1-x} (Fig. 3). This is due to the reduced amount of positron annihilations with core electrons, when Zn atoms with *3d* electrons are substituted by Mg atoms that do not have *d* electrons. Second, the data in N-doped $Mg_yZn_{1-y}S_xSe_{1-x}$ form a straight line in the (S, W) plane, indicating that a single type of vacancy is detected in positron experiments. This vacancy can be characterized by the same slope $R = |\Delta S / \Delta W| \approx 5$ as that found in N-doped ZnS_xSe_{1-x}, implying that the vacancy defect is the same. Hence, Se vacancies are observed by positrons also in heavily N-doped $Mg_yZn_{1-y}S_xSe_{1-x}$ (x = 0.16, y = 0.11) layers.

The detection of positron trapping at Se vacancies indicates that the total charge of the observed defect is neutral or negative in N-doped ZnS_xSe_{1-x} at 300 K. On the other hand, the isolated Se vacancy in p-type ZnSe is double positive according to theoretical calculations [2]. Positive vacancies are repulsive to positrons and the isolated Se vacancy is not expected to act as a positron trap in p-type ZnS_xSe_{1-x}. The Se vacancy detected in the positron experiments must thus be a part of a complex, where the Se vacancy is closely associated with a negatively charged acceptor. The present positron data can not be used to identify the details of this acceptor. However, such complexes as V_{Se} - N_{Se} are expected to be neutral or negatively charged for at least certain positions of the Fermi level in the energy gap [2].

The concentration of the vacancy complexes in N-doped ZnS_xSe_{1-x} can be estimated using the positron data of Fig. 2 at room temperature. The relative S parameter at monovacancies in semiconductors is typically $S_v / S_b \leq 1.03$ [9,13]. This value can be used to estimate the lower limit of the vacancy concentration, even if the exact parameter S_v / S_b is not known. The positron trapping coefficient at negative vacancies is $\mu \approx 10^{15}$ s^{-1} [11,14] and it is roughly by a factor of 2 - 6 less for a neutral than for a negative vacancy [14,15]. Taking $\mu = 10^{14}$ - 10^{15} s^{-1}, we get a vacancy concentration of $[V_{Se}] = 10^{18}$ - 10^{19} cm^{-3} in heavily N-doped ZnS_xSe_{1-x}. This is of the same order of magnitude as the nitrogen doping concentration, thus indicating that the Se vacancy complex plays a substantial role in the electrical compensation of ZnS_xSe_{1-x}.

Several theoretical calculations have been recently published in order to explain the microscopic origin of the p-type doping problems in ZnSe. Garcia and Northrup have proposed that an effective compensation results from the formation of defect complexes involving the nitrogen dopant and charged native defects such as Se vacancies or Zn interstitials [2]. The present positron experiments show that a high concentration of Se vacancies is present in N-doped ZnS_xSe_{1-x} and that these vacancies are probably complexed with an acceptor defect. A most natural candidate for the acceptor is the nitrogen dopant atom. The V_{Se} - N_{Se} pair is thus a defect compatible with the observed annihilation characteristics.

CONCLUSIONS

We have identified the Se vacancy in N-doped ZnS_xSe_{1-x} and $Mg_yZn_{1-y}S_xSe_{1-x}$ alloys and the Zn vacancy in Cl-doped ZnS_xSe_{1-x} by positron annihilation experiments. The total charge of the defect involving V_{Se} is neutral or negative, suggesting that the Se vacancy is in a complex with an acceptor defect, possibly with the nitrogen dopant. The concentration of Se vacancy complexes is of the same order of magnitude as the nitrogen doping concentration ($\geq 10^{18}$ cm^{-3}), indicating that the V_{Se} is important in the electrical compensation of p-type ZnSe based alloys.

ACKNOWLEDGMENTS

We acknowledge R. M. Nieminen and M. J. Puska for discussions and comments and J. Likonen for performing the SIMS experiments. This work has been supported by the Academy of Finland (EPIMATTER project).

REFERENCES

[1] D. B. Laks, C. G. Van de Walle, G. F. Neumark, and S. T. Pantelides, Phys. Rev. Lett. **66**, 648 (1991); D. B. Laks, C. G. Van de Walle, G. F. Neumark, P. E. Blöchl, and S. T. Pantelides, Phys. Rev. B **45**, 10965 (1992).
[2] A. Garcia and J. E. Northrup, Phys. Rev. Lett. **74**, 1131 (1995).
[3] C. G. Van de Walle, D. B. Laks, G. F. Neumark, and S. T. Pantelides, Phys. Rev. B **47**, 9425 (1993).
[4] D. J. Chadi and K. J. Chang, Appl. Phys. Lett. **55**, 575 (1989); D. J. Chadi, ibid. **59**, 3589 (1991).
[5] K. W. Kwak, R. D. King-Smith, and D. Vanderbilt, Phys. Rev. B **48**, 17827 (1993).
[6] D. J. Chadi, Phys. Rev. Lett. **72**, 534 (1994).
[7] C. H. Park and D. J. Chadi, Phys. Rev. Lett. **75**, 1134 (1995).
[8] K. Saarinen, T. Laine, K. Skog, J. Mäkinen, P. Hautojärvi, K. Rakennus, P. Uusimaa, A. Salokatve, and M. Pessa, Phys. Rev. Lett. **77**, 3407 (1996).
[9] P. Hautojärvi and C. Corbel, in *Positron Spectroscopy of Solids*, edited by A. Dupasquier and A. P. Mills Jr. (IOS Press, Amsterdam, 1995).
[10] M. Alatalo, H. Kauppinen, K. Saarinen, M. J. Puska, J. Mäkinen, P. Hautojärvi, and R. M. Nieminen, Phys. Rev. B **51**, 4176 (1995); M. Hakala, M. Puska, B. Barbiellini, and R. M. Nieminen, private communication.
[11] C. Corbel, F. Pierre, K. Saarinen, P. Hautojärvi, and P. Moser, Phys. Rev. B **45**, 3386 (1992).
[12] L. Liszkay, C. Corbel, L. Baroux, P. Hautojärvi, M. Bayhan, A. W. Brinkman, and S. Tatarenko, Appl. Phys. Lett. **64**, 1380 (1994).
[13] R. Ambigapathy, A. A. Manuel, P. Hautojärvi, K. Saarinen, and C. Corbel, Phys. Rev. B **50**, 2188 (1994).
[14] J. Mäkinen, P. Hautojärvi, and C. Corbel, J. Phys. Condens. Matter **4**, 5137 (1992).
[15] K. Saarinen, A. P. Seitsonen, P. Hautojärvi, and C. Corbel, Phys. Rev. B **52**, 10932 (1995).

ELECTRICAL CHARACTERIZATION OF NITROGEN ACCEPTORS IN p-ZnSe/p-GaAs GROWN BY MOLECULAR BEAM EPITAXY

D. SEGHIER, H.P. GISLASON
Science Institute, University of Iceland, Dunhaga 3, IS-107 Reykjavik, Iceland

ABSTRACT

Using current-voltage measurements, deep-level transient spectroscopy and admittance spectroscopy we investigated nitrogen doped ZnSe grown on p-GaAs substrates by molecular beam epitaxy. Three major hole traps were observed with energy levels at 0.11, 0.46, and 0.56 eV from the valence band. We attribute the level at 0.11 eV to a nitrogen acceptor. No other direct observations of this important acceptor level in p-ZnSe have been reported in the literature so far. The two remaining levels may originate from the nitrogen doping process. In addition, reverse current-voltage characteristics of the ZnSe/GaAs heterojunction show a hysteresis at low temperature and a soft saturation. At a constant reverse bias the current increases slowly until it reaches a steady state value. This behavior is attributed to a slow voltage-induced barrier lowering due to the presence of mismatch interface states. Therefore, these analyses are of a major interest for applications of ZnSe/GaAs based devices and illustrates the necessity of improving the growth conditions of such structures.

INTRODUCTION

Much work has been done on epitaxial layers of ZnSe on GaAs because of the small lattice mismatch (0.27%) in this heterojunction (HJ). The inability to grow high quality and low resistivity p-type ZnSe has been a long standing obstacle in the way of applications of this material [1]. The observation that only a fraction of the nitrogen dopants contributes to the active acceptor concentration makes it necessary to characterize the defect spectrum in order to understand the compensation mechanism. There are only a few reports on defects in p-type ZnSe and energy levels introduced by nitrogen in the band gap are not known. Moreover, mismatch-induced defects are widely present in and near the heterointerface between ZnSe and GaAs. These defects can affect the mobility [2,3] and the interface barrier height [4]. Therefore, characterization and control of the ZnSe/GaAs heterointerface are key points in obtaining high-quality ZnSe epilayers on GaAs substrate. Despite many reports on this topic it is still a subject of great interest. In this work we report on hole traps in N-doped ZnSe grown by molecular beam epitaxy (MBE) which were measured by deep level transient spectroscopy (DLTS) and admittance spectroscopy (AS). In particular the nitrogen-related acceptor level was investigated. We also report the presence of slow mismatch-induced interface defects at the HJ as observed in current-voltage (I-V) measurements. These defects result in a voltage-induced lowering of the barrier at the heterointerface and in a long time-constant relaxation in the electrical properties of ZnSe/GaAs.

SAMPLE PREPARATION

ZnSe epilayers were grown by MBE on a (001) p-type GaAs substrates [5]. Nitrogen was introduced via free radicals generated from radio frequency nitrogen plasma source. Growth temperatures were in the range 250-300 °C. The ZnSe epilayers were 2 μm thick. Their nitrogen concentration was around 2×10^{18} cm^{-3} as determined by SIMS analysis. The GaAs substrate was Zn-doped to $p = 3\text{-}5\times10^{18}$ cm^{-3}. A thick Be-doped GaAs buffer layer with $p = 1\times10^{18}$ cm^{-3} was grown. Schottky diodes with diameter 1 mm were made by evaporating Au on the ZnSe. Ohmic

Mat. Res. Soc. Symp. Proc. Vol. 442 © 1997 Materials Research Society

contacts on the GaAs substrate were formed by evaporating Au-Zn alloy or using In-Ga. The acceptor concentration determined from capacitance-voltage was about 1×10^{17} cm^{-3}.

EXPERIMENT

The I-V curves of the studied device can be well understood by modeling the structure as two diodes connected back-to-back: a Au/p-ZnSe Schottky barrier diode (SD), and a p-ZnSe/p$^+$-GaAs HJ. Because of a large valence band discontinuity in the HJ and a high doping level in the GaAs buffer layer the depletion regions of both junctions are in the ZnSe layer. The applied voltage V is divided between the two junctions. When V is positive most of the applied bias drops across the SD. The negative voltage drops first across the SD until $\phi_{SD} - V = \phi_{HJ}$, where ϕ is the barrier. Further increase of V appears as a reverse bias across the HJ, which will limit the current in the circuit.

DLTS and Admittance measurements

Figure 1a shows a DLTS spectrum from the SD depletion region. A reverse bias of $V = 5$ V, a carrier filling pulse of 3 V and a DLTS rate window of $\tau = 2\times10^{-4}$ s were used. There are three dominant peaks in the spectrum labeled T1, T2 and T3 from low to high temperature, respectively. All of them originate from hole traps. The trap activation energy E_t and the apparent hole capture cross section $\sigma_{p\infty}$ calculated from the equation of detailed balance are:

$$E_t = 0.46 \text{ eV}, \sigma_{p\infty} = 1\times10^{-15} \text{ cm}^2; \text{ and } E_t = 0.56 \text{ eV}, \sigma_{p\infty} = 3\times10^{-15} \text{ cm}^2$$

for T2 and T3, respectively. For T1 the capacitance transient at low temperature at which this peak is observed is not purely exponential. A typical capacitance transient is composed of an initial rapid decay followed by a subsequent long transient. There can be several reasons for a non exponential capacitance transient [6]. In case of an electric-field dependence of the trap emission, a temperature shift of the DLTS peak should be observed when performing DLTS at different reverse bias keeping the same rate window. For T1 no such a shift occurs, indicating that the emission from T1 is not field dependent. The possibility of several traps with emission rates too close to be separated in the DLTS spectrum cannot be completely excluded. However, due to the strong signal observed for T1, it is very likely that the non exponential behavior also arises from the high concentration of this trap. Furthermore, the second portion of the capacitance decay may well be approximated by an exponential curve. Wang et al. [6] showed that the problem of a trap with a high concentration is equivalent to that of a low one when $t >> 1/e$, where t is the time and e the emission rate of the trap. Then the corresponding part of the transient must be an exponential function of the true emission rate. Using this tail of the transient, we obtain the following values of E_t and $\sigma_{p\infty}$ for T1:

$$E_t = 112 \text{ meV}; \sigma_{p\infty} = 2\times10^{-18} \text{ cm}^2.$$

Due to the non-negligible value of the series resistance (R_s), as will be mentioned later, the concentration of T1 estimated from DLTS to about 10^{16} cm^{-3} has to be regarded as a lower limit for the trap concentration since a high value of R_s tends to reduce the DLTS peak height. It is possible to overcome problems arising from R_s by measuring the sample admittance at lower frequencies [7]. Figure 1b shows the conductance spectrum measured at 10 KHz. A clear peak is observed at low temperature. It is due to a hole trap since only majority carrier traps are observed in admittance spectroscopy. The Arrhenius plot of this peak agrees well to the DLTS data for T1. Hence, we conclude that they are identical.

The temperature dependence of the capacitance of the SD at 1 MHz is shown in Figure 2. At low temperature (~90 K) the capacitance dramatically drops more than 70% in a narrow temperature range, indicating a freeze-out of carriers. This freeze-out of carriers at such a temperature, confirms

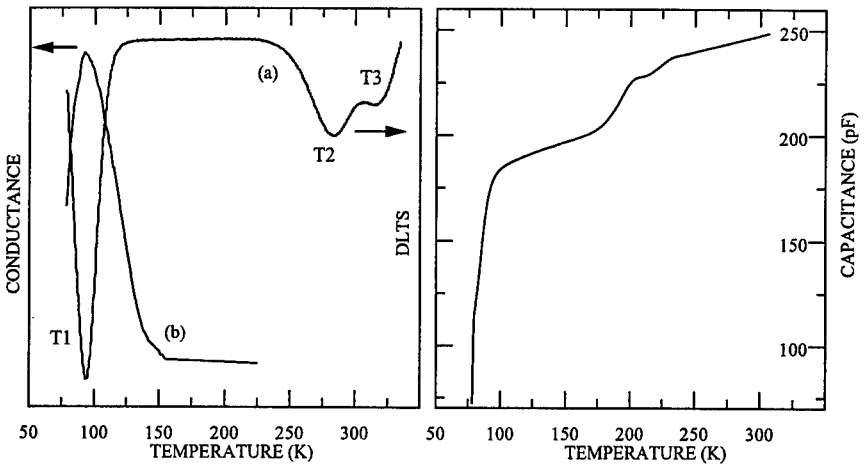


Fig. 1: a) DLTS spectrum, $\tau = 2\times10^{-4}$ s ; b) Conductance spectrum, f=10 KHz, V_r=2V; from the Au/p-ZnSe junction.

Fig. 2: Capacitance vs temperature, *f = 1MHz, from the Au/p-ZnSe junction. V_r = 2V.*

that the ionization energy of the acceptor level is at about E_v+100 meV. The sharp decrease seems to occur in two steps (from high to low temperature): a fast step followed by a second one which is more rapid. This behavior agrees with the hypothesis of two levels with similar concentrations being close in energy.

I-V measurements

Figure 3 shows semilogarithmic plots of I-V characteristics of the device under study at 270 K. The data were acquired by scanning from 6 to -6 V using bias steps of 0.05 V and different scan delays. The I-V characteristic for positive bias is independent of scan direction and scan delay. For negative bias voltages this is also true when the scan delay is long enough. The lower limit for the scan delay is about 15 s for a typical sample at 270 K. For faster scans, however, the I-V curves show a small hysteresis in the range between -6 V and -1.5 V. The current is slightly higher when scanning from -6 to +6 V compared to the opposite direction. In addition, the longer the scan delay is, the higher the current becomes for V between -6 V and -1.5 V. For scan delays longer than the lower limit no significant dependence on the scan delay is observed. In the same bias range the current increases slowly to a steady state value I_∞ if the voltage is kept constant. If the bias voltage is switched to zero there is no current through the device. Restoration of the initial bias results in the current taking an intermediate value between the lowest one ($t = 0$) and the highest one ($t = \infty$) depending on the time for which no bias was applied. If the negative bias is suddenly reduced from steady state conditions at a given bias voltage, the current attains a new equilibrium value characteristic of the new bias. The time needed to reach the new current value in this way is much shorter than that needed from the $t = 0$ condition. At lower temperatures the time needed to reach the steady state is longer whereas the difference between the $t = 0$ and $t = \infty$ current values is smaller.

For bias voltages between 0 V and -1.5 V the current increases exponentially, whereas a smooth saturation takes place for more negative voltages. For long scan delays this second step current can

also be fitted with an exponential (Fig. 3). The first step may be understood in terms of the forward current through the SD limiting the current flow. In this case there is no dependence on scan direction or scan delay. At larger negative bias the current is ultimately limited by the HJ barrier. As seen in Fig. 3, the behavior of the reverse current at higher voltages indicates that the HJ barrier height is itself voltage dependent [8]. The series resistance R_s for the SD was calculated by considering the slope of the linear *I vs dV/d(lnI)* plots in the range $-1.5\ V < V < 0\ V$, according to calculations from Cheung *et al.*[9]. A value of approximately 400 Ω was found. This high value may arise from the neutral region of the material, the ohmic contact on GaAs or a possible interface layer between the ZnSe and the GaAs. Since the bulk resistance is low for highly doped p-type GaAs and the ohmic contact resistance is also known to be low for such material, we conclude that the measured value of R_s mostly arises from an interfacial layer at the heterointerface.

Because the steady current is exponential, it can be described by a relationship of the form

$$I_\infty(V) = I_o exp(aV) \qquad (1)$$

where $I_\infty(V)$ is the voltage-dependent steady state current. The value of I_o deduced from these results lies within the experimental error of the saturation current measured by plotting the I-V characteristics very quickly (the $t = 0$ condition). The factor a is a constant. Assuming that the increase of the reverse-current at constant bias is due to a slow voltage-dependent barrier height lowering (which is a working hypothesis to be justified below), it is required that

$$I_\infty(V) = I_s exp(\Delta\Phi_\infty/kT)) \qquad (2)$$

where $\Delta\Phi_\infty$ is the total barrier height change between the $t = 0$ and $t = \infty$ states and $I_s \approx I_o$ is almost independent of the applied voltage. From Eqs.(1) and (2) we find that the total change of the barrier height is proportional to the applied reverse bias

$$\Delta\Phi_\infty(V) = akTV. \qquad (3)$$

We now show that a relationship of this type can well be caused by the presence of interface states. Let us consider a uniform distribution of energy levels in the interfacial layer filled up to the Fermi level at equilibrium. The case of a discrete interface level leads to similar results. When the system reaches its steady state at constant reverse bias, the change of the hole population in the slow states, assuming a zero-temperature limit for the Fermi-Dirac distribution [10], will be given by

$$\Delta p_o(\infty) = D_s \Delta E_F(\infty) \qquad (4)$$

where D_s is the density of slow states per cm^2 and per eV, and $\Delta E_F(\infty)$ the displacement of the quasi-Fermi level of the slow states relative to E_F in the GaAs substrate. For a small departure from equilibrium it is legitimate to write: $\Delta E_F(\infty) = bV$, where b is a small constant ($b << 1$) and V the applied voltage. This assumption combined with Eq.(4) gives

$$\Delta p_o(\infty) = D_s bV. \qquad (5)$$

By applying Gauss' law to the interfacial layer we can write

$$\Delta V_i(\infty) = (q\delta/\varepsilon_i)\Delta p_o(\infty) \qquad (6)$$

where δ is the thickness of the interfacial layer and ε_i its dielectric constant. Since $\Delta\Phi_\infty = \Delta V_i(\infty)$ we deduce

$$\Delta\Phi_\infty = (q\delta D_s b/\varepsilon_i)V \qquad (7)$$

which means that the total barrier height lowering induced by the interface states is proportional to the applied bias. This is in agreement with the experimental results, thereby proving the working hypothesis of the investigation.

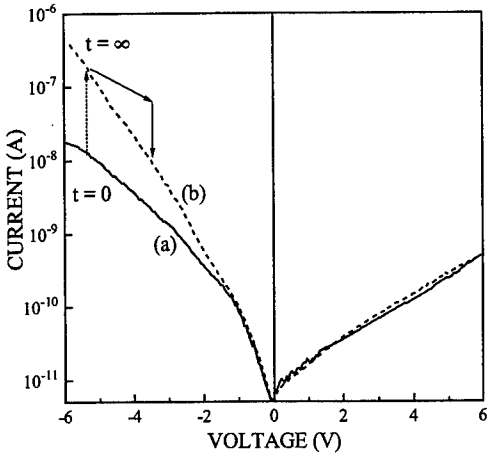


Fig. 3: I-V *characteristics at 270 K for Au/p-ZnSe/p$^+$-GaAs. (a) rapid scan: 0.5 s per bias step; (b) long scan: 15 s per step. The dashed arrow indicates the increase of current at constant reverse bias, and the solid arrows the decrease of current after the bias is decreased.*

DISCUSSION

The peak T1 was observed in all N-doped samples. As pointed out, the freeze-out of carriers around 90 K confirms that T1 is a dominating acceptor. A level at around E_v+0.11 eV has been observed in photoluminescence spectra of ZnSe:N and attributed to nitrogen. Therefore, we attribute T1 to a nitrogen-related acceptor level for reasons of its ionization energy and its correlation with the nitrogen doping. If there are two traps with similar activation energies, as discussed above, this could mean that nitrogen acceptor atoms are present in slightly different configurations in the host material. Hole traps with activation energies similar to T2 and T3 have also been reported in the literature [11-12]. It has been suggested that these traps involve nitrogen impurities. The fact that the density of these traps is quite significant, even comparable to that of T1 leads us to suggest that they are related to the nitrogen doping process. At this point we are not able to speculate on their origin without further studies.

In Fig. 3, the negative part of the applied voltage first increases exponentially which is attributed to the forward characteristic of the SD. The value of R_s estimated from this characteristic strongly indicates the presence of a resistive insulating layer at the heterointerface. Mismatch induced defects between ZnSe and GaAs have been reported by many workers [13-14]. The soft reverse characteristic of the HJ suggests a bias dependent barrier. We propose that the slow reverse-current changes are due to slow voltage-induced barrier height changes at the HJ and, in particular, that the increase of the reverse current at constant bias voltage is due to a voltage-dependent barrier height lowering. Strictly speaking, the voltage drop across the insulating layer depends on the charge on the interface states. This voltage drop induces a barrier change $\Delta\phi$. Hence, when the applied bias is changed, the barrier changes by an amount $\Delta\phi(t)$ which is a slow function of time due to the slow change in the interface states charge. Therefore, the change in the reverse current of the HJ is also a slow function of time. If holes in the valence band of GaAs can tunnel through the interfacial layer, they have to overcome the barrier ϕ at zero bias. When a reverse bias is applied to the HJ, it is divided into a potential drop across the interface layer V_i, and another one across the ZnSe depletion layer V_d, so $V = V_d+V_i$. Therefore, at $t=0$ the barrier height and the saturation current will be determined by the potential drop across the interfacial layer. From this moment

however, the slow voltage-induced barrier height changes determine the current. Then, if the slow states communicate more easily with the ZnSe bulk than with GaAs (as we assume to be the case), they will start to release holes into the valence band of ZnSe or capture electrons from the conductance band of ZnSe or both, leaving an 'effective' negative charge in the interfacial layer. This results in an increase of the potential drop across the interfacial layer which leads to a reduction of the barrier height ϕ and, hence, an increase in the reverse current. This is in agreement with the experiment.

CONCLUSION

In summary, nitrogen-doped p-type ZnSe epilayers grown by MBE on p^+-GaAs substrates were investigated using DLTS and admittance spectroscopy. Three hole traps were observed. We attribute the level at E_v+0.11 eV to a nitrogen acceptor. The remaining ones (at E_v+0.46 and E_v+0.56 eV) may originate from the nitrogen doping process. The smooth reverse characteristic of the HJ and the increase in the current at constant reverse bias suggest a bias-dependent barrier. We attribute this to the presence of mismatch-induced slow defects which results in a slow voltage-induced lowering of the barrier. These results underline that growth conditions and substrate treatment are of prime importance when growing ZnSe/GaAs based devices. Further studies will be performed on samples grown under different conditions on the basis of these observations.

ACKNOWLEDGMENTS

This research was supported by the Icelandic Research Council and the University Research Fund. We are grateful to L.A. Kolodziejski for providing samples, I.S. Hauksson and K. Leosson for discussions, and B.H. Yang for preparing the samples for electrical measurements.

REFERENCES

1. R.M. Park, M.B. Troffer, C.M. Rouleau, J.D. DePuydt and M.A. Haase, Appl. Phys. Lett. **57**, 2127 (1990).
2. W. Stutius and F.A. Ponce, J.Appl. Phys. **58**, 1548 (1985).
3. K. Morimoto, J. Appl. Phys. **64**, 495 (1988).
4. DJ. Olego, J. Vac. Sci. Technol. B6, 1193 (1988).
5. E. Ho, P.A. Fisher, J.L. House, G.S. Petrich, L.A. Kolodziejski, J. Walker and N.M. Johnson, Appl. Phys. Lett. **66**, 1062 (1995).
6. Alex C. Wang, and C.T. Sah, J. Appl. Phys. **55,** 565 (1984).
7. G. Vincent, A. Chantre and D. Bois, J. Appl. Phys. **50,** 5484 (1979).
8. A.G. Milnes and D.L. Feucht in Heterojunctions and Metal-Semiconductor Junctions (Academic Press, New York, 1972), p. 98.
9. S.K. Cheung and N.W. Cheung, Appl. Phys. Lett. **49**, 85 (1986).
10. E. H. Rhoderic and R.H. Williams in Metal-Semiconductor Contacts, 2nd ed. (Clarendon, Oxford, 1988), p.17.
11. B. Hu, G. Karczewski, H. Luo, N. Samarth and J.K. Furdyna, Appl. Phys. Lett. **63**, 358 (1993).
12. H. Goto, T. Tanoi, M. Takemura, and T. Ido, Jpn. J. Appl. Phys. **34,** L827 (1995).
13. T. Marshall, S. Colak and D. Cammack, J. Appl. Phys. **66**, 1753 (1989).
14. A. Singh, Solid State Electron. **28**, 223 (1985).

DEEP CENTERS INFLUENCE ON PHOTORESPONSE CHARACTERISTICS IN HIGH-RESISTIVITY ZnSe

V.A.KOROTKOV, L.I.BRUK, A.V.SIMASHKEVICH, O.S.GOREA, L.E.KOVALEV, L.V.MALIKOVA*
State University of Moldova, Dept. of Physics, Kishinev, MOLDOVA, MD2009
*Brooklyn College, Dept. of Physics, Brooklyn, NY, USA, lmakova@its.brooklyn.cuny.edu

ABSTRACT

The photocurrent peak after preliminary optical excitation with specific wavelength in high resistivity ($\rho \approx 10^{12} \Omega * cm$), unintentionally doped ZnSe monocrystals was observed. To study photocurrent "flash" phenomenon, the photocurrent relaxation spectra, photon-capture cross-section (PCCS) spectra and photo-electron paramagnetic resonance (photo-EPR) were investigated. Two-levels model involving the recombination of an S-center and an acceptor A has been developed to obtain the relation between recombination probability and instantaneous photocurrent value. The S-centers ionization energies (1.06eV and 1.14eV from the bottom of the conduction band) and charge carriers life times were determined. The acceptor's positions in ZnSe band gap are equal to 2.05, 2.11, 2.16 and 2.21eV from the bottom of the conduction band. The photocurrent and PCCS "flash" nature as well as complicated photo-EPR are associated with the relaxation of S-centers attributed to Fe ion in the band gap of semi-insulated ZnSe.

INTRODUCTION

The optical properties of wide energy band gap II-VI compound semiconductor ZnSe material system have received much attention of late because they may prove useful for photodetectors, photodiodes, and laser diodes [1, 2], working in blue and blue-green range of the spectrum. The efficiency of such devices is determined by the concentration of unintentional impurities and defects. At the same time, research into undoped, highly resistive ZnSe, containing a large density of deep centers (DC), is also of interest. This is the subject of our report.

It is known that the intrinsic and impurity stationary photoconductivity (PC) spectral region is the result of a few superimposed bands and does not allow one to obtain the total information about the photosensitive centers position in the semiconductor's band gap. The recording PC stationary signal excludes the possibility to reveal less sensitive, recombination and capture centers. The preliminary excitation can change the state of such levels and leads to their displaying in "flash" phenomenon [3, 4]. These centers, depending on their charge state, can show paramagnetism at different external conditions. In the photosensitivity region of ZnSe with unintentional impurities we have investigated PC "flash" phenomenon, the photocurrent relaxation spectra, photo-EPR and PCCS spectra.

EXPERIMENTAL RESULTS AND DISCUSSION

We have studied highly resistive ($\rho \approx 10^{12} \Omega * cm$) ZnSe crystals with free carrier concentration and mobility of $n \approx 10^{7} cm^{-3}$ and $\mu_n \approx 10 cm^2 / V * s$ respectively. Indium makes an Ohmic contact to ZnSe. One of the contacts was semitransparent.

Mat. Res. Soc. Symp. Proc. Vol. 442 © 1997 Materials Research Society

The PC relaxation spectra and PCCS spectra were measured in the 0.5-1.0μm range at the room temperature. EPR spectra were measured at 20K, 77K with and without optical and X-rays excitation from the fundamental absorption region.

Photocurrent

The "flash" phenomenon of the photocurrent of the investigated ZnSe samples was observed at temperatures of 100-300K. The fall of the photocurrent after "flash" (see Fig.1a, curve 1) from its maximum value I_{PCm} to the stationary signal I_{PCst} (see Fig.1a, curve 2) during illumination with light of the same wavelength, but following preliminary excitation occurred after $10^2 - 10^3 s$ at T=100K and after $10^1 - 10^2 s$ at T=300K. One could distinguish three experimental situations in which this effect was observed: illumination with light from the intrinsic absorption region following preliminary excitation with impurity-absorbed light; illumination with impurity-absorbed light after excitation with light corresponding to the intrinsic absorption region; illumination with impurity-absorption light after excitation with light of a different wavelength within the impurity absorption region.

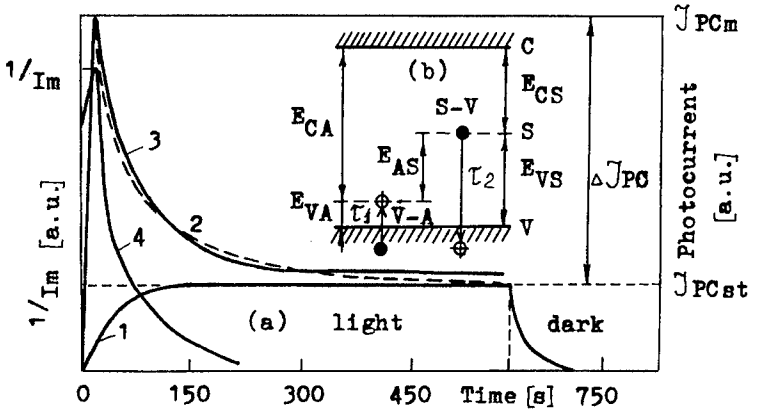


Fig.1. PC decay spectra (a); energy-band diagram of the two-levels model (b).

Figure 2 illustrates typical PC dependence on wavelength without preliminary (curve 1) and with preliminary excitation (curves 2,3), with the wavelength of the PC "flash" (ΔI_{PC}) induced by prior irradiation falling in the 0.46... 0.95 μm range. We measured the spectral dependence of ΔI_{PC} at various wavelengths of prior irradiation, whose "flash" corresponded to energies of 2.05, 2.11, 2.16 and 2.21eV. The dependence of ΔI_{PC} on the wavelength of the prior irradiation measured at a fixed wavelength (Fig.2, curves 2,3) also exhibits a number of peaks. Apparently, nonequilibrium electrons recombine via the above-described local centers, and PC "flash" is probably due to the overcharging of deep centers, which are taken out of equilibrium by prior irradiation in a different frequency range.

A model accounting for the peak of the photoconductivity relaxation curve in the second and third cases was developed by considering the case of a PC "flash" as a result of illumination with light of photon energy E_{CS} after preliminary excitation with light of photon energy E_{CA}. Figure 1b shows the energy band diagram of the two-level model. Levels E_{CS} and E_{CA} are the

energy separation — from the bottom of the conduction band — of a deep level S located near the middle of the band gap and of an acceptor level A. The envelopes of the relaxation curves were obtained by two methods. In the first method we used short light pulses sufficient to reach the quasisteady value of the current (see Fig.3a, curve 1). In the second method we used long light pulses alternating with short intervals in darkness during which the dark value of the current could not be established (see Fig.3a, curve 2). The coincidence of the envelopes of the relaxation curves indicated that relaxation of the nonequilibrium PC after illumination with E_{CS} and the dispersal of the nonequilibrium electrons at the S-level in darkness were both due to the same recombination channel. In other words, dispersal of the charge from the S-centers does not involve the conduction band, in contrary to the model proposed in [5] and [6], and was due to the subsequent illumination of the semiconductor.

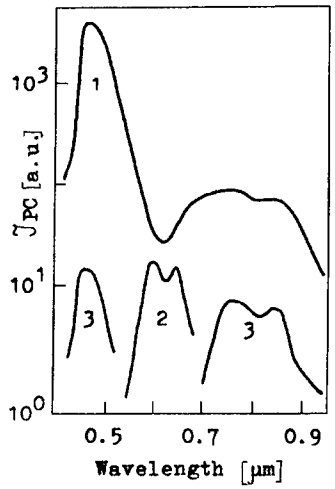


Fig.2. PC spectra without (curv.1) and after preliminary excitation (curv.2) at $\lambda_{exit.}$ = 0.525μm and curv.3 at $\lambda_{regist.}$ = 0.580μm)

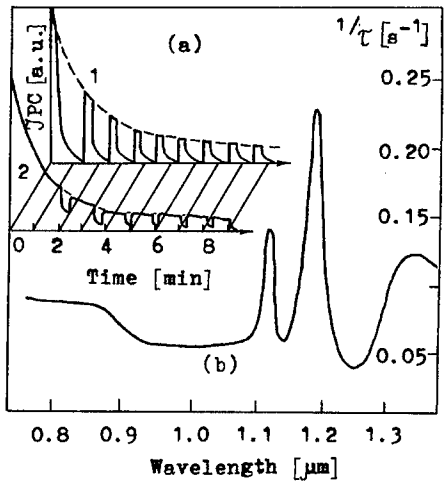


Fig.3. PC decay spectra at $\lambda_{regist.}$ = 0.950μm and $\lambda_{exit.}$ = 0.475μm (a); spectrum after preliminary excitation at $\lambda_{exit.}$ = 0.490μm (b).

We propose that the conditions of optical generation simply transfer electrons to the conduction band and result in repeated trapping on the S-level. We assume that the density of holes in the valence band after a long interval in darkness is zero. This was true if $N_A \langle N_S$, where N_A and N_S the concentration of the A- and S-centers, respectively. If in such a state the sample was illuminated with light of the photon energy $h\upsilon = E_{CS}$, we should observe the usual relation of the nonequilibrium electron density in the conduction band due to the presence of electrons with a density n_{Sst} at the S-centers. However, if a sample is first illuminated with light of the photon energy $h\upsilon = E_{CA}$, the nonequilibrium electrons from the conduction band were captured by the S-centers and these were only partly emptied. Therefore, after preliminary illumination of a crystal nonequilibrium situation was established in which A-centers were partly emptied and the S-enters were almost filled with electrons. The subsequent illumination of the semiconductor with photons of energy $h\upsilon = E_{CS}$ released electrons from the S-level to the conduction band and this gave a steep rise of the photocurrent above the steady-state value, followed by a fall together

with the density of nonequilibrium electrons at the S-centers. Preliminary illumination with photon of the $h\upsilon = E_{CA} - E_{CS}$ energy did not create a "flash". A change in the electron density at the S-level due to their recombination with holes from the valence band is given by the Bernoulli equation [4]:

$$\frac{dn_S}{dt} + \frac{1}{\tau_2}\frac{n_S}{n_{Sst}} - \frac{n_S}{\tau_2}\left(\frac{n_{Sst}}{n_{Sm}} + e^{-t/\tau_1}\right) = 0 \qquad (1),$$

where n_S is the density of electrons at the S centers at any moment in time t; $n_S\big|_{t=0} = n_{Sm}$ (for ΔI_{PCm}); $n_S\big|_{t=\infty} = n_{Sst}$ (for ΔI_{st}) ; the following characteristic times: $\frac{1}{\tau_1} = \gamma_{Ap} N_A$; $\frac{1}{\tau_2} = \gamma_{Sp} n_{Sm}$. The hole capture coefficient of the S centers is γ_{Sp} and γ_{Ap} is the hole capture coefficient of the A-centers.

Equation (1) has the exact solution :

$$n_S = \frac{n_{Sm} n_{Sst} \exp\left[n_{Sst}/n_{Sm}\tau_2 + \tau_1\left(1 - \exp\left[-t/\tau_1\right]\right)/\tau_2\right]}{n_{Sst} + n_{Sm}\exp\left(\tau_1/\tau_2\right)\left[\exp\left(n_{Sst}t/n_{Sm}\tau_2\right) - 1\right]} \qquad (2).$$

Substitution of the experimentally determined parameters $\tau_1 = 10^{-7}s$, $\tau_2 = 10s$, $n_{Sm} = 10^7 cm^{-3}$ and $n_{Sst} = 10^6 cm^{-3}$ into eq. (2) ensured satisfactory agreement between the calculated and experimental dependencies (see Fig.1a, curves 2, 3). Taking into account, that $\tau_1 \langle\langle \tau_2$ and $I_{PC} \approx n_S$, we obtained from equation:

$$\frac{1}{\tau}t = \frac{I_{PSm}}{I_{PCst}} \ln\left(\frac{\left(I_{PCst}/I_{PCm}\right) - 1}{I_{PCst}/I_{st}}\right) \qquad (3).$$

Figure 3b illustrates the dependence of $1/\tau$ on wavelength. It is supposed that the peaks at the energies 1.14eV and 1.06eV from the conductivity band bottom correspond to S-centers, which are characterized by high probability of recombination.

Photon-capture cross-section

The independent determination of the A-centers position is carried out from the PCCS (σ_{ph}) spectral dependence. According to ref.7 spectral dependence is determined by the dependence of photon flux intensity (I) on the photon energy: $\sigma_{ph}(h\upsilon) = const/I(h\upsilon)$, at $I_{PC} = const$ on account of the excitation intensity change. The typical PCCS spectra are given in Fig.4a. By bending points the position of photosensitive A-centers with the energy E= 2.05; 2.11; 2.16; 2.21eV there were established. As one can see from Fig.4a satisfactory coincidence of the calculated and experimental curves is observed.

The deep centers PCCS relaxation after the optical recharging reveals "flash" phenomena. It is supposed that preliminary illumination transfers the electrons from A-centers through conductivity band to the centers of "flash" activation (S-centers). The charge state of deep S-center is changing and the average value of photoionization grows ("flash" on Fig.1a, curve 4).

At the recombination of the electrons from S-center with the holes from the valence band PCCS decreases to its stationary value. Thus apparently, PC "flash" phenomena after optical recharging DL is explained by PCCS relaxation on S-centers.

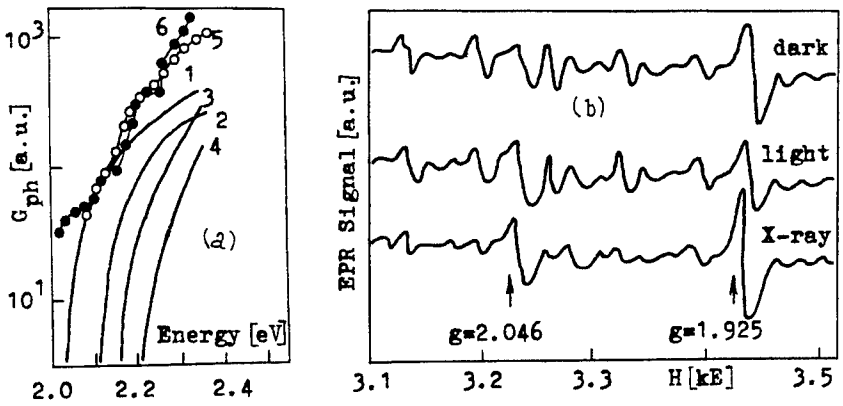


Fig.4. PCCS spectra (curv. for centers 1-E_{CS} = 2.05eV; 2-E_{CS} = 2.11eV; 3-E_{CS} = 2.16eV; 4-E_{CS} = 2.21eV and 5-calculation; 6-experiment) (a); EPR spectra at 77K (b).

Photo-electron paramagnetic resonance

We have studied EPR of unintentionally doped zinc selenide with and without optical and X-ray excitation .

In the EPR spectra of all samples it was observed the Mn^{2+} , consisting from six lines with superfine (HFS) interaction constant A=67.9 Gs, a=9 Gs, g-factor of 2.007 and Fe^{3+} (g=2.046) and lines with g-factor equal to 1.925 at 77K (see Fig.4b) in the dark. The EPR spectra measured at 77K, when magnetic field coincide with the direction of the fundamental symmetry axis H||Z confirms lines structure Mn^{2+} with the intense line with g=2.001. That line is caused by an F-center.

With the illumination of the light corresponding to the fundamental absorption region, the F-center line increases, which can be related to the capture of the electron from neutral selenium vacancy or other impurities or complexes on the double charged vacancy V_{Se}^{2+} destructed by the light. Optical and X-ray excitation intensifies the Fe^{3+} line. The line with g=1.925 also increases with X-ray excitation and decreases with optical excitation. This center may be related to the acceptor center (V_{Zn} -III; V_{Zn} -VII) [8].

Illumination with light from the impurity absorption region, after excitation with the light from the fundamental region, decreases the intensity of lines related to iron up to the level in the dark. It is supposed that this is a result of the destruction of complexes, which consists of the initial inherited defects of the lattice and impurities.

CONCLUSIONS

The properties of unintentionally doped ZnSe using PC spectra, PC relaxation spectra, photon-capture cross-section spectra, EPR and photo-EPR was studied. The results are summarized as follows:

a two-level model involving recombination S-center and an acceptor A has been developed to obtain the relation between the recombination probability and the instantaneous photocurrent value;

the S-centers ionization energies are 1.06eV and 1.14eV from the bottom of the conduction band and charge life times were determined;

the acceptors position are equal to 2.05, 2.11, 2.16 and 2.21eV from bottom of the conduction band;

the photocurrent and PCCS "flash" nature as well as complicated photo-EPR are associated with the relaxation of S-centers attributed to Fe^{3+} ion;

from EPR measurements, F-centers and impurities with g=1.925 (V_{Zn} -III or V_{Zn} -VII) was detected.

REFERENCES

1. M.A.Haase, J.Qiu, J.M.DePuydt, H.Luo et al., Appl. Phys.Lett., **59**, 1273 (1991).
2. A.Ishibashi and Y.Mori, J.Cryst.Growth, **138**, 677 (1994).
3. F.M.Berkovskii and S.M.Ryvkin, Sov.Phys.Solid.St., **5**, 381 (1963).
4. O.S.Gorea, L.E.Kovalev, V.A.Korotkov, L.V.Malicova and A.V.Simashkevich, Sov.Phys.Semicond., **23**, 1294 (1989).
5.E.N.Arkadieva, L.G.Paritskii and S.M.Ryvkin, Sov.Phys.Solid St., **2**, 1051(1960)
6. S.M.Ryvkin, Photoelectric Effects in semiconductors, Consultants Bureau, New York (1964).
7. H.G.Grimmeisec and L.A.Ledebo, J.Appl.Phys., **46**, 2155(1975)
8. S.S.Davless et al., J.Luminescence, **18-19**,322(1970)

COMPLEX DEFECTS IN Cl DOPED ZnTe AND CdTe

V. VALDNA
Tallinn Technical University, Tallinn, EE-0026, Estonia, vello@opto.ttu.ee

ABSTRACT

Photoluminescence and conductivity of doped with chlorine and copper ZnTe, Zn(SeTe) and CdTe are investigated. We suppose that interstitial tellurium and complex defects of Te_i with a donor dopant Cl can significantly affect the luminescence spectra and conductivity value of ZnTe and CdTe. This assumption is confirmed experimentally. We found that copper dopant in CdTe: Cl can increase the resistivity value of p-type CdTe.

INTRODUCTION

ZnTe, CdTe and its solid solutions have a good potential for fabricating room-temperature radiation detectors, electro-optic modulators and low cost large-area solar cells [1-4]. Native defects of ZnTe and CdTe have been studied in recent years by several authors [5-9]. However, very little is known about the intrinsic host interstitials in the group II-VI materials [10] and control of the electrical properties of these materials has not yet been achieved [11]. The donor-cation vacancy pair (A-centre) is the most investigated complex in CdTe and ZnTe. Nevertheless, a correct assignment of A-centers has been possible only resently by ODMR [7]. A-centre $V_{Cd}Cl_{Te}$ is a single acceptor in CdTe with a level position of 125 meV above the valence band, in ZnTe 160 meV above the valence band [7]. B.K. Meyer et al. [12] have found that the A-centre cannot be responsible for the p-type conversion and the selfcompensation in the p-type ZnTe. It is found that nearly at the same energetic level as A-centre in CdTe some other acceptor defect can exist and Cu_{Cd} or Cu complex are proposed as a possible candidate [11,13,14]. W. Stadler et al. [15] have found that the Indium A-centre in CdTe:In has a zero phonon line (ZPL) at 1.45 eV which is almost identical to the copper related PL whereas the chlorine A-centre in CdTe:Cl has a ZPL at 1.475 eV.

Cl plays a multiple role in group II-VI tellurides. Single substitutional Cl acts as a donor. Chlorine A-centre is a shallow acceptor. Chlorine fluxes are widely used for recrystallization of the polycrystalline layers and synthesizing of solid solutions from the mixed powders. $CdCl_2$ treatment improves the junction characteristics of the CdS/CdTe solar cells [16].

From the above reviewed papers we can conclude that there can exist at least one up to now unidentified shallow acceptor in ZnTe and CdTe and that the role of Cl and Cu in ZnTe and CdTe are yet under discussion. The purpose of this work is to investigate which effect interstitial tellurium has upon the electronic properties of ZnTe and CdTe. We also try to clarify the role of the copper dopant in p-type CdTe:Cl.

EXPERIMENT

ZnTe, ZnSe and CdTe powders of semiconductor purity (6N-7N) as starting materials were used. A complementary vacuum treatment of the starting materials to remove oxygen

Mat. Res. Soc. Symp. Proc. Vol. 442 © 1997 Materials Research Society

compounds and excess host components was used. $ZnCl_2$, $CdCl_2$ and $CuCl_2$ were synthesized from extra pure HCl, Zn, Cd and Cu. Mixed ZnTe and ZnSe powders were heated with 5 wt% $ZnCl_2$ and Cu dopant of 0.06 at% for 5 h at 1250 K in the evacuated quartz ampoules, then cooled down to room temperature together within the tube furnace at a rate of ~1.2 $Kmin^{-1}$. Residual $ZnCl_2$ and formed excess Te were removed by the vacuum annealing at 800 K. Then annealing under Zn vapour pressure was carried through.

CdTe layers were prepared from the mixture of CdTe powder, 5 wt% $CdCl_2$ flux and bidistilled water on the chemically and thermally etched 6×6 mm quartz substrates. The thickness of the layers was about 100 μm. Some layers were doped with Cu using $CuCl_2$ solution in water. Layers were recrystallized isothermally in the evacuated quartz ampoules one hour at 870 K. Then the layers were annealed in the evacuated quartz tubes at 800 K 50 hours, with one end of the tube at 300 K. This treatment removed excess $CdCl_2$ from the layers and to some extent diminished the Cl concentration in the layers due to a Cl outdiffusion. Thermal treatment followed under the Te vapour pressure of 0.65 kPa 50 hours in the evacuated quartz tubes, in 2-zone furnace (Te source was hold at 890 K, sample temperature was 20-30 ^{0}C higher). This treatment diminished the Cl concentration in the layers also. With some layers a complementary annealing under Cd vapour pressure was carried through. After all thermal treatments the layers similarly as the powders were slowly cooled down to room temperature. Indium evaporated electrodes with the fused In balls on In layer were used which formed good ohmic contacts.

Photoluminescence (PL) spectra of the samples were measured in the quartz cryostat at 80 K using a 24 mW 441.6 nm He-Cd laser and monochromator SPM-2. A chopped signal from the PbS detector was amplified, recorded and corrected on a computer. Light resistance R_L was measured using a 100 W glow lamp. Conductivity type was determined by measuring the polarity of thermovoltage.

Condensed phases after the thermal treatment were studied using X-ray diffraction (XRD), X-ray microanalysis (XMA) and by microscopic investigations on a scanning electron microscope (SEM).

RESULTS AND DISCUSSION

When stoichiometric ZnTe or CdTe are thermally treated with Cl fluxes, always Te excess is formed. Each $ZnCl_2$ or $CdCl_2$ molecule which dissolves in ZnTe or CdTe forms one excess Te atom.In ZnTe the Te excess is some more increased in case a quartz ampoule is used. Zn reacts with quartz in the event of Cl and Te are present but not Cd at the same conditions [17]. Cl solubility in CdTe is high, up to 10^{18}-10^{19} cm^{-3} [18, 19] whereas native defects concentration at 300 K is much lower in CdTe, about $2 \cdot 10^{16}$ cm^{-3} [5, p.6, 20]. Long vacuum annealing and slow cooling enhanced also the concentration of Zn or Cd vacancies in ZnTe or CdTe, owing to a higher partial pressure of Zn or Cd. When material is cooled down to 300 K, Te precipitates and Te_i are formed, due to a small diffusion coefficient of Te. Te precipitates in annealed ZnTe and CdTe have been detected by different authors [18, 21, 22]. Te_i as one host defect which can compensate donors in CdTe is proposed by M. Tomitori et al. [23]. We supposed that if Te_i and the complex defects with Te_i caused the self-activated (SA) and Cu-Cl PL bands quenching and the 1.05 eV PL band formation, annealing under Zn vapour pressure which can decrease Te_i

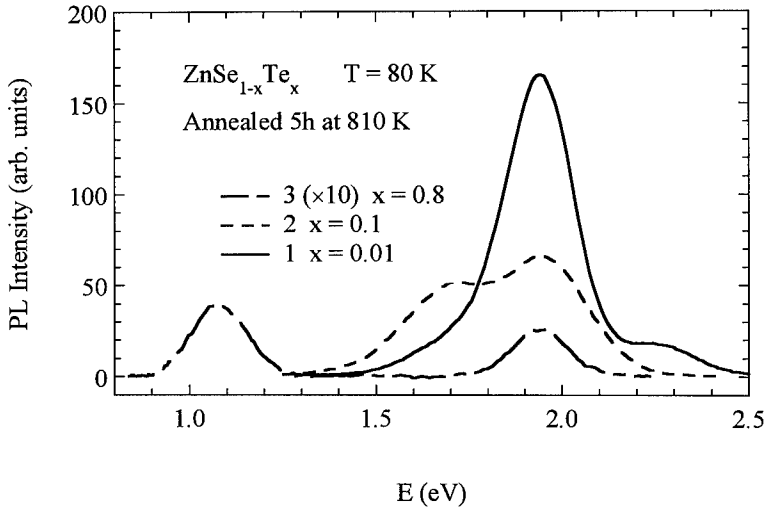


Fig. 1. *Photoluminescence spectra of $ZnSe_{1-x}Te_x$:Cl:Cu vacuum annealed 5 h at 810 K. N_{Cu}=0.06 at%. 5 wt% $ZnCl_2$.*

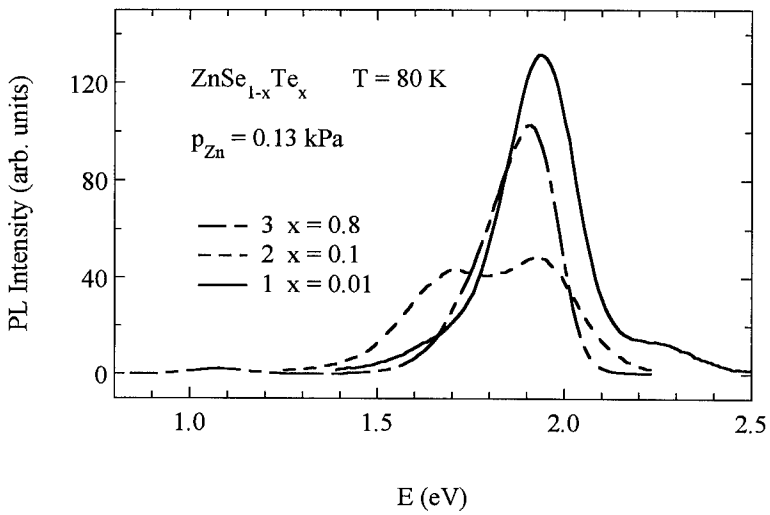


Fig. 2. *Photoluminescence spectra of $ZnSe_{1-x}Te_x$:Cl:Cu annealed 5 h under Zn vapour pressure of 0.13 kPa. N_{Cu}=0.06 at%. 5 wt% $ZnCl_2$.*

Table I. *Resistivity values of CdTe layers.**

Sample No	N_{Cu}, (at%)	p_{Te}, (kPa)	t_a, (h)	ρ, (Ω cm)	K_F	Conductivity type
1	-	0.65	-	120	1	p
2	0.02	0.65	-	160	1	p
3	0.02	0.65	24	380	1	p
4	0.2	0.65	-	1.6×10^6	2.9	p
5	0.2	0.65	24	1100	1	p

* N_{Cu} is copper concentration
p_{Te} is Te vapour pressure
t_a is annealing time under Cd vapour pressure of 1.3 kPa
ρ is resistivity
K_F is dark to light resistance ratio

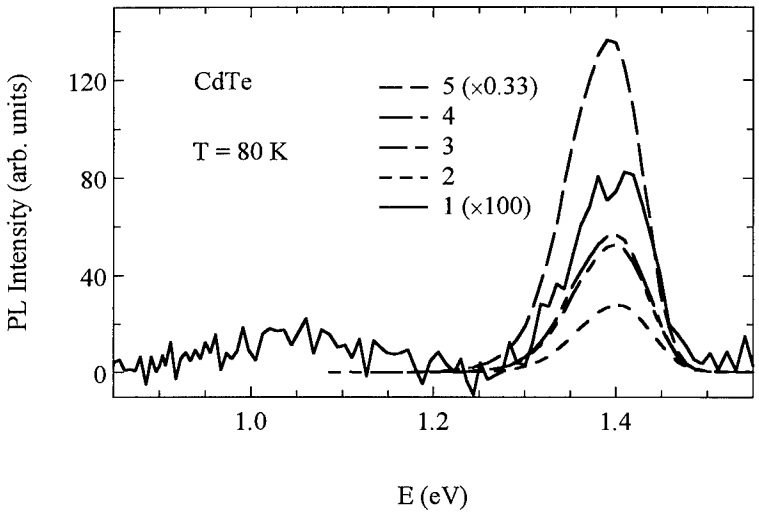


Fig. 3. *Photoluminescence spectra of CdTe layers. Curve No corresponds to the sample No in Table I.*

concentration, must decrease the 1.05 eV PL band and increase the SA and Cu-Cl PL band intensity.

Actually, the results of the carried through experiment well confirmed this assumption, as seen in Fig. 1 and Fig. 2. Vacuum annealed ZnSe-rich compounds have intense broad PL band in the visible region which consists of the SA and Cu-Cl donor-acceptor pair (DAP) parts (curve 1

and 2, Fig. 1). ZnTe-rich compound (curve 3, Fig. 1) has a weak PL band in the visible region and a new PL band near 1.05 eV which is supposed to be formed due to a defect pair V_{Te}-Te_i as the 1.1 eV PL band in CdTe [24]. Thermal treatment under Zn vapour pressure (Fig. 2) increased the intensity of the visible PL band of ZnTe-rich compound about 2 orders of magnitude and supressed the intensity of 1.05 eV PL band. Zn-treatment to some extent decreased the intensity of PL bands of ZnSe-rich compounds (curve 1 and 2, Fig. 2). We can conclude that due to a strong bond with Cl, Te_i which is a deep acceptor in ZnTe as V_{Zn}, can form complexes with Cl_{Te}. As a result the concentration of A-centres and Cl_{Te}-Cu_{Zn} pairs decreases and the intensity of SA and DAP PL bands falls down.

The results of CdTe layers on quartz substrates are shown in Table I and in Fig. 3. Sample No 1 without Cu dopant has a low p-type resistivity 120 Ω cm without photoconductivity (K_F=1) and similar to ZnTe PL spectrum where 1.4 eV PL band is weak and 1.1 eV PL exists. At higher Te vapour pressures the resistivity value of these samples can be decreased to 20-30 Ω cm and the 1.1 eV PL band intensity can be increased. Copper dopant of 0.02 at% somewhat increased the resistivity value, significantly increased the 1.4 eV PL band intensity and supressed the 1.1 eV PL band (No 2). Next annealing under Cd vapour pressure of 1,3 kPa increased the ρ value and 1.4 eV PL band intensity (sample No 3). Cu dopant of 0.2 at% (sample No 4) increased the resistivity value up to 1.6×10^6 Ω cm and photoconductivity is formed (K_F~2.9). Obviously, here Cu_i is formed which is known to be donor in CdTe [25]. Cu_i is known also as luminescence killer owing to which the PL band intensities of samples 3 and 4 are almost equal (Fig. 3). Following annealing of the sample under Cd vapour pressure decreased the ρ value to 1100 Ω cm, K_F to 1 and strongly increased the 1.4 eV PL band intensity (sample No 5). We suppose that in all these samples the Cl concentration has about the same order of magnitude as native defects (V_{Cd} and Te_i) have. It is impossible to get low p-type resistivity at high Cl concentrations (at high recrystallization temperature). Samples have then resistivity values up to 2×10^9 Ω cm and K_F up to 10^3.

Based on our experimental results we can suppose that complex defects Te_iCl_{Te} are responsible for low p-type resistivity of Cl doped CdTe and ZnTe. Te_i can play a greater role in ZnTe than in CdTe if material is termally treated in the closed isothermic space. Zn and Te partial pressures difference is smaller than that of Cd and Te one and formed Te excess is higher in the case of ZnTe. Copper dopant can decrease the concentration of V_{Cd} and Te_i in CdTe:Cl and so decrease the concentration of shallow acceptors A-centre and Te_iCl_{Te}, and as a result, increase the p-type resistivity value of CdTe:Cl. Copper impurity cannot be responsible for low p-type resistivity in Cl doped CdTe.

CONCLUSIONS

We have investigated the photoluminescence spectra of Cl doped ZnTe, Zn(SeTe) and CdTe and the formation of p-type resistivity in CdTe:Cl. We suppose that Te_i and complex defects of Te_i with chlorine can cause the quenching of the SA and DAP PL bands and low p-type resistivity in ZnTe and CdTe. Copper dopant can increase the resistivity value of p-type CdTe.

ACKNOWLEDGMENTS

This work was partly supported by the European Materials Research Society. The author is indebted to Dr. R. Triboulet from Laboratoire de Physique des Solides, Meudon, whose support initiated this investigation. The author would like to thank Dr. J. Hiie and Dr. J. Krustok for valuable discussion and help in the experiment.

REFERENCES

1. T. Asahi, O. Oda, Y. Taniguchi and A. Koyama, J. Crystal Growth **161**, 20 (1996).

2. M. Laasch, R. Schwarz, W. Joerger, C. Eiche, M. Fiederle, K.W. Benz and K. Grasza, J. Crystal Crowth **146**, 125 (1995).

3. M. Ohmori, Y. Iwase and R. Ohno, Mater. Sci. Eng. **B 16**, 283 (1993).

4. P.C. Pande, S. Bocking, S. Duke, R.W. Miles, M.J. Carter, I.D. Latimer and R. Hill, J. Crystal Growth **159**, 930 (1996).

5. K. Zanio, in *Semiconductors and Semimetals. Cadmium Telluride, Vol. 13*, edited by R.K. Willardson and A.C. Beer (Academic Press, New York, 1972).

6. B.K. Meyer and W. Stadler, J. Crystal Growth **161**, 119 (1996).

7. D.M. Hofmann, W. Stadler, K. Oettinger, B.K. Meyer, P. Omling, M. Salk, K.W. Benz, E. Weigel and G. Müller-Vogt, Mater. Sci. Eng. **B 16**, 128 (1993).

8. G.D. Watkins, J. Crystal Growth **159**, 338 (1996).

9. W. Stadler, D.M. Hofmann, A.C. Alt, T. Muschik, B.K. Meyer, E. Weigel, G. Müller-Vogt, M. Salk, E. Rupp and K.W. Benz, Phys. Rev. **B 51**, 10 619 (1995).

10. G.D. Watkins, Materials Science Forum **143-147**, 9 (1994).

11. B. Yang, Y. Ishikawa, T. Miki, Y. Doumae, T. Tomizono and M. Isshiki, J. Crystal Growth **159**, 171 (1996).

12. B.K. Meyer, W. Stadler, D.M. Hofmann, P. Omling, D. Sinerius and K.W. Benz, J. Crystal Growth **117**, 656 (1992).

13. B. Biglari, M. Samimi, M. Hage-Ali, J.M. Koebel and P. Siffert, J. Crystal Growth **89**, 428 (1988).

14. B.K. Meyer, P. Omling, E. Weigel and G. Müller-Vogt, Phys. Rev. **B 46**, 15 135 (1992).

15. W. Stadler, B.K. Meyer, D.M. Hofmann, B. Kowalski, P. Emanuelsson, P. Omling, E. Weigel, G. Müller-Vogt and R.T. Cox, Materials Science Forum **143-147**, 399 (1994).

16. H.M. Al-Allak, A.W. Brinkmann, H. Richter and D. Bonnet, J. Crystal Growth **159**, 910 (1996).

17. V. Valdna, J. Hiie, U. Kallavus, A. Mere and T. Piibe. J. Crystal Growth **161**, 177 (1996).

18. P. Höschl, R. Grill, J. Franc, P. Moravec and E. Belas, Mater. Sci. Eng. **B 16**, 215 (1993).

19. C. Eiche, W. Joerger, M. Fiederle, D. Ebling, R. Schwarz and K.W. Benz, J. Crystal Growth **146**, 98 (1995).

20. R. Krause-Rehberg, Th. Drost and A. Polity, Materials Science Forum **143-147**, 429 (1994).

21. J. Shen, D.K. Aidun, L. Regel and W.R. Wilcox, Mat. Sci. Eng. **B 16**, 182 (1993).

22. N.V. Sochinskii, E. Dieguez, U. Pal, J. Piqueras, P. Fernandez and F. Agullo-Rueda, Semicond. Sci. Technol. **10**, 870 (1995).

23. M. Tomitori, M. Kuriki and S. Hayakawa, Japan. J. Appl. Phys. **26**, 588 (1987).

24. J. Krustok, V. Valdna, K. Hjelt and H. Collan, J. Appl. Phys. **80**, 1757 (1996).

25. U. Reislöhner, N. Achtziger, M. Rüb and W. Witthuhn, J. Crystal Growth **159**, 372 (1996).

THE EFFECTS OF SUBSTITUTIONAL ALKALINE METALS IN ZINC VACANCY OF ZINCSELENIDE SINGLE CRYSTALS GROWN BY THE SUBLIMATION METHOD

Kenji Yoshino, Kouji Maeda, Atsuhiko Fukuyama*, Yoshito Akashi*, Kiyohisa Imada* and Tetsuo Ikari
Department of Electrical and Electronic Engineering, Faculty of Engineering, Miyazaki University, 1-1 Gakuen Kibanadai-nishi, Miyazaki 889-21, Japan.
*Department of Materials Science, Faculty of Engineering, Miyazaki University, 1-1 Gakuen Kibanadai-nishi, Miyazaki 889-21, Japan.
TEL : +81-895-58-2811, FAX : +81-985-58-2876, E-MAIL : yoshino@pem.cc.miyazaki-u.ac.jp

ABSTRACT

The photoluminescence measurements of alkaline metal doped zincselenide (ZnSe) single crystals were carried out to investigate how the impurity atoms substitute the intrinsic vacancy. Sample are grown by the sublimation method and the Li and Na with the concentrations of 0.1, 0.25 and 0.5 mol% were incorporated simultaneously. In the PL spectra with lower impurity concentrations, bound exciton lines of deep acceptor and donor-acceptor pair (DAP) bands were clearly observed accompanied by a weak free exciton line. Although the bound exciton lines becomes smaller with increasing the impurity concentration, the DAP band remains strong and its peak energy shift to lower energy side with the concentration. The decrease of the bound exciton lines is drastic for Li-doped sample than Na-doped sample. This indicates that Li atoms more easily occupy the Zn vacancies than Na.

INTRODUCTION

Zincselenide (ZnSe) single crystals have been widely investigated because of the essential application to luminescence devices in the blue emission region [1]. However, efficient blue laser diode and blue light emitting diode have never been available yet in ZnSe compound semiconductor. One of the reasons is that the p-type ZnSe single crystals are very difficult to grow by reason of the presence of the self-compensation and intrinsic defects in the crystals [2]. Actual p-type ZnSe single crystals have been obtained only from the nitrogen doped ZnSe grown by molecular beam epitaxy [3]. It is known that the alkaline metals substituted in Zn site act as acceptor type impurities in ZnSe crystals. In our previous paper, we confirmed that the alkaline metals (Li, Na, K, Rb and Cs) act as acceptors in the ZnSe single crystals by the photoluminescence (PL) measurement. The activation energy was found to increase with the decrease of the atomic number of the dopant [4].

In the present work, Li and Na with the concentrations of 0.1, 0.25 and 0.5 mol% were successively doped to the ZnSe single crystals by the self-closed growth method which is a sort of the sublimation method. These samples were examined by means of the PL measurement at 4.2 K. The effects of substitutional alkaline metals in Zn vacancy in the ZnSe single crystals are discussed.

Mat. Res. Soc. Symp. Proc. Vol. 442 © 1997 Materials Research Society

EXPERIMENTAL PROCEDURE

ZnSe single crystals doped with LiCl and NaCl were grown by the sublimation method at 1250 ℃ for 48 hours in a stream of argon gas at a flow rate of 0.1 *l* / min. The doping fraction of Li and Na are 0.1, 0.25 and 0.5 mol%. During the crystal growth, the temperature of the opened side of the ampoule was maintained at 1250 ℃ and that of the closed side was maintained at 1050 ℃. This temperature gradient of about 200 ℃ was found to be the optimum condition for the growth of large crystal ingots. The average size of the obtained ingots was about 0.5 cm^3. The PL spectra were measured at 4.2 K immersing the crystals directly in liquid helium in the glass cryostat. The PL spectra excited by ultra-violet light from a Hg lamp (365 nm) were obtained with a monochromator (HR-640 produced by JOVIN YVON instruments) and a photomultiplier (R2368 produced by Hamamatsu Television Co. Ltd.).

RESULTS AND DISCUSSIONS

The PL spectra of Li-doped ZnSe with three different Li concentrations are shown in fig. 1. In the PL spectrum of 0.1 mol% doped sample, bound exciton emission lines of the donor (I_2), the shallow acceptor (I_1^{Li}) and the deep acceptor (I_1^{deep}) with longitudinal optical (LO) phonon replica are clearly observed. Very weak free exciton (FE) line is also observed. Donor-acceptor pair (DAP) emission bands with LO phonon replica are clearly observed. These DAP bands are reported to be due to the recombination between Li_{Zn} (substitutional Li in Zn site) and Cl_{Se} [3]. It is known that the I_1^{deep} line is due to a bound exciton line of the Zn Vacancy (V_{Zn}) [4].

In the PL spectrum of 0.25 mol% doped sample, the I_2, I_1^{Li} lines and the DAP bands with LO phonon replicas are observed. However, the FE and I_1^{deep} lines disappeared. This is understood by considering that Zn vacancies (V_{Zn}) are substituted by Li atoms with the increase of Li atoms. In the PL spectrum of 0.5 mol% doped sample, I_2 and I_1^{Li} lines are completely disappeared but the DAP bands with LO phonon replicas are observed. The halfwidths of these band become large. This is due to that Cl donors and Li acceptor impurities increase in the crystal with increasing of the Li concentration, since Li and Cl atoms were doped at the same time.

PL spectra of Na-doped ZnSe with various Na concentration are shown in fig. 2. In the PL spectrum of 0.1 mol% doped sample, the I_2, I_1^{Na} (bound exciton emission line of Na acceptor) and I_1^{deep} lines, and the DAP bands with LO phonon replica are clearly observed. Weak free exciton (FE) line is also observed as in the case for Li-doped ZnSe with the concentration of 0.1 mol% shown in fig. 1. Additional free to Na-acceptor (FA) emission bands with LO phonon replica are clearly observed in the present sample. Since the decrease of the intensity of I_1^{deep} line is not so drastic compared with that for Li-doped sample, the occupation of the Zn vacancy by Na atoms is more difficult than that of Li atoms.

Similar results for the PL spectrum of K-doped ZnSe with concentration of 0.25 mol% are observed in the previous paper [4]. The I_2, I_1^K (bound exciton emission line of K acceptor) and I_1^{deep} line and the FA line and DAP bands with LO phonon replica are clearly observed. Since we could not obtained K-doped sample with different impurity concentrations, the detailed discussions could not be carried out yet.

Since the I_1^{deep} line and DAP band are due to Zn vacancy (V_{Zn}) and the pair of Cl_{Se} -alkaline atoms in Zn site, respectively, it is interesting to plot the intensity ratio of I_1^{deep} line / DAP emission bands as a function of the doping concentration. The results are shown in fig. 3. In the Li- and Na-doped ZnSe, the intensity ratio decreases with increasing the doping concentration.

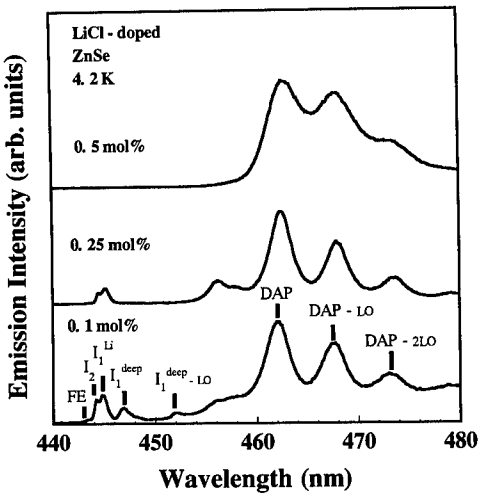


Fig. 1 Photoluminescence spectra of Li-doped ZnSe single crystals with Li concentrations of 0.1, 0.25 and 0.5 mol%.

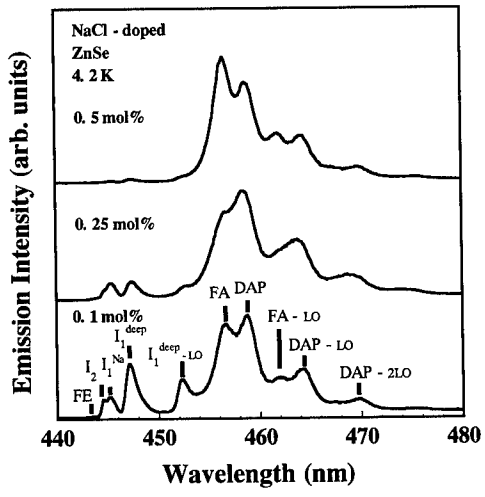


Fig. 2 Photoluminescence spectra of Na-doped ZnSe single crystals with Na concentrations of 0.1, 0.25 and 0.5 mol%.

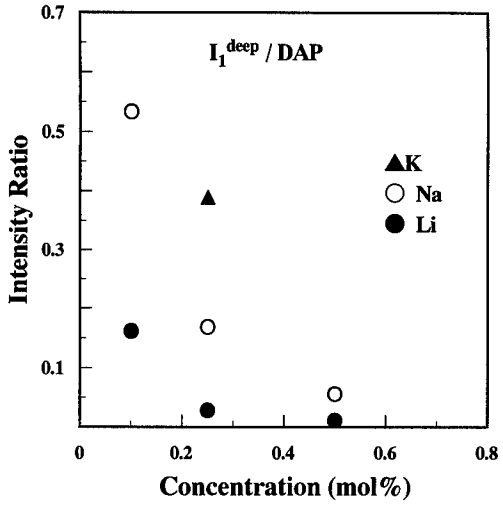


Fig. 3 The peak energies of DAP emission bands as a function of doping concentration in Li- and Na-doped ZnSe single crystals .

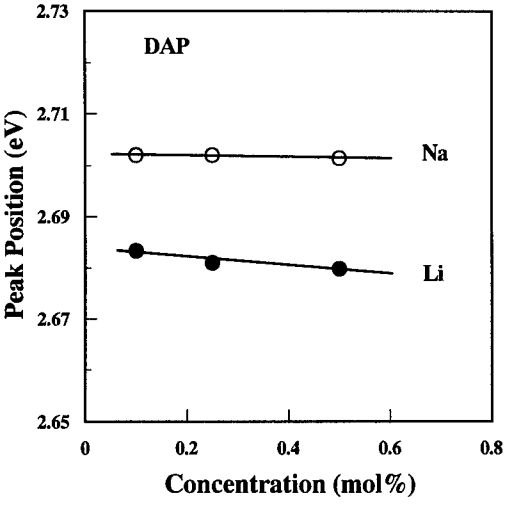


Fig. 4 The intensity ratio of I_1^{deep} line / DAP emission bands as a function of doping concentration in Li- and Na-doped ZnSe single crystals .

The intensity of the DAP bands becomes larger than that of the I_1^{deep} line. A decrease of the intensity ratio of Na-doped ZnSe is more drastic than that of Li-doped ZnSe. This indicates that Li atoms can easily substitute the Zn site in comparison with Na atoms. It is considered that alkaline atoms with larger ionic radii is more difficult to substitute or occupy the Zn site.

The peak energies of the DAP emission bands as a function of the doping concentration in Li- and Na-doped ZnSe single crystals are shown in fig. 4. In the Na-doped ZnSe, the peak positions of DAP band is almost constant with doping Na concentration from 0.1 to 0.5 mol%. On the other hand, in the Li-doped ZnSe, the peak positions of DAP band decrease with doping Li concentration from 0.1 to 0.5 mol%. One possible reasons is that the binding energy of acceptor (E_A) and/or donor (E_D) changes with the impurity concentration. Zhu *et al.* reported that E_D of N-associated donor increases with N concentration by means of temperature dependence of PL spectra [6]. The another possibility arises from the fact that the distance between the constituent donor and acceptor of DAP decreases with the increase of the concentration of the impurities. This may lead to the decrease of the peak energy of DAP. However, we do not have enough data for explaining these results. More detailed discussions are in progress.

CONCLUSIONS

The doping effect of the Li and Na with various concentrations on the photoluminescence spectra are investigated for the ZnSe single crystals grown by the sublimation method. The main results obtained are as follows: (1) The Zn vacancies are easy to be substituted by Li atoms in comparison with Na atoms. It is considered that alkaline atoms with larger ionic radii is more difficult to substitute or occupy the Zn site. (2) The peak energy of the DAP bands shift to lower energy side with increasing the impurity concentrations. This may be understood by supposing that acceptor and/or donor binding energies increase with increasing the impurity concentrations.

ACKNOWLEDGMENTS

The authors would like to express our sincere thanks to Mr. H. Yokoyama, M. Kawahara and D. Maruoka for their experimental assistances and useful discussions.

REFERENCES

[1] K. Yoshino, Jpn. J. Appl. Phys. **34**, 6331 (1995).
[2] G. F. Neumark, J. Appl. Phys. **51**, 3383 (1980).
[3] K. Ohkawa, A. Ueno and T. Mitsuyu, J. Cryst. Growth **117**, 375 (1992).
[4] K. Yoshino, Y. Matsushima and M. Hiramatsu, Jpn. J. Appl. Phys. **34**, 61 (1995).
[5] M. Ohishi, Jpn. J. Appl. Phys. **25**, 1546 (1986).
[6] Z. Zhu, K. Takebayashi, K. Tanaka, T. Ebisutani, J. Kawamata and T. Yao, Appl. Phys. Lett. **64**, 91 (1994).

SURFACE OF Li-DOPED ZnSe GROWN ON MISORIENTED GaAs(001) SUBSTRATES

Minoru Yoneta, Masakazu Ohishi, Hiroshi Saito, Mitsuhiro Ohura, Katsumoto Fujii and Yoshihiko Hioe
Department of Applied Physics, Okayama University of Science,
Ridai-cho 1-1, Okayama 700, Japan

ABSTRACT

The surface of Li-doped ZnSe grown on misoriented GaAs(001) substrates by molecular beam epitaxy is studied by means of reflection high energy electron diffraction. Sharp and curved streaky RHEED patterns are observed for all the layers grown on the misoriented substrate towards [$\bar{1}$10], irrespective of off-angles. No curved pattern, however, is observed on ZnSe layers grown on misoriented GaAs(001) towards [110] with off-angle larger than 5°. We confirmed that the Li-array is surely formed along [110], and that the length of the Li-array is longer than 32Å to be observable as curved streaks. It is also confirmed that the growth rate of Li-doped ZnSe is proportional to the step density, and that the growth rate on the misoriented substrate towards [110] is higher than that on the misoriented substrate towards [$\bar{1}$10]. The photoluminescence spectra of Li-doped ZnSe layers grown on misoriented GaAs are reported.

INTRODUCTION

In the last few years, considerable progress has been made in preparing p-type ZnSe and related materials, particularly with regard to make use of nitrogen plasma [1-2]. Until now, blue and green lasers at room temperature are successfully fabricated [3]. However, the p-type doping level needs to be further improved in MBE-grown materials, since nobody has succeeded in growing highly doped p-type ZnSe with hole concentrations above several 10^{18} cm^{-3}.

Among alkali-metal acceptors in II-VI compounds, Li is easily supplied from a conventional effuser cell. So far, we have reported that the RHEED pattern of ZnSe/GaAs(001) grown under Li beam exposure shows sharp and curved streaks, which is attributed to the one-dimensional (1D) Li-array selectively adsorbed along B-steps on the surface terraces [4]. We studied the epitaxial growth of Li-doped ZnSe on a misoriented GaAs(001) surface to confirm that the 1D Li-array is surely formed along [110]. In this paper, the RHEED pattern of Li-doped ZnSe grown on misoriented GaAs(001), the misorientation dependence of growth rate, and the photoluminescence property of the grown layer are reported.

EXPERIMENTAL PROCEDURE

ZnSe layers were grown by using molecular beams effused from a cracking cell on semi-insulating GaAs(001) substrates. We call the epitaxial growth using molecular beams effused from cracking cell as post-heated molecular beam epitaxy (PH-MBE). The temperatures of the cracker region are kept at 600°C for both Zn- and Se-cells. The misorientation directions of the substrate are [110] and [$\bar{1}$10], and the off-angles are 2°, 5°, 10° and 15°, which correspond to terrace length of 10.2Å, 16.0Å, 32.3Å and 78.1Å, respectively.

Prior to MBE growth, the GaAs wafers were chemically etched in the conventional sulfuric acid solution, and were rinsed with deionized water and dried with N_2 gas blow before mounting onto a Mo block. The substrates were thermally cleaned at a typical temperature of 600°C for 10min. Typical molecular beam pressures P_{Zn} and P_{Se}, which are merely measured by an ion gauge at the substrate position, are 3.6×10^{-7} and 1.8×10^{-6} Torr, respectively. The dopant Li beam is supplied from a conventional effusion cell using elemental Li. The epitaxial growth was monitored by reflection high energy electron diffraction (RHEED).

Mat. Res. Soc. Symp. Proc. Vol. 442 © 1997 Materials Research Society

RESULTS AND DISCUSSION

RHEED patterns of a Li-doped ZnSe surface grown on GaAs substrates observed from [010] direction are depicted in Fig.1. All the layers grown on misoriented GaAs(001) towards [$\bar{1}$10] show the sharp and curved streaks, irrespective of off angles (Fig.1a). These patterns are the same as those observed from ZnSe layer grown on conventional GaAs(001) substrates. The RHEED pattern observed from [110] are long and sharp streaks, and that from [$\bar{1}$10] are short streaks, though as not shown in the Fig.1. The RHEED pattern of ZnSe surface grown on misoriented GaAs (001) towards [110] depends on off-angle, ie, no curved streak is observed on the substrate with off-angle above 10°, and the curved streak is observed for off-angle below 5° as shown in Fig 1b. Since the maximum length of 1D Li-array is restricted by terrace length,

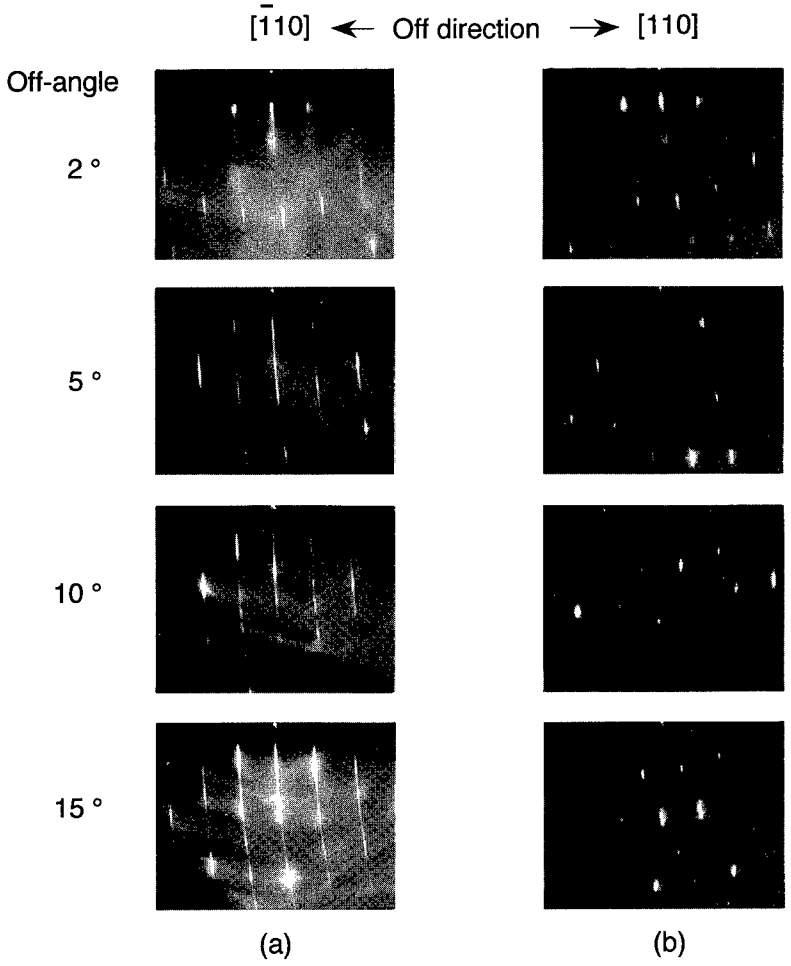


Fig. 1 RHEED patterns of Li-doped ZnSe layers grown on the misorientated GaAs(001) with an off-angle towards (a) [$\bar{1}$10] and (b) [110]. The electron beam azimuth is [010].

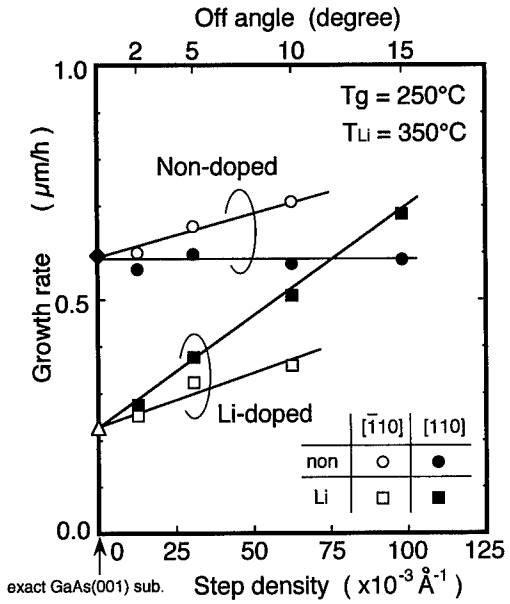


Fig.2 Growth rate of Li-doped ZnSe as a function of the step density on the misorientated GaAs(001) towards two directions of [110] and [$\bar{1}$10]. The step density is the reciprocal of calculated terrace length.

then we see the terrace length longer than 32Å is needed to observe the curved streaks. The curved streaks observed in this experiment indicate that Li-related 1D arrays are surely formed along [110] direction, irrespective of the misorientation direction of the substrate.

Fig.2 shows the growth rate of Li-doped ZnSe layers as a function of calculated step density of misoriented GaAs(001) towards [110] and [$\bar{1}$10]. The growth rate of non-doped ZnSe layer grown on the misoriented substrate under the same molecular beam condition is studied to make clear the influence of Li supply on growth rate. The step density of zero in Fig.2 means the step density on exact GaAs(001) surface. The Li beam is supplied from the effusion cell temperature of 350°C. Comparing the growth rates of non- and Li-doped ZnSe layer at the step density 0, we notice that the marked reduction in growth rate is caused by Li beam supply as reported before [4, 5].

We first discuss the dependence of the growth rate on the step density for a non-doped layer. The growth rate of non-doped ZnSe on misoriented GaAs(001) towards [110], GR (non,[110]), has almost no dependence on the step density. The growth rate of non-doped ZnSe on misoriented GaAs(001) towards [$\bar{1}$10], GR(non,[$\bar{1}$10]), however, is proportional to the step density. This result shows the layer growth from B-step is dominant and the growth from A-step is quite small in case of non-doped ZnSe grown by PH-MBE. This is consistent with the results which RHEED streak line observed from [$\bar{1}$10] is sharper than that observed from [110], suggesting the surface terrace develops towards [$\bar{1}$10] [6]. It is reported on GaAs stepped surface that Ga steps (A-step) are straight over long distance and the terrace length has large fluctuation in terrace length, whereas As-steps (B-step) has high kink density but the fluctuation in terrace length is small [7]. The high kink density along B-step can explain the step density dependence of GR(non, [$\bar{1}$10]).

On the other hand, the growth rates of Li-doped ZnSe on misoriented GaAs(001) substrates towards [110] and [$\bar{1}$10], GR(Li,[110]) and GR(Li,[$\bar{1}$10]), are proportional to step density. It is noticed that the slope of GR(Li,[110]) is larger than that of GR(Li,[$\bar{1}$10]), which is different from the undoped case. This is explained as follows. Li atoms captured by the B-step obstruct the further layer growth towards [$\bar{1}$10]. Li atoms impinged at A-step are randomly captured without forming 1D arrays, which give rise to high kink density. Thus, the layer growth towards [110] becomes possible and the growth rate has the dependence on step density.

Fig.3 shows the photoluminescence (PL) spectra of Li-doped ZnSe grown on misoriented GaAs(001) towards [110]. The emission due to the exciton bound to neutral Li acceptor (I_1) and donor-acceptor pair (DAP) band dominate the spectrum regardless of off-angles. Except for 2° off substrate, the marked difference in spectra is not found. Fig.4 shows the PL spectra of Li-doped ZnSe grown on misoriented GaAs(001) towards [$\bar{1}$10]. The intensity of free-to-acceptor (FA) emission is comparable to that of DA emission. Usually, Li doped ZnSe grown by conventional MBE presents the DAP emission only at 4.2K, and the FA emission band appears at elevated temperature around 70K. The appearance of FA emission at 4.2K indicates that Li atoms are highly incorporated as acceptors. The appearance of DAP band means the existence of shallow donors even if any donor species is supplied. The donor species responsible to present DAP is unknown at present. The dominance of FA band suggests that Li atoms are effectively incorporated into Zn sites.

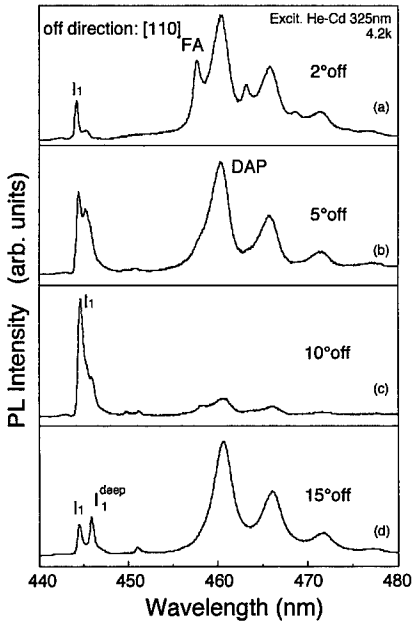


Fig.3 Photoluminescence spectra measured at 4K of Li-doped ZnSe grown on the misorientated GaAs(001) substrates towards [110] with an off-angle (a) 2°, (b) 5°, (c) 10° and (d) 15°, repectively.

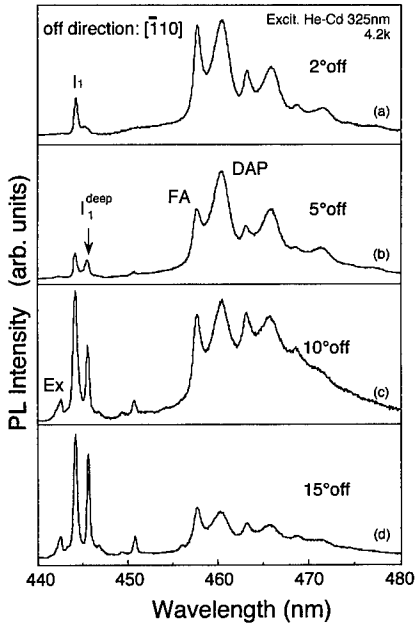


Fig.4 Photoluminescence spectra measured at 4K of Li-doped ZnSe grown on the misorientated GaAs(001) substrates towards [$\bar{1}$10] with an off-angle (a) 2°, (b) 5°, (c) 10° and (d) 15°, respectively.

CONCLUSIONS

The epitaxial growth of non-doped and Li-doped ZnSe using post-heated molecular beams on misoriented GaAs(001) surface was studied by RHEED observation and growth rate measurement. RHEED pattern observation showed the Li-related 1D array is surely formed along [110]. From the misorientation dependence of growth rates of non-doped ZnSe layers, it is found that the growth rate towards [110] is proportional to step density, but the growth rate towards [$\bar{1}$10] has almost no step density dependence. Whereas, in case of Li-doped layer, we confirmed that the layer growth towards [110] is superior to that toward [$\bar{1}$10], which shows the Li 1D array along [110] obstruct the layer growth towards [$\bar{1}$10]. From the photoluminescence measurement, it is also found that Li atoms are effectively incorporated into ZnSe when the Li-doped ZnSe layers are grown on misoriented GaAs(001) towards [110].

REFERENCES

1. R. M. Park, M. B. Troffer, C. M. Rouleau, J. M. DePuydt and M. A. Hasse, Appl. Phys. Lett. **57**, 2127 (1990).
2. J. Qiu, J. M. DePuydt, H. Cheng and M. A. Hasse, Appl. Phys. Lett. **52**, 2992 (1991).
3. R. L. Gunshor and A. V. Nurmikko, MRS Bulletin, July (1995) 15.
4. M. Ohishi, M. Yoneta, N. Ishii, M. Ohura, Y. Hiroe and H. Saito, J. Cryst. Growth. **159**, 376 (1996).
5. M. Yoneta, H. Saito, M. Ohishi, K. Kitani, H. Kobashi and C. Hatano, J. Cryst. Growth. **150**, 817 (1995).
6. M. Ohishi, H. Saito, H. Torihara, Y. Fujisaki and K. Ohmori, Jpn. J. Appl. Phys.**30**, 1647 (1991)
7. P. R. Pukite, G. S. Petrich, S. Batra and P. I. Cohen, J. Crystal Growth **95**, 267 (1989)

INVESTIGATION OF DEEP ENERGY LEVELS IN II-VI COMPOUNDS

A.CASTALDINI, A.CAVALLINI, P.FERNANDEZ*, B.FRABONI and J.PIQUERAS*
INFM and Department of Physics, University of Bologna, Bologna, Italy
* Departamento de Fisica de Materiales, Facultad de Ciencias Fisicas, Universidad Complutense, 28040 Madrid, Spain

ABSTRACT

Deep levels in II-VI compounds have been investigated to understand their role in the compensation mechanism and their influence on the material electrical and optical properties. The electrical properties have been studied by current and capacitance transient spectroscopy, while the optical properties have been studied by cathodoluminescence. We have focused our attention on the traps involved in the compensation process, such as centre A and the deep levels located near midgap.

INTRODUCTION

Cadmium telluride (CdTe) has long been known as a suitable material for nuclear radiation detector and electro-optic devices. The combination of a high average atomic number, good mobility-lifetime product and large band gap, enables an efficient charge collection for γ- and X-rays. The most important requirement is the high resistivity of the material.Semi-insulating CdTe can be obtained by growing impurity free stoichiometric crystals or, more easily, by growing the material from a Te-rich phase and introducing during the growth group III or VII donors. The highest resistivities have been obtained with Cl (up to $\rho>10^9\Omega$cm) [1]. The dopants thus introduced act as shallow donors and the formation of compensating defects has to be considered to explain the observed high resistivities. The main problem for the technical application of II-VI compounds is the control of the electrical properties which depend on the nature and distribution of the related point defects which are formed by reactions between intrinsic defects and impurities during and after the growth. During growth under Te-rich conditions a high concentration of Cd vacancies (V_{Cd}) acting as native acceptors is generated. Some of the vacancies are compensated by the intentionally introduced shallow donors, thus forming V_{Cd}-donor complexes of the type generally called centre A [2,3]. However, the existence of such A center in CdTe:Cl has been experimentally proved only recently with optical investigations [2], and its electrical role remains still unclear. As the energy level of A centre in the forbidden gap is quite shallow ($\approx$0.15eV), it has been suggested that it cannot be the sole responsible for the semi-insulating behaviour of CdTe:Cl [2,3]. The pinning of the Fermi level near midgap, observed in highly resistive II-VI compensated materials, could be explained by assuming the existence of a deep donor level located at approximately $\approx$0.8eV. Various experimental techniques have been developed to study deep levels in semiconducting materials. We have used the DLTS (Deep Level Transient Spectroscopy) technique, one of the most convenient and powerful methods for the detection and characterisation of deep levels [4]. In order to study semi-insulating materials we have utilized PICTS (Photo-Induced Current Transient Spectroscopy) [4,5] and P-DLTS (Photo-DLTS) [6], two particularly interesting techniques developed and based on the same approach as DLTS. They allow the determination of deep trap parameters (activation energy and capture cross section) in high resistivity materials with good resolution, even though the data interpretation is more complex than in DLTS. As optical characterization technique we have employed cathodoluminescence (CL) to investigate recombination processes at deep levels in semi-insulating (SI) materials and to complement the electrical transient spectroscopy methods.

Luminescence investigations carried out on II-VI compounds provide evidence for the existence

Mat. Res. Soc. Symp. Proc. Vol. 442 © 1997 Materials Research Society

of an emission band centered at approximately 1.4eV, independently of the material doping and growth method [2,3,7,8]. Junction spectroscopy methods, such as thermally stimulated current (TSC) and photo-induced current transient spectroscopy (PICTS), have also revealed single deep energy levels scattered around E_V+0.15eV [1,9,10], which is the complementary transition of the 1.4eV in CdTe, its band gap being Eg=1.54eV at room temperature [11]. We have resolved, in our samples, three different levels located at this energy. The exact structure of the complex 1.4eV luminescence band is still under discussion, as are its nature and origin. This implies that there might be other native defects/complexes, extended defects or residual impurities which either emit in the spectral range 1.3-1.5eV or form complexes with the available V_{Cd}. Therefore, the 1.4eV band might not be necessarily related to an actual A-center [3,7,12].

We have studied the various components of the 1.4eV band in order to understand which ones could be reliably attributed to A-center and a comparison of the results obtained with the different and complementary spectroscopies used allowed us to determine the character of each deep trap (either donor or acceptor).Moreover, we have investigated the deep traps located near midgap, in order to study their role in the pinning of the Fermi level and to provide a deeper insight on the compensation process in CdTe based II-VI compounds.

EXPERIMENTAL

We have investigated both semiconducting and semi-insulating II-VI compounds, all p-type: CdTe undoped (ρ=30Ωcm), CdTe:Cl ($\rho>10^8\Omega$cm) and $Cd_{0.8}Zn_{0.2}Te$ ($\rho=10^{11}\Omega$cm). The CdTe:Cl and CdTe undoped samples were grown by the travelling heater method (THM) while the $Cd_{0.8}Zn_{0.2}Te$ ones were grown by the high pressure Bridgman (HPB) method. Some CdTe:Cl samples have been annealed at T=600°C for t=5h in an Ar atmosphere, to study the evolution with temperature of the defective states. While CdTe:Cl is made semi-insulating by the presence of Cl via a compensation process, $Cd_{0.8}Zn_{0.2}Te$ is intrinsically highly resistive, as Zn occupies Cd site and decreases the V_{Cd} concentration. We have utilized CL and three different junction spectroscopy methods: DLTS, PICTS and P-DLTS. While DLTS analyzes capacitance transients and can only be applied to semiconducting materials, PICTS and P-DLTS, which study current transients generated by optical excitation, can be used for the investigation of semi-insulating samples. These last two methods are complementary as PICTS reveals both majority and minority carrier traps without being able to distinguish between them, and P-DLTS reveals only majority carrier traps. Thus, a direct comparison between the PICTS and the P-DLTS spectra in the same SI sample can provide indication on the donor or acceptor character of the deep levels. Schottky diodes have been prepared by evaporating Al or In, while the ohmic contacts have been obtained by electroless Au deposition. Junction spectroscopy analyses have been carried out with a SULA Tech. system. The DLTS method has been applied to CdTe undoped samples while PICTS and P-DLTS analyses have been utilized to study CdTe:Cl and $Cd_{0.8}Zn_{0.2}Te$. The excitation wavelength utilized was λ=880nm and the applied bias was V=30V. The heating rate was 0.2K/sec and the emission rates varied from 5 to 2×10^4 s^{-1}. CL analyses have been performed in an Hitachi S-2500 scanning electron microscope at a temperature of 80K, with an accelerating voltage of 25keV. Luminescence emission was measured with a North Coast E0-817 germanium detector. Spectra are recorded under different focusing conditions of the electron beam on the sample, to account for the radiative centres with low concentration. Usually by defocusing the intensity of the deep band increases.

RESULTS

The results of the CL investigations are summarized in figure 1. The spectra are obtained under defocusing conditions and the 1.4eV band is clearly visible in all CdTe samples. The band in the $Cd_{0.8}Zn_{0.2}Te$ spectrum is shifted to approximately 1.5eV, which arises from the fact that the band gap of $Cd_{0.8}Zn_{0.2}Te$ ($E_g \approx 1.65$eV) is larger than the band gap of CdTe ($E_g \approx 1.54$eV) [11].

The junction spectroscopy methods utilised in this work revealed in the CdTe:Cl material three different peaks in the region corresponding to the 1.3-1.5eV emission range. A comparison of PICTS spectra from these three different materials is reported in figure 2. The three peaks observed in the region of interest, i.e. the low temperature region of the spectrum, have been named A_0, A and A_1. Their activation energies are 0.12, 0.14, 0.16 eV and their apparent capture cross section 2×10^{-16}, 1×10^{-16} and 4×10^{-17} cm^2, respectively. These peaks are labelled with the same letters for all samples as they actually correspond to the same deep levels. This has been verified by comparing the Arrhenius plot of each level, which is usually considered the "fingerprint" of the trap. As the three peaks are also present in the corresponding P-DLTS spectrum, i.e. obtained in identical experimental conditions, we can conclude that they are all majority carrier (hole) traps (figure 3).

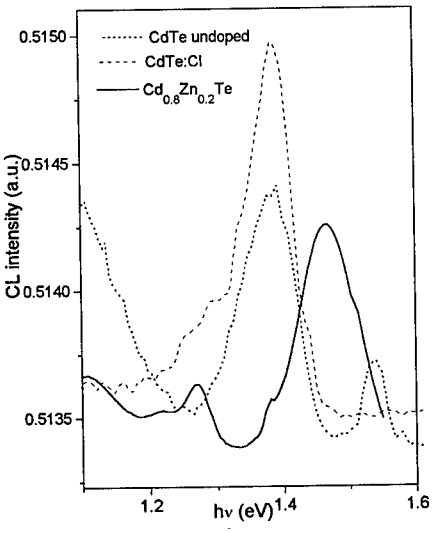


Fig.1: CL spectra of CdTe:Cl, undoped CdTe and $Cd_{0.8}Zn_{0.2}Te$

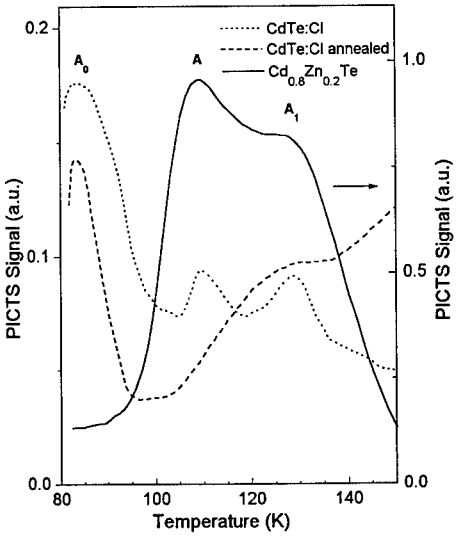


Fig.2: PICTS spectra for CdTe:Cl, CdTe:Cl annealed and $Cd_{0.8}Zn_{0.2}Te$

After the annealing treatment of CdTe:Cl, peak A disappears. In $Cd_{0.8}Zn_{0.2}Te$ samples only two peaks are present: peak A and A_1. The DLTS results of the undoped CdTe samples have not been included in figure 2 together with the other PICTS measurements as they derive from capacitance transients and the determination of the emission rate is different in the current (PICTS, P-DLTS) and capacitance case (DLTS) [5]. In order to reliably compare the activation energy and the capture cross section of the levels in undoped CdTe to those in CdTe:Cl and $Cd_{0.8}Zn_{0.2}Te$, we have also performed some P-DLTS analyses at low temperature. Both DLTS and P-DLTS revealed the presence of

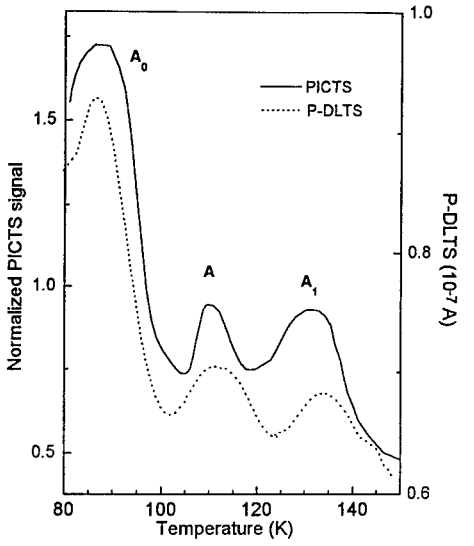


Fig.3: PICTS (soild line) and P-DLTS (dotted line) spectra of CdTe:Cl.

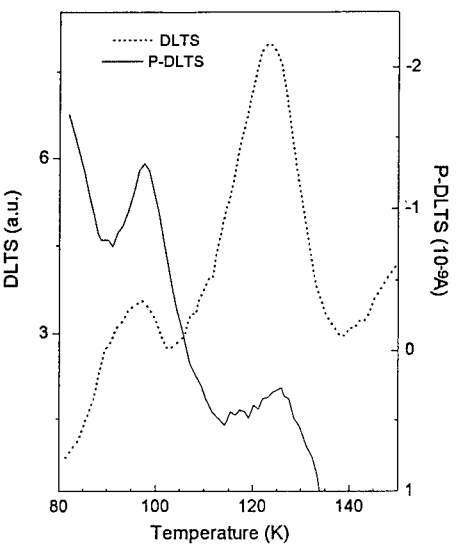


Fig.4: DLTS (solid line) and P-DLTS (dotted ine) spectra of CdTe undoped

a peak in the 0.12-0.18eV energy range and by comparing these results to those relative to CdTe:Cl and $Cd_{0.8}Zn_{0.2}Te$, the peak resulted to correspond to level A (figure 4). Table I summarises the results obtained for the levels related to centre A.

Table I: Crosses indicate the levels observed in the various materials investigated

	CdTe:Cl	CdTe:Cl annealed	CdTe undoped	$Cd_{0.8}Zn_{0.2}Te$
A_0	X	X		
A	X		X	X
A_1	X	X		X

We have then focused our attention on the deep traps located near midgap, whose peaks appear in the high temperature region of PICTS and P-DLTS spectra, arising from complexes involved in the compensation process. The high temperature region of a PICTS spectrum obtained from a CdTe:Cl sample (solid line) exhibits two peaks, labelled H and E, with an activation energy of 0.76 and 0.79eV respectively. Their apparent cross sections, calculated from the Arrhenius plot, are 6×10^{-13} and 4×10^{-14} cm^2. These traps are the dominant deep levels, but their concentration can be only qualitatively deduced from a comparison with the amplitudes of the other peaks in the spectrum, as the determination of trap concentration from PICTS measurements is quite difficult [13]. The PICTS

spectrum of the CdTe:Cl samples after the annealing treatment still clearly shows both peaks H and E. The corresponding CdTe:Cl P-DLTS spectrum indicates that only level H is a hole trap, while level E is a deep donor.

DISCUSSION AND CONCLUSIONS

The junction spectroscopy mesurements (PICTS, P-DLTS and DLTS) carried out in the low temperature region allow to resolve three possible components of the 1.4eV luminescence band observed in CL which correspond to peaks A_0, A and A_1 observed in PICTS and PDLTS spectra. The acceptor nature of the traps has been inferred from the comparison of PICTS and P-DLTS spectra obtained from a CdTe:Cl sample in identical experimental conditions: the peaks that are present in the P-DLTS spectrum correspond to majority carrier traps, i.e. acceptor traps being all materials p-type.

Most levels are found, with identical Arrhenius plots, in more than one investigated material.The activation energies of the deep levels in $Cd_{0.8}Zn_{0.2}Te$, which has a larger band gap than CdTe, are the same as in CdTe despite the fact that the luminescence band of interest is shifted to higher energies (1.5eV); this can be explained if one considers that the change in the band gap from CdTe to $Cd_{0.8}Zn_{0.2}Te$ affects mainly the conduction band which shifts up in energy while the valence band remains in the same position as in CdTe [14]. As the deep levels A_0, A and A_1 are acceptor traps, their energy levels are measured from the valence band and, therefore, remain constant in all investigated materials.

In order to obtain some information on the origin of the revealed traps, we have compared the results obtained from the different materials analysed. As can be observed in Table I, the shallowest level, A_0, is only present in Cl doped CdTe samples and this suggests how its origin is related to the presence of Cl. Therefore, it can be assigned to the (V_{Cd}-Cl_{Te}) complex, the actual chlorine centre A [2].

The other two levels, A and A_1, are present in $Cd_{0.8}Zn_{0.2}Te$ which is not intentionally doped. These levels, recently observed in photoluminescence investigations of undoped CdZnTe [7], could be related to complexes involving a V_{Cd} and a V_{Te}, respectively, as similar peaks have been observed to move or to disappear after annealing treatments [7], as occurs for level A in CdTe:Cl annealed samples. Other experimental results suggest an attribution to residual impurities, such as Cu or Li, which may form complexes with native defects, showing different properties than the Cl centre A [2,3,15].

The level H, present in the high temperature region of PICTS spectra of CdTe:Cl, is a deep trap that has been observed in the past in semiconducting and semi-insulating II-VI compounds by luminescence [2,8] and electrical [1,16] characterization methods. It has been widely attributed to a complex related to a V_{Cd}^- and an impurity, which seems to be a recombination centre, i.e. a trap both for electrons and holes [16]. Such deep trap cannot be responsible for the semi-insulating behaviour of CdTe:Cl, as it is also present in semiconducting materials. The deep level E and its donor character, on the other hand, have never been to our knowledge assessed before, and it could play a major role in the pinning of the Fermi level and in the compensation process of CdTe:Cl .

ACKNOWLEDGEMENTS

This research has been partially supported by the Cooperation Programme "Azione Integrata" between Italy and Spain and by DGICYT (Project PB 93 - 1256). The authors are indebted to Prof.

F.Casali for the $Cd_{0.8}Zn_{0.2}Te$ samples and to Japan Energy Corporation for the undoped and Cl doped samples.

REFERENCES

[1] M.Fiederle, D.Ebling, C.Eiche, D.M.Hofmann, M.Salk, W.Stadler, K.W.Benz and B.K.Meyer, J.Crystal Growth **138**, 529 (1994)
[2] D.M.Hofmann, D.Omling, H.G.Grimmeiss, B.K.Meyer, K.W.Benz and D.Sinerius, Phys.Rev.B **45**, 6247 (1992)
[3] W.Stadler, D.M.Hoffman, H.C.Alt, T.Muschik, B.K.Meyer, E.Weigel, G.Müller-Vogt, M.Salk, E.Rupp and K.W.Benz, Phys.Rev.B **51**, 10619 (1995)
[4] P.Blood and J.W.Orton, The Electrical Characterization of Semiconductors: Majority Carriers and Electron States, (Academic Press, U.K., 1992).
[5] O.Yoshie, M.Kamihara, Jpn.J.Appl.Phys. **22** 629 (1983).
[6] Mooney P.M. J.Appl.Phys. **54**, 208 (1983).
[7] C.Barnett Davis, D.D.Allred, A.Reyes-Mena, J.Gonzalez-Hernandez, O.Gonzales, B.C.Hess and W.P.Allred, Phys.Rev.B **47**, 13363 (1993)
[8] U.Pal, P.Fernandez, J.Piqueras, N.V.Sochinskii and E.Dieguez, J.Appl.Phys. **78**, 1992 (1995)
[9] C.Eiche, D.Maier, D.Sinerius, J.Weese, K.W.Benz and J.Honerkamp, J.Appl.Phys. **74**, 6667 (1993)
[10] J.P.Zielinger, M.Tapiero, Z.Guellil, G.Roosen, P.Delaye, J.C.Launay and W.Mazoyer, Mat.Sci.Eng. **B16**, 273 (1993)
[11] E.Lopez-Cruz, J.Gonzalez-Hernandez, D.D.Allred and W.P.Allred J.Vac.Sci.Technol. **A8**, 1934 (1990)
[12] M.Samimi, B.Biglari, M.Hage-Ali, J.M.Koebel and P.Siffert, Phys.Stat.Sol.(a) **100**, 251 (1987)
[13] M.Tapiero, N.Benjelloun, J.P.Zielinger, S.El Hamd, and C.Noguet J.Appl.Phys. **64** 4006 (1988).
[14] D.M.Hofmann, W.Stadler, K.Oettinger, B.K.Meyer, P.Omling, M.Salk, K.W.Benz, E.Weigel and G.Müller-Vogt, Mat.Sci.Eng. **B16**, 128 (1993)
[15] J.W.Allen, Semicond.Sci.Technol. **10**, 1049 (1995)
[16] T.Takebe, J.Saraie and H.Matsunami J.Appl.Phys. **53**, 457 (1982).

NONDESTRUCTIVE CHARACTERIZATION OF THE SURFACE AGING OF HgI_2 CRYSTAL

H. YAO*, J.C. ERICKSON*, R.B. JAMES**, M. NATARAJAN***
*University of Nebraska, Center for Microelectronic and Optical Materials Research, and Department of Electrical Engineering, Lincoln, NE 68588-0511, hyao@unl.edu
**Sandia National Laboratories, Livermore, CA 94551
***TN Technologies, Round Rock, TX 78680

ABSTRACT

Variable angle spectroscopic ellipsometry (VASE) and atomic force microscopy (AFM) measurements have been employed to characterize the surface aging of HgI_2 crystals. A surface model including top surface roughness and subsurface defects was established and studied by VASE analysis, as a function of real time, after the 10% KI chemical etching. In this model, the surface defects associated with the surface aging were modeled by the Bruggeman effective-medium approximation (EMA) as a HgI_2/voids mixed layer. The relative 2-dimensional (2D) surface-defect-densities were monitored as the surface aging proceeds. The VASE measurements indicated that high surface aging rates were related to high initial effective 2D surface-defect densities. The AFM profile revealed increasing physical surface roughness as surface aging took place. The cleaved HgI_2 crystal surface presented a smooth surface and the lowest surface aging rate, while the as-grown HgI_2 surface also presented a very low surface aging. The HgI_2 surfaces baked at elevated temperatures presented accelerated surface aging phenomena after a 30 min. baking.

INTRODUCTION

Crystal mercuric iodide (HgI_2) is an important technological material for room-temperature X-ray and nuclear detectors [1-5]. It is a well-known fact that the bare surface of a HgI_2 crystal will be aging in air. The origin of surface aging is still under study [6-8]. It has been suggested that the surface aging is related with the deviation from stoichiometry of HgI_2 by losing I_2 from the crystal surface, due to its higher vapor pressure [7]. In this paper, we report, results of surface aging studies of several different HgI_2 surface conditions characterized by variable angle spectroscopic ellipsometry (VASE) and atomic force microscopy (AFM) measurements.

EXPERIMENTAL BACKGROUND

The spectroscopic ellipsometry (SE) is a surface-sensitive, nondestructive optical technique used to characterize surface changes, overlayer thicknesses, multilayer structures, optical constants of bulk materials, and surface or interface roughness [9,10]. Ellipsometry determines the complex reflectance ratio r_p to r_s from the sample, where r_p and r_s are the reflectance coefficients of light polarized parallel to (p) or perpendicular to (s) the plane of incidence. The ratio is defined as:

Mat. Res. Soc. Symp. Proc. Vol. 442 © 1997 Materials Research Society

$$\rho = r_p / r_s = \tan(\psi) e^{i\Delta}, \quad (1)$$

where the values of $\tan(\psi)$ and Δ are the amplitude and projected phase of the complex reflectance ratio, respectively.

AFM measurements provide surface probes with atomic layer scale. In this application it is utilized to monitor the top surface roughness changes, as a function of real time, in the surface aging process of HgI_2.

SAMPLE PREPARATIONS

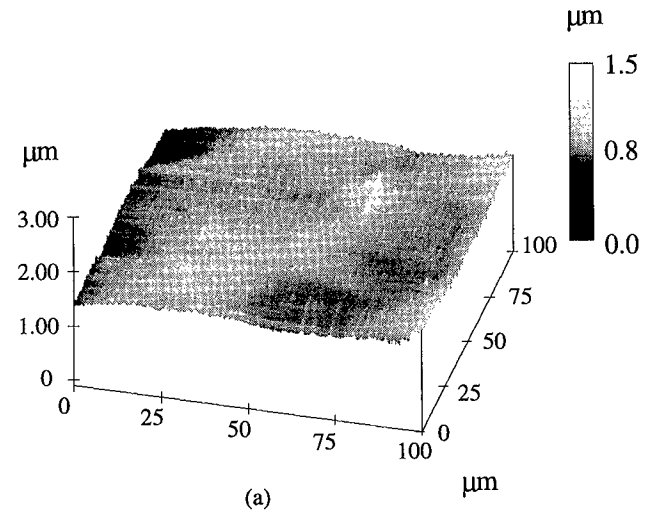
Three HgI_2 surfaces were cut from a same crystal grown at EG&G/EM Inc. Santa-Barbara, with different initial surface conditions, i.e., (1) as-grown surface; (2) cleaved surface; (3) mechanically and chemically polished surface. All three samples are c-plane surfaces, to which the c-axis of the crystal is perpendicular.

The as-grown and cleaved surfaces were characterized by VASE and AFM about 48 hours after the sample being exposed to air. The mechanically and chemically polished sample was subjected to a 10% KI etching to ensure clean and fresh surface before the characterization[6,11]. In the etching process, the sample was immersed in a 10% KI (by weight) solution for about 2 min. After the KI etching, the sample was rinsed immediately with deionized water for ~ 2-3 min. Separate pieces of the KI etched HgI_2 samples were baked in an oven for 30 min. at elevated temperatures of 45 and 55 °C, respectively. The VASE and AFM measurements were made on all those samples in air at room temperature over a period of several months after the samples being exposed to air.

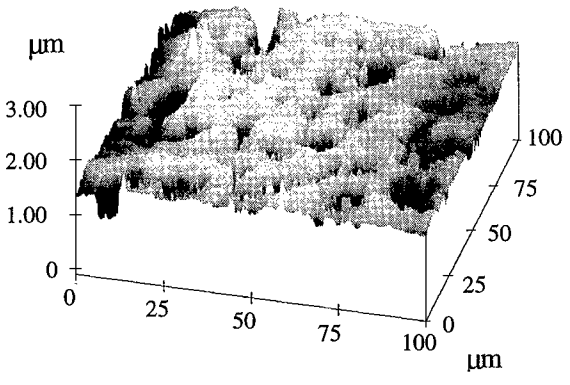
MEASUREMENTS AND ANALYSIS

Fig. 1 includes a pair of AFM images showing a typical surface aging process of a c-plane HgI_2 crystal surface: (a) 12 minutes after etching; and (b) 545 hours after etching with 10% KI. The AFM measurements were made in a fixed position of a 100 μm window on the sample surface. It is clearly shown in (a), that the 10% KI etching removed the old aged materials, and provided a clean and ruby red fresh HgI_2 surface. After 545 hours of exposure to air after the KI etching, the surface became rough and aged, as shown in (b). The visible color change of the top surface layer, from ruby red into whitish, indicated a possible stoichiometry change.

VASE measurements were made, side by side with AFM probes, in a spectral range of 1.24 to 5.1 eV, with an increment of 0.05 eV and angles of incidence of 67.5°, 70°, 72.5° and 75°. A surface model was established, for the VASE analysis, to describe the top surface roughnesses and possible subsurface defects, as shown in Fig. 2 (b). The HgI_2 surface was modeled as two graded layers containing voids, labeled as d_1 and d_2 in thickness. The top layer (d_1) is mainly used to describe the physical roughness of the sample surface, while the sublayer (d_2) is designed to reflect the possible subsurface defects. In the top layer (d_1), the volume voids percentage was graded from 50% to x%, while in the sublayer (d_2) the voids percentage was graded from x% to 0%. The effective optical constants of the mixed graded layers used in the VASE analysis were calculated using the Bruggeman effective-medium approximation (EMA) [12,13]. The determination of the anisotropic dielectric



(a)



(b)

Fig. 1 Atomic force microscopy (AFM) images of a typical c-plane surface of HgI_2 crystal. (a) 12 minutes after etching; and (b) 545 hours after etching with 10% KI. The depth scale is shown on the right side of the figure.

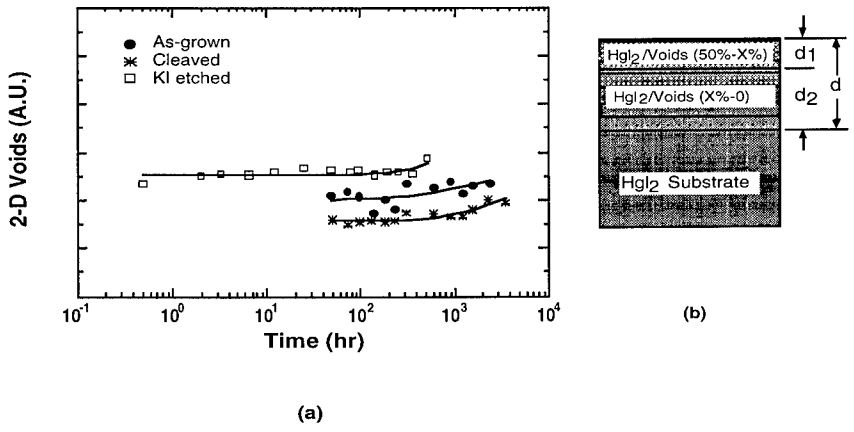


Fig. 2 (a) A comparison of VASE determined 2D voids densities in arbitrary units, as a function of aging time, of three different surface conditions: (●) as-grown; (✳) cleaved; (❑) KI etched. (b) The surface model of HgI_2 crystal for VASE analysis including the top layer (d_1) and the sub-surface layer (d_2).

function of HgI_2 crystals is reported in a separated paper [14]. During the VASE analysis, the voids volume percentage x, the top and sub-surface layer thicknesses d_1 and d_2 were allowed to vary, and a regression process was employed to minimize differences between the measured and calculated parameter values. The fitted value of volume voids percentage was then converted into an effective 2D voids density representing the surface layer ($d= d_1 + d_2$), as shown in Fig. 2 (a).

The physical meaning of the voids may be explained as following: (1) it can be used to describe the physical surface roughness of HgI_2 sample (i.e., on the very top surface); (2) the voids, especially in the sub-surface layer, may represent possible surface defects. It is shown, in Fig. 2 (a), different 2D voids densities associated with different initial surface conditions: the lowest 2D voids densities for cleaved surface, followed by higher voids densities for as-grown surface, and the highest 2D voids densities for 10% KI etched HgI_2 surface. The AFM surface images have revealed, as shown in Fig. 1 and ref. 8, increasing physical surface roughness as surface aging took place. This is consistent with the VASE analysis results. The surface aging rates of HgI_2 surfaces are closely related with the 2D voids densities: in general, the relative higher 2D voids density, the higher surface aging rate.

A comparison of VASE determined 2D voids densities of HgI_2 surfaces, that were baked for 30 min. at elevated temperatures, are shown in Fig. 3. It is noticeable that the 2D voids densities keep nearly unchanged in the initial period of time and then start increasing at certain hours reflecting the start of surface aging. As shown in Fig. 3, the starting points of increasing 2D voids densities for baked HgI_2 surfaces are earlier than unbaked surface, i.e., ~6 hours for surface baked at 55 °C, ~10 hours for surface baked at 45 °C, and ~100 hours for unbaked HgI_2 surface. This indicates that baking the HgI_2 surfaces for 30 min. accelerates the surface aging of HgI_2. The

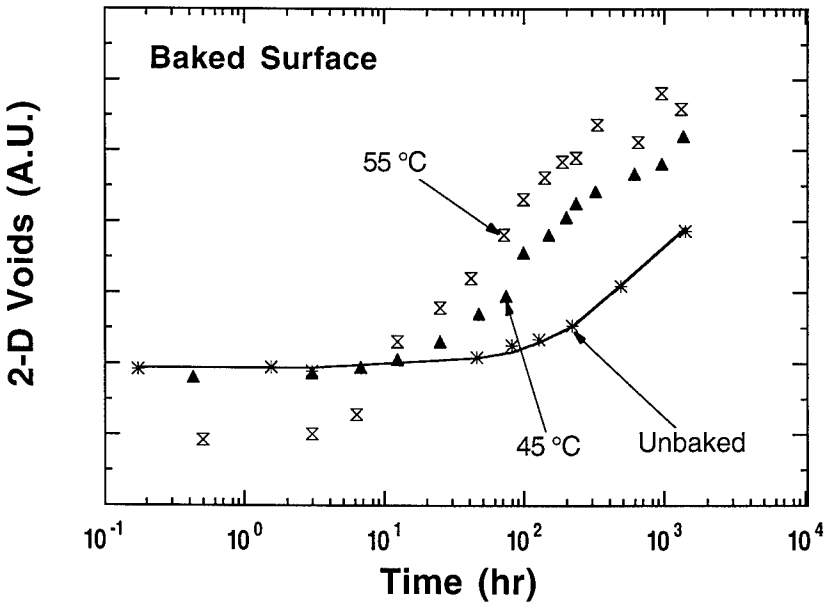


Fig. 3 A comparison of VASE determined 2D voids densities in arbitrary units, as a function of aging time, of baked HgI_2 surface conditions: (✳) unbaked; (▲) baked at 45 °C; (⧖) baked at 55 °C.

start of surface aging for baked HgI_2 surfaces is much earlier than unbaked surface. The higher the baking temperature is, the faster the surface aging occurs. This phenomenon indirectly supports the origin of surface aging mentioned in ref. 7 suggesting that by losing I_2 from the crystal surface, due to its higher vapor pressure, it causes stoichiometry deviation of HgI_2. Obviously, the higher baking temperature accelerates the evaporation of I_2 from the HgI_2 crystal surface. Further studies to confirm the loss of I_2 and the change of stoichiometry are needed.

SUMMARY

We have presented results of surface aging studies of HgI_2 crystals characterized by VASE and AFM. HgI_2 c-plane surfaces cut from the same crystal with different initial surface conditions, i.e., cleaved, as-grown and mechanically and chemically etched surfaces, were studied. The results indicated that the cleaved surface had the lowest aging rate among the three, while the chemically etched surface aged at the highest rate. A low aging rate was also observed from the as-grown surface. An effective 2D voids density representing the surface roughness and defects was obtained through VASE analysis. The surface aging rates of HgI_2 crystals were closely related with the 2D voids densities: in general, the relative higher 2D voids density, the higher surface aging rate. KI etched HgI_2 surfaces baked for 30 min.

show accelerated surface aging phenomena. The start of surface aging for baked HgI_2 surfaces are much earlier than unbaked surface, i.e., ~6 hours for surface baked at 55 °C, ~10 hours for surface baked at 45 °C, and ~100 hours for unbaked HgI_2 surface.

ACKNOWLEDGMENTS

This work was supported by Department of Energy via Sandia National Laboratories.

REFERENCES

1. W. R. Wing, Nucl. Instrum. Meethods **96,** 615 (1971).
2. S. P. Swierkowski, G. A. Armantrout, and R. Wichne, IEEE Trans. Nucl. Sci. **NS-21,** 302 (1974).
3. J. P. Ponpon, R. Stuck, P. Siffert, B. Meyer, and C. Schwab, IEEE Trans. Nucl. Sci. **NS-22,** 182 (1975).
4. A. J. Dabrowski, W. M. Szymczyk, J. S. Iwanczyk, J. H. Kusmiss, W. Drummond, and L. Ames, Nucl. Instrum. Methods **213,** 89 (1983).
5. J. H. Howes and J. Watling, Mat. Res. Soc. Symp. Proc. **16,** 207 (1983).
6. H. Yao and B. Johs, Mat. Res. Soc. Symp. Proc. **302,** 341 (1993).
7. M. Schieber, M. Roth, H. Yao, M. DeVries, R. B. James, and M. Goorsky, J. Crystal Growth **146,** 15 (1995).
8. H. Yao, L. A. Lim, R. B. James, M. Schieber, and M. Natarajan, Nucl. Instrum. Methods (to be published) (1996).
9. R. M. A. Azzam and N. M. Bashara, *Ellipsometry and Polarized Light* (North-Holland, Amsterdam, 1977).
10. D. E. Aspnes, in *Handbook of Optical Constants of Solids*, edited by E. D. Palik (Academic, New York, 1985), p. 89.
11. X. J. Bao, T. E. Schlesinger, R. B. James, R. H. Stulen, C. Ortale, and A. Y. Cheng, J. Appl. Phys. **68,** 86 (1990).
12. D. E. Aspnes, J. B. Theeten, and F. Hottier, Phys. Rev. B **20,** 3292 (1979).
13. H. Yao and P. G. Snyder, Thin Solid Films **206,** 283 (1991).
14. H. Yao, B. Johs, and R. B. James, Phys. Rev. B (to be published).

Part XIII

Wide-Bandgap Materials: SiC

THE MICROSCOPIC STRUCTURE OF SHALLOW DONORS IN SILICON CARBIDE

J.-M. SPAETH, S. GREULICH-WEBER, M. MÄRZ, E.N. KALABUKHOVA**, S.N. LUKIN**
*Department of Physics, University of Paderborn, 33095 Paderborn, Germany
**Institute of Semiconductors, Kiev, Ukraine

ABSTRACT

The electronic structure of nitrogen donors in 6H-, 4H- and 3C-SiC is investigated by measuring the nitrogen hyperfine (hf) interactions with electron nuclear double resonance (ENDOR) and the temperature dependence of the hf split electron paramagnetic resonance (EPR) spectra. Superhyperfine (shf) interactions with many shells of ^{13}C and ^{29}Si were measured in 6H-SiC. The hf and shf interactions are discussed in the framework of effective mass theory. The temperature dependence is explained with the thermal occupation of the lowest valley-orbit split A_1 and E states. It is proposed that the EPR spectra of P donors observed previously in neutron transmuted 6H-SiC at low temperature (<10K) and high temperature (>60K) are all due to substitutional P donors on the two quasi-cubic and hexagonal Si sites, whereby at low temperature the E state is occupied and at high temperature the A_1 state. The low temperature spectra are thus thought not to be due to P-vacancy pair defects as proposed previously.

INTRODUCTION

SiC has attracted considerable attention recently because of its potential for high temperature electronics and as a wide band gap material for optoelectronics. For any device one must understand shallow donors and acceptors. The most important shallow donor is nitrogen which is inadvertently incorporated into SiC by the Lely growth. Although N donors have been investigated for many years by electron paramagnetic resonance (EPR) in several polytypes [1-4], open questions have remained with respect to the differences in hyperfine (hf) interactions observed in EPR for the various lattice sites. In order to obtain a better picture of the electronic ground state, the N hf interaction was measured with electron nuclear double resonance (ENDOR) in 6H-SiC with higher precision than possible in EPR. It was shown that the hexagonal site donor has an unexpectedly small isotropic hf interaction constant as well as an anisotropic hf interaction constant [5]. An explanation of the small isotropic hf constant (it is a factor of 14 smaller than that of the quasi-cubic sites) was attempted by considering the Kohn-Luttinger interference factors and the differences in the stacking order along the c-axis [5]. It is the purpose of the present work to extend the ENDOR investigations of N donors to 4H-SiC and 3C-SiC as well as to investigate in detail the superhyperfine (shf) interactions in 6H-SiC. It is also shown that the temperature dependence of the hf splitting of the EPR spectra can be understood on the basis of the thermal occupation of the two lowest effective mass states with A_1 and E symmetry split by the valley-orbit interaction. The interpretation of the temperature dependence of the N hf interactions led us to propose that EPR spectra of P donors observed hitherto in neutron transmuted 6H-SiC [5,6] and ascribed to substitutional P donors [6] as well as to P-vacancy pair defects [5,6] may all be due to substitutional P donors occupying a ground state with E symmetry at low temperature and a state with A_1 symmetry at high temperature.

RESULTS AND DISCUSSION

NITROGEN DONORS

The EPR spectra of N donors in 6H-, 4H- and 3C-SiC had been measured previously [1-5]. At high microwave frequencies (e.g. 142 GHz [3,4]) the spectra of the hexagonal site donors in 6H- and 4H-SiC appear separated from those of the quasi-cubic site donors. The g-tensor has axial symmetry about the c-axis in 6H- and 4H-SiC for all sites, while it is isotropic in 3C-SiC. The g-

Mat. Res. Soc. Symp. Proc. Vol. 442 © 1997 Materials Research Society

	site	E_D [meV]	v.o. splitting [meV] ERS/IR	v.o. splitting [meV] EPR	hf interaction a/h [MHz]	hf interaction b/h [MHz]	ground state
3C E_g = 2.40 eV	cubic	54 [11]	8.37 [11]	8.0 [14]	3.500	0	A_1
4H	cubic	91.8 [12]		45.5 [14]	50.970	0.004	A_1
E_g = 3.28 eV	hex	52.1 [12]	7.6 [12]		2.900	0.080	$\alpha A_1+\beta E$
6H	cubic	137.6 [13]	60.3 [13]	61.1 [14]	33.221	0.004	A_1
E_g = 3.10 eV	cubic	142.4 [13]	62.6 [13]		33.564	0.009	A_1
	hex	81.0 [13]	12.6 [13]	13.0	2.468	0.137	$\alpha A_1+\beta E$

Table 1: Experimental hyperfine interaction constants of N donors in 3C-, 4H- and 6H-SiC determined from ENDOR, valley-orbit splitting and the lowest donor energy levels E_D with respect to the conduction band minimum. The precision of the hf interactions is ±2kHz.

values are all very near to the free electron value. The hf structure consists of triplets ($I(^{14}N)=1$) and is mostly resolved in EPR [1-4]. With ENDOR the hf interactions can be determined with higher precision, in particular the small anisotropic interactions. In table 1 previous data on 6H-SiC [5] are collected together with new ones for 4H-SiC and 3C-SiC. The hf interactions are given in terms of the isotropic hf constant a/h and the anisotropic hf constant b/h, which are related to the usual axially symmetric hf tensor by

$$A_{xx}=A_{yy}=a-b \qquad A_{zz}=a+2b \tag{1}$$

In 6H-SiC a very small quadrupole interaction was found [5], similarly also in 4H-SiC but none in 3C-SiC. For the cubic site donors in 3C-, 4H- and 6H-SiC the hf interaction is isotropic. There is only a very small anisotropy in 6H- and 4H-SiC (table 1). However, the sizes of the interaction constants differ substantially. In 3C-SiC a/h is about one order of magnitude smaller than in 6H- and 4H-SiC, while there is almost a factor of 2 between the latter two. The hexagonal site interaction constants in 6H- and 4H-SiC show, besides a very small isotropic constant, also an anisotropic hf constant.

Similarly, as was found for the shallow donor P, As and Sb in Si [7], one cannot explain the measured isotropic hf constants using effective mass theory. In 6H- and 4H-SiC one calculates values for the isotropic hf constant which are far too low, as was found in Si. The discrepancy is of the order of a factor between 10 and 20 depending on the values used for the effective mass. In Si a central cell correction was introduced considering the chemical nature of the different donors. Such an explanation cannot be used here to account for the differences on the various sites in one polytype. Only in 3C-SiC effective mass theory would predict a/h=2.08 MHz, which is about the measured value. For the calculation the dielectric constant ε_r=9.75 [8] and the effective mass m*=0.33 [9] was used. One cannot relate with each other the hf interactions of the different polytypes by effective mass theory.

The anisotropic hf constant seen for the hexagonal site donors in 6H- and 4H-SiC indicates that the ground state has lower than tetrahedral symmetry. According to effective mass theory for a state with A_1 symmetry one expects a≠0, b=0 and for one with E symmetry a=0, b≠0. It is proposed that the hexagonal crystal field mixes the nearby symmetry allowed excited state 1s(E) into the 1s(A_1) state which causes the anisotropic interaction. Qualitatively, a similar effect was observed for donors in Si, where the application of uniaxial stress caused the appearance of an anisotropic hf interaction as well as a reduction in the isotropic hf constant [10].

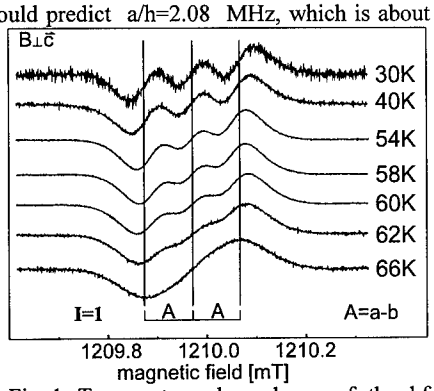


Fig. 1: Temperature dependence of the hf interaction of the hexagonal site N donor in 6H-SiC (B⊥c-axis, ν_{ESR}=35GHz).

The influence of the nearby excited state 1s(E) is also seen from the temperature dependence of the hf interaction. In Fig. 1 the temperature dependence of the hf splitting of the hexagonal site donor in 6H-SiC is shown. The hf interaction decreases upon increasing the temperature exponentially by approximately 0.4 MHz between 30 and 66K. The activation energy determined from this decrease is 13±0.1meV. This value is in agreement with the valley-orbit splitting between the $1s(A_1)$ and 1s(E) states determined previously with optical spectroscopy [13] and from intensities of EPR lines [14] for 6H-SiC. The decrease in hf splitting by 0.4MHz is larger than the value of the anisotropic hf constant. Thus, in the excited state the a-value must be smaller than in the ground state. Therefore, the ground state cannot be of pure E symmetry. We propose that the ground state is mainly A_1 with some admixture of E and the excited state vice versa (Fig. 2). For the cubic site defects the splitting between A_1 and E is much larger. When the 1s(E) state is thermally occupied, the hf splitting has disappeared in the EPR spectrum [14].

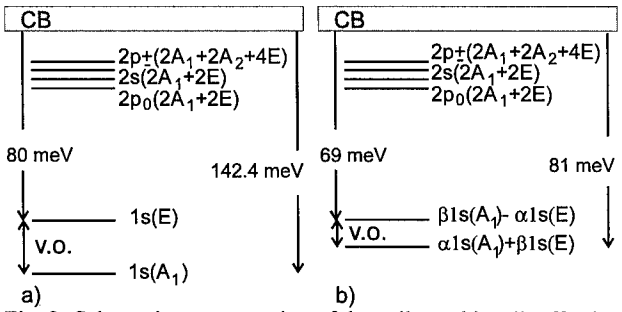


Fig. 2: Schematic representation of the valley-orbit split effective mass states of N donors in 6H-SiC. a) quasi-cubic donors b) hexagonal site donors.

From Fig. 2 it is seen that the lowest excited states of the quasi-cubic and hexagonal site donors have a very similar energy, while the ground states differ considerably. It is thought that the hexagonal crystal field lifts the ground state at the hexagonal site very much and still has some influence on the excited state showing again the mixing of the two states. The small differences in the properties of the two quasi-cubic sites are probably also due to differences in the crystal fields at these sites.

It seems that there is a striking linear relationship between the value of the valley-orbit splitting between $1s(A_1)$ and 1s(E) divided by E_D according to EMT and the size of the isotropic hf constants. A large splitting results in a large isotropic constant, a small splitting in a small constant, irrespective of polytype and site (table 1). A physical explanation for the linear relation is not available at present.

Besides the ENDOR lines of the central N nuclei, also many lines of ^{13}C and ^{29}Si lattice nuclei have been measured. A spectrum of the quasi-cubic N donors in 6H-SiC has been published in [5] with a preliminary analysis. Most of the lines are isotropic. One can therefore not assign them to any particular lattice nuclei of the surrounding without theoretical interpretation of the isotropic shf constants [5]. In the EPR spectrum no shf interactions are resolved [1-4]. Because of the many lines observed and because of the rather small nuclear g-factors of ^{29}Si and of ^{13}C, it was difficult to determine beyond doubt isotropic ^{29}Si and ^{13}C lines for interaction constants smaller than 2.5MHz [5,18]. However, some anisotropic lines were observed of which the angular dependence could be followed. Three anisotropic ^{29}Si lines showed axial symmetry about the c-axis. Therefore, the corresponding ^{29}Si nuclei could only be on the c-axis. Fig. 3 shows their possible location. The assignment was made according to the anisotropic shf constants with the nearest ^{29}Si nucleus having the largest b-value (see table 2 and Fig. 3). Many more ^{29}Si interactions were identified compared to ^{13}C interactions.

It was attempted to interpret the isotropic shf interactions within the framework of effective mass theory. The wave function for the indirect semiconductor 6H-SiC is given by

$$\Psi(\vec{r}) = \sum_{j=1}^{6} \alpha^{(j)} F^{(j)}(\vec{r}) u^{(j)}(\vec{r}) e^{i\vec{k}^{(j)}\vec{r}} \qquad (2)$$

whereby j is the conduction band minimum j, $F^{(j)}(r)$ the hydrogenic envelope function and $u^{(j)}(r)$

^{29}Si		^{13}C	
a/h [MHz]	b/h [MHz]	a/h [MHz]	b/h [MHz]
a) 1.70	1.26	4.577	<0.005
b) 0.21	0.17	4.486	<0.005
c) 0.88	0.14	4.424	<0.005
6.447	<0.005	3.936	<0.005
5.810	<0.005	3.716	<0.005
4.767	<0.005	3.624	<0.005
4.479	<0.005		
3.891	<0.005		
3.757	<0.005		
3.459	<0.005		
3.139	<0.005		
3.021	<0.005		
2.839	<0.005		
2.593	<0.005		
2.573	<0.005		

Table 2: Shf interaction constants for quasi-cubic N donors in 6H-SiC determined from ENDOR.

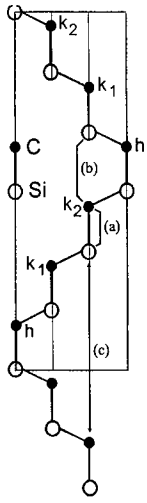


Fig. 3: (1120)-plane of a unit cell of 6H-SiC showing the 3 Si neighbours for which the anisotropic shf interactions could be resolved. (a)=1.89Å, (b)= 3.15Å and (c) = 8.31Å (see also table 2). The c-axis is parallel to z. k_1 and k_2 describe the quasi-cubic C sites, h the hexagonal C site.

e^{ikr} the Bloch function. $|\alpha^{(j)}|^2$ are the probabilities to find the electron in the j^{th} valley. Since $a/h \propto \psi^2$ [15], one has to calculate $\psi(r)$. For this the Kohn-Luttinger interference factor

$$S = \sum_{j=1}^{6} \alpha^{(j)} e^{i\vec{k}^{(j)}\vec{r}} \tag{3}$$

has to be calculated for each lattice site.

One also needs to know F(r) as well as the $u^{(j)}(r)$. For F(r) a hydrogenic wave function with the Bohr radius a_{qH} and a factor K to describe the central cell correction were assumed:

$$F(r) = \frac{K}{\sqrt{\pi a_{qH}^3}} \exp\left(\frac{r}{a_{qH}}\right) \tag{4}$$

K, a_{qH} and the ratio $\eta = u^{(j)}(Si)/u^{(j)}(C)$ were used as fit parameters, whereby K was fitted to the largest isotropic ^{29}Si interaction (K=3.55). An open question was the position of the conduction band minimum (L point [16], M point [17] or somewhere between L and M) and the site for N. No anisotropic ^{13}C lines were found, and in total much less ^{13}C lines compared to ^{29}Si lines. Already this suggested that N occupies a C site. The details of the calculation cannot be described here (see [18]). It may be noted, however, that the Kohn-Luttinger factor causes oscillations of the isotropic constants by 6 orders of magnitude for the nearer lattice nuclei, while the isotropic constants of further distant nuclei are mainly influenced by the envelope function. A satisfactory explanation of the experimental data was obtained for the following electronic structure (Fig. 4) (Note, that only interactions above 2.5MHz could safely be assigned to either ^{29}Si or ^{13}C): (i) N is on a C site. (ii) a_{qH}=(17±1.5)Å. (iii) The conduction band minimum is near the L point. The best fit was obtained for L+0.03 LM towards M±15%. (iv) $\eta = u^{(j)}(Si)/ u^{(j)}(C)$ = 1.45±0.05. (v) K=3.55. No satisfactory explanation of the data was obtainable for N on an Si site, nor for the conduction band minimum at the M point as calculated theoretically [16]. The Bohr radius is in the range of 12-20Å calculated with the different published values of the effective masses [9].

It was found in Si that the shf interactions measured in the lattice surroundings of different donors did differ very little, while the spin density of the central nuclei showed large differences making the central cell correction necessary [7]. It seems that in SiC also the shf interactions can

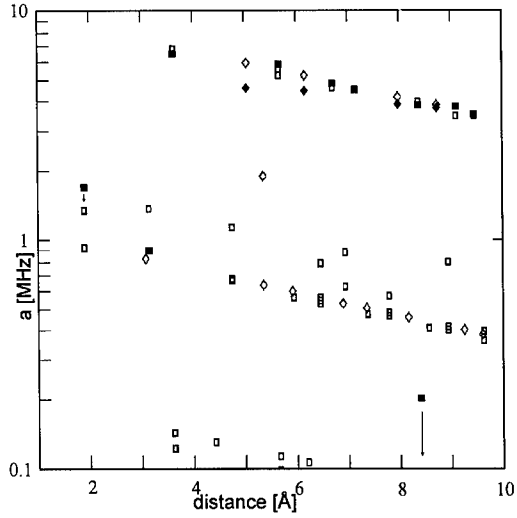


Fig. 4: Isotropic shf interaction of quasi-cubic N donors in 6H-SiC as a function of the distance of the lattice neighbours assuming a C lattice site for N. Full symbols are the experimental values (■^{29}Si, ◆^{13}C) above 2.5 MHz, except for the 3 Si neighbours along the c-axis, which could be identified. The calculated values (open symbols) were determined from effective mass theory assuming a Bohr radius of 17Å and the conduction band minimum near the L point (for details see text).

be described much better than the central nuclei by the effective mass theory.

PHOSPHORUS DONORS IN 6H-SIC

In a neutron-transmuted 6H-SiC sample (neutron irradiation with a flux of $\varphi=2\cdot10^{20}$cm^{-2}, annealed after irradiation at 2100°C) several P donors were found in EPR. At temperatures above about 60K two hf split axially symmetric spectra about the c-axis with almost only isotropic hf interaction were observed with a rather large isotropic hf constant [6] (see table 3, donors P_a, P_b). In addition, an anisotropic hf split P spectrum was observed (P-V, table 3) at T>60K with a much smaller isotropic hf constant, which was interpreted as a P-vacancy pair defect. At low temperature two anisotropic P spectra were found, which show a relatively high anisotropic constant and a low isotropic hf constant (table 3, spectra P_1, P_2 [5]). One spectrum could be assigned to the quasi-cubic sites and one to the hexagonal site due to the EPR line intensities. The spectra are axially symmetric about the c-axis. Tentatively, the spectra were also assigned to a P-V complex, in which, however, it had to be assumed that the vacancy is always along the c-axis [5]. At about 10K the spin lattice relaxation time of these centres becomes too short to observe the EPR spectra. Inspection of table 3 shows that the g-factors of all defects are very similar, the g-tensors are all axially symmetric about the c-axis as was found for the N donors in 6H-SiC. As there $g_{||}>g_{\perp}$ is observed, the absolute values of $g_{||}$ and $g_{\perp}$ are very much the same.
It is tempting to propose that all these P spectra, which are observed in the same neutron-transmuted 6H-SiC sample, belong to the same isolated shallow P donors similarly as the N donors in 6H-SiC. If the effective mass 1s(E) state is lowest and the 1s(A_1) state split off by the valley-orbit interaction is higher, then we have an analogue situation as in the case of the N donors. (Note, that the P donor occupies an Si site, since it is produced from ^{30}Si isotopes). It is also assumed here that the valley-orbit splitting is smaller for the hexagonal site donor than for

	site	temperature	$g_{||}$	$g_{\perp}$	a/h [MHz]	b/h [MHz]
P_a [6]	cubic	T > 60 K	2.0040	2.0029	156	0.7
P_b [6]	cubic	T > 60 K	2.0040	2.0025	145	0
P-V [6]	hex	T > 60 K	2.0044	2.0025	22	1.9
P_1 [5]	hex	T ≤ 10 K	2.0049	2.0031	1.562	0.894
P_2 [5]	k_1, k_2	T ≤ 10 K	2.0041	2.0028	8.7	4.2

Table 3: g-values and hf constants of several P donors in 6H-SiC generated in a neutron- transmuted sample.

the quasi-cubic site donors, such that E and A_1 states mix considerably for the hexagonal site donors. The P_1 spectrum belongs to the low temperature hexagonal site, while at high temperature (where P_1 is not observed because of the spin lattice relaxation effects) this donor has the properties assigned hitherto to a P-V complex: the isotropic hf constant increases due to the higher A_1 character of the thermally occupied excited state. Similar arguments hold for the quasi-cubic site defects. Comparison of the isotropic hf constants devided by the nuclear g-factors a/g_I shows that for the quasi-cubic N donors this value of about 83 is near that for the high temperature cubic P donors, which is about 70. The corresponding values for the hexagonal donors are 6 for N and 10 for P, i.e. of the same order of magnitude. The larger difference compared to cubic site defects is probably due to the different E-A_1 mixing. Recently, the value for E_D for the high temperature quasi-cubic P donors was determined to be 130meV [19], which is slightly shallower than that of the N donors (140meV). This is qualitatively seen in a somewhat smaller isotropic constant. Thus, it seems that all P spectra observed are due to isolated shallow donors on Si sites thermally occupying the two lowest effective mass states split by the valley-orbit splitting.

CONCLUSION

The isotropic hf constants of the N donors cannot be explained by simple effective mass theory. It seems that for all polytypes investigated only the donor in 3C-SiC can be explained by effective mass theory. The experimental results indicate that there is a linear relationship between the size of the valley-orbit splitting between the 1s(A_1) and 1s(E) states and the isotropic N hf constants.
The several EPR spectra of P donors observed in a neutron-transmuted 6H-SiC all seem to be originating from isolated P donors on Si sites and not partly due to P-V pair defects as suggested previously. The electronic structure is characterized by the 1s(E) state being lowest for the cubic site donors and mixed with the 1s(A_1) state for the hexagonal site donors. Thus, a unifying picture of the P donors is proposed.

REFERENCES

1. H.H. Woodbury and G.W. Ludwig. Phys. Rev **124** 1033 (1961)
2. Yu.M. Altaiskii, I.M. Zaritskie, V.Ya. Zevin and A.A. Konchits, Sov. Phys. Solid State **12** 2453 (1971)
3. E.N. Kalabukhova, S.N. Lukin, B.D. Shanina, L.V. Artamona, E.N. Mokhov, Sov. Phys. Solid State **32** 482-6 (1980)
4. E.N. Kalabukhova, N.N. Kabdin, S.N. Lukin, Sov. Phys. Solid State **29** 1461-2 (1987)
5. S. Greulich-Weber, M. Feege, J.-M. Spaeth, E.N. Kalabukhova, S.N. Lukin and E.N. Mokhov, Solid Sate Commun. **93** 393 (1995)
6. A.I. Veinger, A.G. Zabrodskii, G.A. Lomakina and E.N. Mokhov, Sov. Phys. Solid State **28** 917 (1986)
7. W. Kohn and J.M. Luttinger, Phys. Rev. **97** 4 p883 (1955)
8. L. Patrick, W.J. Choyke, Phys. Rev. **B2** p2255 (1970)
9. S. Yoshida, in Properties of Silicon Carbide, ed. G.L. Harris, IEE, inspec, p69 (1995)
10. D.K. Wilson and G.Feher, Phys. Rev. **124** 4 (1961)
11. P.J. Colwell and M.V. Klein, Phys. Rev. **B6** 2 p498 (1972)
12. W. Goetz, G. Pensl, W.J. Choyke, R. Stein, S. Leibenzeder, J. Appl. Phys. **72** p3332 (1993)
13. W. Suttrop, G. Pensl, W.J. Choyke, R. Stein, S. Leibenzeder, J. Appl. Phys. **72** p3708 (1992)
14. C. Kisielowski, K. Maier, J. Schneider and V. Oding, Mat. Sci. Forum **83-87** p1171 (1992)
15. J.-M. Spaeth, J.R. Niklas and R.H. Bartram, Structural Analysis of Point Defects in Solids, Series of Solid State Sciences **43** (1992)
16. W. E. Carlos, in Properties of Silicon Carbide, ed. G.L. Harris, IEE, inspec, p42 (1995)
17. P. Käckel, B. Wenzien, F. Bechstedt, Phys. Rev. **B50** (15) 10761 (1994)
18. M. Feege, Doctoral Thesis, Paderborn, 1995
19. T. Troffer, C. Peppermüller, G. Pensl, K. Rottner and A. Schöner, J. Appl. Phys. **80** (7) (1996)

VACANCIES IN ELECTRON IRRADIATED 6H-SiC

T. FRIESSNEGG *, S. DANNEFAER **
*Institut für Kernphysik, Technische Universität Graz, A-8010 Graz, Austria
**Department of Physics, University of Winnipeg, Winnipeg, MB R3B 2E9, Canada

ABSTRACT

Annealing of electron irradiated bulk n-type 6H-SiC has shown that neutral carbon vacancies and neutral silicon vacancies undergo a major reduction in concentration in the 20-200 °C temperature interval after which only slight changes occur up to 1200 °C. The experiments suggest that the positively charged carbon vacancy, detected by electron paramagnetic resonance, constitutes only a small fraction of all carbon vacancies.

INTRODUCTION

Progress has recently been made in characterizing defects in SiC. Itoh *et al.* [1] found in 2 MeV proton irradiated p-type 3C-SiC films an electron paramagnetic resonance (EPR) line (T5) which was ascribed to a singly-positive carbon vacancy (V_C^+); this resonance was not observed in n-type material. Itoh *et al.* [2] also found an EPR line (T1) after 1 MeV electron irradiation of n-type 3C-SiC, which was interpreted as arising from negatively charged silicon vacancies (V_{Si}^-); however Itoh *et al.* did not report on the presence nor absence of the T1 line in p-type 3C-SiC. We are not aware of any EPR investigations which identify defects in as-grown SiC.

Positron lifetime experiments have shown [3] that electron irradiation of n-type bulk 6H-SiC formed neutral V_C and V_{Si} and that no such defects could be detected in p-type 6H-SiC. They also showed the presence of a small concentration of vacancy clusters in as-grown 6H-SiC independent of conductivity type.

Albeit having established responses arising from fundamental vacancy-type defects there remains to investigate important features such as association of vacancies with dopants which plays an important role in silicon and diamond. The role of interstitials is equally important but may well prove as elusive as in silicon and diamond.

Another important topic pertains to the thermal stability of the irradiation-produced vacancies and the mechanisms by which they anneal. Itoh *et al.* [4] showed that annealing of V_C^+ took place in *two* stages, one close to room temperature and one around 700 °C, which removed all of the EPR detected radiation damage. It is not clear why two annealing stages are found for the same defect. In the present work we extend our former work [3] by investigating annealing of electron irradiated 6H-SiC using both positron lifetime spectroscopy and Doppler broadening.

EXPERIMENTAL DETAILS

The samples were bulk n-type 6H-SiC with a carrier concentration of 6×10^{17} /cm^3 and were obtained from Cree research, USA. Two samples were irradiated to electron doses of 6×10^{16} e$^-$/cm^2 and 2×10^{17} e$^-$/cm^2, respectively. The electron energy was 2.2 MeV and the irradiation was done at 10 °C. Isochronal heat treatments were done up to 1200 °C for 30 minutes at each temperature. Above 600 °C the samples were placed in a projective ambient.

Mat. Res. Soc. Symp. Proc. Vol. 442 © 1997 Materials Research Society

Each lifetime spectrum contained at least 6×10^6 counts which makes possible resolving individual lifetime components when they differ by ~50 ps. Doppler broadened energy spectra were obtained using a Ge detector with an energy resolution of 1.2 keV and were analyzed in terms of the usual S parameter.

RESULTS

Before irradiation the lifetime spectrum is dominated by one component, τ_1, with an intensity of 94% (see Table I). This component arises from annihilations in the bulk while the weak 300 ps component is due to vacancy clusters, and from the simple trapping model [5] the trapping rate due to these clusters can be calculated. For the irradiated sample two new lifetimes are observed which are both larger than the value for τ_1 in the as-grown material. As argued in ref. 3, the ~160 ps lifetime arises from V_C and the ~250 ps component from V_{Si}.

Table I. Lifetime and Doppler broadening results for as-grown sample and for the unannealed 6×10^{16} e^-/cm^2 and 2×10^{17} e^-/cm^2 irradiated samples. τ's denote resolvable lifetimes and the I's their intensities. Trapping rates are denoted by κ, and S is the Doppler parameter.

Sample	τ_1 (ps)	τ_2 (ps)	τ_3 (ps)	I_1 (%)	I_2 (%)	I_3 (%)	κ_2 (ns^{-1})	κ_3 (ns^{-1})	S
As-grown	140 ±2	300 ±10	-	94 ±1	6 ±1	-	0.4	-	0.4380± 0.0009
Irradiated 6×10^{16} e^-/cm^2	100 ±5	170 ±5	275 ±10	30 ±2	61 ±2	9 ±1	2.5	0.6	0.4457± 0.0009
Irradiated 2×10^{17} e^-/cm^2	-	145 ±3	245 ±4	-	61 ±3	39 ±3	-	-	0.4517± 0.0009

The long-lived component in the as-grown material is no longer observable in the irradiated sample because the newly created defects overwhelm the weak response from the vacancy clusters. The trapping rates due to each of the vacancy types are calculated from the trapping model and we note that these trapping rates are proportional to the vacancy concentration. S values are listed last in Table I: S increases with irradiation dose as one might expect because of the introduction of vacancies.

Annealing data for the 6×10^{16} e^-/cm^2 irradiated sample are shown in Fig. 1 (we restrict ourselves to show only the important vacancy-related lifetimes and trapping rates). The τ_2 lifetime is essentially constant at 176±2 ps (see Fig. 1(a)) while the scatter in τ_3 obscures any systematic trend. However, by fixing τ_2 (at 176 ps) the scatter can be reduced significantly (as shown in Fig. 1(b)), and based on these analyses the trapping rates κ_2 (due to τ_2) and κ_3 (due to τ_3) are shown in Fig. 1(c). Some increase is observed for τ_3 with annealing temperature, but the striking feature is the rapid decrease of the two trapping rates in the 20-200 °C temperature interval.

Similar analyses on the 2×10^{17} e^-/cm^2 irradiated sample yield results as shown in Fig. 2(a). τ_2 was found constant at 164±1 ps, but trapping rates are now too large to be calculable in the 20-200 °C temperature interval because τ_1 could not be resolved (commensurate with the significantly higher S parameter for this sample, Table I). For this reason trapping rates are only shown (in Fig. 2(b)) above 200 °C. There is, however, no doubt that also in this sample a significant reduction in the concentration of V_C and V_{Si} takes place between 20 and 200 °C.

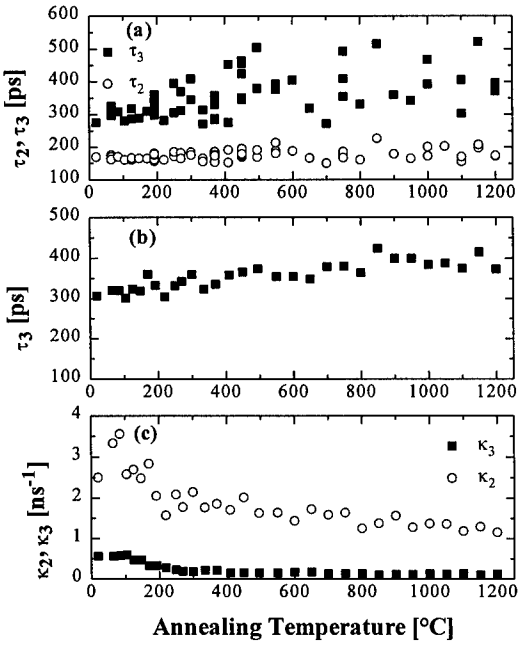


Figure 1: (a) Defect lifetimes τ_2 and τ_3 obtained from free fits for the 6×10^{16} e^-/cm^2 irradiated sample. Multiple entries at each temperature indicate results from repeated measurements. (b) τ_3 obtained from fits with τ_2 fixed at 176 ps. (c) Trapping rates for τ_2 and τ_3 with τ_2 fixed. In (b) and (c) only averaged values from repeated measurements are shown.

DISCUSSION

One feature of the positron data is that a comparatively modest dose of 6×10^{16} e^-/cm^2 results in a total trapping rate (see Table I) of about 3 ns^{-1}, which according to Ref. 3 indicates a vacancy concentration of 3×10^{17} $/cm^3$. Compared to electron irradiation of C (diamond) or Si, vacancies are introduced (at room temperature) much more efficiently in SiC, which seems contradictory to the established radiation-hardness of electrical properties. We propose therefore that the majority of the positron-detected vacancies are not carrier traps. A similar "discrepancy" also emerges when comparing EPR and positron data, although we caution that EPR data were obtained on a 3C-SiC film while we used bulk 6H-SiC. The EPR data indicated that about 10^{17} spins/cm^3 (V_C^+) were created by a dose of 3×10^{18} e^-/cm^2, while the positrons indicate a concentration of V_C^0 (superscript "0" denotes a neutral V_C) of 2.5×10^{17} $/cm^3$ after a dose of 6×10^{16} e^-/cm^2, i.e. EPR detects ~100 times less V_C than does positron annihilation. We do not hold plausible that this discrepancy would simply be a matter of crystallographic differences affecting the introduction of V_C (although differences in impurity content could well play a role), but rather

that EPR only observes a small fraction of V_C being positively charged while positrons observe the dominant and neutral V_C.

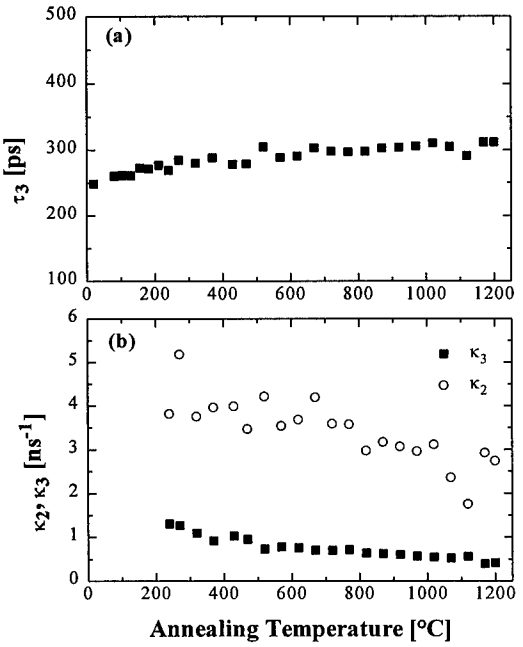


Figure 2: (a) Defect lifetime τ_3 obtained for the 2×10^{17} e^-/cm^2 irradiated sample with τ_2 fixed at 164 ps from free fits. (b) Trapping rates for τ_2 and τ_3. Only above 200 °C was it possible to calculate trapping rates.

The data for the 2×10^{17} e^-/cm^2 irradiated sample supports at least qualitatively the notion of large V_C^0 concentrations. Even though trapping rates can only be calculated above 200 °C (see Fig. 2(b)) comparison with the data in Fig. 1 (c) points to a 3-fold increase of vacancies (both V_C and V_{Si}) in agreement with the increase in dose. This predicts a trapping rate of 9 to 12 ns^{-1} before annealing which indeed would not be possible to measure.

Annealing between 20 and 200 °C occurs for both V_C^0 and V_{Si}^0 and a similar annealing step was observed for V_C^+ and V_{Si}^- by EPR. Nearly 50 % of V_C^0 disappears (Fig. 1(c)) which compares well with the 30 % observed by EPR. We note that an annealing stage situated this close to room temperature would suggest that annealing could occur during the irradiation as well as during storage at room temperature over an extended period of time. Low temperature electron irradiations are clearly called for to ascertain if long-range migration of vacancies takes place at room temperature.

During annealing between room temperature and 1200 °C the τ_2 lifetime is constant, but differs slightly (by 12±3 ps) between the two samples. This may arise from slight differences in the environment of the V_C^0 defects for example as a consequence of trapping by impurities. The

τ_3 lifetime also differs between the two samples (by 50 ps, see Figs. 1 (b) and 2(b)) and increases perceptibly with annealing temperature. It is quite possible that τ_3 should not be viewed as arising from a single defect type (although V_{Si}^0 still would be dominating), but could contain unresolved contributions from larger vacancy clusters such as divacancies. Notwithstanding the possible composite nature of τ_3 it is noteworthy that both τ_2 and τ_3 are constant during the annealing up to 200 °C, during which about 50% of the vacancies disappear. This suggests that vacancy agglomeration is not a dominant process and that the vacancies mainly disappear by means of vacancy-interstitial recombination, possibly from Frenkel-pair recombination.

Annealing up to 700 °C does not reduce perceptively the vacancy concentration, but above ~700 °C there might be an indication therefor (Fig. 2b). This contrasts the total disappearance of V_C^+ at ~700 °C as observed by EPR, which, although the positrons could not observe V_C^+, indicates that V_C^+ and V_C^0 might have different thermal stabilities. Other positron experiments indicate that another significant reduction in positron-detected vacancies first takes place above 1300 °C. [6,7]

CONCLUSION

Positron lifetime experiments have shown that V_C^0 and V_{Si}^0 are introduced at rates much higher than in silicon or diamond. About 50% of these vacancies anneal in the 20-200 °C temperature interval, possibly by Frenkel-pair recombination. Up to the maximum temperature of annealing (1200 °C) some vacancy agglomeration is indicated but the overall concentration of vacancies is nearly constant. At this point it is unclear if vacancies (either V_C or V_{Si} or both) are initially associated - or become associated - with impurities during the annealing.

ACKNOWLEDGEMENTS

This work was supported by the Natural Sciences and Engineering Research Council of Canada.

REFERENCES

1. H. Itoh, M. Yoshikawa, I. Nashiyama, S. Misawa, H. Okumura and S. Yoshida, J. of Electronic Materials **21**, 707 (1991).

2. H. Itoh, M. Yoshikawa, L. Wei, S. Tanigawa, I. Nashiyama, S. Misawa, H. Okumura and S. Yoshida, in Defect Engineering in Semiconductor Growth, Processing and Device Technology, edited by S. Ashok, J. Chevallier, K. Sumino and E. Weber (Mat. Res. Soc. Symp. Proc. 262, Pittsburgh, PA 1992), p. 331

3. S. Dannefaer, D. Craigen and D. Kerr, Phys. Rev. B **51**,1928 (1995).

4. H. Itoh, N. Nayakawa, I. Nashiyama and E. Sakuma, J. Appl. Phys. **66**, 4529 (1989).

5. R.N. West, Adv. Phys. **22**, 263 (1973).

6. A.I. Girka, V.A. Kuleshin, A.D. Mokrushin, E.N. Mokhov, S.V. Suirida and A.V. Shishkin, Sov. Phys. Semicond. **23**, 1337 (1989).

7. W. Puff, A.G. Balogh, P. Mascher and H. Baumann, in Proc. of Intern. Symposium on Materials Science Applications of Ion Beam Techniques, Seeheim, Germany (1996).

DEFECTS IN 4H SILICON CARBIDE CVD EPILAYERS

L. Zhou **, P. Pirouz and J. A. Powell *
Dept. of Materials Science and Engineering, Case Western Reserve University, 10900 Euclid Ave., Cleveland, OH 44106
*NASA Lewis Research Center, 21000 Brookpark Road, MS 77-1, Cleveland, OH 44135
**Now at: Dept. of Materials Science and Engineering, 1304 W. Green St., University of Illinois, Urbana, IL 61801, lingzhou@uiuc.edu*

ABSTRACT

The characteristic defects of 4H-SiC homoepitaxial thin films grown on bulk substrates using chemical vapor deposition (CVD) are described based on transmission electron microscopy (TEM), atomic force microscopy (AFM) and surface decoration studies. Emphasis is placed on understanding the formation mechanism of surface triangular defects. Cross-sectional TEM observations revealed the existence of two variants of 3C-SiC inclusions in 4H epitaxial films. In the plan-view orientation, $\mathbf{g}_{4H} = 3\bar{3}04$ type reflections were found useful for distinguishing the two variants of 3C-SiC platelets that are present in the 4H epilayer. A decoration technique was employed to reveal the relationship between the 3C platelets and surface features, e.g., surface steps. A formation mechanism for surface triangular defects is proposed, which is partially confirmed by the etch pit patterns obtained on the epilayer surfaces after a molten KOH etch.

INTRODUCTION

SiC is currently the most developed wide bandgap material in terms of materials growth. In situ CVD doping is widely used to produce both *n*-type and *p*-type SiC epilayers with desired carrier concentrations. The earlier problem of randomly mixed polytype formation during CVD growth of 6H-SiC has been largely overcome by the use of off-axis substrates promote step-flow and suppress island nucleation of 3C-SiC. Since bulk 4H-SiC became commercially available a few years ago, and because 4H-SiC possesses superior intrinsic properties compared to 6H, a number of groups have tried to grow homoepitaxial 4H-SiC on off-axis substrates [1-5]. Growth experiments have indicated that 4H films are more prone to morphological defects with more pronounced step bunching than 6H surfaces[2,7]. A curious type of large surface defect with triangular shapes was observed on 4H epilayers [2,4-6]. Oxidation experiments indicated that some of the triangles were possibly 3C islands and their formation is probably due to surface damages caused by wafer polishing [5,6].
In this paper, we report preliminary results from a comprehensive study on the dislocation content in 4H CVD epilayers and its link to the surface triangles. A possible formation mechanism for the surface triangles will be discussed, and a method for eliminating them suggested.

EXPERIMENT

The samples were 2-μm thick 4H-SiC films grown homoepitaxially by CVD at NASA Lewis Research Center on off-axis (0001) 4H wafers supplied by Cree Research Inc. The growth process and equipment have been described elsewhere [2,8]. TEM specimens were prepared by

Mat. Res. Soc. Symp. Proc. Vol. 442 © 1997 Materials Research Society

mechanical backthinning and ion milling to electron transparency at room temperature from the substrate side only. Ion milling was performed using 5 kV Ar ions at 1 mA. AFM observations were performed using a Nanoscope III scanning probe microscope working in the contact mode in air at room temperature.

RESULTS

Nomarski differential interference contrast microscopy (NDIC) observation of the as-deposited surface revealed several types of surface triangles. Two representative basal plane surfaces are shown in Figure 1. All of the triangular defects in Sample A (shown in Figure 1*a*) have two equal and curved sides, while those in Sample B (Figure 1*b*) have straight sides. A triangle with the longer side to the left will be called a "left-handed" triangle subsequently. In addition to left-handed triangles, right-handed triangles appear with almost equal frequency on the surface of Sample B. Somewhat less numerous are isosceles triangles which are not in the field of view in Figure 1*b* (there is one in Fig.6). A triangle on the surfaces of either samples is always oriented in such a way that one of the three corners—referred to as "apex"—is pointed up-step; the side which is parallel to the surface steps will be referred to as the "base". It should be pointed out that both of the sample surfaces have an off-axis angle of about 2.5 degrees toward the $[11\bar{2}0]$ direction, and therefore the step edges are parallel to $[\bar{1}100]$. A feature common to both samples is that the distance from apex to base is the same for all triangles on the same surface. The epilayer thickness can be calculated easily from the size of the triangles [2], and this suggest that they are not formed randomly during growth.

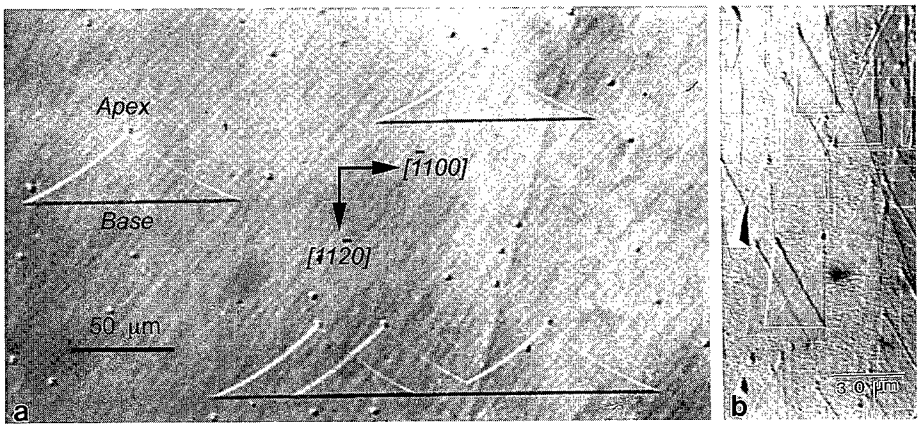


Fig.1. NDIC micrograph of triangular surface defects in ***a***. Sample A (left), ***b***. Sample B

AFM studies revealed that the base of a triangle is a large, bunched-up, step 10-15 nm in height (Figure 2*a*). The "nodule" which can be seen on the tip of every triangle on Sample A is a double depression, which initiated the step bunching (Figure 2*b*). The other two sides bounding a triangle are steep, bunched-up steps on Sample A. Despite a similar appearance on NDIC micrographs, the sides of a triangle on Sample B are only gentle uplifts. It will become clear later that the sides of a triangle on Samples A and B are formed through different mechanisms.

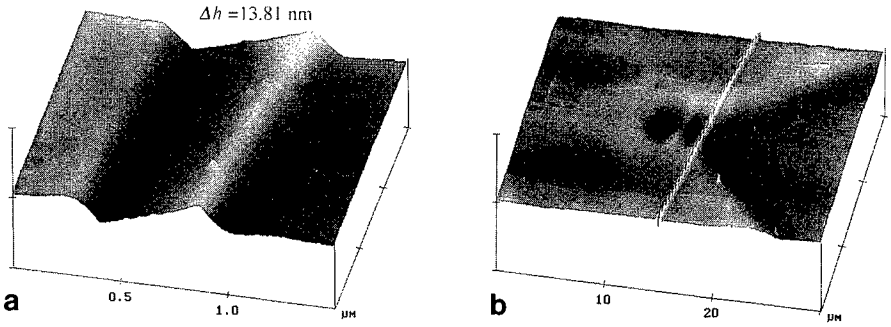


Fig.2. AFM images: ***a***. bunched steps at triangle base (left); ***b***. double depression at triangle apex.

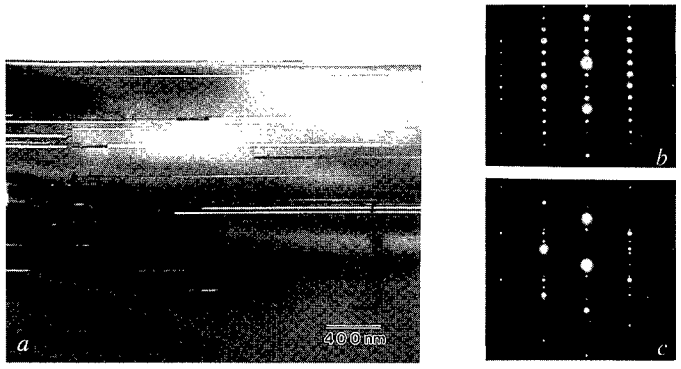


Fig.3. ***a***. BF TEM micrograph of 3C platelets (20-50 nm thick) in the 4H epilayer. The beam direction is $[11\bar{2}0]$; ***b***. SADP of the 4H matrix; ***c***. SADP of the epilayer containing 3C platelets.

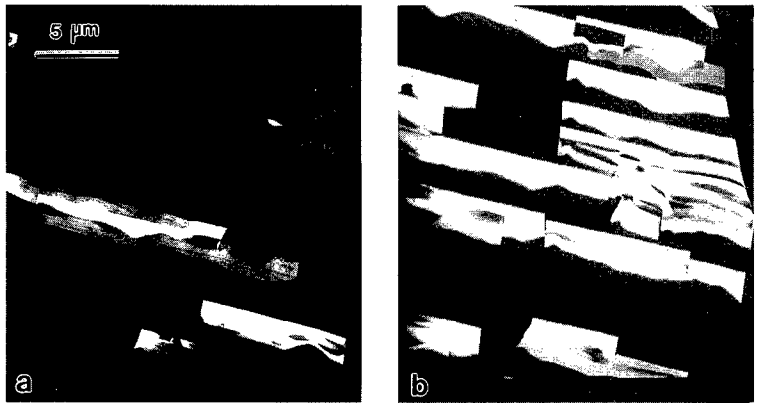


Fig.4. DF TEM images of 3C platelets in plan-view direction ***a.*** variant 1 (left); ***b.*** variant 2.

Only Sample B contained defects of sufficient density that allowed consistent TEM observations. Cross-sectional studies, i.e., imaging with the beam direction within $\pm 30°$ to the $[11\bar{2}0]$ zone-axis, showed existence of both basal plane stacking faults and 3C platelets of various thickness within the 4H epilayer. An on-zone bright-field (BF) micrograph is shown along with two selected area diffraction patterns (SADP) in Figure 3. Figure 3*b* is a SADP obtained from the defect-free 4H-SiC substrate, whereas Figure 3*c* is obtained from the faulted region in the epilayer which revealed two variants of 3C-SiC in syntaxy with the 4H matrix. The orientation relationships for variant 1 is $(1\bar{1}1)_{3C}$ // $(0001)_{4H}$, $[110]_{3C}$ // $[11\bar{2}0]_{4H}$; and $(1\bar{1}1)_{3C}$ // $(0001)_{4H}$, $[110]_{3C}$ // $[2\bar{1}\bar{1}0]_{4H}$ for variant 2. Plan-view studies on triangular areas in Sample A showed no structural defects or inclusions of other polytypes, which is consistent with results obtained from micro-Raman spectroscopy (μRS) [9]. Since 3C platelets were found in Sample B during the cross-sectional study, it would be informative to know their distribution from a plan-view direction. A diffraction intensity calculation was carried out for various reflections accessible under TEM when the SiC sample was in the near plan-view orientation [9]. The imaging vector, **g**, which maximizes the contrast between the 3C platelets and the 4H matrix was found to be a $\mathbf{g}_{4H} = 3\bar{3}04$ type which allows one of the $\mathbf{g}_{3C} = 11\bar{1}$ reflections to be operative also, thus giving a ratio of 5:1 of the extinction distance of 4H:3C. Figures 4*a* and 4*b* are two dark-field (DF) micrographs from the same area showing the two complimentary variants of 3C platelets. The length of these 3C platelets, which was typically about 8-10 μm, matches the average length of triangle bases. All the above observations suggested that the 3C platelets are related to the surface triangles. In order to confirm this, a surface decoration technique was used to deposit fine copper debris onto the TEM specimen during ion-milling. It was found that the shape of the platelets exactly matches the contours of the surface steps outlined by the copper debris, and that surface steps stop at where the platelets terminate [Figure 5].

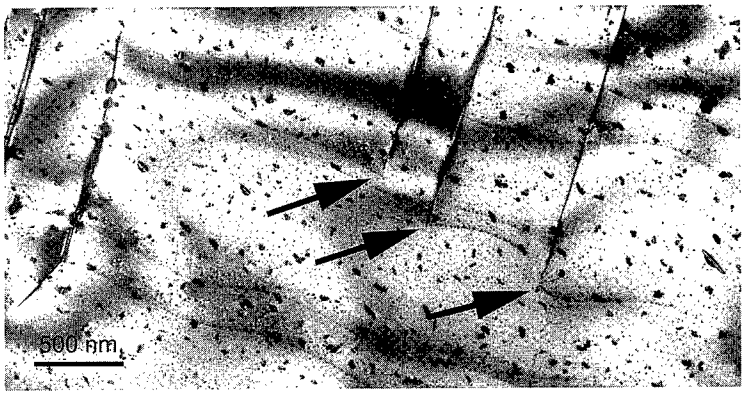


Fig.5. Decoration of surface steps by copper debris (BF TEM micrograph). The steps begin at the 3C/4H boundaries as indicated by the arrows.

DISCUSSION

TEM observations suggest that the two variants of 3C platelets are the result of a partial transformation of the 4H matrix . Further tilting experiments allowed us to find dislocation loops

which were physically connected to multiple 3C plates, and they were found to have an edge character in their vertical (parallel to [0001]) sections. In addition, no screw dislocations with a line direction close to [0001] were found inside the film, while prismatic stacking faults similar to those observed in martensitic transformations in other polytypic structures were observed. All these features support a solid state phase transformation model [10].

The link between these subsurface defects and surface triangles were clearly revealed by the combination of diffraction imaging of 3C platelets in a near-[0001] zone-axis direction and surface decoration. Also, the observed average size of subsurface defects using TEM matches that obtained for surface defects using NDIC, SEM and AFM imaging [9]. Therefore, this work provides strong evidence that surface triangles have a dislocation origin. It is a reasonable assumption that there will be dislocations located near the surface of the substrate before thin film deposition. They might have formed during bulk growth, or generated during the cutting, grinding and polishing process. Since the Peierls valleys in α-SiC are along the $\langle 11\bar{2}0\rangle$ directions, the partial components of a dissociated dislocation intersecting a step edge are likely to lie in one set of these valleys. One such set of valleys lies perpendicular to the step edges since the step flow direction is $[11\bar{2}0]$. Energetic considerations favor the rotation of these partial dislocations such that their line direction will no longer be perpendicular to the step edge [11]. During the subsequent deposition, these dislocations will be replicated and, depending on the angles formed between their lines, they can either be constricted or spread out and form triangular regions. Our experimental results show that in fact these dislocations will lead to 4H→3C solid state transformations under appropriate conditions.

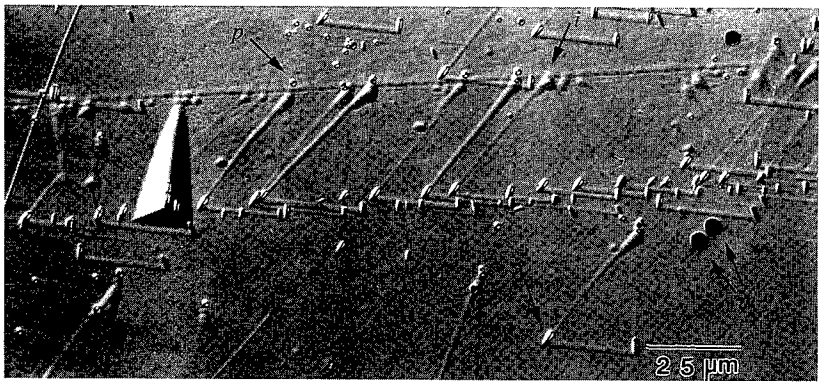


Fig.6. A region of Sample B after a molten KOH etch. (***i***). The apex of an isosceles triangle; (***p***). a pit due to a perfect dislocation discussed in the model; (s) one of the two pits formed due to a partial pair; (m) pits due to micropipes.

The most convincing evidence in support of this model comes from a molten KOH etching experiment. Figure 6 shows an area on Sample B after etching. Dislocation etch pits can be found at the positions discussed in the model: the partials pairs are located at the ends of the triangle base, and their progenitor—the perfect dislocation—leaves a small circular pit near the apex of the triangles. This image also shows that triangles are clustered around a scratch, in direct support of the hypothesis that process-induced dislocations were responsible for their formation. Etching results from Sample A showed no pits at the triangle base, an indication that the majority of the triangles (with curved sides) are purely due to step bunching.

CONCLUSIONS

The current work provids strong evidence that both variants of 3C can be formed from in a 4H epilayer by a solid state phase transformation mechanism. The 3C inclusions observed on the surface can be initiated by solid state phase transformation, in addition to the 2D-nucleation mechanism proposed by others [5]. This mechanism clearly shows why sometimes only the base of the triangles appear to be 3C in oxidation experiments [6], an observation that the 2D-nucleation mechanism can not adequately explain. This model also offers an explanation for the absence of such defects in 6H-SiC: since step bunching is less severe, it is less likely that dislocations will intersect the vertical riser of a step and propagate during growth. Our investigation further pointed to unremoved surface damage as the source of dislocations which then lead to surface triangles during growth. The result of this investigation has provided us with the motivation for using chemomechanical polishing to substitute the current mechanical polishing used in wafer production [12].

ACKNOWLEDGMENTS

This work was supported by grant #NAG3-1702 from NASA.

REFERENCES

[1] A. Itoh, H. Akita, T. Kimoto and H. Matsunami, Appl. Phys. Lett. **65**(11), 1400 (1994).
[2] J.A. Powell, D.J. Larkin and P.B. Abel, J. Elec. Mater. **24**(4), 295 (1995).
[3] O. Kordina, A. Henry, J.P. Bergman, N.T. Son, W.M. Chen, C. Hallin and E. Janzen, Appl. Phys. Lett. **66**(11), 1373 (1995).
[4] V.F. Tsvetkov, S.T. Allen, H.S. Kong and C.H. Carter Jr., Inst. Phys. Conf. Ser. **142**,17 (1996).
[5] C. Hallin, A.O. Konstantinov, O. Kordina and E. Janzen, Inst. Phys. Conf. Ser. **142**, 85 (1996).
[6] J.A. Powell, D.J. Larkin and P.B. Abel, Inst. Phys. Conf. Ser. **142**, 77(1996).
[7] T. Kimoto and H. Matsunami, J. Appl. Phys. **75**, 850 (1994)
[8] J.A. Powell, L.G. Matus and M.A. Kuczmarski, J. Electrochem. Soc. **134**, 1558 (1987)
[9] L. Zhou, M.S. Thesis, Case Western Reserve University, (1996).
[10] P. Pirouz, Inst. Phys. Conf. Ser. **104**, 49 (1989)
[11] R. Gevers, S. Amelinckx. and P. Delavignette, Phil. Mag. **6**, 1515 (1961)
[12] L. Zhou, V. Audueir, P. Pirouz and J.A. Powell, *to be published.*

THEORY OF $3d$ TRANSITION METAL DEFECTS IN 3C SiC

HARALD OVERHOF
Fachbereich Physik, Universität-GH Paderborn, D-33098 Paderborn, Federal Republic of Germany
E-mail: fover1@pbhrzc.uni-paderborn.de

ABSTRACT

The electronic properties of $3d$ transition metal (TM) defects located on one of the four different tetrahedral positions in 3C SiC are shown to be quite site-dependent. We explain the differences for the $3d$ TMs on the two substitutional sites within the vacancy model: the difference of the electronic structure between the carbon vacancy V_C and the silicon vacancy V_{Si} is responsible for the differences of the $3d$ TMs. The electronic properties of $3d$ TMs on the two tetrahedral interstitial sites differ even more: the TMs surrounded tetrahedrally by four Si atoms experience a large crystal field splitting while the tetrahedral C environment does not give rise to a significant crystal field splitting at all. It is only in the latter case that high-spin configurations are predicted.

INTRODUCTION

The electronic properties of the $3d$ transition metal (TM) impurities in silicon have successfully been explained within the model of Ludwig and Woodbury [1] who predicted high-spin ground states both for interstitial and substitutional TMs in Si. The model has been challenged by Beeler et al.[2] who showed that for some of the early interstitial and late substitutional TMs a low-spin ground state is observed. Discrepancies between theoretical results and the Ludwig-Woodbury model, however, have been predicted by Beeler *et al.* for those TMs only, for which experimentally the spin of the ground state has been and still is unknown.

Cubic (3C) SiC is isoelectronic to Si and crystallizes in the zinc-blende structure which is the analog to the diamond crystal structure for a compound semiconductor. Although both constituents of the SiC lattice are group IV elements, several properties of the SiC crystal are more common to an ionic compound than for a covalent semiconductor. It therefore appeared interesting to theoretically investigate the electronic properties of $3d$ TM impurities located on the different high-symmetry positions in the SiC lattice by means of an *ab-initio* method. In this paper we shall discuss the single particle energies of all $3d$ TMs as substitutional defects substituting for carbon (TM_C)and for silicon (TM_{Si}). We shall also discuss as typical examples the Sc and Fe TMs as interstitial point defects on the highly symmetrical sites where the TMs are tetrahedrally surrounded by four carbon (TM_{TC} in the notation of Wang *et al.* [3]) or by four silicon (TM_{TSi}) ligands.

COMPUTATIONAL

Our calculations have been performed using the standard Local Spin-Density Approximation of the Density Functional Theory (LSDA-DFT) for the inclusion of exchange and correlation effects. We have used a self-consistent Greens-function based on the Linear Muffin-Tin-Orbitals (LMTO) method in the Atomic-Sphere approximation (ASA) [4]. In the LMTO-ASA method the crystal is represented by overlapping spheres centered around the atomic sites ("atomic spheres"). In order to fill the space without too much overlap one further introduces spheres which are centered around the tetrahedral interstitial TM_{TC} and TM_{TSi} ("empty")sites. The application of this method to $3d$ TM defects in Si has been described by Beeler *el al.* [2].

When this method is applied to cubic SiC the major change with respect to the Si case

Mat. Res. Soc. Symp. Proc. Vol. 442 © 1997 Materials Research Society

stems from the fact that the lattice is made up from two different atoms, C and Si, with quite different covalent radii and ionicities. If we use the same radius (the Wigner-Seitz radius) for all atomic and empty sites we end up with Si atomic spheres that contain two valence electrons only, while the C atomic sphere contains 4.3 electrons. Fixing the sphere radii in such a way that the number of valence electrons contained in the Si and C sphere are nearly equal we would end up with a C atomic sphere volume that is only 1/3 of that of the Si atomic sphere. Such a small atomic sphere presents severe problems for $3d$ TM defects substituting for C: we have to divide the electron states into core states of the inner s and p shells and into valence states in our approach. This cannot be done properly unless the core states fit into the atomic spheres. With the very small C atomic sphere and with the lighter $3d$ TM elements this is not the case.

We, therefore, have taken the atomic sphere radii as 2.14 r_B and 1.885 r_B, respectively which results in 2.37 (3.88) valence electrons in the Si (C) atomic sphere. The rest of the valence charge is found in the larger TC (1.14 unit charges) and the smaller TSi atomic sphere (0.60 unit charges). We have further made use of the scissors operator technique by Baraff and Schlüter [5] in order to adjust the LDA fundamental bandgap for cubic SiC (1.3 eV) to the experimental value of 2.3 eV.

RESULTS

Substitutional TMs on a Si site

The single particle energies for a Sc atom in a d^3 configuration, a hypothetical spinless Fe atom in a d^8 configuration, a silicon vacancy Vac_{Si} and the substitutional Sc_{Si} and Fe_{Si} point defects are are displayed in Fig. 1. As has been demonstrated by Zunger [6] and also bei Beeler et al. [2] the electronic states of substitutional $3d$ TM defects can be understood in the simple vacancy model where the electronic states of the $3d$ TM interact with the vacancy that must be generated prior to the incorporation of the substitutional TM. For the silicon vacancy Vac_{Si} the dangling bond states that transform according to the t_2 irreducible representation are located in the lower half of the fundamental band gap (the state that transforms according to a_1 gives rise to a resonance just below the valence band edge). The $3d$ states are split by the crystal field into states that transform according to the e and the t_2 irreducible representations, respectively. For

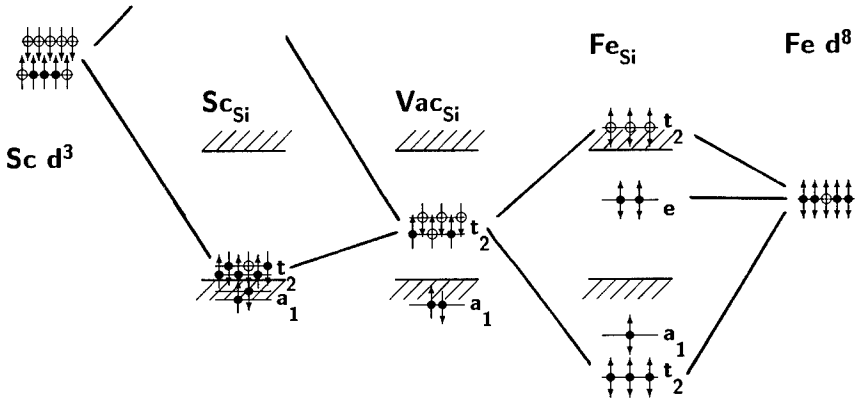
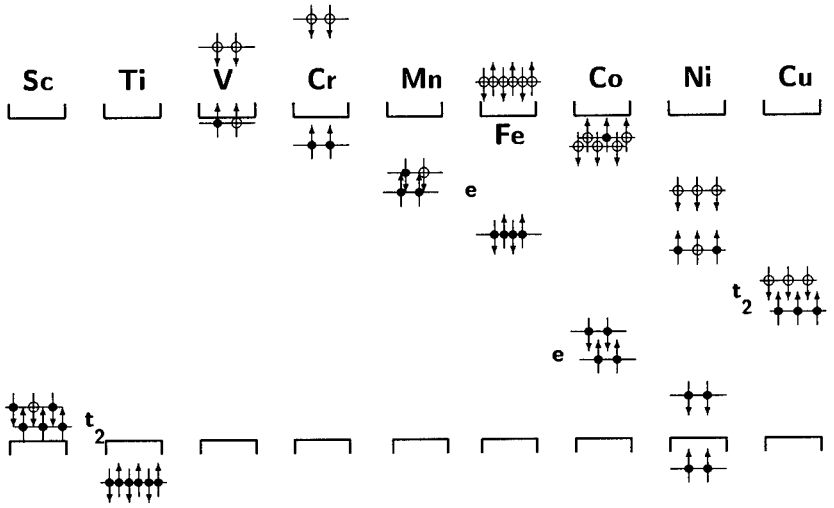


Figure 1: Single particle energies for Sc (left), a hypothetical spinless Fe atom (right), and a carbon vacancy Vac_{Si} (center) in comparison with the Sc_{Si} and Fe_{Si} point defects

Figure 2: Single particle energies for the neutral substitutional $3d$ TM ions on a Si lattice site in the ground states which are the low-spin states.

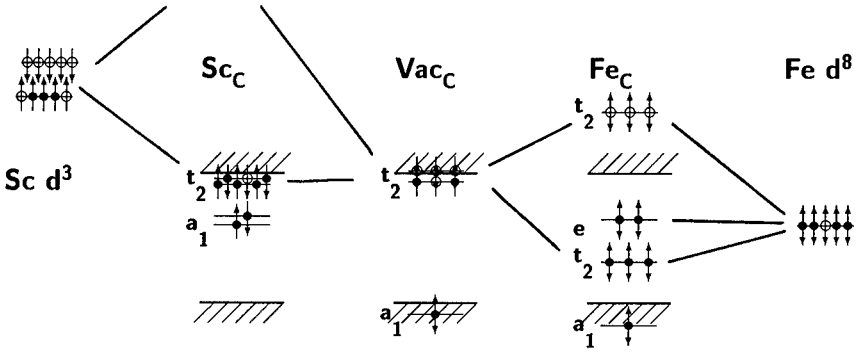


the e-like states there are no vacancy orbitals to interact with. These states, therefore, mark the energetic position of the "undisturbed" d-levels. For Sc, however, the d-states are only loosely bound and, therefore, the e-like states are resonances above the conduction band edge which are hardly resolved at all. Only for $3d$ TMs that are heavier than vanadium the e-like states form localized states in the gap. The d-states that transform according to t_2 interact with the dangling-bond states and form bonding and anti-bonding states. For Sc the larger energetic distance from the bonding t_2 states to the TM-derived d-states as compared to the distance to the t_2 states of the Vac_{Si} ensures that the t_2 of the TM defect Sc_{Si} are essentially dangling-bond like with ($\sim$ 12 %) d-admixture. Since the p-like spin density is with $\sim$ 4% only a factor of three smaller than the d-like spin density, the dipolar hyperfine coupling for Sc_{Si} stems predominantly from the p-like dangling bonds and is similar to the dipolar coupling of the Vac_{Si} vacancy states. The antibonding states that transform according to t_2 are resonances that are situated in the lower conduction band. These resonances are more d-like in character.

If we replace Sc $3d^3$ by Fe in a $3d^8$ state the d-states are significantly lower in energy. The states that transform according to the e irreducible representation are now situated in the fundamental band gap, the bonding t_2 states are resonances in the upper valence band, while the anti-bonding states are resonances in the lower conduction bands. Note the large energetic splitting between bonding and anti-bonding states which is much larger than the fundamental band gap. Since for the substitutional Fe the single particle energies of the t_2-like dangling bond states and the atomic $3d$-states virtually coincide, both occupied bonding and unoccupied anti-bonding t_2 states have essentially a mixed character: the bonding states show a strong d-admixture, however the dangling-bond character is still dominant.

For the iron substitutional Fe_{Si} point defect the crystal field splitting exceeds by far the exchange splitting. As a result the state is spinless. We show in Fig. 2 the single particle energies of the gap states for all $3d$ substitutional TMs on a Si lattice site in the neutral charge state. We find that for all TMs the ground state is a low-spin state. In some cases (Mn_{Si}, Fe_{Si},

Figure 3: Single particle energies for Sc (left), a hypothetical spinless Fe atom (right), and a carbon vacancy Vac_C (center) in comparison with the Sc_C and Fe_C point defects



Co_{Si}, and Ni_{Si} the states that transform according to e ant to t_2 are both localized states in the gap. It is only in these cases that a high-spin configuration could be possible. We find, however, that in the case of Mn_{Si} and Ni_{Si} the total energy of the low-spin configuration is lower by 0.8 eV as compared to the total energy of the high-spin state. For Fe_{Si} and for Co_{Si} this difference is reduced to 0.2 eV, but still the low-spin configuration is the ground state according to our calculations.

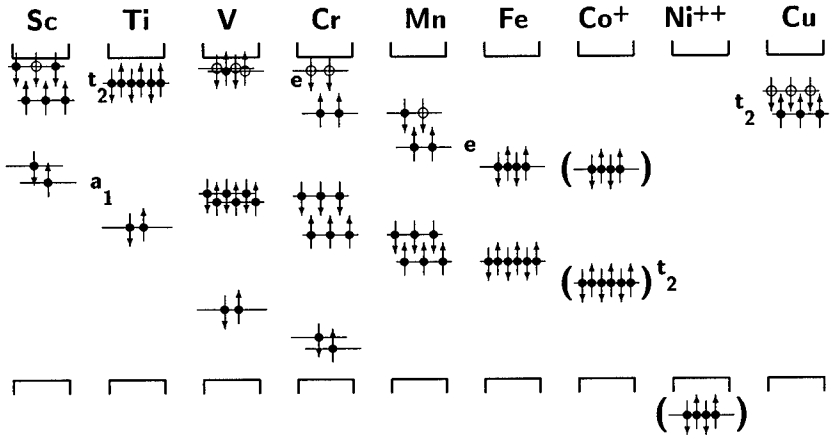
If we compare our results in Fig. 2 for cubic SiC with the results of Beeler et al. [2] Fig. 17 obtained for Si we find a general similarity in spite of the fact that the fundamental band gaps for both crystals differ by a factor of two. In cubic SiC the d-states systematically are located at higher energies with respect to the center of the gap. Furthermore, the energetic differences between the analogous electronic states for different TM ions are significantly larger compared to substitutional TMs in Si if one follows the $3d$ TM series from Sc to Cu. This observation also holds if we scale the energetic differences with the respective fundamental band gaps.

Substitutional TMs on a C site

For the $3d$ TMs on the carbon lattice site the electronic structure of the C vacancy leads to remarkable differences: The dangling bond states of the carbon vacancy Vac_C (see Fig. 3) give rise to localized gap states that transform according to the a_1 (fully occupied) and the t_2 irreducible representations and these states are located in the upper half of the fundamental band gap. As in the case of Vac_{Si} the t_2 states are only partially occupied. We, therefore, expect that the neutral carbon vacancy will show a static Jahn-Teller distortion. Since the energetic position of the t_2 states of Vac_C is close to the conduction band edge, for most TMs these dangling band states will be higher in energy than the TM-derived d-states.

This has of course the consequence that the bonding t_2 states of the substitutional TM on a carbon site will be predominantly d-like with little resemblance to dangling bonds. Even for Sc_C the t_2-like bonding gap state shows a 40 % d-admixture. Hence the dipolar hyperfine interaction of Sc_C is due to the d-like spin density. Comparing the dipolar hyperfine interactions of the Sc_{Si} and Sc_C point defects we find that both dipolar interactions with the Sc nucleus are comparable: Experimentally [7] however it is known that the paramagnetic state observed in 6H SiC is due to a Sc_C point defect and only for this configuration do calculated and experimental

Figure 4: Single particle energies for the neutral substitutional $3d$ TM ions on a carbon lattice site. For Co and Ni no neutral charge state is possible.



results agree for the ligand hyperfine interaction.

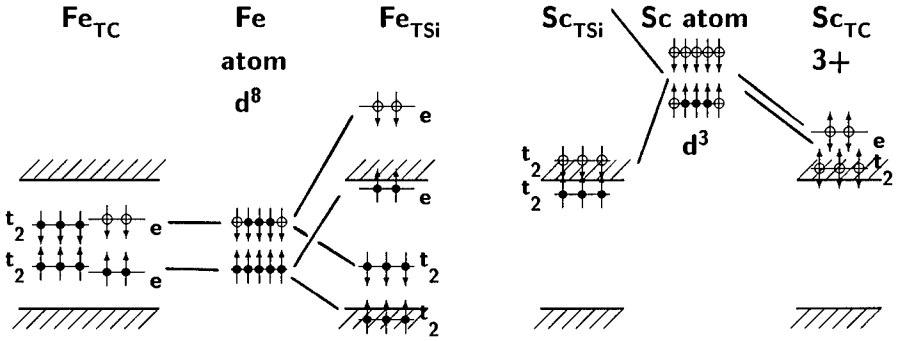
We show in Fig. 4 the single particle states for the full sequence of the $3d$ TMs on a carbon lattice site. These defect states differ from the corresponding TM states on a silicon site with respect of the higher energy position of all states which is explained by the energy position of the corresponding vacancy. The bonding t_2-like state remains a localized gap state until we reach Ni. In perfect agreement with the predictions of the vacancy model the energetic positions of the gap states that transform according to the e irreducible representation for the TM_C point defect virtually coincide with the energies of the corresponding states for TM_{Si}. The bond strength of the TM on a C site is comparable to that of a TM on a Si site and, therefore, the bonding-anti-bonding splitting of the two sets of t_2 states is hardly reduced. This is the reason why the anti-bonding t_2 states are located at higher energies and do not enter the gap before we reach Cu. This is also the reason why we do not obtain neutral charge states for the Co_C and Ni_C point defects. It further gives rise to the fact that we cannot even find the states that would be required to have any of the $3d$ TMs in a high-spin state except for V_C. Only for this TM a high-spin configuration is possible, the total energy of this state, however, is by 0.5 eV higher than that of the low-spin ground state.

Interstitial TM

For interstitial point defects there are two distinct highly symmetrical tetrahedral positions in the zinc-blende lattice. In the TC position the interstitial TM in has relatively much space because it is surrounded tetrahedrally by the four small carbon atoms. Note, however, that this TM is also surrounded by six relatively large silicon atoms which, although somewhat farther apart, nearly balance the crystal field of the nearest neighbors. The crystal field splitting in this case is very small and we have a high-spin ground state for Fe_{TC} shown in Fig. 5. This high-spin ground state is consistently found for all $3d$ TM_{TC} defects in all the charge states investigated thus far.

For the TSi position of the TM interstitials the nearest neighbors are the rather large Si

Figure 5: Single particle energies for the neutral Fe and Sc impurities on the higly symmetrical TSi and TC interstitial positions in comparison with the respective atomic levels.



atoms which give rise to a large crystal field splitting which is not significantly reduced by the smaller and more distant carbon next nearest neighbors. Consequently the interstitials at the TSi positions have a low-spin ground state (which for Fe interstitials leads to the same single particle occupancy than the high-spin state).

CONCLUSIONS

Our numerical results from numerical *ab-initio* Greens-function calculations for the substitutional TMs can be understood by the simple orbital interaction picture where the dangling bond orbital of the respective vacancy interact (with the t_2-like) d-states of the TM. We find that the differences between TM_{Si} and TM_C point defects originates from the different energetic positions of the t_2 -like dangling bond states of the two vacancies. We find for all substitutional TMs and also for the TC interstitials that the ground state is a low-spin state. The reverse is true for the TSi interstitials: here the crystal fields of the nearby Si and next nearest C neighbors virtually cancel. The exchange splitting, therefore, leads to a high-spin ground state.

REFERENCES

1. G.W. Ludwig and H.H. Woodbury, in Solid State Physics, ed. by H. Ehrenreich, F. Seitz, and D. Turnbull (Academic Press, New York, 1962), Vol. 13, p. 223.
2. F. Beeler, O.K. Andersen, and M. Scheffler, Phys. Rev. B **41**, 1603, (1990).
3. C. Wang, J. Bernholc, and R.F Davis, Phys. Rev. B **38**, 12 752, (1988).
4. O. Gunnarsson, O. Jepsen, and O.K. Andersen, Phys. Rev. B **27**, 7144, (1983).
5. G. A. Baraff and M. Schlüter, Phys. Rev. B **30**, 3460, (1984).
6. A. Zunger, in in Solid State Physics, ed. by H. Ehrenreich, F. Seitz, and D. Turnbull (Academic Press, New York, 1986), Vol. 39, p. 275.
7. M. März, J. Reinke, S. Greulich-Weber, J.-M. Spaeth, H. Overhof, E.N. Mokhov, A.D. Roenkov, and E.N. Kalabukhova, Semic. Science and Technol. **98**, 439, (1996).

IMAGING OF MICROPIPES IN SILICON CARBIDE UNDER HIGH FIELD STRESS

G. GRADINARU, M. HELMI, Y. KHLEBNIKOV, G. KORONY, W. C. MITCHEL*, and T. S. SUDARSHAN
ECE Department, University of South Carolina, Columbia, SC 29208, sudarsha@ece.sc.edu
* Wright-Patterson AFB, WL/MLPO Bldg. 651, 3005 P st Ste 6, OH 45433-7707

ABSTRACT

A new technique for investigation of the electrical effects of micropipes in single-crystal 6H-SiC is presented. The setup allows the application of a parallel or normal electric field to MSM (metal-semiconductor-metal) test structures and the visualization of light emission sites in the test gap, including light activity underneath the metal contact. A special transparent metal [indium-tin-oxide(ITO)] was chosen for the metallic contacts. A map of micropipe locations was initially obtained at zero applied field using a laser scattering method. The initial map is compared with that of light emissions at different applied fields.

Several tests on undoped and vanadium-doped (compensated) SiC, using NiCr/Au or ITO contacts, indicated the rapid activation of micropipes at relatively low fields in vertical MSM devices. A good match between the laser imaging map of micropipes at zero field and the map of field-induced light emission sites indicates that micropipes are the main current paths in vertical devices, carrying a large current density, and leading to light emissions and partial or total bulk breakdown of the test device.

INTRODUCTION

Silicon carbide boules and the resulting substrates and epitaxial layers have a high density of defects - both classical crystallographic defects and micropipes - diminishing device performance [1-3]. Premature breakdown phenomena with damaging effects were observed in high voltage SiC based pn junction diodes due to lateral or edge breakdown [4,5]. Large leakage currents and premature reverse failure, due, especially, to micropipes in SiC material, limit severely the device areas to $\leq 1 mm^2$, even though high voltage/high power devices require much larger areas.

Considerable effort is underway in the field of material (SiC) growth technology in order to minimize the density of micropipes and other defects. New and, if possibly, non-destructive methods to determine the location and density of micropipes, are necessary. At the same time, reliable and efficient characterization methods, able to evaluate the electrical effects of micropipes at high applied fields in different conditions, should be developed.

A new electrical method to investigate the quality of SiC material, especially the preflashover and surface flashover [6] properties and the electrical effects of micropipes, namely the high field (HF) characterization method, was presented by the USC group in Ref. [7]. In this paper, an improvement of the HF characterization method in order to study, along with electrical effects, the light emission from micropipes, especially those located under the metallic contact in vertical devices, is presented. At the same time, a nondestructive method, to map micropipes at zero field, is proposed. The correlation of the zero field micropipe maps with field-induced light emission maps and the corresponding electrical characteristics of test devices at high fields is discussed.

EXPERIMENTAL

The material investigated in this work was high resistivity 6H-SiC grown in boules at Westinghouse (now Northrop Grumman) in the 1992-1994 period. Undoped and vanadium-doped 6H-SiC single crystals, <0001> oriented, were grown by the physical vapor transport (PVT) method [8]. Two types of undoped [~1 kΩcm(A) and ~5 kΩcm(B)] and one type of vanadium-doped material [>50 kΩcm(C)] were tested. Note that the density of micropipes was not measured, but a 200 to 800 cm^{-2} was typical for the growth processes used in the mentioned period.

The substrate wafers were cut into several rectangular (5 mm x 10 mm) samples, having ~450 μm thickness and the Si face mirror polished in all cases. Lateral and vertical test structures (separated or combined) (Fig. 1) were fabricated using normal metallic contacts (NiCr/Au) or transparent contacts (ITO). The normal metallic contacts were produced by in situ high temperature (300 °C) sputter deposition of a 600 Å NiCr mixture, followed by evaporation of a 1000 Å Au layer at the same temperature.

Transparent contacts were produced by depositing indium tin oxide (ITO) thin films using RF magnetron sputtering technique. Fairly good results, in terms of optical transparency, electrical conductivity, and mechanical resistance, were obtained with 35-50 W RF power, 150 °C substrate temperature, and 5 mtorr Ar pressure.

Mat. Res. Soc. Symp. Proc. Vol. 442 © 1997 Materials Research Society

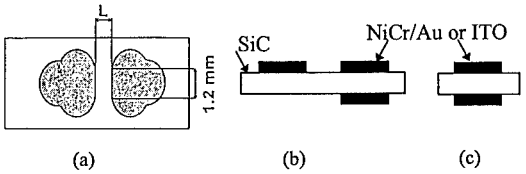


Fig. 1. (a) Top view of the lateral device geometry; (b) combined lateral and vertical SiC-MSM structures; and (c) a separate vertical device.

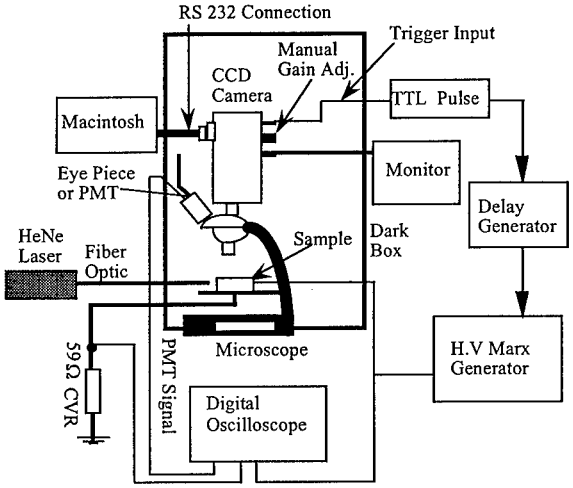


Fig. 2. Experimental setup of the high field characterization method with enhanced imaging capabilities.

All lateral MSM devices have rounded contacts in order to reduce field enhancement effects and a gap of 0.6-0.7 (Fig. 1a). Vertical test structures were fabricated combined with lateral ones (Fig. 1b) or separately. For vertical devices the gap length is equal to the thickness of the wafer (~450 μm) and the cross-sectional area for the current transport was taken as the area of of the contacts.

For devices with non-transparent (NiCr/Au) contacts, we have used our HF characterization method as presented in Ref. [7]. The tests were performed at room temperature in certain dielectric ambients, namely vacuum (~10^{-6} torr), SF_6 (1.5 atm) and air (1 atm). The applied voltage is a double-exponential pulse with 0.39 μs rise time and ~3 μs FWHM in a 0.5-100 kV range and 0.2 kV steps. The test system incorporates advanced optical diagnostics (photomultiplier tubes in UV, visible, and IR ranges and ICCD camera), computer data acquisition interfaces, and a microprocessor-based control circuit. The response of the MSM test structure to the applied HV pulse is obtained by analyzing the time-resolved (nanosecond scale) characteristics of voltage, current, and light emissions.

The setup was modified in order to obtain the visualization of emission sites located under the (transparent) contact in vertical devices. The CCD camera and the PMT (visible-range) were mounted on a modified microscope base and placed in a dark box (Fig. 2). All tests in this box were performed in air. The gating of the CCD guaranteed image acquisition during the period that the voltage pulse was applied to the device under test. The emission sites presented in the images, recorded by the CCD camera, are compared with a map of structural defects and micropipes obtained at zero field by optical methods.

Initially, a CCD image (map) of structural defects is obtained using a simple back illumination (visible light) of the structure. A laser scattering method is used in this work to obtain a map of micropipes in the SiC device (in the gap area for lateral device and contact area for vertical devices). A laser beam provides an incident light with a wavelength smaller than the range of diameters of micropipes in SiC (1-100 μm), penetrating the SiC sample from the side, i.e. the laser beam's direction is perpendicular to the side plane of the sample (Fig. 2). Bright (reddish) spots of light were observed only on certain sites of the device surface. We conclude, based on the results presented below, that these bright sites correspond to micropipe locations.

RESULTS

The electrical results on lateral and vertical MSM SiC devices with NiCr/Au contacts were presented in Ref. [7]. While in lateral devices the response is ohmic and the current density (J_L) corresponds to the nominal resistivity of the device up to high fields in the prebreakdown stage, in vertical devices the current density (J_V) significantly and randomly increases (up to 2000 times) for the same applied field, starting at relatively low fields (5-

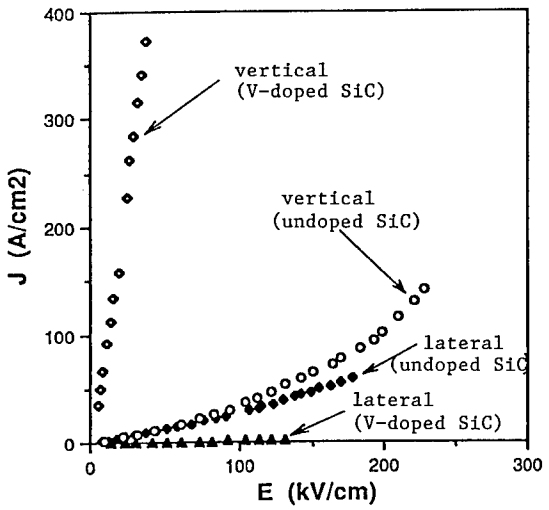


Fig. 3. Comparison between current density-electric field (J-E) characteristics in SF_6 ambient for lateral and vertical SiC-MSM devices with NiCr/Au contacts.

20 kV/cm). In lateral devices the breakdown is produced by surface flashover [6, 9] at relatively large fields (150-180 kV/cm) in vacuum and SF_6, with no defect activation or surface filamentation [10] in the prebreakdown stage. However, in most vertical MSM devices, bulk breakdown is produced at very low fields (15-50 kV/cm) compared with the large intrinsic breakdown field of SiC. It is important to note that in only one out of six tested devices, a vertical MSM device of ~1kΩcm undoped SiC supported more than 225 kV/cm without breakdown and showed nominal current density up to large fields. Figure 3 shows a comparison of J-E characteristics between vertical and lateral devices, including one frequent case ($J_V >> J_L$) and the exception case ($J_V \sim J_L$).

The electrical characteristics of lateral and vertical devices with ITO contacts were similar to those obtained on devices with NiCr/Au contacts, as briefly described above. Let us now focus on micropipe effects.

The large increase of current density, along with the reduction of the bulk breakdown field of vertical devices, were correlated with light emission sites appearing on the (transparent) contact face of the device under stress, which is supposed to match the sites of the main paths of the current in the vertical MSM structure. At the same time, the map of field-induced light emission sites can be analyzed by comparison with the map of structural defects, including micropipes, obtained at zero applied field using the laser scattering method. Due to limited space, only one example will be presented here, for a vertical device of undoped SiC type B.

A reference image (Fig. 4a), obtained using back illumination, shows different structural defects (darker spots) in the material (the contour of the ITO contact is shown by a fine solid line). In Fig. 4b a map of defects, including micropipes, obtained by our laser scattering method, is presented. The location of bright spots exactly coincide with the areas of structural defects shown in Fig. 4a. Note that only small zones are very bright in the map shown in Fig. 4b, indicating that the structural defects zones are not uniformly transmitting the light from the incident transversal laser beam. In fact, this can be proved by slightly changing the incident angle of the laser beam, resulting in small discrete bright sites (Fig. 4c) which cluster in the area of structural defects shown in Fig. 4a. There are reasons to believe that the discrete light emitting sites correspond to micropipe terminations on the device surface.

Under the electric field stress, at low voltages, the electric response is essentially ohmic, with no visible light emission that can be observed using PMT or CCD camera. However, when the current response begins to increase suddenly and significantly, a clear light emission is recorded. For example, using the above noted device of type B material, no light emission was observed up to 22.5 kV/cm, when the current peak was ~0.1 A. Then, at E = 23 kV/cm, the current peak increased suddenly to 0.9 A, and a clear CCD image of emission sites was captured (Fig. 4d). Superimposing the image from Fig. 4d with the reference image (Fig. 4a), the location of bright spots vs. the map of structural defects is obtained (Fig. 4e). Fig. 4e clearly shows that the field-induced emission sites are located in some of the structural defect zones, therefore coincident with the location of micropipes. At the next voltage shot, at a similar field, the current was increased up to 1.15 A, resulting in a new bright zone that indicates a new highly activated micropipe cluster (Fig. 4f), located also in a structural defect zone obstructed in Fig. 4a, but appearing in Fig. 4b.

In the prebreakdown stage, relatively small increases of current coincide with singular micropipe activation (1-3 bright spots). However, at higher applied fields, a relatively large increase in the current results in a large bright site, much larger than the area of the initiating structural defect zone.

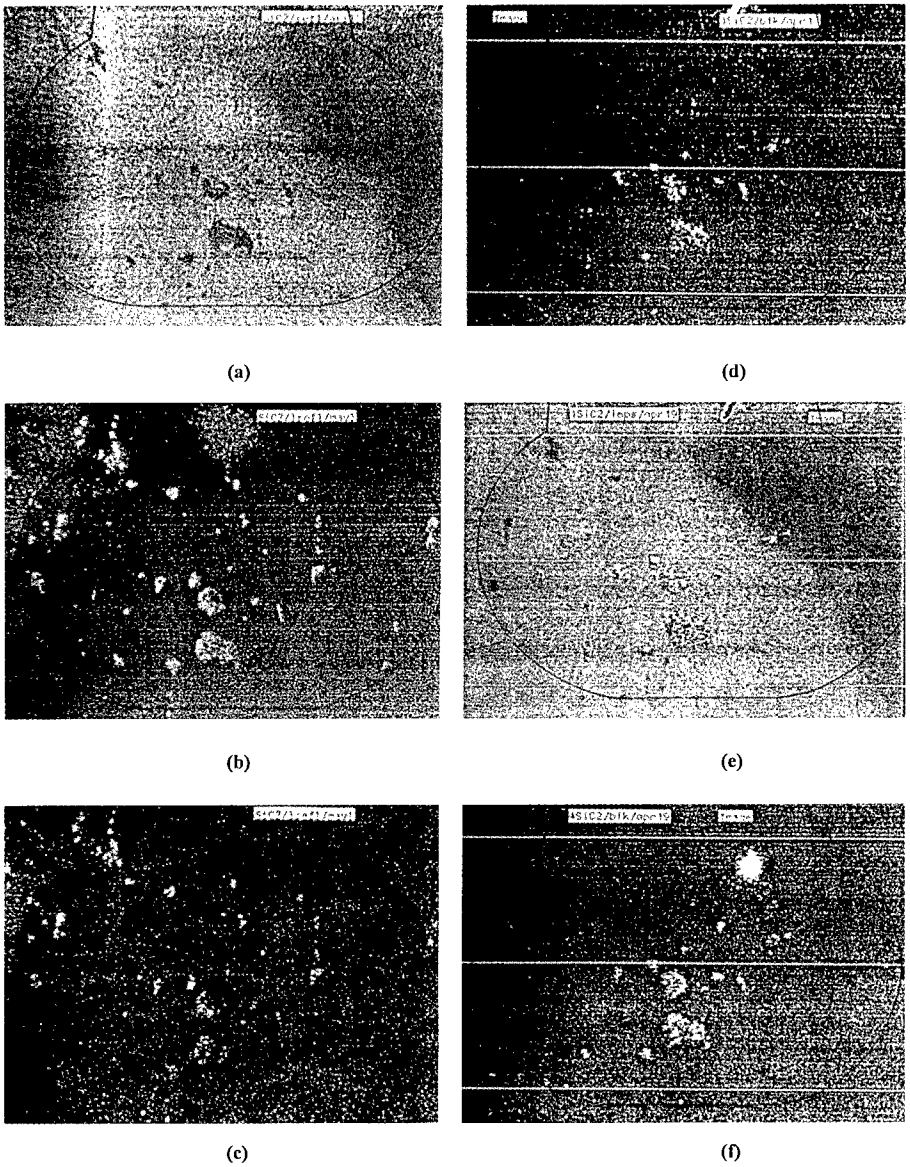


Fig. 4. Examples of zero field and high field-induced defect imaging in a vertical device structure of 6H-SiC with ITO contacts: (a) initial reference image of structural defects using back illumination; (b) micropipe map obtained by the laser scattering method; (c) similar to (b) with lower intensity of the incident light; (d) CCD image of light emission sites at E = 23 kV/cm and sudden increase of I from 0.1 A to 0.9 A; (e) images (d) and (a) superimposed; (f) similar to (d) for I = 1.15 A.

DISCUSSION

The results presented above indicate, on one hand, the significant influence of the growth defects on the electrical response of the high resistivity SiC devices at high fields and, on the other hand, a specific behavior of these defects, related to the orientation of the applied field.

For lateral devices, when E is parallel to the surface of the device, the only high field limitation of the SiC devices is the surface flashover process. No defect activation, notably no light emission from the gap region, is observed up to fields as large as 180 kV/cm in SF_6 or vacuum. In fact, by modeling the field distribution in a lateral configuration, significant field enhancement factors of 1.5-5 (depending mostly on the gap geometry) are expected in the active area of the device, allowing a correction of the applied field value. At the same time, the limiting process, that is the surface flashover phenomenon, is not a bulk process, but it is the final stage of a field dominated time evolving process at the semiconductor-ambient dielectric interface under the HF stress, when a total breakdown of the system, due to a streamer or arc discharge, is produced. The surface flashover process is greatly influenced by the material nature and quality, device parameters (surface, contacts, gap length and geometry) and ambient dielectric properties [6, 9].

In the vertical device configuration all the current flows between the two contacts and no surface leakage can be accounted in the total current. Also, the breakdown processes are localized in the bulk, in the material between the two contacts, where the field is applied. Therefore, the much higher current densities obtained in the vertical than in lateral devices, along with much smaller breakdown fields, should be correlated with particular defects which may be easily activated when E is perpendicular to the surface of the device, but are not activated when E is parallel to the surface, even for large field values (180 kV/cm). The only defects in SiC which can be implied in such a situation are the micropipes, specific growth defects as empty tubes of 1-100 μm diameter, traversing, in most cases, the wafer thickness between the two faces and being, generally, perpendicular to the wafer surface. Then, the map of the light emission sites is truly the map of activated micropipes. Considering the micropipes as the main conduction paths in the vertical MSM devices under high field, we have calculated that for a density of micropipes of ~500 cm^{-2} the current density in micropipes should be in the range of 400-800 kA/cm^2, based on the measured J_V = 0.2-0.4 kA/cm^2. Note that in lateral devices of the same material (6H-SiC:V) J_L~0.4 A/cm^2, corresponding to the nominal resistivity of the V-doped material. Therefore, the current density in micropipes is ~10^6 times larger than the nominal current density, with no defect activation. The high current density in micropipes is caused, we suppose, by various field/thermal-induced generation processes in a thin wall region around the micropipe, where most of the atomic impurities (V, B, Ti, Al, Cr, Fe, Co, Ni, etc.) and other defects are precipitated. The huge current densities generate microplasmas, therefore, causing light emission. The problem here is to explain how these wall-zones around the pipes, so sensitive in parallel fields (to their orientation), are insensitive even for large perpendicular fields. It appears that the generated carriers can move only in a confined region around the micropipe.

Considering that the map of light emission sites is, in fact, a map of activated micropipes, we can conclude that, due to an almost perfect match, as shown above, the laser scattering method is truly a map of non-activated (no-field) micropipes in the SiC material. We propose the following qualitative explanation for the laser scattering method: the laser light entering the side of the device is transmitted in the free-defect regions of the crystal (which appear black to the microscope normally oriented to the surface of the device), but can be scattered and even amplified by multiple reflections in the micrometric wave-guides perpendicular to the surface (micropipes), appearing as bright spots. The relatively large structural defect zones appear slightly illuminated due, probably, to refraction effects at the edge and, more importantly, due to the clustering of micropipes in these regions.

From the optical observations, we conclude that micropipes are preferentially located in the structural defect zones of the material, as clusters. A similar result was presented in Ref. [12]. Therefore, a reduction of structural defects (darker spots in the material, possibly different polytypes), during the growth process, can lead to a reduction in the density of micropipes. Another important conclusion is that the sensitivity of micropipes to field activation depends more on the density of atomic impurities precipitated around rather than on their dimensions. This fact can explain why in vertical devices of 6H-SiC:V the current densities increased up to 2000 times compared with lateral devices, but much less (1-5 times) in the undoped material. At the same time, the random increase in the J_V/J_L ratio can be explained by the random distribution of the micropipes in a SiC wafer.

CONCLUSIONS

The unique property of micropipes to activate easily in parallel electric fields, but to be insensitive to fields perpendicular to their direction, is demonstrated. A map of light emission spots obtained under high field excitation, in vertical devices, is well correlated with the map obtained using the Laser Scattering Method, confirming that the latter is truly a map of micropipes. Thus, a new, non-destructive method, based on laser scattering in SiC single-crystal, is presented.

ACKNOWLEDGMENTS

This work is supported by the Department of the Army, Army Research Office, Research Triangle Park.

REFERENCES

1. R. F. Davis, Proceedings of the Fifth Conference on Silicon Carbide and Related Materials (Washington, DC, 1993), p. 7.

2. J. A. Powell, P. G. Neudeck, D. J. Larkin, J. W Yang, and P. Pirouz, ibid., p.161.

3. P. G. Neudeck, and J. A. Powell, IEEE Electron Dev. Lett. **15**, 63 (1994).

4. P. G. Neudeck, D. J. Larkin, C. S. Salupo, J. A. Powell, and L. G. Matus, op. cit., p. 475.

5. L. G. Matus, J. A. Powell, and C. S. Salupo, Appl. Phys. Lett. **59**, 1770 (1991).

6. G. Gradinaru and T. S. Sudarshan, J. Appl. Phys. **73**, 7643 (1993).

7. T. S. Sudarshan, G. Gradinaru, G. Korony, W. Mitchel, and R. H. Hopkins, J. Electr. Mat. **25**, 893 (1996).

8. H. M. Hobgood, D. L. Barett, J. P. McHugh, R. C. Clarke, S. Sriram, A. A. Burk, J. Greggi, C. D. Brandt, R. H. Hopkins, and W. J. Choyke, J. Cryst. Growth **137**, 181 (1994).

9. G. Gradinaru, V. P. Madangarli, and T. S. Sudarshan, IEEE Trans. Electron Devices **41**, 1233 (1994).

10. G. Gradinaru and T. S. Sudarshan, J. Appl. Phys. **79**, 8557 (1996).

11. V. P. Madangarli, G. Korony, G. Gradinaru, and T. S. Sudarshan, IEEE Trans. Electron Devices **43**, 793 (1996).

12. R. C. Glass, L. O. Kjellberg, V. F. Tsvetkov, J.E. Sundgren, and E. Janzen, J. Cryst. Growth **132**, 504 (1993).

DEEP LEVEL TRANSIENT SPECTROSCOPY STUDY OF HIGH-TEMPERATURE ALUMINUM IMPLANTED 6H-SiC

Yuri A. STOTSKI*, Igor O. USOV*, Alexander V. SUVOROV**
*Ioffe Physical Technical Institute, St. Petersburg, 194021, Russia
**CREE Research Inc., Durham, NC, 27713, USA, e-mail: asuvorov@cree.com

ABSTRACT

Deep levels in 6H-SiC wafers implanted with Al^+ ions at high-temperature were studied using current deep level transient spectroscopy (iDLTS). Aluminum was implanted at a temperature of 1800 °C with an energy of 40 keV and a dose of 2×10^{16} cm^{-2} into n-type epitaxial layers with different carrier concentration. Four levels were found, at E_C–0.12, E_C–0.13, E_C–1.06 and E_V+0.35 eV. It was established that modification of the carrier concentration in original n-type 6H-SiC epitaxial layers affects the deep levels concentration. The relationship between the thickness of the space charge region and the relative deep level concentration was considered.

INTRODUCTION

Ion implantation is the prevailing doping method for semiconductors device technologies. The recent availability of good quality 6H and 4H-SiC wavers makes ion implantation an attractive doping technique for the production of SiC devices. Previously it was established that high temperature implantation is required to reduce crystal lattice damage and to increase the electrical activation of the implanted dopants in SiC [1, 2].There are some reports on DLTS studies of SiC p-n structures formed by room temperature ion implantation followed with furnace annealing [3, 4]. However, the DLTS study of the diodes formed by high-temperature ion implantation is not available, to our knowledge. In this paper we present the parameters of deep centers of p^+-n diodes produced by Al implantation into n-type 6H-SiC wafers at the temperature of 1800 °C.

THE SAMPLES

In this work we investigated five n-type 6H-SiC samples obtained from CREE Research Inc [5]. Nitrogen doped 3 μm thick epitaxial layers were grown on Si-faced 6H-SiC substrates. The p^+-n diodes were formed by implantation of Al ions with an energy of 40 keV and a dose of 2×10^{16} cm^{-2} at a target temperature of 1800 °C. Ohmic contacts were made using Ni and Al on the n- and p^+-sides of the samples, respectively.

There are two kinds of the samples in our investigation. The original donor concentration in the n-type epitaxial layers for the first three diodes were found to be 1×10^{17} cm^{-3} and 2×10^{15} cm^{-3} for the rest. Other characteristics and preparing conditions were equal for all samples.

Mat. Res. Soc. Symp. Proc. Vol. 442 © 1997 Materials Research Society

THE METHODS OF MEASUREMENTS

To determine the capture cross section and activation energy of deep levels the method of current deep-level transient spectroscopy (iDLTS) was applied. The reverse current of the p – n junction can be expressed as [6]:

$$I(t) = (A/\tau)\exp(-t/\tau)\,, \tag{1}$$

$$\tau = (\sigma_n V_T N_C)^{-1}\exp(\Delta E/kT)\,, \tag{2}$$

where A is proportional to the concentration of the deep level, σ_n is the electron capture cross section, V_T is the mean thermal velocity of electrons, N_C is the effective density of states in the conduction band, ΔE is the thermal activation energy of the trap refered to the lower edge of the conduction band, k is the Boltzman constant, t is the time interval from the front of reverse bias impulse, T is the temperature and τ is the deep level relaxation time.

Experimental iDLTS signal is the function $\Delta I=\Delta I(T)$, where $\Delta I=I(t_1)-I(t_2)$. The time points t_1 and t_2 determine the rate window and are chose during measurements. The position of the maximum of this function defines temperature T_{max}. It corresponds to the characteristic relaxation time τ_{max}, that can be calculated from the equation:

$$(t_1-\tau_{max}) / (t_2-\tau_{max}) = \exp[(t_1-t_2)/\tau_{max}]\,. \tag{3}$$

The relationship $\tau_{max}=\tau_{max}(T_{max})$ can be obtained from (3) and the temperature dependence of ΔI, which is measured with various t_1 and t_2. Then the deep level ionization energy and the carriers capture cross section is calculated from (2).

In our measurements we were storing a record of the time dependence of the current by using a digital oscilloscope with resolution of 50 ns/point. The data from oscilloscope was transmitted to the computer for analysis. Such a method of measurement is not traditional. Usually at first t_1 and t_2 are specified, then the p – n junction current for these time points are measured [7]. Our method allows one to obtain experimental data for every time point t during one cycle of temperature variation. So there is complete information about p – n junction current in the computer. We choose the time positions t_1 and t_2 during data processing, so we can vary τ_{max} dynamically depending on the preliminary results. It allows to improve the measurement accuracy.

RESULTS

The characteristics of observed deep levels are listed in the Table:

Energy position	Cross section, cm^2	Source of level
E_C–0.12 eV	2×10^{-16}	N
E_C–0.13 eV	3×10^{-15}	
E_C–1.06 eV	2×10^{-15}	Al implantation
E_V+0.35 eV	4×10^{-15}	B related

The iDLTS spectra obtained for the samples with low (2×10^{15} cm^{-3}) and high (1×10^{17} cm^{-3}) background carrier concentration are presented in Fig. 1 and 2, respectively. We applied 1.0 V forward bias for filling minority carrier traps and then 5.0 V reverse bias to the p^+ – n junction during these measurements. Two iDLTS maxima were observed.

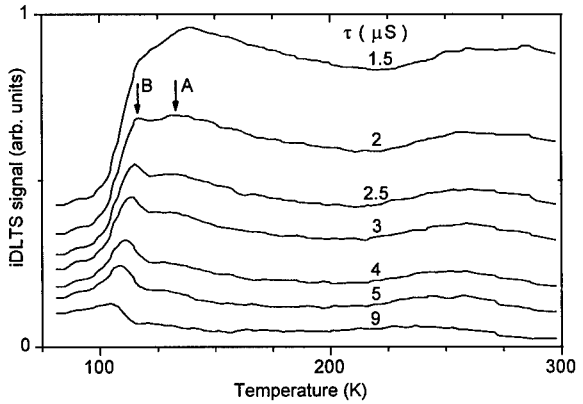


Fig. 1. iDLTS spectra from the p^+-n diodes formed by implantation of Al ions at a temperature of 1800 °C into n-type 6H-SiC sample with low (2×10^{15} cm^{-3}) background carrier concentration (τ is the rate window).

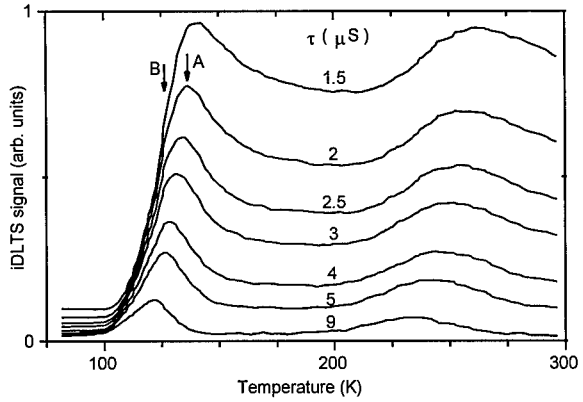


Fig. 2. iDLTS spectra from the p^+-n diodes formed by implantation of Al ions at a temperature of 1800 °C into n-type 6H-SiC sample with high (1×10^{17} cm^{-3}) background carrier concentration (τ is the rate window).

The first maximum (situated near 120 K) consists of two peaks (named A and B). The activation energies E_C–0.12 eV, E_C–0.13 eV and the electron capture cross sections 2×10^{-16} cm^2, 3×10^{-15} cm^2 of the deep levels A and B, respectively, are estimated from the Arrhenius plot (Fig. 3). It follows from formula (1) that the concentration of deep level is proportional to the iDLTS peak intensity. We can see from Fig.1, the concentration of level A is more relative to the concentration of level B for the samples with high background carrier concentration. The inverse ratio of A and B level concentrations is observed for samples with low background carrier concentration (Fig. 2). We emphasize that difference in activation energy of level A and B is less than experimental error. By this means energy position of the first level relative to the second one must be defined more accurately.

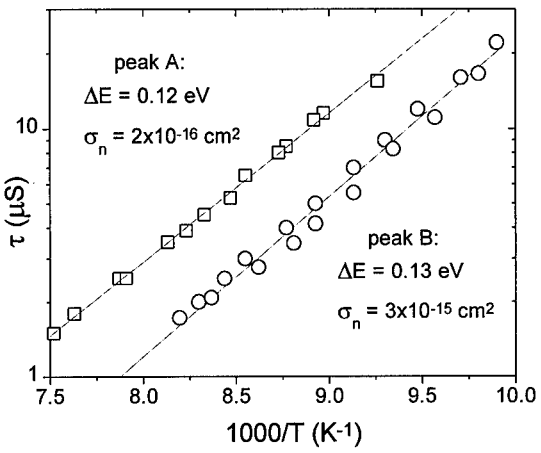


Fig. 3. Arrhenius plots of the deep levels relaxation time τ as a function of $1000/T$ for two iDLTS peaks situated near 120 K.

The additional measurements of the iDLTS spectra with various values of reverse bias were made in temperature range from 200 K to 300 K. The typical plots of relaxation time as a function of 1000/T for various reverse bias are shown in Fig. 4. The 5.0 V forward bias for filling minority carrier traps was applied to samples in this set of experiments.

The second iDLTS maximum (situated near 250 K) corresponds to one minority carrier and one majority carrier deep level. For these levels, the activation energy positions were estimated to be E_V+0.35 eV, E_C–1.06 eV and the capture cross sections were calculated to be 4×10^{-15} cm^2, 2×10^{-15} cm^2, respectively.

From Fig. 4 we notice that the slopes of the straight lines fitted to the experimental points for the Arrhenius plots depend substantially on the value of reverse bias. It can be explained by existence of two iDLTS peak at a short distance and their interdependence. If the value of reverse bias equals zero, only the minority carrier levels affect the iDLTS signal. In this case the majority carrier traps at the full length of the space charge region are below Fermi level and electrons do not leave theirs. The greater the reverse bias the wider region in which majority carrier deep levels are above Fermi level. In this case their contribution to the iDLTS signal is enhanced. So the activation energy of the minority carrier deep level at E_V+0.35 eV estimated from the Arrheniuse plot shown in Fig. 4a (the reverse bias is zero) is valid. If the reverse bias is high (Fig. 4c) the peaks from levels at E_V+0.35 eV and E_C–1.06 eV are overlapped, so it needs to apply special data processing for separate nearby iDLTS peaks. For some special value of reverse bias the points that specified to the different levels are separated. This case is presented on Fig. 4b (lines 1). The activation energies estimated from the slopes of these lines are valid also.

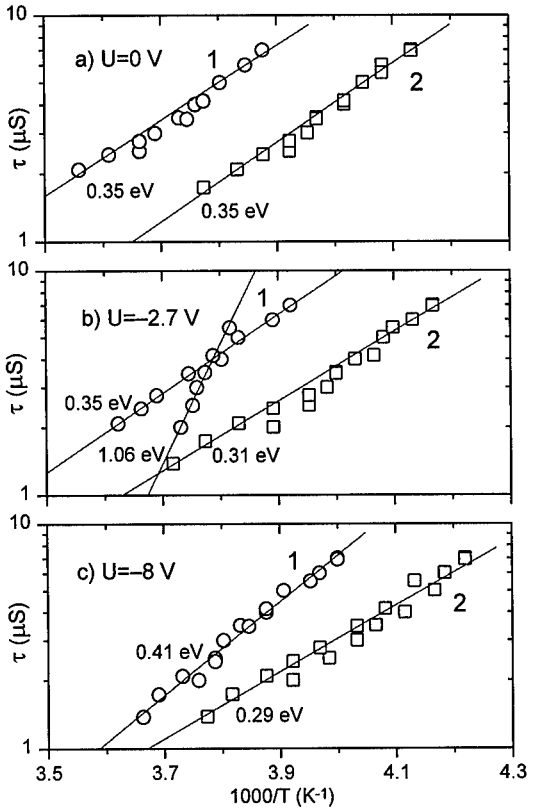


Fig. 4. Arrhenius plots of the deep levels relaxation time τ as a function of 1000/T for two iDLTS peaks situated near 250 K. Three plots correspond to three different value of reverse bias applied to the samples during the iDLTS measurements (0, –2.7 and –8 V).
lines 1 – background carrier concentration of the sample is 2×10^{15} cm^{-3}
lines 2 – background carrier concentration of the sample is 1×10^{17} cm^{-3}

DISCUSSION AND CONCLUTIONS

Two deep levels were found at E_V+0.35 eV and E_C–1.06 eV, and two nearby levels were found at E_C–0.12 eV and E_C–0.13 eV. These four levels were observed in p^+– n junction formed by implantation of Al into the epitaxial layers at high temperature.

The obtained activation energies for levels A and B agree with the reported values of nitrogen in the cubic lattice sites k1 and k2 [9], respectively. The fact is that background carrier (nitrogen) concentration affects the relative concentration of two nearby levels, E_C–0.12 eV and E_C–0.13 eV. The level observed at E_C–0.12 eV predominates over the level at E_C–0.13 eV in the samples with high background carrier concentration (Fig. 2). The concentration of level at E_C–0.13 eV is more than the concentration of level at E_C–0.12 eV for the samples with low carrier concentration (Fig. 1). Since the amplitude of iDLTS peak for the electron trap (peak A in Fig. 1, 2) with an activation energy of 0.12 eV correlates with the carrier concentration we have

suggested that this level is associated with nitrogen atoms sitting in the cubic lattice sites (k1, k2) [8–11]. The amplitude of iDLTS peak associated with the level at E_C–0.13 eV (peak B at Fig. 1, 2) does not depend on the carrier concentration. The value of level B capture cross section is an order of magnitude larger than that of level A. Thus, we hypothesize that nitrogen atoms are not responsible for level B formation.

Fig. 4 shows that correlation between appearance of the Arrhenius plot and the value of reverse bias is not similar for the samples with high or low carrier concentrations. The increase in the value of reverse bias affects strongly on the slopes of lines 1 (the carrier concentration is 2×10^{15} cm^{-3}). It is explained by approximately equal contribution of the levels at E_V+0.35 eV and E_C–1.06 eV to the carrier relaxation process. In the case of high (1×10^{17} cm^{-3}) carrier concentration the slopes of lines are changed insignificantly. It can be explained by higher concentration of the level at E_V+0.35 eV relative to the concentration of the trap at E_C–1.06 eV. So the first level affects the iDLTS signal more strongly than other one.

The amplification of the E_C–1.06 eV level contribution to the carrier relaxation process is observed with the increase of the reverse bias. The spatial distribution of the traps in n-region of the p^+– n junction may account for this effect. The reverse bias value affects the width of the space charge region. By this means the traps placed far from the edge of junction affect the iDLTS signal if the reverse bias is high only. At any value of reverse bias the traps that locate near the edge of junction is observed.

It is probable the deep level at E_V+0.35 eV is related to the boron impurities [3, 12]. The deep level at E_C–1.06 eV was observed in p – n junction formed by room temperature implantation of Al ions [13].

REFERENCES

1. A.V. Suvorov, P.A. Ivanov, Y.V. Morozenko and V.N. Makarov, Third All-Union Conference on Wide-Gap Semiconductors (in Russian), Mahachkala, **28**, (1986).
2. J.A. Edmond, S.P. Withrow, W. Wadlin and R.F. Davis, in *Interfaces, Superlattices and Thin Films*, edited by John D. Dow and Ivan K. Schuller (Mater. Res. Soc. Proc. **77**, Pittsburgh, PA, 1987), pp. 193-198.
3. G. C. Rybicki, J. Appl. Phys. **78**(5), 2996, (1995).
4. A. Uddin and T. Uemoto, Jpn. J. Appl. Phys. **34**, 3023, (1995).
5. CREE Research Inc., 2810 Meridian Parkway, Suite 176, Durham, NC 27713, USA.
6. L.S. Berman and A.A. Lebedev, in *Capacitance Deep Level Spectroscopy in Semiconductors*, St. Petersburg, Nauka, (1981).
7. N.I. Kuznetsov, Sov. Phys. Semicond, **27**, 1674, (1993).
8. J. Schneider and K. Maier, Physica B **185**, 199, (1993).
9. W. Suttrop, G. Pensl, W.J. Choyke, R. Stein and S. Leibenzeder, J. Appl. Phys. **72**, 3708, (1992).
10. P.J. Colwell and M.V. Klein, Phys. Rev. **B6**, 498.
11. A.I. Veinger, A.A. Lepneva, G.A. Lomakina, E.N. Mokhov and I.V. Sokolov, Sov. Phys. Semicond. **18**, 1256, (1984).
12. M.M. Anikin, A.A. Lebedev, A.L. Syrkin and A.V. Suvorov, Sov. Phis. Semicond. **19**(1), 69 (1985).
13. M.M. Anikin, A.A. Lebedev, I.V. Popov, V.N. Rastegaev, A.M. Strel'chuk, A.L. Syrkin, Y.M. Tairov, V.F. Tsvetov and V.E. Chelnokov, Sov. Phys. Semicond. **22**, 181, (1988).

HRTEM Characterization of 6H-15R Polytype Boundaries in Silicon Carbide Grown by Physical Vapor Transport

E. K. SANCHEZ, M. DE GRAEF, W. QIAN*, M. SKOWRONSKI
Department of Materials Science & Engineering, Carnegie Mellon University, Pittsburgh, PA 15213-3890, esanchez@andrew.cmu.edu
*Currently at Department of Materials Science & Engineering, Northwestern University, Evanston, IL 60208

Abstract

The interface between 6H and 15R polytypes of silicon carbide, grown by Physical Vapor Transport, was studied by high-resolution transmission electron microscopy. The sample was investigated in cross-section cut perpendicular to the [11.0] direction. The atomic stacking sequence at the interface of the polytypes was determined. Polytype boundaries with orientations parallel and perpendicular to the 6H c-axis were investigated. Stacking faults associated with low angle grain boundaries in both 6H and 15R regions were observed and the 15R regions systematically showed a higher fault density than the 6H regions.

Introduction

In recent years Silicon Carbide (SiC) has sparked much attention as a wide-bandgap semiconductor. This interest is due to SiC's unique set of properties, among them, its large bandgap, high saturation electron velocity, high thermal conductivity and high dielectric breakdown field strength. These properties make it the most promising material for high power/high temperature/high voltage devices.[1, 2] However, there are still several unresolved problems which prevent the fabrication of reliable SiC devices. One of the most troublesome problems is the growth of defect-free crystals. This defect problem is compounded by the phenomenon of *polytypism*. SiC has been found to take the form of over 170 different polytypes,[3] each with a different bandgap and different electronic properties. The most common polytypes are 6H, 15R, 4H and 3C. Recent developments in physical vapor transport growth have allowed the growth of large single crystals of both 6H and 4H polytypes.[4] Even though the growth of large single polytypes has been demonstrated, the control over polytypes throughout the crystal is still difficult since all four of the most common polytypes coexist over a wide range of temperatures. Previous studies have reported observations of the interface between 4H and 6H polytypes,[5] but the characterization of the boundary between 15R and 6H has not been previously reported.

Experimental

TEM thin foils were prepared with a foil normal parallel to the [11.0] direction. The samples were first lapped with 6 μm diamond paste on a titanium plate to a thickness of 100 μm. They were then polished with finer diamond paste and/or alumina in a Gatan dimpler to a thickness of 20 μm. Electron transparency was obtained by ion sputtering with Ar^+ in a Gatan Duomill. The TEM high resolution images were obtained on a JEOL top entry 4000EX operated at 400 kV (spherical aberration = 1mm, point resolution = 0.17nm). Digital images were acquired in zero loss mode using a Gatan post-column energy filter or GIF (slit width = 10 eV) and a 1024x1024 grade B CCD camera.

Mat. Res. Soc. Symp. Proc. Vol. 442 © 1997 Materials Research Society

Results and Discussion

At low magnification the thin foil appears to consist of regions, often several microns across, separated by nearly planar boundaries. Some of the boundaries are sharp and can change direction from parallel to perpendicular to the 6H c-axis, others are somewhat wavy, with an average orientation parallel to the 6H c-axis. Selected area electron diffraction revealed that most of the regions are of the 6-H type, with large 15R sections scattered throughout the thin foil. Both 6H and 15R polytypes contain low angle grain boundaries, such as the one shown in the [00.n] systematic row image of Figure 1. Note the difference in background contrast, indicating a small misorientation across the boundary. From electron diffraction patterns it could be deduced that such boundaries have both a tilt and a twist component, with tilt/twist angles of less than a degree. The boundary in Figure 1 is made up of planar faults, parallel to the 6H basal plane. Some faults continue across the boundary, while others end at the boundary. It is remarkable that many of the faults end at some unique distance away from the boundary, as shown in Figure 2. The strong diffraction contrast at the tip of the fault indicates the presence of a strain field, possibly associated with terminal dislocations. The fault density is rather high in the 15R regions, with typically one fault per 10 nm or so. In 6H regions the observed fault density is much lower, and large defect-free areas are found.

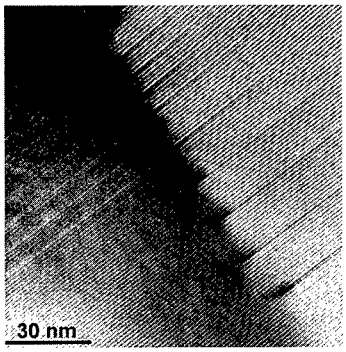


Figure 1 - Low angle grain boundary in 15R with associated planar faults.

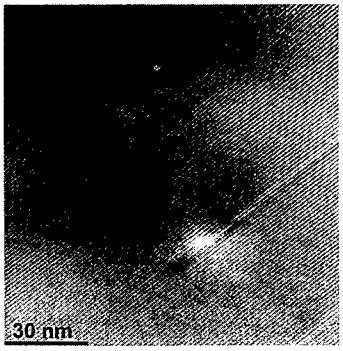


Figure 2 - Faults ending in the center of a 15R region.

Figure 3 shows a low magnification image of a typical interface between a 6H and 15R region near the edge of the thin foil. The boundary has a complex non-planar structure and the associated contrast is not continuous. The somewhat wavy trail of bright elongated contrast patches actually delineates the polytype interface. The distance between subsequent bright patches is constant along the boundary, indicating that the interface has a periodic structure. On average the interface is parallel to the 6H c-axis but locally there are lateral shifts of as much as 10 nm between subsequent bright patches. Occassionaly the distance between the bright regions is different; this invariably is associated with the intersection of planar basal faults with the polytype interface, as indicated by the white arrow in Figure 3.

Figure 4 shows a high resolution micrograph of the polytype interface (center image). All high resolution images presented in this paper were acquired in zero-loss energy filtering mode, with a 10 eV energy selecting slit. The micrograph shows a short segment of the interface, with three neighbouring bright patches. Selected area diffraction patterns taken on both sides of the interface correspond with the 6H (lower left) and 15R (lower right) structures. The inset on the upper left shows a high resolution micrograph of the perfect 6H lattice, taken close to the edge of

the foil. The six-layer stacking sequence can clearly be observed; the c lattice parameter for 6H is 1.512 nm.[6,7] The rightmost inset shows the ideal 15R structure with a periodicity of 3.779 nm measured along the 6H [00.1] direction. The alternating bright and dark bands in the center micrograph are a common artifact in high resolution micrographs of layered structures and are a consequence of either beam tilt or crystal misorientation. If the crystal was perfectly aligned along the [11.0] zone axis, and if the electron beam tilt were completely eliminated, then all six planes in the 6H unit cell should show the same image contrast, as shown in the inset.

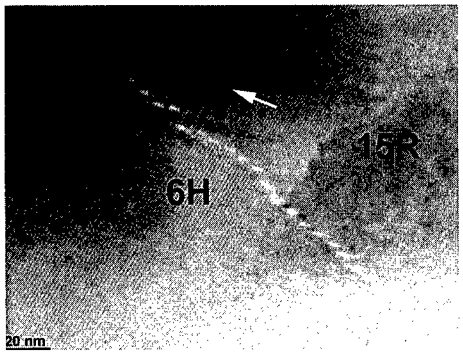


Figure 3 - Interface between polytypes. The white arrow indicates the position of two faults associated with the boundary.

The stacking sequences of the 6H and 15R polytypes can be determined directly from the high resolution micrographs. It is therefore possible to analyze the structure of the polytype interface by comparing the stacking sequences on either side of the interface. Looking at the center micrograph from a glancing angle view (from lower left to upper right) we observe that the regions in between the bright patches have continuous planes across the interface, whereas the patches themselves correspond to regions of substantial misfit between the two polytypes. The stacking sequence of 6H can be represented by the symbol ABCACB, whereas that of 15R is given by ABCAC BCABA CABCB (see Figure 5).

Figure 6 shows a high magnification view of a single bright patch. From a glancing angle view (left to right) one can determine that the contrast is approximately symmetrical with respect to the center of the patch. A detailed analysis of this micrograph reveals the following: on either side of the patch there are groups of 8 lattice planes which cross the polytype interface uninterrupted (see vertical arrows in Figure 6). In between those bands there are 22 lattice planes; of those 22, a total of 6 cross the interface without interruption (indicated by horizontal arrows), the remaining 16 change type from A to B or C (or any equivalent change).

From these observations we can derive that the repeat distance across the interface corresponds to 30 layers: 5 unit cells of 6H match up with 2 unit cells of 15R. Since the interplanar spacing for the 6H (00.1) planes is 0.252 nm, we find an interface periodicity of 7.56 nm, in good agreement with the average spacing between the bright patches in Figure 3. The lateral shifts between subsequent patches (as seen in Figure 3) can also be explained: two subsequent bright patches are separated from each other by 8 continuous planes, which means that the misfit areas need not perfectly align with each other. The presence of misfit strains may put limitations on the magnitude of the lateral shift, but insufficient information is available at this time.

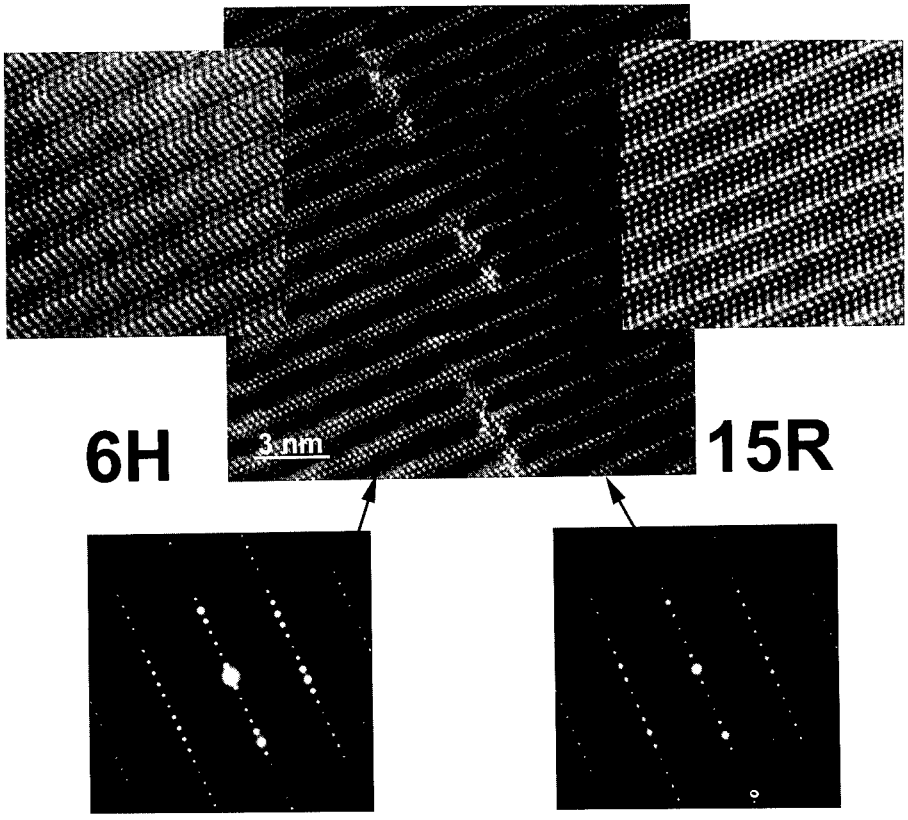


Figure 4 - Center: close up of 6H-15R polytype interface. The stacking sequences of 6H (left) and 15R (right) can be determined from the higher magnification insets. Selected area diffraction patterns of the 6H [11.0] and corresponding 15R zone axes are shown at the bottom.

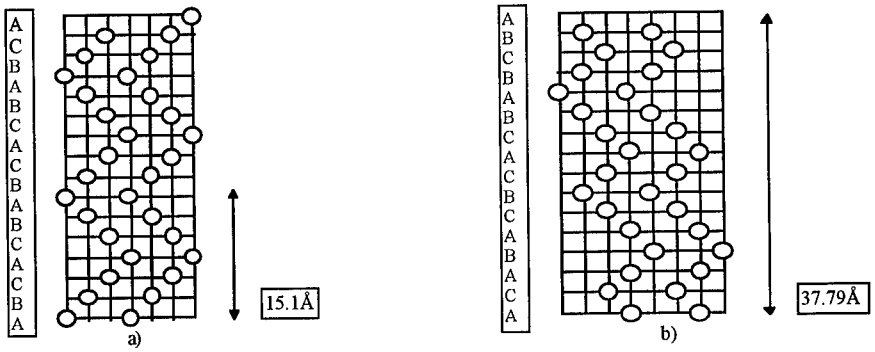


Figure 5 - Stacking sequences of a) 6H and b) 15R polytypes.

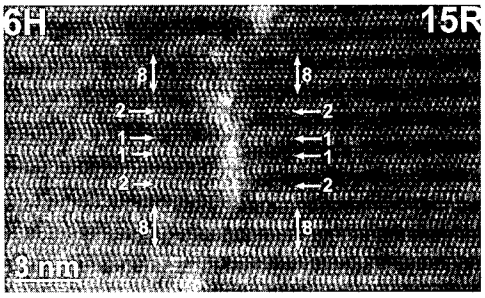


Figure 6 - Close up of interface, showing matching layers.

CBABCACB**CAB**AC**ABCB**A**BC**A**CBCA**BA**CAB**CB <--**15R**

CBABCACB**ABC**AC**BABC**A**CB**A**BCAC**BA**BCA**CB <-- **6H**

8 3 2 4 1 2 1 4 2 3 8

Figure 7 - The planes that do not match are in bold and underlined. The number of matching and non-matching planes is indicated at the bottom.

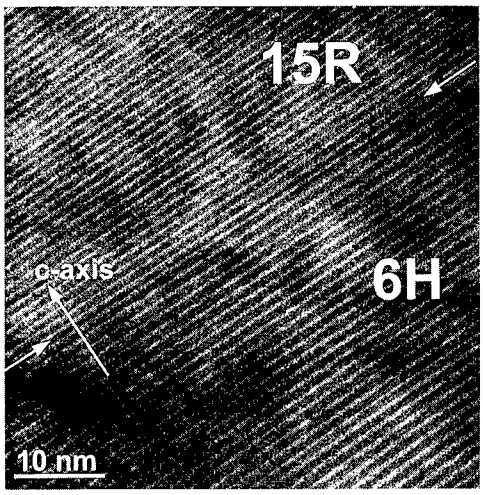


Figure 8 - Interface between 15R and 6H polytypes perpendicular to the 6H c-axis.

In addition to the 6H-15R polytype interface discussed above, we have also observed a second type of 6H-15R polytype interface. An example of this second type is shown in Figure 8. This image was obtained with the 6H [00.n] systematic row and shows the 6H polytype in the lower half, and the 15R polytype in the upper half. The interface is indicated by white arrows and is *perpendicular* to the 6H c-axis. On several occasions we observed 90 degree turns in this type of boundary, converting it to the type discussed earlier. The exact nature of those bends, and their interaction with other planar stacking defects, is at present poorly understood and is the subject of further research.

There is substantial evidence that the polytype boundaries reported in this paper are mechanically weak features in the microstructure. We frequently observed cracks in the thin foils, running from the foil edge to thicker regions along the 6H-15R polytype boundaries. It appears that the 15R regions not only degrade the electrical properties of these SiC samples, but may also compromise their mechanical strength.

Conclusions

The polytype boundaries between 6H-SiC and 15R-SiC were studied by means of HRTEM. Stacking sequences and electron diffraction patterns were used to determine the structure of a polytype boundary parallel to the 6H c-axis. The interface between the polytypes is periodic, with a 7.56 nm repeat distance. Out of every 30 basal lattice planes, 14 match up perfectly between 6H and 15R, while the remaining 16 give rise to misfit contrast in HRTEM micrographs. Polytype boundaries perpendicular to the 6H c-axis were also observed, and there is evidence that all 6H-15R boundaries are mechanically weak. 15R regions were found to have a high planar fault density, and both 6H and 15R polytypes contain low angle twist and/or tilt boundaries from which large numbers of planar faults emerge. A more detailed study of these faults and their interactions with low angle grain boundaries and polytype interfaces is currently underway.

References

1. Shenai, R.S. Scott and B.J. Baliga, IEEE Trans. Electron Devices **36**, 1811-1823 (1989).
2. M. Bhatnagaer and B.J. Baliga, IEEE Trans. Electron Devices **40**, 645-655 (1993).
3. G. Muller, G. Krotz, E. Niemann, Sensors and Actuators A **43**, 259 (1994).
4. M. Kanaya, J.Takahashi, Y. Fujiwara and A. Moritani, Appl. Phys. Lett. **58**, 56 (1991).
5. H. Iwasaki, S. Inoue, T. Yoshinobu, M. Tarutani, Y. Takai, R. Shimizu, A. Ito, T. Kimoto and H. Matsunami, Appl. Phys. Lett. **63**, 2636-2637 (1993).
6. A.H. Gomes de Mesquita, Acta Cryst., **23,** 610-617 (1967).
7. JCPDS Database (1992).

X-RAY TOPOGRAPHY OF A SINGLE SUPERSCREW DISLOCATION IN 6H-SiC THROUGH ALL {100} FACES

W. M. Vetter, M. Dudley
Dept. of Materials Science and Engineering, SUNY at Stony Brook, Stony Brook, NY 11794-2275

ABSTRACT

Micropipes, the hollow cores of superscrew dislocations that lie along the c-direction in SiC single crystals, are quite deleterious to the performance of semiconductor devices. In the x-ray topography of longitudinal-cut samples of these crystals, topographs in the reflection (006) show dislocation image contrast associated with the superscrew dislocations lying along the c-axis of the crystal, which is also the direction of the dislocations' Burgers vectors. In the (110) reflection, whose g-vector is perpendicular to the c-axis and the dislocations' Burgers vector, there is also an image of the superscrew dislocation formed, albeit weaker than the corresponding image in the (006) reflection. This dislocation image is thought to represent stress components of the superscrew dislocation in directions perpendicular to the c-axis.

In order to investigate the origin of these stress components, steps have been carried out to determine whether the dislocation image is anisotropic in all possible reflections where $\mathbf{g}=\{110\}$. To achieve this we have excised a hexagonal prism-shaped sample from a 6H-SiC wafer, 100μm wide, polished along the six {100} crystallographic faces, such that a single micropipe ran along the axis of the sample. This enabled x-ray topographs to be taken through each of these {100} faces.

INTRODUCTION

Crystals of silicon carbide, and other polytypic materials often have screw dislocations running along their axial dimensions whose Burgers vectors are multiples of the c-parameters of their unit cells[1]. These have been termed superscrew dislocations. Typically, when superscrew dislocations have a Burgers vector of more than several c, hollow tubes, referred to as micropipes, can be observed coinciding with the position of their dislocation cores. Micropipes present in SiC crystals are of particular importance, being considered the most deleterious to the performance of semiconductor devices fabricated from this material. Micropipe diameters in high quality SiC wafers typically range from 0.5 to 10Å.

In the x-ray topography of longitudinal-cut samples of these crystals[2], topographs in the reflection (006) show dislocation image contrast associated with the superscrew dislocations as double lines along the c-axis of the crystal, which is also the direction of the dislocations' Burgers vectors. X-ray topographs using the (110) reflection, where the g-vector is perpendicular to the c-axis and the dislocations' Burgers vector, also show images of the superscrew dislocations, albeit weaker than the corresponding images in the (006) reflection. Normally, by the $\mathbf{g}\cdot\mathbf{b}=0$ criterion, dislocation images formed with reflections perpendicular to the Burgers vector should extinguish. The presence of this residual image clearly indicates the presence of strain components associated with the superscrew dislocations in directions perpendicular to the c axis. It has earlier been established that superscrew dislocations are decorated with loops of basal plane dislocations[2,3]. Since the Burgers vectors of these basal plane dislocations are perpendicular to the c axis, a dense distribution of such dislocations close to the superscrew dislocation core may possibly create the perpendicular strain components in question. If this is the case, the residual contrast from the superscrew dislocation might be expected to be anistropic in equivalent crystallographic directions, and this could be determined by comparing a set of topographs using all the $\mathbf{g}=\{110\}$ reflections possible.

This experiment, however, is precluded by the geometry of a longitudinal-cut wafer, where only one $\mathbf{g}=(110)$ reflection may be observed through the wafer's single pair of beam entrance and exit faces. To make this experiment possible, we have prepared a sample in the shape of a hexagonal prism, whose prism and basal faces are the {100} prism and basal crystallographic faces. The lone micropipe running along the axis of the sample is positioned so that x-ray topographs of it may be taken through any of the {100} faces.

Mat. Res. Soc. Symp. Proc. Vol. 442 © 1997 Materials Research Society

EXPERIMENTAL

The sample was prepared from a commercially available Cree basal-cut 6H-SiC wafer whose micropipes were impregnated with dye-doped epoxy, rendering them more easily visible[4]. A strip was cut along a (100) plane from the wafer about 2mm x 1cm. The basal faces were polished to an optical finish with ¼μm diamond paste on a Mastertex cloth. A suitable target micropipe was selected by searching the sample under an optical microscope.

A piece cut from a glass microscope slide was attached to the side of a tripod polisher as shown in figure 1a. The sample was glued to the side of this glass support as shown with the long (100) face downward. Material was then polished away with a series of diamond lapping films until the face was 50μm from the target micropipe. The progress of the polishing operation was followed by frequent observation under a 110x optical microscope equipped with a eyepiece measuring reticle. It is important to measure the position of the micropipe through the basal faces only, as this is the optical axis of 6H-SiC, which is a hexagonal crystal. The image of the micropipe is strongly displaced from its true position when viewed through a prism face, because of the high refractive index of SiC. The surface was then finished with ¼μm diamond paste as above. A second prism face of the sample was similarly formed and polished after reattachment to the polishing support as in figure 1b, and another as in 1c. The sample was then attached to the edge of the slide piece by the first prism face that was formed, as in 1d, then a fourth prism face was formed, resulting in a splinter shape. By following this polishing sequence, the sample remained macroscopic throughout most of the procedure, so that it could be manipulated more safely. The sliver was cleaved along the dashed line in 1e, then glued by one of its small prism faces to the slide's edge, between two glass supports, as in 1f. The supports were cut from microscope coverslips, with an edge beveled to a 60° angle. The fifth prism face was carefully polished in this geometry, and the hexagonal prism was completed by polishing away an edge of the sample in the arrangement in 1g.

Topographs were obtained by allowing the highly collimated beam of synchrotron white x-rays obtained from beamline X19-C at the National Synchrotron Light Source, Brookhaven National Laboratory, to fall onto the SiC sample, glued on the tip of a quartz fiber, while recording the diffracted beams on sheets of Kodak Industrex SR-5 film placed normal to the incident beam direction at a distance of 10cm from the crystal.

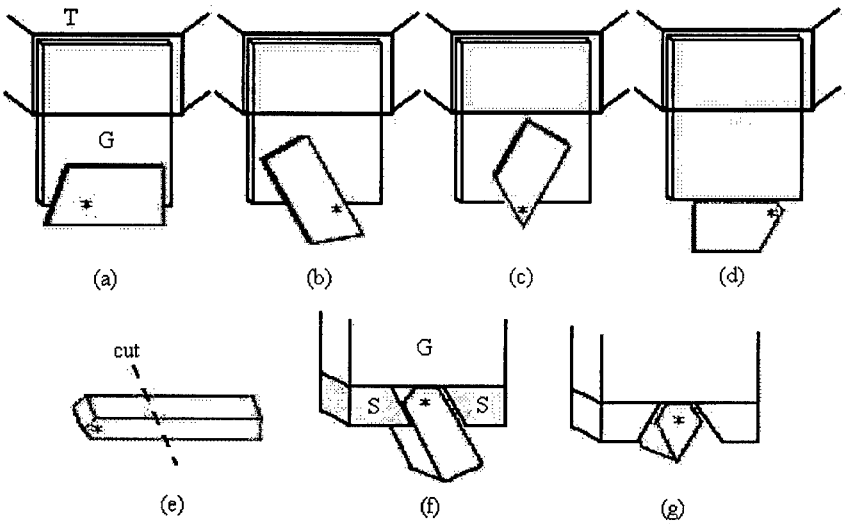
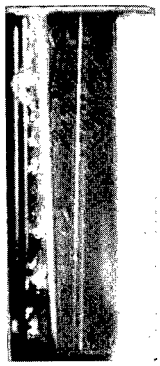


Figure 1. Steps in the preparation of the hexagonal prism-shaped sample. T = edge of tripod polisher, G = glass slide, S = glass supports, * = position of micropipe.

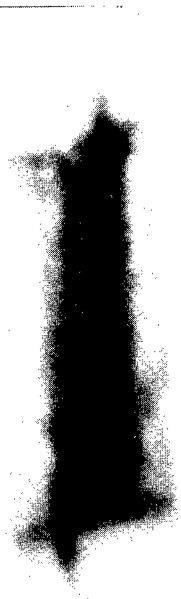
RESULTS AND DISCUSSION

The sample is shown in figure 2. Its dimensions are 100μm wide and 270μm long. The micropipe is seen as a bright line running down the center of the sample. The x-ray topograph in figure 3 uses the **g**=(006) reflection. The two vertically displaced dark lines are characteristic of a superscrew dislocation.



100μm

Figure 2. Photomicrograph of hexagonal prism-shaped sample.



100μm

Figure 3. Transmission x-ray topograph, where g=(006).

Figure 4 shows three topographs, taken through different faces of the crystal, representing members of the set **g**={110}, lying in the basal plane. They show double lines coinciding with the position of the superscrew dislocation also, although more widely spaced, and basal plane dislocations (**B**) in high contast extending off into the crystal, whose Burgers vectors are **b**={110}. The double lines are in higher contrast at certain places (**H**) along the micropipe, especially where the basal plane dislocations originate. When **H** are compared in different **g**={110}, the intensity of the contrast is consistent. In areas of the lines that are of lower contrast (**L**), where basal plane dislocations are not seen streaming away from the micropipe, contrast varies somewhat from one **g**={110} to another.

These changes may be explained by a population of **g**={110} dislocations, where the ratio of the three pairs of possible Burgers vectors, **b**=±(110), **b**=±(1$\bar{2}$0), **b**=±($\bar{2}$10), varies along the micropipe's length. In the darkest areas of the image, **H**, where the level of stress at the micropipe

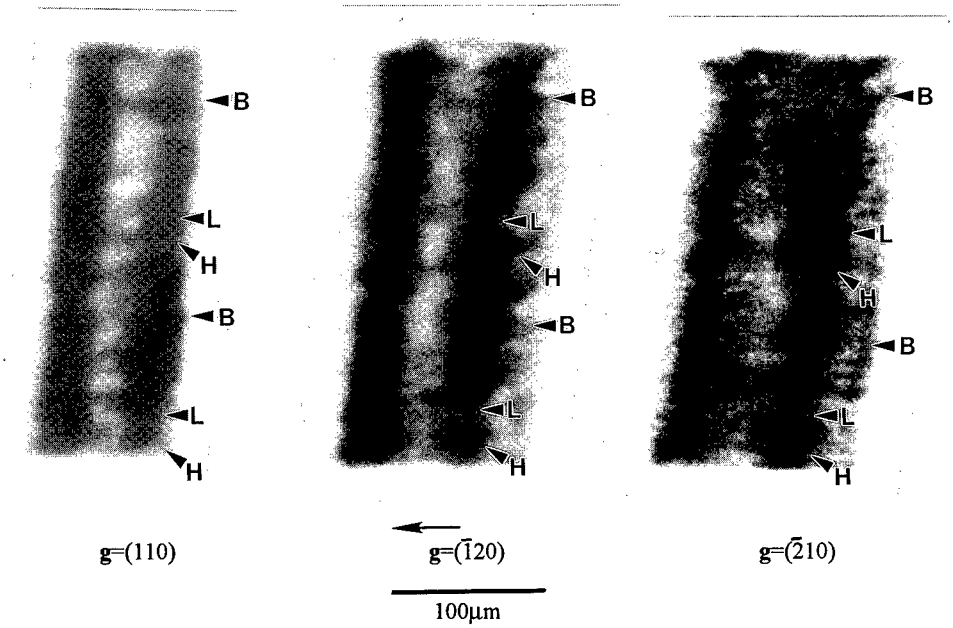


Figure 4. Transmission x-ray topographs using basal plane reflections of the set **g**={110}.

is higher, and more **b**={110} dislocations are generated, some extend far out into the crystal as at **B**. Close to the micropipe, at **H**, the bulk of the **b**={110} dislocations curve back to the micropipe's surface, originating and terminating there. There, the dislocation density is quite high, and therefore, the **g•b**=0 criterion is expected to fail[5]. This might cause the contrast at **H** to be about equal for all **g**={110}. At points along the micropipe such as **L**, the **g**={110} dislocations similarly occur, except they are fewer, and extend from the micropipe's surface only a few microns. Here, their dislocation density is low enough for the image contrast to change as some of the dislocation contrast extinguishes as **g•b**=0.

In this way, the apparent failure of the **g•b**=0 criterion for the screw dislocation in the **g**={110} reflections may be explained by a rather high density of **b**={110} dislocations that are confined to within about 5μm of the micropipes' surfaces. These dislocations are not easily recognizable by x-ray topography, whose maximum resolution is about 1μm and generally fails to separate individual dislocations in regions of high stress, such as where dislocations occur in high density.

CONCLUSIONS

When x-ray topographs are taken of the same micropipe using different g-vectors lying in the basal plane, the image contrast in the double line associated with the micropipe may vary somewhat. It therefore seems reasonable to postulate that the residual contrast from superscrew dislocations when **g•b**=0 originates in a dense and anisotropic distribution of basal plane dislocations which are confined to within a few microns of the dislocation core or micropipe.

ACKNOWLEDGEMENTS

Research Supported by the U.S. Army Research Office under contract numbers DAAH04-94-G-0091 and DAAH04-94-G-0121 (contract monitor Dr. John T. Prater). Topography carried out at the Stony Brook Synchrotron Topography Facility, Beamline X19-C, at the NSLS, which is supported by the U.S. Department of Energy.

REFERENCES

1. A.R. Verma, Crystal Growth and Dislocations, (Academic Press, New York, 1953).

2. M. Dudley, S. Wang, W. Huang, C. H. Carter, Jr., V. F. Tsvetkov and C. Fazi, J. Phys. D: Appl. Phys. **28**, A63, (1995).

3. S. Wang, M. Dudley, C. Carter, Jr., D. Asbury and C. Fazi, Mat. Res. Soc. Symp. Proc., **307**, 249, (1993).

4. W. M. Vetter, M. Dudley, T.-F. Wong and J. T. Fredrich, Mat. Res. Soc. Symp. Proc., **406**, 561 (1995).

5. J. Wu, T. Fanning, M. Dudley, V. Shastry and P. Anderson, Mat. Res. Soc. Symp. Proc., **262**, 265, (1992).

THE INFLUENCE OF THE INCORPORATION AND DESORPTION OF CH_n GROUPS ON THE DEFECT STRUCTURE OF *a*-SiC:H FILMS

T. FRIESSNEGG *, M. BOUDREAU **, P. MASCHER **, P.J. SIMPSON ***, W. PUFF *
*Institut für Kernphysik, Technische Universität Graz, A-8010 Graz, Austria
**Centre for Electrophotonic Materials and Devices, Department of Engineering Physics, McMaster University, Hamilton, Ontario L8S 4L7, Canada
***The Positron Beam Laboratory, Department of Physics, The University of Western Ontario, London, Ontario, Canada

ABSTRACT

Changes in the defect structure in carbon rich *a*-SiC:H films deposited on various substrates using ditertiary butyl silane were investigated as a function of thermal treatment. Films grown at high deposition rates exhibit hydrogen trapped in voids. The incorporation of CH_n groups is thought to be the origin for these microvoids. With increasing annealing temperature the effusion of CH_n groups as determined by thermal desorption experiments promotes void growth which was studied using a variable energy positron beam. At annealing temperatures above 600 °C the films densify due to the breaking of C-H bonds and the formation of additional C-C bonds when the voids anneal out.

INTRODUCTION

The variation of the bandgap of *a*-SiC:H films with C-content is useful for many applications such as solar cells and optoelectronic devices. However, the increase in the defect density associated with carbon incorporation limits its potential use as a wide band gap electronic material [1]. Also, the role of hydrogen on the defects created is not completely understood, yet is important for the thermal stability of the film. El Khakani *et al.* [2] pointed out that the hydrogen bond dissociation during annealing causes compressive stress relaxation, whereas the stress becomes tensile at increasing temperatures due to additional Si-C bond formation. Results of gas evolution measurements coupled with IR absorption data [3] suggest that the hydrogen evolution from *a*-SiC:H films involves two processes: One is related to microvoids and/or polyhydride bonding, the other is related to the dense network structure.

Recent positron beam experiments [4] indicate that annealing in vacuum produces large voids in carbon rich films. Contrary to this, rapid thermal annealing at higher temperatures in an N_2 atmosphere causes film densification and additional SiC formation. Because of these differences it is interesting to examine the vacuum annealing behavior in more detail by combining hydrogen effusion experiments with defect sensitive measurements such as positron beam experiments in order to study the influence of hydrogen desorption on the bond and defect structure in *a*-SiC:H films.

EXPERIMENTAL DETAILS

The deposition of the *a*-SiC:H films was carried out in the electron cyclotron resonance chemical vapour deposition (ECR-CVD) system at McMaster University [5] using ditertiary butyl silane (DTBS) as the silicon source [6]. A 1 min pure Ar-discharge was used prior to film

Mat. Res. Soc. Symp. Proc. Vol. 442 © 1997 Materials Research Society

deposition to remove contaminants from the substrate surface. Films were deposited on various substrates to allow for different techniques in the post deposition characterization. The film thickness was measured after deposition using an alpha-stepper. The deposition temperature was estimated from temperature calibrations performed in similar plasmas using a surface mounted thermocouple. The Si/C ratio was determined from the Si and C peak to peak ratios of Auger electron spectra. The film density was measured by depositing the film on a 2 μm Al foil and weighing the foil before and after the deposition. Table I summarizes the deposition parameters and some film characteristics for the sample sets A and B.

Table I: Deposition and film characteristics of the investigated *a*-SiC:H films.

	Sample A	Sample B
Substrates	FZ-Si (hi res.), Quartz	Tantalum
Deposition rate [Å/min]	180	250
Deposition temperature [°C]	250	200
Power [W]	1000	1000
Thickness [μm]	2.1	15.5
Si/C ratio	0.36	0.30
Density [g/cm^3]	2.21	1.90

Isochronal annealing was carried out in steps of 50 °C from 200-650 °C for 30 min at each temperature. The annealing was performed by introducing an evacuated quartz tube ($p<10^{-5}$ Torr) containing the samples into a furnace at a fixed temperature. After annealing the samples were cooled down to room temperature very quickly by pushing the samples into the cold zone of the quartz tube.

After each annealing step FTIR and UV-VIS absorption measurements were performed. The energy gap of the *a*-SiC:H films was deduced from the transmittance spectra of the film deposited on a quartz substrate using a Perkin-Elmer UV-VIS spectrometer in the range of 300-700 nm. The FTIR spectra were recorded at room temperature relative to an uncoated FZ-Si substrate and the Si-C, Si-H and C-H absorption bands were analyzed. Due to space limitations, the detailed FTIR results will be published in a more comprehensive paper.

A variable energy positron beam was used to observe changes in the defect structure during *in-situ* annealing by measuring the Doppler broadening of the annihilation line [4]. The spectra were analyzed in terms of the conventional lineshape "S" parameter, defined as the ratio of the integral over a fixed, central position of the peak and the total counts, reflecting the "sharpness" of the annihilation line. While heating the samples the positron energies were kept constant at 2 keV and 20 keV for samples A and B, respectively in order to implant the positrons in the film region of the samples.

For the gas evolution experiments the samples were inserted into a desorption chamber and heated to 800 °C at heating rates of 2 and 10 °C/min. The partial pressures of H, H_2, CH, CH_2, CH_3, and other species were monitored by a quadrupole mass analyzer and were used as a measure of the evolution rate. The amount of hydrogen desorbed from the bare substrate was found to be negligible and was therefore not taken into account.

RESULTS AND DISCUSSION

Figure 1 shows the temperature dependence of the Doppler broadening S parameter in the film region of samples A and B. The samples were heated at an average rate of 1 °C/min. The

measured S parameters were normalized to the S parameter value of silicon at room temperature (0.5080). Since the density of our films is low (see Table I) compared to crystalline SiC (ρ=3.21 g/cm^3), most of the positrons are being trapped by open volume defects. The observed S parameter thus is due to annihilations of positrons from two basic modes: One is the annihilation of free positrons from the bulk or from a trapped state, while the other is the annihilation from a bound state between a positron and an electron, the so-called positronium atom (Ps). Whether Ps is formed or not depends on several factors, an important one being the availability of sufficient space to accomodate Ps. Ps is formed initially in two states, para-Ps with spin zero and ortho-Ps with spin 1, with a probability of 1:3 due to the energy difference between these states. The annihilation of para-Ps contributes a very narrow component to the Doppler broadening spectrum and is therefore reflected by much higher S parameter values.

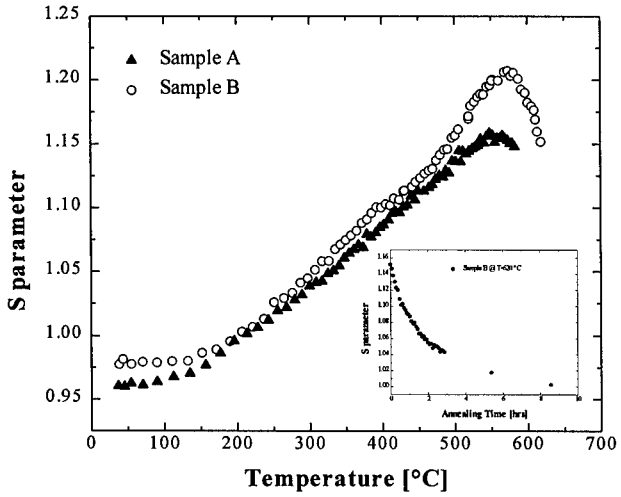


Figure 1: Film S parameter as a function of temperature during heating sample B. The inset shows the S parameter as a function of annealing time at 620 °C.

The S parameter for the as deposited sample B is 2% higher than for sample A, indicating that the higher deposition rate for this sample creates larger positron traps. However, upon increasing the temperature to 200 °C, the S parameter in sample A increases and reaches the value of sample B. In the temperature range from 200 °C to 500 °C, the S parameters for both samples increase at the same rate, indicating that the type and size of defects created is the same. It is well documented that large open volume defects lead to increases in the S parameter values by up to ~15% in Si [7] and GaAs [8]. In this study, the S parameter increases from its original value by this amount when the sample temperature is increased up to 500 °C, which unambiguously indicates that open volumes larger than individual vacancies are formed. The significantly sharper increase of the S parameter in the temperature range 500-550 °C in sample B indicates the formation of even larger voids.

At temperatures above 550 °C the S parameter decreases for both samples indicating a decrease in the trap density for positrons. We attribute this decrease to densification processes in

the film during which the size and the concentration of the voids are reduced. This was reported in a recent paper [4]. The inset in Figure 1 shows the S parameter versus annealing time while holding sample B at 620 °C. Annealing the film for more than 8 hours results in an S parameter close to that of the as deposited sample. At these high temperatures the thermally created voids are essentially removed as a consequence of the observed densification process.

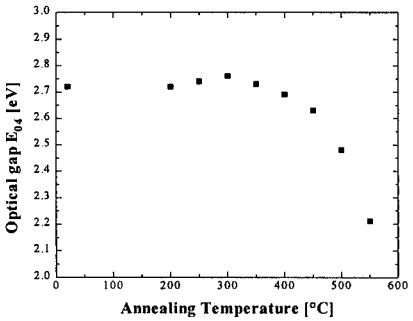


Figure 2: Energy gap, E_{04}, as a function of annealing temperature for sample A.

In Figure 2 we present the values of the optical gap as a function of annealing temperature in sample A. Since it is difficult to define a linear dependence of $(\alpha E^{1/2})$ as a function of E in the fundamental absorption region for films having a high carbon content [9], we used the optical gap E_{04} defined as the energy at which the absorption coefficient is 10^4 cm^{-1}. The relatively high value of E_{04} is a result of the high carbon content in our sample. The optical gap increases slightly with increasing annealing temperature and has a maximum after annealing at 300 °C. This result suggests a recovery stage in this low temperature range, where structural disorder frozen-in after growth is annealed out, reducing the number of dangling bonds on internal surfaces and voids, and leading to a reorganization of the random network. The positron experiments, however, show an increase of the void size and concentration already at these low annealing temperatures. These differences indicate that the optical gap is primarily governed by the density of occupied dangling bonds rather than the variation of the trap density in this temperature range. At annealing temperatures above 300 °C, E_{04} decreases significantly indicating the creation of new defect gap states most likely due to the effusion of hydrogen [10] or other species.

We conducted thermal desorption experiments in order to investigate the mechanism of hydrogen release and to study its influence on the film structure. Typical hydrogen and hydrocarbon evolution spectra for sample B are shown in Figure 3. It should be noted that the observed yield for hydrogen was more than two orders of magnitude higher than for the CH_n groups. This has partly experimental reasons and has to be considered in the interpretation of the data: First, hydrocarbons will be removed from the desorption chamber by the used turbomolecular pump more efficiently than hydrogen. Second, there is a possibility that the hydrocarbon molecules are cracked in the RGA and therefore hydrogen will be detected. Both effects lead to a higher observed hydrogen yield than was actually desorbed from the sample. As is shown in Figure 3 the effusion of loosely bonded CH_n groups is already observable at relatively low temperatures. It is likely that hydrocarbons are desorbed from internal surfaces and voids in the film at these temperatures. This is supported by the enhanced positron trapping in open volume defects observed in the S parameter data. The thermal energy would be too low to break any Si-H or C-H bonds at these temperatures. The hydrogen yields for heating rates of 2 and 10 °C/min show a common feature in the desorption curves: At lower heating rates desorption peaks shift to lower temperatures and need more time to reach a maximum rate.

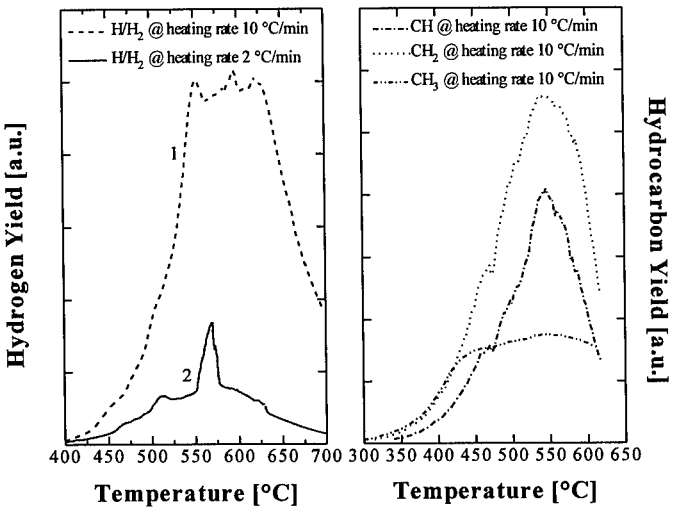


Figure 3: Hydrogen and Hydrocarbon desorption spectra for sample B.

The hydrogen peak at 550 °C in the desorption curve 1 recorded at a ramp rate of 10 °C/min is shifted in curve 2 to 510 °C. We attribute this peak to H from the dissociation of CH, CH_2 and CH_3 molecules in the RGA, since these species show a maximum of the desorption rate at the same temperature. A second peak is observable close to 600 °C in curve 1 and arises most likely from the thermal breaking of C-H bonds. This peak can be seen more pronounced at 570 °C in the desorption curve 2 recorded at the lower ramp rate. The area of this peak indicates that a high concentration of hydrogen is bonded to carbon in the film. The small shoulder seen at 500 °C in curve 1 and located at 470 °C in curve 2 possibly originates from the breaking of Si-H bonds, because a lower activation energy is required to break these bonds. Since the Si/C ratio is low in our films this peak is expected to be much smaller than the peak for the thermal dissociation of C-H. From the size of the molecule it is obvious that the desorption of hydrocarbons from the film has a much higher impact on the film structure than the desorption of trapped hydrogen and can very well explain the observed void formation in our films upon annealing.

The possible origin of the microvoids and the nature of the microvoid surfaces can be discussed by considering the structure of the DTBS molecule used for depositing the *a*-SiC:H films. In the DTBS molecule each C-atom is bonded to 3 methyl groups. At high DTBS flow rates, as used in the growth of our samples, the $C\text{-}H_3$ bonds are not sufficiently broken by the plasma and therefore, these groups are incorporated into the film. This interrupts the film growth in three of the four tetrahedral directions [11] and as a consequence, a microvoid structure is formed. During deposition, hydrogen, CH_n and SiH_n groups can be trapped in these open volumes, partly filling these voids but increasing the number of dangling bonds in the film. At low temperatures some of these dangling bonds are annealed and the optical properties of the films are slightly improved. At the same time desorption of loosely bound hydrocarbons and hydrogen from the internal surfaces of these voids occurs and increases the void size. At sufficiently high temperatures hydrogen bonded to silicon and carbon effuses from the film. This

breaking of C-H bonds is accompanied by more C-C formation and films become more interconnected. As a result the size and density of the defects drops significantly at higher annealing temperatures. This rearrangement of the amorphous network introduced tensile stress in the films and was especially noticeable for the much thicker sample B by the appearance of micro cracks.

CONCLUSION

The defect structure in ECR-CVD *a*-SiC:H films was identified to originate from the incorporation of CH_n groups. At high gas flow rates CH_3 groups are not sufficiently broken by the plasma and are directly incorporated into the film. These groups terminate the matrix around this configuration and create microvoids which are filled with hydrogen and CH_n groups. With increasing temperatures these trapped species are successively released increasing the void size. At sufficiently high temperatures, Si-H and C-H are broken and the films become more interconnected due to the formation of additional C-C bonds. As a consequence the void structure is annealed out and the film become more tensile.

ACKNOWLEDGEMENTS

We wish to thank Dr. R. Macaulay-Newcombe for assisting with the thermal desorption experiments and Dr. G. Balcaitis for the the Auger measurements. This work has been supported by the Natural Sciences and Engineering Research Council of Canada and the Ontario Centre for Materials Research.

REFERENCES

1. D. Kruangani et al. in Amorphous Silicon Semiconductors - Pure and Hydrogenated, edited by A. Madan, M. Thompson, D. Adler, and Y. Hamakawa (Mater. Res. Soc. Symp. Proc. 95, Pittsburgh, PA 1987), p. 609
2. M.A. El Khakani, M. Chaker, A. Jean, S. Boily, H. Pépin, J.C. Kieffer and S.C. Gujrathi, J. Appl. Phys. **74**, 2834, (1993)
3. J. Park, J.Choi, H. Kim, K. Lee and J. Lee, Thin Solid Films, **266**, 129, (1995)
4. T. Friessnegg, M. Boudreau, J. Brown, P. Mascher, P.J. Simpson and W. Puff, J. Appl. Phys., **80**, 2216, (1996)
5. M.G. Boudreau, M. Boumerzoug, P. Mascher and P.E. Jessop, Appl. Phys. Lett., **63**, 3014, (1993)
6. M. Boumerzoug, M. Boudreau, P. Mascher and P. E. Jessop in Diamond, SiC and Nitride Wide Bandgap Semiconductors, edited by C.H. Carter, G. Gildenblat, S. Nakamura, and R.J. Nemanich (Mat. Res. Soc. Symp. Proc. 339, Pittsburgh, PA 1994), p. 381
7. D.D. Perovic, G.C. Weatherly, P.J. Simpson, P.J. Schultz, T.E. Jackman, G.C. Aers, J.-P. Noël and D.C. Houghton, Phys. Rev. B, **43**, 14257 (1991)
8. P.J. Simpson, P.J Schultz, S.-Tong Lee, Samuel Chen and G. Braustein, J. Appl. Phys., **72**, 5 (1992)
9. L.R. Tessler and I. Solomon, Phys Rev. B, **52**, 10962, (1995)
10. F. Demichelis, C.F. Pirri, E. Tresso, V. Rigato and G. DellaMea, J. Non-Cryst. Solids, **128**, 133, (1991)
11. D.H. Williamson, A.H. Mahan, B.P. Nelson and R.S. Crandal, Appl. Phys Lett., **55**, 783, (1989)

Part XIV

Wide-Bandgap Materials: Diamond

BEHAVIOR OF THE POTENTIAL N-TYPE DOPANTS P AND AS IN DIAMOND AFTER LOW DOSE ION IMPLANTATION

H. HOFSÄSS, M. DALMER, M. RESTLE, C. RONNING, K. BHARUTH-RAM*,
H. QUINTEL, AND THE ISOLDE-COLLABORATION**
Universität Konstanz, Fakultät für Physik, Postfach 5560, D-78434 Konstanz, Germany
*University of Durban-Westville, Physics Department, P.B. X54001, 4000 Durban, South Africa
**CERN/PPE, CH-1211 Geneva 23, Switzerland

ABSTRACT

We have studied the lattice sites of P and As impurities in natural IIa diamond after room temperature ion implantation at very low doses of 10^{11} P/cm^2 and $\leq 10^{13}$ As/cm^2 and subsequent annealing. We implanted radioactive ^{33}P and ^{73}Se/^{73}As probe atoms and used the sensitive emission channeling technique to determine the impurity lattice sites. In this technique the channeling effects of emitted decay electrons are measured for different crystal axes. By comparison with calculated electron emission distributions the fractions of emitter atoms on different lattice sites can be quantitatively determined. After annealing of the implanted samples above 900 °C we find high substitutional fractions of 70 ± 10 % for ^{33}P and 55 ± 5 % for ^{73}As.

INTRODUCTION

Boron doped p-type diamond exists as natural type IIb diamond, and can be produced in the laboratory by high temperature high pressure (HTHP) synthesis [1], CVD growth techniques [2,3] and by ion implantation [4]. On the other hand, all attempts at n-type doping of diamond have met with limited success and a convincing proof of n-type conductivity in diamond does not yet exist. Nitrogen, which is present as impurity in natural type I diamond, is a well known deep-level impurity [5] and hence unsuitable for producing n-type semiconducting diamond.

Possible candidates for n-type doping of diamond are the alkali elements Li and Na and the group V elements P, As and Sb [6-9]. HTHP synthesis of P doped diamonds [6,7] and also P doping during CVD growth [10,11] have been attempted. Arsenic-doped diamond single crystals were prepared by Rotner et al. using the HTHP method [12]. Most experimental studies on doping of diamond were carried out by ion implantation [13], including studies on doping with P [14-21] and As [22-24]. Ion implantation is possible for almost any dopant atom and provides the best control of impurity concentration levels and impurity depth distribution. However, it always goes along with radiation damage, which, in the case of diamond, cannot be removed completely by post-implantation annealing procedures [17]. Therefore, the effect of dopant atoms on the electronic properties of an implanted diamond may be obscured by residual implantation defects.

The knowledge of dopant atom lattice sites is essential for the understanding of doping effects in semiconductors. The group I elements Li and Na may act as shallow donors in diamond if they occupy interstitial sites, in analogy to the well known behavior in Si. P and As should be incorporated on substitutional sites as a presupposition for n-type conductivity. Calculations done by Kajihara et al. predict that P may occupy substitutional sites [9,25]. However, depending on the chemical bonding and the presence of defects, P may also occupy other lattice sites, including displacements from geometrically ideal positions. In a recent theoretical work by Jones et al. a

Mat. Res. Soc. Symp. Proc. Vol. 442 © 1997 Materials Research Society

strong binding energy of P with vacancies (V) is suggested, giving rise to deep acceptor P-V complexes with interstitial P [26]. To our knowledge, theoretical studies on the behavior of As in diamond do not exist.

Direct determination of impurity lattice sites is usually done by ion beam channeling. In most of these studies high implantation doses of typically 10^{15} atoms/cm^{-2} were used. To prevent graphitization, samples are usually heated to 600 - 1000 °C during implantation. Gorbatkin et al. estimated a substitutional fraction of 40-50 % for As ions implanted at 600 °C [22]. Recently, Correia et al. determined a 50 % substitutional fraction of As after room temperature implantation of 10^{14} As/cm^2 into IIa diamond and annealing to 1200 °C [23]. Braunstein et al. estimated a substitutional fraction of only 25 % for P implanted at 1150 °C with doses > 10^{15} cm^{-2} [18]. In a similar experiment Zhang et al. estimated a somewhat higher substitutionality for P after 800 °C implantation at a dose of 10^{15} cm^{-2} [19].

Emission channeling is a much more sensitive technique for direct determination of impurity lattice sites [27,28]. This technique makes use of implanted radioactive probe atoms and measures the channeling effects of emitted decay particles such as conversion electrons, ß-particles or α-particles. Hereby, implantation doses below 10^{13} ions cm^{-2} are sufficient for a lattice site determination. In particular, in the present study with ^{33}P the implantation dose was only 10^{11} cm^{-2}. The quantitative determination of site fractions is done by comparison with calculated emission channeling effects [28,29]. Therefore, the emission channeling technique allows to study ion implanted diamond at significantly reduced implantation damage, compared to the conventional ion channeling techniques.

In this paper, we present emission channeling studies to determine the lattice site occupation of radioactive ^{33}P [14] and ^{73}As [24] in natural IIa diamond after low dose room temperature implantation and subsequent annealing.

EXPERIMENTAL

Our samples were natural IIa diamonds of size 3 x 3 x 0.25 mm with polished (110) surface supplied by Drukker International. Several diamonds were implanted at room temperature with either 30 keV ^{33}P ions ($t_{1/2}$ = 25.3 d) or 60 keV ^{73}Se ions ($t_{1/2}$ =7.1 h). ^{33}P decays to ^{33}S, emitting ß$^-$ with end point energy of 250 keV, whose channeling effects in the diamond lattice were measured. ^{73}Se decays to ^{73}As ($t_{1/2}$ = 80.3 d) and finally to ^{73}Ge. Here, the channeling effects of 43 keV conversion electrons emitted in the decay ^{73}As to ^{73}Ge were measured.

^{33}P ions were produced by evaporation of radioactive orthophosphoric acid ($H_3{}^{33}PO_4$) in a Sidenius type ion source. The implantation dose of 10^{11} P/cm^2 was checked by the ß$^-$ activity of the sample. Monte-Carlo simulations using the TRIM code [30] gave a mean ion range of 22 nm (FWHM 13.5 nm), corresponding to a peak concentration of about 10^{17} P/cm^3.

^{73}Se ions were produced at the on-line isotope separator ISOLDE at CERN in a Nb hot plasma ion source and extracted as isotopically pure 60 keV ^{73}Se ion beam [31]. The implantation dose of 10^{13} As/cm^2 was determined by measurements of both the implanted ion charge and the activity of the sample. TRIM calculations gave a mean range of 240 Å (FWHM 60 Å), which yields a peak dopant concentration of about 10^{19} As/cm^3.

Annealing was done in vacuum at 1200 °C for 5 minutes using a DC-current heated graphite boat. The annealing temperature lies well above a pronounced annealing stage around 900 °C, which we observed in previous emission channeling studies using ion implanted As, In and Cd

impurities [24,32]. No loss of activity was measurable so that diffusion of ^{33}P and ^{73}As during annealing can be excluded.

Emission channeling measurements were done using a three-axis goniometer. Samples were pre-oriented by Laue X-ray photographs. The emitted decay electrons were detected with a silicon surface barrier detector as a function of tilt angle to different crystallographic directions with an angular resolution of $\sigma \approx 0.2°$. The normalized emission yield is obtained after background subtraction and normalization to the off-axis random emission yield.

RESULTS

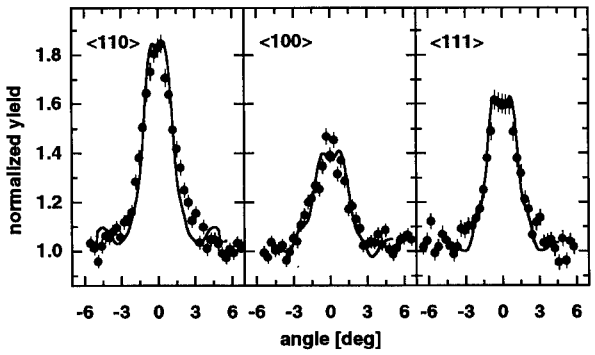


Figure 1: Emission-channeling yields of the 43 keV electrons emitted by the ^{73}As decay along the <110>-, <100>-, and <111>-axial direction from the diamond. The solid lines represent fits to the data of calculated yields based on the dynamical theory of electron diffraction [24].

Fig. 1 shows the normalized conversion electron intensities measured along the three axial directions for an ^{73}As doped diamond after annealing at 1273 K. The normalized β^--intensities measured along the three axial directions for a ^{33}P implanted diamond after annealing to 1473 K is plotted in fig. 2. The differences in height and shape of the spectra for different axial directions are due to different atomic spacing along the axes, which determine the strength of the attractive potential responsible for electron flux peaking. Consequently, we get the strongest channeling effect for the dense <110>-axis and the weakest channeling effect for the <100>-axis.

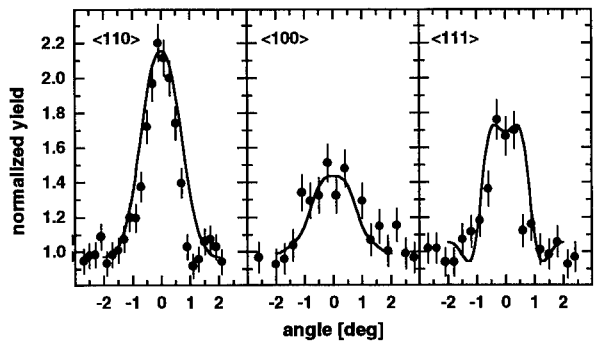


Figure 2: Emission-channeling spectra of β^- from the decay of ^{33}P measured for the principal axial directions after implantation and subsequent annealing at 1200°C of the diamond sample. The solid lines are calculated emission yield distributions fitted to the experimental points [14].

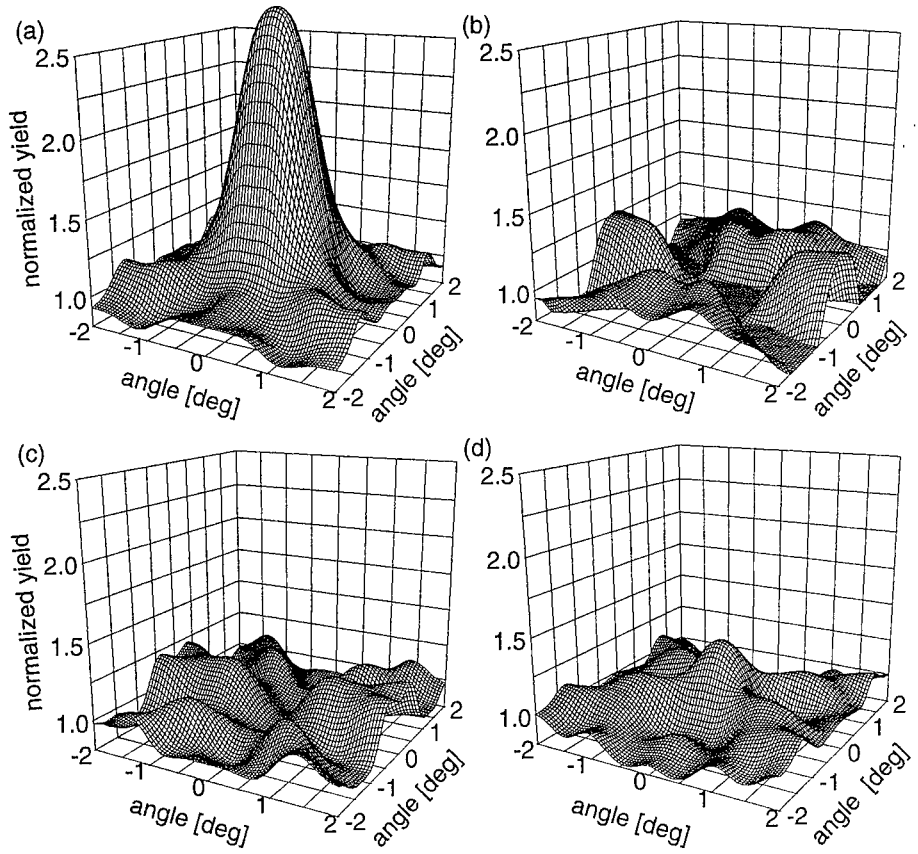


Figure 3: Calculated electron emission distributions around the <110>-axis of diamond for 150 keV electrons. The ^{33}P emitters are located on substitutional (a), tetrahedral interstitial (b), antibonding (c), and bond-center sites (d). The spectra take into account the experimental angular resolution of $\sigma = 0.2°$.

For electron emitting probe nuclei we get channeling peaks, i.e. maximum emission yields, along the <111>- and <100>-axes for both substitutional (S) and tetrahedral interstitial (T) sites. Along the <110>-direction, however, an S site yields a channeling maximum and a T site an almost isotropic emission distribution. Probe nuclei on other interstitial sites like bond-center (BC) and antibonding (AB) sites would also give rise to nearly isotropic emission distributions around the <110>-direction. This is illustrated for electrons from ^{33}P in fig. 3. A corresponding calculation for ^{73}As gives qualitatively the same result [28]. Thus, the channeling peak height observed in <110>-direction is a direct measure of the substitutional fraction of probe nuclei. For both ^{33}P- and ^{73}As-implanted diamond a pronounced <110> channeling peak is observed, which

is evidence for a large substitutional fraction f_S of P and As probe nuclei. Even small displacements from ideal substitutional sites strongly reduce the channeling effects. For example, the distance of AB sites to a <110>-atom row is only 0.44 Å, but the emission distribution for AB sites is almost isotropic (fig. 3). Therefore, the measured channeling effects are compatible with static displacements from S sites of at most 0.2 Å.

By comparing the <110> and <111> channeling effects we can determine the fraction f_T of probe nuclei on tetrahedral interstitial sites. Additionally, we also consider a fraction f_R on random sites (R). These sites comprise other interstitial sites and irregular sites leading to isotropic emission. Quantitative site fractions are determined by fitting calculated channeling spectra to the experimental data shown in fig.1 and fig.2 with site fractions f_S ,f_T and f_R as fit parameters. The calculated one-dimensional channeling spectra are obtained from suited cuts through the calculated 2-dimensional distributions, like the ones shown in fig. 3.

The calculated emission spectra fit well to all measured spectra in figs. 1 and 2, not only regarding the maximum emission yield but also the width and the shape of the spectra. From the fit we obtain for ^{33}P a high substitutional fraction $f_S = 70 \pm 10$ % and a vanishing fraction $f_T \approx 0$ % of tetrahedral interstitial sites and a remaining random fraction $f_R \approx 30$ %. In the case of ^{73}As implanted diamond we get $f_S = 55 \pm 5$ %, $f_T \approx 0$ % and $f_R \approx 45$ %.

CONCLUSION

We have determined the lattice sites of radioactive ^{33}P and ^{73}As implanted into natural IIa diamonds. The majority of the atoms are incorporated on substitutional sites with substitutional fractions of 70 ± 10 % for P atoms and 55 ± 5 % for As and with a limit of 0.2 Å for the maximum deviation from the ideal substitutional positions. We exclude the occupation of tetrahedral interstitial sites. Such a high substitutional fraction of P is measured for the fist time and contradicts the proposed efficient formation of P-V complexes with interstitial P [26]. Our experiments demonstrate that a high substitutionality is achieved by conventional room temperature implantation followed by annealing in vacuum above 900 °C, as long as implantation doses are below about 10^{13} cm^{-2}. No special implantation procedures such as the CIRA technique [4] or hot implantation are necessary. Moreover, low dose room temperature implantation and subsequent annealing is sufficient to create electrically active dopants, giving rise to dopant-related bound-exciton signals in cathodoluminescence spectra [33]. A combination of emission channeling and cathodoluminescence, using identical implantation and annealing conditions, appears therefore very attractive for a detailed investigation of P, As and other impurities in diamond.

ACKNOWLEDGMENT

This work was financially supported by the Bundesminister für Bildung und Forschung.

REFERENCES

1. V.S. Vavilov and E.A. Konorova, Sov. Phys. Usp **19**, 301 (1976).
2. E. Fritsch and A.W. Phelps, Diam. Relat. Mat **2**, 70 (1993).
3. C.F. Chen, S.H. Chen, Diam. Relat. Mat. **4**, 451 (1995).
4. J.F. Prins, Phys. Rev. **B 38**, 5576 (1988).
5. P.R. Briddon and R. Jones, Physica **B 185**, 179 (1993).
6. M. Akaishi, H: Kanda and S. Yamaoka, Science **259**, 1592 (1993).

7. J. Isoya, H. Kanda, M. Akashi, Y. Morita and T. Oshima, Diam. Relat. Mater. (1997) (to be published).
8. S. Prawer, C. Uzan-Saguy, G. Braunstein, R. Kalish, Appl. Phys. Lett. **63**, 2502 (1993).
9. S.A. Kajihara, A. Antonelli, J. Bernholc and R. Car, Phys. Rev. Lett. **66**, 2010 (1991).
10. G.Z. Cao, L.J. Giling, P.F.A. Alkemade, Diam. Relat. Mat. **4**, 775 (1995).
11. M.I. Landstrass, M.A. Plano, M.A. Moreno, S. McWilliams, L.S. Pan, D.R. Kania and S. Han, Diam. Relat. Mater. **2**, 1033 (1993).
12. S.M. Rotner, Y.M. Rotner, G.V. Krishchuk, E.M. Khrakovskaya, N.S. Stephanova, V.A. Laptev, Sov. Phys. Semicond. **17**, 128 (1983).
13. M.S. Dresselhaus and R. Kalish, Ion Implantation in Diamond, Graphite and Related Materials, Springer Series in Materials Science Vol. **22** (Springer, Heidelberg, 1992).
14. H. Hofsäss, M. Dalmer, M. Restle, C. Ronning, J. Appl. Phys (1997), (to be published).
15. M.G. Allen, S. Prawer, D.N. Jamieson and R. Kalish, Appl.Phys.Lett. **63**, 2062 (1993).
16. G. Braunstein and R. Kalish, Appl. Phys. Lett. **38**, 416 (1981).
17. J.D. Hunn, N.R. Parikh, M.L. Swanson and R.A. Zuhr, Diam. Relat. Mat. **2**, 847 (1993).
18. G. Braunstein and R. Kalish, Nucl. Instr. Meth **182/183**, 691 (1981).
19. Z. H. Zhang, Nucl. Instr. Meth **B 118**, (1996).
20. J.F. Prins, Diam. Relat. Mat. **4**, 580 (1995).
21. J.F. Prins, Diam. Relat. Mat. **5**, (1996), (to be published).
22. S.M. Gorbatkin, R.A. Zuhr, J. Roth, H. Naramoto, J. Appl. Phys. **70**, 2986 (1991).
23. J.G. Correia, J. Marques, E. Alves, D. Forkel-Wirth, S.G. Jahn, M. Restle, M. Dalmer, H. Hofsäss, K. Bharuth-Ram, Nucl. Instr. Meth. B , (1997), (to be published).
24. K. Bharuth-Ram, H. Quintel, M. Restle, C. Ronning, H. Hofsäss and S.G. Jahn, J. Appl. Phys. **78**, 5180 (1995).
25. S.A. Kajihara, A. Antonelli, J. Bernholc, Physica **B 185**, 144 (1993).
26. R. Jones, J.E. Lowther, J. Goss, Appl. Phys. Lett. **69**, 2489 (1996)..
27. H. Hofsäss and G. Lindner, Phys. Rep. **201**, 121 (1991).
28. H. Hofsäss, Hyp. Int. **87/88**, 247 (1996).
29. H. Hofsäss, U. Wahl and S.G. Jahn, Hyp. Int. **84**, 27 (1994).
30. J.F. Ziegler, J.P. Biersack and U. Littmark, The Stopping and Ranges of Ions in Solids, (Pergamon Press, New York, 1985).
31. E. Kugler, D. Fiander, B. Jonson, H. Haas, A. Przewloka, H. L. Ravn, D. J. Simon, K. Zimmer and the ISOLDE Collaboration, Nucl. Instr. Meth. **B 70,** 41 (1992).
32. H. Quintel, K. Bharuth-Ram, H. Hofsäss, M. Restle, C. Ronning, Nucl. Instr. Meth. **B 118**, 72 (1996).
33. H. Sternschulte, T. Albrecht, K. Thonke, R. Sauer, M. Dalmer, C. Ronning, H. Hofsäss, presented at Diamond Films '96, Tours, 1996 ; Appl. Phys. Lett. (1997), (submitted).

Correlation Between Defects and Electrical Conduction in Surface Conductive Layer of CVD-diamond Films

Y. Show, F. Matsuoka, S. Ri, Y.Akiba, T. Kurosu, M. Iida, and T. Izumi

Dept. of Electronics, Fac. of Engineering, Tokai University
1117 Kitakaname, Hiratsuka, Kanagawa, JAPAN

Correlation between defects and electrical conduction in surface conductive layers of CVD diamond films has been studied using electron spin resonance (ESR) and two points probe technique methods. The ESR analysis revealed the presence of P_{ac}-center with spin density of 10^{20} spins/cm^3. The P_{ac}-center is composed from two ESR signals : ESR signal from carbon dangling bond with carbon atom neighbors and ESR signal from carbon dangling bond associated with nearest neighbor hole (hole associated P_{ac}-center). The hole associated P_{ac}-center is an electrically active defect.

1. Introduction

It is well known that the surface of diamond films, which is deposited by chemical vapor deposition (CVD) method, indicates low resistivity, while high pressure synthetic diamond and natural diamond (except IIb type one) have high resistivity with ~10^{16} Ω·cm. Landstrass *et al.* [1] postulated that low resistivity of as-grown film is due to hydrogen passivation of traps in the film. Grot *et al.* [2] reported that a thin nondiamond surface layer is formed on top of CVD diamond films and the resistance of as-grown diamond films increases after removing the nondiamond surface layer. Moreover, Ri *et al.* [3] proposed the formation mechanism of a p-type conductive layer on the diamond surface. According to Ri's model, the ionization of acid produces oxonium ion (H_3O^+) which reacts with hydrogen on diamond films, and a hole is created in the diamond films. However, the mechanism of surface conductive layers has not been completely clarified up to the present, in spite of a large number of studies about the surface conductive layer.

In this paper, we present defect structures in the surface conductive layer of diamond film by the ESR method. Moreover, we discuss the correlation between the defects and electrical conduction.

2. Experimental

Diamond films were deposited by the hot filament chemical vapor deposition (HF-CVD) method on p- and n-type silicon. The methane (CH_4) gas diluted in hydrogen (H_2) gas at 1% was used as source gas. The total source gas flow rate was kept 100 sccm. The filament was positioned approximately 3 mm above the substrate. The filament temperature, chamber pressure and substrate temperature were maintained at 2100℃, 100 Torr and 800℃, respectively. The

Mat. Res. Soc. Symp. Proc. Vol. 442 © 1997 Materials Research Society

diamond films with thickness of ~13 μm and with grain size of ~2μm were formed on the substrate after the deposition time of 2 hours.

Thermal treatments were carried out in oxygen and argon atmosphere at 600℃ for 10 min. After the thermal treatment in the oxygen atmosphere, the hydrogen treatment was carried out using the HF-CVD equipment at the filament temperature of 2100℃ for 10 min in pure hydrogen gas. The temperature of the diamond films increased up to 800℃ during the hydrogen treatment.

The defect structures in the diamond films were investigated by the ESR method. The ESR measurements were performed using X-band spectrometer at room temperature. The g-value, the line width (ΔH_{PP}) and the signal intensity were determined using the signals of Mn^{2+} and 1,1-diphenyl-2-picryl- hydrazyl (DPPH) as the calibration references.

Electrical properties were investigated using points probe technique and Seebeck effect measurement. An ohmic electrode of 1 mm in diameter was formed by sputtered Au. The distance between the two electrodes was 1 mm. The Seebeck effect measurement was carried out in the following manner : (a) the heating point is about 500 K and the cold point (reference) is room temperature; (b) the distance between two probe points was 1 mm.

3. Results and Discussion

Fig. 1(a) shows typical ESR signal from as-grown diamond film. The ESR signal has a Lorenzian line shape with g=2.003 and ΔH_{PP}=3 Oe and has a tail at its foot. We deconvoluted the ESR signal into two kinds of centers as shown in Fig. 1(b) and 1(c), that is, the P_{dia}-center with g=2.003, ΔH_{PP}=3 Oe and the P_{ac}-center with g=2.003, ΔH_{PP}=8 Oe. The P_{dia}-center originates from a carbon dangling bond in the diamond layer. On the other hand, the P_{ac}-center originates from a carbon dangling bond in the non-diamond region [4, 5].

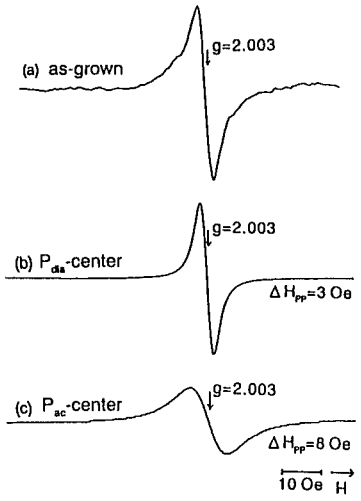


Fig. 1 (a) the ESR signal from the as-grown diamond film. The ESR signal can be deconvoluted into two kinds of ESR centers. (b) P_{dia}-center : g=2.003 ΔH_{PP}=3 Oe. (c) P_{ac}-center : g=2.003, ΔH_{PP}=8 Oe.

Fig. 2 shows correlation between the ESR centers and the resistance of diamond films. The P_{dia}-center and the P_{ac}-center were observed from as-grown diamond films. If these ESR centers are distributed uniformly in the diamond films, the spin densities in the diamond film would be ~10^{17} spins/cm^3 for the both ESR centers. Resistance of the as-grown diamond film was 1.8×10^6 Ω. Moreover, Seebeck effect measurement showed that the as-grown diamond surface was p-type conduction layer.

When thermal treatment of the diamond film was carried out in oxygen atmosphere at 600℃, the intensity of the P_{ac}-center decreased to two-thirds compared with that of the as-grown sample, while the intensity of the P_{dia}-center decreased slightly under approximately 10 percent. On the other hand, the resistance of the diamond film increased from 1.8×10^6 to 9×10^8 Ω. In case of the thermal treatment in argon atmosphere, however, both the ESR intensities and the electrical resistance did not change.

When hydrogen treatment was carried out for the diamond film after the thermal treatment in an oxygen atmosphere, the intensity of the P_{ac}-center increased again. It's value was almost the same as that of as-grown diamond films, while the intensity of the P_{dia}-center did not change. On the other hand, the resistance of the diamond film decreased to 6×10^6 Ω after the hydrogen treatment.

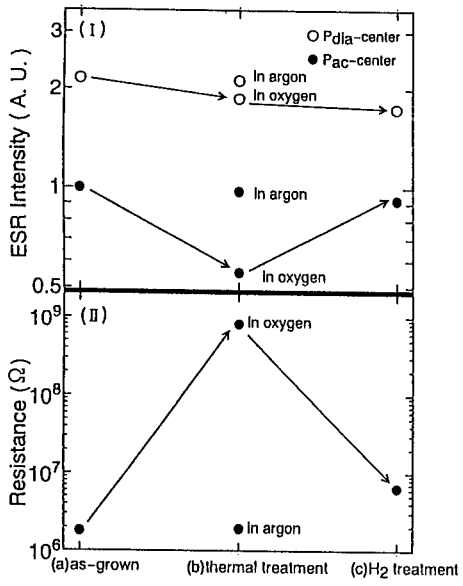


Fig. 2 Correlation between the ESR centers and the resistance. (a) as-grown diamond film. (b) after the thermal treatment. (c) after the hydrogen treatment.

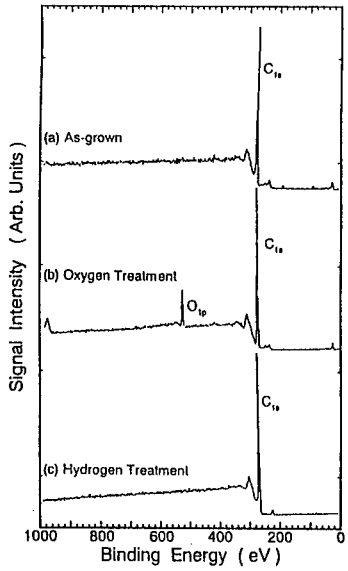


Fig. 3 XPS signals observed from (a) as-grown, (b) thermal treated and (c) hydrogen treated diamond films.

Fig. 3 shows the X-ray photoelectron spectroscopy (XPS) signals from Fig. 3(a) as-grown, Fig. 3(b) thermal treated in oxygen atmosphere and Fig. 3(c) hydrogen treated diamond films. The XPS signal from C_{1S} (286 eV) was commonly observed from these samples. When the thermal treatment was carried out in an oxygen atmosphere at 600℃, the XPS signal from O_{1S} (530 eV) was newly observed. After the hydrogen treatment, the XPS signal from O_{1S} disappeared. Aizawa *et al.* [6] reported that hydrogen is chemisorbed on the diamond (111) and (100) surfaces epitaxially grown by the plasma CVD method from the result of the high resolution electron-energy loss spectroscopy (HREELS). Ando *et al.* [7] reported oxidation of the hydrogenated diamond occurred above 300℃ and the maximum chemisorption of oxygen onto the diamond surface was obtained in the oxidation between 480 and 500℃. Therefore, our XPS measurements show the hydrogen terminated surface is formed on the diamond film during the film deposition. When the thermal treatment was carried out in an oxygen atmosphere, the diamond surface modified the hydrogen termination into oxygen termination. After the hydrogen treatment, the oxygen terminated diamond surface was converted again into the hydrogen terminated surface.

Above results indicate that as-grown and hydrogen treated diamond surfaces, which have hydrogen termination, give low resistivity by forming the surface conductive layer. Moreover, high density of P_{ac}-center exists in the surface conductive layer. Since thickness of surface conductive layer was assumed to be 5 nm [8], the spin density of the P_{ac}-center in the surface conductive layer is of the order of 10^{20} spins/cm^3 or more. The spin density in the surface conductive layer is three order higher than that of inner part of diamond films. When the diamond

surface was oxidized by the thermal treatment, the P_{ac}-center in the surface conductive layer is removed. This means that the density of the carbon dangling bonds (P_{ac}-center) in the oxygen terminated diamond surface layer is lower than that of the hydrogen terminated diamond surface layer.

We propose the defect model of diamond surface region from above results as shown in Fig. 4. The as-grown and the hydrogen treated diamond surfaces are terminated with hydrogen atoms (Fig. 4 (a)). In case of the hydrogen termination to diamond surfaces, P_{ac}-center, which originates from carbon dangling bond with carbon atom neighbors, exist in the surface region, because the hydrogen termination of diamond surface cannot compensate completely to the dangling bonds near the surface. The density of the P_{ac}-center in the surface region is in the order of 10^{20} spins/cm^3 or more. In addition, the as-grown and hydrogen treated diamond surfaces give low resistance of 1.8×10^6 and 6×10^6 Ω, respectively. Nakahata *et al.* [9] reported the surface conductive layer with the resistance of 10^4 - 10^6 Ω is caused by hydrogen which reacted with the diamond surface. Maki *et al.*, [10] observed that the carrier in the conductive layer with the resistance of ~10^6 Ω, which produced by hydrogenation of single-crystal diamond (type-Ia), is a hole and the carrier concentration is estimated to be ~3.0×10^{18} /cm^3 at 500 K from the result of the Seebeck effect measurement. The resistance observed from the as-grown and the hydrogen treated diamond films in our study is comparable to that of their reports. Moreover, we also obtained the fact that a p-type conductive layer exists in the surface region of these diamond films.

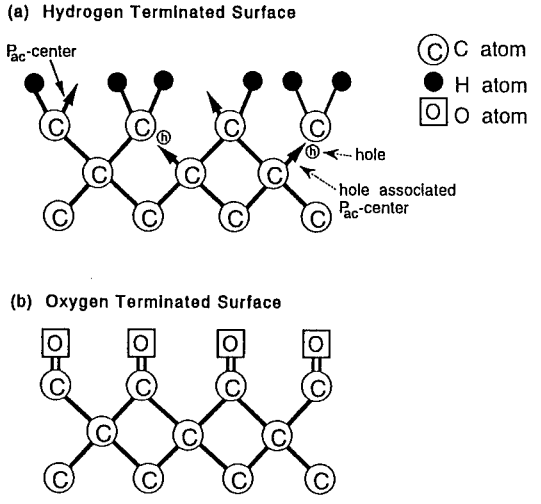


Fig. 4 Defect model of the diamond surfaces. (a) the surface of as-grown and hydrogen treated diamond films. (b) the thermal treated diamond film in oxygen atmosphere.

Therefore, it seems that the hydrogenation of the diamond surface produces holes in the surface region and the resistance of the surface region decreases. When the holes are generated in the surface region, the paramagnetic defect (hole associated P_{ac}-center), which originates from a carbon dangling bond associated with the nearest neighboring hole, is formed. The hole associated P_{ac}-center is an electrically active defect. The spin density of the ESR center is considered to be almost on the same order as that of the hole in the surface conductive layer. When the thermal treatment is carried out in the oxygen atmosphere, the diamond surface is terminated with oxygen atoms (Fig. 4(b)). The P_{ac}-center is removed by the termination of oxygen atom to diamond surface. Moreover, the hole associated P_{ac}-center also disappeared, because no hole exists in the oxygen terminated diamond surface region.

4. Conclusions

Correlation between the defect structures and electrical conduction in surface conductive layers of diamond films has been investigated by the ESR and two points probe technique methods. The ESR analysis revealed the presence of P_{ac}-center (g=2.003 ΔH_{PP}= 8 Oe) with spin density of 10^{20} spins/cm^3 in the surface conductive layer. The P_{ac}-center consists of two types of defect, that is, carbon dangling bond with carbon atom neighbor, and carbon dangling bond associated with the nearest neighboring hole (the hole associated P_{ac}-center). The hole associated P_{ac}-center is an electrically active defect. The P_{ac}-center is removed by thermal treatment in oxygen atmosphere.

References

1. M. I. Landstrass and K. V. Ravi : Appl. Phys. Lett. **55**, 975 (1989)
2. S. A. Grot, G. S. Gildenblat, C. W. Hatfield, C. R. Wronski, A. R. Badzian and R. Messier : IEEE Electron Device Lett. **12**, 100 (1990)
3. Ri S. G, T. Mizumasa, Y. Akiba, Y. Hirose, T. Kurosu and M. IIda : Jpn. J. Appl. Phys **34**, 5550 (1995)
4. Y. Show, M. Iwase and T. Izumi : Thin Solid Films **50**, 274 (116)
5. Y. Show, Y. Nakamura, T. Izumi, M. Deguchi, M. Kitabatake, T. Hirao, Y. Mori, A. Hatta, T. Ito, A. Hiraki : Thin Solid Films **281-282**, 275 (1996)
6. T. Aizawa, T. Ando, M. Kamo and Y. Sato : Phys. Rev. B **48**, 18348 (1993)
7. T. Ando, K. Yamamoto, M. Ishii, M. Kamo and Y. Sato : J. Chem. Soc. Frans **89**, 2685 (1993)
8. Y. Mori, Y. Show, M. Deguchi, H. Yagi, H. Yagyu, N. Eimori, T. Okada, A. Hatta, K.Nishimura, M. Kitabatake, T. Ito, T. Hirao, T. Izumi and A. Hiraki : Jpn. J. Appl. Phys. **31**, L987 (1993)
9. H. Nakahata, T. Imai and N. Fujimori : Proc. of the Second Int. Sympo. on Diamond Material 487 (1991)
10. T. Maki, S. Shikama, M. Komori, Y. Sakaguchi, K. Sakuta and T. Kobayashi : Jpn. J. Appl. Phys. **31**, L1446 (1992)

CHARGE TRANSIENT SPECTROSCOPY STUDY OF DEEP CENTERS IN CVD DIAMOND AND DIAMOND-LIKE FILMS

V.I. POLYAKOV *, A.I. RUKOVISHNIKOV *, N.M. ROSSUKANYI *, V.P. VARNIN **, I.G. TEREMETSKAYA **, B.L. DRUZ ***, E. OSTAN ***, and A. HAYES ***

* Institute of Radio Eng. & Electronics, RAS, 11 Mohovaya str., Moscow 103907, Russia, vip197@ire216.msk.su
** Institute of Physical Chemistry, RAS, Moscow, Russia
*** Veeco Instruments Inc., Plainview, NY

ABSTRACT

The parameters of trapping centers in CVD diamond and Diamond-Like Carbon (DLC) films were studied by Charge Deep Level Transient Spectroscopy (Q-DLTS). The concentrations, activation energies, captures cross-section and location of the trapping centers were determined. The influence of post deposition heat treatment on the defect center parameters was studied. The Q-DLTS measurements showed that micro defects are acting as point trapping centers and have the continuous energy spectrum with one or two maximums at different energies. The nature of the trapping centers is discussed.

INTRODUCTION

CVD diamond and Diamond-Like Carbon (DLC) films are the most promising materials for electronic and optoelectronic devices due to inherently superior properties such as wide bandgap, high thermal conductivity, high breakdown field, very good insulating and passivation quality. For electronic device application, it is of great importance to understand the electrical properties and conduction mechanisms as well as the junction properties of these films. Detailed information about the defect states (including deep levels) is needed in order to understand completely the behavior of the devices, since these defects are electrically active, behaving as trapping or recombination centers. Although a dominant trap level is obtained from the temperature dependence of diamond film current-voltage (I-V) characteristics, further studies of trap levels which have a strong influence on electrical properties are necessary in addition to I-V measurements [1]. For example, deep-level transient spectroscopy (DLTS) has already been used extensively to study the parameters of the deep levels in conventional semiconductors [2-5]. The results on DLTS boron doped diamond films were reported in [6]. However, standard DLTS methods can not be used for the study of defect states in undoped wide bandgap and insulating materials.

In this paper, we demonstrate the opportunity of the isothermal charge-based deep level transient spectroscopy (Q-DLTS) for obtained information about trapping centers (TC) in doped (semiconducting) and undoped (insulating) diamond and diamond-like films. In comparison to the widely used capacitance-based (C-DLTS) method [7], our method measuring the charge but not capacitance, provides the possibility of investigating the structures with the high frequency capacitance independent of the charge state of the interface and bulk traps. This is true, for example, for metal / insulator / metal structures or MIS structures in the case of pinning of the Fermi level. As other transient techniques, the Q-DLTS method is based on the measurement of the trapped charge transient process after voltage or light stimulation on the structure. It provides

Mat. Res. Soc. Symp. Proc. Vol. 442 © 1997 Materials Research Society

information about activation energy, capture cross section, density of states, and space distribution of active trapping centers.

EXPERIMENTAL DETAILS

The Q-DLTS method is described in detail in Refs. [8-10]. The block diagram of the Q-DLTS apparatus is shown in Fig. 1. The Q-DLTS measurement uses cyclic bias pulses to change the charge state of the trapping centers. During the first part of a cycle, the switch S1 is open, S2 is closed, and the trapping centers are filled by applying a forward bias pulse to the sample from DAC_V (Fig. 1). In the next part of the cycle, the trapped charge is emitted by changing the bias on the sample to zero. The charge emitted during the emission process is collect by using an integrator circuit shown in Fig. 1. The integrator circuit includes a high-speed operational amplifier OPA with capacitance in the feedback loop. The measured value of the Q-DLTS signal can be written as $\Delta Q = Q(t_2) - Q(t_1)$, where t_1 and t_2 are the times from the beginning of discharge. The charge ΔQ flowing through the circuit during the time period $\Delta t = t_2 - t_1$ is measured as a function of parameters of the bias pulse, temperature, and rate window $\tau_m = (t_2 - t_1) / \ln(t_2/t_1)$.

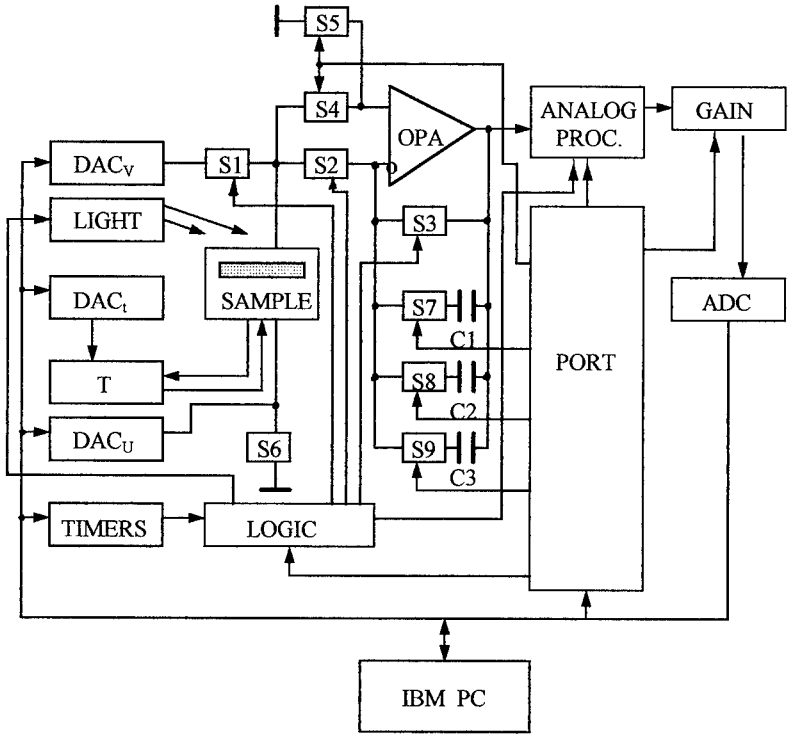


Fig. 1. Block diagram of the Q-DLTS apparatus, S1-S9 - analog switches OPA - operational amplifier, DAC - digital to analog converter, ADC - analog to digital converter, C1-C3 - capacitances.

If assuming that the charge emission from the TC varies exponentially with time and the integration time constant is much smaller than the trap emission time, the signal at the integrator output represents the trapped charge emission $Q(t) = Q_0 [1 - \exp(-e_{p(n)} t)]$. The Q-DLTS signal is given by

$$\Delta Q = Q_0 [\exp(-e_{p(n)} t_1) - \exp(-e_{p(n)} t_2)], \quad (1)$$

where $Q_0 = \int_0^\infty Q_0(t)dt$. For acceptor-like (or donor-like) traps,

$$e_{p(n)} = \sigma \Gamma_{p(n)} T^2 \exp(-E_a/kT) \quad (2)$$

is the hole (electron) emission rate, $\Gamma_{p(n)} = 2 * 3^{1/2} (2\pi/h^2)^{3/2} k^2 m^*_{p(n)}$, σ is the capture cross-section, T is the temperature, E_a is the activation energy, h is the Planck constant, k is the Boltzmann constant, $m^*_{p(n)}$ is the effective mass of the hole (electron).

The cycle DLTS algorithm used in the present work is different from that of Lang [7]. In Lang's algorithm, the time period Δt (or rate window τ_m), is kept fixed while the sample temperature is scanned to obtain the DLTS spectrum. The alternative algorithm used in the present work obtains the spectrum by scanning the rate window τ_m while keeping the temperature of the sample fixed. If we keep the ratio $t_2 / t_1 = \alpha$ constant and vary $\tau_m = t_1 (\alpha - 1)/\ln\alpha$, the functional dependence $\Delta Q(\tau_m)$ has a maximum that can be used to determine the trapping center parameters. Indeed, differentiating Eq. (1) with respect to τ_m, we find that the maximum in $\Delta Q(\tau_m)$ occurs at the rate window equal to the emission rate of the traps, i.e. $\ln\alpha /(\alpha - 1)t_1 = e_{p(n)}$. The maximum value of the DLTS signal ΔQ_{max} is $Q_0[\alpha^{1/(1-\alpha)} - \alpha^{\alpha/(1-\alpha)}]$. In the present measurements $\alpha = 2$ is selected such that $e_{p(n)} = \ln 2/t_1$ and $\Delta Q_{max} = Q_0 /4$. We find the emission rate of the traps without recourse to temperature scanning, which takes considerable time. The density of TC can be obtained from Q-DLTS spectra measured at room temperature as $N_t = 4 \Delta Q_{max} / qAd$, where q - the electron charge, A - the contact area, d - the thickness of the film. The activation energy E_a and capture cross-section σ are defined from an Arrhenius type plot of $\ln(\tau_m^{-1} * T^{-2})$ over T^{-1} [as can be seen from Eq.(2)] after measurements of Q-DLTS at several temperatures.

Q-DLTS measurements were made by the computerized system ASMEC in which the charge sensitivity is ΔQ_{min} - 10^{-16} Coulomb, deep level density sensitivity N_t/N - 10^{-7} (N - concentration of noncompensated shallow impurities), and range of rate window duration τ_m - 10^{-6} - 200 s .

RESULTS AND DISCUSSION

The polycrystalline B-doped and undoped diamond films were fabricated on Si or W substrates by hot filament CVD method. The used methods and techniques of chemical vapor deposition were described in [6]. Diamond films were grown from a mixture of 0.5 - 1.5% methane or acetone and hydrogen. The substrate temperature was varied from 870 to 920^0 C .

The insulating diamond-like carbon films with thickness of 4-400 nm were deposited on silicon substrates using RF inductively coupled CH_4 - plasma source [11].

The Ni and Ti electrodes with area about 2 mm^2 were deposited on the polycrystalline CVD and DLC films by evaporation of Ni in vacuum and d.c. magnetron sputtering of Ti. The films prepared had polycrystalline or amorphous structures and their thickness varied from $5*10^{-7}$ to $5*10^{-3}$ cm.

Figures 2-4 show the Q-DLTS spectra taken at room temperature from the sample consisting of boron-doped polycrystalline diamond film with Ni top electrode, before (Fig. 2) and after annealing at low (Fig. 3) and high (Fig. 4) temperatures. From the temperature dependencies of the DLTS peak positions, two activation energies E_{aA} = 0.4 and E_{aB} = 0.2 eV, were obtained for boron-doped diamond films, as is shown in Fig. 5. These values were not changed by the temperature treatments. However, annealing even at such low temperature as 130^0 C resulted in redistribution of the deep level density in favor of the deeper levels, see Fig. 3. The temperature treatment at high temperatures (650^0 C for Fig. 4) practically removed the levels with the activation energy 0.2 eV and strongly enhanced the higher activation energy peak. For all the samples trapping centers are working like point micro defects with average capture cross-sections 0 - $\sigma = 10^{-22} - 10^{-20}$ cm^2.

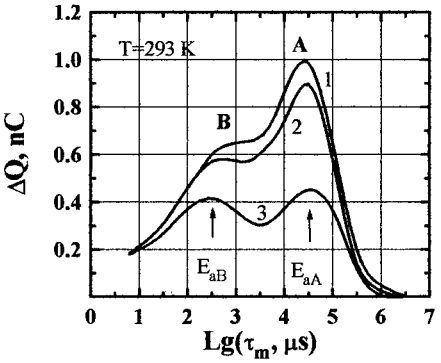


Fig. 2. Q-DLTS spectra of HF CVD diamond film for amplied pulse 1 V and different pulse duration: 1 - 2 ms; 2 - 1 ms; 3 - 0.5 ms. E_{aA} and E_{aB} - activation energies of the trapping centers.

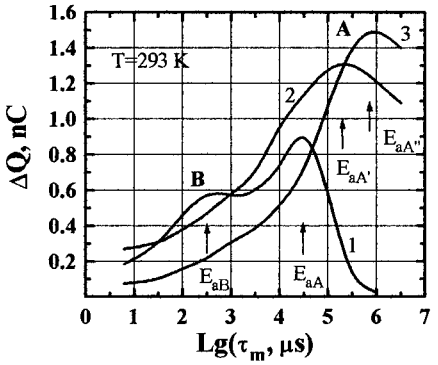


Fig. 3. Q-DLTS spectra of HF CVD diamond films: 1 - before annealling; 2 - after annealing on air at 130^0 C; 3 - after annealing on air at 220^0 C.

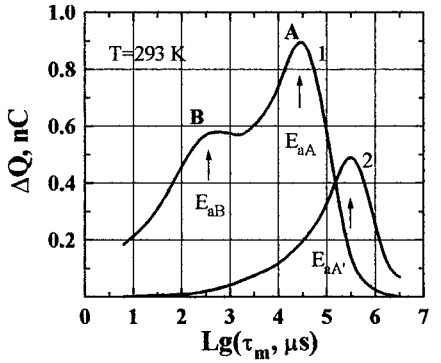


Fig. 4. The influence of annealling on air at 650^0 C on Q-DLTS spectra of HF CVD diamond film: 1 - before and 2 - after heat treatment.

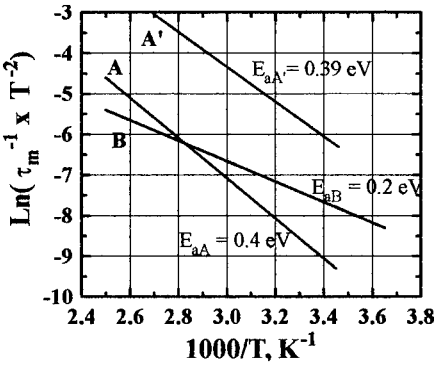


Fig 5. The Arrhenius plot (HF CVD diamond film). The capture cross-sections for different TC are: $\sigma_A = 7.4 \cdot 10^{-19}$ cm^2; $\sigma_A = 9.2 \cdot 10^{-19}$ cm^2; $\sigma_B = 6.8 \cdot 10^{-22}$ cm^2.

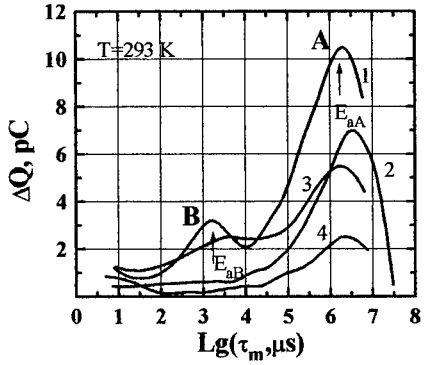


Fig. 6. Q-DLTS spectra of DLC films deposited at different CH_4 flow rates and beam currents: 1 - 12.5 sccm, 250 mA; 2 - 20 sccm, 130 mA; 3 - 12.5 sccm, 170 mA; 4 - 20 sccm, 250 mA.

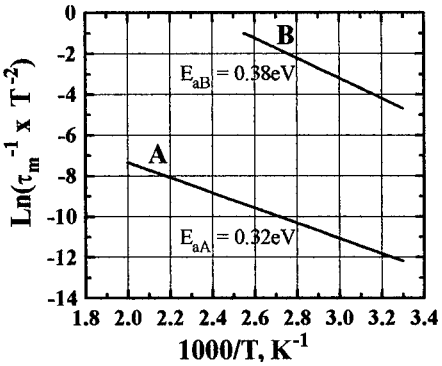


Fig. 7. The Arrhenius p lot (DLC film). The capture cross sections are: $\sigma_A = 3.5 * 10^{-22}$ cm^2 and $\sigma_B = 7.0 * 10^{-18}$ cm^2.

From the analysis of the results, a possible model is suggested describing the effect of annealing on electrical properties of diamond films as result of the decreased conductivity along the grain boundaries with the activation energy 0.2 eV after the heat treatment.

One or two peaks "A" and "B" usually were distinguished by investigation of trapping center parameters in DLC films (Fig. 6). The traps corresponding to these peaks possess average activation energies - E_a = 0.3 - 0.5 eV, and capture cross-sections: $\sigma_A = 10^{-22}$ - 10^{-20} cm^2, $\sigma_B = 10^{-18}$ - 10^{-16} cm^2 (see Arrhenius plot in Fig. 7). To reveal the nature and locations of peaks, Q-DLTS spectra were taken under different charging voltages and light illumination conditions. The variation of the applied voltage affects the amplitude and position of the peaks in the Q-DLTS spectra. Under light illumination, peak B and A shift to the lower relaxation time. The relaxation time correlates with the activation energy E_a. Therefore, when the relaxation time (e.g. peak position on the Q-DLTS spectra) shifts to lower τ_m values, it causes us to believe that the peak is stipulated by the continuous energy spectrum of TC with one or two peaks, and localized on the interface and bulk [12]. The obtained results showed that micro defects are working like point trapping centers.

Before annealing, the TC density N_t was about 10^{14} cm^{-3} and can decrease substantially after annealing (to 1-2 10^{13} cm^{-3}). It seems, dangling bonds are the main reason for point trapping centers in DLC films. The annealing effect in diamond and DLC films can be the result of the oxygen saturating the dangling bonds.

ACKNOWLEDGMENTS

The authors are indebted to Dr. A.I.Krikunov for contacts manufacture and Dr. A.V. Khomich for valuable discussions.

REFERENCES

1. S. Nath, J.I.B. Wilson, Diamond and Related Materials, **5**, 65 (1995).

2. W.Chu, J. Matthey, and T. Purcell, III-Vs Reviev, **9**, 44 (1996).

3. Y. Okamoto, H.Yonekura, J. Morimoto, and T. Miyakava, Rev Sci. Instrum., **67**, 809, (1996).

4. S.Libertino, S.Coffa, G, Franzo, and F. Priolo, J.Appl.Phys., **78**, 3867, (1995).

5. Z.Chen and A. Mandelis, Appl. Phys. Lett., **59**, 1861, (1991).

6. H.Kiyota, H.Okushi, K.Okano, Y. Akiba, T. Kurosu, and M.Iida, Diamond and Related Materials, **2**, 1179, (1993); K.Srikanth, S.Asok, W.Zhu, A.Badzian, and R.Messier, Diamond, Boron Nitride, Silicon and Related Widebandgap Semicond., edited by J.T.Glass et al (Mater. Res. Soc. Proc. 148, Pittsburgh, PA, 1990); J.W.Glesener, Appl. Phys. Lett., **63**, 767, (1993).

7. D.V. Lang, J.Appl. Phys. **45**, 3023 (1974).

8. V.I. Polyakov, P.I. Perov, A.I. Rukovishnikov, O.N. Ermakova, A.L. Aleksandrov, B.G. Ignatov, Mikroelektronika, **16**, 326 (1987).

9. B.M. Arora, S. Chakravarty, S. Subramanian, V.I. Polyakov, M.G. Ermakov, O.N. Ermakova, P.I.Perov., J.Appl.Phys., **73**, 1802 (1993).

10. V.I. Polyakov, A.I. Rukovishnikov, P.I. Perov, A.V. Khomich, A.A. Sukhanov, B.F. Dorfman, B.N. Pypkin, M.G. Abraizov, B. Druz, Thin Solid Films, (1996), to be published.

11. B.L.Druz, A.Hayes, E.Ostan, V.I.Polyakov, N.M. Rossukanyi, A.I.Rukovishnikov, A.V. Khomich, Diamond and Related Materials, (1997), to be published.

12. V.Polyakov, M.Ermakov, O.Ermakova, P.Perov, V.Sleptsov, V.Elinson, A.Baranov, 2nd International Conference on the Applications of Diamond Films and Related Materials, edited by M. Yoshikawa, Y. Tzeng, and W.A. Yarbrough (The 2nd Internation Conference - ADFRM Proc., Tokyo, Japan 1993), p.381-386.

COEXISTENCE OF TWO CARBON PHASES AT GRAIN BOUNDARIES IN POLYCRYSTALLINE DIAMOND

O. SHENDEROVA, D.W. BRENNER

Department of Materials Science and Engineering, North Carolina State University, Raleigh, NC 27695-7907

ABSTRACT

Energies and structures for two models of <001> tilt grain boundaries in diamond have been calculated using a many-body empirical bond-order potential. The first model contains all four-fold coordinate atoms. The second model is a two-phase system in which a graphitic region connects the diamond grains. At selected misorientation angles we predict that the two-phase structures are energetically competitive with the sp^3 bonded structures when the width of the graphitic regions exceed 10-15Å.

INTRODUCTION

The chemical vapor deposition of diamond coatings over large areas results in polycrystalline films with defects that include grain boundaries and regions of sp^2-bonded carbon. The latter can be characterized with Raman spectroscopy, which typically shows a sharp diamond peak at 1332 cm^{-1} plus a broad background arising from sp^2 bonded carbon. This background has been interpreted as a graphitic phase[1-3], amorphous or diamond-like carbon[4], linear assembles of sp^2 bonded carbon[2] and polycyclic aromatic molecular species[5].

Coexistence of diamond and graphitic phases and the transformation from one phase to the other have been studied with several theoretical methods. De Vita et al.[6] have explored the surface induced diamond-to-graphite transition with first-principles simulation. The electronic structure of diamond-graphite hybrids at the boundary of the two carbon phases has been investigated with a tight-binding model by Balaban *et al.*[7] Davidson and Pickett[8] have used a tight-binding model to simulate graphitization of bare and hydrogenated stepped diamond surfaces and to calculate corresponding electronic structures. A microscopic model of diamond nucleation by hydrogenation of the edges of graphitic precursors has been proposed by Lambrecht *et al.*,[9] where a many-body analytic potential was used for energy minimization.

Although coexistence of diamond and graphitic phases at grain boundaries in vapor deposited diamond films was proposed as long ago as 1989[3], possible structures and associated energetics for these interfaces have not been theoretically characterized. In this work we report structures and energies for two models of <001> tilt grain boundaries in diamond predicted using a many-body analytic bond-order potential function. The first model, which is based on similar grain boundaries in silicon and germanium, contains all four-fold coordinate atoms. The second model is a two-phase system in which a graphitic region connects the diamond grains. The underlying structure for this model, which is composed of graphitic sheets containing an in-plane grain boundary chemically-bonded to (111) planes of the diamond grains, was predicted from a simulation of the melting and recrystallization of an initially sp^3

Mat. Res. Soc. Symp. Proc. Vol. 442 © 1997 Materials Research Society

bonded grain boundary. At selected misorientation angles these calculations predict that the two-phase grain boundaries have energies lower than the all sp^3 bonded structures when the widths of the graphitic regions exceed 10-15Å.

GRAIN BOUNDARY STRUCTURES

The <001> symmetrical tilt grain boundaries with all four-fold coordinate carbon atoms were constructed from coincident site lattice models previously developed for silicon and germanium[10]. They are formed by rotation of two crystals around a common <001> axes at an angle θ with a median (110) plane. The resulting structures consist of an array of edge dislocations whose cores contain five- and seven-membered rings. In a [001] projection these rings correspond to either a straight (Figure 1(a)) or zig-zag (Figure 1(c)) arrangement of 3-5 structure units. The computational cell used in the calculations is periodic in the plane of the grain boundary with a hydrogen-terminated free surface perpendicular to the grain boundary plane.

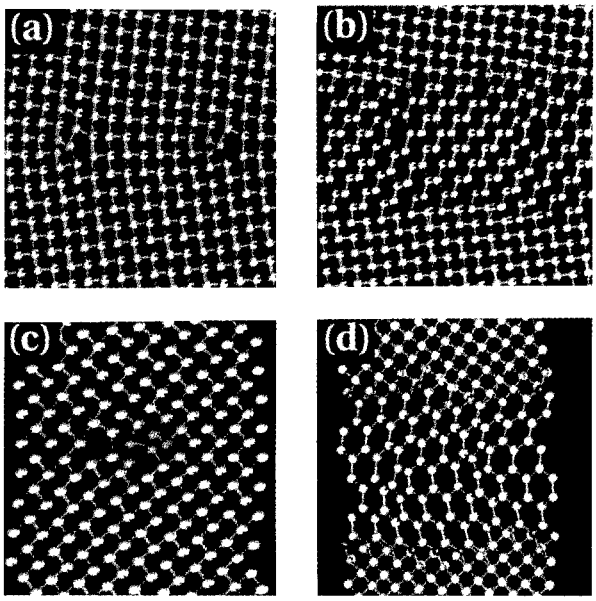


Figure 1: *Illustrations of the* [001] *projection of one and two-phase grain boundary models. (a)*$\sum$ = 41(450), θ = 12.68°. *(b) Resulting two-phase system constructed as described in the text. (c)*$\sum$ = 41(190), θ = 77.32° *(d) Two-phase system constructed from (c).*

Minimum energy structures were obtained using an empirical many-body bond-order interatomic potential.[11] This function is based on a second moment approximation to the electronic local density of states. It is composed of pair-additive short-range repulsive and attractive terms that model core-core repulsion and bonding due to valence electrons, respectively. The attractive terms are coupled to a many-body analytic bond order function which depends on local bonding topologies, bond angles and conjugation. The overall function reproduces a relatively large data base of solid-state and molecular properties, including the lattice constant, cohesive energy and elastic properties of bulk diamond and individual graphite sheets. Nonbonded interactions between graphite sheets are neglected in this model. Possible implications of this approximation are discussed below.

The underlying structure for the two-phase system was discovered via a molecular-dynamics simulation of the melting and quenching of an approximately 10Å region in the vicinity of an initially sp^3-bonded grain boundary. During the quench, in which the temperature of the melted region was continuously decreased from a maximum of 7000K to 2000K over 500 ps, the relative positions of atoms in the grain boundaries were held rigid while the crystalline grains as a whole were allowed to move according to the average forces on the grains. As the system was quenched a graphitic region formed consisting of defected graphite planes chemically bonded to the (111) planes of the diamond grains (Figures 1 and 2). The graphite sheets contain a defect composed of pairs of 5 and 7-membered rings (Figure 2, right) which produces a misorientation angle within the graphite sheets that accommodates the tilt angle between diamond grains. Because the defect appears as a pair of 5 and 7-membered rings, it does not introduce significant local curvature into the planes such as occurs in fullerenes.

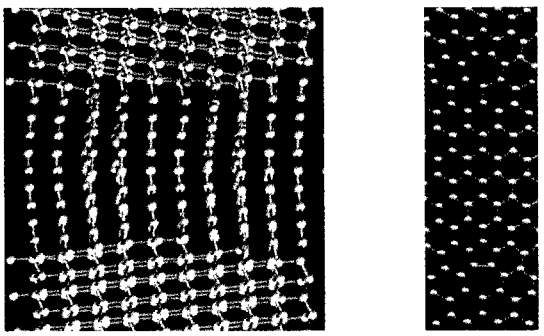


Figure 2: *Illustrations of the two-phase grain boundary model. Left: Rotated view showing graphitic planes connecting diamond grains. Right: Single graphitic plane at the grain boundary. The pairs of 5 and 7-membered rings at dislocation cores are at the top and bottom of the figure.*

The defected graphitic sheets within the grain boundary are essentially pairs of 'flattened' (111) planes in diamond. Thus another way to construct the diamond-graphite structures is to 'cut' bonds between every other (111) planes in the vicinity of the grain boundary starting with the coincident site structures discussed above. This procedure was used to generate the two-phase grain boundaries at the other tilt angles. With this relationship the origin of the 5 and 7-membered rings within the graphitic sheets is clear; they correspond to 'flattened' cores of the dislocations in the original sp^3-bonded structure. It should be noted that for angles θ>53.13° using this procedure to construct the mixed system from a straight arrangement of 3-5 structure units (cores of 45°-mixed dislocations) results in dangling bonds in the dislocation cores of the graphitic sheets. This is because of the screw component in the dislocation cores. Thus for θ>53.13° only grain boundaries with an initial zig-zag arrangement of structure units (cores of partial edge dislocations) can be used to construct the graphitic phase.

GRAIN BOUNDARY ENERGIES

Energies for the one and two-phase grain boundary models versus misorientation angle are shown in Figure 3. The widths of the graphitic regions perpendicular to the grain boundary planes are between 11 and 15 Å. At misorientation angles of 0° and 90° (graphite inclusions in perfect crystallites with <011> and <001> orientations respectively), the all sp^3 structures are more stable than those with the graphitic defects despite graphite being the energetically lower phase. This is due primarily to relatively weak binding at the graphite-diamond interface, where atoms with one graphite neighbor and two diamond neighbors have significantly lower binding energies compared to atoms in the two pure structures. In addition, there is a strain energy contribution arising from a lattice mismatch of approximately 2% between the graphitic sheets and the <111> projections of the diamond bond lengths. As the size of the graphitic inclusions increase, the lower energy of the graphitic phase will eventually dominate over destabilization at the diamond-graphite boundary and the system with graphitic inclusions will eventually become more stable than pure diamond.

At intermediate misorientation angles both the single and mixed phase models have higher energies and qualitatively similar energy trends involving cusps at 36.87° and 53.13° misorientation angles. At the cusps the single-phase model is more stable, but at other misorientation angles the two models become energetically competitive. This can be understood through detailed analysis of the energy contributions in each of the models. For the single-phase model the energy can be divided into two contributions, dislocation core energies and elastic strain energies. For the two-phase model there are four major contributions to the energy: energies from the dislocation cores within the graphitic sheets; elastic strain energies within the sheets from the cores plus the lattice mismatch between the graphitic sheets and the diamond bond length <111> projections; the energy difference between bulk graphite and diamond phases; and the relatively weak atomic binding energies at the boundary between the graphitic and diamond phases. As discussed above, the latter contribution significantly destabilizes the two-phase structure, while the elastic contributions from both models are nearly the same. However, the dislocation core energies within the

all sp^3-bonded model are much larger than those within the graphitic sheets. This is because maintaining four-fold coordination at the cores requires significant bond angle and length distortions, while the core structures in the graphitic sheets do not require large changes in bond angles and distances. Hence the larger core energy contributions in the single-phase model can roughly cancel the energy destabilization due the graphite-diamond interface, making both models energetically competitive at grain boundaries.

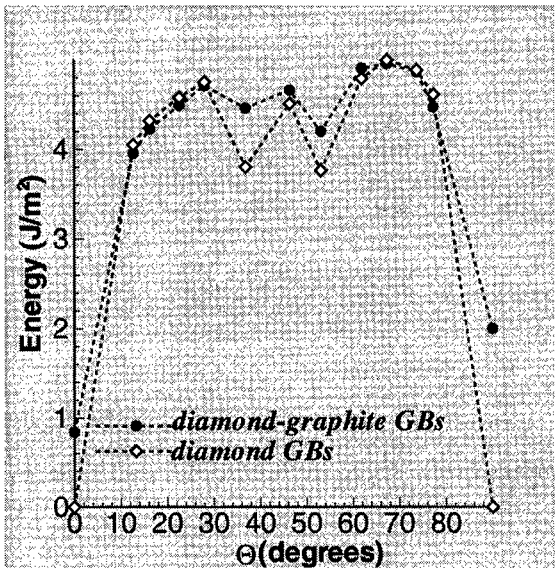


Figure 3: *Energy versus tilt angle for the two grain boundary models*

The distance between the graphite planes varies between about 2.1Å and 2.5Å depending on the tilt angle of the grain boundary. Because our bond-order potential model is short ranged (it has a cut-off at 2.0Å), the influence of interplanar distance on energy is neglected in the present calculations. We are currently examing these effects.

There are two important implications of these results for understanding the structure and properties of polycrystalline diamond films. First, as the size of graphitic inclusions in the bulk decreases, eventually the instability of the diamond-graphite interface makes bulk diamond energetically favorable. At grain boundaries, however, defects consisting of graphitic inclusions remain energetically competitive with

single-phase structures to very small defect sizes. Hence sp^2-bonded carbon in otherwise high-quality diamond films will likely remain at grain boundaries. Second, graphitic inclusions at grain boundaries will contain dislocations themselves. These dislocations combined with potential 'bowing' of the graphitic sheets to relieve strain may contribute to the broad background observed between two graphite peaks in Raman spectra of diamond films. Finally, because the one and two-phase structures are energetically competitive for small inclusions at grain boundaries, they may play a significant role in nucleating graphitization of diamond at high temperatures. Simulations of this and related dynamic phenomena such as strain-induced fracture are currently being carried out.

ACKNOWLEDGMENTS

This work is support by the Office of Naval Research through award N00014-95-1-0270.

REFERENCES

1. L. Abello and G. Lucazeau, Diam. Relat. Mater. **1**, p. 512 (1992).
2. Y. Sato and M. Kamo, in The Properties of Natural and Synthetic Diamond, edited by J.E.Field (Academic Press Limited, San Diego, 1992) p.423.
3. W. Zhu,C.A. Randall, A.R. Badzian and R. Messier, J. Vac. Sci. Technol. **A7**, p. 2315(1989).
4. P.J.Fallon and L.M.Brown, Diam. Relat. Mater. **2**, p. 1004 (1993).
5. D.S.Knight and W.B.White, J. Mater. Res. **4** p. 385 (1989).
6 A. De Vita, G. Galli,A. Canning and R. Car, Nature, **379**, p. 523 (1996).
7. A.T. Balaban, D.J. Klein, C.A. Folden, Chem. Phys. Lett. **217**, p. 266 (1994).
8. B.N. Davidson and W.E. Pickett, Phys. Rev. B **49**, p. 14770 (1994).
9. W.R. Lambrecht, C.H. Lee, B.Segall, J.C. Angus, Z. Li and M. Sunkara, Nature **364**, p. 607 (1993).
10. M. Kohyama, R. Yamamoto, Y. Ebata, M. Kinoshita, J. Phys. C **21**, p. 3205 (1988);J.L. Rouviere and A. Bourret, J. Physique **51**, C1-329 (1991). Energies and structures for similar four-fold coordinate structures modeling <011> tilt grain boundaries in diamond have been also been calculated (J. Narayan and A.S. Nandedkar, Phil. Mag. B **63**, p. 181 (1991)).
11. D.W.Brenner, Phys. Rev. B **42**, 9458(1990).

HYDROGEN-INDUCED LUMINESCENT STATES IN THE SUBSURFACE REGION OF HOMOEPITAXIAL DIAMOND FILMS

KAZUSHI HAYASHI [*,a], HIDEYUKI WATANABE [*,b], SADANORI YAMANAKA [*,c], TAKASHI SEKIGUCHI [**], HIDEYO OKUSHI [*], AND KOJI KAJIMURA [*,c]

[*] Electrotechnical Laboratory, 1-1-4, Umezono, Tsukuba, Ibaraki 305, Japan

[**] Institute for Materials Research, Tohoku University, 2-1-1, Katahira, Sendai 980-77, Japan

ABSTRACT

We found the existence of hydrogen-induced luminescent states in the subsurface region of chemical-vapor-deposited homoepitaxial diamond films by means of cathodoluminescence (CL). A specific broad peak at around 540 nm is observed in both as-deposited diamond films and those treated by hydrogen plasma at 800 °C, but not in conventional oxidized films. The accelerating voltage dependence of the CL spectra indicates that the luminescent states related to the 540 nm peak exist in the surface region and decrease abruptly with increasing the depth from the surface, showing that the depth distribution of the states slightly depends on the hydrogenation duration. Although the 540 nm peak is not observed in the films hydrogenated at 500 °C, it appears once the films are irradiated by an incident electron beam. It indicates the existence of a metastable configuration of hydrogen or its complex forms in the diamond films hydrogenated at low temperatures and a relaxation occurs into a stable one which produces luminescent states by the electron-beam irradiation.

INTRODUCTION

Diamond is considered to be a promising material for electronic devices which can operate at high temperatures and/or in chemically harsh environments. Detailed information about electronic properties induced by impurities or point defects is required for realizing the practical diamond devices.

Hydrogen, which is a common impurity for many semiconductors, is known to have a great influence on both electrical [1-7] and optical [8-10] properties of diamond. Owing to its hydrogen-rich growth environments, diamond films prepared by chemical vapor deposition (CVD) have high-conductivity layers near the surface, which can be removed by oxidation using acid solutions or oxygen-ambient annealing. At present, the electronic states in the surface region of the hydrogenated diamond films are not well understood and need to be clarified.

Cathodoluminescence (CL) is a powerful tool to obtain information about optical centers existing in the subsurface region by using a low-energy electron beam excitation. CL also has an advantage to obtain the depth distribution of gap states by changing the accelerating voltage. In this study, we investigated the CL spectra of the subsurface region of as-deposited homoepitaxial diamond films, which are

Mat. Res. Soc. Symp. Proc. Vol. 442 © 1997 Materials Research Society

compared with those of conventional oxidized diamond films. We also examined the CL spectra of hydrogenated diamond films which were treated in various hydrogenation conditions in order to clarify the effect of hydrogen on its electronic properties.

EXPERIMENT

Diamond films used in this study were deposited on synthetic Ib diamond (001) substrates ($4.0 \times 4.0 \times 0.3$ mm^3) with 0.5 % CH_4 diluted by H_2 gas [11]. The gas pressure, the total gas flow rate, and the microwave power were 25 Torr, 400 sccm, and 750 W, respectively. The growth duration was 6 h and the resultant film thickness was approximately 2 μm. The substrate temperature measured by a thermocouple attached to the backside of the susceptor was maintained at 800 °C. Therefore, actual surface temperature was slightly different from the measured one due to plasma radiation. After deposition, the films were cooled down in H_2 atmosphere in order to avoid the formation of nondiamond carbon layers on the surface. Further, the films were oxidized by acid solution of H_2SO_4 and HNO_3 at 200 °C for 15 min, followed by a thermal annealing at 400 °C for 30 min in N_2 atmosphere. After oxidation of the samples, they were again exposed to hydrogen plasma under various conditions listed in Table 1.

Table 1. Sample descriptions and hydrogenation conditions

Sample No.	Sample type	Treatments	Duration	Temperature
AS	as-deposited	-	(6 h)	(800 °C)
OX	oxidized	acid solution	15 min	200 °C
		+ N_2 annealing	+ 30 min	+ 400 °C
HP1	hydrogenated	plasma	10 sec	800 °C
HP2	hydrogenated	plasma	15 min	800 °C
HP3	hydrogenated	plasma	6 h	800 °C
HP4	hydrogenated	plasma	15 min	500 °C

The CL from the surface region was observed at room temperature using a quantitative electron-beam tester [12] with a CCD array detection system (Jobin Yvon, Spectra View-2D) . Typical CL spectrum obtained from diamond films used in this study is shown in Fig. 1. The spectrum was taken with an accelerating voltage of 10 kV. The peaks at both 533 nm [13] and 575 nm [14] are attributed to the nitrogen related centers, which were previously reported. In the present study, the accelerating voltage of the electron beam was varied between 1.5 and 5 kV, while the beam current was kept at approximately 1 nA. The electron range, which nearly corresponds to the depth of the probe from the surface, varied between approximately 30 and 280 nm according to Kanaya and Okayama's analysis [15].

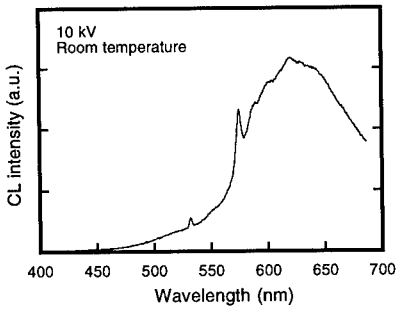


Fig. 1. Typical CL spectra obtained from diamond films used in this study.

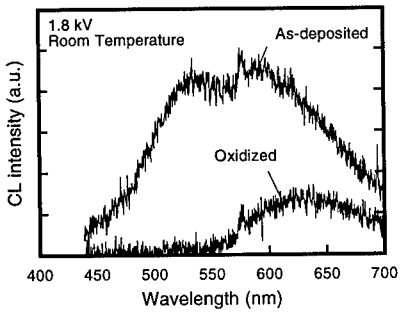


Fig. 2. CL spectra obtained from the near surface region of both as-deposited and oxidized diamond films.

RESULTS AND DISCUSSION

Figure 2 shows the CL spectra obtained from the near surface region of both as-deposited and oxidized films. They were taken at room temperature with an accelerating voltage of 1.8 kV, which corresponds to an electron range of about 50 nm. In addition to the features shown in Fig. 1, a broad peak at around 540 nm is observed in the as-deposited diamond films. On the other hand, the peak is not observed in the oxidized films, while the other features remain. The peak at 540 nm is close to the hydrogen related luminescence observed at 546 nm in hydrogen implanted diamonds reported by Gippius *et al* [8].

The accelerating voltage dependence of the CL spectra of the as-deposited films is shown in Fig. 3 (a). The intensities of all the peaks generally increase since generation of electron-hole pairs increases with the accelerating voltage. Although a similar structure is observed over the whole voltage range, the relative intensities of peaks between 540 and 575 nm are different. As the accelerating voltage, namely, the probing depth increases, the intensity of the peak at around 540 nm decreases relative to that at 575 nm. The CL spectrum at 5 kV is similar to that obtained at 10 kV (see Fig. 1). It means that the peak signal observed at around 540 nm was not detected in the deeper region of the as-deposited films. On the other hand, an apparent change in the CL spectra is not observed over the whole voltage range for the oxidized sample as shown in Fig. 3 (b).

Figure 4 shows the CL spectra obtained from the diamond films hydrogenated at 800 °C for (a) 10 sec, (b) 15 min, and (c) 6 h. They were taken with an accelerating voltage of 1.5 kV at room temperature. Although the relative intensities of the peaks at 540 nm to that at 575 nm are not the same, the broad peak at around 540 nm appears after hydrogenation of the oxidized diamond films even in the film of 10-sec hydrogenation. Contrary to the above mentioned results, the features observed in the films of 500 °C hydrogenation are quite different from those observed at 800 °C. As shown in Fig. 5, the peak at around 540 nm is not observed at first. However, it appears once the films are irradiated by the incident electron beam of 5 kV. This change indicates that low-temperature hydrogenation forms a metastable configuration of hydrogen related defects, which is different from that achieved at

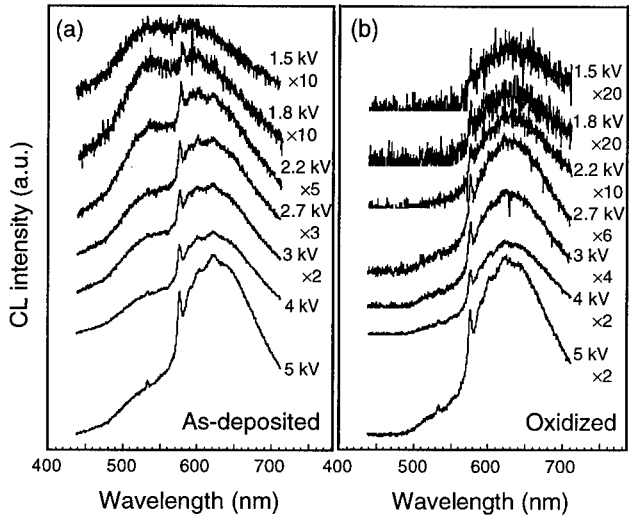


Fig. 3. Accelerating voltage dependence of the CL spectra obtained from (a) as-deposited and (b) oxidized diamond films.

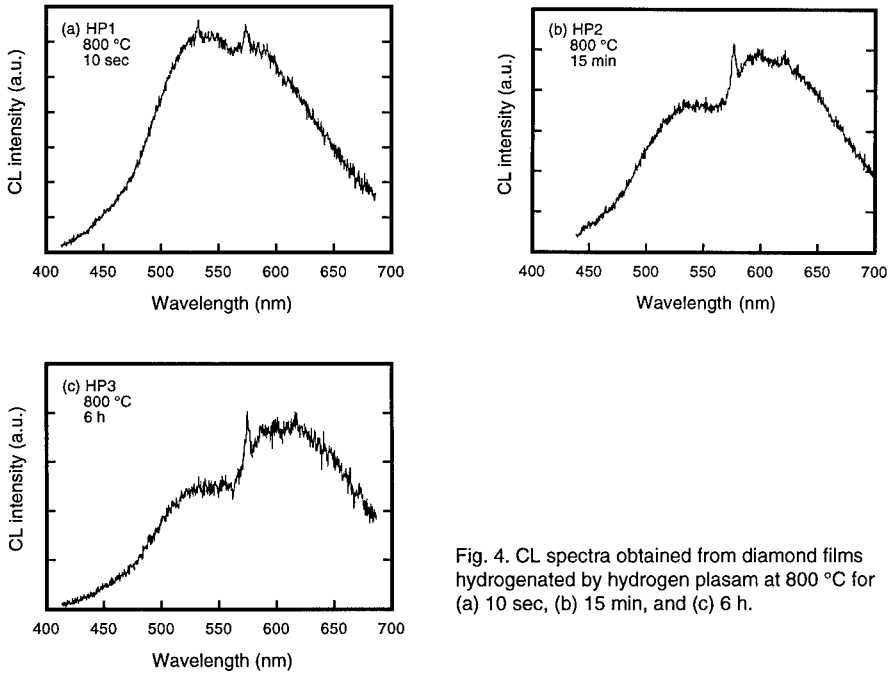


Fig. 4. CL spectra obtained from diamond films hydrogenated by hydrogen plasam at 800 °C for (a) 10 sec, (b) 15 min, and (c) 6 h.

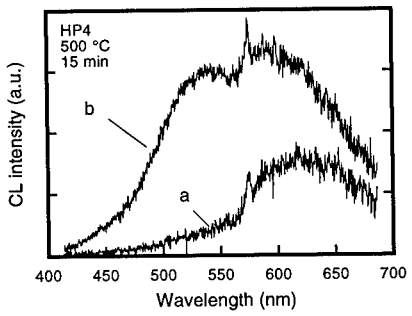


Fig. 5. CL spectra of diamond films hydrogenated at 500 °C (a) before and (b) after electron-beam irradiation.

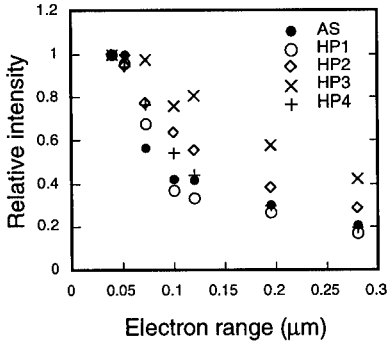


Fig. 6. Relative intensities of the peaks at 540 nm to that at 575 nm as a function of an electron range.

800 °C, and that it is relaxed by the electron-beam irradiation of as low as 5 kV into the stable configuration which produces the 540 nm-luminescent states.

The relative intensities of the peaks at 540 nm of all the hydrogenated diamond films to that at 575 nm as a function of an electron range are summarized in Fig. 6 (note: plots for HP4 stand for the intensities after electron-beam irradiation). The intensity of all the samples decreased rapidly with increasing the electron range and tends to saturate in the deeper region. In addition, the depth distribution of the gap states seems to slightly increases with the hydrogenation duration, as compared to HP 1-3. In other words, the depth distribution becomes broader as increasing the hydrogenation duration. This result leads to an conclusion that the gap states related to the peak at 540 nm exist spatially in the surface region. Using secondary ion mass spectroscopy (SIMS), we reported that high-concentration of hydrogen incorporated in the subsurface region of as-deposited CVD diamond films and that hydrogen concentration decreased rapidly with increasing the distance from the surface [5]. Therefore, we can conclude that the gap states related to the broad peak at 540 nm originate from hydrogen incorporated in the subsurface region. This conclusion is consistent with the fact that a longer hydrogenation duration leads to a deeper distribution of the gap states from the surface. The dominant factors for determining the depth distribution of the gap states is not clear at present. Detailed investigation is now in progress.

CONCLUSIONS

The electronic structure in the subsurface region of chemical-vapor-deposited homoepitaxial diamond films is found to be different from that in the bulk region. The hydrogen-induced luminescent states are observed in the hydrogenated diamond films inclusive of the as-deposited films. The accelerating voltage dependence of the CL spectra indicates that the luminescent states related to the 540 nm peak exist in the surface region and decrease abruptly with increasing the depth from the surface. The depth distribution of the states slightly depends on the

hydrogenation duration. In the case of hydrogenation at 500 °C, the peak is not observed, but it appears after the irradiation of the incident electron beam, suggesting that the possible configurations of hydrogen related defects in the subsurface region of diamond films are not unique and that the structural relaxation of the configurations from the metastable position into the stable one occurs by electron beam irradiation.

ACKNOWLEDGMENTS

The authors would like to acknowledge S. Hara, T. Shimizu, Y. Toyoshima, K. Arai, and P. L. Hacke for their useful discussion. Useful advice from K. Kobashi and Y. Yokota of Kobe Steel Ltd., is also gratefully acknowledged.

REFERENCES

[a] On leave from Kobe Steel Ltd., Electronics Research Laboratory, 1-5-5, Takatsukadai, Nishi-ku, Kobe 651-22, Japan.
[b] On leave from Tokai University, 1117, Kitakaname, Hiratsuka, Kanagawa 259-12, Japan.
[c] Also at Institute of Materials Science, University of Tsukuba, 1-1-1 Tennoudai, Tsukuba, Ibaraki 305, Japan.

1. M. I. Landstrass and K. V. Ravi. Appl. Phys. Lett. **55**, 1391 (1989).
2. T. Maki, S. Shikama, M. Komori, Y. Sakaguchi, K. Sakuta, and T. Kobayashi, Jpn. J. Appl. Phys. **31**, L1446 (1992).
3. Y. Mori, A. Hatta, T. Ito, and A. Hiraki, Jpn. J. Appl. Phys. **31**, L1718 (1992).
4. H. Kiyota, E. Matsushima, K. Sato, H. Okushi, T. Ando, M. Kamo, Y. Sato, M. Iida, Appl. Phys. Lett. **67**, 3596 (1995).
5. K. Hayashi, S. Yamanaka, H. Okushi, and K. Kajimura, Appl. Phys. Lett. **68**, 376 (1996).
6. J. Shirafuji and T. Sugino, Diamond and Related Materials **5**, 706 (1996).
7. H. Kawarada, H. Sasaki and A. Sato, Phys. Rev. B **52**, 11351 (1995).
8. A. A. Gippius, V. S. Vavilov, A. M. Zaitsev, and B. S. Zhakupbekov, Physica **116B**, 187 (1983).
9. X. Yang, A. V. Barnes, M. M. Albert, R. G. Albridge, J. T. McKinley, N. H. Tolk, and J. L. Davidson, J. Appl. Phys. **77**, 1758 (1995).
10. K. Hayashi, H. Watanabe, S. Yamanaka, H. Okushi, K. Kajimura, and T. Sekiguchi, Appl. Phys. Lett. **69**, 1122 (1996).
11. K. Hayashi, S. Yamanaka, H. Okushi, and K. Kajimura, Appl. Phys. Lett. **68**, 1220 (1996).
12. T. Sekiguchi and K. Sumino, Rev. Sci. Instrum. **66**, 4277 (1995).
13. V. S. Vavilov, A. A. Gippius, A. M. Zaitsev, B. V. Deryagin, B. V. Spitsyn, and A. E. Aleksenko, Sov. Phys. Semicond. **14**, 1078 (1980).
14. A. T. Collins, Diamond and Related Materials, **1**, 457 (1992).
15. K. Kanaya and S. Okayama, J. Phys. D **5**, 43 (1972).

AUTHOR INDEX

Abernathy, C.R., 387
Abrosimov, N.V., 43
Agarwal, A.M., 231
Ahn, S.H., 169
Akashi, Yoshito, 423, 459, 593
Akiba, Y., 681
Alavanja, C.M., 441
Aleksandrov, O.V., 237
Alex, V., 411
Alvarez, A., 429
Amekura, H., 287
Astafiev, O.V., 43
Auret, F.D., 51, 75, 87
Aziz, Michael J., 305

Balk, P., 143
Bayerl, M.W., 511
Beechinor, J.T., 51, 75
Benton, J.L., 231
Bharuth-Ram, K., 675
Bliss, D., 447
Boudreau, M., 667
Brandl, T., 511
Brandt, M.S., 511
Brenner, D.W., 693
Brown, S.W., 25
Bruk, L.I., 579
Bryant, G., 447
Buyanova, I.A., 355

Carter, C. Barry, 503
Castaldini, A., 605
Cavallini, A., 605
Chafai, M., 429
Chaldyshev, V.V., 491
Chalfoun, L.L., 169
Chen, W.M., 355
Chevallier, J., 523
Chisholm, M.F., 213
Chu, J.O., 325
Clement, M., 143
Cockayne, D.J.H., 367
Cohen, Dov, 503
Cook, M.J., 479
Corni, F., 293
Crean, G.M., 51, 75

Dalmer, M., 675
Danbata, M., 107
Dannefaer, S., 625
De Graef, M., 655
de Nijs, J.M.M., 143
Deenapanray, P.N.K., 51, 75, 87
Dokumaci, O., 151
Drechsler, M., 399
Druz, B.L., 687
Duan, X., 249
Dudley, M., 661

Elliman, R.G., 367
Emerson, D.T., 479
Emtsev, V.V., 243
Erickson, J.C., 611
Evans, M.J., 275

Faleev, N.N., 491
Fang, Z-Q., 405
Fernandez, P., 605
Fitz Gerald, J., 367
Fitzgerald, E.A., 343
Fraboni, B., 605
Friessnegg, T., 625, 667
Fujii, Katsumoto, 599
Fujimura, S., 269
Fujinami, M., 125
Fujioka, H., 485
Fujita, Shigeo, 561
Fujita, Shizuo, 561
Fukata, N., 269
Fukuyama, Atsuhiko, 423, 459, 593

Gammon, D., 25
Ganichev, S.D., 465
Gao, Huajian, 373
Geva, M., 441
Giles, N.C., 555
Gilmer, G.H., 231
Gislason, H.P., 453, 573
Glasko, J.M., 367
Gonzalez, M.A., 429
Goodhew, P.J., 473, 523
Goodman, S.A., 75
Goorsky, M.S., 343
Gorea, O.S., 579
Gornstein, M.G., 275
Gossmann, H-J., 151, 157
Gotoh, Hideki, 63
Gradinaru, G., 643
Gräf, D., 137
Greulich-Weber, S., 619
Grillot, P.N., 313
Gutkin, A.A., 497

Halliburton, L.E., 555
Haneda, H., 269
Harada, H., 125
Hardtdegen, H., 399
Hasebe, Masami, 113, 125
Hashimoto, K., 255
Hautojärvi, P., 567
Hayafuji, N., 517
Hayashi, Kazushi, 699
Hayes, A., 687
Helmi, M., 643
Herner, S.B., 157
Hieslmair, H., 261
Hioe, Yoshihiko, 599

Hiraiwa, Atsushi, 37
Hirata, M., 435
Hofmann, D.M., 399, 511
Hofsäss, H., 675
Hollfelder, M., 399
Horikawa, Mitsuhiro, 175, 181
Hu, X.W., 541

Iida, M., 681
Iino, T., 411
Ikari, Tetsuo, 423, 459, 593
Ikematsu, Y., 125
Imada, Kiyohisa, 593
Inaba, M., 31
Inoue, N., 131
Iseler, G., 447
Ishida, Hidetsugu, 37
Ishioka, K., 269
Ito, Akira, 205, 281
Itsumi, Manabu, 95
Iwamoto, T., 193
Iwasaki, Toshio, 113, 125
Iwata, Hiroyuki, 205, 281
Izumi, T., 681

Jablonski, J., 107
James, R.B., 611
Jimenez, J., 429
Jones, K.S., 151, 157

Kajimura, Koji, 699
Kalabukhova, E.N., 619
Kalejs, J.P., 261
Kalinushkin, V.P., 43
Kanbe, Hiroshi, 63
Kanemoto, Kei, 163
Kato, Masahiro, 119
Kawaguchi, Daisuke, 561
Kennedy, T.A., 25
Khlebnikov, Y., 643
Kikuchi, J., 269
Kim, S.J., 535
Kimerling, L.C., 169, 231, 249
Kirchner, R., 137
Kishimoto, N., 287
Kitagawara, Yutaka, 119
Kitajima, M., 269
Kitano, Tomohisa, 175, 181
Klockenbrink, R., 485
Koizuka, M., 31
Kono, K., 287
Korony, G., 643
Korotkov, V.A., 579
Kovalev, L.E., 579
Kringhøj, P., 367
Krishnamoorthy, V., 157
Kunitsyn, A.E., 491
Kurosu, T., 681

Laine, T., 567
Larkin, J., 447
Lavine, James P., 187
Law, M.E., 151
Lee, Sanboh, 199
Leigh, W.B., 447
Leosson, K., 453
Liang, Junwu, 349
Look, D.C., 405
Lukin, S.N., 619
Luysberg, M., 485

MacPherson, G., 473
Maeda, Kouji, 423, 459, 593
Magerle, R., 3
Mahony, J., 547
Maiti, A., 213
Makihara, K., 193
Malherbe, J.B., 87
Malikova, L.V., 579
Mallee, R., 143
März, M., 619
Mascher, P., 547, 667
Masterson, H.J., 51, 75
Matsumoto, S., 81
Matsuoka, F., 681
McColgin, William C., 187
Mchedlidze, T., 381
McHugo, S.A., 261
Mera, T., 107
Meyer, B.K., 399, 511
Meyer, W.E., 51, 75, 87
Michel, J., 249
Mitchel, W.C., 643
Mitha, Salman, 305
Mizokawa, Y., 131
Mizuta, M., 511
Mochizuki, Y., 511
Mogi, T.K., 157
Moldovan, M., 555
Monemar, B., 355
Moon, Y.B., 535
Mooney, P.M., 325
Morita, S., 15
Morooka, Y., 423, 459
Morse, M., 249
Murakami, K., 269
Murtagh, M., 51, 75
Myburg, G., 51, 75, 87
Myers, T.H., 555

Nagai, K., 107
Nagata, Tsuyoshi, 175
Nakada, Akira, 163
Nakai, Katsuhiko, 113
Nakamura, K.G., 269
Nakanishi, H., 69
Nakashima, H., 169
Natarajan, M., 611
Nix, William D., 373
Nordhoff, H., 51

Ogata, Ken-ichi, 561
Ohishi, Masakazu, 599
Ohmi, Tadahiro, 163, 193

Ohno, Takahisa, 529
Ohno, Y., 435
Ohta, M., 15
Ohura, Mitsuhiro, 599
Oila, J., 567
Oka, Mauricio Massazumi, 163
Okamoto, M., 255
Okumura, Tsugunori, 417
Okushi, Hideyo, 699
Ostan, E., 687
Otsubo, M., 517
Ottaviani, G., 293
Overhof, Harald, 637
Ozkan, Cengiz S., 373

Palm, J., 249
Paloura, E.C., 523
Pantelides, S.T., 213
Pearton, S.J., 387
Peng, Zhi Gang, 561
Pennycook, S.J., 213
Pessa, M., 567
Petkos, G., 523
Pinzone, C.J., 441
Piontek, H., 137
Piqueras, J., 605
Pirouz, P., 631
Pivac, B., 293
Platero, M., 169
Poloskin, D.S., 243
Polyakov, V.I., 687
Powell, J.A., 631
Prasad, A., 485
Preobrazhenskii, V.V., 491
Prettl, W., 465
Puff, W., 667
Putyato, M.A., 491

Qian, W., 655
Quintel, H., 675

Raab, W., 465
Rakennus, K., 567
Rakvin, B., 293
Reinacher, N.M., 511
Reshchikov, M.A., 497
Restle, M., 675
Ri, S., 681
Ridgway, M.C., 87
Ringel, S.A., 313
Romanato, F., 343
Ronning, C., 675
Rosenblum, M.D., 261
Rossukanyi, N.M., 687
Rukovishnikov, A.I., 687

Saarinen, K., 567
Saito, Hiroshi, 599
Saito, T., 287
Saitoh, Tadashi, 63
Salokatve, A., 567
Samavedam, Srikanth, 343
Sanchez, E.K., 655
Sasaki, S., 269
Sasaki, Taizo, 529
Sato, K., 517
Schiferl, David, 305
Schmolke, R., 137
Schut, H., 143
Schutte, C., 87
Sedov, V.E., 497
Seghier, D., 573
Sekiguchi, Takashi, 699
Semyagin, B.R., 491
Setzler, S.D., 555
Shealy, J.R., 479
Shek, E.I., 237, 243
Shenderova, O., 693
Shibata, Tadashi, 163
Shigematsu, T., 15
Shimizu, T., 81
Shinagawa, Tatsuyuki, 417
Shinozuka, Yuzo, 225
Show, Y., 681
Shum, Kai, 325
Si, S.K., 535
Simashkevich, A.V., 579
Simpson, P.J., 667
Skog, K., 567
Skowronski, M., 655
Smith, A.L., 169
Sobolev, N.A., 237, 243
Sogawa, Tetsuomi, 63
Sohn, H., 485
Spaeth, J-M., 619
Specht, P., 485
Sputz, S.K., 441
Stancampiano, Charles V., 187
Stavola, Michael, 275, 387
Steude, G., 399
Stotski, Yuri A., 649
Stutzmann, M., 511
Sudarshan, T.S., 643
Sugawara, Y., 15
Suhren, M., 137
Suvorov, Alexander V., 649
Suzuki, M., 15
Sveinbjörnsson, Einar Ö., 331

Taguchi, Akihito, 529
Takano, J., 193
Takayanagi, K., 255
Takeda, Kazuo, 37
Takeda, S., 435
Takeno, Hiroshi, 119
Takeuchi, J., 81
Tamai, Yukio, 163
Tanahashi, K., 131
Tanaka, K., 125
Teremetskaya, I.G., 687
Theys, B., 523
Tokuda, Yutaka, 205, 281
Tonini, R., 293
Tretyakov, V.V., 491

Tsumori, Yasuo, 113

Uchihashi, T., 15
Ueyama, H., 15
Usov, Igor O., 649
Uusimaa, P., 567

Valdna, V., 585
van Veen, A., 143
Varnin, V.P., 687
Vetter, W.M., 661

Wada, K., 69, 81
Wagner, P., 137
Wan, Xueyuan, 349
Wang, Q.M., 541
Wang, X.J., 541
Wankerl, A., 479
Watanabe, Hideyuki, 699
Watanabe, M., 107
Weber, E.R., 261, 485
Weber, Jörg, 331, 411
Wijaranakula, W., 299
Wimbauer, T., 511
Wolk, J., 447

Xiao, Z.B., 541

Yamada-Kaneta, H., 31
Yamamoto, Y., 517
Yamanaka, Sadanori, 699
Yanase, Y., 15
Yao, H., 611
Yaoita, Akihiko, 175
Yassievich, I.N., 465
Ye, Shu-Ren, 51, 75
Yonenaga, I., 337, 381
Yoneta, Minoru, 599
Yoon, E., 535
Yoshino, Kenji, 423, 459, 593
Yu, Z., 555

Zaitsu, Y., 81
Zepezauer, E., 465
Zhang, Tong-Yi, 199
Zhang, Xin, 199
Zhang, Z.P., 541
Zhao, S., 169, 231
Zhao, Yuechao, 305
Zheng, B., 249
Zheng, J-F., 387
Zheng, L.X., 541
Zhou, L., 631
Zohar, Yitshak, 199
Zou, J., 367

SUBJECT INDEX

ab initio method, 637
activation energy, 299
actuator level, 429
AFM, 75, 137, 611
  noncontact, 15
alignment, growth induced, 387
annealing, 175, 205, 237, 243, 547, 625, 667
  reverse bias, 81
antiphase boundaries, 503
antisite, 3
  arsenic, 417
arsenic activation, 151

band-to-band transition, 331
boron cluster, 255
breakdown B-mode, 107
bulk alloy, 337

capacitance transient spectroscopy, 605
carbon acceptor, 423, 459, 479
carrier transport, 381
  concentration profiles, 205
C_{As}, 387
cathodoluminescence (CL), 605, 699
charge-coupled devices, 187
chemical
  beam epitaxy (CBE), 523
  identification, 3
chlorine, 529
cluster calculation, 255
compensation, 535, 567
complex(es), 497, 585
  C_{As}-H, 387
  gold-hydrogen, 275
copper, 453, 585
critical thickness, 473, 541
crystal-originated particles (COP), 107
CV, 75
CVD, 681

damage, 367
  subsurface, 199
DAP distant, 535
dark current spectroscopy (DCS), 187
deep
  center, 405
  level, 313, 605, 649
  trap, 523
defect(s)
  grown-in, 31
  morphology, 137
  nonradiative, 355
  reaction, 225
  structural, 261
degradation, 225
depth profile, 163
desorption, 667

diffusion, 299, 435, 529
  length of minority carriers, 181
diodes, Schottky barrier, 51, 87
dislocation(s), 313, 367, 523
  center, 331
  core, 213
  loop, 125, 157, 249
  structure, 343
  superscrew, 661
  threading, 325, 473
  velocity, 337
dissociation, 81
divacancy, 547
D-lines, 325, 331
DLTS, 51, 75, 87, 169, 181, 281, 287, 573, 649, 687
donor-acceptor pair (DAP), 593
doping, isovalent impurity, 491

EBIC, 169
EDMR, 511
EL2, 411, 417, 423, 429, 459
EL6, 459
electrical
  conduction, 681
  parameter, 237
  properties, 485
electrochemical reaction, 517
electroluminescence, 331
electron
  irradiation, 625
  traps, 281
electronic properties, 699
ENDOR, 619
energy calculations, 693
enhanced generation rate, 299
epitaxial layer, 31
epitaxy
  hetero, 373
  homo, 699
EPR, 293, 555, 681
  photo, 579
erbium, 237, 243, 249
  related donor centers, 237
etching
  chemical, 199
  dry, 63
  RF sputter, 87
excited state, 465

Fe, 181
first-principle
  calculations, 529
  local density functions approach, 255
flow-pattern defects (FPD), 119
fluorine, 517, 529
flux ratio, As/Ga, 485

FP-SEP, 125
Frank-Read, 473

gateoxide, 95, 107
  integrity, 113
gettering, 175, 181, 261
grain boundaries, 213, 693
grown-in defects (GOI), 113, 119, 131

Hall effect measurements, 243, 381, 447, 547
heterojunction, 573
heterostructures, 313, 511
hole
  photoionization, 423
  saturation, 535
HRTEM, 249, 373
hydrogen, 293, 447, 453, 667, 699
  molecules, 269
  passivation, 479
  plasma, 699
  profile, 205
  related donor, 205
  thermal equilibrium concentration, 299
hydrogenation, 417

imaging, 643
  atomic resolution, 15
implantation, 163, 237, 249, 649, 675
  H^+, 281, 293
  high temperature, 649
  induced damage, 205
  P^+, 281
in situ, 287
interaction chemical bonding, 15
interface, 541
  SiO_2/Si, 143
interstitial, 435, 637
  defects, 281
  oxygen, 299
  pair, 435
ion irradiation, 367
IR absorption, 31, 447
iron-boron pairs, 169, 187
isotope(s)
  radioactive, 3
  shift, 269

Jahn-Teller, 497

laser scattering tomography (LSTD), 119
lattice site, 675
leakage current, 163, 175
lifetime, 169
  contrast, 43, 169
light
  illumination, 69
  scattering, 31, 137
lithium, 453
  array, 599
low-temperature growth, 355, 479, 485, 491

MBE, 355, 555, 573, 599
mechanical strength, 337
metal impurities, 175, 261
metastable, 51, 417, 429
micro(-)
  defects, 687
  Raman spectroscopy, 199
micropipes, 643, 661
  electrical effects, 643
  light emission, 643
microscopic structure, 619
MOCVD, 441
monovacancy, 547
morphological evolution, 373
MOS
  devices, 193
  LSI, 95
  systems, 143
MOVPE, 399

nitridation, 157
nitrogen, 619, 573
NMR, 25
nondestructive characterization, 611
nonradiative, 331

octahedron, 95
ODMR, 355
OMVPE, 479
optical
  pumping, 25
  shallow defect analyzer (OSDA), 31
optically detected cyclotron resonance (ODCR), 399
Overhauser shift, 25
oxidation-induced stacking fault (OSF), 131
oxygen
  concentration, 31
  enhanced diffusion, 299
  precipitation, 31, 131
    profiler, 113

passivation, 453, 529
phonon kick, 225
phosphorous defect complexes, 81
photocurrent
  flash phenomenon, 579
  relaxation spectra, 579
photoinduced interaction, 405
photoluminescence, 3, 63, 497, 535, 555, 593
  dislocation related, 325
photoquenching, 429, 459
photoreflectance, 63, 75
photorefractive, 447
photoresponse, 579
piezoelectric photoacoustic, 423, 459

planar faults, 503
plasma(-)
  induced defects, 81
  irradiation, 69
  processing, 51, 87
point defect clusters, 163
point trapping centers, 687
polyhedral, 107
  cavities, 131
polysilicon, 143
positron, 143, 567
  beam, 667
  lifetime, 547, 625
precipitates, 249
  oxygen, 125
proton irradiation, 287
PV materials, 43

quantum
  well, 511, 541
  dot, 25
quenching, 169

radiation damage, 287
radiative efficiency, 355
Raman spectrum, 269
recombination, 43, 331
  enhanced, 225
  nonradiative, 423
reliability, 193
remote treatment, 269
reorientation, 497
resonant excitation, 497
reverse bias annealing, 69
RHEED, 599
RIE, 63, 75

segregation, 175, 213, 541
selenium vacancy, 555
semi-insulating, 405, 411, 429
shallow donor, 465, 619
  centers, 243
Si(111)7x7, 15
Si surface, 31
SiC:H, 667
SiGe
  Czochralski grown, 337
  graded layer, 343
silicon
  heavily doped, 31
  multicrystalline, 261
size distribution, 137
solubility, 169
strain(ed), 541
  layer, 373
    heterostructures, 367
  relaxation, 313
  relief, 367
stress, bias-temperature, 517
stretching vibration hydrogen, 275
structural instability, 225
sublimation method, 593
substitutional defects, 637
supersaturation vacancy, 157
surface
  aging, 611
  InP, 15
  microroughness, 193
synchrotron, 261

tellurium interstitial, 585
TEM, 119, 125, 249, 435, 503, 523, 631
thermal donor, 299
thin film, 631
transition metal, 275
  hydrogenated, 275
  metal impurities, 637
transport properties, 399
trapping centers, 687
thermally stimulated current spectroscopy (TSC), 405

upconversion, 411, 465

vacancy, 157, 567, 625
  defects, 281
  injection, 151
variable angle spectroscopic ellipsometry, 75, 611
vibrational
  spectroscopy, 275
  spectrum, 387, 535
void defects, 95, 119, 125

X-ray
  fluorescence, 261
  reciprocal space map, 343
  topography, 661

zero field micropipe map, 643
zinc
  diffusion, 441
  vacancy, 593